

PHOTOGRAPH THIS SHEET

DTIC FILE COPY

INVENTORY

AD-A217 804

DTIC ACCESSION NUMBER

LEVEL

AFOSR TR 90 0113

DOCUMENT IDENTIFICATION

2 DEC 1988

DISTRIBUTION STATEMENT A

Approved for public release;
Distribution Unlimited

DISTRIBUTION STATEMENT

ACCESSION FOR

NTIS GRA&I ☒

DTIC TAB ☐

UNANNOUNCED ☐

JUSTIFICATION

BY

DISTRIBUTION /

AVAILABILITY CODES

DIST

AVAIL AND/OR SPECIAL

A-1 21

DISTRIBUTION STAMP PRICE-\$49.00

Materials Research Society
9800 McKnight Rd.
Pittsburgh, PA 15237

DTIC
ELECTE
FEB 09 1990
S E D

DATE ACCESSIONED

DATE RETURNED

REGISTERED OR CERTIFIED NO.

DATE RECEIVED IN DTIC

90 02 06 282

PHOTOGRAPH THIS SHEET AND RETURN TO DTIC-FDAC

DOCUMENT PROCESSING SHEET

PREVIOUS EDITION MAY BE
STILL BEING USED

AD-A217 804

VOLUME 129

Laser- and Particle-Beam Chemical Processes on Surfaces

EDITORS

A. Wayne Johnson

Gary L. Loper

T.W. Sigmon

90 02 06 282



REPORT DOCUMENTATION PAGE

Form Approved
OMB No. 0704-0188

Public reporting burden for this collection of information is estimated to average 1 hour per response, including the time for reviewing instructions, searching existing data sources, gathering and maintaining the data needed, and completing and reviewing the collection of information. Send comments regarding this burden estimate or any other aspect of this collection of information, including suggestions for reducing this burden, to Washington Headquarters Services, Directorate for Information Operations and Reports, 1215 Jefferson Davis Highway, Suite 1204, Arlington, VA 22202-4302, and to the Office of Management and Budget, Paperwork Reduction Project (0704-0188), Washington, DC 20503.

1. AGENCY USE ONLY (Leave blank) 2. REPORT DATE 26 Dec 1989 3. REPORT TYPE AND DATES COVERED Final Report/15 Nov 88-14 May 90

4. TITLE AND SUBTITLE
Materials Research Society Symposia

5. FUNDING NUMBERS

6. AUTHOR(S)

61102F/2301/A1
61102F/2306/B1

John Ballance

7. PERFORMING ORGANIZATION NAME(S) AND ADDRESS(ES)

Materials Research Society
9800 McNight Road, Suite 327
Pittsburgh, PA 15237

AFOSR-TR- 90-0118

8. PERFORMING ORGANIZATION
REPORT NUMBER

9. SPONSORING/MONITORING AGENCY NAME(S) AND ADDRESS(ES)

AFOSR/NP
Bolling AFB DC 20332-6448

10. SPONSORING/MONITORING
AGENCY REPORT NUMBER

AFOSR-89-0142

11. SUPPLEMENTARY NOTES

12a. DISTRIBUTION/AVAILABILITY STATEMENT

Approved for public release; distribution is available from:
Materials Research Society, 9800 McNight Rd, Publications
Department, Pittsburgh, PA 15237

12b. DISTRIBUTION CODE

13. ABSTRACT (Maximum 200 words)

The Materials Research Society held their symposium "Laser & Particle-Beam
Chemical Processes on Surfaces" in Boston, Massachusetts on November 28 -
December 3, 1988

14. SUBJECT TERMS

15. NUMBER OF PAGES

640

16. PRICE CODE

17. SECURITY CLASSIFICATION
OF REPORT

18. SECURITY CLASSIFICATION
OF THIS PAGE

19. SECURITY CLASSIFICATION
OF ABSTRACT

20. LIMITATION OF ABSTRACT

UNCLASSIFIED

UNCLASSIFIED

UNCLASSIFIED

UL
CAP

Laser- and Particle-Beam Chemical Processes on Surfaces

Symposium held November 29-December 2, 1988, Boston, Massachusetts, U.S.A.

EDITORS:

A. Wayne Johnson

Sandia National Laboratories, Albuquerque, New Mexico, U.S.A.

Gary L. Loper

The Aerospace Corporation, Los Angeles, California, U.S.A.

T. W. Sigmon

Stanford University, Stanford, California, U.S.A.



MATERIALS RESEARCH SOCIETY
Pittsburgh, Pennsylvania

This work was supported by the Air Force Office of Scientific Research, Air Force Systems Command, USAF, under Grant Number AFOSR 89-0142.

CODEN: MRSPDH

Copyright 1989 by Materials Research Society.
All rights reserved.

This book has been registered with Copyright Clearance Center, Inc. For further information, please contact the Copyright Clearance Center, Salem, Massachusetts.

Published by:

Materials Research Society
9800 McKnight Road
Pittsburgh, Pennsylvania 15237
Telephone (412) 367-3003

Library of Congress Cataloging in Publication Data

Laser- and particle-beam chemical processes on surfaces : symposium held November 29- December 2, 1988, Boston, Massachusetts, U.S.A. : editors, A. Wayne Johnson, Gary L. Loper, T.W. Sigmon.

p. cm. — (Materials Research Society symposium proceedings : ISSN 0272-9172 ; v. 129)

Includes bibliographical references.

ISBN 1-55899-002-X

1. Materials—Effect of radiation on—Congresses. 2. Surface chemistry—Congresses. 3. Laser beams—Industrial applications—Congresses. 4. Particle beams—Industrial applications—Congresses. I. Johnson, A. Wayne. II. Loper, Gary L. III. Sigmon, T. W. IV. Materials Research Society. V. Series: Materials Research Society symposium proceedings : v. 129.

TA418.6.L36 1989
620'.44—dc20

89-27866
CIP

Manufactured in the United States of America

Contents

PREFACE	xiii
ACKNOWLEDGMENTS	xv
MATERIALS RESEARCH SOCIETY SYMPOSIUM PROCEEDINGS	xvi
PART I: OVERVIEW OF LASER- AND BEAM-INDUCED SURFACE PROCESSES	
*SOME RECENT RESULTS OF FUNDAMENTAL STUDIES OF BEAM-INDUCED SURFACE PROCESSES J. Dieleman	3
*ION BEAM PROCESSING OF OPTICAL MATERIALS F.L. Williams, L.L. Boyer, D.W. Reicher, J.J. McNally, G.A. Al-Jumaily, and J.R. McNeil	17
*ATOMIC-SCALE MODELING OF LOW-ENERGY ION-SOLID PROCESSES B.W. Dodson	29
PART II: LASER-INDUCED DEPOSITION OF METAL FILMS	
*THE SPECTROSCOPY AND SURFACE CHEMISTRY OF METAL-ALKYL MOLECULES P. Shaw, J. O'Neill, E. Sanchez, Z. Wu, and R.M. Osgood, Jr.	45
THERMAL AND PHOTOLYTIC DECOMPOSITION OF ADSORBED CADMIUM AND TELLURIUM ALKYL C.D. Stinespring and A. Freedman	57
ArF LASER-INDUCED CHEMICAL-VAPOR DEPOSITION OF TUNGSTEN FOR GATE ELECTRODES H. Matsushashi, S. Nishikawa, and S. Ohno	63
MECHANISTIC STUDY OF LASER CHEMICAL VAPOR DEPOSITION OF TRIMETHYLINDIUM M. Kawasaki, K. Kasatani, A. Sato, H. Sato, and N. Nishi	69
PHOTOCHEMICAL VAPOR DEPOSITION OF ALUMINUM THIN FILMS M. Hanabusa, A. Oikawa, P.Y. Cai, S. Furuno, and S. Iguchi	73
TUNABLE UV LASER PHOTOLYSIS OF ORGANOMETALLIC COMPOUNDS WITH PRODUCT DETECTION BY LASER MASS SPECTROSCOPY Th. Beuermann and M. Stuke	79
LICVD OF Cr(C,O) FILMS FROM Cr(CO) ₆ AT 248 NM: GAS-PHASE AND SURFACE PROCESSES R. Nowak, L. Konstantinov, and P. Hess	85

*Invited Paper

LIF-DIAGNOSTICS OF Cr DURING LASER-INDUCED DEPOSITION FROM Cr(CO) ₆ D. Rieger, B. Rager, and F. Bachmann	91
FINE METAL PARTICLE FORMATION FROM ORGANOMETALLIC COMPOUNDS BY LASER IGNITED MILD EXPLOSIVE REACTION N. Shimo and K. Yoshihara	99
PART III: LASER-INDUCED WRITING OF METAL LINES	
*MODELING OF PYROLYTIC LASER DIRECT-WRITING FROM THIN METALORGANIC FILMS P.E. Price, Jr. and K.F. Jensen	107
LASER-INDUCED CHEMICAL VAPOR DEPOSITION OF HIGH PURITY ALUMINUM T.H. Baum, C.E. Larson, and R.L. Jackson	119
STUDIES OF LASER-INDUCED SURFACE REACTIONS BY SURFACE TEMPERATURE MODULATION TECHNIQUES P.B. Comita, D.R. Strongin, and T.T. Kotas	125
LASER DEPOSITION OF GOLD J.A. Sell, M.S. Meyer, and G.P. Meisner	133
LASER CLADDING WITH A Ni-Fe-Cr-Al ALLOY K.M. Jasim and D.R.F. West	139
PART IV: LASER-INDUCED DEPOSITION OF SEMICONDUCTORS	
*SELECTED AREA GROWTH OF GaAs BY LASER INDUCED PYROLYSIS OF ADSORBED Ga-ALKYLS V.M. Donnelly, J.A. McCaulley, V.R. McCrary, and C.W. Tu	147
LASER INDUCED DECOMPOSITION OF TRIETHYLGALLIUM AND TRIMETHYLGALLIUM ADSORBED ON GaAs(100) J.A. McCaulley, V.R. McCrary, and V.M. Donnelly	159
LATTICE DISTORTION INDUCED BY LASER ASSISTED MOCVD OF GaAs S.A. Hussien, N.H. Karam, S.M. Bedair, A.A. Fahmy, and N.A. El-Masry	165
PATTERNED CRYSTAL GROWTH OF GaAs BY LASER ASSISTED ATOMIC LAYER EPITAXY S. Iwai, T. Meguro, Y. Aoyagi, and S. Namba	171
ARGON ION AND EXCIMER LASER INDUCED EPITAXY OF GaP U. Sudarsan, N.W. Cody, T. Dosluoglu, and R. Solanki	177
LASER PATTERNING OF II-VI EPITAXIAL THIN FILMS S.J.C. Irvine, H. Hill, J.E. Hails, G.W. Blackmore, and J.B. Mullin	183
GROWTH MECHANISM OF DIRECT WRITING OF SILICON IN Ar ⁺ LASER CVD T. Nagahori and S. Matsumoto	189
*Invited Paper	

A COMPARISON OF THE GAS PHASE PROCESSES RESULTING FROM SiH ₄ and Si ₂ H ₆ PHOTODISSOCIATION WITH A PULSED ArF EXCIMER LASER	195
E. Boch, C. Fuchs, E. Fogarassy, and P. Siffert	
LASER PHOTOCHEMICAL VAPOUR DEPOSITION OF EPITAXIAL Ge FILMS ON GaAs FROM GeH ₄ USING NH ₃ AS A SENSITISER	201
C.J. Kiely, C. Jones, V. Tavitian, and J.G. Eden	
LASER-INDUCED CHEMICAL VAPOR DEPOSITION OF Ge-Se THIN FILMS	207
T.D. Xiao and P.R. Strutt	
SYNTHESIS OF DIAMOND FILMS BY LASER-INDUCED CHEMICAL VAPOR DEPOSITION	213
Y. Goto, T. Yagi, and H. Nagai	
LOW TEMPERATURE DEPOSITION OF HARD, AMORPHOUS DIAMOND- LIKE FILMS BY LASER EVAPORATION	219
J. Krishnaswamy, A. Rengan, A. Srivatsa, J. Narayan, Y. Cong, R. Collins, and K. Vedam	
PART V: LAMP-INDUCED CHEMICAL VAPOR DEPOSITION	
WINDOWLESS WIDE AREA VUV LAMP FOR ENERGY ASSISTED CVD	227
Z. Yu, T.Y. Sheng, H. Zarnani and G.J. Collins	
LOW TEMPERATURE EPITAXY OF Hg _{1-x} Cd _x Te	233
N.W. Cody, U. Sudarsan, and R. Solanki	
LOW TEMPERATURE OMVPE OF ZnSe FROM ALKYL SOURCES USING A PLASMA DISK LAMP	239
K.L. Tokuda, B. Pihlstrom, D.W. Kisker, M.L. Schnoes, and G.J. Collins	
PHOTOREACTIONS OF Mo(CO) ₆ ON POTASSIUM PRECOVERED SILICON SURFACE WITH UV TO IR RADIATION	245
Z.C. Ying and W. Ho	
Al PHOTODEPOSITION AND LIGHT-INDUCED NUCLEATION ON p-TYPE Si FROM TMA	251
J.E. Bouree, J. Flicstein, J.F. Bresse, J.F. Rammelueere, and A.M. Pougnet	
UV ENHANCEMENT OF SURFACE CATALYTIC POLYMERIZATION OF ETHYLENE	259
P.V. Purohit, M. Rothschild, and D.J. Ehrlich	
PART VI: LASER-INDUCED CHEMICAL ETCHING	
*SELECTIVE PHOTOCHEMICAL DRY ETCHING OF COMPOUND SEMICONDUCTORS: ENHANCED CONTROL THROUGH SECONDARY ELECTRONIC PROPERTIES	269
C.I.H. Ashby	
PHOTOGENERATED CARRIER CONFINEMENT DURING THE LASER- CONTROLLED AQUEOUS ETCHING OF GaAs/AlGaAs MULTILAYERS	279
M.N. Ruberto, A.E. Willner, D.V. Podlesnik, and R.M. Osgood, Jr.	
*Invited Paper	

HIGH RESOLUTION DIRECT-WRITE PHOTOCHEMICAL ETCHING OF InP USING METHYL IODIDE K. Durose, J.P.L. Summersgill, M.R. Aylett, and J. Haigh	285
LASER-INDUCED ATOMIC CHLORINE ETCHING OF SILICON G.V. Treyz, R. Scarmozzino, H.H. Burke, and R.M. Osgood, Jr.	291
ANGLE RESOLVED TIME-OF-FLIGHT MEASUREMENTS OF THE EXCIMER LASER INDUCED ETCHING OF SILICON IN A CHLORINE ENVIRONMENT T.S. Baller, J. van Zwol, S.T. de Zwart, G.N.A. van Veen, H. Feil, and J. Dieleman	299
PHOTODISSOCIATION OF CHLORINE ON A COOLED SILICON WAFER M. Kawasaki, H. Sato, and N. Nishi	305
REACTIONS OF PHOTOGENERATED CF ₂ AND CF ₃ ON SILICON AND SILICON OXIDE SURFACES J. Langan, J.A. Shorter, X. Xin, and J.I. Steinfeld	311
EXCIMER LASER INDUCED ETCHING OF SILICON-CARBIDE M. Murahara, H. Arai, and T. Matsumura	315
COMPARISON OF CW AND PULSED UV LASER ETCHING OF LiNbO ₃ K.W. Beeson and N.S. Clements	321
KrF* LASER-INDUCED CHEMICAL ETCHING OF NICKEL WITH Br ₂ G.W. Tyndall and C.R. Moylan	327
LASER INDUCED CHEMICAL ETCHING OF COMPOSITE STRUCTURE OF FERRITE AND SENDUST S. Nagatomo, M. Takai, Y.F. Lu, and S. Namba	333
LASER INDUCED WET-CHEMICAL ETCHING OF Mn-Zn FERRITE IN H ₃ PO ₄ Y.F. Lu, M. Takai, S. Nagatomo, and S. Namba	339
PART VII: LASER-INDUCED SURFACE ABLATION	
PATTERNING OF HIGH T _c SUPERCONDUCTOR FILMS WITH A FOCUSSED EXCIMER LASER J.M. Hagerhorst, J.D. Mannhart, M.M. Oprysko, M.R. Scheuermann, and C.C. Tsuei	347
MASS SPECTROMETRIC PROBING OF LASER-INDUCED MATERIALS VAPOR TRANSPORT: GRAPHITE AND SUPERCONDUCTING YBa ₂ Cu ₃ O _x D.W. Bonnell, P.K. Schenck, and J.W. Hastie	353
EJECTED PRODUCT ENERGY DISTRIBUTIONS FROM LASER ABLATED SOLIDS H. Helvajian and R.P. Welle	359
SPACE/TIME RESOLVED ANALYSIS IN μm/nsec SCALE OF LASER BEAM-SOLID SURFACE INTERACTION IN GROUP IV ELEMENTS A. Kasuya and Y. Nishina	365
ULTRAVIOLET LASER ABLATION OF A SILICON WAFER M. Kawasaki, H. Sato, and G. Inoue	371

ABLATION OF UV-TRANSPARENT MATERIALS WITH FEMTOSECOND UV EXCIMER LASER PULSES S. Küper and M. Stuke	375
EXCIMER LASER ABLATION OF SODIUM TRISILICATE GLASS P.A. Eschbach, J.T. Dickinson, and L.R. Pederson	385
LASER-INDUCED REACTIVE EVAPORATION AND CONDENSATION G-M. Chow and P.R. Strutt	393
EXCIMER LASER THIN METALLIC FILM PATTERNING ON POLYVINYLENE DIFLUORIDE M. Gauthier, R. Bourret, C-K. Jen, and E.L. Adler	399
ABLATION OF POLYMERS WITH PAIRS OF ULTRAVIOLET LASER PULSES WITH CONTROLLED TEMPORAL SEPARATION B. Braren and R. Srinivasan	405
MASS AND ENERGY ANALYSIS OF IONIC FRAGMENTS FROM PHOTO- ABLATION OF POLYIMIDE G. Ulmer, K. Bues, and E.E.B. Campbell	411
PART VIII: LASER-INDUCED SURFACE MODIFICATION	
*ULTRATHIN SILICON DIOXIDE FILMS: PHOTO-INDUCED GROWTH I.W. Boyd	421
LASER PHYSICAL AND LASER CHEMICAL VAPOR DEPOSITION OF TiN and TiN _x O _y FILMS J. Narayan, N. Biunno, A.R. Srivatsa, R. Singh, and B. Chen	435
REVERSIBLE LASER MODIFICATION OF HIGH TEMPERATURE SUPERCONDUCTING Y-Ba-Cu-O FILMS R.R. Krichavek, S-W. Chan, C.T. Rogers, F. De Rosa, P.F. Miceli, and S.J. Allen, Jr.	441
SELECTIVE-AREA LASER PHOTODEPOSITION OF TRANSPARENT CONDUCTIVE SnO ₂ FILMS R.R. Kunz, M. Rothschild, and D.J. Ehrlich	447
LASER-INDUCED MULTI-CRYSTALLIZATION OF THIN GERMANIUM FILMS C. Ortiz, K.A. Rubin, and S. Ajuria	455
PULSED LASER CLEANING OF ANTIMONY SINGLE CRYSTAL <111> SURFACE E.J. Petit and R. Caudano	461
PULSED LASER PROCESSING OF TARGETS IMMERSED IN LIQUID MEDIA J.P. Partridge, P.R. Strutt, and P.G. Klemens	469
PART IX: ION-, ELECTRON-, AND PLASMA-ASSISTED CHEMISTRY	
PHYSICAL AND CHEMICAL SPUTTERING AT VERY LOW ION ENERGY: THE IMPORTANCE OF THE SPUTTERING THRESHOLD C. Steinbruchel	477
*Invited Paper	

THE MICROSTRUCTURE OF GOLD FILMS WRITTEN BY FOCUSED ION BEAM INDUCED DEPOSITION	483
P.G. Blauner, J.S. Ro, Y. Butt, C.V. Thompson, and J. Melngailis	
TEMPERATURE DEPENDENCE OF ETCH RATE AND RESIDUAL DAMAGE IN REACTIVELY ION ETCHED GaAs AND AlGaAs	489
S.J. Pearton, K.S. Jones, U.K. Chakabarti, B. Emerson, E. Lane, M.J. Vasile, T.R. Fullowan, W.S. Hobson, K.T. Short, and N.M. Haegel	
SURFACE MORPHOLOGICAL CHANGES OF POLYIMIDE WITH OXYGEN REACTIVE ION BEAM ETCHING (RIBE)	495
K.W. Paik and A.L. Ruoff	
ON THE USE OF MÖSSBAUER NUCLEI AS PROBES OF RADIATION INDUCED EFFECTS AT INTERFACES	501
P.A. Ingemarsson, T. Ericsson, G. Possnert, and R. Wäppling	
EPITAXIAL RELATIONSHIPS IN ESD PROCESSES ON OXIDE SURFACES	509
M.R. McCartney and D.J. Smith	
HIGH CURRENT DENSITY ELECTRON BEAM INDUCED DESORPTION	515
S.D. Berger, J.M. Macaulay, L.M. Brown, and R.M. Allen	
FORMATION OF A Ni_3O_4 SPINEL PHASE ON THE SURFACE OF NiO DURING ELECTRON IRRADIATION	521
M.I. Buckett and L.D. Marks	
ELECTRON-BEAM ASSISTED CVD OF SILICON HOMOEPITAXIAL FILMS	527
J.P. West and C.B. Fleddermann	
THE INITIAL STAGES OF PLASMA SYNTHESIS OF DIAMOND FILMS	533
R. Meilunas, M.S. Wong, K. Sheng, T.P. Ong, and R.P.H. Chang	
RF PLASMA CVD USING HOLLOW CATHODE DISCHARGE	539
S. Araki, H. Kamaji, and K. Norimoto	
PART X: I. C. FABRICATION TECHNOLOGY	
*SELECTIVE-AREA LASER-ASSISTED PROCESSING FOR MICRO- ELECTRONIC MULTI-CHIP INTERCONNECT APPLICATIONS	547
R.F. Miracky	
*PROCESS MARGINS FOR LASER PLANARIZATION OF 1 to 5 μm GOLD FILMS	559
A.F. Bernhardt, R.J. Contolini, D.B. Tuckerman, and A.H. Weisberg	
FLASHLAMP-PUMPED DYE AND EXCIMER LASER PLANARIZATION OF THIN METAL FILMS	569
P.F. Marella, D.B. Tuckerman, and R.F. Pease	

*Invited Paper

LASER SURFACE MODIFICATION FOR COPPER DEPOSITION ON POLYIMIDE Y.S. Liu and H.S. Cole	579
PATTERNED EXCIMER LASER ETCHING OF GaAs WITHIN A MOLECULAR BEAM EPITAXY SYSTEM P.A. Maki and D.J. Ehrlich	585
BORON DOPING OF SILICON USING EXCIMER LASERS A. Slaoui, F. Foulon, M. Bianconi, L. Correra, R. Nipoti, R. Stuck, S. Unamuno, E. Fogarassy, and S. Nicoletti	591
HEAVILY DOPED ULTRA-SHALLOW JUNCTIONS FORMED BY ArF EXCIMER LASERS S. Yoshioka, J. Wada, H. Saeki, and S. Matsumoto	597
LASER PATTERNING OF HIGH TEMPERATURE SUPERCONDUCTING OXIDE FILMS A. Gupta, B.W. Hussey, R. Jagannathan, E.I. Cooper, and E.A. Giess	603
EPITAXIAL SILICON LAYERS MADE BY REDUCED PRESSURE/ TEMPERATURE CVD J.L. Regolini, D. Bensahel, J. Mercier, C. D'Anterrockes, and A. Perio	609
X-RAY LITHOGRAPHY STUDIES OF POLYSILANE USING A LASER PLASMA X-RAY SOURCE G.D. Kubiak, D.A. Outka, and J.M. Zeigler	615
LASER TRIM REVISITED IN THE LIGHT OF AN EXCIMER LASER M. Gauthier, R. Bourret, G. Gavrel, and R. Carnegie	621
SINGLE & MULTIPLE PULSE ABLATION OF POLYMERIC AND HIGH DENSITY MATERIALS WITH EXCIMER LASER RADIATION AT 193NM AND 248NM D.J. Elliott and B.P. Piwczyk	627
AUTHOR INDEX	637
SUBJECT INDEX	641

*Invited Paper

Preface

The symposium Laser- and Particle-Beam Chemical Processes on Surfaces, presented at the Fall 1988 Meeting in Boston, MA, was devoted to a discussion of recent advances in the use of photon, electron, and ion beams to induce or enhance chemical reactions on surfaces. These reactions are the basis for fabrication techniques that have particularly important applications to microelectronic and optoelectronic technologies. It was shown that thin films can be formed, modified, or removed in highly localized regions with submicrometer dimensions as well as over broad areas. The symposium served as a forum on the science of beam-induced materials processing and the implications of this science to practical implementation.

The symposium was the seventh in a series of MRS Fall symposia dealing with beam-induced chemical processes on surfaces. Work was described in a variety of areas, including (a) the deposition or etching of metal, semiconductor, and dielectric films by photon-, ion-, electron-, or plasma-enhanced chemical processes; (b) the laser-or-ion-induced ablation or sputtering of metal, semiconductor, dielectric, superconductor, and polymer films; (c) the laser-induced physical or chemical modification of surfaces, such as the planarization of metal films, the doping or crystallization of semiconductors, and the formation of dielectrics on semiconductors; and (d) the use of ion or electron beams to affect material properties, for example, by modifying interfacial bonding, inducing surface desorption, or writing conducting or superconducting lines in precursor films.

Research in beam-induced chemical processes on surfaces has matured rapidly in the last few years. An increased emphasis on obtaining an understanding of the fundamental mechanisms of beam-induced surface processes was a major trend observed at this year's symposium. This has resulted in the increased use of advanced diagnostic techniques and modeling studies to determine the rate-controlling steps in these processes. A better understanding of the chemical and physical phenomena that control these processes will allow further improvements in beam-induced processing techniques that will have many technological applications. The combination of a wide variety of technological applications and scientific approaches made this year's meeting especially interesting. This symposium once again demonstrated the ability of scientific and application research efforts to stimulate each other. The MRS is to be thanked for its role in enabling this symposium to flourish. We hope that the MRS Fall Meeting will continue to serve as the major international conference for this topic.

Symposium Cochairmen

A. Wayne Johnson
Gary L. Loper
T.W. Sigmon

October 1989

Acknowledgments

We thank the invited speakers for describing their latest work and providing perspective on various exciting areas of laser- and particle-beam induced chemistry on surfaces:

Joint Plenary Session Speakers

J. Dieleman
B.W. Dodson
J.R. McNeil
J.-E. Sundgren

Invited Speakers

C.I.H. Ashby
A.F. Bernhardt
I.W. Boyd
V.M. Donnelly
K. Kompa
K.V. Jensen
R.F. Miracky
R.M. Osgood, Jr.
H. Schroder

as well as contributors and referees for a successful symposium.

We thank the session chairs for their assistance in conducting the symposium:

C.I.H. Ashby	J.C. Hemminger
G.J. Collins	I.P. Herman
V.M. Donnelly	G.S. Higashi
D.J. Ehrlich	M.M. Oprysko
C.B. Fleddermann	R.M. Osgood, Jr.

We are especially grateful to the Air Force Office of Scientific Research for providing the primary financial support for the symposium. We thank H.R. Schlossberg of AFOSR for arranging this funding. We also greatly appreciate the important additional support provided for the symposium by Lambda Physik, Inc., Newport Corporation, and Applied Electron Corporation.

MATERIALS RESEARCH SOCIETY SYMPOSIUM PROCEEDINGS

ISSN 0272 - 9172

- Volume 1—Laser and Electron-Beam Solid Interactions and Materials Processing, J. F. Gibbons, L. D. Hess, T. W. Sigmon, 1981, ISBN 0-444-00595-1
- Volume 2—Defects in Semiconductors, J. Narayan, T. Y. Tan, 1981, ISBN 0-444-00596-X
- Volume 3—Nuclear and Electron Resonance Spectroscopies Applied to Materials Science, E. N. Kaufmann, G. K. Shenoy, 1981, ISBN 0-444-00597-8
- Volume 4—Laser and Electron-Beam Interactions with Solids, B. R. Appleton, G. K. Celler, 1982, ISBN 0-444-00693-1
- Volume 5—Grain Boundaries in Semiconductors, H. J. Leamy, G. E. Pike, C. H. Seager, 1982, ISBN 0-444-00697-4
- Volume 6—Scientific Basis for Nuclear Waste Management IV, S. V. Topp, 1982, ISBN 0-444-00699-0
- Volume 7—Metastable Materials Formation by Ion Implantation, S. T. Picraux, W. J. Choyke, 1982, ISBN 0-444-00692-3
- Volume 8—Rapidly Solidified Amorphous and Crystalline Alloys, B. H. Kear, B. C. Giessen, M. Cohen, 1982, ISBN 0-444-00698-2
- Volume 9—Materials Processing in the Reduced Gravity Environment of Space, G. E. Rindone, 1982, ISBN 0-444-00691-5
- Volume 10—Thin Films and Interfaces, P. S. Ho, K.-N. Tu, 1982, ISBN 0-444-00774-1
- Volume 11—Scientific Basis for Nuclear Waste Management V, W. Lutze, 1982, ISBN 0-444-00725-3
- Volume 12—In Situ Composites IV, F. D. Lemkey, H. E. Cline, M. McLean, 1982, ISBN 0-444-00726-1
- Volume 13—Laser-Solid Interactions and Transient Thermal Processing of Materials, J. Narayan, W. L. Brown, R. A. Lemons, 1983, ISBN 0-444-00788-1
- Volume 14—Defects in Semiconductors II, S. Mahajan, J. W. Corbett, 1983, ISBN 0-444-00812-8
- Volume 15—Scientific Basis for Nuclear Waste Management VI, D. G. Brookins, 1983, ISBN 0-444-00780-6
- Volume 16—Nuclear Radiation Detector Materials, E. E. Haller, H. W. Kraner, W. A. Higinbotham, 1983, ISBN 0-444-00787-3
- Volume 17—Laser Diagnostics and Photochemical Processing for Semiconductor Devices, R. M. Osgood, S. R. J. Brueck, H. R. Schlossberg, 1983, ISBN 0-444-00782-2
- Volume 18—Interfaces and Contacts, R. Ludeke, K. Rose, 1983, ISBN 0-444-00820-9
- Volume 19—Alloy Phase Diagrams, L. H. Bennett, T. B. Massalski, B. C. Giessen, 1983, ISBN 0-444-00809-8
- Volume 20—Intercalated Graphite, M. S. Dresselhaus, G. Dresselhaus, J. E. Fischer, M. J. Moran, 1983, ISBN 0-444-00781-4
- Volume 21—Phase Transformations in Solids, T. Tsakalakos, 1984, ISBN 0-444-00901-9
- Volume 22—High Pressure in Science and Technology, C. Homan, R. K. MacCrone, E. Whalley, 1984, ISBN 0-444-00932-9 (3 part set)
- Volume 23—Energy Beam-Solid Interactions and Transient Thermal Processing, J. C. C. Fan, N. M. Johnson, 1984, ISBN 0-444-00903-5
- Volume 24—Defect Properties and Processing of High-Technology Nonmetallic Materials, J. H. Crawford, Jr., Y. Chen, W. A. Sibley, 1984, ISBN 0-444-00904-3
- Volume 25—Thin Films and Interfaces II, J. E. E. Baglin, D. R. Campbell, W. K. Chu, 1984, ISBN 0-444-00905-1

MATERIALS RESEARCH SOCIETY SYMPOSIUM PROCEEDINGS

- Volume 26—Scientific Basis for Nuclear Waste Management VII, G. L. McVay, 1984, ISBN 0-444-00906-X
- Volume 27—Ion Implantation and Ion Beam Processing of Materials, G. K. Hubler, O. W. Holland, C. R. Clayton, C. W. White, 1984, ISBN 0-444-00869-1
- Volume 28—Rapidly Solidified Metastable Materials, B. H. Kear, B. C. Giessen, 1984, ISBN 0-444-00935-3
- Volume 29—Laser-Controlled Chemical Processing of Surfaces, A. W. Johnson, D. J. Ehrlich, H. R. Schlossberg, 1984, ISBN 0-444-00894-2
- Volume 30—Plasma Processing and Synthesis of Materials, J. Szekely, D. Apelian, 1984, ISBN 0-444-00895-0
- Volume 31—Electron Microscopy of Materials, W. Krakow, D. A. Smith, L. W. Hobbs, 1984, ISBN 0-444-00898-7
- Volume 32—Better Ceramics Through Chemistry, C. J. Brinker, D. E. Clark, D. R. Ulrich, 1984, ISBN 0-444-00898-5
- Volume 33—Comparison of Thin Film Transistor and SOI Technologies, H. W. Lam, M. J. Thompson, 1984, ISBN 0-444-00899-3
- Volume 34—Physical Metallurgy of Cast Iron, H. Fredriksson, M. Hillerts, 1985, ISBN 0-444-00938-8
- Volume 35—Energy Beam-Solid Interactions and Transient Thermal Processing/1984, D. K. Biegelsen, G. A. Rozgonyi, C. V. Shank, 1985, ISBN 0-931837-00-6
- Volume 36—Impurity Diffusion and Gettering in Silicon, R. B. Fair, C. W. Pearce, J. Washburn, 1985, ISBN 0-931837-01-4
- Volume 37—Layered Structures, Epitaxy, and Interfaces, J. M. Gibson, L. R. Dawson, 1985, ISBN 0-931837-02-2
- Volume 38—Plasma Synthesis and Etching of Electronic Materials, R. P. H. Chang, B. Abeles, 1985, ISBN 0-931837-03-0
- Volume 39—High-Temperature Ordered Intermetallic Alloys, C. C. Koch, C. T. Liu, N. S. Stoloff, 1985, ISBN 0-931837-04-9
- Volume 40—Electronic Packaging Materials Science, E. A. Giess, K.-N. Tu, D. R. Uhlmann, 1985, ISBN 0-931837-05-7
- Volume 41—Advanced Photon and Particle Techniques for the Characterization of Defects in Solids, J. B. Roberto, R. W. Carpenter, M. C. Wittels, 1985, ISBN 0-931837-06-5
- Volume 42—Very High Strength Cement-Based Materials, J. F. Young, 1985, ISBN 0-931837-07-3
- Volume 43—Fly Ash and Coal Conversion By-Products: Characterization, Utilization, and Disposal I, G. J. McCarthy, R. J. Lauf, 1985, ISBN 0-931837-08-1
- Volume 44—Scientific Basis for Nuclear Waste Management VIII, C. M. Jantzen, J. A. Stone, R. C. Ewing, 1985, ISBN 0-931837-09-X
- Volume 45—Ion Beam Processes in Advanced Electronic Materials and Device Technology, B. R. Appleton, F. H. Eisen, T. W. Sigmon, 1985, ISBN 0-931837-10-3
- Volume 46—Microscopic Identification of Electronic Defects in Semiconductors, N. M. Johnson, S. G. Bishop, G. D. Watkins, 1985, ISBN 0-931837-11-1
- Volume 47—Thin Films: The Relationship of Structure to Properties, C. R. Aita, K. S. SreeHarsha, 1985, ISBN 0-931837-12-X
- Volume 48—Applied Materials Characterization, W. Katz, P. Williams, 1985, ISBN 0-931837-13-8
- Volume 49—Materials Issues in Applications of Amorphous Silicon Technology, D. Adler, A. Madan, M. J. Thompson, 1985, ISBN 0-931837-14-6

MATERIALS RESEARCH SOCIETY SYMPOSIUM PROCEEDINGS

- Volume 50—Scientific Basis for Nuclear Waste Management IX, L. O. Werme, 1986, ISBN 0-931837-15-4
- Volume 51—Beam-Solid Interactions and Phase Transformations, H. Kurz, G. L. Olson, J. M. Poate, 1986, ISBN 0-931837-16-2
- Volume 52—Rapid Thermal Processing, T. O. Sedgwick, T. E. Seidel, B.-Y. Tsaur, 1986, ISBN 0-931837-17-0
- Volume 53—Semiconductor-on-Insulator and Thin Film Transistor Technology, A. Chiang, M. W. Geis, L. Pfeiffer, 1986, ISBN 0-931837-18-9
- Volume 54—Thin Films—Interfaces and Phenomena, R. J. Nemanich, P. S. Ho, S. S. Lau, 1986, ISBN 0-931837-19-7
- Volume 55—Biomedical Materials, J. M. Williams, M. F. Nichols, W. Zingg, 1986, ISBN 0-931837-20-0
- Volume 56—Layered Structures and Epitaxy, J. M. Gibson, G. C. Osbourn, R. M. Tromp, 1986, ISBN 0-931837-21-9
- Volume 57—Phase Transitions in Condensed Systems—Experiments and Theory, G. S. Cargill III, F. Spaepen, K.-N. Tu, 1987, ISBN 0-931837-22-7
- Volume 58—Rapidly Solidified Alloys and Their Mechanical and Magnetic Properties, B. C. Giessen, D. E. Polk, A. I. Taub, 1986, ISBN 0-931837-23-5
- Volume 59—Oxygen, Carbon, Hydrogen, and Nitrogen in Crystalline Silicon, J. C. Mikkelsen, Jr., S. J. Pearton, J. W. Corbett, S. J. Pennycook, 1986, ISBN 0-931837-24-3
- Volume 60—Defect Properties and Processing of High-Technology Nonmetallic Materials, Y. Chen, W. D. Kingery, R. J. Stokes, 1986, ISBN 0-931837-25-1
- Volume 61—Defects in Glasses, F. L. Galeener, D. L. Griscom, M. J. Weber, 1986, ISBN 0-931837-26-X
- Volume 62—Materials Problem Solving with the Transmission Electron Microscope, L. W. Hobbs, K. H. Westmacott, D. B. Williams, 1986, ISBN 0-931837-27-8
- Volume 63—Computer-Based Microscopic Description of the Structure and Properties of Materials, J. Broughton, W. Krakow, S. T. Pantelides, 1986, ISBN 0-931837-28-6
- Volume 64—Cement-Based Composites: Strain Rate Effects on Fracture, S. Mindess, S. P. Shah, 1986, ISBN 0-931837-29-4
- Volume 65—Fly Ash and Coal Conversion By-Products: Characterization, Utilization and Disposal II, G. J. McCarthy, F. P. Glasser, D. M. Roy, 1986, ISBN 0-931837-30-8
- Volume 66—Frontiers in Materials Education, L. W. Hobbs, G. L. Liedl, 1986, ISBN 0-931837-31-6
- Volume 67—Heteroepitaxy on Silicon, J. C. C. Fan, J. M. Poate, 1986, ISBN 0-931837-33-2
- Volume 68—Plasma Processing, J. W. Coburn, R. A. Gottscho, D. W. Hess, 1986, ISBN 0-931837-34-0
- Volume 69—Materials Characterization, N. W. Cheung, M.-A. Nicolet, 1986, ISBN 0-931837-35-9
- Volume 70—Materials Issues in Amorphous-Semiconductor Technology, D. Adler, Y. Hamakawa, A. Madan, 1986, ISBN 0-931837-36-7
- Volume 71—Materials Issues in Silicon Integrated Circuit Processing, M. Wittmer, J. Stimmell, M. Strathman, 1986, ISBN 0-931837-37-5
- Volume 72—Electronic Packaging Materials Science II, K. A. Jackson, R. C. Pohanka, D. R. Uhlmann, D. R. Ulrich, 1986, ISBN 0-931837-38-3
- Volume 73—Better Ceramics Through Chemistry II, C. J. Brinker, D. E. Clark, D. R. Ulrich, 1986, ISBN 0-931837-39-1
- Volume 74—Beam-Solid Interactions and Transient Processes, M. O. Thompson, S. T. Picraux, J. S. Williams, 1987, ISBN 0-931837-40-5

MATERIALS RESEARCH SOCIETY SYMPOSIUM PROCEEDINGS

- Volume 75—Photon, Beam and Plasma Stimulated Chemical Processes at Surfaces, V. M. Donnelly, I. P. Herman, M. Hirose, 1987, ISBN 0-931837-41-3
- Volume 76—Science and Technology of Microfabrication, R. E. Howard, E. L. Hu, S. Namba, S. Pang, 1987, ISBN 0-931837-42-1
- Volume 77—Interfaces, Superlattices, and Thin Films, J. D. Dow, I. K. Schuller, 1987, ISBN 0-931837-56-1
- Volume 78—Advances in Structural Ceramics, P. F. Becher, M. V. Swain, S. Sōmiya, 1987, ISBN 0-931837-43-X
- Volume 79—Scattering, Deformation and Fracture in Polymers, G. D. Wignall, B. Crist, T. P. Russell, E. L. Thomas, 1987, ISBN 0-931837-44-8
- Volume 80—Science and Technology of Rapidly Quenched Alloys, M. Tenhover, W. L. Johnson, L. E. Tanner, 1987, ISBN 0-931837-45-6
- Volume 81—High-Temperature Ordered Intermetallic Alloys, II, N. S. Stoloff, C. C. Koch, C. T. Liu, O. Izumi, 1987, ISBN 0-931837-46-4
- Volume 82—Characterization of Defects in Materials, R. W. Siegel, J. R. Weertman, R. Sinclair, 1987, ISBN 0-931837-47-2
- Volume 83—Physical and Chemical Properties of Thin Metal Overlayers and Alloy Surfaces, D. M. Zehner, D. W. Goodman, 1987, ISBN 0-931837-48-0
- Volume 84—Scientific Basis for Nuclear Waste Management X, J. K. Bates, W. B. Seefeldt, 1987, ISBN 0-931837-49-9
- Volume 85—Microstructural Development During the Hydration of Cement, L. Struble, P. Brown, 1987, ISBN 0-931837-50-2
- Volume 86—Fly Ash and Coal Conversion By-Products Characterization, Utilization and Disposal III, G. J. McCarthy, F. P. Glasser, D. M. Roy, S. Diamond, 1987, ISBN 0-931837-51-0
- Volume 87—Materials Processing in the Reduced Gravity Environment of Space, R. H. Doremus, P. C. Nordine, 1987, ISBN 0-931837-52-9
- Volume 88—Optical Fiber Materials and Properties, S. R. Nagel, J. W. Fleming, G. Sigel, D. A. Thompson, 1987, ISBN 0-931837-53-7
- Volume 89—Diluted Magnetic (Semimagnetic) Semiconductors, R. L. Aggarwal, J. K. Furdyna, S. von Molnar, 1987, ISBN 0-931837-54-5
- Volume 90—Materials for Infrared Detectors and Sources, R. F. C. Farrow, J. F. Schetzina, J. T. Cheung, 1987, ISBN 0-931837-55-3
- Volume 91—Heteroepitaxy on Silicon II, J. C. C. Fan, J. M. Phillips, B.-Y. Tsaur, 1987, ISBN 0-931837-58-8
- Volume 92—Rapid Thermal Processing of Electronic Materials, S. R. Wilson, R. A. Powell, D. E. Davies, 1987, ISBN 0-931837-59-6
- Volume 93—Materials Modification and Growth Using Ion Beams, U. Gibson, A. E. White, P. P. Pronko, 1987, ISBN 0-931837-60-X
- Volume 94—Initial Stages of Epitaxial Growth, R. Hull, J. M. Gibson, David A. Smith, 1987, ISBN 0-931837-61-8
- Volume 95—Amorphous Silicon Semiconductors—Pure and Hydrogenated, A. Madan, M. Thompson, D. Adler, Y. Hamakawa, 1987, ISBN 0-931837-62-6
- Volume 96—Permanent Magnet Materials, S. G. Sankar, J. F. Herbst, N. C. Koon, 1987, ISBN 0-931837-63-4
- Volume 97—Novel Refractory Semiconductors, D. Emin, T. Aselage, C. Wood, 1987, ISBN 0-931837-64-2
- Volume 98—Plasma Processing and Synthesis of Materials, D. Apelian, J. Szekely, 1987, ISBN 0-931837-65-0

MATERIALS RESEARCH SOCIETY SYMPOSIUM PROCEEDINGS

- Volume 99—High-Temperature Superconductors, M. B. Brodsky, R. C. Dynes, K. Kitazawa, H. L. Tuller, 1988, ISBN 0-931837-67-7
- Volume 100—Fundamentals of Beam-Solid Interactions and Transient Thermal Processing, M. J. Aziz, L. E. Rehn, B. Stritzker, 1988, ISBN 0-931837-68-5
- Volume 101—Laser and Particle-Beam Chemical Processing for Microelectronics, D.J. Ehrlich, G.S. Higashi, M.M. Oprysko, 1988, ISBN 0-931837-69-3
- Volume 102—Epitaxy of Semiconductor Layered Structures, R. T. Tung, L. R. Dawson, R. L. Gunshor, 1988, ISBN 0-931837-70-7
- Volume 103—Multilayers: Synthesis, Properties, and Nonelectronic Applications, T. W. Barbee Jr., F. Spaepen, L. Greer, 1988, ISBN 0-931837-71-5
- Volume 104—Defects in Electronic Materials, M. Stavola, S. J. Pearton, G. Davies, 1988, ISBN 0-931837-72-3
- Volume 105—SiO₂ and Its Interfaces, G. Lucovsky, S. T. Pantelides, 1988, ISBN 0-931837-73-1
- Volume 106—Polysilicon Films and Interfaces, C.Y. Wong, C.V. Thompson, K-N. Tu, 1988, ISBN 0-931837-74-X
- Volume 107—Silicon-on-Insulator and Buried Metals in Semiconductors, J. C. Sturm, C. K. Chen, L. Pfeiffer, P. L. F. Hemment, 1988, ISBN 0-931837-75-8
- Volume 108—Electronic Packaging Materials Science II, R. C. Sundahl, R. Jaccodine, K. A. Jackson, 1988, ISBN 0-931837-76-6
- Volume 109—Nonlinear Optical Properties of Polymers, A. J. Heeger, J. Orenstein, D. R. Ulrich, 1988, ISBN 0-931837-77-4
- Volume 110—Biomedical Materials and Devices, J. S. Hanker, B. L. Giammara, 1988, ISBN 0-931837-78-2
- Volume 111—Microstructure and Properties of Catalysts, M. M. J. Treacy, J. M. Thomas, J. M. White, 1988, ISBN 0-931837-79-0
- Volume 112—Scientific Basis for Nuclear Waste Management XI, M. J. Apter, R. E. Westerman, 1988, ISBN 0-931837-80-4
- Volume 113—Fly Ash and Coal Conversion By-Products: Characterization, Utilization, and Disposal IV, G. J. McCarthy, D. M. Roy, F. P. Glasser, R. T. Hemmings, 1988, ISBN 0-931837-81-2
- Volume 114—Bonding in Cementitious Composites, S. Mindess, S. P. Shah, 1988, ISBN 0-931837-82-0
- Volume 115—Specimen Preparation for Transmission Electron Microscopy of Materials, J. C. Bravman, R. Anderson, M. L. McDonald, 1988, ISBN 0-931837-83-9
- Volume 116—Heteroepitaxy on Silicon: Fundamentals, Structures, and Devices, H.K. Choi, H. Ishiwara, R. Hull, R.J. Nemanich, 1988, ISBN: 0-931837-86-3
- Volume 117—Process Diagnostics: Materials, Combustion, Fusion, K. Hays, A.C. Eckbreth, G.A. Campbell, 1988, ISBN: 0-931837-87-1
- Volume 118—Amorphous Silicon Technology, A. Madan, M.J. Thompson, P.C. Taylor, P.G. LeComber, Y. Hamakawa, 1988, ISBN: 0-931837-88-X
- Volume 119—Adhesion in Solids, D.M. Mattox, C. Batich, J.E.E. Baglin, R.J. Gottschall, 1988, ISBN: 0-931837-89-8
- Volume 120—High-Temperature/High-Performance Composites, F.D. Lemkey, A.G. Evans, S.G. Fishman, J.R. Strife, 1988, ISBN: 0-931837-90-1
- Volume 121—Better Ceramics Through Chemistry III, C.J. Brinker, D.E. Clark, D.R. Ulrich, 1988, ISBN: 0-931837-91-X
- Volume 122—Interfacial Structure, Properties, and Design, M.H. Yoo, W.A.T. Clark, C.L. Briant, 1988, ISBN: 0-931837-92-8

MATERIALS RESEARCH SOCIETY SYMPOSIUM PROCEEDINGS

- Volume 123—Materials Issues in Art and Archaeology, E.V. Sayre, P. Vandiver, J. Druzik, C. Stevenson, 1988, ISBN: 0-931837-93-6
- Volume 124—Microwave-Processing of Materials, M.H. Brooks, I.J. Chabinsky, W.H. Sutton, 1988, ISBN: 0-931837-94-4
- Volume 125—Materials Stability and Environmental Degradation, A. Barkatt, L.R. Smith, E. Verink, 1988, ISBN: 0-931837-95-2
- Volume 126—Advanced Surface Processes for Optoelectronics, S. Bernasek, T. Venkatesan, H. Temkin, 1988, ISBN: 0-931837-96-0
- Volume 127—Scientific Basis for Nuclear Waste Management XII, W. Lutze, R.C. Ewing, 1989, ISBN: 0-931837-97-9
- Volume 128—Processing and Characterization of Materials Using Ion Beams, L.E. Rehn, J. Greene, F.A. Smidt, 1989, ISBN: 1-55899-001-1
- Volume 129—Laser and Particle-Beam Chemical Processes on Surfaces, G.L. Loper, A.W. Johnson, T.W. Sigmon, 1989, ISBN: 1-55899-002-X
- Volume 130—Thin Films: Stresses and Mechanical Properties, J.C. Bravman, W.D. Nix, D.M. Barnett, D.A. Smith, 1989, ISBN: 0-55899-003-8
- Volume 131—Chemical Perspectives of Microelectronic Materials, M.E. Gross, J. Jasinski, J.T. Yates, Jr., 1989, ISBN: 0-55899-004-6
- Volume 132—Multicomponent Ultrafine Microstructures, B.H. Kear, D.E. Polk, L.E. McCandlish, 1989, ISBN: 1-55899-005-4
- Volume 133—High Temperature Ordered Intermetallic Alloys III, C.T. Liu, A.I. Taub, N.S. Stoloff, C.C. Koch, 1989, ISBN: 1-55899-006-2
- Volume 134—The Materials Science and Engineering of Rigid-Rod Polymers, W.W. Adams, R.K. Eby, D.E. McLemore, 1989, ISBN: 1-55899-007-0
- Volume 135—Solid State Ionics, G. Nazri, R.A. Huggins, D.F. Shriver, 1989, ISBN: 1-55899-008-9
- Volume 136—Fly Ash and Coal Conversion By-Products: Characterization, Utilization, and Disposal V, R.T. Hemmings, E.E. Berry, G.J. McCarthy, F.P. Glasser, 1989, ISBN: 1-55899-009-7
- Volume 137—Pore Structure and Permeability of Cementitious Materials, L.R. Roberts, J.P. Skalny, 1989, ISBN: 1-55899-010-0
- Volume 138—Characterization of the Structure and Chemistry of Defects in Materials, B.C. Larson, M. Ruhle, D.N. Seidman, 1989, ISBN: 1-55899-011-9
- Volume 139—High Resolution Microscopy of Materials, W. Krakow, F.A. Ponce, D.J. Smith, 1989, ISBN: 1-55899-012-7
- Volume 140—New Materials Approaches to Tribology: Theory and Applications, L.E. Pope, L. Fehrenbacher, W.O. Winer, 1989, ISBN: 1-55899-013-5
- Volume 141—Atomic Scale Calculations in Materials Science, J. Tersoff, D. Vanderbilt, V. Vitek, 1989, ISBN: 1-55899-014-3
- Volume 142—Nondestructive Monitoring of Materials Properties, J. Holbrook, J. Bussiere, 1989, ISBN: 1-55899-015-1
- Volume 143—Synchrotron Radiation in Materials Research, R. Clarke, J.H. Weaver, J. Gland, 1989, ISBN: 1-55899-016-X
- Volume 144—Advances in Materials, Processing and Devices in III-V Compound Semiconductors, D.K. Sadana, L. Eastman, R. Dupuis, 1989, ISBN: 1-55899-017-8

MATERIALS RESEARCH SOCIETY CONFERENCE PROCEEDINGS

**Tungsten and Other Refractory Metals for VLSI Applications, R. S. Blewer, 1986;
ISSN 0886-7860; ISBN 0-931837-32-4**

**Tungsten and Other Refractory Metals for VLSI Applications II, E.K. Broadbent, 1987;
ISSN 0886-7860; ISBN 0-931837-66-9**

Ternary and Multinary Compounds, S. Deb, A. Zunger, 1987; ISBN 0-931837-57-x

**Tungsten and Other Refractory Metals for VLSI Applications III, Victor A. Wells, 1988;
ISSN 0886-7860; ISBN 0-931837-84-7**

**Atomic and Molecular Processing of Electronic and Ceramic Materials: Preparation,
Characterization and Properties, Ilhan A. Aksay, Gary L. McVay, Thomas G. Stoebe,
1988; ISBN 0-931837-85-5**

**Materials Futures: Strategies and Opportunities, R. Byron Pipes, U.S. Organizing Com-
mittee, Rune Lagneborg, Swedish Organizing Committee, 1988; ISBN 0-55899-000-3**

**Tungsten and Other Refractory Metals for VLSI Applications IV, Robert S. Blewer,
Carol M. McConica, 1989; ISSN: 0886-7860; ISBN: 0-931837-98-7**

PART I

**Overview of Laser- and
Beam-Induced Surface Processes**

SOME RECENT RESULTS OF FUNDAMENTAL STUDIES ON BEAM-INDUCED SURFACE PROCESSES

JAN DIELEMAN
Philips Research Laboratories
5600 JA Eindhoven, The Netherlands

Recent results of studies on the mechanism of processes induced by the interaction of beams of (reactive) particles with surfaces in UHV, often combined with concurrent bombardment of the surface with low-energy ion or excimer laser beams, are reviewed. Angular-resolved mass spectrometry combined with time-of-flight studies on the desorbing products is used as a key diagnostic. A more complete picture is obtained using several other diagnostic tools to characterize the surface before, during or after the interaction. Interactions at Si and Cu surfaces will be emphasized. The review will deal successively with data for interaction with a single beam of Cl_2 , low-energy noble gas ions or excimer laser pulses, followed by data on the concurrent interaction of crossed beams of Cl_2 and low-energy noble gas ions or excimer laser pulses with these surfaces. Some conclusions will be drawn.

1. INTRODUCTION

Growth and etching of thin films, usually via the gas phase, plays a dominating role in the technology of present-day integrated circuits. The ever increasing complexity of these devices has necessitated the development of techniques providing improved quality at reduced substrate temperatures. The reduced substrate temperatures are a necessity because the delicate structures already present in the substrate should not be damaged and the improved quality is essential to get a high yield of well-performing devices. Typically these techniques use dissociation and excitation of gas molecules by plasmas or by photons to enhance surface adsorption and reaction and/or apply surface-localized energy deposition by bombardment of the adsorbate layer and nearby surface region by low-energy electrons, ions, excited neutrals or photons to stimulate surface

reactions and desorption of products. A qualitative and certainly a quantitative understanding of the crucial steps in these important reaction chains is largely lacking. This hampers assessment of basic possibilities and limitations of most of these techniques.

It is the object of this paper to review some recent results of studies on the mechanisms of surface reactions stimulated by low-energy noble gas ion bombardment or by nanosecond excimer laser pulses. These studies have been performed in UHV chambers in which surfaces can be exposed to one beam of particles like chemically active molecules, low-energy noble gas ions or excimer laser photons or concurrently to two beams, one consisting of chemically active molecules and the other of low-energy noble gas ions or excimer laser photons. The discussion will be restricted to the comprehensive studies on the interaction of low-energy noble gas ion beams or excimer laser beams with Si or Cu surfaces in most cases in the presence of chlorine adsorbed on the surfaces from a beam of Cl_2 molecules. For studies on other systems the reader is referred to several recent review papers [1-6]. The main features of the most important diagnostic tool used, viz. mass spectrometry combined with time-of-flight measurements on the neutral "desorption" products, can be found in another recent review [7].

This review paper will deal successively with some data on the interaction of separate Cl_2 beams, low-energy noble gas ion-, or excimer laser-beams with Si and Cu surfaces, the concurrent action of crossed Cl_2 and low-energy noble gas ion beams on Si surfaces, the simultaneous exposure of Si or Cu surfaces to crossed beams of Cl_2 and nanosecond excimer laser pulses and will end with some conclusions. The data on the interaction of only one of these beams with Si or Cu surfaces will be reviewed only for ranges of parameter values also used in the experiments with crossed beams.

2. Cl_2 BEAMS

In the temperature range of 300 to 850 K Cl_2 sticks to Si(111) surfaces with an initial sticking coefficient of about 0.1 until a coverage of about one monolayer is reached. At this saturation coverage the sticking coefficient drops rapidly. Both the initial sticking coefficient and the saturation coverage decrease only slightly with

increasing temperature [8]. At 300 K Si does not react measurably with Cl_2 . At somewhat higher temperatures the main etch product is SiCl_4 , while at temperatures above about 800 K up to 1500 K the main etch product observed is SiCl_2 [9,10]. A comparison of an estimate of the relative contribution of the etch products SiCl_2 and SiCl_4 as a function of temperature from mass spectra alone [10], with an estimate using a combination of mass spectroscopy and time-of-flight [7] clearly shows the very qualitative character of the former estimate. Time-of-flight distributions, using modulation of the product beam, have the form of Maxwell-Boltzmann (MB) distributions at target temperature, suggesting thermal desorption [7]. The desorption of SiCl_2 has been reported to show an activation energy of about 1.75 eV at 1400 K decreasing to about 0.8 eV below 1000 K, with a surface residence time of about 10^{-2} s at 1400 K and accompanied by "unusually" low preexponential (frequency) factors of $3 \times 10^8 \text{ s}^{-1}$ at 1400 K to $8 \times 10^6 \text{ s}^{-1}$ below 1000 K. (which is about 10^5 to 10^6 times lower than "usual"). Calculations have confirmed that chlorine has a high activation energy barrier for diffusion from the surface into the Si [11]. It is difficult to derive from recent literature [12-14] a unified, quantitative picture of the reaction of Cl_2 with Cu surfaces. In the pressure and temperature ranges of interest in the crossed beams experiments to be described later on, i.e. for effective Cl_2 pressures up to about 10^{-4} Torr and temperatures up to about 1000 K, the situation seems to be as follows. At very low pressures (about 10^{-8} Torr) and room temperature the surface coverage increases linearly with dose up to about 2 Langmuir (L) where it saturates at about half of a monolayer. The initial sticking probability is about 0.5 and drops drastically at saturation coverage. The Cl_2 seems to be dissociatively chemisorbed without forming a halide-like overlayer. The overlayer has been reported to contain "free" halogen. This holds even for exposures up to 20 kL in the temperature range 300 to 700 K. However, when the effective pressures are chosen much higher or when Cl_2 at low pressures is condensed on a Cu surface at temperatures of 200 K, thicker Cu halide films are formed. The reaction probability of Cl_2 first decreases with increasing temperature till about 500 K and then increases. This has been explained by a rapidly decreasing sticking probability of Cl_2 on the CuCl surface film and rapid evaporation of Cu-halide, thus exposing "fresh" Cu surface with a high sticking probability, at temperatures above about 500 K. At 300 K thermal etching is immeasurably slow. At temperatures up to about 850 K the dominant etch product is Cu_3Cl_3 , while above 925 K the main desorbing molecule is CuCl .

3. LOW-ENERGY NOBLE GAS ION OR EXCIMER LASER BEAMS

Only a few data are available on physical sputtering of Cu and Si with Ar^+ ion beams of a few keV in UHV [15,16]. At these projectile energies the energy distributions of the main products, sputtered atoms, are described well with a collision cascade (CC) distribution, i.e. the flux of sputtered atoms $\phi(E)$ is proportional to $E / (E+U_0)^3$ where U_0 is the binding energy of the atom. $U_0(\text{Cu}) = 3.5$ eV and $U_0(\text{Si}) = 7.8$ eV. For quite a number of elements U_0 is equivalent to the value of the sublimation energy [5], only U_0 of Si is somewhat higher. Sputtering yields at 6 keV are 3.7 atoms/ Ar^+ for Cu and 1.3 atoms/ Ar^+ for Si. The values of these yields are consistent with yield formulas (see eq. 6 of ref. 5). Sputtering yields decrease with decreasing projectile energy to values of a few 0.1 atoms/ Ar^+ at 100 eV. With decreasing projectile energy the energy distribution of the sputtered atoms deviates at the high energy end progressively to lower values. This is especially significant for oblique incidence and ejection angles [17,18].

Low-energy noble gas ion bombardment of solids also leads to implantation. The resputtering of these noble gases has been studied for bombardment of Si with Ar^+ [19]. The time-of-flight (TOF) distributions consisted of two contributions, an MB distribution at target temperature which is ascribed to ion bombardment-enhanced diffusion to the surface followed by evaporation (or, below the solidification temperature, sputtering) and a contribution which may be reasonably well simulated with an MB distribution *but at a much higher temperature*. The latter contribution has tentatively been interpreted as opening of noble gas "bubbles" by ion impact. Recent studies [20], for more noble gases and more solid targets, have shown that the TOF distributions always have a high kinetic energy component and often an MB contribution at target temperature. It also appeared that steady state resputtering is reached already with a fluence of no more than about 10^{15} ions per cm^2 . The latter observation is not easily understood by assuming sputter opening of noble gas bubbles. Hopefully, incidence- and exit angle-dependent studies will shed more light on the mechanism responsible.

The interaction of 308 and 248 nm nanosec laser pulses at laser pulse fluences up to 0.82 and 1.0 Jcm^{-2} respectively with pure Si and Cu surfaces in UHV did not lead to significant etching.

4. CROSSED BEAMS OF LOW-ENERGY NOBLE GAS IONS AND OF Cl_2

By using a combination of TOF studies and mass spectroscopy the composition of the various neutral products desorbing from e.g. a Si surface exposed to crossed beams of low-energy noble gas ions and Cl_2 can be determined [7]. If care is taken to prevent the desorbing products from colliding with each other above the surface [21] also information about the desorption mechanism(s) is obtained. It is much more difficult to make a more quantitative estimate of the relative proportions of the various products. For this quantification one needs to know what the TOF distributions of the various products are to be able to make a $1/v$ correction for the ionization probability in the ionization chamber of the mass spectrometer. Since we have measured these TOF distributions for the products, this correction can be applied. Of course one must take care of collecting the ions produced properly. The important problem remaining is that for most of the molecules encountered in our studies no ionization cross sections are known and it takes a lot of effort to measure them [22]. To get a qualitative impression of the neutral products leaving a Si surface along the surface normal, when exposed to crossed beams of 1 keV Ar^+ ions incident at 60° to the surface normal and of 300 K Cl_2 , the series of experiments illustrated in Fig. 1 have been performed [23].

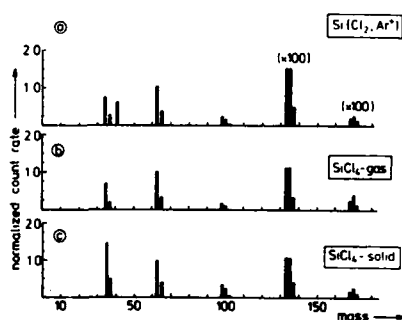


Fig. 1. (a) Mass spectrum of species emitted from silicon under simultaneous exposure to a chlorine-gas beam ($\phi_{\text{Cl}_2} = 3 \times 10^{16} \text{ mol cm}^{-2} \text{ s}^{-1}$) and an argon-ion beam ($E_{\text{Ar}} = 1 \text{ keV}$, $\phi_{\text{Ar}} = 2 \times 10^{14} \text{ ions cm}^{-2} \text{ s}^{-1}$). The signals for SiCl_3^+ and SiCl_4^+ have been multiplied by a factor of 100. (b) Mass spectrum of room-temperature SiCl_4 gas. (c) Mass spectrum of species sputtered by an argon-ion beam ($E_{\text{Ar}} = 1 \text{ keV}$) from solid SiCl_4 , condensed at liquid air temperature. The mass spectra have been obtained with 10 mA of 70 eV ionizing electrons and are normalized to the SiCl^+ signals.

Using the same settings of the mass spectrometer and a modulation frequency of 10 Hz, the mass spectrum of SiCl_4 gas was measured (b) followed by the mass spectrum of the products sputtered from solid SiCl_4 (c) and then by the crossed beams experiment for a relatively high flux ratio R of Cl_2 to Ar^+ of 150 (a) (Note that in Fig. 1a the SiCl_3^+ and SiCl_4^+ peaks have been multiplied by a factor of 100.) A comparison between the mass spectrum of the gas and the bombarded solid SiCl_4 indicates that part of the SiCl_4 molecules in the solid have been fragmented by the Ar^+ ion impact. TOF measurements on the neutral sputtering products from solid SiCl_4 showed that indeed neutral SiCl molecules are sputtered as such with a CC distribution and a binding energy of only 0.08 eV. A comparison of the results of the crossed beams experiment shown in Fig. 1a with those presented in 1b and 1c proves that SiCl and SiCl_2 are major etch products. A recent repetition of these experiments [24] reproduces these early results very well. This work also shows that the TOF distributions of the more chlorinated products SiCl_3 and SiCl_4 lie at about the same position as those of e.g. SiCl_2 . Even a relatively large difference in ionization cross section of the various neutral products, like for SiF_x neutrals [22], does not change this conclusion. The above conclusion remains valid when R is enhanced to about 500 and when the Ar^+ ion energy is reduced to 250 eV, both measures which cause a relative increase in more halogenated products.

More extensive studies on this system [25,26] have shown that

- a. The main species ejected are Si, Cl, SiCl and SiCl_2 and resputtered Ar
- b. The kinetic energy distributions of these products are composed of two contributions: first a CC distribution comprising more than 80% of the total emission and second an MB distribution at target temperature. The latter contribution is ascribed to ion-bombardment enhanced outdiffusion, followed by evaporation at target temperature. The CC distribution shows that the main removal process is physical sputtering of these molecules. An example of a TOF distribution showing both contributions is given in Fig. 2.

Recently [7] TOF distributions can be measured either by modulation of the ion beam or by chopping the product beam: no significant differences have been found for SiCl^+ . This means that the above-mentioned two contributions are far the most important ones and contributions from higher chlorinated SiCl_x are insignificant. Also long residence times do not seem to play an important role, which is, of course, to be expected for

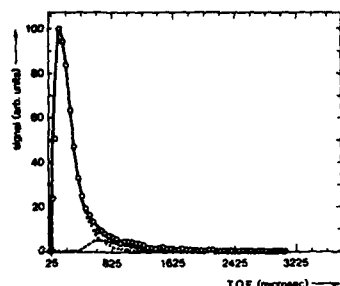


Fig. 2 Time-of-flight distribution of the product SiCl for $\phi_{Cl}/\phi_{Ar^+} = 40$. $\theta_{inc} = 50^\circ$, $\theta_{det} = 0^\circ$. As demonstrated, a combination of 90% of a collision cascade distribution and of 10% of a Maxwell-Boltzmann distribution at $T = 300$ K fits the data quite well.

physical sputtering processes.

In other recent work [27] a systematic study of the effect of R and of the angle-of-incidence of Ar^+ has confirmed earlier indications [26] that the binding energy of the product SiCl increases from values below 0.2 eV at high values of R and incidence close to the normal to values near 0.6 eV for low R values and high incidence angles. These results have been related to the effective amount of chlorine mixed into the Si by the ion bombardment as measured by Mayer's group [28,29]. The value of U_0 decreases with increasing concentration of chlorine mixed into the Si. As expected the sputtering yield increases in the same way [30].

A most intriguing aspect of this chemically enhanced physical sputtering is that the values of U_0 are so low, i.e. only a few tenths of an eV. As discussed in section 3 there is a one-to-one relation between U_0 and the sublimation energy. If the molecules would have been formed in one Ar^+ impact at the surface and then sputtered from there in a following impact it is difficult to understand why they did not evaporate thermally, except when the frequency factor for this thermal process is exceptionally low. That this could be the case may be derived from the data mentioned in Section 2. If the frequency factor has a value near 10^{13} s^{-1} other explanations have to be found for the high sputtering yields of SiCl (and SiCl₂). Essentially three different explanations have been put forward (except the one with the low frequency factor for desorption). All of them [2,3,26,27] agree about the importance of bond breaking and mixing of chlorine into the Si. Mayer's group [3] assumes subsequent reformation of small molecules and sputtering of the molecules by the tail of the same collision cascade that caused the bond breaking. However, reformation of bonds takes more time than the collision cascade takes. Winters [2] assumes direct formation of molecules during the early bond breaking stage of the collision cascade and sputtering of the molecules thus formed by the tail of the same collision cascade. However, it is difficult to understand why, except for a dissociation correction

[32], a complete collision cascade distribution develops, i.e. with also high-velocity molecules, when only the tail of the collision cascade is used. Finally, Dieleman et al. [26,27] have proposed formation of these molecules in the top film during and after one impact and sputtering of these molecules in a subsequent impact. More research into this interesting and technologically important phenomenon will hopefully lead to a more definitive answer.

Very recently measurements have been extended to Ar^+ ion energies down to 75 eV and to bombardment with Xe^+ ions at higher energies [24]. At the lower energies or for the heavier projectile masses the TOF distribution lose their high velocity part or, differently stated, "shift" to longer flight times. For bombardment with very low ion energies the TOF distributions could be fitted reasonably well with MB distributions at about the same high temperature and an MB distribution at target temperature. These results have been interpreted by assuming evaporation from an ion-induced hot spot. More research will have to be done to decide whether this picture (which holds perhaps also for noble gas resputtering) holds or whether this is simply due to insufficiently developed collision cascades or whether this is equivalent.

For Cu exposed to crossed beams of Cl_2 and low-energy Ar^+ ions the sputtering yield decreases slightly as compared to sputtering with Ar^+ ions alone [13]. Further studies, as described above for Si, will have to be performed to understand this behaviour.

5. CROSSED BEAMS OF EXCIMER LASERS AND Cl_2

The results to be reviewed in this section pertain to the etching of Si and Cu surfaces when exposed to crossed beams of nanosecond excimer laser pulses of mostly 308 nm and a continuous Cl_2 beam (or background pressure) corresponding to an effective pressure at the Si or Cu surface of at most about 10^{-4} Torr. This means that experiments performed at much higher Cl_2 background pressures [32-34] will not be reviewed here.

Recently, some studies on the mechanism of nanosecond excimer laser etching of Si concurrently exposed to Cl_2 at an effective pressure up to about 10^{-4} Torr have been performed [35-38]. At laser pulse fluences up to 0.4 Jcm^{-2} for 308 nm and 1.0 Jcm^{-2} for 248 nm and in the Cl_2 pressure range indicated above Si is easily etched with a maximum etch rate of 30

A per laser pulse. The main products observed are Cl, SiCl and SiCl₂. The TOF distributions can be fitted quite well with MB distributions at temperatures in the range 1400 to 4000 K. The temperature increases with laser pulse fluence and with chlorine pressure up to a pressure of about 10⁻⁴ Torr (at least for a repetition rate of 4 Hz). Each pulse removes all of the chlorine absorbed in the time between two pulses. The most intriguing observation is the increase of the particle temperature with Cl₂ pressure (which is equivalent to surface coverage) until a surface coverage of one monolayer between two laser pulses is reached. Studies on the rovibrational excitation of the product SiCl have shown that these molecules are also internally very hot. This is at least partially consistent with time-resolved reflectivity studies, which indicate that for the higher Cl₂ pressures and laser pulse fluences the laser pulse melts the Si surface. No definitive conclusion has been reached as yet about the desorption mechanism. The most recent studies [38] indicate that, except at the lowest pressures, the desorbing particles interact above the surface. Of course this effect has to be separated from the desorption-induced external and internal energy distributions.

Also for Cu exposed to crossed beams of nanosecond excimer laser pulses at various wavelengths and Cl₂ at effective pressures below 10⁻⁴ Torr relatively little studies have been published [39-42]. In none of these publications attention has been paid to effects of interaction of desorbed particles above the substrate, like described in Ref. 21. This holds almost completely for the work of Osgood et al. [40] and completely for that of Chuang et al. [39]. So it is not possible to draw more definitive conclusions about the mechanisms responsible for the observed high velocities of the desorbed species. In our own work some experimental conditions occurred where this interaction was absent. In addition some data have been collected about the laser-induced modification of Cu surfaces in the presence of a Cl₂ beam. For these reasons the discussion here will be restricted to some of our data.

When Cu containing minute amounts of chlorine is exposed to nanosecond excimer laser pulses at 308 nm in UHV, some Cu₃Cl₃ is desorbed. The kinetic energy distribution of these molecules can be fitted by a Maxwell-Boltzmann distribution at temperatures corresponding very well to those calculated on the basis of the temperature induced in the Cu surface by absorption from the laser pulse. This temperature rises linearly with laser pulse fluence. Of course, this indicates a thermal desorption mechanism. When a clean Cu sample is exposed to crossed beams of nanosecond excimer laser pulses and low pressure Cl₂ beams, the etch

rate at the start of the experiment is no more than about 1% of a monolayer. The TOF distributions of the main products Cu_3Cl_3 and CuCl are fitted quite well with Maxwell-Boltzmann distributions at temperature not very different from those mentioned above. However, the etch rate increases with exposure till a steady state etch rate level is obtained. The TOF distributions of the products remain Maxwell-Boltzmann, but the corresponding temperature rises with exposure till the steady state is reached.

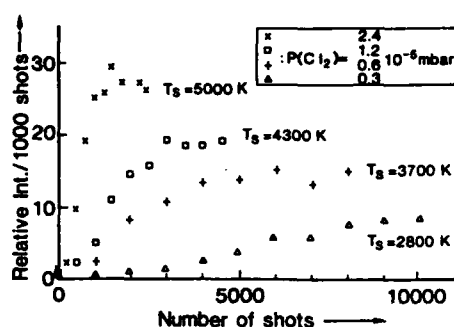


Fig. 3. Evolution of the flux of Cu_3Cl_3 leaving the target as a function of the number of laser shots after the beginning of exposure of a clean Cu surface to Cl_2 for the four values of P_{Cl_2} indicated in the figure. The laser pulse fluence is fixed at 0.45 J cm^{-2} . The steady-state temperature of the ejected Cu_3Cl_3 is also indicated. $1 \text{ mbar} = 10^2 \text{ Pa}$.

As illustrated in Fig. 3 the steady state level is reached faster the higher the Cl_2 pressure and the steady state "temperature" increases.

Fig. 4 shows that the build-up to the steady state (S) etch rate level is accompanied by a build-up of a rather thick chlorinated Cu surface film. The explanation of these observations is rather straightforward. At the start of the exposure the chlorine adsorbed is only for a small part desorbed from the surface. Because the Cu surface is heated by the laser pulse part of the chlorine remaining will diffuse into the Cu. This process will go on till the chlorinated surface film is so thick that all chlorine sticking to the surface in between laser pulses is removed.

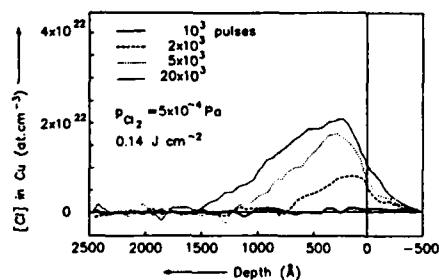


Fig. 4. Cl profiles in etched single-crystal Cu (100) at various stages of the buildup to S for $F = 0.14 \text{ J cm}^{-2}$, $P_{\text{Cl}_2} = 5 \times 10^{-4} \text{ Pa}$, and $n = (1, 2, 5, \text{ and } 20) \times 10^3$, respectively. The latter is the S profile. The zero is indicated for ^{35}Cl only. Resolution is 200 Å .

Because the heat conductivity of the CuCl is lower than that of Cu metal also higher temperatures may occur, as observed. But because the TOF distributions will be obscured by interaction between the desorbing species, the temperature corresponding to the MB distribution measured will not be a true measure of the surface temperature.

6. CONCLUSION

The review clearly demonstrates the fascinating and important role chemically active adsorbates play in low-energy ion- and laser-assisted etching. It also shows that much remains to be done to get a better qualitative understanding of the underlying mechanisms.

REFERENCES

1. H.F. Winters, J.W. Coburn and T.J. Chuang, J. Vac. Sci. Technol. B1, 469 (1983)
2. H.F. Winters, J. Vac. Sci. Technol. A6, 1997 (1988)
3. T.M. Mayer, M.S. Ameen and D.J. Vitkavage, in The Chemical Physics of Solid Surfaces and Heterogeneous Catalysis Vol. 5: Surface Properties of Electronic Materials, edited by D.A. King and D.P. Woodruff (Elsevier Science Publishers, New York, 1988), p. 427
4. D.J. Oostra and A.E. de Vries, Nucl. Instr. and Meth. B18, 618 (1987)
5. P.C. Zalm, Vacuum 36, 787 (1986); Surf. Interf. Anal. 11, 1 (1988)
6. A.W. Kofschoten, Nucl. Instr. and Meth. B19/20, 1001 (1987)
7. J. Dieleman, in Photon, Beam and Plasma Enhanced Processes, edited by A. Golanski, V.T. Nguyen and E.F. Krimmel (European Mat. Res. Soc. Proc. XV, les éditions de physiques, Les Ulis, France), p. 363 (1988):
8. J.V. Florio and W.D. Robertson, Surf. Sci. 18, 398 (1969)
9. R.J. Madix and J.A. Schwarz, Surf. Sci. 24, 264 (1971)
10. F.H.M. Sanders, A.W. Kofschoten, J. Dieleman, R.A. Haring, A. Haring and A.E. de Vries, J. Vac. Sci. Technol. A2, 481 (1984)

11. M. Seel and P.S. Bagus, Phys. Rev. B28, 2023 (1983)
12. H.F. Winters, J. Vac. Sci. Technol. A3, 786 (1985)
13. S. Park, T.N. Rhodin and L.C. Rathbun, J. Vac. Sci. Technol. A4, 168 (1986)
14. W. Sesselman and T.J. Chuang, Surf. Sci. 176, 32 (1986); 176, 67 (1986)
15. M. Szymonski, Appl. Phys. 23, 89 (1980)
16. J. Dieleman, Le Vide-Les Couches Minces, Suppl. to Vol. 218, 3 (1983)
17. J. Dembovski, H. Oechsner, Y. Yamamura and M. Urbassek, Nucl. Instr. and Meth. B18, 464 (1987)
18. R.A. Brizzolara, C.B. Cooper and T.K. Olson, Nucl. Instr. and Meth. B35, 36 (1988)
19. G.N.A. van Veen, F.H.M. Sanders, J. Dieleman, A. van Veen, D.J. Oostra and A.E. de Vries, Phys. Rev. Lett. 57, 739 (1986)
20. J. van Zwol, S.T. de Zwart, and J. Dieleman, to be published
21. R. Kelly and R.W. Dreyfus, Surf. Sci. 198, 263 (1988)
22. T.R. Hayes, R.C. Wetzel, F.A. Baiocchi and R.S. Freund, J. Chem. Phys. 88, 823 (1988); T.R. Hayes, R.J. Thul, F.A. Baiocchi, R.C. Wetzel and R.S. Freund, *ibid.* 89, 4035 (1988); R.J. Shul, T.R. Hayes, R.C. Wetzel, F.A. Baiocchi and R.S. Freund, *ibid.* 89, 4042 (1988)
23. A.W. Kolfschoten, R.A. Haring, A. Haring and A.E. de Vries, J. Appl. Phys. 55, 3813 (1984)
24. D.J. Oostra, A. Haring, R.P. van Ingen and A.E. de Vries, J. Appl. Phys. 64, 315 (1988)
25. F.H.M. Sanders, A.W. Kolfschoten, J. Dieleman, R.A. Haring, A. Haring and A.E. de Vries, J. Vac. Sci. Technol. A2, 487 (1984)
26. J. Dieleman, F.H.M. Sanders, A.W. Kolfschoten, P.C. Zalm, A.E. de Vries and A. Haring, J. Vac. Sci. Technol. B3, 1384 (1985)
27. J. van Zwol, J. van Laar, A.W. Kolfschoten and J. Dieleman, J. Vac. Sci. Technol. B5, 1410 (1987)
28. T. Mizutani, C.J. Dale, W.K. Chu and T.M. Mayer, Nucl. Instr. and Meth. B7/8, 825 (1985)
29. E.L. Barish, D.J. Vitkavage and T.M. Mayer, J. Appl. Phys. 57, 1336 (1985)
30. P.C. Zalm, A.W. Kolfschoten, F.H.M. Sanders and P. Vischer, Nucl. Instr. and Meth. B18, 625 (1987)
31. R.A. Haring, H.E. Roosendaal and P.C. Zalm, Nucl. Instr. and Meth. B28, 205 (1987)
32. Y. Horiike, N. Hayasaka, M. Sekine, T. Arikado, M. Nakase and H. Okano, Appl. Phys. A44, 313 (1987)

33. R. Kullmer and D. Bäuerle, Appl. Phys. A43, 227 (1987); P. Mogyrosi, K. Piglmayer, R. Kullmer and D. Bäuerle, *ibid.* 45, 293 (1988)
34. J.J. Ritsko, F. Ho and J. Hurst, Appl. Phys. Lett. 53, 78 (1988)
35. T. Baller, D.J. Oostra, A.E. de Vries and G.N.A. van Veen, J. Appl. Phys. 60, 2321 (1986)
36. R. de Jonge, J. Majoor, K. Benoist and D. de Vries, Europhys. Lett. 2, 843 (1986)
37. T. Baller, G.N.A. van Veen and J. Dieleman, in Photon, Beam and Plasma Enhanced Processes, edited by A. Golanski, V.T. Nguyen and E.F. Krimmel (European Mat. Res. Soc. Proc. XV, les éditions de physique, Les Ulis, France), p. 415 (1988)
38. T.S. Baller, J. van Zwol, S.T. de Zwart, H. Feil and J. Dieleman, paper B3.3 this symposium
39. W. Sesselman, E.E. Marinero and T.J. Chuang, Appl. Phys. A41, 209 (1986)
40. L. Chen, V. Liberman, J.A. O'Neill and R.M. Osgood, in Laser and Particle-Beam Chemical Processing for Microelectronics, edited by D.J. Ehrlich, G.S. Higashi and M.M. Oprysko (Mat. Res. Soc. Proc. 101, Pittsburgh, PA 1988) p. 463
41. T.S. Baller, G.N.A. van Veen and J. Dieleman, J. Vac. Sci. Technol. A6, 1409 (1988)
42. G.N.A. van Veen, T.S. Baller and J. Dieleman, Appl. Phys. A47, 183 (1988)

ION BEAM PROCESSING OF OPTICAL MATERIALS

F. L. Williams, L. L. Boyer, D. W. Reicher, J. J. McNally[†],
G. A. Al-Jumaily^{††}, and J. R. McNeil

University of New Mexico
Department of Electrical and Computer Engineering
Center for High Technology Materials
Albuquerque, NM 87131

ABSTRACT

We have deposited thin films of optical materials using ion beam sputtering and ion assisted deposition techniques. It is possible to obtain good quality film material deposited on substrates at temperatures lower than normally required. Ion assisted deposition influences film stoichiometry and packing density, which in turn determine optical and mechanical properties of the film material. We discuss two general indicators which appear helpful in predicting the degree to which these occur.

1.0 Introduction

The technique of processing optical and electronic materials using low energy ion beams ($E_i < 1500\text{eV}$) has been a subject of research for many years. Two techniques that are used in producing high-quality thin films are ion assisted deposition (IAD)¹⁻⁵ and ion beam sputtering (IBS).^{6,7} The former technique involves bombarding a substrate with ions during deposition of thin film material generated from evaporation or sputtering, and the latter method entails the use of ion beams to produce thin films by sputtering. In the case of IAD, additional surface energy is imparted to the adatoms via ion bombardment during deposition. One distinct advantage of IAD over conventional deposition techniques is that it allows the production of coatings at moderate deposition rates ($1\text{\AA s}^{-1} \leq R_{\text{depo}} \leq 10\text{\AA s}^{-1}$) that have improved properties. Both IBS and IAD allow the production of improved coatings at low substrate temperature ($T_{\text{sub}} \approx 100^\circ\text{C}$). Standard deposition techniques typically require heating substrates to high temperatures ($T_{\text{sub}} \approx 300^\circ\text{C}$) in order to achieve thin films of acceptable optical performance.⁸

Present Address:

[†] Department of Physics
USAF/DFP
United States Air Force Academy, CO 80840
^{††} Barr Associates
Westford, MA 01886

This work supported in part by the Air Force Weapons Laboratory and Los Alamos National Laboratory.

We have investigated the use of both IAD and IBS to produce metal oxide thin films. The first section of this paper will summarize results of IAD applied to thin films of materials typically used in optical coatings, while the second section of this paper describes results of using IBS to deposit an optical nonlinear material, PLZT.

2.0 Ion Assisted Deposition of Optical Coatings at Reduced Substrate Temperature

IAD can increase film packing density and stoichiometry, resulting in improvements in optical properties, environmental stability, abrasion resistance and adhesion.^{1-5,9} Low temperature deposition processes have become increasingly important in practical applications involving certain substrate materials (e.g., plastics¹⁰ and heavy metal fluoride glass^{9,11}), and for increasing throughput for coating large, precision elements. Results presented here will be restricted to substrate temperatures of approximately 100°C.

Thin films were deposited in an apparatus that is described in detail in Reference 12. The thin film starting material was electron beam evaporated at a deposition rate of $\sim 2\text{\AA s}^{-1}$, and the chamber was backfilled with oxygen during deposition to a pressure of $P_{O_2} \sim 10^{-4}$ Torr. Substrates were heated to $\sim 100^\circ\text{C}$ prior to starting the coating process, with the substrate temperature rising to $\sim 125^\circ\text{C}$ at the end of the coating due to heat from the evaporative sources. A Kaufman ion source¹³ provided either argon or oxygen ions for bombarding the substrates. Substrates were ion precleaned with $75\text{ }\mu\text{Acm}^{-2}$ of 500 eV argon ion bombardment for 4 minutes prior to deposition, and then bombarded with oxygen ions during film deposition. The ion current density was measured with a probe mounted on a shutter near the substrate surface.

Coatings of SiO_2 , Al_2O_3 , Ta_2O_5 and TiO_2 were deposited at different levels of oxygen ion energy and current density, and were analyzed for refractive index and extinction coefficient. A homogeneous envelope technique developed by Manafacier *et al.* (1976) was used to determine optical constants from the spectral transmittance of coated samples.¹⁴

Results

Figure 1 illustrates the variation of the index of refraction of Ta_2O_5 films with respect to ion energy and current density deposited using IAD. The upper horizontal axis of the figure represents the arrival ratio γ , which is the ratio of the flux of oxygen atoms from the ion beam to the flux of film atoms arriving at the substrate. It can be seen that the film refractive index of IAD Ta_2O_5 initially increases for a corresponding increase in ion current density, and the rate of increase is greater for greater ion energy. This increase continues until γ reaches a so-called "critical value." Note that essentially bulk values of refractive index (~ 2.28) are attained for the Ta_2O_5 film material for 300 eV ion

bombardment. Films deposited at bombardment levels greater than the critical value exhibit refractive indices that are less than those obtained at current densities below the critical value. The critical value is never attained for films deposited with 150 eV ion energy. Similar characteristics have been observed in films of Al_2O_3 and TiO_2 deposited using IAD.

Thin films of SiO_2 deposited using IAD do not display any significant increase in refractive index. Unbombarded films of SiO_2 have refractive indices (measured at $\sim 350\text{nm}$), of ~ 1.42 , while SiO_2 films deposited using IAD display values of ~ 1.44 . Transmittance spectra of SiO_2 films recorded around the $2.8\ \mu\text{m}$ water optical absorption band, however, show that use of IAD dramatically reduces film water content. Thus, the lack in variation of IAD SiO_2 film refractive index is most likely attributable to the small difference between the index of refraction of water and bulk SiO_2 , rather than a lack of film densification.

The extinction coefficient of IAD Ta_2O_5 also depends on bombardment conditions. Figure 2 illustrates the effect of oxygen IAD on the extinction coefficients of Ta_2O_5 thin films deposited at reduced substrate temperature. Low temperature deposition of Ta_2O_5 by conventional means typically results in absorbing films,¹⁵ as illustrated in Figure 2 by appreciable extinction coefficient ($\sim 15 \times 10^{-4}$) for $J=0$. The extinction coefficient is reduced to values $< 2 \times 10^{-4}$, however, by low-level oxygen ion bombardment, presumably due to improvements in film stoichiometry caused by oxygen ions. *Similar in nature to the effect of IAD on refractive index*, the rate of decrease is greater for greater bombardment energy in the region of decreasing extinction coefficient. For current densities near the critical value, the extinction coefficient begins to increase for increasing current density.

This result is *not* obtained for thin films of Al_2O_3 and TiO_2 deposited using IAD. For these materials, the extinction coefficients are typically low ($k < 4 \times 10^{-4}$) for unbombarded films, and the effect of IAD is to further reduce the extinction coefficients of these materials to values that are less than the sensitivity of our measurement technique. No increase in absorption is observed for an increase in current density.

Discussion

For the materials investigated, the presence of suboxide material can dramatically increase the amount of optical absorption measured in thin films. Because of this, the optical extinction coefficient is a sensitive indicator of metal oxide film stoichiometry.¹⁶ We have examined samples of tantalum and titanium oxides using Rutherford backscattering spectrometry (RBS). In the case of large amounts of absorption there is a correlation between film extinction coefficient and sample substoichiometry. However,

for films of low absorption, RBS techniques are not sufficiently accurate to determine film stoichiometry.¹⁷

A qualitative picture of the response of film extinction coefficient to ion bombardment is provided by the fractional sputtering yield (Y_O/Y_M), which gives the ratio of the oxygen atomic sputtering yield to the metal atomic sputtering yield of a compound metal oxide target. A value of (Y_O/Y_M) > 1 implies that oxygen atoms are more readily sputtered from the surface than are metal atoms, so that ion bombardment results in a reduced metal oxide material. This process is known as preferential sputtering,¹⁸ and is most likely responsible for the increase in extinction coefficients observed from thin films of Ta₂O₅.

Malherbe *et al.* (1986) have developed a method for predicting the composition of metal oxides reduced by ion bombardment.¹⁹ Their argument gives the fractional sputtering yield of a compound target as

$$\frac{Y_O}{Y_M} = \left(\frac{A_M}{A_O} \right)^{1/3} \left(\frac{U_M}{U_O} \right)^{2/3},$$

where A_j and U_j are the atomic weight and surface binding energy, respectively, of the metal (M) and oxygen (O). While the expression for (Y_O/Y_M) was derived for bulk target material, the preferential sputtering for thin films is expected to be approximately the same. Values of (Y_O/Y_M) calculated for the metal oxides investigated in this study are listed in Table 1. The values in Table 1 show that the theory of Malherbe *et al.* is reasonably accurate in predicting the experimental result that use of IAD to deposit Ta₂O₅ produces films having significantly greater optical absorption compared to that of films of Al₂O₃, SiO₂ and TiO₂.

Table 1 Fractional Sputtering Yields

Target	A_M/A_O	U_M/U_O	Y_O/Y_M
Al ₂ O ₃	1.69	0.77	1.00
SiO ₂	1.76	0.81	1.00
TiO ₂	2.99	1.09	1.50
Ta ₂ O ₅	11.31	1.23	2.50

The model for preferential sputtering does not include the effects of bombarding with reactive ions. Reactive ions may engage in specific chemical interactions with the target to synthesize compound thin films.²⁰ Also, oxygen IAD of metal oxides occurs in a reactive atmosphere, where ion bombardment may induce chemical reactions between

neutral gas species and the surface. Such chemically reactive mechanisms are probably responsible for the low values of extinction coefficient observed in TiO_2 thin films deposited with oxygen IAD, even though the theory of preferential sputtering predicts that IAD of TiO_2 should result in reduced thin film material.

Much work has been done in recent years to model the effects of ion bombardment during film growth. The most successful model uses binary collisions and molecular dynamics to explain the densification of ion assisted thin films in terms of surface atom recoil implantation.^{21,22} The results of this model indicate that an increase in sputtering yield increases the probability of a recoil implantation event occurring. For the same material, the sputtering yield will be greater for greater ion energy.²³ Since film refractive index strongly depends on film density, a change in index of refraction is assumed to represent a change in density. Therefore, greater bombardment energies result in greater increases in refractive index for the same increase in ion current density (i.e. greater $\partial n/\partial J$). Greater sputtering yields are also expected for smaller values of target mass. This can be characterized by the kinematic factor κ , which is a measure of the fraction of energy imparted to a target by an energetic projectile. For a projectile of mass M_1 and a target of mass M_2 , the kinematic factor is given by

$$\kappa = \frac{4M_1M_2}{(M_1+M_2)^2}$$

Table 2 lists values of κ for the collisions $\text{O} \rightarrow \text{TiO}_2$, $\text{O} \rightarrow \text{Al}_2\text{O}_3$ and $\text{O} \rightarrow \text{Ta}_2\text{O}_5$. From Table 2, it is seen that the kinematic factor is greater for TiO_2 than for Al_2O_3 , and that the value of κ is greater for Al_2O_3 than for Ta_2O_5 . Thus, although the kinematic factors are consistent with the result that IAD of Al_2O_3 exhibits greater rates of increase in refractive index ($\partial n/\partial \gamma$) than is observed for Ta_2O_5 , there is an inconsistency with the results that ($\partial n/\partial \gamma$) for Al_2O_3 is also greater than that for TiO_2 . This may be due to the fact that oxygen IAD results in generation of crystalline material in thin films of TiO_2 , but does not promote the growth of crystallites in thin films of the other materials investigated.^{5,24}

Table 2 Kinematic factors for O on various metal oxides

Collision	κ
$\text{O} \rightarrow \text{SiO}_2$	0.66
$\text{O} \rightarrow \text{TiO}_2$	0.56
$\text{O} \rightarrow \text{Al}_2\text{O}_3$	0.47
$\text{O} \rightarrow \text{Ta}_2\text{O}_5$	0.13

Competing with bombardment-induced film densification is the mechanism of ion incorporation associated with ion bombardment. Three important observations have been made by researchers investigating the effects of ion bombardment on reactor materials: (1) the ion incorporation probability η is greater for greater ion energy, (2) it is possible for the ion incorporation mechanism to become saturated and (3) there is a threshold ion energy E_T below which no ion incorporation occurs (i.e., $\eta = 0$ for $E_i < E_T$). For the low-energy regime, Carter et al. (1980)²⁵ have derived an approximate expression for E_T

$$E_T \approx 100\pi N a^2 (Z_1 Z_2)^{3/4} ,$$

where E_T is in eV, N is the areal atomic density of the target (atoms m^{-2}), Z_1 and Z_2 are the atomic numbers of the ion and target, respectively, and a is the Andersen-Sigmund range ($a = 2.2 \times 10^{-11} m$).²⁶ The expression for E_T shows that, for the same ion species and flux, bombardment of a lighter target material will result in greater values of η compared to values of η for a heavier target material.

The results reported above may be used to develop a picture which is consistent with material-dependent differences in maximum packing density obtained from IAD of thin films. There is evidence indicating that ion incorporation causes a reduction in film density due to the presence of trapped gas in the film. Therefore, there will be a maximum film density obtained using IAD due to the competing mechanisms of recoil implantation and ion incorporation.

Table 3 lists values of E_T for the collisions $O \rightarrow Al_2O_3$, $O \rightarrow TiO_2$ and $O \rightarrow Ta_2O_5$. Mean atomic numbers were used for Z_1 and Z_2 in the calculation for E_T . For example, in the case of $O \rightarrow Al_2O_3$, $Z_1 = 8$, $Z_2 = 10.5$, and $N = 2.40 \times 10^{19}$ atoms m^{-2} , yielding a value of $E_T = 101$ eV. It can be seen that the estimated threshold energies for ion incorporation to occur in Ta_2O_5 is roughly twice that value for Al_2O_3 and TiO_2 . Thus, for a given ion energy and flux, there is a greater probability of ion incorporation occurring for both Al_2O_3 and TiO_2 compared to the ion incorporation probability for Ta_2O_5 . This result is consistent with the fact that IAD of Ta_2O_5 yields a greater value of maximum film packing density than is achieved using IAD to deposit either Al_2O_3 or TiO_2 . The decrease and saturation in packing density of IAD metal oxide thin films at high ion flux levels may be explained in terms of saturation of the gas trapping mechanism.

Table 3 Ion incorporation threshold energy (E_T) for various collisions

Collision	E_T (eV)
O→SiO ₂	72
O→Al ₂ O ₃	101
O→TiO ₂	108
O→Ta ₂ O ₅	212

3.0 PLZT Film Deposition

Lanthanum-modified lead zirconate-titanate, $Pb_{1-x}La_x(Zr_yTi_{1-y})_{1-x/4}O_3$ or PLZT, is a very attractive class of ceramic material because of its pronounced electro-optic characteristics. In addition, the stoichiometry can be varied to produce material with different characteristics. The material has been investigated in bulk form for a number of years, and more recently in thin film form.^{27,28} Thin film PLZT has numerous possible applications in electronic and electro-optic devices such as FET nonvolatile memory, optical switches, optical displays, and image storage. Most recently, thin film PLZT has been used to frequency double light at 1.06 microns wavelength.²⁹

PLZT thin films were prepared by IBS. The experimental apparatus included a 5 cm Kaufman ion source directed at a pressed powder target of composition (x/y/z) of (28/0/100). The substrates were heated to temperatures ranging from 500°C to 650°C prior to deposition. The ion source was operated with Ar at a pressure of 5×10^{-5} Torr. The chamber was backfilled during deposition with O₂ to a pressure of 2×10^{-4} Torr. Substrates used for this investigation include Si <100>, Si <111>, Si <100> with 2 μ m of SiO₂ as a buffer layer, and fused silica. The thickness of the films were approximately 5000Å. Thin film crystallography was determined by x-ray diffraction (Cu K α radiation). The thin film composition was determined by SEM/EDAX measurements.

Results

Highly oriented PLZT thin films have been obtained with ion beam sputtering. Figure 3 illustrates the x-ray diffraction characteristics of three samples of PLZT deposited on Si at substrate temperatures of approximately 500, 550, and 650°C. The sample deposited at a substrate temperatures of 550°C is highly oriented with only the <100> crystalline orientation of the perovskite form of the material detectable. This is very desirable for applications of the material. The sample deposited at 650°C is very polycrystalline, while the sample deposited at 500°C illustrates the x-ray diffraction characteristics of pyrochlore PLZT. Neither of these other forms of PLZT is desirable for electro-optic applications. Good quality PLZT was also deposited on Si wafers having

a buffer layer of SiO_2 approximately 2 microns thick. This is very encouraging because the configuration can be used as a waveguide structure, and also because this illustrates the compatibility of Si and PLZT technologies. Devices of Si (*e. g.* drivers, etc.) can be produced with PLZT on the same wafer. Good quality PLZT has also been deposited on fused silica substrates.

We have observed second harmonic generation in ion beam sputtered PLZT deposited on the buffer layer of SiO_2 on a Si substrate. The second harmonic conversion increases quadratically with applied electric field in the configuration shown in figure 4, indicating this is a third order effect. The incident wavelength was 1.06 microns, and the reflected beams were 0.53 and 1.06 microns. We are presently characterizing this effect more thoroughly, including extending the incident wavelength to 10.6 μm .

In addition we have observed a significant difference in the surface morphology of IBS and magnetron sputtered samples of PLZT. The IBS sample had an rms roughness approximately 60 percent of that of the magnetron sputtered sample. Excessive surface roughness can prohibit use of the material in applications requiring low optical scatter loss, such as waveguiding. A possible explanation for this difference in surface roughness is the lower pressure at which the ion beam sputtered material was deposited. In addition, the magnetron deposited sample was exposed to an unknown level of ion bombardment as a result of being immersed in the discharge of the arrangement; this was not the case for the ion beam sputtered sample.

4.0. Conclusions

Good quality oxide materials have been deposited on substrates at reduced temperature using IAD techniques. For some film materials, values of bulk refractive index are obtained. Preferential sputtering of oxygen from the film material is sometimes an issue. General indicators of these two behavioral characteristics promoted by ion bombardment include threshold energy for ion incorporation and relative sputter yields of film atomic species. Good quality, highly oriented films of PLZT have been deposited on substrates of Si, Si with a buffer layer of SiO_2 , and fused silica using ion beam sputtering. The material has displayed strong second harmonic generation at 1.06 microns incident wavelength. In addition the surface morphology of the ion beam deposited PLZT appears to be of higher quality than that of r.f. magnetron sputtered films of the same composition.

The authors thank A. Mukherjee and S. R. J. Brueck for second harmonic characterization of PLZT. We also thank Feiling Wang for his photolithography work necessary to characterize these films.

REFERENCES

1. W. C. Herrmann, Jr., and J. R. McNeil, "Ion Beam Applications for Optical Coating," *Optical Thin Films*, Proc. SPIE, 325, 101 (1982).
2. J. M. E. Harper, J. J. Cuomo, and H. R. Kaufman, "Technology and Applications of Broad-Beam Ion Sources Used in Sputtering. Part II. Applications," *J. Vac. Sci. Technol.* 21, 737 (1982).
3. E. H. Hirsch, and I. K. Varga, "Thin Film Annealing by Ion Bombardment," *Thin Solid Films*, 69, 99 (1980).
4. P. J. Martin, H. A. MacLeod, R. P. Netterfield, G. C. Pacey, and W. G. Sainty, "Ion Beam-Assisted Deposition of Thin Films," *Appl. Opt.* 22, 178 (1983).
5. F. L. Williams, D. W. Reicher, C.-B. Juang, and J. R. McNeil, "Metal Oxides Deposited Using Ion Assisted Deposition at Low Temperature," *J. Vac. Sci. Technol.* A7, in press (1989).
6. J. R. Sites, P. Gilstrap, and R. Rujkorakarn, "Ion Beam Sputter Deposition of Optical Coatings," *Opt. Eng.* 22, 447, (1983).
7. J. M. E. Harper, J. J. Cuomo, and H. T. G. Hentzell, "Quantitative Ion Beam Process for the Deposition of Compound Thin Films," *Appl. Phys. Lett.*, 43, 547 (1983).
8. S. Ogura, and H. A. Macleod, "Water Sorption Phenomena in Optical Thin Films," *Thin Solid Films*, 34, 371 (1976).
9. J. J. McNally, G. A. Al-Jumaily, J. R. McNeil, and B. Bendow, "Ion Assisted Deposition of Optical and Protective Coatings for Heavy Metal Fluoride Glass," *Appl. Opt.*, 25, 1973 (1986).
10. R. E. Hurley, and E. W. Williams, "Ion Plating on Plastic Substrates," *Thin Solid Films*, 92, 99 (1982).
11. D. C. Tran, G. H. Sigel, Jr., and B. Bendow, "Heavy Metal Fluoride Glasses and Fibers, A Review," *J. Lightwave Technol.*, 2, 566 (1984).
12. J. J. McNally, K. C. Jungling, F. L. Williams, and J. R. McNeil, "Optical Coatings Deposited Using Ion Assisted Deposition," *J. Vac. Sci. Technol.*, A5, 2145 (1987).
13. H. R. Kaufman, J. J. Cuomo, and J. M. E. Harper, "Technology and Applications of Broad-Beam Ion Sources Used in Sputtering. Part I. Ion Source Technology," *J. Vac. Sci. Technol.*, 21, 725 (1982).
14. J. C. Manafacier, J. Gasiot, and J. P. Fillard, "A Simple Method for the Determination of the Optical Constants n , k and the Thickness of a Weakly Absorbing Thin Film," *J. Phys. E. Sci. Instru.*, 9, 1002 (1976).
15. W. C. Herrmann, Jr., "E-Beam Deposition Characteristics of Reactively Evaporated Ta_2O_5 for Optical Interference Coatings," *J. Vac. Sci. Technol.*, 18, 1303 (1981).
16. H. Demiryont, J. R. Sites and K. Geib, "Effects of Oxygen Content on the Optical Properties of Tantalum Oxide Films Deposited by Ion-Beam Sputtering," *Appl. Opt.* 24, 490 (1985).
17. R. Behrisch, and B. M. U. Scherzer, "Rutherford Backscattering as a Tool to Determine Electronic Stopping Powers in Solids," *Thin Solid Films*, 19, 247 (1973).
18. S. Hofmann, and J. M. Sanz, "Quantitative XPS Analysis of the Surface Layer of Anodic Oxides Obtained During Depth Profiling by Sputtering with 3 keV Ar^+ Ions," *J. Trace Microprobe Tech.*, 1, 213 (1982-1983).
19. J. B. Malherbe, S. Hofmann, and J. M. Sanz, "Preferential Sputtering of Oxides: A Comparison of Model Predictions with Experimental Data," *Appl. Surf. Sci.*, 27, 355 (1986).
20. R. P. Netterfield, K. -H. Mueller, D. R. McKenzie, M. J. Goonan, and P. J. Martin, "Growth Dynamics of Aluminum Nitride and Aluminum Oxide Thin-Films Synthesized by Ion-Assisted Deposition," *J. Appl. Phys.*, 63, 760 (1988).
21. K. -H. Mueller, "Model for Ion Assisted Thin-Film Densification," *J. Appl. Phys.*, 59, 2803 (1986).

22. K. -H. Mueller, "Ion-Beam-Induced Epitaxial Vapor-Phase Growth: A Molecular-Dynamics Study," *Phys. Rev.*, **B35**, 7906 (1987).
23. P. Sigmund, "Theory of Sputtering, I. Sputtering Yield of Amorphous and Polycrystalline Targets," *Phys. Rev.*, **184**, 383 (1969).
24. F. L. Williams, R. D. Jacobson, J. R. McNeil, G. J. Exarhos and J. J. McNally, "Optical Characteristics of Thin Films Deposited at Low Temperature Using Ion Assisted Deposition," *J. Vac. Sci. Technol.*, **A6**, 2020 (1988).
25. G. Carter, D. G. Armour, S. E. Donnelly, and R. P. Webb, "The Injection of Gas Ions into Solids: Their Trapping and Escape," *Rad. Eff.*, **53**, 143 (1980).
26. H. H. Andersen, and P. Sigmund, "Defect Distributions in Channeling Experiments," *Nucl. Instru. Meth.*, **38**, 238 (1965).
27. H. Higashino, T. Kawaguchi, H. Adachi, T. Makino, and O. Yamazaki, "High Speed Optical TIR Switches Using PLZT Thin-Film Waveguides on Sapphire," *Proc. of the 6th Intl. Meeting on Ferroelec.*, Kobe 1985, *Jap. J. Appl. Phys.*, **24**, supplement 24-2, 284 (1985).
28. H. Adachi, T. Mitsuyu, O. Yamazaki, and K. Wasa, "Bragg A-O Deflector Using A Piezoelectric PLZT Thin Film," *Proc. of the 6th Intl. Meeting on Ferroelect.*, Kobe 1985, *Jap. J. Appl. Phys.*, **24**, supplement 24-3, 287 (1985).
29. A. Mukherjee, S. R. J. Brueck, and A. Y. Wu, "Electric Field Induced Second Harmonic Generation in PLZT," to be published, (1989).

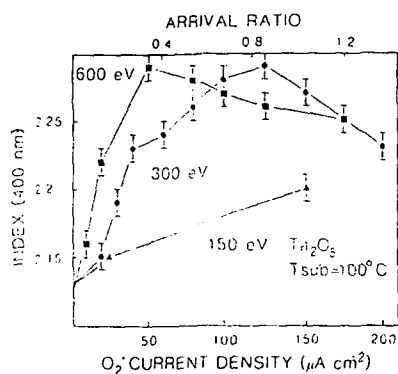


Fig. 1. Variation of film index of refraction with bombarding oxygen ion energy and current density

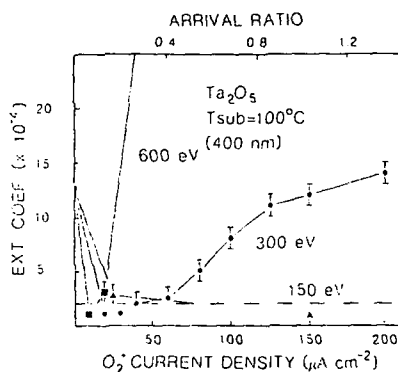


Fig. 2. Variation of film extinction coefficient with bombarding oxygen ion energy and current density.

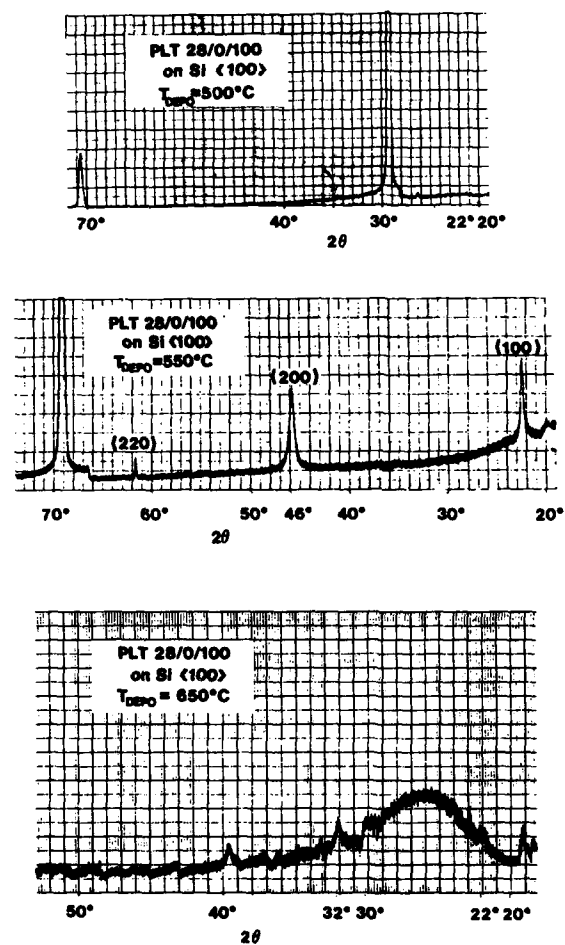


Fig. 3. X-ray diffraction characteristics of PLZT thin film material ion beam sputter deposited on Si substrates at temperature of 500, 550 and 650°C .

ELECTRIC FIELD INDUCED SECOND HARMONIC GENERATION

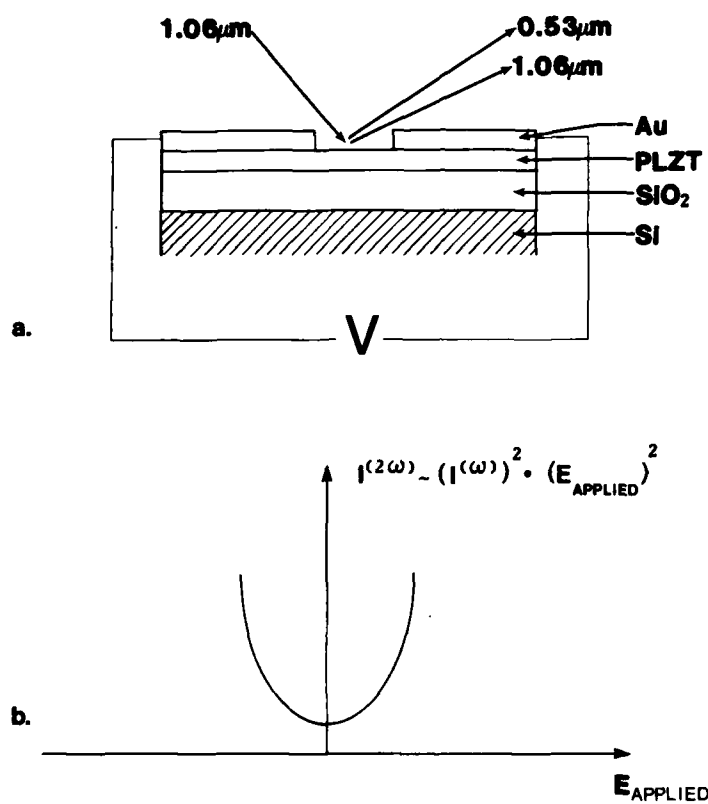


Fig. 4. Field induced second harmonic generation of PLZT thin film material ion beam sputter deposited onto a Si substrate having a buffer layer of SiO₂; (a) schematic illustration of the process; and (b) variation of the intensity of the second harmonic signal with applied field.

ATOMIC-SCALE MODELING OF LOW-ENERGY ION-SOLID PROCESSES

BRIAN W. DODSON

Sandia National Laboratories, Albuquerque, NM 87185-5800

ABSTRACT

Various techniques which have been applied to modeling low-energy ($\ll 1$ keV) ion-solid interactions on an atomistic scale are described. In addition to their individual strengths, all such methods also have a number of drawbacks, both fundamental and practical. The range of validity, and the problems encountered external to this range, will be outlined for the different approaches. Finally, examples of molecular dynamics simulations of low-energy ion-solid interactions will be presented.

INTRODUCTION

Growth, surface modification, and doping of artificially structured materials (both metals and semiconductors) using low-energy ($\ll 1$ keV) ion-beams is currently under intense experimental study. The kinetic energy associated with the ion beam can control important effects in near-surface structural kinetics. Such effects include reactive ion cleaning/etching¹, control of surface growth nucleation sites², control over growth morphology³, including relative orientation of epitaxial growth⁴, production of non-equilibrium doping profiles⁵, growth of metastable epitaxial semiconductor alloys⁶, and depth-limited oxidation of semiconductor surfaces.⁷ The growth and fabrication opportunities presented have generated considerable excitement in this field of research.

Rather than pursuing the purely empirical approach of doing every possible experiment, however, it appears more reasonable to establish the behavior of the dominant mechanisms through a carefully chosen subset of experiments, and then develop procedures to predict the behavior of those mechanisms under a wide range of conditions. Such considerations have driven considerable effort on atomic-scale modeling of low-energy ion-solid processes.

This paper reflects an attempt to review the special aspects of modeling low-energy ion beam processes on an atomistic scale. The low-energy regime is defined in physical terms, and the general nature of ion collisions, cascade formation, and healing of the target material is described. The interaction of a low-energy ion with the target is described in detail, because many of the relevant interactions are not important in conventional high-energy beam processes. The three major classes of simulation techniques are then outlined, along with a discussion of the validity of their underlying assumptions in the low-energy regime. Finally, we illustrate the current status of atomic-scale modeling as applied to low-energy ion beam processes through examples of state-of-the-art simulations.

WHAT ARE 'LOW-ENERGY' ION BEAMS?

It is useful to establish physically based limits on the "low-energy" ion beam regime. (Note that we shall call any energetic species impinging on a solid surface an ion, even if it is uncharged.) At the lower end, a reasonable cutoff provides that the kinetic energy of the incoming ions is similar to chemisorption energies for that ionic species on the substrate in question. Note that this energy can, for chemically reactive species, be much higher than typical thermal energies of, e.g., an MBE source. (Thermal energies in an MBE deposition process are typically 0.1-0.2 eV, whereas chemisorption energies for most semiconductors are several eV.) The reason for this choice is that the energy released in forming the chemical bonds is largely dissipated as phonon-like excitations and lattice distortions, which serve to perturb the local environment of the chemisorbed species in a manner similar to the effect of excess kinetic energy supplied by ion beam deposition. A reasonable lower limit for the "low-energy" beam regime in most cases is thus 5-10 eV.

Establishing an upper limit for the "low-energy" regime is not as straightforward. For example, one physically based limit is that the beam velocity should be less than the Fermi velocity of the valence electrons of the target material. This limit generally corresponds to beam energies of several hundred keV, and thus appears much larger than appropriate for our current purposes. A more reasonable limit can be set by determining in what energy range the approximations used in modeling high-energy ($>>10$ keV) ion beam interactions begin to break down. In the high-energy regime, the energetic particles are modeled as "soft-spheres", having monotonically decreasing pairwise repulsive interactions. This is quite reasonable, as rapidly moving atoms do not have time to form chemical bonds (to do so, the residence time Δt of the atoms must be $>> \hbar/\Delta E$; at typical bonding energies ($\Delta E \approx 1$ eV), Δt is about 1 femtosecond (fsec); in fact, Δt for a 100 keV particle is about 0.1 fsec). In addition, the bonds between substrate atoms do not contribute significant inelastic losses, again because of the disparity in energy scales. At the same time, the pairwise interaction approximation is also appropriate because the dominant interactions take place at small interatomic radii. As a result, the "soft-sphere" approximation is quite reasonable in the high-energy regime.

When does this "soft-sphere" pairwise interaction approximation break down? Discussion of this multifaceted question will take up a significant part of this review. However, various approaches to this question suggest that the high-energy interaction approximation breaks down noticeably at beam energies of a few hundred eV. In addition, the 'breakeven' energy for substrate sputtering (where the beam flux equals the sputtering rate) is on the order of 1000 eV for many systems. For this review, then, the low-energy regime encompasses beam energies of roughly 10-1000 eV. This criterion also agrees with the requirement, in ion-beam deposition, that sputtering processes are limited enough that a positive net flux to the surface is retained.

ATOMIC-SCALE SIMULATION OF LOW-ENERGY ION-SOLID PROCESSES

The overall process of interaction of an energetic ion with a solid can be broken down into three major regimes, each occurring on a different timescale. The first is the collisional regime, in which the incoming ion transfers its kinetic energy to the solid. This can take place either through direct nuclear collisions with the atoms of the solid, or by inducing transitions in the electrons of the solid. The nonequilibrium structure of displaced and/or highly energetic atoms formed within the solid in this period is usually called the collision cascade. The underlying crystal structure of

the solid is often completely disrupted in the cascade, with an accumulation of vacancies in the central region of the cascade and a corresponding number of interstitials generated around the periphery by the action of 'dynamic crowdions'.⁸ The characteristic timescale for development of this structure is a few tenths of a picosecond in the low-energy regime.

The second major process is that of thermalization of the cascade region. Energetic atoms will lose their excess kinetic energy through generation of phonons in the surrounding material. The thermalization regime ends when the cascade region has settled to local thermal equilibrium with the surrounding material, so that the temperature is constant across the region. This will generally occur within a few psec for cascades generated by low-energy ion impact.

Following the collisional and thermalization regimes, the cascade region still exhibits a considerable degree of damage. Over the course of time, this damage may be healed by diffusional processes, or by the action of other incoming ions or atoms (e.g., in ion-assisted growth). The rate of further evolution is a strong function of the experimental conditions, but will typically take place on a timescale which is not amenable to direct atomic-scale simulation. As a result, the primary foci for atomistic simulation of ion-beam processes are the collisional and thermalization regimes, where the relevant physics takes place during the first few psec of interaction.

There are three general classes of simulation techniques for study of atomic-scale structure generated by low-energy ion-solid events. The simplest, and most widely used for high-energy ion processes, are the Monte Carlo methods, with the TRIM-based codes⁹ providing the best-known examples. In this approach, a moving particle approaches an initial atom with a randomly chosen impact parameter. The binary collision approximation, which assumes that the collision dynamics is dominated by the interaction of only the closest atom, allows the collision to be treated as a simple binary scattering event. The impact parameter, the particle masses, and the relative velocity of the two particles, when combined with an interaction potential, allow calculation of the scattering integral, which yields the amount of energy transferred to the solid atom. The ion follows a straight line between subsequent collisions. The angle of deviation in the collision, however, is not used (in pure TRIM-type simulations) to evaluate the distance to the next collision. Instead, the solid is assumed to be amorphous, and the distance and impact parameter for the next collision are chosen randomly based on the average properties of the solid lattice. (One common technique is to rotate the lattice to a random orientation, and project the initial ion trajectory until an impact parameter less than a cutoff value is found.) The scattering integral for this binary collision is then evaluated, and the procedure iterated until the kinetic energy of the incoming ion is dissipated.

The previous paragraph describes only the simplest Monte Carlo ion range simulations. For treatment of cascades, the solid atoms to which substantial amounts of kinetic energy have been transferred must also be followed, as they can produce secondary cascades. To obtain the lateral extent of a cascade, more information about the lattice structure and deflection angle of the collisions must be included in the simulation. Evaluation of the extent of permanent damage is accomplished by identifying an average 'displacement energy' for formation of an interstitial-vacancy pair. In all cases, however, Monte Carlo simulations are essentially pragmatically defined stochastic descriptions with limited basis in first-principles. They provide reasonable accuracy for the collisional regime of high-energy ions because the various approximations applied to the collisions apply there and a given ion experiences a large number of collisions. Thus treating each collision as a statistical average is reasonable, and a highly refined empirical fitting process has been developed over several decades. In the low-energy regime,

however, essentially all of the approximations used in development of Monte Carlo techniques break down. As a result, it is not reasonable to blindly apply this class of simulation to low-energy ion-solid processes. In addition, Monte Carlo techniques are incapable of treating the thermalization regime. Despite these limitations, these are the most commonly used procedures at this time.

A significant refinement of the Monte Carlo techniques is sometimes called the binary-collision lattice technique. The best-known code of this type is probably MARLOWE.¹⁰ These techniques follow the Monte Carlo procedures, save for two factors. First, rather than assuming an amorphous lattice, the actual lattice of the solid determines the trajectories of the incoming ions. Second, the angle of deflection is calculated in each binary collision. The trajectory through the lattice is then followed from collision to collision throughout the lattice until the kinetic energy is dissipated. The result is a deterministic calculation of the ion trajectory and the corresponding cascade, fixed by the crystal lattice, interaction potential, and the initial beam trajectory. Much of the stochastic nature which is the downfall of the Monte Carlo techniques is absent in these binary-collision lattice simulations. This procedure is more accurate for range calculations, because lattice effects, such as channeling, are included. It also provides a more natural description of cascade structure, since the lateral evolution of the cascade is included naturally. However, the treatment of lattice damage is still probabilistic in nature (based on an average displacement energy), the collisions are still assumed to be binary in nature, and the moving particle is assumed to travel on straight lines between these binary collisions. All of these assumptions are questionable in the low-energy regime. Again, the thermalization process cannot be properly treated by this class of techniques.

Finally, the molecular dynamics techniques¹¹ provide a description of ion-solid processes as accurate as the description of interactions between the various parts of the system. In this approach, the Newtonian equations of motion of the individual atoms are integrated in time to obtain the actual trajectory of the entire system through phase space. (For beam energies above 10 eV, the deBroglie wavelength of an ion is several orders of magnitude less than interatomic spacings. The classical trajectory approximation is therefore justified.) This is a wholly deterministic procedure, and naturally includes lattice damage, collective effects of the solid, and simultaneous interactions amongst several particles. In principle, then, the molecular dynamics techniques are the ideal approach toward low-energy ion-solid process simulation, including both the collisional and thermalization phases. The difficulty is that these techniques are orders of magnitude more difficult to carry out from a computational viewpoint. As a result, only a handful of such simulations have been performed at this time.

In this section, three general classes of ion-solid simulations were outlined. Application of these techniques requires various approximations which are perhaps reasonable (at least on average) in the high-energy regime, but which appear likely to fail at low ion energies. The amorphous solid approximation does not even include particle channeling, which is a common effect in the high-energy regime. The binary collision approximation is likely to break down at low energies, where the distance of closest approach is not dramatically smaller than interatomic distances on average. In addition, inelastic interaction with collective modes of the solid can become a dominant influence at low beam energies. The approximation that trajectories are straight between collisions is seriously wrong when the kinetic energy is within an order of magnitude of binding energies in the solid. The statistical approach toward generation of lattice damage is questionable when an ion interacts with only a small number of atoms before thermalizing. Most of the above approximations can be avoided in molecular dynamics simulations.

However, choice of appropriate interactions between the atoms of the solid, and between those atoms and the incoming ion, will always represent a significant approximation. The description of these interatomic interactions defines the fundamental physics controlling the ion-solid processes. Various approximations used to describe these interactions are described in the following section.

ENERGETICS OF LOW-ENERGY ION-SOLID INTERACTIONS

The overall interaction of an energetic ion with a solid results from a complex combination of electronic and nuclear (collisional) interactions. Contributions from electronic interactions include the classical Bohr stopping power, in which kinetic energy is lost to the work required to displace a stationary electron gas, particle-hole creation, excitation of plasmons, charge transfer reactions, and related effects. A classical image charge interaction with the surface may also be present. The nuclear interactions, which are usually treated as interatomic potentials, include the ion-solid interaction potential as well as the solid-solid atomic interaction potential.

Fully accurate treatment of all these interactions poses an extremely difficult problem. Fortunately, in any given energy region, some factors of the overall interaction dominate. In the high-energy regime, for example, the usual approximation is that the ion-solid interaction potential is a sum of purely repulsive pairwise screened Coulomb potentials between the cores of the interacting particles, combined with exchange and correlation energies based on a simple density-functional model and superposition of static charge densities. (An example is the widely used "universal" nuclear interaction potential developed by Ziegler, Biersack, and Littmark.¹²) The electronic interaction is often treated by invoking an electron-density and velocity-dependent "frictional force", which is primarily due to the Bohr stopping power. Factors which are generally ignored in this limit are the image potential, the interaction between the atoms of the solid, and the various localized electronic excitations.

The interactions appropriate for the low-energy regime differ considerably. At low energies, the Bohr electronic stopping power is very small, and can usually be ignored; however, the image potential, charge exchange reactions, and the localized electronic excitations can be quite important. The repulsive nuclear ion-solid interaction used in the high-energy regime is also inappropriate for low-energy interactions, because there can be time for atomic polarization and chemical bonding effects to provide significant attractive interactions. It is also necessary to include solid-state bonding in the target, as the ion trajectories and rate of energy transfer to collective excitations of the solid lattice can also be significant for low-energy ion-solid processes.

In order to model low-energy ion-solid interactions with any of the atomic-scale simulation techniques, tractable approximations for the dominant scattering mechanisms are necessary. The primary difficulty is presented by the ion-solid nuclear and image potentials. In both cases, the high-energy formalism assumes that the ion-atom interaction time is short enough (or equivalently, the ion approaches the surface quickly enough) that redistribution of the valence electrons does not take place. As a result, at sufficiently high beam energies screened Coulomb potentials provide an adequate description of the ion-atom interaction, and there is little or no image potential.

If the ion is moving slowly enough, however, the high-energy formalism breaks down. In the limit of very slow motion, both the ion-solid and the image charge interactions should be treated as adiabatic processes using the

Born-Oppenheimer approximation. In adiabatic interactions, the electrons are always in stationary eigenstates of the current nuclear configuration. As a result, chemical bonding interactions will form, and methods developed for treatment of chemical and solid-state bonding are appropriate for obtaining the ion-solid potential energy surface describing the collision dynamics. Similarly, the polarization of the valence electrons which is responsible for the image potential also has time to develop, and the conventional description in terms of the dielectric constant of the solid is appropriate in this limit. Note that in both high-energy and extremely low-energy processes these effects depend only on the instantaneous positions of the interacting atoms.

NONADIABATIC EFFECTS IN LOW-ENERGY ION-BEAM PROCESSES

In the low-energy regime, the system may not have time during the residence period to fully attain the adiabatic limit. Some degree of electronic redistribution, which may perhaps be described as formation of nascent chemical bonds (which we may term 'protobonds' or 'protobonding interactions'), should occur during the interaction, but the adiabatic (or equilibrium) bonding configurations may not have time to form. (Equivalent statements apply for the image potential.) In this situation, the nature and strength of the ion-atom nuclear interaction will depend not only on the present positions of the particles, but also on the relative velocity and past trajectories of the ion-atom pair. In this intermediate energy range, then, the ion-atom interaction must be treated using a velocity and history-dependent description.¹³

The crossover energy between the high-energy and adiabatic beam energy regimes can be estimated by comparing the timescale for development of bonding interactions with the ion-atom residence period. A typical residence period for low-energy ions is several femtoseconds. It is very difficult, however, to calculate the timescale for formation of protobonds within a time-dependent quantum-mechanical framework. Because of this, several relevant semiclassical estimates are considered, which together establish a qualitative lower limit on the timescale for formation of significant bonding interactions. The uncertainty principle can be used to determine if there is sufficient residence time for bonding interactions to be physically meaningful. From the energy-time uncertainty relation, the residence time required to make bonding interactions physically meaningful is about 0.5 fsec. Protobond formation during low-energy ion-atom encounters is thus meaningful within a quantum-mechanical framework.

Formation of protobonds within the residence period also requires that the electrons move fast enough to redistribute within the residence period, and that the force on the electrons from the forces driving the formations of the protobonds be large enough to drive the redistribution on the same timescale. The first condition requires that the ion be moving much slower than the Fermi velocity, which for metals and semiconductors is generally about two orders of magnitude higher than low-energy ion velocities. The second condition requires that the bonding force on the valence electrons be large enough to cause the electrons to drift on the order of 1 Å during the residence period. This force is on the order of $\Delta E/\Delta x$, or about 1 eV/Å. Upon integration, the time required for an electron distribution to drift 1 Å in a field of this magnitude is about 0.3 fsec, again very small compared to the residence timescale.

These independent semiclassical estimates agree in that the timescale for redistribution of valence electrons, and hence formation of bonding interactions, is potentially sub-femtosecond. (Note again that formation of adiabatic bonding configurations may take a considerably longer period. Only

the initial stages of redistribution of the valence electrons in the dynamically modified nuclear potential are considered here.) Since the residence period for low-energy beam particles in a lattice is generally several femtoseconds, it appears possible that there is an important regime (probably below a few hundred eV) in which non-adiabatic (and hence velocity and history-dependent) bonding interactions can influence beam-solid interactions.

It seems clear that non-adiabatic nuclear interactions may result from dynamic redistribution of the valence electrons during low-energy beam-solid processes. It is not immediately clear, however, that these effects will have a significant influence on the overall nature of the beam-substrate interaction. This question has recently been examined by the present author using molecular dynamics simulations of beam-solid interactions in the two extreme

limits (non-bonding versus adiabatic bonding).¹³ A neutral Si beam normally incident on a (2x1) reconstructed Si(100) substrate was chosen for study. Beam energies of 12.5 eV, 50 eV, and 200 eV were considered to study the effect of bonding interactions over a range of velocities. A random distribution of impact positions was chosen so that the effect of uncharacteristic initial conditions could be eliminated. The interaction between the substrate

atoms was treated in both limits using an empirical many-body potential¹⁴, which provides a natural description of cascade processes, vibrational excitation, and other effects due to the incoming beam particles. The non-bonding ion-solid interaction was modeled using the Ziegler, Biersack, and Littmark "universal" nuclear interaction potential. The adiabatic ion-solid interaction is described using the same semiempirical many-body potential as used to describe the solid-solid atomic interactions.

These simulations revealed very significant differences between the bonding and non-bonding ions. For example, the average penetration depth of the 12.5 eV non-bonding ions is 10.5 Å, compared to 2.8 Å for the case of adiabatic bonding. At beam energies of 12.5 and 50 eV, energy loss is substantially more rapid for the bonding ions than for the non-bonding ions. At 200 eV, however, the energy loss is similar for the two cases. This is because the beam energy in this case is much larger than the characteristic bonding energies.

Figure 1 shows examples of collision cascades resulting from identical initial configurations for non-bonding and bonding ions at 12.5 and 50 eV. Major differences appear as the simulation conditions are varied. First, the trajectory of the non-bonding ions is only slightly deflected by interaction with the substrate atoms, whereas the bonding ions follow a strongly curved path through the substrate. This is a simple consequence of the strongly directional covalent bonding active in the latter case. For the same reason, the cascade resulting from the non-bonding ion extends far into the substrate, but has moderate lateral extent and density, whereas the bonding ion produces a cascade restricted to a region near the surface, but having a larger lateral extent and density of displaced atoms (this is best seen in the 50 eV simulations). Another interesting feature of the bonding ions is that the number of displaced atoms is a strong function of the beam energy, with only 3 atoms displaced at 12.5 eV, but 16 atoms displaced in the 50 eV event, despite the fact that the total energy deposition is similar in both cases. (The kinetic energy lost by the 50 eV non-bonding ion during penetration of the substrate lattice is 11.3 eV in this example.) As a result, the beam energy should affect low-energy ion-solid processes not only by varying the available energy, but also by controlling the ion-substrate coupling. As a result, beam energy could take on a new importance in optimization of very-low-energy ion-beam processing.

The simulations presented above establish that the effect of an ion beam on a surface depends strongly on the nature of the interaction of a rapidly moving ion with the substrate atoms. The nature of the interaction should

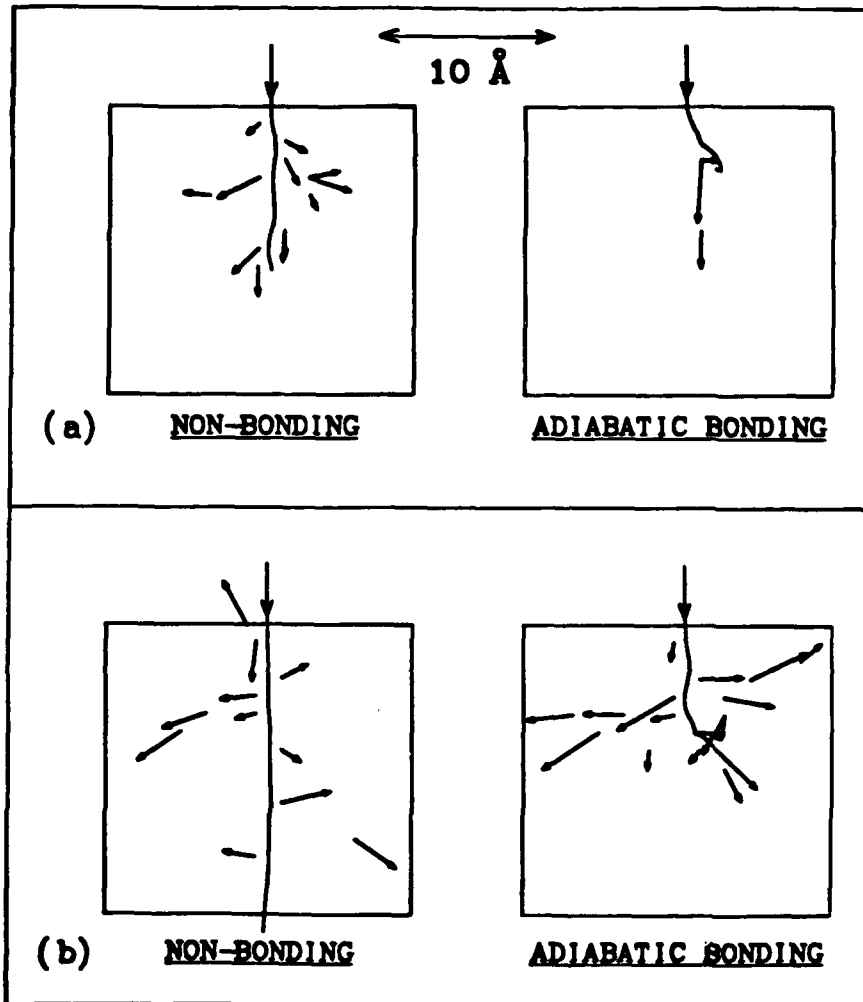


Figure 1. Collision cascades produced in a Si(100) substrate by a very-low energy neutral Si ion at normal incidence. The impact location is the same for all examples shown. The beam energy is 12.5 eV in (a), and 50 eV in (b). The cascades marked "non-bonding" result from use of the universal nuclear potential of Ziegler et. al.¹² to describe ion-atom interactions, whereas those marked "adiabatic bonding" use an empirical many-body potential¹⁴ for ion-atom interactions. In all cases, the substrate atoms interact via this many-body potential to accurately include the effect of lattice vibrations. The distinction between the non-bonding and adiabatic bonding ion-atom interactions is clearly seen.

change with relative velocity of the interacting particles, from nearly adiabatic bonding at the low end of the low-energy regime to repulsive screened Coulomb potentials at the high end. As always, the intermediate regime is the most difficult to treat. Preliminary efforts have been made by various groups toward a time-dependent quantum description of ion-atom interactions in the non-adiabatic energy regime.¹⁵ Although this area of research is progressing rapidly, simulations complex enough to treat the non-adiabatic interactions described in the present paper are apparently beyond the current state-of-the-art.

EXAMPLES OF LOW-ENERGY MOLECULAR DYNAMICS SIMULATIONS

In this section, some low-energy beam-solid simulations which are representative of the current status of the molecular dynamics technique are presented. There are two main areas being studied at this time, concentrating either on ion-beam processes which are not amenable to experimental study or on the problem of identifying appropriate interaction potentials by comparison with relevant experimental studies. Both types of efforts have produced encouraging results.

Many studies have been made of processes which are difficult or impossible to study experimentally. An obvious problem of this type is ion-beam deposition, in which the relevant physics takes place primarily on a psec-nsec timescale. The ion-beam deposition of Lennard-Jones atoms on a two-dimensional substrate over a range of incident kinetic energies has been simulated by Muller.^{16,17} He found that, whereas thermal deposition processes carried out at very low substrate temperatures yielded a spongy, porous microstructure, beam energies equivalent to a few eV were sufficient to drive formation of a nearly perfect epilayer (Figure 2). Similarly, in the case of ion-assisted deposition (ion bombardment simultaneous with thermal deposition), small beam energies were found adequate to greatly improve the epilayer microstructure. It is certainly possible that, in this particular system, the porous microstructure of the thermally deposited epilayer may be an artifact of the extremely short timescales available for structural relaxation in molecular dynamics simulations. The qualitative effect of the incident kinetic energy of the impinging atoms however, is probably valid for general systems.

More commonly, the initial stages of the low-energy ion-solid interaction are studied using molecular dynamics techniques. Simulations of the interaction of low-energy (<50 eV) neutral Si beams with a (111) silicon substrate have recently been carried out by the present author.^{18,19} The interactions amongst the substrate atoms and between the ion and the substrate atoms are treated using an empirical many-body potential¹⁴ which captures the essence of the covalent solid-state bonding. (The tacit assumption of fully adiabatic bonding was made here. This is probably reasonable in this very-low energy regime.) In the case of near-normal incidence, both the range of the ions and the extent of lattice damage were found to be greater than expected from the conventional Monte Carlo or binary-collision lattice models. The extended range is caused by interactions which efficiently steer the ions into lattice channeling directions, allowing deeper penetration than expected. The increase in lattice damage has at least two sources. First, the range of the potential combined with the collective response of the lattice produces a near-surface region in which the cage effect of the surrounding atoms is less than expected by the simple displacement energy description. Second, the highly directional nature of covalent bonding produces more effective coupling between the kinetic energy of the ion and a given substrate atom. The overall

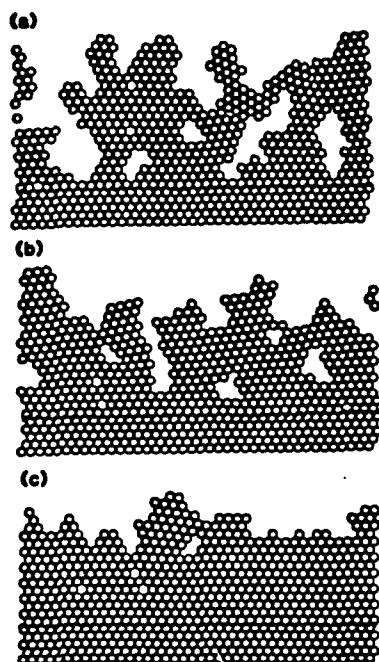


Figure 2. Molecular dynamics simulation of growth of two-dimensional Lennard-Jones crystals. The kinetic energy of the beam atoms is a) 0.05ϵ , b) 0.3ϵ , and c) 1.5ϵ , where ϵ sets the scale of the binding energy. [Roughly, a) corresponds to thermal deposition, and b) to ~ 10 eV beam deposition.] The influence of added kinetic energy is clearly shown, with beam deposition resulting in growth of material having nearly the ideal crystal density.

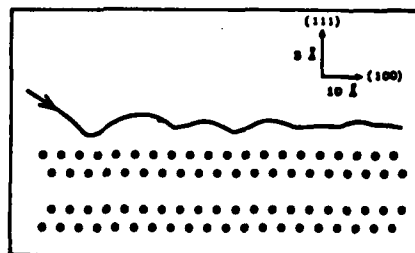


Figure 3. The surface channeling trajectory of a 40 eV silicon atom incident at an angle of 10° on the Si(111) surface. The perpendicular momentum of the beam atom is lost by inelastic generation of collective substrate excitations, causing the beam atom to be trapped at the surface. The resulting trajectory is nearly parallel to, and about 2 Å above, the surface of the substrate.

picture resulting from this study is very different from that suggested by the stochastic simulation techniques.

Grazing incidence trajectories were also studied.¹⁹ In these, incoming neutral Si ions were directed at grazing (3-30°) angles of incidence along the (110) rows of atoms on the substrate surface. Again, all interactions were described by the empirical many-body potential. At larger angles of incidence, the ions were found either to scatter off the surface or stick near the impact site. As the incidence angle is reduced, however, the vertical momentum is absorbed by phonon-mediated inelastic interaction with the substrate, and the ion is steered into a trajectory parallel to and above the substrate, where it is trapped by the chemical bonding between the ion and the substrate atoms (Figure 3). Ions following these 'surface channeling' trajectories experience very little energy loss, and can travel large distances (hundreds of Å) from the point of impact. A closely related effect was recently observed experimentally for low-energy K ions incident on a Si substrate.²⁰

A problem of considerable importance to the plasma/wall interactions which limit the performance of some types of fusion research devices is that of low-energy hydrogen reflection from metal surfaces. Experimental study of this phenomenon is extremely difficult at energies below 100 eV, which is perhaps the most important regime for the applications of interest. In response to this need, Baskes²¹ has studied reflection of neutral H ions from a (100) nickel surface for ion energies from 0.1 to 100 eV. The Ni-Ni and the H-Ni interactions are treated within the framework of the embedded atom method, which is a semiempirical many-body potential with an excellent record of success in treating fcc metals. In the absence of chemical interactions, one expects that the reflection coefficient will go to unity at very low energies. In contrast, the EAM simulations predict that the reflection coefficient goes to zero, consistent with a finite chemical binding energy. The effect of the many-body surface bonding effects begins to appear at ion energies of about 10 eV in this system (Figure 4).

Another interesting study has recently been performed by Garrison and coworkers^{22,23}, who studied the use of the embedded atom method in calculating sputtering from metal surfaces, in particular Rh and Cu sputtering driven by 5 keV Ar ion bombardment. (Although the beam energy is considerably above the low-energy regime, the atomic interactions within the substrate which lead to sputtering generally occur at much lower energies.) The primary result of including the many-body interactions is to approximately double the energy of the peak of the energy distribution, and to increase the size of the high-energy tail (Figure 5). They find that the energy and angular distributions predicted by molecular dynamics simulations are in agreement with the relevant experimental data, although the form of the EAM interactions had to be adjusted to obtain this result. This provides a clear example of the need to include many-body interactions to accurately model low-energy ion-solid processes.

SUMMARY

In this review, we have attempted to establish that there is a physically defined low-energy regime for ion-solid processes. This regime is distinguished from thermal adsorption processes by having incident kinetic energy greater than typical chemisorption energies, and from the high-energy ion-solid regime by the breakdown of the 'soft-sphere' and binary collision approximations. These considerations establish a low-energy regime from about 10-1000 eV, in which collective excitations of the crystal lattice, many-body effects, and ion-solid bonding interactions cannot be safely ignored. The primary atomic-scale simulation techniques applied to high-energy ion-solid

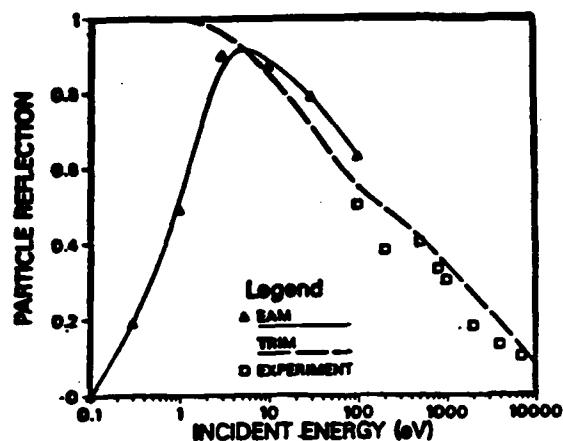


Figure 4. Probability of hydrogen reflection off a Ni(100) surface as a function of incident energy. The solid line represents a many-body treatment, whereas the dashed line is the result of a TRIM-type Monte Carlo code. Below an incident energy of about 10 eV, major differences in reflection coefficient appear.

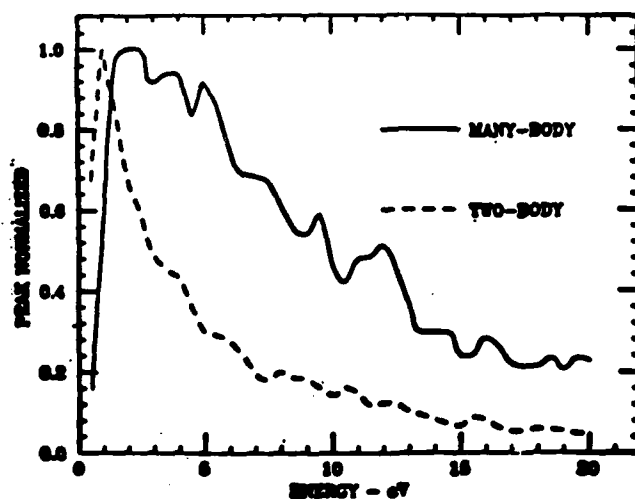


Figure 5. Energy distribution of sputtered atoms from a Cu(111) surface bombarded with 5 keV Ar ions. The two-body interaction is a Moliere core combined with a chemical Morse potential, whereas the many-body interaction is based on the embedded-atom method. When many-body interactions are included, the peak in the distribution shifts to higher energies, and the high-energy tail is much larger than for pairwise interactions.

processes were described, and their shortcomings for the low-energy regime were outlined. Even though the best founded technique is clearly molecular dynamics, there remain fundamental problems concerning appropriate potentials for this non-adiabatic regime. The many-body and non-adiabatic effects are not yet well understood. As a result, atomic-scale simulations of low-energy ion-solid interactions should not yet be regarded as routine tools, but rather as active objects of research in themselves.

REFERENCES

1. N. Herbots, B.R. Appleton, T.S. Noggle, R.A. Zuhr, and S.J. Pennycook, Nucl. Instr. Methods **B13**, 250 (1986).
2. See, e.g., J.E. Greene, CRC Critical Reviews of Solid State and Materials Science **11**, 47 (1983).
3. T.C. Huang, G. Lim, F. Parmigiani, and E. Kay, J. Vac. Sci. Tech. **A3**, 2161 (1985).
4. L.S. Yu, J.M.E. Harper, J.J. Cuomo, and D.A. Smith, J. Vac. Sci. Tech. **A4**, 443 (1986).
5. H. Jorke, H.-J. Herzog, and H. Kibbel, Appl. Phys. Lett. **47**, 511 (1985).
6. J.E. Greene, J. Vac. Sci. Tech. **1**, 229 (1983).
7. N. Herbots, P. Cullen, S.J. Pennycook, B.R. Appleton, T.S. Noggle, and R.A. Zuhr, Nucl. Instr. and Meth. B (in press).
8. A. Seeger, Proc. 2nd UN Int. Conf. on Peaceful Uses of Atomic Energy, vol 6. (IAED, Vienna, 1958) p. 250.
9. J.P. Biersack and L.G. Haggmark, Nucl. Instr. Meth. **174**, 257 (1980).
10. M.T. Robinson and I.M. Torrens, Phys. Rev. **B9**, 5008 (1974).
11. J.B. Gibson, A.N. Goland, M.M. Milgram, and G.H. Vineyard, Phys. Rev. **120**, 1229 (1960).
12. J.F. Ziegler, J.R. Biersack, and U. Littmark, The Stopping and Range of Ions in Solids, (Pergamon, New York, 1985).
13. B.W. Dodson, Phys. Rev. Lett. (in press).
14. B.W. Dodson, Phys. Rev. **B35**, 2795 (1987).
15. e.g., B.M. Deb and P.K. Chattaraj, Chem. Phys. Lett. **148**, 550 (1988).
16. K-H. Muller, Surf. Sci. **184**, L375 (1987).
17. K-H. Muller, Phys. Rev B
18. B.W. Dodson, Phys. Rev. **B36**, 1068 (1987).
19. B.W. Dodson, Appl. Surf. Sci. **22**, 334 (1987).
20. K.J. Snowden, D.J. O'Conner, and R.J. MacDonald, Phys. Rev. Lett. **61**, 1760 (1988).
21. M.I. Baskes, J. Nuc. Mat. **128-129**, 676 (1984).
22. B.J. Garrison, N. Winograd, D.M. Deaven, C.T. Reimann, D.Y. Lo, T.A. Tombrello, D.E. Harrison, and M.H. Shapiro, Phys. Rev. **B37**, 7197 (1988).
23. D.Y. Lo, T.A. Tombrello, M.H. Shapiro, B.J. Garrison, N. Winograd, and D.E. Harrison, J. Vac. Sci. Tech. **A6**, 708 (1988).

PART II

**Laser-Induced Deposition of Metal
Films**

THE SPECTROSCOPY AND SURFACE CHEMISTRY OF METAL-ALKYL MOLECULES

P. SHAW, J. O'NEILL, E. SANCHEZ, Z. WU, and R.M. OSGOOD, JR.
Microelectronics Sciences Laboratories, Columbia University,
New York, NY 10027

ABSTRACT

Metal-alkyl molecules provided an early source molecule for photodeposition of metal. They continue to be of interest for patterned and unpatterned laser deposition and for contact formation on compound semiconductors. This article provides a brief review of what has been learned about the surface photo-physics of this class of molecules based on several years of study with UV and IR absorption spectroscopy, UHV surface analysis, and thermal and photodesorption mass spectroscopy.

INTRODUCTION

Some of the earliest demonstrations of both the fundamental chemistry and practical applications of laser chemical processing techniques involved photofragmentation of relatively simple metal-alkyl molecules [1-5]. For example, laser direct writing of metal lines [1] and direct doping of compound semiconductors were first demonstrated [2] with two related organometallics, e.g. dimethylcadmium (DMCd) and dimethylzinc (DMZn). Both of these molecules were also used in the first demonstration of additive mask repairs [5], and circuit testing and restructuring [6]. Metal alkyls were attractive sources because they are easily fragmented in the medium UV with readily available pulsed and UV laser sources.

The photochemical processing techniques utilizing these molecules involve a complex series of heterogeneous chemical processes. For example, in the photodeposition of metal films most metal atoms in a deposition result from photolysis of either gas-phase or physisorbed species. On the other hand, the patterning or spatial resolution of the process results to a large degree from photolysis of chemically adsorbed molecules [7,8].

Metal alkyls form an excellent class of model compounds for investigating interfacial phenomena. Metal-containing parent molecules appear in both the divalent and trivalent forms with a variety of substituted ligands (e.g. DMCd, DECD and TMAI), allowing the effects of various molecular properties to be studied. Their ultraviolet spectra occur in the near-to-medium ultraviolet and exhibit scientifically useful shifts from one member of a sequence to another. The vapor pressures of most compounds at room temperature are in the range where both gas and adsorbed phases can be conveniently studied. Finally, their molecular structure is simple enough to allow clear physical interpretation.

In this review, we will attempt to summarize briefly what has been learned about the interfacial photochemistry of metal-alkyl molecules. The review will concentrate on results with dimethyl-metal alkyls [9]. In addition, we will focus on discussing work in the authors' laboratory. The paper will be divided into four sections: a brief review of the experimental techniques used, a description of gas-phase photochemistry, a summary of what is known regarding the photo-physics and structure of the physisorbed layers, and finally more recent studies of the chemisorbed phase.

EXPERIMENTAL TECHNIQUES

The study of the photochemistry of metal alkyls has relied on the use of an array of standard and novel experimental techniques. For the gas phase, the approach has been to use ultraviolet and infrared spectroscopy for the studies of basic molecular structure, and to rely on metal-atom resonance-line-lamp absorption for the study of metal-atom transport and lifetime. In addition synchrotron-radiation-induced dissociation has been used by Yu, *et al* [10] to probe the very diffuse emission from monomethyl fragments [11]. Finally, Chu, *et al* [11] have used infrared fluorescence to detect vibrational excitation in methyl ligands following pulsed excimer dissociation.

Surface studies have more often required the development of new techniques. For spectral measurements involving physisorbed layers, the central experimental problem is to distinguish a rather small surface signal from the strong absorption in the gas overlayer that is necessary to maintain the film on the surface [12]. In the case of ultraviolet absorption surface spectroscopy, we solved this problem by using multiple, flat, adsorption surfaces and spacing these surfaces sufficiently closely that the absorbing gas path between the windows had an optical depth smaller than the optical depth of the physisorbed layer [13]. For infrared spectroscopy on surfaces, we have used monolayer-sensitive total-internal-reflection spectroscopy [14]. The evanescent wave of the multiple-reflected infrared beam preferentially samples the adsorbed layer. For our experiments, the total-internal-reflection element was silicon. However, the composition of the surface was reliably chemically altered to study adsorption on SiO₂ and hydrogen-passivated surfaces.

For chemically-adsorbed molecules, the relatively high heat of adsorption permits experimentation in an UHV ambient. As a result, it is possible to use standard UHV analysis techniques such as XPS and Auger spectroscopy [15]. In addition, we have developed a sensitive single-pass adsorption technique to look at adsorption on a single surface of transparent material [16]. The simplicity of the optical path allows significant *in situ* surface preparation. We have also used the total-internal-reflection technique mentioned above since it is sensitive to even submonolayer molecular coverages. Finally, we have recently begun the study of the thermal desorption and the photofragmentation of the adsorbed

molecules using an SiO_2 -covered silicon substrate on a heatable holder and an *in situ* mass spectrometer. A summary of the techniques used for the experiments reviewed here is shown in Fig. 1.

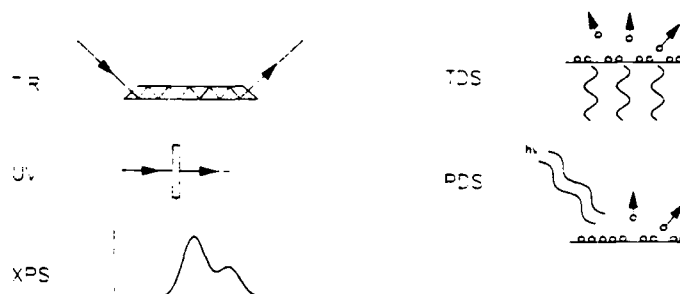


Fig. 1. Different techniques used for the study of adsorbed molecules.

MOLECULAR STRUCTURE AND ULTRAVIOLET SPECTRA

At first glance, the multiplicity of atoms (nine) and electrons (~100) in the dimethyl metal molecules would seem to make understanding of the metal-alkyl vibrational and electronic spectra a formidable task. However, to a high level of approximation, the electronic states of these species can be understood upon consideration of only the four outer electrons which are active in the bonding process. In particular, all three of the Group IIB metal atoms, Zn, Cd, and Hg, have a compact core and two outer s electrons with relatively large radii. Only these outermost valence s electrons are involved in the bonding process. For the methyl groups, the four valence electrons of carbon occupy four tetrahedral hybrid sp^3 orbitals. In the metal alkyls, three of them are fixed as C-H bonds. Only one of the sp^3 hybrid orbitals bonds with the metal atom.

Within this four electron approximation, these dimethyl metal alkyls resemble closely the case of the simplest polyatomic molecules: metal dihydrides with four active electrons, that is, BeH_2 , MgH_2 , ..., CdH_2 , HgH_2 . As pointed out by Walsh, [17] these four-electron dihydrides should be linear in their ground state and bent in their first excited state. This four-electron picture has been verified by an *ab initio* calculation of the electron structure of the ground state of dimethylcadmium.

According to the above model the dissociation process occurs as follows (see Fig. 2) [18]. Excitation of the molecule to the first excited state, results in the immediate production of a bent "quasitriatomic" molecule. The excited

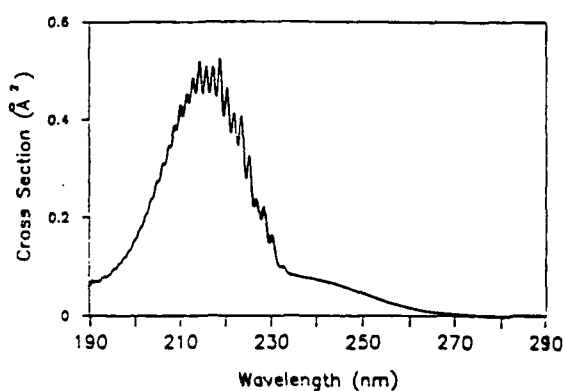
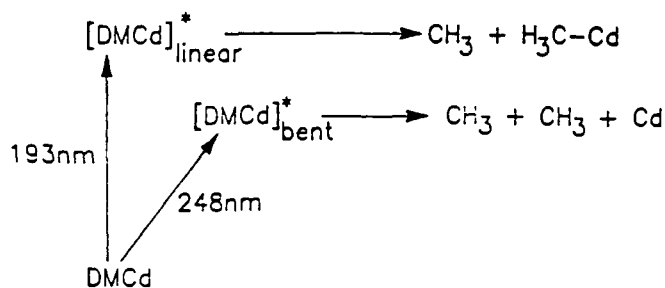


Fig. 2.
Gas-phase
DMCd
photochemistry.

molecular orbital a_1^* is made of, essentially the outer s atomic orbital of the metal atom and electrons in one of the tetrahedral orbitals of the methyl groups. Since one of the valence bonds is broken, the molecule will disintegrate immediately into a monomethyl molecule in the ground state and a methyl radical. Notice that since the excited DMCD molecule is highly vibronically excited and the binding energies of the monomethyl molecules are very small (less than 6 kcal/mol), complete dissociation of the monomethyl occurs as well. The second excited state, which is linear, contains a nonbonding, excited Π orbital. Thus, the metal atom behaves just as a column I atom; for example, Ag. Consequently, the molecule will disintegrate immediately into a monomethyl molecule in its excited state and a methyl radical. The potential surface of this excited state will have a saddle point and two troughs, and a structured continuum can be observed in the absorption spectra, since the lifetime of the excited state is longer than a vibrational period. Finally, the electronically excited monomethyl molecule, in either the $^2\Pi_{1/2}$ or $^2\Pi_{3/2}$ state will radiatively decay to the ground state. This has recently been observed by Yu, *et al* [10].

PHOTOPHYSICS IN THE PHYSISORBED LAYERS

The infrared and ultraviolet spectroscopic studies of the physisorbed layers illustrate different aspects of the photophysics of the physisorbed molecular layer. In particular, the infrared studies are most useful for determining the thermodynamics and molecular environment for the adsorbed molecules. The ultraviolet measurements directly address the question of the UV absorption spectra.

Regarding the infrared studies of the physisorbed layers, Fig. 3 compares the IR spectra of both the gas (done by conventional FTIR absorption spectroscopy) and adsorbed DMCD in the region of the CH stretch frequency [14]. As can be seen, the spectral features are very similar for both the gas and physisorbed state except that, as might be expected, the rotational motion is quenched upon adsorption, and some narrowing of the rotational envelope is seen.

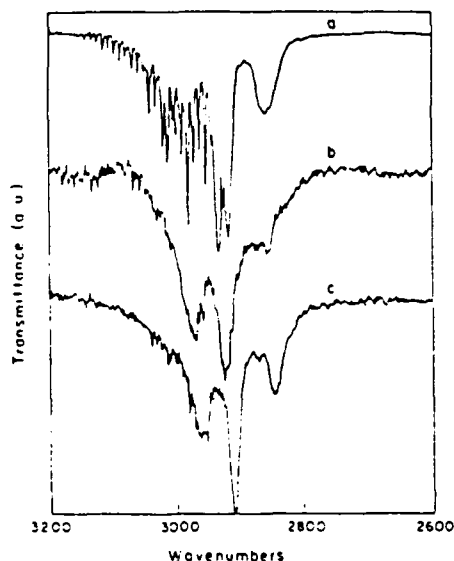


Fig. 3. FTIR absorption spectra of gas phase and adsorbed DMCD. The transmittance scale for each spectrum is different in this figure. Intensities were normalized to the peak intensity of each trace (a) Gas-phase spectrum path length 5 cm, pressure 10 Torr (b) IR spectrum of chemisorbed species, background pressure 1×10^{-7} torr (c) IR spectrum of physisorbed species, ambient DMCD pressure 30 torr.

In addition, infrared spectral changes are observed as the ambient DMCD pressure is varied. As illustrated in Fig. 4, the frequency of each vibrational band is seen to red-shift gradually from the gas-phase absorption frequency at low coverages toward that exhibited by the liquid state at higher multilayer coverages. The magnitude of the red-shifts

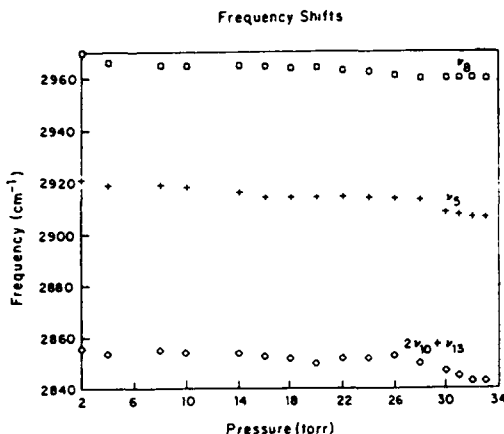


Fig. 4. A plot of the absorption frequency as a function of ambient DMCD pressure for all three vibrational bands in the spectrum of the physisorbed species. The band positions gradually red-shift from the gas-phase absorption frequency at low coverages toward that exhibited by the liquid state at pressures near the vapor pressure.

measured in the present experiments ($\approx 20\text{cm}^{-1}$) is consistent with that expected for a weakly interacting system dominated by dispersive interactions. Also, the intensity of each vibrational band grows with increasing DMCD pressure. This behavior is reversible with ambient gas pressure except for a small residual signal which remains upon evacuation to 10 Torr and which is attributed to a non-negligible chemically adsorbed film. The intensity development of the $2\nu_{10} + \nu_{13}$ combination vibration lags behind that of the fundamental stretching modes at higher surface coverages ($p > 15$ Torr).

Isotherms of the ν_5 absorption intensity, which can be related to total molecular surface density versus ambient gas pressure, are presented in Fig. 5 for measurements at various temperatures. Similar plots were obtained for the other vibrational bands observed in the DMCD spectrum. Near the vapor pressure of dimethylcadmium (35 Torr at 25°C), the adlayer signal increases dramatically, indicating the incipient formation of the condensed liquid. At a given gas pressure, the measured absorption intensity decreases abruptly with increasing surface temperature, as expected for physisorbed molecules. By analyzing the integrated absorption intensity as a function of substrate temperature at constant gas pressure, the energy of this adsorption process was determined to be approximately 9 kcal/mole, which is in close agreement with the heat of vaporization of liquid DMCD. The loss of intensity from the rotational wings of the ν perpendicular CH stretching vibration arises as collisions and dephasing interactions between molecules on the surface broaden the individual rovibrational transitions which are resolved in the gas phase.

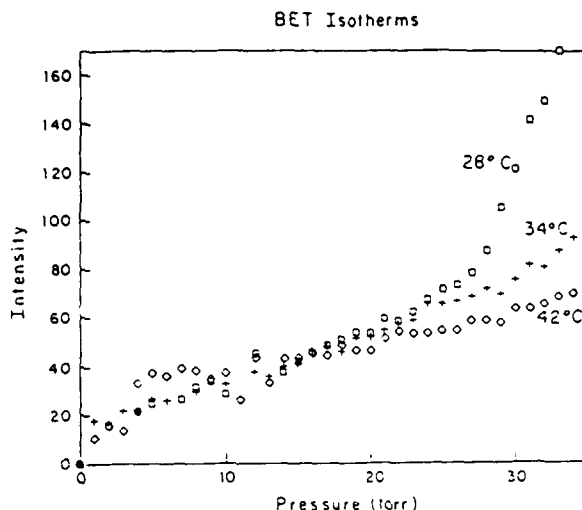


Fig. 5. Isotherms of absorption intensity versus ambient DMCD pressure for the v_5 absorption band. These data were obtained at 28, 34 and 42° C, and they can be shown to yield a heat of adsorption of 9 kcal/mol.

Recently, infrared measurements have shown that the degree of physisorption is sensitive to the nature of the substrate. For example, on carefully hydrogen-passivated silicon, the number of physisorbed molecules is very small. We believe this effect stems from the fact that physisorption occurs primarily on the sites of chemisorbed molecules, which, as we will show below, adsorb negligibly on passivated silicon. The opposite of this behavior, which causes an enhancement of both the physi- and chemisorbed molecular densities, is seen on surfaces containing metal. Similar effects were observed previously in a system involving trimethylaluminum on alumina [9].

The changes in the ultraviolet spectrum upon molecular physisorption are more pronounced than in the IR. Figure 6 shows, for example, the ultraviolet spectra of physisorbed DMCD [13]. Notice that both of the gas-phase bands mentioned above appear to have coalesced into a single feature, indicating significant shifts and broadening in the energy levels of the adsorbed molecules. The peak optical cross section of the adsorbed molecules is, however, comparable to that of the B state of the gas phase.

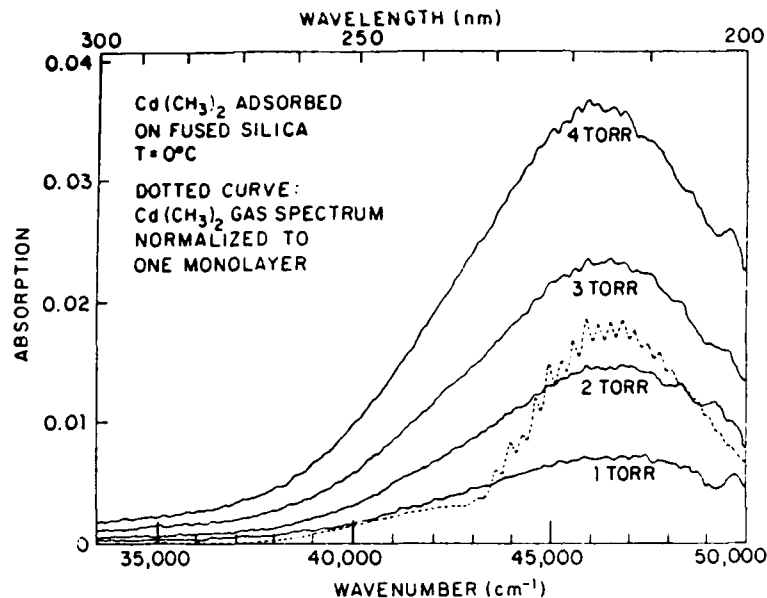


Fig. 6. UV spectrum of physisorbed DMCD on fused silica.

For most practical applications it is also important to know the yield for surface photodissociation. Unfortunately, very little data has been gathered on the yield for physisorbed molecules. However, we do know from the more practically oriented studies of photodeposition, that photodissociation can occur in physisorbed molecules; in fact in some cases it may dominate the photodeposition process [19].

PHOTOPHYSICS AND THE NATURE OF THE CHEMICALLY ADSORBED LAYERS

The possibility of studying the chemically adsorbed layer under UHV conditions has led to a more precise understanding of its physical properties. The two most basic questions to be answered are 1) What is the species of the chemisorbed molecule? and 2) What is the site at which chemisorption occurs?

First, regarding the nature of the adsorbed molecule, recent experiments using thermal desorption spectroscopy (TDS) have confirmed that the molecule leaving the surface has the same mass spectrum as that of DMZn. This result is also supported by the strong similarity between the infrared spectroscopy of the physisorbed layers with that of the chemisorbed layer (see Fig. 3), although the latter evidence cannot be regarded as convincing because of the strong binding within the methyl ligand.

Second, the degree of adsorption of the DMCD molecules on the various substrates that we have investigated can be used to help identify the sites on which the molecule adsorbs. In

particular, we have found, using IR spectroscopy, that chemisorption does not occur on hydrogenated silicon but instead appears to correlate well with the amount of oxide on the surface (see Fig. 7). Further, UV spectroscopic studies on fused silica substrates have shown that the amount of absorption is also controlled by the extent of preheating of the silica surface [16]. As shown in Fig. 8, preheating temperatures of $\sim 500^\circ\text{C}$, are sufficient to reduce by 1/4 the amount of surface adsorption on the silica. This result correlates well with the known thermal removal of hydroxyl surface radicals with temperature. Hydroxyl radicals are formed readily on an oxide surface through the reaction with ambient water. The preheating results indicate that the primary absorption site is these surface OH groups and not the simple oxide sites. Infrared measurements have shown that the hydroxyl peaks disappear (or possibly broaden into the background noise) after the chemisorption of DMCD. Again this result is consistent with chemisorption on an OH site.

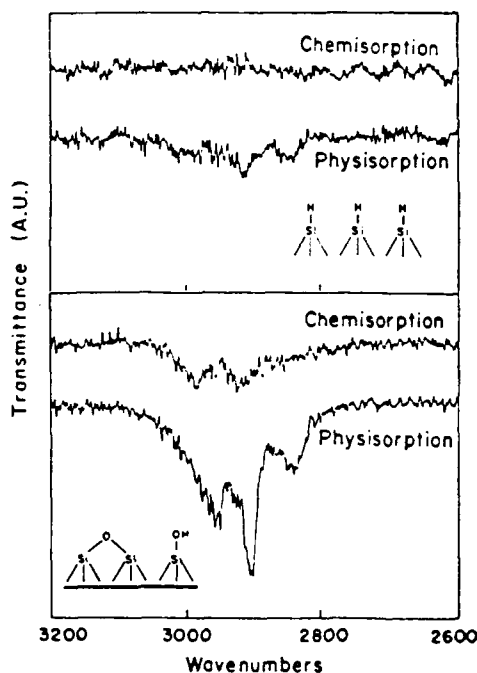


Fig. 7. IR spectra of both chemisorbed and physisorbed DMCD on an H-passivated silicon surface and on an oxidized silicon surface.

The TDS measurement alluded to earlier can be used to determine the strength of the adsorption bond. For both DMZn and DMCD the bond energy found in this way is approximately 1 eV. Further, it is found that absorption will reoccur

after thermal desorption has taken place. Both of these observations are consistent with a mechanism which relies on a weak bond between the surface OH and the dimethyl molecule.

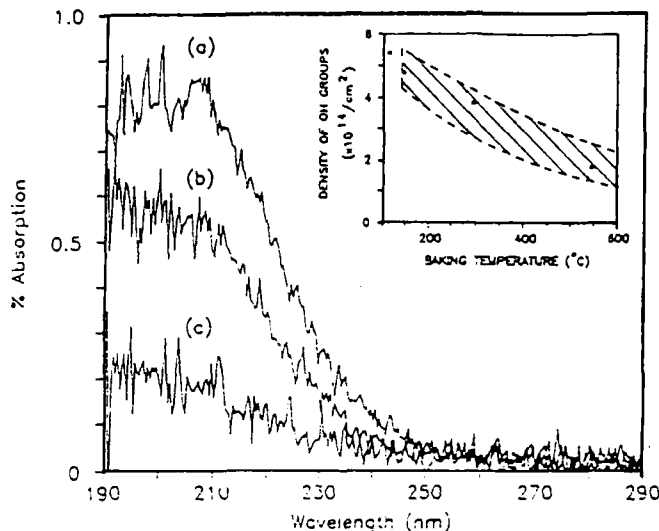


Fig. 8. Absorption spectra of chemisorbed DMZn molecules on one quartz surface which had been prepared by baking and evacuating the surface at (a) 120°C, (b) 300°C and (c) 550°C for 24 h. The insert describes the surface concentration of OH groups as a function of the temperature of thermal treatment. The hatched area is the range of OH concentration on silica samples measured by previous workers (Ref. 20). The points are obtained by the present absorption measurement as described in the text. Since only relative values of OH density can be estimated in our absorption measurement, we have assumed, in plotting the points, the OH concentration at 120°C to be equal to the value given in Ref. 20.

A final aspect of our work on chemisorbed species concerns its photochemistry. Unlike in the case of the physisorbed molecules, we now have very good evidence on the yield and fragmentation pattern of the chemisorbed molecules. First based on our assumed surface density of the DMcd molecules, we find that the total cross section for optical absorption agrees reasonably with that expected from the gas-phase molecule; oscillator strength in the mid-UV bands is not lost or gained upon absorption. Second, we used a mass spectrometer attached to our photolysis chamber to determine

that the fragmentation following surface irradiation at 193 nm (ArF) produces only CH_3 radicals; gas-phase Cd species are not seen. Finally we have found that the yield during irradiation is considerably lower than for gas-phase molecules. As shown in Table 1, irradiation at 248 nm produces little or no photodissociation. At 193 nm significant photodissociation does occur but still with yields much less than that seen for gaseous molecules. This data was obtained both by observing the disappearance of the CH_3 IR spectra and by observing the instantaneous production of CH_3 fragments with a continuously vacuum-pumped mass spectrometer. The former measurement gives a measurement of the integrated photodecrease in the metal alkyl while the latter provides a "snapshot" of the photodissociation cross section at a given moment in time.

	193 nm	248 nm
DMZn	CH_3	Nothing
DMCd	CH_3	Nothing

Table 1. Fragmentation of surface adsorbed molecules under UV laser irradiation measured by a mass spectrometer.

One of the results of these measurements is to show that the yield for photodissociation is much less than unity, i.e. $\sim 1/20$. This small yield may result from quenching through the OH-DM metal complex to the surface. Note that the quenching appears to be far more effective at 248 nm, indicating that the lower lying A state is more amenable to de-excitation than the B state.

CONCLUSION

In this review, we have presented an overview of the photophysics of dimethyl metal-alkyls. Through an extended study of the photochemistry of these molecules, we have obtained a nearly complete picture of their photophysics at interfaces on passive surfaces. Important questions do still remain unanswered. For example, the photochemistry on the deposited (or even pre-existing) metal surfaces remains unstudied. In particular, questions remain on the nature of the chemisorption process on pure metal, the shift in the dominant alkyl UV spectra as methyl ligands are ejected from the surface, and, finally, the value of yield on the bare surface.

We would like to acknowledge support for this work from ARO, JSEP, and IBM.

REFERENCES

1. T. F. Deutsch, D. J. Ehrlich, and R. M. Osgood, Appl. Phys. Lett. 35, 175 (1979).
2. D. J. Ehrlich, R. M. Osgood, and T. F. Deutsch, Appl. Phys. Lett. 36, 916 (1980).
3. T. F. Deutsch, D. J. Ehrlich, R. M. Osgood, and Z. L. Liao, Appl. Phys. Lett. 36, 847 (1980).
4. D. J. Ehrlich, J. Y. Tsao, D. J. Silversmith, J. H. Sedlacek, W. S. Graber, R. Mountain, IEEE Elect. Device Lett., EDL-5, 32 (1984).
5. D. J. Ehrlich, T. F. Deutsch, D. J. Silversmith, and R. M. Osgood, Elect. Dev. Lett. EDL-1, 101 (1980).
6. T. Cacouris, R. R. Krchnavek, H. H. Gilgen, R. M. Osgood, S. Kulick, and J. Schoen, Proceedings of the IEDM (1985).
7. D. J. Ehrlich and R. M. Osgood, and T. F. Deutsch, J. Vac. Sci. Technol. 20, 738 (1982).
8. D. J. Ehrlich, R. M. Osgood, and T. F. Deutsch, Appl. Phys. Lett. 38, 1 (1981).
9. For a series of studies on TMAI the reader is referred to G. Higashi and references cited therein.
10. C. F. Yu, F. Youngs, K. Tsukiyana, R. Bersohn, and J. Preses, J. Chem. Phys., 85, 1382 (1986).
11. J. O. Chu, G. W. Flynn, C. J. Chen, and R. M. Osgood, Chem. Phys. Lett. 119, (1985).
12. D. J. Ehrlich and R. M. Osgood, Chem. Phys. Lett. 79, 381 (1981).
13. C. J. Chen and R. M. Osgood, Chem. Phys. Lett. 98, 363 (1983).
14. E. Sanchez, P. Shaw, J. O'Neill and R. M. Osgood, Chem. Phys. Lett. 147, 153 (1988).
15. C. D. Stinespring and A. Freedman, Chem. Phys. Lett. 143, 584 (1988).
16. P. S. Shaw, E. Sanchez, Z. Wu, and R. M. Osgood, Chem. Phys. Lett., 151, 449 (1988).
17. J. Walsh, J. Chem. Soc. 2260 (1953).
18. C. J. Chen and R. M. Osgood, J. Chem Phys., 81, 327 (1984).
19. R. R. Krchnavek, H. H. Gilgen, J. C. Chen, P. S. Shaw, T. J. Licata and R. M. Osgood, Jr., J. of Vac. Sci. and Tech., 5, 20 (1987).
20. L. H. Little, Infrared Spectra of Adsorbed Species, (Academic Press, NY, 1966).

THERMAL AND PHOTOLYTIC DECOMPOSITION OF ADSORBED CADMIUM AND TELLURIUM ALKYLs

C.D. Stinespring and A. Freedman
Center for Chemical and Environmental Physics, Aerodyne Research, Inc.,
45 Manning Road, Billerica, MA 01821

ABSTRACT

Studies of the thermal and photon-induced surface chemistry of dimethyl cadmium (DMCd) and dimethyl tellurium (DMTe) under ultrahigh vacuum conditions have been performed for substrate temperatures in the range of 133 K to 295 K. Results on GaAs(100) and Si(100) surfaces indicate that for DMTe, the predominant adspecies, dimethyl tellurium, can be photodissociated to a metal adspecies at both 193 and 248 nm. For DMCd, the major adspecies, monomethyl cadmium, is unreactive to photon stimulation.

INTRODUCTION

Thermal and photon-assisted deposition processes involving organometallic precursor species are currently being investigated for II-VI and III-V compound semiconductors.[1] These processes provide the potential for reduced growth temperatures and increased process flexibility. Illustrations include reduced pressure laser assisted chemical vapor deposition (LCVD) of CdTe[2] and ultra high vacuum (UHV) metalorganic molecular beam epitaxy (MOMBE) of GaAs.[3] These relatively new deposition processes raise important questions concerning chemical mechanisms which must be answered if the processes and materials they produce are to be optimized.

This paper describes ongoing experimental studies[4,5] of the thermal and photon-induced surface reactions of dimethyl cadmium (DMCd) and dimethyl tellurium (DMTe). The objectives of these studies are to provide an understanding of the underlying chemical and physical processes and to explore novel approaches to CdTe heteroepitaxy. The work focuses on CdTe heteroepitaxy because of the importance of this material in electro optical systems.[6] DMCd and DMTe were the first precursor species selected for investigation because of their inherent scientific interest. The gas phase photochemistry of DMCd and DMTe has been extensively investigated; these molecules are known to undergo one photon dissociation to produce ground state metal atoms.[7-9] This behavior contrasts with that of trimethyl gallium and trimethyl arsenic which dissociate in the gas phase via a multiphoton excitation process.[10] The basic questions we attempt to answer in this study are: i) How do DMCd and DMTe interact with the surface of a substrate or growing thin film? and ii) Is this interaction such that single photon (as opposed to multiphoton) processes can be used to produce metal adspecies and, ultimately, epitaxial CdTe thin films?

EXPERIMENTAL

The experimental apparatus used in these studies is shown in Figure 1. It consists of a turbomolecular pumped, liquid nitrogen trapped UHV reaction cell interfaced to an ion/sublimation pumped UHV analysis chamber. The diagnostics used in these studies were X-ray photoelectron

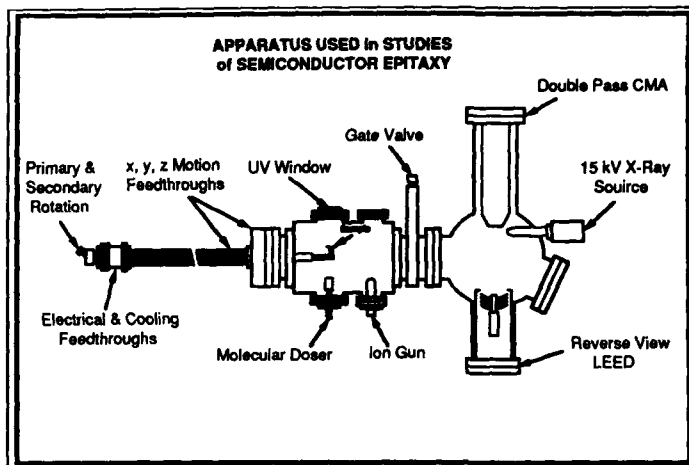


Figure 1. Schematic diagram of the experimental apparatus.

spectroscopy (XPS) and low energy electron diffraction (LEED). The sample was transferred between chambers using a linear motion feedthrough with sample heating (1200 K) and cooling (133 K) capabilities. Samples were exposed to reactive gas species using an effusive molecular beam doser. For the sample-source geometry used here, the angular distribution of the effusive beam produced only a nominal 10% variation in exposure over the analyzed area of the surface. Photon-induced processes were studied by irradiating the surface with UV photons produced by an excimer laser. These were introduced through a Conflat mounted MgF_2 window (Harshaw). The wavelengths used in these experiments were 193 nm and 248 nm. Laser fluence, controlled using a simple beam expander, ranged from 0.25 mJ cm^{-2} to 2.5 mJ cm^{-2} to minimize the effects of surface heating ($<3 \text{ K}$ to 30 K) [11].

The samples used in these studies were GaAs(100), Si(100), SiO_2 , and Au. The GaAs and Si samples were p-type electronic grade single crystal substrates provided by Litton and Monsanto, respectively. The SiO_2 sample was amorphous quartz, and the Au sample was a polycrystalline foil (Alfa Products). In situ sample cleaning involved Ar^+ ion etching at 1 kV. For the GaAs and Si surfaces, this was followed by annealing at 850 K [12] and 1100 K [13], respectively, to restore surface order. The DMCd and DMTc (Alfa), except where noted, were purified using a series of freeze-thaw cycles.

The XPS analyses were performed using a PHI 15 kV, $\text{Mg K}\alpha$ source and a PHI double pass cylindrical mirror electron energy analyzer operated at a pass energy of 50 eV. The analyzer was calibrated using the Au $4f_{7/2}$ photoelectron peak at 83.8 eV. For the SiO_2 , sample charging effects were taken into account by referencing the spectra to the Si 2p peak at 103.4 eV. Adsorption coverages were calculated from known values of the X-ray mass absorption coefficients, electron mean free paths, and peak intensities using a technique developed by Madey, et al. [14]. Following Wedler and Klemperer, [15] reactive sticking coefficients were determined from the slope of plots of surface coverage versus exposure.

RESULTS

As discussed elsewhere[4], XPS analyses of the Cd and Te $3d_{5/2}$ peaks for adspecies on the various substrates led to the identification of three distinct binding energies for each peak. As an example, Figure 2 shows Cd $3d_{5/2}$ spectra for the Si(100) 2x1 surface exposed to DMCD at 133 K. The initial exposure produces a peak at 404.6 eV (FWHM = 2.0 eV) which corresponds well with Cd metal. At higher exposures, the spectrum is dominated by a monomethyl Cd (MMCd) peak at 405.2 eV. The details of how this surface reaction product distribution evolves with DMCD exposure are shown in Figure 3 where Cd adspecies coverage is plotted against DMCD exposure. From the slope of this plot, the reactive sticking coefficient of DMCD is found to be ~ 0.1 for the indicated conditions. Under similar conditions, DMTe is found to adsorb as the dimethyl and metal adspecies with Te metal representing a relatively minor component. The reactive sticking coefficient of DMTe on the Si(100) 2x1 surface was found to be ~ 0.5 at 133 K. Interestingly, while the saturation surface coverage for the Cd-adspecies at 133 K is ~ 0.7 monolayers, multilayer DMTe coverages may be produced.

Table 1 summarizes the adspecies which have been observed on the various substrates at 295 K[4] and 133 K. Where multiple adspecies are observed, the dominant species at high coverage/exposure is listed first. As indicated, measurements for SiO_2 and Au at 133 K are currently in progress. The measurements of DMTe adsorption on Si and SiO_2 at 295 K showed very limited uptake. This was originally attributed to a low DMTe sticking coefficient, but we are currently investigating the possibility that the DMTe used in the original measurements was contaminated by decomposition products.

Upon irradiation by 193 nm photons, no effect was observed for either the Cd or the Te metal adspecies. For the monomethyl adspecies, some desorption ($<50\%$) but no conversion to the metal was observed. For the dimethyl adspecies, conversion to the metal adspecies ($\sim 25\%$ to 75%) and some desorption ($<25\%$) were observed. The DMTe adspecies formed on Si and GaAs at 133 K were found to dissociate to metal adspecies with 248 nm photons. Studies using this wavelength have not been extended to other adspecies.

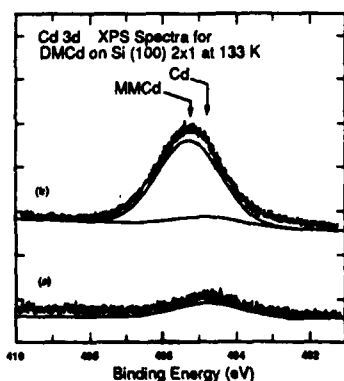


Figure 2. Cd $3d_{5/2}$ XPS spectra for the Si(100) 2x1 surface exposed at 133 K to a) $5 \times 10^{14} \text{ cm}^{-2}$ and b) $6 \times 10^{15} \text{ cm}^{-2}$ DMCD molecules.

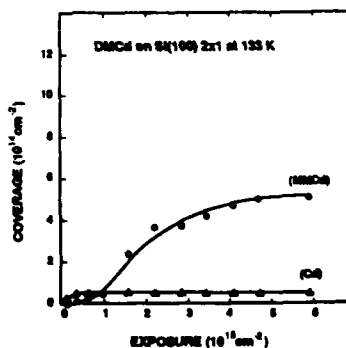


Figure 3. Plot of Cd adspecies surface coverage versus DMCD exposure for the Si(100) 2x1 surface at 133 K.

Table 1: Summary of Observed Adspecies^a

Substrate	Cd-Adspecies		Te-Adspecies	
	133 K	295 K	133 K	295 K
Si(100)	MMCd + Cd	MMCd	DMTe + Te	ND ^c
GaAs(100)	MMCd	MMCd	DMTe + Te	MMTe
SiO ₂	NA ^b	DHCd	NA ^b	ND ^c
Au	NA ^b	Cd	NA ^b	Te + DMTe

^aDominant species at high coverage/exposure listed first.

^bNA = not available, measurement in progress

^cND = no adspecies detected

The effects of photon irradiation on the dimethyl-adspecies is illustrated in Figure 4.[5] The lower spectrum shows the Te 3d_{5/2} XPS peak for Au exposed to DMTe at 295 K. The total adspecies coverage represented here corresponds to about 0.5 monolayers which is distributed between the metal (~60%) and dimethyl (~40%) peaks. The upper spectrum shows the effects of laser irradiation. Here it may be seen that ~80% of the dimethyl adspecies was converted to metal, ~5% was desorbed, and ~15% remained on the surface after irradiation. Further irradiation by an additional 5000 pulses did not eliminate the residual dimethyl adspecies.

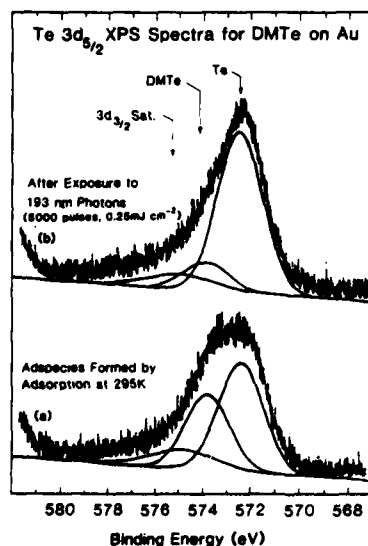


Figure 4. Te 3d_{5/2} XPS spectrum for DMTe adspecies on Au (a) before and (b) after irradiation by 5000 pulses of 193 nm laser light at 0.25 mJ cm⁻² per pulse. Each spectrum has been resolved into metal (572.6 eV) and a dimethyl (573.6 eV) peaks. The low intensity peak at 574.8 eV is an X-ray satellite associated with the Te 3d_{3/2} peak.

DISCUSSION

The thermal surface chemistry of DMCD and DMTe appears to be quite diverse. Disregarding the minor channel to form metal adspecies on Si and GaAs at 133 K (probably due to defect sites), DMCD appears to be more reactive than DMTe. Simple thermodynamic considerations might argue that this trend is due to the relatively weak average Cd-carbon bond strength, 36.2 kcal mole⁻¹ compared to 57.5 kcal mole⁻¹ for DMTe[9]. On the other hand, substrate-metal bond strengths are probably stronger for Te than for Cd. Furthermore, the increased propensity for dissociation as the substrate changes from insulator to conductor does not follow any simple thermodynamic argument. We intend to pursue studies on single crystal quartz and gold substrates as well as n-doped semiconductors to further investigate this trend.

The photochemistry results are important for several reasons. First they demonstrate that species present on the surface in the dimethyl chemical state can be photodissociated. This finding is critical to the success of any CdTe deposition process based on laser induced surface chemistry of DMCD and DMTe. Studies now in progress will provide additional insight into the nature of these photon-assisted processes. Second, the photochemistry results also demonstrate clear differences in the behavior of the surface species we have assigned as dimethyl-, monomethyl-, and metal-adspecies. Further, the observed differences in behavior are the same for each metal alkyl. Thus, as a secondary result, the observed photochemistry helps to corroborate the peak assignments made on the basis of ligand shifts and bulk standards. In future work, we will add additional corroborating evidence obtained from thermal desorption measurements.

ACKNOWLEDGMENT

This research was sponsored by the Air Force Office of Scientific Research under Small Business Innovative Research Program Contract No. F49620-86-C-0089.

REFERENCES

1. J.A. O'Neill, P. Shaw, E. Sanchez, Z. Wu and R.M. Osgood, Jr., "Surface Spectroscopic Studies of Organometallic Deposition," Mat. Res. Soc. Symp., this volume.
2. J.J. Zinck, P.D. Brewer, J.E. Jensen, G.L. Olsen and L.W. Tutt, Appl. Phys. Lett. **52**, 1434 (1988); J.B. Mullin and S.J.C. Irvine, J. Vac. Sci. Technol. **A4**, 700 (1986).
3. E. Tokumitsu, Y. Kurow, M. Kanogai and K. Takahashi, J. Appl. Phys. **55**, 3163 (1984).
4. C.D. Stinespring and A. Freedman, Chem. Phys. Lett. **143**, 584 (1988).
5. C.D. Stinespring and A. Freedman, Appl. Phys. Lett. **52**, 1959 (1988).
6. R.A. Wood and R.J. Hager, J. Vac. Sci. Technol. **A1**, 1608 (1983).
7. C. Jonah, P. Chandra, and R. Bersohn, J. Chem Phys. **55**, 1903 (1971), C.F. Yu, F. Youngs, K. Tsukiyama, R. Bersohn, and J. Preses, J. Chem. Phys. **85**, 1382 (1986).
8. C.J. Chen and R.M. Osgood, J. Chem. Phys. **81**, 327 (1984).
9. P.D. Brewer, J.E. Jensen, G.L. Olsen, L.W. Tutt and J.J. Zinck, Proc. Mat. Res. Soc. Symp. **101**, 327 (1988); P.D. Brewer, Chem. Phys. Lett., **141**, 301 (1987).

10. V.M. Donnelly, J.A. McCaulley, V.R. McCrary, C.W. Tu and J.C. Beggy, "Selective Area Growth of GaAs by Laser Induced Pyrolysis of Absorbed Gallium-Alkyls," Proc. Mat. Res. Soc. Symp., this volume.
11. D. Burgess, P.C. Stair, and E. Weitz, J. Vac. Sci. Technol. A4, 1362 (1986); P.C. Stair and E. Weitz, J. Opt. Soc. Am. B4, 255 (1987).
12. L.A. Kolodziejski, R.L. Gunshor, N. Otsuka, S. Datta, W.M. Becker and A.V. Nurmikko, IEEE J. Quantum Electron. QE-22, 1666 (1986).
13. M. Henzier, Surface Sci. 36, 109 (1973).
14. T.E. Mady, J.T. Yates and N.E. Erickson, Chem. Phys. Lett. 19, 487 (1973).
15. G. Wedler and W.F. Klemperer, Chemisorption: An Experimental Approach (Butterworths, London, 1976).

ArF LASER-INDUCED CHEMICAL-VAPOR DEPOSITION OF TUNGSTEN FOR GATE ELECTRODES

H. Matsuhashi, S. Nishikawa, and S. Ohno
Semiconductor Technology Laboratory, OKI Electric Industry Co., Ltd.,
550-5 Higashiasakawa-cho, Hachioji-shi, Tokyo 193, Japan

ABSTRACT

The deposition of W films by ArF laser-induced chemical-vapor deposition (LCVD) was investigated as a function of incident laser power, WF_6 and H_2 partial pressures, and substrate temperature. The deposition of W films by LCVD is discussed dividing that into two parts, thermal CVD (TCVD) and photon assisted CVD (P_n CVD). The rate of P_n CVD has been defined as the difference between the rates with and without laser irradiation. The reaction orders for P_n CVD are 1, 0 with respect to WF_6 and H_2 partial pressures, respectively, and the rate linearly increases with increase in laser repetition rate. The activation energy in P_n CVD is 0.17 eV. These facts indicate that, in LCVD, P_n CVD takes place independently of TCVD and that the deposition rate in P_n CVD is determined by the formation of F radicals in the dissociation of WF_6 molecules by laser irradiation.

MOS capacitors with LCVD-W gates were fabricated and their characteristics were compared with those with sputtered-W gates. It was shown that the level of contamination due to mobile ions in the capacitor with the LCVD-W gate was extremely low.

INTRODUCTION

Tungsten is an attractive alternative to poly-Si or polycide for VLSI CMOS gates because of its low resistivity and near midgap workfunction. To realize W gate CMOS VLSIs, it is important to establish the method for depositing W films on SiO_2 without damage. The CVD method has several advantages including no damage, low contamination and low resistivity. In the usual thermal CVD (TCVD), W film is selectively deposited on Si, but not on SiO_2 , at temperatures around 400 °C. To deposit W film nonselectively, ArF laser-induced CVD (LCVD) using WF_6 and H_2 gases has been studied by several authors [1-2]. However, the reaction mechanism of deposition of W film in LCVD has not been fully understood. In order to make this method applicable to device fabrication, a deeper understanding of the reaction mechanism is quite important.

The purpose of this study is to examine the reaction mechanism of deposition of W film in LCVD using WF_6 and H_2 gases in comparison with that in TCVD. The characteristics of MOS capacitors with LCVD-W gates were also studied.

EXPERIMENTAL

Tungsten films were deposited on Si or SiO_2 using WF_6 , H_2 and Ar gases by ArF laser induced CVD. The ArF excimer laser was operated typically at 50 Hz and 150 mJ/pulse and the laser beam (22 x 8 mm) was passed 10 mm above the wafer. The wafer was heated in the range from 200 to 400 °C. The gas flow rates of WF_6 , H_2 and Ar were 0 ~ 30, 0 ~ 700, and 400 sccm, respectively. In these experiments, except for MOS capacitor fabrication, W was deposited on Si because W film is not deposited on SiO_2 in TCVD, which was used to compare

with LCVD.

MOS capacitors with W gates were fabricated using (100) oriented p-type silicon wafers ($3 \Omega \cdot \text{cm}$). After gate oxidation, W films about 300 nm-thick were deposited by LCVD or sputtering. Sputtered-W was deposited using a target whose purity is 99.995%. For preventing contamination from photo-resist, silicate glass and phospho-silicate glass whose thicknesses were both about 100 nm were deposited onto W films. Then these samples were annealed at high temperatures. W gate electrodes were patterned by dry etching and the photo-resist was removed by plasma ashing. Finally these samples were annealed in N_2 at 500 °C for 30 min [3]. The characteristics of MOS capacitors were evaluated by C-V, I-V and triangular voltage sweep (TVS) [4] methods.

RESULTS and DISCUSSION

Reaction mechanism of deposition of W film in ArF laser induced CVD

Fig.1 shows the distribution of W film thickness over a substrate across the laser beam deposited with and without laser irradiation. The abscissa indicates the lateral distance from the center of laser beam. In TCVD (without laser irradiation), the distribution is almost uniform over a substrate. On the other hand, in LCVD, the distribution has a peak under the laser beam. We observed [5] similar distributions in the case of the SiN deposition by LCVD, except that the thickness approaches zero far from the laser beam. We concluded that the peaklike distribution is due to the diffusion of radicals formed in the laser beam. In the W deposition by LCVD, TCVD also occurs. Here we consider the difference between the distribution of W film thickness with and without laser irradiation. This difference is considered as the net contribution of the deposition due to radicals and/or activated atoms formed in the laser beam, which is defined as $P_h\text{CVD}$ shown in Fig.1. This is true if no interferences between TCVD and $P_h\text{CVD}$ exist as discussed later.

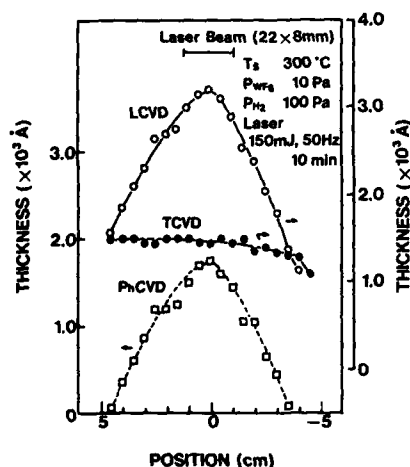


Fig.1 Distribution of W film thickness over a substrate across the laser beam.

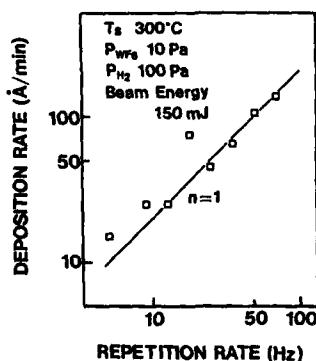


Fig.2 Deposition rate of W films in $P_h\text{CVD}$ as a function of repetition rate.

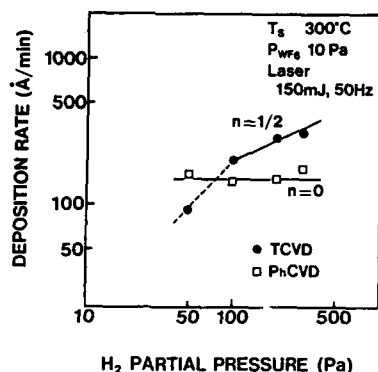


Fig. 3 Deposition rate of W films in PnCVD and TCVD as a function of H_2 partial pressure.

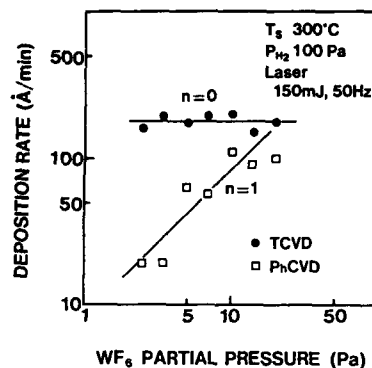


Fig. 4 Deposition rate of W films in PnCVD and TCVD as a function of WF_6 partial pressure.

Fig. 2 shows the dependence of the deposition rate of W film (r_p) in PnCVD on the repetition rate (R) and by keeping the beam energy (E) at 150 mJ/pulse. r_p has been defined as the difference between deposition rates beneath the center of laser beam with and without laser irradiation. With increasing repetition rate, r_p increases linearly.

Fig. 3 shows the deposition rates of W films in TCVD and PnCVD (r_T and r_P respectively) as a function of the H_2 partial pressure (P_{H_2}). During these depositions, the WF_6 partial pressure (P_{WF_6}) was constant. r_T depends on a square root of P_{H_2} . At the lower P_{H_2} region, r_T increases linearly with P_{H_2} . In this region, the H_2 supply is insufficient and r_T is controlled by H_2 mass transport. On the other hand, r_P was independent of P_{H_2} . The reaction order with respect to P_{H_2} for TCVD and PnCVD are thus determined to be 1/2 and 0, respectively.

Fig. 4 shows r_T and r_P as a function of P_{WF_6} , where P_{H_2} was maintained constant. r_T is independent of P_{WF_6} . On the other hand, r_P increases

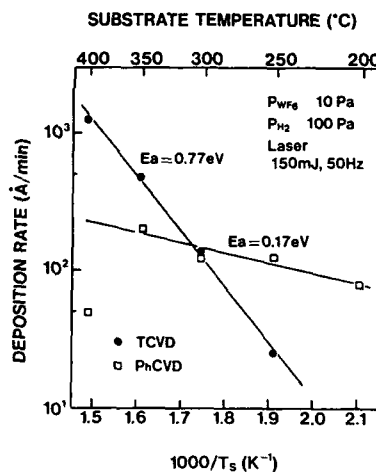


Fig. 5 Deposition rate of W films in PnCVD and TCVD as a function of substrate temperature.

linearly with P_{WF_6} . The reaction orders with respect to P_{WF_6} for TCVD and P_nCVD are thus determined to be 0 and 1, respectively.

Fig.5 shows the Arrhenius plots for r_T and r_P in the range of substrate temperature (T_s) from 200 °C to 400 °C. The activation energies in TCVD and P_nCVD are estimated to be 0.77 eV and 0.17 eV, respectively. The former value is almost the same as those estimated by others [6-8]. On the other hand, the latter value is much smaller than those in TCVD. These facts suggest that r_P is controlled by gas phase reaction. At 400 °C, the value of r_P is smaller than the expected value. It is considered that, at 400 °C, the WF_6 supply is insufficient and the reaction mechanism is a little different from that at the substrate temperature lower than 350 °C.

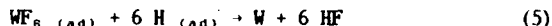
In summary of the results, when the H_2 and WF_6 supplies are sufficient, the experimentally determined rate equations for P_nCVD and TCVD can be expressed as

$$r_T = k_T P_{H_2}^{1/2} P_{WF_6}^0 \quad (1)$$

$$r_P = k_P(E) P_{H_2}^0 P_{WF_6}^1 R \quad (2)$$

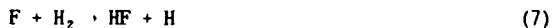
where k_T and $k_P(E)$ are rate constants for TCVD and P_nCVD , respectively.

Equation (1) agrees with those reported by others [6-7]. The reaction mechanism of deposition of W film in TCVD has been reported as follows [6]. H_2 molecules are adsorbed on the surface of W and then these adsorbed H_2 molecules dissociate to adsorbed H atoms. Next, these adsorbed H atoms react with adsorbed WF_6 molecules, producing metal W. These phenomena can be expressed as

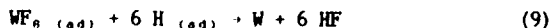


Bryant [6] has reported that, in these reactions, the dissociation of adsorbed H_2 molecules is the rate-limiting step.

Although TCVD involves no gas phase reaction, LCVD involves the gas phase dissociation, which results in excited atoms and molecular radicals, in addition to the surface reaction. This dissociation process in the gas phase is considered as follows. Photons from laser irradiation, photon dissociate WF_6 molecules into WF_x radicals and F atoms. These F atoms react in the gas phase with H_2 molecules and produce H atoms. These gas phase phenomena can be expressed as



The H atoms are then adsorbed on the surface of W and react with adsorbed WF_6 molecules, producing metal W.



In LCVD, it is supposed that reactions (3) to (5) take place in addition to reactions (6) to (9) simultaneously. We consider that reactions (6) to (9)

are operative in P_nCVD defined before. It is a question whether these two deposition paths, TCVD and P_nCVD, take place independently. For example, if adsorbed H atoms increase by reaction (8) so that the reverse reaction of (4) becomes predominant, the rate of TCVD may decrease. Another possibility is that reaction (6) occurs intensively near the laser beam, as a result, P_{WF₆} decreases locally and the rate of TCVD decreases. However the following considerations may exclude the former possibilities. First, the duration time of the laser irradiation (about 20 nsec) is much shorter than the repetition period of the laser pulse (about 20 msec) and the related reactions may cease in the interval less than a few msec after the laser irradiation as in the case of SiN deposition [5]. Second, the increase in deposition rate by the laser irradiation is the same as, or smaller than, r_T under our experimental conditions, so that the increase of adsorbed H atoms by reaction (8) may be too small to affect reaction (4).

Here we assume that r_p is determined by the formation of F atoms in the dissociation of WF₆ molecules by laser irradiation and that almost all the F atoms produced by laser irradiation react with H₂ because the number of H₂ molecules are much larger than those of F atoms. Thus, it is clear that r_p depends linearly on P_{WF₆} and the incident laser power (R·E) because F atoms formed in the dissociation of WF₆ molecules by laser irradiation increase linearly with the absorbed laser power by WF₆ molecules. The rate equation would be

$$r_p' = k_p' P_{H_2}^0 P_{WF_6}^{-1} R E \quad (10)$$

This result is in agreement with experimentally determined rate equation (2). In this experiment, the dependence of r_p on E was not studied. However the linear dependence of r_p on E is expected from this equation.

Furthermore, as the r_p is controlled by reaction (6) in the gas phase, r_p is independent of the substrate temperature. Consequently, the activation energy seems to be very small. It is also in good agreement with the fact that the activation energy in P_nCVD is very small (0.17 eV).

In previous reports [1-2], the reaction order and activation energy were determined for the rate of LCVD of tungsten, which is equal to r_p+r_T in our notations. Their experimental conditions are quite similar to ours, where r_p is the same as, or smaller than, r_T. In such situations, to understand the deposition mechanism of LCVD, it is essential to divide the rate of LCVD into r_p and r_T as discussed above.

MOS characteristics

We have reported [9] that in LCVD the intrinsic stress of W films can be controlled from a large tensile to a small compressive stress by selecting the H₂/WF₆ gas flow ratio. W films with low intrinsic stress less than 4X10⁸ dyne/cm² are reproducibly deposited on SiO₂ without peeling.

Using W film having low intrinsic stress, MOS capacitors with LCVD-W gates were fabricated and the characteristics were compared with those with sputtered-W gates. The typical characteristics of the LCVD-W MOS capacitors are shown in Table I as compared with the sputtered-W ones. The flatband voltage of the LCVD-W capacitors is a little higher than those with sputtered-W gates as a result of the higher work function of LCVD-W compared with sputtered-W. The work functions of LCVD-W and sputtered-W annealed at 900 °C were found to be 5.0 eV and 4.9 eV, respectively. The maximum breakdown fields (E_m), the fixed charge density (N_f) and the interface state density at midgap (D_{it}) of the LCVD-W capacitors are almost the same as the sputtered-W

Table | Comparison of characteristics of MOS capacitors with LCVD-W and sputtered-W gates.

	LCVD-W	Sputtered-W
V_{FB} [V]	0.11	- 0.04
E_{ox} [MV/cm]	11	11
N_t [cm^{-2}]	1.6×10^{10}	6.1×10^{10}
D_{it} [$\text{eV}^{-1} \text{cm}^{-2}$]	$< 1.0 \times 10^{10}$	4.7×10^{10}
D_{ion} [cm^{-2}]	$< 5.0 \times 10^9$	3.1×10^{10}

THICKNESS OF GATE OXIDE : 22nm

ANNEALING CONDITIONS : 900°C - 30min

ones. It was found that the mobile ion density (D_{ion}) of the LCVD-W capacitors is below the detection limit of the TVS method. The mobile ion density of the LCVD-W capacitors is one order of magnitude smaller than that of the sputtered-W capacitors. These results indicate that highly purified W films can more easily be obtained by LCVD than by sputtering.

CONCLUSION

In ArF excimer laser CVD (LCVD) of W films, there are two deposition paths TCVD and P_nCVD. The reaction orders for P_nCVD are 1,0 with respect to WF₆ and H₂ partial pressures, respectively, and the rate linearly increases with increase in laser repetition rate. The activation energy in P_nCVD is 0.17 eV. These results indicate that, in LCVD, P_nCVD takes place independently of TCVD and that the deposition rate in P_nCVD is determined by the formation of F atoms in the dissociation of WF₆ molecules by laser irradiation.

The characteristics of the MOS capacitors with LCVD-W gates are almost the same as those with sputtered-W gates. The level of contamination due to mobile ions in the LCVD-W gate MOS capacitor is much lower than that with the sputtered-W gate. These results indicate that LCVD-W is a promising material for the gate electrode for future VLSI.

REFERENCES

- [1] T.F. Deutsch and D.D. Rathman, Appl. Phys. Lett. 45, 623 (1984)
- [2] A. Shintani, S. Tsuzuku, E. Nishitani and M. Nakatani, J. Appl. Phys. 61, 2365 (1987)
- [3] B.J. Fishbein, T.T. Watt and J.D. Plummer, J. Electrochem. Soc. 134, 674 (1987)
- [4] N.J. Chou, J. Electrochem. Soc. 118, 601 (1971)
- [5] S. Nishikawa, H. Matsuhashi, T. Ishida, S. Ohno and S. Ushio in Amorphous Silicon Semiconductors—Pure and Hydrogenated, edited by A. Maden, M. Thompson, D. Adler and Y. Hamakawa (Mater. Res. Soc. Proc. 95, Pittsburgh, PA 1987) pp. 267-272
- [6] W.A. Bryant, J. Electrochem. Soc. 125, 1534 (1978)
- [7] E.K. Broadbent and C.L. Ramiller, J. Electrochem. Soc. 131, 1427 (1984)
- [8] C.M. McConica and K. Krishnamani, J. Electrochem. Soc. 133, 2542 (1986)
- [9] H. Matsuhashi, S. Nishikawa and S. Ohno, Jpn. J. Appl. Phys. 27, L2161 (1988)

MECHANISTIC STUDY OF LASER CHEMICAL VAPOR DEPOSITION OF TRIMETHYLINDIUM

MASAHIRO KAWASAKI, KAZUO KASATANI * , AKIHIKO SATO * , HIROYASU SATO *
and NOBUYUKI NISHI**

Research Institute of Applied Electricity, Hokkaido University, N2W6, Sapporo
060, Japan

*Chemistry Department of Resources, Mi'e University, Tsu 514, Japan

**Institute for Molecular Science, Okazaki 444, Japan

Laser photodissociation of trimethylindium on a quartz substrate has been studied by the laser-induced fluorescence and photofragment mass-spectrometric techniques. Translational energy distributions of photofragments are measured.

1. Introduction

Nonthermal photochemistry of organic and inorganic compounds adsorbed on substrates is induced by photon irradiation and leads to processes different from those observed in the gas phase. Photodissociation of monolayers on substrates has been reported for Cl_2 , CH_3Cl [1], CH_3Br_2 , H_2S [2], CH_3Al [3], and trimethylgallium[4]. In the photodissociation of trimethylgallium on the substrate at room temperature, Ga atoms were detected by the laser-induced fluorescence (LIF) technique[4]. In the gas phase, organometallic compounds absorb UV photons at $< 200 \text{ nm}$, resulting in dissociation into methyl radicals and other fragments. In order to understand the nature of how photon/adsorbate interactions change in different environments, our study investigates the UV photodissociation of molecules which have been deposited as a monolayer or as multilayers (solid) on a substrate.

2. Experimental

2.1 Laser-Induced-Fluorescence Measurements of Photoejected Metal Atoms.

Figure 1 shows the schematic drawing of the essential part of our experimental apparatus[4]. Briefly, a quartz substrate was dosed with a pulsed molecular beam of trimethylindium (TMIn) seeded in He. Photolysis was performed with either a KrF excimer laser or the third or fourth harmonics of a YAG laser (355 or 266nm, respectively). Indium atoms are produced by a two-photon process. After a variable time delay, the probe laser light from a dye laser pumped by an excimer laser traversed the space above the substrate at a certain distance, l (in our case, $l = 1 \text{ mm}$). Metal atoms in their ground state were detected by LIF through a monochromator with a gated MCP photomultiplier tube.

2.2 Time-of-Flight Measurements of Photoejected Radicals

The experimental apparatus[5] is schematically drawn in Fig. 2. Two chambers for reaction and detection were differentially pumped by turbomolecular pumps. The quartz substrate was cooled to 100 K, after which the sample molecules, TMIn, were deposited through a capillary tube until the molecules formed multilayers on the substrate. An ArF excimer laser (193 nm) was used to irradiate the molecules on the substrate. Radicals ejected from the substrate were detected by a quadrupole mass spectrometer with an electron bombardment ionizer.

3. Results

3.1 Laser-Induced Fluorescence Measurement of Photoejected Indium Atoms

First, the dependence of LIF intensity on the substrate temperature was studied. The LIF intensity of metal atoms decreased with increasing the temperature. This phenomenon can be explained as follows; the desorption rate of TMI_n is expected to be higher at higher substrate temperature. Thus, fewer parent molecules remain before photolysis at higher substrate temperature. We simulated the dependence of surface coverage on substrate temperature assuming several values of activation energies for desorption. It was found that the activation energy of less than one kJ mol⁻¹ could explain the temperature dependence of the LIF intensity for photoejection of indium. Therefore, the adsorption of TMI_n on the substrate is thought to be physical adsorption.

Next, the translational energy distribution of metal atoms was studied. Time-of-flight (TOF) spectra of In atoms were obtained by scanning the delay time between the photolysis laser and the LIF probe laser. In the analysis of the TOF spectra we simulated the TOF distributions assuming a Maxwell-Boltzmann translational energy distribution for In atoms. In this calculation, the distribution of flight lengths, the angular distribution of metal atoms, and the response function of the detection system were taken into account. The TOF function is given as,

$$P(t) = \int_0^\infty w(\ell) \exp[-m(\ell/t)^2/2kT] (\ell^3/t^4) d\ell, \quad (1)$$

where $w(\ell)$ is a distribution function of the flight length. Figure 3 shows a TOF spectrum of In atoms produced upon photodissociation of TMI_n at 248 nm or 193 nm and also the simulated one after deconvolution of Eq.(1) for the response function of our apparatus.

Figure 3 indicates the uniform angular distribution of fast In atoms and that the translational temperature of fast In atoms was estimated to be 3000 K. The relatively large translational energy of metal atoms means that the photodissociation of adsorbed TMI_n is so fast that there is little time for the available energy to randomize among the molecular vibrational modes of fragments.

3.2 Mass Spectroscopic Measurement of Photoejected CH₃ Radicals

When the 193 nm laser light irradiated TMI_n deposited on a quartz plate cooled to 100 K, CH₃ radicals were detected by the mass spectrometer. The TOF spectrum is given in Fig. 4 where a fast and a slow signal peak is observed. The threshold TOF is observed at 25 μs and the spectrum peaks at 70 μs for the fast component and at 270 μs for the slow one. This bimodal distribution is typical of photodissociation of molecular solids. The TOF spectrum of CH₃ radicals is converted to the translational energy distribution as given in Fig. 5, in which signal intensity peaks toward zero translational energy in addition to the high energy component.

The high-energy component in the TOF spectrum is attributable to the direct dissociation of the topmost layer of TMI_n.

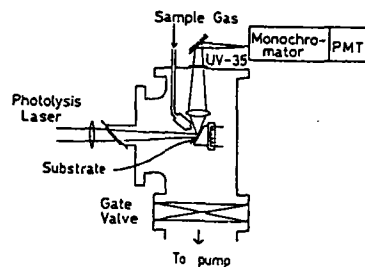


Fig. 1 Experimental apparatus for laser-induced fluorescence measurements. Probe dye laser light (not shown) passes parallel to the substrate (i.e., normal to the text paper).

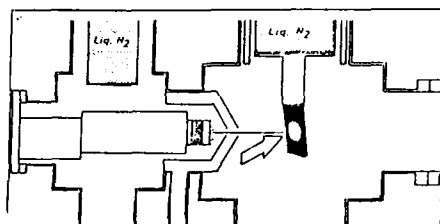


Fig. 2 Experimental apparatus for time-of-flight measurements.

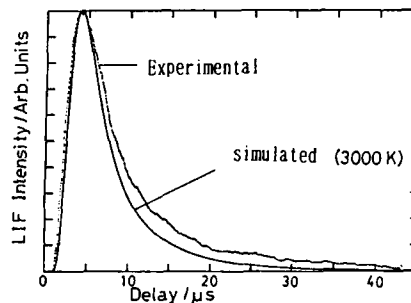


Fig. 3 TOF spectrum of In atoms produced upon photodissociation of TMIIn at 193 nm

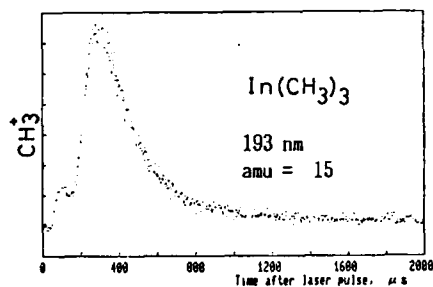


Fig. 4 TOF spectrum of CH_3 radicals produced upon photodissociation of solid TMIIn at 193 nm.

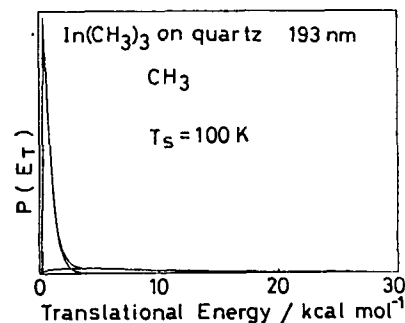
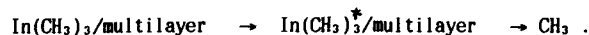


Fig. 5 Translational energy distribution of CH_3 radicals produced upon photodissociation of TMIIn at 193 nm. (·····); observed data, (—); simulated curves with two Maxwell-Boltzmann distributions.



In the direct photodissociation process, the fastest CH_3 radicals can carry all the excess energy as the translational energy. The maximum translational energy is given by,

$$E_T(\text{max}) = \hbar\omega - D_0 - \Delta E_{\text{ads}}, \quad (2)$$

where ΔE_{ads} is the difference in adsorption energies between TMI and CH_3 .

The observed $E_T(\text{max})$ of $(73 \pm 21) \text{ kcal/mol}$ is in fair agreement with the calculated value of 101 kcal/mol obtained from $\hbar\omega = 148$ and $D_0 = 47 \text{ kcal/mol}$ using Eq. (2).

ΔE_{ads} could be large in this case because TMI is adsorbed by interaction between the substrate and the In atom while the leaving CH_3 interacts weakly with the substrate through the carbon or hydrogen atoms.

Concerning the low-energy component, Higashi[3] has stated in his report on photodissociation of trimethylaluminum monolayers that the dissociative transition of monolayered molecules is not direct since so little energy is imparted to the ejected methyl radicals. These subthermal desorption distributions have been observed in the past in thermal desorption experiments[7].

The TOF spectra have a rather wide width in Fig. 4. The FWHM is as wide as $100 \mu\text{s}$. This wide distribution reflects rapid energy flow among the oscillators of molecular solids and the lattice model of the substrate. Lin and his co-workers[6] have developed a theoretical model for photodesorption using transition state theory,

$$P(E_T) = 2\pi (1/\pi kT)^{3/2} \times E_T^{-1/2} \exp(-E_T/kT). \quad (3)$$

The smooth curves through the experimental traces of Fig. 5 are best fits to composites of two Maxwell-Boltzmann distributions as given above. Thus, the surface photodissociation competes with relaxation of electronic energy to the substrate lattice modes.

References

- 1.a) M. Kawasaki, K. Kasatani, H. Sato, N. Nishi, and G. Inoue, 12th. Internat. Conf. Photochem., (Tokyo, Aug. 4-7, 1985) 1A6
- b) M. Kawasaki, H. Sato and N. Nishi, J. Appl. Phys., **65**, 792 (1989)
- 2.a) E. B. D. Bourdon, J. P. Cowin, I. Harrison, J. C. Polanyi, J. Seger, C. D. Stanners, and P. A. Young, J. Phys. Chem., **88**, 6100(1984)
- b) F. L. Tabares, E. P. Marsh, G. A. Bach, and J. P. Cowin., J. Chem. Phys., **86**, 738(1987)
3. G. S. Higashi, J. Chem. Phys., **88**, 422 (1988)
4. H. Suzuki, K. Mori, M. Kawasaki and H. Sato, J. Appl. Phys., **64**, 371 (1988)
5. N. Nishi, H. Shinohara, and T. Okuyama, J. Chem. Phys., **80**, 3898 (1984)
6. S.H. Lin, I. S. T. Tsong, A. R. Ziv, M. Symonski, and C. M. Loxton, Phys. Scrip., **T6**, 106 (1983)
7. T. Kawai and T. Sakata, Chem. Phys. Lett., **69**, 33 (1980); B. Schafer and P. Hess. ibid., **105**, 563 (1984)

PHOTOCHEMICAL VAPOR DEPOSITION OF ALUMINUM THIN FILMS

MITSUGU HANABUSA*, AKIRA OIKAWA*, PENG YING CAI*, SHIGEO FURUNO** AND SATOSHI IGUCHI**

*Toyohashi University of Technology, Tenpaku, Toyohashi 440, Japan

**Toyota Motor Corporation, Higashifuji Technical Center, 1200 Mishuku, Susono-shi, Shizuoka 410-11, Japan

ABSTRACT

Using dimethylaluminum hydride as the source gas and an ArF laser as the light source, aluminum thin films with low electrical conductivity were deposited via photochemical reactions. To emphasize surface reactions, vapor pressure was kept low with a typical value of 6.7×10^{-3} Pa. The laser energy density was typically 23 mJ/cm^2 per pulse. The deposition rate of aluminum films became reasonably high above a substrate temperature of 90°C and increased thereafter with substrate temperature. The electrical resistivity was about four times greater than the bulk aluminum value. A strongly non-linear dependence of the deposition rates on laser energy density was observed. The incremental change in thickness per pulse increased with the inverse of the pulse repetition rate, which indicated, together with area selectivity, the importance of surface photolysis of absorbed molecules.

INTRODUCTION

Last year in this conference, the interesting results of photochemical vapor deposition (photo-CVD) of aluminum thin films were reported using a new source gas of dimethylaluminum hydride (DMAIH),¹ and subsequently they were published elsewhere.² It was shown then that DMAIH was a promising source gas for photo-CVD of aluminum films as an alternative to such traditionally used gases as trimethylaluminum (TMA) or tri-isobutylaluminum (TIBA). For successful application of photoinduced processes to deposition of metal thin films of high quality at low temperature, the choice of source gases and light sources is critically important. In the works cited above, the goal was to draw fine aluminum lines with focused UV beams with high electrical conductivity, and either 257-nm or 275-nm beams generated by argon-ion lasers were used as the light source. However, since the source gas showed strong absorption only below 220 nm,² light with shorter wavelengths should be more adequate. With such light sources, adequateness of this new source gas for the wider use in photo-CVD of aluminum films can be examined.

For the reason described above we carried out an experiment using a deuterium lamp and DMAIH to deposit aluminum thin films.³ The lamp generates UV light with two broad peaks near 160 nm and 240 nm, and the vacuum ultra-violet (VUV) should be particularly suitable for photolysis of DMAIH. At substrate temperatures above about 130°C , deposition rates became large with a typical value of 20 nm/min at 200°C . The temperature required for photo-deposition was lower than that for thermal decomposition (about 250°C). The electrical resistivity varied with substrate temperature only weakly, and it was $6.2 \mu\Omega\cdot\text{cm}$ for a film deposited at 270°C . The film can be produced at the same temperature without irradiation, even though the deposition rate was about one third of what was obtained with irradiation. However, the electrical resistivity was much higher ($140 \mu\Omega\cdot\text{cm}$) for the thermally produced film than the value for the film produced with the photo-assisted process. Light helps not only to enhance deposition, but also to improve the electrical property of the deposits.

The results to be described in the present paper were obtained as an extension of the previous work with a different UV light source, namely, an ArF excimer laser (193 nm). The use of the laser was of great interest; then

the reaction mechanism responsible for deposition via photolysis of DMAIH might be understood better by comparison of the results obtained with different light sources. Also, while deposition with the deuterium lamp is suitable for production of large-area films, patterned aluminum films can be obtained with the excimer laser via pattern transfer from masks. The present work was intended partly as a preparation for such a work to be carried out in the near future.

EXPERIMENTAL

In the present work, as well as in the previous one performed with the deuterium lamp, the vapor pressure was kept low deliberately. This was done so because surface reactions, rather than gas-phase reactions, were to be emphasized. For selective-area deposition gas-phase reactions are not desirable. Also, the quartz window used to introduce light into the reaction cell was expected to be kept free from the coverage of unwanted deposits at low pressures. The vapor pressure was 6.7×10^{-3} Pa unless specified otherwise.

The experimental arrangement used in the present experiment is shown in Fig. 1. The rectangular laser beam was shaped into a size of 4×8 mm with the help of a cylindrical lens. The substrate was irradiated perpendicularly. The energy density was 23 mJ/cm^2 per pulse unless specified otherwise. The window was contaminated gradually, so that it was cleaned occasionally to restore transparency.

The source gas was synthesized by a thermal reaction of $(\text{CH}_3)_2\text{AlCl}$ and NaH and provided for this work by Toyo Stauffer Chemical Company.

The reaction cell was made of a stainless steel tube with a diameter of 100 mm and a height of 180 mm. It was evacuated by a turbomolecular pump. Back pressure was about 2×10^{-4} Pa. The source gas was introduced through a nozzle directed toward the substrate and separated from it about 10 mm. No carrier gas was used.

The substrate was *n*-doped, single-crystal silicon wafer, which was etched in buffered HF for 2 min, cleaned ultrasonically in methanol for 10 min, and then blown dry with N_2 prior to loading into the cell. Substrate temperature was controlled by an electric heater.

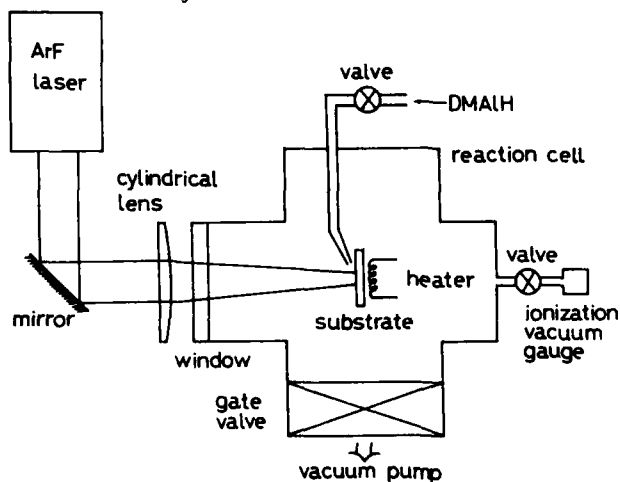


Fig. 1. Experimental arrangement used for photo-CVD of aluminum films using an ArF laser.

RESULTS AND DISCUSSIONS

Figure 2 shows the dependence of deposition rates, defined as the increase in thickness per pulse, on substrate temperature for the photo-deposited aluminum thin films. Below 90 °C deposition occurred too slowly to be significant for the practical application. Near 250 °C deposits were recognized even outside the irradiated area because of the thermal reaction. At lower temperatures deposition took place only in the irradiated area. The observed area-selectivity confirmed the importance of surface reactions.

The electrical resistivity of the photodeposited films was measured as a function of substrate temperature (Fig. 3). The values were about four times higher than the bulk value of $2.7 \mu\Omega\cdot\text{cm}$. They were about the same magnitude as those obtained from photo-CVD with the deuterium lamp.

In the case of the lamp irradiation, the growth rates were almost independent of the light power density above a certain level. A nonlinear dependence on pulse energy density was also observed in the present case, as shown in Fig. 4. After the initial rapid increase, the deposition rate became nearly constant above 5 mJ/pulse. As for the dependence of deposition rates on vapor pressure, we observed a linear behavior (up to 9×10^{-3} Pa), as was the case with the deuterium lamp. The surface of the deposited films was rough, as evidenced on scanning electron microscopic pictures by spatial irregularity with the average size of a few tenths of a micrometer.

Finally, we show the result obtained when the pulse repetition rate was changed, as shown in Fig. 5. This was observed at 200 °C. Note that if gas-phase reactions are important, the deposition rate defined as above should be independent of the repetition rate. On the other hand, the general trend can be expressed well by a solid curve shown in Fig. 5, which takes the functional form of $[1 - \exp(-t/\tau)]$, where t is the inverse of repetition rate, or the time interval between two pulses. This kind of time dependence is expected for the temporal increase of adsorbed molecules with an average lifetime of τ . The deposition rate is then given by the probability of photolysis per molecule times the number of adsorbed molecules. To fit the experimental points, the value of τ should be about 0.22s. The observed

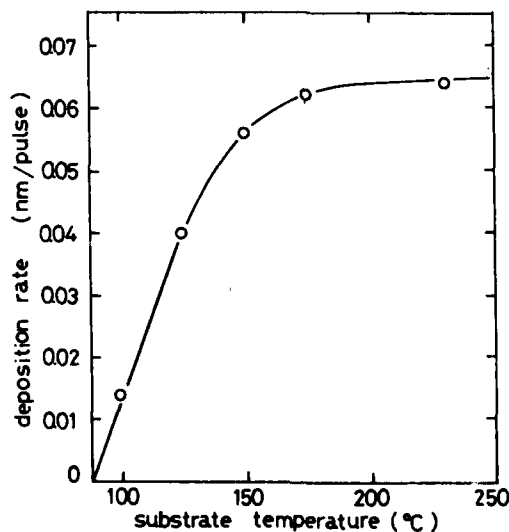


Fig. 2. Dependence of deposition rates on substrate temperature.

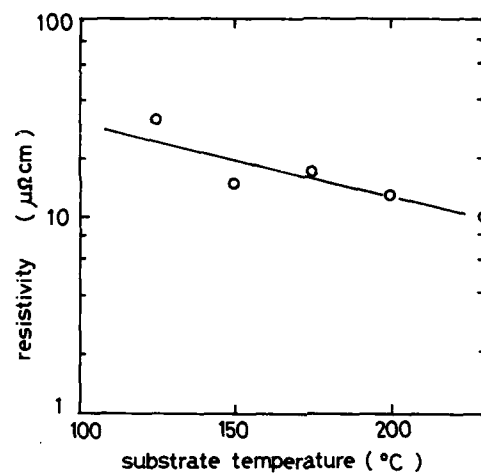


Fig. 3. Dependence of electrical resistivity on substrate temperature.

temperature dependence can be accounted for if the probability of surface photolysis increases with temperature, as postulated elsewhere.⁴ However, a further study is required before a definite conclusion is drawn.

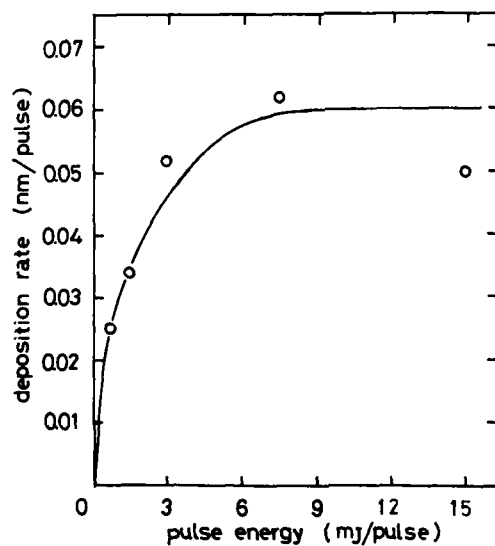


Fig. 4. Dependence of deposition rates on laser pulse energy.

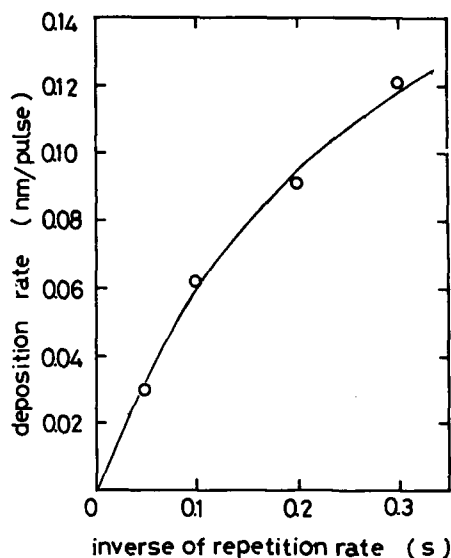


Fig. 5. Dependence of deposition rates on inverse of pulse repetition rate.

CONCLUSION

Aluminum thin films with their electrical resistivity about four times the bulk value could be produced via photo-CVD using DMAIH at temperatures lower than possible with thermal reactions. The vapor pressure was chosen low (typically 6.7×10^{-3} Pa). Then, surface reactions became more important than gas-phase reactions, as evidenced by area selectivity and the pulse-interval dependence of deposition rates.

ACKNOWLEDGEMENT

We thank Toyo Stauffer Chemical Company for the supply of DMAIH. This work was partly supported by the Spetial Fund from the Ministry of Education.

REFERENCES

1. T. Cacouris, G. Scelsi, R. Scarmozzino and R.M. Osgood, presented at the 1987 MRS Fall Meeting, Boston, MA, 1987 (unpublished).
2. T. Cacouris, G. Scelsi, P. Shaw, R. Scarmozzino, R.M. Osgood and R.R. Krchnavek, *Appl. Phys. Lett.* **52**, 1865 (1988).
3. M. Hanabusa, K. Hayakawa, A. Oikawa and K. Maeda, *Jpn. J. Appl. Phys.* **27**, L1392 (1988).
4. Y. Aoyagi, A. Doi, S. Iwai and S. Namba, *J. Vac. Sci. Technol.* **B5**, 1460 (1987).

TUNABLE UV LASER PHOTOLYSIS OF ORGANOMETALLIC COMPOUNDS WITH PRODUCT DETECTION BY LASER MASS SPECTROSCOPY

TH. BEUERMANN AND M. STUKE

Max-Planck-Institut für biophysikalische Chemie, P.O.2841, D-3400 Göttingen,
F. R. Germany

ABSTRACT

We use tunable UV laser light in the region 200-320 nm, produced by frequency doubling the output of a dye laser for the decomposition of organometallic compounds. This method has been applied to TMA, trimethylaluminum $\text{Al}(\text{CH}_3)_3$. Only the TMA monomer absorbs UV light for $\lambda > 220\text{nm}$. TMA decomposes by one-photon absorption mainly into two channels: aluminum plus organic fragments and aluminummonomethyl plus organic fragments. The ratio $[\text{Al}]/[\text{AlCH}_3]$ is wavelength dependent. Finally, we present a mechanism to explain the photolysis of trimethyl compounds of group III elements (Al, Ga, In).

INTRODUCTION

How do organometallics interact with UV laser light ?

Metalorganic compounds play an important role in the chemical vapour deposition (CVD) and Laser-CVD. A better understanding of the photolysis of these compounds is essential to optimize the deposition rate and the purity of the deposited metal film, among other important parameters, for practical purposes. We use laser mass spectroscopy for the detection and identification of neutral photoproducts.

ABSORPTION SPECTRUM OF TMA

The absorption spectrum of TMA is shown in Fig.1. The structureless spectrum points to a dissociative continuum of TMA in the far UV region. The cross section begins to rise at about 250 nm till 220 nm, where a new channel seems to open. The cross section is pressure dependent due to dimer formation. For a given temperature the monomer / dimer ratio strongly depends on the pressure (Fig.2) [1]. For example, at room temperature the monomer fraction in TMA amounts to only 4% at $p=1\text{Torr}$ while it amounts to 33% at $p=0.01\text{Torr}$ (compare Fig.2), i.e. by decreasing

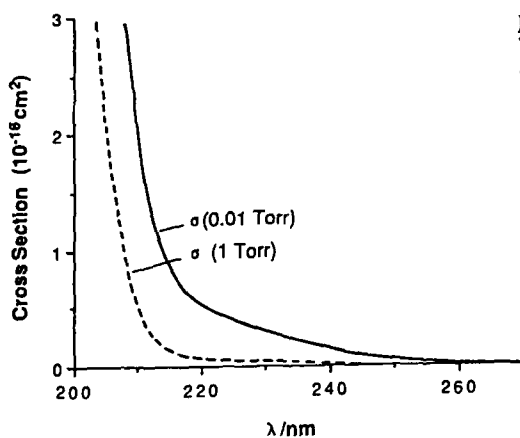


Fig.1: UV absorption spectrum of TMA for a pressure of 0.01 Torr and 1 Torr, respectively.

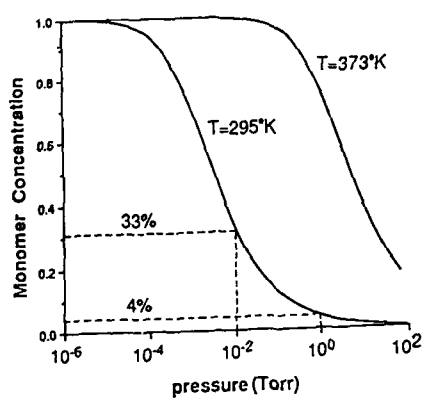


Fig.2: Pressure dependence of the monomer concentration in TMA for a temperature of 295 K and 373 K (the curves were calculated by using the equilibrium constant given in Ref.1).

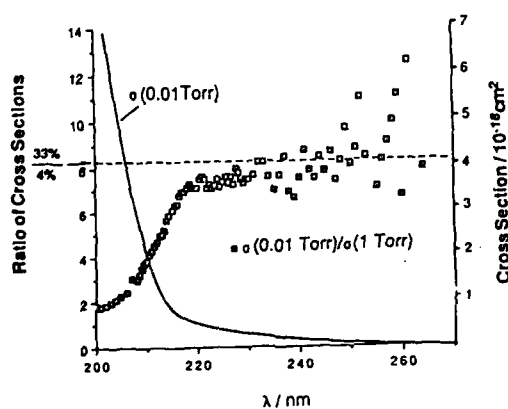


Fig.3: Ratio of the UV absorption cross sections for a pressure of 0.01 Torr and 1 Torr as a function of the wavelength. The cross section for 0.01 Torr is plotted for comparison.

the pressure between these two values the monomer fraction is multiplied by a factor 8. For $\lambda > 220\text{nm}$ only the monomer absorbs. This can be seen from Fig.3, where the ratio of the cross sections at $p=0.01\text{Torr}$ and $p=1\text{Torr}$ is plotted versus laser wavelength, showing an asymptotic approach to the predicted value $\sigma(0.01\text{Torr})/\sigma(1\text{Torr})=8$.

EXPERIMENTAL SETUP

A detailed description of the experimental setup can be found in [2]. The excimer laser is replaced by a tunable UV laser light source to photolyse the investigated compounds. Tunable UV output is generated by frequency doubling (SHG) the output of a XeCl excimer laser pumped dye laser in a β -bariumborate crystal (BBO). With this arrangement it is possible to tune the photolysis laser wavelength between 205 and 320nm [3]. Moreover, one can cover the range 200-207nm by sum frequency generation (SFG) [3]. We use a weakly focussed KrF excimer laser ($\lambda=248\text{nm}$) to detect the photoproducts by non-resonant two-photon ionization similar to the detection of GaCH₃ as a photoproduct of trimethylgallium described earlier [4]. Alternatively, photoproducts can be detected by resonant multiphoton ionization (REMPI). Applying this technique, it was shown [5] that AlCH₃ is a photoproduct of TMA.

The data presented here were obtained by exposing TMA molecules (Alfa Ventron) in the ionization region of the laser time-of-flight mass spectrometer to the UV laser light source described above. Then, after a time delay of 200ns, the neutral photoproducts were ionized by a KrF laser.

RESULTS

Typical time-of-flight mass spectra of TMA at $\lambda=193\text{nm}$ (ArF) can be seen in Fig.4. Ions generated by the photolysis laser alone (top trace) are Al⁺ and Al(CH₃)₂⁺. The detection laser (KrF) alone generates only a small amount of Al⁺ (bottom trace). If the detection laser is triggered after a suitable delay of $\Delta t=0.2\mu\text{s}$ with respect to the photolysis laser, the mass spectrum shown in the middle trace is obtained. In addition to the ions from the top trace, AlCH₃⁺ and Al⁺ ions are detected, due to the corresponding neutral species. Other photoproducts were not found. The enhancement of the Al⁺ and AlCH₃⁺ peaks with respect to the bottom line is a measure of the relative amount of the corresponding neutral fragments produced by the photolysis laser. Since the energy of the photolysis laser is wavelength dependent, one has to divide the above mentioned enhancement by the pulse energy to derive the yield Y of a photoproduct. Measurements reported here show a linear dependence of the Al and AlCH₃ signals upon the laser energy, a fact, which strongly suggests that TMA decomposes by a one-photon process. The obtained yields Y(Al) and Y(AlCH₃) are shown in Fig.5 as a function of the photolysis laser wavelength. The threshold for Al production is at about 255nm, whereas

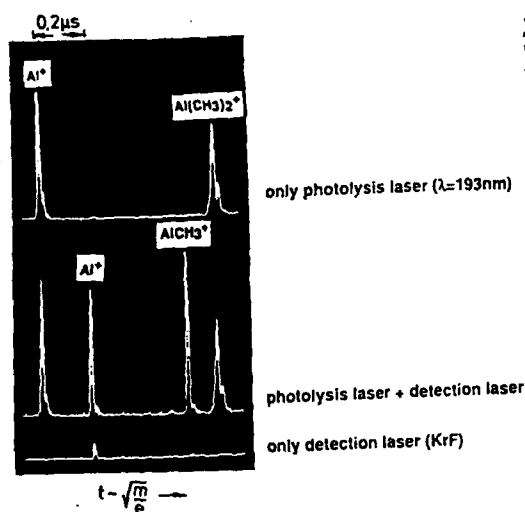


Fig. 4: Ion time-of-flight signal of trimethylaluminum $\text{Al}(\text{CH}_3)_3$, induced by the photolysis laser at 193 nm alone (top trace), and after ionization of neutral species, formed by the photolysis laser, by a weakly focussed KrF excimer laser (detection laser) delayed by 200 ns (middle trace). The control experiment, with the detection laser alone, is shown in the bottom trace (see text for details).

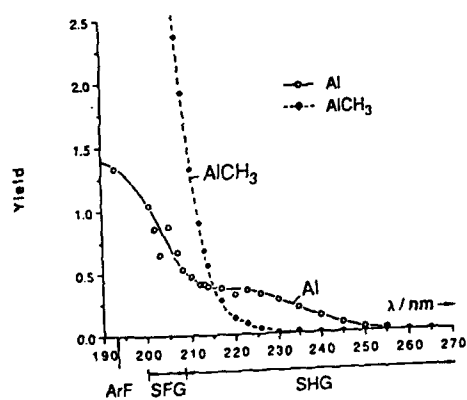


Fig. 5: Yields of Al and AlCH_3 as a function of the photolysis laser wavelength.

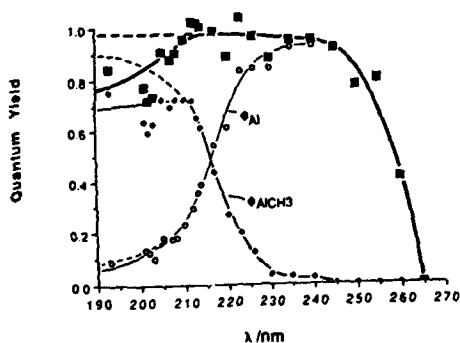


Fig. 6: Quantum yield Φ for the two fragmentation channels Al , AlCH_3 and the sum of both. The yields were calculated from $\Phi = Y/A$, where Y is the measured yield of a photoproduct and A the absorption coefficient of TMA at 0.01 Torr.

the AlCH_3 yield has its onset at 230nm. The latter channel becomes even dominant below $\lambda=215\text{nm}$. It should be further mentioned that, since the ionization probabilities of Al and AlCH_3 are different, the ratio of both yields depends on the experimental conditions.

An important issue is whether there is any correlation between the yields $Y(\text{Al}), Y(\text{AlCH}_3)$ and the absorption spectrum of TMA. Therefore, we calculate the quantum yield $\Phi_x := N_x/N$, where x stands for Al or AlCH_3 , N_x is the number of photons in the x-channel and N is the total number of absorbed photons. From the proportionalities $Y_x \sim N_x$ and $A(\lambda) \sim N$, for the absorption coefficient A being much smaller than 1, follows $\Phi_x \sim Y_x/A$.

In Fig. 6 we have plotted Φ against the wavelength of the photolysis laser. One sees that the quantum yield for Al production remains constant between 220 and 260nm. This means that absorption of a UV photon leads in this interval predominantly to the decomposition of TMA into aluminum and organic fragments. Below 230nm the AlCH_3 production becomes more and more important, but both quantum yields sum up to a constant all the way down to 210nm. Below this value, the sum of both channels begins to decrease. A reason for this behaviour can be the uncertainty of the absorption spectrum for low pressures ($p < 0.001$ Torr). Nevertheless, no significant amounts of other photoproducts have been seen in this region, so that we are confident that the dotted line in Fig.6 reflects the real photochemistry of TMA. Finally, Fig.7 illustrates the relative amounts of Al and AlCH_3 compared to the absorption spectrum of TMA. Observe again that for $\lambda \geq 235\text{nm}$ TMA decomposes only to Al and organic fragments, while otherwise AlCH_3 is detected as well.

DISSOCIATION MECHANISM OF TMA

One striking feature of our results is that aluminum atoms are produced at lower photon energies than AlCH_3 . Since the average bond energy of an Al-C bond in TMA is reported to be about 2.7eV [6], one expects 8.1eV to be necessary in order to separate all three CH_3 ligands.

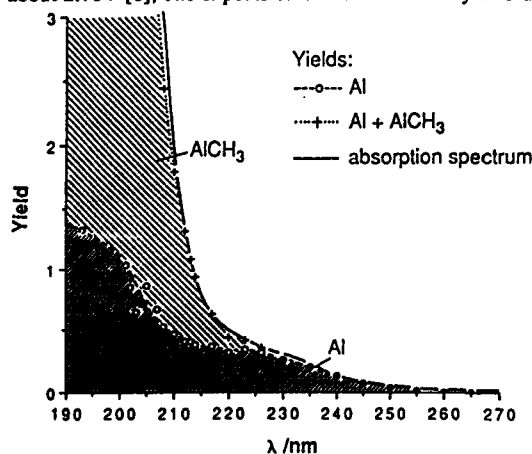


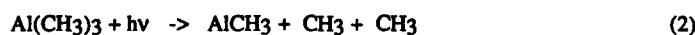
Fig.7: The relative amounts of TMA decomposition products as a function of photolysis laser wavelength in comparison to the absorption spectrum.

On the other hand, our experiments show that one 5eV photon is sufficient to isolate the Al atom. In order to explain the energy mismatch of 3.1 eV, we propose a mechanism which sets energy free, for example by the following :



Unfortunately, C_2H_6 has no dipole moment and a high ionization potential making the collision-free detection difficult.

The mechanism for the production of AlCH_3 is :



without the gain of energy through the formation of a stable molecule like C_2H_6 . Taking the average binding energy of 2.7eV, one would expect the onset of the AlCH_3 production at about 230nm (5.4eV), in agreement with the experimental results (comp. Figs. 5-7).

For Ga (TMG) and In (TMI) the mechanism is the same.

Conclusion

From our results on the decomposition of TMA by UV laser light we conclude:

only the monomer of TMA absorbs radiation for $\lambda \geq 220\text{nm}$
 the decomposition of TMA is a one-photon process
 the main photoproducts are Al and AlCH_3
 the ratio $[\text{AlCH}_3]/[\text{Al}]$ is wavelength dependent

REFERENCES

1. A. Almendinger, S. Halvorsen, A. Haaland, Acta Chem. Scand. **25**, 1937 (1971)
2. R. Larciprete and M. Stuke, J. Phys. Chem. **90**, 4586 (1986)
3. P. Lokai, B. Burkhardt, D. Basting, W. Mückenheim, Laser und Optoelektronik **3**, 296 (1987)
4. Y. Zhang, Th. Beuermann, M. Stuke, Appl. Phys. B, rapid communications, Jan. 1989
5. Y. Zhang and M. Stuke, Jap. J. Appl. Phys. **27**, L1349-L1351 (1988)
6. Y. Rytz-Froideveux, R. P. Salathé, H. H. Gilgen, Appl. Phys. A **37**, 121 (1985)

LICVD OF $\text{Cr}(\text{C},\text{O})$ FILMS FROM $\text{Cr}(\text{CO})_6$ AT 248 NM:
GAS-PHASE AND SURFACE PROCESSES

R. NOWAK, L. KONSTANTINOV AND P. HESS
Institute of Physical Chemistry, University of Heidelberg,
Im Neuenheimer Feld 253, D-6900 Heidelberg, F.R.G.

ABSTRACT

The influence of laser fluence and carbon monoxide partial pressure on the deposition rate of thin $\text{Cr}(\text{C},\text{O})$ films was investigated. The films were deposited from $\text{Cr}(\text{CO})_6$ mixtures with CO and Ar using a KrF excimer laser. The observed results are discussed with respect to the relative importance of gas-phase and surface processes. The results reveal that under the present experimental conditions chromium atoms produced in the gas phase play only a minor role as direct film precursors in KrF laser-induced film deposition.

INTRODUCTION

Recent experiments on LICVD of thin $\text{Cr}(\text{C},\text{O})$ films using chromium hexacarbonyl as a precursor have shown that in pulsed laser and especially cw laser deposition at UV wavelengths the grown films are heavily contaminated by carbon and oxygen impurities. Typical chromium concentrations for pulsed deposition with 248 nm light (KrF laser) were approximately 50-60% Cr with equal or unequal amounts of carbon and oxygen (1-3). Films deposited with cw 257 nm light (frequency-doubled Ar⁺ laser) contained only 30-40% Cr and oxygen with no or only small amounts of carbon (4-7). In order to reduce the level of impurity incorporation, a better understanding of the basic processes leading to $\text{Cr}(\text{C},\text{O})$ film deposition is of extreme importance. For the case of KrF laser-induced film deposition it has been shown that a variety of excited chromium atoms are produced in the gas phase by both direct multiphoton dissociation and sequential dissociation via an intermediate, but in addition a large number of unsaturated chromium carbonyl molecules are produced in the gas phase (8). Further experiments revealed that in the case of $\text{Cr}(\text{C},\text{O})$ film deposition on quartz substrates the growth rate increases upon heating the substrate in the temperature interval between 20°C and 65°C (3) and that the process can be described in terms of a diffusion length for buffer gas pressures greater than about 20 torr (2,3). In the present work results concerning the influence of KrF laser fluence and carbon monoxide partial pressure on the growth rate of film deposition from $\text{Cr}(\text{CO})_6$ mixtures are reported. These results are discussed with respect to a possible mechanism for $\text{Cr}(\text{C},\text{O})$ film deposition in the case of pulsed laser irradiation.

EXPERIMENTAL

The experimental setup used for the present studies is shown schematically in Fig.1. The output energy of the KrF excimer laser, which was operated at a repetition rate of 20 Hz in most experiments, was attenuated by a dielectric beam

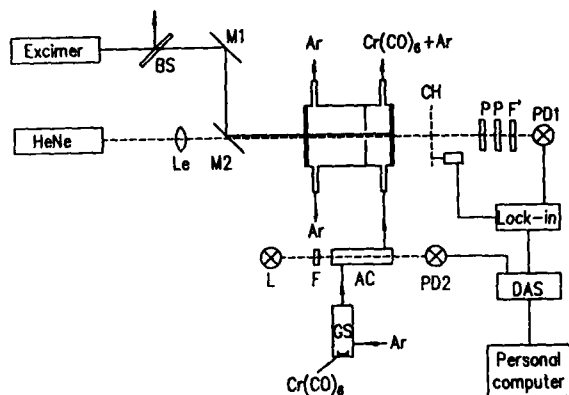


Fig.1: Experimental setup; abbreviations as follows: AC: absorption cell, Ar: carrier gas (argon), BS: beam splitter, CH: chopper, DAS: data acquisition system, F, F': bandwidth filters, GS: gas saturator, L: low pressure mercury lamp, Le: lens ($f=300$ mm), M1, M2: dielectric mirrors for 248 nm, P: polarizer, PD1, PD2: photodiodes for visible and ultraviolet wavelengths, respectively.

splitter. The gas flows through the deposition cell were adjusted by mass flow controllers (not shown in Fig.1). After saturating the carrier gas (argon, purity: 99.999%) with chromium hexacarbonyl vapor in the saturator, the number density of $\text{Cr}(\text{CO})_6$ in the carrier gas was monitored by measuring the absorption at 253 nm in a quartz cuvette before the mixture entered the deposition cell. The film deposition was performed on quartz substrates (Suprasil I) at a laser beam spot diameter of 3 mm and an ambient temperature of about 24°C . Monitoring the film growth by the transmission of a HeNe laser probe beam (633 nm) in situ revealed that under the conditions of the present experiments the change of the optical density with time was nearly constant for film thicknesses greater than approximately 200 Å. Therefore, a calibration of the optical transmission curves with mechanically measured film thicknesses was possible (Talystep profilometer). In all cases the film growth could be monitored up to a film thickness of about 4000 Å using a sensitive photodiode for probe beam detection. The partial pressure of carbon monoxide in the carrier gas was adjusted by mixing the argon gas flow with a controlled CO mass flow (purity: 99.996%) while keeping the total gas flow through the deposition cell constant. During all experiments of this work the total gas pressure, which was measured by a capacitance manometer, was kept constant at 200 mbar.

RESULTS AND DISCUSSION

The deposition of thin $\text{Cr}(\text{C},\text{O})$ films under the conditions of the present study results from a complex combination of gas-phase and surface processes. The importance of surface processes is already evident from the observation that a metallic film is formed only on the area irradiated by the laser

beam; outside of this area a nonadhesive black to brown deposit may be formed under certain experimental conditions. For this reason the amount of energy absorbed in the gas phase and at the surface, respectively, will be indicative of the importance of both processes. In Fig.2 the fluence absorbed in the gas phase is presented as a function of the incident laser fluence under the given conditions. This dependence was obtained upon firing two or three laser pulses through the deposition cell at a very low repetition rate ($\ll 1$ Hz). It can clearly be seen that the amount of energy absorbed in the gas phase reaches saturation for fluences higher than about 100 mJ cm^{-2} and this suggests that in the saturation limit practically all absorbing molecules are dissociated or excited.

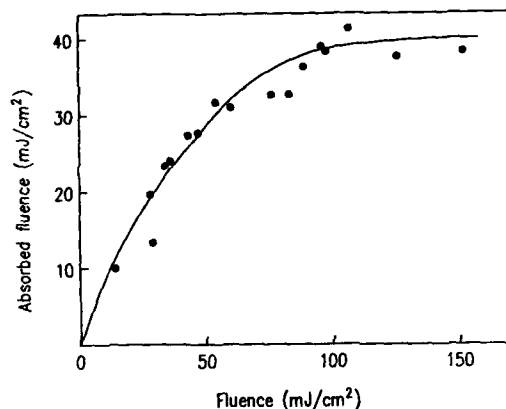


Fig.2: The fluence absorbed in the gas phase as a function of the incident laser fluence for $\text{Cr}(\text{CO})_6$ -Ar mixtures at a total pressure of 200 mbar, an absorption length of 4 cm and a gas flow of 50 sccm.

In Fig.3 the dependence of growth rate on the incident laser fluence is given for the same conditions as in Fig.2. The figure presents the time-averaged growth rates determined by mechanical thickness measurements with a profilometer. This is compared with the temporal change of the optical thickness which was obtained from the linear part of the transmission curves. It is interesting to note that the characteristic behavior of both dependences is nearly identical. For laser fluences below about 70 mJ cm^{-2} the growth rate increases approximately linearly with incident laser fluence up to about 6 Å/s and for higher fluences it drops to about half of this value. The linear part of this dependence suggests a rate-limiting one photon process, while the interpretation of the decreasing part is more difficult. Obviously the similar behavior of the temporal change of optical thickness and that of the time-averaged growth rate suggests that the optical properties of the deposited films do not change very much in the interval studied. Therefore, we believe that to a first approximation the morphology of the films does not change drastically during growth but that the main reason for the decrease in growth

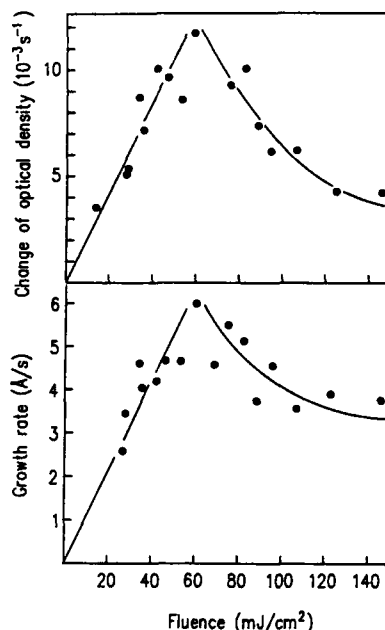


Fig.3: Bottom: The dependence of the time-averaged growth rate on the incident laser fluence at a repetition rate of 20 Hz for Cr(CO)_6 -Ar mixtures at a total pressure of 200 mbar and a gas flow of 50 sccm. Top: The dependence of the temporal change of the optical density on the incident laser fluence under the same conditions.

rate is a mechanistic one. In the following, two simple explanations are discussed in detail. Homogeneous gas phase nucleation leads to heavy inert particles and clusters which, to some extent, are lost for film growth because of diffusion and flow out of the deposition region. Such an explanation is supported by the observation that under the present conditions and incident fluences higher than 70 mJ cm^{-2} the deposition of black nonadhesive powder on non-illuminated substrate areas increases with rising incident laser fluence. On the other hand, we observed that for laser fluences higher than those given in Fig.3 no homogeneous film formation is obtained. From this result we conclude that thermal re-evaporation from the growing film might be an additional loss channel for film growth, which may also contribute to the decrease of the growth rate above 70 mJ/cm^2 .

Further mechanistic information is obtained from the dependence of growth rate on the carbon monoxide partial pressure, as shown in Fig.4, where the carbon monoxide partial pressure was increased up to somewhat less than the total gas pressure. Interestingly, the deposition rate decreases only slowly within the studied pressure interval, in contrast to the results obtained from the cw experiments by Jackson and

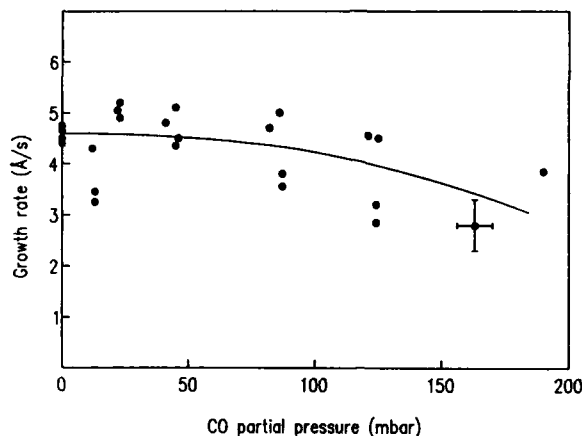


Fig.4: The dependence of the growth rate on carbon monoxide partial pressure at an incident laser fluence of 72 mJ/cm^2 , a repetition rate of 20 Hz and a total gas pressure of 200 mbar.

Tyndall (6), on the other hand, the nucleation time rises (not shown). An experiment performed with pure carbon monoxide yielded a brown and porous adhesive deposit with a time-averaged growth rate of 15 Å/s , but with a rather long nucleation time. While all films prepared for the data shown in Fig.4 had a metallic appearance, the morphology and composition of this latter deposit is clearly different.

In this paragraph some remarks concerning a possible mechanism of Cr(C,O) film deposition under the present experimental conditions will be made. The present growth rate is on the order of 6 Å/s . Therefore, approximately 2×10^{14} atoms cm^{-2} are deposited per laser pulse, when taking the bulk density of pure chromium into account. Due to the low vapor pressure of about 0.2 torr a column height of chromium hexacarbonyl molecules on the order of 1 mm above the substrate is necessary to explain the magnitude of the present growth rate. However, the mean free path length at the given total pressure of 200 mbar is only about 0.2 μm . It is very unlikely that chromium atoms separated from the substrate surface by more than a few mean free path lengths will reach the surface in the above reactive environment. Thus, we believe that the direct contribution of chromium atoms to film growth will play only a minor role under the conditions of the present experiments, because it has been shown that the recombination of unsaturated chromium carbonyl molecules with CO molecules requires less than ten collisions (9). Taking into account that the growth process can be described by a diffusion length (3), a substantial contribution of unsaturated and saturated chromium carbonyl molecules to film growth is very likely. Previously we have shown that the growth rate increases with rising substrate temperature and this finding has been

interpreted in terms of an activated chemisorption and/or pyrolytical decomposition (3). Therefore, film formation by an adsorbed layer of unsaturated chromium carbonyl molecules which may be partly decomposed by the high transient surface temperature and completely decomposed by the next laser pulse is supported by these experiments.

CONCLUSIONS

The present measurements show that the effect of increasing partial pressure of CO on the nucleation time and the growth rate is surprisingly small. The nucleation time increased by less than a factor of two when the CO partial pressure was changed from zero to about 200 torr. The decrease in the deposition rate was also very small, as shown in Fig.4, for a repetition rate of 20 Hz, but was somewhat more pronounced at lower pulse repetition rates. This is consistent with the following scenario for Cr(CO)₆ film deposition from Cr(CO)₆. The excimer laser pulse photolyses most of the Cr(CO)₆ molecules in the irradiated gas volume. However, only chromium atoms and coordinatively unsaturated chromium carbonyls located within a few mean free path lengths have a chance to reach the surface before the efficient recombination with CO molecules occurs. These highly active species may be responsible for nucleation, but the lifetime is too small to explain the measured growth rate. This indicates an important contribution of more stable carbonyl molecules and possibly clusters to the deposition process. This would imply that most of the CO groups are removed at the surface either by photolysis during the laser pulse and/or by pyrolysis during and between laser pulses.

ACKNOWLEDGEMENTS

We would like to thank Professor Schmidt and Dr. Oetzmann from Corporate Research of Asea Brown Boveri AG in Heidelberg for their contributions to this work. Financial support by the Bundesministerium für Forschung und Technologie (BMFT) under contract No. 13N5363 8 and by the Fonds der Chemischen Industrie is gratefully acknowledged.

REFERENCES

- (1) H. Yokoyama, F. Uesugi, S. Kishida, K. Washio, Appl.Phys. A **37**, 25 (1985)
- (2) L. Konstantinov, R. Nowak, P. Hess, Appl.Phys.A **47**, 171 (1988)
- (3) R. Nowak, L. Konstantinov, P. Hess, Appl.Surf.Sci., to be published.
- (4) N.S. Gluck, Z. Ying, C.E. Bartosch, W. Ho, J.Chem.Phys. **86**,4957 (1987)
- (5) N.S. Gluck, G.J. Wolga, C.E. Bartosch, W. Ho, Z. Ying, J.Appl.Phys. **61**, 998 (1987)
- (6) R.L. Jackson, G.W. Tyndall, J.Appl.Phys. **64**, 2092 (1988)
- (7) K.A. Singmaster, F.A. Houle, R.J. Wilson, Appl.Phys.Lett. **53**,1048 (1988)
- (8) G.W. Tyndall, R.L. Jackson, J.Chem.Phys. **89**, 1364 (1988)
- (9) E. Weitz, J.Phys.Chem. **91**, 3945 (1987)

LIF-DIAGNOSTICS OF Cr DURING LASER-INDUCED DEPOSITION FROM $\text{Cr}(\text{CO})_6$

D. Rieger, B. Rager and F. Bachmann

Siemens AG, Corporate Production and Logistics Department, Otto-Hahn-Ring 6,
D-8000 München 83, Federal Republic of Germany

ABSTRACT

The spatial and temporal distribution of Cr^* in a laser-CVD arrangement has been studied by laser-induced fluorescence (LIF). Low excited $\text{Cr}^*(a^5S_2)$ atoms are produced by dissociation of $\text{Cr}(\text{CO})_6$ by a KrF laser ($\lambda = 248 \text{ nm}$) via two photon absorption. An observed disappearance of Cr^* after photolysis is due to reaction with photofragments, quenching via collision relaxation and deposition. The diffusion constants for Cr^* in $\text{He}/\text{Cr}(\text{CO})_x$ mixtures could be determined. The Cr^* density in the vicinity of a sample drops sharply by heating the sample. The decrease is due to thermal decomposition of $\text{Cr}(\text{CO})_6$ with an activation energy of 0.11 eV.

Introduction

The use of laser-induced deposition (Laser-CVD) processes holds substantial promise for application. The knowledge of gas phase and (or) surface dissociation, transport of radicals and reaction mechanism are important clues for the understanding of the deposition process [1,2]. Laser-induced fluorescence is a sensitive and selective method for monitoring atoms or molecules and is therefore in use to investigate plasmas in etch processes [3] and CVD reactors [4]. In this work we monitor Cr^* atoms produced by photolysis of $\text{Cr}(\text{CO})_6$ with a KrF excimer laser radiation to study the gas phase processes and the changes in the vicinity of a surface due to deposition and substrate temperature.

Experimental

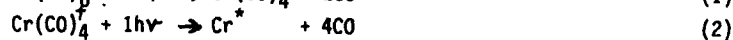
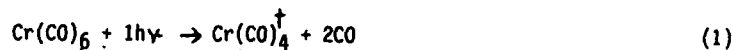
The experimental setup consists of a photolysis laser, a dye-laser, a reaction chamber and a photon detection system. The photolysis laser (Lambda Physik, EMG 1003i) was focussed into the chamber onto a heatable sample

(Si(100)). The focal dimensions were about $90 \times 500 \mu\text{m}$ and the fluence could be adjusted between 0.05 and 1.8 J/cm^2 . The Cr^* atoms were excited by a dye laser (Lambda Physik, FL 3002), whose focussed beam ($\phi \leq 20 \mu\text{m}$) crosses the focus of the photolysis laser perpendicular and passes parallel to the sample surface. The dye laser beam could be moved relative to the KrF laser beam 0.1 - 10 mm parallel and vertical to the sample. The fluorescence was collected perpendicular to both laser beams by a lens and imaged onto the entrance slit of a 0.35 m-monochromator. The signal was averaged with a boxcar integrator. In order to observe the temporal change of the Cr^* density after photolysis, the time delay between the pulses of the KrF and dye laser was varied. The repetition rate was 30 Hz. $\text{Cr}(\text{CO})_6$ seeded in Helium was flowing through the reaction chamber, and a separate window purge with He reduced deposition on the windows. The partial pressure of $\text{Cr}(\text{CO})_6$ could not be measured directly, but was estimated from the vapor pressure, the He flow and the LIF intensity.

Results and Discussion

The emission spectrum observed is very similar to that reported by Tyndall et al. [5]. All lines can be assigned to $\text{Cr}(\text{I})$ transitions [6]. A LIF spectrum of $\text{Cr}(a^5S_2)$ is shown in Fig. 1. The dye laser excites a transition of Cr^* from the metastable initial state a^5S_2 to $y^5P^o_3$ ($\lambda = 449.7 \text{ nm}$) and the red shifted fluorescence at 464.6 nm ($y^5P^o_3 \rightarrow a^5D_4$) was monitored. Therefore we detect in all experiments slightly excited Cr^* atoms starting from the metastable initial a^5S_2 state, about 0.94 eV above the ground state a^7S_3 . The fluorescence was saturated at dye laser fluences of 0.1 - 1 J/cm^2 .

We observed a quadratic dependence between the fluence of the photolysis laser and the LIF intensity, exhibiting that $\text{Cr}(a^5S_2)$ is formed by a two-photon process. Since the total dissociation energy of $\text{Cr}(\text{CO})_6$ is 6.45 eV [5], at least two photons of 5.0 eV are necessary to produce Cr atoms. Tyndall et al. give evidence [5], that Cr^* in the low excited a^5S and a^5D states is formed in a high yield by a sequential process and higher excited states are produced in a direct process. In the sequential process vibrationally hot $\text{Cr}(\text{CO})_4^\dagger$ serves as an intermediate photoproduct, from which excited Cr^* is produced by absorption of a second photon:



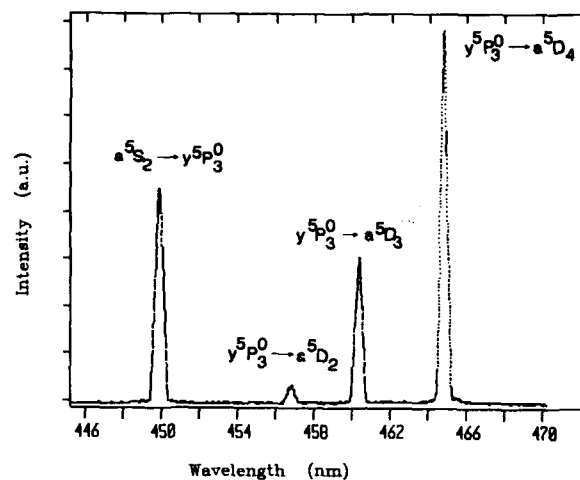


Fig. 1 LIF spectrum of $\text{Cr}(a^5S_2)$ showing the excitation wavelength $\lambda = 449.7 \text{ nm}$ ($a^5S_2 \rightarrow y^5P_3^0$) and the red-shifted fluorescence ($y^5P_3^0 \rightarrow a^5D_{2/3/4}$).

If collisional cooling of the hot $\text{Cr}(\text{CO})_4^\dagger$ intermediate occurs, the Cr^* states a^5S and a^5D may not be reached energetically with a 5.0 eV photon. Our experiments support this model, because as shown in Fig. 2, the Cr deposition drops sharply for total pressures $> 10 \text{ Torr}$. For this pressure regime, the

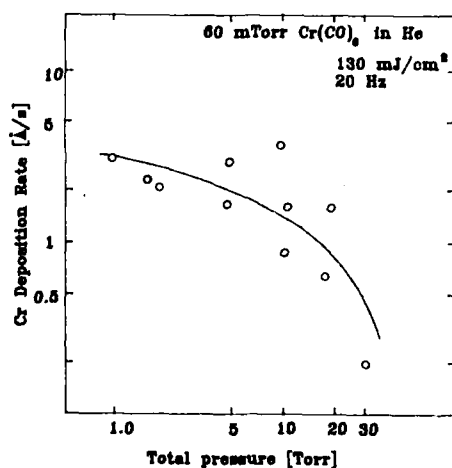


Fig. 2 Laser-induced Cr deposition rate as a function of total pressure.

number of collisions exceeds unity during the photolysis time (~ 20 ns) allowing for collisional cooling of the intermediate, whereby the production of Cr^* and also the deposition seems to be inhibited.

In Fig. 3 the spatial distribution of the Cr^* density in the region of the KrF laser focus is shown for various time delays after photolysis. The width of the Cr^* distribution curve ($\sim 140 \mu\text{m}$) with no time delay is somewhat larger than the focus of the KrF laser due to saturation of the LIF excitation which increases the focal volume of the interaction [7]. Broadening of the Cr^* distribution curves with increasing time delay shows the diffusion of Cr^* out of the focal region of the KrF laser focus. However, the integral intensity of the Cr^* distribution curves decreases with increasing time, indicating a disappearance of Cr^* . As shown in Fig. 4, the disappearance follows an exponential dependence on time and is faster for higher $\text{Cr}(\text{CO})_6$ partial pressures. The disappearance rate (slope of the curve) exhibits a linear dependence to the $\text{Cr}(\text{CO})_6$ partial pressure (Fig. 5), indicating that the disappearance of Cr^* is due to reaction with photofragments of $\text{Cr}(\text{CO})_6$ or with $\text{Cr}(\text{CO})_6$ itself. Quenching of the low excited $\text{Cr}(a^5\text{S}_2)$ state by collision relaxation with $\text{Cr}(\text{CO})_6$ and photofragments is also possible but could not be separated in this experiment. Collisions with He have a low cross section for quenching the Cr^* states [7]. The disappearance rate varies slowly with time: In the initial regime $\Delta t < 4 \mu\text{s}$ (Fig. 4) the rate is about 2.8 faster than in a later regime $10 \mu\text{s} < \Delta t < 40 \mu\text{s}$ (Fig. 5,6). This behaviour is probably due to the higher density of photoproducts in the initial time regime. The disappearance rate increases by a factor of about 1.7 when the total pressure is lowered from 5.0 Torr to 1.6 Torr. A higher He density provides a better prevention for reaction (or collision relaxation) probably caused by an increased screening of the reaction partners.

The widths (FWHM) of the Cr^* distribution curves (Fig. 3) follow a $(\Delta t)^{1/2}$ law, from which the diffusion constants D can be derived. We find for $P_{\text{tot}} = 1.6$ Torr (5.0 Torr) the value $D = 330 \text{ cm}^2/\text{s}$ ($105 \text{ cm}^2/\text{s}$). A mean velocity of Cr can be calculated using the expression $D = 1/3 \cdot \bar{v} \cdot \lambda$ and a mean free path for Cr in He of $\lambda = 86 \mu\text{m}$ ($27 \mu\text{m}$) (simple collision model). We get $\bar{v}_{\text{Cr}} = 1150 \text{ m/s}$, which is about 3 times larger than the thermal velocity, demonstrating, that Cr^* obtains excess translational energy during dissociation.

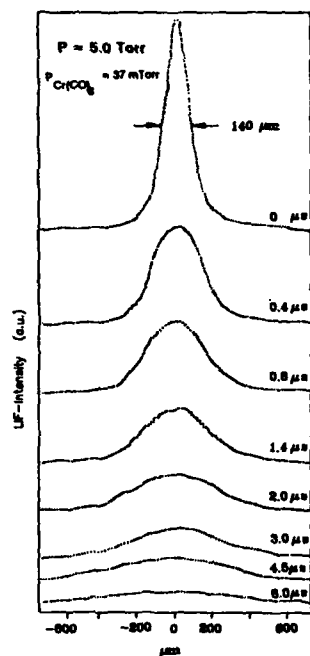


Fig. 3
Spatial distribution of the LIF-signal in the region of the KrF laser focus for various delay times between photolysis and detection. The LIF-signal is proportional to the Cr^+ density.

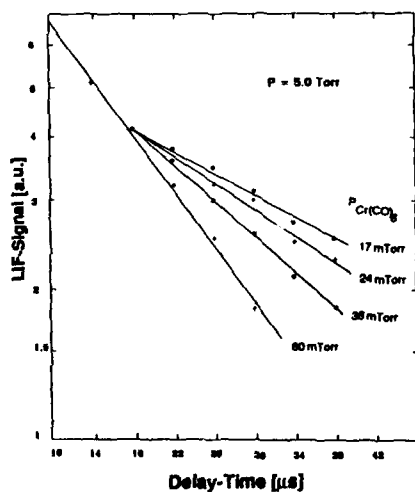


Fig. 4 Disappearance of Cr^+ as a function of delay time.

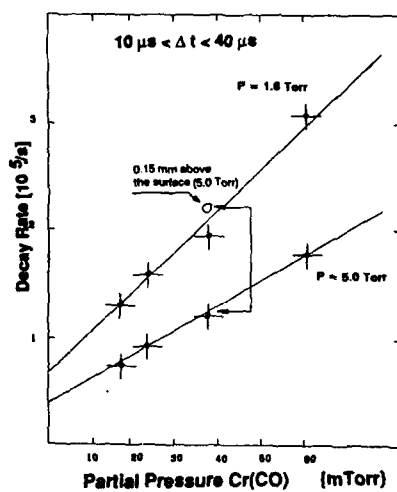


Fig. 5 Disappearance rate of Cr^+ as a function of Cr(CO)_6 partial pressure for $\Delta t > 10 \mu\text{s}$.

An additional channel for the disappearance of Cr^* is the deposition on a sample surface. The disappearance rate 0.15 mm above a Si(100) surface is unchanged in the initial time regime ($< 4 \mu\text{s}$), but doubles approximately for $\Delta t > 10 \mu\text{s}$ (see additional point in Fig. 5). The surface acts as a sink, from where diffusion out of this half space is reduced. From our observation we derive a sticking coefficient for Cr on the film close to unity. The Cr^* signal and the laser-induced deposition rate drop sharply when the sample is heated. Fig. 6 shows an Arrhenius plot of the Cr^* density 0.5 mm above the surface and of the laser-induced deposition rate. We explain the observed result by a decrease of the $\text{Cr}(\text{CO})_6$ density: $\text{Cr}(\text{CO})_6$ is decomposed thermally and may not be accessible for further laser-induced dissociation.

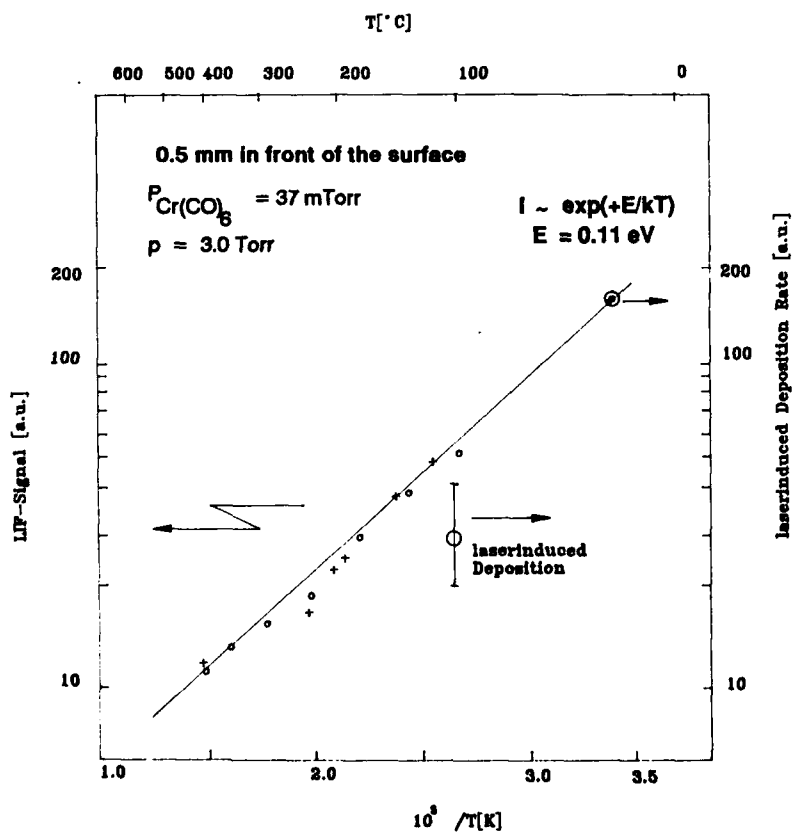


Fig. 6 Arrhenius plot of the Cr^* LIF signal. Two extra circles show the laser-induced deposition rate.

Assuming equilibrium for the thermal decomposition rate $k_0 N_{\text{Cr}(\text{CO})_6} e^{-E/kT}$ (k_0 = preexponential factor, E = activation energy) and the flow rate $S = \partial N / \partial t$, the concentration of $\text{Cr}(\text{CO})_6$ in the vicinity of the substrate is:

$$N_{\text{Cr}(\text{CO})_6} = \frac{S}{k_0 T} e^{+E/kT} \quad (3)$$

From Fig. 6 we obtain an activation energy of 0.11 eV, indicating the instability of $\text{Cr}(\text{CO})_6$ against thermal decomposition. Therefore a higher laser-induced deposition rate should be possible for cooled substrates. Further advantage might be a reduced C and O contamination, because it is known [8] that CO adsorption on Cr leads to dissociative chemisorption, while on cold Cr samples molecular adsorption dominates.

Conclusion

Using the method of LIF, we could investigate the production, the disappearance due to reaction and collision relaxation and the diffusion of Cr^* for various $\text{Cr}(\text{CO})_6/\text{He}$ mixtures. Our measurements in the vicinity of a substrate showed marked changes in the disappearance rate due to deposition and a large influence of the substrate temperature on the Cr^* density in front of a sample surface.

References

1. L. Konstantinov, R. Nowack, and P. Hess, Appl. Phys. A 47, 171, (1988)
2. N.S. Gluck, G.J. Wolga, C.E. Bartosch, W. Ho, Z. Ying, J. Appl. Phys. 61, 998 (1987)
3. O.N. Singh, H.J. Hopman, Microelectronics Journal, 18, 39, (1987)
4. W.G. Breiland, P. Ho, M.E. Coltrin, J. Appl. Phys. 60, 1505 (1986)
5. G.W. Tyndall, R.L. Jackson, J. Am. Chem. Soc. 109, 582, (1987) and J. Chem. Phys. 89, 1364 (1988)
6. C.C. Kiess, J. Res. Natl. Bur. Stand. 51, 247 (1957)
7. J.W. Daily, Appl. Optics 17, 225 (1987)
8. N.D. Shinn and T.E. Madey, J. Chem. Phys. 83, 5928 (1985)

FINE METAL PARTICLE FORMATION FROM ORGANOMETALLIC COMPOUNDS BY LASER IGNITED MILD EXPLOSIVE REACTION

NOBUO SHINO AND KEITARO YOSHINARA*

Idemitsu Kosan Cent. Res. Lab., 1280, Kasilizumi, Sodegaura, Chiba
298-02, JAPAN

*Inst. Mol. Sci., Hyodaiji, Okazaki, 444, JAPAN

ABSTRACT

Fine metal particles are deposited on a surface by explosive decomposition of organometallic compounds with single pulse laser irradiation. This new technique has the following characteristics:

- (1) High quantum efficiency of ca. 10^5 , that depends on the size of the reaction chamber used and the concentration of organometallic compounds.
- (2) Formation of uniform spherical particles of ca. 0.3μ m size under some reaction conditions.
- (3) Rapid formation of metal particles. Most of the starting materials are decomposed within a few milliseconds.

The key points of this decomposition reaction are:

- (1) Formation of high density active species in the gas phase by the irradiation with high power lasers.
- (2) Propagation of a thermal chain reaction.

1. INTRODUCTION

Recently chemical vapor deposition processes have attracted much attention for the preparation of thin films and fine particles. For example, amorphous silicon is deposited from silane or disilane, silicon carbide is deposited from organosilicon compounds, and various metals are deposited from organometallic compounds.

In these processes, laser beams as well as conventional light sources, thermal energy sources, and plasmas are used for the decomposition of starting gaseous materials. However so-called quantum efficiency for the production of deposited materials is usually very low.

We have found a highly efficient process for producing fine metal particles, in which laser light is used only for igniting a decomposition reaction of organometallic compounds. The quantum efficiency exceeds 2×10^5 . Since this reaction is initiated by only one shot of laser irradiation just like an explosive reaction, we will call this type of decomposition reaction a "laser ignited mild explosive reaction (LINER)."

In this article we report some features of this unique decomposition reaction of organometallic compounds and fine metal particles produced by LINER.

2. EXPERIMENTAL

Excimer laser output, ArF (193 nm) and KrF (248 nm), having a power of 10-350 mJ, and a pulse width of ca. 10 ns was used for the decomposition of organometallic compounds. In some cases of the KrF excimer laser irradiation, the laser beam was focused with a convex lens of $f = 100$ mm in order to make active organometallic compounds at high concentration. Tetramethyllead (TML), tetraethyllead (TEL), and trimethylbismuth (TNBi) were purified by at least 5 freeze-pump-thaw cycles followed by trap-to-trap distillation in vacuum before transferring to a reaction chamber. Nitrogen, helium, and hydrogen were from Nippon Sanso, stated purities 99.9 %, and were used without further purification.

Organometallic compounds were introduced into the reaction chamber of about 100 ml volume. A reaction chamber with a volume of 10 liters was used for the quantum efficiency measurement. Background pressure of 10^{-5} Torr was achieved by using an oil diffusion pump.

Gaseous products were analyzed by a gas chromatograph (Hewlett Packard, model 5890A) using a methyl silicon gum column (HP-1, 5 m x 0.53 μ m) with a flame ionization detector.

The shape and the size of metal particles were measured by scanning electron microscope (Hitachi S-800).

3. RESULTS AND DISCUSSION

After organometallic compounds such as tetramethyllead (TML) and trimethylbismuth (TNBi) were introduced into the reaction chamber, the sample was irradiated by a single laser pulse through a quartz window. Immediately after laser irradiation, most of the organometallic compounds decompose within a few tens of milliseconds accompanied by a strong orange emission. After that, spherical black fine metal particles having a size of below 1 μ m were deposited on the wall of the reaction chamber.

There are two key points which make possible this unique reaction. One is the formation of high density active species by a single laser pulse irradiation, and the second is the propagation of a thermal chain reaction.

Since 10 Torr of TML has a molar extinction coefficient of 10300 at 193 nm, 99 % of the ArF excimer laser light is absorbed within 5 mm. Therefore high density active species such as metal atoms and methylmetal radicals are formed in a relatively confined volume by a single shot irradiation from an excimer laser. Then these active species can cause the propagation of a thermal chain reaction with an emission of orange light. After the explosive reaction, most of the tetramethyllead compound is decomposed to produce fine metal particles and gaseous products such as ethane, ethylene, methane, and propane in the reaction chamber and finally these fine particles adhere on the chamber surface.

Now let us consider the reaction efficiency. The irradiated laser light, for example ArF 193nm, 25mJ, contains 2.4×10^{16} photons per pulse. On the other hand, 20 Torr of TML in the 10 l volume reaction chamber at room temperature (22°C) corresponds to 6.5×10^{21} molecules. Consequently reaction efficiency becomes 2.7×10^{-5} .

In order to elucidate the reaction mechanism, we have investigated the reaction conditions for LINER, that is irradiated laser (power and wavelength), organometallic compounds (variety and concentration), and added foreign gases (variety and concentration).

3.1 Laser power and laser wavelength

Figure 1 shows the laser power and laser wavelength dependence for LINER. In this figure, the vertical axis is the ratio of pressure after laser irradiation to that before irradiation. If the decomposition reaction of TML proceeds completely according to scheme 1, the ratio should be about 2 because the main gaseous products are 2 molecules of ethane which is obtained by the recombination reaction of methyl radicals.

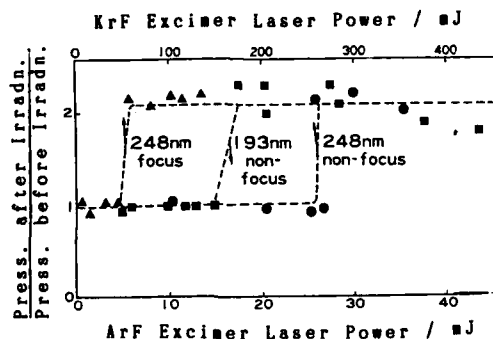
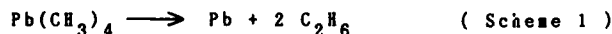


Fig.1. Laser power and wavelength dependence for LINER



In fact, 85 % of ethane, several percent of methane and ethylene, and a few percent of propane are detected by gas chromatography. As is clearly shown in this figure, for 5 Torr of TML, there exists a threshold laser power, about 17 mJ in the case of 193 nm irradiation and 270 mJ in the case of 248 nm irradiation without focusing the laser beam. When the KrF excimer laser beam is focused with a convex lens, having 100 mm focal length, at a distance of 80 mm from the window, the threshold laser fluence goes down to 60 mJ. These results indicate that a multi-photon process is necessary for the formation of active species.

The difference in the threshold laser power between 193 nm and 248 nm irradiation can be interpreted by the difference in absorption coefficients of TML at these wavelengths. The molar extinction coefficient is 10300

$M^{-1}cm^{-1}$ at 193 nm, while it is $120 M^{-1}cm^{-1}$ at 248 nm. Accordingly, the absorbance at 193 nm is about two orders of magnitude greater than the one at 248 nm. These results on laser power dependence and laser wavelength dependence clearly show that it is very important for LINER to produce high density active species.

3.2 Effect of concentration of organometallic compounds for LINER

LINER does not take place below the concentration of ca. 1 Torr in the cases of both 193 nm and 248 nm irradiations. This pressure effect can be interpreted as follows. When the concentration of starting materials is low, active species which are formed by the laser irradiation, cannot collide with the other parent molecule and will be deactivated. On the other hand, with high pressures active species can collide with the other parent molecule and transfer the internal energies to it. The frequency of collision is attributed to the pressure of the parent molecule. The excited parent molecules then decompose to form active species again and a thermal chain propagation process proceeds. Fine metal particles and gaseous products are probably formed during the propagation of the chain reaction.

3.3 Organometallic compounds possible to induce LINER

Among the organometallic compounds we have investigated to date, TNL and TNBi can undergo LINER. These two compounds have a weak metal-to-methyl group bond dissociation energy. As the bond dissociation energy decreases, organometallic compounds can be expected to decompose to smaller fragments such as methylmetal radicals and metal atoms. Actually we have detected absorption spectra of lead atom which are obtained by the photolysis of tetraethyllead using a nanosecond laser flash photolysis technique.[1] While in the case of the photolysis of hexamethyldisilane, trimethylsilyl radical can be detected and no other small fragments were detected.[2] Accordingly active species are expected to be generated in the case of the photolysis of the compounds which have a weak bond dissociation energy. These compounds are also advantageous for the propagation of thermal chain reactions.

Among the various types of organometallic compounds, alkylmetal, metallocarbonyl, and metallocene compounds have weak bond dissociation energies. In these compounds, some of the alkylmetal compounds can proceed by an exothermic reaction because recombination of alkyl-alkyl radicals have large bonding energies. Table 1 shows the average bond dissociation energies (D_{av}) and energy balances (ΔH) of some alkylmetal compounds. The average bond dissociation

energy means the energy D_0 per one metal-alkyl bond, and D_0 is the energy necessary for the formation of a metal atom, that is $D_0 = D_1 + D_2 + D_3 + D_4$ in the case of tetramethyl-metal compounds. ΔH is the bond dissociation energy of an alkylmetal (D_{av}) minus the bond formation energy of the alkyl-alkyl radicals, for instance bonding energy of the methyl-methyl is 88 kcal mol⁻¹. The compound which has a minus ΔH value, that is the one that proceeds by an exothermic reaction, has a possibility of LINER. In fact, TML and TMBi can cause LINER, but others cannot presumably because of threshold ΔH value for LINER and because of insufficient vapor pressure at room temperature ($Pb(C_2H_5)_4$).

Table I. Average bond dissociation energies and energy balances of some alkylmetal compounds

alkylmetal compounds	$D_{av} /$ kcal mol ⁻¹	$\Delta H /$ kcal mol ⁻¹
Bi (CH ₃) ₃	38	-26
Pb (CH ₃) ₄	37	-30
Pb (C ₂ H ₅) ₄	32	-45
Sn (CH ₃) ₄	52	33
Ge (CH ₃) ₄	57	50
Zn (CH ₃) ₂	43	-2
Zn (C ₂ H ₅) ₂	36	-15
Cd (CH ₃) ₂	34	-20

3.4 Effect of foreign gases

The last reaction condition for LINER is the effect of added foreign gases as shown in figure 2. LINER is prohibited by the addition of foreign gases at pressures above 7 Torr. These results can be interpreted as the deactivation of active species by added foreign gases. When the concentration of foreign gases is low, the formed active species can collide with the other parent molecules. However, with increased pressure of added foreign gases, the possibility of collisions with foreign gases increases more than with the parent molecules. This may prevent the active species from propagating the thermal chain reaction.

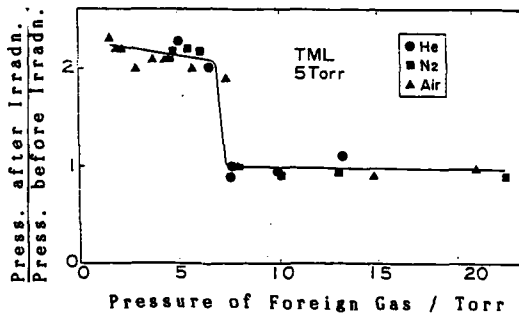


Fig.2. Effect of Foreign Gases.

3.5 Fine metal particles formed by LINER

After laser irradiation, fine metal particles are formed in the reaction chamber. Figure 3 shows a microphotograph of lead particles which were obtained by the decomposition of TML under a certain reaction condition. It is recognized from this figure that spherical shape fine particles of $0.3\text{ }\mu\text{m}$ size are formed.



Figure 3. Microphotograph of lead particles

3.6 Conclusion

We have discovered the unique decomposition reaction named LINER. (Laser Ignited Mild Explosive Reaction) The key points of LINER are the high density formation of active species and the propagation of a thermal chain reaction caused by these active species. The formed metal particles are spherical shape of $0.3\text{ }\mu\text{m}$ size.

References

- [1] N. Shimo, N. Nakashima, and K. Yoshihara, in preparation.
- [2] N. Shimo, N. Nakashima, and K. Yoshihara, Chem. Phys. Lett., 125 (1986) 303.

PART III

**Laser-Induced Writing
of Metal Lines**

MODELLING OF PYROLYTIC LASER DIRECT-WRITING FROM THIN METALORGANIC FILMS

Peter E. Price Jr. and Klavs F. Jensen

Department of Chemical Engineering and Materials Science, University of Minnesota,
Minneapolis, Minnesota 55455

ABSTRACT

A one-dimensional model for pyrolytic laser direct-writing of metal features from thin metalorganic films is presented. The model extends previous results for scanning laser crystallization by including separate but coupled mass and energy balances and allowing for variations in the optical properties and thermal conductivity in the film as it decomposes. A finite element approach is used to obtain solutions to the steady state and transient model forms. The model predicts the existence of multiple steady states for a range of laser powers when the optical absorbance is a nonlinear function of the fractional conversion in the film. These predictions agree qualitatively with multiple steady states that have been observed in direct-writing of palladium features from palladium acetate films. Experimental results that demonstrate multiplicity in the palladium acetate system are presented. The model also predicts the existence of periodic solutions that correspond to the periodic features that have been reported for direct-writing of gold features from organogold films.

INTRODUCTION

Laser direct-writing of micron-scale metal features by pyrolytic decomposition of thin metalorganic films has been reported in a number of recent publications, demonstrating the potential of the technique in applications such as device interconnects and photolithographic mask repair [1-11]. It was the pioneering work of Fisanick, Gross, and coworkers at Bell Labs on the deposition of micron-scale gold features from organogold films [3-6] that revealed the wide variety of dynamic behavior that can occur during direct-writing. In particular, they observed pronounced periodic oscillations in features written over a range of laser powers and scan speeds. They studied the thermochemistry of the film decomposition using differential scanning calorimetry and thermogravimetric analysis and found that the decomposition took place in several steps with a strongly exothermic overall heat of reaction. This suggested that the observed periodic features were a chemical analog to the periodic features that had been widely observed in laser induced crystallization [12-18].

Fisanick *et al.* [3] used the concept of cooperativity to explain the existence of periodic solutions. The concept is that when the rate of energy released by reaction in the film is comparable to the rate of energy input by the laser, periodic features may develop by the following mechanism. Initially, the scanned laser beam causes the film to undergo a chemical transformation during direct-writing or a physical transformation during scanned laser crystallization. The heat released by this transformation causes the transformation front to expand beyond the laser beam. However, the front loses heat by conduction to the substrate and the surrounding film as it is expanding. If this rate of heat loss is sufficient, the transformation front will be quenched. Upon reaching the quenched front, the scanning beam initiates this process again, resulting in periodic features.

Fisanick *et al.* [3] noted that their experimental results were in qualitative agreement with the model presented by Kurtze *et al.* [18] for scanning laser crystallization. This model consists of a one-dimensional energy balance that describes the behavior of a step front at the amorphous-crystalline boundary as an infinite laser slit is scanned across a thin film of amorphous material, e.g., Si or Ge, on an insulating substrate. Their results

extended a previous model for explosive crystallization presented by Gilmer and Leamy [19] and further examined by van Saarloos and Weeks [20] by including a laser term in the energy balance. Kurtze *et al.*'s model also overcame the physically unrealistic results obtain by Zeiger *et al.* [15] by properly accounting for the temperature dependence of the interface kinetics. The application of Kurtze *et al.*'s model to laser direct-writing is, however, limited by the assumptions of a step transformation front and constant optical and physical properties in the film. As noted by Fisanick *et al.* [3], changes in the thermal conductivity and optical properties of the film can be significant, and the assumption of a step transformation front may not accurately describe the decomposition reaction of the metalorganic film. The model presented herein is a further extension of Kurtze *et al.*'s laser crystallization model insofar as it includes a separate mass balance to describe the extent of reaction in the film and allows for variations in the optical properties and thermal conductivity as the film decomposes. These extensions provide a more accurate description of the laser direct-write process.

More recently, Gross and coworkers [7-9] have presented several papers describing the direct-writing of palladium features from palladium acetate films. Although the overall heat of reaction for the decomposition of palladium acetate is endothermic or at most weakly exothermic [7,9,21], the palladium features also exhibit periodic behavior. Baufay and Gross [9] have attributed this periodic behavior to nonlinear variations in the optical absorbance of the film as it decomposes. At low conversions, the optical absorbance is reported to increase with fractional conversion. Thus, once the reaction is initiated, the absorbed laser energy increases, causing the reaction front to expand. As the conversion increases, the reflectivity of the film begins to rise and the absorbed laser energy decreases. This causes the front velocity to decrease. When the scanning beam catches up to the reaction front, the process begins again, leading to optically induced periodic features. Here, we limit the discussion to optical effects in the steady state behavior.

In this paper, we use a reaction engineering approach to derive a one-dimensional model for laser direct-writing that contains the essential characteristics of the process. This approach follows a long history in the chemical engineering literature that is replete with studies of steady state multiplicities and instabilities in chemical reactors [22,23]. To facilitate understanding of the relative importance of the various processes, e.g., reaction, conduction, and convection, that occur during direct-writing, the model is put in dimensionless form. Using parameters derived from reported results for direct-writing from palladium acetate [7-9] and organogold [3-6] films, as well as new experimental results, we present computational results that are in qualitative agreement with observed multiplicity and periodicity in direct-write features.

THE MATHEMATICAL MODEL AND NUMERICAL METHODS

The laser direct-write process is complex, and a general model would require three-dimensional, time dependent mass and energy balances. Performing the extensive calculations needed to solve such a system would clearly be impractical. Rather than proposing such a detailed model, we seek to develop a model that remains computationally tractable, yet captures the essential qualitative behavior of the process. The model system we consider is pictured in Figure 1.

In laser direct-writing, the substrate is typically much larger than the reaction zone. The domain is therefore modelled as a thin film of reactant on a semi-infinite substrate. We consider a laser slit source, infinite in the y -direction, with a Gaussian power distribution and scanning at a constant velocity, V_x , in the x -direction. The mass and energy balances are developed by considering a volume element, infinite in the y -direction and of depth d . The volume element includes the film, of depth ϵd , and some portion of the substrate, of depth $(1 - \epsilon)d$. The thickness of the film, as well as the density and specific heat of the film and substrate, are assumed to be constant. The thermoconductivity of the film is assumed to vary with conversion. The film is assumed

to decompose in the solid state, i.e., no melting is assumed, and diffusion of reactants and products in the film is neglected. The incident laser energy is assumed to be absorbed evenly throughout the volume element, although the degree of absorbance may vary with conversion in the film. The film is assumed to initially contain only reactant, A, that reacts irreversibly to form product, B, with first order Arrhenius kinetics. Transport of reactants and/or products to and from the surface is not considered. Finally, heat loss from the volume element to the surroundings is described by a *Newton's law of cooling* term. The resultant mass and energy balances are:

$$\frac{\partial(\epsilon C)}{\partial t} = V_L \frac{\partial(\epsilon C)}{\partial x} - \epsilon k_0 C \exp\left[\frac{-E_a}{RT}\right] \quad (1)$$

and

$$\begin{aligned} \frac{\partial(\epsilon \rho_l c_{p,l} T + (1-\epsilon) \rho_s c_{p,s} T)}{\partial t} &= \frac{\partial}{\partial x} \left(\kappa_{eff} \frac{\partial T}{\partial x} \right) + V_L \frac{\partial(\epsilon \rho_l c_{p,l} T + (1-\epsilon) \rho_s c_{p,s} T)}{\partial x} \\ &- \frac{\Gamma}{d} (T - T_w) + \frac{2P_0 A}{\pi^{1/2} \omega d} \exp\left[\frac{-x^2}{\omega^2}\right] + (-\Delta H) \epsilon k_0 C \exp\left[\frac{-E_a}{RT}\right] \end{aligned} \quad (2)$$

The initial and boundary conditions are:

$$C(x, 0) = C_0(x), \quad T_0(x, 0) = T(x); \quad C(\infty, t) = C_0, \quad T(-\infty, t) = T_w, \quad T(\infty, t) = T_w \quad (3)$$

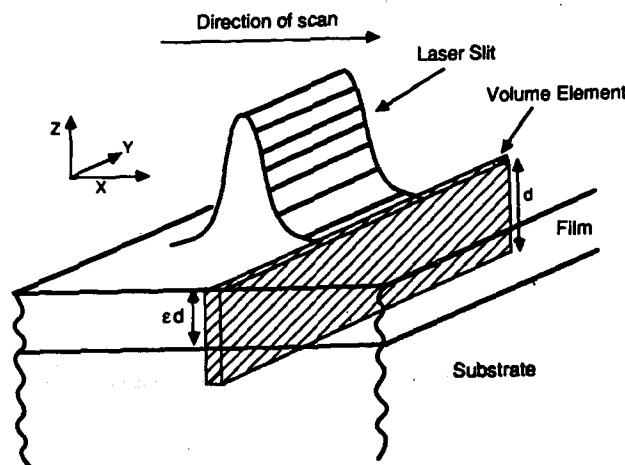


Figure 1. Schematic of slit laser direct-write model system.

For constant densities and heat capacities of the film and substrate the above equations are similar to the pseudohomogeneous axial dispersion model for tubular reactors. The steady state and dynamic behavior of the tubular reactor model has been studied in detail [24 and references therein]. Further development of the direct-write model will follow the approach used previously for the tubular reactor [24]. The model equations are made dimensionless by defining:

$$\begin{aligned} X_1 &= \frac{C_0 - C}{C_0}, \quad X_2 = \frac{T - T_0}{T_0}, \quad X_{2w} = \frac{T_w - T_0}{T_0}, \quad \gamma = \frac{E_a}{RT_0} \\ \tau &= \frac{t V_L}{\omega}, \quad z = \frac{x}{\omega}, \quad Le = \frac{\epsilon \rho_l c_{p,l} + (1-\epsilon) \rho_s c_{p,s}}{\epsilon \rho_l c_{p,l}}, \quad Pe = \frac{V_L \omega \epsilon \rho_l c_{p,l}}{\kappa_{eff}} \end{aligned} \quad (4)$$

$$B = \frac{(-\Delta H)C_0}{c_{p,t}T_0}, \quad \beta = \frac{\Gamma\omega}{V_\ell d \epsilon \rho_t c_{p,t}}, \quad Da = \frac{k_0\omega}{V_\ell}, \quad Q_0 = \frac{2P_0}{\pi^{1/2}T_0 V_\ell d \epsilon \rho_t c_{p,t}}$$

X_1 is the conversion of the reactant. X_2 is the dimensionless temperature. X_{2w} is the dimensionless temperature of the surroundings. γ is the dimensionless activation energy. τ and z are the dimensionless time and length scales. To account for the change in effective thermal conductivity between the metalorganic film and the final metal structure, Pe is assumed to vary linearly with conversion X_1 . Using the above definitions, the model equations can be written as:

$$\frac{\partial X_1}{\partial \tau} = \frac{\partial X_1}{\partial z} + Da(1 - X_1) \exp\left[\frac{-\gamma}{1 + X_2}\right] \quad (5a)$$

$$\begin{aligned} Le \frac{\partial X_2}{\partial \tau} = & \frac{\partial}{\partial z} \left(\frac{1}{Pe(X_1)} \frac{\partial X_2}{\partial z} \right) + Le \frac{\partial X_2}{\partial z} - \beta(X_2 - X_{2w}) \\ & + BDa(1 - X_1) \exp\left[\frac{-\gamma}{1 + X_2}\right] + Q_0 A \exp[-z^2] \end{aligned} \quad (5b)$$

Taking the reference temperature, T_0 , to be the temperature of the surroundings, T_w , and the reference concentration, C_0 , to be the pure unreacted precursor, the dimensionless initial and boundary conditions become:

$$X_1(z, 0) = X_{10}(z), \quad X_2(z, 0) = X_{20}(z); \quad X_1(\infty, \tau) = 0, \quad X_2(-\infty, \tau) = 0, \quad X_2(\infty, \tau) = 0 \quad (6)$$

Several of the dimensionless parameters have physical interpretations similar to those given in the tubular reactor analysis of Jensen and Ray [24]. Le is the Lewis number, which gives the ratio of the intrinsic thermal time constant to the intrinsic material time constant. Pe is the Peclet number for heat transfer, which describes the relative importance of energy transfer by convection and conduction. B is a dimensionless heat of reaction. β is a dimensionless heat transfer coefficient. Da is the Damköhler number, which gives the ratio of the reaction rate to the space velocity. Q_0 is the dimensionless laser power per dimensionless unit length.

NUMERICAL METHODS

The Galerkin finite element method has been used to solve both the steady state and transient forms of the model equations. This method is well described in a number of textbooks [25,26]. Although the direct-write model is formulated on an infinite domain, solutions to the finite element problem were obtained by considering a truncated domain that was sufficiently large that further increases in size had a negligible effect on the solution. To investigate the dependence of the steady state solutions on the laser power, a pseudo-arclength continuation scheme was used. This method, which has been described previously by Keller [27], makes it possible to obtain solutions near bifurcation points where natural parameter continuation would fail. Time integrations of the transient problem were performed using the implicit integrator LSODI [28]. To reduce numerical difficulties a small degree of diffusion was added to the mass balance. This diffusion term was chosen so that any oscillations in the conversion profile behind the laser would not reflect back towards the laser upon reaching the truncated left boundary. The short time behavior and steady state behavior were indistinguishable with or without this diffusion term.

For both the steady state and transient calculations, several measures have been used to characterize the solutions. The first measure is the feature width. When metal lines are written using a scanning beam, the width of the lines can easily be measured.

For the one-dimensional model, no such width exists. For the case of a scanning laser slit, however, the position of the reaction front relative to the center of the slit should be a comparable characteristic of the system. Hence, we define the feature width for the one-dimensional model to be the distance from the slit center to the point in the reaction front where the conversion has reached half of its maximum value.

The other two measures, the conversion and temperature integrals, are suggested by the shape of the conversion and temperature profiles. These integrals are defined as follows:

$$\text{conversion integral} = \int_0^{\infty} X_1 dz; \quad \text{temperature integral} = \int_0^{\infty} X_2 dz \quad (7)$$

These integrals measure the area under the conversion and temperature profiles, respectively, from the beam center to the right boundary. They reflect the total degrees of conversion and of energy input plus generation in the film.

EXPERIMENTAL

The experimental apparatus consisted of a 5W Ar⁺ laser operating in TEM₀₀ mode at 514.5 nm. The beam was either focused through a cylindrical lens to give a slit source or expanded 3X and then focused through a 0.22 NA microscope objective to give a beam source. Using a scanning knife edge technique, the slit was determined to have an elliptical profile with approximate 1/e, principle radii of 28 μm and 900 μm . The 1/e beam radius was determined to be approximately 4.0 μm . Palladium acetate films were spin coated onto quartz substrates from chloroform solution. The samples were mounted on a stepping motor driven X-Y stage with a scan speed range of 1 to 1200 $\mu\text{m/s}$. Palladium features were written by exposing the films under ambient conditions.

RESULTS AND DISCUSSION

Steady State Behavior

A set of base parameters for the mathematical model was determined by using the scanning laser slit to deposit palladium features from a 1.0 μm palladium acetate film. Although the slit source is actually elliptic, the laser power in the central region of the slit is nearly constant and provides a good approximation to the infinite slit used in the model. At a laser power of 1.3W and scan speed of 100 $\mu\text{m/s}$, the slit was scanned across the film. The laser slit was blocked during the scan. The resultant feature appeared as a sharp palladium/palladium acetate front propagating 92 μm ahead of the slit center. This experimental result was used in conjunction with maximum film temperatures estimated by Gross *et al.* [4] and the analytical solution for the temperature profile induced by a laser slit scanning across a substrate. The choice of parameters is discussed in more detail below. Additional experiments using the scanning laser slit are currently underway and will be used for further comparison to and refinement of the mathematical model in the future. At present, we compare the qualitative behavior predicted by the model to new, as well as previously published, experimental results for a scanning laser beam.

Table 1 contains the physical properties, reaction parameters, and laser slit properties for the base case. The thermal conductivity of the unreacted film was taken to be the same as for the quartz substrate. The thermal conductivity of the completely reacted film was taken to be approximately 50% of the bulk value for palladium to account for impurities in the final feature, as suggested by measured electrical resistivities for direct written palladium features [8]. The density and heat capacity of the film were taken to

be order of magnitude estimates of the average values. The reaction rate constant and activation energy were obtained from Baufay and Gross [9]. The reaction was assumed to be thermoneutral. The thickness of the volume element, d , was taken to be that of the film, and the heat transfer coefficient, Γ , was selected so that the predicted feature width matched the 92 μm size obtained experimentally.

Table 1. Base Parameters for One-Dimensional Laser Direct-Write Model

Laser Film and Substrate Properties		
$\omega = 28 \mu\text{m}$	$d = 1 \mu\text{m}$	$\kappa_{\text{eff}}(X_1 = 0) = 0.005 \text{ cal}/(\text{cm s K})$
$P_0 = 1.71 \text{ cal}/(\text{cm s})$	$\rho_f = 10 \text{ g}/\text{cm}^3$	$\rho_s = 2.2 \text{ g}/\text{cm}^3$
$V_f = 0.01 \text{ cm}^3/\text{s}$	$c_{p,f} = 0.1 \text{ cal}/(\text{g K})$	$c_{p,s} = 0.18 \text{ cal}/(\text{g K})$
		$\Gamma = 0.017 \text{ cal}/(\text{cm}^2 \text{ s K})$
<hr/>		
Palladium Parameters:	$k_0 = 1.1 \cdot 10^{11} \text{ s}^{-1}$	$-\Delta H = 0 \text{ cal/g}$
	$E_a = 30.3 \text{ kcal/mol}$	$\kappa_{\text{eff}}(X_1 = 1) = 0.0875 \text{ cal}/(\text{cm s K})$
<hr/>		
Gold Parameters:	$k_0 = 1.1 \cdot 10^{11} \text{ s}^{-1}$	$-\Delta H = 630 \text{ cal/g}$
	$E_a = 36.9 \text{ kcal/mol}$	$\kappa_{\text{eff}}(X_1 = 1) = 0.375 \text{ cal}/(\text{cm s K})$

Baufay and Gross [9] calculated the variation in optical absorbance of a 1.0 μm palladium acetate film on a quartz substrate with the fractional conversion in the film. This nonlinear dependence of the laser absorbance was included in the model by using the following functional form for A obtained by fitting the data given by Baufay and Gross [9]:

$$A(X_1) = 0.05 + 100.0X_1^{1.32} \exp(-5.88 X_1^{0.495}) \quad (8)$$

The conversion and temperature integrals for the base case are shown as a function of laser power in Figure 2. The nonlinear variation in laser absorbance with fractional conversion leads to the existence of multiple steady states over a range of laser powers. The low conversion state exists because most of the laser energy is transmitted through the film and substrate, causing only slight heating of the film and thus a small degree of reaction. Along the upper branch of the curve the conversion is high, and enough laser energy is absorbed to maintain the nearly complete reaction despite the high reflectivity. Additional calculations suggest that the existence of a maximum in the absorbance as function of conversion, not the specific functional form, is all that is needed to obtain multiple steady states.

This sort of multiplicity behavior has not, to the authors' knowledge, been previously reported for direct-writing from thin films. To investigate the existence of multiple steady states, a series of experiments were conducted using a scanning laser beam. At a scan speed of 100 $\mu\text{m}/\text{s}$ and for a range of laser powers, palladium lines were written from a 0.6 μm film of palladium acetate. At each power, lines were written from starting points on the unreacted film and on a previously written line. At laser powers below 80 mW, extremely low conversion lines, like that shown in Figure 3a were observed regardless of the state of the film at the starting point of the scan. In Figure 3a, the starting point of the scan was a high conversion reference line. The direct-write feature rapidly dies down to the low conversion state. Between 99 mW and 145 mW, low conversion features similar to that shown in Figure 3b were obtained when the scan was initiated on an unreacted portion of film. When the scan was started from an existing high conversion line, a high conversion line was obtained, as shown in Figure 3c. Above 145 mW, high conversion lines similar to that shown in Figure 3d were obtained regardless of the state of the film at the start of the scan.

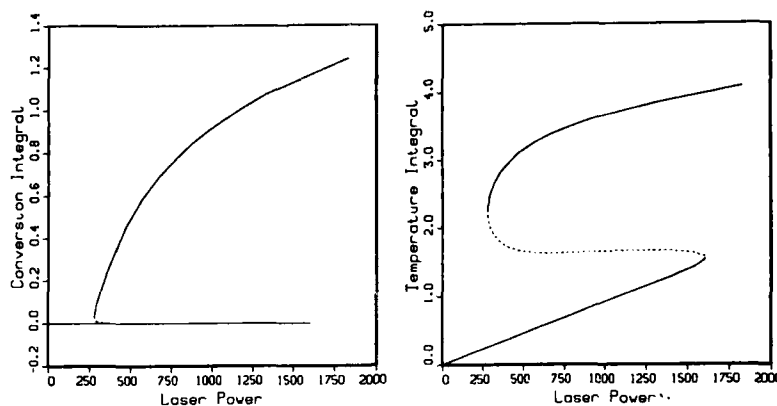


Figure 2. Predicted multiple steady states for the palladium system for varying laser power. $Pe(X_1 = 0) = 5.6 \cdot 10^{-3}$, $Pe(X_1 = 1) = 3.2 \cdot 10^{-4}$, $Da = 3.08 \cdot 10^{10}$, $\beta = 48$, $B = 0$, $Le = 1$, $\gamma = 50.8$, $x_{2w} = 0$.

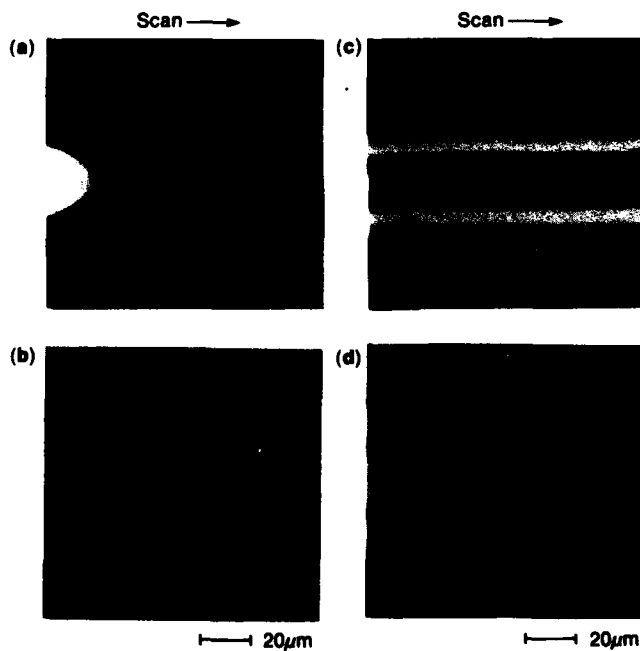


Figure 3. Observed multiple steady states in laser direct-writing of palladium films from palladium acetate. (a) Unique low conversion state, laser power 80 mW; (b) low conversion state of two possible stable steady states, $95 \text{ mW} < \text{laser power} < 145 \text{ mW}$; (c) high conversion state of two possible stable steady states, $95 \text{ mW} < \text{laser power} < 145 \text{ mW}$; (d) unique high conversion state, laser power 165 mW. Laser scan speed $100 \mu\text{m/s}$ in all cases.

Attempts to demonstrate reproducibility of these results showed that the solvent, chloroform, can have a significant impact on the region of multiplicity. In the initial experiments, the spin coated films were not baked to remove excess solvent. When lines were written within several hours after spin coating, the region of multiplicity was considerably larger and shifted toward higher powers, extending from 145 mW to 280 mW. Attempts to reproduce these results on the same film the following day yielded a smaller region of multiplicity in a lower power range. The same reduction in the region of multiplicity was obtained when the films, after spin coating, were baked at 100°C for several hours to remove excess chloroform. This shows that sample preparation can have a major impact on the nature of direct-written features and suggests that residual chloroform may also have some effect on the periodicity observed in palladium features. The multiplicity phenomena may also have practical consequences in terms of efforts to reduce feature size. If the scan is initiated at a high conversion state, perhaps by using a short pulse at higher power, lower laser powers can be used for direct-writing, leading to smaller line widths. Adherence of the features, however, may restrict the minimum writing power.

Transient Behavior

The development of periodic behavior in gold features written from films of Engelhard Bright Gold NW screen ink has been attributed to the concept of cooperativity [3]. To investigate the model predictions for an exothermic system, the second set of parameters shown in Table 1 were chosen to represent the gold system being processed with the laser slit. Order of magnitude estimates were again used for the average density and heat capacity of the film. The thermal conductivity of the completely converted film was taken to be approximately 50% of the value for bulk gold to account for impurities in the final features, as suggested by electrical resistivity measurements reported by Gross *et al.* [4]. The reaction parameters were also obtained from Gross *et al.* [4]. The optical absorbance was assumed to vary with conversion according to the formula:

$$A(X_1) = 0.32 + X_1^{0.4} \exp(-1.7 X_1^{3.2}) \quad (9)$$

This functional form is based on transmission and reflectance data presented by Gross *et al.* [6]. This function is based on absorbance values at low and high conversions. Values for the absorbance in the middle range of fractional conversion may be inaccurate. From the reported data, however, it is clear that the gold system also exhibits a nonlinear variation in laser absorbance with fractional conversion. This nonlinear absorbance function again permits multiple steady states. Below, we consider only the high conversion states.

The concept of cooperativity suggests that periodic features should develop when the heat of reaction is sufficiently high. We have calculated transient solutions as the dimensionless heat of reaction was increased. These calculations suggest that as the heat of reaction is increased to the point where the rate of energy generated by the reaction is comparable the absorbed laser energy, the system undergoes a Hopf subcritical bifurcation to stable oscillations corresponding to periodic features in laser direct-write. We have also found that the Lewis number can have a strong effect on the nature of the oscillations as also observed in the analogous tubular reactor case [24]. The Lewis number is expected to be greater than one because of the thermal capacitance of the substrate, but the exact value is difficult to fix without a detailed heat transfer analysis. Lewis numbers near unity led to numerical stiffness problems that meant that solutions could not be obtained in reasonable computing times. Since our interest is in the qualitative behavior of the system, we performed calculations at high Lewis numbers (100), where the equations are less stiff.

The dynamic behavior of the system is described in terms of phase plane diagrams approximated by plots of the conversion integral versus the temperature integral. Since the conversion and temperature integrals represent projections of the solutions to the

partial differential equation (5), it is possible for trajectories in the plane spanned by the conversion and temperature integrals to cross without the intersection corresponding to identical conversion and profile temperature. Figure 4a shows the phase plot for the system with $B = 155$ and the remaining parameters with the same values as in Table 1. In this case the phase portrait is that of a stable spiral. This was found to be the case regardless of how far from the steady state profile the initial state was. Increasing B to 166.1 and starting the system from the steady state solution corresponding to perturbed laser power and heat of reaction, the system appears to be a weakly attracting spiral, as shown in Figure 4b. However, if the initial profile is perturbed significantly, the phase plot reveals a stable limit cycle, as shown in Figure 4c. Additional calculations for $B > 166.1$ suggest that the domains of attraction of the spiral and the limit cycle are separated by an unstable limit cycle. Finally, if the heat of reaction is increased to 170, then the system approaches the limit cycle from even the slightest perturbation of the corresponding steady state solution. This limit cycle is shown in Figure 4d.

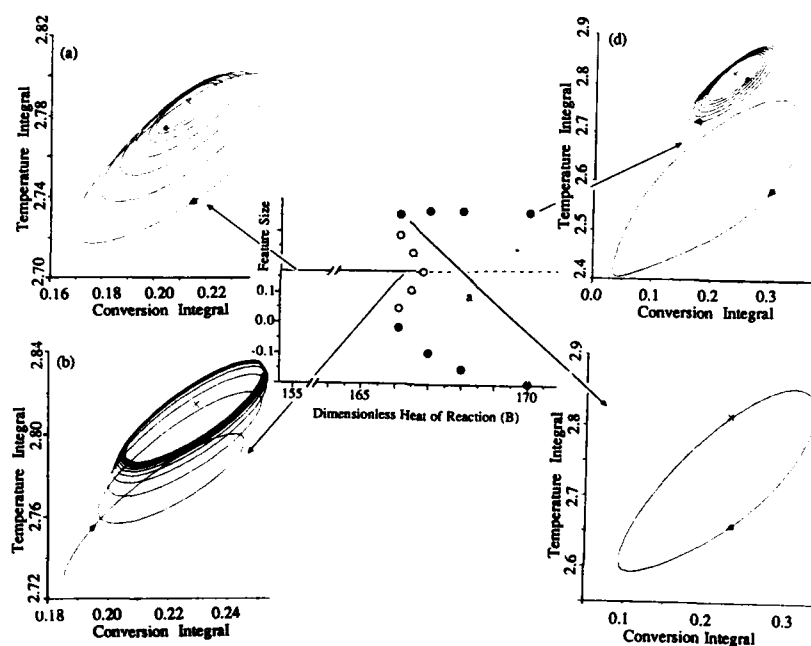


Figure 4. Subcritical Hopf bifurcation to periodic deposits in laser direct-writing of gold films from organogold films with increasing heat of reaction (B). Figures a-d show phase plane behavior approximated by plots of the temperature integral versus the conversion integral. (a) $B = 155$, stable spiral; (b) $B = 166.1$, stable spiral; (c) $B = 166.1$, stable limit cycle; (d) $B = 170$, stable limit cycle. Other parameters: $Pe(X_1 = 0) = 5.6 \cdot 10^{-3}$, $Pe(X_1 = 1) = 7.5 \cdot 10^{-5}$, $Da = 3.08 \cdot 10^{10}$, $\gamma = 61.9$, $Le = 100$, $B = 155$, $\beta = 4.8$, $X_{2w} = 0$, $Q_0 = 500$.

Figure 5 shows the variation in the feature size as a function of time corresponding to the stable limit cycle for $B = 170$ (cf. Figure 4d). Even at Lewis numbers of 100, the speed of the front as it expands is large, and therefore the stiffness of the problem is

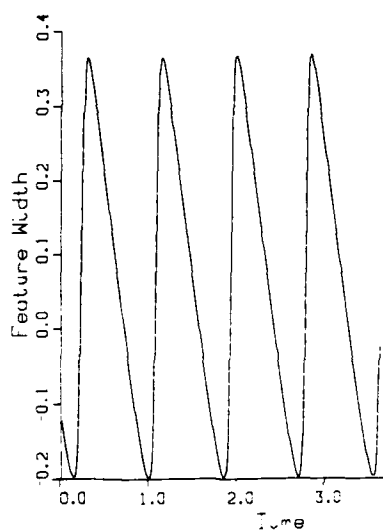


Figure 5. Feature width as a function of time corresponding to the limit cycles in Figure 4d.

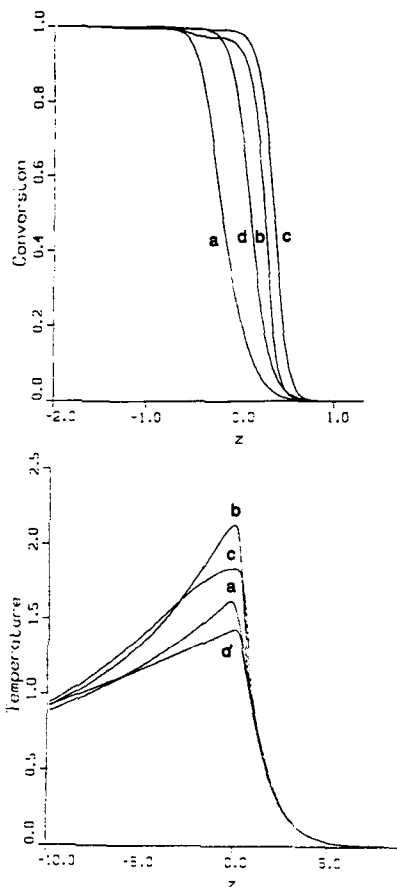


Figure 6. Conversion and temperature profiles relative to the laser slit position at four different times during a period of oscillation for the limit cycle in Figure 4d. (a) $\tau = 0.1$, (b) $\tau = 0.26$, (c) $\tau = 0.3$, (d) $\tau = 0.6$.

apparent. Finally, Figure 6 shows the corresponding conversion and temperature profiles at different times during one period of oscillation. The importance of the metal tail as a heat sink is clearly reflected in these profiles. Stability analysis shows that at $B = 166.82$ the steady state loses stability as a pair of complex conjugate eigenvalues cross the imaginary axis. The behavior of the system is characteristic of a subcritical Hopf

bifurcation [29]. This bifurcation behavior is summarized in Figure 4, where the dark circles represent the maxima and minima in the feature width of the stable oscillations and the open circles represent, qualitatively, the unstable limit cycles. At the bifurcation point, the ratio of the rates of energy generated by the reaction to the energy input from the laser is 0.324. These results suggest that there should be values of the laser power and scan speed at which both smooth and periodic features can be written. While such behavior has been noted for direct-writing from the gas phase [30], it has not been reported for gold features written from organogold films.

In closing, we note that qualitatively similar bifurcation and oscillatory behavior was observed when a linear absorbance function was used, although the specific bifurcation point depends on the absorbance function. The relationship between the absorbance function and both the heat of reaction at the bifurcation point and the variation in the period of oscillation with laser power are subjects that will be further investigated. This should lead to a better understanding of the differences between the variation in period with laser power seen in laser induced crystallization [17] and laser direct-writing [3].

CONCLUSIONS

A one-dimensional model for pyrolytic laser direct-writing of metal features from thin metalorganic films has been described. The model predicts qualitatively the multiple steady state behavior observed experimentally for direct-writing of palladium lines from palladium acetate films. The observed multiplicity is caused by a nonlinear dependence of the absorbance on conversion in the film. For sufficiently exothermic reactions, the model predicts periodic solutions corresponding to experimentally observed periodic features in laser writing of gold features from organogold films. The development of oscillations in endothermic systems by an optically activated mechanism, as observed in palladium features written from palladium acetate films, is currently under investigation.

ACKNOWLEDGEMENTS

This work was supported by an IBM Materials and Processing Science Grant and by the Minnesota Supercomputer Institute. The authors are grateful to Dr. Paul Comita, IBM Almaden Research Center for permission to use his laser direct-writing experimental system.

REFERENCES

1. R.B. Gerassimov, S.M. Metev, S.K. Savtchenko, G.A. Kotov and V.P. Veiko, *Appl. Phys. B* **28**, 266 (1982).
2. R.Y. Jan and S.D. Allen, SPIE Vol. 459 Laser Assisted Deposition, and Doping (1984) pp. 71-6.
3. G.J. Fisanick, M.E. Gross, J.B. Hopkins, M.D. Fennell, K.J. Schnoes and A. Katzir, *J. Appl. Phys.* **57**, 1139 (1985).
4. M.E. Gross, G.J. Fisanick, P.K. Gallagher, K.J. Schnoes, and M.D. Fennel, *Appl. Phys. Lett.* **47**, 923 (1985).
5. G.J. Fisanick, J.B. Hopkins, M.E. Gross, M.D. Fennell, and K.J. Schnoes, *Appl. Phys. Lett.* **46**, 1184 (1985).
6. M.E. Gross, A. Appelbaum and K.J. Schnoes, *J. Appl. Phys.* **60**, 529 (1986).
7. M.E. Gross, A. Appelbaum and P.K. Gallagher, *J. Appl. Phys.* **61**, 1628 (1987).
8. M.E. Gross, W.L. Brown, J. Linnros, L.R. Harriott, K.D. Cummings and H.O. Funsten, in *Photon, Beam, and Plasma Stimulated Chemicals at Surfaces*, Vol. 75 of the Proceedings of the Materials Research Society, V.M. Donnelly, I.P. Herman and M. Hirose (eds.), Elsevier: New York (1987), pp. 91-97.

9. L. Baufay and M.E. Gross, in *Laser and Particle-Beam Chemical Processing for Microelectronics*, Vol. 101 of the Materials Research Society Symposium Proceedings, D.J. Ehrlich, G.S. Higashi, and M.M. Oprysko (eds.), Materials Research Society: Pittsburgh, PA (1988), pp. 89-94.
10. A. Gupta and R. Jagannathan, *Appl. Phys. Lett.* **51**, 2254 (1987).
11. A. Gupta, R.C. Sausa and J.R. White, in *Photon, Beam, and Plasma Stimulated Chemical Processes at Surfaces*, Vol. 75 of the Proceedings of the Materials Research Society, V.M. Donnelly, I.P. Herman and M. Hirose (eds.), Elsevier: New York (1987), pp 83-90.
12. J.C.C. Fan, H.J. Zeiger, R.P. Gale and R.L. Chapman, *Appl. Phys. Lett.* **36**, 158 (1980).
13. R.L. Chapman, J.C.C. Fan, H.J. Zeiger and R.P. Gale, *Appl. Phys. Lett.* **37**, 292 (1980).
14. H.J. Zeiger, J.C.C. Fan, B.J. Palm, R.P. Gale and R.L. Chapman, in *Laser and Electron Beam Processing of Materials*, C.W. White and P.S. Percy (eds.), Academic Press: New York (1980), pp. 234-240.
15. H.J. Zeiger, J.C.C. Fan, B.J. Palm, R.L. Chapman and R.P. Gale, *Phys. Rev. B* **25**, 4002 (1982).
16. R.A. Lemons and M.A. Bosch, *Appl. Phys. Lett.* **39**, 343 (1981).
17. D. Bensahel and G. Auvert, in *Laser-Solid Interactions and Transient Thermal Processing of Materials*, Vol. 13 of the Materials Research Society Symposium Proceedings, J. Narayan, W.L. Brown and R.A. Lemons (eds.), Materials Research Society: Pittsburgh, PA (1983), pp. 165-176.
18. D.A. Kurtze, W. van Saarloos and J.D. Weeks, *Phys. Rev. B* **30**, 1398 (1984).
19. G.H. Gilmer and H.J. Leamy, in *Laser and Electron Beam Processing of Materials*, C.W. White and P.S. Percy (eds.), Academic Press: New York (1980), pp. 227-233.
20. W. van Saarloos and J.D. Weeks, *Physica D* **12**, 279 (1984).
21. P.K. Gallagher and M.E. Gross, *J. Therm. Anal.* **31**, 1231 (1986).
22. M. Morbidelli, A. Varma and R. Aris, in *Chemical Reaction and Reactor Engineering*, J.J. Carberry and A. Varma (eds.), Marcel Dekker: New York, pp. 973-1054.
23. L.F. Razón and R.A. Schmitz, *Chem. Eng. Sci.* **42**, 1005 (1987).
24. K.F. Jensen and W.H. Ray, *Chem. Eng. Sci.* **37**, 199 (1982).
25. G. Strang and G.J. Fix, *An Analysis of the Finite Element Method*, Prentice Hall: Prentice Hall, NJ (1973).
26. G. Dhatt and G. Touzot, *The Finite Element Method Displayed*, Wiley: Chichester, England (1984).
27. H.B. Keller, in *Applications of Bifurcation Theory*, P.H. Rabinowitz (ed.), Academic Press: New York (1977), pp. 359-384.
28. A.C. Hindmarsh, *ACM SIGNUM Newsletter* **15**, 10 (1980).
29. J.M.T. Thompson and H.B. Stewart, *Nonlinear Dynamics and Chaos*, John Wiley and Sons: New York (1986).
30. D. Bäuerle, *Chemical Processing with Lasers*, Springer Verlag: Berlin (1986), p. 113.

LASER-INDUCED CHEMICAL VAPOR DEPOSITION OF HIGH PURITY ALUMINUM

THOMAS H. BAUM, CARL E. LARSON and ROBERT L. JACKSON
IBM Almaden Research Center, San Jose, California 95120-6099

ABSTRACT

The laser-induced chemical vapor deposition (LCVD) of aluminum metal has been achieved via the pyrolytic decomposition of trimethylamine aluminum hydride (TMAAH). This material is a volatile, crystalline solid which is non-pyrophoric, in contrast to many other aluminum precursors. Laser-driven pyrolysis of TMAAH enables the selective deposition of high purity, highly conducting aluminum deposits. The volatility of the TMAAH precursor is directly responsible for the rapid rates of aluminum deposition and permits rapid scan velocities to be utilized. The relationship between the chemical structure of TMAAH and the high purity of the aluminum deposits is described.

INTRODUCTION

The synthesis of metal precursors for conventional and laser-induced chemical vapor deposition has become an area of increasing activity. The number of metal precursors that are volatile, easy to handle and decompose cleanly to high purity metals is rapidly expanding. The syntheses of organogold [1,2] precursors have led to laser [3], ion [4] and electron [5] beam-induced depositions of gold. Similarly, organopalladium [6] and organoaluminum [7] precursors have been used to deposit pure palladium and aluminum films. We report here the use of trimethylamine aluminum hydride (TMAAH) complex for the production of pure aluminum films via laser-induced chemical vapor deposition.

EXPERIMENTAL

Trimethylamine aluminum hydride was synthesized by reported procedures [8]. The isolated crude product was purified by sublimation at 40 °C (30 μ m Hg) to obtain a white crystalline solid. The ambient vapor pressure of the purified product was measured with a capacitance manometer after several freeze-pump-thaw cycles and is approximately 2 Torr at 25 °C. This measurement is consistent with that reported for the 2:1 adduct [9] of trimethylamine to aluminum hydride, as shown in Figure 1. Although this precursor is air and water sensitive, it will not spontaneously ignite in air. The purified material has a melting point of 75 °C and is thermally decomposed to aluminum metal between 250 and 300 °C. Thermal decomposition has been observed to be catalysed by the presence of aluminum metal. The complex was allowed to equilibrate into a static vacuum chamber for the deposition experiments. The sample and chamber are translated with respect to the focused laser beam, thereby allowing the deposition of lines.

The laser-induced deposition of aluminum was carried out with the TEMgo mode of an argon ion laser (American Laser 909 and Coherent Innova 20) operating at 514 nm. The beam was expanded (3X) and collimated with a telescope then focused through a microscope objective (0.2 NA). The measured beam

diameter is approximately $9 \pm 1.0 \mu\text{m}$ at $1/e$ intensity points and was roughly Gaussian. The substrates used for deposition consisted of silicon wafers with a thermally grown oxide layer ($0.2 \mu\text{m}$ thickness) or a cured polyimide layer. In some cases, lines were deposited between evaporated $0.2 \mu\text{m}$ thick Cr/Au pads to enable the measurement of the resistance of the laser-deposited lines by a 4 point electrical probe. The resistivities were calculated after measuring the thickness and widths of lines by stylus profilometry. Several lines were examined by scanning Auger electron spectroscopy (SAES) at Surface Science Labs in Mt. View, California. The lines were also examined by SEM using a Philips 505 microscope with computer enhanced imaging.

RESULTS AND DISCUSSION

The molecular structure of the 2:1 complex of trimethylamine to aluminum hydride is depicted in Figure 1. The trimethylamine ligands are used to stabilize the highly reactive aluminum trihydride species and other alkyl substituted amines may be used for this same purpose.

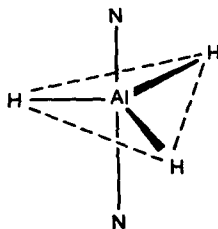


Figure 1

Molecular structure of the trimethylamine aluminum hydride (TMAAH) species used for the laser-induced deposition of aluminum. The 2:1 complex is depicted without the methyl groups on the amine ligands.

Lines of aluminum were deposited under varying conditions of laser power, scan velocity and onto various substrates. The ability to 'write' lines of aluminum at rapid velocities was noted at several laser powers. Lines with resistivities of 2 to 4 times bulk aluminum ($2.7 \mu\Omega\text{-cm}$) were produced on SiO_2/Si substrates, independent of the scan velocity up to $150 \mu\text{m/s}$. Using a smaller focal spot size ($3 \mu\text{m}$), $2 \mu\text{m}$ wide lines were formed at scan velocities up to $600 \mu\text{m/s}$. Several laser-deposited lines were analyzed by SAES. In general, the top-surface was highly oxidized from environmental exposure and contained some carbon. Argon ion sputtering to 200 Å revealed relatively clean aluminum (95 to 97 at. %). Some oxygen content was noted, but was believed to arise in part from the SiO_2 surface (silicon peak is observed) and in part from the surface roughness of the aluminum lines, which may cause uneven sputter etching. As can be seen in Figure 2, the laser-deposited lines formed on SiO_2 over silicon have a rough surface morphology and are highly crystalline. Limited analytical data indicates that the deposit resistivity correlates with the deposit purity. An aluminum line with a resistivity of $7.4 \mu\Omega\text{-cm}$ was found to be 97% aluminum, while a line with a resistivity of $14.2 \mu\Omega\text{-cm}$ was 95% aluminum after depth profiling to 200 Å with oxygen being the only impurity observed.

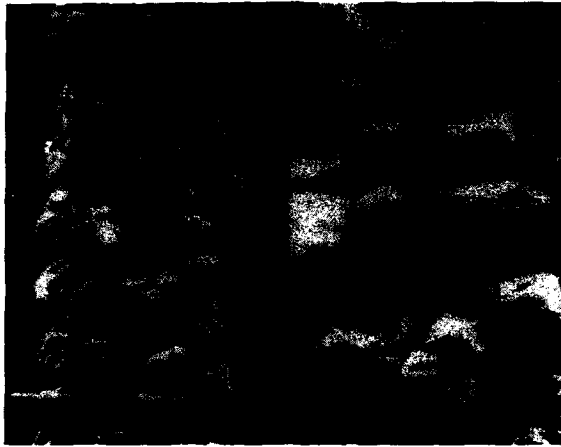


Figure 2

Scanning electron micrograph of a laser-deposited aluminum line produced from TMAAH. The line thickness is $3.6\text{ }\mu\text{m}$ with a calculated resistivity of $7.2\text{ }\mu\Omega\text{-cm}$.

The high volatility of TMAAH (2 Torr) affords rapid rates of deposition and enables rapid scan velocities to be used. At this time, the rates of aluminum deposition are believed to be mass-transport limited and further detailed experiments are underway. Thus, after heterogeneous nucleation, the rate of diffusion of TMAAH to the laser-heated reaction zone may be the rate-limiting step.

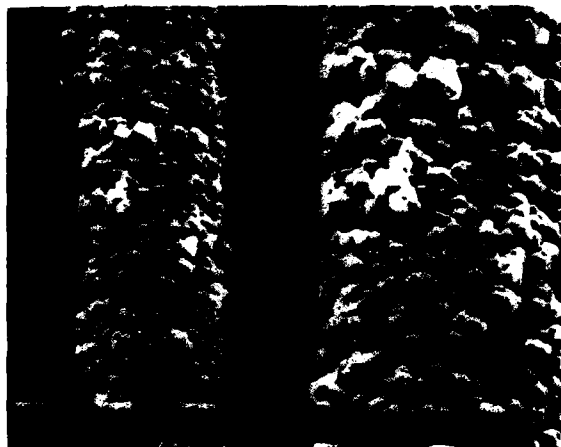


Figure 3

Scanning electron micrograph of aluminum line deposited onto polyimide from TMAAH.

The laser-induced deposition of aluminum onto polyimide films has also been demonstrated. The aluminum lines formed on this substrate have been found to possess smaller grain sizes (Figure 3) than the deposits formed on SiO₂ on silicon substrates. This is presumably due to the lower laser powers required for deposition onto polyimide without damage. Also, at low laser powers and fast scan velocities, the formation of periodic line structures is observed. These structures are produced because of the much higher surface reflectivity of the thin, aluminum deposits relative to the polyimide substrates. At the low laser powers, the surface temperature decreases with the increasing thickness of the reflecting aluminum deposit and deposition stops [10]. Deposition begins again as the focused laser beam encounters a fresh absorbing polyimide surface. This cycling of surface temperature results in the formation of periodic aluminum structures on polyimide.

The laser-induced deposition of aluminum has been extensively explored through the use of trialkyl aluminum complexes. In general, the trimethyl and triethyl complexes yield poor quality deposits. On the other hand, triisobutyl aluminum (TIBA) has been utilized to produce pure aluminum films by CVD [11] and by a clever two-step, laser process [12]. TIBA decomposition is believed to occur via β -hydride elimination, forming a surface-adsorbed diisobutyl aluminum hydride species [13]. The formation of aluminum hydride species were also implicated by Zhang and Stuke [14] as being important for the production of pure aluminum films in photochemically initiated deposition from several trialkylaluminum complexes. Recently, dimethyl aluminum hydride (DMAH) [15] was used to prepare pure aluminum films by high-power UV laser-induced decomposition. Although both photo and thermal effects are important in the latter work, the use of the aluminum hydride precursor appears critical to achieving pure films of aluminum. Further evidence supporting the importance of aluminum hydride species in producing pure aluminum films is demonstrated in this study via the pyrolytic decomposition of TMAAH.

CONCLUSIONS

The laser-induced deposition of high purity aluminum has been achieved through the use of trimethylamine aluminum hydride (TMAAH). This precursor is volatile, non-pyrophoric and yields high purity, highly conducting aluminum deposits under a variety of process conditions on SiO₂/Si and polyimide substrates. The hydride structure is believed to be an important factor in the formation of pure aluminum films. The volatility of TMAAH affords rapid rates of deposition and enables rapid 'writing' velocities to be realized.

REFERENCES

1. T. H. Baum, J. Electrochem. Soc., **134**, 2616 (1987); T. H. Baum, Mat. Res. Soc. Symp. Proc., **75**, 141 (1987).
2. M. R. Aylett, Chemtronics, **1**, 146 (1986).
3. T. H. Baum and C. R. Jones, Appl. Phys. Lett., **47**, 538 (1985); T. T. Kodas, T. H. Baum and P. B. Comita, J. Appl. Phys., **62**, 281 (1987).
4. G. M. Shedd, A. D. Dubner, H. Lezec and J. Melngailis, Appl. Phys. Lett., **49**, 1584 (1986).
5. H. W. P. Koops, R. Weiel, D. P. Kern and T. H. Baum, J. Vac. Sci. Tech. B **6**, 477 (1988).
6. J. E. Gozum, D. M. Pollina, J. A. Jensen and G. S. Girolami, J. Amer. Chem. Soc., **110**, 2688 (1988); G. T. Stauf and P. A. Dowben, Thin Solid Films, **156**, L31 (1988).
7. R. Bhat, M. A. Koza, C. C. Chang, S. A. Schwarz and T. D. Harris, J. Crystal Growth, **77**, 7 (1986).
8. J. K. Ruff and M. F. Hawthorne, J. Amer. Chem. Soc., **82**, 2141 (1960).

9. C. W. Heitsch, *Nature*, **195**, 995 (1962).
10. T. T. Kodas, T. H. Baum and P. B. Comita, *J. Appl. Phys.*, **61**, 2749 (1987).
11. K. Ziegler, K. Nagel and W. Pfohl, *Justus Liebigs Ann. Chem.*, **629**, 210 (1960); A. Malazgirt and J. W. Evans, *J. Metal. Trans. B*, **11B**, 225 (1980).
12. G. E. Blonder, C. G. Fleming and G. S. Higashi, *Appl. Phys. Lett.*, **50**, 766 (1987); G. S. Higashi, L. J. Rothberg and C. G. Fleming, *Chem. Phys. Lett.*, **115**, 2771 (1985).
13. B. E. Bent, R. G. Nuzzo and L. H. Bubeis, *Mat. Res. Symp. Proc.*, **101**, 177 (1987).
14. Y. Zhang and M. Stuke, *Mat. Res. Soc. Symp. Proc.*, **101**, 70 (1987).
15. T. Cacouris, G. Scelsi, P. Shaw, R. Scarmozzino, R. M. Osgood and R. R. Krachnevsk, *Appl. Phys. Lett.*, **52**, 1865 (1988).

STUDIES OF LASER-INDUCED SURFACE REACTIONS BY SURFACE TEMPERATURE MODULATION TECHNIQUES

PAUL B. COMITA*, DANIEL R. STRONGIN*, and TOIVO T. KODAS**

*IBM Research Division, Almaden Research Center, 650 Harry Road, San Jose, CA 95120

**Chemical and Nuclear Engineering Dept., University of New Mexico, Albuquerque, NM 87131

ABSTRACT

Two relaxation techniques are described, both of which use surface temperature modulation as their basis. In these techniques, modulation of laser light intensity results in a modulation of surface reaction rates. The first technique, a diffusive transport relaxation technique, has been developed to study the chemical reactions occurring under the high pressure conditions used in laser-induced chemical vapor deposition. Perturbation of the reaction rate in a high pressure reactor produces transients in the gas phase reactant and product concentrations for the case of gas phase transport-limited deposition. The product species are differentiated from species formed from the reactant during ionization and fragmentation due to the phase-sensitive nature of the detection scheme. The system response is examined theoretically by examining the response of the gas phase reactant and product concentrations to the modulated surface reaction. The second technique is a new technique which has been developed for obtaining detailed information concerning reaction energetics and pathways of elementary surface reactions. This technique also employs a laser to generate a surface temperature modulation. The laser light is incident on a pure metal film which is mounted within an ultra high vacuum chamber. By modulating the laser intensity, the surface chemical reaction rates are modulated. The combined use of surface temperature modulation and appropriate linearization methods allows a quantitative analysis of the overall reaction energetics to be made, and is used here to investigate the surface processes in a thermal laser-induced reaction.

INTRODUCTION

The surface chemical reactions which occur during laser-induced chemical vapor deposition determine the purity of the deposit and the deposition rate, two characteristics which determine the usefulness of a particular reactive system[1]. High pressures, on the order of 1 to 1000 Torr, are needed in many cases in order to achieve the rapid surface reaction rates which are required in a number of practical applications[2]. Under these conditions, a number of physico-chemical processes can influence the laser-induced surface reactions. The high deposition rates can result in a surface reaction rate limited by the flux of reactant from the gas phase to the heated region of the surface. A further complication is that reactions can occur both on the surface and in the gas phase. Thus, in order to study laser-induced reactions which occur in the high pressure regime, the influence of gas phase processes such as diffusion and chemical reaction on the surface reactions must be understood. In an effort to study laser-induced processes under high pressure conditions, we have developed a technique in which the concentrations of gas phase species above a surface reaction zone are modulated by perturbing the laser light intensity[3], and have used it for determining the products of laser-induced chemical vapor deposition reactions.

In order to investigate the detailed elementary chemical processes which occur only on the surface, a different experimental technique must be employed. The experiment in this case again uses the surface temperature modulation to produce a perturbation in the surface reaction rate, but in this case the perturbations in surface reaction rates result in fluctuations in the scattered intensity of product molecules. The fluctuations are measured directly using a line-of-sight detector. For the reaction under study, the mass balances of the adsorbed species are formulated. These are given by the rate expressions describing adsorption, desorption, and surface reactions. The set of coupled differential equations which describe the surface reaction system are linearized about steady state values and combined with a linearized mass balance

on the gas phase reaction products. The system transfer function developed in this way is then compared to the experimentally determined input and output signals, and the validity of the proposed kinetic model can be examined. The energetics of the elementary surface reactions can be extracted directly from the experimental response using this surface temperature modulation technique.

EXPERIMENTAL SYSTEM

The experimental design for the high pressure experiment consisted of three differentially pumped vacuum chambers. The high pressure chamber, to which the reactant gas was admitted, contained the substrate which formed the interface between the high pressure region and the high vacuum region. At sufficiently low laser modulation frequencies, the surface temperature can be modulated thereby producing transients in the surface reaction rate which in turn result in modulation of the reactant and product fluxes to the surface. At sufficiently high pressures, the transients in reactant and product fluxes to the surface result in modulated reactant and product concentrations in the gas above the surface. The beam passing through the aperture enters a differentially pumped chamber which contains a quadrupole mass spectrometer. See Reference 3 for a more complete description of this experimental apparatus.

In the experimental design for the UHV scattering experiment, the reactant is admitted to a heated metal surface mounted in a UHV chamber (base pressure 1×10^{-10} Torr) by a collimated molecular beam formed by either a multicapillary array or a nozzle apertured by a skimmer (see Figure 1). The reactant beam impinges on the surface and the scattered products are detected with a quadrupole mass spectrometer. The product ions are detected synchronously with the laser light modulation, and are digitized to enable signal averaging. The experimental apparatus also incorporates Auger electron spectroscopy and secondary ion mass spectrometry to determine the surface composition before and after reactive scattering. In addition to laser heating, the film can be resistively heated to determine the energetics of the desorption reactions independently of the surface temperature modulation experiment.

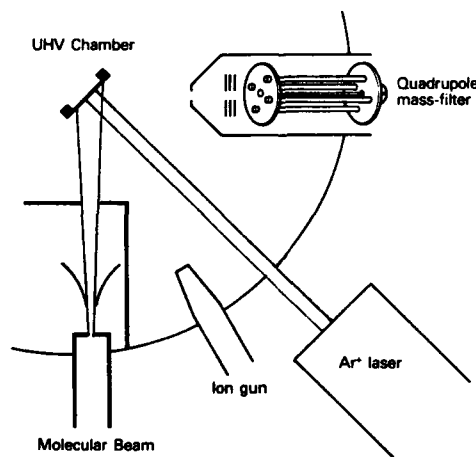


Figure 1. Schematic of UHV Reactive Scattering Apparatus.

RESULTS AND DISCUSSION

High Pressure Experiment

The amplitude of the reactant signal from the molecular beam is proportional to the change in the reactant concentration at the surface as the surface temperature is modulated. Thus, the reactant signal amplitude can be obtained by solving the steady state diffusion equation in spherical coordinates if the reactant and product concentration profiles reach a steady state with respect to the temperature during each laser on cycle.

$$I_A \sim n_{A\infty} - n_A(a) = \frac{n_{A\infty}}{1 + \frac{4Kn}{3\alpha}} \quad (1)$$

Equation (1) gives the signal amplitude dependence on the surface reaction rate and total pressure, where I_A is the reactant signal amplitude, $n_{A\infty}$ is the reactant concentration far from the deposit, $n_A(a)$ is the reactant concentration at the surface, Kn is the Knudsen number, and α is the reaction probability[3]. For an efficient surface reaction ($\alpha \sim 1$) and high pressure ($Kn \ll 1$), $n(a)$ goes to zero when the laser is on, while the sampled reactant concentration is equal to $n_A(a) = n_{A\infty}$ when the laser is off. If a phase sensitive detector, such as a lock-in amplifier is used, the signal amplitude will be proportional to the gas phase concentration far from the deposit, $I_A \sim n_{A\infty}$. This situation can be achieved experimentally by operating at sufficiently high pressures and laser powers since Kn is inversely proportional to the total pressure and α is usually an increasing function of the laser power. It is difficult to obtain information about the details of the surface chemical kinetics since the signal amplitude I_A does not depend on α for these conditions. However, the time to approach steady state during each laser pulse can provide information about the time for the surface temperature profile and the gas phase concentration profile to reach a steady state. In addition, this case provides the strongest reactant and product signals and as a result is the most useful operating regime for determining the product distribution.

Equation 1 shows that for sufficiently large Kn/α , the reactant signal I_A from a phase-sensitive detector is proportional to $3n_{A\infty}\alpha/4Kn$. In practice, this behavior can be obtained for sufficiently low pressures and low laser powers. In this regime, the reactant signal depends on α , but signal amplitudes are weaker than for the case of diffusion-limited operation. Indeed, in the limiting case of $Kn/\alpha \gg 1$, the reactant concentration at the surface during reaction is always nearly the same as its concentration far from the deposit and no signal should be observed.

The amplitude of the product signals is related to that of the reactant signals through Eq. 2. The concentration of a product (C) at the surface can be obtained as long as the reactant and product concentrations are much less than the buffer gas concentration. For the case where the laser modulation frequency is sufficiently low to allow a steady state product concentration to be achieved during each laser on cycle, of the product/buffer gas system. The product signal amplitude is proportional to the concentration of the product at the surface when the laser is on,

$$I_C \sim n_C(a) = \frac{D_{AB}}{D_{CB}} \left(\frac{n_{A\infty}}{1 + \frac{4Kn}{3\alpha}} \right) \quad (2)$$

and $I_C \sim (D_{AB}/D_{CB})I_A$ for all Kn/α , where D_{CB} is the binary diffusion coefficient. Thus the product signal amplitude is different from the reactant signal amplitude because of the factor D_{AB}/D_{CB} and should exhibit the same dependence on the reactant and total pressures and laser power and modulation frequency as the reactant signal amplitude. Equation 2 shows that for a sufficiently high reaction rate and total pressure, the reactant concentration near the surface goes to zero when the laser is on and a negative signal (out of phase with the laser light) is obtained for the reactant. Similarly, the concentration of product at the surface increases to some value when the laser is turned on and a positive signal (in phase with the laser light) is obtained for the product. Thus, the signs or phases of reactant and product signals are opposite. This suggests that if the parent molecular ion can be detected, product and reactant signals can be differentiated.

The predictions of the theory for the dependence of the signals on the total pressure and reactant partial pressure can be compared to the experimentally observed dependences for the case of gold deposition using $\text{Me}_2\text{Au}(\text{hfac})$. Transient signals were observed due to modulation of the laser light for sufficiently high pressures and laser powers (small Kn/α) as expected theoretically (Eqs. 1 and 2). Both reactant and product signals were observed (see Figure 2). Since the products undergo many collisions prior to being sampled by the orifice, the product distribution can be influenced by reactions occurring in the gas phase. The ion signals can be used to deduce the identity of the desorbed product species formed by the surface chemical reactions since theory predicts that reactant and product signals will be opposite in phase. This is important for complex precursor molecules such as $\text{Me}_2\text{Au}(\text{hfac})$ which can fragment during ionization in the mass spectrometer to form species identical or similar to reaction products.

Figure 2 compares a spectrum from m/e 70 to 230 obtained with this technique (top spectrum) and a reference mass spectrum of $\text{Me}_2\text{Au}(\text{hfac})$ in the same mass region obtained in the absence of surface reaction (bottom spectrum). The molecular ion signal is out-of-phase with the laser light due to depletion of the gas phase reactant number density by surface chemical reaction. The high m/e signals with the same phase as the molecular ion are daughter ions of the molecular ion, and have been assigned by analogy to other metal acetylacetonates[4].

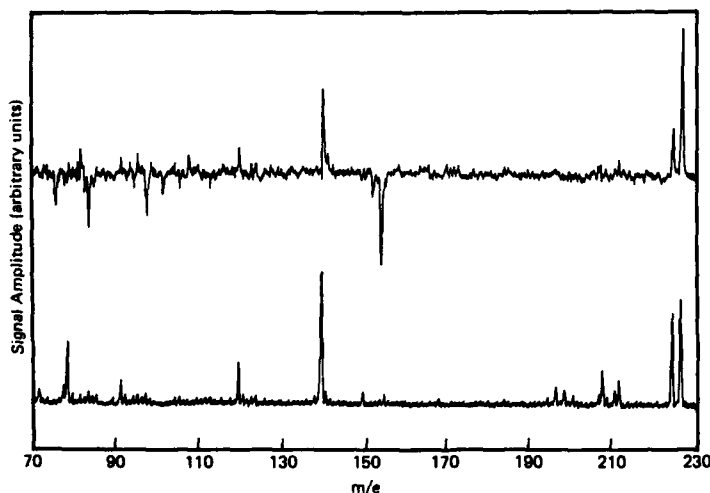


Figure 2. Mass spectrum obtained during reaction with modulated surface temperature technique (top spectrum) and spectrum obtained in absence of deposition (bottom spectrum).

The low m/e signal transients are derived mainly from reaction products and their daughter ions. These transients increase in amplitude when the laser light turns on since the gas phase concentration of these species increases as the result of production by surface chemical reaction. An effect that can complicate the interpretation of a mass spectrum is that the intensity of a product ion can have two sources: the product ion itself and daughter ions of the reactant and other products. Since the product and reactant signals have opposite phases, the product ion signal intensity can be reduced or possibly inverted depending on the relative intensity of the sources. Thus, complete reactant and product mass spectra must be obtained in order to determine quantitatively the product distribution.

UHV Reactive Scattering Experiment

The general theoretical formulation for this experiment has been described recently by Engstrom and Weinberg [5]. The measured responses for the reactive scattering experiment are described by the transfer function $G(p)$ for the reactions which are under investigation. The detailed form of the transfer function is dependent upon the rate expressions which describe adsorption, desorption, and surface reactions. For the use of line-of-sight detection, the scattered intensity $R_E(t)$ of the product molecules is measured. To relate this quantity to the transfer function and the driving function (the surface temperature modulation), the detailed mass balances on the surface species and the gas phase species must first be found. These equations are linearized about their steady state values, and the Laplace transform of these equations are evaluated. After combining transformed equations, the general form of the equations are

$$R_E^+(p) = G(p)T^+(p) \quad (3)$$

where p is the transform variable, $T^+(p)$ is the input function, and $R_E^+(p)$ is the output function. By making the substitution $p = i\omega$ for the transform variable, we can find the experimentally measured quantities, the amplitude ratio $AR(\omega)$ and the phase difference $\phi(\omega)$ of the input and output functions, which are given by

$$AR(\omega) = |G(i\omega)| \quad \phi(\omega) = \arg[G(i\omega)]. \quad (4)$$

The technique therefore involves finding the specific form of the transfer function for the specific class of surface reaction being investigated.

It is useful to restrict the scope of this discussion to the particular class of surface reaction which we have chosen to study, the surface reactions of aluminum alkyls. These molecules have in some cases been shown to deposit pure aluminum [6], and are also useful in the formation of compound semiconductors [7]. The experiments which establish the rate equations are described first for the dissociation of $Al(CH_3)_3$ on aluminum surfaces, and the class of surface reactions and the transfer functions are then described.

The reactant beam is composed almost entirely of the dimer of $Al(CH_3)_3$ at room temperature. The scattered product species from the dimer molecular beam which we have identified are CH_4 , CH_3 (methyl radical), and the monomer $Al(CH_3)_3$. Temperature programmed desorption experiments were carried out in order to establish the temperatures which are relevant to each specific reaction channel. These experiments were performed in the UHV chamber on a clean aluminum surface, using a linear temperature ramp of 16K/second. The CH_4 and CH_3 signals increase in intensity starting at 350°C to 400°C, and continue to rise up to the highest temperature achievable on the aluminum surface. The signal from $Al(CH_3)_3$ has a completely different behavior and the rate of desorption of this species has a maximum at 39±2°C and is shown in Figure 3. The signal observed (m/e 57) corresponds to a signal from the monomer $Al(CH_3)_3$ and not the dimer $(Al(CH_3)_3)_2$. This is determined by observing

the signal intensity of m/e 129, which shows no temperature dependence in this region (see Figure 3).

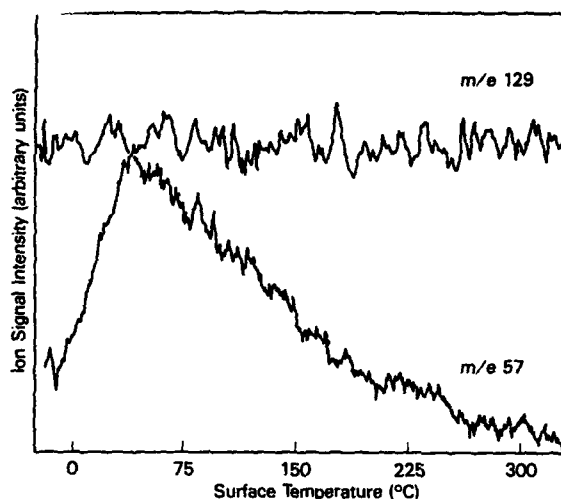


Figure 3. Temperature programmed desorption spectrum of product ions m/e 57 and 129 after dosing Al surface with $(TMA)_2$.

The surface temperature modulation experiments were performed in the pressure range of 10^{-8} to 10^{-7} Torr. Each scattered product species displays a modulated intensity which is time correlated with the surface temperature modulation. The signal intensity as a function of time for m/e 57, the ion signal which corresponds to the $Al(CH_3)_3$ monomer, are the result of the dimer unimolecularly reacting on the surface to form the monomer of $Al(CH_3)_3$. The product is trapped in this case for a significant period of time with respect to the average residence time of the reactant on the surface and the modulation period of the temperature forcing function. The subsequent analysis will be concerned with only this reaction channel and not with the higher temperature CH_4/CH_3 reaction channel. In order to compare these signals to an experimentally predicted signal, the transfer function for this case must be obtained.

A limiting form of the system transfer function can be obtained if a number of simplifying assumptions are applied[5]. These assumptions are approximations to the parameters involved, but are physically realistic for this case. They are (i) the adsorption reaction of the reactant is essentially independent of coverage and surface temperature with respect to the desorption and surface reactions; (ii) both the desorption of the reactant and the surface reaction are first order; and (iii) the rate parameters are independent of coverage. The transfer function has the form

$$t_{d,2}G(p) = t_{d,2} \left[\frac{(p/a_{22})}{(p/a_{22}) + 1} \right] + t_r \left[\frac{1}{1 + (p/a_{22})} \right] G'(p) \quad (5)$$

where

$$G'(p) = 1 + [x_1 H'_1(p)/h_r], \quad x_1 = \left[\frac{\partial(xk_r)}{\partial\theta_1} \right]_s, \quad H'_1(p) = \frac{-h_1}{(p + a_1)}, \quad h_r = (xk_r)_s t_r / T_s.$$

The data has been acquired as a function of steady state temperature, and agrees reasonably with the temperature dependence of this form of the transform function, using energies which have been either measured or can be well approximated.

SUMMARY AND CONCLUSIONS

Two experimental techniques have been developed to investigate laser-induced surface reactions. The first allows the rapid and simple identification of reaction products from a laser-driven, thermally activated surface chemical reaction carried out at high pressures, typical of the conditions which are most useful for high deposition rates. The second technique is useful for studying surface reaction dynamics in detail, in that elementary surface reaction parameters can be evaluated in a straightforward manner.

REFERENCES

1. R. L. Jackson, T. H. Baum, T. T. Kodas, D. J. Ehrlich, and P. B. Comita, *Laser Microfabrication: Thin Film Processes and Lithography*, Ed. D. J. Ehrlich and J. Y. Tsao, in press.
2. T. T. Kodas, T. H. Baum, and P. B. Comita, *J. Appl. Phys.*, **62**, 281 (1987).
3. P. B. Comita and T. T. Kodas, *Appl. Phys. Lett.*, **51**, 2059 (1987); T. T. Kodas and P. B. Comita, *J. Appl. Phys.*, **hp2/65/**, 2513 (1989).
4. C. Reichert and J. B. Westmore *Can. J. Chem.* **48**, 3213 (1970); C. Reichert, G. M. Bancroft and J. B. Westmore *Can. J. Chem.* **48**, 1362 (1970); I. W. Fraser, J. L. Garnett and I. K. Gregor, *J. Chem. Soc. Chem. Comm.* 365 (1974).
5. J. R. Engstrom and W. H. Weinberg, *J. Chem. Phys.*, **87**, 4211 (1987).
6. T. Cacouris, G. Scelsi, P. Shaw, R. Scarmozzino, and R. M. Osgood, *Appl. Phys. Lett.*, **52**, 1865 (1988).
7. R. Bhat, M. Koza, C. C. Chang, S. A. Schwarz, and T. D. Harris, *J. Crystal Growth*, **77**, 7 (1986).

LASER DEPOSITION OF GOLD

JEFFREY A. SELL, MARTIN S. MEYER, AND GREGORY P. MEISNER

Physics Department, General Motors Research Laboratories, Warren, MI, 49090-9055

ABSTRACT

Metallic gold was deposited on several different substrates by laser pyrolysis of a gold-containing ink. The gold was deposited in the form of lines by translating the substrate during laser pyrolysis; linewidths ranged from 10 μm to 1.5 mm. This process was performed in open air. Prior to annealing, the films contain 40 to 50 % carbon impurity and the resistivity is extremely high. After a 1 hour anneal in air, the carbon content is reduced to < 5 %, and the resistivity is reduced to roughly 13 times bulk gold. Further improvement may be possible with a different annealing schedule.

INTRODUCTION

The field of laser direct-write metallization has received a great deal of attention lately due to the prospect of maskless pattern generation for integrated circuit fabrication or repair. Laser deposition of Au has been demonstrated previously[1-14]. Indeed, the literature in this area is so extensive that we can not attempt to review it here. However, in order to distinguish the present work from that published previously, it is helpful to categorize the different types of laser deposition of metals. One method of categorizing laser-induced metallization is based on the type or phase of precursor used. We use the term precursor here to mean the metal-containing species from which the metal is deposited. Many experiments utilize an organometallic compound which may be a liquid or a solid at room temperature. Typically,[2-7] the precursor is held at a fixed temperature and the small but finite vapor pressure is admitted into an evacuated cell where the deposition is conducted. This points out the difficulty of potential scaleup of these types of laser deposition, namely the need for a cell or chamber. In addition, maintaining deposit-free windows is often a problem. Another category is experiments where metals are deposited from electrolytic plating solutions using laser assist.[13,14] Lately, much attention has been devoted to laser deposition from thin metallopolymer films,[8,9] a technique which can be accomplished in air without the need for a vacuum cell. Closely related to this is laser deposition from metal-containing inks.[1]

Another method of categorizing laser metallization experiments is based on whether the deposition mechanism is predominantly photothermal (pyrolytic) or photochemical (photolytic).[15] The advantage of deposition using the photolytic mechanism is that the thermal stress to the substrate is not as severe as in photothermal deposition. However, the thermal stress may not actually be too damaging in cases where the linewidth is small and a large fraction of the thermal energy is generated and dissipated above the substrate within the gaseous or liquid layer containing the precursor. In addition, photolytic type precursors are often more difficult to handle due to their sensitivity to room light. Finally, photothermal deposition rates often exceed photolytic rates by several orders of magnitude.[15]

In the present work, we discuss deposition of gold from a gold-containing ink on various substrates. Gold was deposited on glass and quartz using a CO_2 laser and on Si, alumina, brass, sapphire, and SrTiO_3 using an argon laser. We believe the mechanism to be largely thermal in both cases, involving heating of the substrate and subsequent decomposition of the ink in the case of the CO_2 laser. In the case of the argon laser, the beam is absorbed directly by the ink which decomposes, leaving a gold film. Although this study is an extension of previous work by Jan and Allen[1], Fisanick, Gross, and coworkers[8,9], and Houlding *et al.*[10,11] we used a different gold-containing ink, worked with several additional substrates, and characterized our resulting films extensively.

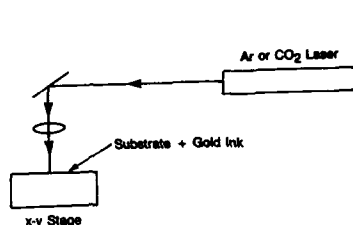


Figure 1. Block diagram of the experiment.

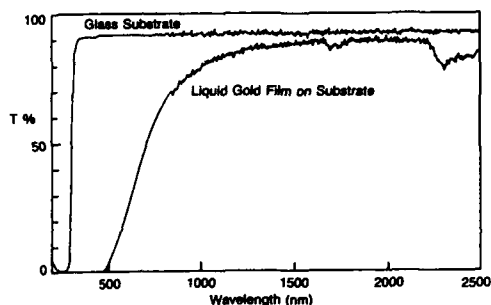


Figure 2. Transmission spectrum of the gold-containing ink.

EXPERIMENTAL

The laser direct-write deposition experiments were conducted in the geometry shown in Fig. 1. The substrate was mounted on a xy translator driven by a constant velocity actuator. Translation speed was controllable between 32 and 320 $\mu\text{m/s}$, allowing localized temperature regulation and thus precise patterning. Heating was provided by a beam from either a CO_2 laser or argon ion laser focused and directed normally onto the substrate. The CO_2 laser was a GTE Sylvania Model 950 which was operated typically at 0.2 to 1 Watt power. The argon laser was a Spectra Physics Model 171 tuned to the 514.5 nm spectral wavelength line with up to 3 Watt power. A 10 cm focal length lens was utilized for the argon beam and a 25 cm focal length ZnSe lens was used for the CO_2 laser beam.

Although a variety of substrates were used, the surface preparation of each was quite similar. The gold ink solution[16] was diluted 50/50 by xylene and dropped onto the substrate. Some redistribution of the drops was required to achieve a fairly uniform coating of ink. The sample was then translated under the laser beam in air, decomposing the ink and leaving a gold film. The residue left behind was washed away with xylene.

Resistance measurements were performed utilizing a standard 4-point probe technique. Electrical contacts between the gold stripes and 2 mil platinum wires were made with silver paint baked at 60 $^\circ\text{C}$ for 5-10 minutes. Voltages were measured at various dc currents which were reversed at each measurement to eliminate thermal and other background voltages. Resistances were determined by averaging the voltage divided by current for the forward and reversed current directions. Resistances at 77 $^\circ\text{K}$ were measured by immersing the samples in liquid nitrogen.

RESULTS AND DISCUSSION

Gold Ink

The gold ink used here[16] was a proprietary mixture of an unknown organometallic gold compound and various solvents, resins, and oils. Briefly, the ink contains 8 to 10 % gold by weight, and 62 % solvents by volume. Lower concentrations of Fe and Bi have also been detected.

Fig. 2 shows a visible transmission spectrum of the ink, where strong absorption in the blue is found. The 488 and 514.5 nm lines from the argon laser are both strongly absorbed. Converting this data into an absorption coefficient requires an accurate value for the thickness of the liquid layer which we have not yet been able to determine. Likewise,

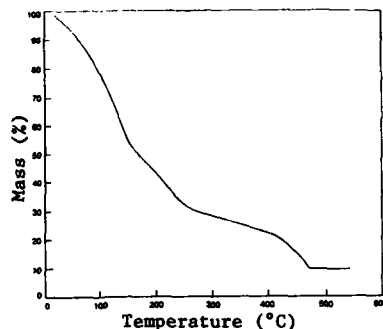


Figure 3. Thermal gravimetric analysis of gold ink.

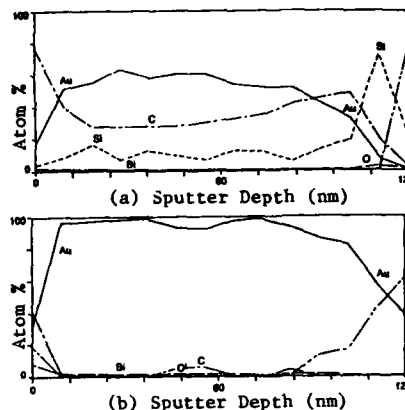


Figure 4. ESCA depth profile (by ion sputtering) of Au film: (a) as-deposited (b) annealed at 425 °C for 1 hr. in air.

10.6 μm radiation is absorbed by the ink, but we do not yet have an absorption coefficient for the same reason.

Fig. 3 shows a thermal gravimetric analysis (TGA) of the ink. This first wave in the TGA shows rapid weight loss at low temperature which could be due to both turpentine and perchloroethylene evaporation. The second wave is probably due to evaporation of cyclohexanol, commencing about 160 °C. The last wave may well be decomposition of higher boiling components as well as the organometallic, which typically decompose at higher temperatures such as in this 275-470 °C range.

Substrates

We demonstrated deposition on several different substrates, many of which have different potential applications. Deposition of fine gold lines on Si may be important for integrated circuit interconnects and contacts. Conducting lines on alumina have potential use in hybrid circuits. Gold conductors on sapphire and SrTiO_3 may be useful for connecting to high T_c superconductors for resistivity measurements and for future circuit applications. Finally, we demonstrated deposition on zinc and brass since gold is commonly used on electric contacts.

CO_2 Laser Deposition

With the CO_2 laser, gold was deposited on glass and quartz substrates. In these cases, we were not attempting to write fine lines, but rather desired lines on the order of 1 mm wide which would be used for characterization. Here, the thermal decomposition was quite obvious since a "bow wave" preceded the beam and a gold colored film was left behind. The best results have been obtained with ink layers that are not completely dry. Ink films that are either too dry or too thick seem to only partially decompose, leaving bubble-filled resin along with some gold. Quantification of the optimum thickness will be attempted in the future as well as spin-depositing the liquid ink to improve uniformity.

Figure 4 (a) shows a depth profile of the film before annealing obtained by x-ray photoelectron spectroscopy with ion sputtering and Figure 4 (b) shows it after annealing at 425 °C for 1 hour. Before annealing, the film contained 50 to 60% gold with carbon as the main impurity, as well as some Bi. After annealing, the film was roughly 95% gold.

X-ray diffraction of the annealed gold film showed only fcc gold to be present, and the lattice parameter derived matched the handbook value for gold within 0.09 %. An x-ray analysis of the unannealed film showed the same peaks, but less intense than the annealed film. This is probably due to partial disordering from the impurities present (mainly C).

SEM analysis of the films revealed a granular morphology with very prominent cracks near the edges of the film. However, the cracks did not appear to be present in the center of the films. A granular morphology in gold films has been observed previously[11] and attributed to the high interfacial surface tension between the gold and the glass as well as the high surface mobility of gold.

Determination of the thickness of the films proved to be a difficult task. Stylus profilometry was unsuccessful due to a slight sag in the center of the films due to softening of the glass by the CO_2 laser beam. Thickness determination by XPS depth profiling was uncertain due to lack of a suitable standard for sputtering rate of thin gold films. Optical transmission measurements were complicated by lack of an accurate value of the index of refraction of contaminated gold films and by microcracks in the films. Thickness measurements by electron microprobe scans[17] across the films finally revealed a thickness of the order of 300 Å. The ultimate thickness of the gold films that can be achieved is not yet known. It is expected that the film thickness will ultimately be self-limiting since the reflectivity of Au at $10.6\text{ }\mu\text{m}$ is $> 99\%$ for bulk gold. The reflectivity of thin films will depend strongly on the film thickness, increasing as the thickness increases.

The resistance of an air-annealed film (AU1) and an as-deposited film (AU3) both at room temperature and liquid nitrogen temperature were ohmic in nature over at least four orders of magnitude of applied currents. Sample AU3 had a room temperature resistance of $5904\text{ }\Omega$ and decreased to $4928\text{ }\Omega$ at $77\text{ }^\circ\text{K}$. Sample AU1 had a resistance at room temperature of more than two orders of magnitude lower, $39.1\text{ }\Omega$ and dropped to $30.3\text{ }\Omega$ at $77\text{ }^\circ\text{K}$. The dimensions of the films were 0.095 cm wide by 0.732 cm long by 250 Å thick for AU3 and 0.15 cm wide by 0.673 cm long by 320 Å thick for AU1, giving resistivities of $1.9 \times 10^3\text{ }\mu\Omega\text{cm}$ and $28\text{ }\mu\Omega\text{cm}$ for samples AU3 and AU1, respectively, at room temperature. The resistivity of the air-annealed film is hence about 13 times the resistivity of bulk gold, $2.214\text{ }\mu\Omega\text{cm}$. [18] A measure of the thermal coefficient of the resistivity for these gold films is given by the ratio of the room temperature to the low temperature resistance. This ratio is 1.2, 1.3, and 4.85 for AU3, AU1, and bulk gold, respectively. Both the lower resistivity and the larger resistance ratio for the annealed film AU1 are consistent with substantially less disorder in the annealed film compared to the as-deposited film. Another possible source of high resistivity could be the thinness of the films. However, by considering the dependence of the resistivity on thickness and electron mean free path[19], we estimate that the contribution to the resistivity from the thickness is only on the order of $1\text{ }\mu\Omega\text{cm}$. Hence the main source of resistance in the films is impurity and disorder. Further improvement in resistivity may be possible through optimization of the annealing schedule.

The only measure of adhesion we have at this time is the scotch tape test. The gold films on glass and quartz passed the test repeatedly; it was also found that the tape helped remove some of the resin residue at the edges of the gold film. The films on the other substrates were less adherent; in general they passed the test in some regions but did not adhere in others. We believe that this is at least partially due to the fact that we did not pretreat or clean the substrates prior to deposition.

Argon Laser Deposition

Figure 5 shows an optical micrograph of lines deposited on Si using the argon laser at 3 W with the sample translated at $320\text{ }\mu\text{m/s}$. It can be seen that the edges of the gold line are reasonably sharp and that the film is free of ripples. Some of the residue that did not get removed in the xylene wash can be seen clinging to the edge of the film. A more vigorous wash with the solvent is expected to remove the residue. We expect that lines more narrow than $10\text{ }\mu\text{m}$ can be deposited with a more tightly focused beam. Jan and Allen[1] have shown that film widths considerably smaller than the laser diameter can be deposited due to the nonlinearity of the process.



Figure 5. Optical micrograph of gold lines deposited on Si.

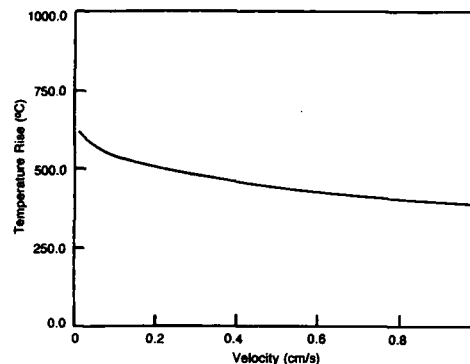


Figure 6. Temperature versus translation velocity calculated for a CO₂ laser beam on quartz. Laser parameters: R=0.01 cm, P=0.6 W.

Laser Pyrolysis of Ink

In this section we discuss a tentative mechanism for the deposition, namely pyrolysis of the gold-containing ink. We are describing the deposition of gold on quartz or glass by the CO₂ laser since the substrate in this case absorbs the beam. As stated above, the ink also absorbs the CO₂ laser radiation. However, the heating of the ink and substrate seems to cause a forced convection current in the ink that effectively thins the ink ahead of the beam. Based on the ratio of densities of gold (19.3 g/cc) to the ink (roughly 2 g/cc) and the final gold layer thickness of 300 Å, we estimate that the ink layer thickness prior to decomposition is 3000 Å. The absorption of the CO₂ by this thin layer of ink compared to that by the substrate is estimated to be small. Thus, for simple modeling purposes, the ink absorption will be ignored. The goal here is merely to calculate the surface temperature of the substrate and show that it is high enough to decompose the ink.

We follow the procedure of Cline and Anthony[20], assuming a semi-infinite solid and a laser beam moving with velocity v . For a gaussian beam of total power P and spot radius R ,

$$Q = \frac{P}{2\pi R^2} e^{-(r/\sqrt{2}R)^2}$$

where

$$r^2 = (x - vt)^2 + y^2$$

the temperature rise $T(x, y, z, v)$ at point x, y and depth z is given by

$$T(x, y, z, v) = \frac{P(1 - R_s)}{\rho C} \int_0^\infty \frac{1}{\sqrt{\pi^3 D t}} \frac{e^{-[(x+vt)^2 + y^2](2R^2 + 4Dt)^{-1} + \frac{z^2}{4Dt}}}{(2R^2 + 4Dt)} dt$$

where ρ is the density, C is the specific heat, and D is the thermal diffusivity and R_s is the surface reflectivity. Note that this expression was derived assuming complete absorption of the radiation at the surface of the solid. It would therefore be valid for the materials that have a large absorption coefficient. We have evaluated this expression using the IMSL routine QDAG to perform the integration. A resulting plot of temperature at the surface versus translation velocity is shown in Figure 6, for thermal properties of quartz and 0.6 W of CO₂ laser power. As expected, the peak temperature decreases slowly with increasing velocity, since the thermal diffusion length is greater than the distance moved in this velocity range.

At the velocity used in the experiment, 320 $\mu\text{m/s}$, the peak temperature rise calculated is 585 $^{\circ}\text{C}$ for 0.6 W. From the TGA analysis of the ink (Fig. 3), this temperature should be sufficient to decompose the ink. In fact, from Fig. 6, substantially higher writing speeds should still decompose the ink.

Note that this assumes that the peak temperature of the ink is the same as that of the substrate. This probably is not quite true due to thermal diffusion, but the thermal conductivity and heat capacity of the ink are not known presently, so that a calculation of the peak ink temperature is not possible at this time.

Acknowledgements

The authors would like to thank Tony Catalan, Bruce Clemens, Audrey Dow, Don Morelli, Noel Potter, Dave Roessler, Steve Swarin, Rick Waldo, and Curt Wong for assistance in various stages of these experiments and Gary Eesley for access to the argon laser and for helpful discussions.

REFERENCES

1. R.Y. Jan and S.D. Allen, Proc. SPIE 459, Laser Assisted Deposition, Etching, and Doping, 71 (1984).
2. T.H. Baum and C. R. Jones, Appl. Phys. Lett., 47, 538 (1985).
3. T.H. Baum and C.R. Jones, J. Vac. Sci. Technol. B, 4, 1187 (1986).
4. T.H. Baum and E.E. Marinero, Appl. Phys. Lett., 49, 1213 (1986).
5. T.T. Kostas, T.H. Baum, and P.B. Comita, J. Appl. Phys., 62, 281 (1987).
6. T.T. Kostas, T.H. Baum, and P.B. Comita, Matl. Res. Soc. Symp. Proc., 76, 57 (1987).
7. T.H. Baum, Matl. Res. Soc. Symp. Proc., 76, 141 (1987).
8. G.J. Fisanick, J.B. Hopkins, M.E. Gross, M.D. Fennell, and K.J. Schones, Appl. Phys. Lett., 46, 1184 (1985).
9. M.E. Gross, G.J. Fisanick, P.K. Gallagher, K.J. Schones, and M.D. Fennell, Appl. Phys. Lett., 47, 923 (1985).
10. V.H. Houlding, N.S. Clements, K.W. Beeson, and G.A. West, in *Photon, Beam, and Plasma Stimulated Chemical Processes at Surfaces*, edited by V.M. Donnelly, I.P. Herman, and M. Hirose, (Matl. Res. Soc. Symp. Proc., 75, Pittsburgh, PA 1986) p. 165.
11. V.H. Houlding, N.S. Clements, and K.W. Beeson, J. Appl. Phys., 62, 1070 (1987).
12. Y. Ye and R.G. Hunsperger, Appl. Phys. Lett., 51, 2136 (1987).
13. R.J. von Gutfield, M.H. Gelchinski, L.T. Romankiw, and D.R. Vigliotti, Appl. Phys. Lett., 43, 876 (1983).
14. R.J. von Gutfield, E.E. Tynan, R.L. Melcher, and S.E. Blum, Appl. Phys. Lett., 35, 651 (1979).
15. D. Bauerle, in *Laser Processing and Diagnostics*, D. Bauerle, Ed., Springer-Verlag, Berlin, 1984, p. 166.
16. Liquid bright gold fire cone 19 available from Johnson Matthey, Inc., 1397 King Road West, West Chester, PA, 19380.
17. R.A. Waldo, "Proceedings of the Microbeam Analysis 1988 Conference," Microbeam Analysis Society, Milwaukee, Aug. 7, 1988.
18. C.Y. Ho, et al., J. Phys. Chem Ref. Data, 12, 183 (1983).
19. G.T. Meaden, "Electrical Resistance of Metals," (Plenum Press, New York, 1965), p. 138. Also see K. Fuchs, Proc. Cambridge Phil. Soc., 34, 100 (1938).
20. H.E. Cline and T.R. Anthony, J. Appl. Phys., 48, 3895 (1977).

LASER CLADDING WITH A Ni-Fe-Cr-Al ALLOY

K. Mohammed Jasim* and D.R.F. West

Department of Materials, Imperial College, London

* On leave from Scientific, Research Council, Baghdad, Iraq.

ABSTRACT

An investigation is reported of the laser surface cladding of an alloy of nominal composition Ni-4Fe-30Cr-6Al (wt%) on a mild steel substrate, using a continuous powder feed of the elemental powder mixture into the melt pool. The effect of laser processing conditions has been investigated in relation to clad dimensions, bonding, dilution level, hardness and microstructural features. A 2 kW CW CO₂ laser was used working at 1.6 kW power and 2.5 mm beam diameter at different traverse speeds ranging from 1.8 to 25 mm/s; clad layers were produced in the range of 0.15-3 mm thick. Fine microstructures were obtained (corresponding to the rapid solidification rates). Good metallurgical bonding was observed between the clad layer and substrate within the range of specific energies, 50-130 J/mm². For all the conditions studied, no cracking was observed in single tracks; low specific energy conditions gave little porosity.

INTRODUCTION

The availability of high power lasers in recent years has led to a range of applications in materials processing, including the field of surface engineering. Surface alloying and cladding have been investigated using prealloyed powders on mixtures of elemental powders e.g (1). The objectives of these investigations include the attainment of improved surface properties such as resistance to corrosion and wear. Control of the dimensions, structure, and properties of the processed layers (tracks) is achieved by control of laser parameters (power, traverse speed, and beam diameter) and of powder composition and feed rate.

Lasers have also been used to deposit ceramic clad layers of zirconia based material by continuous powder feed (2), and to surface melt ceramic layers predeposited by plasma spray techniques in order to seal some of the porosity (3).

In superalloy technology for gas turbine components, there is currently extensive interest in the application of coatings, including both metallic alloys and ceramics, by plasma spraying (4). MCrAlY coatings (where M can be Fe, Ni, Co or combinations of these elements) confer protection from degradation by oxidation and hot corrosion (5). They may also be applied to superalloy substrates to produce a base (intermediate layer) on which a ceramic insulating layer can be deposited.

Recently a CO₂ laser has been used to remelt as-cast NiCrAlY (6). It was found that the microstructure after laser melting consists of two phases, intermetallic NiAl (β phase) and Ni solid solution (γ phase).

In another investigation (7), laser clad layers of FeCrAlY and CoCrAlY were produced using preplaced powder on a stainless steel (type 304) substrate. Complete melting of the coating powder was achieved with metallurgical bonding to the substrate and excellent oxidation resistance. However, the compositions of the clad layers were not uniform and microcracks were observed in the CoCrAlY coating.

The present investigation has explored the feasibility of producing a clad layer of a M-30Cr-6Al (nominal wt%) type alloy by laser cladding on a mild steel substrate, using a mixture of elemental powders. M consisted predominantly of nickel (nominal 60%) but a small addition of iron was incorporated (nominal 4%); yttrium was not included in the alloy.

EXPERIMENTAL PROCEDURE

A mild steel substrate in plate form was used and the upper surface was sand-blasted prior to laser treatment to improve the absorptivity. The cladding powder was a mixture of pure nickel, chromium, aluminium and iron. The analysed composition of the powder mixture was (wt%), Ni 60, Cr 30, Al 6 and Fe 4: (at%), Ni 54.3, Cr 30.3, Al 11.65 and Fe 3.75. This was continuously fed into the laser melt pool generated in the substrate which was traversed relative to a 3 mm diameter laser beam at speeds in the range of 1.8 to 25 mm/s. The powder feed rate was 10 g/min. Single and partially overlapping tracks were produced. The laser used was a 2 kW CW CO₂ type (Control Laser Ltd) operated at 1.6 kW. During processing, interaction with the environment was reduced only by an argon flow through the laser nozzle; no special shielding "dome" was used.

The single tracks were sectioned and metallographically examined. An etching solution consisting of 10ml HNO₃ + 30 ml HCl + 20 ml glycerol was used for microstructural studies by optical and scanning electron microscopy. Microhardness measurements were made using a Leitz Miniload 2. Compositional analysis was carried out by electron probe microanalysis (EPMA) using a JEOL JSM 35 instrument. The phases present were determined by X-ray diffractometry from partially overlapping tracks.

RESULTS

Dimensions and Quality of Laser Clad Layers

Fig. 1 shows the effect of traverse speed at constant power, beam diameter and powder feed rate on the dimensions of the clad layer. The width of the layer changed relatively little, lying in a range 1.7-2.3 mm, which is smaller than the beam diameter. The height of the clad layer (measured from the original substrate surface level) varied little from (0.5 to 0.3 mm) for traverse speeds between 8 and 12.5 mm/s, and then increased in the speed range 3-5 mm/s to values of 1-1.4 mm. The degree of dilution as measured from the area of substrate melted (8) was small (around 10%).

Within the traverse speed range 5-12.5 mm/s there was good bonding to the substrate (fig. 1a and b); however, at less than

3 mm/s the clad tracks were discontinuous (fig. 1c). Optical microscopic examination of the surface of clad tracks produced at speed from 5-12.5 mm/s did not detect any cracking. There was only a small amount of porosity, which increased with increasing traverse speed. However, cracking occurred in overlapping tracks at speeds less than 5 mm/s; cracks mainly started from the upper surface of the tracks.

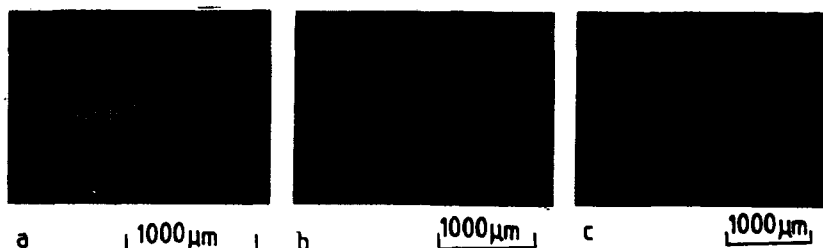


Fig. 1 Clads produced at different traverse speeds (a) 12.5 mm/s, (b) 5 mm/s and (c) 1.8 mm/s.

Microstructural and Compositional Features

Microstructural examination and electron probe microanalysis was carried out on a track 2 mm in height, produced with a traverse speed of 3 mm/s. Substantial variations in structure and composition were found as a function of position in the track.

In the dilution region adjoining the substrate, the microstructure appeared to be single phase as viewed by optical microscopy, for a distance of 10-20 μm (fig. 2a). This region was characterized by a high iron content, as a result of dilution from the substrate, with a consequent decrease in content of nickel, chromium, and aluminium as compared with the bulk analysis. The iron content at a distance of 10 μm from the substrate was ~55 at%, but decreased markedly with increasing distance, e.g., values of ~16 at% and ~7 at% were obtained at distances of 60 μm and 100 μm , respectively.

At a distance of 50 μm from the bottom of the processed zone, a fine-scale, two-phase structure occurred (fig. 2b). Regions of dendritic morphology were present in a "matrix" of eutectic type structure, the latter apparently being two-phase in nature with interphase spacings of the order of a few microns. The aluminium content of the dendrites was ~12 at%, indicative of nickel based solid solution (γ).

With increasing distance from the substrate the structure became predominantly eutectic (fig. 3a), with an analysed composition (at%) of 15 Al; 28 Cr; 2.5 Fe; balance Ni. Some small phase regions of high Al content were also present; these contained (at%): 37 Al; 20 Cr; 2 Fe; balance Ni consistent with β phase (based on NiAl). X-ray diffraction examination of overlapping clad layer (carried out at a central position corresponding to the predominantly eutectic structure) showed the presence of β and γ phases; the eutectic structure is

interpreted as consisting of β and γ . No superlattice lines corresponding to γ' phase were detected, but this does not exclude its possible presence.

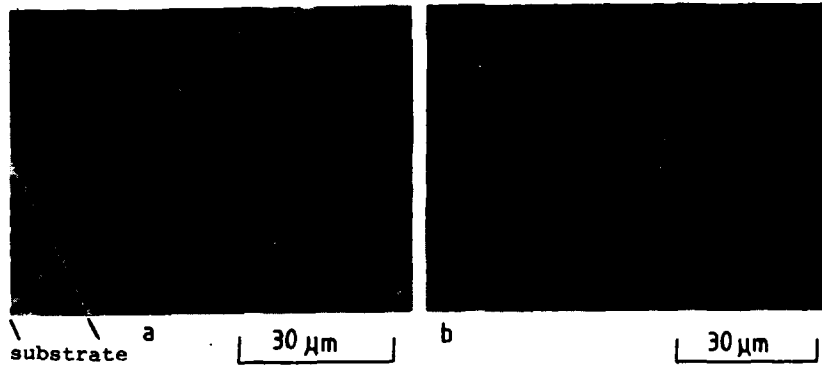


Fig. 2 Clad produced at 3 mm/s. Microstructures of clad region (a) adjacent to substrate (Fe content 60 at% near substrate), and (b) further from the substrate (average Fe content 12 at%).

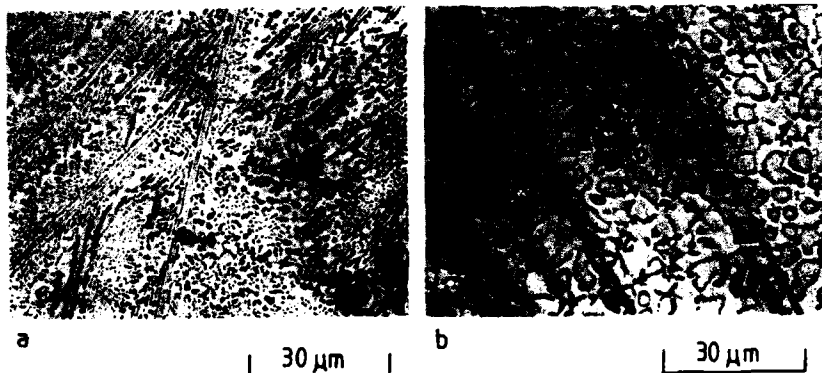


Fig. 3 Clad produced at 3 mm/s. Microstructure of (a) central region of clad zone; predominantly eutectic and (b) upper region of clad zone.

The upper part of the track to a distance of 9.0 μm from the top surface showed a different microstructure (fig. 3b). The dendritic type phase contained ~ 25 at% Al, indicating that it was γ' (based on Ni_3Al), but with a chromium content substantially less than that of the bulk alloy. The aluminium content of the matrix (~ 10 at%), indicated that it was γ . The small dark regions were not sufficiently large for EPMA. The bulk analysis of this region showed a substantially higher

aluminium and lower chromium content than that of the nominal powder mixture.

The hardness was reasonably uniform throughout the clad zone, at a high value of about 600 Hv.

DISCUSSION

The microstructural features indicate the attainment of complete melting and alloying of the powder, followed by rapid solidification; a cooling rate of the order of 10^2 - 10^3 °C/s is anticipated from other work on laser cladding (9). The compositional variations in the clad zone reflect the dilution effect, taking iron from the substrate into solution in the clad melt zone; significant solution of iron extends over a distance of about 100 μ m from the substrate. The decrease in chromium and increase in aluminum near the upper surface may result from selective loss of chromium by evaporation during the final stage of solidification.

The microstructures can be interpreted in conjunction with the analysis data by reference to the Ni-Fe-Cr-Al system considering compositions (at%) up to 60 at% Ni, 60 at% Fe, 30 Cr, 15 Al; this range covers the bulk cladding mixture and the modifications produced by dilution. The quaternary phase diagram is not reported in the literature but certain features can be deduced, based on liquidus and isothermal section data from the constituent ternary systems: Ni-Al-Cr, Ni-Cr-Fe and Ni-Al-Fe (10).

The Ni-Cr-Al system provides a good basis for interpreting the undiluted alloy composition (containing only 4 at% Fe). The phases for consideration are the fcc solid solution of Fe, Cr and Al in Ni (γ), the ordered cubic phase based on Ni_3Al (γ') and the ordered cubic phase based on NiAl (β). All of these phases show substantial solubility for chromium. The liquidus includes the reactions: $L \xrightarrow{\gamma} \gamma + \gamma'$; $L + \beta \xrightarrow{\gamma} \gamma$; $L + \gamma' \xrightarrow{\gamma} \gamma + \gamma'$; $L \xrightarrow{\beta} \gamma + \beta$.

The Fe-Cr-Ni system, in a range of elevated temperatures, shows a complete series of solid solutions between chromium and δ -iron (bcc), and between nickel and γ -iron (fcc). The structure shows a eutectic/peritectic reaction involving the two solid solutions.

In the Ni-Al-Fe system, the phase FeAl shows complete solid solubility with NiAl, and in the nickel rich region the liquidus reactions involving γ , γ' and β are of the same type as in the Ni-Al-Cr system.

In the iron enriched regions near the substrate the solidification sequence is interpreted as primary γ , followed by formation of the $\beta + \gamma$ eutectic and this is consistent with the phase diagram data. The main region of the clad material appears to be of composition close to the $\beta + \gamma$ eutectic.

The high hardness observed throughout the clad layer (~600 Hv) is interpreted as deriving from the presence of β and also from fine scale γ' precipitation from supersaturated γ which is expected to occur during cooling in the solid state.

CONCLUSIONS

1. Single clad tracks of Ni-4Fe-30Cr-6Al (wt%) can be successfully produced from a mixture of elemental powders in

the range of specific energies 50-130 J/mm².

2. There is relatively small dilution from the substrate, and freedom from cracking and significant porosity.

3. In the iron rich regions near the substrate the solidification sequence is interpreted as primary γ followed by $\beta + \gamma$ eutectic; the central regions of the clad layers are predominantly $\beta + \gamma$ eutectic.

ACKNOWLEDGEMENTS

Acknowledgements are due to Iraqi Government and Scientific Research Council, Baghdad, Iraq for support and interest during the investigation.

REFERENCES

1. J.D. Ayers, Thin Solid Films 84, 323 (1981).
2. K. Mohammed Jasim, D.R.F. West, W.M. Steen and R.D. Rawlings, presented at the 1988 TMS Fall-Meeting, Chicago, Illinois, Sept. 25-29 (unpublished).
3. K. Mohammed Jasim and D.R.F. West, to be published in J. Mat. Sci. Letts.
4. A.S. Grot and J.K. Martyn, Ceram. Bull. 60, 807 (1981).
5. T.W. Vogan, L. Hsu and A.R. Stetson, Thin Solid Films 84, 75 (1981).
6. J.G. Smeggil, A.W. Funkenbusch and N.S. Bornstein, Thin Solid Films 119, 327 (1984).
7. C.A. Liu, J.H. Humphries and R.C. Kratenat, Thin Solid Films 107, 269 (1983).
8. G.J. Bruck, J. of Metals 39, 10 (1987).
9. W.M. Steen, presented at ECLAT' 88, Bad Nauheim, W. Germany, 1988 (published).
10. G.V. Raynor and V.G. Rivlin, Phase equilibria in iron ternary alloys, Institute of Metals, London, 1988.

PART IV

**Laser-Induced Deposition
of Semiconductors**

SELECTED AREA GROWTH OF GaAs BY LASER INDUCED PYROLYSIS OF ADSORBED Ga-ALKYLS

V. M. DONNELLY, J. A. McCAULLEY, V. R. McCRARY, AND C. W. TU*
AT&T Bell Laboratories, 600 Mountain Ave., Murray Hill NJ, 07974; current address: Department of Electrical and Computer Engineering, University of California, San Diego, La Jolla CA, 92093

ABSTRACT

We compare three approaches to excimer laser assisted growth of GaAs: 1) *Film growth is dominated by gas phase photolysis of deposition precursor gases at 193 nm under low pressure metal organic chemical vapor deposition (MOCVD) conditions.* This approach leads to rapid deposition at low substrate temperature, but with very low spatial resolution (~1 cm). 2) *Growth is controlled by laser induced pyrolysis of adsorbed triethylgallium (TEGa) at 193 nm under metal organic molecular beam epitaxy (MOMBE) conditions.* Films grown under these conditions have the potential for high spatial resolution (i.e. sub-micron), but geometric constraints in MBE conflict with the requirement of a short working distance between the lens and substrate, making it difficult to attain this limit. 3) *Area-selective growth is controlled by laser induced pyrolysis of adsorbed TEGa at 351 nm (XeF excimer laser) under low pressure MOCVD conditions.* This approach combines the advantage of laser controlled surface chemistry with the potential for much shorter working distances.

Selected area growth of GaAs occurs in this latter mode because TEGa dissociatively chemisorbs at 400°C to form a stable layer which decomposes further under laser irradiation to liberate hydrocarbon products. The Ga left behind on the surface reacts with As₂ and As₄ (formed by pyrolysis of trimethylarsine or triethylarsine in a side tube) to grow GaAs in irradiated areas. Since the gas does not absorb at 351 nm the process is highly area-selective. Patterned films with feature sizes of ~70µm (limited by the mask dimensions) were grown by this method. Interference between the incident beam and light scattered along the surface also causes a substructure of parallel lines to form on the features with a line spacing about equal to the laser wavelength 0.35µm. This indicates that the ultimate spatial resolution is comparable to that predicted by thermal diffusion calculations (~0.3µm).

INTRODUCTION

Selected area growth of III-V semiconductor films would simplify the fabrication of complex integrated optical devices. Consequently, there has been considerable interest in using lasers to stimulate growth.¹⁻¹⁰ Previously, we have deposited InP^{1,2} and GaAs^{3,4} by low pressure photo-induced MOCVD from group-III and group-V methyl compounds. In those studies, the ArF excimer laser was chosen as the photolysis source because the laser wavelength (193 nm) overlapped strong gas-phase absorption to dissociative states in both the group-III and group-V sources.^{11,12} Photodissociation in the gas phase resulted in growth of epitaxial films at low substrate temperature. Irradiation of the surface improved crystallinity and decreased the carbon incorporation rate. However, film growth was not area-selective, i.e. material grew in regions adjacent to where the laser irradiated the surface. This is because photodecomposition products generated in the gas phase diffuse large distances (i.e. ~1 cm) before reaching and sticking to the surface.

Control of the growth rate by laser initiated surface (rather than gas phase) chemistry is necessary to achieve high resolution, selected area growth. More recently,¹³ we have shown that ArF excimer laser irradiation can enhance the rate of growth of GaAs in metal-organic molecular beam epitaxy (MOMBE), resulting from laser induced decomposition of an adsorbed layer. Subsequent X-ray photoelectron spectroscopy (XPS) studies showed that decomposition of the chemisorbed triethylgallium (TEGa) layer was a result of pyrolysis caused by pulsed laser induced transient heating.¹⁴ Consequently, it should also be possible

to induce selected area growth of GaAs in a higher pressure MOCVD environment (compared to MOMBE) by choosing a wavelength which is absorbed by the GaAs substrate, but not by gas phase TEGa. Selected area growth by pattern projection is more easily carried out under MOCVD conditions, than under MOMBE conditions, since the objective lens can more easily be positioned close (i.e. ~ 2 cm) to the substrate surface. Pattern projection has a large advantage over direct laser writing in that it is a parallel process, i.e. features grow simultaneously over a large (~ 1 cm²) area. In this paper we describe growth of GaAs under conditions where growth results from laser stimulated reactions occurring either in the gas phase, or on the surface. With proper choice of conditions (i.e. pressure and laser wavelength), surface reactions can be enhanced, and gas phase reactions suppressed, resulting in selected area growth of GaAs.

DEPOSITION CONTROLLED BY GAS PHASE PHOTOLYSIS

These experiments have been described in detail elsewhere.^{3,4} Briefly, the deposition system consisted of a multiport stainless steel chamber and gas mixing manifold. Trimethylgallium (TMGa) and trimethylarsine (TMAs) flows were mixed with He and H₂ carrier gas and window purge gas and flowed over the substrate. The GaAs(100) substrates were irradiated at normal incidence with ~ 15 ns pulses from a 193 nm ArF excimer laser. The 0.5×1 cm rectangular laser beam passed through roughly 4 cm of gas before reaching the substrate. Semi-insulating, undoped GaAs(100) ($10^7 \Omega\text{-cm}$) substrates were used. Polished substrates were degreased, etched, and rinsed in deionized water. Cleaned samples were mounted on molybdenum sample holders and placed in a load-lock chamber that is isolated from the growth reactor by a gate valve. Samples were then transferred into the growth chamber and heated to a temperature of between 100 and 500°C.

The absorption spectra of TMGa and TMAs are shown in Figure 1. At 193 nm, the wavelength of the ArF excimer laser, both gases absorb strongly (cross sections of 2.62×10^{-17} and 4.46×10^{-17} cm², for TMGa and TMAs, respectively).¹² The energy of a 193

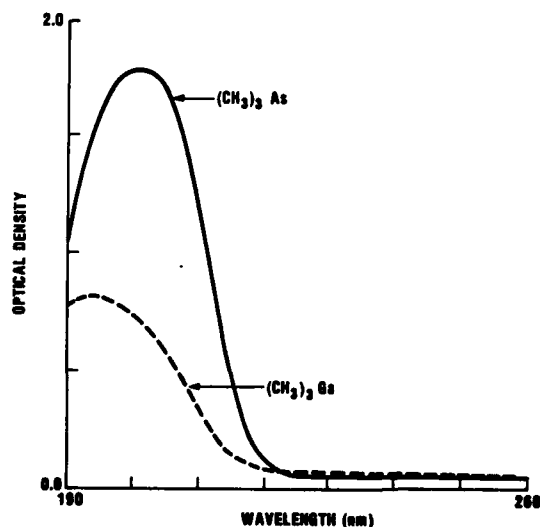


Figure 1. Room temperature absorption spectra of trimethylgallium (---) and trimethylarsine (—). Pressure=0.30 Torr; pathlength=7.5 cm. From reference 12.

nm photon (6.42 eV) exceeds the energy required to break two Ga-CH₃ or As-CH₃ bonds. At a typical laser fluence of 100mJ/cm²/pulse, TMGa and TMAAs are largely dissociated following each laser pulse. Species formed in primary and secondary photolysis in the gas phase, as well as products formed in reactions occurring after the laser pulse, diffuse to the surface, where they stick to grow GaAs. This process is depicted in Figure 2. Irradiation of the surface stimulates desorption of carbon-containing species and enhances the degree of epitaxy. However, absorption in the gas phase attenuates the laser beam so that the intensity at the surface is not sufficient to promote efficient decomposition of adsorbed TMGa (see below). Consequently, under these conditions the deposition rate is limited by gas phase photolysis, and material deposits not only where the laser irradiates the surface, but also adjacent to it. This leads to a loss of spatial resolution, such that this process could not produce features smaller than a few millimeters.

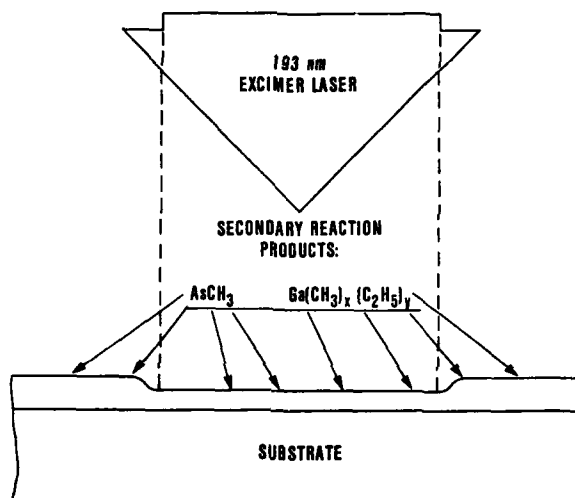


Figure 2. Schematic depiction of laser induced deposition of GaAs where gas phase photolysis is the rate limiting process.

LASER ASSISTED DEPOSITION FROM METAL-ALKYL MOLECULAR BEAMS

One method of suppressing gas phase photolysis and enhancing decomposition of an adsorbed layer is to use molecular beams. Under typical MOMBE conditions, gas phase photolysis can be ignored, and the full laser intensity reaches the substrate. We have recently demonstrated selected area growth of GaAs under MOMBE conditions.¹³ In those experiments, the Ga-alkyl source was triethylgallium (TEGa) and the arsenic source was an effusive beam of As₄. As above, the GaAs(100) substrate surface was irradiated with a 193 nm ArF excimer laser beam. Deposition of GaAs occurred only where the beam irradiated the surface. A plot of film thickness as a function of intensity across the ~1cm dia. beam is shown in Figure 3. The deposition rate rises rapidly with laser intensity and saturates at 120mJ/cm²/pulse, where it is limited by the flux of TEGa. The deposition rate is independent of substrate temperature in regions irradiated with full laser intensity. Outside the irradiated regions, the deposition rate is negligible below 350°C, and rises steeply with temperature such that above 550°C the growth rate is not enhanced by laser irradiation. These results suggest that a relatively stable, saturated layer of TEGa forms on the surface below

400°C, and that this layer is efficiently dissociated at 193 nm. One possible mechanism is photolysis of the adsorbed layer. Gas phase TEGa has a strong, dissociative absorption band at 193 nm (see Figure 4). Even if the absorption band of the adsorbate shifts by the amount seen for dimethylcadmium and trimethylaluminum adsorbed on quartz¹⁵, the absorption at 193 nm would still be strong enough to be important. The highly nonlinear fluence dependence rules out a single photon absorption process. However, two photon photodissociation is possible, as well as carrier mediated chemistry, and thermal decomposition due to laser induced heating of the substrate.

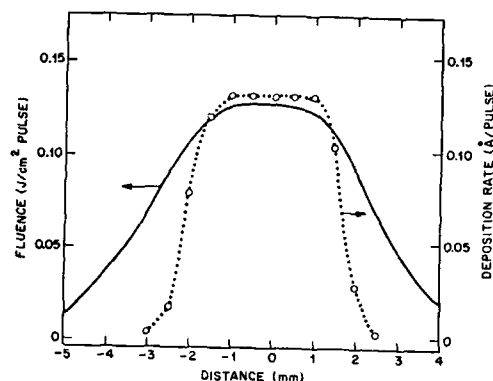


Figure 3. Deposition rate and laser intensity as a function of distance from the center of the laser beam across the short dimension, for GaAs grown under laser assisted MOMBE conditions. TEGa and As₄ beam pressures were 1.5×10^{-6} and 5×10^{-6} Torr, uncorrected for ionization gauge sensitivity. Substrate temperature = 400°C. (○): deposition rate at a laser repetition rate of 20 Hz. Solid curve: laser intensity.

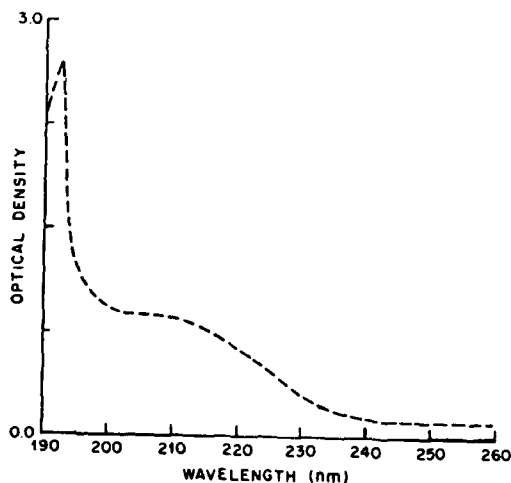


Figure 4. Absorption spectrum of triethylgallium at 0.9 Torr (measured at room temperature). The sealed cell was heated to 100°C to prevent condensation. Path-length=7.5 cm. From reference 12.

Deposited films exhibit photoluminescence at 1.486 eV, associated with a carbon acceptor level. Those areas grown with higher laser intensity exhibit more intense photoluminescence, indicating that laser annealing during growth reduces defects. However, the overall yields are rather low. In addition, the films contain high carbon impurity levels ($\sim 10^{19} \text{ cm}^{-3}$, based on SIMS measurements). To gain further insight into the growth mechanism, and specifically the carbon incorporation process, we have begun studies of decomposition of Ga-alkyls adsorbed on GaAs(100), described below.

While laser assisted MOMBE has the potential for selected area growth of small features, we were not able to demonstrate even low resolution patterned growth by image projection, due to the long distance between the window and substrate (1 m). This problem is common to all MBE systems, and would make growth of micron sized features difficult, since the working distance between the lens and substrate must be only a few cm. These short distances could more easily be accommodated under MOCVD conditions. We show below that this could be accomplished without loss of resolution due to gas phase photolysis, by choosing a wavelength (351 nm) which is not absorbed in the gas phase, but which induces efficient decomposition of adsorbed Ga-alkyls.

X-RAY PHOTOELECTRON SPECTROSCOPY STUDIES OF LASER INDUCED DISSOCIATION OF ADSORBED GA-ALKYLS

These experiments were described in detail elsewhere¹⁴, and have been summarized in this symposium proceedings.¹⁶ Wafers were loaded into ultrahigh vacuum and heated to desorb the native oxide. After cooling, they were dosed to saturated coverage with TEGa. Carbon coverage was measured as a function of the number of laser pulses, at various laser intensities. Between 100 and 200 mJ/cm²/pulse, decomposition of TEGa is dominated by pyrolysis due to transient laser induced heating of the substrate. One piece of supporting evidence is the lack of a wavelength dependence at high fluence, at two wavelengths (193 and 351 nm) strongly and equally absorbed by the substrate (Figure 5). This efficient dissociation at long wavelength can also be exploited to selectively dissociate TEGa on the surface and not in the gas phase, making possible highly area-selective growth at pressures much higher than in MOMBE (i.e. under MOCVD conditions).

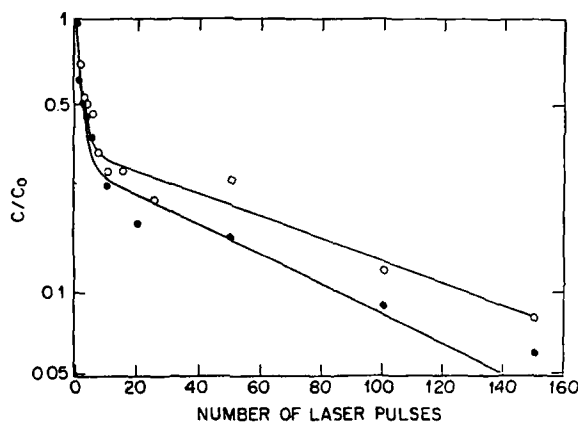


Figure 5. Relative carbon coverage vs number of laser pulses for saturated monolayer coverage of TEGa on GaAs(100), at 193 nm (●) and 351 nm (○), at a laser fluence of 180 mJ/cm²-pulse. From reference 14.

DEPOSITION CONTROLLED BY LASER INDUCED PYROLYSIS OF ADSORBED TEGa

Our approach to selected area growth of GaAs is to use the laser to decompose the Ga-alkyl on the surface, and desorb hydrocarbon species. Ga atoms left on the surface subsequently react with arsenic which is continuously flooding the surface. The process must be done at low temperature ($<450^{\circ}\text{C}$ for TEGa and $<500^{\circ}\text{C}$ for TMGa), otherwise thermal pyrolysis (not induced by the laser) of Ga-alkyls on the surface becomes the rate determining step, and selectivity is lost.

The deposition system was the same as that used in the experiments described above, where deposition was dominated by gas phase photolysis. The growth chamber has been coupled to an ultrahigh vacuum (UHV) chamber equipped with an X-ray photoelectron spectrometer (XPS), which has also been described in detail elsewhere.¹⁴

The beam irradiated a stencil mask with U-shaped features. A 20 cm focal length suprasil lens was placed nearly equidistant between the mask and the substrate to project the image of the mask onto the surface (see Figure 6). The relatively large mask features were compatible with the low resolution projection optics used in this preliminary study.

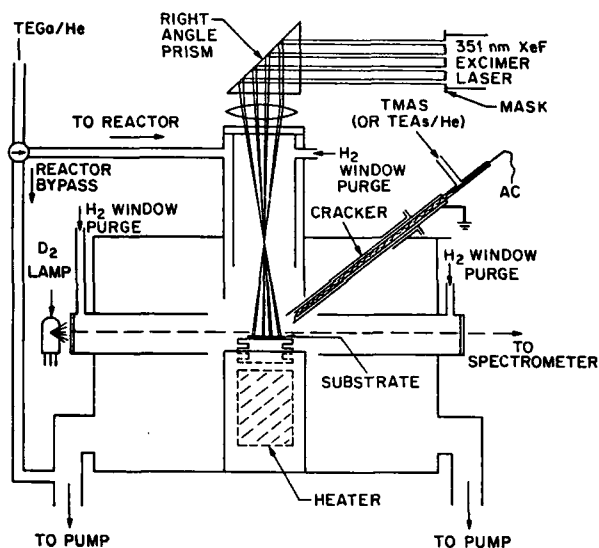


Figure 6. Schematic diagram of the apparatus used for selected area growth under MOCVD conditions.

All experiments were carried out at a total pressure of 10 Torr. TEGa vapors were transported to the growth reactor by bubbling He through the liquid source, held at a temperature of -7°C (measured vapor pressure of 0.49 Torr). After further downstream dilution with He, TEGa was mixed with H_2 window purge gas just above the substrate (Figure 6). We estimate the flow rate of TEGa to be 0.4 sccm (in some experiments, 4 sccm), while the total He carrier gas flow rate was typically 100 sccm. The window through which the laser light is transmitted was purged with a flow of H_2 (410 sccm). The TEGa/He flow was then injected into this H_2 gas stream ~ 4 cm above the substrate. The gallium source could also be bypassed around the reactor until growth conditions were established and then switched to flow over the wafer. Gas switching time was estimated to be ~ 2 sec under typical conditions.

The arsenic precursor (triethylarsine, TEAs) was flowed through a side tube (alumina or quartz) which contained a tantalum filament. TEAs flow rates (either ~ 4 or 40 sccm) were adjusted to be about 10 times higher than the TEGa flow rate. The end of the tube was injected into the gas stream ~2 cm above the substrate surface. The filament was resistively heated to thermally crack the arsenic compound, and its resistance was determined by simultaneously measuring the voltage and current applied, typically 55 V (a.c.) and 2 A. The measured resistance was related to the filament temperature using published resistivity data.¹⁷ Temperature is given by:

$$T(K) = 46.2 + 200.4R + 50.19R^2 - 2.48R^3 \quad (1)$$

where R is the ratio of the resistance at high temperature to that at 300 K. The cracking efficiency and the partial pressures of As_2 and As_4 products were measured by UV absorption spectroscopy.

Semi-insulating, undoped GaAs(100) ($10^7 \Omega\text{-cm}$) wafers were used. Polished substrates were degreased, etched, and rinsed in deionized water. Cleaned samples were mounted on stainless steel or molybdenum sample holders and placed in a load-lock chamber that is isolated from the growth reactor and UHV system by gate valves. The sample holder was then transferred under vacuum into the UHV chamber. The native oxide was desorbed by heating the sample holder from the back side by electron bombardment from a negatively biased, hot filament. Oxygen coverage was continuously monitored by XPS. Heating was stopped immediately after oxide sublimation was completed.

The sample was then transferred under vacuum back into the growth chamber. After establishing a constant substrate temperature in the range 300-560°C, the TMAs (or TEAs) flow and window purge flows were begun. The filament in the cracker was then heated to the desired temperature. TEGa flow was allowed to stabilize while bypassing the reactor (see Figure 6). After a constant laser power was obtained, a shutter was opened, exposing the substrate to irradiation. TEGa flow was subsequently switched to flow through the reactor and growth began.

At the low temperatures needed to achieve selected area growth, the arsenic alkyl compounds decompose slowly on the surface, hence they must be cracked before reaching the surface to grow GaAs. As_2 and As_4 generated in the cracker react at Ga sites to grow GaAs. However, As_2 and As_4 will not react with either arsenic terminated GaAs, or Ga-alkyl terminated GaAs (the steady state surface in regions not exposed to laser light).

Trimethylarsine will decompose, when heated, by the following overall reaction



The concentrations of $As(CH_3)_3$, As_2 , and As_4 , measured by UV absorption, are plotted as a function of the filament temperature in Figure 7. With an estimated transit time in the cracker of 30 ms, TMAs begins to decompose at ~530°C and is 95% dissociated by ~730°C. Although we did a more complete study of TMAs decomposition as a function of temperature, TEAs was used as the As-source in the growth studies presented here. The weaker As-C bond energies in TEAs (vs. TMAs) lead to more complete dissociation, and should result in reduced carbon incorporation. We chose to operate at 730°C, where TEAs is at least 95% dissociated. We have estimated the sticking coefficient of TEGa on GaAs(100) to be >0.1, and possibly as high as unity.¹⁸ A sticking coefficient close to unity was reported in previous studies of laser-assisted¹³ and thermally induced¹⁹ deposition from TEGa molecular beams. Our previous XPS study¹⁴ showed that dissociation occurs rapidly after adsorption (even at temperatures as low as room temperature) to form a more strongly bound chemisorbed layer.

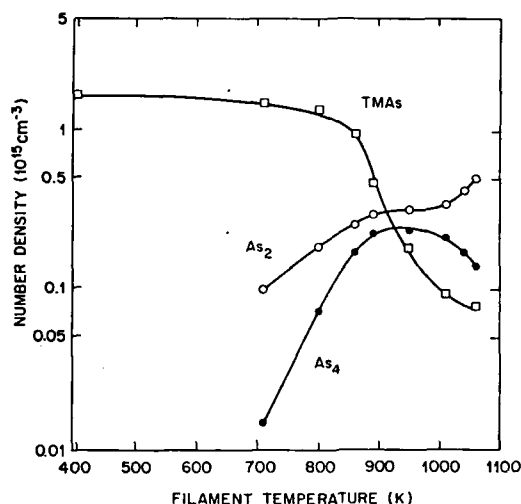


Figure 7. Number densities of $\text{As}(\text{CH}_3)_3$, As_2 and As_4 emerging from the cracker, above the substrate, as a function of cracker filament temperature. The temperature of the region probed by the absorption measurements was ~ 400 K. TMA flow rate = 7.4 sccm. Total pressure = 9.9 Torr. Top window purge = 450 sccm H_2 , side window purges = 260 sccm He through each of the two side windows. Cracker tube length = 15 cm. The gas residence time through the hot region of the cracker was ~ 30 ms at 1000 K. Cross sections used to extract number densities from UV absorption data are $5.5 \times 10^{-17} \text{ cm}^2$, for TMA at 200 nm, $1.7 \times 10^{-17} \text{ cm}^2$ for As_2 at 226.5 nm, and $1.7 \times 10^{-17} \text{ cm}^2$ for As_4 at 260.0 nm. The latter two values were determined in this study.

In the absence of laser light, or As species, adsorbed TEGa could dissociate as previously proposed.¹⁴



On the GaAs surface this reaction would be exothermic by $\sim 35 \text{ kcal/mol}$.¹⁴ When saturated monolayer coverage is reached, the sticking coefficient at room temperature (and presumably at temperatures up to those where TEGa decomposes rapidly, i.e. $\sim 450^\circ\text{C}$) drops to zero.

At a partial pressure of 4.4 mTorr TEGa used in these experiments, the adsorbed TEGa layer is expected to reach saturated monolayer coverage in 0.3 ms, assuming a sticking coefficient of unity, a temperature of 300°C and a saturated coverage of $1 \times 10^{14} \text{ cm}^{-2}$.¹⁴

Our previous XPS studies showed that adsorbed TEGa is not efficiently photolyzed at 351 nm (or at 193 nm).^{14,16} However, deposition of $\sim 90\%$ of the absorbed energy of an XeF laser pulse in the top $\sim 300 \text{ \AA}$ of a smooth GaAs surface leads to rapid heating, and desorption of hydrocarbon products. The efficiency of this process increases rapidly with laser fluence, reaching a rate of 1 pulse^{-1} at $200 \text{ mJ/cm}^2 \text{ pulse}$ at room temperature (i.e. 1 pulse at this fluence reduces the carbon coverage to $1/e$ of its initial value). Reactive Ga sites formed by this process react with impinging As_2 , or As_4 to grow GaAs. However, even if one laser pulse removes all the adsorbed hydrocarbon, self-limiting growth of about one monolayer of GaAs and subsequent saturated coverage of chemisorbed TEGa occurs

long before the next laser pulse (i.e. $\ll 50$ ms).

A patterned film grown by this technique is shown in Figure 8. GaAs grew only in areas where the laser irradiated the surface. Films up to $\sim 0.5\mu\text{m}$ thick were deposited in 30 min growth runs. The smallest feature size ($70\mu\text{m}$) was limited by the mask feature size and the 1-to-1 magnification used in these preliminary studies. Since selected area growth is a thermally initiated process, the ultimate resolution is expected to be limited by thermal diffusion. The 1-dimensional thermal diffusion length is given by²⁰

$$l = \sqrt{\kappa t / \rho C_p} \quad (5)$$

where t is the laser pulse duration (1.5×10^{-8} s), ρ is the density (5.317 g/cm^3)²¹ and where C_p and κ are the specific heat (0.40 J/gK)²¹ and thermal conductivity coefficient (0.09 W/cmK)^{14,22} for GaAs at a typical peak temperature (1200 K) induced by pulsed laser heating. Using these values, the one dimensional thermal diffusion length is $0.25 \mu\text{m}$. This value is about the distance, below the surface, where the peak temperature rise will be $1/e$ of that at the surface. Using our activation energy of 25 kcal/mol for decomposition of TEGa on GaAs,¹⁴ we predict that the smaller temperature rise will cause the growth rate to decrease by about four orders-of-magnitude. The minimum feature size possible by this technique is expected to be on the order of $0.2\mu\text{m}$. Diffusion in three dimensions will become important when the desired feature size becomes comparable to the 1-dimensional diffusion length. Temperature will therefore fall off more steeply than that predicted by 1-dimensional heat flow. Consequently the resolution limit should be somewhat better.

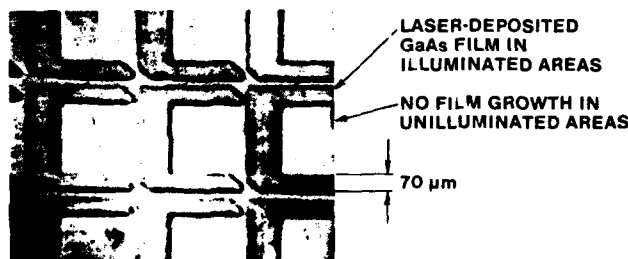


Figure 8. Patterned GaAs film. The substrate temperature was 400°C . Film thickness = $\sim 0.3\mu\text{m}$

In fact, we have experimental verification of this resolution limit. The GaAs features exhibit a diffraction easily discerned in visible light. This is due to the formation of a grating in the film caused by interference between the incident laser beam and light scattered off surface defects, propagating along the surface. This leads to a periodic modulation of intensity and hence peak temperature and growth rate. Grating formation with a $0.35\mu\text{m}$ period was observed by scanning electron microscopy. In addition, by measuring the approximate wavelength and angle of diffracted light, we confirmed that the grating period is about equal to the laser wavelength (i.e. $0.35\mu\text{m}$), as expected for normal incidence radiation with little dispersion of the surface wave (see ref. 4 and references contained therein). This effect could be enhanced or suppressed by increasing or decreasing the coherence and polarization of the laser.

To study the effects of laser intensity on film growth rate and morphology, we irradiated

the mask with a spatially nonuniform laser beam which was most intense in the center. We found that the growth rate reached a maximum at a laser intensity that we estimate to be $\sim 220 \text{ mJ/cm}^2/\text{pulse}$, falling below zero at the highest laser powers. That is, the substrate was etched or ablated at high fluence. This effect is shown in Figure 9, where each point is the growth rate at the center of a feature across the full 4.5 mm field. The same effect is observed across individual features deposited at the highest powers (see Figure 10, top), while at lower powers, the maximum growth rate is more nearly constant across the feature (Figure 10, bottom)

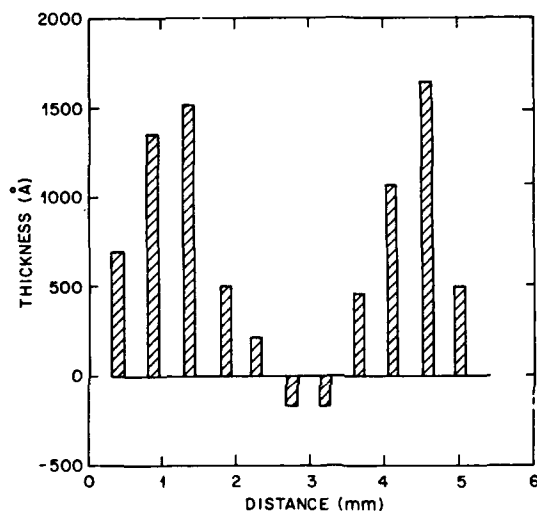


Figure 9. Feature thickness vs position across a patterned GaAs film deposited under conditions similar to those for figure 4. The maximum laser power in the center of the pattern resulted in etching.

Examination of films with XPS-sputter depth profiling revealed a 1:1 Ga:As stoichiometry (when corrected for preferential As sputtering), no detectable oxygen ($<0.2\%$), and carbon levels ranging from $\sim 1\%$ to below our detection limit ($<0.5\%$). In most cases, film morphology was rough, apparently due to nonuniform nucleation. This is probably caused by contamination of the substrate before growth began. In one instance, we began the procedure leading to film growth, but did not turn on the laser or TEGa flow. The sample was then transferred back to the UHV chamber under vacuum and analyzed by XPS. The Ga/As surface stoichiometry was 1.0, with no detectable oxygen ($<0.2\%$), and a carbon coverage $\sim 1/2$ that present when saturated coverage of TEGa is reached. It is unclear whether this level of carbon could inhibit growth. Incomplete removal of carbon species by laser induced heating could also lead to nonuniform nucleation. Carbon incorporation, as well as oxygen incorporation from trace H_2O and O_2 in the growth chamber, is an important issue that needs to be addressed in any low temperature and/or selected area growth process. We are currently evaluating the crystallinity of patterned films, as well as studying thermal decomposition of TEGa on GaAs(100) in attempts to improve surface morphology, crystal structure, and reduce carbon incorporation.

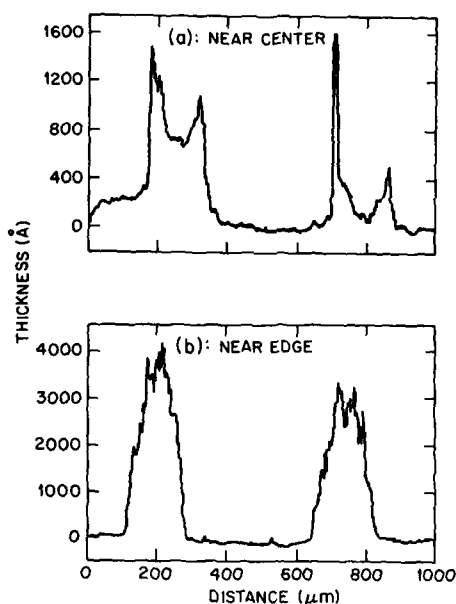


Figure 10. Dektak scan across individual features deposited near the center of the patterned film at high laser power (a), and near the edge of the pattern at low laser power (b).

SUMMARY

We have shown that GaAs can be selectively deposited on GaAs(100) under low pressure MOCVD conditions by choosing a wavelength (351 nm XeF excimer laser) which is not absorbed by the gas phase precursor species, but is absorbed by the substrate. Absorption of 15 ns XeF laser pulses by the substrate caused rapid transient heating which decomposed adsorbed TEGa. Subsequent reactions at these surface sites, between adsorbed Ga and impinging As_2 or As_4 formed by pyrolysis of arsine alkyls in a side tube, leads to selected area growth of GaAs. Since the mechanism for laser induced growth is mainly thermal, it is advantageous to use longer wavelengths such as the 351 nm XeF excimer laser to avoid gas-phase photochemistry that causes material to deposit over a relatively large area and thus blurs small features grown by laser induced surface chemistry in the high pressure MOCVD process.

Patterned films $\sim 0.3\mu\text{m}$ thick were formed by projecting the image of a mask onto the substrate surface. The minimum feature size of $70\mu\text{m}$ was limited by the mask feature size in these preliminary attempts to grow patterned films. However, periodic lines (separated by $\sim 0.35\mu\text{m}$) caused by laser interference were formed, indicating that the ultimate resolution may be close to that expected, based on thermal diffusion calculations.

ACKNOWLEDGMENTS

We would like to thank R. Kopf for assistance in substrate preparation, R. J. Shul for assistance in data collection during several experiments, and M. Geva for scanning electron micrographs.

REFERENCES

1. V. M. Donnelly, M. Geva, J. Long, and R. F. Karlicek, *Appl. Phys. Lett.*, **44**, 951 (1984).
2. V. M. Donnelly, D. Brasen, A. Appelbaum, and M. Geva, *J. Appl. Phys.*, **58**, 2022 (1985).
3. V. M. Donnelly, V. R. McCrary, A. Appelbaum, D. Brasen, and W. P. Lowe, *J. Appl. Phys.*, **61**, 1410 (1987).
4. V. R. McCrary, V. M. Donnelly, D. Brasen, A. Appelbaum, and R. C. Farrow, in *Photon, Beam, and Plasma Stimulated Chemical Processes at Surfaces*, ed. V. M. Donnelly, I. P. Herman, and M. Hirose, Vol. 75, (Materials Research Society, Pittsburgh PA, 1987), pp. 223-231.
5. P. Balk, H. Heinecke, C. Plass, N. Pütz, and H. Lüth, *J. Vac. Sci. Technol.*, **A4**, 711 (1986).
6. J. Haigh, *J. Vac. Sci. Technol.*, **A4**, 1456 (1985).
7. J. Nishizawa, H. Abe, T. Kurabayashi, and N. Sakurai, *J. Vac. Sci. Technol.*, **A4**, 706 (1986).
8. A. Doi, Y. Aoyagi, and S. Namba, in *Photon, Beam, and Plasma Stimulated Chemical Processes at Surfaces*, ed. V. M. Donnelly, I. P. Herman, and M. Hirose, Vol. 75, (Materials Research Society, Pittsburgh PA, 1987), pp. 217-222.
9. N. H. Karam, S. M. Bedair, N. A. El-Masry, and D. Griffis, in *Photon, Beam, and Plasma Stimulated Chemical Processes at Surfaces*, ed. V. M. Donnelly, I. P. Herman, and M. Hirose, Vol. 75, (Materials Research Society, Pittsburgh PA, 1987), pp. 241-248.
10. S. J. C. Irvine, J. B. Mullin, J. Tunnicliffe, *J. Crystal Growth*, **68**, 188 (1984).
11. R. F. Karlicek, J. Long, and V. M. Donnelly, *J. Crystal Growth*, **68**, 123 (1984).
12. V. R. McCrary and V. M. Donnelly, *J. Crystal Growth*, **84**, 253 (1987).
13. V. M. Donnelly, C. W. Tu, J. C. Beggy, V. R. McCrary, M. G. Lamont, T. D. Harris, F. A. Baiocchi, and R. C. Farrow, *Appl. Phys. Lett.* **52**, 1065 (1988).
14. J. A. McCaulley, V. R. McCrary, and V. M. Donnelly, *J. Phys. Chem.*, in press (1988).
15. D. J. Ehrlich and R. M. Osgood, Jr., *Chem. Phys. Lett.* **79**, 381 (1981).
16. J. A. McCaulley, V. R. McCrary, and V. M. Donnelly, this volume.
17. *Metals Handbook Ninth Edition, Volume 2 Properties and Selection: Nonferrous Alloys and Pure Metals*, (American Society for Metals, Metals Park, Ohio, 1979), p. 801.
18. V. M. Donnelly and J. A. McCaulley, unpublished data.
19. A. Robertson, Jr., T. H. Chiu, W. T. Tsang, and J. E. Cunningham, unpublished data.
20. P. Baeri and P. Campisano, in *Laser Annealing of Semiconductors*, eds. J. M. Poate and J. M. Mayer (Academic Press, New York 1982), pp. 75-109.
21. J. S. Blakemore, *J. Appl. Phys.* **53**, R123 (1982).
22. A. Amith, I. Kudman, and E. F. Steigmeier, *Phys. Rev.* **138**, A1270 (1965).

LASER INDUCED DECOMPOSITION OF TRIETHYLGALLIUM AND TRIMETHYLGALLIUM ADSORBED ON GaAs(100)

J. A. McCauley, V. R. McCrory, AND V. M. Donnelly
AT&T Bell Laboratories, 600 Mountain Ave., Murray Hill NJ, 07974

ABSTRACT

We report X-ray photoelectron spectroscopy (XPS) studies of excimer laser stimulated decomposition of triethylgallium (TEGa) and trimethylgallium (TMGa) adsorbed on Ga-stabilized GaAs(100) surfaces in ultrahigh vacuum. TEGa and TMGa dissociatively chemisorb on GaAs at room temperature, whereupon irradiation by an excimer laser (at 193 or 351 nm) leads to further dissociation and desorption of carbon-containing species. The carbon removal rate (per laser pulse) decreases as carbon is removed suggesting multiple reaction sites, coverage dependent Arrhenius parameters, or second-order reactions. Based on the dependence of the rate on laser wavelength and fluence, we conclude that at low fluence, a two-photon electronic excitation of the adsorbate occurs, while at high fluence, laser induced pyrolysis dominates.

INTRODUCTION

Laser enhanced growth of GaAs in high vacuum¹ underscores the importance of laser initiated surface chemistry. Control of the growth rate by laser initiated surface (rather than gas phase) chemistry is necessary to achieve high resolution, selected area growth.

Here we present results of studies of laser induced decomposition of monolayer coverages of triethylgallium (TEGa) and trimethylgallium (TMGa) chemisorbed on Ga-stabilized GaAs(100). A detailed account of this work will be published elsewhere.² X-ray photoelectron spectroscopy (XPS) was used to monitor Ga, As, and C surface concentrations before and after irradiation with either an ArF laser (193 nm) or a XeF laser (351 nm) at fluences varying between 10 and 220 mJ/cm²/pulse. We conclude that laser induced pyrolysis dominates above 100 mJ/cm²/pulse while 2-photon photolysis dominates at lower fluences.

EXPERIMENTAL PROCEDURE

The apparatus² comprises an ultrahigh vacuum (UHV) chamber equipped with an X-ray photoelectron spectrometer (Surface Science Instruments) and gas doser, an excimer laser (Quik), and computer controlled data acquisition. The pressure during XPS characterization was $\sim 2 \times 10^{-10}$ Torr. In most experiments, semi-insulating GaAs(100) (10⁷ Ω cm) wafers were used. Chemically cleaned samples, mounted on stainless steel or molybdenum sample holders, were transferred to a manipulator in the UHV chamber via a turbo-pumped load-lock chamber.

The GaAs sample was positioned for XPS measurements and heated by electron beam bombardment of the sample holder to $\sim 585^\circ\text{C}$ to desorb the native oxide and carbon impurities. The O(1s) XPS signal was monitored during oxide desorption, and the heating was stopped immediately after the oxide desorbed. The sample was allowed to cool to near room temperature and then dosed to saturated coverage with either TEGa or TMGa (Strem, 99.999%) using an effusive doser. Before dosing, the purity of the gas was ascertained mass spectrometrically (Extranuclear, Model 7-162-8). The dosed sample was characterized (for Ga, As, C, and O) by XPS.

A spot was then alternately irradiated with excimer laser pulses (either 193 or 351 nm) and analyzed by XPS. Calibrated quartz attenuators were used to obtain fluences between 10 and 250 mJ/cm²/pulse at 193 nm, while glass filters (Corning, 5860 and 5874) were used to obtain the same range of fluences at 351 nm. This irradiation-analysis cycle was repeated to obtain a decay plot of the relative carbon coverage as a function of the

irradiation dose. As little as 10%, to as much as 95% of the carbon was removed, depending on laser fluence.

RESULTS

For TEGa- and TMGa-dosed surfaces the C(1s) peak is centered at 284.1 eV and 283.4 eV, respectively. The integrated C(1s) peak intensity is twice as large for TEGa-dosed surfaces as it is for TMGa-dosed surfaces. High resolution spectra of TEGa-dosed GaAs(100) exhibit at least two overlapping features separated by ~ 1.0 eV, while no such structure was seen for TMGa-dosed GaAs(100). Absolute coverages of Ga and C, in the adlayer, are obtained by analysis² of the integrated intensities of the Ga(3d), As(3d), and C(1s) peaks before and after dosing. For TEGa- and TMGa-dosed GaAs(100), the saturated coverage of Ga is $1.1 \times 10^{14} \text{ cm}^{-2}$ and $0.96 \times 10^{14} \text{ cm}^{-2}$, respectively. The carbon coverages, $6.1 \times 10^{14} \text{ cm}^{-2}$ and $3.0 \times 10^{14} \text{ cm}^{-2}$, yield C/Ga ratios of 5.8 and 3.0 for TEGa and TMGa, respectively, in agreement with the precursor stoichiometries.

Upon exposure to laser radiation, the XPS C(1s) intensity decreases as carbon-containing species desorb. As carbon was removed, no shift of the C(1s) peak was observed for either TEGa or TMGa. Figure 1 shows the integrated C(1s) intensity vs laser exposure (at 193 nm) at several fluences for TEGa-dosed GaAs(100). Least-squares

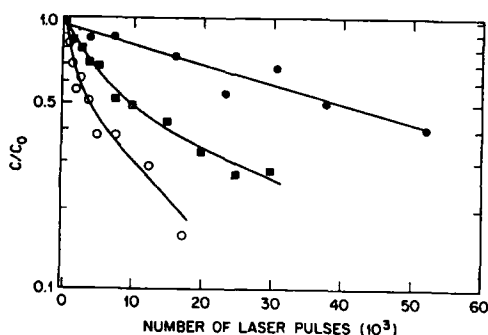


Figure 1. Relative carbon coverage vs number of laser pulses for TEGa-dosed GaAs(100) at: 30 mJ/cm², ●; 110 mJ/cm², ■; 150 mJ/cm², ▲, ○.

fits were obtained with a biexponential expression

$$C/C_0 = a_1 \exp(-a_2 n_p) + a_3 \exp(-a_4 n_p) \quad (1)$$

where n_p is the number of laser pulses, and a_2 and a_4 are rate coefficients (pulse⁻¹) of the first and second decay processes. At fluences below 100 mJ/cm² pulse, the decay of carbon coverage could not be followed as far toward completion. Consequently, little or no curvature was observed in the semilogarithmic decay plots, and only the initial decay coefficient was obtained. The fraction of surface carbon removed in the initial decay process ($a_1/(a_1+a_3)$), varies nearly linearly with fluence, increasing from ~ 0.2 to ~ 0.6 over the range 50–220 mJ/cm² pulse. Similar behavior was observed for TMGa-dosed surfaces, however the rate coefficients were a factor of ~ 20 smaller than those obtained for TEGa-dosed GaAs. A log-log plot of carbon removal rate coefficients (in pulse⁻¹) vs laser fluence for TEGa-dosed GaAs(100) is presented in Figure 2.

Figure 3 presents the Ga(3d)/As(3d) intensity ratio before dosing, immediately after dosing, and as a function of removed carbon ($1-C/C_0$). This figure contains data from all the TEGa experiments at 193 nm, including fluences between 12 and 220 mJ/cm² pulse. For TMGa-dosed GaAs the Ga(3d)/As(3d) ratio is also nearly constant as hydrocarbons are removed from the adlayer. If Ga were desorbed, the Ga/As ratio would return to that observed for clean GaAs as the carbon was removed.

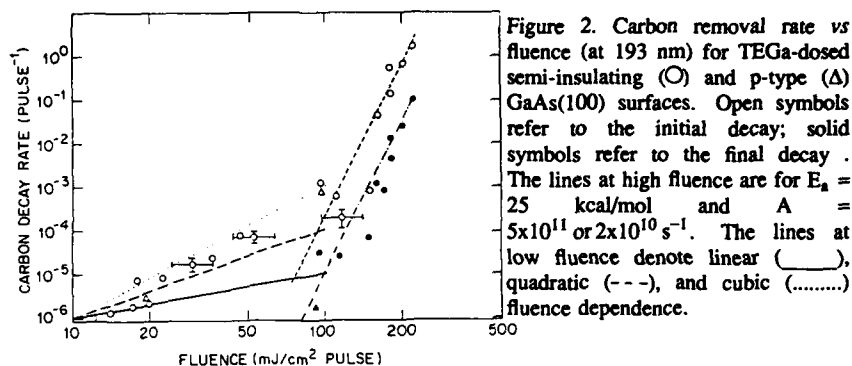


Figure 2. Carbon removal rate vs fluence (at 193 nm) for TEGa-dosed semi-insulating (○) and p-type (Δ) GaAs(100) surfaces. Open symbols refer to the initial decay; solid symbols refer to the final decay. The lines at high fluence are for $E_a = 25$ kcal/mol and $A = 5 \times 10^{11}$ or $2 \times 10^{10} \text{ s}^{-1}$. The lines at low fluence denote linear (—), quadratic (---), and cubic (.....) fluence dependence.

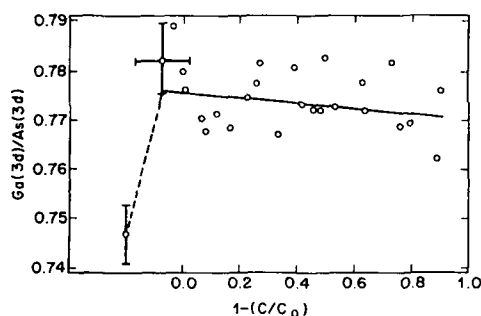


Figure 3. Ga(3d)/As(3d) intensity ratios vs carbon coverage for TEGa experiments, at fluences (193 nm) between 12 and 220 mJ/cm^2 . Slope = -0.007 ± 0.004 .

Several experiments were performed with 351 nm XeF excimer laser radiation. In each case an experiment at 351 nm was immediately followed by an experiment, with the same fluence, at 193 nm. At 180 mJ/cm^2 pulse the decay curves obtained for 193 and 351 nm irradiation are identical, while at 18 mJ/cm^2 pulse the rate is a factor of six faster at 193 nm.

DISCUSSION

The rate of carbon removal increases supralinearly with laser fluence. Linear dependence is shown by the solid line (slope = 1) in Figure 2. This precludes single-photon photodissociation over the range of fluences studied.

GaAs has nearly the same reflectivity and extinction coefficient at 193 nm and 351 nm (R (at normal incidence) = 0.44 vs. 0.42 and k = 2.03 vs. 1.94, respectively).³ Therefore, at constant fluence, the peak surface temperature should be similar for irradiation at these two wavelengths. This enables one to distinguish between resonant photolysis (which depends on photon energy) and laser induced pyrolysis (which depends only on absorbed power density, not photon energy). At 180 mJ/cm^2 pulse the decomposition rate is identical for 193 nm and 351 nm irradiation. At 18 mJ/cm^2 pulse, where laser induced heating is negligible (see below), carbon removal is a factor of six faster for 193 nm irradiation than for 351 nm.

Thermal decomposition cannot explain the small, but significant, rates at the lowest fluences, nor is it consistent with the dependence on wavelength at low fluence. A plausible explanation is that carbon removal is caused by resonant photodissociation of the

adsorbate. The rate of a two-photon dissociation process would depend quadratically on fluence if neither step were saturated. The quadratic fluence dependence expected of two-photon dissociation (slope = 2) is shown as a dashed line in Figure 2. While the two-photon mechanism provides a reasonable fit at low fluence, the apparent slope is closer to three. The apparent slope is, however, biased toward higher values;² we expect the true value to be closer to two, supporting a two-photon process.

About 50% of the energy in an ArF (or XeF) laser pulse incident (at 45°) on a smooth GaAs surface is absorbed. Most of this energy is deposited in the top ~100 Å. This causes rapid heating, which can initiate thermal reactions on the surface. The results of a first-order, thermal model of carbon removal were compared to the observed dependence of the rate of laser induced carbon removal vs laser fluence. The first-order rate coefficient is expressed in Arrhenius form:

$$k \text{ (s}^{-1}\text{)} = A \exp(-E_a/RT) \quad (2)$$

where R is the molar gas constant (1.987×10^{-3} kcal/mol K). As a result of pulsed laser irradiation, the surface temperature, and thus the rate coefficient, is a function of time. At each time, t_i , the carbon concentration is

$$C_i = C_{i-1} \exp(-A \exp(-E_a/RT_{avg}) \Delta t) \quad (3)$$

where Δt is the time interval between t_{i-1} and t_i , and T_{avg} is the average surface temperature during that interval. The rate coefficient of carbon removal is

$$k \text{ (pulse}^{-1}\text{)} = -\ln(C_{\infty}/C_0) \quad (4)$$

where C_{∞} is the carbon concentration remaining after a single laser pulse. To compare this model with measured carbon removal rates (pulse⁻¹), we numerically integrated the time-dependent rate expression over *calculated* temporal profiles of surface temperature. These profiles were obtained by numerical solution of the 1-dimensional heat flow equation, using the finite element technique described by Baeri and Campisano.⁴

The first-order rate expression was integrated over surface temperature profiles while varying the Arrhenius parameters, A and E_a . The curvature in Figure 2 cannot be reproduced using a single E_a and A -factor. This is consistent with our interpretation that below ~100 mJ/cm² carbon removal is due mainly to photolysis. The break in the data at ~100 mJ/cm² suggests the onset of thermal decomposition. The dashed line through the open circles (90-220 mJ/cm²/pulse) in Figure 2 is obtained from the first-order, thermal model using

$$k_{\text{TEGa}}^{\text{fast}} \text{ (s}^{-1}\text{)} = 10^{11.7 \pm 1.2} \exp(-25 \pm 5/RT) \quad (5)$$

where the uncertainties in A and E_a are correlated. This yields a 1/e lifetime of one month at room temperature, consistent with our observation that the carbon concentration in the adlayer changes negligibly in one week. For the slow component of the biexponential decay, the line through the solid circles in Figure 2 is obtained.

$$k_{\text{TEGa}}^{\text{slow}} \text{ (s}^{-1}\text{)} = 10^{10.4 \pm 1.2} \exp(-25 \pm 5/RT) \quad (6)$$

The activation energy (for both components) agrees with the 22-33 kcal/mol activation energies extracted from the TEGa heterogeneous decomposition data of Putz, *et al.*,⁵ and with the values of 18 and 21 kcal/mol taken from the growth rate of GaAs from TEGa.^{6,7}

Similarly, if we consider the TMGa data above 100 mJ/cm^2 we estimate

$$k_{\text{TMGa}}^{\text{fast}} (\text{s}^{-1}) = 10^{-10.4} \exp(-25/RT) \quad (7)$$

This agrees well with the activation energy ($26 \pm 3 \text{ kcal/mol}$) for desorption of methyl radicals from GaAs continuously dosed with TMGa.⁸ The observed activation energies are much smaller than the R-GaR₂ bond strengths in TEGa (46 kcal/mol ⁹) and TMGa (60 kcal/mol ¹⁰). This could be due to formation of a new Ga-As or Ga-Ga bond as a Ga-R bond breaks.

Biexponential decay would be observed for simultaneous first-order removal, with different rate coefficients, of two indistinguishable (by XPS) populations of carbon-containing species (e.g. desorption of R from GaR vs AsR sites, or from R₂Ga vs GaR). Desorption from these sites might have similar activation energies because the Ga-R and As-R and R-GaR bond strengths are similar. The disparity between the A-factors of the first and second decay process could reflect the participation of different mechanisms at the two sites. Non-exponential decay may also result from coverage-dependent Arrhenius parameters. A mechanism that includes second-order elementary reactions can also yield non-exponential decay. We are currently studying thermal decomposition (with slow heating, $\sim 1^\circ\text{C/min}$) of TEGa and TMGa adsorbed on GaAs(100) to further clarify the detailed mechanism.

Hall and coworkers¹¹ have shown that, in some cases, rapid laser induced heating favors desorption of intact molecules over decomposition, even in instances where decomposition dominates if the sample is heated slowly. We observe, however, that for TEGa (and TMGa) adsorbed on GaAs(100) the Ga remains on the surface after the hydrocarbon fragments are completely removed. This rules out laser induced desorption of intact TEGa or TMGa molecules (or Ga-containing intermediates).

From these studies, it is clear that at fluences where efficient laser enhanced growth of GaAs is achieved ($>150 \text{ mJ/cm}^2$ pulse at room temperature) laser induced pyrolysis of adsorbed Ga-alkyl is rate-limiting. Since the mechanism of laser enhanced growth is mainly thermal, it has proven¹² to be advantageous to use a longer wavelength (XeF, 351 nm), thereby avoiding gas-phase photolysis which causes material to deposit over a relatively large area.

SUMMARY

Exposure of Ga-stabilized GaAs (100) to TEGa or TMGa at $\sim 300 \text{ K}$ results in formation of a dissociatively chemisorbed layer with a C/Ga ratio (determined by XPS) equal to that of the precursor compound. When this layer is irradiated with an excimer laser, carbon coverage decays non-exponentially, with the Ga in the adlayer remaining on the surface. The decay of carbon coverage is fit well by a biexponential function, with slow and fast components that contribute nearly equally to carbon removal.

Above 100 mJ/cm^2 pulse, laser induced pyrolysis dominates and the decomposition rates are identical for irradiation at 193 and 351 nm. Numerical solution of the one-dimensional heat flow equation yielded temporal profiles of surface temperature for exposure to laser pulses of various energies. These profiles were then used to calculate rates from numerical integration of a first-order Arrhenius model. For TEGa, the best fit to the fast component was obtained with $E_a = 25 \text{ kcal/mol}$ and $A = 5 \times 10^{11} \text{ s}^{-1}$. The slow process has the same activation energy but a smaller A-factor ($2.5 \times 10^{10} \text{ s}^{-1}$). For TMGa, $E_a = 25 \text{ kcal/mol}$ is consistent with data for the initial decay process at fluences above $\sim 100 \text{ mJ/cm}^2$ pulse. The A-factor is a factor of 20 smaller than for TEGa. The activation energies are lower than the Ga-C bond energy. This is rationalized by invoking a concerted reaction, where breaking a Ga-C bond is accompanied by formation of a Ga-As, or Ga-Ga bond. Below $\sim 100 \text{ mJ/cm}^2$, carbon coverage on TEGa-dosed GaAs decays

slowly, and irradiation at 193 nm is more efficient than at 351 nm. We ascribe this reaction to a two-photon excitation of the adsorbate.

These studies show that laser enhanced epitaxial growth of GaAs from TEGa and As₄ molecular beams, observed in our previous studies, is initiated by laser induced thermal decomposition of adsorbed TEGa. Based on these studies, we have recently deposited patterned GaAs films by projecting a XeF excimer laser beam through a stencil mask and selectively decomposing TEGa adsorbed on GaAs(100), in the presence of excess As₂ and As₄.¹²

ACKNOWLEDGMENTS

We thank R. Kopf for help in substrate preparation and R. J. Shul for help in data collection.

REFERENCES

1. V. M. Donnelly, C. W. Tu, J. C. Beggy, V. R. McCrary, M. G. Lamont, T. D. Harris, F. A. Baiocchi, and R. C. Farrow, *Appl. Phys. Lett.*, in press, 1988.
2. J. A. McCaulley, V. R. McCrary, and V. M. Donnelly, *J. Phys. Chem.*, in press, 1988.
3. H. R. Philipp and H. Ehrenreich, *Phys. Rev. Lett.*, **8**, 92 (1962); *Phys. Rev.*, **129**, 1550 (1963); H. Ehrenreich, H. R. Phillips, *Phys. Rev. Lett.*, **8**, 59 (1962).
4. P. Baeri and S. V. Campisano, in *Laser Annealing of Semiconductors*, ed. J. M. Poate and J. M. Mayer (Academic Press, New York, 1982), pp 75-109.
5. N. Putz, H. Heinecke, M. Heyen, P. Balk, M. Weyers, and H. Luth, *J. Crystal Growth*, **74**, 292 (1986).
6. W. T. Tsang, *Appl. Phys. Lett.*, **45**, 1234 (1984).
7. P. Balk, M. Fischer, D. Grundmann, R. Luckrath, M. Luth, and W. Richter, *J. Vac. Sci. Technol.*, **B5**, 1453 (1987).
8. D. W. Squire, C. S. Dulcey, and M. C. Lin, in *Laser and Particle-beam Chemical Processing for Microelectronics*, edited by D. J. Ehrlich, G. S. Higashi, and M. M. Oprysko (Mater. Res. Soc. Proc. **101**, Pittsburgh, PA 1988) pp. 301-306.
9. M. G. Jacko and S. J. W. Price, *Can. J. Chem.*, **41**, 1560 (1963).
10. M. C. Paputa and S. J. W. Price, *Can. J. Chem.*, **57**, 3178 (1979).
11. R. B. Hall, A. M. DeSantolo, and S. J. Bares, *Surf. Sci.*, **161**, L533 (1985).
12. V. M. Donnelly, J. A. McCaulley, V. R. McCrary, C. W. Tu, and J. C. Beggy, in *Laser and Particle-beam Chemical Processing for Microelectronics*, this volume, 1989.

LATTICE DISTORTION INDUCED BY LASER ASSISTED MOCVD OF GaAs

S. A. HUSSEIN*, N. H. KARAM** S. M. BEDAIR** A.A. FAHMY* AND N. A. EL-MASRY*

*Department of Materials Science and Engineering North Carolina State University, Raleigh,
NC 27695-7907

**Department of Electrical Engineering North Carolina State University, Raleigh, NC
27695-7911

ABSTRACT

Laser induced chemical vapor deposition (LCVD) of GaAs has been achieved at low temperature using trimethylgallium and arsine precursors. The deposited film traces the path of the Ar⁺ laser, thus making it attractive for several applications. The localized thermal expansion resulting from the laser induced temperature rise has to be elastically accommodated in order to prevent lattice distortion during the LCVD process. We report on the growth conditions that can be used without the occurrence of plastic deformation in the epitaxial films. A model is presented to explain the thermal expansion induced distortion during the deposition process and will be compared with experimental results.

INTRODUCTION

Metalorganic chemical vapor deposition (MOCVD)[1] is typically accomplished by inductively heating an appropriate substrate, and the pyrolytic reaction of the gases at the heated substrate surface provides the basis for the crystal growth. Deposition occurs over the entire substrate surface and subsequent masking and etching are used for device fabrication. In contrast to the standard CVD process, laser-induced chemical vapor deposition (LCVD) would allow direct generation of material patterns. LCVD offers the advantage of spatial selectivity in deposition through focusing of the beam rastering optics. Laser-induced chemical vapor deposition (LCVD) of thin films has been recently demonstrated by either pyrolysis or photodissociation of polyatomic molecules near the gas/surface interface [2-5]. In the pyrolytic reaction the laser beam is used to provide localized heating of the substrate to endothermically decompose gas phase molecules resulting in film deposition. Photolytic LCVD on the other hand is based upon the photodecomposition of molecules near the substrate with subsequent deposition of the desired species. For an Ar⁺-laser, photons do not have enough energy ($\lambda = 0.514\mu\text{m}$) to dissociate the parent OM molecules such as TMG in the gas phase, but they can induce a localized heating of the substrate surface. However, it has been argued that the enhancement process in the LCVD is a result of a photocatalytic reaction on the locally heated substrate surface. Thus, the LCVD induced by the Ar⁺ laser is not completely pyrolytic.

However, this localized heating and the accompanied temperature rise can lead to thermal stresses. If these stresses exceed a critical value, plastic deformation will occur in the substrate or the epitaxial films. This plastic deformation is undesirable since it will create dislocations and lattice distortions which will affect the device quality of the LCVD films. In this paper we present experimental results and a model to estimate the allowed temperature rise during

the LCVD process, and thus the laser power density that can be applied without the creation of any plastic deformation.

MODEL FOR THERMAL STRESSES DURING THE LCVD PROCESS

The temperature rise ΔT induced by a cw laser beam impinging on a solid is estimated from Lax's model [6] for Gaussian power density distribution

$$\Delta T = \Delta T_{max} N(R, W, Z), \quad (1)$$

where $N(R, W, Z)$ is the temperature profile normalized to ΔT_{max} . $R = r/w$, $Z = z/w$, and $W = \alpha w$ where r is the radial distance from the beam center, z is the beam depth in the solid, w is the beam width which is equivalent to the laser spot radius, α is the attenuation coefficient and ΔT_{max} is given by [6]

$$\Delta T_{max} = \frac{P(1 - \Theta)}{2(\pi)^{1/2} K w}, \quad (2)$$

where K is the thermal conductivity, P is the total incident power, and Θ is the reflection coefficient. ΔT_{max} is defined as the maximum temperature rise at $r=0$ for large values of w . For a given value of w , the temperature rise ΔT is gradually decreasing with r to the substrate temperature T_b . Plots of the temperature profile $N(R, W, 0)$ as a function of R (or r/w) are given in figure 1.

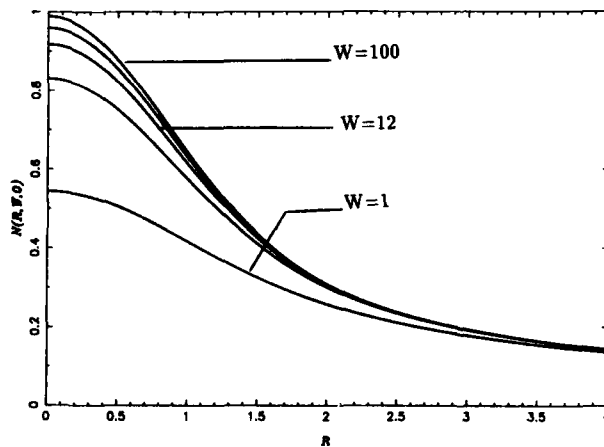


Fig.1 Variation of the temperature profile normalized to ΔT_{max} with the radial distance from the center of the beam $R=r/w$ (measured in the units of beam width)

The stresses σ induced due to this radial temperature gradient can be approximated by assuming a locally heated thin circular disk with radius b , by the expression:

$$\sigma_r = \beta E \left[\frac{1}{b^2} \int_0^b \Delta T r dr - \frac{1}{r^2} \int_0^r \Delta T r dr \right], \quad (3)$$

$$\sigma_\theta = \beta E \left[-\Delta T + \frac{1}{b^2} \int_0^b \Delta T r dr + \frac{1}{r^2} \int_0^r \Delta T r dr \right], \quad (4)$$

where σ_r and σ_θ are the principal radial and hoop stresses, β is the linear thermal expansion coefficient, and E is Young's modulus. This approximate model is valid for the case of GaAs since the attenuation length $\frac{1}{\alpha} \approx 1 \mu m$ is much smaller than the laser spot sizes considered in this study ($10 \mu m$ - $1000 \mu m$). Equations 1, 2, 3 and 4 show the dependence of σ_r and σ_θ on the temperature profile and the laser power. The plastic deformation starts to take place when the maximum shear stress, τ_{max} , is equal to the critical shear, τ_{cr} . τ_{max} and τ_{cr} are defined by Tresca criterion [7] for the isotropic case as

$$\tau_{max} = \frac{\sigma_{max} - \sigma_{min}}{2}, \quad (5)$$

$$\tau_{cr} = \frac{Y}{2}, \quad (6)$$

where Y is the yield stress, and σ_{max} and σ_{min} are the maximum and minimum principal stresses, respectively. Once β , E , K and Y are known for GaAs, it is possible to predict the maximum temperature rise and the critical laser power at which the material starts to yield, i.e. the onset of plastic deformation. Details of this calculation will be represented elsewhere.

For each radial point in the heated area there is a maximum shear stress which can be evaluated from equation 5. Figure 2 shows the variation of this maximum shear stress with the radial distance normalized to the beam width ($T_b = 250^\circ C$ and $w = 100 \mu m$). In this figure the value of this shear stress decreases as the radial distance increases. The onset of plastic deformation due to these thermal stresses will thus appear at the center of the heated area. Figure 3 shows the variation of the laser critical power density, $I_0 = P/\pi w^2$, to produce plastic deformation with the beam width at a substrate temperature $T_b = 250^\circ C$. This figure represents guidelines for the choice of the maximum applied laser power density for a given beam width (w) and substrate temperature (T_b) that will allow the LCVD process to take place without plastic deformation.

The conditions for the onset of plastic deformation were also determined experimentally. GaAs films were epitaxially grown on GaAs substrate using the LCVD technique with the multiple scanning approach previously described [8]. For fixed laser spot size ($w = 300 \mu m$) and substrate temperature $T_b = 250^\circ C$ a series of GaAs lines were deposited using different laser powers. The nature of these deposited lines were studied by optical microscopy and X-ray topography (XRT) and the results are shown in figure 4. Figure 4.a shows the optical micrograph, where for laser

power of 2.5W (line L_2), $I_0 = 884\text{W}/\text{cm}^2$, the surface is smooth whereas for 3.5W (lines L_1 and L_3), $I_0 = 1238\text{W}/\text{cm}^2$, the surface is rough with a cross-hatched pattern. The corresponding XRT reflection mode is given in figure 4.b. Lines L_1 and L_3 appear in XRT since they are fairly defective, whereas line L_2 is absent indicating no lattice distortion induced during LCVD. Thus from these preliminary experimental data it seems that under these conditions, the onset of plastic deformation appears for laser power greater than 3W. These experimental results compare favourably with the model as shown in figure 3 where L_1 and L_3 correspond to a condition yielding plastic deformation whereas for L_2 the thermal stresses are accommodated elastically.

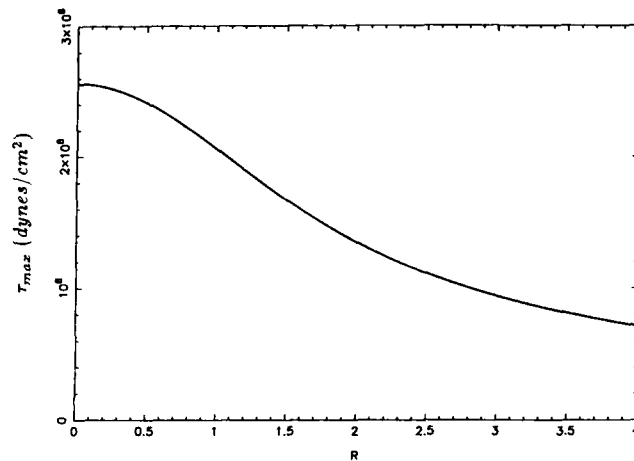


Fig.2 Variation of the maximum shear stress with the radial distance R

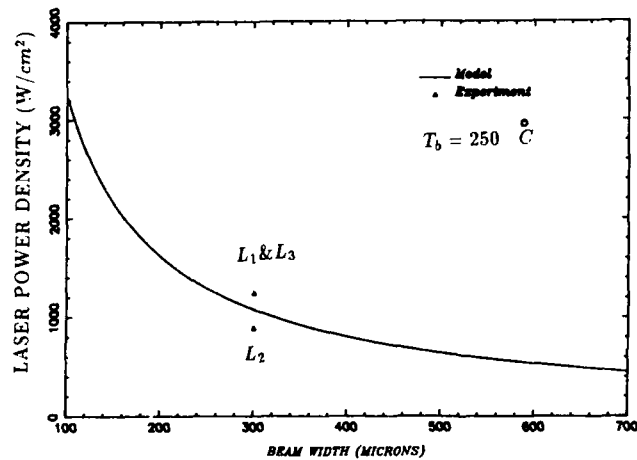


Fig.3 Variation of the critical laser power density with beam width. Points L_1 , L_2 and L_3 are obtained from experimental results presented in Figure 4.

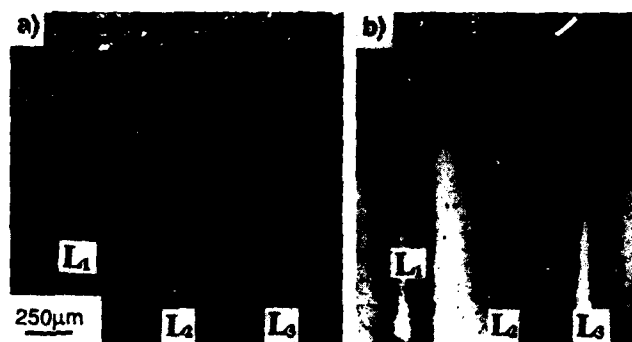


Fig.4 (a) Optical micrograph of homo-epitaxial GaAs grown by LCVD at $T_s = 250^\circ\text{C}$ and $P = 2.5\text{ W}$ (L_2) and $P = 3.5\text{ W}$ for L_1 and L_3 ,
(b) X-ray diffraction topography in the reflection mode $g = 511$

Line L_2 does not appear in XRT; presumably the LCVD film does not suffer any plastic deformation.

CONCLUSION

LCVD technique using Ar^+ laser is accompanied by localized heating and thus thermal stresses takes place in the substrate or in epitaxial film. LCVD with good crystalline quality can be achieved by allowing the stress to be accommodated elastically. A model is presented to predict the critical growth conditions such as laser power, beam size and substrate temperature that will not result in plastic deformation of these LCVD films. The model compared favourably with the available experimental results based on XRT technique.

ACKNOWLEDGEMENT

This work is supported by the NSF, ONR and SDIO/IST. We would like to thank B.L. Jiang for his help.

REFERENCES

- 1) G. Ghosh and R. L. Layman, Appl. Phys. Lett., **45**, 1229 (1984).
- 2) C. P. Christensand and K. M. Lakin, Appl. Phys. Lett., **32**, 254 (1978).
- 3) V. M. Donnelly, D. Brasen and M. Geva, J. Appl. Phys., **58**, 2022 (1985).
- 4) S. D. Allen, J. Appl. Phys., **52**, 6502 (1981).
- 5) N. H. Karam, N. El-Masry and S. M. Bedair, Institute of Phys. Conf., **83**, 171 (1986).
- 6) M. Lax, J. Appl. Phys., **48**, 3919 (1977).
- 7) W. A. Backofen, "Deformation Processing", Addison-Wesely (1972).
- 8) S. M. Bedair, M. A. Tischler, and T. Katsuyama, Appl. Phys. Lett., **48**, 30 (1986).

PATTERNED CRYSTAL GROWTH OF GaAs BY LASER ASSISTED ATOMIC LAYER EPITAXY

SOHACHI IWAI, TAKASHI MEGURO, YOSHINOBU AOYAGI AND SUSUMU NAMBA

The Institute of Physical and Chemical Research, Wako-shi, Saitama, 351-01, Japan

ABSTRACT

Atomic layer epitaxy (ALE) of GaAs is achieved by metalorganic vapor phase epitaxy (MOVPE) under irradiation by Ar ion laser. The self-limiting mechanism for gallium deposition at one atomic layer on an arsenic atomic surface is realized by the site-selective decomposition of triethylgallium on the arsenic surface. A patterned growth of ALE is obtained by scanning a laser beam on a substrate.

INTRODUCTION

Atomic layer epitaxy (ALE) is an attractive method to obtain abrupt interfaces in heterostructures and narrow doped layers at one atomic level [1]. ALE of GaAs has been reported by metalorganic vapor phase epitaxy (MOVPE) [2][3][4]. In order to realize an ideal ALE, means of arresting the deposition of the element at one monolayer are required in the growth mechanism. We have found that the growth rate is enhanced by laser irradiation and ALE is achieved by a switched-laser MOVPE technique using trimethylgallium (TMG) [5][6]. The laser-induced MOVPE has an advantage of selective area growth [7]. In conventional laser MOVPE by an argon ion laser, photochemical decomposition of the source gases has been considered to be dominant. However, it is difficult to obtain a uniform thickness because of the intensity profile of laser beam [8]. In laser assisted ALE (laser ALE), it has been shown that the photochemical surface effect is an important mechanism to realize ALE although optical absorption in the visible region does not exist in metalorganic compounds [6]. It seems to be important for a patterned growth with uniform thickness that the epitaxial layer is grown by the surface reaction and the growth rate is independent of the laser intensity. Direct writing of GaAs has been reported in the epitaxial layer grown by scanning a laser beam on the substrate surface in the laser ALE [9] [10].

In this paper, ALE of GaAs in triethylgallium (TEG)-AsH₃ system under irradiation by an argon ion laser is described. The laser ALE technique is applied to the patterned growth by the scanning of laser beam.

EXPERIMENTAL

Epitaxial layers were grown on (100) oriented GaAs substrates in a low pressure MOVPE system at 350 °C. The pressure in the reactor was 75 Torr during the crystal growth. The growth procedure for laser ALE has been reported previously [5]. AsH₃ and TEG were supplied on a substrate alternately for 1 s. H₂ carrier gas was continuously flowed into the growth chamber at the rate of 2800 sccm to ensure purging of residual source gases. The purging time of 1 s between TEG and AsH₃ pulses was enough to prevent mixing of source gases. In our laser MOVPE system, visible light of 514.5 nm from an argon ion laser was used in order to enhance the decomposition of TEG at a substrate surface, not in gas phase. The laser beam was switched on by a shutter to irradiate the substrate during desired periods. For the ALE growth, the substrate was irradiated at the same time as the TEG flux was supplied. In order to get a patterned crystal growth, the laser beam was also scanned on the substrate surface by deflecting mirrors or a lens.

RESULTS AND DISCUSSION

ALE of GaAs has been achieved by controlling one monolayer adsorption of source element on the substrate. One atomic layer deposition of arsenic atoms seems to be easily achieved during the supply of AsH_3 under a proper growth condition because of the high pressure of As atoms. On the other hand, in case of the Ga layer, the mechanism to arrest the deposition at one atomic layer is necessary because of the low vapor pressure of Ga. The stopping of Ga deposition at 1 atomic layer has been realized by the adsorption of diethylgallium chloride on the substrate [4]. Recently, the self-limiting of Ga deposition has been realized by pulsed jet epitaxy (PJE) using TMG [11]. In PJE, methylgalliums were carried to the substrate by a fast pulsed gas stream without thermal decomposition and were adsorbed selectively on the As surface. However, in general, it is difficult for metalorganic compounds to realize an ideal ALE by the adsorption process. In the case of TEG, the 100% surface coverage by the TEG adsorbate is difficult to attain because of the steric hindrance of TEG molecules.

In order to study the surface coverages of TEG adsorbate on an arsenic surface, the laser pulse was supplied just after the end of the TEG pulse. The adsorbed TEG molecules desorb from the substrate surface in a gas stream with the time constant of about 0.6 s, as measured by the delayed laser pulse technique [8]. If the switching time of the laser pulse was very short compared with the desorption time constant and the TEG adsorbate is mostly decomposed by the delayed laser pulse, the surface coverage of TEG can be obtained from the layer thickness grown by the delayed laser pulse. The growth rate by the delayed laser pulse is shown by curve 2 in Fig. 1. This growth rate corresponds to the surface coverage by the TEG adsorbate and increases with the TEG flux. However, the growth rate saturates at a value of less than one monolayer thickness. Curve 1 in Fig. 1 shows the growth rate under the irradiation at the same time as the TEG pulse. ALE is realized for the TEG flux above 1×10^{-7} mole per cycle even if the surface coverage of TEG is less than 100%. When TEG is supplied on the substrate under irradiation, the decomposition of TEG occurs immediately after the adsorption and the decomposed gallium atoms cover the whole surface of the arsenic layer without the steric hindrance of TEG.

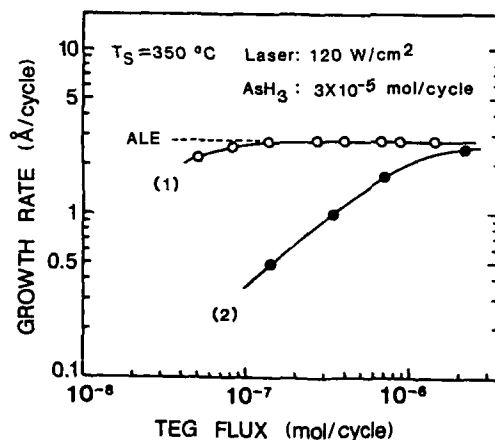


Fig. 1. Growth rate as a function of TEG flow rate under irradiation by laser pulse at the same time as the TEG pulse (1) and just after the TEG pulse (2).

In order to explain the self-limiting of gallium deposition, another TEG pulse with a laser pulse was supplied between the TEG and the AsH_3 pulses. Even if the number of TEG pulses were increased within one cycle of AsH_3 pulse, the growth rate per cycle remained constant at 1 monolayer thickness. Once the whole surface of the arsenic layer is covered with gallium atoms, no decomposition of TEG occurs on the gallium layer under irradiation. Thus, 100% surface coverage by gallium atoms is realized on the arsenic surface. The growth mechanism of laser ALE seems to be based on the fact that the decomposition rate of TEG on an arsenic layer is much larger than that on a gallium layer under irradiation. The selective enhancement of photochemical reaction on the arsenic surface has been observed from the signal of RHEED (Reflection High Energy Electron Diffraction) at 350 °C in MOMBE (metalorganic molecular beam epitaxy) system [12].

Figure 2 shows the growth rate as a function of the average laser power density at 350 °C. In this experiment, visible light of 514.5 nm and IR light of 1.06 μm were used in order to clarify the difference between the photochemical and the photothermal effects in laser ALE. For low power density, the grown layer showed a hillock shape similar to the gaussian profile of the laser beam intensity. At the power density above 60 W/cm^2 of an argon ion laser, the growth rate per cycle saturates at the thickness of 1 monolayer on a (100) oriented GaAs surface. The selective growth of GaAs was clearly observed in the irradiated area and no deposition occurred without irradiation. The selectively grown area showed a flat mirror surface in spite of the intensity profile of a laser beam.

On the other hand, for the irradiation by IR light, the growth rate per cycle did not saturate at 1 monolayer thickness. The IR light is absorbed in the bulk crystal and the temperature rise is much larger than that by visible light irradiation. The large increase of growth rate is due to the increase of the thermal decomposition rate of TEG. This result suggests that the self-limiting of Ga deposition is achieved by the photochemical effect on the surface, not by the photothermal effect.

Laser MOVPE has been applied to a patterned crystal growth by scanning a laser beam. However, it is difficult to grow a flat epitaxial layer with uniform thickness, because the growth rate strongly depends on the laser intensity and the scanning speed in a conventional MOVPE system. On the contrary, in laser ALE, the growth rate is independent of the laser power density, as shown in Fig. 2. In the case of laser scanning, the laser power density must be adjusted to perform the crystal growth under the ALE condition. Compared with the result obtained by TMG [6][10], TEG seems to be a more suitable material for the patterned growth than TMG because ALE is realized in the wide range of laser power density for TEG.

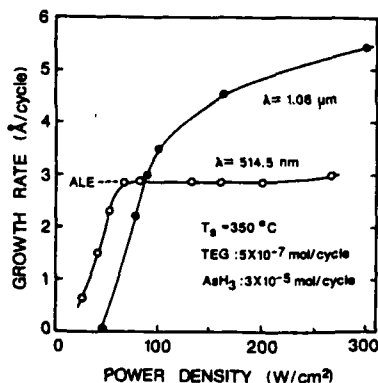


Fig. 2. Growth rate as a function of power density of an argon ion laser (514.5 nm) and a YAG laser (1.06 μm).



Fig. 3. Micrograph of GaAs surface grown by scanning a laser beam.



Fig. 4. Photograph of a crossed pattern grown by laser scanning.

A typical photograph of a line pattern grown by scanning a laser beam under the ALE growth condition is shown in Fig. 3. The epitaxial layer showed a flat mirror surface in spite of the laser intensity profile. The thickness of the epitaxial layer was uniform along the line pattern although the scanning speed varied within the power density to satisfy the ALE condition.

A crossed pattern grown by the laser ALE is shown in Fig. 4. The crossing part of two lines is also flat in contrast to the pattern by the conventional laser MOVPE. In case of the conventional laser MOVPE, the thickness is proportional to the number of scans and the thickness of the crossed part of two lines are almost twice of that of each line. However, in the laser ALE, the thickness is limited by the number of the growth cycles. Therefore, the thickness at the crossing part is the same as that of the line if the pattern is written within the period of one cycle. This characteristic is an advantage of the patterned growth by the laser ALE.

For the patterned crystal growth, a laser beam was swept several times on the substrate surface during the period of one laser pulse. The thickness of the epitaxial layer per cycle saturated to the monolayer thickness with an increase in the number of scans between two AsH_3 pulses because the self-limiting mechanism is involved in the gallium deposition. However, when the scanning rate per second was increased above 30 Hz, the growth rate decreased below one monolayer thickness, as shown in Fig. 5. In this case, the length of scanning was maintained at the constant value. The decrease of the growth rate is caused by the insufficient decomposition rate of TEQ due to the increase of scanning speed. The scanning speed is about 9 cm/sec at the scanning rate of 30 Hz for the line pattern of about 3 mm. The spot size

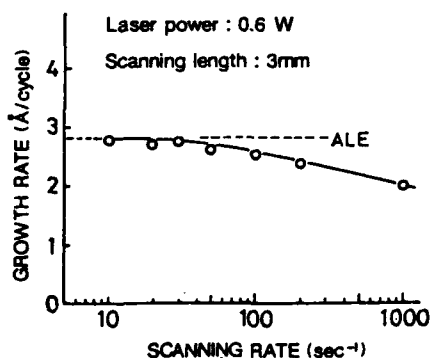


Fig. 5. Growth rate as a function of the scanning rate for the scanning length of about 3 mm.

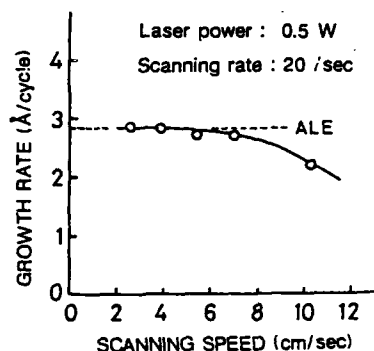


Fig. 6. Growth rate as a function of the scanning speed at the scanning rate of 20 Hz.

of laser beam was estimated to be about 0.1 mm from the width of the line pattern. The irradiation time at each point on the surface must be adjusted more than about 1 ms in order to realize ALE.

Figure 6 shows the growth rate as a function of the scanning speed at the scanning rate of 20 Hz. The growth rate remains constant at the value of one monolayer thickness up to the scanning speed of 6 cm/sec. These results mean that the thickness of line pattern is uniform even if the scanning speed fluctuates within the ALE growth condition.

CONCLUSION

An ideal ALE of GaAs was realized by the pulsed laser MOVPE technique. The 100% surface coverage by gallium atoms on arsenic surface was achieved by the selective photochemical decomposition of TEG at the arsenic surface with irradiation by visible light. The patterned growth of ALE with uniform thickness was obtained by scanning a laser beam.

REFERENCES

1. T. Suntola and M. Anton, U.S. Patent 4058430, (1977).
2. J. Nishizawa, H. Abe and T. Kurabayashi, J. Electrochem. Soc. **132** 1197 (1985).
3. S.M. Bedair, M.A. Tishler, T. Katsuyama and N.A. Elemsary, Appl. Phys. Lett. **47**, 51 (1985).
4. A. Usui and H. Sunakawa, Jpn. J. Appl. Phys. **47**, 51 (1986).
5. A. Doi, Y. Aoyagi and S. Namba, Appl. Phys. Lett. **48**, 1787 (1986).
6. A. Doi, Y. Aoyagi and S. Namba, Appl. Phys. Lett. **49**, 785 (1986).
7. H. Kukimoto, Y. Ban, H. Takechi and M. Ishizaki, J. Cryst. Growth **77**, 223 (1986).
8. S.M. Bedair, J.K. Whisnant, N.H. Karam, M.A. Tischler and T. Katsuyama, Appl. Phys. Lett. **48**, 174 (1986).
9. S. Iwai, A. Doi, Y. Aoyagi and S. Namba, in Proceedings of 14th Symposium on GaAs and Related Compounds, Heraklion, 1987 (Institute of Physics, Bristol and Philadelphia, 1988), p. 191.
10. N.H. Karam, H. Liu, I. Yoshida and S.M. Bedair, Appl. Phys. Lett. **52**, 1144 (1988).
11. M. Ozeki, K. Mochizuki, N. Ohtsuka and K. Kodama, to be published in Appl. Phys. Lett.
12. K. Nagata, S. Den, Y. Iimura, Y. Aoyagi and S. Namba, to be published in J. Cryst. Growth.

ARGON ION AND EXCIMER LASER INDUCED EPITAXY OF GaP

U. SUDARSAN, N. V. CODY, T. DOSLUOGLU, AND R. SOLANKI
Department of Applied Physics and Electrical Engineering, Oregon Graduate
Center, Beaverton, OR 97006-1999

ABSTRACT

Laser-induced epitaxial growth of GaP has been achieved using both pyrolytic and photolytic reactions. A focused beam from an argon ion laser operating at 514.5 nm was used to 'direct-write' epitaxial microstructures of GaP on silicon using a pyrolytic process. An ArF excimer laser has also been used to demonstrate homoepitaxy utilizing the photolytic process.

INTRODUCTION

One of the attractive features of laser-induced processing is spatial selectivity which allows in-situ patterned growth or etching of a wide range of materials [1]. An application of this attribute that has generated considerable interest is selective epitaxial growth of III-V compound semiconductors which has been reported by several researchers using either laser-induced photolytic [2,3] or pyrolytic reactions [4-9]. These reactions are characterized by the laser wavelength and the absorption spectra of the reactant gases and the substrates. We describe below epitaxial growth of GaP utilizing both these processes.

The precursor gases for this investigation were electronic grade trimethylgallium (TMG) and tertiarybutylphosphine (TBP), which is a new phosphorous source. TBP was selected over phosphine due to lower safety risks. Although several substrates were examined, discussion here is limited to heteroepitaxy of GaP on silicon (lattice mismatch 0.4%) using the argon ion laser and homoepitaxy of GaP using an excimer laser-induced photolytic reaction.

Argon Ion Laser-Induced Epitaxy

The experimental configuration is sketched in Fig. 1. The 514.5 nm output from the Ar⁺ laser is first passed through a beam expander and then steered into a multiple element focusing lens which produced a focused spot of 6 μ m diameter at the substrate. The lens was mounted on a precision X-Y stage, which could be translated a maximum of 50 mm along each axis by stepper motors in increments of 0.1 μ m. By programming the motions of the stepping motors, it was possible to 'write' various geometric patterns. A vidicon camera allowed us to visually monitor the location of the deposition and in-process growth.

The (100) oriented silicon substrates were first etched in 10% HF, rinsed in deionized water, dried by blowing nitrogen, and then placed in a stainless steel reaction cell. A quartz window allowed the light into the cell. The cell was first pumped down to 10^{-6} Torr and then brought up to 100 Torr by flowing hydrogen. The native oxide on silicon was thermally desorbed in the presence of hydrogen. The thermal cycle consisted of raising the substrate temperature to 850°C for half an hour and then dropping down to 200°C. The deposition temperature was kept at 200°C to avoid condensation of the precursor gases on the window in the static cell.

Several deposition parameters were examined, including partial pressures of the precursor gases. At high partial pressures of the reactants, thick

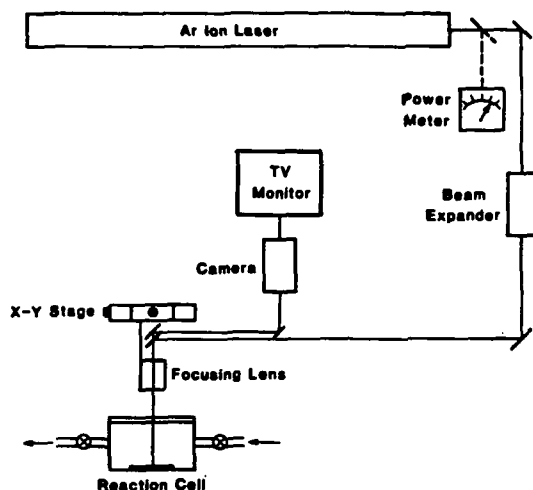
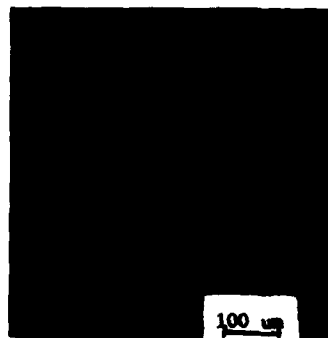


Figure 1. Schematic of the argon laser direct-write system.

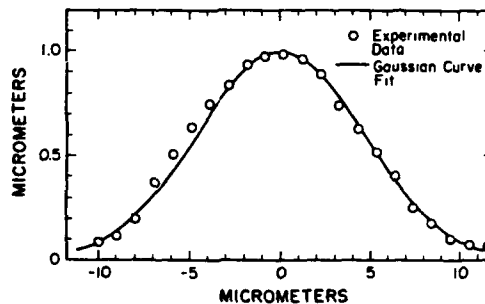
depositions were obtained, however these structures were polycrystalline. To obtain epitaxial growth, the partial pressures were reduced and multiple laser passes were used to slowly grow the films. Typical deposition conditions were as follows:

TMG pressure:	3 Torr
V/III ratio:	10
Total pressure:	1 Atm (balanced by hydrogen)
Laser power:	0.4 W
Laser scan speed:	100 $\mu\text{m/s}$
Growth/scan:	0.05 μm

An example of a 'patterned' growth of epitaxial GaP lines on silicon is shown in Fig. 2a and its cross-sectional profile (measured with a profilometer) is presented in Fig. 2b. It can be seen that the cross-



(a)



(b)

Figure 2. (a) Epitaxial growth of GaP lines on silicon. (b) Gaussian curve fit to a cross-sectional profile of an epitaxial line.

sectional profile of the growth is in reasonably good agreement with the Gaussian curve fit. By raster scanning the laser beam, we obtained epitaxial pads as illustrated in Fig. 3a, which is a Nomarski micrograph. The crystalline properties of these deposits were determined using cross-sectional transmission electron microscopy (TEM). An example of the transmission electron diffraction pattern of the laser deposited pad is shown in Fig. 3b. The diffraction pattern shows slight streaking and a few double spots. There could be several reasons for the streaking, however the double spots are most likely due to the presence of twins. Auger electron spectroscopy was used to examine the stoichiometry of these deposits. The Ga and P atomic concentrations were typically 51% and 49%, respectively. The incorporation of carbon was negligible.

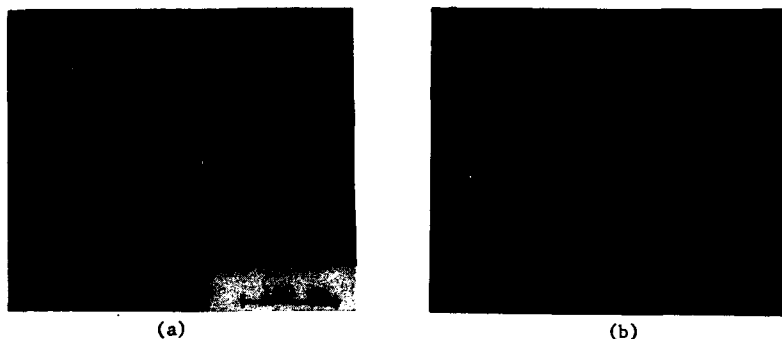


Figure 3. (a) Nomarski micrograph of an epitaxial pad. (b) Transmission electron diffraction pattern of the pad showing the epitaxial growth.

The thickness of these structures was controlled by the number of passes made with the focused laser spot. Therefore, to obtain a thick deposit, one has to increase the number of scans, which can be time consuming for a large patterned growth. One way to increase the throughput is to use an excimer laser where pattern projection can be used for in-situ growth and the thickness can be controlled by the number of pulses. This process is described below for homoepitaxial growth of GaP.

Excimer Laser-Assisted Epitaxy

The excimer laser deposition system used for this investigation is sketched in Fig. 4. The output from an ArF (193 nm) laser was focused to a 2×0.5 mm spot size on a substrate which was placed in a stainless steel reactor. The substrate temperature could be varied from 200 to 600°C. The UV radiation entered the reactor through a sapphire window, which was kept clear of deposits with a hydrogen purge system.

The (100) oriented GaP substrates were first degreased in organic solvents and then etched in 10:1:1 solution of $H_2SO_4:H_2O_2:H_2O$. This was followed by a deionized water rinse and dry blowing with nitrogen before they were loaded into the deposition cell. The cell was pumped down to 10^{-6} Torr before the flow of the precursor gases was started. TMG (at $-15^\circ C$) and TBP ($5^\circ C$) were flowed at 2 and 24 sccm, respectively, with hydrogen as the carrier gas. The total pressure in the reactor was about 30 Torr.

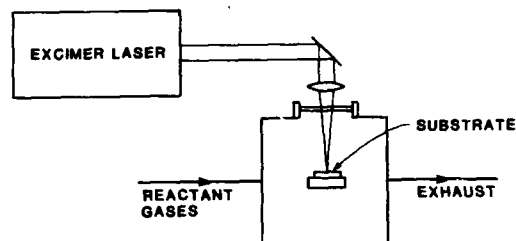


Figure 4. Schematic of the excimer laser deposition system.

Growth rate of GaP versus the substrate temperature is shown in Fig. 5. At a laser energy density of 0.13 J/cm^2 , the growth rate first increases with the substrate temperature up to 300°C , then stays constant, and finally drops above 500°C . Crystalline properties of these films were examined using cross-sectional TEM and were found to be polycrystalline. When the energy density was increased to 0.21 J/cm^2 , growth rate was higher, as expected due to more gas-phase dissociation. Films grown at 300°C and 400°C were polycrystalline and their surfaces appeared to be cracked. However, at 500°C the film had a smooth surface and the growth was epitaxial. Above 500°C , the films were damaged due to sputtering.

In Fig. 5, the thermal growth at 500°C is also indicated. Cross-sectional TEM analysis of this growth (Figs. 6a and b) show a fine grain polycrystalline morphology. Even at a temperature of 600°C , the pure thermal

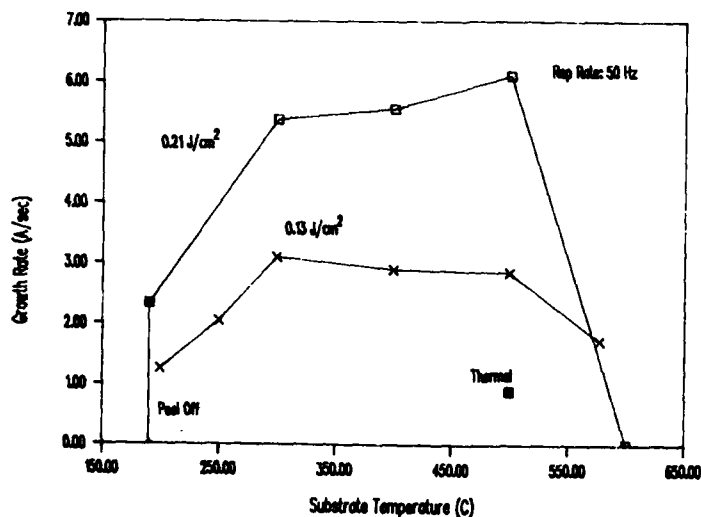


Figure 5. Plot of growth rate versus the substrate temperature at two laser energy densities.

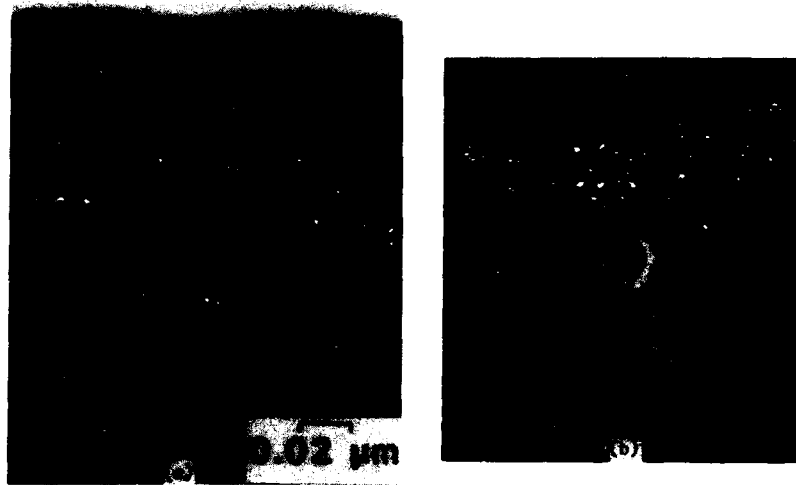


Figure 6. (a) Cross-sectional TEM view of the GaP grown thermally at 500°C. (b) Electron diffraction pattern showing the polycrystalline nature of the film.

growth consisted of pyramid-like structures with spherical tips that were determined to be polycrystalline. However, with a laser energy density of 0.2 J/cm², epitaxial growth was achieved at 500°C, as shown in Figs. 7a and 7b which are TEM micrographs. Besides inducing epitaxial growth, the laser radiation also increased the growth rate by a factor of 6 compared to the thermal growth. The phase change from polycrystalline to single-crystal was believed to be due to the transient heating by the pulsed laser radiation. This was further checked by changing the laser wavelength to 248 nm (KrF) while keeping all other conditions the same. However, only polycrystalline films were obtained suggesting that other factors besides transient heating are responsible for assisting epitaxial growth.

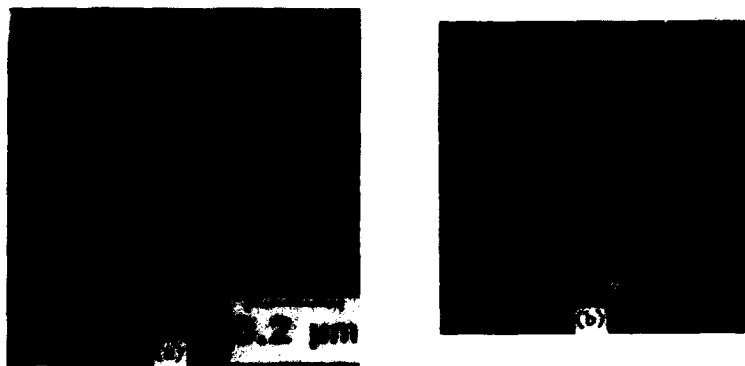


Figure 7. (a) Cross-sectional TEM showing the epitaxial growth at 500°C and laser energy density of 0.21 J/cm². (b) Electron diffraction pattern confirming the single crystal growth.

Summary

Both an argon ion and an excimer laser have been used to achieve epitaxial growth of GaP. With the Ar⁺ laser, 'direct-write' of microstructures has been demonstrated. Excimer laser assisted epitaxial growth was achieved at lower temperatures and higher growth rates.

References

- [1] D. Bauerle, Chemical Processing with Lasers (Springer, New York, 1986).
- [2] F. M. Donnelly, M. Geva, J. Long, and R. F. Karlieck, Appl. Phys. Lett. 44, 10 (1984).
- [3] V. R. McCrary, V. M. Donnelly, D. Brasen, A. Applebaum, and R. C. Farrow, Mater. Res. Soc. Proc. 75, 223 (1987).
- [4] W. Roth, H. Beneking, A. Krings, and H. Krautle, Microelectron. J. 15, 26 (1984).
- [5] N. H. Karam, N. A. El-Masry, and S. M. Bedair, Appl. Phys. Lett. 49, 880 (1986).
- [6] S. M. Bedair, J. K. Whisnant, N. H. Karam, D. Griffis, N. A. El-Masry, and H. H. Stadelmaier, J. Cryst. Growth 77, 229 (1986).
- [7] Y. Aoyagi, M. Kanazawa, A. Doi, S. Iwai, and S. Namba, J. Appl. Phys. 60, 3, 131 (1986).
- [8] R. Solanki, U. Sudarsan, and J. C. Johnson, Appl. Phys. Lett. 52, 919 (1988).
- [9] U. Sudarsan, T. Dosluoglu, N. W. Cody, and R. Solanki, J. Crystal Growth (to be published).

LASER PATTERNING OF II-VI EPITAXIAL THIN FILMS

S.J.C. IRVINE, H. HILL, J.E. HAILS, G.W. BLACKMORE AND J.B. MULLIN
 Royal Signals and Radar Establishment, St Andrews Road, Malvern Worcs. WR14 3PS UK

ABSTRACT

The laser induced photo-MOVPE (photolytic-metal organic vapour phase epitaxy) technique has been used to grow epitaxial films onto CdTe or GaAs substrates (with a 257nm frequency doubled Argon ion laser). The growth temperature was chosen to be below the normal pyrolysis temperature so that decomposition of the metal-organics will only occur within the illuminated parts of the substrate. A measure of enhancement of growth rate by UV illumination is the photo-enhancement factor which has been determined for CdTe deposits onto Si(100) substrates using the precursors dimethyl cadmium (Me_2Cd) together with either diethyl telluride (Et_2Te) or dimethyl ditelluride (Me_2Te_2). For patterned epitaxial layers at 300°C, Et_2Te was preferable to Me_2Te_2 because Et_2Te was more stable, yielding a higher photo-enhancement factor. A 2-D array of CdTe mesas (60 x 60µm) has been deposited onto a GaAs (100) substrate. Using imaging SIMS (secondary ion mass spectrometry) the distribution of major elements and impurities have been studied.

INTRODUCTION

The need for increasing device complexity and monolithic integration of different semiconductor materials is exemplified in 2-D arrays of photovoltaic infra-red detectors for thermal imaging. Epitaxial cadmium mercury telluride (CMT) has been used for preparation of photovoltaic arrays using conventional processing technology [1]. This paper explores the possibility of using a radically new technology of selective area epitaxy of II-VI semiconductors onto different substrate materials which could themselves form part of the complete device structure. Photo-MOVPE (photolytic-metal organic vapour phase epitaxy) has been used to reduce epitaxial growth temperatures by UV photo-dissociation of the precursors with either Hg arc lamps or excimer lasers. Photo-epitaxy of CdTe from dimethyl cadmium (Me_2Cd) and diethyl telluride (Et_2Te) has been reported at 250°C by Kisker et al [2] using a low pressure Hg arc lamp and by Zinck et al [3] at 165°C by parallel illumination to the GaAs substrate using a KrF laser. The present work uses a 257nm frequency doubled argon ion laser to illuminate the substrate through suitable masks. A recent report [4] demonstrated the localised nature of the photochemical reaction stimulated in this way. Unlike an excimer laser, there was no significant heating effect due to direct illumination of the substrate; the maximum power density in these experiments was 5W/cm². Also, no laser damage or ablation of Hg containing films would be expected using this method.

EXPERIMENTAL

All the deposition experiments were carried out in a horizontal silica reactor cell similar to that described previously for UV lamp-induced deposition [5]. The photo-patterning experiments used a modified reactor cell with optically polished, hydroxyl free, silica mounted on a turret side arm on top of the reactor shown in fig 1. The carrier gas was molecular sieve dried helium, which was also used as a purge gas to avoid deposition onto the cell window. Transmission of the window could be checked after a deposition experiment, ex situ, on a Perkin-Elmer Lambda 15 spectrometer. Attenuation at 257nm was typically less than 5% provided that the purge and reactant flows were properly balanced. The precursors were Me_2Cd together with either Et_2Te or dimethyl ditelluride (Me_2Te_2).

Illumination of the substrate was either by direct illumination with the laser beam which has a diameter of approximately 2mm or by using a collimator to expand the beam to illuminate a 1-2cm diameter region of the substrate. A stainless steel mesh with a 120µm pitch was used as a simple mask, shown in fig 4a. The mask could be situated

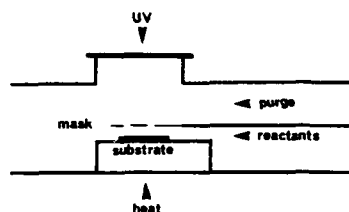


Fig 1 Schematic of reactor cell with mesh mask aligned with the flow separator.

either (a) before the collimator to project an image onto the surface; (b) above the window in order to create a 2-D diffraction pattern or (c) inside the reactor adjacent to the flow separator and in line with the substrate and UV window, as shown in fig 1.

The laser was an intra-cavity, frequency-doubled argon ion laser. Components included a Spectra Physics 2020-5 argon ion laser with a 3958 doubler. The cw power at 257nm was between 100 and 150mW with a typical stability over a 1 to 2 hour growth run of $\pm 7\%$.

Si(100) substrates were prepared using a 2% HF etch and deionised water rinse. CdTe(100) 2° -(110) substrates were prepared by a chemo-mechanical polish of 2% bromine in methanol with a heat clean at 430°C in hydrogen. GaAs(100) 2° -(110) substrates were etched in 1:10 KMnO₄:HCL solution [6] and heat cleaned at 350°C in hydrogen. The heat cleans for CdTe and GaAs were both in-situ.

CdTe ON Si(100) SUBSTRATES

Si(100) was used as a suitable substrate for photo-deposition rate experiments. Thickness profiles of these layers could be obtained by energy dispersive x-ray analysis (EDX) whereby the relative intensities of the Cd and Te L lines could be compared with the SiK α radiation from the underlying substrate [4]. Using a 2mm beam width at 150mW, the resulting intensity of $\approx 5\text{W/cm}^2$ would be expected to decompose all the reactants in the beam (for absorption cross sections $\approx 5 \times 10^{-18}\text{cm}^2$). The thickness of these CdTe layers will therefore give the maximum photolytic growth rate for a given substrate temperature and reactant partial pressures. The thermal growth rate was determined by measuring CdTe film thickness away from the illuminated part of the substrate, and hence the maximum photo-enhancement factor could be obtained. Two thickness profiles for CdTe are shown in Fig 2 for the Te precursors Et₂Te (a) and Me₂Te₂ (b), grown at 250°C. Both films have a similar thickness, 0.8 μm , corresponding to a growth rate of 1.6 $\mu\text{m/h}$. The slightly higher vapour pressure used for Et₂Te (0.4 torr) would be more than offset by the Te₂ dimer released by photolysis of Me₂Te₂, as proposed by Larciprete and Stuke [7]. The thermal growth using Me₂Te₂ is represented in fig 2(b) as the cross hatch region at the bottom of the graph, corresponding to a growth rate of 0.15 $\mu\text{m/h}$. The thermal growth component for Et₂Te was much smaller at around 0.01 $\mu\text{m/h}$ which is consistent with the known pyrolytic properties of these precursors [1]. The different thermal growth rates are reflected in the widely varying photo-enhancement factors of 7.3 and 125 for Me₂Te₂ and Et₂Te respectively. For good photo-selectivity, the photo-enhancement factor needs to be as large as possible so that, ideally, no deposition will occur in the unilluminated regions.

Another important consideration in determining the photo-selectivity of growth is the extent to which decomposition of the precursors in the vapour will lead to a spread of the photo-pattern arising from vapour diffusion of Cd and Te atoms. The thickness profiles in fig 2 give some clue as to the possible extent of this effect. Fig 2(a) is asymmetric with thicker deposit on the left hand side of the graph corresponding to the downstream side of the deposit. Fig 2(b) is more symmetric, indicating that under these conditions of growth there was less vapour spread with Me₂Te₂. However, in both examples the pattern of deposition is predominantly replicating the substrate illumination with most of the CdTe confined to a 2mm diameter disc shape. If the photo-deposition

reaction was purely in the vapour with no surface photo-chemical reaction, then for a reactant boundary layer 1cm thick, flow velocity of 5cm/s, the CdTe deposition would extend more than 5cm downstream from the point of illumination. This is clearly not the case. The SEM micrograph shown in fig 3 for CdTe deposited onto Si from Et_2Te not only shows a well defined boundary (replicating the beam shape) but also shows diffraction patterns due to inhomogeneities in the reactor cell wall.

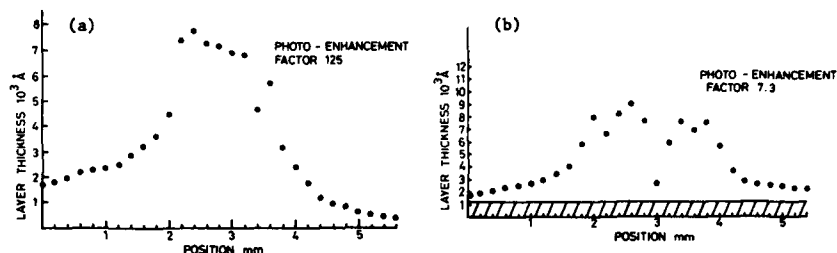


Fig 2 EDX thickness profiles for laser deposited CdTe onto a Si(100) substrate held at 250°C and exposure for 30 minutes.
(a) 0.4 torr Et_2Te and 0.4 torr Me_2Cd ,
(b) 0.3 torr Me_2Te_2 and 0.3 torr Me_2Cd .

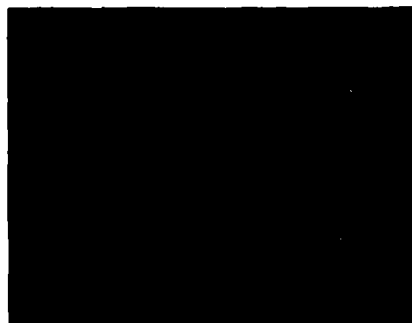


Fig 3 SEM micrograph of the surface of CdTe layer profiled in Fig 2(a), scale markers are 0.1 μm wide.

CdTe ON CdTe(100)2' AND GaAs(100)2'

Epitaxial growth of CdTe has been shown to occur by either pyrolytic or photolytic decomposition of Cd and Te precursors [2, 8]. The purpose of these experiments was to combine both epitaxial growth and laser modulation of the growth pattern, the potential for the latter demonstrated with the deposition onto Si(100) substrates. Different beam conditions for epitaxial growth onto CdTe(100)2' substrates were used. UV intensity was reduced by expanding the UV beam with a X10 collimator. The reduced intensity was $\approx 50\text{mW/cm}^2$ and the larger area of UV enhanced growth was $\approx 2\text{cm}$ diameter. Epitaxial layers were grown using either Et_2Te or Me_2Te_2 together with Me_2Cd , both resulted in similar growth rates of $0.35\mu\text{m/h}$. 100 channeling patterns were observed in these layers, as reported previously, indicating that they were homoepitaxial [4].

Epitaxial growth onto GaAs(100)2' was carried out at a slightly higher temperature of

300°C which improved nucleation. The UV beam was 1cm diameter, with an intensity of $\sim 100\text{mW/cm}^2$. This is a highly mismatched layer/substrate system with an increase in lattice spacing of 14.6% for CdTe compared with GaAs. X-ray texture patterns were used to establish the crystalline nature of these films. These results will be described in some detail elsewhere [9].

Layers 1–2 μm thick were grown using Et_2Te and Me_2Cd at partial pressures of 1.5 torr and 2.4 torr respectively. Previous reports have shown that improved epitaxial nucleation of CdTe onto GaAs can be obtained by using Cd rich conditions [2, 9]. Me_2Te_2 was not used for photo-patterning at 300°C because of the large component of thermal decomposition of Me_2Te_2 at this temperature. In all the films examined, the CdTe grew with a (100) surface on (100) substrates, no evidence was found for the (111)/(100) configuration.



Fig 4 Micrographs of (a) 120 μm pitch mesh mask and (b) Nomarski contrast of CdTe epitaxial mesa structure on GaAs substrate.

A micrograph of a 2-D array of CdTe epitaxial squares is shown in fig 4(b) with a micrograph of the mesh mask used shown in fig 4(a). The layer was confirmed to be epitaxial by x-ray diffraction. A 1:1 correspondence exists between the CdTe mesas and the grid pattern showing that photo-enhanced patterning has occurred. Each of the deposited squares is approximately 60 x 60 μm in size. Superimposed on this pattern are additional features attributed to diffraction and interference from the mask. This can explain the additional structure, including small ridges between the mesas, indicating that much smaller feature sizes could be defined by the UV beam.



Fig 5 SIMS imaging for As and Te from CdTe mesas on a GaAs substrate.

This layer has been analysed using imaging SIMS (secondary ion mass spectrometry). Major element images for arsenic and tellurium are shown in fig 5. The CdTe mesas are delineated by the tellurium map and corresponding absence of signal on the arsenic map. Depth profiles for the impurity elements Al, Si, Na and K are shown together with the Te depth profile in fig 6. The featureless profile for Al is thought to be due to background contamination and not representative of the impurity level in the layer. The profiles for Si, Na and K show dips in concentration in the layer with high levels at the CdTe/GaAs interface which is attributed to substrate contamination. The maps for ^{23}Na , ^{39}K and ^{28}Si corresponding to the interface are shown in fig 7. By comparison with the tellurium map, it can be seen that these impurities lie underneath the CdTe islands. The surrounding GaAs has been milled by the primary beam to below the original substrate surface and therefore does not show high concentrations. Similar impurity maps corresponding to the dips in the profiles in fig 6 (i.e. in the middle of the CdTe layer) do not show these concentrations of impurities.

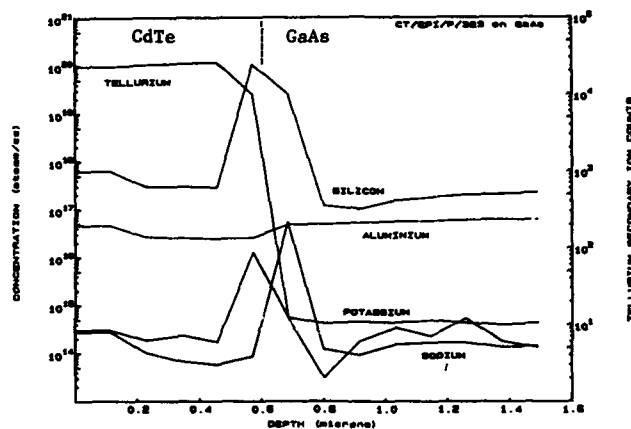


Fig 6 SIMS depth profiles through CdTe/GaAs mesas for ^{27}Al , ^{28}Si , ^{23}Na , ^{39}K ions. The interface is shown by the impurity peaks.



Fig 7 SIMS imaging of CdTe/GaAs interface region for ^{23}Na , ^{39}K , ^{28}Si and ^{125}Te .

CONCLUSIONS

Some of the factors determining the localisation of epitaxial growth by projection of a UV beam have been considered. Localised deposition of CdTe onto Si(100) substrates has indicated a higher photo-enhancement factor using Et_2Te than Me_2Te_2 , although the latter appears to show less vapour diffusion of Cd and Te. Epitaxial layers have been grown onto CdTe(100)2' and GaAs(100)2' substrates at 250 and 300°C respectively. A 2-D array of epitaxial CdTe mesas have been grown for the first time onto a GaAs(100)2' substrate and the pattern analysed using imaging SIMS.

ACKNOWLEDGEMENTS

The authors gratefully acknowledge the technical assistance of Mrs J Clements in the preparation of these films and Mrs O D Dosser for SEM micrographs and EDX analysis. Also, Professor D Cole-Hamilton and Dr D.V. Shenai-Khatkhate of St Andrews University for the preparation of the Me_2Te_2 precursor.

REFERENCES

1. S.J.C. Irvine, J.B. Mullin, J.Giess, J.S. Gough, A. Royle and G. Crimes. J. Crystal Growth (in press).
2. D.W. Kisker and R.D. Feldman, J. Crystal Growth 72(1985) 102.
3. J.J. Zinck, P.D. Brewer, J.E. Jensen, G.L. Olson and L.W. Tutt, Appl. Phys. Lett. 52 (1988) 1434.
4. S.J.C. Irvine, H. Hill, O.D. Dosser, J.E. Hails, J.B. Mullin, D.V. Shenai-Khatkhate and D. Cole-Hamilton, Materials Lett. 8 (1988) 25.
5. S.J.C. Irvine, J. Giess, J.B. Mullin, G.W. Blackmore and O.D. Dosser, J. Vac. Sci. Technol. B3 (1985) 1450.
6. D.S. Buhaenko, S.M. Francis, P.A. Goulding and M.E. Pemble, J. Vac. Sci. Technol. B (in press).
7. R. Larciprete and M. Stuke, J. Crystal Growth, 77 (1986) 235.
8. S. Haq, P.S. Dobson and S.J.C. Irvine, Les Editions de Physique, Vol 15, Photon Beam and Plasma Enhanced Processing (1987) 199.
9. S.J.C. Irvine, H. Hill, G.T. Brown, J.E. Hails and J.B. Mullin, (to be published).

GROWTH MECHANISM OF DIRECT WRITING OF SILICON IN Ar^+ LASER CVD

Takeshi Nagahori and Satoru Matsumoto
Department of Electrical Engineering, Keio University
Hiyoshi, Yokohama 223 Japan

Abstract

Silicon lines are directly written using argon ion laser CVD. The thickness profile of the line has a Gaussian-like shape. The thickness profile is calculated with the model based on Arrhenius behavior. A good agreement is obtained.

The effective exposure time is used to analyze the direct writing process. Using it, the average growth rate is estimated to be about 100 times faster than that of conventional large area CVD with the activation energy of 2.4 ± 0.4 eV.

INTRODUCTION

Direct writing of thin films of various kinds of materials has been performed using the laser-induced chemical vapor deposition (LCVD) method[1]. LCVD has been recognized as a promising technique in fabricating micro-electronic and -optic devices by a maskless, low-temperature process. This technique has now been developed in application to the fabrication of MOSFETs[2] and interconnections[3] in integrated circuits(IC).

A cw argon ion laser has been used chiefly in writing Si lines with pyrolytic LCVD[4]. Highly-conductive, fine Si lines with submicrometer spatial resolution have been realized[5]. However, the mechanism of direct writing of Si lines with pyrolytic LCVD remains obscure.

In writing interconnect lines in IC with the LCVD technique, the cross sectional shape of lines becomes important with the reduction of device dimension. The detailed analysis of the shapes of lines has, however, not been carried out.

In this paper, we perform direct writing of Si lines by argon ion laser CVD, make the qualitative analysis of the line cross sectional shape by relating it with the laser power density, and discuss the mechanism of LCVD.

EXPERIMENTAL

A LCVD apparatus consists of an argon ion laser, optics, and a chamber. A multiline, cw, argon-ion laser beam was focused on the substrates with a 6-cm focal length lens. The focused beam radius ($1/e^2$ intensity points) was $14.3 \mu m$. No special effort to focus the laser beam finely was made in the present work.

Substrates used in this work were p-type, single-crystal

(100) Si wafers and Si wafers covered with thermally grown SiO_2 of 3400 Å thickness. This thickness of SiO_2 was selected to equate the reflectivity of Si covered with SiO_2 at the wavelength of argon laser to that of bare Si.

After setting substrates in a chamber, 5 % SiH_4 diluted in nitrogen gas was introduced in the chamber at atmospheric pressure. The chamber was mounted on an x-y stepping motor translation stage, which was moved with the scan speed of 1~4 mm/s. The laser beam irradiated the substrate perpendicularly, leading to direct writing of Si lines. The backside substrate temperature was kept at 300 °C. As the scan time was long, a steady state was established in this work.

One of the key parameters in pyrolytic LCVD is the spatial distribution of temperature on the substrates induced by laser irradiation. Since the line width is so narrow, it is difficult to measure the temperature on the substrate accurately. Therefore the steady-state temperature distribution on the substrate was calculated using the Lax [6] method including the temperature dependence of thermal conductivity. The cross-sectional shape of the Si lines was determined with SEM observation of cleaved lines or Nomarski microscope observation of angle lapped lines.

RESULTS AND DISCUSSION

The deposited line of direct writing with LCVD was confirmed to be Si with Auger electron spectroscopy.

Figure 1 (a) and (b) show Nomarski microscope photographs of an angle lapped Si line on a Si substrate. In Fig. 1(a), a convex cross section is observed, corresponding to the distribution of laser power density. On the other hand, in cases of larger laser power (Fig. 1(b)), a dip is observed in the center of line and interference fringes, which indicate the occurrence of Si melting in the dip region.



Fig. 1 Nomarski microscope photograph of angle lapped Si line on the Si substrate, (a) laser power 2.34 W, (b) laser power 2.45W.

These are typical characteristics of the cross sectional shapes of Si lines in pyrolytic LCVD. Such a laser power dependence of the line shape has previously been reported by Bäuerle[7]. Here we investigate the laser power dependence of Si line shape in detail, particularly under the conditions of nonmelting Si.

Figure 2 shows data of the maximum thicknesses of deposited lines as a function of the temperature on the substrate at the beam center for different scan speeds. The temperature on the substrate corresponding to laser power density was calculated by the Lax method as described previously. The laser power density required to melt Si in the calculation was corrected with the laser power density needed to melt Si actually as a reference. With no melting of Si, the thickness at the center of scan axis is the maximum thickness as shown in Fig. 1(a).

The cross sectional shape of a Si line can be analyzed with the model that the growth rate of the deposited line is characterized only by Arrhenius behavior. It is assumed that the growth rate V is given by

$$V = V_0 \exp(-E_a/kT), \quad (1)$$

where E_a is the activation energy of the chemical reaction in the LCVD process. Using this expression of growth rate, the thickness of the Si line at the center of scan axis, $d(0)$, can be expressed as

$$d(0) = \int_{-\infty}^{\infty} V_0 \exp(-E_a/kT(0,t)) dt, \quad (2)$$

where $T(0,t)$ is the temperature at time t at the center of the

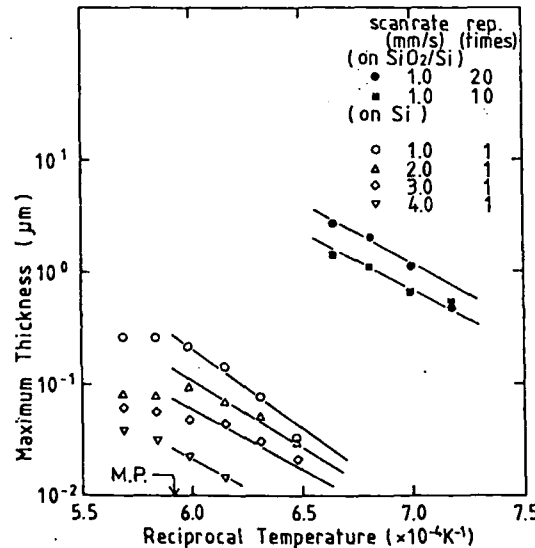


Fig. 2 Maximum thicknesses of Si lines versus reciprocal temperature at the beam center

scan axis. $T(0,t)$ can be obtained by relating the temperature distribution curve for static laser heating to scanning conditions and $d(0)$ can be calculated numerically.

By fitting the calculated results of Eq. (2) to the experimental results of Fig. 2, E_a and V_0 are determined.

The thickness of Si lines at a distance x from the center of scan axis, $d(x)$, can be written as in Eq. (2) as follows.

$$d(x) = \int_{-\infty}^{\infty} V_0 \exp[-E_a/kT(x,t)] dt, \quad (3)$$

where $T(x,t)$ is the temperature at time t at the distance x from the center. Substituting E_a and V_0 determined from the above procedure, $d(x)$ can be calculated. That is, the cross sectional shape of a Si line can be simulated using the values of E_a and V_0 at the center of scan axis. Figure 3 shows the experimental and calculated results. Good agreement is obtained. Thus the thickness of the Si line at any distance from the center can be predicted using the model based on the Arrhenius behavior of growth rate.

The growth rate, which is an essential parameter in the direct writing of LCVD, is generally expressed as

$$V = d \cdot v / w, \quad (4)$$

where d is the line thickness, w is beam radius and v is scan

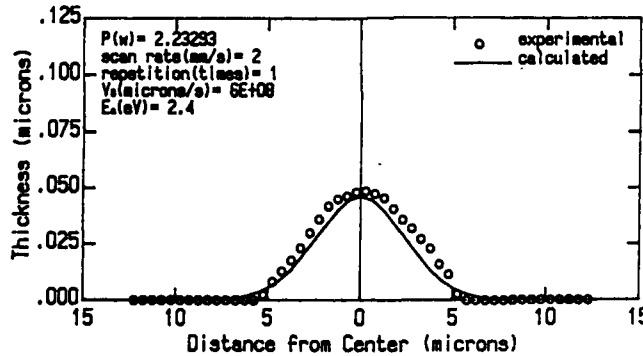


Fig. 3 Thickness profile of laser CVD Si line

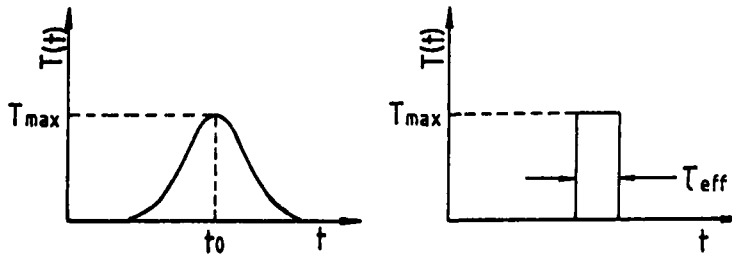


Fig. 4 Scan beam process with effective exposure time T_{eff}

speed. In order to characterize the scanning beam process, we use the effective exposure time.

The temperature at the center of the scan axis at time t , $T(0,t)$ is schematically shown in Fig. 4(a). The thickness $d(0)$ at the center is given by Eq. (2) as stated previously using $T(0,t)$. Now $T(0,t)$ is replaced by the rectangular pulse of width τ_{eff} and height T_{max} as shown in Fig. 4(b). Thus Eq. (2) can be expressed using the effective exposure time τ_{eff} ,

$$d(0) = V_0 \exp(-E_a/kT_{\text{max}}) \tau_{\text{eff}} \quad (5)$$

Substituting V_0 and E_a determined from Eq. (2) into Eq. (5), τ_{eff} is found to be given by w_{eff}/v , where w_{eff} is the FWHM of the Si line. τ_{eff} is on the order of several msec in the present work.

In order to compare conventional large area CVD with direct writing LCVD, it is appropriate to use the average growth rate, \bar{V} , which is defined as $d(0)/\tau_{\text{eff}}$.

The data of the average growth rate are shown in Fig. 5 as a function of reciprocal temperature using the data of Fig. 2. The activation energy of $2.4 \pm 0.4 \text{ eV}$ is obtained. This value is similar to the value (1.93 eV) reported by Bäuerle et al. [4] for Si deposition by Ar ion laser. The present activation energy is also similar to that (1.9 eV) of the conventional thermal CVD, indicating that the growth of the Si lines in LCVD is limited by surface reaction, too. It is also found that the average growth rate falls on a single line for scan speed of $1 \sim 3 \text{ mm/s}$. This indicates that the growth of a Si line on a Si substrate proceeds at steady state within several msec.

For a scan speed of 4 mm/s , the maximum thickness was so thin that the accuracy of measurement was considered to be

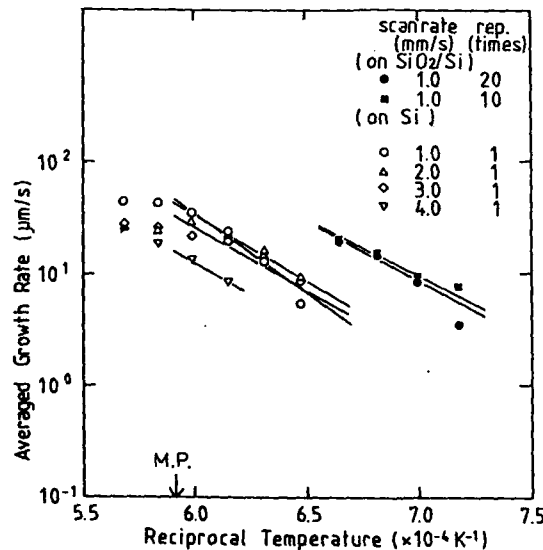


Fig. 5 Growth rate of Si line versus reciprocal temperature at the beam center

insufficient. As compared with large area thermal CVD, the average growth rate of LCVD is almost 100 times faster than that of large area CVD.

A higher growth rate is obtained for a Si substrate covered with SiO_2 . The reason for this is that the surface temperature rises with the deposition of Si because of the change of reflectivity on the surface and the smaller thermal conductivity of SiO_2 than that of Si.

SUMMARY

Direct writing of Si lines by Ar ion laser CVD has been performed. The cross sectional shape of the Si lines are investigated in detail. They are analyzed by a model based on the Arrhenius behavior of growth of Si lines.

In order to analyze the scanning beam process, the effective exposure time is introduced. It is found that the growth rate of direct writing LCVD is estimated to be 100 times faster than that of large area CVD.

REFERENCES

1. R. M. Osgood and H. H. Gilgen, Ann. Rev. Mater. Sci. 15, 549(1985).
2. B. M. McWilliams, I. P. Herman, F. Mitlitsky, R. A. Hyde, and L. L. Wood, Appl. Phys. Lett. 43, 946(1983).
3. J. G. Black, S. P. Doran, M. Rothschild, and D. J. Ehrlich, Appl. Phys. Lett. 50, 1016(1987).
4. D. Bäuerle, P. Irsigler, G. Leyendecker, H. Noll, and D. Wagner, Appl. Phys. Lett., 40, 819(1982).
5. D. J. Ehrlich, R. M. Osgood, and T. F. Deutsch, Appl. Phys. Lett. 39, 957(1981).
6. M. Lax, Appl. Phys. Lett., 33, 786(1978).
7. D. Bäuerle, Laser Processing and Diagnostics, Edited by D. Bäuerle(Springer-Verlag, Berlin) Vol.39, p.166.

A COMPARISON OF THE GAS PHASE PROCESSES RESULTING FROM SiH_4 AND Si_2H_6 PHOTODISSOCIATION WITH A PULSED ArF EXCIMER LASER

E. BOCH, C. FUCHS, E. FOGARASSY, P. SIFFERT

Centre de Recherches Nucleaires (IN2P3), Laboratoire PHASE (ER du CNRS n°292),
23, rue du Loess, F-67037 Strasbourg Cedex, France

ABSTRACT

We present in this paper a comparison of the photodissociation processes of SiH_4 and Si_2H_6 under pulsed excimer laser at 193 nm. The experimental curves of the gas composition as a function of laser energy density show that the dissociation of Si_2H_6 results from both one and two-photon absorption whereas SiH_4 only absorbs two photons. The deposition yield of Si_2H_6 has also been determined as a function of the number of laser pulses or initial pressure. These experimental results show the establishment of a stationary state in the gas phase and prove the existence of reverse reactions in the disilane kinetic model. The photodissociation of Si_2H_6 under UV laser excitation (193 nm) presents, therefore, similar properties to those of SiH_4 .

INTRODUCTION

Thin film deposition at low temperature of hydrogenated amorphous silicon by dissociating silane or disilane with UV light is now well recognized as an interesting technique. We propose in this work a comparison of the photochemical processing in the gas phase resulting from the decomposition of SiH_4 and Si_2H_6 at 193 nm, using a pulsed ArF excimer laser.

There are differences between SiH_4 and Si_2H_6 in the number of photons absorbed by the electronic states of the two molecules. At 193 nm, silane is only excited by a two-photon process, whereas disilane can be dissociated by absorption of one photon. We show here that a two-photon excitation of Si_2H_6 is also possible.

Using a condensation technique, we determined the gas composition after laser irradiation of Si_2H_6 and silane by measuring the partial pressure of different species created in the sealed chamber during the photodissociation.

These results prove the existence of a steady state in the disilane dissociation process and demonstrate the presence of reverse reactions in the chemical kinetic model.

EXPERIMENTAL

Pure disilane, sealed in a suprasil quartz cylindrical reaction chamber (diameter = 3 cm, $L = 10$ cm) at pressure ranging between 1 and 100 Torr, was irradiated under normal incidence with a Lambda Physik (EMG 201 MSC) ArF excimer laser providing 193-nm pulses of 20 ns duration with fluences ranging between 5 and 300 mJ/cm². The irradiated area (≈ 0.25 cm²) is continuously moved along the reactor in order to prevent the deposition of silicon on the walls.

The final pressures of stable species (H_2 , SiH_4 , Si_2H_6) were determined after different irradiation times (i.e. number of laser pulses) or different initial pressures of Si_2H_6 using a condensation technique previously described (1).

We do not take into account Si_3H_8 or higher silanes, whose concentration in the cell is low enough to be neglected.

RESULTS AND DISCUSSION

As described in a previous paper (2), the photodissociation of SiH_4 at 193 nm is achieved through a two-photon excitation process:

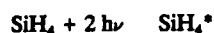


Fig. 1 shows the non-linear behavior of SiH_4 decomposition (and deposition) as a function of the laser energy and proves the existence of a two-photon energy threshold of $\approx 35 \text{ mJ/cm}^2$.

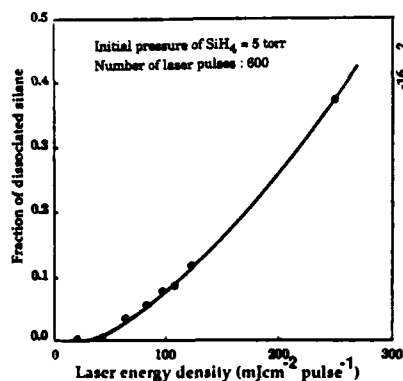


Fig. 1 : Deposition yield of SiH_4 as a function of laser energy density.

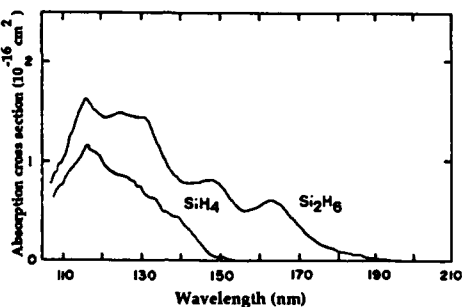


Fig. 2 : Absorption spectrum of SiH_4 and Si_2H_6 in the UV range (4).

As shown by the absorption spectrum of disilane in the UV range (Fig. 2), the dissociation of Si_2H_6 at 193 nm can be described by a single photon excitation process



and the deposition yield of disilane should be linear with the laser energy density.

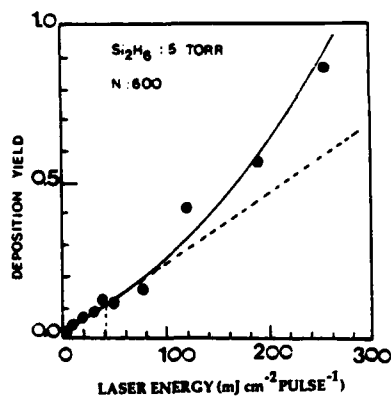


Fig. 3 : Deposition yield of Si_2H_6 as a function of laser energy density.

Fig. 3 shows that in fact, for Si_2H_6 , the process is linear at low energy and becomes non-linear above a laser energy threshold of about 40 mJ/cm^2 . The fluence threshold value depends on the molecular virtual state life time. Since the bond energies involved in the SiH_4 molecules are close to those corresponding to Si_2H_6 molecules, the two intermediate state life times, and consequently the threshold values, cannot be very different. This is well confirmed by the experimental results of 35 and 40 mJ/cm^2 .

The single photon process is not the only way of excitation: disilane can also be decomposed above 40 mJ/cm^2 by a two-photon excitation process. The difference between the experimental curve and the straight line represents the part of the two photon process. The quantum yield for single and two-photon processes depends on the values of the absorption cross sections. These Si_2H_6 absorption cross sections will be determined and presented in a further paper.

The deposition yield of disilane is simply the ratio of silicon atoms deposited on the wall,

$$\frac{\Sigma^{\text{initial}} - \Sigma^{\text{gas}}}{\Sigma^{\text{initial}}}$$

This ratio can be easily calculated by the relation

$$r = 1 - \frac{\text{Si}_2\text{H}_6 + 1/2 \text{SiH}_4}{\text{Si}_2\text{H}_6^0} \quad \text{for disilane}$$

and

$$r = 1 - \frac{\text{SiH}_4 + 2\text{Si}_2\text{H}_6}{\text{SiH}_4^0} \approx 1 - \frac{\text{SiH}_4}{\text{SiH}_4^0} \quad \text{for silane.}$$

Si_2H_6 created in the gas phase during the silane photodissociation can indeed be neglected (1).

The experimental deposition yield of SiH_4 as a function of the number of laser pulses or irradiation time (Fig. 4) shows the establishment of an equilibrium state which proves the existence in the chemical model of reverse reactions to regenerate SiH_4 (1).

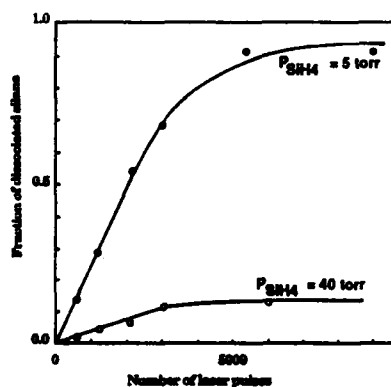


Fig. 4 : Deposition yield of SiH_4 as a function of the number of laser pulses.

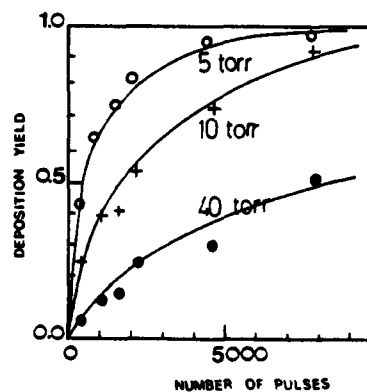


Fig. 5 : Deposition yield of Si_2H_6 as a function of the number of laser pulses.

Similar results are observed when using disilane as the active gas. Fig. 5 shows clearly that the deposition yield tends to a constant value even if the equilibrium state is reached after a number of pulses much higher than in the silane dissociation. Indeed, the number of equations involved in the kinetic models is larger for Si_2H_6 than for SiH_4 ; the radical species have a greater choice of possible reactions, which delay the establishment of the equilibrium state. It is also proved that the process is more efficient when the initial pressure of disilane decreases. This equilibrium state is also observed on Fig. 6, which represents the final pressure of silane divided by the final pressure of disilane as a function of number of laser pulses. This result can only be explained if we assume the existence of reverse reactions to regenerate Si_2H_6 and to keep the gas phase in an equilibrium composition. The importance of reverse reactions increases with pressure since the number of shocks between molecules and radicals is favored.

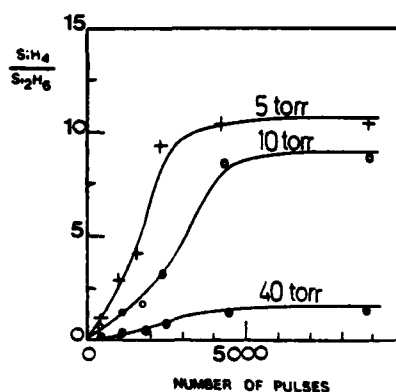


Fig. 6 : $\frac{\text{SiH}_4}{\text{Si}_2\text{H}_6}$ (final pressure) as a function of the number of laser pulses in the disilane photodissociation.

We deduce from these experimental results that kinetics processes for silane and disilane are based on the same model. We suggest in Table I (see next page) the principal reactions involved in the dissociations of SiH_4 and Si_2H_6 . The reactions leading to the formation of higher silanes are neglected.

We emphasize that the dissociation of Si_2H_6 is more efficient at low pressure. We have measured the deposition yield of Si_2H_6 as a function of initial pressure (Fig. 7), by

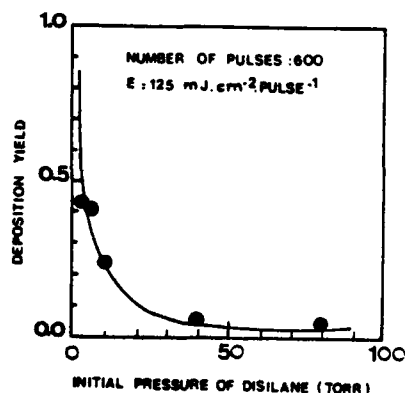


Fig. 7 : Deposition yield of Si_2H_6 as a function of disilane initial pressure.

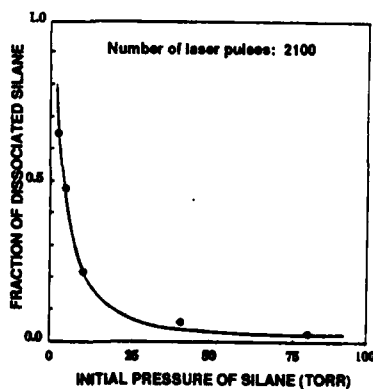


Fig. 8 : Deposition yield of SiH_4 as a function of silane initial pressure.

comparison with silane (Fig. 8). Both gases present the same behavior: the dissociation is more efficient at low pressure.

Table I: Principal reactions of the SiH_4 and Si_2H_6 photodissociation processes.

Silane (1)	Disilane (3)
$\text{SiH}_4 + 2 h\nu \rightarrow \text{SiH}_4^*$	$\text{Si}_2\text{H}_6 + 1 h\nu \rightarrow \text{Si}_2\text{H}_6^*$
	$\text{Si}_2\text{H}_6 + 2 h\nu \rightarrow \text{Si}_2\text{H}_6^*$
<i>Formation of radicals</i>	
$\text{SiH}_4^* \rightarrow \text{SiH}_3 + \text{H}$	$\text{Si}_2\text{H}_6 \rightarrow \text{SiH}_3 + \text{SiH}_2 + \text{H}$
$\text{SiH}_4^* \rightarrow \text{SiH}_2 + \text{H}_2$	$\text{Si}_2\text{H}_6 \rightarrow \text{SiH}_3 + \text{SiH} + 2\text{H}$
	$\text{Si}_2\text{H}_6 \rightarrow \text{Si}_2\text{H}_5 + \text{H}$
	$\text{Si}_2\text{H}_6 \rightarrow \text{SiH}_2 + \text{SiH}_4$
<i>Formation of stable species</i>	
$\text{H} + \text{SiH}_4 \rightarrow \text{H}_2 + \text{SiH}_3$	$\text{H} + \text{Si}_2\text{H}_6 \rightarrow \text{SiH}_3 + \text{SiH}_4$
$\text{SiH}_2 + \text{SiH}_4 \rightarrow \text{Si}_2\text{H}_6$	$\text{H} + \text{Si}_2\text{H}_6 \rightarrow \text{Si}_2\text{H}_5 + \text{H}_2$
$\text{SiH}_3 + \text{SiH}_3 \rightarrow \text{SiH}_2 + \text{SiH}_4$	$\text{SiH}_3 + \text{SiH}_3 \rightarrow \text{SiH}_4 + \text{SiH}_2$
<i>Reverse reactions</i>	
$\text{Si}_2\text{H}_6 + \text{H} \rightarrow \text{SiH}_4 + \text{SiH}_3$	$\text{SiH}_3 + \text{SiH}_3 \rightarrow \text{Si}_2\text{H}_6$
$\text{H}_2 + \text{SiH}_2 \rightarrow \text{SiH}_4$	$\text{Si}_2\text{H}_5 + \text{H} \rightarrow \text{Si}_2\text{H}_6$
	$\text{SiH}_4 + \text{SiH}_2 \rightarrow \text{Si}_2\text{H}_6$
<i>Deposition</i>	
$\text{SiH}_3 + \text{wall} \rightarrow \text{solid}$	$\text{SiH}_3 + \text{wall} \rightarrow \text{solid}$
$\text{SiH}_2 + \text{wall} \rightarrow \text{solid}$	$\text{Si}_2\text{H}_5 + \text{wall} \rightarrow \text{solid}$

CONCLUSION

We have shown in this work that the dissociation of Si_2H_6 at 193 nm occurs by both one and two-photon processes.

We have proposed a general model for the kinetics of the dissociation including in both cases reverse reactions to regenerate the initial gas. These reactions are necessary to explain the establishment of an equilibrium state observed in the two cases.

Finally, we have shown that the deposition yield increases at low pressures.

In conclusion, silane and disilane, despite their different ways of excitation (one or/and two-photon processes), present the same general kinetic behavior in the gas phase under pulsed UV light (193 nm).

REFERENCES

- (1) E. Boch, C. Fuchs, E. Fogarassy, P. Siffert
Eighth Photovoltaic Solar Energy Conference, Florence, Italy, May 1988.
- (2) C. Fuchs, E. Boch, E. Fogarassy, B. Aka and P. Siffert
in Laser and Particle Beam Chemical Processing for Microelectronics, edited by
D.J. Ehrlich, G.S. Higashi and M.M. Oprysko (Mater. Res. Soc. Proc. 101,
Pittsburgh, PA, 1988).
- (3) G.G.A. Perkins, F.W. Lampe
J. Am. Chem. Soc. 102, 3764 (1980).
- (4) U. Itoh, Y. Toyoshima, H. Onuki
J. Chem. Phys. 85 (9), 4867 (1986).

LASER PHOTOCHEMICAL VAPOUR DEPOSITION OF EPITAXIAL Ge FILMS ON GaAs FROM GeH₄ USING NH₃ AS A SENSITISER.

C.J.KIELY, C.JONES*, V.TAVITIAN and J.G.EDEN.

Dept. of Electrical Engineering, University of Illinois at Urbana-Champaign, Ill. 61801.

*NCCMR, University of Illinois, 104 S.Wright St., Urbana, Ill. 61801.

ABSTRACT

The viability of ammonia as a sensitiser for the epitaxial growth of Ge on GaAs by laser photochemical vapour deposition (LPVD) has been investigated. Specifically NH₃/GeH₄/He (0.8/5/95 sccm, 5.5 Torr total pressure) mixtures have been irradiated by a 193nm ArF excimer laser in parallel geometry for substrate temperatures, T_s < 400°C. As evidenced by a dramatic acceleration in Ge film growth rate, the NH₃ efficiently couples the laser radiation to the GeH₄ precursor molecule. The microstructures of LPVD Ge films grown with and without NH₃ have been examined by TEM, and the epitaxial nature of both types of films has been verified, although some subtle differences are noted. Chemical analysis of the deposited films has been carried out using Auger spectroscopy, X-ray photoelectron spectroscopy and secondary ion mass spectroscopy. Our results show that there is little or no nitrogen incorporation into the Ge films grown in the presence of NH₃, and that hydrogen contamination in our films is minimal. The beneficial effect of NH₃ on the growth rate of LPVD Ge films is attributed to the photolytic production of hydrogen atoms which efficiently decompose GeH₄ by hydrogen abstraction collisions.

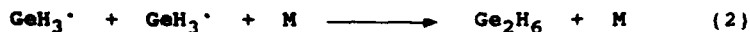
INTRODUCTION

Tavitian et. al.[1,2] and Kiely et.al.[3] have previously reported the epitaxial growth of Ge on GaAs(001) from GeH₄ using parallel geometry laser photochemical vapour deposition (LPVD). Microstructural characterisation of the films was carried out by transmission electron microscopy (TEM) and these authors found that the Ge grew epitaxially for ~200-700Å before turning amorphous in character. Ge epitaxy was achieved for substrate temperatures (T_s) as low as 280°C, which is close to the pyrolytic threshold of GeH₄. This represents a 120°C reduction in growth temperature from those typically used in conventional low pressure chemical vapour deposition, which is desirable in order to reduce autodoping effects.

The gas phase reaction mechanism proposed was that the GeH₄ was photolytically decomposed, yielding predominantly GeH₃·:



The GeH₃· then reacts via a three body process to form Ge₂H₆ which has a lower pyrolytic threshold (<200°C) than that for GeH₄ (280°C) [4,5]



where M is any third body such (such as He). The Ge₂H₆ typically

diffuses a distance of 10-60 mean free paths to the substrate where it is adsorbed and subsequently pyrolytically decomposes to form Ge. The switch from crystalline to amorphous material after 700 Å was attributed by Kiely et al. [3] either to low Ge adatom mobility at such low growth temperatures or to the differing catalytic behaviour of GaAs and Ge surfaces to the Ge_2H_6 molecule.

The GeH_4 precursor molecule is virtually transparent at the rare gas-halide excimer laser wavelengths of 193 and 248 nm (the photodissociation cross section, σ , for GeH_4 at 193nm being only $2-3 \times 10^{-20} \text{ cm}^2$ [6,7]). A possible way of increasing the efficiency of the photolytic decomposition of GeH_4 is to employ a photosensitiser which absorbs strongly at the source wavelength and efficiently transfers its internal energy to the GeH_4 precursor. In this study we examine the effect of NH_3 as a photosensitiser (σ at 193nm = 10^{-17} cm^2 [8]) on the LPVD reaction kinetics. Furthermore, we have characterised the microstructure of the deposited films by TEM, and the chemical composition of the films by AES, XPS and SIMS.

APPARATUS AND GROWTH RATE RESULTS

The experimental apparatus has previously been described in detail [1,3] and will only be reviewed briefly here. Mixtures composed of NH_3 , GeH_4 and He (0.8, 5.0, 95 sccm mass flow rates respectively and 5.5 Torr total pressure) were dissociated by an ArF laser beam directed parallel to and 2.2mm above the substrate surface. At all times the laser fluence was maintained at or below 17 mJ cm^{-2} and substrate temperatures in the range 410°C to room temperature were investigated. The film growth rate was measured in-situ by monitoring with a pyrometer the GaAs (5 μm) IR fringes produced as the Ge film grows. Alternatively the growth rate on an SiO_2 substrate placed directly next to the GaAs substrate in the growth chamber was determined by He-Ne laser transmission measurements.

The dramatic rise in the Ge film growth rate that occurs upon adding 1sccm of NH_3 to the GeH_4/He gas stream is shown in

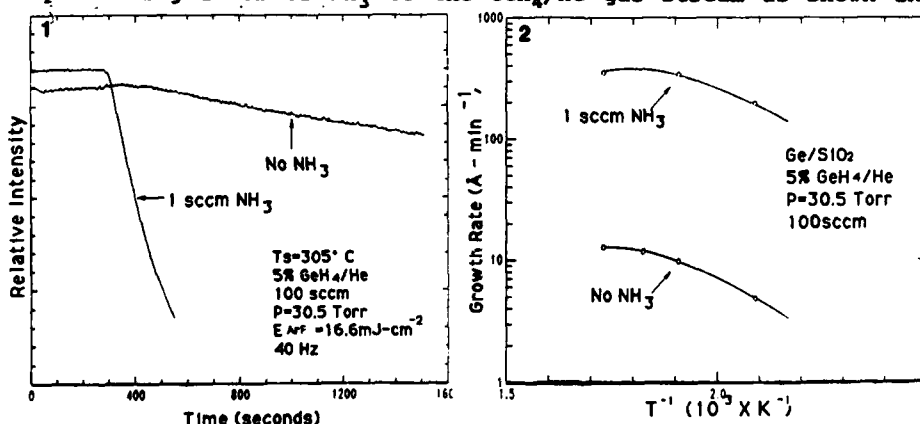


Fig.1. Raw He-Ne laser transmission curves for LPVD growth.

Fig.2. Growth rates as a function of temperature for conventional LPVD and NH_3 assisted LPVD growth.

Figs.1 and 2. Fig.1 gives the raw He-Ne laser transmission curves that were obtained at $T_s=305^\circ\text{C}$. Film growth leads to an exponential decay of the red laser intensity with time, allowing one to extract the film growth rate. In the absence of NH_3 , the Ge film growth rates vary from 4.8\AA min^{-1} at 205°C to 11.8\AA min^{-1} at 305°C . However, as shown in Fig.2 the addition of NH_3 to the gas flow results in a growth rate increase of 30-40x in this temperature range. Although this effect was observed for every T_s studied, it becomes increasingly pronounced as the temperature is reduced.

STRUCTURAL AND CHEMICAL ANALYSIS OF FILMS

Despite a more than order of magnitude improvement in the Ge film growth rate, cross sectional TEM (eg. see Fig.3 for a $T_s=305^\circ\text{C}$ sample) shows that the Ge overlayer grows epitaxially for the first $\sim 250\text{\AA}$ before turning amorphous. This result is broadly similar to the microstructures reported previously [1,3] for conventional LPVD films except that the epitaxial to a-Ge transition occurs sooner. One subtle difference noted in the microstructure of films grown by conventional LPVD and NH_3

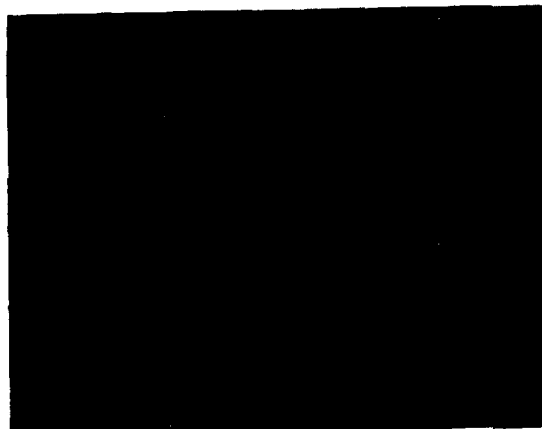
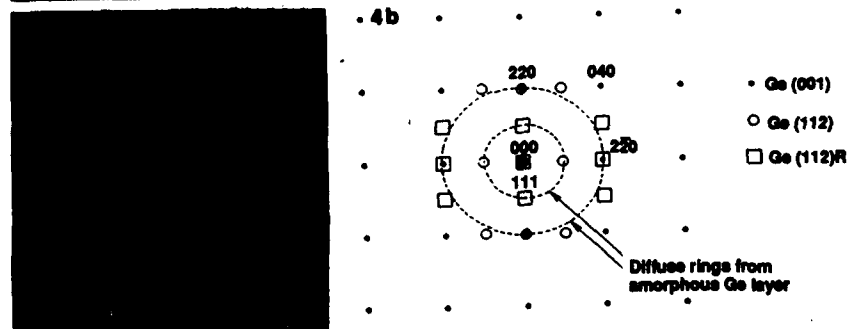


Fig.3. Cross-sectional micrograph of an NH_3 assisted LPVD film with $T_s=305^\circ\text{C}$.



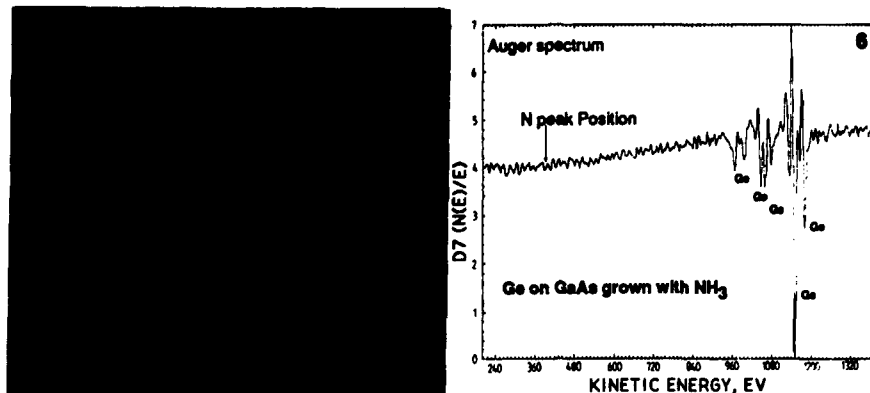


Fig.5. DF image showing $\langle 112 \rangle$ R Ge microcrystals in film.
Fig.6. Auger spectrum from an NH_3 assisted LPVD film.

assisted LPVD is that the latter shows the presence of Ge microcrystals (typically 70-100Å in diameter) within the a-Ge layer. Analysis of SADPs obtained from plan view samples of such films indicate that the Ge microcrystals are not randomly oriented (Fig.4a). The schematic indexing of this (001) pattern (Fig.4b) demonstrates the presence of (001)Ge and a-Ge along with Ge microcrystals which are oriented with their [112] axis parallel to the film normal. Two epitaxial variants of the microcrystals exist (which are related by a 90° rotation about [112]Ge) and have been defined as $\langle 112 \rangle$ and $\langle 112 \rangle$ R type such that:

$\langle 112 \rangle$ type :- Ge[112]//GaAs[001], Ge[110]//GaAs[110]
 $\langle 112 \rangle$ R type :- Ge[112]//GaAs[001], Ge[110]//GaAs[110]

The Ge microcrystals are identified as such from lattice fringe spacing measurements from HREM images, and they are most clearly seen in DF images of plan view samples (Fig.5). The fact that they are only present in NH_3 assisted films suggests that their nucleation may be associated with the increased growth rate and/or a recrystallisation process seeded from the epitaxial Ge layer.

An Auger spectrum from an NH_3 assisted LPVD film is shown in Fig.6. The expected N signal (395eV) is not observed (as indicated); only those due to the Ge are present, with the main peak being at 1148eV. Similarly, the N1s signal was not detected in the XPS spectrum. It can be concluded from these results that nitrogen was not present in the film at concentrations greater than 1%. This result is a radical departure from previous LPVD experiments [8-11] involving NH_3 in which the primary purpose of NH_3 was to act as a nitrogen donor in the growth of stoichiometric Si_3N_4 . In such a situation the amidogen radical NH_2^\cdot is the critical species.

The Ge3d XPS spectra for the LPVD Ge film and the commercial Ge(001) substrate standard are shown in Fig.7. If GeH were present in the film in significant quantities, a broadening of the 3d signal would be expected. However, the FWHM for both peaks are identical at 1.46eV.

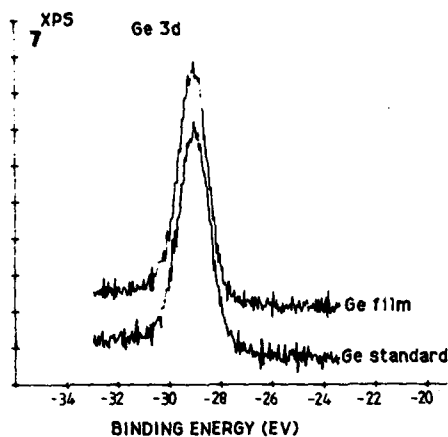


TABLE 1(a)

Mass	Species
70	^{70}Ge
72	^{72}Ge
82	$^{70}\text{Ge}+^{12}\text{C}$
84	$^{72}\text{Ge}+^{12}\text{C}$ and $^{70}\text{Ge}+^{14}\text{N}$

TABLE 1(b) Mass Ratios

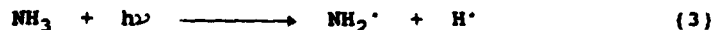
	70/72 (isotopic)	82/84
Ge standard	0.76	0.42
Ge film	0.75	0.75

Fig.7. Ge3d XPS spectra for the NH_3 assisted film and a Ge standard.

To check whether N is present in concentrations less than 1%, depth profiles of these samples were obtained using SIMS. Relevant isotopic masses and intensity ratios are shown in Table 1. It can be seen that in the Ge standard substrate, the ratio of mass 82 to 84 is not the same as the isotopic ratio for mass 70 to 72. The intensity of mass 84 is higher than would be expected and suggests the presence of nitrogen in small concentrations. However, in our NH_3 LPVD films the 82 to 84 mass ratio is identical to that of the 70 to 72 isotopic ratio, indicating the absence of nitrogen. The count levels of mass 82 and 84 were also much higher suggesting the presence of carbon throughout the film. The carbon contamination most likely originated from hydrocarbon associated with the pumping system and appears to be a further possible cause of the crystalline to a-Ge phase transition. Since the solubility of C in Ge is low, crystalline Ge may initially form pushing the carbon contaminant along with the growth front, until eventually the C concentration exceeds a critical level at which only a-Ge (containing C) may form.

CONCLUSIONS

Addition of trace amounts of NH_3 to the gas flow stream dramatically enhances the film growth rate and yet: 1) the films are still initially epitaxial for $T_s > 300^\circ\text{C}$ and 2) nitrogen and hydrogen incorporation into the films is negligible. The beneficial effect of NH_3 is attributed to the efficient single photon dissociation of NH_3 which yields free hydrogen:



The highly reactive hydrogen atoms liberated by reaction (3) rapidly produce GeH_3^\cdot radicals by the hydrogen abstraction process:-



which subsequently enhances the Ge_2H_6 production rate by the three body process:-



Hence, the major role played by the NH_3 is to artificially enhance the H atom production rate which in turn accelerates Ge_2H_6 production. The Ge_2H_6 then subsequently pyrolyses at the substrate.

ACKNOWLEDGEMENTS

This work has been supported by the Air Force Office of Scientific Research (H.Schlossberg) under contract F49620-85-C-0141 and the National Science Foundation under grant DMR 86-12860. The electron microscopy and surface analysis were carried out in the Center for Microanalysis of Materials at the University of Illinois which is supported by the U.S. Department of Energy.

REFERENCES

- [1] V.Tavitian, C.J.Kiely, D.B.Goehegan and J.G.Eden, Appl.Phys. Lett. 52, 1710, (1988).
- [2] V.Tavitian, C.J.Kiely and J.G.Eden, Mater.Res.Soc.Symp.Proc 101, 349, (1988).
- [3] C.J.Kiely, V.Tavitian and J.G.Eden, Submitted J.Appl.Phys.
- [4] L.H.Hall, J.Electrochem.Soc, 119, 1593, (1972)
- [5] T.R.Gow, D.G.Coronell and R.I.Masel, J.Mat.Res. (in press).
- [6] J.F.Osmundsen, C.C.Abele and J.G.Eden, J.Appl.Phys. 57, 2921, (1985).
- [7] U.Itoh, Y.Toyoshima, H.Onuki, N.Washida and T.Ibuki, J.Chem Phys, 85, 4867, (1986).
- [8] K.Watanabe, J.Chem.Phys., 22, 1564, (1964).
- [9] P.K.Boyer, G.A.Roche, W.H.Ritchie and G.J.Collins, Appl. Phys.Lett., 40, 716, (1982).
- [10] D.H.Lowndes, D.B.Goehegan, D.Eres, S.J.Pennycook, D.N. Mashburn and G.E.Jellison, Appl.Phys.Lett. 52,1868,(1988).
- [11] T.F.Deutch, D.J.Silversmith and R.W.Mountain, Mat.Res.Soc. Symp.Proc., 17, 129, (1983).

LASER-INDUCED CHEMICAL VAPOR DEPOSITION OF Ge-Se THIN FILMS

Tongsan D. Xiao and Peter R. Strutt.
The University of Connecticut, Institute of Materials Science and Department of
Metallurgy, U-136, Storrs, CT 06268.

Abstract

The synthesis of Ge-Se deposits has been demonstrated by using continuous wave CO₂ laser excited reactions of GeCl₄ and Se₂Cl₂ precursors, each transported in an argon carrier gas. The deposited Ge-Se layers are rich in Ge with a composition of 70% of Ge and 30% of Se. Microstructural examinations reveal that the microstructure consists of amorphous Ge-Se particles ranging in diameter from 2000 Å to 7000 Å. Suggestions are made for the possible mechanisms that might occur during film deposition including, pyrolytic reactions, multiphoton dissociations, and Volmer-Weker film growth.

Introduction

Ge-Se films have generated considerable interest as infrared photonic material [1-3]. Several alternative techniques have been developed for deposition of optical films, including conventional CVD and PECVD [1,4,5]. Japanese investigators have deposited GeO₂-Sb₂ and other chalcogenide glassy films inside a fused quartz tube by reacting GeCl₄ and SbCl₃ with an oxygen flame and hydrogen gas [6]. Wilson has successfully deposited Ge-Se films on fused quartz [1]. In Wilson's work, rf and microwave radiation were used as the energy source for the dissociation of GeCl₄ and Se₂Cl₂ inside the quartz tube.

Recently, laser chemical vapor deposition (or LCVD) has been explored [7-13]. The reasons for the rapidly growing importance of LCVD lies primarily in its versatility for depositing a very large variety of elements and compounds at low temperatures in the forms of amorphous and crystalline layers having a high degree of perfection and purity. The deposits, including those of metallic elements and compounds, semiconductors, and insulators, form in the amorphous and crystalline states. Although this technique has proved to be efficient in the development of thin film technology, little attention has been paid to synthesizing infrared photonic materials by LCVD.

The nature of laser-vapor-substrate interaction depends upon the radiation characteristics (wavelength, intensity) and optical properties of the vapor and substrate. The selection of a particular reaction system involves a knowledge of the optical behavior of the reactants and the substrate under specific radiation conditions. In the current experiments, for instance, Fourier transform infrared spectroscopy shows GeCl₄ to be transparent at a wavelength near 10.6 μm, while fused silica and Se₂Cl₂ are strongly absorbant.

Experimental

The experiment setup is shown in Figure 1. Fused SiO₂ samples of 1 cm² × 0.6 cm were mounted on the sample holder with the surface being modified perpendicular to the incoming laser beam. The reaction chamber was first evacuated to about 0.4 torr, and then back-filled with argon at 0.1 atmosphere pressure. The mixtures of

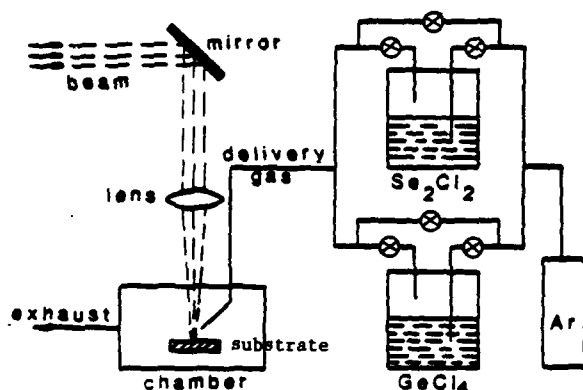


Figure 1. Schematic diagram of the LCVD system.

GeCl_4/Ar and Se_2Cl_2 were combined prior to injection through a delivery nozzle into the beam-substrate interaction zone, with argon flow rates of 100 sccm and 200 sccm for GeCl_4 and Se_2Cl_2 , respectively. The Se_2Cl_2 precursor liquid was heated up to about 35°C to ensure complete vaporization in the flowing stream of argon. In these situations where the substrate was stationary, the laser-radiation duration was 10 minutes using a power density of $2.54 \times 10^3 \text{ W/cm}^2$. Another type of experiment involved deposition of successive Ge-Se layers onto quartz substrates mounted on a rotating stage. Using a beam-substrate relative velocity of 1.4 cm/s, thin films were deposited in a total interaction time of 11 seconds during successive rotations.

Characterization of the deposited layers was done using wavelength-dispersive x-ray analysis, Fourier transform infrared spectroscopy in reflection mode, scanning electron microscopy, transmission electron microscopy, and x-ray diffraction analysis.

Results and Discussions

Several interesting phenomena were observed during the deposition process, both in the case of a stationary and moving substrate. For a stationary substrate, an intense plume formed during the initial period of laser interaction, this existed for several seconds. Extinction of the laser plume occurred which would appear to result from momentary depletion of reactants in the vicinity of the interaction zone. Interestingly, although the plume did not form again, the deposition process continued at an appreciable rate. However, the initial plume is important, since it appeared to play a critical role in initiating the deposition process.

Examination of the SEM micrographs (Figure 3a) suggests that the film growth might be due to the Volmer-Weber mechanism [14]. Initial nucleation could be caused by the chemisorption of species that led to the growth of 3 dimensional Ge-Se islands which later coalesced to form a continuous film. Figure 2 is a typical SEM micrograph at low magnification which indicates that most of the Ge-Se film was deposited in regions away from the beam-substrate interaction zone. Typically, particle sizes of about 7000 Å average diameter are observed in the heavily deposited region (Figure 3b).

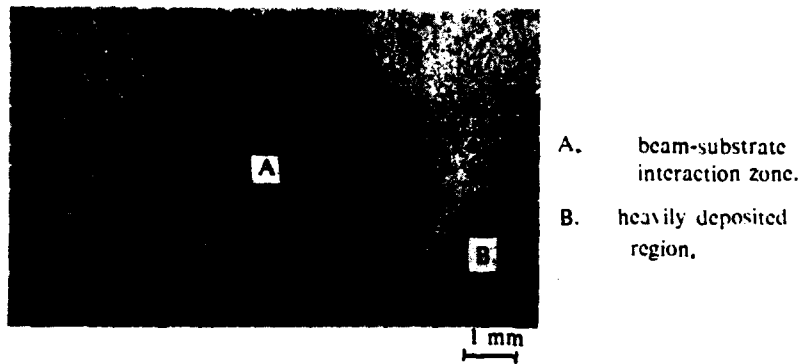


Figure 2. A SEM photograph showing profile of the deposited film.

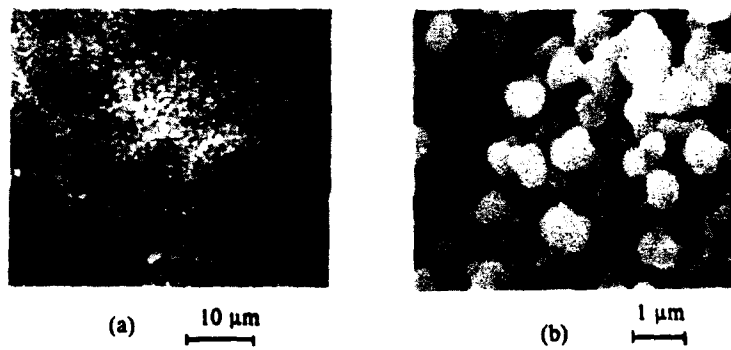


Figure 3. SEM photographs showing (a) surface roughness (b) uniform distribution of the particles.

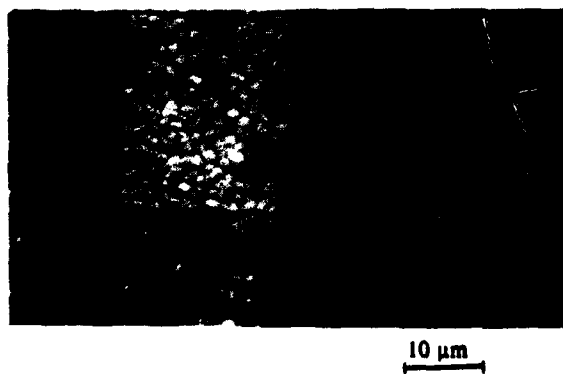


Figure 4. Ge-Se deposits (rotating substrate) showing the progressive build-up of each layer.

For a rotating substrate, the product material was progressively deposited (Figure 4), as the substrate passed beneath the incident laser beam. The average particle size was smaller than the case of stationary specimens, typically about 2000 Å mean diameter.

Wavelength-dispersive x-ray analysis indicated the film composition to be 70% Ge, 30% Se, together with trace amounts of Cl (less than 1 percent). This result is in agreement with that obtained by other workers [1]. X-ray analysis showed the deposited layers to be amorphous. Fourier transform infrared analysis revealed peaks at 1072 and 1045 cm^{-1} , which correspond to Ge-Se bonds as shown previously [15-17]. A small peak corresponding to Ge-O bond was also observed in the analysis which could be due to the presence of the oxygen within the deposits. Transmission electron microscope replicas also revealed that single crystals of diameter of about 2000 Å had formed within the deposited films. Figure 5 shows a bright field image of such a crystal and the diffraction patterns suggested that the Ge-Se crystals had a distorted BCC lattice structure.

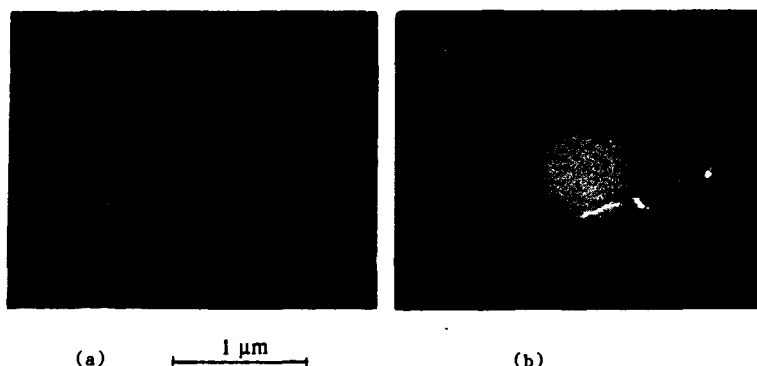


Figure 5. TEM micrographs (a) bright field image of a Ge-Se single crystal (b) diffraction pattern of this crystal.

In considering mechanisms within the interaction zone, two basic features are that, for 10.6 μm radiation: (i) GeCl_4 vapors are highly transparent and probably undergo pyrolytic dissociations; and (ii) molecules of Se_2Cl_2 are strongly absorbant and possibly dissociate via a multiphoton process. In a model which has been developed, the calculations indicate that most of the laser-beam energy reaches the substrate surface [18]. Since the electromagnetic field of the beam has an optical absorption distance of 40 μm , there is significant substrate heating. Actual temperatures obtained during this process have been measured experimentally. At the relatively low power density employed, substrate melting did not occur even after continuous irradiation of stationary specimens for 600 seconds. During most of this time the surface temperature was in the range of 1000 to 1500°C. Factors limiting the maximum obtainable temperature include heat conduction, convection, and emissive losses.

In considering the nature of the plume formation, the electric field (E_0) of radiation, for a beam power density of $2.54 \times 10^3 \text{ W/cm}^2$ was about $8.9 \times 10^4 \text{ volts/m}$. In the presence of an intense electric field, a gas switches from being an almost ideal insulator to become a rather good conductor, and a plasma state can be obtained. According to established data, electric breakdown can only occur when the applied electric field is exceeding the maximum field (E_{max}) strength of the insulator:

$E_{\max} = 9 \times 10^6$ volts/m for glass and $E_{\max} = 3 \times 10^6$ volts/m for air, for instance. The electric field in these experiment was almost 100 times smaller than the required value to initiate the electric breakdown. It can be concluded that the electric field alone could not cause electric breakdown of the gas precursors and the solid substrate. Therefore, the plume observed in these experiments would not be in a plasma state, rather, the plume was caused by the radiation emitted from the excited vapor molecules.

The vapor molecules were excited by the absorption of the laser beam or the thermal energy resulting from the heating of the substrate, and were promoted to higher energy states. Collisions and vibrations of these molecules resulted in dissociation to form reaction intermediates. Thermal radiation from these excited molecules provided the observation of an intense plume.

Acknowledgements

The authors wish to thank the state of Connecticut, Department of Higher Education, under the industrial collaborative program with Ensign-Bickford Optics Corporation for the financial support of this program.

References

1. J. I. B. Wilson & D. Blanc, SPIE, **618**, 118 (1986).
2. A. Goswami & P. S. Nikam, Indian J. Pure & Appl. Phys., **8**, 798 (1970).
3. C. R. Kannewurf & R. J. Cashman, J. Phys. Chem. Solids, **22**, 293 (1961).
4. J. Irvén & A. Robinson, phys. & Chem. Glass, **21**, 47 (1987).
5. K. Inada, IEEE, J. Quant. Elect., **QE-18**, 1424 (1982).
6. H. Takahashi, I. Sugimoto, T. Sato, & S. Yoshida, SPIE, **320**, 88 (1982).
7. M. Hanabusa & K. M. Lakin, Appl Phys. Lett., **35**, 662 (1979).
8. V. Barananskas & C. I. Z. Mammanna, Appl. Phys. Lett., **36**, 930 (1980).
9. P. K. Boyer, C. A. Moore, R. Solanki, W. K. Ritchie, G. A. Roche, & G. J. Collins, Mat. Res. Soc. Symp. Proc. (Laser Diagn. Photochem. Process Semicond. Devices), **17**, 119 (1983).
10. P. K. Boyer, G. A. Roche, W. H. Ritchie, & G. J. Collins, Appl. Phys. Lett., **40**, 716 (1982).
11. R. Solanki & G. J. Collins, Appl. Phys. Lett., **42**, 662 (1983).
12. S. C. Danforth & J. S. Haggerty, J. Amer. Cerami Soc., **66**, 58 (1983).
13. Y. R. Froidevaux, H. H. Gilgen, Appl Phys., **A 37**, 121 (1985).
14. M. Volmer & A. Weber, Z. Phys. Chem. (Leipzig), **119**, 277 (1926).
15. Kanamori, Y. Terunuma, S. Takahashi, & T. Miyashia, J. Non-Cryst. Solids, **69**, 231 (1985).
16. A. R. Hilton, D. J. Hayes, & M. D. Rechtin, J. Non-Cryst. Solids, **17**, 319 (1975).
17. T. Katsuyama, K. Ishida, S. Satoh, & H. Matsumura, Appl. Phys. Lett., **45**, 925 (1984).
18. T. Xiao, M. S. Thesis, The University of Connecticut, 1987.

SYNTHESIS OF DIAMOND FILMS BY LASER-INDUCED CHEMICAL VAPOR DEPOSITION

Yoshiyuki Goto, Toshinori Yagi and Haruhiko Nagai*

Manufacturing Development Laboratory

*Central Research Laboratory

Mitsubishi Electric Corp., 1-1, Tsukaguchi-honmachi, 8-chome, Amagasaki, Hyogo, 661 Japan.

ABSTRACT

An experimental study of diamond formation by laser-induced chemical vapor deposition (CVD) technique using a gaseous mixture of H_2 and CCl_4 is reported. The laser used in this work is an ArF excimer laser which emits 80 - 200 mJ pulses with 20 ns duration. We have succeeded in obtaining thin films of diamond by the activation of hydrogen to enhance the removal of graphite and the production of CH radicals. Films obtained without the activation were composed of amorphous carbon and graphite. Hydrogen was activated by a microwave discharge tube or a hot tungsten filament. Films were characterized by Raman scattering and reflection electron diffraction. The diagnostic study using a visible optical emission spectroscopy shows that the emission intensity ratio of CH to C_2 radicals increases in the system with the activation.

INTRODUCTION

Temperatures higher than 1500°C and pressures higher than 5 GPa are generally needed to synthesize diamond from the crystallization of carbon. At lower pressures, graphite is the stable structure of carbon and diamond is the metastable structure. The applications of diamond are now limited to diamond needles and machining tools for grinding, sawing and drilling. This is because diamonds produced under the above conditions are made of particles.

Recently many attempts to synthesize diamond have used the gas-phase method. This technique allows the formation of thin film of diamonds on a substrate and, therefore, extends the applications of diamond to semiconductors and passivation films. The diamond films were produced by a variety of methods, including thermal CVD using a hot tungsten filament, plasma CVD, and photo-induced CVD (1-4). Among these techniques, photo-induced CVD seems promising for deposition at a low temperature.

This paper reports the results obtained with the excimer laser CVD processes by using carbon tetrachloride as a reactant source.

EXPERIMENTAL

A gaseous mixture of CCl_4 and H_2 was used as a reactant gas, and the film formation was made by laser irradiation. A schematic diagram of the experimental apparatus is shown in Fig. 1. The apparatus is made up of an excimer laser irradiation system, a growth chamber, a gas flow system and an evacuation system. Thin films were deposited onto a Si wafer at a given temperature, gas flow rate and pressure by vertical or horizontal irradiation with focused laser beams. The pulsed ArF excimer laser at 100 pps repetition rate provides a power of 80 - 200 mJ; the average output power is 5 - 12 W. The laser beam was focused by a F300 cylindrical lens. The flow rate of the reactant gas was mass controlled and the pressure inside the chamber was 6 - 50 Torr. The standard gas flow rate for H_2 is 1000 SCCM, and 1 - 10 SCCM for CCl_4 . Some of the hydrogen was blown onto the window to prevent the adhesion of reaction products. Si wafers were temperature controlled from room

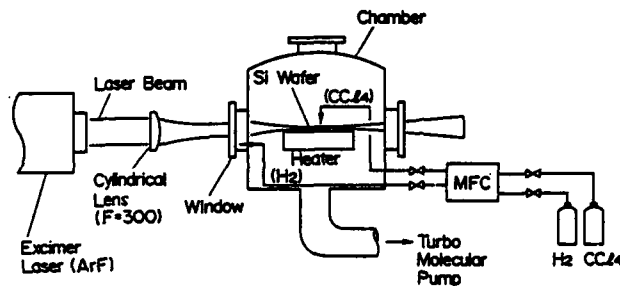


Fig. 1. Schematic diagram of the laser CVD apparatus.

temperature to 600°C. The deposition duration was 30 - 180 minutes. Film properties were evaluated by SEM, RHEED and Raman scattering, and film constituents measured by AES and FTIR. An emission spectroscopic study was carried out for the identification of reaction species.

RESULTS AND DISCUSSION

It is known that methyl radical and active hydrogen play an important role in the process of film formation. Therefore the hydrocarbon of methane series is usually used as a reactant gas. The main issue is how to produce numerous active species.

Although CCl_4 has no methyl group, it is considered to be a very good candidate for the reactant gas because C and Cl are more weakly bonded than C and H and therefore more easily decomposed by ArF excimer laser irradiation. Moreover, the process described here which uses the CVD method but no methyl group may develop into a new approach to diamond formation.

Film formation by the laser CVD method

The excimer laser has a short duration of 20 ns and a peak power of more than 10 MW. The wavelength of the ArF excimer laser (193 nm) is short enough to decompose the reactant gas for diamond formation. A uniform film is obtained, as shown in Fig. 2. The uniformity of the film is caused by a large number of nuclei due to the high peak power and short duration of the ArF laser which results in insufficient nuclei growth. The film thickness is 3 μm . The Raman spectrum of the film is shown in Fig. 3. The Raman spectroscopy can

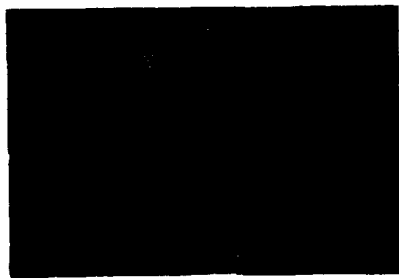


Fig. 2. SEM image of a film obtained by laser CVD technique using a gaseous mixture of CCl_4 and H_2 .

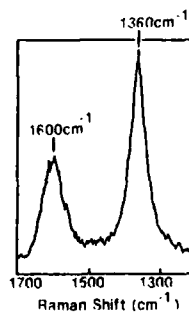


Fig. 3. Raman spectrum of a film obtained by laser irradiation alone.

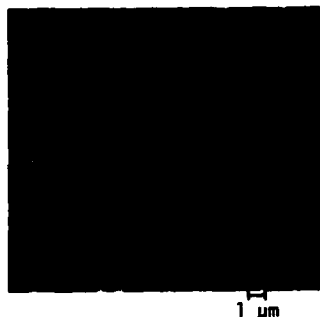


Fig. 4. SEM image of a film obtained by laser irradiation in an atomic hydrogen atmosphere.

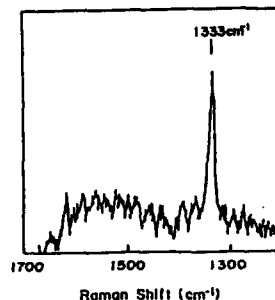


Fig. 5. Raman spectrum of a film obtained with activation of hydrogen.

detect graphite and amorphous carbon with high sensitivity and therefore is excellent for the evaluation of diamond. The two peaks at 1360 cm^{-1} and 1600 cm^{-1} are usually found in the spectra of defective amorphous carbon. No specific peak of diamond is observed at 1333 cm^{-1} . The constituents of the film are determined by AES and FTIR. The results show that the film is composed dominantly of carbon, with very little amounts of chlorine and oxygen (less than 100 ppm). The presence of chlorine in the film suggests that the dechlorination is insufficient during the film formation process and the inclusion of oxygen is thought to be due to the background gas in the growth chamber. Diffraction rings as well as halo patterns are observed by electron diffraction images. From those results we can conclude that this film contains amorphous carbon with incomplete crystalline structures.

Effect of hydrogen activation

Films obtained by laser irradiation alone are amorphous, though they have incomplete crystalline structures. The incomplete structures must be due to the fact that the absorbance of hydrogen is very small in the region around 193 nm, resulting in insufficient activation of hydrogen. In order to produce atomic hydrogen, either a hot tungsten filament or a microwave generator was added to the laser CVD system. Fig. 4. shows a SEM image of a typical film obtained in an atomic hydrogen atmosphere. This image shows that the film is composed of particles with a diameter of $2 - 3\text{ }\mu\text{m}$. Raman spectrum of the film is shown in Fig. 5. A main peak observed at 1333 cm^{-1} is specific to diamond and has a FWHM of 15 cm^{-1} , 5 times larger than that peak of natural diamond. This high value suggests that the crystal structure is somewhat incomplete. Small peaks observed at $1500 - 1600\text{ cm}^{-1}$ are assigned to "i-carbon". The crystal structure is confirmed by an electron diffraction image. The results are shown in Fig. 6. Rings are clearly observed on the diffraction pattern. The



Reported (ASTM)		Observed
hkl	d(Å)	d(Å)
111	2.06	2.07
220	1.261	1.27
311	1.075	1.06
222	—	1.02
400	0.892	0.89
331	0.818	0.81
422	0.728	0.72
511,333	0.686	0.68
440	0.631	0.62
531	0.603	0.60
620	0.565	0.56

Fig. 6. RHEED pattern and interplanar spacings of a film obtained with activation of hydrogen.

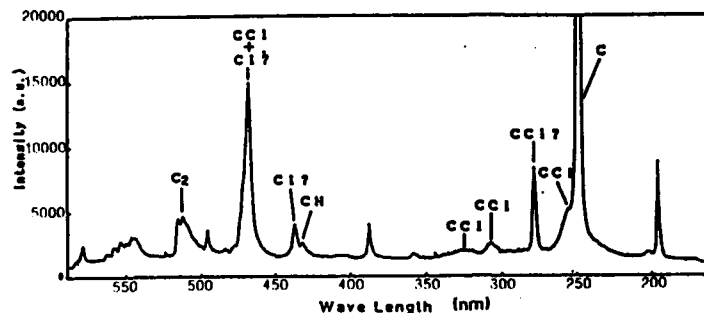


Fig.7. Optical emission spectrum of a gaseous mixture of CCl_4 and H_2 irradiated by ArF excimer laser.

diffraction radii are identical with the interplanar spacings of diamond reported by ASTM within the accuracy of measurement error. These data show that the film obtained is made of diamond. The fact that this diamond film is obtained at the relatively low temperature of 450°C by laser irradiation on the surface suggests that the laser irradiation enhances the photochemical and/or thermal reactions on the surface. Activation of hydrogen is found to be essential for the diamond formation from carbon tetrachloride.

Emission spectroscopic study

Methyl radical and active hydrogen are considered essential for the process of diamond formation. Emission spectroscopic analysis is carried out to determine the reaction species. Fig. 7 shows an emission spectrum of a gaseous mixture of CCl_4 and H_2 irradiated by 5 W excimer laser. The initial process of the reaction (5) can be expressed as



and thereafter complicated reactions, such as dechlorination of CCl_4 or

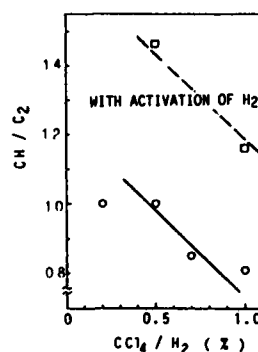


Fig. 8. Effect of hydrogen activation on the ratio of CH to C_2 radicals

generation of atomic hydrogen seem to occur. The occurrence of C, C₂ and CH, in addition to CCl and Cl, is shown in Figure 7. It is reported that C₂ influences the growth of graphite and that CH is important for the diamond formation (6). Therefore, the intensity ratio of CH to C₂ was calculated. Fig. 8 shows the relation between CH/C₂ and CCl₄/H₂ ratios. Open circles and open squares show the values obtained when atomic hydrogen is not added and added, respectively.

A large ratio of CH/C₂ is observed in an atomic hydrogen atmosphere. The deposition rate increases with increasing CCl₄/H₂, but the ratio CH/H₂ decreases. Therefore, the optimal ratio of CCl₄/H₂ seems to be around 0.5%. Further study is under way to confirm this conclusion.

From these results it is concluded that when atomic hydrogen is added, diamond is formed due to large enough amounts of CH and the effective removal of graphite by atomic hydrogen; whereas when atomic hydrogen is not added, amorphous carbon is formed due to the lack of the CH species.

SUMMARY

Laser-induced CVD is an attractive technique to obtain thin films with low damage at a low temperature. By this technique, diamond films with thickness of 1 - 3 μm are successfully deposited onto Si wafers at a temperature of 450°C. An ArF laser is used to irradiate the sample in the gaseous mixture of CCl₄ and H₂. Activation of H₂ is found essential for obtaining diamond films. With more work on the formation mechanism, the process temperature could be lowered further.

REFERENCES

- (1) A. Aisenberg and R. Chabot, J. Appl. Phys. **42**, 2953 (1971)
- (2) B.V. Derjaguin, Soc. Phys. Dokl. **21**, 676 (1976)
- (3) M. Kamo, Y. Sato, S. Matsumoto and S. Setaka, J. Cryst. Growth **62**, 642 (1983)
- (4) A. Sawabe and T. Inuzuka, Appl. Phys. Lett. **46**, 146 (1985)
- (5) D.L. Baulch, R.A. Cox, P.J. Crutzen, J. Troe, R.F. Hampson Jr., J.A. Kerr and R.T. Watson, J. Phys. Chem. Ref. Data **11**, 487 (1982)
- (6) Y. Mitsuda, Y. Kojima, T. Yoshida and K. Akashi, J. Mater. Sci. **22**, 1557 (1987)

LOW TEMPERATURE DEPOSITION OF HARD, AMORPHOUS DIAMONDLIKE FILMS BY LASER EVAPORATION

J. Krishnaswamy*, A. Rengan*, A. Srivatsa*, J. Narayan*, Y. Cong**, R. Collins**,
and K. Vedam**.

*Materials Science and Engg., North Carolina State University, Raleigh, N.C.- 27695.

**Materials Research Lab., Pennsylvania State University, University Park, PA-16802.

ABSTRACT

Substrate temperature during deposition of hard carbon films by short pulse (40 nsec, FWHM) eximer (308 nm) laser ablation ($\sim 1.25 \times 10^8$ W/cm²) of solid carbon affects the optical and mechanical properties of deposited films. Films deposited at 25° C are superior to those deposited at 500° C. Deposited films were characterized by spectroscopic ellipsometry, microhardness, TEM, Raman and FT-IR techniques.

INTRODUCTION

Hydrogen incorporation in CVD deposited carbon films [1-4] have problems of adhesion [5], hardness [6] and internal stress [7]. These problems are somewhat mitigated by the use of high substrate temperatures and substrate bias during film growth [8]. Adhesion and hardness are however important properties for the use of films in various non-microelectronic applications [9-12]. Ion deposited techniques have been used in the past [13]. Here, the formation of diamondlike carbon films by laser ablation of a carbon target is reported [see also, 14]. Deposited films are characterized by TEM, Raman spectroscopy, spectroscopic ellipsometry and microhardness measurements. It was found that laser ablation of carbon leads to the formation of hard, amorphous, adherent, acid resistant, hydrogen free films and that the substrate temperature had substantial effect both on the optical properties as well as on hardness.

FILM DEPOSITION BY LASER EVAPORATION

The apparatus used for laser evaporation and deposition is described elsewhere [15]. Briefly samples were loaded into a chamber maintained at a base pressure of 10^{-7} Torr. The separation between the substrate, placed on a substrate heater, and the graphite target was about 2.5 cm. A 40 nsec (FWHM), XeCl laser beam was focussed by a lens onto the target at a power density of $\sim 1.25 \times 10^8$ W/cm². Under these conditions the visible extent of the plasma plume formed by laser evaporation and excitation (without filter) is less than 5 mm. Growth rate of the deposit formed by impinging carbon atoms and ions is estimated to be 0.03 to 0.05 nm/pulse.

CHARACTERIZATION OF FILMS

A. Spectroscopic ellipsometry:

Films on <100> Si substrates were analysed by spectroscopic ellipsometry. The details of the apparatus and method of obtaining n , k , absorption coefficient and Tauc plots are described elsewhere [16-18]. Refractive index and extinction coefficient parameters for these films for three deposition parameters are shown in Figure 1 (a) and Figure 1 (b) respectively. Higher temperature deposition gives a smaller optical band gap compared to those deposited at a lower substrate temperature. Refractive index values (2.3 to 2.4) of films at ~2.5 eV deposited between 25° C to 100° C are nearer to those of diamondlike films.

B. TEM characterization:

Plan view and cross-section samples were examined by transmission electron microscopy. A cross-section image of the hard carbon film is seen in Figure 2. The 'layered' appearance of the film is attributed to the occasional interruption of the deposition process for maintaining constant fluence during ablation. A characteristic electron diffraction pattern from a hard carbon film on silicon is shown in Figure 3. The rings from the hard carbon film are diffuse indicating the amorphous nature of these films. Though the position of the two strongest amorphous rings correspond well with the positions of the first two rings in diamond, the close correspondence of positions of rings due to graphite and diamond complicates unequivocal identification of the structure. Consequently correlations with physical properties of the films are necessary to ensure positive identification of the nature of the films.

C. Microhardness measurements:

Microhardness measurements were carried out on a Nanoindenter at the Oak Ridge National Laboratory by Drs. McHargue and O'Hern. The sapphire indenter tip was slowly pushed into the surface of the specimen at a constant rate of less than 10 nm/sec until the desired load was reached. The indenter tip was then retracted at the same rate. Load vs. position was measured with a resolution of 1.8 μ N in the 0 - 120 mN load range with a resolution of 0.4 nm in position. The results of hardness measurements averaged over several areas of the films deposited at three different temperatures are summarized below.

Table 1

Deposition Temp. ° C	Hardness at 25 nm from surface GPa
25	13.6 \pm 20 %
100	12.9 \pm 10 %
500	7.3 \pm 10 %

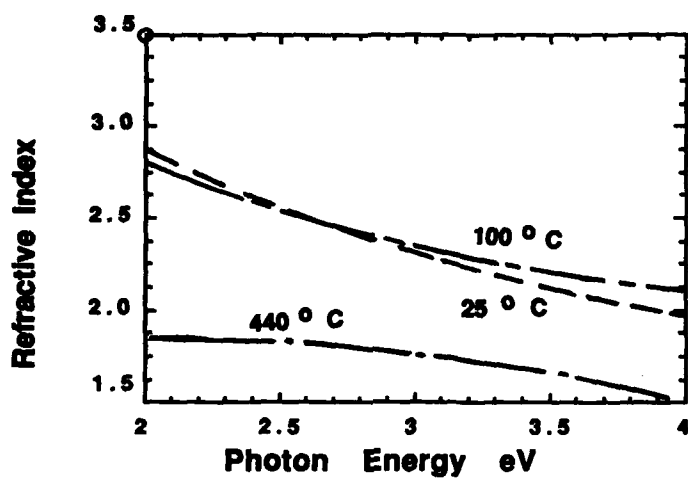


Figure 1(a) Refractive index vs. Photon energy at three temperatures for the hard carbon films. The 440 °C sample was deposited under biased conditions.

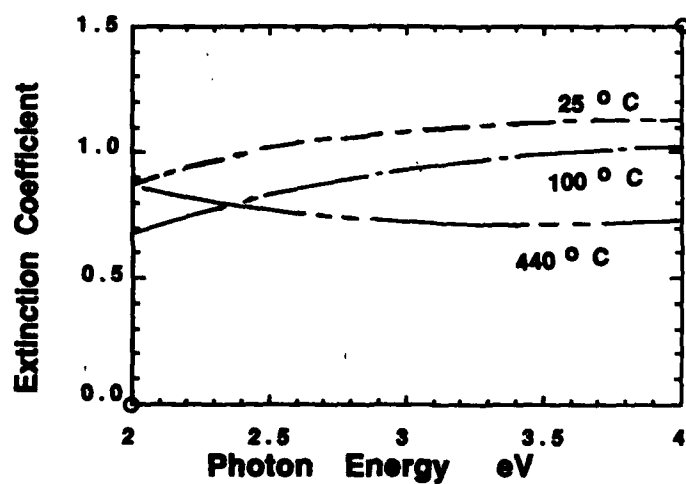


Figure 1(b) Extinction coefficient vs. Photon energy at three temperatures for the hard carbon films. The 440 °C sample was deposited under biased conditions

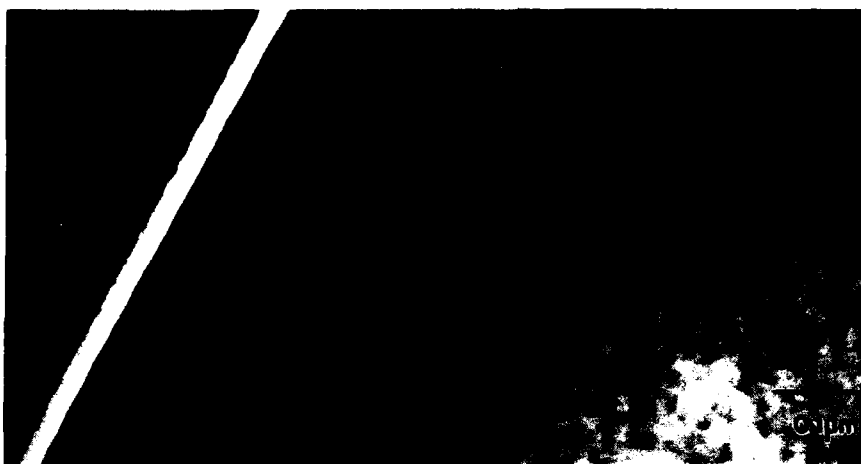


Figure 2 TEM cross-section image of a hard carbon film on Silicon substrate. Notice the layered structure

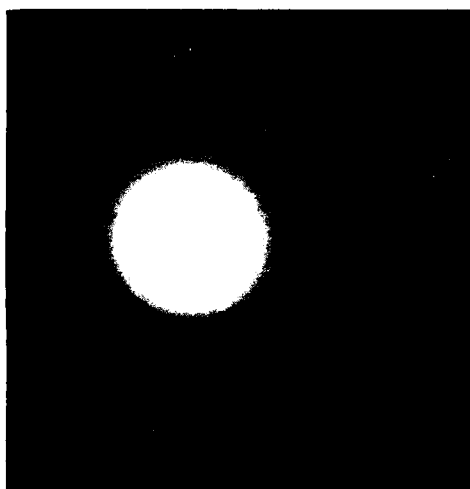


Figure 3 Transmission electron diffraction pattern from a hard carbon film. The diffuse rings are indicative of amorphous film

D. Raman and FT-IR characterization:

Raman characterization was carried out with a 4W Ar ion laser (2.41 eV) in the usual Raman Scattering geometry at Crystallume Inc. CA. Predominantly two peaks were found at $1380\text{--}1400\text{ cm}^{-1}$ (D peak) and $\sim 1600\text{ cm}^{-1}$ (G peak). Higher temperature deposition favors enhancement of "G" peak tending towards graphite formation. These peaks have been attributed to scattering by disorder activated optical zone edge phonons and graphite optic zone center phonons respectively [19]. FT-IR characteristics of the films in 1300 cm^{-1} to 1400 cm^{-1} region revealed no extra absorption due to the carbon film.

DISCUSSION AND CONCLUSIONS:

- #1. Tem cross section study revealed a very smooth, featureless, layered film. A diffraction pattern showing a diffuse ring structure is characteristic of an amorphous film.
- #2. The microhardness values are inferior to those of polycrystalline diamond films. Substrate temperature during deposition has substantial effect on the hardness. Lower substrate temperatures are conducive to growth of harder films.
- #3. The n and k values vs. photon energy of deposited films (25 to 100°C) lie intermediate to those of diamond and graphite. Substrate temperature during deposition has substantial effect on the optical constants. Lower substrate temperature during deposition is conducive to film growth with optical constants nearer to diamondlike films i.e. lower absorption coefficient and greater optical bandgap.
- #4. Raman diamond signature at 1333 cm^{-1} is absent in the film. Two broad peaks at $\sim 1400\text{ cm}^{-1}$ and at 1600 cm^{-1} were found for films deposited at 25°C and 500°C . The temperature of the substrate appears to influence the relative intensities of these peaks. Higher temperature deposition gives larger "G" peak as compared to "D" peak.
- #5. FT-IR spectroscopy on films deposited on silicon substrates in the limited range investigated reveals absence of extra absorption peaks due to the film.

In conclusion, extremely smooth, hard, adherent, hydrogen-free, acid resistant and IR transparent carbon films were deposited by the laser evaporation of solid carbon. Substrate temperature has substantial effect on the deposited film properties. Room temperature deposition is conducive to growth of films with optical constants and hardness nearer to those of diamondlike films.

Acknowledgements:

We acknowledge the help of Dr. C. McHargue and Dr. O'Hern of Oak Ridge National Laboratory for the Nanoindentation tests and Dr. Ravi of Crystallume Inc., for the Raman measurements. We sincerely thank the National Science Foundation for supporting this research.

REFERENCES:

- (1) R.C.DeVries, *Synthesis of diamond under metastable conditions*, GE Corporate Research and Development, Technical Information Series, Class1, Report No.86 CRD (1987) p.247.
- (2) J.C.Angus and C.C.Hayman, *Science*, 913, August (1988).
- (3) T.Kawato and K.Kondo, *Jpn.J.Appl.Phys.* 26, 1429 (1987).

- (4) N.Setaka, Sym.N, MRS Fall Meeting, Boston (1987).
- (5) A.Sawabe and T.Inuzuka, Appl.Phys.Lett., 46(2), 146 (1985).
- (6) J.Koskinen, J.P.Hirvonen and A.Antilla, Appl.Phys.Lett., 47(9), 941 (1985).
- (7) K.Enke, Thin Solid Films, 80, 227 (1981).
- (8) L.Holland and S.J.Ohja, Thin Solid Films, 58, 107 (1979).
- (9) J.Zelez, RCA Review, 43, 665 (1982).
- (10) E.Bergman and J.Vogel, J.Vac.Sci.and Technol., 5, 3287 (1987).
- (11) Hsia-Chu Tsai and D.B.Bogy, J.Vac.Sci.and Technol., 5, 2867 (1987).
- (12) A.T.Howe, J.Electrochem.Soc:Electrochemical Sci.and Technol., 134, 2470 (1987).
- (13) Y.Namba and T.Mori, J.Vac.Sci.and Technol., 3, 319 (1985).
- (14) T.Sato, S.Furuo, S.Iguchi and M.Hanabusa, Jpn.J.Appl.Phys., 26, 1487 (1987).
- (15) J.Narayan, N.Buinno, R.Singh, O.W.Holland and O.Auciello, Appl.Phys.Lett., 51, 1845 (1987).
- (16) K.Vedam, MRS Bulletin, Jan.I., 21 (1987).
- (17) D.E.Aspnes and A.A.Studna, Appl.Opt., 15, 10 (1975).
- (18) W.Budde, Appl.Opt., 1, 201 (1962).
- (19) M.Ramsteiner and J.Wagner, Appl.Phys.Lett., 51, 135 (1987).

PART V

Lamp-Induced
Chemical Vapor Deposition

WINDOWLESS WIDE AREA VUV LAMP FOR ENERGY ASSISTED CVD*

Z. YU, T. Y. SHENG, H. ZARNANI AND G. J. COLLINS, Department of Electrical Engineering, Colorado State University, Fort Collins, CO 80523

ABSTRACT

A ring shaped cold cathode electron gun provides a large area disc shaped vacuum ultraviolet (VUV) light source up to 20 cm in diameter. The windowless disc plasma is also a source of radical and excited atomic gas species. VUV photons, excited species, and radicals can all assist dissociation of CVD feedstock reactants via volume photo-absorption and sensitized atom-molecule collisions, respectively. In addition, the excited radical flux and VUV impingement on the film may also assist heterogeneous surface reactions and increase surface mobility of absorbed species. Thin films of aluminum nitride, Si_3N_4 , and hydrogenated amorphous silicon have been deposited at temperatures between 100°C - 400°C. The deposited films show significant improvement over other photo-assisted CVD processes in the film quality achieved, the substrate temperature required and the maximum deposition rates.

I. INTRODUCTION

There is a need for both low temperature and low radiation damage film deposition methods for use in III-V, II-VI and submicron silicon semiconductor processing as well as in coating sensitive optical materials. In-situ plasmas while effective for lowering required deposition temperatures may also bring undesired fluxes of charged particles via sheath electric fields which can cause film damage.

Thin film deposition has been reported previously using in-situ lamps[1], and remote plasmas[2]. Remote plasma or in-situ lamp processing, as compared to conventional plasma methods, reduces charged particle fluxes at reactor walls, substrates and fixtures. Simple photodissociation, using an external photon source, also minimizes deleterious plasma damage but VUV photon induced damage remains an issue. The photon absorption cross sections of many polyatomic reactant gases used in CVD processes have peak values in the VUV region beyond the reach of commercial photon sources. Photo deposition of hydrogenated amorphous silicon, for example, requires a VUV light source ($\lambda < 180 \text{ nm}$) when using monosilane as a feedstock gas since monosilane does not absorb photons with wavelengths above 180 nm.

Conventional VUV light sources employ both high pressure and low pressure gas discharges excited by either a radio frequency, microwave, or a D.C. electrical source. A window transmits the VUV resonance light generated in the enclosed plasma. VUV window materials, such as LiF, are hydroscopic, their VUV transmission degrades with time and the window cost is high.

An in-situ windowless lamp would avoid many of the above problems. Hollow cathode lamps are used without a VUV window but their geometry is usually cylindrical and the emission region is of small area ($< 3 \text{ cm}^2$). Moreover, the VUV resonance radiation emitted from an optically thick cylindrical plasma is trapped and the output intensity limited via self-absorption. Finally, the hollow cathode discharge uses a closed wall cylindrical structure open only to one end which restricts wide area and

*Supported by Naval Research Laboratory, National Science Foundation and Applied Electron Corporation.

uniform outdiffusion of atomic species and free radicals created in the localized cylindrical plasma region.

II. WIDE AREA WINDOWLESS LAMP

In the present study a ring shaped cold cathode electron gun shown in Figure 1 provides a large area disc shaped VUV light source up to 20 cm in diameter [3]. A conventional D.C. power supply is used to drive the cold ring cathode which emits secondary electrons following ion bombardment, metastable impingement, or the absorption of a VUV photon. The secondary electrons are accelerated in the ring shaped cathode sheath, thereby providing a disc-shaped electron beam created plasma [4]. The grounded wall of the reactor chamber adjacent to the ring cathode is used as a discharge anode. It is noteworthy that no sheath driven fluxes of charged particles are present on downstream substrate or reactor walls. Electric fields are localized to the cold cathode electron gun regions only. The energetic electron beam excites the ambient gas species via electron-atom or electron-molecule collisions. Using molecular gases the disc-shaped plasma acts as a large area source of atomic radicals, charged particles, metastables, as well as a characteristic photon emission spectra. Excited atomic species within the disc-shaped electron beam created plasma emit VUV radiation primarily on their resonance lines. Because of the thin (1 mm) spatial thickness of the beam created disc plasma compared to conventional plasmas (several cm) the resonant photon mean free path is comparable to the lamp plasma thickness and trapping of photons emitted by atomic species is reduced. In a H_2 lamp atomic hydrogen resonance radiation can propagate far from the disc-shaped plasma since H_2 outside the plasma does not significantly absorb 121 nm photons. Neither does atomic hydrogen cause appreciable absorption inside the mm thick disc plasma. Clearly, resonance absorption effects outside the disc plasma for atomic helium emission are quite different from those of atomic H since outside the disc plasma atomic helium absorbs resonant light over a long path. Hence, the He I resonance lines at 668 Å are rapidly diminished with distance towards the substrate. Ionized He spectra emitted from the disc plasma do not suffer the resonance absorption of neutral helium since outside the disc plasma the He ground state density is small. In fact, we observe that at the substrate the He II VUV spectra dominates over the He I VUV spectra.

In operation He, H_2 or N_2 gas is flowed through the disc shaped beam plasma creating unique VUV photon spectra and atomic radicals. The excited and radical species, created in the wide area electron beam plasma, move downstream and interact with feedstock gases which are introduced upstream from the substrate. Feedstock reactant dissociation occurs primarily via volume photo-absorption and sensitized atom-molecule collisions. A specific lamp gas may better assist dissociation of a specific feedstock gases because its unique VUV emission spectra and free radical species are better matched energetically for the task. The excited radical flux and VUV impingement on the film assist heterogeneous surface reactions and will also increase surface mobility of adsorbed species. This occurs at lower substrate temperatures than possible with conventional pure thermal methods. We emphasize that the plasma species which impinge on the downstream substrate do so at thermal kinetic energy typically below 0.1 eV even though the internal energy may be 1-20 eV for these same species.

The intensity of VUV emission has a measured uniformity of $\pm 6\%$ over the central 15 cm of the 20 cm diameter plasma discs using atomic helium, molecular N_2 and H_2 . The Lyman alpha emission, $2p^2p^0 - 1s^2S$ at a wavelength of 121.6 nm, dominates when running a hydrogen discharge while

the N I line $3s^4p - 2p^4s^0$ at 120.0 nm, dominates in the disc shaped nitrogen discharge. Due to self absorption the He II VUV emission dominates.

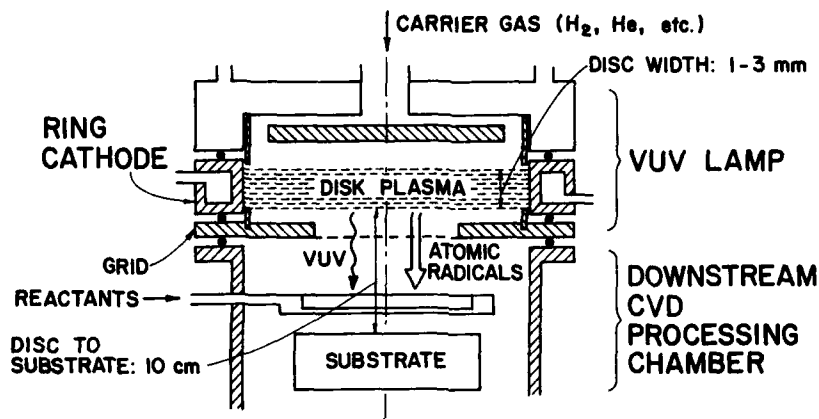


Figure 1. Windowless VUV Lamp CVD reactor.

III. ENERGY ASSISTED CHEMICAL VAPOR DEPOSITION

The feedstock CVD gas species are introduced into the processing chamber downstream from the VUV lamp. A reactant gas inlet jet is located just above the substrate shown in Figure 1. The distance from the disc plasma to the substrate is typically 10 cm. Ground state ions, metastables or free radicals created in the confined disc plasma flow over a distance of 10 cm before reaching the substrate. The carrier gas flow is less than 10^4 cm/sec implying that the downstream plasma is more than 1 ms into the plasma afterglow and are fully thermalized. By way of comparison all electrons and ions outside an applied electric field thermalize within fractions of a millisecond to gas kinetic temperatures. Note however that the confined plasma disc does emit narrow band resonance radiation which may be resonantly absorbed by the downstream diffusing species raising their internal energy but leaving their kinetic energy thermal. Excited thermal atoms may participate in sensitized atom-molecule collisions which dissociate the reactant feedstock gas molecules either in the volume or at the substrate surface.

Amorphous silicon, Si_3N_4 , aluminum nitride, as well as gallium nitride thin films have been deposited when using: Si_2H_6 ; SiH_4 and N_2 ; TMA and NH_3 ; and TMG and He- N_2 feedstock gases, respectively. Detailed windowless disc lamp assisted deposition conditions for two of films are listed in Table I.

TABLE I. WINDOWLESS DISC LAMP CVD OPERATION CONDITIONS

Films	AlN	a-Si:H
Light Source	H ₂ Lamp H: 121.6 nm	He ⁺ Lamp He ⁺ : 121.5 nm
Cathode Current	0.2A	0.5A
Cathode Voltage	500V	600V
Reactant	TMA/NH ₃	Si ₂ H ₆
Gas Flow	1/40 NH ₃ 60SCCM H ₂ 200SCCM	Si ₂ H ₆ 20SCCM He 200SCCM
Total Pressure	1Torr	1-1.5Torr
Substrate Temp.	100-400°C	50-400°C
Deposition Rate	60-200Å/min	>200Å/min

A. Aluminum Nitride Films [5]

Aluminum nitride thin films (AlN) are deposited on three substrates: heavy metal fluoride glass (HMF), silicon wafers and III-V wafers. CVD feedstock gases employed are trimethylaluminum (TMA) and ammonia (NH₃) [5]. The feedstock reactants are both photo dissociated and decomposed via atom-molecule reactions. Details of TMA and NH₃ photodissociation pathways has been studied previously [6]. The atom-molecule reactions involve atomic hydrogen excited atoms colliding with the molecular feedstock and dissociating it. The deposition rate varied from about 20 nm/min for a 400°C substrate temperature to about 6 nm/min for a 100°C substrate temperature.

The AlN film properties measured include: refractive index; film resistivity; and dielectric constant. See Table II. It is especially noteworthy that with windowless lamp CVD we can deposit good quality AlN films at 100°C whereas the laser CVD technique is not able to do so below 200°C and that the deposited film thickness variation is within 5% over a 10 cm diameter substrate. The wet etch rate at 60°C of lamp deposited AlN in 85% phosphoric acid (H₃PO₄) was also examined. Windowless lamp deposited AlN films show a 2-3 times lower etch rate than laser deposited films indicating both the lower hydrogen content and the higher film density. The refractive index of deposited AlN films was measured to be 2.06 at 400°C substrate temperature and is comparable to excimer laser deposited AlN which has a refractive index of 1.95 for a 400°C deposition temperature [7]. Moreover, AlN deposited at 400°C with the windowless lamp CVD exhibits a resistivity similar to that reported for bulk AlN ($>5 \times 10^{13} \Omega \text{ cm}$) [8].

The deposited AlN film was examined using complementary Auger electron spectroscopy (AES) and infrared absorption spectroscopy (FTIR) to determine the elemental Al/N ratio and the amount as well as the form of hydrogen bonding. Windowless lamp and laser assisted CVD films have nearly equivalent aluminum to nitrogen ratios. However, the hydrogen bonding of lamp deposited AlN films have a low concentration at all substrate temperatures. In contrast the hydrogen bonding increases for laser CVD AlN films over one order of magnitude when substrate temperatures are lowered to 200°C from 400°C. Note that at 400°C the

hydrogen bonding concentrations have same level for both laser and in lamp deposited films. The hermetic properties of hydrogen lamp deposited AlN films on HMF glass were examined by the chemical leach rate method. The leach rate of the HMF samples coated using windowless lamp assisted CVD of AlN is $\sim 10^{-6}$ ppm/min.

In conclusion, the hydrogen lamp assisted CVD achieves equivalent or even higher quality AlN films at lower substrate temperature than prior art excimer laser CVD methods [7].

TABLE II PROPERTIES OF AlN FILMS

	VUV Lamp-CVD	193 nm Laser-CVD
Refractive Index	1.7-2.0 (100-400°C)	1.7-1.9 (200-400°C)
Dielectric Constant (at 1 MHz)	7.5-8.0	7.0-8.0
Breakdown Voltage (MV/cm)	2 - 4 (200-400°C)	2 - 3 (300-400°C)
Resistivity (ohm-cm)	5×10^{13} (400°C)	10^{13} (400°C)
Wet Etch Rate (Å/sec at H_3PO_4)	460-50 (100-400°C)	500-100 (200-400°C)
Relative NH Bonding Concentration(α ΔH) from FTIR (arb.unit)	0.1-0.1 (100-400°C)	1.0-0.1 (200-400°C)

B. Helium Lamp Assisted Deposition of Hydrogenated Amorphous Silicon Films [9]

A VUV lamp employing helium as a carrier gas is used for deposition of amorphous silicon using disilane as a downstream feedstock. Hydrogenated amorphous silicon films are deposited on crystalline silicon wafers or glass substrates. Helium is introduced upstream to the lamp and in addition to He VUV radiation plasma products created in the disc plasma (He , He 2¹S, He 2³S) flow downstream toward the substrate at thermal kinetic energy.

The hydrogenated amorphous silicon films deposited by the VUV helium lamp dissociation of disilane have film properties comparable to photo-CVD films deposited by either excimer lasers or mercury lamps. See Table III. Typically a film deposited at a substrate temperature of 350°C has a refractive index of 3.62, an optical band gap of 1.76 eV, a photoconductivity of 4×10^{-4} (Ω -cm)⁻¹, and a dark conductivity of 3.5×10^{-9} (Ω -cm)⁻¹. The conductivity activation energy was measured to be 0.71 eV. The optoelectronic properties of Table III are comparable with that of R.F. plasma films[10]. The hydrogen concentration which includes only Si-H bonding for our films is found to vary from 4 to 8% as the substrate temperatures varies from 350° to 300°C. The hydrogenated amorphous silicon films, photoconductivity drops 25% during first day it is exposed in AMI light. This drop is comparable to conventional plasma deposited a-Si:H films [9].

IV. Conclusions

A windowless VUV lamp operates in a variety of carrier gases (H_2 , N_2 , He) and provides a wide area source of VUV photons and free radicals which assist downstream CVD processes. The chosen gas species have compatible VUV emission spectra and free radical species with the chosen CVD reactants. Large area film deposition occurs uniformly on substrates up to 15 cm in diameter. AlN, Si_3N_4 and amorphous silicon thin films were

deposited with physical, chemical and electrical properties comparable or better than other photo-assisted methods.

TABLE III PROPERTIES OF a-Si:H FILMS

	VUV Lamp	193 nm Laser	R.F. Plasma
Photoconductivity ($\text{ohm}^{-1} \text{cm}^{-1}$)	4×10^{-4}	1.2×10^{-5}	1×10^{-3}
Dark Conductivity ($\text{ohm}^{-1} \text{cm}^{-1}$)	3.5×10^{-9}	2.5×10^{-11}	3×10^{-9}
Optical Band Gap (eV)	1.76	1.7	1.7-1.8
Conductivity Activation Energy(eV)	0.71	0.85	0.76
Refractive Index	3.62	3.5	3.43
Hydrogen Concentration(%)	4.3	12	14

REFERENCES

1. Paul A. Robertson, et al., Mat. Res. Soc. Symp. Proc. 75, 257 (1987) and M. Hanabusa and T. Kaneoka, J. Vac. Sci. Technol. B5, 1432, 1987.
2. Sang S. Kim, D. V. Tsu, and G. Lucovsky, J. Vac. Sci. Technol. A6(3), 1740, May/June 1988.
3. Applied Electron Corp., U.S. Patents 4,509,451, 4,782,267 and Pending Applications.
4. B. Shi, J. D. Meyer, Z. Yu, and G. J. Collins, IEEE Transactions on Plasma Science, PS-14, 523 (1986). See also R. J. Carman and A. Maitland, J. Phys. D20, 1021 (1987).
5. T.Y. Sheng, Z. Yu, and G.J. Collins, Appl. Phys. Lett. 52, 576 (1988).
6. D.J. Ehrlich, R.M. Osgood, Jr., and T.F. Duetsch, IEEE J. Quantum Electron. QE-16, 1233 (1980). See A.W. Laubengayer, J.D. Smith, and G.G. Ehrlich, Am. Chem. Soc. 83, 542 (1961). See V.M. Donnelly, A.P. Barowavski, and J.R. McDonald, Chem. Phys. 213, 218 (1979). See also D. Eres, T. Motooka, S. Gorbatkin, D. Lubben, and J.E. Greene, J. Vac. Sci. Technol. B 5, 848 (1987).
7. C.A. Moore, Z. Yu, L.R. Thompson, and G.J. Collins, in Handbook of Thin Films Deposition Processes and Technologies, edited by K. Schuegraf (Noyes, Parkridge, NJ, 1988), Chap. 10.
8. Y. Kurokawa, K. Utsumi, H. Takamizawa, T. Kamata, and S. Noguchi, IEEE Trans. Components, Hybrids, Manuf. Technol. CHMT-8, 247 (1985).
9. H. Zarnani, Z. Yu, and G.J. Collins, E. Bhattacharya and J. I. Pankove, Appl. Phys. Lett. 53, 131 (1988).
10. M. Mirose, "Hydrogenated Amorphous Silicon," Part A, edited by, J. I. Pankove, Vol. 21, page 9.

LOW TEMPERATURE EPITAXY OF $Hg_{1-x}Cd_xTe$

N. V. Cody, U. Sudarsan, and R. Solanki
Department of Applied Physics and Electrical Engineering
Oregon Graduate Center, Beaverton, OR 97006-1999

ABSTRACT

Mercury cadmium telluride epitaxial layers have been grown using methylallyltelluride (MATE), dimethylcadmium (DMCd), and elemental Hg. Using these precursors high quality films have been achieved over the temperature range of 200-300°C. Comparisons are made between UV photon-assisted and thermally deposited films. Composition, growth rate, and electrical properties are compared for the two processes under various parameter conditions. Properties of films deposited on various substrates including CdTe, GaAs, and GaAs/Si are also described.

INTRODUCTION

Until recently, the chemical vapor deposition (CVD) temperature of $Hg_{1-x}Cd_xTe$ (MCT) was limited to about 400°C mainly due to the dissociation temperature of diethyltellurium, a commonly used Te precursor. Techniques such as ultraviolet (UV) photon-assisted CVD were utilized to lower the effective activation energy and hence reduce MCT growth temperature to about 250°C [1,2]. However, with the availability of new Te compounds, which can dissociate around 250°C [3], the obvious question asked is why use photo-CVD? The work described below was undertaken to compare the MCT film properties produced by thermal and photo-CVD using methylallyltelluride (MATE) and to determine if there is any merit for using the latter technique.

EXPERIMENTAL

The deposition system was an all stainless steel horizontal reactor with a sapphire viewport for the admission of UV radiation. The source of the UV photons was a medium pressure, microwave excited Hg lamp with 100 mW/cm² intensity between 200-250 nm spectral range. The substrate holder was resistively heated and monitored using a thermocouple placed on the surface of the holder to account for any added heating due to the UV source. Before loading, the substrates were cleaned and etched using 2% bromine in methanol for CdTe and a 5:1:1 ($H_2SO_4:H_2O:H_2O$) for GaAs substrates. After loading, the system was evacuated using a diffusion pump to a base pressure of 10⁻⁵ Torr and then brought up to atmospheric pressure and desired temperature. All flows including the window purge system (kept window clean for > 7 hrs.) were controlled using mass flow controllers. The organometallic partial pressures were controlled using constant temperature baths and appropriate hydrogen carrier gas flows.

RESULTS AND DISCUSSION

Growth vs. Parameters

The parameters investigated include variations of all reactant partial pressures as well as a temperature study for a fixed reactant condition. This study showed that there was some prereaction occurring upstream of the

substrate. This prereaction resulted in deposition of mainly HgTe. This was significantly decreased by reducing the Hg source temperature from 300°C to 250°C and by also using an internal extension to the MATe line. This combination reduced the time during which MATe was in contact with the Hg vapor and resulted in doubling the growth rate.

Shown in Figure 1 is a plot of the growth rate against Hg partial pressures. The growth was investigated using both CdTe and GaAs substrates and results in a linear relationship for the photon-assisted case and an exponential relationship for the purely thermal growth conditions for both substrates. At Hg partials of 0.01 Atm. films are Hg deficient resulting in films of CdTe being deposited and thus near equal growth rates. At high partials (≥ 0.04 Atm.), Hg condensation was observed which formed many ring patterns on the films surface due to etching.

The partial pressure of MATe was varied from 1.5-3.0 E-3 Atm. with the other reactants held constant with values of Hg = 0.03 Atm. and DMCD = 5.8 E-4 Atm. The resulting growth rates varied linearly from 2.4-2.8 $\mu\text{m/hr}$ for CdTe and 2.0-2.4 $\mu\text{m/hr}$ for GaAs. This 0.4 μm difference in growth rate could be attributed to the initial nucleation time required for growth and is equivalent to the difference observed in Figure 1 for photo-assisted growth. For the thermal growth this nucleation difference appears to be twice that of the photon-assisted growth as evidenced by a 0.8 μm difference between the CdTe and GaAs substrates.

By holding Hg = 0.03 Atm. and MATe = 1.9 E-3 Atm. constant and varying the DMCD partial pressure from 3.2-8.5 E-4 Atm. a change in x-value as well as growth rate results for both photo and thermal growths. For the photo-

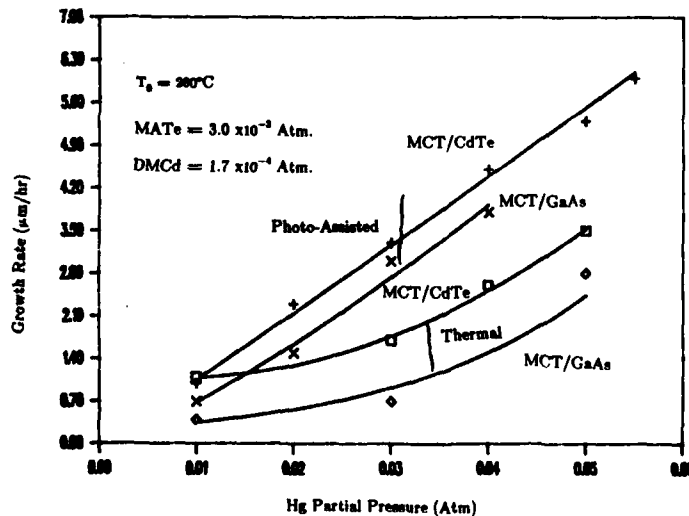


Figure 1. Growth rate vs. Hg partial pressure for photon-assisted and thermally grown MCT epilayers on CdTe and GaAs substrates.

assisted case the growth rate decreases from 4.3-2.0 $\mu\text{m/hr}$ with a corresponding change in x -value from 0.01-0.4. There is also an increase in hillock density from $3.2 \text{ E}+2 - 4.0 \text{ E}+5 \text{ cm}^{-2}$. For the thermal case this hillock density increases from $1.0 \text{ E}+4 - 1.5 \text{ E}+5 \text{ cm}^{-2}$ indicating that the photo-assisted growth does not increase this density but rather tends to be a function of the x -value only. This is evident as the defect density values are equal at a x -value of about $x = 0.3$. The possibility of the defects being a function of thickness is also eliminated as the growth rate for the thermal case varied from 2.2-0.8 $\mu\text{m/hr}$ with a corresponding variation in x -value of 0.3-0.35. Thus a photo-assisted process allows selection of a much wider range of x -values than in the thermal case.

A plot of growth rate against substrate temperature is shown in Figure 2. As can be seen the photo-assisted process gives a nearly constant growth rate over the temperature range investigated. Also, this process does allow for good growth rates at temperatures of 230°C which is one of the lowest reported values for MCT epitaxial growth at such a high growth rate. At a temperature of 210°C the film does grow, but is polycrystalline and appears to be the lower limit to film growth for this particular condition. The thermal growth rate reaches a maximum at a substrate temperature of 280°C and then drops off rapidly. This sharp drop is also present for higher partial pressures of both Hg and MATe which indicates a temperature related process. This region of the temperature dependence curve is still under investigation and will be reported at a later date.

Substrates

The substrates investigated for this study included CdTe (100) $2^\circ \rightarrow$

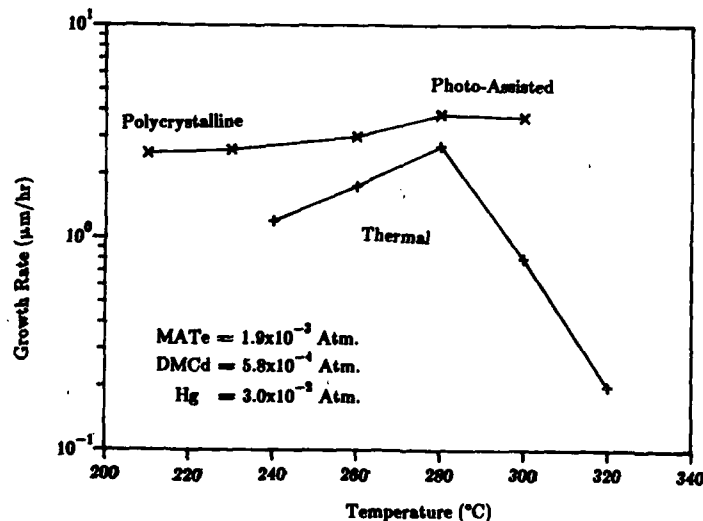


Figure 2. Dependence of growth rate on substrate temperature for photon assisted and thermally grown films.

(110), CdTe (100) $3.5^\circ \rightarrow (110)$, CdTe (110), GaAs (100), and GaAs/Si (100) $3^\circ \rightarrow (110)$. For the CdTe substrates the smoothest films were obtained on 3.5° offset which resulted in a decrease in vertical height of the hillocks. However the density remained constant with a pyramidal shape tilted according to the offset. The (110) CdTe orientation density is very high with an average size much greater than for the offset substrates which resulted in a much poorer morphology. The GaAs (100) substrates also have a high density of hillocks resulting in pyramidal growths of varying sizes. Analysis of films grown on GaAs using transmission electron microscopy showed that MCT films grown thermally and photon-assisted are both of a poor crystalline quality due to the large number of dislocations present throughout the film. Thus to decrease the amount of dislocations a buffer layer of CdTe was grown [4]. This buffer layer accommodated the lattice mismatch within the first micron and allowed for a much improved MCT epilayer. Growth of films grown on GaAs/Si, also employing the buffer, resulted in a specular surface with a slight cellular-type surface morphology observed under high magnification.

Electrical Measurements

In order to compare the thermal and photon-assisted processes, films were grown with equivalent x-values and film thicknesses. Hall measurements were made using the Van der Pauw technique where In was used to form ohmic contacts. Shown in Figure 3 is a plot of mobility against temperature and corresponding carrier concentration ($N_A - N_D$) for films grown thermally and photon-assisted with a x-value of 0.32. As can be seen the mobility of the photon-assisted film grown at a substrate temperature of 250°C does not decrease due to impurity scattering as does the thermally (280°C) grown film. This is believed to be due to impurities in the source reactants which would not be completely dissociated at 280°C but could be during the photon-assisted deposition allowing for incorporation into the film as acceptor sites. Comparisons are also made for films grown on CdTe and GaAs/Si substrates as

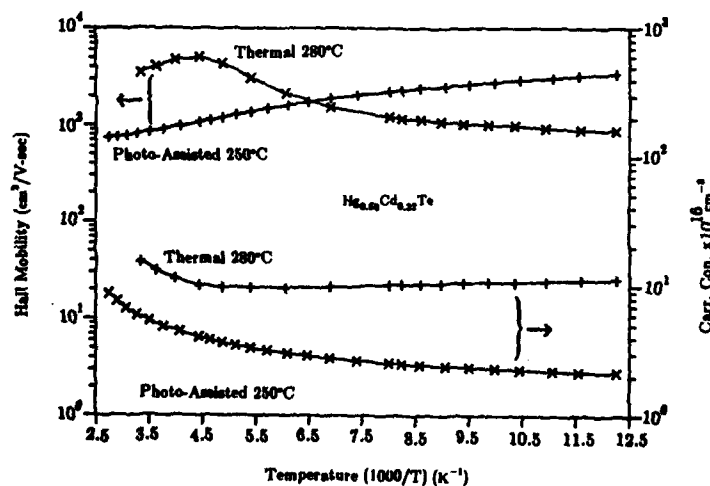


Figure 3. Hall mobility and carrier concentration for thermally grown and photon-assisted MCT grown on CdTe.

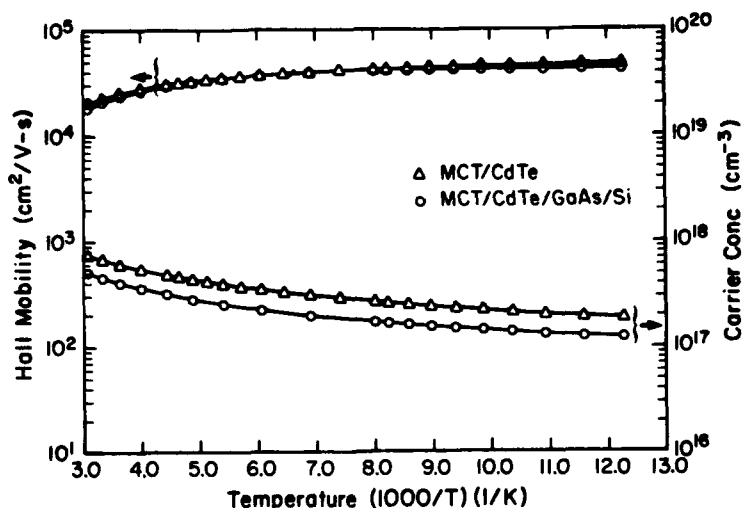


Figure 4. Hall mobility and carrier concentration for MCT grown on CdTe and CdTe/GaAs/Si substrates.

shown in Figure 4. Both of these films are grown under identical conditions except the GaAs/Si substrate has a CdTe buffer layer followed by MCT growth. The CdTe films typically have room temperature mobilities of 100-120 cm²/Volt-sec and carrier concentrations of 10 E+15 cm⁻³. Thus the improvement in film quality is not considered to be due to a contribution from the CdTe buffer but rather a result of having a clean and improved CdTe starting surface on which the MCT is grown.

Crystal Quality

The crystalline quality of the epilayers was characterized using x-ray double crystal rocking curves (DCRC) from the (004) reflection. The x-ray source used was CuK_α obtained from a four crystal Si monochromator. The values obtained are listed in Table I for the different substrates together with the range of thicknesses used. The variation in the full width at half maximum (FWHM) can be attributed mainly to the different x-values studied as this table includes values from 0.01-0.4. One trend which is observed is that as the thickness is increased the FWHM does decrease indicating that the epilayer is of good quality away from the substrate interface.

Table I. Double crystal rocking curve FWHM values for substrates studied.

Substrate	Film Thickness (μm)	FWHM (arc-sec)
CdTe	3-9	100-200
GaAs	4-6	200-250
Si with buffer layers	MCT 3-4 (1-1.5 μm buffer)	250-300

SUMMARY

The organometallic tellurium source MATE has been studied using both a thermal and a photon-assisted growth process. Advantages using the photon-assisted process include epitaxial growth at temperatures as low as 230°C at high growth rates (3 $\mu\text{m/hr}$) and better electrical properties. Also films grown on GaAs and GaAs/Si with intermediate buffer layers tend to yield better films than those grown on bulk CdTe substrates. These results indicate that MCT films grown on large substrates can be achieved using the photon-assisted growth process.

REFERENCES

1. J. B. Mullin and S. J. C. Irvine, J. Vac. Sci. Technol. A 4, 700 (1986).
2. D. W. Kisker and R. D. Feldman, J. Crystal Growth 72, 102 (1985).
3. V. E. Hoke, P. J. Lemonias, and R. Korenstein, J. Mater. Res. 3, 329 (1988).
4. N. W. Cody, U. Sudarsan, and R. Solanki, J. Mater. Res. 3, 1144 (1988).

LOW TEMPERATURE OMVPE OF ZnSe FROM ALKYL SOURCES USING A PLASMA DISK LAMP

K. L. Tokuda*, B. Pihlstrom***, D. W. Kisker*, M. Lamont Schnoes** and G. J. Collins***

*AT&T Bell Laboratories, Holmdel, NJ 07733

**AT&T Bell Laboratories, Murray Hill, NJ 07974

***Dept. of Electrical Engineering, Colorado State Univ., Ft. Collins, CO 80523

ABSTRACT

The growth of high quality ZnSe by organometallic vapor phase epitaxy (OMVPE) has generally been hindered because of parasitic source pre-reactions or relatively high source decomposition temperatures. In this work, we have used vacuum ultraviolet photons generated by a disk-plasma lamp to assist the ZnSe growth process using diethylselenium and diethylzinc as source materials. This approach has resulted in satisfactory growth rates and high material quality at temperatures as low as 250°C, without the limitations of prereaction typically observed when H₂Se is used for the selenium source material. In addition, the alkyl selenium compound offers advantages due to reduced toxicity compared to H₂Se. This new, low-growth-temperature process thus offers the possibility of improved stoichiometry and impurity incorporation control as well as a reduced thermal effect on the underlying substrate during growth. At the same time, the advantages of excellent morphology and uniformity typically exhibited by the alkyl-based growth processes are retained.

I. INTRODUCTION

The epitaxial growth of II-VI semiconductor compounds and alloys has been greatly improved by the recent development of techniques such as Molecular Beam Epitaxy (MBE) and Organometallic Vapor Phase Epitaxy (OMVPE). The advantages of these techniques over other techniques such as vapor phase transport occur largely because of the reduced growth temperatures in these processes. Both MBE and OMVPE have been used to successfully grow ZnSe, CdTe, ZnTe etc. at temperatures in the range of 200°C to 450°C,¹⁻⁵ compared to more typical vapor transport temperatures of over 500°C^{6,7}. The reduction of growth temperature results in improved control of properties, such as native defect concentration, and minimizes unintentional impurity incorporation due to substrate outdiffusion and autodoping.

In the case of MBE growth, because the growth temperature is largely independent of the source temperatures, it can be adjusted, while maintaining constant beam flux, thus eliminating any variation in source characteristics. However, especially for the OMVPE growth of II-VI compounds, the source properties and the resulting growth parameters are closely coupled. Typically, lower bounds on growth temperatures are incurred because of the stability of the alkyl group VI sources. When hydride group VI sources are used, as in ZnSe and ZnS growth, there is an additional limitation due to a parasitic pre-reaction between the group II and VI sources.

There has been considerable recent work toward lowering the OMVPE growth temperature of ZnSe growth using alternative selenium⁸⁻¹⁰ or zinc¹¹ chemistry, or using methods such as plasma-assisted growth with solid sources^{12,13} or OM sources,^{14,15} and photo-assisted growth.¹⁶⁻¹⁸ For example, the thermal growth rate using diethylzinc (DEZ) and dimethylselenium (DMSe) was enhanced by a factor of two using a mercury arc lamp;¹⁶ however, the enhanced rate was only 0.2 $\mu\text{m/hr}$ at 400°C, probably due to the low intensity of the lamp. Use of a higher intensity Hg-Xe lamp, resulted in a growth rate of 0.4 $\mu\text{m/hr}$ using DMZ and DMSe.¹⁷ More recently, a growth rate of 1.5 $\mu\text{m/hr}$ at 300 °C using a Xe lamp and DMZ and DMSe has been reported.¹⁸ In that work, growth rate enhancement was observed even when the irradiation was limited to wavelengths longer than the OM photo-dissociation threshold of 240 - 260 nm, suggesting enhancement was due to another mechanism, such as increased surface energy. Although these efforts have shown some success, photo-assisted techniques using a light source external to the deposition chamber are often hindered by window deposits, limited intensity, and spatial variation of the light source over large areas.

An alternative approach to reducing growth temperature is the use of a plasma to decompose OMs and increase surface energy. For example, Mino et al.¹⁴ report a growth rate of 0.5 $\mu\text{m/hr}$ using DEZ and DESe in a RF plasma at 250°C. Similar results were obtained by Oda and coworkers¹⁵ using a microwave plasma. Two potentially serious problems of this type of plasma-assisted process are damage to the substrate and the growing film due to ion bombardment and unintentional incorporation of C or H due to the high density and variety of organic radicals present in an OM-containing plasma. As an alternative, remote plasma-assisted depositions, i.e. systems in which the substrate and sources are not exposed directly to the plasma, have been reported for germanium,¹⁹ aluminum nitride,²⁰ amorphous Si.²¹

In this work, we have used a remote hydrogen plasma to enhance the growth of ZnSe in the range of 250°C using DESe and DEZ as source materials. The plasma primarily provides 10.21 eV photons, the Lyman alpha line of atomic hydrogen. As such, it is a wide-area *in situ* ultraviolet lamp. In addition, atomic hydrogen carried from the plasma region to the growth chamber, may also promote the decomposition of the organometallic sources.

II. EXPERIMENTAL

The experimental apparatus used in this work is described in previous publications by Collins and co-workers^{20,21}. Briefly, it consists of a conventional OMVPE gas handling system with mass flow controlled lines, etc., with the ability to operate at low pressure, plus a lamp to provide plasma-generated vacuum ultraviolet (VUV) photons. As in Ref. 20, the system is configured vertically, as shown in Figure 1, with the plasma about 15 cm above the substrate. The plasma lamp was operated under DC conditions similar to those previously reported, with the cathode at -600V with respect to the grounded anode. Under our typical growth conditions, using a lamp current of about 300 mA, a total flow of about 400 sccm H_2 and a pressure of 800 mtorr in the lamp, the plasma is a relatively uniform disk, which is spatially confined in height to about 1 cm.

For the depositions discussed here, typically 9 $\mu\text{mole/min}$ of DEZ and 36 $\mu\text{mole/min}$ of DESe were introduced about 1 cm above a GaAs substrate through a perforated ring inlet. Because of the downstream position of the substrate, no window which might prevent either VUV photons or hydrogen atoms from reaching the deposition region is necessary.

Due to limitations in pumping capacity, system pressure was a function of total gas flow. As a result, it was not possible to vary all growth parameters independently. For example, at a pressure of 1 torr and a current of 300 mA applied to the lamp, a typical value of plasma power was 240 W. However, since the impedance of the plasma was effected by pressure, the plasma power varied by 3 - 4% for pressure differences of 10 - 20 mtorr caused by different gas flow rates. As a result, in this work, we will primarily explore the effect of substrate temperature and lamp current, but it should be understood that other parameters also affected growth rate.

Characterization of the grown layers included optical microscopy, double crystal x-ray diffraction, and photoluminescence (PL). For the x-ray diffraction (XRD) measurements, Cu K_α radiation was collimated using a (100) InP crystal, thus resulting in a small amount of broadening at the ZnSe/GaAs lattice parameter. PL measurements were made at 5°K using a spectrophotometer with a cryostat attached. Excitation energy was very low, about 50 $\mu\text{Watts/cm}^2$.

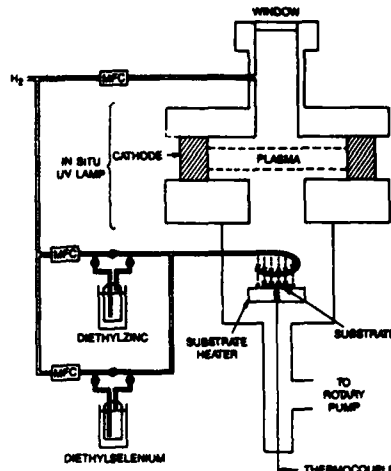


Figure 1. Schematic diagram of OMVPE apparatus showing *in situ* UV lamp.

III. RESULTS

The first notable result of our plasma-assisted growth of ZnSe is the ease with which we were able to obtain high quality surface morphology. In other OM growth processes in which hydrogen selenide is used, it is frequently very difficult to obtain specular surfaces, apparently due to the tendency for powder formation due to a parasitic pre-reaction. In contrast, in this work, if we started with a substrate holder which was cleaned of all previous deposits, we were able to obtain smooth surfaces for temperatures above 250°C. Below this temperature, there was a tendency to form surface structures, as seen in Figure 2.

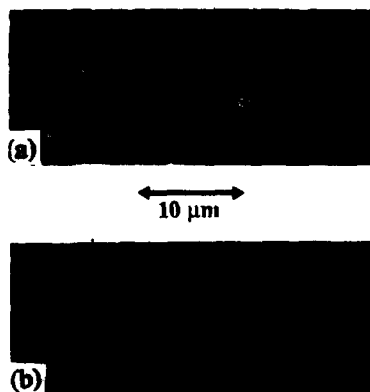


Figure 2. Morphology using a Nomarski microscope. (a) At a deposition temperature of 200°C, surface structures are observed. (b) At 250°C, surfaces are essentially featureless.

Apparently, although the plasma-supplied photons are able to dissociate the OM compounds, some heating is required to supply sufficient surface energy to achieve good morphology. The results of XRD measurements support the observation of higher material quality at increased temperature. The half width was reduced from about 400 arc-sec to about 225 arc-sec as the substrate temperature was raised from 200°C to 250°C. In addition, as shown in Figure 3, the photoluminescence also improved with an increase in substrate temperature.

At a temperature of 250°C, the luminescence is dominated by donor-acceptor pair bands (DAP), but in fact, the bound exciton (BE) at about 443 nm is beginning to appear. The very low pumping intensity of our current PL system results in an overestimate of the relative peak intensities of the DAP and BE bands. However, the increased intensity, more well-defined structure and reduced deep level (>480 nm) luminescence are all consistent with improved material quality.

In addition to temperature, the lamp current also dramatically affected the material quality of our ZnSe films. In Figure 4, we show the notable improvement in luminescence properties as the lamp current is increased from 200 to 300 mA. For these same 1 μ m thick films grown at 250°C, this increase in current resulted in a decrease in x-ray peak width from 450 arc-sec to 325 arc-seconds. However, because the growth rate depended on lamp current, these growth times were not equal. In Figure 5, we present our data for the dependence of growth rate on lamp current at 250°C. In addition, we found that at this temperature, if the plasma was not present, then no measurable growth occurred. In fact, using these source compounds, we would not expect that there would be measurable growth from a purely thermal process until the temperature reached the range of 400-450°C. Thus, we feel that the plasma is lowering the required temperature for high quality growth by at least 150-200°C!

If we compare our results to the properties of ZnSe films grown by other means, we find that there is some problem of impurity incorporation, as shown by the dominance of the PL by the DAP bands. At this time, we do not know if this is related to the lamp's construction materials or another source. At the same time, the results are promising, since we have significantly lowered the temperature for growth using these alkyl sources. In addition, at the higher lamp power and substrate temperature, there seems to be little evidence of major incorporation of deep level impurities, which can severely degrade

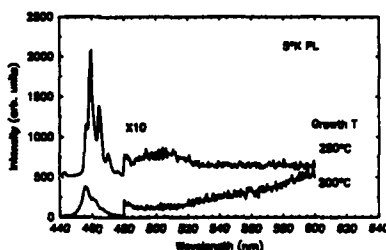


Figure 3. Composite plot showing improvement in photoluminescence data with increase in substrate temperature.

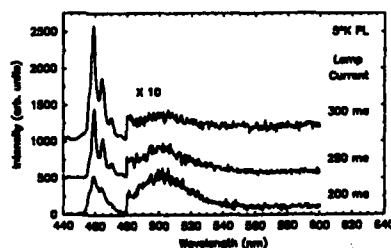


Figure 4. Composite plot showing improvement of photoluminescence data with increase in lamp current.

the optical properties of ZnSe. Additional evidence of this is that several of these samples exhibit bright blue luminescence at room temperature under HeCd laser pumping.

IV. CONCLUSIONS

High quality ZnSe has been deposited using a remote-plasma lamp at 250 °C. In comparison to our thermal process, the plasma depositions have better crystalline quality and improved morphology. However, the most significant advantage is that using the plasma process has reduced the growth temperature from 500°C using DEZ and DESe to ~250°C while maintaining a growth rate of 1.5 $\mu\text{m/hr}$.

Low temperature OMVPE of ZnSe from alkyl sources using a plasma-disk lamp has been successfully demonstrated and shown to have distinct advantages over conventional thermal OMVPE. The reduction in deposition temperature realized using this technique should lower the level of native defects in this material. This reduction of temperature will also help to minimize interdiffusion in multi-layer structures. In addition, the plasma process allows the use of a variety of source compounds, possibly even thermally-stable sources, while maintaining a low deposition temperature. Therefore, further applications of this technique are encouraging. Already, our attempts at doping ZnSe using plasma-assisted OMVPE have been successful and current efforts to deposit other materials are promising.

ACKNOWLEDGEMENTS

The authors are grateful to Z. Q. Yu, at Colorado State University, for his technical support in solving operational problems with the plasma lamp, and to T. D. Harris for his efforts promoting and facilitating photoluminescence analyses at Bell Labs. Special thanks are due to A. M. Glass for his continued support of this work.

REFERENCES

- [1] W. Stutius, Appl. Phys. Lett. **33** (7), 656 (1978).
- [2] T. Yao, M. Ogura, S. Matsuoka, T. Morishita, Appl. Phys. Lett. **43** (5), 499 (1983).
- [3] R. D. Feldman, D. W. Kisker, R. F. Austin, K. S. Jeffers, and P. M. Bridenbaugh, J. Vacuum Sci. Tech., **A4** (4), 2234 (1986).
- [4] D. W. Kisker, P. H. Fuoss, J. J. Krajewski, P. M. Amirthiraj, S. Nakahara, J. Menendez, J. Cryst. Growth, **86**, 210 (1988).
- [5] T. Yao and S. Maekawa, J. Cryst. Growth, **53**, 423 (1981).
- [6] P. J. Dean, Phys. Stat. Sol., **A81**, 625 (1984).
- [7] H. Hartmann, R. Mach and N. Testova, J. Cryst. Growth, **84**, 199 (1987).

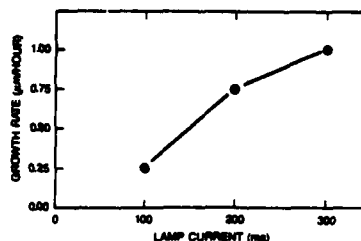


Figure 5. Dependence of growth rate on the current applied to the lamp, at a substrate temperature of 250°C.

- [8] B. Cockayne, P. J. Wright, M. S. Skolnick, A. D. Pitt, J. O. Williams and T. L. Ng, *J. Cryst. Growth*, 72, 17 (1985).
- [9] S. Fujita, T. Sakamoto, M. Isemura, S. Fujita, *J. Cryst. Growth*, 87, 581 (1988).
- [10] D. W. Kisker and K. L. Tokuda, Paper E9.23, Fall Meeting of the Materials Research Society, 1988.
- [11] P. J. Wright, B. Cockayne and A. J. Williams, *J. Cryst. Growth*, 84, 552 (1987).
- [12] H. Sato, O. Osada, K. Matsushita, T. Hariu and Y. Shibata, *Vacuum*, 36 (1-3), 133 (1986).
- [13] T. Matsumoto, S. Yoshida and T. Ishida, *Jpn. J. Appl. Phys.*, 25 (5), L413 (1986).
- [14] N. Mino, M. Kobayashi, M. Konagai and K. Takahashi, *J. Appl. Phys.* 59 (6), 2216 (1986).
- [15] S. Oda, R. Kawase, T. Sato, I. Shimizu and H. Kokado, *Appl. Phys. Lett.*, 48 (1), 33 (1986).
- [16] H. Ando, H. Inuzuka, M. Konagai and K. Takahashi, *J. Appl. Phys.*, 58 (2) 802 (1985).
- [17] W. E. Johnson and L. A. Schlie, *Appl. Phys. Lett.*, 40 (9), 798 (1982).
- [18] S. Fujita, A. Tanabe, T. Sakamoto, M. Isemura and S. Fujita, *Jpn. J. Appl. Phys.*, 26 (12) L2000 (1987).
- [19] R. A. Rudder, G. G. Fountain and R. J. Markunas, *J. Appl. Phys.* 60 (10), 3519 (1986).
- [20] T. Y. Sheng, Z. Q. Yu and G. J. Collins, *Appl. Phys. Lett.*, 52 (7), 576 (1988).
- [21] H. Zamani, Z. Q. Yu, G. J. Collins, E. Bhattacharya and J. I. Pankove, to be published.

PHOTOREACTIONS OF Mo(CO)_6 ON POTASSIUM PRECOVERED SILICON SURFACE WITH UV TO IR RADIATION

Z. C. Ying and W. Ho

Laboratory of Atomic and Solid State Physics and Materials Science Center
Cornell University, Ithaca, New York, 14853

ABSTRACT

The adsorption and photoreactions of Mo(CO)_6 coadsorbed with K on $\text{Si(111)7}\times\text{7}$ at 90 K have been studied under ultra-high vacuum conditions. It is found that dissociative adsorption of Mo(CO)_6 on the K preadsorbed surface occurs for coverages below a monolayer. A multilayer of physisorbed Mo(CO)_6 molecules is formed on top of the monolayer. Under photon irradiation physisorbed Mo(CO)_6 molecules are dissociated and CO desorption is observed. The photoreactions of Mo(CO)_6 occur over a wide wavelength range from the UV to IR. In contrast, only UV radiation induces photoreactions of Mo(CO)_6 on the K-free $\text{Si(111)7}\times\text{7}$ surface. Evidently K opens a new channel for the photoreactions of Mo(CO)_6 on the surface. A mechanism involving interactions between photogenerated charge carriers and the substrate-adsorbate complex is proposed.

INTRODUCTION

Investigation of photoreactions of metal carbonyls adsorbed on solid surfaces is important for understanding photodeposition of metals using carbonyls. A number of studies have recently been reported on the surface of various materials, including semiconductor,¹⁻⁴ metal,⁵ and insulator.⁴ These studies show that UV radiation induces dissociation of adsorbed carbonyls, via a mechanism involving direct electronic excitation of adsorbed carbonyl molecules. Similar to photoreactions of carbonyls in the gas phase, the photoreactions on these surfaces are observed under UV irradiation but not visible irradiation.

This paper reports our recent experiments of Mo(CO)_6 coadsorbed with K on $\text{Si(111)7}\times\text{7}$ at 90 K. It is found that photoreactions of Mo(CO)_6 occur even under visible and infrared irradiation. The experiments were performed under ultra-high vacuum (UHV) conditions, using photon induced desorption spectroscopy (PIDS), thermal desorption spectroscopy (TDS), high resolution electron energy loss spectroscopy (HREELS), and work function change ($\Delta\phi$) measurements.

To give a background for understanding the adsorption and reactions of Mo(CO)_6 on the K preadsorbed $\text{Si(111)7}\times\text{7}$ surface, the main results of previous studies of Mo(CO)_6 on the K-free $\text{Si(111)7}\times\text{7}$ surface are briefly reviewed in the following.^{2,3} Mo(CO)_6 molecules are observed to be physisorbed on $\text{Si(111)7}\times\text{7}$ at 90 K without dissociation; HREELS of Mo(CO)_6 on $\text{Si(111)7}\times\text{7}$ reveals vibrational features which are similar to those of Mo(CO)_6 molecules in the gas phase. Physisorbed Mo(CO)_6 molecules can be thermally desorbed from the surface at 200 K. UV radiation induces photodissociation of Mo(CO)_6 molecules. CO molecules, which are products in the photodissociation process, are desorbed from the surface during irradiation. The mechanism of the photoreactions is attributed to the direct excitation of the electronic states of the adsorbates, a process which also occurs in the gas phase carbonyls. However, it is found that adsorbed Mo(CO)_6 , unlike Mo(CO)_6 in the gas phase, do not completely dissociate into Mo and CO; Mo(CO)_x ($0 < x < 6$) are observed on the surface after photon irradiation. These

carbonyl fragments can be further dissociated with thermal heating, which gives rise to CO desorption at higher temperatures (250–500 K).

EXPERIMENTAL ARRANGEMENT

The experiments were performed in a stainless steel UHV chamber. An *n*-type ($5.5 \times 10^{14} \text{ cm}^{-3}$) Si(111) sample was used. The surface was cleaned by repeated cycles of sputtering and annealing. The clean surface was then exposed to K from a heated K getter, followed by an exposure of $\text{Mo}(\text{CO})_6$. A Xe arc lamp was used as the photon source. Radiation in various spectral regions from the lamp was selected using appropriate combinations of bandpass and longpass filters, giving rise to a bandwidth of approximately 60 nm. The photon flux absorbed by the sample is approximately 10 mW/cm^2 . In addition, the 514-nm output from a cw Ar ion laser was used for the power dependence study.

The K exposure was achieved reproducibly by controlling the heating time of the getter. Compared to the clean surface, the work function of the K-exposed surface shows a monotonic decrease with increasing K exposure until a maximum decrease of $2.6 \pm 0.2 \text{ eV}$ is reached. Additional exposures of K result in a slight increase in the work function. The K exposure corresponding to the maximum decrease in the work function was used in the present experiments. No attempt was made to calibrate the absolute coverage of K deposited on the surface. Detailed description of the apparatus and the data collection procedures have been published elsewhere.^{2,6}

RESULTS

Figure 1 presents thermal desorption spectra obtained from Si(111)7×7 with different exposures of K and $\text{Mo}(\text{CO})_6$. A TD spectrum for the K-free surface is shown in Fig. 1(a). When the surface is exposed with a high exposure of $\text{Mo}(\text{CO})_6$ ($\sim 3 \text{ Langmuir}$, $1 \text{ L} = 10^{-6} \text{ Torr s}$), a multilayer of physisorbed $\text{Mo}(\text{CO})_6$ molecules is formed on the surface. The TD spectrum is characterized by a single desorption peak at 200 K. The desorbed species is molecular $\text{Mo}(\text{CO})_6$; the mass 28 signal, as shown in the figure, is one of the cracking fragments of $\text{Mo}(\text{CO})_6$ in the mass spectrometer.^{2,3} When the same amount of $\text{Mo}(\text{CO})_6$ is exposed on the K preadsorbed surface, a broadening of the molecular desorption peak at 200 K is observed, as shown in Fig. 1(b). Furthermore, additional CO desorption peaks are observed between 250 and 500 K. These higher temperature desorption peaks dominate in the TD spectrum for a low $\text{Mo}(\text{CO})_6$ exposure ($\sim 0.6 \text{ L}$) on the K preadsorbed surface, as shown in Fig. 1(c). Molecular desorption is not observed at low exposures of $\text{Mo}(\text{CO})_6$ on the K preadsorbed surface.

Photon induced desorption spectra from Si(111)7×7 at 90 K under visible irradiation (550 nm) are shown in Fig. 2. The exposures of K and $\text{Mo}(\text{CO})_6$ for the spectrum in each panel are identical to those in the corresponding panel of Fig. 1. On the K-free surface photoreactions of $\text{Mo}(\text{CO})_6$ occur only with UV radiation; visible radiation does not induce desorption, as shown in Fig. 2(a). However, Figs. 2(b) and 2(c) show desorption of CO under visible irradiation on the K preadsorbed surface for both the high and low exposures of $\text{Mo}(\text{CO})_6$. (In the UV region desorption signal is more than 10 times higher on the K preadsorbed surface than the K-free surface.) The desorption signal reaches the maximum within a small fraction of a second, which is limited by the pumping speed of the UHV chamber, and decays with further irradiation. The lineshape of the desorption signal reveals that the photodesorption is not due to thermal effects. The nonthermal process is further confirmed by direct measurement of the temperature rise of the sample

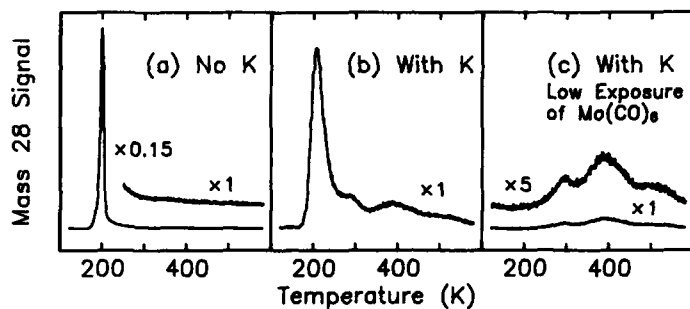


Figure 1. Thermal desorption spectra monitoring mass 28 for Mo(CO)_6 adsorbed on (a) the K-free, and (b)–(c) the K preadsorbed $\text{Si(111)7}\times\text{7}$ surface at 90 K. The same Mo(CO)_6 exposure (~ 3 L) was used for spectra (a) and (b), and a lower exposure (~ 0.6 L) was used for spectrum (c). A heating rate of 2 K/s was used.

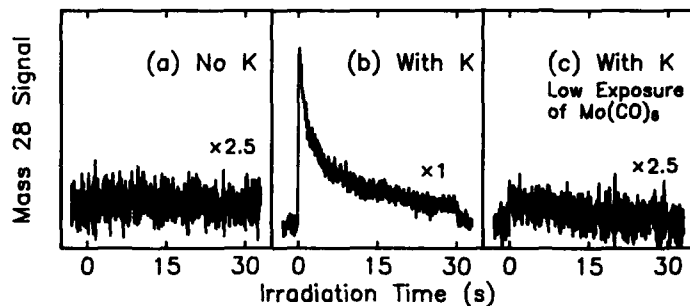


Figure 2. Photodesorption of CO from Mo(CO)_6 adsorbed on $\text{Si(111)7}\times\text{7}$ at 90 K. The K and Mo(CO)_6 exposures are the same as those in Fig. 1. Photon irradiation, started at 0 s and blocked at 30 s, is carried out in the visible region, centered at 550 nm and with a bandwidth of 65 nm.

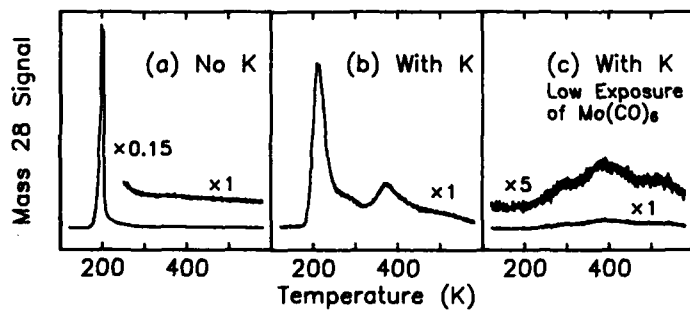


Figure 3. Thermal desorption spectra for Mo(CO)_6 on $\text{Si(111)7}\times\text{7}$ at 90 K after 10 min irradiation of visible photons at 550 nm. The K and Mo(CO)_6 exposures are the same as those in Fig. 1.

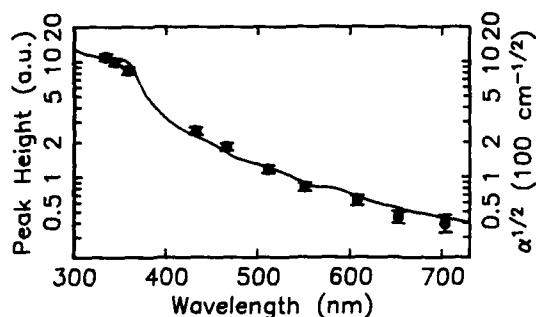


Figure 4. Peak height of the photodesorption signal as a function of photon wavelength. The surface at 90 K was coadsorbed with K and $\text{Mo}(\text{CO})_6$ ($\sim 3 \text{ L}$). The solid line is the square root of the absorption coefficient of Si.

($\sim 1 \text{ K}$). The photodesorption spectra for the K preadsorbed surface [Figs. 2(b) and (2c)] show a factor of 20 difference in the maximum peak height, while the $\text{Mo}(\text{CO})_6$ exposures are different only by a factor of 5. It can be immediately concluded that the photodesorption yield is larger at the higher $\text{Mo}(\text{CO})_6$ exposure.

Thermal desorption spectra taken after visible irradiation (550 nm) are shown in Fig. 3. The spectrum shown in Fig. 3(a) is recorded after irradiation of the K-free surface and is identical to the TD spectrum without irradiation [Fig. 1(a)]. This is expected since visible radiation does not induce any reaction of $\text{Mo}(\text{CO})_6$ on the K-free surface. However, changes in TD spectra are observed for the K preadsorbed surface. At the higher exposure of $\text{Mo}(\text{CO})_6$, a noticeable decrease in the peak height of the molecular desorption at 200 K is observed [Fig. 3(b)]. In addition, the intensity of the CO desorption peaks observed at higher temperatures is increased after photon irradiation. At the low exposure of $\text{Mo}(\text{CO})_6$, TD spectrum in Fig. 3(c) shows a slight decrease in the intensity of the CO desorption peaks compared to the spectrum without irradiation [Fig. 1(c)].

In sharp contrast to the K-free surface, a nonlinear power dependence is observed for the photodesorption of CO from $\text{Mo}(\text{CO})_6$ on the K preadsorbed Si(111)7 \times 7 surface. The peak height of the photodesorption signal at a fixed wavelength approximately follows the square root of the photon flux. In addition, the wavelength dependence of the photodesorption is shown in Fig. 4. The figure presents the measured peak height of the desorption signal as a function of photon wavelength. The data have been normalized to the square root of the photon flux absorbed by the Si substrate, i.e., $[I(1-R)]^{1/2}$, where I is the incident photon flux and R is the reflectivity. It is clear from the figure that the photodesorption occurs over a wide wavelength range (335–700 nm). The desorption intensity is higher under UV irradiation and monotonically decreases as the wavelength increases. The desorption signal is still clearly observed when radiation with wavelengths shorter than 830 nm is blocked by a longpass filter. These results indicate that the photoreactions of $\text{Mo}(\text{CO})_6$ on the K preadsorbed surface occur even with IR radiation of wavelengths longer than 830 nm.

DISCUSSION

Adsorption of $\text{Mo}(\text{CO})_6$ on Si(111)7 \times 7 at 90 K is modified by coadsorption with K. Thermal desorption of CO on the K preadsorbed surface is observed at 250–500 K. Desorption of CO in the same temperature range has been observed for the K-free Si(111)7 \times 7

surface after UV irradiation of adsorbed Mo(CO)_6 , and is attributed to the thermal dissociation of carbonyl fragments produced from UV irradiation.^{2,3} The observation of the high temperature desorption peaks on the K preadsorbed surface (without irradiation) indicates that Mo(CO)_6 molecules are at least partially dissociated during adsorption. In contrast, Mo(CO)_6 molecules are physisorbed on the K-free surface and thermally desorb at 200 K. The molecular desorption of Mo(CO)_6 is also observed on the K preadsorbed surface at high exposures of Mo(CO)_6 but not at low exposures. It can be concluded that low exposures of Mo(CO)_6 result in dissociative adsorption of Mo(CO)_6 on the K preadsorbed Si(111)7×7 surface at 90 K. A multilayer of physisorbed Mo(CO)_6 molecules is formed on top of the dissociated carbonyl fragments at higher exposures of Mo(CO)_6 .

Photoreactions of Mo(CO)_6 occur on the K preadsorbed surface. A higher photoreaction yield is observed at high Mo(CO)_6 exposures than at low exposures. Since a multilayer of physisorbed Mo(CO)_6 molecules is formed at high exposures, it is suggested that photoreactions mainly occur for physisorbed carbonyl molecules in the multilayer and not for carbonyl fragments in the monolayer. This is confirmed by the changes in the TD spectrum with high exposures of Mo(CO)_6 after photon irradiation; the intensity of the Mo(CO)_6 desorption is decreased and the intensity of the CO desorption is increased. Photon radiation dissociates Mo(CO)_6 molecules into CO and Mo(CO)_x ($0 < x < 6$). CO molecules are desorbed from the surface during irradiation; and resulting Mo(CO)_x can be thermally dissociated and give rise to CO desorption at 250–500 K.

Although it is likely that direct electronic excitation of Mo(CO)_6 molecules with UV radiation partially contributes to the photoreactions of Mo(CO)_6 observed on K the preadsorbed Si(111)7×7 surface, this mechanism can not fully explain the observed photoreactions. On the K preadsorbed surface photoreactions mainly occur for the physisorbed Mo(CO)_6 molecules. Modification of the electronic states for the physisorbed Mo(CO)_6 molecules is not expected to be appreciable. Therefore, direct electronic excitation should occur only with UV radiation, as is the case for Mo(CO)_6 both in the gas phase and adsorbed phase on the K-free Si(111)7×7 surface. However, photoreactions on the K preadsorbed surface are observed over a wide wavelength range extending to the IR. Moreover, in the UV region, where photoreactions occur on the surface both with and without K, the desorption signal is significantly higher for the K preadsorbed surface. Furthermore, an approximate square root power dependence at a fixed wavelength is observed for the photoreaction yield on the K preadsorbed surface, in contrast to a linear power dependence observed for the photoreaction yield due to direct electronic excitation of Mo(CO)_6 on the K-free surface.

A square root power dependence has been observed previously for the photoreactions of NO on Si(111)7×7⁷ and GaAs(110).⁸ The mechanism of photoreactions is attributed to the electron-hole pair excitation followed by coupling between the photogenerated charge carriers and the adsorbate-substrate complex. In addition, the peak height should follow the square root of the optical absorption coefficient of the substrate.⁹ The square root of the absorption coefficient, α , of Si¹⁰ is plotted as the solid line in Fig. 4. Good agreement with the experimental data is obtained. Both the power and wavelength dependences suggest that photogenerated charge carriers induce photoreactions of Mo(CO)_6 on the K preadsorbed surface.

It is desirable to determine whether it is the electrons or holes which induce the photoreactions. A consideration of the energetics rules out the possibility of holes. Photoreactions are observed over a wide wavelength range with the lowest photon energy at 1.5 eV (830 nm) in the present experiments. The upper limit for the energy of holes created by these photons is therefore 1.5 eV from the edge of the conduction band. Using the work function for the clean Si surface of 4.5 eV¹¹ (actually the work function

is much reduced after K deposition), the energy of these holes can not exceed 6.0 eV below the vacuum level. On the other hand, since $\text{Mo}(\text{CO})_6$ involved in the photoreactions are physisorbed on the surface and their electronic states are not expected to be appreciably modified, the energy of the highest occupied state of adsorbed $\text{Mo}(\text{CO})_6$ can be approximated by the ionization energy of $\text{Mo}(\text{CO})_6$ measured in the gas phase (8.4 eV¹²). Therefore, if the holes to be captured by the $\text{Mo}(\text{CO})_6$, their energies must be approximately 8.4 eV from the vacuum level, which is much greater than the upper limit of 6.0 eV for the energy of the photogenerated holes estimated above. Thus the observed photoreactions are attributed to an interaction with the photogenerated electrons, instead of the holes. The electron mediated mechanism has been observed for carbonyls adsorbed on solid surfaces via electronic stimulated dissociation¹ and in the gas phase via dissociative electron attachment.¹³

CONCLUSIONS

Coadsorption of K on $\text{Si}(111)7\times7$ has been found to enhance the photodissociation of physisorbed $\text{Mo}(\text{CO})_6$ molecules and the photodesorption of CO ligands. The photoreactions are observed over a wide wavelength range from the UV to IR. It is suggested that the photoreactions are initiated by photogenerated electrons.

ACKNOWLEDGMENTS

Support of this research by the Office of Naval Research Under Grant No. N00014-81-K-0505 is gratefully acknowledged. We would like to thank Professor J.H. Freed for the generous loan of the Xe arc lamp and F.-J. Kao for technical assistance. In addition, one of us (ZCY) is a recipient of the Materials Research Society Graduate Student Award.

REFERENCES

- ¹J.S. Foord and R.B. Jackman, *Chem. Phys. Lett.* **112**, 190 (1984); *Surf. Sci.* **171**, 197 (1986).
- ²C.E. Bartosch, N.S. Gluck, W. Ho, and Z. Ying, *Phys. Rev. Lett.* **57**, 1425 (1986); N.S. Gluck, Z. Ying, C.E. Bartosch, and W. Ho, *J. Chem. Phys.* **86**, 4957 (1987).
- ³J.R. Creighton, *J. Appl. Phys.* **59**, 410 (1986); C.-C. Cho and S.L. Bernasek, *J. Vac. Sci. Technol. A* **5**, 1088 (1987); J.R. Swanson, C.M. Friend, and Y.J. Chabal, *J. Chem. Phys.* **87**, 5028 (1987).
- ⁴F.G. Celii, P.M. Whitmore, and K.C. Janda, *J. Phys. Chem.* **92**, 1604 (1988).
- ⁵F.G. Celii, P.M. Whitmore, and K.C. Janda, *Chem. Phys. Lett.* **138**, 257 (1987); T.A. Germer and W. Ho, *J. Chem. Phys.* **89**, 562 (1988).
- ⁶Z. Ying and W. Ho, *Surf. Sci.* **198**, 473 (1988).
- ⁷Z. Ying and W. Ho, *Phys. Rev. Lett.* **60**, 57 (1988).
- ⁸S.K. So and W. Ho, *Appl. Phys. A* **47**, 000 (1988).
- ⁹Y. Shapira, R.B. McQuistan, and D. Lichtman, *Phys. Rev. B* **15**, 2163 (1977).
- ¹⁰D.E. Aspnes and A.A. Studna, *Phys. Rev. B* **27**, 985 (1983).
- ¹¹R. Bachmann, *Phys. Kondens. Mater.* **8**, 31 (1968).
- ¹²G.A. Junk and H.J. Svec, *Z. Naturforsch.* **23b**, 1 (1968).
- ¹³P.M. George and J.L. Beauchamp, *Thin Solid Films* **67**, L25 (1980); *J. Chem. Phys.* **76**, 2959 (1982).

Al PHOTODEPOSITION AND LIGHT-INDUCED NUCLEATION ON p-TYPE Si FROM TMA

J.E. BOURKE*, J. FLICSTRIN**, J.F. BRESSE**, J.P. ROMMELUERE*
and A.M. POUGNET**

* CNRS, Laboratoire de Physique des Solides, 92195 MEUDON,
France

** CNET, Laboratoire de Bagneux, 92220 BAGNEUX, France

ABSTRACT

Photodecomposition of trimethylaluminum (TMA) flowing with H_2 on p-type Si under UV irradiation is shown to be exclusively a reaction confined to surface species. Thus photonucleation and photodeposition of Al on Si is controlled either by Si-H or Si-O and Si-OH bonds. In the regions where Si-O and Si-OH are present, Al-O forms, which inhibits Al deposition either directly or via the adsorption of C containing photoproducts. In the other regions where Si is H terminated, it is assumed that H_2 adsorbs dissociatively on Al clusters, thus leading to the formation followed by the desorption of methane from the adsorbed phase. For this reason, Al thin films are C contamination free.

INTRODUCTION

In the search for metallization processes for large scale integrated (LSI) devices, the use of lasers or monochromatic incoherent light sources to induce chemical reactions at gas-solid interfaces, may offer attractive potential applications in a low-temperature, high-resolution process [1,2]. Al is one of the most important metals used in integrated circuit (IC) technology. However, Al deposition constitutes a challenge to be overcome for both technological and scientific reasons. First of all, oxygen and carbon contamination are the main problems to be solved when Al is deposited using TMA as the metalorganic parent molecule. TMA has the highest vapor pressure at room temperature among the various known metalorganic parent gases. From a fundamental viewpoint, it is essential for further process development to devote much more effort to the understanding of the mechanisms of photochemical or thermochemical deposition and particularly of photonucleation where the surface adsorbates can play the major role [3,4].

The present paper aims to give a better insight into the photolytic and the pyrolytic processes of decomposition of TMA flowing along with hydrogen carrier gas, by combining ex situ [5] and in situ [3,6-9] analytical techniques. The role of H_2 (by changing the flux) as well as that of O_2 (by working with a normal-vacuum and a high-vacuum cell) will be emphasized.

EXPERIMENTAL

Experimental apparatus

The experimental set-up for the deposition by photo-induced chemical processing is composed of a gas feeder which can

be connected to two different cells (a normal-vacuum cell and a high-vacuum cell) and any of three light sources: a visible laser, a UV lamp or a UV laser.

The gas handling system has been described earlier [5]. Both cells are stainless steel, vacuum-tight cells. The normal-vacuum one, which can be pumped out using a sorption pump to 10^{-3} Torr, has an optical length of 13mm, a volume of 60 ml and a 1.5mm thick fused silica window. The high-vacuum one, which can be pumped out using an ion pump to 10^{-9} Torr (see Fig. 1), has an optical length of 17mm, a volume of 0.7l and a 5mm thick synthesized-quartz window.

The electronic grade TMA, which is purified under vacuum [10], is carried by hydrogen and further diluted [11]. The mole fraction of TMA in H_2 is allowed to vary in the range $4 \cdot 10^{-4}$ - $1.2 \cdot 10^{-2}$ [11].

The scanning speed of the laser beams along the x-axis can vary between 2 and 100 $\mu\text{m/s}$ [5, 11].

The laser used as the source of visible radiation is a cw monomode (514.5 nm line) Ar ion laser with a maximum available output power of 2 W. The laser beam is focused on the Si surface by means of 80 mm or 40 mm focal length lenses. Typical gaussian radii are 25 μm and 16.5 μm , respectively. The experimental set-up concerning the UV lamp (low pressure mercury lamp emitting at 254nm) and the cw UV laser (intracavity frequency doubler emitting at 257nm) have been described earlier [5,11].

Experimental procedure

Since TMA reacts spontaneously with O_2 and H_2O , even in traces, the gas handling system is baked and flushed with N_2 just after the introduction of the sample into the cell to lower the dew point below -76°C (H_2O concentration less than 1ppm vol). Then, so as to remove residual gas impurities and passivate the cells, the cells are pumped out using either the sorption pump or the ion pump in the case of the high-vacuum cell, and flushed with pure H_2 . Experimental conditions have been listed previously [5,11].

RESULTS

Let us summarize the previous results obtained by using the normal-vacuum cell [5, 11]. From the mechanistic point of view, there is no real difference between the reactions induced by the UV lamp and those induced by the UV laser in the low fluence regime [11]; these latter results will be skipped in the present paper.

Reactions induced by the UV lamp

When a silicon substrate, placed in flowing TMA, is exposed to the UV lamp for at least 30 min, its surface is subject to a microscopic change which, analyzed by SEM, results in the nucleation of a fine-grain Al structure [5, 12]. Obviously photonucleation effects are very sensitive to the local chemical nature of the substrate surface (O atom or -OH group).

Thus, the sample preparation is crucial. The fine-grain structure is found to be made up mostly from spherical caps and a few spheroids, the former presumably being the sign of heterogeneous nucleation resulting from photodissociation of adsorbed TMA molecules, whereas the latter are associated with homogeneous nucleation in the gas phase [12]. Ex situ Auger microanalysis indicates the presence of metallic Al, of oxidized Al (Al-O) and of non-carbidic carbon [5]. The carbon containing species, which can be also observed by SEM + EDAX, nucleate on the surface and locally inhibit further coalescence and growth. However, this inhibiting effect is observed to decrease when TMA is more diluted in H₂ [10].

Sequential reactions induced by the UV lamp and the cw visible laser

Following the work of Tsao and Ehrlich [13], we used this two-step, two-source process for direct writing of Al on Si [5]. The first step corresponds to a prenucleation step, while the second one corresponds to a continuous growth step. By using the high-vacuum cell compared to the normal-vacuum cell for the previous studies [5,11], we obtain the Al lines shown in Fig. 2. Both lines have been written with the same scanning speed ($v = 72 \mu\text{m/s}$) and by using the same mole fraction of TMA in H₂ ($3.4 \cdot 10^{-3}$). The line shown in the upper part of the figure is drawn with a gaussian radius of $25 \mu\text{m}$ and a laser power of 1.7W whereas the line of the lower part is drawn with a gaussian radius of $16.5 \mu\text{m}$ and a laser power of 1.1 W. Auger microanalysis performed with Ar ion sputter profiling on the deposited lines indicates metallic Al, Al-O, C and O signals in atomic concentration ratio 37:3:12:48. Thus, even though Al-O is very weak compared to previous work, the O signal is high, which is unexpected in our high-vacuum conditions.

Fig. 3 shows an Al line ($v = 72 \mu\text{m/s}$, $\text{CTMA} = 3.4 \cdot 10^{-3}$, $P = 1.3\text{W}$, $\omega = 16.5 \mu\text{m}$) which is interrupted. The lower part of Fig. 3 is a magnified view of the interrupted region and exhibits a grain structure with random distribution which, analyzed by Auger microspectroscopy in the integral mode, is clearly made up of Al-O. Thus Al-O (presumably Al₂O₃) grain structure apparently inhibits Al film deposition (Al does not stick on Al₂O₃).

Finally by diluting TMA in H₂, we have observed a change in Al grain size. Fig. 4 shows that by decreasing the mole fraction of TMA in H₂ ($1.17 \cdot 10^{-3}$ in the upper part, $4.8 \cdot 10^{-4}$ in the lower part), the typical grain size decreases from $2\text{-}3 \mu\text{m}$ to less than $0.1 \mu\text{m}$. This result should be correlated to the change in deposited film morphology (mirrorlike with excess H₂ and granular without H₂) observed by other workers [8].

DISCUSSION

Higashi and Rothberg [3,8], using optoacoustic infrared absorption, have shown that about one monolayer of hydrogen bonded -OH groups is adsorbed on silica or sapphire substrates. More recently Chabal et al [14], using multiple-internal-reflection infrared spectroscopy, have shown that chemically

oxidized and subsequently HF stripped Si surfaces are terminated mostly with hydrogen (monohydride and dihydride termination). Thus in our experiments, it is likely that we are faced with Si-H, SiH₂ and Si-OH bonds on Si (100) surface. TMA, when introduced into the cell, can be chemisorbed on the hydroxylated oxides forming locally at least one monolayer of Al(CH₃)₃ adsorbates [3].

Moreover the carrier gas H₂ flowing with TMA under atmospheric pressure may have three major effects:

(1) H₂ limits the gas phase mean free path for photoproducts to less than 300 Å, a value that is much smaller than the radii of the laser beams.

(2) H₂ may presumably adsorb dissociatively on Al at room temperature, as it does on transition metals [15].

(3) The flow of TMA along with H₂ induces, in our conditions of light source fluences, a permanent replenishment of parent molecules at the center of the photoreaction zone.

Combining all these experimental facts, it can be inferred that photoreactions will be for the most part confined to surface species (chemisorbed and physisorbed phases).

Reactions induced by the UV lamp

It is easily demonstrated that the UV lamp, due to its low fluence intensity, induces a negligible temperature rise at the substrate surface. Thus at 254nm, pure photolysis occurs which is consistent with the non-carbidic carbon observed in the deposits. In the gas phase, it has been shown independently [7,9] at 248 nm that Al and a small amount of Al-CH₃ and of CH₃ and a tiny amount of CH are generated according to the cascade one-photon absorption process. In the adsorbed phase, the amount of Al-CH₃ is slightly higher [9]. Thus the gas phase contributions are not significant and at 254nm the photodecomposition of TMA adsorbed on the Si substrate is supposed to be the primary source of deposited Al, as was inferred by other investigators [8]. More precisely it has been observed that organoaluminum adsorbates are insignificantly dissociated at 248nm [7], so that methyl radicals cannot be removed easily from the surface [3,6]. This explains the small generation of methane as observed from mass spectroscopic analysis and the quite high level of C concentration in the deposited films [8]. One must infer from our experiments that the presence of H radicals originating in the dissociative adsorption of molecular hydrogen on existing Al clusters makes possible, in the physisorbed layers in the vicinity of Al clusters, the following reaction :



Thus methane is formed and desorbs readily at room temperature, which leads to the elimination of methyl radicals. As the residence time of H on the surface is expected to be very short [16], the higher the flux of H₂, the more efficient the elimination of methyl radicals. On the contrary, in the surface areas where silicon oxide or Si-OH are present, Al atoms getter oxygen or -OH groups and form Al-O bonds. Unfortunately C containing photoproducts chemisorb readily on Al-O and further inhibit Al nucleation and deposition.

Fig. 1. Schematic diagram of the high-vacuum cell.

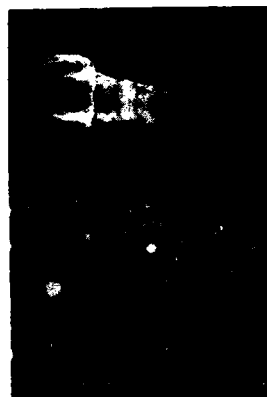
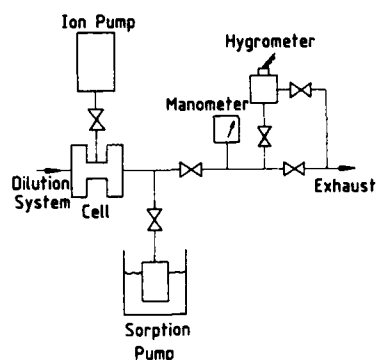


Fig 3. Upper view: SEM micrograph of an Al line using UV lamp+visible laser: $v = 72\mu\text{m/s}$, $\text{CTMA} = 3.4 \cdot 10^{-3}$, $P = 1.3\text{W}$, $\omega = 16.5\mu\text{m}$. Lower view: magnified SEM micrograph of the interrupted region of the line.

Fig. 2. Scanning electron micrographs of Al lines using UV lamp + visible laser. Upper view: $v = 72\mu\text{m/s}$, $\text{CTMA} = 3.4 \cdot 10^{-3}$, $P = 1.7\text{W}$, $\omega = 25\mu\text{m}$. Lower view: $v = 72\mu\text{m/s}$, $\text{CTMA} = 3.4 \cdot 10^{-3}$, $P = 1.1\text{W}$, $\omega = 16.5\mu\text{m}$.

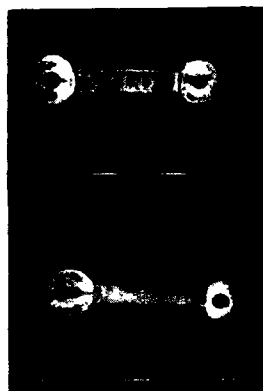


Fig. 4. SEM micrographs of two Al lines using UV lamp+visible laser. Upper view: $\text{CTMA} = 1.2 \cdot 10^{-2}$. Lower view: $\text{CTMA} = 4.8 \cdot 10^{-4}$. All other parameters are identical.

Sequential reactions induced by the UV lamp and the cw visible laser

In this two-step, two-light-source process, the maximum temperature induced by the visible laser at the laser spot center on the Si surface ranges from 70°C up to 180°C, depending upon the laser power and the focal length used. In the case of Fig. 2, the temperature induced at the center of both Al lines is about 114°C. Thus most of the physisorbed TMA adlayers desorb, as observed from a thermal desorption experiment [8], which means that the Al photodeposition proceeds via the photodissociation of the chemisorbed TMA monolayer. An argument similar to that developed in the preceding section explains why an Al line can be stopped and replaced by the fine grain Al-O structure (see Fig. 3).

Finally the decrease of Al grain size inside a written line when dilution of TMA in H₂ increases (see Fig. 4) may have the same origin as the change in morphology of the Al deposit (mirrorlike) when processing with excess H₂ under ArF irradiation [8]. It is thought that the H₂ flux reacts with surface Al, thus forming AlH₃ which promotes Al cluster formation [8]. This is consistent with a smooth sample surface allowing shallow oxide penetration [8].

CONCLUSION

Photodeposition of Al on Si substrates from TMA flowing in H₂ using a UV lamp or a combination of a UV lamp and a cw visible laser involves the photodecomposition of adsorbed TMA. Consequently this deposition may be controlled either by surface silicon oxide and surface hydroxylated groups or through a surface reaction with flowing H₂. In the case of Si-O and Si-OH, there is a possibility of Al-O formation which inhibits Al film nucleation and deposition either directly or indirectly via the adsorption of carbon containing photoproducts. In the surface areas with negligible Si-O and Si-OH bonds, it is assumed that H₂ adsorbs dissociatively on Al clusters, which makes possible a reaction with methyl radicals in the adsorbed phase, thus explaining the elimination of carbon in the deposited film by desorption of methane. In the same areas, the formation of aluminum hydride by contact of H₂ with surface Al may lead to the increase of the Al nucleation center density.

ACKNOWLEDGEMENTS

This work has been partly supported by a contract from CNET-Meylan. The authors would like to acknowledge Mr J.M. LAROCHE, Mr R. DRUILHE and Mr B. FENAILLE for their respective support in the experimental part and the characterization. One of the authors (JEB) has benefited from stimulating discussions with Dr G.S. HIGASHI, Dr Y.J. CHABAL, Dr T.E. ORLOWSKI, Dr T. BEUERMANN and Dr S.J.C. IRVINE.

REFERENCES

1. D.J. Ehrlich and J.Y. Tsao, J. Vac. Sci. Technol. B1, 969 (1983).
2. R.M. Osgood and H.H. Gilgen, Ann. Rev. Mater. Sci. 15, 549 (1985).
3. G.S. Higashi and L.J. Rothberg, J. Vac. Sci. Technol. B3, 1460 (1985); Appl. Phys. Lett. 47, 1288 (1985).
4. E. Sanchez, P.S. Shaw, J.A. O'Neill and R.M. Osgood, Chem. Phys. Lett. 147, 153 (1988); P.S. Shaw, E. Sanchez, Z. Wu and R.M. Osgood, Chem. Phys. Lett. 151, 449 (1988).
5. J.E. Bourée, J. Flicstein and Y.I. Nissim, in Photon, Beam and Plasma Stimulated Chemical Processes at Surfaces, MRS Symp. Proc. 75, 129 (1987); J.E. Bourée and J. Flicstein, NATO ASI Series E139, 121 (1988).
6. G.S. Higashi, J. Chem. Phys. 88, 422 (1988).
7. T. Motooka, S. Gorbatskin, D. Lubben, D. Eres and J.E. Greene, J. Vac. Sci. Technol. A4, 3146 (1986); D. Lubben, T. Motooka, J.F. Wendelken and J.E. Greene, NATO ASI Series B (1989), to be published.
8. T.E. Orlowski and D.A. Mantell, in Laser and Particle-Beam Chemical Processing for Microelectronics, MRS Symp. Proc. 101, 165 (1988); in Laser and Particle-Beam Chemical Processes on Surfaces, MRS Symp. Proc. 129 (1989), to be published.
9. Y. Zhang and M. Stuke, J. Cryst. Growth 93, 143 (1988); T. Beuermann and M. Stuke, Appl. Phys. B (1989), to be published.
10. J. Flicstein, J.E. Bourée, J.F. Bresse and A.M. Pougnet, in Laser and Particle-Beam Chemical Processing for Microelectronics, MRS Symp. Proc. 101, 49 (1988).
11. J.E. Bourée and J. Flicstein, NATO ASI Series B198, 33 (1989); J.E. Bourée and J. Flicstein, in Laser and Particle-Beam Chemical Processing for Microelectronics, MRS Symp. Proc. 101, 55 (1988).
12. J. Flicstein and J.E. Bourée, Appl. Surf. Sci., 36, 443 (1989).
13. J. Y. Tsao and D.J. Ehrlich, Appl. Phys. Lett. 45, 617 (1984); J. Cryst. Growth 68, 176 (1984).
14. V.A. Burrows, Y.J. Chabal, G.S. Higashi, K. Raghavachari and S.B. Christman, Appl. Phys. Lett. 53, 998 (1988); Y.J. Chabal, G.S. Higashi, K. Raghavachari and V.A. Burrows, J. Vac. Sci. Technol. A7, 2104 (1989).
15. L. Schlapbach, NATO ASI series B 136, 397 (1986).
16. G.S. Higashi, private communication.

UV ENHANCEMENT OF SURFACE CATALYTIC POLYMERIZATION OF ETHYLENE

PARUL VORA PUROHIT, MORDECHAI ROTHSCHILD, AND DANIEL J. EHRLICH
Lincoln Laboratory, Massachusetts Institute of Technology,
244 Wood Street, Lexington, MA 02173

ABSTRACT

The polymerization of ethylene on surfaces sequentially dosed with TiCl_4 and trimethylaluminum was studied by Fourier transform infrared spectroscopy. The polymer film was observed *in situ* as a function of time and under the influence of 254-nm cw radiation. The rate of polymerization and the saturation thickness of the polyethylene are strongly dependent on the order of dosing and the partial pressures of the reactants that form the catalyst. UV enhancement of polymerization was demonstrated to occur through two separate photochemical channels: gas-phase photolysis of the reactants and solid-phase chemical transformation of a noncatalytic thin film.

INTRODUCTION

The UV photodeposition of a thin film of a catalyst is among the more complex photoprocesses from a molecular and structural standpoint. In earlier studies [1,2] it was shown that the 257-nm photolysis of a gaseous mixture of TiCl_4 and trimethylaluminum (TMA) can form an organometallic thin film which, upon subsequent exposure to ethylene (C_2H_4) vapor induces catalytic polymerization at room temperature. This thin film was shown to behave similarly to a Ziegler-Natta catalyst [3-6].

In this paper, we describe an investigation of the mechanisms whereby UV irradiation enhances the catalytic activity of a film formed by dosing surfaces with TiCl_4 and TMA. The study was performed *in situ* with Fourier transform infrared (FTIR) spectroscopy with and without UV stimulation. FTIR spectroscopy, if used in conjunction with an internally reflected element (IRE) can be a powerful surface sensitive technique which allows for the investigation of very thin films on the IRE. It is demonstrated that gas-phase photolysis of TiCl_4 and TMA, as well as solid-state photochemistry contribute to the formation of a catalyst film, which can induce polymerization of ethylene.

EXPERIMENTAL

The experimental setup consists of a vacuum-tight stainless steel cell placed in an FTIR spectrometer, and connected to a gas handling and a pumping system. Pumping is performed with a

mechanical pump to a base pressure ~ 10 mTorr. The IRE and a UV-grade fused silica flat serve as two opposing sides of the cell. UV radiation at 254 nm from a low-pressure mercury lamp is introduced to the cell through the fused silica window.

The experimental procedure consists of sequential dosing of the IRE with TiCl_4 and TMA, and then exposing it to C_2H_4 . Each dosing stage is followed by pumping. The UV lamp is turned on and off at selected times during the experiment. Any polymerization on the surface of the IRE is monitored *in situ* through the absorption spectrum of the growing thin film. A typical example of the polymer spectrum and its temporal evolution is shown in Fig. 1. The sharp double peak at 2851 and 2919 cm^{-1} represents the C-H symmetric and antisymmetric stretching frequencies of polyethylene, respectively [7], and is the signature of a polymer film growing on the surface of the IRE. The procedure of sequential dosing of reactants to form the catalyst is in contrast with the co-dosing in the earlier work [1,2]. It enables the isolation of the effects of several chemical and photochemical processes which would otherwise take place simultaneously.

RESULTS

The thin film formed on the IRE by the sequential dosing described above, has catalytic properties even in the absence of UV irradiation. Its catalytic activity, as determined by polymer growth, strongly depends on experimental conditions. In particular, the order of dosing plays a dramatic role on the formation of the catalyst. If the first dosant is TMA, no subsequent polymerization is seen without UV, even at the highest dosing pressures used in our studies (Fig. 2). When the first dosant is TiCl_4 , however, a catalyst is indeed formed on the surface, as evidenced by polymer growth when the IRE is exposed to C_2H_4 vapor. The initial rate of polymerization and the saturation thickness of the polymeric thin film are complex functions of dosing pressures and pressure ratios, as shown in Fig. 2. In general, the higher the dosing pressures the more pronounced the polymerizing effects of the metalorganic thin film.

UV irradiation at 254 nm can enhance polymer formation, if it is applied at the appropriate stage in the sequence dose-pump-dose-pump-polymerize. Figure 3 shows two such instances. In the first case, TiCl_4 at a pressure of 2 Torr is added to the cell followed by TMA at 9 Torr. UV is turned on during TMA dosing, and in an independent experiment during TiCl_4 dosing. The presence of UV during TMA dosing has no effect, whereas the rate of polymerization of ethylene is considerably enhanced when the UV is on during TiCl_4 dosing (Fig. 3, curves (a) and (b)). In the second case, the role of the UV is studied when dosing with TMA occurs before the dosing with TiCl_4 . As mentioned above, no polymerization without UV takes place in this case.

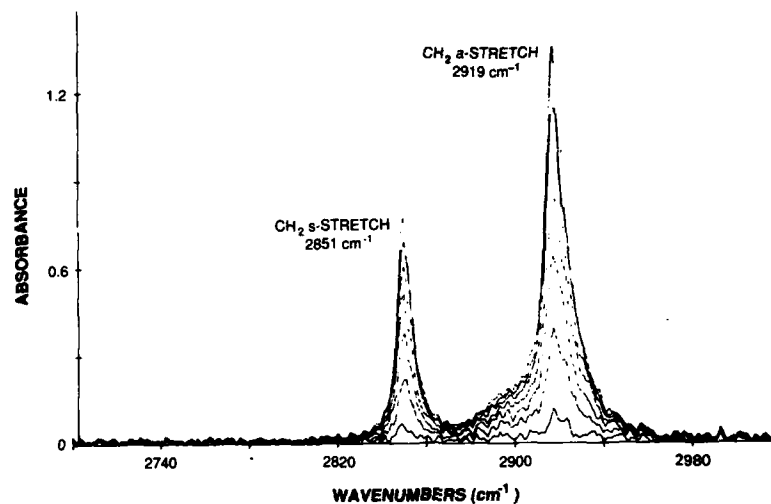


Fig. 1 Representative IR absorption spectra in the 2700- to 3020-cm⁻¹ range taken at 10-min intervals. The double peaks at 2851 and 2919 cm⁻¹ indicate the presence of polyethylene on the IRE surface. The growth of the polymer film is manifested by the increasing amplitude of these peaks. From independent measurements, an absorbance value of 1.0 correlates with a film thickness of 0.45 μm .

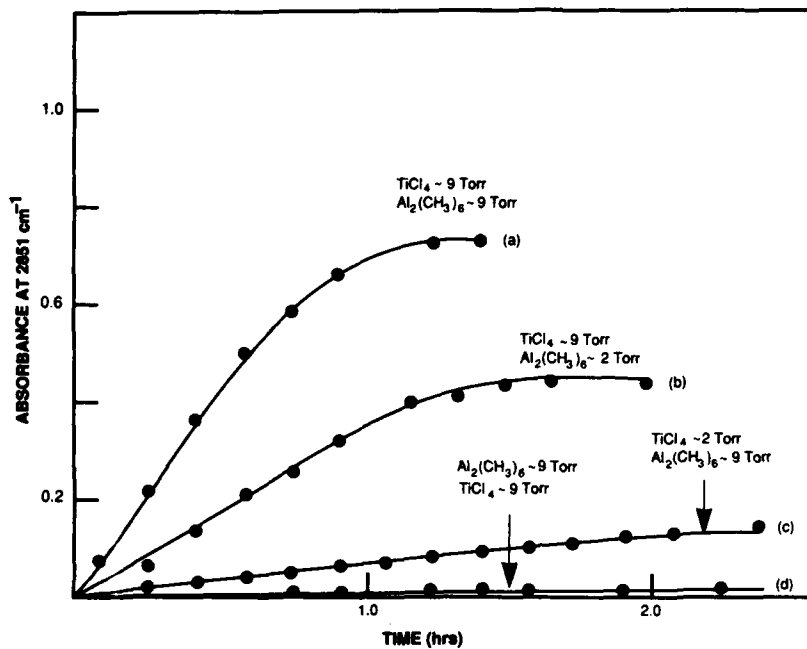
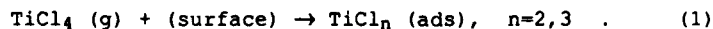


Fig. 2 The growth of polyethylene as a function of time for various different experimental conditions without the presence of UV. Curves (a)-(c) represent the growth when TiCl_4 was the first dosant whereas curve (d) indicates the growth when TMA was the first dosant.

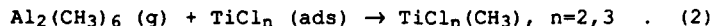
The UV is turned on during the presence of ethylene in the chamber, that is after the formation of a thin film. As gaseous ethylene does not absorb at 254 nm, any effect on the polymerization must occur due to photochemistry of the film. As seen in curve (c) of Fig. 3, polymerization does occur after the UV is turned on; this indicates UV enhanced surface effects. Further experiments where the UV is turned on during TMA and TiCl_4 dosing shows similar effects as observed earlier, i.e., there is no enhancement if the UV was turned on during TMA dosing but there is significant enhancement if the UV is turned on during TiCl_4 dosing.

DISCUSSION

The experimental observations presented above are interpreted within accepted models of Ziegler-Natta type catalysts and the photochemical properties of the precursors TiCl_4 and TMA. Specifically, UV enhancement of polymerization can occur via two separate channels: gas-phase photolysis of TiCl_4 (absorption cross section $\sim 5 \times 10^{-19} \text{ cm}^2$ at 254 nm), and solid state photochemistry of a titanium chloromethyl thin film. Because the effects studied here are partly heterogeneous reactions, information on the chemical nature of any adsorbates is also of importance. Therefore we observed the spectrum of the adsorbed species following TiCl_4 dosing, but before exposure to TMA. The characteristic Ti-Cl stretch frequency of gaseous TiCl_4 , around 500 cm^{-1} , is reduced by $\sim 20 \text{ cm}^{-1}$ in the adsorbate. We interpret this result as indicative of partial dechlorination [8,9], possibly as a result of chemical reactions with surface contaminants such as residual water:



The addition of gaseous TMA to this adsorbate probably yields a titanium compound of the form shown below.



The compound indicated in Eq. (2) has been shown to be a catalyst by Gray et al. [6] and thus polymerization takes place as shown in Fig. 2, curves (a)-(c). The enhancement of catalyst formation by UV irradiation during TiCl_4 dosing (compare Fig. 3, curves (a) and (b)), is interpreted as a result of photolytic dechlorination of gaseous TiCl_4 , and the formation of additional TiCl_2 and TiCl_3 on the surface. The absence of any noticeable UV enhancement during TMA dosing is similarly understood as the result of negligible photochemical decomposition of TMA vapor ($\sigma < 5 \times 10^{-21} \text{ cm}^2$).

When dosing with TMA occurs first, TMA is stripped of methyl radicals and an unsaturated aluminum compound resides on the surface [10,11]:

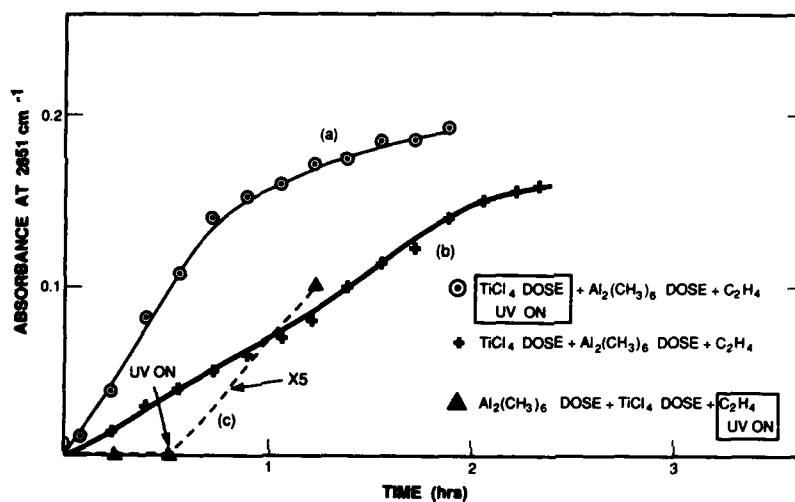
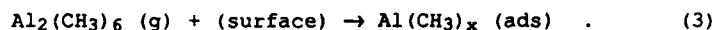
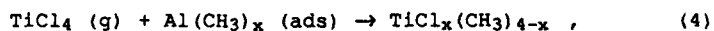


Fig. 3 The effects of UV on polymer growth. Curves (a) and (b) represent the growth with and without UV on during TiCl_4 dosing, respectively. Curve (c) shows the formation of the polymer in the case when dosing by TMA was first. Here, the UV was off for the first 0.5 hrs, during which no polymerization was observed; the lamp was then turned on (see arrow), and growth of the polymer film was noted.



Upon exposure of this adsorbate to TiCl_4 , a surface Ti compound may be formed, in which the Ti has fully saturated bonds, and which therefore does not have catalytic properties as evidenced by the absence of polymer formation in Fig. 2 curve (d):



with $x = 1-3$. In the presence of UV that has been turned on after the formation of this non-catalyst, a solid-phase photochemical reaction apparently takes place, which results in the formation of a catalytically active, coordinatively unsaturated Ti compound, and UV enhanced surface polymerization takes place (Fig. 3, curve (c)).

SUMMARY

Polymerization of ethylene due to catalytic action of a thin film formed by sequential dosing of TiCl_4 and TMA was observed with and without UV radiation. Catalytic activity was shown to depend strongly on the order of dosing and gas pressures. UV enhancement of the rate of polymerization was seen to occur through gas phase decomposition of TiCl_4 and by surface photochemistry of a non-catalytic film. However, UV irradiation of gaseous or adsorbed TMA alone had no effect upon the subsequent activity of the film.

ACKNOWLEDGMENTS

We would like to thank A. K. McIntosh and T. J. Pack for their expert technical assistance. This work was sponsored by the Defense Advanced Research Projects Agency and by the Department of the Air Force, in part under a specific program supported by the Air Force Office of Scientific Research.

REFERENCES

1. J. Y. Tsao and D. J. Ehrlich, *J. Chem. Phys.* **81**, 4620 (1984).
2. J. Y. Tsao and D. J. Ehrlich, *Appl. Phys. Lett.* **46**, 198 (1985).
3. W. Cooper, in *Progress in High Polymers*, Vol. 1, edited by J. C. Robb and F. W. Peaker (Heywood and Co., London, 1961) pp. 79-340.
4. J. Boor, Jr., *J. Polym. Sci. C* **1**, 257 (1963).
5. A. P. Gray, A. B. Callear, and F. H. C. Edgecombe, *Can. J. Chem.* **41**, 1502 (1963).

6. G. Natta and F. Dannusso, Stereoregular Polymers and Stereospecific Polymerizations, Vols. 1 and 2 (Pergamon, Oxford, 1967).
7. T. Shimanouchi, Tables of Molecular Vibrational Frequencies, Vol. 1, (NSRDS-NBS3, 1972), p. 222.
8. W. B. Person and W. B. Maier, J. Chem. Phys. 62, 297 (1978).
9. T. C. Devore and T. N. Gallaher, High Temp. Sci. 16, 269 (1983).
10. G. S. Higashi and L. J. Rothberg, Appl. Phys. Lett. 47, 1288 (1985).
11. G. S. Higashi, L. J. Rothberg and C. G. Fleming, Chem. Phys. Lett. 115, 167 (1985).

PART VI

Laser-Induced Chemical Etching

SELECTIVE PHOTOCHEMICAL DRY ETCHING OF COMPOUND SEMICONDUCTORS:
ENHANCED CONTROL THROUGH SECONDARY ELECTRONIC PROPERTIES

CAROL I. H. ASHBY*

*Sandia National Laboratories, P. O. Box 5800, Albuquerque, NM 87185

ABSTRACT

When laser-driven etching of a semiconductor requires direct participation of photogenerated carriers, the etching quantum yield will be sensitive to the electronic properties of a specific semiconductor material. The band-gap energy of the semiconductor determines the minimum photon energy needed for carrier-driven etching since sub-gap photons do not generate free carriers. However, only those free carriers that reach the reacting surface contribute to etching and the ultimate carrier flux to the surface is controlled by more subtle electronic properties than the lowest-energy band gap. For example, the initial depth of carrier generation and the probability of carrier recombination between the point of generation and the surface profoundly influence the etching quantum yield. Appropriate manipulation of process parameters can provide additional reaction control based on such secondary electronic properties. Applications to selective dry etching of GaAs and related materials are discussed here.

INTRODUCTION

Lasers have been used in a variety of ways to produce spatially localized etching of semiconductors. The simplest application of the laser beam is as a highly localized source of heat to increase the rate of a thermally activated chemical reaction. A second application uses the laser photons to photolyze a reactant precursor molecule to produce a highly reactive species that reacts more rapidly with the semiconductor material than does the precursor. Both these approaches have been demonstrated to produce highly localized etching (1), but their ability to etch compositionally similar materials selectively is limited by the chemical selectivity of the particular chemical reaction employed. For many materials, such as the different stoichiometric compositions of a ternary compound semiconductor, differences in chemical reactivity are so small as to be essentially nonexistent. In contrast, laser-driven processes that require the direct participation of photogenerated carriers (electrons and/or holes) can be made more selective than expected from simple chemical selectivity since one can also employ the specific electronic properties of the semiconductor to control the carrier-driven reaction. The primary electronic property of a semiconductor for carrier-driven etching is the lowest band-gap energy, since this determines the minimum photon energy for free-carrier generation and, therefore, etching to occur. However, other secondary electronic properties, such as the depth profile of photon absorption, field-induced carrier drift, and carrier recombination can also play significant roles in determining the efficiency of carrier-driven photochemical etching for a specific semiconductor material. It is this latter dependence on secondary electronic properties that is the subject of this paper.

Carrier-driven photochemical etching processes can be divided into two broad categories: photoelectrochemical (PEC) and photochemical (PC). In a PEC process, the semiconductor serves as one electrode of an electrochemical cell and the other electrode is generally a metal counter-electrode. Because the etching of the semiconductor proceeds through the oxidation portion of the redox reaction with reduction occurring at the counter-electrode, PEC processes are generally restricted to n-type materials; p-type materials require no photons to drive the corresponding reaction. An external voltage is applied to the cell to drive the flow of minority carriers (holes) to the surface of the semiconductor electrode, thereby producing etching. An ample supply of holes is provided by the creation of electron-hole pairs through the absorption of photons with energies greater than or equal to the band-gap energy. The applied electric field is chosen

to efficiently sweep photogenerated holes to the surface but to simultaneously preclude significant etching in the absence of photogenerated holes. Because the applied field plays a dominant role in controlling hole flux to the surface, PEC processes are not as strongly influenced as PC processes by some of the secondary electronic properties of the semiconductor, as will be made clear later.

In contrast to PEC processes, PC processes do not inherently employ an external voltage source to drive etching. In most cases, no external voltage source is employed. Both oxidation and reduction occur at the semiconductor surface, with the semiconductor being oxidized and the etchant species being reduced. Consequently, both n-type and p-type materials can be etched with a suitable reactant. Without an externally applied field to dominate carrier flow to the surface, PC processes are more responsive to the secondary electronic properties than are PEC processes. The relationships between these properties, processes parameters, and selective etching will be discussed below using the carrier-driven etching of GaAs and Ga(As,P) by Cl atoms to exemplify the selectivity that is achievable through electronic-property control.

EXPERIMENT

GaAs and Ga(As,P) were etched using Cl atoms generated 10 cm upstream from the semiconductor sample in a d.c. glow discharge. No current due to charged particles from the plasma was detected at the sample in reactions that did not involve deliberate application of a bias voltage. Discharge parameters were selected to produce negligible thermal etching during the course of 60-minute photochemical etching reactions. Under the conditions employed (2), the carrier-driven reaction is essentially independent of substrate temperature between 353 and 383 K. Most reactions reported here were performed at 363 ± 6 K. For wavelength-dependent studies, 514.5-nm (2.41 eV) photons from an Ar-ion laser and 607-nm to 613-nm (2.04 to 2.02 eV) and 766-nm (1.62 eV) photons from a cw dye laser were employed (3,4,5,6). Photon fluxes were selected to produce an etched depth that is linear in photon fluence; the calculated temperature rise at beam center is less than 10 degrees unless otherwise specified (2). Samples of GaAs were implanted with 40-keV ^{11}B ions to fluences of 10^{10} , 10^{12} , and 10^{14} ions/cm² (5,6). Further experimental details are reported in the appropriate references. The quantum yield is defined as the number of atoms removed per incident photon.

DISCUSSION:

For an n-type semiconductor under steady-state illumination, the general behavior of the minority carrier holes can be described by the form of the continuity equation given as Eqn. 1.

$$D_p \frac{d^2 p}{dx^2} - \frac{d(\mu p F)}{dx} + \frac{\alpha I_0}{h\nu} \exp(-\alpha x) - \frac{(p-p_0)}{\tau(x)} = 0 \quad (1)$$

Here p is the hole concentration at a given depth, x , D the hole diffusivity, μ the hole mobility, F the electric field at x , α the absorption coefficient at the excitation wavelength, I_0 the incident intensity in ergs/cm²-sec, p_0 the equilibrium hole concentration in the bulk, and τ the hole recombination lifetime. Whether a carrier-driven reaction proceeds with a substantial quantum yield depends on the minority carrier flux to the surface and the surface lifetime of those carriers that reach the surface. The concentration of holes as a function of depth, $p(x)$, is determined by the balance between diffusion away from the surface due to the concentration gradient, field-induced drift, the depth profile of initial carrier photogeneration, and carrier recombination; these factors

determine the minority carrier surface concentration that is finally available to drive a chemical reaction. This can be calculated for specific materials and process conditions from Eqn. 1. In practice, the solution to Eqn. 1. requires detailed knowledge of specific material parameters, including surface recombination behavior as a boundary condition, and numerical solution techniques; this is beyond the scope of this paper and we will employ Eqn. 1 primarily as a reference point for examining qualitatively the effects on etching behavior of varying one of its terms while holding the other terms constant.

The relative importance of the different terms of Eqn. 1 will vary with the depth beneath the surface. Figure 1 illustrates the general form of the band edges for an n-type semiconductor with no external field applied and with the Fermi level unpinned from mid-gap, as is the case in the Cl-atom etching of (100) GaAs (7). One can approximate the depth of the space-charge region as $d = N_s/N_d$, where N_s is the density of surface states below the Fermi level (E_f) and N_d is the donor concentration. At $x \geq d$, the potential, ψ , is zero. E_i is the Fermi-level energy in intrinsic material. Assuming a constant space-charge density of eN_s from $x=0$ to $x=d$, the surface potential, $\phi = \psi(x=0)$, is $eN_s^2/2\epsilon N_d$ (8). The field in the space-charge region is $F = -d\psi/dx$. In the absence of an externally applied field, one can divide the material into two characteristic regions: the region from the surface to $x=d$, where one must consider the effects of all four terms in Eqn. 1, and the region with $x \geq d$, where field-induced drift term is zero.

The first significant effect of secondary electronic properties on etching quantum yields is due to the relative fraction of photogenerated carriers created in the surface-field region. The relative probability that a photon of a specific wavelength will create carriers that reach the surface to promote etching depends on the relative values of d and α , assuming carrier loss through recombination within the bulk (same τ) and through surface recombination are equal. Clearly, if the photon energy does not exceed the band gap, α is essentially zero and no significant carrier production occurs. This is illustrated by the total selectivity between GaAs_{0.63}P_{0.37} ($E_g = 1.81$ eV at 363 K) and GaAs_{0.8}P_{0.2} ($E_g = 1.59$ eV at 363 K) using 766-nm (1.62 eV) photons (3). No etching occurs for the higher-gap material.

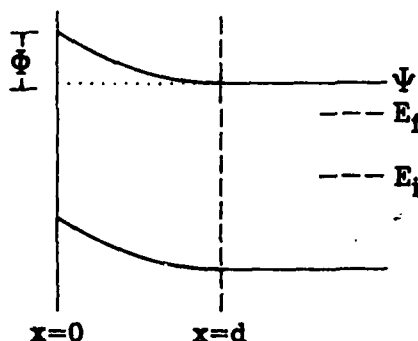


Fig. 1. General form of the band edges for a n-type semiconductor with an unpinned Fermi level.

However, etching quantum yields can be strongly wavelength dependent even when the photon energy exceeds the band gap. This is illustrated by the wavelength-dependence of the quantum yield for Ga(As,P). In Fig. 2, the band-gap energy as a function of composition for GaAs_{1-y}P_y at 363 K is illustrated. Near $y=0.45$, the nature of the lowest-energy gap, E_0 , changes from direct to indirect. There is, however, a higher-energy gap, E_1 , which is direct in nature. The energies of 514.4- and 610-nm photons relative to these two types of gaps are also shown in Fig. 2 for several Ga(As,P) compositions whose etching behavior has been examined. While 514.5-nm photons possess energy well in excess of the direct gap of all these materials, with an expected α in excess of $10^4/\text{cm}$ (9), 610-nm photons lie below the direct-gap energy of material with $y=0.59$. For this latter material, α should be on the order of 10^3 at 610 nm.

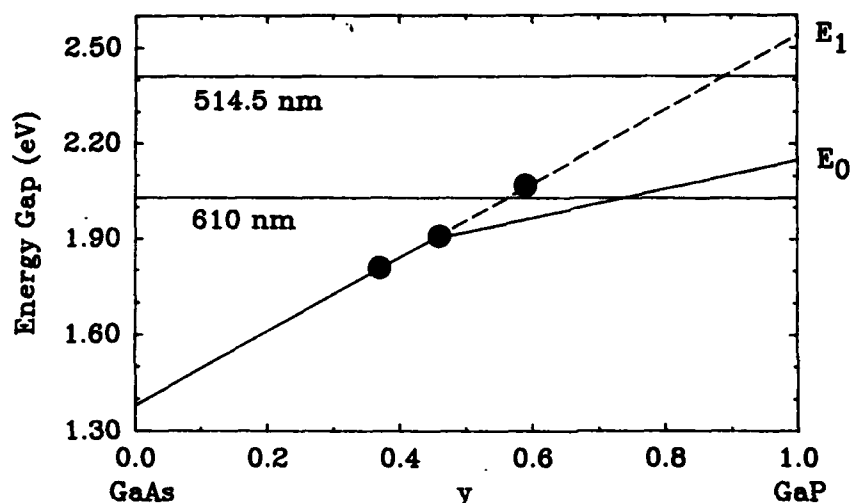


Fig. 2. Band Gaps for GaAs_{1-y}P_y at 363 K. Data points correspond to materials shown in Fig. 3.

The difference in etching quantum yield at these two wavelengths is illustrated in Fig. 3. Whereas both direct-gap and indirect-gap materials etch at comparable rates with direct-gap excitation at 2.41 eV (514.5 nm), the quantum yield for indirect-gap excitation of the $y=0.59$ material is much lower than that for the direct-gap excitation of the other two materials at 2.03 eV (610 nm). This behavior may be attributed to the smaller fraction of photogenerated carriers generated in or within a diffusion length of the field-induced drift region of the semiconductor (x_{sd} in Fig. 1) with the lower α ; consequently, a smaller fraction of the carriers reach the surface and the quantum yield is reduced.

Even when direct-gap excitation is employed, a dependence of quantum yield on wavelength can be observed since the absorption coefficient continues to increase gradually above the direct-gap energy. This can lead to a slightly higher quantum yield with higher energy photons, as shown in Fig. 3, due to the difference in overlap between the regions of significant carrier generation and the space-charge region. Similar wavelength-dependent behavior is seen in the wet PC etching of GaAs with UV and visible light (10,11). However, this effect is generally not observed in PEC etching (12), since the external field is dominant over the space-charge field in determining carrier drift to the surface.

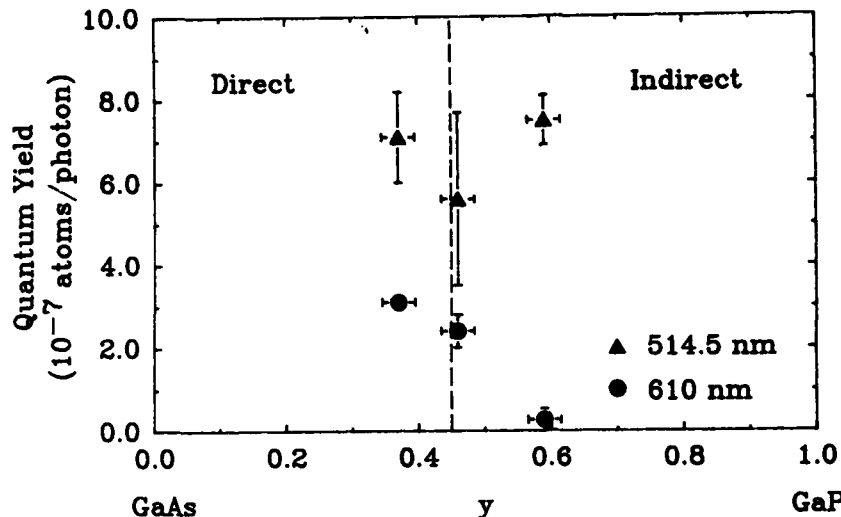


Fig. 3. Etching quantum yields for $\text{GaAs}_{1-y}\text{P}_y$ at 363 K with 514.5-nm and 610-nm photons. Compositions with $y \leq 0.45$ are direct-gap materials; those with $y \geq 0.45$ are indirect-gap materials.

The second significant effect of secondary electronic properties is seen in the selective suppression of carrier-driven etching by alteration of field-induced drift by applying a bias voltage to the semiconductor. This concept is related to the application of an external field in PEC etching; however, the purpose of applying the field is opposite in the two cases. In PEC etching, the field is applied to increase the flow of holes to the semiconductor surface. In this particular approach to PC etching, the field is applied to selectively decrease the flow of minority carriers to the surface, permitting doping-level selective etching (13).

In a semiconductor where the Fermi level is not pinned by a high density of in-gap states, the depth of the space-charge region is approximated by $d = N/N_d$. Although the Fermi level is generally pinned for (100) GaAs in vacuum or air ambients, the Cl atoms employed in our PC process serve a dual role as both etchant and the means whereby the dominant surface states are altered to unpin the Fermi level. This effect is seen in both photoluminescence and photorefectance spectra of (100) GaAs in a Cl-atom ambient (7). With an unpinned Fermi level, the depth of the space-charge region and hence the region of field-induced drift is greater for lower doping levels and can change in response to an applied voltage. In addition, the magnitude of the surface potential, ϕ , in Fig. 1 is smaller in more heavily doped materials, since $\phi = eN_s^2/2\epsilon N_d$.

When a negative bias is applied to n-GaAs in the presence of a slightly conducting Cl-atom ambient, the near-surface bending of the bands is decreased, thereby decreasing the depth from which carriers are swept to the surface (7). Because the band bending is initially less in n⁺-GaAs than in n-GaAs, a less-negative applied voltage is required to reduce the depth of the field region to zero, i.e., to produce the flat-band condition. Under flat-band conditions, the minority carrier flux to the surface is reduced to that from diffusion only; this is insufficient to produce significant etching in GaAs. Consequently, the etching of n⁺-GaAs can be selectively shut off relative to the etching of n-GaAs materials differing by less than a factor of three in doping level, as shown in Fig. 4 (13). Similarly, the etching of n⁺-GaAs can be suppressed relative to p-GaAs (13).

The depth profile of the damage produced by 40-keV $^{11}\text{B}^+$ ions in GaAs, as calculated with the Monte Carlo TRIM code (16), is presented in Fig. 5. Also shown in Fig. 5 is the carrier-generation profile for the two etching wavelengths in GaAs at 363 K. It is clear that a larger fraction of the carriers produced by 607-nm photons must travel a greater distance through the damaged region than with 514.5-nm photons. Consequently, for a given ion fluence, the relative decrease in etching quantum yield due to damage-mediated recombination is greater with 607-nm excitation than with 514.5-nm excitation (Fig. 6), suggesting that a lower total ion fluence may be required to produce total suppression of etching with the longer wavelength. However, the same smaller α that enhances the sensitivity to ion damage also results in a lower total quantum yield. Therefore, attempts to maximize damage sensitivity by wavelength selection will be limited by reduction in overall quantum yield. The use of an externally applied field to sweep carriers to the surface overrides wavelength-related effects in the PEC process (12).

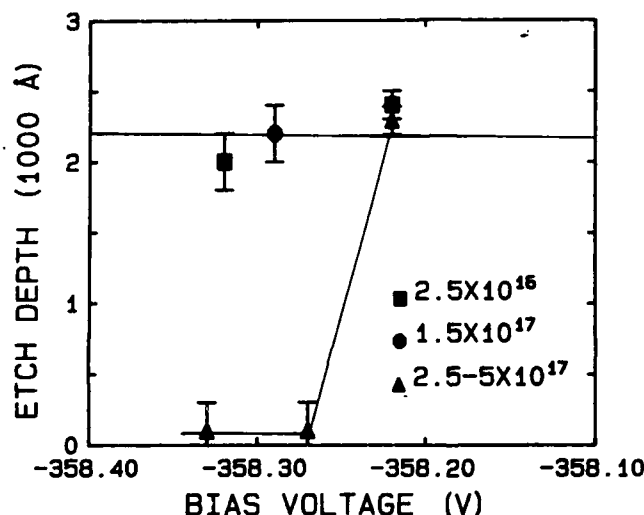


Fig. 4. Etching quantum yields as a function of applied bias voltage for three doping levels of n-GaAs. Voltage dropped in semiconductor is small fraction of total applied voltage (10).

The utility of implantation-enhanced recombination is dependent on the dominance of τ_{damage} over τ_{impurity} in Eqn. 1. When bulk recombination is already large due to large impurity concentrations, the efficacy of implantation for selective suppression of PC or PEC etching is greatly reduced. The quantum yields for etching p-GaAs ($7 \times 10^{18} \text{ cm}^{-3}$) are shown in Fig. 7. The quantum yield of unimplanted n-GaAs is substantially reduced relative to n-GaAs ($1 \times 10^{17} \text{ cm}^{-3}$) due to the shorter τ_{impurity} characteristically found in very heavily doped semiconductors. While substantial reduction in quantum yield is seen with 10^{12} B/cm^2 in $1 \times 10^{17} \text{ cm}^{-3}$ n-GaAs (Fig. 6.), quantum yield reduction is only seen at the 10^{14} cm^{-2} damage level in the n-GaAs.

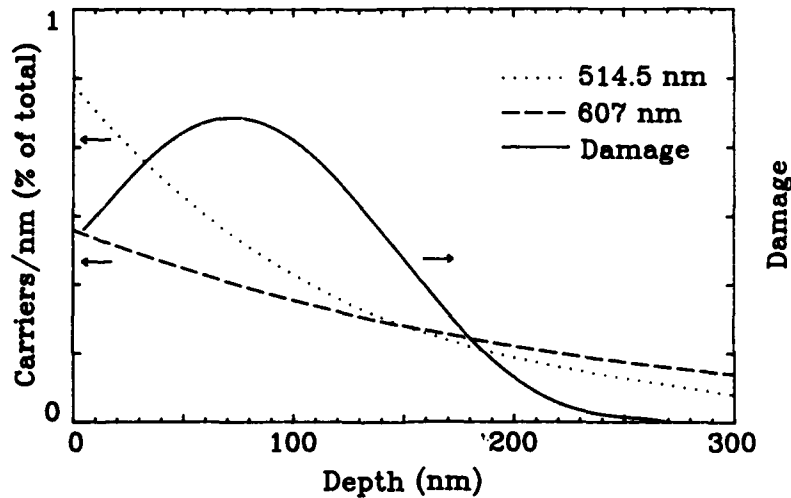


Fig. 5. Depth profile of damage from 40-keV $^{11}\text{B}^+$ ions implanted into GaAs and carrier-generation depth profiles for 607- and 514.5-nm light.

The third significant effect of secondary electronic properties is seen in the selective suppression of carrier-driven etching resulting from increased carrier recombination rates. The recombination term in Eqn. 1 can have several contributing terms; these can be divided into direct and trap-mediated processes. It is the latter which prove especially amenable to alteration to produce selective etching. One way to enhance recombination and thereby reduce the carrier concentration at the surface is through the deliberate introduction of recombination-mediating defects by ion implantation. This effect has been shown to be highly effective in producing total reaction suppression in both PEC (12,14,15) and PC (5,6) processes.

One can describe the carrier lifetime, τ , by Eqn. 2, where τ_{damage} is determined by the number and type of defects created by ion implantation and τ_{impurity} is determined by the number and types of recombination-mediating sites present prior to implantation.

$$1/\tau = 1/\tau_{\text{damage}} + 1/\tau_{\text{impurity}} \quad (2)$$

When a semiconductor is implanted to a sufficiently high fluence, τ_{damage} will be the dominant recombination term. This term will be a function of the distance below the surface, x ; the depth profile of implantation-induced damage will depend on both the ion species and energy. The peak in the damage profile moves to greater depths with increasing ion energy and, generally, with decreasing ion mass.

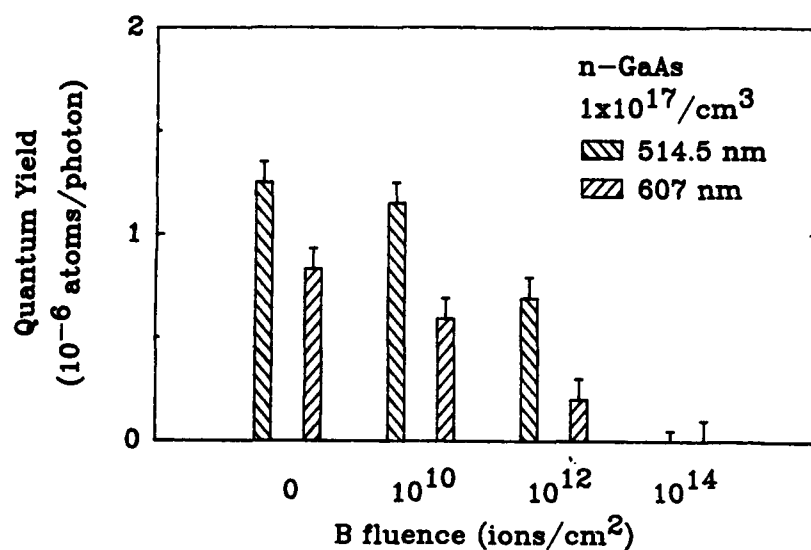


Fig. 6. Wavelength and ion-fluence dependence of etching quantum yields for $1 \times 10^{17}/\text{cm}^3$ n-GaAs implanted with 40-keV $^{11}\text{B}^+$ ions.

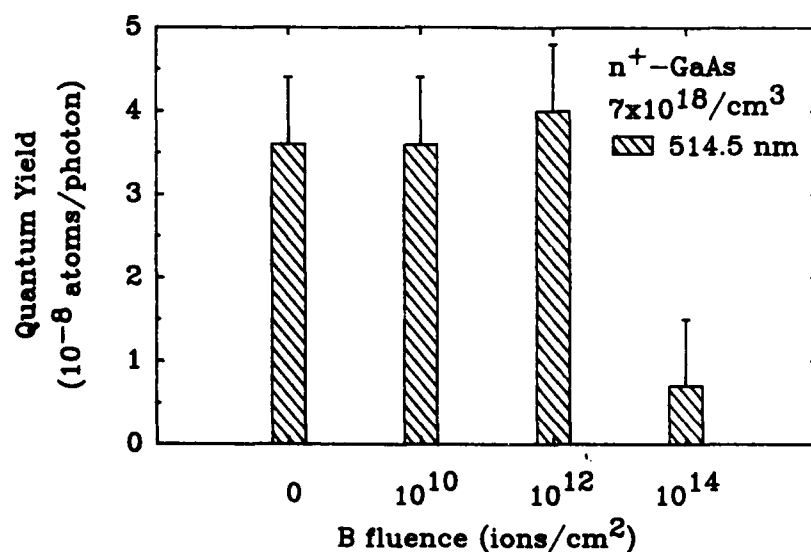


Fig. 7. Ion-fluence dependence of etching quantum yields for $7 \times 10^{18}/\text{cm}^3$ n^+ -GaAs with 40-keV $^{11}\text{B}^+$ ions.

The interplay of the different terms in Eqn. 1 will vary as the electronic properties of the specific semiconductor vary and, consequently, the relative importance of different secondary properties in determining quantum yield will vary. This is clearly illustrated by the comparison in quantum yields for moderate- and low-doped GaAs and Ga(As,P) relative to high purity Si. Both GaAs and GaP are characterized by relatively high bulk recombination rates and surface recombination velocities (10^6 - 10^8 cm/s in air). These properties make it essential to create most of the photogenerated minority carriers relatively near the surface (high α) to achieve etching quantum yields in the technologically useful range of 10^{-7} - 10^{-8} atoms/photon. In contrast, high-purity Si has longer bulk minority carrier lifetimes and lower surface recombination velocities (10-1000 cm/s in air). Consequently, carriers generated deeper beneath the surface have a higher probability of contributing to etching in Si than they have in GaAs. This is illustrated by the etching of Si by indirect-gap excitation with quantum yields which are likewise 10^{-6} - 10^{-7} atoms/photon (17).

SUMMARY

The carrier-driven photochemical dry etching of semiconductors depends on the minority-carrier concentration at the semiconductor surface. This concentration is determined by the complex interplay of a number of semiconductor electronic properties, including depth of photocarrier generation, carrier loss through bulk and surface recombination, field-induced drift, and diffusion. The relative importance of some of these properties can be altered through judicious selection of etching process conditions. This, in turn, can produce highly selective photochemical etching to discriminate among chemically similar semiconductor materials.

ACKNOWLEDGEMENTS

The author wishes to acknowledge R. M. Biefeld, L. R. Dawson, and D. R. Myers for their collaborative efforts and J. L. Dishman for technical assistance. This work, performed at Sandia National Laboratories, was supported by the U.S. Department of Energy under Contract DE-AC04-76DP00789 for the Office of Basic Energy Sciences.

REFERENCES

1. C. I. H. Ashby, in "Physics of Thin Films," Vol. 13, ed. M. H. Francombe and J. L. Vossen, Academic Press, New York, 1987, pp. 151-197.
2. C. I. H. Ashby, Appl. Phys. Lett. **45**, 892 (1984).
3. C. I. H. Ashby and R. M. Biefeld, Appl. Phys. Lett. **47**, 62 (1985).
4. C. I. H. Ashby and R. M. Biefeld, J. Electrochem. Soc., to be published (1989).
5. C. I. H. Ashby and D. R. Myers, in Laser and Particle-Beam Chemical Processing for Microelectronics, edited by D. J. Ehrlich, G. S. Higashi, and M. M. Oprysko, (Mater. Res. Soc. Proc. **101**, Pittsburgh, PA), p. 429-434.
6. C. I. H. Ashby, D. R. Myers, and F. L. Vook, J. Electrochem. Soc., to be published, (1989).
7. C. I. H. Ashby, Technical Digest, Conf. Lasers and Electro-optics, 4/26-5/1/87, Baltimore, MD, p. 300.

8. R. A. Smith, Semiconductors, 2nd Ed., Cambridge Univ. Press, New York, 1978, p. 229.
9. J. J. Tietjen and J. A. Amick, *J. Electrochem. Soc.* 113, 724 (1966).
10. G. C. Tisone, and A. W. Johnson, *Appl. Phys. Lett.* 42, 530 (1983).
11. D. V. Podlesnik, H. H. Gilgen, and R. M. Osgood, Jr., *Appl. Phys. Lett.* 45, 563 (1984).
12. G. C. Chi, F. W. Ostermayer, Jr., K. D. Cummings, and L. R. Harriott, *J. Appl. Phys.* 60, 4012 (1986).
13. C. I. H. Ashby, *Appl. Phys. Lett.* 46, 752 (1985).
14. K. D. Cummings, L. R. Harriott, G. C. Chi, and F. W. Ostermayer, Jr., *Appl. Phys. Lett.* 48, 659 (1986).
15. A. Yamamoto and S. Yano, *J. Electrochem. Soc.* 122, 260 (1975).
16. J. P. Biersak and L. G. Haggmark, *Nucl. Instrum. Meth.* 174, 257 (1980).
17. G. M. Reksten, W. Holber, and R. M. Osgood, Jr., *Appl. Phys. Lett.* 48, 551 (1986).

**PHOTOGENERATED CARRIER CONFINEMENT DURING THE
LASER-CONTROLLED AQUEOUS ETCHING OF GaAs/AlGaAs MULTILAYERS**

M.N. RUBERTO, A.E. WILLNER, D.V. PODLESNIK, and R.M. OSGOOD, JR.
Microelectronics Sciences Laboratories and the Center for Tele-
communications Research, Columbia University, New York, NY 10027

ABSTRACT

The sensitivity of the laser-controlled aqueous etching to the optical and electrical properties of semiconductors was utilized during the etching of n-GaAs/n-AlGaAs multilayers to produce novel microstructures. Since this process is controlled by the transport of photogenerated holes to the semiconductor/solution interface, we found that the morphology of etched features is dependent on the bandgap and hole diffusion length of each layer within the heterostructure.

INTRODUCTION

Utilizing the varying properties of III-V layered materials provides many possibilities for novel fabrication techniques. The laser-controlled aqueous etching of semiconductors is very attractive since this process is sensitive to both the electrical and optical properties of the material. We applied this maskless, direct-write technique to the GaAs/AlGaAs system which is the basis for many electro-optic devices used in optical communication networks.

In the photochemical etching of bulk n-GaAs, the dissolution process is controlled precisely by the number of photogenerated holes at the semiconductor/solution interface [1]. These carriers initiate a redox reaction that results in the formation of an oxide which is then soluble in the solution. The transport of photogenerated holes to the surface and their resultant spatial distribution will therefore determine the morphology of the etched structures. In layered structures the same basic etching mechanism for bulk material is expected to be operable. The chief difference is that the bandgap discontinuity at the interface between two layers controls the flow of photogenerated carriers within the structure. This results in the confinement of these carriers to various layers within the sample which changes the morphology of the etched feature relative to what is seen in bulk materials.

EXPERIMENTAL

For our etching experiments, an Ar⁺ laser operating at 514 nm was focused onto the semiconductor surface to a spotsize of 3-4 μm . The cleaved samples were mounted within a quartz cell and immersed in a solution that produced no dark etching. The laser intensity of 50 W/cm² used in most of our experiments was well below the level of significant thermal excitation of both the semiconductor and solution. By rastering the sample below the fixed laser spot, features were masklessly engraved onto the semiconductor surface. The MOCVD-grown heterostructure which was used in the majority of our experiments consisted of the following layers: 2 μm n-GaAs, 2 μm n-AlGaAs, 2 μm n-GaAs, 2 μm n-AlGaAs, and 0.15 μm undoped-AlAs

on an n'-GaAs substrate. The layers were doped to $n=10^{16}/\text{cm}^3$ and the Al concentration in AlGaAs was 30%. The etching solution used was 5% HNO₃, since this reagent etched both GaAs and AlGaAs under 514 nm illumination.

RESULTS AND DISCUSSION

The lateral confinement of etched features to the micron-sized laser beam spot is dependent on the hole diffusion length. To demonstrate this point, we compared the etched profiles of n and n' bulk GaAs. In low doped ($n=10^{16}/\text{cm}^3$) bulk n-GaAs samples with hole diffusion lengths of 3 μm [2,3], a width of 8.5 μm from the center of the trench was observed for a 4 μm beam diameter. Similarly in higher doped ($n=10^{18}/\text{cm}^3$) bulk n'-GaAs samples with diffusion lengths of 1.5 μm [2,3], a trench width of 5 μm was observed. The trench width dependence on the diffusion length is also seen in a laser-etched line through an n-GaAs epilayer ($n=10^{16}/\text{cm}^3$) on an n'-GaAs substrate. A lateral width of 8 μm from the center of the trench was observed in the lower doped, higher diffusion length epilayer in comparison to the 2.5 μm width seen in the substrate with a lower diffusion length.

In layered structures, an additional effect has to be accounted for. The bandgap discontinuity at the interface between two layers may affect the flow of photogenerated carriers. Figure 1 shows a typical cross-section of a laser-etched line using a 4 μm beamspot at 50 W/cm², which revealed that rapid lateral material removal occurred in the sandwiched n-GaAs layer. The undercut was bounded vertically by the n-AlGaAs layers and the bottom of the trench was flat along the AlAs layer. Note that the trench width in the n-AlGaAs layers are smaller than that of n-GaAs. We estimate that the hole diffusion lengths for n-GaAs and n-AlGaAs are 14 μm and 2 μm , respectively [4-6].



Fig. 1. Cross-section of a laser-etched line through the GaAs/AlGaAs heterostructure.

The effect of the layer interfaces on the etching process became evident from the temporal evolution of the etched trench, which was obtained by varying the scan velocity of the laser beam. Experimental results are shown schematically in Figure 2 for different etch times. As the beam started etching the top n-GaAs layer at a rate of $10\text{ }\mu\text{m/min}$, it engraved a profile similar in shape to that of the Gaussian beam profile. As soon as etching into the AlGaAs layer occurred, a faster vertical rate of $18\text{ }\mu\text{m/min}$ was observed and the trench profile was more confined to the beam spot. However, when the third layer (GaAs) was reached, both vertical and lateral etching occurred with etch rates of 17 and $26\text{ }\mu\text{m/min}$, respectively, resulting in the undercut of the AlGaAs layers to a lateral width of $10\text{ }\mu\text{m}$ from the center of the trench. Finally upon etching the fourth layer (AlGaAs), the trench width of this layer was the same as that of layer 2 (AlGaAs), which would be the case if the etching is material dependent. The etching then stopped at the AlAs layer.

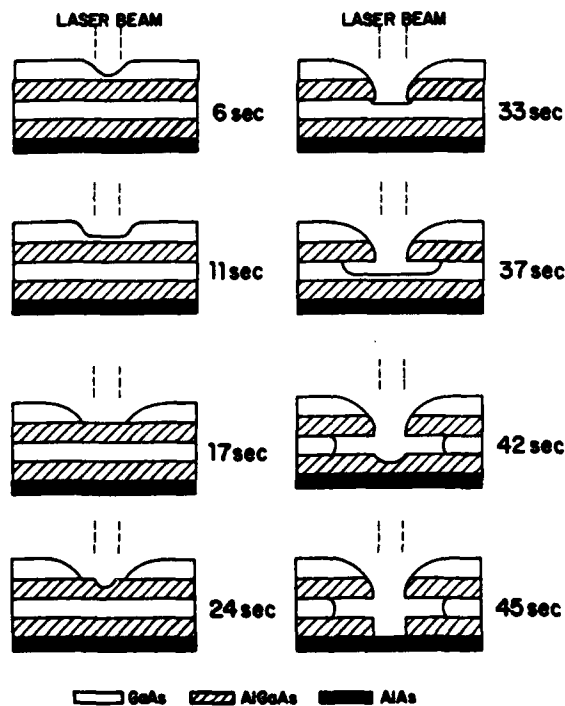


Fig. 2. Temporal evolution of the laser-etched trench on the GaAs/AlGaAs heterostructure.

Lateral etching is a carrier diffusion phenomena which results from a spread in the photogenerated hole distribution at the semiconductor/solution interface due to longer diffusion lengths. This was seen first on bulk n-GaAs and then on the n/n'-GaAs sample, as well as the GaAs/AlGaAs heterostructure. To account for the undercutting in the sandwiched n-GaAs material, photogenerated holes are confined to this layer by the valence band discontinuity of 0.4 eV between the GaAs and AlGaAs layers, which constrains the entire population of holes at the semiconductor/solution interface to the small GaAs contour exposed to the electrolyte. Therefore, undercutting occurs only within the sandwiched n-GaAs layer, whose lateral width is controlled by the hole diffusion length. The possibility that the lateral etching results from light reflected off the trench bottom and onto the sidewalls can be excluded since the lateral etch rate is faster than the vertical etch rate.

To illustrate the effect of the hole diffusion length, L_p , the layer thickness, d , and the vertical confinement of photogenerated holes from a Gaussian laser beam on the carrier distribution at the surface of a semiconductor slab with $d < L_p$, consider the diffusion equation which is given in cylindrical coordinates by:

$$D_p \left[\frac{1}{\rho} \frac{\partial}{\partial \rho} \rho \frac{\partial \Delta p}{\partial \rho} + \frac{\partial^2 \Delta p}{\partial z^2} \right] - \frac{\Delta p}{\tau} + \frac{\alpha \phi}{\pi \rho_0^2} e^{-\alpha z} e^{-\rho^2/\rho_0^2} = 0 \quad (1)$$

where $\Delta p(\rho, z)$ is the angularly independent excess hole density. D_p and τ are the hole diffusivity and lifetime. α , ρ_0 , and ϕ are the absorption constant, beam radius, and absorbed photon flux, respectively. The boundary condition of surface recombination was used to account for the flow of holes during the etching process into the uniform layer of etchant solution covering the top of the slab. The constraint of no diffusion current through the bottom of the layer provided hole confinement to the slab of thickness d , i.e.

$$\left. \frac{\partial \Delta p}{\partial z} \right|_{z=0} = \frac{S \Delta p(0)}{D_p}, \quad \left. \frac{\partial \Delta p}{\partial z} \right|_{z=d} = 0 \quad (2)$$

where S is the surface recombination velocity. Equations (1) and (2) were numerically solved for $\Delta p(\rho, z=0)$, the photogenerated hole distribution at the slab surface, using a Hankel transform.

$\Delta p(\rho, 0)$ was varied for different values of L_p for a 2 μm n-GaAs slab for $\rho_0=2 \mu\text{m}$ as shown in Figure 3(a). The width of this distribution, and thus the trench width, spreads for larger values of L_p . The layer thickness d was also varied for $L_p=14 \mu\text{m}$ and $\rho_0=2 \mu\text{m}$ as shown in Figure 3(b). This revealed that the width of the distribution increased as the layer thickness decreased, thereby increasing the degree of carrier confinement, from the bulk ($d \gg L_p$) to the thin layer case ($d < L_p$). This trend is also seen experimentally on the top GaAs layer in Figure 2 by comparing etch times 6 and 11 s. Not only does this model predict the same trench width dependence on L_p , but it also reveals that increased lateral etching occurs as the layer becomes thinner.

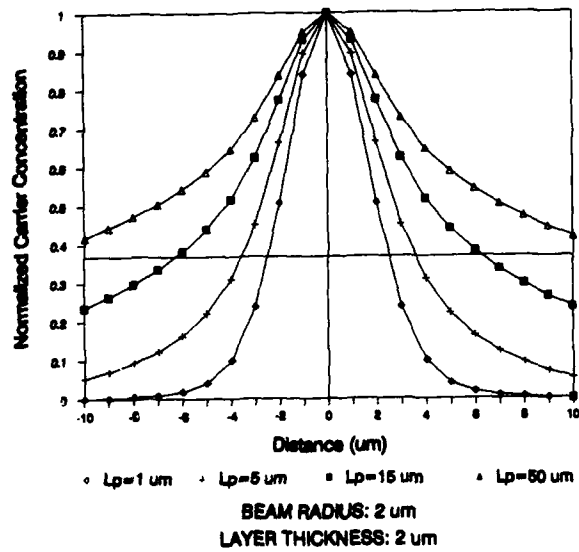


Fig. 3(a). The dependence of the (normalized) surface distribution of photogenerated holes on the diffusion length.

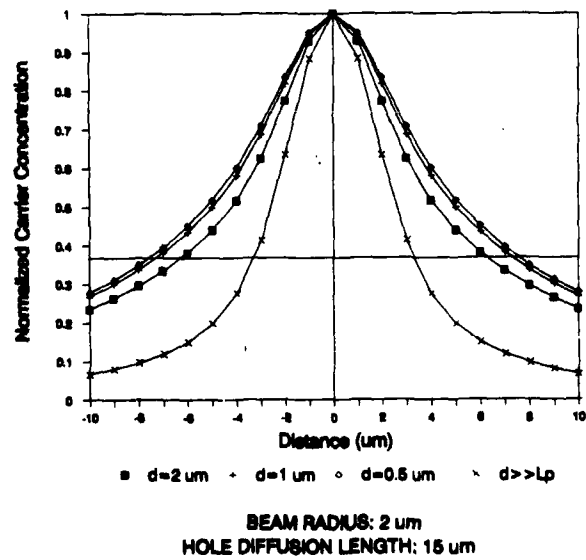


Fig. 3(b). The dependence of the (normalized) surface distribution of photogenerated holes on the layer thickness

CONCLUSION

We were able to utilize the carrier confining properties of GaAs/AlGaAs heterostructures to control the direction of etching within these multilayers. The morphology of laser-etched features depends on the diffusion length and bandgap of each layer within the sample. Although our theoretical model neglected the deformation of the etched surface, lateral etching was accounted for on the simple premise of the confinement of diffusing minority carriers. The laser-controlled aqueous etching of the GaAs/AlGaAs system shown in this paper has been used for the fabrication of optoelectronic components [7], such as rib waveguides and directional couplers. In addition, this technique has been applied to the maskless fabrication of microcleaved semiconductor facets by utilizing the structure shown in Fig. 1 [8].

ACKNOWLEDGMENTS

We would like to thank Wen Wang, Ulrich Stimming, Rob Scarmozzino, Zhen Wu, Shangheng Xin, and Jim O'Neill for many hours of helpful discussions. The lab assistance of Aaron Fleischman was also invaluable during the formative stages of this work. This project was supported by the National Science Foundation, the IBM Materials and Processing Science Grant Program and the Defense Advanced Research Projects Agency.

REFERENCES

- [1] D.V. Podlesnik, H.H. Gilgen, A.E. Willner, and R.M. Osgood, Jr., *J. Opt. Soc. Am. B* **3**, 775 (1986)
- [2] A.V. Dudenkova and V.V. Nikitin, *Soviet Physics-Solid State* **8**, 2432-2433 (1967)
- [3] S.M. Sze, *Physics of Semiconductor Devices*, 2nd ed. (Wiley, New York, 1981), p. 29-30
- [4] G.W. 't Hooft, C. van Opdorp, H. Veenvliet, and A.T. Vink, *J. Crystal Growth* **55**, 173 (1981)
- [5] G.B. Stringfellow, *J. Crystal Growth* **53**, 45 (1981)
- [6] J.S. Blakemore, *J. Appl. Phys.* **53**, 10 (1982)
- [7] A.E. Willner, M.N. Ruberto, D.J. Blumenthal, D.V. Podlesnik, and R.M. Osgood, Jr., *Appl. Phys. Lett.*, **54**, 1839 (1989)
- [8] M.N. Ruberto, A.E. Willner, D.V. Podlesnik, and R.M. Osgood, Jr., to appear in *Appl. Phys. Lett.*

HIGH RESOLUTION DIRECT - WRITE PHOTOCHEMICAL ETCHING OF InP USING METHYL IODIDE

K. DUROSE, J.P.L. SUMMERSGILL*, M.R. AYLETT and J. HAIGH
British Telecom Research Laboratories, Martlesham Heath, Ipswich, IP5 7RE, United Kingdom.
* Lincoln College, Oxford University, United Kingdom.

ABSTRACT

Photochemical etching of InP using a cw frequency doubled Ar⁺ laser is evaluated with a view to the production of optoelectronic device features. The diffusion-limited resolution of the unmodified etching process is discussed and a new method of etching high resolution grooves which utilises a native oxide coating is described. Grooves produced in this way have widths comparable to that of the laser beam.

INTRODUCTION

Increasing interest in InP based opto-electronic integrated circuitry (OEIC's) has led to greater demands being made of conventional processing techniques such as ion beam sputtering and wet chemical etching. For example, in the horizontal integration scheme it is desirable to separate the optical and electronic components of the circuit by a shallow angled step in the substrate [1,2]. This is currently made prior to epitaxy by the 'graded step' method [1,2] of ion beam milling samples which have been pre-masked with baked photoresist. Photoetching offers practical alternative solutions to processing requirements of this type. The purpose of this work was to evaluate and develop the CH₃I/H₂ photoetching system with a view to generating features of use in OEIC fabrication.

Previous work has demonstrated the ability of uv photolysed halogenated methanes, for example CF₃Br [3], CH₃Br [3-6] and CH₃I [4,6,7] to etch GaAs and InP at temperatures of around 200-300°C. The reaction products are mixed halogenated and methylated species [5] and since these are all volatile the process is a dry one which is compatible with MOVPE growth. We have used a CH₃I/H₂ mixture, the hydrogen being necessary to provide chemical reduction. Initial work [4,6] demonstrated the production of directly written grooves in InP, InGaAs, and InGaAsP using this reagent in conjunction with an excimer laser operating at 249 nm which is close to the CH₃I absorption peak. However, grooves produced in this way were not of device quality since they were roughened as a result of beam damage.

The present work investigates the use of a cw frequency doubled Ar⁺ laser operating at 257 nm in the production of high quality features in InP using CH₃I/H₂. A modified process which utilises deliberately oxidised surfaces is also described.

EXPERIMENTAL

Atmospheric pressure etching was carried out using a partial pressure of 10 torr of CH₃I in H₂ and at substrate temperatures in the range 150-250°C. UV illumination was provided by a Spectra-Physics 2020 Ar⁺ laser with 359B intracavity frequency doubler which gave a 257 nm output of up to 150 mW cw. The reaction cell was fitted with a silica window and was positioned on a computer controlled x-y stage having 0.1 μm resolution. Both direct-write and pattern projection imaging were carried out using an optical arrangement similar to that described by Aylett and Haigh [8]. In the direct-write configuration both single and multiple scans were used at rates of between 0.3 and 200 μm/s. Clean InP surfaces were prepared by degreasing the samples and then heating them briefly in the reaction cell at 400°C to remove surface oxides immediately prior to etching. The influence of surface oxides on the direct-write process was also investigated. Thermal oxidation of InP wafers was carried out in a 20:1 mixture of N₂:O₂ at 450°C.

RESULTS

Photochemical Etching of Clean InP Surfaces

Optimised direct-write etching conditions were established under which smooth, clean channels could be produced at the highest etch rate. The effect of varying the substrate temperature was as follows -

- a) at 150 - 160°C reaction products in the form of a thick oily looking film developed (maybe $\text{In}_3\text{P}(\text{CH}_3)_2$ complex [9]).
- b) at 180°C etching developed cleaner but rougher surfaces.
- c) between 210 and 220°C smoother etching was obtained which was surrounded by a thin halo of reaction products at a radius of 200 - 300µm. This was removable by heating briefly to 350°C in hydrogen.
- d) between 220 and 250°C the etch rate diminished and cleaner surfaces were observed, presumably due to faster reactant and product desorption.

The parallel channels illustrated in figure 1 were drawn at 220°C using a spot size of approximately 30µm and a linear scan rate of 0.5µm/s. Relatively low power densities are preferred ($600\text{W}/\text{cm}^2$ in this case) since high power (eg $6\text{KW}/\text{cm}^2$) worsens the roughness which is visible in the centres of the channels in the figure. Using low power densities virtually eliminates this roughness.

Figure 2 shows a depth profile of a 1.3µm deep channel which was drawn under similar conditions to those shown in figure 1. Both multiple scanning and the use of slower scan rates enabled these features to be deepened to several microns or more. An important aspect of channels produced by the direct-write process is that their overall widths, which are in excess of several hundred microns (see figure 2), are many times greater than that of the illuminating beam. This is caused by the gas phase diffusion of photolysed species away from their points of origin [3].

The circular dips in InP illustrated in figure 3 were etched by pattern projecting a mask consisting of circular holes for 15 minutes using a beam power density of $0.1\text{W}/\text{cm}^2$. All other conditions were the same as those described above for direct-write etching. Clean, smooth features were generated and the depth profile in figure 4 indicates a vertical etch rate of approximately 1µm/hour. In addition the edges of the features have undergone considerable broadening which has resulted in shallow step angles. Indeed, pattern projected straight steps etched in InP under identical conditions had measured step angles of 15 - 30°.

Direct-Write Etching of Oxidised InP Surfaces

Coating InP surfaces with thermal oxide prior to photochemical etching enabled grooves to be etched which had widths which were comparable to that of the laser beam. However, the definition achieved in the examples shown in figures 5a/b and 6 was related to the thermal oxidation time, the scan rate and the power density. Prolonged thermal treatment (eg 30 mins at 450°C) generated a surface oxide coating which completely resisted attack under the direct write etching conditions for InP described in the previous section. Oxidation for 5 minutes under the same conditions yielded surfaces which could be etched to produce a band of pits using relatively high power densities (around $12\text{KW}/\text{cm}^2$) and low scan rates (eg 1µm/s). The optimum oxidation time was around 1-2 minutes and this corresponds to an oxide thickness of about 60Å as measured by ellipsometry. Surfaces with such a coating were used to produce the grooves illustrated in the figures in conjunction with a laser scan rate of 200µm/s and beam power density of $12\text{KW}/\text{cm}^2$. Deepening of the grooves, as in figure 6, could be achieved by performing multiple scans, each scan increasing the etched depth by approximately 0.05 µm without degrading the edge quality. Indeed the widths of the lines drawn at high scan rates was governed solely by the spot size rather than the diffusion of the reactive species. Nevertheless, at slow scan rates (eg 1µm/s), although the etching was largely confined to the width of the focussed beam there was some broadening which gave rise to funnel shaped channels.

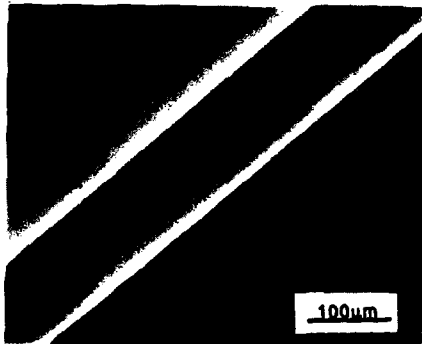


Figure 1 (left). A pair of direct-write channels etched in oxide-free InP. Normarski micrograph.

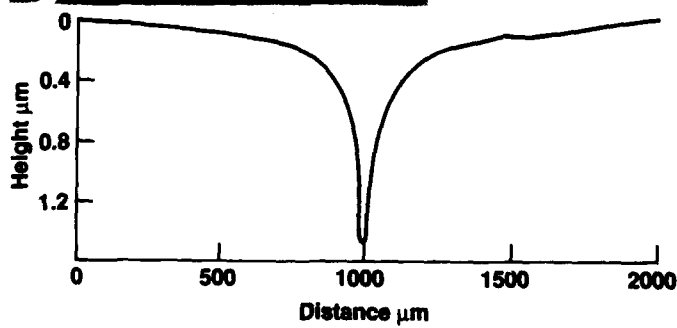


Figure 2 (below). Depth profile of a channel similar to one of those in figure 1. Note the broad overall feature width.

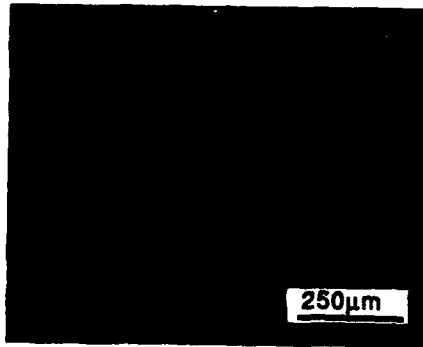


Figure 3 (left). Pattern projected dips etched in InP. Normarski micrograph.

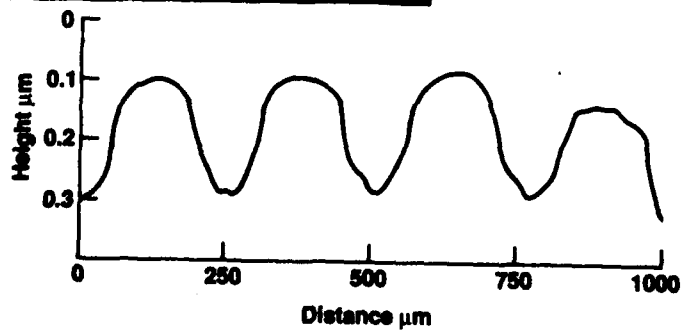


Figure 4 (below). Depth profile of etched dips illustrated in figure 3.

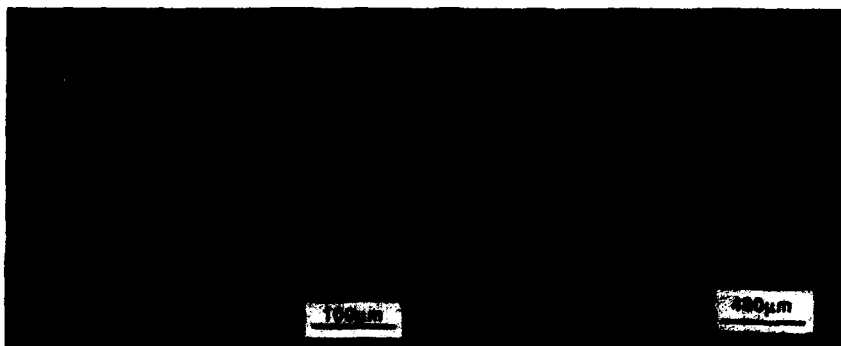


Figure 5a/b. Direct-write grooves etched in oxide coated InP. Normarski micrographs.

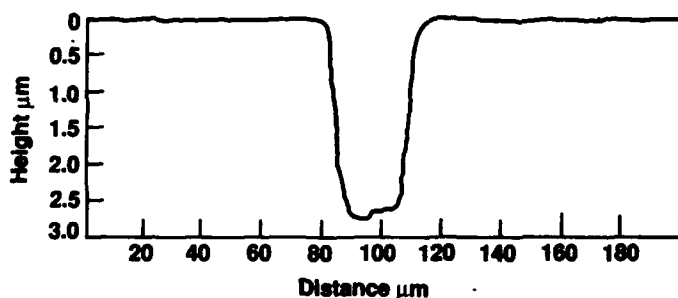


Figure 6. Depth profile of a deepened (multi-scan) direct-write groove etched in oxide coated InP.

RESOLUTION OF PHOTOCHEMICALLY ETCHED FEATURES IN InP

Clean (Oxide Free) Surfaces

The mechanisms responsible for the dry photoetching of semiconductor surfaces have been discussed by a number of authors (see [3,10 and 11] for example). The first step in the process is the photolysis of molecular species in the gas phase to produce photo-fragments which are capable of reacting with the substrate. In the process investigated in this work, CH_3I is photolysed to yield the reactive species, namely methyl radicals and excited iodine atoms [12]. These species undergo collisions with the substrate and some of them react with it to yield volatile reaction products, namely phosphorus and indium iodides [7] and probably some methylated products in addition. In a case where each reactive entity which strikes the surface and reacts locally with it then the profile of the etched feature is governed solely by the spatial distribution of those reactive species at the substrate [3]. This in turn is influenced by factors such as the laser spot size, shape and intensity, the lifetime of the reactive species, the overall pressure in the reaction cell and the presence or absence of any scavengers. Further modifications to the etched profile might arise from surface parameters such as the sticking coefficient of the reactants, the proportion of the reactive species reacting with the substrate, and the efficiency with which the reaction products desorb.

The wide, gently sloping profiles produced by CH_3I on InP indicate that reactive species strike the substrate up to several hundred microns either side of the centre of the focussed spot. Since the spot diameter used in this work was measured to be about $30\text{ }\mu\text{m}$ it is apparent that the breadth of the etched features is not controlled by the quality of the focus but rather by the mobility of the reactive species (methyl radicals and excited iodine atoms) which are capable of diffusing in excess of $200\text{ }\mu\text{m}$ before reacting with the substrate.

The relatively long lifetime of photolysis products in the dilute $\text{CH}_3\text{I}/\text{H}_2$ mixture used in this work is a result of the absence of gas-phase scavenging which is prevalent when high methyl halide concentrations are used. By contrast, in work reported by Ehrlich et al. [3] in which neat CH_3Br was used at atmospheric pressure to photoetch InP with 257nm radiation, it was estimated that the reactive species travelled no further than $30\text{ }\mu\text{m}$. This was thought to be the result of the high probability of gas phase scavenging reactions involving Br atoms and intact CH_3Br molecules. Apparently, however, the long lifetimes observed in the present work do not preclude the formation of high periodicity ($<1\text{ }\mu\text{m}$) fringes in etched features produced by a slightly defocussed stationary spot; features of this type which were produced with CH_3Br [3] were readily reproduced by the present authors with CH_3I . As Ehrlich et al. [3] point out this phenomenon is only possible because reactive species generated close to the surface will remain localised to a greater extent than those generated at greater distances. Nevertheless such features will be superimposed on a much broader, smooth, shallow background and hence direct written etched features produced using the unmodified process (i.e. as described in this work) can never be expected to yield micron scale features of device quality. The value of the technique rests in its suitability for the production of shallow angled steps and sloping features, such as those which are currently being used in OEIC fabrication.

Oxide Coated Surfaces

The etching behaviour of oxidised InP surfaces differs greatly from that of clean surfaces in that the use of an optimised thickness of oxide enables a significant degree of contrast enhancement to be achieved. The properties of thermal oxide which enables this are -

- a) the oxide coating is not degraded significantly by CH_3I or its photolysis products under the processing conditions in the absence of laser irradiation.
- b) the oxide coating is removed where the focussed laser light interacts with the surface to reveal clean InP which is then susceptible to etching by the CH_3I photolysis products.

These two properties of the oxide modify the process characteristics - oxide is stripped away where uv light falls and this allows localised attack by CH_3I radicals and I atoms. Since the process works best for relatively high laser power densities (eg $12\text{KW}/\text{cm}^2$) it seems likely that the oxide removal mechanism is thermal and takes place by either reduction or sublimation [13]. If this is indeed the case then thermal conduction would appear to be responsible for the broadening of the grooves which is observed at low scan rates. Sub-micron roughness in the bottoms of the channels might also be attributed to damage of the InP surface by the high power density - similar roughness observed in channels drawn on clean InP surfaces was eliminated using reduced beam powers. An improvement to the high resolution process would therefore be to use a high power density direct-write configuration to pattern the oxide layer rapidly, followed by the use of low-power, broad-area illumination to initiate the photolytic etching.

APPLICABILITY TO DEVICE PROCESSING

Features in optoelectronic device structures typically have both widths and depths of around several microns. However, due to the resolution limits imposed by gas phase diffusion, the unmodified process is incapable of producing discrete structures such as waveguides or mesas. Nevertheless both of these illumination geometries are capable of producing smooth, gently sloping steps having slopes of $15^\circ - 30^\circ$. These are of use in modifying substrates prior to epitaxy as in the graded step process [1,2], although since the direct-write process is very slow ($0.5\text{ }\mu\text{m}/\text{s}$), any serious device application will require them to be made by pattern projection.

Coating the InP surfaces with thermal oxide prior to photochemical etching is an important modification to the process since it allows high resolution grooves to be drawn having widths

comparable to that of the focussed beam hence making the process more suitable for the production of discrete features. A practical limitation is that the direct-writing and deepening of the grooves described in this work is slow. A faster version of the process incorporating a combination of direct-write and broad area illumination, as described in the previous section, should however be feasible.

A major advantage of dry photoetching with CH_3I in hydrogen is that since all of the reaction products are volatile the etching can potentially be carried out in conventional MOVPE equipment without interfering with subsequent epitaxial growth. The use of *in-situ* etching techniques to avoid sample contamination between conventional processing stages for example could be a major advantage in device fabrication.

ACKNOWLEDGEMENTS

The authors would like to thank Dick Hobbs for carrying out the thermal oxidation of the InP substrates which were used in this work. Acknowledgement is made to the Director of Research at British Telecom and BT&D Technologies for permission to publish this paper.

REFERENCES

1. S. Miura, H. Machida, O. Wada, K. Nakai and T. Sakurai, *Appl. Phys. Lett.*, **46** (4), 389 (1985).
2. O. Wada, T. Sakurai, and T. Nakagami, *J. Quantum Electronics*, **QE-22** (6), 805 (1986).
3. D.J. Ehrlich, R.M. Osgood and T.F. Deutsch, *J. Quantum Electronics*, **QE-16** (11), 1233 (1980).
4. M.R. Aylett and J. Haigh, *Extended Abstracts of 1984 MRS Fall Meeting, Symposium D*.
5. P. Brewer, S. Halle and R.M. Osgood Jr, *Mat. Res. Soc. Symp. Proc.*, **29**, 179 (1984).
6. M.R. Aylett, *PhD. Thesis, Queen Mary College, University of London*, 1988.
7. J. Haigh, *UK patent N° 8516684* (1985).
8. M.R. Aylett and J. Haigh, *Laser Processing and Diagnostics*, Ed Bauerle, D., Springer Series in Chemical Physics, **39**, 263 (1984).
9. A.J. Carty, T. Hinsperger and P.M. Boorman, *Canadian Journal of Chemistry*, **48**, 1959 (1970).
10. P.D. Brewer, G.M. Reiksten and R.M. Osgood Jr, *Solid State Technology*, **28** (4), 273 (1985).
11. M.E. Pemble, *Chemtronics*, **2**, 13 (1987).
12. T. Donohue and J.R. Wiesenfeld, *J. Chemical Physics*, **63** (7), 3130 (1975).
13. W.M. Lau, R.N.S. Sodhi and S. Ingre, *Appl. Phys. Lett.*, **52** (5), 386 (1988).

LASER-INDUCED ATOMIC CHLORINE ETCHING OF SILICON

G.V. TREYZ, R. SCARMOZZINO, H.H. BURKE and R.M. OSGOOD, JR.,
Microelectronics Sciences Laboratories,
Columbia University, New York, NY 10027

ABSTRACT

UV laser photolysis of chlorine ($\lambda = 350\text{-}360\text{ nm}$) has been used to produce a microscopic atomic chlorine source. Crystalline silicon has been etched and deep, through-wafer vias have been fabricated. The etching process has been modeled and both theoretical and experimental results are given.

INTRODUCTION

Laser processing of semiconductors is of interest because unique features can be obtained that are difficult or impossible to fabricate using conventional techniques. Laser photolysis of Cl_2 by a cw-laser can be used to etch smooth vertical features in crystalline silicon without using a multistep photomasking procedure. Previously, the etching of silicon by laser photolysis of chlorine has been studied in the low-power cw[1] and pulsed[2] regimes. In this work, we examine silicon etching by laser photodissociated molecular chlorine using a high-power cw laser source operating at wavelengths (350-360 nm) near the chlorine absorption peak at 330 nm. We show that this photolysis scheme produces a microscopic source of chlorine atoms which can be used to produce localized etching of a silicon substrate. As a particular example we have demonstrated the etching of smooth via holes in a silicon wafer. Due to the local nature of the Cl-atom source, etching only occurs in the interior of the via into which the laser beam is directed. Since the process is driven by a photolytic mechanism, etching occurs at low temperature and the thermal damage to the surrounding silicon is avoided.

EXPERIMENT

In these experiments crystalline silicon, typically n-type, 4-6 ohm-cm resistivity, and (100)-orientation, was etched in a chlorine ambient (0-600 Torr). The samples were cleaned with a standard RCA cleaning process before loading into a vacuum chamber. The etching chamber consisted of a nickel-plated, stainless-steel cell with a fused-silica window. The chamber was evacuated to $< 10\text{ mTorr}$ before filling with chlorine. The 350-360 nm lines of an Ar^+ laser were focused with a UV-transmitting microscope objective to a spot size of $1.5\text{ }\mu\text{m}$

(FWHM) at the sample surface. The sample was located 3 mm below the lower surface of the window.

RESULTS AND DISCUSSION

The focused beam photodissociated chlorine into reactive atomic chlorine, which diffused to the sample and spontaneously etched the silicon surface. Initially, the focused beam produces a temperature rise of $\approx 100^\circ\text{C}$ on the silicon surface (estimated using the formulas given in [3]). However, as the etched structure becomes enlarged the laser spot size on the surface increases due to the beam divergence. Because the maximum laser-induced temperature rise varies inversely with the spot size, the temperature rise drops off rapidly as the structure becomes larger. The maximum temperature rise of the substrate has been calculated to be $\approx 15^\circ\text{C}$ for the structures studied here. Therefore, thermal contributions to the etch rate can be neglected because it has been previously shown[4] that a substantial temperature increase ($> 1000^\circ\text{C}$) and phase change are necessary for a substantial heat-driven etch rate.

The profile of the etched features changed with the length of exposure time. For short etching times, the features were characterized by clear crystallographic planes (Figure 1a). At longer times, the etched feature increased in size, and the straight edges of the square pattern as seen along the wafer axis were replaced by increasingly curved sides until finally a perfectly rounded perimeter was observed (Figure 1b). For long etch times, cylindrical through wafer vias were formed. Note that the tapering near the bottom of the via in Figure 1b is probably due to the spreading of the laser beam, which is focused at the top of the sample, and diverges near the bottom to a diameter comparable to that of the via.

To characterize the etching process as a function of laser etching parameters, we studied the development of etched via holes as a function of etch time, laser power, and chlorine pressure. For example, as seen in Figure 2a, the etched via area, as measured at the surface, increased linearly with time (the solid lines in Figures 2a-c are based on the model given below). A similar behavior was also seen for the depth of the vias. This linear dependence persisted over a large range of etch times and laser powers, showing that via area is a good indicator of the etch rate for this Cl/Si system. Figure 2b shows that via area was also found to be linearly dependent on incident laser power. In contrast, a plot of via area vs. chlorine pressure displayed a more complex dependence (see Figure 2c). For low pressures, via area increased roughly linearly with pressure, while at higher pressures the via area saturated.

To explain the data exhibited in Figures 2a-c, and to understand more fully the reaction physics, a model has been developed that contains the key features of the etching process. In order to obtain an analytical solution, we assumed the

simplified via geometry shown in the inset to Figure 2c. Atomic chlorine is generated in the beam path by the following photodissociation process which has a peak in cross section near our laser wavelength[5]:



The Cl atoms created in the beam diffuse radially, to the silicon surface. We have estimated the loss of Cl due to gas-phase recombination to be a subdominant effect for our relatively low pressure conditions. At the surface Cl atoms may react with and etch the silicon, or may recombine to form Cl_2 . We will assume both the etch rate and the recombination rate to be linearly proportional to the incident Cl particle flux at the surface. However it can be shown that our model is independent of the order of these reactions, provided that the order is the same for both etching and recombination. The ratio of the etch rate to the recombination rate is the one free parameter in our model.

In order to calculate the concentration of Cl at the etching surface, the generation of Cl atoms in the beam was calculated. Absorption by Cl_2 , for the pressures studied here, was small enough that the chlorine ambient could be considered to be optically thin in the region of the via ($1/\alpha \approx 4.5 \text{ mm}$ at $P_{\text{Cl}_2} = 400 \text{ Torr}$, [6] wafer thickness $\approx 0.2 \text{ mm}$). Thus, the source s_0 becomes:

$$s_0 = 2 \frac{\alpha P_s}{h\nu} \quad (2)$$

where P_s is the calculated laser power at the sample surface, $\alpha(P_{\text{Cl}_2})$ is the Cl_2 absorption coefficient ($\alpha[\text{cm}^{-1}] \approx 5.5 \times 10^{-3} P_{\text{Cl}_2}[\text{Torr}]$, [6]) and $h\nu$ is the energy per photon ($h\nu \approx 3.5 \text{ eV}$ for $\lambda = 350\text{--}360 \text{ nm}$). In the steady state, the continuity equation ($\nabla \cdot J = 0$) implies that the net flux of Cl to the surface at radius R is $J_{\text{surf}} = s_0/2\pi R$. This flux is balanced by the etching and recombination processes at the sample surface:

$$J_{\text{surf}} = J_{\text{etch}} + J_{\text{rec}} \quad (3)$$

$$J_{\text{etch}} = \eta_e n_R \bar{v}/4 \quad (4a)$$

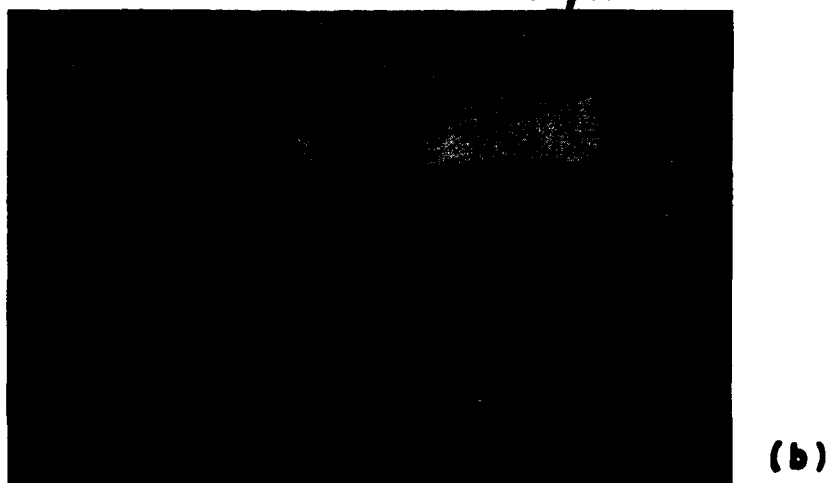
$$J_{\text{rec}} = \eta_r n_R \bar{v}/4 \quad (4b)$$

where η_e and η_r are the reaction efficiencies for etching and recombination, respectively, \bar{v} is the Cl atom thermal velocity, and n_R is the Cl atom density at the via surface. The flux J_{etch} etches the surface via the net reaction[7]:





50 μm



200 μm

Figure 1. (a) Scanning Electron Microscope (SEM) micrograph showing crystallographic dependence of etched via in silicon. The sample was (100) silicon cleaved parallel to the (110)-plane. Laser power P_L was 0.08 W. Chlorine pressure was 400 Torr. Etch time was 1000 s. (b) SEM micrograph showing via morphology for high-power, long-etch-time regime. Laser power P_L was 0.48 W. Chlorine pressure was 500 Torr. Etch time was 600 s.

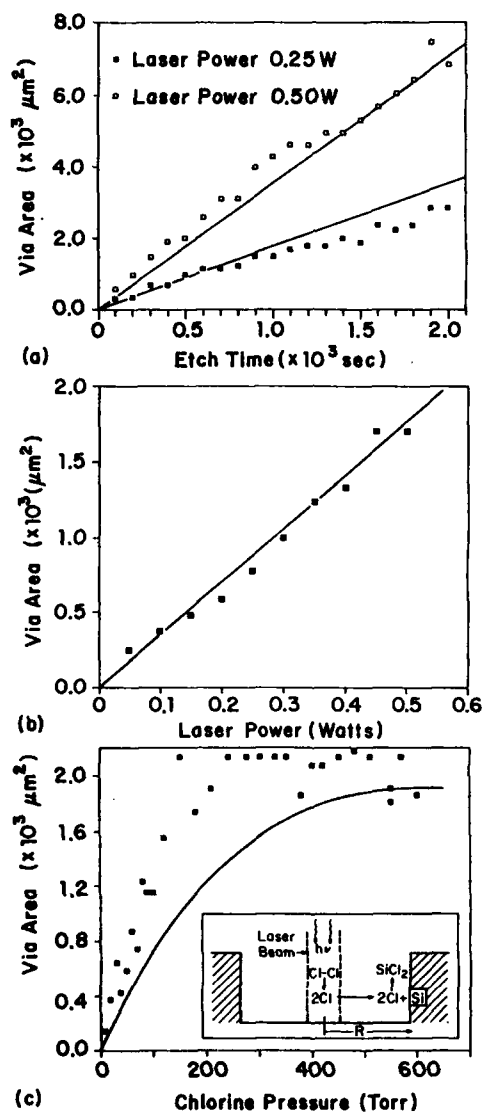


Figure 2. (a) Etched via area vs. etch time. Chlorine pressure was 400 Torr. (b) Etched via area vs. laser power. Chlorine pressure was 400 Torr. Etch time was 500 s. In (a) and (b) the laser power P_L at the vacuum chamber was 16% of the indicated laser power. (c) Etched via area vs. chlorine pressure. Laser power P_L was 0.08 W. Etch time was 500 s. Solid lines in (a-c) are model predictions. The inset shows a schematic diagram of the simplified geometry used in the theoretical model. The via is represented as a cylinder, of radius R . The source is a cylinder in the center of the via.

increasing the via radius at a rate:

$$dR/dt = \frac{1}{2} J_{\text{etch}} / N_{\text{Si}} \quad (6)$$

Combining (1)-(6) and integrating the resulting equation for $R(t)$ yields the following expression for via area:

$$\pi R^2 = \frac{\eta_e}{\eta_r + \eta_e} \frac{\alpha P_L \exp(-\alpha l)}{h\nu N_{\text{Si}}} t \quad (7)$$

where R is the via radius, t is the etch time, P_L is the laser power incident on the vacuum chamber, and l is the distance between the window and the sample surface (3 mm). The dependence on chlorine pressure is through α , which is proportional to P_{Cl_2} . The ratio η_e/η_r , the only adjustable parameter in the model, was found to be 0.011.

The experimental data plotted in Figures 2a-c are in good agreement with this mathematical model. Because of the linear dependence of the via area on t and P_L as shown in Eq. 7, the model predicts the observed linear dependence of the etched via area on etch time and laser power. The saturation that is observed in the etch rate at higher pressures is shown by the model to be explainable by absorption of the laser power in the space above the sample.

Finally, we have recently begun applying this UV laser etching technique to the fabrication of practical device structures. Although we could not routinely operate at high laser powers for the UV wavelengths reported here, smooth, cylindrical vias were etched through a 250 μm thick wafer in less than 5 min at a power of 0.8 W. These vias have been employed in the fabrication of a novel low-loss fiber-optic tap[8]. In that work, laser etched vias were shown to have good electrical properties and to be ideally suited to the insertion of optical fibers due to the matching cylindrical geometry and similar aspect-ratio. With even higher power (4 W), multiline (458-514 nm) operation, through-wafer vias could be etched in silicon in under a minute using a combination of the present photolytic process, and a melt-enhanced reaction studied earlier[4].

In conclusion, we have demonstrated the etching of silicon using a photolytically generated source of atomic chlorine. The process has been used to form smooth through-wafer vias in silicon, and may be useful in other applications requiring a microscopic source of chlorine atoms. A model has been presented that describes the etching process as a function of etching time, laser power, and chlorine pressure, and which yields excellent agreement with experimental data.

The authors would like to thank R. Beach for his help in the early stages of this work, as well as J. O'Neill for helpful discussions regarding the possible chemical reaction mechanisms. This work was supported by the Semiconductor Research Corporation.

REFERENCES

1. D.J. Ehrlich, R.M. Osgood, Jr., and T.F. Deutsch, Appl. Phys. Lett. 38, 1018 (1981).
2. H. Okano, Y. Horiike, and M. Sekine, Jpn. J. Appl. Phys. 24, 68 (1985).
3. M. Lax, J. Appl. Phys. 48, 3919 (1977).
4. G.V. Treyz, R. Beach, and R.M. Osgood, Jr., Appl. Phys. Lett. 50, 475 (1987).
5. M.C. Heaven and M.A.A. Clyne, J. Chem. Soc., Faraday Trans. 78, 1339 (1982).
6. G.E. Gibson and N.S. Bayliss, Phys. Rev. 44, 188 (1933).
7. G.V. Treyz, R. Beach, and R.M. Osgood, Jr., J. Vac. Sci. Technol. B 6, 37 (1988).
8. E. Harstead, S.D. Elby, and P.R. Prucnal, in Optical Fiber Communications Conference Proceedings (Optical Society of America, Washington, DC, 1988), p. THE3.

ANGLE RESOLVED TIME-OF-FLIGHT MEASUREMENTS OF THE EXCIMER LASER INDUCED ETCHING OF SILICON IN A CHLORINE ENVIRONMENT

T.S. Baller, J. van Zwol, S.T. de Zwart, G.N.A. van Veen, H. Feil and J. Dieleman
Philips Research Laboratories, P.O. BOX 80.000, 5600 JA Eindhoven, The Netherlands

ABSTRACT

Si (100) samples have been irradiated with excimer laser pulses ($\lambda = 308\text{nm}$, pulsewidth = 28ns) in a low pressure chlorine environment, at a fluence just enough to melt the surface. Time-of-flight spectra of the particles desorbed due to the laser irradiation have been measured as a function of effective chlorine pressure and desorption angle. Maxwell-Boltzmann distributions have been used to fit the measurements. The mean kinetic energy per particle increases with increasing chlorine pressure. Angular distributions of the desorbed particles are found to be cosine like at a chlorine coverage much less than a monolayer and sharply peaked along the surface normal at coverages on the order of a monolayer. Monte-Carlo simulations of the desorption process show that due to collisions between the desorbed particles the change in angular distribution can be explained. The increase in mean energy with increasing chlorine coverage however cannot be explained by gas phase collisions. A possible desorption process is suggested.

INTRODUCTION

In the past decade the search for new dry etching methods especially in the microelectronics industry has initiated research in the field of laser assisted processing. Much work has been presented on the etching of metals and semiconductors under UHV conditions by nanosecond or picosecond laser pulses [1]. Also cw laser etching of semiconductors in the presence of reactive gases at relatively high pressures has been studied extensively [2]. However, the etching with the assistance of short pulse lasers in combination with low reactive gas pressures is a fairly new field of interest. The selective adsorption of the etching gas and the reduced effect of diffusion of gas-phase reactants will possibly lead to higher selectivity and high anisotropy. Also from a fundamental point of view it would be interesting to know which processes occur under these desorption conditions. In a foregoing paper the time-of-flight (TOF) distributions of the excimer laser enhanced etching of silicon at low chlorine pressures have been presented [3]. In this paper the results will be extended with measurements of the angular dependence of the desorption flux and the energy distributions. The importance of angular dependent measurements will be shown with the help of preliminary results of Monte-Carlo simulations of the desorption process.

EXPERIMENTAL

The experimental set-up used has been described earlier [4]. The main differ-

ences are that the ion source is replaced by an excimer laser and the pseudo-random chopper facility is replaced by a pulse-and-wait detection system. In this paper only the most important technical aspects are given. A Si (100) sample is placed in the center of a UHV chamber with a base pressure of 1.10^{-9} mbar. Before mounting, the samples are cleaned using a HF dip method. The effectiveness of the cleaning procedure has been studied separately by Auger measurements [5]. It has been shown that after cleaning only a fraction of a monolayer oxide is present at the surface. In the time between cleaning and mounting an oxide layer with a maximum thickness of 6 Å will grow. During the experiments the sample has been directly exposed to chlorine which flows through a capillary. Experiments have shown that the exposure obtained in this way is 14 times higher than the measured background pressure. This factor has been taken into account in the results presented below. In the experiments effective chlorine pressures between 1.10^{-8} and 1.10^{-5} mbar are used. As a light source an excimer laser is used with a pulse width of 28 ns operating at a wavelength of 308 nm. All the experiments are performed at a laser power density just enough to melt the silicon. This is checked by probing the reflectivity of the surface during irradiation with a frequency stabilized HeNe laser. The angle of incidence of the excimer laser is 57.5° and its spot size is a few mm^2 . Repetition frequencies between 1 and 80 Hz are used.

In the UHV chamber a differentially pumped quadrupole mass spectrometer equipped with an electron impact ionizer can be rotated around the midpoint of the sample. The detection angle is defined as the angle with respect to the surface normal. The distance between the ionizer and the sample is 300 mm. The entrance angle is large enough that at all detection angles the whole sample can be viewed. Neutral particles, desorbed in a short time, are counted as a function of time after the pulse. The signals of a series of pulses, are accumulated in a multi channel scaler with a time resolution of 5 microseconds.

RESULTS

From the mass distribution, given in a foregoing paper [3], it can be seen that in the system studied the main etch product using 308 nm is SiCl. Only a minor fraction of SiCl₂ and SiCl_{3,4} has been detected.

In this study TOF spectra are measured at the mass of SiCl at 5 different effective chlorine pressures and 6 detection angles. The effective chlorine exposure between the laser pulses is varied by changing the repetition frequency of the laser or the gas pressure. All the measured TOF spectra are fitted with a Maxwell-Boltzmann (MB) distribution with the temperature as fit parameter. The temperatures found under the different conditions are summarized in figure 1. At low Cl₂ exposures the temperature found in the fit is only slightly dependent on the detection angle. At higher exposures the temperature found at a small detection angle increases drastically, whereas at a large detection angle the temperature decreases only slightly.

To calculate the flux of desorbed particles as a function of chlorine exposure the measured TOF flux distributions are integrated. In figure 2 these integrals are plotted as a function of detection angle and chlorine pressure. At low chlorine exposure the angular distribution resembles almost a cosine distribution whereas at high exposure the distribution is sharply peaked along the surface normal. The

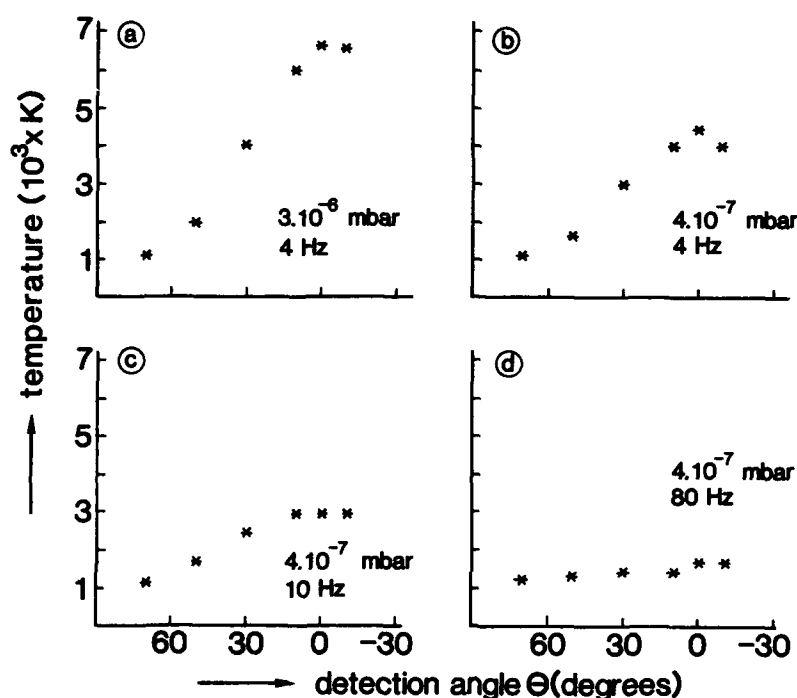


Figure 1 : Temperatures found in Maxwell-Boltzmann fits of the measured TOF distributions, as a function of chlorine exposure and detection angle.

combination of the data from figures 1 and 2 shows an increase of mean energy per particle with increasing exposure. In figure 3 the relative change in mean energy per particle is plotted versus the effective Cl_2 pressure. The values are calculated by weighing the mean energy at each detection direction, obtained by the MB fit, by the flux of particles in that direction. The flux in each direction is corrected for the $\sin(\Theta)$ dependence of the measured flux.

Angular distributions at mass 98 ($SiCl_2$) are measured at four of the coverages used for $SiCl$ as well. These angular distributions resemble in all cases the distributions of the $SiCl$ measurements at the same conditions. Because of the small signal at mass 98, TOF spectra at this mass are only measured at zero degrees detection angle as a function of chlorine exposure. In the Maxwell-Boltzmann fits temperatures have been found which are comparable to the values found for $SiCl$ under the same etch conditions. In figure 4 the relative desorption flux as function of Cl_2 pressure is plotted for $SiCl$ and $SiCl_2$. The data for the latter one are obtained using the angular distributions found for $SiCl$ and the relative fluxes measured at zero degrees. The desorption of $SiCl$ is linearly dependent on chlorine

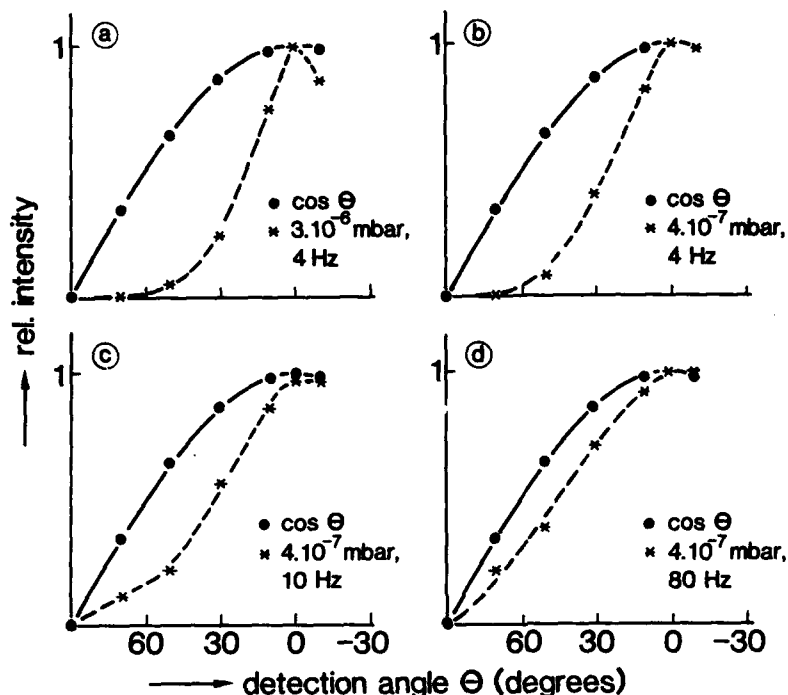


Figure 2 : Measured flux as a function of chlorine exposure and detection angle.

exposure whereas the desorption of SiCl_2 is almost independent of exposure. Saturation takes place above an effective chlorine pressure of about $1 \cdot 10^{-6}$ mbar.

DISCUSSION

The adsorption of Cl_2 on Si has been studied in detail in the past [6]. Chlorine dissociatively adsorbs on the silicon up to one monolayer with a high sticking probability, after which the sticking probability drops drastically. At the chlorine pressures used in our experiments a maximum coverage of one monolayer Cl atoms will be obtained after an exposure of about 16 Langmuir ($1\text{L} = 1 \cdot 10^{-6}$ Torr.s). The saturation behaviour in figure 4 is in reasonable agreement with this. From the linear increase of the etch yield with chlorine pressure it can be inferred that all or almost all of the chlorine is removed in each pulse. During etching no etch time dependent effects are found in contrast to similar experiments on copper published earlier [7]. The most important results are the peaking of the desorbed particle flux and the increase of the mean energy per particle with increase of

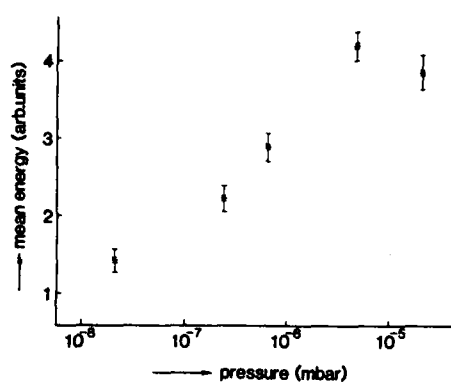


Figure 3 : Mean energy per particle as a function of effective chlorine pressure. Repetition frequency is 4 Hz.

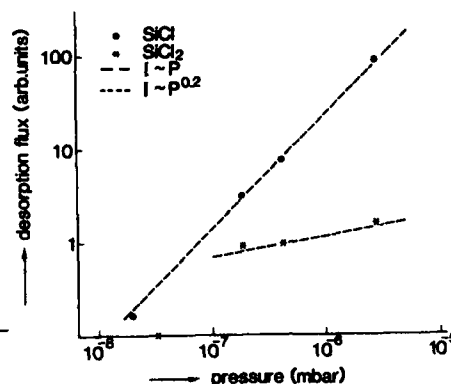


Fig.4 Desorption flux integrated over the whole angular distribution as a function of effective Cl_2 pressure for SiCl and SiCl_2 . Repetition frequency is 4 Hz.

chlorine exposure of the sample. How can these results be explained?. Cowin et al. [8] suggested that during fast desorption of particles from a surface, collisions between these particles would occur just above the surface. Recently Noorbach et al. [9] calculated with a Monte-Carlo method that these collisions indeed should take place in the laser desorption of D_2 from tungsten and NO from LiF . We performed the same kind of calculations for the desorption of SiCl from silicon. Results from these calculations will be presented in a forthcoming paper [10]. Preliminary results show that collisions between the desorbed molecules give rise to peaking of the flux along the surface normal if per laser pulse a whole monolayer is desorbed. The mean temperature of the particles along the surface normal increases only a few hundred degrees above the desorption temperature whereas the temperature at large angles decreases much more. This is of course plausible because in this kind of simulation the mean energy per particle is preserved. Neither heating nor cooling of internal degrees of freedom are taken into account. This seems reasonable because measurements of the internal excitation of the SiCl molecules in a similar etching system indicated that the molecules were not sufficiently internally cooled to explain the increase in translational energy [11]. From the number of collisions between the desorbed particles and the knowledge that only a few collisions between particles with different kinetic energy and mass are enough to share the kinetic energy it can be understood why under equal conditions but different masses, MB distributions are found at similar temperatures.

To explain the change of the mean energy per particle with changing chlorine exposure, yet another mechanism has to be included. A possible mechanism is the photo-dissociation of desorbed SiCl or SiCl_2 molecules. In this case the photon

energy minus the dissociation energy would be shared by collisions. However, even at the lowest chlorine coverages used, in which case no collisions can take place, no increase in SiCl_2 flux is found. Also neither fast SiCl molecules nor Cl atoms have been detected. Although gas phase absorption cannot be excluded beforehand, more optical measurements have to be performed to be sure, it seems that these will not lead to the very high kinetic energies.

Electronic effects at the surface are other ways to increase the kinetic energy. Different electronic mechanisms for the the desorption of fast particles from laser-irradiated surfaces have been suggested in the literature [12,13]. In none of these theories has the concentration of adsorbates been taken into account. It may be suggested that because of a decrease of the work function of the surface due to the chlorine at the surface the emission of electrons and ions is changed. If ionized SiCl particles will be repelled out of the surface and afterwards neutralized by the electrons, relatively fast neutral SiCl particles will be created. The possible characteristic energy distribution will be lost by collision effects. At the moment, it is not clear if such a model is reasonable. More detailed experiments have to be done concerning other aspects of the etching system (e.g. thermal radiation of the surface, electron and ion yield) to obtain more indications for the correctness of this explanation.

In conclusion, it can be stated that angular resolved measurements are necessary when TOF measurements are used to study fast desorption processes. With the results of Monte Carlo calculations, the angular dependence of the measured distributions can be explained. The increase in mean energy with increasing chlorine coverage suggests that additional effects have to be taken into account to understand the processes that take place at the surface during particle emission.

REFERENCES

1. R.R. Alfano, *Semiconductors Probed by Ultrafast Laser Spectroscopy*, (Academic Press, New York, 1984)
2. D. Bauerle, *Chemical Processing with Lasers*, 1st ed. (Springer, Berlin, 1986)
3. T. Baller, D.J. Oostra, A.E. de Vries and G.N.A. van Veen, *J. Appl. Phys.* **60**, 3221 (1986)
4. J. Dieleman, in *Photon, Beam and Plasma Enhanced Processing*, Proc. E-MRS 1987 (editors A. Golanski, V.T. Nguyen and E.F. Krimmel)
5. P.A.M. van der Heide, M.J. Baan Hofman and J. Ronde, *Philips technical note* 1987
6. J.V. Florio and W.D. Robertson, *Surf. Sci.* **18**, 398 (1969)
7. T.S. Baller, G.N.A. van Veen and J. Dieleman, *J. Vac. Sci. Technol.* **A6**, 1409 (1988)
8. J.P. Cowin, D.J. Auerbach, C. Becker and L. Wharton, *Surf. Sci.* **78**, 545 (1978)
9. I. Noorbach and R.R. Lucchese, *J. Chem. Phys.* **86**, 5816 (1987)
10. I. Noorbach and R.R. Lucchese, *Phys. Rev. B*, **36**, 4978 (1987)
11. H. Feil and T.S. Baller, to be published
12. R. de Jonge, J.W.F. Majoor, K.W. Benoit and A.E. de Vries, *Eur. Phys. Lett.* **2**, 843 (1986)
13. P.R. Antoniewicz, *Phys. Rev. B* **21**, 3811 (1980)
14. S.A. Buntin, L.J. Richter, R. Cavanagh and D.S. King, *Phys. Rev. Lett.* **61**, 1321 (1988)

PHOTODISSOCIATION OF CHLORINE ON A COOLED SILICON WAFER

MASAHIRO KAWASAKI, HIROYASU SATO* and NOBUYUKI NISHI**

Research Institute of Applied Electricity, Hokkaido University, Sapporo 060, Japan

* Chemistry Department of Resources, Mi'e University, Tsu 514, Japan

**Institute for Molecular Science, Okazaki 444, Japan

Laser irradiation at 193 nm of multilayered Cl_2 on an Si wafer cooled to 100 K leads to both photodissociation of Cl_2 and formation of photoetching products.

1. Introduction

Reduction of side etching has been studied to create small lines and holes for highly integrated devices. Wafer temperature control during dry etching provides an excellent possibility of allowing device processing at the nanometer level[1]. Laser surface chemistry on a cryosubstrate will provide basic information for this new method of surface processing. Photodissociation of monolayers on substrates has been reported by some groups[2-4]. They have measured the translational energy distribution of photofragments ejected from the substrate in photodissociation of CH_3Br [2,3], H_2S [4], and trimethylaluminum[5], and report that the fragments have low translational energy components. This result is similar to that reported in photo-desorption of molecules from surfaces[6]. We have intended to study UV laser photodissociation of chlorine molecules on silicon substrates in order to understand the radical behavior on the substrate for etching processes[7].

2. EXPERIMENTAL

The substrate (an Si wafer or a quartz plate) was cooled to 100 K, on which sample molecules were deposited through a stainless capillary until sample molecules formed solid on the substrate. An excimer laser (pulse width ~ 10 ns) was used to irradiate the substrate at glancing incidence (80° to the normal). The laser wavelengths used were 193, 248 and 351.1 or 353.1 nm. The laser energy fluence was 10 mJ/cm^2 . The molecules and radicals ejected from the surface were detected by a quadrupole mass spectrometer equipped with an electron bombardment ionizer as shown in Fig. 1. Signals were accumulated as a function of time after laser pulses. The time-of-flight (TOF) signals were converted to a translational energy distribution using a suitable Jacobian factor[8]. An n-type Si (100) wafer was used after doping with P^+ ions. The dose rate was $3 \times 10^{15} \text{ cm}^{-2}$, and ρ_a was $19 \text{ } \Omega/\square$. Undoped Si (111) wafers were also used.

3. RESULTS AND DISCUSSION

a) Effect of thickness of Cl_2 multilayers on TOF distributions of photoproducts

When Cl_2 deposited on the Si wafer was irradiated at 193 nm, Cl atoms were detected as one of the photoproducts. The TOF distributions for thin- and thick-depositions of Cl_2 on the substrate are contrasted in Fig. 2. The TOF distribution is bimodal for the thin-deposition case. The low-energy component appeared only in photodissociation of the thin-deposited Cl_2 , since Cl atoms photogenerated on the substrate surface are decelerated by strong interaction between the atoms and the

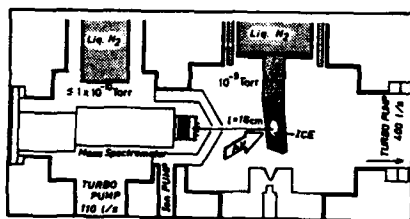


Fig. 1 Experimental setup.

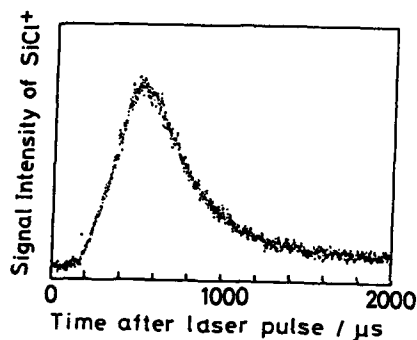
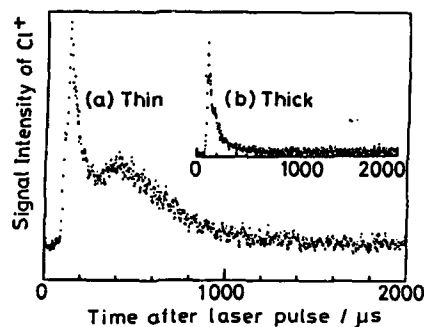
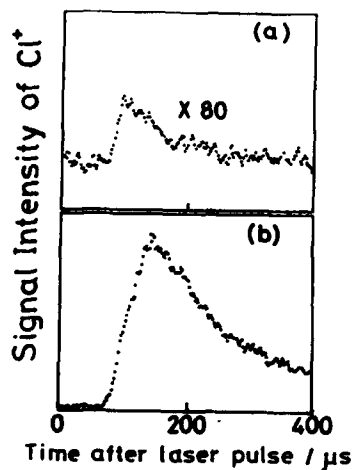
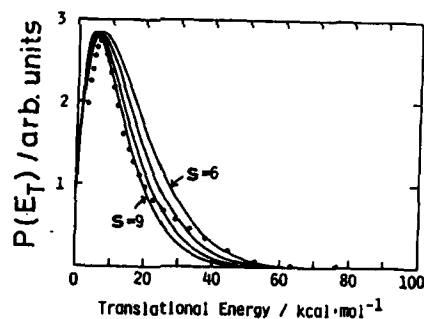
Fig. 3 TOF distribution of SiCl from photodissociation of Cl₂ on an Si wafer at 193 nm. Drift time in the mass filter is 35 μs for SiCl⁺.Fig. 2 Time-of-flight distribution of Cl atomic photofragments obtained in photodissociation of Cl₂ molecules deposited thin(a) and thick(b) on an Si wafer cooled to 100 K. Drift time in the mass filter is 26 μs for Cl⁺.Fig. 4 Translational energy(E_T) distribution of Cl atomic photofragment obtained in photodissociation of Cl₂ molecule deposited thick on an Si wafer cooled to 100 K (Fig. 2(b)). Laser wavelength is 193 nm. Open circles are experimental results. Solid lines are obtained by Eq. (1) in the text or $E_T^{-1/2} (E_{AVL} - E_T)^{s-1}$, for $s = 6-9$.

Fig. 5 Change in the yield of Cl photofragments (a) on a quartz plate and (b) on an Si wafer. The sensitivity of (a) is higher than that of (b) by a factor of 80.

surface.

The high-energy component of Cl atoms observed in Fig. 2 is considered to be formed by photodissociation of the Cl₂ molecules on the top molecular layer of the multilayered Cl₂. Similar dependence of kinetic energies on the surface coverage was reported for photodissociation of CH₂I₂ on Al₂O₃ and Al surfaces with a pulsed 308 nm laser[9].

Cl atoms photo-generated on the Si surface may result in generation of etching products for the thin-deposition case.



Mass analysis gave signals at $m/e = 63$ (SiCl⁺) and 98 (SiCl₂⁺) but not at 133 (SiCl₃⁺) nor 168 (SiCl₄⁺). The TOF distributions of these products consist only of the low-energy component as shown in Fig. 3. Sanders et al. [11] investigated the products of ion-bombardment-induced reaction of Cl₂ with Si surfaces at temperature of 300 K. SiCl₃ and SiCl₂ radicals and Cl atoms are preferentially emitted. These observations resemble the Si etching with both XeF₂ and Ar⁺, that is, SiF and SiF₂ are preferentially generated[10]. Cl(F) produced on an Si substrate results in the formation of SiCl(SiF) and SiCl₂(SiF₂) molecules.

b) Translational energy of photoproducts

The fast moving photofragments from solid Cl₂ (Fig. 2(b)) have a rather large width, compared with that of gas-phase photodissociation. The full width at half maximum was as wide as 100 μs. The energy partition among solid parent molecules makes the width of the TOF spectrum larger than that of gas-phase photodissociation. This wide distribution reflects energy flow among the oscillators in the Cl₂ solid.

Based on phase space theory, the number of effective modes may be estimated by using the following equation for the translational energy distribution.

$$P(E_T) = E_T^{-1/2} (E_{AVL} - E_T)^{s-1} \quad (1)$$

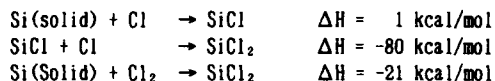
where s is the number of modes over which the vibrational energy is distributed among the multilayer of Cl₂ molecules. Figure 4 shows the simulated and experimental spectra for the Cl fragment obtained at 193 nm. The number of effective oscillators (s) is between 6-9 for this case, that is, the vibrational energy is relaxed among the lattice modes of the Cl₂ solid with this effective number of the oscillator modes.

c) Formation of etching products

By irradiation at 193 and 248 nm, SiCl and a small amount of SiCl₂ were detected as photoproducts. Neither SiCl₃ nor SiCl₄ were detected in the present experiment. When SiCl₄ solid was irradiated at 193 nm, Cl atoms were detected as primary photoproducts but SiCl and SiCl₂ were not. This result suggests that in the photodissociation of Cl₂ on the Si wafer, SiCl and SiCl₂ are produced by reaction of Cl atoms with the Si wafer and not by the secondary photodissociation of SiCl₄ on the substrate. It is reported that SiCl and SiCl₂ are detected by mass spectrometry in an ion-assisted Cl atomic reaction with an Si wafer[11]. F atomic

reaction produces SiF_2 that has been detected by the laser-induced-fluorescence technique[12]. SiF_2 radicals on the Si surface has been proposed in the interaction between the vibrationally excited SF_6 molecules with silicon[11]. Photogenerated Cl atoms may have kinetic energies up to 25, 58 or 91 kcal/mol in the photodissociation at 351, 248 or 193nm, respectively.

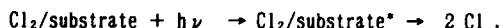
Since the reaction of Cl atoms with an Si substrate to form SiCl or SiCl_2 is endo- and exo- thermic, respectively, hot Cl atoms initiate the reactions by attacking the substrate to form these products.



The relaxation of energy is so fast on the substrate surface that the photodesorbed SiCl and SiCl_2 have the Maxwell-Boltzmann kinetic energy distributions. The average E_T value is 1.0~1.2 kcal/mol. Since desorbed SiCl and SiCl_2 are produced on the substrate surface by reactions of the Cl atoms with the top atomic layers of the Si wafer, their kinetic energy is as low as that of the Cl atoms desorbed from the substrate surface.

d) Effect of substrates on photodissociation of Cl_2

The signals of Cl atoms were observed for two different kinds of substrates: an Si wafer and a quartz plate. The results at 193 nm for both substrates are contrasted in Fig. 5. On the Si wafer, the signal intensity was larger than on the quartz plate. Since Cl_2 gas has a weak absorption cross section at this wavelength, some enhancement must occur on the Si wafer. This enhancement may be caused by energy transfer from the Si substrate excited electronically by the laser photons. The absorbance of an Si substrate is as large as 10^6 cm^{-1} . The underlying Si wafer can absorb UV photons quite well and thus electronically excites the Cl_2 molecules on the Si substrate.



where substrate* denotes the electronically excited Si substrate by UV photon absorption. The substrate excitation has been observed experimentally[13]. The etch rates achieved with the laser excitation of the solid surfaces are always higher than those obtained by the excitation of the gas phase alone.

REFERENCES

1. S. Tachi, K. Tsujimoto, and S. Okudaira, Appl. Phys. Lett., **52**, 616 (1988)
2. E.B.D. Bourdon, J.P. Cowin, I. Harrison, J.C. Polanyi, J. Segner, C.D. Stanners, and P.A. Young, J. Phys. Chem., **88**, 6100 (1984)
3. F.L. Tabares, E.P. Marsh, G.A. Bach, and J.P. Cowin, J. Chem. Phys., **86**, 738 (1987)
4. E.B.D. Bourdon, P. Das, I. Harrison, J.C. Polanyi, J. Segner, C.D. Stanners, R.J. Williams, and P.A. Young, Discuss. Faraday Soc., **82**, 343 (1986)
5. G.S. Higashi, J. Chem. Phys., **88**, 422 (1988)
6. a) D. Burgess, Jr., R. Viswanathan, I. Hussla, P.C. Stair, and E. Weitz, J. Chem.

- Phys., 79, 5200 (1983)
b) D. Burgess, Jr., D.A. Mantell, R.R. Cavanagh, and D.S. King, J. Chem. Phys., 85, 3127 (1986)
7. M. Kawasaki, K. Kasatani, H. Sato, N. Nishi, and G. Inoue, 12th Internat. Conf. Photochem. (Tokyo, Aug. 4-9, 1985), 1A06
8. N. Nishi, M. Shinohara, and T. Okuyama, J. Chem. Phys., 80, 3898 (1984)
9. T.J. Chuang and K. Domen, J. Vac. Sci. Technol., A5, 473 (1987)
10. U. Gerlach-Meyer, J.W. Coburn and E. Kay, Surface Sci., 103, 524 (1981)
11. F.H.M. Sanders, A.W. Kofschoten, J. Dielman, R.A. Haring, A. Haring, and A.E. de Vries, J. Vac. Sci. Technol., A2, 487 (1984); D.J. Oostra, A. Haring, R.P. Van Ingen, and A.E. de Vries, J. Appl. Phys., 64, 325 (1988)
12. a) D.L. Flamm, V.M. Donnelly, and J.A. Mucha, J. Appl. Phys., 52, 3633 (1981).
b) Y. Matsumi, S. Toyoda, T. Hayashi, M. Miyamura, H. Yoshikawa, and S. Komiya, J. Appl. Phys., 60, 4102 (1986)
13. a) D. J. Ehlich, R. M. Osgood, Jr, and T.F. Deutsch, Appl. Phys. Lett., 38, 1018 (1981)
b) T.J. Chuang, IBM J. Res. Develop., 26, 145 (1982)
c) F.A. Houle, J. Chem. Phys., 80, 4851 (1984)

REACTIONS OF PHOTOGENERATED CF_2 AND CF_3 ON SILICON AND SILICON OXIDE SURFACES

JOHN LANGAN**, J.A. SHORTER*, XU XIN*, AND J.I. STEINFELD*

*Department of Chemistry, Massachusetts Institute of Technology, Cambridge, Massachusetts 02139

**Present address: Air Products and Chemicals, Allentown, Pennsylvania 18105

ABSTRACT

We have investigated the reactions of neutral fluorocarbon fragments, generated by laser photolysis of suitable precursors, with single-crystal silicon and thermally deposited silicon oxide surfaces. CF_3 free radicals are generated by infrared multiple-photon dissociation of C_2F_6 . While CF_3 undergoes dissociative chemisorption on Si, it adsorbs very little on annealed SiO_2 surfaces, and even on ion-damaged oxide surfaces, CF_3 adsorbs but does not undergo transfer of fluorine from the fluorocarbon to surface silicon atoms. CF_2 , produced by excimer-laser photolysis of C_2F_4 , is adsorbed on SiO_2 surfaces. As with CF_3 , no transfer of fluorine from carbon to silicon is observed, even after argon-ion sputtering or ultraviolet irradiation of the surface. These measurements have been extended to NF_3 ; this species chemisorbs and dissociates on a silicon surface, but even a monolayer of oxide is sufficient to block this process. A simple model based on the relative strengths of C-F, N-F, Si-F, Si-C, Si-O, and Si-N bonds appears to account for the observed behavior of CF_3 , CF_2 , and NF_3 species on silicon and silicon oxide surfaces. In other cases, however, a barrier appears to be implicated in the chemisorption process.

INTRODUCTION

The reactions of neutral fluorine-containing free radicals and molecules at semiconducting and insulating surfaces constitute an important aspect of plasma-assisted reactive etching processes for these materials. However, elucidating the details of such reactions in the complex plasma environment is difficult, if not impossible, due to the presence of ions, electrons, and high-energy (vacuum-u.v.) radiation along with the reactive neutral species in the plasma. In a recent series of publications [1-8], we have reported investigations of the reactions occurring at silicon and silicon oxide surfaces in the presence of fluorocarbon free radicals (CF_3 and CF_2) produced by gas-phase laser-driven photodissociation of suitable precursor molecules, as well as of reactive fluorinating species such as XeF_2 and NF_3 . In this report, we summarize the results of those investigations, and discuss a simple model based on the relative energies of chemical bonds being formed and broken at the reacting surface, which can account for much of the observed behavior.

EXPERIMENTAL RESULTS

The measurements are carried out in a two-stage UHV chamber as described in earlier publications [2,6,9]. In the upper part of the apparatus, samples of single-crystal silicon (previously sputter-cleaned and annealed) or of thermally grown silicon oxide may be exposed to fluorinating agents such as XeF_2 (PCR, Inc.) or NF_3 (Air Products) at pressures between 10^{-7} and 10^{-4} Torr. Fluorocarbon free radicals are produced above the sample surfaces by photolysis using an appropriate laser source [8]: the 9R(30) CO_2 laser line at 1084.64 cm^{-1} to generate CF_3 from C_2F_6 [2, 6], or the ArF excimer laser emission at 193 nm to generate CF_2 from C_2F_4 [7]. The laser beams are admitted to the

vacuum chamber through differentially pumped windows of the appropriate optical material (ZnSe for the CO₂ laser, S-UV quartz for the excimer laser).

Following exposure and/or irradiation, the samples are transferred into the lower UHV chamber for analysis. The principal method used is XPS with the MgK_α line; thermal desorption spectrometry is also employed to identify species desorbing from the surfaces following exposure.

Both CF₃ and CF₂ undergo dissociative chemisorption on silicon surfaces [2,6,7]. NF₃ has also been found to adsorb and dissociate on silicon surfaces, with formation of the nitride [10]. On thermally grown silicon oxide surfaces, neither CF₃ [6], XeF₂ [5], nor NF₃ [10] are found to undergo chemisorption, unless the oxide layer has been damaged by argon-ion bombardment. There is uptake of CF₂, however, on the undamaged oxide surface [7]. In no instance do we observe transfer of fluorine from species chemisorbed on silicon oxide surfaces such as occurs readily in the case of XeF₂ [4], CF₃ [2, 6], CF₂ [7], and NF₃ [10] on silicon surfaces.

DISCUSSION

The observed behavior of the fluorocarbon radicals and other fluorine-containing species on silicon and silicon oxide surfaces can be understood in terms of a simple model based on the net thermodynamic energy changes associated with bonds made and broken at the surface [8, 11]. The single-bond energies used in these calculations, which are given in Table I, are taken from standard tables and reference works [12,13].

Table I.

Single-Bond Energies (kJ mole ⁻¹)		Notes
Si-O	430	(a)
Si-F	550	(b,c,d)
Si-Si	180 ^{d,e} , 330 ^c	
C-F	460	(c,d)
Si-C	300	(f,d)
Xe-F	17	(c)
O-F	200	(g)
C-O	270	(c)
N-F	340(c), 270(d)	
Si-N	439	(c)

^aFrom value of 4.5 eV, Reference [11].

^bFrom value of 5.6 eV, Reference [11].

^cFrom Reference [12].

^dFrom Reference [13].

^eFrom value of 1.9 eV, Reference [11].

^fAverage of C-C and Si-Si single-bond energies, from Reference [12].

^gAverage of values from References [12] and [13].

All of the species studied (CF_3 , CF_2 , XeF_2 , and NF_3) readily react with the "dangling bonds" on the silicon surface to produce a fluorine-containing overlayer. In each instance, fluorine transfer from the donor species to silicon is an exothermic process, and proceeds spontaneously with room-temperature samples. The remaining C and N atoms are incorporated into the surface, as carbide or nitride, respectively; in the case of XeF_2 , the Xe atom desorbs except at very low temperatures [14]. On an oxide surface, however, there is little or no uptake of CF_3 , XeF_2 , or NF_3 ; in the case of NF_3 , even the native oxide monolayer appears to be sufficient to block chemisorption [10]. Adsorption on an oxide surface would require breaking pre-existing Si-O bonds at the surface, which would convert a net exothermic process into an endothermic (and therefore unfavorable) one; however, if the Si-O bonds are weakened by argon-ion bombardment of the surface prior to exposure, uptake of CF_3 or XeF_2 can occur. The CF_2 species appears to adsorb spontaneously on undamaged oxide surfaces, because insertion of the CF_2 at a Si-O bond produces both a new Si-C bond (-300 kJ/mole) and a new C-O bond (-270 kJ/mole), compensating for the energy required (+430 kJ/mole) in the Si-O bond breaking step. Subsequent transfer of fluorine atoms from the donor species does not occur on oxide surfaces, however, because there is no simple exothermic process which can take place without a good deal of lattice rearrangement.

This model clearly does not take account of energy changes associated with lattice rearrangement or surface reconstruction [15], nor of possible barriers to chemisorption [16]. The importance of barriers is clearly demonstrated by the lack of reactivity of valence-saturated molecular species on surfaces at which the net reaction would appear to be exothermic: F_2 on Si [17], XeF_2 on SiO_2 [5, 8], and undissociated fluorocarbons such as CF_4 on Si are all examples. The presence of a significant barrier to dissociative chemisorption is also demonstrated by the work of Suzuki *et al.* [18] on etching of silicon with a heated molecular beam of SF_6 . In the case of NF_3 , the initial chemisorption step is so exothermic (-650 kJ/mole) that the barrier, if present, can be overcome at room temperature; reaction on the oxide, however, would be endothermic and is not predicted to occur. Further development of this model will need to consider both lattice rearrangement and surface reconstruction energies as well as energy barriers along the reaction path.

ACKNOWLEDGEMENTS

This work was supported under Air Force Office of Scientific Research Contract F49620-860C-0003 and by a graduate fellowship from the Perkin-Elmer Corporation. We thank Dr. S.A. Joyce for helpful discussion.

REFERENCES

1. B. Roop, S. Joyce, J.C. Schultz, N.D. Shinn, and J.I. Steinfeld, *Appl. Phys. Letts.* **46**, 1187 (1985).
2. B. Roop, S. Joyce, J.C. Schultz, and J.I. Steinfeld, *J. Chem. Phys.* **83**, 6012 (1985).
3. S. Joyce and J.I. Steinfeld, in *Photon, Beam and Plasma Stimulated Chemical Processes at Surfaces*, edited by V.M. Donnelly, I.P. Herman, and M. Hirose, (*Mater. Res. Soc. Proc.* **75**, Pittsburgh, Pennsylvania, 1986).
4. B. Roop, S. Joyce, J.C. Schultz, and J.I. Steinfeld, *Surf. Sci.* **173**, 455 (1986).
5. S. Joyce, J. Langan, and J.I. Steinfeld, *Surf. Sci.* **195**, 270 (1988).
6. S. Joyce, J. Langan, and J.I. Steinfeld, *J. Chem. Phys.* **88**, 2027 (1988).

7. J.G. Langan, J.A. Shorter, Xu Xin, S.A. Joyce, and J.I. Steinfeld, *Surf. Sci.* (in press).
8. J.I. Steinfeld, *Chem. Reviews* (to be published).
9. B. Roop, Ph.D. Thesis, Massachusetts Institute of Technology, (1985); S.A. Joyce, Ph.D. Thesis, *ibid.* (1987).
10. J.A. Shorter, J.G. Langan, and J.I. Steinfeld (to be published).
11. J.D. Oostra, A. Haring, and A.E. de Vries, *J. Vac. Sci. Tech.* B4, 1278 (1986).
12. R.C. Weast, ed., *CRC Handbook of Chemistry and Physics*, 67th ed. (CRC Press, Inc., Boca Raton, Florida, 1986), pp. F-167 to F-184.
13. L. Pauling, *The Nature of the Chemical Bond* (Cornell University Press, Ithaca, New York, 1960), p. 85.
14. J.E. Demuth and A.J. Schell-Sorokin, *J. Vac. Sci. Tech.* A2, 808 (1984).
15. I. Oppenheim and R.D. Levine (to be published).
16. S.T. Ceyer, *Ann. Rev. Phys. Chem.* 39, 479 (1988).
17. J.A. Mucha, V.M. Donnelly, D.L. Flamm, and L.M. Webb, *J. Phys. Chem.* 85, 3529 (1981).
18. K. Suzuki, K. Ninomiya, S. Nishimatsu, and O. Okada, *Jap. J. Appl. Phys.* 25, L373 (1986); *ibid.* 26, 166 (1987).

EXCIMER LASER INDUCED ETCHING OF SILICON-CARBIDE

M. MURAHARA*, H. ARAI** AND T. MATSUMURA***

*Faculty of Engineering, Tokai Univ., 1117 Kitakaname, Hiratsuka, Kanagawa, 259-12, JAPAN.

**Central Glass Corporation, Chiyodaku, Tokyo, JAPAN.

***Iwatani Corporation, Atsugi, Kanagawa, JAPAN.

ABSTRACT

Resistless photoetching of SiC was performed by using XeF and KrF excimer laser beams. In this method, ClF₃ gas was used for etchant. ClF₃ gas has a unique absorption band in the range of 300- 430 nm. The strongest absorption band corresponds to the wavelength of the XeF laser (350 nm). So ClF₃ gas is decomposed effectively. On the other hand, the absorption factor of SiC is about 30% in the range of 200-400 nm, and the bonding energy of SiC is lower than the photon energy of the KrF laser beam. For these reasons, it is possible to cut the bond of SiC directly. Thus, two laser beams were used. Fluence of the KrF laser beam was 200 mJ/cm², of the XeF, 50 mJ/cm². Total flow rates through the cell were 0.05 l/min. We can fabricate the etched feature of reticle pattern by reductive projection. Line and space was 10 μm and etching rate was 50Å/pulse.

INTRODUCTION

There is a need to develop semiconductor devices which can operate under extreme conditions. However, the allowable operating temperature of Si and GaAs semiconductors is low, being 100°C. On the other hand, the melting point of SiC is as high as 2830°C, and its critical operating temperature is expected to exceed 600°C. In addition, its band gap is as wide as 2.3 eV, and the electron mobility is high, being from 500 to 1000. For these reasons, it is expected that a superior heat resistance device or blue light emitting device can be developed with SiC. On the other hand, etching of SiC is difficult, and selective etching of minute patterns is almost impossible. Only a few successful experiments in this area have been reported. Methods of selective etching that have been reported recently include etching of Si by means of Cl radicals excited by XeCl excimer laser [1], and etching TiC-Al₂O₃ using a Ar⁺ or YAG laser in CCl₄ or SF₆ atmosphere[2].

In this paper, a new and simple etching method is reported by which SiC is etched with XeF and KrF excimer lasers. The etchant used, ClF₃ gas, has high reactivity. Use of this gas has been reported in relation to etching experiments on Si, Ta, Ta₂N, Ta₂O₅, TaSi, SiO₂, and Si₃N₄[3,4,5]. Recently, we have verified that this gas has various interesting photochemical features[6,7].

PHOTOCHEMICAL REACTIONS

In photochemical reactions, the raw material gas must absorb photons directly, and the photon energy must be larger than the binding energy of constituent molecules[8]. As illustrated in Figure 1, ClF₃ gas has discrete absorption in the band of 300 to 430 nm, and its strongest absorption coincides with the oscillation wavelength of the XeF laser (350 nm). The photon energy of XeF laser light is 80 Kcal, while the binding energy between Cl-F is 60 Kcal/mol. One shot of the XeF laser beam having 100 mJ on ClF₃ gas almost eliminates its absorption by photodissociation. On the other hand, when the KrF laser beam (249 nm) is used to irradiate in a similar manner, the efficiency of photodissociation is low.

In this experiment, fifty percent of 1.5 X 10⁻⁴ mol of ClF₃ gas is dissociated by a single shot of a 20-mJ/cm²-fluence XeF-laser pulse. Only 0.2% of the gas was photodissociated under the same conditions when KrF laser irradiation was applied as shown in Figure 2.

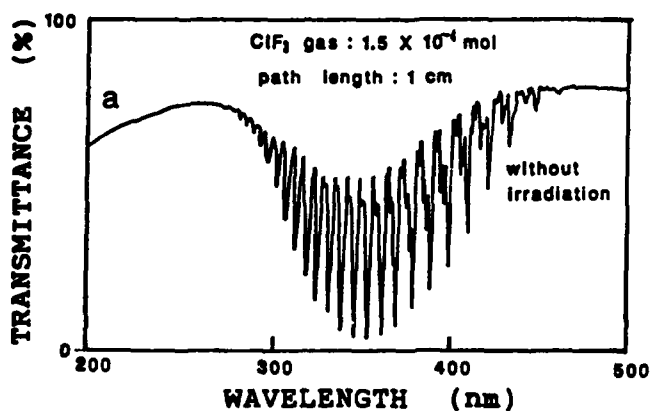


Figure 1 UV transmittance of gaseous ClF_3 .

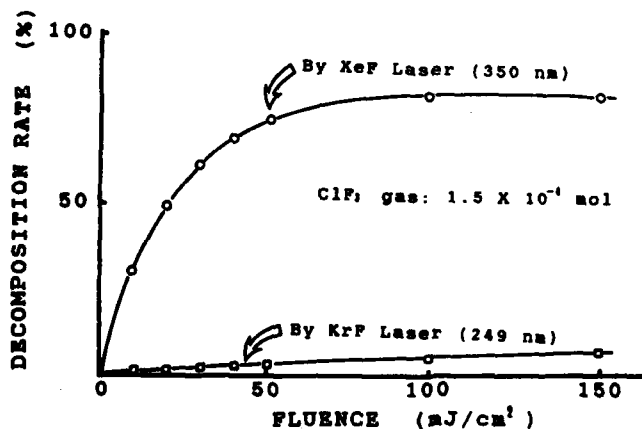


Figure 2 Dependence of decomposition rate of laser beam fluence for XeF and KrF lasers using a single shot.

On the other hand, the photon absorption of SiC is approximately 30% near the wavelength of 249 nm, the binding energy of Si-C bond is 104 Kcal/mol, and the photon energy of the KrF laser beam is 114 Kcal. Therefore, the SiC bond can be cut directly by means of the KrF laser beam. If photodissociations of ClF_3 and SiC occur simultaneously, it is possible to etch the surface of SiC materials.

EXPERIMENTAL SETUP

To verify this concept, we applied two laser beams having different wavelengths to the SiC substrate, one parallel and another perpendicular to the substrate surface as in Figure 3. The parallel XeF laser beam was used to photodissociate ClF_3 gas in the proximity of the substrate, and the perpendicular KrF laser beam was used to locally excite the substrate.

The experimental conditions were as outlined below: 100% ClF_3 gas was sealed in the cell with a pressure of 200 Torr, and a gas flow of 0.05 liters per minute was maintained. The two laser beams were applied to the cell simultaneously. The KrF laser fluence was 200 mJ/cm^2 , and that of XeF laser beam 50 mJ/cm^2 .

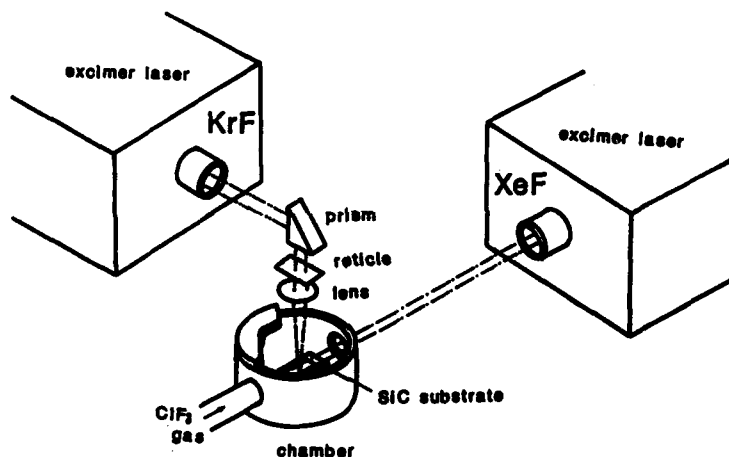


Figure 3 Schematic diagram of etching system using two color excimer lasers.

RESULTS

Polycrystalline SiC films of thickness $4 \mu\text{m}$ were used. Specimen were created on stainless substrate by plasma-enhanced chemical vapor deposition. A pattern was formed in the laser beam with a reticle and projected onto the specimen with a 2:1 optical system. The resulting photo-etched pattern is shown in Figure 4. The line and space were $10 \mu\text{m}$, etching depth 5000 \AA , and etching rate 50 \AA/pulse . In this experiment, etching can never be done by irradiation of the XeF laser beam only. When the KrF laser only is used to irradiate the sample, faint etching is produced because this laser is weakly absorbed by ClF_3 gas, as shown in Figure 1. However, virtually all that happens on the etched part is the change in color to black. When the flow of ClF_3 is small, or the energy of XeF laser beam is low, or synchronization of the XeF and the KrF lasers is substantially out of phase, the SiC surface turns to black. This is because the C in SiC is dissociated to deposit on the substrate surface.

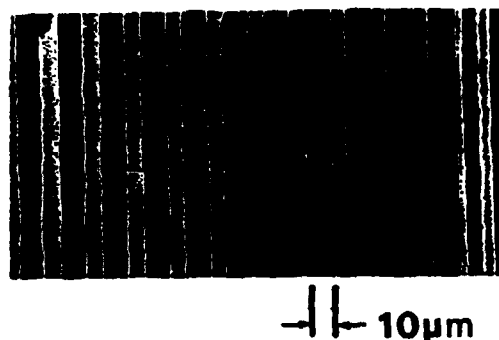


Figure 4 Etched feature of reticle pattern by reductive projection.
Sample is SiC. Line and space is 10 μm .

DISCUSSION

The flow chart of the photochemical reaction that occurs when two laser beams of different wavelengths are applied in parallel and perpendicular directions is given in Figure 5. The Si and C atoms, released from SiC by photo and thermal dissociation brought about by the KrF laser, promptly react with F radicals which are released from ClF_3 gas by the XeF laser beam. The reason for the reaction is that F has a higher electronegativity than Cl in general: the binding energy of C-F is 12k Kcal/mol, that of C-Cl 95, Si-F 129, and Si-Cl 107. For these reasons, then, it can be assumed that Si-C is converted to SiF_4 and CF_4 . The temperature at which the vapor pressure of SiF_4 becomes 200 Torr is -107.2°C , while the value for CF_4 is -143.6°C . Therefore, chemical compounds are evaporated without substrate heating, thereby making it possible to create etching patterns of high contrast.

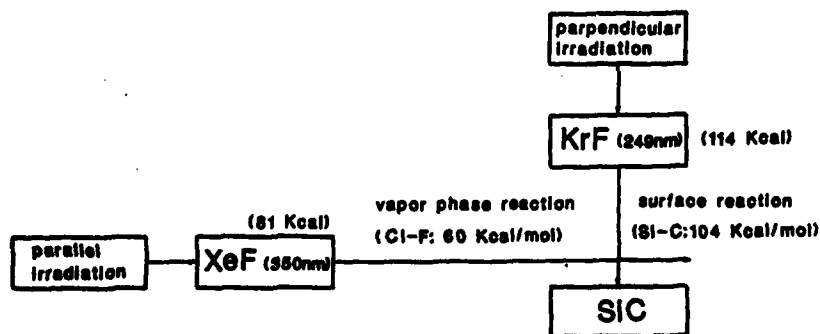


Figure 5 Flow chart of the photoetching process for SiC
by vapor phase and surface reactions.

CONCLUSION

This photochemical reaction was created by the cumulative effect of surface reaction and gas phase reaction caused by laser beams of different wavelengths. In this method, resistless pattern etching of SiC was performed.

REFERENCES

1. M. Sekine, H. Okano, K. Yamabe, N. Hayasaka and Y. Horiiki in "Dry Process" (Proc. 6th Symp. Inst. Electr. Eng., Tokyo, 1984) p.74.
2. T. J. Chuang, "Laser-Controlled Chemical Processing of Surfaces" ed. by A. W. Johnson, D. J. Ehrlich, H. R. Schlossberg, (North-Holland, NY 1984) p. 185.
3. Daniel L. Flamm, David N. K. Wang, and Dan Maydan, J. Electrochem. Soc., 129(12), 2757(1982)
4. D. E. Ibbotson, J. A. Mucha, D. L. Flamm, and J. M. Cook, J. Appl. Phys. 56(10), 2939(1984).
5. D. E. Ibbotson, J. A. Mucha, D. L. Flamm, and J. M. Cook, Appl. Phys. Lett. 46(8), 794(1985).
6. S. Asahara, A. Sakai, T. Matsumura, H. Arai, and M. Murahara, Extended Abstract of the 48th Autumn Meeting of the Japan Society of Applied Physics, 682(1987).
7. S. Asahara, T. Matsumura, H. Arai, and M. Murahara, Extended Abstract of the 35th Spring Meeting of the Japan Society of Applied Physics, 527(1987).
8. M. Murahara and K. Toyoda, Springer Series in Chemical Physics 39, 252(1984).

COMPARISON OF CW AND PULSED UV LASER ETCHING OF LiNbO_3

K.W. Beeson and N.S. Clements
Allied-Signal, Inc., P.O. Box 1021R, Morristown, NJ 07960

ABSTRACT

The results of CW frequency-doubled argon-ion laser etching and pulsed excimer laser etching of lithium niobate (LiNbO_3) are compared. Argon-ion laser etching occurs in the presence of Cl_2 at laser intensities of 1.1 MW/cm^2 or higher. The 257 nm laser beam with up to 25 mW power is focused to a $1.5 \mu\text{m}$ diameter spot and scanned at speeds of $10 \mu\text{m/s}$ or less. Excimer laser etching is done at 248 nm (KrF) with the laser beam focused onto the sample with cylindrical optics. Trenches $>20 \mu\text{m}$ wide and several millimeters long are produced by ablating the target and without scanning the beam. Excimer laser etching of lithium niobate has been attempted in the presence of Cl_2 , O_2 , N_2 , H_2 or air. Excellent results are obtained with air as the etching medium.

INTRODUCTION

Lithium niobate has important device applications in the emerging field of integrated optics. Despite its useful optical and acoustic properties [1], LiNbO_3 is very difficult to etch by standard wet or dry chemical means. Recently laser processing [2-7] has been examined as a possible alternative technology for etching LiNbO_3 .

LiNbO_3 is an insulator which is transparent in the visible spectrum but absorbs light in the UV region at wavelengths shorter than 330 nm. At 248 nm and 257 nm, the absorption coefficients are $>10^5 \text{ cm}^{-1}$ [7] which allows easy coupling of energy from a 257 nm frequency-doubled Ar^+ laser or from 248 nm KrF excimer laser irradiation. In this paper, we examine both 257 nm CW laser etching in a Cl_2 atmosphere and pulsed 248 nm excimer laser etching in the presence of Cl_2 , O_2 , N_2 , H_2 or air and compare the two techniques.

EXPERIMENTAL

Polished LiNbO_3 wafers cut perpendicular to the z-axis or y-axis were purchased from Crystal Technologies and cleaned with acetone and methanol prior to etching. Etching at 257 nm was done on z-cut samples placed in a vacuum chamber with a 5-in. diameter fused silica window and a 0.125-in. gap between the inside surface of the window and the sample. The chamber was evacuated and backfilled with 500 Torr of Cl_2 . The cell was then sealed and subsequent experiments were done without changing the gas. The intracavity frequency-doubled Ar^+ laser beam was focused with a microscope objective to give a $1/e$ spot diameter of $1.5 \mu\text{m}$ and a maximum power at the sample of 25 mW. This corresponded to a maximum light intensity of 1.4 MW/cm^2 . To make an etched groove, the beam was scanned one or more times along the same line at velocities ranging from 0.5 – $10 \mu\text{m/s}$.

Excimer laser etching was done with a Lambda Physik EMG-200 laser operating at 248 nm and 1–10 Hz. The pulse width was approximately 15 ns. The rectangular beam was focused to a line

on the LiNbO_3 surface either by a single plano-convex cylindrical lens or by a simple projection arrangement using two cylindrical lenses (one condenser lens and one projection lens) and a metal slit as a mask. Excimer laser etching was done mostly on y-cut LiNbO_3 . A few experiments conducted on z-cut LiNbO_3 showed no apparent differences with the y-cut results. Lithium niobate samples were placed in a gas cell with a fused silica window and filled with the appropriate gas to a pressure of 1 atmosphere. Laser fluence was calculated from the pulse energy and focal area on the substrate surface. The beam width was determined by the scanning knife edge technique. Measurements of etch rate versus laser fluence were done with a $1/e$ beam width of approximately $125 \mu\text{m}$ and the resulting etch depths after 250 laser pulses were measured with a scanning profilometer. The fluence was varied by inserting partially transmitting mirrors into the laser beam.

Etched samples were cleaned with methanol before analysis. Some samples were cleaved across the etched lines and examined in cross-section by scanning electron microscopy (SEM). The surface elemental composition of etched lines was determined by Auger electron spectroscopy (AES) using standard sensitivity factors.

RESULTS AND DISCUSSION

We have determined [7] that, for 257 nm frequency-doubled Ar^+ laser etching, Cl_2 is necessary for any etching to take place at the laser beam intensities used in this study ($<1.4 \text{ MW/cm}^2$). Etching is not observed in an evacuated cell under identical laser operating conditions. Even in the presence of Cl_2 , a laser intensity threshold for etching is observed. With a beam diameter of $1.5 \mu\text{m}$ and a scan speed of $2.7 \mu\text{m/s}$, the observed threshold is 1.1 MW/cm^2 corresponding to a laser power of 20 mW. The observation of a threshold is consistent with a thermal etching process involving surface melting. From a simple theoretical calculation [8], the approximate power needed to achieve surface melting of LiNbO_3 (m.p. 1240°C) is given by

$$P = (2\sqrt{\pi} Kw \Delta T) / (1-R) \quad (1)$$

where P is the laser power in watts (W), K is the thermal conductivity ($\text{W cm}^{-1} \text{ deg}^{-1}$) of the substrate, w is the laser beam radius (cm), ΔT is the change in temperature, and R is the reflectivity of the surface. The term $1/(1-R)$ accounts for reflection losses. Using $K = 0.04 \text{ Wcm}^{-1}\text{deg}^{-1}$, $w = 0.75 \mu\text{m}$, and $R = 0.32$, the calculated value of P needed to reach the melting point of LiNbO_3 is 19 mW which is consistent with the experimental results. The parameters K and R are assumed not to change with temperature.

Etched trenches in z-cut LiNbO_3 can be produced by single or multiple laser scans along the same line. Single scans produce trenches approximately 0.5 – $0.8 \mu\text{m}$ deep and $2 \mu\text{m}$ wide. Material removed from an etched trench is redeposited both within the trench and along the edges of the trench where it forms ridges approximately $2 \mu\text{m}$ wide. Multiple laser scans in z-cut LiNbO_3 result in deeper trenches which have a v-shaped cross section. Figure 1 shows SEM micrographs of a trench formed by eight laser scans at $1.4 \mu\text{m/s}$ and a laser power of 25 mW. After etching, the sample is cleaned with methanol which removes a thin blanket layer of easily dissolved material which deposits on the sample during etching and is not shown in the micrographs. The blanket

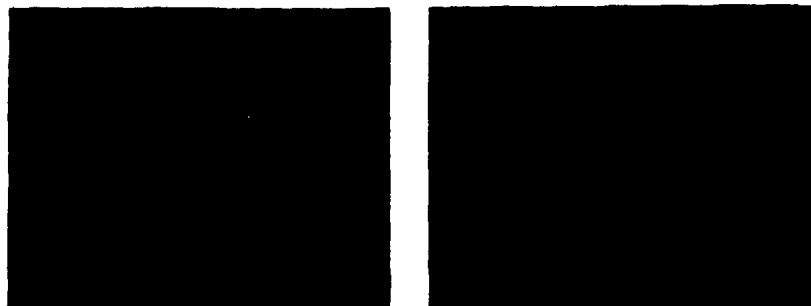


Fig. 1. SEM micrographs of a trench etched by 8 laser scans at $1.4 \mu\text{m/s}$ using a 257 nm frequency-doubled CW Ar^+ laser operating at an incident power of 25 mW. The trench has been cleaned with methanol. (a) Tilted view. (b) Edge view.

layer is due to a photochemical reaction from scattered laser light that dissociates Cl_2 into radicals which can react with the LiNbO_3 surface at light intensities much below the threshold for etching [7]. The granular deposits from the etching process shown in and near the trench in Fig. 1 are not affected by the methanol cleaning but can be removed afterwards by strong bases or acids.

The trench depth for 257 nm CW laser etching does not increase linearly with the number of laser scans but saturates after about eight scans. A typical result is shown in Fig. 2. The saturation effect may be due to the increasing difficulty of etching through the redeposited material remaining in the trench from previous laser scans. Surface analysis has been done by AES on the redeposited material and a surface composition of approximately $\text{Li}_{0.3}\text{NbO}_{1.1}$ (assuming $\text{Nb}=1$) has been observed [7].

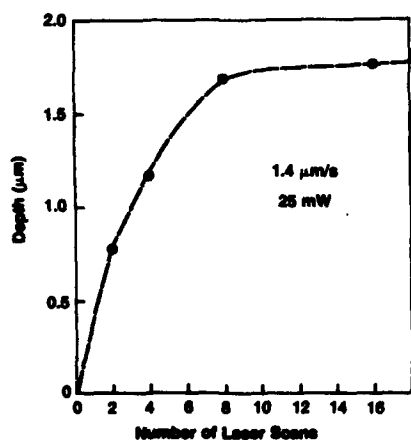


Fig. 2. The variation of trench depth with increasing number of 257 nm CW laser scans at $1.4 \mu\text{m/s}$ and 25 mW.

The resulting material in the bottom of the trench will likely have a different melting point and a different reactivity to Cl_2 than the original LiNbO_3 surface.

The above data for 257 nm CW laser etching are consistent with the following mechanism. The scanning laser beam melts the LiNbO_3 surface. If the experiment is done in vacuum, no chemical reaction takes place and the material merely resolidifies in place after the laser beam has passed resulting in no trench. If Cl_2 is present, the molten material reacts with the Cl_2 forming volatile products which vaporize to form a trench and then redeposit in the colder regions both near the trench and in the trench itself after the laser beam has passed. The layer of redeposited material is not very susceptible to further reaction with Cl_2 which causes the etching process to terminate after several laser scans.

A significant improvement in overall LiNbO_3 etch rates can be achieved using pulsed 248 nm excimer laser etching in place of 257 nm Ar^+ laser etching. With an excimer laser beam of rectangular cross section focused by one or more cylindrical lenses, trenches several millimeters long can be etched in LiNbO_3 without scanning the laser beam. The width of the trenches can be easily varied from a few μm to hundreds of μm depending on the beam optics and the laser pulse energy. These are significant advantages over 257 nm CW laser etching where low available laser powers severely restrict the dimensions of etched trenches and the rate at which trenches can be produced.

Pulsed excimer laser etching experiments were done in a gas cell filled with Cl_2 , O_2 , N_2 , H_2 , or air at one atmosphere pressure to determine if the ambient atmosphere has any effect on etch rates. The laser beam was passed through a 1 mm wide slit approximately 1 cm long and focused to a $1/e$ width of 125 μm using a single cylindrical lens. The results are shown in terms

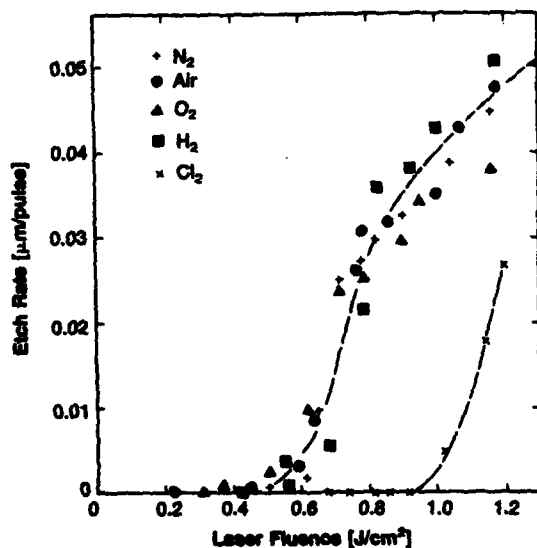


Fig. 3. Excimer laser etch rate in the presence of Cl_2 , O_2 , N_2 , H_2 or air vs. laser incident fluence.

of etch rate per pulse versus laser fluence in Fig. 3. A fluence threshold is observed for etching in all cases. The threshold fluences for O_2 , N_2 , H_2 , and air are nearly identical at about 0.6 J/cm^2 . On the other hand, the threshold fluence for Cl_2 is significantly higher at about 0.9 J/cm^2 . Surface compositional analysis by AES of the bottom of trenches etched in Cl_2 indicates that the trench surface is 50-70% depleted of Li relative to Nb which is similar to the results obtained for 257 nm CW laser etched trenches. AES results for excimer laser etching in air indicate less than 20% depletion of Li. The higher threshold for pulsed excimer laser etching in Cl_2 relative to the other gases is probably due to the changed surface composition. This result is consistent with the overall 257 nm CW laser etching results since there too etching is inhibited once a buildup of a surface layer of reacted material has taken place after the first laser scan.

The etching threshold fluence of 0.6 J/cm^2 at 248 nm which we obtained in air is similar to the value 0.9 J/cm^2 obtained by Bäuerle and coworkers at 308 nm [4-6]. This is surprising since the absorption depth ($1/\alpha$ where α is the absorption coefficient) at 308 nm is $100 \mu\text{m}$ [1] which is much larger than the absorption depth of $0.03 \mu\text{m}$ at 248 nm. Although the 248 nm results are consistent with a thermal ablation process, the 308 nm results cannot be explained by a purely thermal process and would indicate that a non-thermal mechanism is important. In view of the nearly identical thresholds at 308 nm and 248 nm, it cannot be ruled out that a non-thermal mechanism is responsible for etching at both wavelengths.

The morphologies of excimer laser etched grooves have been examined by SEM. Two examples of etched grooves are shown in cross section in Fig. 4. These grooves are formed by projecting the image of a 1 mm slit onto the $LiNbO_3$ surface using one cylindrical lens. The trench in Fig. 4(a) is a result of 1000 laser pulses and the groove in Fig. 4(b) results from 2000 pulses under the same conditions. The grooves are approximately $100 \mu\text{m}$ wide at the top and several millimeters long. The trenches

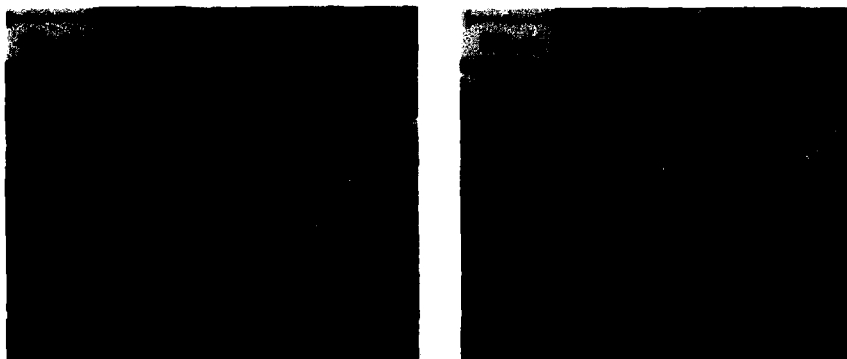


Fig. 4. SEM micrographs of 248 nm excimer laser etched trenches. (a) 1000 laser pulses at 1.0 J/cm^2 . (b) 2000 laser pulses.

initially have a flat bottom and sloping sidewalls. As the trench deepens, the sidewall slope remains nearly constant and the flat bottom becomes narrower. If etching is continued, eventually the cross section of the trench becomes v-shaped. Etching does not stop at that point, however, but continues at the point of the "v" forming a narrow channel via waveguiding. The etching of deep waveguide channels is slow relative to the initial etching of the LiNbO_3 surface due to the difficulty of removing ablated material from the channel.

SUMMARY

Frequency-doubled CW Ar^+ laser etching has been shown to occur in the presence of Cl_2 but not in vacuum at the same laser powers. However, the process is slow at the laser powers available to us and the etching process saturates due to redeposited material which forms in the trenches. Etched channels typically have width and depth dimensions of only a few micrometers. Compared to CW laser etching, pulsed excimer laser etching is much more rapid with etch rates of $.03 \mu\text{m}$ or more per pulse easily achieved. Trenches with widths and depths $>100 \mu\text{m}$ and lengths of several millimeters can be produced by simple projection optics without scanning the laser beam. Air works well as an etching medium but Cl_2 increases the threshold fluence for etching. It is surprising that the etching thresholds at 248 nm and 308 nm are similar even though the absorption depths are much different at the two wavelengths. A non-thermal etching process is needed to explain the 308 nm results and may also dominate the etching process at 248 nm. It would be interesting in future experiments to probe the etching mechanism at the two wavelengths by examining the fragments ejected from the surface by mass spectroscopy or other means.

ACKNOWLEDGMENTS

We would like to thank R. Beach, R.M. Osgood, and V.H. Houlding for their assistance in doing the CW argon-ion laser experiments.

REFERENCES

- [1] A. Rauber, in Current Topics in Materials Science, edited by E. Kaldis (North-Holland, New York, 1978), Vol. 1, p. 481.
- [2] C.I.H. Ashby and P.J. Brannon, Appl. Phys. Lett. **42**, 475 (1986).
- [3] T.C. Rice and F.H. Fisher, in Materials Research Society 1986 Fall Meeting Abstracts (Materials Research Society, Pittsburgh, PA, 1986), p. 85.
- [4] M. Eyett and D. Bäuerle, Appl. Phys. Lett. **51**, 2054 (1987).
- [5] D. Bäuerle, M. Eyett, U. Kolzer, R. Kullmer, P. Mogyrosi, and K. Piglmayer, Mater. Res. Soc. Symp. Proc. **101**, 411 (1988).
- [6] D. Bäuerle, Appl. Phys. B **46**, 261 (1988).
- [7] K.W. Beeson, V.H. Houlding, R. Beach, and R.M. Osgood Jr., J. Appl. Phys. **64**, 835 (1988).
- [8] M. Lax, J. Appl. Phys. **48**, 3919 (1977).

KrF⁺ LASER-INDUCED CHEMICAL ETCHING OF NICKEL WITH Br₂

GEORGE W. TYNDALL and CHRISTOPHER R. MOYLAN, IBM Almaden Research Center, 650 Harry Rd., San Jose, CA 95120.

ABSTRACT

A quartz crystal microbalance (QCM) has been used to study the 248 nm laser-induced etching of nickel by Br₂. The experiment consists of focusing a pulsed UV laser beam at normal incidence onto the surface of a quartz crystal coated with 1 μ m of polycrystalline nickel. Absolute etch rates of nickel, in terms of mass removed per unit time, are determined from the integrated sensitivity function of the 6 MHz crystals used in this work. The dependence of the etch rate on Br₂ pressure and laser fluence was measured. The kinetic data obtained from these measurements show that the mechanism of the etching process is dominated by the formation and the subsequent removal of a Ni_xBr_y monolayer.

INTRODUCTION

The use of lasers in the microelectronics industry has become widespread in recent years. The ability to promote localized chemical reactions with laser light is currently used for the deposition of metals with submicron resolution. In addition to depositing materials, lasers are also suitable sources for inducing localized chemical etching processes. Photochemical etching of solid surfaces has been demonstrated for a variety of gas-solid systems [1-5]. Because laser etching can potentially lead to improvements in resolution and a decrease in the number of defects, this process is an attractive alternative to the wet lithographic techniques currently employed for microcircuit patterning.

Metals are in general difficult to etch via dry processes, which makes the laser-induced chemical etching technique particularly appealing. Recently the laser-induced chemical etching of Ag [1], Cu [1-3], Al [1,4], Mo [1,5], and Ti [5] have all been reported, but nickel, owing to its chemical inertness, has proven difficult to etch [1]. In the present work we demonstrate that nickel can be etched at reasonable rates in the presence of Br₂ at moderate KrF⁺ (248 nm) laser powers.

EXPERIMENTAL

The kinetic measurements reported in this work were performed using a quartz crystal microbalance (QCM) as the substrate. The experimental apparatus is shown in figure 1. The vacuum cell was constructed from standard 3-3/8" vacuum flange hardware and contained the QCM crystal. We used 6 MHz quartz crystals obtained from Inficon with 14.0 mm diam. gold coated electrodes. Polycrystalline nickel films with thicknesses of < 2 μ m were either sputtered or evaporated onto the surface of the front electrode. The crystals were mounted in the vacuum cell via a water cooled mount and connected to a homebuilt oscillator circuit via standard vacuum feedthroughs. The QCM frequency was monitored with a frequency counter interfaced to an IBM PC. With this apparatus, we find the noise associated with the QCM to be < 25 x 10⁻⁵ Hz, and the drift in the resonant frequency to be < 0.5 Hz/hr.

The vacuum cell was typically pumped to a base pressure of < 1 x 10⁻⁵ torr with a 4" diffusion pump prior to starting an etching run. Br₂ (Aldrich-ACS Reagent Grade) was introduced to the cell through a molecular leak valve, and the pressure measured with a capacitance manometer. Except for a number of freeze-pump-thaw cycles, the bromine was used without further purification. Once the bromine pressure stabilized at the desired value, data collection was started. Then after approximately 10 seconds, the laser was admitted to the cell and the etching initiated. The change

in the QCM frequency due to the etching of the crystal surface was typically monitored as a function of time for 2 minutes. The laser beam was then blocked and the cell was pumped out. The KrF laser (pulse width = 20 ns FWHM) was operated at 10 Hz for all the work presented here. A uniform portion of the beam was selected with a variable width iris, and then focused onto the surface of the microbalance at normal incidence. Typically the laser focal spot size at the crystal surface was between 1 - 1.5 mm radius. The entire cell was mounted on x-y translation stages to align the laser beam on the center of the quartz crystal.

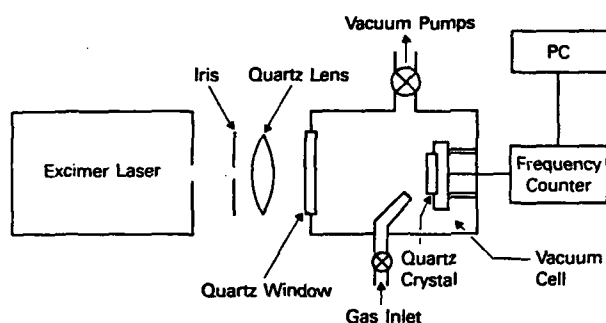


Figure 1. Experimental apparatus.

RESULTS

Upon addition of Br_2 to the vacuum cell, a slight decrease in the crystal frequency is observed (approximately 2 Hz/min) indicating that some adsorption onto the crystal surface occurs. There is also evidence suggesting that Br_2 diffuses into the bulk of the Ni. For example, the frequency of the oscillator exposed to Br_2 for 5 hrs showed a steady decrease of approximately 40 Hz/hr. These effects are, however, small compared to the frequency changes observed via the etching process, and as such do not pose a problem in obtaining quantitative etching rates from the experimental data. The change in the QCM frequency vs. time for a typical etching experiment is shown in figure 2. The dramatic increase in the resonant frequency of the QCM at approximately 10 seconds is caused by heating the surface of the microbalance when the laser beam is admitted to the vacuum cell. In the absence of Br_2 , the frequency increases dramatically upon irradiation of the QCM with the laser, but unlike the data in figure 2, the frequency reaches a constant value after a few seconds. Upon blocking the beam, the frequency drops to its original value. While heating of the QCM surface obscures the first few seconds of the etching process, it does not prohibit measurement of the etching rate, which is obtained from the slope of the linear portion of the data. As is suggested in figure 2, the etch rate of Ni by Br_2 is found to be independent of the number of laser pulses.

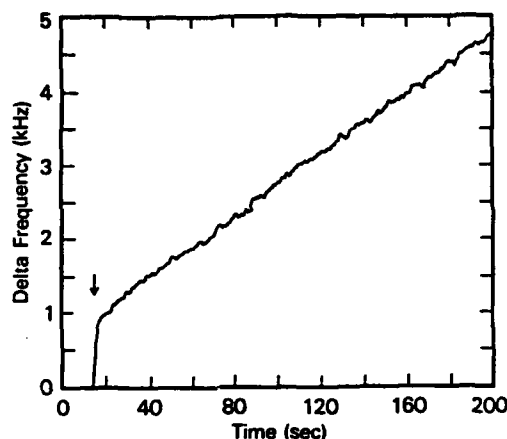


Figure 2. Results of a typical etching experiment. The arrow denotes the time at which the laser beam is admitted to the cell. The Br_2 pressure was 0.100 torr and the laser fluence was 600 mJ-cm^{-2} .

To determine the etch rate of Ni from the change in resonant frequency of the QCM, we start with the general equation relating the frequency change ($\Delta\nu$) to the change in mass (Δm):

$$\Delta\nu = -C \Delta m \quad (1)$$

where C is the mass sensitivity constant of the QCM. In the case of a uniform mass change over the entire crystal, C is given by:

$$C = \frac{\nu_r^2}{N\rho A} \quad (2)$$

In equation (2), ν_r is the fundamental frequency of the quartz crystal, N is the frequency constant of quartz, $1.668 \times 10^5 \text{ Hz-cm}$, ρ is density of quartz, 2.648 g-cm^{-3} and A is the active area of the quartz crystal (see below). Equations (1) and (2) are valid provided that the mass loading of the crystal is small, i.e. $< 2\%$ [6]. The thickness of the nickel films used in this work were thus limited to $< 2 \text{ } \mu\text{m}$. As is noted above, equation (2) assumes that the mass change is uniform over the active area of the crystal. To test the validity of using equation (2) in obtaining etch rates from our experiments, we determined the active area of the crystals used in this work. This was done by measuring the change in the resonant frequency of a set of quartz crystals onto which a known thickness (4200\AA) of Cu was evaporated. By loading the crystals with concentric films of different area (radii between 1 and 5 mm) we obtained the integrated sensitivity function shown in figure 3. The active area is determined from these measurements by noting the point at which increasing the radius of the deposited film has no effect on the frequency change of the quartz crystal. From figure 3, the active area of the crystals used in this work is defined by a radius of approximately 2.5 mm. Since we are etching an area with a radius of between 1 - 1.5 mm, i.e. an area smaller than the active area, we cannot use equation (2) directly but must use figure 3 to obtain the sensitivity constant C . Thus, from the change in the QCM frequency and the measured radius of the etched spot, the mass of the nickel removed is easily determined.

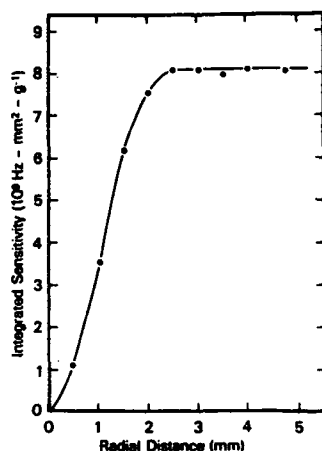


Figure 3. Integrated sensitivity function of the 6Mhz Inficon crystals.

The QCM was used to measure the rates of the 248 nm laser-induced etching of Ni by Br_2 as a function of the incident laser fluence, and the Br_2 pressure. The laser fluence dependence of the etch rate was measured between $200 - 830 \text{ mJ} \cdot \text{cm}^{-2} \cdot \text{pulse}^{-1}$ and is shown in figure 4. We find the etching threshold to be approximately $300 \text{ mJ} \cdot \text{cm}^{-2}$. Above this threshold, the etch rate increases roughly as the cube of the laser fluence up to the highest laser fluences used. We note that the laser fluences shown in figure 4 are incident on the entrance window of the vacuum cell. The actual laser fluence at the surface of the QCM will be approximately 10% lower than the values reported in figure 4 due to reflection from the cell window (approximately 8%) and to absorption by the Br_2 within the cell (approximately 2%). Over the range of laser fluences used, no net change in the QCM frequency is found in the absence of Br_2 . Thus the material is not removed by ablation of the pure Ni surface, but requires interaction of the nickel surface with either Br_2 , or photochemically produced Br radicals (see below).

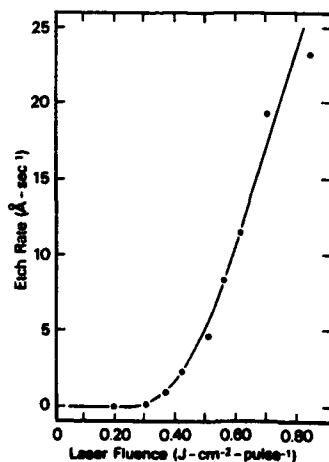


Figure 4. Dependence of the etch rate on laser fluence. The Br_2 pressure was 0.100 torr and the laser repetition rate was 10 Hz.

The dependence of the Ni etch rate on Br_2 pressure was measured between 0.005 - 2.00 torr and is shown in figure 5. The etch rate increases rapidly over the pressure range of 0.005 - 0.070 torr. Above 0.070 torr the etch rate is independent of Br_2 pressure up to the highest pressures studied. This pressure dependence is very similar to a Langmuir adsorption isotherm, which is characteristic of chemisorption of a gas-phase species on the surface that stops at one monolayer coverage.

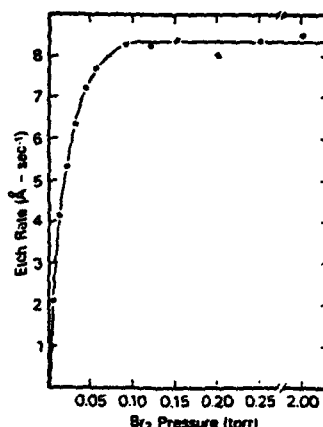


Figure 5. Effect of Br_2 pressure on etching rate. The laser fluence was $500 \text{ mJ} - \text{cm}^{-2} - \text{pulse}^{-1}$.

DISCUSSION

There are three general classes of etching reactions [1]: 1) spontaneous etching which occurs in the absence of any radiation, 2) passive etching which is characterized by the formation of a relatively thin passivation layer on the surface, and 3) diffusive etching in which the etchant diffuses into the bulk of the metal. While we do observe a small amount of Br_2 diffusion into the bulk of the Ni films (see above), based on the pressure dependence of the etching rate, we believe that the etching of nickel by Br_2 is an example of a passive etching system. The etching kinetics are thus easily understood in terms of the formation and the subsequent removal of a Ni_2Br_3 monolayer.

At Br_2 pressures of < 0.070 torr and laser fluences greater than the etching threshold, the rate limiting step is the formation of the Ni_2Br_3 monolayer. This Ni_2Br_3 monolayer could be formed from the reaction of the Ni surface with either Br_2 , photochemically produced Br radicals, or both. The fact that in the absence of 248 nm radiation, the microbalance frequency is found to decrease with the addition of Br_2 implies that adsorption does occur on the Ni surface. The rate of Br_2 adsorption on the Ni surface that we observe in the absence of the 248 nm laser is not, however, sufficiently fast to explain our etch rates. Dissociative chemisorption of Br_2 could, however, be enhanced by the increase in the temperature of the surface caused by the laser beam. In addition, the presence of the 248 nm radiation could remove any oxide layer present on the surface, resulting in an increase in the Br_2 sticking probability. It is also possible that photochemically

produced bromine radicals contribute significantly to the formation of the Ni_xBr_y monolayer. The absorption cross section of Br_2 at 248 nm is approximately $3 \times 10^{-19} \text{ cm}^2$ [7]. At the laser fluences used in this work, considerable dissociation of Br_2 should occur at or near the nickel surface. It is therefore probable that both dissociative chemisorption of Br_2 and chemisorption of photochemically produced Br radicals contribute to the formation of the Ni_xBr_y monolayer.

At Br_2 pressures above 70 mtorr, the rate limiting step is the removal of the entire Ni_xBr_y monolayer from the surface by the laser pulse. The removal of this monolayer most probably occurs via thermal ablation. At the fluences used in this work, removal of the entire monolayer was never realized as shown by the lack of a maximum in the etch rate with increasing laser fluence. This is most probably due to the relatively low volatility of the Ni_xBr_y products.

CONCLUSION

We have demonstrated that nickel can be etched at reasonable rates with Br_2 at moderate laser fluences. The results show that the 248 nm laser induced etching of nickel in a bromine atmosphere consists of the formation and the subsequent removal of a Ni_xBr_y monolayer. It is postulated that the monolayer is formed by a combination of the chemisorption of photochemically produced Br radicals and the dissociative chemisorption of Br_2 . The removal of this monolayer is postulated to occur via thermal ablation of the surface by the 248 nm laser pulse. This mechanism suggests that the maximum etch rate of nickel via this process will be inherently limited to values of less than approximately 10 Å-pulse^{-1} . This limitation can to some extent be overcome by the high repetition rate excimer lasers currently available. It should be noted that, in general, passive etching reactions have potential advantages compared to diffusive and spontaneous etching processes. For example, photoprojection patterning is possible with a passive etching process while it is not possible using spontaneous etching system. Also in contrast to etching processes which rely on diffusion, the passive process described in this paper has the advantage that the unetched metallurgy will not be contaminated with the etchant. In closing, the laser induced chemical etching technique holds promise in greatly simplifying the fabrication of sub-micron linewidth devices by eliminating photoresist patterning and wet etching steps.

REFERENCES

1. W. Sesselmann and T. J. Chuang, J. Vac. Sci. Technol. B, 3, 1507, (1985).
2. W. Sesselmann, E. E. Marinero, and T. J. Chuang, Appl. Phys., A 41, 209, (1986).
3. J. J. Ritsko, F. Ho, and J. Hurst, Appl. Phys. Lett., 53, 78, (1988).
4. G. Koren, F. Ho, and J. J. Ritsko, Appl. Phys. Lett., 46, 1006, (1985).
5. G. L. Loper and M. D. Tabat, Appl. Phys. Lett., 46, 654, (1985).
6. C.-S. Lu and O. Lewis, J. Appl. Phys. 43 4385, (1972).
7. H. Okabe, The Photochemistry of Small Molecules (Wiley-Interscience, New York, 1978), p.186, and references therein.

LASER INDUCED CHEMICAL ETCHING OF COMPOSITE STRUCTURE OF FERRITE AND SENDUST

S. Nagatomo, M. Takai*, Y. F. Lu*, and S. Namba*

D.S. Scanner Company Ltd., Higasi-ku, Osaka 560, Japan

*Faculty of Engineering Science and Research Center for Extreme Materials,
Osaka University, Toyonaka, Osaka 560, Japan

ABSTRACT

Maskless etching of the composite structure of Mn-Zn ferrite and sendust (Fe-Si-Al alloy) was performed by focused argon-ion-laser irradiation in a CCl_4 atmosphere and aqueous solutions. Only a mixture of KOH and NaOH aqueous solutions was found to smoothly etch the composite structure by thermochemical reaction using laser irradiation. A maximum etching rate of $14 \mu\text{m}/\text{sec}$ was obtained for sendust-on-ferrite substrates.

INTRODUCTION

Laser-induced chemical-etching techniques for material processing have extensively been studied [1-3]. Materials such as polymers, thin metal films and semiconductors have been studied in detail [3,4]. On the other hand, laser induced chemical etching of ceramics has been performed in a few cases [4-6], in which few materials having composite structures including ceramics were investigated.

Recently, etching of single crystal ferrite, which is one kind of ceramic, has been studied in detail using laser-induced chemical processing [7,8]. Ferrite is an important magnetic material which has been used for magnetic heads of video tape recorders and floppy or hard disk drives. In particular, recent increases in recording density of magnetic tapes and disks, i.e., high track-per-inch or bit-per-inch values, require magnetic heads made of single crystal ferrite and processed with accuracies in the micron-to-submicron range. However, it is very difficult to realize accuracies in the micron-to-submicron range by conventional mechanical or simple wet chemical etching techniques [7]. Therefore, laser induced chemical processing will be an important method, realizing sufficient accuracy and etching rates [7,8]. A composite structure of sendust deposited on single crystal ferrite for magnetic heads increases coercive force in a magnetic media, since sendust provides higher magnetic flux density than ferrite. Hence, this material with composite structures will be more important than ferrite alone for magnetic application. However, micro processing of sendust is very difficult owing to its hard and brittle characteristics when conventional mechanical processing methods are used.

In this study, maskless, dry and wet etching of a composite structure of ferrite and sendust have been performed by laser induced chemical reaction using focused argon-ion-laser irradiation. Etched shapes were measured by scanning electron microscopy (SEM) and optical microscopy for various laser powers and etchants.

EXPERIMENTAL PROCEDURES

About 3 μm thick sendust thin films (Fe:Si:Al=85:9.5:5.5) were deposited by sputtering on (100)-faced Mn-Zn ferrite substrates. Samples were mounted on the bottom of an irradiation cell or a chamber, which was mounted on an electronically controlled X-Y-Z stage. The laser beam was scanned over the sample by moving the stage. For dry etching in CCl_4 , the chamber was evacuated to about 10^{-3} Torr. Ambient CCl_4 gas was introduced in the chamber at a pressure of about 80 Torr. For wet etching, a mixture of KOH and NaOH solutions (KOH : NaOH : H_2O = 15 : 15 : 70 wt %) was used as an etchant. The etchant level was controlled so that the etchant surface was just over the sample surface.

The 514.5 nm-line of an argon laser was focused by a convex lens, with a focal length of 40 mm, down to a spot diameter of about 13.2 μm (at 1/e intensity) on the sample surface. Etched shapes were measured by SEM and optical microscopy. Auger electron spectroscopy (AES) was used to measure the surface chemical composition after etching. Etched depth and width are defined as maximum values of an etched groove.

RESULTS AND DISCUSSION

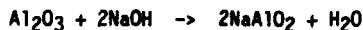
Although ferrite was etched with high etching rates by a focused argon ion laser in 80 Torr CCl_4 gas [7], sendust layers on ferrite were not etched under the same conditions and peeled from the ferrite substrate when the scanning speed was low or laser power was too high. This result suggests that the difference in thermal expansion between ferrite and sendust gives rise to the peeling of the sendust films from the ferrite substrate.

An H_3PO_4 aqueous solution, on the other hand, was a conventional etchant for ferrite. Laser induced chemical etching of ferrite in H_3PO_4 has high etching rates and aspect-ratios [8]. However, H_3PO_4 aqueous solution, and other acid etchants were not suitable for laser induced etching of sendust, because all sendust surfaces were eroded and, hence, the grooves etched using a focused laser beam were not well defined.

Furthermore, sendust was not etched in alkaline solutions at room temperature and was also not etched by focused laser beam irradiation in an alkaline solution such as aqueous KOH.

However, sendust was found to be etched by laser irradiation in an NaOH aqueous solution. The etched grooves were, in this case, not well defined because of the fast etching rate.

These results suggest the following chemical reaction of oxidized surfaces of sendust e.g.



The addition of KOH to the NaOH solution during laser irradiation resulted in smooth etching of both sendust films and ferrite substrate. In this case the KOH suppressed the fast etching reaction of the NaOH solution.

Fig.1 shows the top view of the groove etched in a composite layer of sendust and ferrite in a KOH and NaOH aqueous solution by a single scan of a laser beam at 120nm with a scanning speed of 6 $\mu\text{m}/\text{sec}$. The part with a dark contrast at the center is an etched ferrite layer. The top sendust layer was etched smoothly and the lower ferrite substrate was continuously etched.

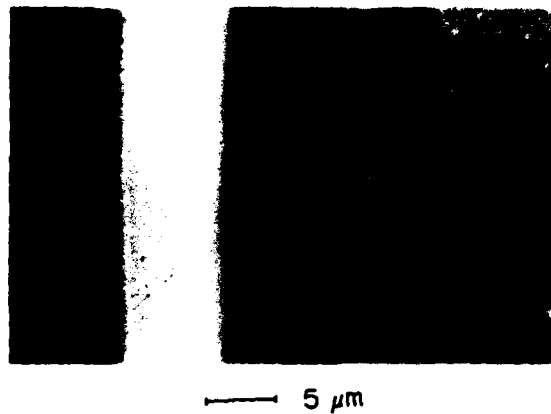


Fig. 1 A top view of the groove etched in a composite layer of sendust and ferrite by laser irradiation at 120 mW in NaOH + KOH solution with a scanning speed of 6 $\mu\text{m/s}$

Such a groove becomes wider and deeper as the laser power increases from 120 mW to 250 mW. Further increases in laser power resulted in the saturation of the etched depth.

Fig. 2 shows the top view of the sample etched at 300 mW. The sendust layer was not etched at the center of the laser scanning trace. This result suggests that the etching reaction is governed by a surface temperature, in which the center of the laser spot has a higher temperature than the edge and the etching reaction takes place only in low temperature regions.

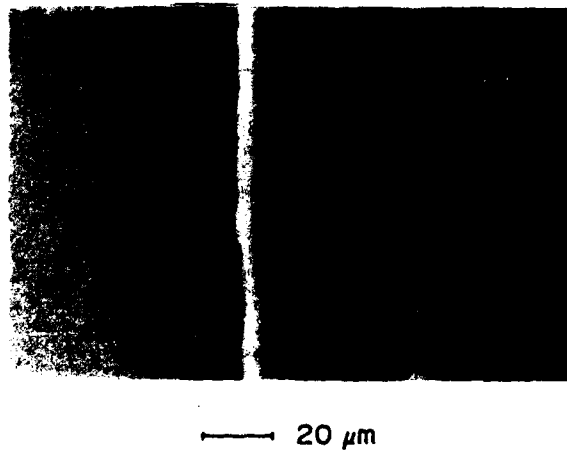


Fig. 2 A top view of the groove etched in a composite layer of sendust and ferrite by laser irradiation at 300 mW in NaOH + KOH solution with a scanning speed of 6 $\mu\text{m/s}$

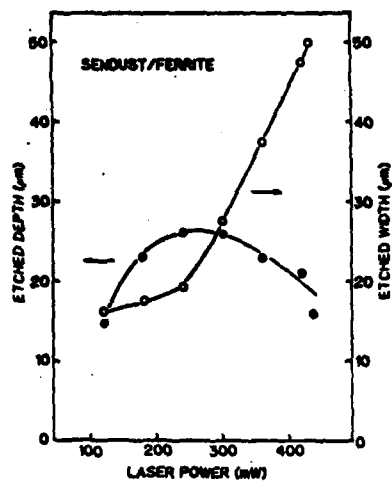


Fig. 3 Etched depth and width as a function of laser power

Fig.3 shows the etched depth and width as a function of laser power. The etched depth increases from 15 μm to 25 μm and saturates as the laser power increases from 110 mW to 250 mW. Further increases in laser power resulted in a decrease in etched depth. The central part of the laser trace was not etched, as shown in Fig.2. Therefore, two parallel grooves with width of 16 μm were etched.

Fig.4 shows Auger spectra for samples before and after etching by focused laser irradiation in the aqueous solution containing KOH and NaOH. A spectrum for the etched groove after sputter cleaning is also shown. The Auger spectrum before etching (bulk spectrum) shows peaks for constituent

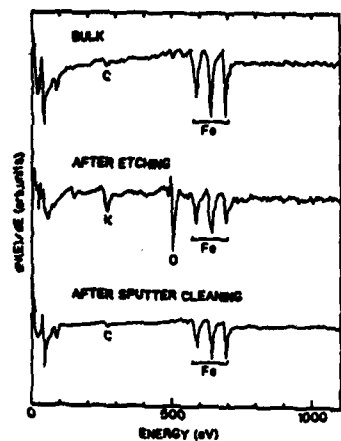


Fig. 4 Auger spectra for sendust layers before and after laser etching in NaOH + KOH solution

elements of sendust such as Fe and C contamination, while, after laser chemical etching, additional peaks for O and K appear. Residual surface oxygen suggests the formation of oxide during etching. After sputter cleaning for 70 min by Ar ions, corresponding to a removal of several hundred nm, K and O signals disappear in the spectrum. In this several hundred nm layer, strong K signals were observed. Thus, K atoms from the etchant seem to diffuse into sendust during laser irradiation.

SUMMARY

Laser-induced chemical etching of a composite structure of Mn-Zn ferrite and sendust was performed by focused argon-ion-laser irradiation in a CCl_4 atmosphere and aqueous solutions. It was found that the composite structure could not be etched by laser irradiation in a CCl_4 atmosphere or KOH solutions. Laser etching in an NaOH solution resulted in erosion and staining. A mixture of NaOH and KOH solutions was found to give a smooth etching surface for laser processes. A maximum etching rate of about 14 $\mu\text{m}/\text{sec}$ was obtained for 3 μm thick sendust on a ferrite substrate.

It was also shown in this study that sendust was not etched at the center of a laser beam spot under some special conditions of laser power and scanning speed. Further investigation on the application of this technique to the etching of the composite structure of ferrite, sendust, and glass, representing a real magnetic head structure, is on progress.

ACKNOWLEDGMENTS

The authors are indebted to M. Matsuzawa, M. Shimizu, F. Takeya, and H. Sandaiji of NGK insulator, Ltd. for their supplying single crystalline ferrite samples. The authors would also like to thank E. Hiraki for his technical assistance during this study.

REFERENCES

1. G. Koren, F. Ho, and J.J. Ritsko, *Appl. Phys. Lett.* **46**, 1006 (1981)
2. D.J. Ehrlich, R.M. Osgood, Jr, and T.F. Deutsh, *Appl. Phys. Lett.* **38**, 1018 (1981)
3. M. Takai, J. Tokuda, H. Nakai, K. Gamo and S. Namba, Japan, *J. Appl. Phys.* **22**, L757 (1983)
4. R.J. von Gutfeld and R.T. Hodgson, *Appl. Phys. Lett.* **40**, 352 (1982)
5. C.I.H. Ashby and P.J. Brannon, *Appl. Phys. Lett.* **49**, 457 (1986)
6. M. Eyett, D. Bauerle, W. Wersing, K. Lubitz, and A. Thomann, *Appl. Phys.* **A40**, 235 (1986)
7. M. Takai, Y.F. Lu, T. Koizumi, S. Nagatomo, and S. Namba, *Appl. Phys.* **A46**, 89 (1988)
8. Y.F. Lu, M. Takai, S. Nagatomo, and S. Namba, to be published in *Appl. phys. A*.

LASER INDUCED WET-CHEMICAL ETCHING OF Mn-Zn FERRITE IN H_3PO_4

YONG FENG LU, MIKIO TAKAI, SYOHEI NAGATOMO*, and SUSUMU NAMBA

Faculty of Engineering Science and Research Center for Extreme Materials,
Osaka University, Toyonaka, Osaka 560, Japan

*D.S. Scanner Co., Ltd., Izumimachi, Higashiku, Osaka 540, Japan

ABSTRACT

Maskless etching of single crystalline Mn-Zn ferrite in an H_3PO_4 aqueous solution by Ar^+ laser irradiation has been investigated to obtain high etching rates and aspect-ratios of etched grooves. The etching processes have been found to be photochemical in a low laser power region and thermochemical in a high laser power region. High etching rates of up to 340 $\mu\text{m/s}$ and an aspect-ratio of 50 for slab structures have been achieved. Periodic ripple structures have been observed under specific etching conditions due to the local surface melting.

INTRODUCTION

Ferrite, one kind of ceramic material, has been widely used as an important magnetic material for magnetic heads of audio and video tape-recorders or floppy and hard disk drives. These kinds of heads have conventionally been fabricated by both wet chemical etching and mechanical processes. Increases in recording capacity, requiring higher recording density of magnetic devices, could be simply satisfied by reducing the gap width of the magnetic head. However, because of the intrinsic characteristics of ferrite such as high hardness and brittleness like other ceramics, it is very difficult to fabricate fine structures in ferrite by both mechanical and wet chemical etching with mask processes. Recently, laser-induced dry etching of single crystalline ferrite in a CCl_4 atmosphere has been developed[1,2] for the maskless microfabrication of magnetic heads in order to increase the recording density. However, the etching rate of 68 $\mu\text{m/s}$ obtained was not high enough for practical device applications.

Laser-induced wet etching, on the other hand, would provide higher etching rates than those in gas phase reactions[3-5]. In this study, Ar^+ laser-induced, maskless, wet-etching of single crystalline Mn-Zn ferrite in a H_3PO_4 solution has been performed to obtain higher etching rate. The results were also compared with dry etching in CCl_4 gas and conventional wet-chemical etching in H_3PO_4 .

EXPERIMENTAL

The single crystalline ferrite used was higher quality in mechanical and magnetic characteristics than poly-crystalline ferrite which has conventionally been used as a head material[2]. (100)-oriented single crystalline Mn-Zn ferrite ($MnO : ZnO : Fe_2O_3 = 31 : 17 : 52$) samples were mounted on the bottom of the irradiation cell and immersed in the etchant solution. The irradiation cell was fixed on an electronically controlled X-Y-Z stage. The laser beam was scanned over the sample by moving the cell with a speed ranging from 2 $\mu\text{m/s}$ to 36 $\mu\text{m/s}$.

The 514.5 nm-line of an Ar⁺ laser was focused by a convex lens, with a focal length of 40 mm, down to a spot diameter of about 13.2 μm (at 1/e intensity) on the sample surface. The distance from the sample surface to the etchant surface was adjusted to 2 mm. 43% - 85% phosphoric acid (H_3PO_4) solution was used as an etchant.

Etched patterns were observed by scanning electron microscopy (SEM) and a stylus measurement (DEKTAK) to obtain etched depth and width. The etching rate was defined as the maximum etched depth divided by the beam dwell time.

RESULTS AND DISCUSSION

Figure 1 shows the etched depth and width as a function of laser power in a low power region at and below 160 mW. The etched depth increases linearly with the increase in laser power from 40 to 132 mW. This suggested that the etching reaction in this power range might be a photochemical process. In order to verify this point, laser etching with irradiation parallel to the sample surface was also performed in H_3PO_4 . An etched groove with a depth of 1.2 μm was formed by a laser power of 10 mW within 30 minutes in this case (etching rate of 40 nm/min).

Figure 2 shows the etched depth and width as a function of laser power in a higher power range. The etching rate and aspect-ratio of etched grooves increased as the laser power increased. The etching rate reached 340 $\mu\text{m/s}$ in the case of a laser power of 660 mW and a scan speed of 9 $\mu\text{m/s}$ in 85% H_3PO_4 . This etching rate is about two to six orders of magnitude

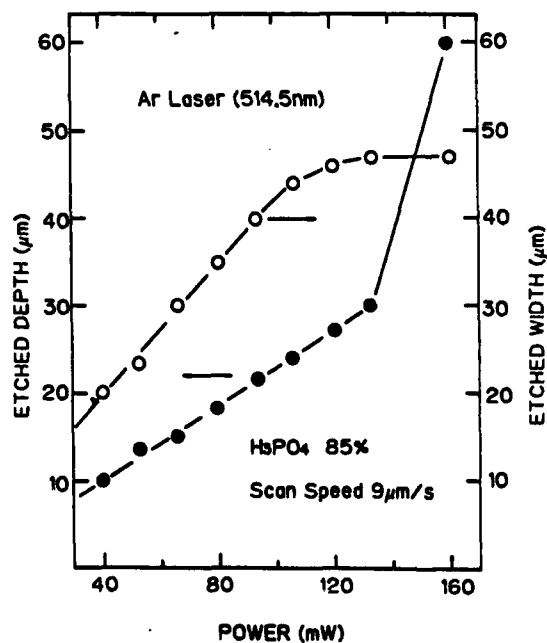


Fig. 1 Etched depth (solid circle) and width (open circle) as a function of incident laser power at and below 160 mW

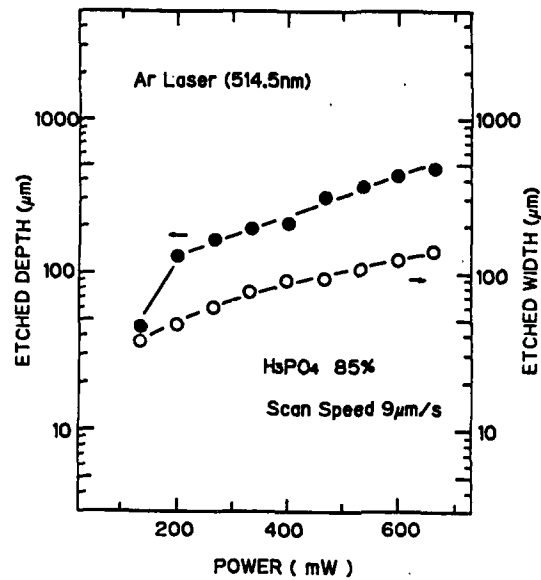


Fig. 2 Etched depth (solid circle) and width (open circle) as a function of incident laser power at and above 120 mW

greater than those achieved by laser induced dry etching in CCl_4 ($2.7\mu\text{m/s}$ [2]) and conventional wet-chemical etching with H_3PO_4 at room temperature (0.33 nm/s).

Periodic ripple structures have been observed during the etching

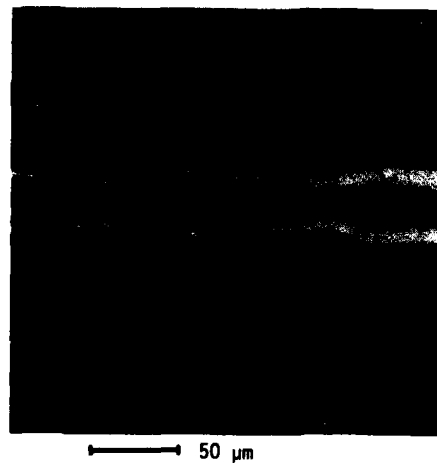


Fig. 3 Ripple structure induced by laser irradiation: laser power 173 mW, scan speed $21\mu\text{m/s}$

processing under specific etching conditions though the sample surface was irradiated by a constant laser power. A period of the ripple structure is shown in figure 3. It was produced by scanning a laser beam from the left to the right with a laser power of 173 mW and a scan speed of 21 $\mu\text{m/s}$. The periodic length is 130 μm , about four times larger than the groove width. The time to form this period is about 6 seconds.

According to our recent study[3], the ripple structure occurred when the laser power exceeded the threshold value for local surface melting. This threshold value for surface melting (local temperature rise of 1600 °C) is estimated to be 120 mW by solving the three dimensional heat equation[2]. The procedure to form the ripple is described as follows. First, the ferrite surface was locally heated and made molten by a high intensity laser beam. The boundary of the molten area expanded isotropically due to the high thermal diffusivity of the liquid phase. The absorption of the laser light was decreased because of the high reflectivity of the molten surface. When the laser beam was scanned from the left to the right, the molten area became narrower and thinner due to the poor absorption of the laser light. Under some specific etching conditions, the boundary of the molten area moved with a lower velocity than the scan speed of the laser beam. The laser beam reached the boundary and started a new period because of the strong absorption of laser power on the new solid surface. A periodic intensity change of the reflected light has been observed during the etching process.

The specific etching condition for the ripple structure has been investigated for the laser induced wet-chemical etching with a laser beam diameter of 13.2 μm in a 85% H_3PO_4 solution (figure 4). In the low laser power region, the low incident intensity keeps the local temperature rise below the melting point of the ferrite material so that a smooth etched groove without the ripple structure can be obtained. When the laser power increased and reached the threshold for surface melting, the ripple structure occurred. The threshold laser power became higher when the scan

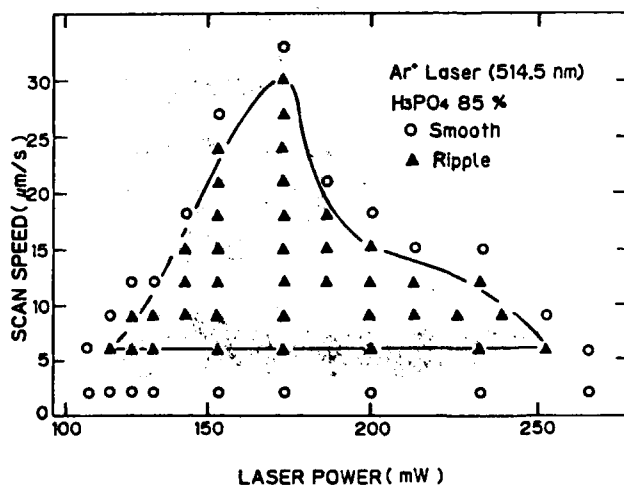


Fig. 4 Specific etching condition for periodic ripple structure

speed increased. In the low scan speed region, below $5 \mu\text{m/s}$, the ripple structure can not be formed, though the surface melting took place, because the laser beam was scanned with such a low speed that it is impossible to reach the molten boundary and start a new period on the solid phase area. In this case, a groove with a high aspect ratio and smooth vertical side walls can be achieved[3]. In the case of the high laser power region, the ripple structure vanished again when the laser power or the scan speed became higher. When the sample surface was irradiated by a laser beam with a strong intensity, a large area with a great spatial volume would become molten and the interface of the liquid phase and the solid phase would move with a slow velocity. Because of the large heat of melting and the poor absorption of the molten surface, the interface of the two phases moves with a lower velocity as the incident laser power increases. Finally, the laser beam reaches the boundary and achieves an equilibrium state. As a result, the threshold velocity for the vanishing of ripple structure decreases with a higher laser power.

The periodicity of the ripple strongly depends on the incident laser power, whereas it is weakly affected by the beam scan speed. This is because the temperature distribution produced by laser is weakly dependent upon scan speed at the low scan speeds used in this study. The ripple structure decreases in frequency when the laser power increases.

By an appropriate choice of etching parameters, a slab structure with a high aspect-ratio can be fabricated. Figure 5 shows the SEM micrograph of the vertical slabs achieved in 43% H_3PO_4 with a laser power of 224 mW, a scan speed of $10 \mu\text{m/s}$ and a beam spot size $1.2 \mu\text{m}$. The slabs have a depth of $200 \mu\text{m}$ and a minimum width of $4 \mu\text{m}$, corresponding to an aspect-ratio of 50. The shape, with a high aspect-ratio and smooth side walls, greatly differs from that of grooves obtained in ceramics by laser induced dry etching[5,6]. The measured focus depth is about $10 \mu\text{m}$, much smaller than

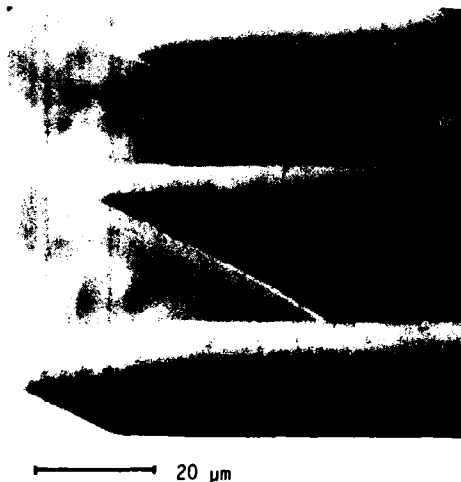


Fig. 5 Slab structures with a high aspect-ratio fabricated under an etching condition: H_3PO_4 43%, laser power 224 mW, scan speed $10 \mu\text{m/s}$, and beam spot size $1.2 \mu\text{m}$

the groove depth. The incoming beam would, therefore, be confined inside the wall, which prevents the beam from diverging, and the beam propagates to the reacting layer by light guiding[3]. Such a light guiding effect has also been found in laser induced etching of GaAs in dilute HNO_3 solution[7] or laser induced vaporization of CdTe[8].

CONCLUSIONS

Laser induced wet-etching of single-crystalline ferrite has been performed to fabricate micro-structures with high aspect ratios such as vertical wall structures. High etching rates of up to $340 \mu\text{m/s}$ and high aspect-ratios of up to 50 have been achieved due to the light guiding effect. The etching process can be considered to be a photochemical reaction in the low laser power region and thermochemical in the high power region. Periodic ripple structures occurred within a specific region of etching conditions, in which local melting of ferrite surfaces took place. The periodicity of the ripple strongly depends on the laser power and the frequency of ripple structure decreased as the laser power increased.

ACKNOWLEDGMENTS

The authors are indebted to M. Matsuzawa, M. Shimizu, F. Takeya, and H. Sandaiji of NGK Insulators, Ltd. for their supplying single crystalline ferrite samples. The authors would also like to thank K. Mino and K. Kawasaki for their technical assistance.

REFERENCES

1. M.Takai, S.Nagatomo, T.Koizumi, Y.F.Lu, K.Gamo, and S.Namba: Laser Processing and Diagnostics(II), ed. by D.Bauerle, K.L.Kompa and L.Lande (Les Editions de Phys., Cedex, 1986) P.57
2. M.Takai, Y.F.Lu, T.Koizumi, S.Nagatomo, and S.Namba: Appl. Phys., **A46**, 197(1988)
3. Y.F.Lu, M.Takai, S.Nagatomo, and S.Namba: Appl. Phys. A (in press)
4. J.T.Tsao and D.J.Ehrlich: Appl. Phys. Lett., **43**, 146(1983)
5. M.Eyett, D.Bauerle, W.Wersing, K.Lubitz, and H.Thomann: Appl. Phys. **A40**, 235(1986)
6. M.Eyett, D.Bauerle, W.Wersing, and H.Thomann: J. Appl. Phys., **62**, 1511(1987)
7. D.V.Podlesnik, H.H.Gilgen, and R.M.Osgood, Jr.: Appl. Phys. Lett., **48**, 496(1986)
8. C.Crnone, M.Rothschild, and D.J.Ehrlich: Appl. Phys. Lett., **48**, 736(1986)

PART VII

Laser-Induced Surface Ablation

PATTERNING OF HIGH T_c SUPERCONDUCTOR FILMS WITH A FOCUSED EXCIMER LASER

J.M. Hagerhorst, J.D. Mannhart, M.M. Oprysko, M.R. Schenemann, and C.C. Tsuei
IBM Research Division
Thomas J. Watson Research Center
Yorktown Heights, New York 10598

Abstract

Laser ablation using focussed excimer light has been found to be an effective technique for the direct, maskless patterning of High T_c superconductor films. The apparatus used in the work consists of an adjustable aperture which is illuminated by a 193 nm excimer laser beam. The aperture is imaged by a microscope onto the substrate into an area as large as 200 x 200 to an area as small as 2 x 2 square microns. The superconductor films are placed on a 0.5 micron resolution, computer controlled x-y stage. Laser fluences up to 5 J/cm² and repetition rates of 10 Hz were found to be sufficient to ablate (pattern) the High T_c films with no apparent effect on their superconducting properties as evidenced by the films' resistance as a function of temperature (R vs T) before and after patterning.

The technique and apparatus are flexible enough to allow patterning across entire substrates and/or the definition of isolated features as small as one micron. To date, the technique has been successfully used to pattern a wide variety of films (based on material and thickness), to fabricate transmission lines several millimeters long, to pattern superconducting quantum interference devices (SQUIDs) which operate at liquid nitrogen temperatures, and to study the behavior of individual grain boundaries within films.

Introduction

High temperature superconductor films hold the promise of dispersion-free electronic interconnects, zero-loss transmission lines, sensitive magnetic field detectors (SQUIDs), etc. For these applications to bear fruit requires the continuing development and understanding of the films, substrates, processing technologies, etc. One key processing technology is the patterning step which requires the definition of micron scale superconductor film features with no degradation of the superconducting properties of the film (such as the onset of superconductivity and critical current handling capability). Numerous approaches have been developed and practiced with a varying degree of success. These include: lift-off processes¹, reactive ion etching², chemical etching^{3,4}, ion implantation⁵, laser thermal processing⁶, and laser ablation^{7,8}. Laser ablation, using focussed excimer laser light, has been found to be an effective technique for the rapid, direct, and maskless patterning of high temperature superconductors.

The apparatus and the general nature of the films are described along with etching results and the effect of laser radiation on the superconducting properties of the films. The viability of the technique is demonstrated through several examples including the generation of isolated structures of micron size dimensions, transmission lines several millimeters long, SQUIDs, and finally the use of the focussed beam to selectively pattern features in and around individual grain boundaries.

Excimer Laser-Micropatterning Apparatus

The apparatus consists of an excimer laser, Lambda Physik 103, operating at a wavelength of 193 nm and an optical delivery system.⁹ The firing or repetition rate of the excimer laser is controlled with a computer or manually via a pulse generator. Rates from "single shot" to 200 Hz are readily obtainable.

The optical delivery system, Leitz-IMS¹⁰, consists of a modified Leitz microscope. The excimer laser beam enters the microscope via a dichroic mirror which directs the beam into a 36X / 0.5 NA "reflective" objective.

A variable-size rectangular aperture is introduced into the excimer laser beam path. This aperture is directly imaged by the objective at its focal point so that a final excimer laser beam "target" area as large as 200×200 down to $2 \times 2 \mu\text{m}^2$ can be obtained. A spot marker illuminator is placed in line with the excimer beam for targeting.

The highest available fluence (at the target) is approximately 5.5 J/cm^2 at 193 nm. The fluence is fine tuned or selected by placing dielectric filters between the excimer laser and optical delivery system. Laser fluence is routinely measured during experiments with a miniature energy meter, Gentec, placed directly under the objective. The laser energies reported here have been adjusted (1.15x) to compensate for the meter sensitivity at 193 nm.

Eyepieces or a video monitor provide real time viewing of the sample. A computer-controlled xy stage makes possible the automated patterning of substrates as well as targeting of specific areas. The entire xy stage is mounted on a z stage providing ca. 25 mm of fine and 150 mm of coarse vertical motion.

High-T_c Films

The films patterned in this report are of the Y-Ba-Cu-O system although Tl- and Bi-based superconductors have also been patterned. Polycrystalline and epitaxial single crystalline Y-Ba-Cu-O films were used in this work, but in addition single crystals of the Y- and of the Bi- systems have been patterned.

The polycrystalline films were deposited at room temperature by dc-magnetron sputtering of BaCu and YCu targets onto a variety of substrates including MgO, SrTiO₃, and LiNbO₃.¹¹ The deposition was performed in an Ar/O₂ atmosphere of 10 microns with an oxygen partial pressure of 0.2 microns. The high-T_c phase was formed in a two-step annealing process: one at 400°C and a second at 900°C. Typical film thicknesses ranged from 0.5 to 1.3 microns.

Alternatively, films were deposited by an e-beam technique¹². The epitaxial films used in the grain boundary experiments were deposited onto polycrystalline SrTiO₃ substrates consisting of grains approximately 100 microns in diameter. The films were epitaxially aligned to the grain orientation of the substrate during the annealing process resulting in a large-grained superconductor film. These films were approximately 0.5 micron thick.

Material Removal

It is important to establish the rate of material removal using the ablation process, the local and global effects of the ablation process on the film, and the resolution which can be obtained.

Care was taken to choose superconductor films whose surface roughness was no greater than 1,000 Å, since the total film thickness was approximately 1 micron. The etch depth as a function of number of pulses is shown in Fig. 1 for several different laser fluences. These data were used to generate the etch rate as a function of laser fluence as shown in Fig. 2.

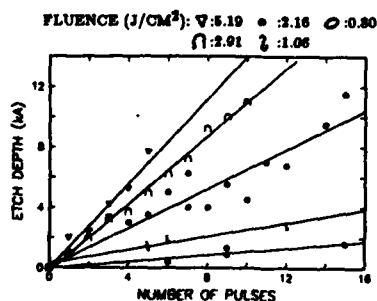


Fig. 1

Etch depth of polycrystalline YBaCuO film as a function of number of laser pulses (at 193 nm) for several fluences as indicated.

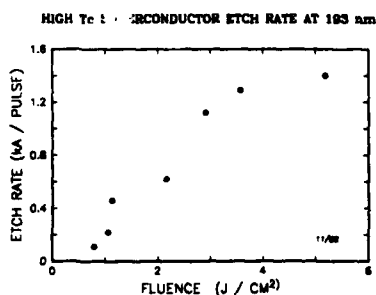


Fig. 2

Etch rate of polycrystalline YBaCuO film as a function of laser fluence (at 193 nm).

The etch rate appears to saturate at fluences greater than 4 J/cm^2 . Qualitatively similar behavior has been observed in the etching of polycrystalline superconductor films at 248 nm^{13} . However, the present work suggests that the absorption depth is smaller at 193 nm which manifests itself as a lower etch rate.

Several lines were patterned and the resistance of the samples was measured as a function of temperature for both patterned and unpatterned samples. No change in the R vs. T behavior was observed for the films after patterning (see Fig.3).

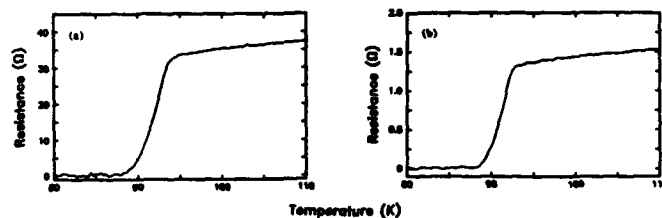


Fig.3

Behavior of resistance as a function of temperature after (a) and before (b) excimer laser micropatterning.

To determine whether fluence had any effect on the films, three narrow lines were patterned into a film at three different fluences ($0.6, 2.3, 4.6 \text{ J/cm}^2$) corresponding to the range of available fluences. The critical current density and transition temperature were measured for each line and found to be the same, within experimental error, indicating that fluences up to 4.6 J/cm^2 have no apparent effect on the film.

A problem generic to excimer laser micromachining and ablation is that of debris formation. This becomes a concern, especially, when critical or fine line resolution is required. Experiments were performed with High- T_c films coated with photoresist. The films were ablated by first "cutting" through the photoresist and then through the High- T_c material. Any debris that was generated was embedded/attached to the photoresist surface. After patterning, the samples were rinsed with ethanol thereby removing the debris along with the photoresist. This procedure was found to have no effect on the superconducting properties of the film and has been extensively used.

The apparatus has been used to generate features as small as $2 \mu\text{m}$ in a routine fashion. Smaller features can and have been made but tend to be difficult to fabricate in a reproducible manner because of mechanical vibrations, optical aberrations, debris formation, etc.

Micropatterned Structures and Devices

Many different structures have been patterned into superconductors both directly and through photoresist. The coplanar transmission lines in Fig. 4 illustrate the feasibility of patterning over large areas. These lines are $12 \mu\text{m}$ wide on $22 \mu\text{m}$ center spacing. It was possible to maintain these dimensions over the 3 mm length to within $0.5 \mu\text{m}$.



Fig.4

Excimer beam micropatterned superconducting "transmission" lines on MgO . Conductors are 3 mm long and $12 \mu\text{m}$ wide on $22 \mu\text{m}$ center spacing.

Fine structures such as High-Tc superconductor "microbridges" have been patterned (Fig. 5). These microbridges are an excellent means for the investigation of important parameters, such as the critical current density. Because the patterning can be viewed in real time, it is possible to avoid patterning in defective areas of a film. These microbridges have been used as the basic building blocks for (SQUIDs), and were used to demonstrate the first SQUID devices operating at liquid nitrogen temperatures.¹⁴



Fig.5

Narrow line patterned in polycrystalline film. Such lines are convenient for measuring critical current densities and are the building blocks of SQUIDs.

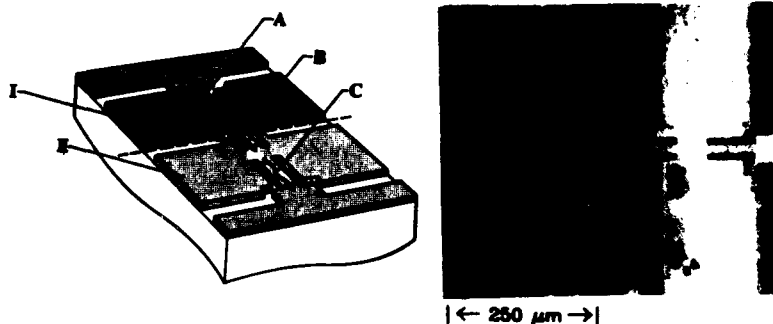


Fig.6

Schematic (left) representation of excimer laser micropatterning of lines within and across single grains. Photo (right) shows actual pattern. Adjacent crystals appear "light" and "dark" using oblique illumination technique.

The selectivity of the process was exploited in the study of grain boundaries. Fig. 6 depicts the type of pattern used to study the transport properties of grain boundaries and their adjacent grains. In the initial work, each grain was approximately 100 microns in diameter. The excimer laser was used to pattern lines within each grain and across the grain boundary. This work gave the first direct proof that grain boundaries are responsible for low critical current densities in polycrystalline films.¹⁵ In addition, these microbridges across grain boundaries were found to act as Josephson Junctions and therefore appear to be a natural way for forming SQUIDs (Fig. 7).

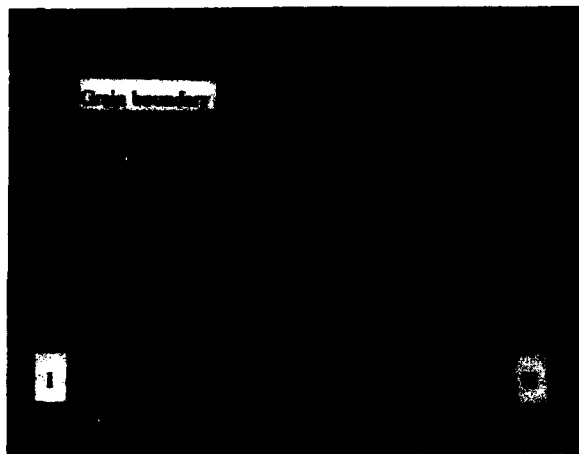


Fig.7
SQUID patterned in an epitaxial film exploiting properties of the grain boundary.

Summary

Focussed excimer laser beams offer a means for the rapid, direct, maskless, patterning of High-Tc films. It is possible to pattern High-Tc films with a resolution on the order of $1\ \mu\text{m}$ with no apparent degradation of the films' superconducting properties. The technique has been used to pattern a variety of structures including transmission lines and SQUIDs as well as help to elucidate fundamental physical properties of High-Tc films such as the role of grain boundaries.

Acknowledgements

We would like to thank P. Chaudhari, D. Dimos, and C.C. Chi for providing films and for their collaboration in the single grain boundary experiments and R.H. Koch and C.P. Umbach for their early contributions.

References

1. P.M. Mankiewich, J.H. Scofield, W.J. Skocpol, R.E. Howard, A.H. Dayem, and E. Good, Appl. Phys. Lett. 51, 1753 (1987)
2. S. Matsui, N. Takado, H. Tsuge, and K. Asakawa, Appl. Phys. Lett., 52, 69 (1988)
3. Y. Yoshizako, M. Tonouchi, and T. Kobayashi, Japan J. Appl. Phys. 26, 1533 (1987)
4. I. Shih and C.X. Qui, Appl. Phys. Lett. 52, 1523 (1988)
5. G.J. Clark, A.D. Marwick, R.H. Koch, and R.B. Laibowitz, Appl. Phys. Lett. 51, 139 (1987)
6. M. Rothschild, J.H.C. Sedlacek, J.G. Black, and D.J. Ehrlich, IEEE Electron Device Lett. 9, 69 (1988)
7. M. Scheuermann, C.C. Chi, C.C. Tsuei, D.S. Yee, J.J. Cuomo, R.B. Laibowitz, R.H. Koch, B. Braren, R. Srinivasan, and M. Plechaty, Appl. Phys. Lett., 51 1951 (1987)

8. J.Mannhart, M.Scheuermann, C.C.Tsuei, M.M.Oprysko, C.C.Chi, C.P.Umbach, R.H.Koch, and C.Miller, Appl. Phys. Lett., 52 1271 (1988)
9. J.Hagerhorst and M.M.Oprysko in "Excimer Beam Applications," Vol. 998 of the Proceedings of SPIE Conf. (Boston, MA, 1988)
10. K.Harte and B.P.Piwczyk in "Excimer Beam Applications," Vol. 998 of the Proceedings of SPIE Conf. (Boston, MA, 1988)
11. M.Scheuermann, C.C.Chi, C.C.Tsuei, and J.D.Mannhart, Vol. 948 of the Proceedings of SPIE Conf. (1988)
12. P.Chaudhari, R.Koch, R.B.Laibowitz, T.R.McGuire, and R.J.Gambino, Phys. Rev. Lett. 58, 2684 (1986)
13. A.Inam, X.D.Wu, T.Venkatesan, S.B.Ogale, C.C.Chang, and D.Dijkkamp, Appl. Phys. Lett. 51, 1112 (1987)
14. R.H.Koch, C.P.Umbach, M.M.Oprysko, J.D.Mannhart, G.J.Clark, A.Gupta, R.B.Laibowitz, M.R.Scheuermann, and C.C.Tsuei, Physica, C153-155, 1685 (1988)
15. J.Mannhart, P.Chaudhari, D.Dimos, C.C.Tsuei and T.McGuire, Phys. Rev. Lett. 61, 2476 (1988)

MASS SPECTROMETRIC PROBING OF LASER-INDUCED MATERIALS
VAPOR TRANSPORT: GRAPHITE AND SUPERCONDUCTING $\text{YBa}_2\text{Cu}_3\text{O}_x$

DAVID. W. BONNELL, P. K. SCHENCK, AND J. W. HASTIE
National Institute of Standards and Technology, Gaithersburg, MD 20899.

ABSTRACT

A very high pressure-sampling mass spectrometer has been used to identify the vapor transport species and determine the thermochemistry and kinetics of laser-induced plumes produced from graphite and superconducting composition $\text{YBa}_2\text{Cu}_3\text{O}_x$ targets ($x = 6.5$ to 7). An electron impact ion source was used for the ionization and detection of neutral plume species. The plumes initially contain ~ 1 atm ($1 \text{ atm} = 101.325 \text{ kPa}$) of neutral and charged atomic and molecular species in a vacuum of $< 10^{-7}$ atm. Time resolved mass spectra were obtained with graphite targets for the neutral plume species C_n ($n = 1-9$) for varying laser fluence, laser-surface interaction geometry, vapor plume-sampling geometry, and target surface morphology. Relatively low abundance charged species C_1^+ , C_2^+ , C_3^+ , and impurities Na^+ and K^+ were also observed in the laser-induced plume.

Mass spectra obtained with superconducting $\text{YBa}_2\text{Cu}_3\text{O}_x$ targets showed a variety of species in the laser-induced plumes including both neutral and ionic Y, Ba, and Cu. In addition, molecular species such as O_2 , BaO , CuO^+ , YO and bimetallics (BaCu , YCu) were observed.

INTRODUCTION

The study of the effects of laser-induced material transport has been the subject of considerable research effort for more than a decade. The use of laser energy as a focused, high-temperature or high energy surface excitation source is an attractive technique for material transport (thin film-making, etching, CVD, etc.) and for surface analysis using either mass spectroscopic or optical techniques. In general, rather different gas-producing processes can be involved: (1) laser desorption, where the laser provides only enough energy to remove adsorbed, chemisorbed, or non-refractory species; (2) laser vaporization, where the laser acts as a thermal source, vaporizing refractory, chemically bonded species in approximate local thermodynamic equilibrium; and (3) laser ablation, where the laser energy is so high that it disrupts chemical bonds indiscriminately, and multiphoton ionization is a significant process. Although all of these processes may participate to some extent in applications, it is important to identify and characterize, on a molecular level, which process(es) predominate in order to relate the vapor deposition process to the properties of the deposit.

Where the substrate is not sufficiently refractory and/or not a sufficiently good thermal conductor, both vaporization and ablation may occur. As ablation begins to dominate, laser disruption and ionization occur, leading to a more uniform emission of the underlying composition. In the extreme limit, only atoms and ions enter the vapor state. Both of these processes are of considerable interest to applications such as film deposition from ceramics and metals, etching of electronic, optical, and high temperature materials, and laser-analytical measurements, as well as to fundamental studies of high temperature thermochemical properties [eg. see 1-8]. The need for thermochemical data of materials at temperatures beyond 2000 K and with vapor pressures above the typical Knudsen experimental collision-free pressure regime of about 10^{-4} atm ($1 \text{ atm} = 101325 \text{ Pa}$) is a major driving force for adapting laser heating processes to fundamental vaporization studies.

We have developed mass spectrometric and concomitant optical diagnostic techniques to explore the gas phase above surfaces under laser attack. The

coupling of a high power laser to a high pressure-sampling molecular beam mass spectrometer, with electron impact ionization for detection of neutral vapor species, shows promise as a new thermochemical characterization tool [9]. In typical laser heating experiments, vapor is generated by a pulsed Nd/YAG laser focused at a target surface. The generated vapor has high instantaneous pressures (> 1 atm), even in a well pumped vacuum system, resulting in a gas-dynamically stabilized plume.

EXPERIMENTAL

Mass Spectrometry

The basic apparatus has been described previously [9, 10], and consists of a four-stage, differentially pumped vacuum system with molecular beam defining collimating apertures separating each pumping stage. The lowest stage (laser impact--plume formation region) has an open geometry with net pumping speed $\gg 2000$ l/s, to minimize background interference with the plume and molecular beam forming processes. No evidence was found in our earlier laser vaporization studies for background-induced perturbation of species identities or the partial pressure distributions. The laser impacts the sample surface at an incident angle from 15° - 45° (75° - 45° from normal incidence), and, for the present study, the system geometry was modified to permit molecular beam sampling normal to the specimen surface.

The mass filter is a quadrupole system with a mass range of 1 - 1600 u (standard unified mass units) and typically unit resolution or better. Neutral species are detected as positive ions generated in a cross-beam configuration electron impact ion source with variable electron energy.

The laser used for the present studies is a Nd/YAG 20 Hz pulsed laser with a typical pulse width of 10 ns. Discrete wavelengths of 355, 532, and 1064 nm, with energies up to 200 mJ per pulse at 1064 nm, are available. For this work, the 532 nm wavelength was used as it provided the best match of energy and vaporization conditions (10 - 40 mJ focused with a 50 cm focal length lens onto a 250 μ m spot). A radiometer was used to directly measure the laser fluence periodically during experimental runs to confirm constant laser power conditions. Alignment of the laser impact point with the mass spectrometer (MS) beam-acceptance axis was monitored using a photodiode located just above the mass filter ion source.

The sample targets were mounted on a two-axis translation stage, allowing samples to be positioned or rastered, as desired, between laser shots. Raster rates up to 200 μ m/sec are possible (100 μ m/sec typical) with a 95 percent heated area overlap and a ~ 250 μ m beam spot diameter.

The primary signal detection technique provides time resolved (time-of-arrival, TOA) ion intensity signals for individual masses by tuning the mass spectrometer to a specific mass value and directly signal-averaging (for typically 100-1000 shots) the detector output.

RESULTS AND DISCUSSION

Graphite Targets

With the perpendicular (on-axis) sampling geometry, the molecular beam pattern deposited on the first collimation aperture plate clearly coincided with the mass spectrometer beam axis, even though the periscoped laser beam was directed at the surface at approximately a 15 - 20° angle (relative to parallel incidence). The mass spectral data indicated that the carbon C_n ($n = 1$ -5) peaks were present at similar intensities to those observed earlier using an off-axis sampling geometry [10].

Using time-of-arrival single peak detection, mass peaks corresponding to C_1^+ - C_5^+ were observed under conditions where these ions were produced both

by electron impact of neutral C_n and directly by the laser. With the electron impact (EI) ion source filaments off, laser-produced ions are the only detected species. Note that the quadrupole system is more sensitive, by a factor of about 10^4 , to ions than to EI-detected neutrals. The on-axis relatively broad peaks were not present with the ionizer off, which establishes their origin as laser-produced neutrals. Figure 1 shows typical TOA profiles for C_1 - C_3 . The C_1 profile clearly shows a bimodal and possibly trimodal structure. The earliest peak is independent of electron impact ionization, showing that it is laser-produced C_1^+ ions. The C_2 and C_3 TOA profiles are also multimodal with the fastest peaks being essentially all laser-produced ions, in marked contrast to the earlier off-axis profiles which showed single peaks [10]. The broad, slower TOA peaks begin earlier in time, but otherwise correspond with TOA peaks observed for the gas-dynamically cooled neutral plume species in the earlier off-axis results [10].

Both the peak width and time-of-arrival indicates the fastest, narrow peaks to be translationally very hot ($\sim 8,000$ K). The time scale for their formation and depletion also suggests that they are not associated with the plume of predominantly neutral species. The peak times-of-arrival for the ions and hot and cool neutrals, correspond to temperatures (directional Maxwell distribution) of 8000 ± 1000 K, 2500 ± 500 K, and 300 ± 100 K, respectively. From our earlier studies, the plume-surface interface region temperature is 4200 ± 200 K, and the plume density and individual species concentrations are consistent with this temperature. Hence the plume formation process has a spatial and temporal temperature distribution which is not unexpected for the gas-dynamic conditions present. The ions are apparently part of the pre-plume formation process and should serve as probes of the plume onset and expansion cooling process. It should be noted, however, that our measured ion concentration is of the same order of magnitude as that expected from a Saha-Langmuir calculation [11] of the thermal concentration in equilibrium with neutrals at 4200 K.

Relative intensities of the neutral C_n species were found to vary with laser fluence and surface morphology due to photochemical and surface accommodation effects, respectively.

YBa₂Cu₃O_x Targets

Typical time-of-arrival signals from the mass spectral analysis of the plume generated from the laser vaporization of the high temperature superconductor YBa₂Cu₃O_x are shown in Fig. 2. Species were identified by isotopic ratio measurements. The mass spectrometer signals for the metal atom species Y, Ba and Cu consisted of bimodal signals like the signal shown in Fig. 2A for mass 63 (Cu). As in the case of graphite, the fast component is identified as coming from ionic plume species and the slower component from cooler neutral plume species. The signal at mass 79, identified as CuO in Fig. 2B, consisted only of ionic plume species.

Figure 2C shows the signal from mass 32 (O₂) which is bimodal also. The observation of molecular O₂ in the plume is noteworthy. Laser deposited films from YBa₂Cu₃O_x targets are usually O-deficient [12], and the observation of molecular oxygen may be indicative of O-atom recombination in the plume or at the plume-surface interface. The much lower reactivity of molecular O₂ relative to O, and consequent lesser incorporation in the deposit, may be one mechanism leading to the observed oxygen deficiency in laser-deposited oxide films.

In addition to the plume species mentioned so far, mass spectrometer signals identified as H₂O, CO₂, BaO, YO, Na⁺, K⁺ and bimetallics (CuBa, YCu) were observed in the plume [10].

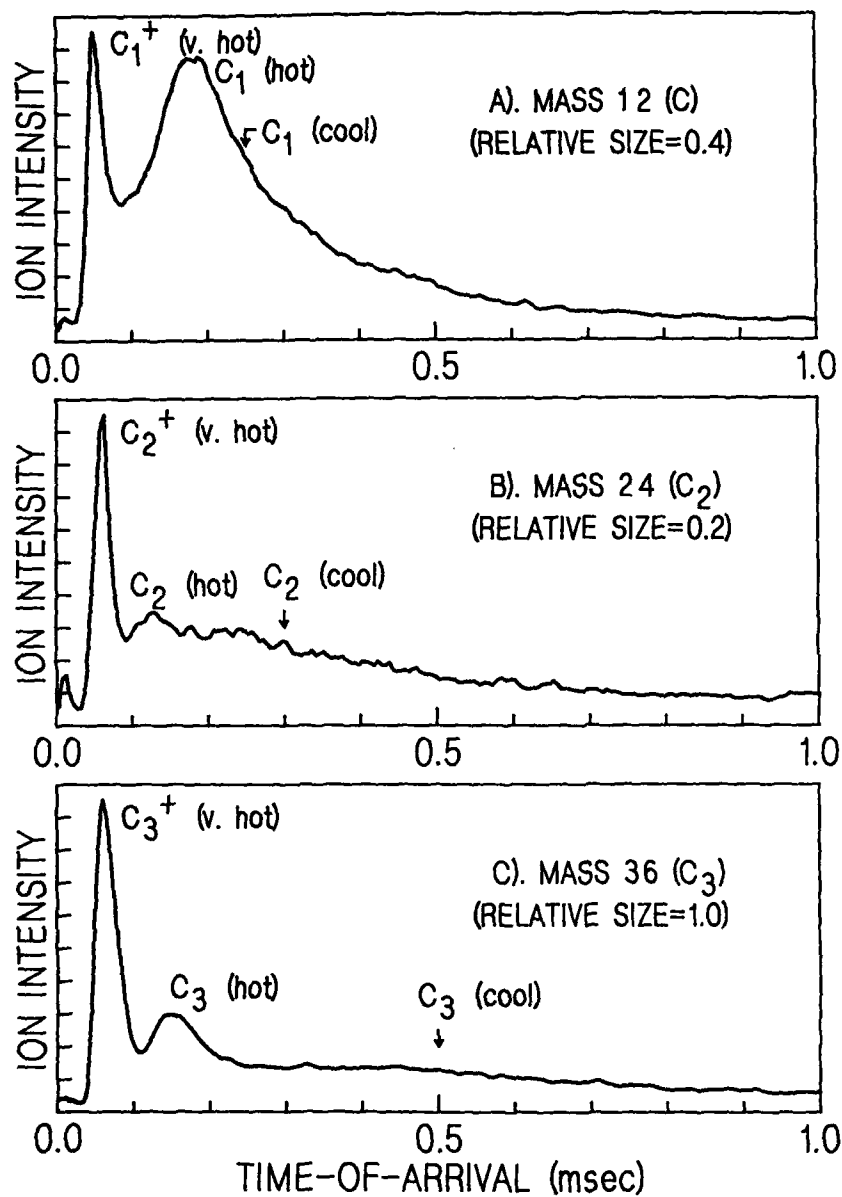


Figure 1. Time-of-arrival intensity profile (arbitrary units) for C_1 , C_2 , and C_3 (Figs. A, B, C respectively) obtained with both the laser and ionizer on and with on-axis sampling of the plume.

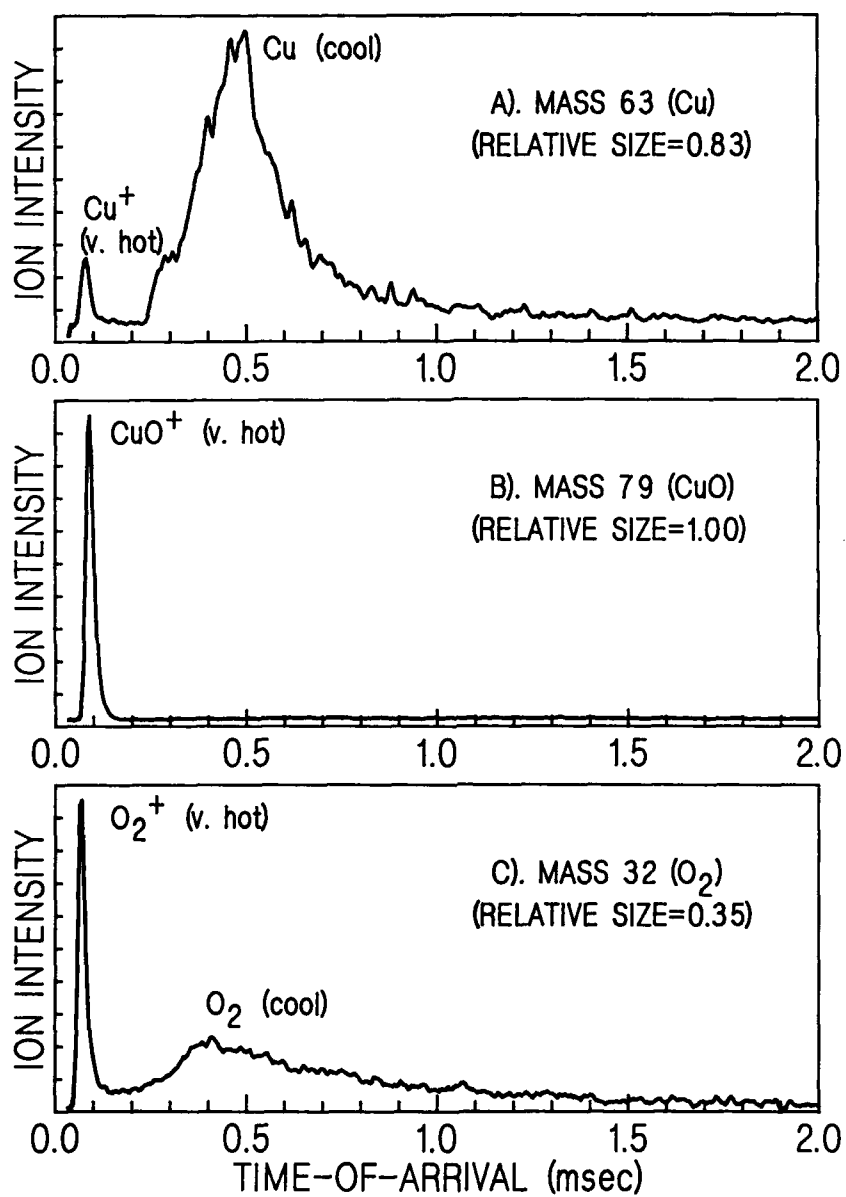


Figure 2. Time of arrival intensity profiles (arbitrary units) for mass 63 (Cu , Cu^+), mass 79 (CuO^+), and mass 32 (O_2 , O_2^+) (Figs. A, B, C respectively) obtained with both the laser and ionizer on and with on-axis sampling of the plume.

CONCLUSIONS

The present results indicate that the vaporization and ejection of vapor species by laser heating and excitation produce both equilibrium and non-equilibrium effects, particularly in relatively low-melting ceramics. Vapor plume formation is non-homogeneous, both in space and time. Fast, very hot, non-equilibrated ions were produced on-axis early in the laser-surface interaction phase. On-axis hot neutrals were also detected prior to the full development of an expansion-cooled plume jet. At later sampling times, and with off-axis sampling, only cool neutrals were observed. Under the latter conditions, which can comprise the bulk of the material transported, the species intensities appear to follow those expected for an equilibrium vaporization process.

ACKNOWLEDGEMENTS

This work was supported in part by the Air Force Office of Scientific Research.

REFERENCES

1. G. Hass and J.B. Ramesey, *Appl Opt.* **8**, 1115 (1969).
2. K.A. Lincoln and M.A. Covington, *Intl. J. Mass Spect. and Ion Phys.* **16**, 191 (1975).
3. R.A. Olstead, and D.R. Olander, *J. Appl. Phys.* **46**, 1499 (1975).
4. M.A. Covington, G.N. Liu, and K.A. Lincoln, *AIAA J.* **15**, 1174 (1977).
5. J.H. Lundell, and R.R. Dickey, *AIAA 16th Aerospace Sciences Meeting*, Huntsville, AL (1978) p. 193-209.
6. R.W. Ohse, J.F. Babelot, C. Cercignani, P.R. Kinsman, K.A. Long, J. Magill, and A. Scotti, in *Proc. 10th Materials Symposium on Characterization of High Temperature Vapors and Gases*, ed J.W. Hastie, (NBS SP 561/1 U.S. Gov. Printing Off., Washington, DC, 1979), p 83.
7. R.L. Baker, M.A. Covington, and G.M. Rosenblatt, "The Determination of Carbon Thermochemical Properties by Laser Vaporization," in *High Temperature Materials II*, ed Z.A. Munir and D. Cubicciotti (Electrochem. Soc., Pennington, NJ, 1983) p. 143.
8. R.W. Dreyfus, R. Kelley, and R.E. Walkup, *Appl. Phys. Lett.* **49**(21), 1478 (1986).
9. J.W. Hastie, D.W. Bonnell, and P.K. Schenck, "Laser-induced Vaporization Mass Spectrometry of Refractory Materials: Part I. Apparatus and the BN system," *High Temp. Sci.* **25**, 117 (1988).
10. J.W. Hastie, D.W. Bonnell, and P.K. Schenck, "Thermochemistry of Materials by Laser Vaporization Mass Spectrometry, Part II Graphite," *High Temp. High Press.*, **20**, 73 (1988).
11. J. Lawton and F. Weinberg, *Electrical Aspects of Combustion*, Chapter 6, (Oxford University Press, 1969).
12. K. Moorjani, J. Bohandy, F. J. Adrian, B. F. Kim, R. D. Schull, C. K. Chiang, L. J. Swartzendruber, and L. H. Bennett, *Phys. Rev. B*, **36**, 4036 (1987).

EJECTED PRODUCT ENERGY DISTRIBUTIONS FROM LASER ABLATED SOLIDS

H. HELVAJIAN, AND R. P. WELLE, Laser Chemistry and Spectroscopy Department, The Aerospace Corporation, P. O. Box 92957, Los Angeles, CA 90009.

ABSTRACT

At laser threshold fluences near ion product formation, we have measured the ejected ion kinetic-energy distributions from the UV laser ablation of crystalline aluminum and silver targets. The mean kinetic energy is found to be hyperthermal.

INTRODUCTION

The recent growth in laser based processing has directed research efforts to better understand the laser/surface interaction phenomena. The hope is that a measure of control could be gained during the laser processing of specialized novel materials. Experiments have shown that the fundamental processes are dependent on both laser intensity and wavelength. Furthermore, the nature of the surface (adsorbed impurities, surface morphology) plays an important role in defining the character of the initial excitation.

We have prepared an experiment which measures, for a single laser shot, the ejected mass and nascent velocity distributions of ablated ionic species at laser threshold fluences for product formation. We have chosen to study first the nascent ionic species as they have the highest potential for reactivity in the above surface chemistry. Using time-of-flight mass spectroscopy, we have measured the nascent kinetic energy (KE) distributions from the UV (248 nm and 355 nm) laser ablation of crystalline silver and aluminum. For these metals, we measure the initial ablated ions to have kinetic energies in excess of that predicted by any thermal process (e.g., 9 eV; 3 eV FWHM for silver). Our laser fluences at threshold (15-150 mJ/cm²) are below the damage threshold of the material and also below that necessary for generating an above surface plasma. Furthermore, at the laser intensities used (1-15 MW/cm²), the calculated localized temperature rise is less than 100 K. The KE distributions are different for each metal but are invariant with wavelength (248 nm and 351 nm) for a given metal. At least for the case of silver, the energy absorbed per ejected ion seems to be constant (58-62 eV/ejected ion) for the two laser wavelengths. The fact that the $N_1(4p_{3/2})$, $N_2(4p_{1/2})$ core excitation energy for silver are at 58.5 eV and 64.5 eV, respectively, suggests the possibility that the initial energy absorption is through an electronic excitation in the solid.

EXPERIMENTAL

The experimental apparatus is drawn schematically in Figure 1. An ultra high vacuum chamber contains the target which is positioned normal to the axis of the time of flight (TOF) mass spectrometer. The chamber pressure is maintained below 4×10^{-10} Torr during the experiment, and at these pressures the time for impurity monolayer formation exceeds that for an experimental run (20 min). The output from an excimer laser (Lumonics) operating either with KrF (248 nm) or XeF (351 nm) laser mixes is collimated to reduce the beam divergence, and is then passed through a gas absorption cell which contains a mixture of F_2/Ne (5%), which allows for variable attenuation of the incident laser intensity without any additional beam steering. The focussed ($f = 50$ cm) laser beam strikes the target at 45 degrees with a 1×2 mm spot size. The intensity distribution, as measured by a reticon array, is uniform horizontally and nearly Gaussian vertically.

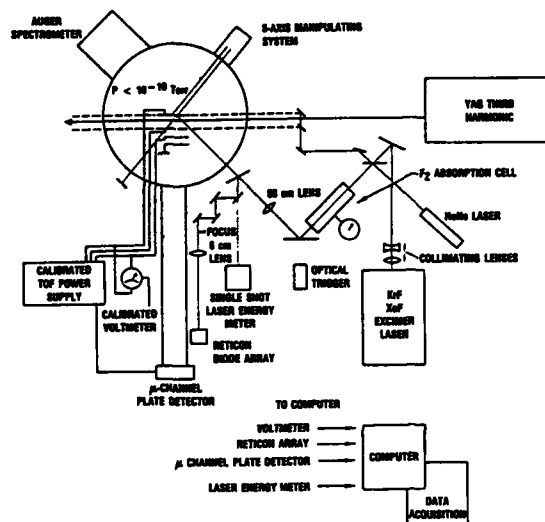


Fig. 1. Experimental Setup.

The TOF mass spectrometer is designed so that the target (13 mm dia. wafer) mounting plate acts as the first plate of the TOF and is biased positive relative to the extractor plate, thereby accelerating ions produced toward the TOF extractor plate. The voltages on the various TOF grids can be independently set, except for the target plate, which is always maintained at a potential 10% higher than the TOF extractor grid. All voltages are calibrated to 1%, and to correct for supply voltage drift, we automatically measure the pertinent voltage differences for each laser shot. The TOF was calibrated by using a second laser to resonantly multiphoton ionize (REMPI) Xe gas at thermal velocity. Our error in measuring the KE is 1 eV, which corresponds to a 10 nsec error in the arrival time.

The signals from the TOF microchannel plate detector (Galileo; response time 1 ns) are amplified by two sequential amplifiers (Lecroy; 200 MHz bandwidth; gain = 10) and then digitized by a transient recorder (Transiac 100 MHz). Data from the transient digitizer is recorded by the computer (DEC 11/73) for each laser firing, along with the TOF voltages and the incident laser energy. The metal targets are single crystal wafers (Atomergics 99.99% pure) and were etched and degreased before inserting them into the UHV chamber. Prior to each data taking the surface is further cleaned by laser ablation with the laser fluence set well above threshold.

RESULTS

It is necessary that the TOF mass spectrum be measured at the laser threshold fluence intrinsic to the ablation process. In this regard, we have found that if we analyze a data set (a number of individually acquired signal traces) by its topography rather than the individual amplitudes, our sensitivity to measuring intrinsic threshold signals increases. By the use of contour type plots, we are able to measure signals with the laser fluence set to a lower level. Figure 2 shows a contour plot of 600 individual TOF traces of the 248 nm laser ablated ion Ag^+ from a crystalline silver target. The figure shows that during the experiment the laser fluence was first held constant and then programmed to slowly increase. At the time of ablation, the kinetic energy (KE) distribution can be calculated from the

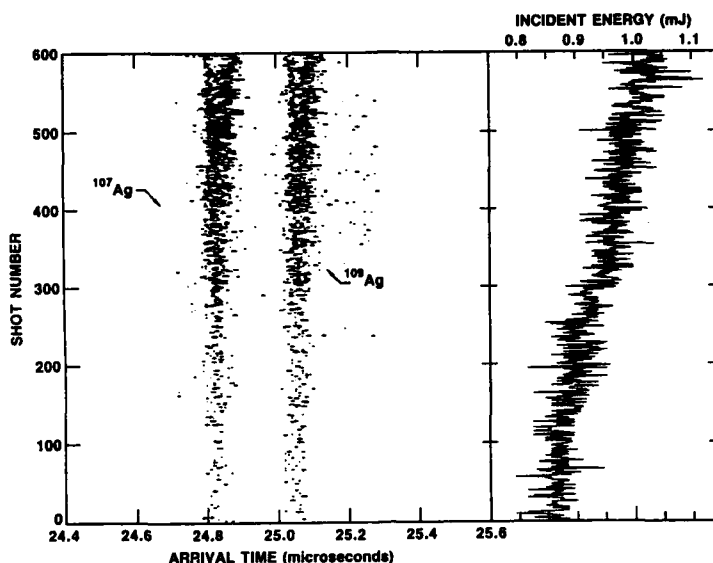


Fig. 2. Contour plot of a series of 600 mass spectra of silver monomer ablated at 248 nm. The spectra are sorted for incident laser energy, which is plotted on the right.

width in the TOF arrival times, and as the figure shows, the distribution broadens after a 20% increase in the laser fluence above threshold. Also seen in the figure is that by controlling the ablation laser fluence (e.g., fixed energy, and uniform intensity profile) consistent product KE distributions can be measured. Figure 3 shows three TOF mass spectra of the substrate ions Ag^+ , Ag_2^+ , and the ionized adsorbed species Fe^+ taken at 248 nm with the laser fluence fixed at the ion production threshold. Each spectrum is a sum of 300 individually acquired laser shots. The two silver isotopes (107, 109 amu) and the three main isotopes of iron (54, 56, 57 amu) are resolved with the ratio of the peak heights as found in natural abundance. Also shown in the upper scale is the ejected ion kinetic energy calculated for a specific mass isotope from the corresponding arrival times. The data show that at threshold laser fluence the ablated ion species regardless of mass and surface binding (substrate/adsorbed) character have a mean kinetic energy $\langle \text{KE} \rangle$ of 9.0 eV with a distribution (3 eV FWHM). We have also taken data at 351 nm laser ablation and measure the same $\langle \text{KE} \rangle$ and distribution. Contrary to these results are the KE distributions with the laser fluence set much higher (>50% above threshold). They tend to be much broader (Fig. 2) and can be fit to a hot Maxwellian distribution. Figure 4 shows a TOF mass spectrum of the Al^+ ion ablated from a crystalline aluminum target. The spectrum shows that the KE distribution for the ablated Al^+ is much broader (10 eV FWHM) than that measured in the silver ablation. We are as yet not sure if the width in the KE distribution is intrinsic to the ion desorption or if it has broadened due to long range interactions in the ablation process. However, the figure does show that the fastest ions have kinetic energies close to 16 eV. This value also corroborated with the results of a retarding potential experiment.

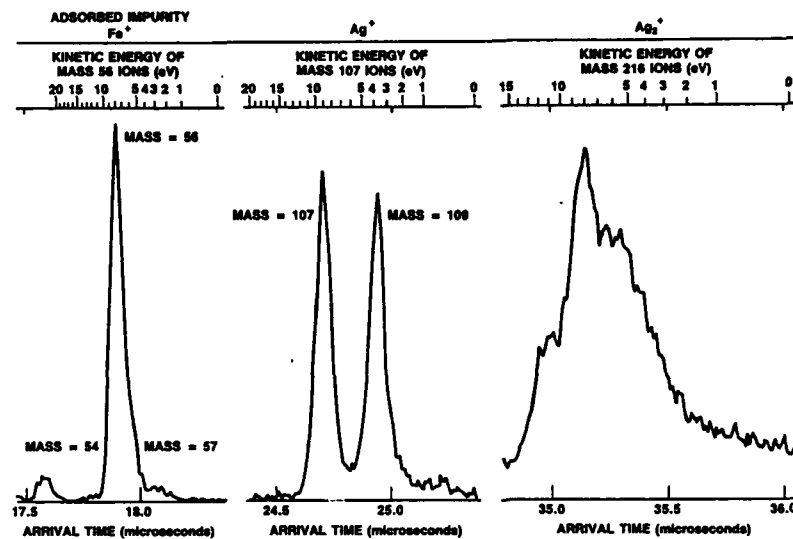


Fig. 3. A 300 shot sum mass spectrum of 248 nm laser ablation from a silver target with adsorbed Fe. Major ablated ions measured at threshold are shown. Kinetic energy for a specific isotope is given in the upper scale. Zero kinetic energy is defined by the arrival time of a REMPI thermal Xe.

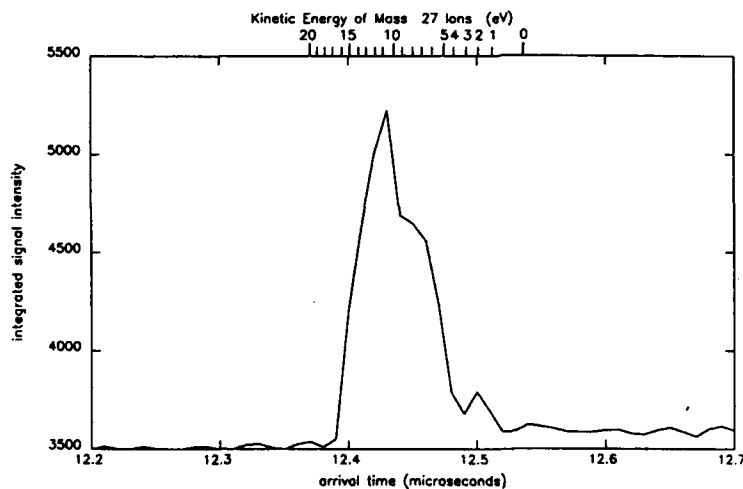


Fig. 4. A 300 shot sum mass spectrum of 351 nm laser ablation of a crystalline aluminum target. Natural abundance of ²⁷Al is 100%.

DISCUSSION

The observation of fast ions in moderate fluence laser ablation experiments is not uncommon [1]. The KE distributions tend to be very broad with the average energy being a function of the laser intensity [2]. To our knowledge our results are the first to show that the threshold laser ablation of certain metals, where plasma effects are negligible, results in hypervelocity ions with very narrow KE distributions.

For a specific crystalline metal target (silver and aluminum), the kinetic energy of the ejecta do not vary with wavelength (248 nm and 351 nm), nor with the ion product mass, and within limits is independent of the incident intensity. These results cannot be explained within the framework of a number of potential mechanisms such as a) laser photolysis of an adsorbate, and b) field ionization of an adsorbate or evaporated substrate species. If the hypervelocity product ions are formed via laser photolysis of an adsorbed precursor, then we would expect variations in the ejected kinetic energy with wavelength as well as some dependence on the differences in binding potentials between physisorbed and lattice bound species. Laser field ionization of thermally desorbed species followed by coulombic repulsion is also difficult to rationalize. At the laser power densities used in this experiment, the electric field strength near the surface ($2-9 \times 10^{-3}$ V/nm) is orders of magnitude lower than that used in field ionization TOF mass spectrometry (10 V/nm) [3]. In addition, a kinetic energy deficit is observed in the TOF mass spectrum by laser field ionization. The energy deficit is due to the ionization of the species at a critical distance above the surface which is laser field dependent [4]. Our results show a kinetic energy enhancement rather than a deficit, and we do not see variation of the kinetic energy with laser fluence near threshold.

It is known that the laser fluence threshold for electron desorption is far below that for ion desorption [5]. Given this fact, our results could be explained by an electrical acceleration mechanism generated by a sheath of electron density above the surface. Two of our experimental results provide evidence contrary to the existence of an electron sheath. In the laser ablation of the Ag target, we observed the same KE distribution at both laser wavelengths, even though the photon energy at 248 nm is above the silver work function. Similarly, we do not see any change in the KE when the laser fluence is increased up to 20% above threshold. One could argue that the electron density in the sheath is space charge limited, it seems that would give KE energy distributions broader than what is measured. We are attempting to model the effects of the space charge limited electron density on the ion KE distributions.

Our results, especially with low laser fluences suggest that a fraction of the absorbed energy must remain localized to permit ion desorption, and furthermore, the desorbing ions are constrained in their KE. From our experimental results, the specific mechanisms by which the ion is actually formed and ejected is not fully apparent. However, we have some evidence which supports the notion that the ion formation and ejection process is induced via an electronic excitation in the solid. The production of ions at the relatively low laser fluences ($15-150$ mJ/cm²) might be the result of electronic resonances in the solid or due to surface impurities which can enhance a process by localizing the deposited energy. The impurity concentration at the surface was minimized during the target preparation cycle. Prior to taking data, roughly 30,000 laser shots are fired at the test area to remove adsorbed contamination. A small amount of contamination could still be present (perhaps the adsorbed Fe) which may artificially lower the threshold for ion production. The KE distribution of all ejected ions from a properly prepared surface is the same and very specific to the target (silver, aluminum). The similarity, regardless of mass, in the ejected kinetic energy distribution, along with the experimental results of the photon dependence where for both laser ablation wavelengths (351 nm 3.5 eV,

and 248 nm 5.0 eV), an average of 58-62 eV is absorbed per ejected ion suggests that the initial energy absorption process is through an electronic excitation in the solid. Further support is the fact that the $N_1(4p_{3/2})$, $N_2(4p_{1/2})$ core excitation energies for silver are at 58.5 eV and 64.5 eV, respectively. An electronic core excitation does not necessarily lead to ion ejection. It can however create ions through a mechanism originally outlined by Knotek and Feibelman [6]. Given that our photon energies are only a few eV, the creation of a core hole in silver requires a multiple photon absorption process. Recently, it has been suggested that electronic surface states due to defects may help, through resonance enhancement, the absorption of multiple photons [7]. We are now planning experiments where we will measure the KE distributions as a function of laser wavelength and temporal pulse shape. What is not immediately clear to us is the mechanism by which this electronic excitation is converted to atomic motion. It is known that two and three hole Auger final states decay at a much lower rate, essentially trapping the excitation at a particular site [8]. It is also known that in an Auger decay process, bulk plasmons can be excited [9]. The values we measure for the ion KE have a fortuitous correlation with the bulk (longitudinal) plasmon frequency of the target metal. Using the free electron metal model, the calculated plasmon frequency for silver and aluminum are 9.0 and 15.8 eV, respectively [10]. The experimentally measured frequencies are 3.78 eV and 8.0 eV for silver [11], and 15.3 eV for aluminum [12]. Our results show that ions are ejected from silver with 9 eV of KE and with 15-16 eV of $\langle KE \rangle$ from aluminum. If in fact our measurements are related to the plasmon frequency, then it is not clear why we do not measure ion KE corresponding to the 3.78 eV bulk plasmon. Otto et al. [11] have concluded from their spectroscopy on silver that the 3.78 eV and 8.0 eV absorption corresponds to the out and in phase oscillations between the free conduction band electrons and the bound d band electrons. Perhaps the in phase oscillation can more readily promote ion acceleration. Clearly, more experiments along with a theoretical model are needed to pin down the underlying mechanisms. We are now preparing experiments to see if this correlation holds with other targets as well, and to see if the predicted laser polarization effects could be observed.

REFERENCES

1. M. R. Bedilov, Yu. A. Bykovskii, D. Kuramatov, A. Kholbaev, and K. Khaibbaev, *Sov. J. Quantum Electron.* **17**, 1068 (1987).
2. V. A. Batanov, P. V. Bunkin, A. M. Prokhorov, and V. B. Fedorov, *Zh. Eksp. Teor. Fiz.* **63**, 1240 (1972).
3. E. R. McMullen, and J. P. Perdew, *Phys. Rev. B* **36**, 2598 (1987).
4. T. T. Tsong, and T. J. Kinkus, *Phys. Rev. B* **29**, 529 (1984).
5. P. G. Strupp, J. L. Grant, P. C. Stair, and E. Weitz, *J. Vac. Sci. Technol.* **A6**, 839 (1988).
6. M. L. Knotek, and P. J. Feibelman, *Phys. Rev. Lett.* **40**, 964 (1978).
7. H. B. Nielsen, J. Reif, E. Matthias, E. Westin, and A. Rosen to be published.
8. D. R. Jennison, in *Desorption Induced by Electronic Transitions DIET I*, Eds. N. H. Tolk, M. M. Traum, J. C. Tully, and T. E. Madey, (Springer-Verlag, New York, NY, 1983), pg. 4.
9. J. W. Gadzuk, in *Desorption Induced by Electronic Transitions DIET I*, Eds. N. H. Tolk, M. M. Traum, J. C. Tully, and T. E. Madey, (Springer-Verlag, New York, NY, 1983), pg. 4.
10. C. Kittel, *Introduction to Solid State Physics*, 5th Ed. (John Wiley & Sons, New York, New York, 1976).
11. A. Otto, and E. Petri, *Solid State Commun.* **20**, 823 (1976).
12. C. J. Powell, and J. B. Swan, *Phys. Rev.* **115**, 869 (1959).

SPACE/TIME RESOLVED ANALYSIS IN $\mu\text{m}/\text{nsec}$ SCALE of LASER
BEAM-SOLID SURFACE INTERACTION IN GROUP IV ELEMENTS

A. Kasuya and Y. Nishina
Institute for Materials Research, Tohoku University, Sendai 980, Japan

ABSTRACT

Dynamical characteristics of laser desorption and chemical processes in Group IV elements have been investigated by means of space/time resolved optical spectrometry in micrometers and nanoseconds scale on the light emitted from desorbed particles. The results suggest that desorbed atoms are coagulated in the form of large size clusters in a few ns after laser excitation. These clusters subsequently decompose into their ultimate forms of monomers. This interpretation is consistent with the conclusion drawn from our time-of-flight analysis of decomposition in 100 ns time scale.

INTRODUCTION

The dynamical process of laser ablation on solid surface is not well understood, particularly in the range of laser intensities from $20 \text{ MW}/\text{cm}^2$ to several GW/cm^2 and of the pulse duration in nanoseconds for group IV elements. The thermal model of laser vaporization has been applied to Si below $20 \text{ MW}/\text{cm}^2$ range in the temperatures up to its melting point [1]. For a higher level of laser power, large discrepancies are found between experimental results and prediction by the model with no account for the extremely high kinetic energies and degree of ionization of emitted particles [1-3]. Our previous measurements show that these particles exhibit a sharp increase (threshold) over three orders of magnitude in their yield under N_2 laser excitation of 10 ns pulse duration [4]. One may note that the pulsive period of laser fluence in nanoseconds is comparable to or longer than that for surface atoms to go through the phase transition from solid to gas. Hence a realistic model has to account for the excitation of surface atoms under transient conditions of the phase change for appropriate prediction of final energies of the desorbed particles. The thermal model deals only with the excitation of surface atoms in the solid before their desorption into vacuum. There are refined models which take into account the energy states of emitted particles after their desorption [2]. These models consider the photo-excitation of desorbed atoms through inverse Bremsstrahlung process [2]. This process becomes significant in the excitation range well above $1 \text{ GW}/\text{cm}^2$, where the desorbed (vaporized) atoms/ions reach a density high enough to absorb sufficient laser energy through collisions with free electrons in the vapor. Hence, this model can neither be applied for excitation below $1 \text{ GW}/\text{cm}^2$, nor predict the presence of a threshold in ion yield [4].

In order to investigate the state of desorbed particles under GW/cm^2 and nanosecond range of excitation, the light emission from the plume of desorbed particles is analyzed both in space and time using a streak camera system. Our preliminary measurements on graphite and Si by KrF laser irradiation [5,6] show a feasibility of analyzing the transient process of laser desorption in a time scale over nanoseconds and in space over micrometers. This paper presents our measurements extended to other group IV elements with the beams of both KrF and ArF lasers with their photon energies of 5.0 eV and 6.4 eV, respectively.

EXPERIMENTAL RESULTS

Our experimental setup consists of a streak camera combined with a single monochromator [5,6]. The streak image records the spectrum for each laser shot by a television camera with a silicon intensified target. In most of our measurements, the excimer laser beam is incident normal (z-axis) to the surface of the target. The plume of emission is viewed from a direction (x-axis) perpendicular to the z-axis. The entrance slit of the camera opens up to 5 mm in width in the y-direction. Three different modes of measurements are performed 1) The z-y mode: The pattern integrated over time and wavelength of the emission in the z-y plane. In this mode, the emitted light in the z-y plane is focused on a photocathode of its area $5 \times 5 \text{ mm}^2$ in the streak camera tube without applying a streak pulse. The monochromator is also removed. 2) The z-t mode: The time evolution of the emission focused along the entrance slit in the z-direction. This mode may be operated with or without a monochromator. 3) The z- λ mode: A time integrated wavelength spectrum of emission along the z-direction. The light is dispersed along the y-direction.

Measurements on graphite and comparison with other group IV elements

Figure 1 shows a z-y pattern of the plume from graphite surface excited by the lasers of KrF, (a) and of ArF (b). Both patterns show that the spot of maximum intensity is not located at the surface but at a few tenths of a millimeter off the surface. In these figures, the maximum intensities are normalized to a common level. Hence, the intensity distribution is much more confined in a small area for Fig. 1(b) than for 1(a). The pattern in Fig. 1(b) is similar to that found in Si for KrF excitation given in [6]. The following experimental observations suggest that the difference between Figs. 1(a) and 1(b) comes from the difference in the wavelength of laser beam rather than the slight difference in the temporal profiles of laser pulse between KrF and ArF: 1) The spectral characteristics of graphite by ArF excitation (shown below in Fig. 3) becomes similar to that of Si by KrF excitation, although they are quite different when excited by the same KrF laser as reported in [5] and [6]. 2) In case of Si, both spatial and spectral characteristics are similar between excitation by KrF and ArF as found in our present measurements.

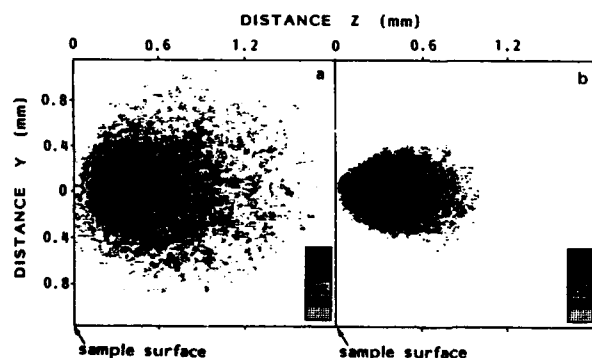


Figure 1. Time-integrated image of the plume emitted from a graphite surface excited by (a) KrF laser, (b) ArF laser pulse at their peak intensity of 50 MW/cm^2 . The distances y and z are measured along the tangential and normal directions with respect to the irradiated surface of graphite, respectively. The relative scale of intensity is digitized linearly by dot patterns shown in the inset.

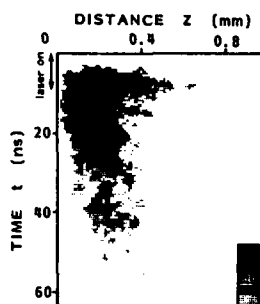


Figure 2. Time evolution of the plume emission along the z-axis from graphite surface excited by an ArF laser pulse of its peak intensity at 50 MW/cm^2 .

Figure 2 shows a z-t pattern of graphite excited by ArF laser. This pattern corresponds to the time evolution of emission intensity along the z-axis of Fig. 1(b). These patterns show that the positions of the maximum intensities are not only off the surface but also delayed with respect to the time of maximum laser intensity. Furthermore, the intensity near the maximum is not a smooth function of both z and t, but exhibits a series of sub-maxima. Figure 2 indicates that there exist two directions of expansion; one points nearly downward, and the other nearly horizontal. The former component of emission in Fig. 2 is concentrated in the region around the maximum intensity in Fig. 1(b), while the latter is distributed over the region of weaker intensity around the maximum in Fig. 1(b). Since the slope of the principal line of the pattern in the z-t plane represents the velocity of expansion, the former expands much more slowly than the latter. These expansion velocities are deduced to be in the order of 10^5 cm/s for the former (slower) component and over 10^6 cm/s for the latter (faster). The presence of the double components of expansion is much more conspicuous in graphite for its excitation by KrF laser, since the intensity of faster component is much higher than the case by ArF laser as shown in [5].

Similar z-y and z-t patterns are obtained for other crystals of group IV elements. The results for Ge is quite similar to the case of Si. The variation in going from Si to Ge, to Sn and to Pb is the increase in the emission intensity of the faster component with respect to the slower as observed in graphite for the change in excitation by ArF to KrF. In case

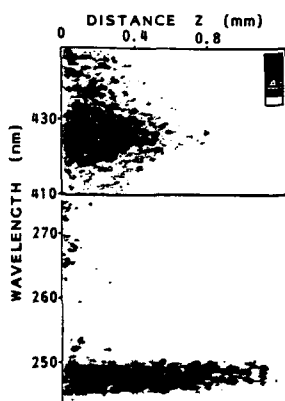


Figure 3. The emission spectrum by ArF laser (193 nm) excitation in the vicinity of 427 nm (ionic), and 248 nm (neutral) lines of the plume along the normal (z) to the surface of graphite.

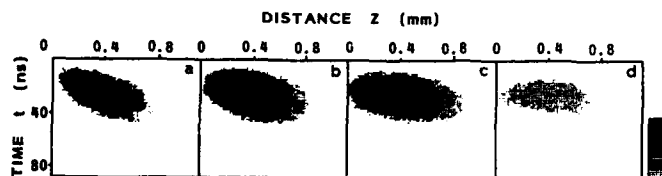


Figure 4. The time evolution of the plume emission from Si surface along the z-direction at (a) $y=0$, the center of the plume, (b) $y=1/8$ mm off-center, (c) $y=1/4$ mm off-center, and (d) $y=3/8$ mm off-center.

of Pb, the two components of emission begin to merge together in z-t plane.

Figure 3 shows the z- λ pattern of emission spectra of graphite for ArF excitation at the wavelength of 193 nm. The broad spectrum at 427 nm corresponds to the emission line ($4f^2F^0$ to $3d^2D$) from atomic ions of C^+ , whereas the sharp one at 248 nm ($3p^1S$ to $2p^3S^0$) from neutrals of C^0 . These spectra are in contrast with those for KrF excitation in which only molecular emissions are observed [6]. These spectroscopic assignments are consistent with our results that the patterns of graphite and Si are quite different from each other for KrF laser excitation, but similar for ArF laser as mentioned previously. The spectral characteristics of emission from other group IV elements are similar to the cases of graphite by ArF laser and of Si by KrF [5,6] and ArF.

Angular dependence of the plume

The emission characteristics of the plume can be analyzed more in detail if the z-t pattern is measured off-axis towards the y-direction. Figure 4 shows the change in the pattern observed in Si by focusing with an increment of 1/8 mm along the y direction. The pattern tends to lie more horizontally in the z-t plane as y increases. The decrease in intensity corresponds to the decrease in the emission intensity in the y-direction away from the center of the plume ($y=0$). The decrease in the slope in the z-t pattern shows that the velocity is faster for particles emitted with greater angle with respect to the surface normal.

Intensity pattern for off-normal incidence of laser beam.

All of the results shown in Figs. 1 through 4 are measured with the laser beam incident normal to the target. Figure 5 shows the emission pattern from Si when the surface of the sample is tilted 45° from the direction of incident laser beam. The z-y pattern depends on the incident

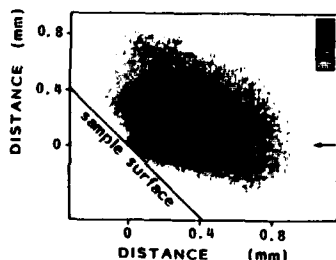


Figure 5. The time integrated image of the plume emitted from Si surface with its surface tilted 45° with respect to the KrF laser beam. Incident direction of the laser beam is indicated by an arrow.

angle of laser beam. The change in the pattern is such that the slower component points towards laser beam, but not the surface normal. On the other hand, the faster component does not change its pattern significantly and remains to spread out in all other directions with respect to the surface normal. This observation is confirmed by measurements similar to those in Fig. 4. The slower component appears only in the pattern in the measurement made along the line coincided with the laser beam (along the arrow in Fig. 5), whereas the faster one persists even in measurements of z-t pattern above this line.

DISCUSSION

The following are the summaries of the experimental results described above:

1) Overall emission patterns in both z-y and z-t planes are similar, but are different in details for different elements as well as different laser photon energies.

2) The intensity of light emission reaches its maximum neither on the surface, nor at the time of the maximum laser intensity, but at a few tenths of a millimeter off the surface and with a delay of about 3 to 15 nanoseconds from the time of laser peak intensity, depending on the substance.

3) The emission intensity is not a smooth function of both z and t, particularly in the vicinity of multi-peak intensities which take place within a narrow region of the z-t plane.

4) The emission pattern consists at least of two velocity components: The faster component is characterized by a) high velocity of expansion (low density) b) isotropic emission intensity regardless of the direction of expansion, and c) small delay in emission with respect to the onset of laser pulse. On the other hand, the slower component is characterized by a) the slow velocity of expansion (high density), b) the high directivity of expansion toward the direction of laser beam, c) and considerable delay in emission with respect to the laser pulse.

The feature 1) indicates that the observed phenomena are general characteristics in laser desorption process and do not depend strongly on detailed electronic or structural properties of the target materials or the final chemical form of desorbed species. The features 2) and 3) imply that desorbed particles continue to change their electronic states after they are removed from the target surface into vacuum. This change in the electronic states continues even after the end of laser pulse. The desorbed particles do not expand immediately into vacuum individually or independently from the surface, but rather tend to keep their initial density for absorbing laser energy before significant degree of expansion accompanied by light emission. Our spectral analysis does not show line emissions from multiply charged atoms [5,6]. Line emissions are observed in the range between 200 nm and 300 nm from excited levels as high as 20.9 eV (4f $^2F^o$) in graphite, and 10.4 eV (3p 2P) in silicon. Hence it is unlikely that electrons in the outermost shell are so highly excited to emit only those lines in the vacuum ultra-violet region in the process of relaxation followed by emission of lines in the visible (200-800 nm) at a later period of time. The feature 4) indicates the presence of extremely high density of desorbed particles near the surface. Otherwise, the faster component of desorbed particles would not gain such high velocities over 10^6 cm/s and the slower component would not emit light of high intensity in a confined area of 1 mm^2 or less.

The above observation may be explained in terms of a simple picture of desorption process that the surface atoms leave the surface in various forms of clusters which eventually decompose into their final forms of monoatoms and their ions. In the case of Si, for example, irradiated by

100 MW/cm² of 10 ns pulse duration, the surface atoms (within the skin depth of laser beam) can not remain in solid for the entire period of irradiation. Under such a transient situation, on the other hand, they do not have enough time to be evaporated individually and uniformly, but may desorb into various sizes of clusters in the region of skin depth [3,7]. These clusters still have a large optical absorption coefficient to absorb further the latter period of a laser pulse but are prevented from dissipating excited energies into the bulk. The surface atoms, therefore, become highly excited as soon as their clustering takes place. These clusters of surface atoms eventually decompose, in the process of relaxation, either into atoms (or small molecules) with high kinetic energies or into smaller clusters with high internal energies. This process of laser desorption can account for observed high kinetic energy and ion yield under a low excitation range where the inverse Bremsstrahlung process is negligible. This proposed model also explains the laser desorption processes in a unified picture under a variety of excitation conditions. In the region of low laser intensity (several MW/cm² or less) and long laser pulse, the cluster desorption process is negligible and thus, the thermal vaporization model is adequate to account for the experimental results. In the region of very high laser fluences, on the other hand, clusters desorb from the surface but decompose very rapidly because of the high intensity of laser beam. Most of the laser energy is absorbed by the desorbed atoms after being decomposed into monoatoms and their ions. Hence the inverse Bremsstrahlung process is the dominant excitation process of desorbed atoms. In the intermediate excitation between the above two cases, strong absorption of laser beam by desorbed clusters is responsible for the observed high kinetic energy and degree of ionization of the desorbed atoms. Hence, the proposed model bridges the gap in the applicability between the two models of thermal vaporization and inverse Bremsstrahlung process.

CONCLUSION

The laser desorption process has been analyzed by space/time resolved spectroscopy in nanosecond time scale and in micrometer space. Our results show that significant changes in both physical and chemical process take place in the desorbed atoms near the surface. This method of investigation can be extended easily to picosecond regime for more detailed analysis of laser beam-solid surface interaction. The authors would like to thank Professor C. Hori and Professor T. Goto, and Professor K. Murakami of Tsukuba University for valuable discussions, and the Mitsubishi Science Foundation for financial support.

- [1] See for example, Laser-solid Interactions and Transient Thermal Processing of Materials, ed by J. Narayan et al., MRS Symposia Proceedings 13 (North Holland, New York, 1983).
- [2] J. F. Ready, Effects of High Power Laser Radiation (Academic Press, New York, 1971) Chap. 4.
- [3] A. Kasuya and Y. Nishina, Phys. Rev. Lett. **57**, 755 (1986).
- [4] A. Kasuya and Y. Nishina, Microclusters, ed by S. Sugano, Y. Nishina and S. Ohnishi, Springer Series in Materials Science 4 (Springer-Verlag, Berlin, 1987) p.249.
- [5] A. Kasuya and Y. Nishina, to be published in Proc. of 19th Int. Conf. on Physics of Semicond., Warsaw (1988).
- [6] A. Kasuya and Y. Nishina, 4th Int. Symp. on Small Particles and Inorganic Clusters, Aix-En-Provence (1988), to be published in Zeitschrift für Physik D.
- [7] H. van Brug, K. Murakami, F. Bijkerk, F.W. Saris and M.J. van der Wiel, J. Appl. Phys. **60**, 3438 (1986).

ULTRAVIOLET LASER ABLATION OF A SILICON WAFER

MASAHIRO KAWASAKI, HIROYASU SATO* and GEN INOUE **

Research Institute of Applied Electricity, Hokkaido University, Sapporo 060, Japan

* Chemistry Department of Resources Mi'e University, Tsu 514, Japan

**National Institute for Environmental Studies, Yatabe, Tsukuba 305, Japan

Pulsed laser irradiation at 248 nm can ablate Si atoms from an Si wafer. The mechanism of this photoablation has been examined by laser-induced fluorescence analysis of the Si products. The Si atoms are measured to leave the wafer surface with averaged translational energy of 2.5 kcal/mol. The distribution of translational energy is well described by the theoretical model for non-cascade ablation processes.

1. Introduction

Recently, a large number of theoretical and experimental attempts have been made to measure and explain the interaction of pulsed laser irradiation with metal and semiconductor surfaces [1-3]. We have undertaken mechanistic studies which are aimed at understanding the dynamics of the photoablation process by which light pulses bring about the breakup of the Si wafer and cause the ejection of the products. From experiments studying the light emitted from excited atoms [3] it is well known that a fraction of the ablated particles are ejected in neutral states as well as ionic states. In this paper we report on translational energy measurements of Si atoms ejected from an Si wafer.

2. Experimental

A schematic diagram of the experiment is shown in Fig. 1. An Si wafer was placed in the vacuum chamber pumped by an oil-diffusion pump. The pressure was less than 10^{-6} Torr. A KrF excimer laser, operating at 248 nm, was used. The power of the laser pulse was ~ 10 mJ and the repetition rate was kept at 10 Hz. The UV laser beam was focused onto an Si (100) wafer (undoped) with a lens of $f=20$ cm.

When the ablation pulse from the excimer laser impinged on the sample, a pulse generator triggered a dye laser pumped by a YAG laser with a variable time delay and subsequently monitored the fluorescence signal via a photomultiplier (RCA 1P28) and a home-made time-resolved data acquisition system assisted by a mini-computer. The time resolution was 10 ns/channel. The photomultiplier was equipped with suitable glass cut-off filters and a two-lens telescope. This telescope limits the observing region of LIF signals in the chamber as small as 1 mm. The cut-off filters were used to reduce the scattered excimer laser light. The photoejected Si atoms were intersected 9 mm in front of the Si (100) wafer by the dye laser beam at right angles. This geometry makes it possible to measure the velocity of the ejected Si atoms. The $3p^3P_0$ state of Si was excited to $4s^3P_1$ at 251.43 nm. The fluorescence from this state was observed at 298.8 nm for $4s^3P_1 \rightarrow 3p^1D$. Typical signal shape is shown in Fig. 2. The photoabsorption spectrum of Si atoms has such a narrow peak that the dye laser wavelength could not be fixed exactly on the electronic transition of the Si atom. The laser wavelength was scanned over the resonant wavelength when measuring the LIF signal intensity for a certain delay time.

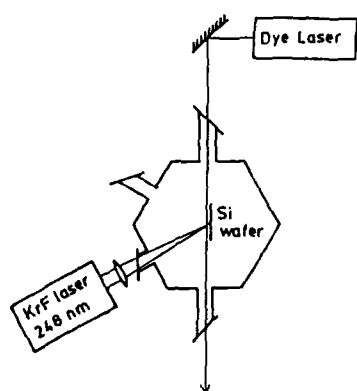


Fig. 1. Experimental setup for KrF excimer laser induced photoablation of an Si wafer. Si atoms are detected by laser-induced fluorescence technique using a YAG laser pumped dye laser. A photomultiplier tube is placed at right angles to two laser beams.

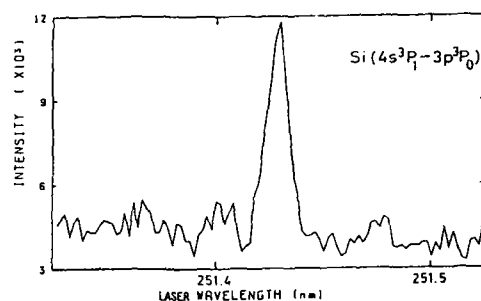


Fig. 2. Laser-induced-Fluorescence spectrum of Si atoms in the transition of $4s^3P_1 \leftarrow 3p^3P_0$.

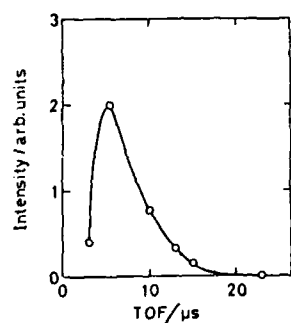


Fig. 3. Time of flight spectrum of Si atoms Photoablated from an Si (100) wafer at 248 nm. Flight length = 9 mm.

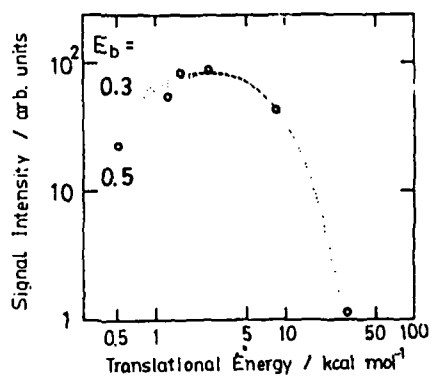


Fig. 4. Translational energy distribution of Si atoms photo-ablated from an Si wafer at 248nm. Open circle: experimental results. dotted lines: calculated curves for $\beta = 0.22$ (kcal/mol) and $E_b = 0.3, 0.4, \text{ and } 0.5$ kcal/mol for eq. (3).

3. Results and Discussion

The LIF signal intensity was observed for the transition of Si at 251.43 nm as shown in Fig. 2. We searched carefully for a transition of Si₂ at 390 - 394 nm [4] but found none. The UV laser ablation produces mainly Si atoms. This result is in agreement with the fact that a doubled YAG laser beam focused onto metal substrates (Si, Al, Nb, Cu etc.) produces only atomic ions of metals but no molecular ions when measured by the quadrupole mass spectroscopic analysis [5]. The signal intensity is shown in Fig. 3 as a function of temporal delay between laser pulses. The single intensity is shown in Fig. 3 as function of temporal delay between two laser pulses.

The velocities (v) were calculated from the temporal delay (t) between the UV pulse and the fluorescence excitation pulse since the ejected metal atom was sampled at a known distance above the surface of the wafer.

$$v = l/t.$$

Figure 4 shows the translational energy distribution $P(E_T)$ of Si, which was obtained by the following equations for E_T and the Jacobian factor for conversion from time (t) to energy.

$$\begin{aligned} E_T &= mv^2/2, \\ J &= t^4/m^2 \end{aligned} \quad (1)$$

$P(E_T)$ thus obtained peaks at ca. 2.5 kcal/mol as shown in Fig. 4. This value is quite low compared with the results of sputtered metals generated in bombardment with a few keV rare gas ions [6]. The ion bombardment causes collisional cascade in solids to result in ejection of metal atoms from the surface [7,8]. Photo-ablation occurs without external momentum transfer. Lin and his coworkers [9] have developed a theoretical model for this non-cascade ablation using the transition state theory. The translational energy of the activated complex along the reaction coordinate becomes a part of the translational energy of the dissociation products. The excess energy of the activated complex is divided into two parts, vibrational energy E_v and translational energy E_T . The calculation of $P(E_T)$ is essentially the problem of calculating the distribution of vibrational energy among a collection of oscillators. In this case the number of ablated particles at translational energy E_T will be proportional to the following equation.

$$P(E_T) = E_T^{-1/2} \exp(-\beta E_T) \quad (2)$$

where β is a parameter that plays the role of "temperature" for the activated complex. Equation (2) is essentially same as the thermodynamical one given by Namiki et al. [2b].

The energy distribution of the ablated Si atoms was compared with eq. (2), changing the β values as a parameter. The calculated result was not satisfactory, then eq. (2) was modified as follows.

$$P(E_T) = (E_T - E_0)^{-1/2} \exp(-\beta E_T) \quad (3)$$

where E_b is considered as a sort of the surface binding energy which is usually identified with the heat of sublimation in the collision cascade model [7,8]. E_b is likely to be of the order of a few eV for the highly energized particles, but as low as 0.1 eV for the slowly ejected molecules, for example, in the ion-assisted etching of silicon by SF_6 [10].

Changing both β and E_b as parameters, the set of experimental data were simulated until a good fit was obtained. The result is shown in Fig. 3 for $\beta = 0.22$ (kcal/mol) $^{-1}$ and $E_b = 0.3 \sim 0.5$ kcal/mol. The best-fit values of β and E_b ranges in $0.20 \sim 0.25$ (kcal/mol) $^{-1}$ for β in $0.3 \sim 0.5$ kcal/mol for E_b . These β values correspond to the temperature of 2000 \sim 2600 K. Pospieszczyk et al. [1] have reported that Si (110) surface is molten by irradiation of a 20 ns ruby laser beam that evaporates Si atoms and that the temperature is estimated to be substantially above 1200 K. If the molten surface and the ejected atoms are in thermal equilibrium, the translational temperature is considered to be same as the surface temperature. Our experimental results of 2000 \sim 2600 K is reasonable as the translational temperature. Concerning the very low value for E_b , however, E_b now can no longer be interpreted as a surface binding energy or the heat of evaporation even though eq. (3) is considered as a weak interaction potential like van der Waals potential between Si atoms ejected and the molten Si surface.

In summary, UV laser photoablation of Si atoms occurs via the mechanism based on the transition state theory described by Lin et al. [9]

References

- 1) A. Pospieszczyk, M.A. Harith, and B. Stritzker, J. Appl. Phys., **54**, 3176(1983).
- 2) a) A. Namiki, H. Fukano, J. Kawai, Y. Yasuda, and T. Nakamura, J. Phys. Soc. Jpn. **54**, (1985) 3162; b) A. Namiki, T. Kawai, and K. Ichige, Surf. Sci., **166**, 129 (1986).
- 3) G.B. Shinn, F. Steigerwald, H. Stiegler, R. Sauerbrey, F.K. Tittel, and W.L. Wilson, Jr., J. Vac. Sci. Technol., **B4**, 1273 (1973).
- 4) P. Ho and W.G. Breiland, Appl. Phys. Lett., **44**, 51 (1984).
- 5) K. Toya, M. Kawasaki and H. Sato, Jpn J. Appl. Phys., **27**, 962 (1988).
- 6) W. Husinsky, G. Betz, and I. Giorgio, Phys. Rev. Lett., **50**, 1689 (1983).
- 7) M.W. Thompson, Phil. Mag., **18**, 377 (1968).
- 8) P. Sigmund, Phys. Rev., **184**, 383 (1969).
- 9) S.H. Lin, I.S.T. Tsong, A.R. Ziv, M. Szymonski, and C.M. Loxton, Phys. Scrip., **T6**, 106 (1983).
- 10) D. J. Oostra, A. Haring, A.E. de Vries, F.H.M. Sanders, and K. Miyake, Appl. Phys. Lett., **46**, 1166 (1985).

ABLATION OF UV-TRANSPARENT MATERIALS WITH FEMTOSECOND UV EXCIMER LASER PULSES

S. Küper, M. Stuke

Max-Planck-Institut f. biophys. Chemie

Dept. Laserphysik, P.O. 2841, D-3400 Göttingen, F.R. Germany

Abstract: Experiments on the ablation of undoped polytetrafluoroethylene (teflon), monocrystalline sodium chloride (NaCl) and polymethyl-methacrylate (PMMA) with 300 fs uv excimer laser pulses at 248 nm are reported. In contrast to standard 16 ns excimer laser pulses, these ultrashort pulses ablate essentially uv-transparent materials, heretofore not accessible to clean ablation, with good edge quality and no signs of thermal damage, with removal rates are on the order of one micrometer per pulse.

Introduction:

Surfaces can be structured by exposure to intense uv laser light [1],[2]. A wide variety of materials with different penetration depths for uv laser light and different chemical constitution show for certain fluence ranges high removal rates of material on the order of micrometers per pulse, along with little or no thermal damage to the edges. Thus the surfaces of many solids can be patterned with a resolution down to less than one micrometer [3].

Essentially uv-transparent materials, such as undoped polytetrafluoroethylene (teflon) or sodium chloride however, are not accessible to clean ablation with standard excimer laser pulses at 308, 248 or 193 nm. Under these conditions teflon is photochemically and thermally degraded [4] and, if at all, rather disrupted than etched by ablation, while sodium chloride shows an undefined etch crater with cracks reaching deep into the surrounding material. Recently, it has been shown that ultrashort excimer laser pulses [5], [6] offer advantages for the structuring of surfaces, and are a valuable tool for mechanistic studies of the ablation process [7],[8]. Furthermore, new materials have become accessible for ablation with 248 nm excimer laser pulses. In the following, we shall describe ablation experiments with PMMA, teflon and sodium chloride at 248 nm for excimer laser pulse durations of 16 ns and 300 fs.

Experimental:

Materials: 4 mm thick commercial sheets of teflon ($\alpha_{248} = 158 \text{ cm}^{-1}$ [10], density = 2.15 g/cm^3) and PMMA (extra purity kind, Röhm GS 214, $\alpha_{248} = 102 \text{ cm}^{-1}$ [7], density = 1.18 g/cm^3) and 5 mm thick commercial sodium chloride infrared windows were used for the determinations of etch depth as a function of fluence. Before irradiation, the surface of the samples was cleaned with methanol.

Procedure: The light sources and the experimental set-up have been described in detail before [7]. The repetition rate of the laser pulses was kept at 1 Hz in order to exclude effects arising from heating of the sample. The laser beam was defined by a metal mask, focussed by a spherical quartz lens ($f = 200 \text{ mm}$) and directed at the sample. Etch depths were measured with a Dektak II A stylus profilometer. In the case of PMMA and teflon, for each given fluence several exposures at varying numbers of pulses were made, and the etch rates were obtained by linear regression from the slope of a plot of the etch depth versus the number of pulses (compare Fig. 3 of [7]). For sodium chloride the etch rate was calculated from the etch depth and the number of ablation pulses. All irradiations were conducted in air atmosphere.

Results:

Figure 1 shows the scanning electron micrograph (SEM) of a PMMA sample, which had been exposed under a contact mask to 50 pulses of 2 J/cm^2 at 248 nm with a pulse duration of 16 ns FWHM (full width at half maximum). The etch pit is well defined, but the bottom exhibits a considerable roughness, which can be seen in a tenfold enlarged detail (see frame in Fig. 1) in Figure 2a. Figure 2b shows the surface of a PMMA sample, ablated under the same conditions, except for the pulse duration, which was 300 fs in this case. The surface is much smoother after fs-ablation and the roughness is reduced by a factor of 10. The etch rates of PMMA for ns- and fs-ablation are shown in Figure 5, and have been described in detail in [7].

Figure 3a shows the scanning electron micrograph of a teflon sample after irradiation with 50 pulses of 2 J/cm^2 at 248 nm with a pulse duration of 16 ns. It is obvious that the observed result cannot be termed ablation, as well as exact etch rates cannot be obtained due to the surface morphology, which prevails the same, also for higher fluences at the same pulse duration. In contrast, 300 fs pulses of the same wavelength smoothly ablate teflon at fluences down to 0.5 J/cm^2 . Figure 3b shows a typical sample which had been subject to 240 pulses of 1 J/cm^2 at 248 nm with a pulse duration of 300 fs. The etch pit is sharply defined. The unevenness of the

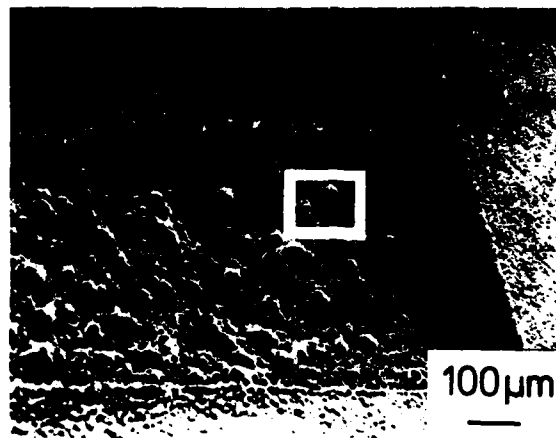


Figure 1: Scanning electron micrograph of a PMMA sample, which was ablated under a contact mask by 40 standard excimer laser pulses of 2 J/cm^2 and 248 nm. The etch pit is well defined, but the surface of the ablated spot is rough.

bottom of the etch hole is due to diffraction at the aperture and inhomogeneities in the beam profile. The ablated surface exhibits a roughness on the order of $1 \mu\text{m}$ and there is practically no solid debris at the edges of the hole. Figure 5 shows the etch rate of teflon for pulses of 300 fs duration at 248 nm plotted versus the fluence. Below 300 mJ/cm^2 virtually no ablation takes place. For higher fluences, a typical etch curve is observed, which levels off into a saturation plateau for fluences above 1 J/cm^2 . A careful measurement of the etch depth versus the number of incident pulses shows a linear rise from the first pulse on. This means, that in the covered fluence range, and for 248 nm, teflon does, in contrast to other materials, not show incubation behaviour [7], [9].

Figure 4a shows the scanning electron micrograph of a typical monocrystalline sodium chloride sample, which had been subject to 15 pulses of 4.2 J/cm^2 at 248 nm with a pulse duration of 16 ns. We observe an undefined etch crater with cracks reaching deep into the surrounding material. For the whole fluence range of ns laser irradiation that induces material removal from sodium chloride, this surface morphology prevails the same. Clearly, this result cannot be termed ablation, and exact etch rates cannot be measured. In contrast, excimer laser pulses of 300 fs duration at 248 nm smoothly etch sodium chloride in a fluence range from 0.3 to 2 J/cm^2 (Figure 4b). Below the threshold fluence of 300 mJ/cm^2 no ablation occurs, while above 2 J/cm^2 cracking also becomes a problem. For sodium chloride we also

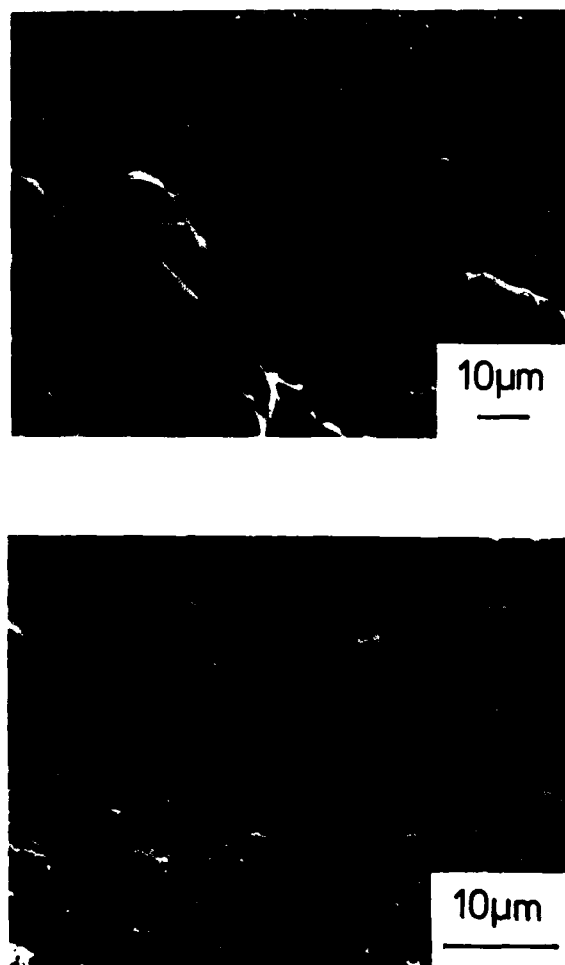


Figure 2: a) Enlarged detail of Figure 1 (see frame). The surface roughness of the etched spot is on the order of 30 micrometers.
b) Detailed view of a PMMA sample ablated under the same conditions, except for the pulse duration, which was 300 fs in this case. Compared to ns-ablation the surface roughness is reduced by one order of magnitude (note the different scales of Fig. 2a and Fig. 2b).

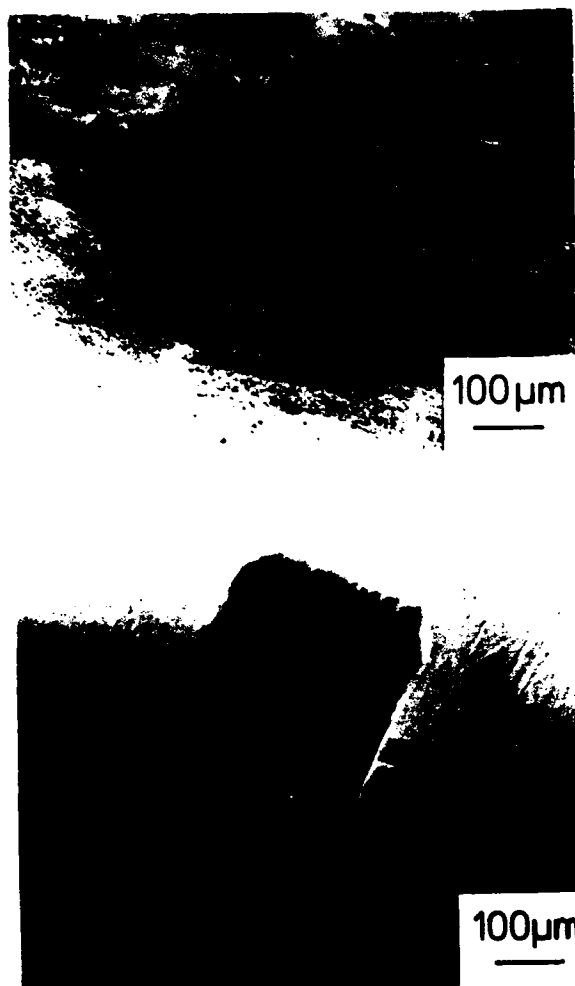


Figure 3: a) Enlarged view of a teflon surface exposed to 50 pulses of 2 J/cm^2 and 16 ns FWHM at 248 nm. The material is severely degraded (see reference 4) and rather disrupted than etched by ablation.

b) SEM photograph of teflon surface subject to 240 pulses of 1 J/cm^2 and 300 fs pulse duration at 248 nm. The material is smoothly ablated with no thermal damage to the edges.

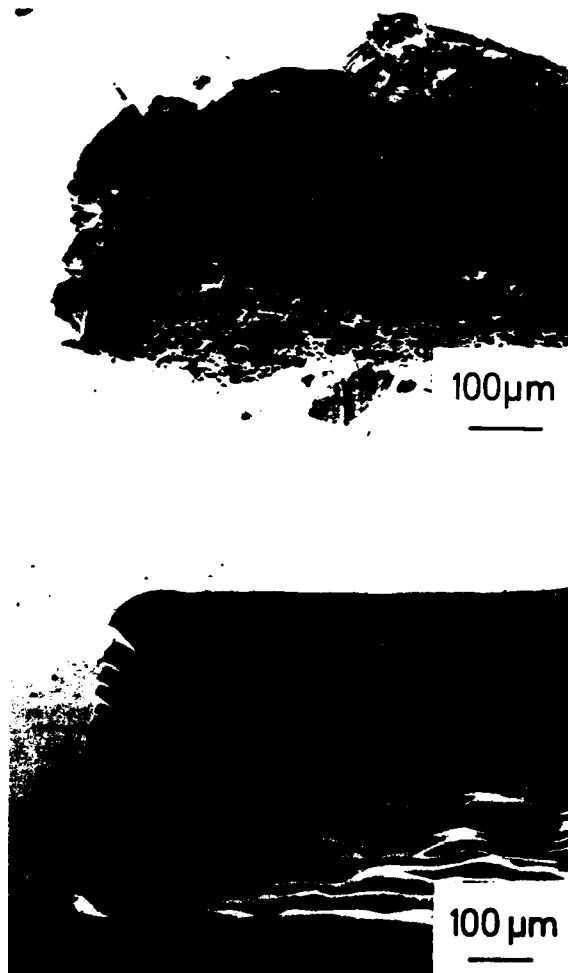


Figure 4: a) Scanning electron micrograph of sodium chloride sample subject to 15 standard excimer laser pulses at 248 nm and a fluence of 4.2 J/cm^2 . An undefined etch crater is observed with cracks reaching deep into the surrounding material. b) Enlarged view of an NaCl sample etched with 500 pulses of 500 mJ/cm^2 at 248 nm with a pulse duration of 300 fs. The material is smoothly etched with good surface quality and no cracks into the surrounding material.

observe a typical etch curve (Fig.5), which levels off into a saturation etch rate on the order of $1 \mu\text{m}$ per pulse for high fluences. In the covered fluence range, sodium chloride, like teflon, starts fs-ablation with the first laser pulse, showing that NaCl does not exhibit incubation behaviour at 248 nm.

Discussion:

In order to ablate a material, it is necessary to absorb a sufficient amount of energy per volume and unit time in the sample. Strong uv-absorbers like polyimide or polystyrene can therefore be readily ablated with standard excimer laser pulses of most laser lines in the ultraviolet range.

Materials, absorbing only weakly in the ultra violet, like teflon or sodium chloride however, are not accessible to clean ablation but show thermal degradation and charring or cracking and, if material is removed at all, a rough surface of the ablated spot.

PMMA, also a weak uv-absorber, can be readily ablated with standard excimer laser pulses only at 193 nm. At 248 nm, in a wide fluence range, PMMA starts ablation only after the material has been sensitized by several incubation pulses [7], [9], and at 308 nm it remains unaffected up to high fluences. During the incubation pulses PMMA is damaged in its chemical structure and exhibits a rapidly growing uv absorption due to the formation of unsaturated species [10]. Both effects finally lead to the start of ablation. Upon ablation with ultrashort, meaning ultra high intensity, excimer laser pulses, two-photon absorption becomes important and limits the penetration depth of the laser light into the material. As a consequence, the observed threshold fluence for the ablation of PMMA at 248 nm is reduced by a factor of five, and the etch rates at higher fluences are limited, compared to ns-ablation [7]. The layers closest to the surface absorb a much higher photon dose than necessary for ablation and, at the same time shield the material deeper in the sample. Thus a sharp border between material that reaches the ablation threshold and material that does not, is produced in the sample. This results in a surface roughness of the etch pit, which is reduced by a factor of 10, compared to standard excimer laser ablation (compare Figures 2a and 2b).

With an absorption coefficient of 158 cm^{-1} [10] teflon is an equally weak absorber at 248 nm as PMMA with 102 cm^{-1} [7]. In the case of teflon however, there is no evidence in the uv- and infrared spectra for a growing uv absorption or formation of unsaturated species [10]. In addition, teflon has no favored sites for bond scission (weak bonds), but a bond energy of at least 406 kJ/mole [11] has to be overcome, whereas in PMMA chain scission is facilitated by a dissociation energy of only

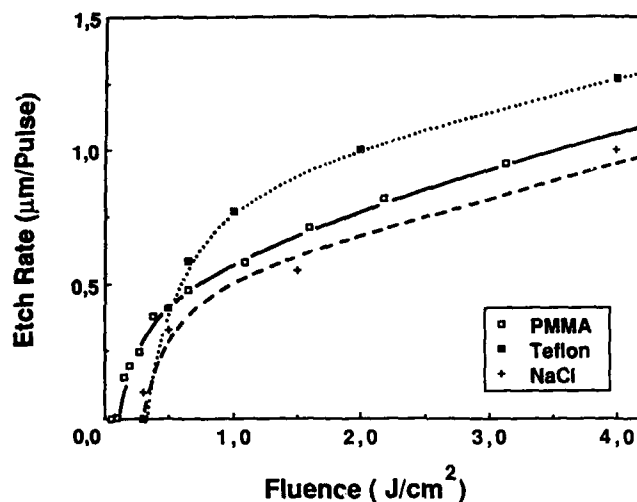


Figure 5: Etch rates of PMMA, teflon and sodium chloride as a function of fluence. All materials show a typical etch curve with a threshold and remarkably similar etch rates for the high fluence range. The lines are drawn to guide the eye.

259 kJ/mole [11] for the weakest bond. Considering energy losses due to various relaxation processes, the probability that sufficient energy for scission is accumulated within one chemical bond, decreases with a rising bond energy and increases with the rate of coupling the energy into the material. The effects of a constant, weak uv absorption along with high bond energies make teflon relatively inert towards intense uv radiation. Their different absorption coefficients and densities taken into account, the photon load per monomer unit and unit time under ns excimer laser irradiation for teflon and PMMA is about the same. However, more than 30,000 pulses of 16 ns duration and 120 mJ/cm² do not induce any observable change in the infrared- and uv-spectra of a 12.5 µm thin teflon film [10], while under the same conditions PMMA undergoes severe photochemical degradation. This shows that teflon requires a higher photon load before suffering damage to its chemical structure. With extremely high light intensities, ultrashort excimer laser pulses induce nonlinear absorption [7], [12] and therefore achieve a high rate of coupling energy into materials, absorbing weakly under low intensity conditions. Thus, the various relaxation processes can be overcome in favor of bond scission, and ablation becomes possible (Fig. 3b). In the case of fs-ablation, the observed threshold fluence for teflon is three times higher than for PMMA under equal conditions, a fact, which is in agreement with its constant, weak absorption and higher bond energies, compared to PMMA.

The most striking example for two-photon ablation however, is sodium chloride, which has a negligible absorption at 248 nm under low intensity conditions. As a result, the ablation of this friable material with ns excimer laser pulses of 248 nm wavelength is not possible (Fig. 4a). High fluences are required before the surface is affected, and induce a breakdown [13] which, due to the long penetration depth, reaches several micrometers into the sample. Again, ultrashort excimer laser pulses induce two-photon absorption [12], reduce the penetration depth of uv light into NaCl, and achieve sufficient energy absorption per unit volume and unit time to ablate the material. The upper layers again receive more energy than necessary for ablation, and shield the material deeper in the sample. Due to the multiphoton absorption most of the pulse energy is absorbed in the first micrometer of material, which will finally be ablated. As a result again, a sharp border between material that will be ablated and material unaffected by the laser pulses forms, and cracking of the sample due to thermal strain can be avoided (Fig. 4b). To our best knowledge, this is the first report of controlled laser material processing of an alkali halide crystal.

In conclusion, we have shown that weak uv absorbers with highly stable molecular structure, such as teflon or sodium chloride, which were heretofore not accessible for ablation, can be cleanly etched with ultrashort excimer laser pulses at 248 nm. For the etching of PMMA, the surface roughness of the ablated spot is reduced by one order of magnitude. Taking advantage of multiphoton absorption, fs excimer laser pulses can create their own absorption, even in materials which are virtually uv transparent under low intensity conditions. The reduced penetration depth of the laser light limits the etch rate at high fluences, but makes new materials accessible to clean ablation.

Acknowledgements:

We would like to thank S. Szatmári and F.P. Schäfer for giving us the opportunity to use their source of 300 fs excimer laser radiation at 248 nm. Technical assistance by K. Müller and W. Sauermann and financial support by Sonderforschungsbereich 93 ("Photochemie mit Lasern", Teilprojekt C2, C15) and Bundesministerium für Forschung und Technologie (Nr. 13N5398/7) are gratefully acknowledged.

References:

- [1] Y. Kawamura, K. Toyoda, S. Namba: Appl. Phys. Lett. 49, 374 (1982); J. Appl. Phys. 53, 6489 (1982)
- [2] R. Srinivasan, V. Mayne-Banton: Appl. Phys. Lett. 41, 576 (1982)

- [3] M. Rothschild, D. J. Ehrlich: *J. Vac. Sci. Technol. B* **5**, 389 (1987)
- [4] M. Stuke, Y. Zhang, in *Proceedings of the Symposium on Laser Processes for Microelectronic Applications*, ed. by J. J. Ritsko, D. J. Ehrlich, M. Kashiwagi, (The Electrochemical Society, Pennington, NJ, 1988), p. 70
- [5] S. Szatmári, F.P. Schäfer, E. Müller-Horsche, W. Mückenheim: *Opt. Comm.* **63**, 305 (1987)
- [6] J. Glowina, J. Misewich, P.P. Sorokin, *J. Opt. Soc. B* **4**, 1061 (1987)
- [7] S. Küper, M. Stuke: *Appl. Phys. B* **44**, 199 (1987)
- [8] R. Srinivasan, E. Sutcliffe, B. Braren: *Appl. Phys. Lett.* **51**, 1285 (1987)
- [9] E. Sutcliffe, R. Srinivasan: *J. Appl. Phys.* **60**, 3315 (1986)
- [10] S. Küper, M. Stuke: Unpublished results
- [11] I. Mita in: *Aspects of Degradation and Stabilization of Polymers*, ed. by H.H.G. Jellinek, (Elsevier, Amsterdam, Oxford, New York 1978) p. 254
- [12] A. J. Taylor, R. B. Gibson, J. P. Roberts, in *Technical Digest, Conference on Lasers and Electro-Optics* (Optical Society of America, Washington, DC, 1988), paper WD 1; and A. J. Taylor, R. B. Gibson, J. P. Roberts: *Opt. Lett.* (1988), submitted
- [13] J. F. Ready in: *Effects of High-Power Laser Radiation*, (Academic Press, New York, London, 1971), p. 277

EXCIMER LASER ABLATION OF SODIUM TRISILICATE GLASS

P. A. ESCHBACH,* J. T. DICKINSON,* AND L. R. PEDERSON**

*Department of Physics, Washington State University, Pullman, WA 99164

**Battelle Pacific Northwest Laboratories, Richland, WA 99352

ABSTRACT

We examine effects resulting from the irradiation of glassy sodium trisilicate ($\text{Na}_2\text{O} \cdot 3\text{SiO}_2$) with 248 nm excimer laser light at fluences from 1-5 J/cm². We observe a threshold for the onset of etching of the surface at 3 J/cm². We present SEM images of the resulting surface topography under etching conditions as well as recent measurements of the particle emission and photon emission from atoms leaving the surface region. A clear correlation is observed between this etching threshold and a) onset of emission of fast excited neutrals, as well as b) the appearance of atomic Na D resonance radiation emitted from particles up to several cm from the surface. We also present identification of the emitted positive ions.

INTRODUCTION

The laser ablation of materials is of considerable importance in microelectronic and micromechanical machining processes.¹⁻³ The ablation mechanisms are complex, often involving both thermal and photochemical processes.²⁻⁸ There is considerable need for intense study of these mechanisms to eventually provide a scientific foundation for future applications, eventually with predictive capability for a wide range of materials.

In this paper, we present measurements of the surface morphology and the emission of particles resulting from exposure of sodium trisilicate glass to intense pulses of 248 nm UV light from an excimer laser. Our results⁹ suggest that significant laser/plume interactions in the near surface region occur, influencing the kinetic energies observed for a number of particle species.

EXPERIMENT

Sodium trisilicate glass was prepared by melting stoichiometric quantities of Na_2CO_3 and SiO_2 powders.¹⁰ The resulting material was transparent and bubble-free. Samples were cut with a diamond saw, mechanically polished, and washed in ethanol. The samples were mounted on a translatable stage in a vacuum chamber maintained at a pressure of 10^{-4} Pa or less. The laser beam was directed through a quartz window at an angle of about 20° to the sample surface normal.

The radiation source was a Lambda Physik Model EMG-203 excimer laser, which produced 20-ns pulses of 248 nm wavelength radiation (KrF). The laser power was measured with a Gentec ED-500 joulemeter. The laser beam was focused by a 1 m focal length lens to produce a 0.2 x 1 mm² rectangular beam with a maximum fluence of 5 J/cm² at the sample. Neutral density filters were used to reduce the fluence by calibrated amounts. The beam profile was examined by burning patterns into unexposed, developed Polaroid film. The beam was generally uniform in the central portion, but showed some irregularities on the edges due to slight misalignment of optical components.

Ions and excited neutral particles were detected with a Channeltron electron multiplier (CEM), Galileo Electro-Optics Model 4039. The CEM front cone was masked so that only a small portion was in line-of-sight with the sample. This was necessary to prevent detector saturation. Various grid and time-of-flight (TOF) arrangements were used to determine charge state, velocity distributions, and (where possible) mass. A quadrupole mass spectrometer

(QMS) was used for mass determinations, although mass resolution was limited. This appeared to be due to high concentrations of electrons entering the mass filter with the ions which modified the electric fields. With the ionizer off and quadrupole rods grounded, excited neutrals and ions emanating from the surface and near surface region would pass down the mass filter in essentially a field-free region and could be detected as a function of time. (A portion of the detector, a CEM, was in sight of the surface.) Experiments with the ionizer on also allowed the detection of otherwise neutral species ionized by electron bombardment in the ionizer region, predominantly ground state neutrals.

Light intensity measurements were made with a Gencom Thorn EMI Model 9924QB photomultiplier tube positioned at the end of a fiber optic cable mounted on a vacuum system flange. The other end of the fiber optic cable was equipped with a slit aperture and collimating lenses to ensure that only light directed along the axis of the cable (perpendicular to the surface normal) was detected. This allowed the observation of temporal variations in light intensity as light emitting atoms/molecules passed in front of the slit. For spectral analysis of this spatially selected light, the output of the fiber optic cable was attached to a Thermo Jarrell Ash Monospec-18 spectrometer employing a 150 lines/mm grating. An EG&G Model 1421 gated, intensified position sensitive detector responsive to light in the region between 200-830 nm was used with an EG&G Model 1460 optical multichannel analyzer to acquire both time-averaged and time-resolved spectra.

RESULTS

Surface Topography When sodium trisilicate glass is exposed to 248 nm excimer laser light at fluences above 3 J/cm^2 , we observe etching of the glass in the central portion of the laser beam. Outside of this central portion there tends to be a gentle modification or clean-up of the defects (e.g., scratches) on the surface which may be of interest to those involved in surface modification. Fig. 1 is a SEM photo showing the edge and bottom of two etched regions each created by ~400 laser shots at a fluence of $\sim 3.5 \text{ J/cm}^2$. A thin metal mask was used to create the edge near the top of the photo. The bottom of the etched region can be described as "coral like", indicating considerable texturing in addition to melting. The walls beneath the mask showed no undercutting but did have a periodic columnar structure normal to the original surface with a spacing of approximately $4 \mu\text{m}$. We also observe a high number of solidified spheres in the vicinity of the etched region. These spheres range in size from 0.5 to $3 \mu\text{m}$ in diameter. Rottenberg and Koren⁶ point out that insulators such as Al_2O_3 are expected to reach higher temperatures than metals such as Al due to the higher heat conductivity of the metals. Thus, it appears that elevated temperatures are reached at these fluences in this particular glass. The coarse features in the etched region observed in this work on sodium trisilicate are quite similar to those seen by Braren and Srinivasan in borosilicate glasses.¹

Even at higher fluences, we found that on polished surfaces there was a necessary "pre-exposure" of several laser pulses before etching was observed. If the surface was highly damaged (e.g., cut with diamond saw), no pre-exposure was required to induce etching. The surface morphology is a strong function of the number of laser shots. For example at a fluence of 3.6 J/cm^2 , up to 20 pulses, we see substantial fracture of the surface in the region and along the edge of highest laser intensity, the latter being where thermal gradients would be high. A small amount of highly localized etching (pitting) can be seen at an exposure of 10 pulses, with a higher concentration occurring at 20 pulses. The fine coral structures continue to grow in between and on top of the fracture areas, eventually smoothing the fractured areas to a great extent. This fine coral structure converged to average spacings of approximately $1 \mu\text{m}$ with melt-like protuberances (Fig. 1).

Particle Emission Emission of negative charge is observed, including a prompt burst of electrons accompanying each laser pulse due to photoemission, probably from defect centers. At higher fluences, there is a significant burst of negative charge moving at velocities greater than 10^4 m/s which we attribute to electrons traveling with the plume.

When particle detectors were positioned at various angles relative to the surface normal we were able to detect additional emission products leaving the exposed region of the sample. As we will explain, the finite pulse width of the laser resulted in considerable interaction of the laser light with the original emission products coming from the surface and near surface region of the sample. Because of the relatively rapid emission process, the detected species were highly correlated in time with the laser pulse. Using the QMS as a TOF analyzer (with rods grounded the drift space is at $V=0$) we can compare the detected particles with ionizer on and off. Fig. 2a shows the dominant TOF signal with the ionizer turned on. The front cone of the CEM in the rear of the drift space was biased at -2700 V to favor detection of positive ions and reject negative particles.

With the quadrupole mass filter activated, we found that only gross mass selection of the peaks created by the ionizer could be achieved due to field distortion from the plasma in the plume. Nevertheless we are able to make the following mass assignments for the neutral peaks labeled 4a, 4b, and 5 as follows: masses 23 (Na), 28 (Si), and 60 (SiO_2). The kinetic energies of these neutral species are on the order of 0.1 eV, which would correspond to an equilibrium temperature of 1100 K. Peaks 1 and 2 were strongly affected by electric fields and were shown to correspond to positive ions. Peak 3 is a robust peak which was frequently limited in peak height due to detector saturation. The peak position was not significantly affected by strong electric fields; it is an excited neutral with sufficient internal energy to release an electron at the surface of the front cone of the CEM. When the ionizer was turned off (Fig. 2b), the faster components of the detected signal were still observed and the slower, neutral species disappeared.

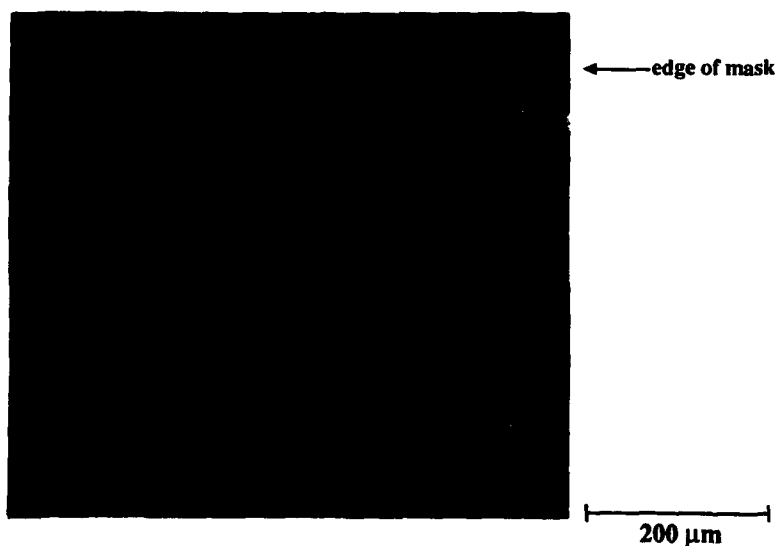


Fig. 1. SEM photograph of two regions etched with 248 nm radiation in $\text{Na}_2\text{O} \cdot 3\text{SiO}_2$ glass.

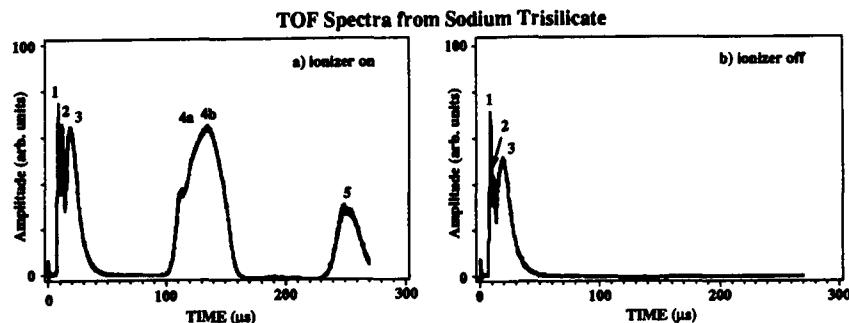


FIG. 2. TOF spectra from $\text{Na}_2\text{O} \cdot 3\text{SiO}_2$ glass taken a) with ionizer on and b) ionizer off.

To confirm that these peaks were not artifacts due to intervening surfaces, a bare CEM was mounted 8.5 cm from the glass surface at an angle of 30° relative to the surface normal (to reduce the particle flux and prevent saturation). Figure 3, curve (i) shows the TOF spectrum for a negatively biased CEM front cone. Again, the initial peak is due to prompt positive ions (unresolved). The broad peak commencing at $6 \mu\text{s}$ is due to the excited neutrals. When the CEM cone is biased positively, the arrival time and general shape of the excited neutral peak is *unchanged*. Because both positive and negative cone voltages can be used to detect this particle, and the TOF is obviously greater than several μs , we suggest that it is a Rydberg species which is being detected by ionization upon collision with the CEM cone. The arrival time of the excited neutral peak decreased with increasing fluence. At fluences below the threshold for the onset of etching, 3 J/cm^2 , the excited neutral peak was not observed. The calculated velocities of this excited species ranged from 10 to 15 km/s.

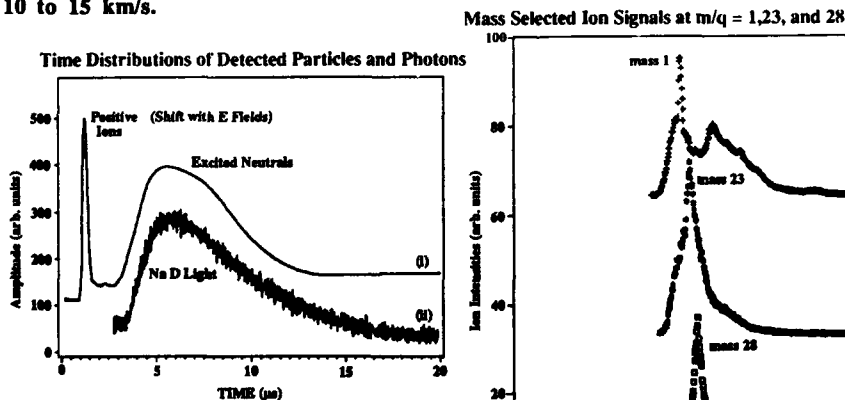


FIG. 3. Time distribution of signals from two different detectors: Curve (i) represents the output of a CEM positioned 8.5 cm from sample. Curve (ii) is Na D light detected with a PMT + filter viewing a region 8.7 cm from the sample.

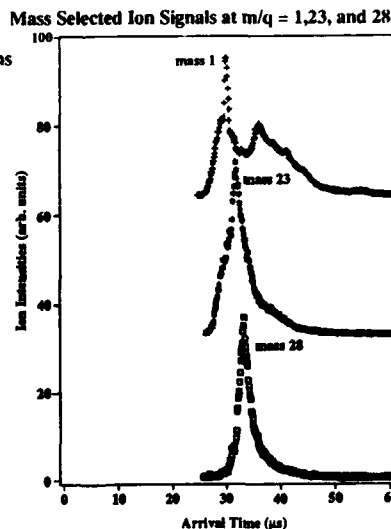


FIG. 4. QMS output with mass filter tuned to $m/q = 1, 23, 28$.

Positive Ion Masses Attempts to mass select the positive ions with the QMS proved unsuccessful due to a broad kinetic energy distribution. By replacing the QMS ionizer with an energy filter (a Bessel Box¹¹) set for ~15 eV positive particles we were able to mass select the ionic species. Probing the mass range from 1-80 amu we found the signals (averaged over 50 shots) when the mass filter was tuned to the masses 1, 23, and 28 as shown in Fig. 4. Na⁺ is by far the major positive ion peak observed, probably due to the low ionization energy of Na. Mass 28, (Si⁺) is readily observed, as is the lowest mass ion, mass 1 (H⁺). We have recently measured the kinetic energies of mass 23 (Na⁺) emission at high fluence⁹. For example, at 3 J/cm² the distribution peaks at 20 eV and extends out to 60 eV. The fluence dependence of the intensities and the kinetic energy distributions of these ions have not yet been determined, but we plan to do so.

Negative Particles Electron emission can also be observed using a bare CEM biased for detection of negative particles. As expected, the TOF of the electrons is considerably shorter than for the massive positive ions and neutrals and the signal is very intense. As we shall explain below, the presence of high densities of photoelectrons in the interaction region will strongly influence the resulting products and their energies. Surprisingly, no negative ion emission was observed.

Photon Emission At fluences sufficient to yield etching, one could easily observe with the naked eye yellow light in the form of a bright sphere near the surface surrounded by a less bright cloud of yellow light which decayed with distance from the surface. A time exposure of this visible light shown in Fig. 5a (insert) indicates a transition in intensity at a radius of ~1 cm from the glass surface. A second, less intense cloud is also spherical and nearly tangent to the surface at the irradiated position with a much larger radius. Time and spatially resolved measurements discussed below show that these patterns are consistent with an expanding plume with a center of mass velocity equal to the radial expansion velocity of the plume in its center of mass frame of reference.

Figure 5b shows the spectrum of the visible plume. The light was collected from a region about 2 cm from and along the normal to the glass surface. The spectrum is dominated by the atomic Na D resonance line. Five other known Na lines are also resolved and identified in Fig. 5b. These lines reveal the presence of highly excited neutral Na atoms in the plume. The lifetime of the 3P_{1/2,3/2} states is only about 15 ns, so that this radiation cannot be due to excitations directly into the 3P state at the surface. The 3P_{1/2,3/2} states appear to be fed by higher lying excited states, suggesting that these atomic spectral lines are due to the decay of long lived, highly excited atomic Na Rydberg states.

Using a PMT with a Na D interference filter and a lens/aperture arrangement to provide wavelength and spatial discrimination, the intensity of the Na D radiation emanating from a narrow cone 8.7 cm from the glass surface was monitored. The Na light appears only at laser fluences above 3 J/cm², in close coincidence with the appearance of the excited neutral peak and the onset of etching. We can examine the velocity of the Na atoms that participate in this emission process by measuring the time distribution of the emitted light. The resulting intensity vs time distribution for a laser fluence of 3 J/cm² is shown in Fig. 3, curve (ii). The temporal variation in photon intensity is nearly identical with that of the excited neutral peak in Fig. 3, curve (i). This is consistent with: (a) the excited neutrals being Na atoms in high lying Rydberg states, and (b) the Na emission [Fig. 3, curve (ii) and Fig. 4] being due to the decay of these long lived Rydberg states to form short lived excited states decaying radiatively by fast, dipole allowed transitions. The TOF spectrum of curve (ii), Fig. 3, therefore reflects variations in the density of Rydbergs in the region viewed by the PMT.

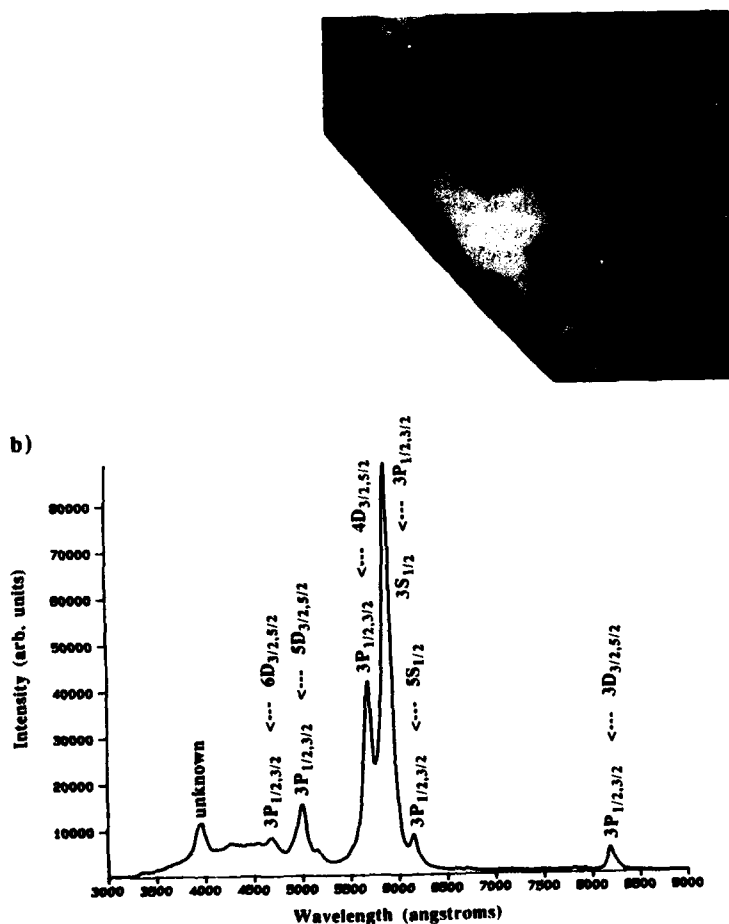


FIG. 5. a) Time exposure on 35 mm black and white film of ablation plume taken over several laser pulses. Note the near-spherical symmetry. b) Visible spectrum of the light emanating from the plume at a distance of 2 cm from the surface.

From the photon TOF peak positions and the known mass (23 amu) we can infer a most probable kinetic energy. This peak translational energy increases with laser fluence from approximately 15 eV at the 3 J/cm² etching threshold to 28 eV at 5 J/cm². Note that these kinetic energies are well in excess of the single photon energy of the laser (5 eV) implying that single photon electronic excitations cannot explain these high energies. It should also be noted that these kinetic energies correspond to unrealistic surface temperatures (e.g., 28 eV ~ 300,000 K). Furthermore, the velocity distributions inferred from the TOF data of Fig. 3 are too narrow for Maxwellian distributions. These high energies cannot be explained by simple thermal mechanisms as well.

DISCUSSION AND CONCLUSION

In the early stages of irradiation, flaws near the surface can lead to localized fracture due to stress induced by differential heating. This is the source of the fracture cones observed early in the irradiation, starting with the first few laser pulses. The gradual onset of etching which we observed here in $\text{Na}_2\text{O}\cdot 3\text{SiO}_2$ was not observed in borosilicate glasses,¹ which are strong UV absorbers at 248 nm. In contrast, the absorption edge of pure sodium trisilicate is well below 240 nm.¹² Devine et. al.¹³ have shown that excimer laser bombardment of amorphous silica at 248 nm can produce E'_1 centers and a non-bridging oxygen defect, both capable of absorbing 248 nm radiation. Tomozawa has observed such defects in crushed fused silica using ESR techniques.¹⁴ Thus, thermally induced fracture at early stages of irradiation may play an important role in etching.

The coral like features observed after the onset of ablation are probably associated with hydrodynamic sputtering which has been observed previously in excimer ablation of several metals.⁴ Once sufficient absorption at 248 nm is attained, etching commences and significant particle emission is observed. These emissions include electrons, positive ions, high velocity Na Rydberg atoms, and slower neutral atoms/molecules. The fast, non-Maxwellian velocity distributions observed for the excited Na species *cannot be explained by photothermal or photochemical processes at the surface*. The most probable mechanism for these high velocities involves the interaction of the 20 ns laser pulse with electrons and products of the decomposition created early in the pulse.

The most likely scenario involves the acceleration experienced by electrons in the field of the laser beam by inverse bremsstrahlung.^{15,16} Initial interaction of the laser pulse with the surface produces a cloud of photoelectrons and desorbed or evaporated atoms near the surface. The photoelectrons are probably excited from filled E' states produced and populated during previous pulses. Mackey et al. have studied these states in sodium silicate glasses.¹⁷ They lie within about 1 eV of the Na ion levels which form the conduction band of this material. When populated by the absorption of a 5 eV photon, the absorption of a second photon can yield a photoelectron. The interaction of the laser beam with the resulting cloud of electrons and atoms then forms a plasma as electron impact yields additional ionization. The Rydberg states are either formed by collisions or electron/ion recombination in the denser part of the plume. The interferometer measurements of Walkup et al.¹⁶ indicate the presence of high electron densities ($> 10^{16}$ electrons/cm³) in plasmas formed by excimer ablation of Al_2O_3 . At these densities, Debye screening maintains local charge neutrality over very small distance scales (~ 20 nm). Thus as electrons are accelerated by inverse bremsstrahlung, ions are accelerated with them by virtue of electrostatic attraction. After the laser pulse decays away, the plume continues to expand and moves away from the surface, carrying with it electrons, positive ions, and Na Rydberg atoms which eventually decay into lower lying states and yield the visible radiation observed. The fast ions that we observe (5-60 eV) strongly support this mechanism. In addition, ion beam deflection experiments performed in the plume from carbon targets also support this charge separation model.¹⁸

Utterback and coworkers¹⁹ have modeled the atomic flux due to plasma formation in laser ablation. Through momentum transfer with the substrate, the expanding plasma pushes off the surface so that the plasma center of mass travels with a velocity v_{cm} normal to the surface. At some distance from the surface, the plasma density remains high enough to allow the plasma to equilibrate at some temperature T , resulting in a spherically symmetric velocity distribution in the center of mass frame of the plasma. As the plasma expands, its components eventually cease to interact appreciably, so that the velocity distribution characterized by temperature T is 'frozen.' v_{cm} and T are

parameters of the model, chosen to fit the data. The atomic fluxes predicted by this model appear to be consistent with the excited neutral fluxes observed in our work. For instance, the temperatures of the excited neutrals inferred from the model are quite high, on the order of 10^5 K, as compared to ~ 1100 K from the TOF data of Fig. 5(a).

Although additional experiments and modeling needs to be done, this work tends to support the scenario described above where an electrostatic acceleration occurs in the plume. The initial decomposition of the substrate is strongly dependent on absorption centers which are induced by repeated laser pulses. Small surface cracks created early in irradiation may significantly modify the etching threshold. In the near future we hope to have more details on the identities of the emitted particles, their relation to material removal by ablation, and the mechanisms involved in the ablation and emission processes including quantitative connections between properties of the emitted species and the etching process.

ACKNOWLEDGMENTS

This work was supported by the Ceramics and Electronic Materials Division of the National Science Foundation under Grant DMR 8601281, the Office of Naval Research under Contract No. N00014-87-K-0514, and the Washington Technology Center.

References

1. B. Braren and R. Srinivasan, *J. Vac. Sci. Technol. B* **6**, 537 (1988).
2. G. B. Shinn, F. Steigerwald, H. Stiegler, R. Sauerbrey, F. K. Tittel, and W. L. Wilson, Jr., *J. Vac. Sci. Technol. B* **4**, 1273 (1986).
3. M. Hanabusa, M. Suzuki, and S. Nishigaki, *Appl. Phys. Lett.* **38**, 385 (1981).
4. R. Kelly and J. E. Rothenberg, *Nucl. Instr. and Meth. in Phys. Res.* **7/8**, 755 (1985).
5. H. Kang and J. L. Beauchamp, *J. Phys. Chem.* **89**, 3364 (1985).
6. J. E. Rothenberg and G. Koren, *Appl. Phys. Lett.* **44**, 664 (1984).
7. J. E. Rothenberg, G. Koren, and J. J. Ritsko, *J. Appl. Phys.* **57**, 5072 (1985).
8. R. W. Dreyfus, R. Kelly, and R. E. Walkup, *Appl. Phys. Lett.* **49**, 1478 (1986).
9. P. A. Eschbach, J. T. Dickinson, S. C. Langford, and L. R. Pederson, *J. Vac. Sci. Technol. A*, in press.
10. D. R. Baer, L. R. Pederson, and G. L. McVay, *J. Vac. Sci. Technol. A* **2**, 738 (1984).
11. J. H. Craig and J. L. Hock, *J. Vac. Sci. Technol.* **17**, 1362 (1980).
12. G. H. Sigel, Jr., *J. Non-Cryst. Solids* **13**, 372 (1973/74).
13. R.A.B. Devine, C. Fiori, and J. Robertson, *MRS Symp. Proc.* **61**, 177 (1986).
14. K. Kokura, M. Tomozawa, and R. K. MacCrone, to appear in *J. Non-Cryst. Solids*.
15. J. M. Green, W. T. Silfvast, and O. R. Wood II, *J. Appl. Phys.* **48**, 2753 (1977).
16. R. E. Walkup, J. M. Jasinski, and R. W. Dreyfus, *Appl. Phys. Lett.* **48**, 1690 (1986).
17. J. H. Mackey, H. L. Smith, and A. Halperin, *J. Phys. Chem. Solids* **27**, 1759 (1966).
18. C. W. Mendel and J. N. Olsen, *Phys. Rev. Lett.* **34**, 859 (1975).
19. N. G. Utterback, S. P. Tang, and J. F. Fritchenicht, *Phys. Fluids* **12**, 900 (1976).

LASER-INDUCED REACTIVE EVAPORATION AND CONDENSATION

GAN-MOOG CHOW and PETER R. STRUTT

Institute of Materials Science, Box U-136, the University of Connecticut, Storrs, CT 06269.

Abstract

A study of laser-induced reactive evaporation-condensation is presented. This considers co-evaporation of metallic, and non-metallic species, by a cw carbon dioxide laser beam, within a reducing environment (98.5% hydrogen, 1.5% methane). A heated W filament placed in proximity of the laser beam-substrate interaction zone produces W for deposition via chemical vapor transport reactions. Composite thin films of a W matrix containing amorphous silica fibers have been deposited on nickel alloy substrates. These films form at rates of about 1 micron/sec, and are found to be adherent to the substrates. The diameter of the fibers is between 25 nm and 120 nm, depending on the interaction time. Various analytical techniques have been employed to characterize as-synthesized layers. Mechanisms of this process are discussed.

Introduction

In the synthesis of materials with desirable phases, microstructures, and morphologies, laser-assisted reactions are frequently employed among many different techniques. Some of the interesting features of the laser reactions include, (i) high intensity irradiation obtainable for rapid heating, (ii) selective laser-beam and material coupling, (iii) small interaction zone resulting in localized reactions, thus acting effectively as cold-wall reactors with minimal contaminations, (iv) high rates of chemical and physical transformations of reactants, (v) generation of metastable phases.

To date, three laser-assisted mechanisms have been employed in surface modification and material synthesis, namely, laser-chemical vapor deposition (LCVD), laser-liquid reaction, and laser-evaporation. Little work has been done by the laser-evaporation technique, thus many potential applications remain [1]. This paper examines the laser-induced coevaporation of a metallic target and a ceramic target, in the presence of a heated tungsten filament, within a reducing environment.

The nature of laser-evaporation depends upon the coupling of the beam with the material to be evaporated. Often a material plume induced by absorption of the beam is observed in evaporation. The plume provides active vapor species that react in a reactive environment and form desirable products. The condensation of the product species, along with the product derived from chemical vapor transport caused by the heated W filament, result in deposited layers on the substrate. This co-employment of laser-evaporation of metallic and ceramic targets and a heated W filament is studied for the first time, and is shown to produce composite layers of silica fibers and a metal matrix. Intriguingly, the diameter of the fibers (25 nm to 120 nm) is considered to be ultrafine. It is well known that fine-diameter fibers are much desirable in fiber reinforcement of composite systems, for their greater enhancement of the ability of the matrix to resist dislocation movement. Therefore, this new approach of synthesizing composite structures provides promising, potential applications.

Experimental

The processing set-up for co-deposition of metal and nanoscale ceramic material is shown schematically in Figure 1. In this arrangement, a nickel alloy disc of composition (wt. %) 58% Ni, 4% Al, 9% Cr, balance of V, Ti, Mn, Co, C is mounted above a ceramic target. The composition of the latter (wt. %) is 55% SiO₂, 42% Al₂O₃, balance TiO₂, MgO, CaO.

Prior to laser-processing, the chamber is evacuated and flushed with nitrogen. Following this, and during laser irradiation, a continuous flow of 98.5% hydrogen / 1.5% methane is maintained at a flow rate of 150 sccm. The 99.9% purity tungsten filament, in proximity to the laser beam-material interaction zone, is switched on 15 minutes before each experiment, and is maintained at 1700°C. It remains on during actual laser irradiation.

The processing procedure involves irradiating the nickel-alloy disc with a cw carbon dioxide laser, using a power density of 2×10^4 W/cm². This intensity is not only sufficient for rapid evaporation, but for complete beam penetration through the disc at the focal spot. This immediately results in interaction with the underlying ceramic target to produce a plume, containing predominantly silica species. Subsequent condensation of these species, together with simultaneous:

- (i) condensation of aluminum, from the aluminum containing nickel-alloy disc, and
- (ii) deposition of tungsten, via chemical transport reactions from the heated filament,

results in deposition of a composite layer, on cooler regions of the nickel-alloy disc. Characterization of the deposits involved X-ray diffraction, electron microprobe analysis, Auger spectroscopy, fourier-transform-infrared spectroscopy, and high resolution transmission electron microscopy.

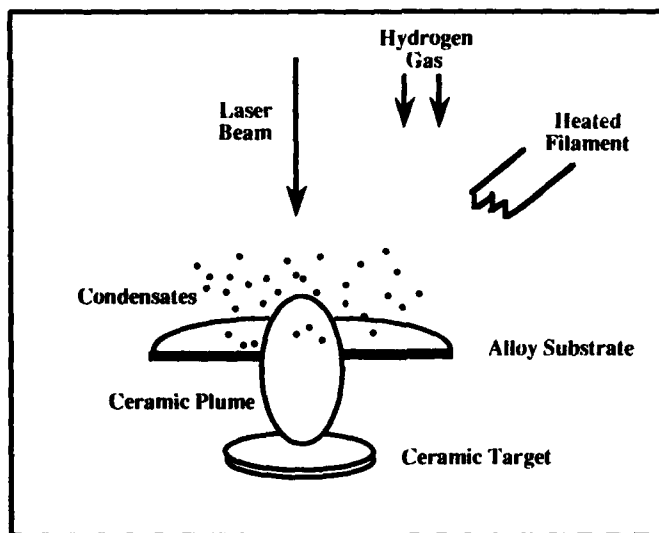


Figure 1. A schematic of processing set-up

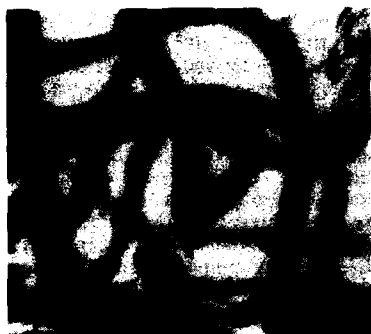


Fig. 2
100 nm



Fig. 3
50 nm

TEM extraction replica micrograph of silica fibers



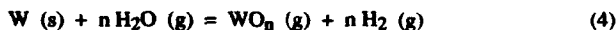
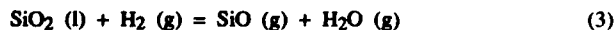
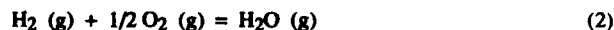
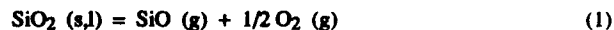
100 nm

Fig. 4 TEM extraction replica micrograph of silica linear aggregates

Results and Discussions

X-ray diffraction data indicated that the as-deposited films contained either W or Al. Al was deposited from evaporation of Ni alloy when short laser-beam / ceramic-target interaction times were used, for instance, 1 sec. At the melting point of Ni alloy (about 1400°C), the vapor pressures for Al, Cr, and Ni are approximately 10^{-1} torr, 10^{-2} torr and 10^{-3} torr respectively. The higher vapor pressure of Al in the molten metal allowed Al to escape and condense on the cooler surrounding regions. Absence of noticeable Ni and Cr in the deposits may be explained by their longer time of stay in the molten pool due to their lower vapor pressures at the temperature concerned, thus allowing these species to be superheated. Atoms of these superheated vapors had too much kinetic energy and would not be able to condense on the Ni alloy substrate. W was not deposited for short laser-beam / ceramic-target interaction times. This is because of the insufficient concentration of water vapor available in the interaction zone to facilitate W transport (see following discussions). When longer laser-beam / ceramic-target interaction times were used (about 8-9 seconds), W was deposited as a matrix. In this case, the underlying ceramic plume heated the Ni alloy substrate by blackbody radiation, and the temperature of the alloy was measured to be in the range of 1200 to 1300°C. At this temperature range, the corresponding vapor pressure of Al would be about 10^{-1} torr. Therefore, the substrate was too hot for Al to condense on it. Simultaneous codeposition of a ceramic dispersed phase was observed in both Al and W matrices. This ceramic phase was found to be amorphous silica fibers with diameter in the range of 25 to 120 nm, as revealed by high resolution TEM extraction replica (Figure 2, Figure 3). Compared with a SiO_2 standard, the chemical compositions of these fibers were found to be $\text{SiO}_{1.86}$. The slight discrepancy of Si-O stoichiometric ratio is explained by the reducing and high temperature environment which caused a small O loss from these fibers. Crystalline, linear, chain-shape aggregates rich in Si and O were deposited when WO_n was adsorbed on the aggregates in the course of their condensation (Figure 4). Fibers were not produced in this case. A I_2O_3 was not produced from the evaporation of the ceramic target because of its negligible vapor pressure at the given temperature. The mechanism for fiber growth is addressed in other papers [2,3,4].

The source of W was the heated W filament. Though the filament temperature was well below the temperature range for any significant W evaporation to occur, W was deposited on the Ni alloy substrate via a chemical vapor transport mechanism. It is well known that a substance A (a solid or liquid) reacts with a gas to form exclusive vapor phase reaction products, which, in turn, undergo the reverse reaction at a different place in the system, resulting in the reformation of A [5]. W was reported to be transported in the presence of a temperature gradient and hydrogen containing water vapor [6]. In this process, the thermal evaporation of SiO_2 produced oxygen upon pyrolysis, and the oxygen atoms reacted with hydrogen to form water vapor. The water vapor molecules reacted with the heated W filament to form volatile WO_n species. These species were transported from the hot filament to the Ni alloy substrate and resulted in reformation of W on the substrate surface. Proposed chemical reactions are as follows:



Reaction (1) is pyrolytic and is coupled with reaction (2). Reactions (2) and (4) as well as (3) and (4) are coupled. Also reactions (3) and (4) are the chemical transport processes. With continuous flow of H_2 into the reaction chamber, reactions (2) and (3) will continue to support the W

transport. The rate limiting step of the W transport is therefore the availability of SiO_2 which is the product of evaporation of the ceramic target.

In addition to serving as a W source, the W filament played other roles. It was experimentally observed that the Ni alloy was heated by thermal radiation from the heated filament. Calculations showed that the temperature of the Ni alloy would be at 975°C due to radiative heating of the filament. The measured temperature due to such heating was in the range of 200 to 300°C , indicating that the thermal loss due to hydrogen conduction was significant. The dissociation of molecular hydrogen to form atomic hydrogen at the filament was calculated to be only 0.23% . Therefore, it is clear that significant dissociation of molecular hydrogen would only occur when the high temperature, laser-assisted reactions took place. It was also observed that the melt-through time of the Ni alloy by the laser beam was less than 2 sec, when the heated tungsten filament was used. This melt-through time was three times faster than that obtained when the filament was not used. FTIR data indicated that a thin film of carbon species was deposited by the dissociation of methane at the heated filament. This film possessed an absorption band that matched the wavelength of the laser beam. Since the Ni alloy has no absorption band in the infrared, the predeposition of this IR active film enhanced the beam-metal coupling, resulting in a faster melt-through time. The W filament also had electron emission of 1×10^{-3} amp / cm^2 when heated to 1700°C . Without externally biasing these electrons, they would form a cloud over the filament, and were at thermal equilibrium with it. Although no experimental verification has been obtained, it is conceivable that these electrons would experience thermal diffusion, collisions with gas molecules, and attachment to neutral molecules. These processes led to the possibility that at any given time, free electrons could be found in the laser beam-material interaction zone. It has been shown [7] that a free electron loses only the fraction of $2m_e / M$ of its energy in an elastic impact with a molecule, where m_e is electronic mass and M is molecular mass. If the electron continues to drift, it will accumulate energy until this relatively slow process balances the rate at which it gains energy from the electric field of the laser beam. Therefore, the few additional free electrons in the interaction zone (due to the heated filament) could interact with the laser beam and promote inverse Bremsstrahlung absorption. This would cause an increase in the rate of heating of the material plume and result in a greater degree of ionization. Under certain conditions, this collection of neutral and ionized particles may become a shield to the laser beam, acting as a reflecting body above the substrate surface [8]. Further work such as direct measurement of free electronic density in the interaction zone is clearly needed to verify to what degree these processes occurred.

The absorption of the laser beam by the gas mixture and evaporants in the infrared depends on whether these molecules possess permanent or induced dipole moments and the matching of the vibrational frequencies of the molecular bonds with that of the electromagnetic radiation. H_2 does not possess dipole moment during vibration and the C-H stretch and the C-H bend frequencies of methane do not match that of the laser radiation. As a result, the gas mixture was transparent to the radiation. The Si-O bond couples with the beam and its optical absorption coefficient determines the fraction of the incident laser power that can be absorbed. Also, the laser beam was scattered by the gas molecules. SiO vapor reacted to form SiO_2 and condensed to form droplets above the Ni alloy substrate. These droplets formed an aerodisperse (aerosols) system with the gas mixture. The power density used in these experiments was too low to cause any major change in the optical properties of these aerosols. IR spectra obtained from the SiO_2 deposits indicated that they absorbed the laser irradiation. Therefore, it is reasonable to believe that SiO_2 droplets would absorb the laser energy and vaporize in the optical path, and the beam merely saw a distribution of unstable SiO_2 nuclei shrinking in time due to revaporization. Direct, in-situ verification of this phenomenon was not performed in this work, however, other workers have observed that absorptive nuclei are unable to form in the laser optical path [8]. The formation of stable nuclei that led to the growth of droplets was only possible outside the optical path. Coagulation of these droplets to form metastable linear chain-shape aggregates is discussed in other publications

[2,3,4]. These linear aggregates are proposed to be responsible for the formation and growth of the silica fibers.

In summary, composite layers with nanometer-size microstructures, such as fibers, were obtained by the coemployment of laser evaporation of metallic and ceramic targets, and a heated filament, in a reactive gaseous environment.

Acknowledgements

The authors wish to thank the Office of Naval Research for its support: Contract N00014-78-C-0580. In addition, they wish to thank C. Burila, G. Lang, B. Laube, D. DeLong of United Technologies Research Center for assistance with the microprobe and Auger analysis.

References

1. I. W. Boyd, Laser Processing of Thin Films and Microstructures, (Springer-Verlag Berlin Heidelberg New York, 1987).
2. G. M. Chow, PhD dissertation, the University of Connecticut, Dec. 1988.
3. G. M. Chow, and P. R. Strutt, Symposium Proceedings " Multicomponent Ultrafine Microstructures", Vol. 132, p61, Materials Research Society.
4. G. M. Chow, P. G. Klemens, and P. R. Strutt, to appear in Journal of Applied Physics.
5. H. Schaffer (translated by H. Frankfort), Chemical Transport Reactions, (Academic Press, New York 1964).
6. H. Alterthum, Z. Physik. Chem., 110, 1, 13 (1924).
7. E. H. Kennard, Kinetic Theory of Gases, (McGraw Hill, New York and London, 1938).
8. H. C. Peebles, and R. L. Williamson, Proceedings of International Conference on Laser Materials Processing, (Osaka, Japan, 1987).

EXCIMER LASER THIN METALLIC FILM PATTERNING ON POLYVINYLENE DIFLUORIDE^{a)}

MICHEL GAUTHIER,* RICHARD BOURRET,*
CHENG-KUEI JEN,** AND ERIC L. ADLER***

*Laser Chemistry Group, Division of Chemistry, National Research Council of Canada,
Ottawa, Ontario, Canada, K1A 0R6

**Industrial Materials Research Institute, NRCC, 75 Boul. de Mortagne, Boucherville,
Québec, Canada, J4B 6Y4

***Department of Electrical Engineering, McGill University, 3480 University St., Montréal,
Québec, Canada, H3A 2A7

ABSTRACT

Tactile sensors and ultrasonic transducers based on the piezoelectric properties of polyvinylidene difluoride, PVF₂, usually take the form of thin 10 - 110 μm polymer films coated on one or both sides with a metallic film. Electrode patterns are usually fabricated by photolithography that requires a 90 °C baking process which may harm the piezoelectric properties of the PVF₂ film. We have developed an alternate method, based on direct patterning with a XeCl laser, yielding complex patterns of lines as narrow as 20 μm which are better than those fabricated by photolithography. The metallic film is ablated on both sides of the polymer while maintaining the intrinsic properties of the PVF₂. The ablation mechanism is investigated using transmission optical, scanning electron, and scanning acoustic microscope images. The performance of an ultrasonic transducer fabricated with this technique is described.

INTRODUCTION

Ablation of thin films on polymeric substrates has been studied for various applications.¹ One of these is the fabrication of ultrasonic transducers from polyvinylidene difluoride (PVF₂) polymer films covered with precisely patterned thin film electrodes. Infrared lasers are used in the industry to cut PVF₂ films, which are strong absorbers at these wavelengths. UV lasers should be a better choice for this non-contact electrode patterning since the optical absorption for metals is high at these wavelengths, whereas for PVF₂, the optical transmission is high.

PVF₂ is a semicrystalline polymer which can possess a high dipole moment and exhibit a reasonably high bulk piezoelectric constant. Because of its flexibility and low acoustic impedance, it has been one of the most attractive materials for underwater ultrasonic transducers and transducer arrays.^{2,3} PVF₂ films have been used for planar and focussed bulk acoustic wave transducers,^{2,4} surface acoustic wave (SAW) transducers,⁵ and phased arrays.^{2,3} Since PVF₂ films are mechanically flexible, they can be bonded to a flat or a curved surface. One of the concerns with PVF₂ is the fabrication of complex electrode patterns which govern the ultrasonic transducer characteristics on such thin and flexible films.

The standard technique for array,^{2,3} and SAW⁵ transducers is to make an electrode pattern on a companion material, and then glue the PVF₂ film on it. The PVF₂ film is electroded one side only and the other side contacts the companion material. Electrode

^{a)}Issued as NRCC # 29821.

patterns are generally fabricated through a rather inconvenient and time consuming photolithographic method which requires a clean room facility, the baking of the photoresist, smooth and flat surfaces, etc. These requirements impose certain limitations on the selection of companion materials. One example is that for phased arrays and SAW interdigital transducers (IDT), the surface of the companion material cannot be conductive or curved.

We report here a noncontact laser ablation technique which circumvents the constraints imposed by the conventional photolithographic method. A XeCl laser is used to ablate some patterns on 10 - 110 μm thick PVF₂ films coated on both sides with a Ni/Al or pure Al coating of 0.3 - 0.8 μm thickness. Throughout this paper LA and NL will represent the PVF₂ regions exposed or not exposed to the laser ablating beam, respectively. For most ultrasonic transducer applications employing complex electrode patterns on PVF₂, the requirements are that: (1) there is high linewidth resolution, (2) there is no loss of piezoelectricity for the NL regions adjacent to the LA regions, and (3) the ablation has little effect on the acoustic properties of LA regions. In this paper, the experimental method, the resolution achievable using laser ablation, the ablation mechanism, patterning considerations, and the performance of an ultrasonic transducer made with this laser patterning method are presented.

EXPERIMENTAL SETUP FOR LASER ABLATION

A schematic of the experimental arrangement is shown in Fig. 1. A Lumonics Model 860 XeCl, 308 nm, pulsed excimer laser was used in the unstable resonator configuration. The central uniform portion of the rectangular beam was selected with a circular 2 mm diameter aperture A₁. Beam divergence was reduced to 0.8 mradian with the use of a L₁-A₂-L₂ spatial filter arrangement. Focal lengths were 150 - 200 mm and 200 - 400 mm respectively, for L₁ and L₂. The spatial filter pinhole was 200 μm in diameter. Beam size and intensity at the target were adjusted precisely for proper ablation by a combination of the following methods: adjustment of the displacement between target and focusing lens L₃, of focal length 20 or 40 mm; adjustment of the beam intensity using attenuators AT; adjustment of the laser pulse repetition rate up to 70 Hz; and adjustment of the lateral displacement speed of the target. Aerotech 4" x 4" X-Y microstepping motor driven translating stages were used. The resolution was 2 μm on both X and Y axes. The patterns were programmed into Aerotech's Unidex XI Motion Controller. The electromechanical beam shutter BS was also activated via the controller.

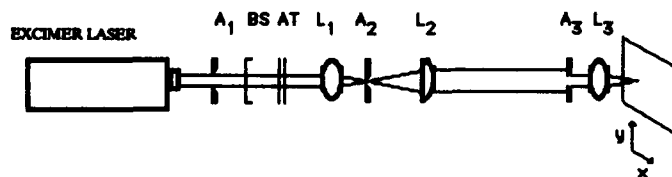


Fig. 1 Schematic of experimental arrangement for laser ablation on PVF₂ films.

ABLATION MECHANISM

PVF₂ films used for the experiment were obtained from Pennwalt (PA) and Kureha Chemical (Japan), and their thicknesses ranged from 10 to 110 μm . We have established that it is possible to draw complex patterns on these thin films very accurately with an excimer laser with little damage to the supporting polymer. To our knowledge, the degree of damage explained below will not compromise the performance of devices employing such films. Looking at the films under an optical microscope, it was quite clear that a certain range of energy densities could ablate the metallic film and leave the underlying polymer as clear and transparent as in unablated uncoated regions. At higher energy densities, the polymer was ablated or burnt, or even ablated right through. At lower energy densities the Al film was only partially ablated.

There is obviously a limit in the acceptable thickness of metallic coating used as conducting electrodes that can be laser-ablated without damaging the PVF₂ film. The standard 0.3 - 0.8 μm metallic coating normally used in commercially available PVF₂ films was fairly easy to handle, but thicker films are much more critical. The optical absorption for the XeCl laser beam (308 nm wavelength) through a 110 μm thick PVF₂ sheet is 50%. With our system the metallic coating on both sides of the film was ablated simultaneously.

Precisely dimensioned circular spots down to 10 μm in diameter were obtainable with a single laser pulse. In principle, line patterns with such resolution should be obtainable. Figure 2 shows an optical transmission image of a line pattern with a period between electrodes (black lines) of 100 μm . With the present setup, the resolution is estimated to be better than 20 μm , and this is mainly limited by the divergence of the excimer beam. This resolution is better than that obtained by photolithographic methods previously reported.^{2,3,5} Expectedly, the energy density available for ablation of the back (bottom) side was reduced by polymer absorption. Figure 3 shows another optical transmission image of only top (left) and bottom (right) electrodes of a line pattern. It can be seen that the electrode width is 10% wider at the bottom surface.

In an attempt to confirm the basic mechanism of this ablation, some patterned films were treated in a weak acid bath to gently etch off the metal coatings in the non-ablated regions, then examined with a scanning electron microscope (SEM), and a 775 MHz

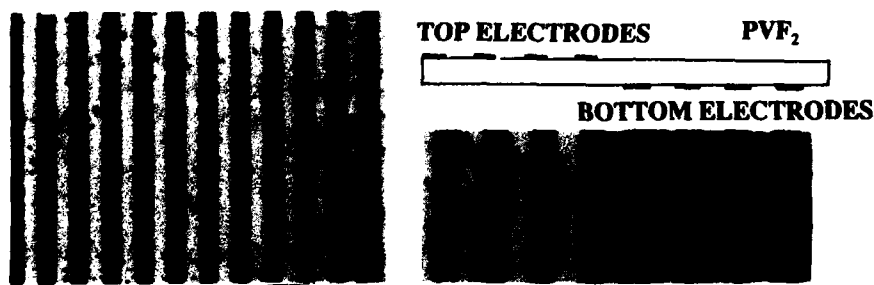


Fig. 2 An optical transmission image of a line pattern. The period between electrodes (black lines) is 100 μm .

Fig. 3 An optical transmission image covering only top (left) and bottom (right) electrodes of a line pattern.

scanning acoustic microscope (SAM). Figure 4a is a SEM picture of a patterned film whose electrodes in NL regions have been removed by chemical etching. The horizontal lines visible in Fig. 4a are scratches normally seen in films obtained from Pennwalt. Figure 4b is a zoomed SEM image of such a scratch and its depth is about $0.1\text{ }\mu\text{m}$. It can be seen that these scratch lines disappear in the LA regions. Therefore, it can be concluded that the laser beam has melted a layer of PVF_2 of about $0.1\text{ }\mu\text{m}$. The source of the heating is coming from the absorption of the laser energy in the metallic coating and not in the PVF_2 film itself. In addition, no distinct height discontinuity between NL and LA region was observed. There is, therefore, no significant ablation of the polymer. The polymer then resolidifies without any significant evaporation. Furthermore, the mechanism is faster than 4 ns , the laser pulse length, since the front and back metal coatings have to be sequentially ablated in single pulse ablations.

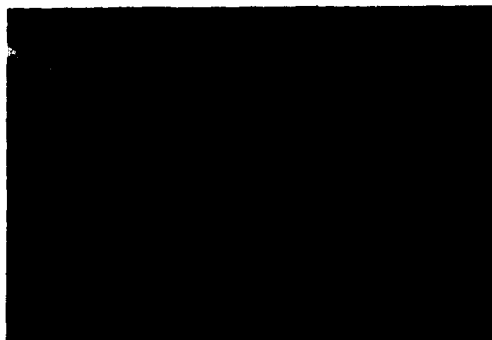


Fig. 4a SEM image covering both laser ablated LA, and non-laser-irradiated NL, regions. The horizontal lines are scratches. The white bar at the bottom is $100\text{ }\mu\text{m}$ long.

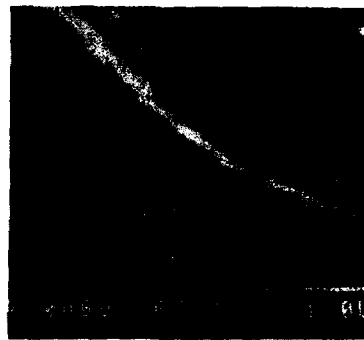


Fig. 4b Zoomed SEM image of one scratch line of Fig. 4a. The white bar is $1.0\text{ }\mu\text{m}$ long.

Since high resolution SAM is very sensitive to small depth variations, it can be seen rather clearly from the SAM images shown in Fig. 5, but barely from the SEM image in Fig. 4a, that the surface texture of the PVF_2 films in NL regions was sharper than that in LA regions. The resolidification process in LA regions smoothes out some irregularities of the surface, in particular, the scratch lines noted in Fig. 4. The depth of the melt is probably not much more than $0.1\text{ }\mu\text{m}$ since the coarser textures still remain continuous when they cross from one region to the other. It was also observed that the depth of the surface melt in the



Fig. 5 775 MHz SAM image covering both laser ablated LA, and non-laser-irradiated NL, regions. Total width: $500\text{ }\mu\text{m}$.

bottom surface was shallower than that in the top surface. Based on the understanding of the ablation mechanism, it is believed that the laser beam will not significantly affect the piezoelectricity of the PVF₂ film at the NL regions. Because there is no elastic contrast observed between NL and LA regions in all the SAM images (see Fig. 5), we believe that the change of acoustic properties of PVF₂ at LA regions, if any, will not affect the performance of devices employing PVF₂ films with laser patterned electrodes.

LASER PATTERNING CONSIDERATIONS

We have produced line patterns of various electrode dimensions on PVF₂ films of different thicknesses. These patterns included line widths of 12, 20, 50, 100, 150, 400, and 800 μm on each of four different thicknesses, 9, 28, 52, and 110 μm of PVF₂. Individual lines, 12 - 800 μm wide, were obtained in single strokes with the translating stage, after proper adjustment of laser energy density and focal spot size. Wider LA bands on each side of the patterns were obtained with a number of adjacent scans. In scanning these lines, the laser pulses overlapped, by a factor N . This factor was optimized to achieve good ablation rates, and good line resolution with minimal damage to the polymer. N depends on the laser pulse repetition rate R , the beam diameter at the target D , and the lateral scanning speed of the object S , according to

$$N = RD/S \quad (1)$$

In the case of the standard 0.3 - 0.8 μm metallic coatings, the energy density at the target was 0.25 J cm^{-2} for the 100 μm pattern in Fig. 2, and a complete pattern was drawn in about 3 minutes. For mass production, since the energy densities involved are quite modest, it should be possible to drastically reduce the processing time by using a mask.

Ultrasonic transducers or piezoelectric sensors employing PVF₂ require low resistance metal electrodes. For this reason, thicker coatings of silver were exposed to similar ablations, but the energy density necessary to remove the silver film was too large, and resulted in melting and charring of the polymer. Aluminium films 1.5 μm thick were subsequently successfully patterned on 28 μm thick PVF₂.

AN EXAMPLE OF ULTRASONIC EXPERIMENT

Due to the high acoustic attenuation of the PVF₂ film,⁶ an ultrasonic transducer consisting of a single line 2 mm wide and 10 mm long was chosen for the Lamb (membrane) wave experiment on a 110 μm thick film. Figure 6a shows the experimental setup, and Fig. 6b, the results. The ultrasonic point probe was a Pinducer from Panametrics. The probing point for the middle and lower traces in Fig. 6b was separated by a distance of 3.2 mm and 9.6 mm from that for the top trace, respectively. In each trace there are two signals. The earlier one was the acoustic signal directly emitted from the line transducer, and the later signal was the one reflected from the edge of the film. The reflected signal was out of phase with the directly transmitted one. The acoustic velocity is about 2000 m/s, therefore the acoustic wave observed in Fig. 6b was the lowest order symmetric Lamb mode. When we replaced the ultrasonic point probe at the probing position with a receiver the same as the transmitting transducer, nearly identical acoustic

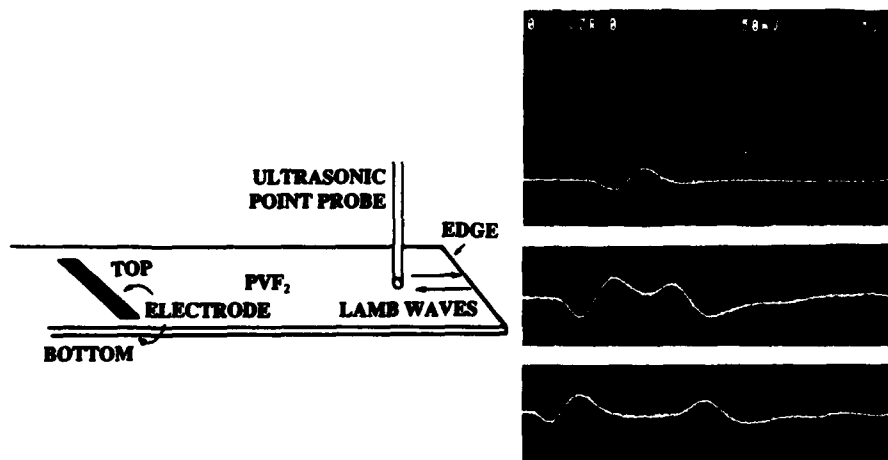


Fig. 6a Ultrasonic Lamb wave experiment setup.

Fig. 6b Observed acoustic signals at three different probing positions.

signals were observed. Interdigital transducers like those reported in Ref. 5 were also fabricated and glued to a glass plate: both symmetric and anti-symmetric Lamb waves were observed.

CONCLUSION

Excimer laser ablation of thin metallic films is a flexible and efficient way of obtaining complex patterns without affecting the intrinsic properties of the supporting polymer. Because of very localized deposition of energy for minimum ablation of the metallic layers, the piezoelectric properties of the polyvinylidene difluoride were maintained. The 20 μm line resolution obtained is much better than that reported using photolithographic methods. Even smaller patterns should be obtainable with a less divergent laser beam, for example with a doubled dye laser, or a doubled or tripled YAG.

REFERENCES

- ¹ One area of intense research is for optical data storage. See, for example, Proceedings of the Symposium on Optical Storage Materials, J. Vac. Sci. Technol. 18, 64 (1981).
- ² H.G. Shaw, D. Weinstein, L.T. Zitelli, C.W. Frank, R.C. DeMattei, and K. Fesler, Proc. IEEE Ultrasonics Symp. 1980, 927.
- ³ H.G. Nguyen, P. Hartemann, and D. Broussoux, Proc. IEEE Ultrasonics Symp. 1982, 832.
- ⁴ N. Chubachi and T. Sannomiya, Proc. IEEE Ultrasonics Symp. 1977, 119.
- ⁵ F. Mattiocco, E. Dieulesaint, and D. Royer, Elect. Lett. 16, 250 (1980).
- ⁶ X.Q. Bao, V.V. Varadan, V.K. Varadan, and R.H. Tancrell, Proc. Ultrasonics Symp. 1988, to be published.

ABLATION OF POLYMERS WITH PAIRS OF ULTRAVIOLET LASER PULSES WITH CONTROLLED TEMPORAL SEPARATION.

Bodil Braren, and R. Srinivasan
IBM, T. J. Watson Research Center,
Yorktown Heights, NY 10598

ABSTRACT

The dependance on the pulse width of the ultraviolet laser ablation and etching of poly(methyl methacrylate) was examined using 40-100 ns pulses. These pulses were created by stitching together two identical pulses, each of 40 ns half-width, which were separated by a set time interval from 0 to 380 ns. The etch depth/pulse is sensitive to the pulse width and, therefore, the power density in this polymer.

The response of PMMA to etching by pairs of pulses suggests that short-lived species which may be electronic states (e.g., triplets) and/or radicals play an important role in the ablation. The shape of the pulse was also found to influence the etch depth/pulse.

The etching of polyimide by these extended pulses shows trends that are opposite to those observed in poly(methyl methacrylate). In this instance the shielding of the latter portion of the incoming pulse by the products that are ablated by the front portion is probably a serious effect.

INTRODUCTION

Considerable interest exists in determining the relationship between the temporal width of an ultraviolet laser pulse and its ability to ablate and etch the surface of an organic polymer. The use of pulses of picosecond [1] or femtosecond [2,3] durations has been shown to result in a striking decrease in the fluence threshold. On the other hand, in one study [4] in which nanosecond pulses (308 nm) whose FWHM were 7 ns or 300 ns were used, the conclusion was reached that for polyimide over a practical etch depth range of 0.1 to 1 μm per laser pulse the etch depth was independent of the pulse duration. It has recently been shown [5] that polyimide is very sensitive to the shielding of the incoming pulse by the products of the ablation. At all three principal wavelengths of the excimer laser (193 nm, 248 nm, 308 nm), the ablation plume was observed to cut off all but the first few (< 5) nanoseconds of the pulse. Since this could be ascribed to the absorption of the laser photons by the decomposition products from the polymer, this material is not a good choice for the study of pulse width effects. UV laser ablation of a weakly absorbing polymer such as poly(methyl methacrylate) (=PMMA) at a laser wavelength and a fluence at which the known products of the ablation [6] do not filter the incoming pulse to any extent would be a more desirable system to look for pulse width effects. We report here the results of such a study. Some results on the ablation of polyimide are also included for comparison.

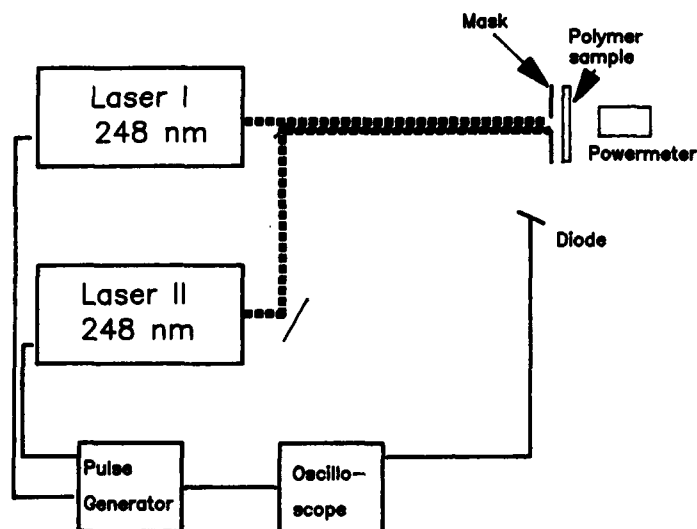


Figure 1. Schematic drawing of arrangement for controlling the temporal separation between the two pulses.

RESULTS

The outputs at 248 nm from two identical excimer lasers (Lambda-Physik 201E) were combined and used. A pulse generator (Philips PM 5716) provided a preset delay of 0 - 600 ns between the pulses. A Tektronix Model 2467 oscilloscope in connection with a silicon photodiode detector was used to monitor a fraction of the energy from the two beams in order to measure the degree of temporal delay that was achieved. The geometry of the setup used is shown schematically in Fig. 1. Since the FWHM of a single pulse was 40 ns, it was possible to create pulse widths from 40 to 100 ns. The jitter from one pair of pulses to the next was ± 10 ns and was most critical when absolute coincidence of the pulses was required. The apparent amplitude of the latter part of the pulse always showed a fall-off which is believed to be due to the fatigue in the silicon photodiode detector. When the temporal separation between the pulses (peak-to-peak) was set at 100 ns the overlap between the pulses was essentially zero. A sample of PMMA sheet ~ 1 mm thick was used. Etch-depths were averaged over 50 to hundreds of pulses. The uncertainty in the measured values of the etch-depth/pulse was $\pm 0.1 \mu\text{m}$.

The etching of PMMA using pairs of pulses is shown in Fig. 2. The fluence of an individual pulse was chosen to be such that it did not fall below the threshold for ablation nor did the sum of the fluences of two pulses fall beyond the limit (for 40 ns pulses) at which the etch curve started to level off [6]. The dashed horizontal lines indicate the depths that can be etched by two pulses with 'infinite' separation (i.e., 1 sec). It is evident that the etch depth does depend upon the pulse width in this

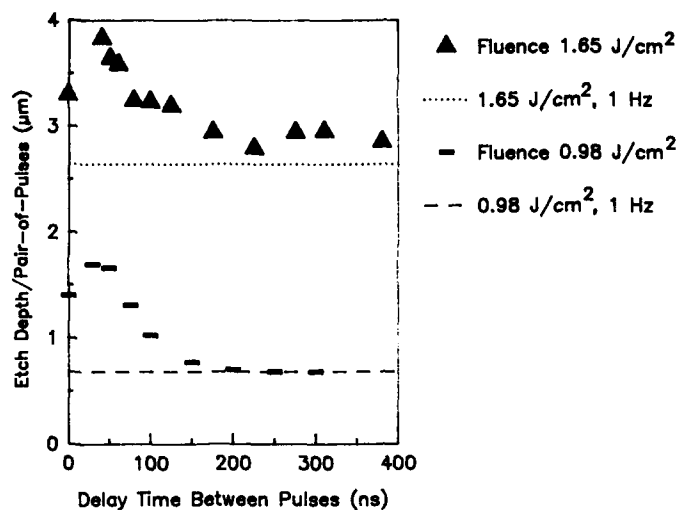


Figure 2. PMMA: Etch-depth/pair-of-pulses plotted against peak-to-peak separation between pulse maxima. Uncertainty in etch-depth measurement is $\pm 0.1 \mu\text{m}$.

polymer even over the small pulse width range of 40 - 100 ns. Of far more interest is the observation that when the peak-to-peak separation is set at 100 ns or even longer, there is a definite catalytic effect produced by the combination of pulses which is not duplicated by two isolated pulses. A separate set of experiments was undertaken to verify the enhancement in the etch-depth that is seen when the separation between the pulses is 30 - 50 ns. This effect can be due to the profile of the pulses. The profile was therefore deliberately distorted as listed in Table I. It is seen that there is an optimum pulse width as well as profile at which the etch-depth per pulse is a maximum.

The dynamic analysis of the UV laser ablation of polymers that was proposed by Sutcliffe and Srinivasan [7] is based on the sequential excitation of the chromophores in a polymer chain by UV photons that is followed by decomposition and ablation. Both a flux threshold and an ablation threshold were postulated for every polymer, the former representing a flux of absorbed photons per unit volume per second which must be exceeded before the photons were effective towards the decomposition process whereas the ablation threshold is defined as the number of 'useful' photons (i.e. those above the flux threshold) per unit volume that are needed to cause ablation. Although the sequential excitation of the chromophores was invoked, the fitting of the experimental curves was done by taking only the first excitation step into account. The predictions based on this analysis with regard to etching at different wavelengths, and the nature of the 'incubation' pulses were close to experiment for weakly absorbing polymers such as PMMA [7], polyethylene, and polypropylene [8].

It has been pointed out [8] that the success of this model can derive from the long radiative lifetime of the first electronically excited states in these polymer molecules so that the relaxation back to the ground state does not compete effectively with the up-

Table I. PMMA: Etch depth/pair of pulses at constant separation and constant total fluence. The relative amounts of photon energies are varied. The first and last row serve as references and correspond to "infinite" (1 sec) and zero separation between the pulses.

Pulse 1	Pulse 2	Peak-to-peak separation (ns)	Etch depth (μm)
0.47J/cm ²	0.47J/cm ²	10 ⁹	0.6
0.66J/cm ²	0.28J/cm ²	50	1.3
0.47J/cm ²	0.47J/cm ²	50	1.7
0.22J/cm ²	0.73J/cm ²	50	1.7
0.95J/cm ²	0	0	1.4

pumping process to the higher electronically excited state from which ablation can occur. The formation of this transient intermediate state whose absorption characteristics would be different from those of the ground state would be consistent with recent demonstrations of increased absorption in PMMA even in the course of a single laser pulse [9,3]. The absorption of PMMA at 248 nm corresponds to an upper singlet state with $n-\pi^*$ character and is weak in intensity because of symmetry considerations. The maximum is at shorter wavelengths but the 0-0 transition has not been clearly placed [10]. The increased absorption during the laser pulse could be initially due to the build-up of the upper singlet but, at longer times, this could undergo intersystem crossing to a triplet state which would be longer-lived than the singlet. The incoming photons could then up-pump the triplet and cause decomposition and ablation from a high triplet state. This is a possible explanation for the influence that both the intensity profile and the temporal width of the laser pulse have on the effectiveness of the UV laser pulse. While pump-probe experiments may appear to be an attractive way to look for the intermediacy of one or more electronically excited states, chromophores in polymers have poorly resolved spectra which would make any definite spectroscopic identification of a transient species difficult.

The behavior of PMMA can be compared to that of polyimide in a similar set of experiments (Fig. 3). In this case, the etch-depth increased consistently as the temporal separation Δt (peak-to-peak) rose from 0 to ∞ . Even at a value of Δt of 600 ns, the etch depth did not correspond to the value at 'infinite' separation between the pulses. Since the electronically excited states of polyimide would be more short-lived than those in PMMA, the trend here is attributable to the shielding of the trailing end of the laser pulse by the solid products (principally carbon [11]) that are generated by the ablation from the leading edge. Solid carbon is an effective absorber of ultraviolet radiation [12]. This result suggests that in much of the quantitative work on the UV laser ablation of polyimide the photon energy is not fully utilized.

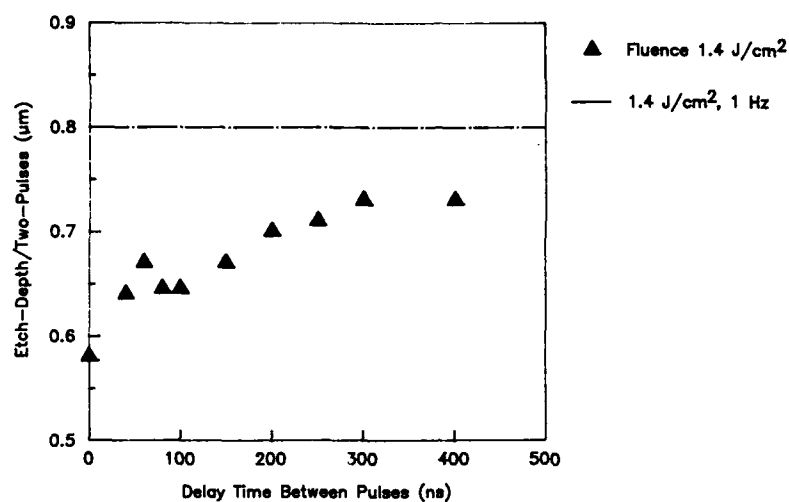


Figure 3. Polyimide (DuPont, Kapton): Etch-depth/pair-of-pulses plotted against peak-to-peak separation between pulse maxima. Uncertainty in etch-depth measurement is $\pm 0.1 \mu\text{m}$.

ACKNOWLEDGMENT

The authors thank Dr. R. W. Dreyfus for his assistance in setting up this experiment.

REFERENCES

1. B. Nikolaus, Conference on Lasers and Electro-Optics, San Francisco (1986).
2. R. Srinivasan, E. Sutcliffe and B. Braren, *Appl. Phys. Lett.* **51**, 1285 (1987).
3. S. Kuper and M. Stuke, *Appl. Phys. B*, **44**, 199 (1987).
4. R.S. Taylor, D. L. Singleton and G. Paraskevopoulos, *Appl. Phys. Lett.* **50**, 1779 (1987).
5. P. Klopotek, B. Burghardt and W. Mückenheim, *J. Phys. E: Sci. Instrum.* **20**, 1269 (1987).
6. R. Srinivasan, B. Braren, D. E. Seeger, and R. W. Dreyfus, *Macromolecules*, **19**, 916 (1986).
7. E. Sutcliffe and R. Srinivasan, *J. Appl. Phys.*, **60**, 3315 (1986).

8. R. Srinivasan, E. Sutcliffe and Bodil Braren, *Laser Chem.* **2**, 147 (1988).
9. G. M. Davis and M. C. Gower, *J. Appl. Phys.*, **61**, 2090 (1987).
10. M. Robin, Higher Excited States of Polyatomic Molecules Academic Press, New York, 22 (1974).
11. R. Srinivasan, B. Braren, and R. W. Dreyfus, *J. Appl. Phys.*, **61**, 372 (1987).
12. M. W. Williams, and E. T. Arakawa, *J. Appl. Phys.*, **43**, 3460 (1972) and earlier references therein.

MASS AND ENERGY ANALYSIS OF IONIC FRAGMENTS FROM PHOTOABLATION OF POLYIMIDE

G. ULMER, K. BUES and E.E.B. CAMPBELL

Fakultät für Physik, Universität Freiburg, Hermann-Herder-Str. 3,
D7800 Freiburg, Federal Republic of Germany.

ABSTRACT

The ionic products from excimer laser photoablation ($\lambda = 308$ nm) of polyimide (Kapton) film have been studied as a function of fluence. Large ion masses up to about 900 a.m.u. are easily observed, the mass distribution depending strongly on the fluence. Velocities of the emitted particles lie between 1400 and 10000 ms⁻¹, again dependent on the fluence. A mechanism to explain the high velocities is suggested consisting of ionisation of the surface polymer molecules followed by a Coulomb explosion combined with expansion of the high density gas formed by the photoablation.

INTRODUCTION

In recent years there has been considerable interest in the interaction of pulsed ultraviolet laser radiation with polymer surfaces /1 - 5/ since this can lead to the precise removal of material in a geometry that is defined by the light beam. It is however not yet clear to which extent photochemical or photothermal effects dominate the ablation process. Until now most investigations have involved detection of either the etch rate produced by different fluences in different polymer materials /1,2/ or the neutral fragments which can be detected by a variety of methods including laser induced fluorescence /2/, photoionisation mass spectrometry /3,4/, and gas chromatography - mass spectrometry /2/. As yet no systematic investigation of the ionic products produced by the ablation has been carried out. Here we present the first preliminary results of such an investigation for ablation of a polyimide (Kapton) film at a laser wavelength of 308 nm. Our results give strong evidence for the dominance of photochemical processes.

EXPERIMENTAL

The apparatus to be used will be described in detail in a forthcoming publication /6/ and will only be briefly discussed here. A schematic diagram is shown in Fig. 1. The light from the excimer laser operating on the 308nm XeCl line passes through a defining aperture, focusing lens ($f = 30\text{cm}$) and quartz window before hitting the sample polymer at an angle of 45° . Changing the distance between focusing lens and sample enables the fluence to be varied. The laser repetition rate is kept at 5Hz during the experiments to avoid polymer heating effects. Ions produced by the photoablation process are formed in a field free region. Those which are ejected normal to the sample surface enter a series of ion optics (IO, EA) where the masses, velocities and energies of the ions can be determined. The ion signal is measured with a transient recorder and averager and stored in an IBM PC.

The experiments were carried out with a free-standing polyimide (Kapton) film, $130\mu\text{m}$ thick.

The vacuum chamber is pumped with an oil diffusion pump and during the experiments is kept at a pressure of $2 - 5 \times 10^{-7}\text{Torr}$. A liquid nitrogen cold trap in the vicinity of the sample helps to maintain a low background pressure during the ablation.

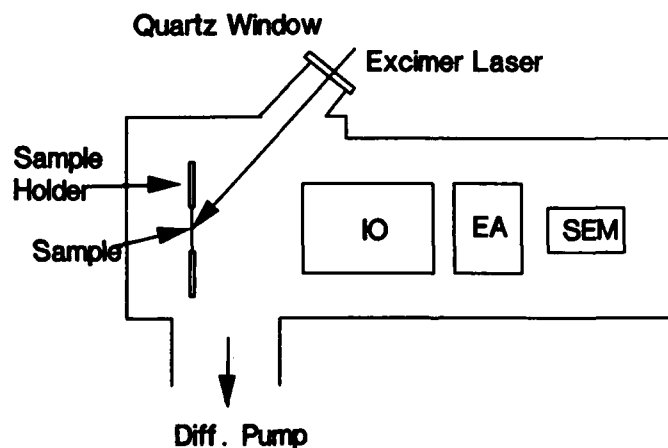


Fig. 1 Schematic diagram of apparatus. IO: ion optics, EA: energy analyser, SEM: electron multiplier

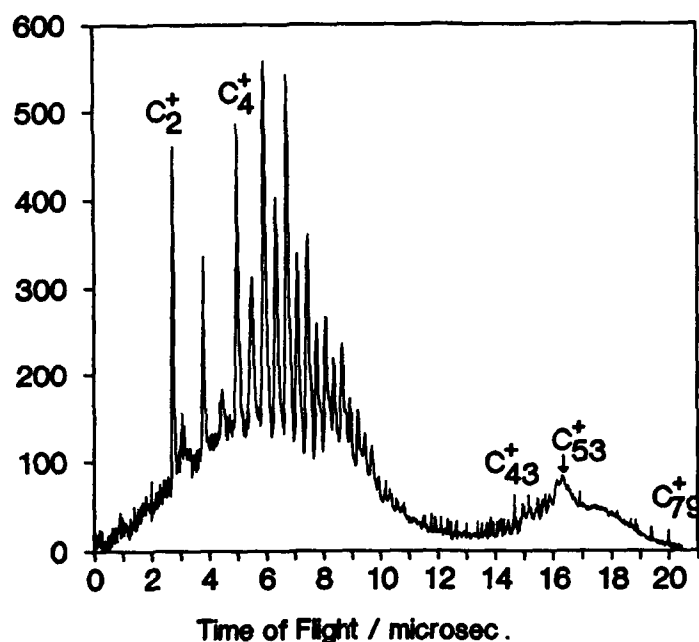


Fig.2 Ion mass spectrum for a fluence of 210 mJ/cm² and a velocity window of 3600 – 5300 ms⁻¹

RESULTS AND DISCUSSIONS

Experiments have been performed in the range of fluences up to 500 mJ/cm². Figure 2 shows a mass spectrum obtained at a fluence of 210 mJ/cm² and a velocity window of 3600 – 5300 ms⁻¹. The spectrum has been averaged over 10 laser shots. Here it can be seen that masses up to 960 a.m.u. (C₈₀) can be detected with a mass difference between the peaks corresponding in most cases to one carbon atom. The mass resolution is unfortunately not adequate to resolve the individual H atoms although, on an expanded scale it is possible to see structure in the main mass peaks which could be due to varying numbers of H atoms or an N or O atom in place of a carbon. It should thus be borne in mind that when we discuss a C_n⁺ mass peak this could be C_n⁺ with a number of hydrogen atoms attached or could be C_{n-1}N or C_{n-1}O again with or without hydrogen atoms. The unresolved double hump structure seen is due to two different species: the hump at low flight times, peaking at approximately 6 μs, is due to ions moving too quickly to be mass resolved, the second structure, peaking at approximately 17 μs, is due to neutral species with a velocity of

approximately 7000 ms^{-1} which produce a signal at the electron multiplier. This spectrum is unlike the carbon cluster spectra observed by Smalley and co-workers /7/ where firstly there was a very strong peak corresponding to C_{60} and secondly for clusters containing more than 40 atoms only those containing an even number of atoms were observed. The mass spectrum which we observe for a given laser intensity depends on the velocity window selected for the measurement as different masses are produced with different velocities, the velocity increasing with increasing

Table 1: Velocities and corresponding kinetic energies for selected ions at two different fluences

Ion	Fluence/ mJcm^{-2}	Observed vel. range / ms^{-1}	Av. Vel. / ms^{-1} ($\pm 10\%$)	Av. Kin. Energy eV ($\pm 20\%$)
C_2^+	110	1500 – 8000	5300	4
C_3^+	110	1500 – 7000	4800	4
C_5^+	110	2000 – 6000	3500	3.5
C_2^+	210	4000 – 8000	6500	6
C_3^+	210	3000 – 8000	5500	7
C_5^+	210	3000 – 7000	5300	8.5

fluence. Table 1 gives some examples of the velocities and corresponding kinetic energies of some ions at different fluences. As can be seen from Fig. 2 very large kinetic energies are produced by the photoablation. In order for us to observe the largest dominant mass peak corresponding to C_{79}^+ , fragments of this mass must have kinetic energies around 60 eV. This would support the photochemical ablation model suggested by Garrison and Srinivasan /8/ where the laser light initiates a chemical reaction or dissociation process the products of which have a larger specific volume than the original sample so that an explosion occurs and the particles are ejected with supersonic velocities, the velocities of different masses being of a similar magnitude. The velocities observed here are however significantly larger than those predicted by this model ($1000 - 2000 \text{ ms}^{-1}$) and also larger than the velocities observed for neutral particle production in the photoablation of polystyrene as reported by Feldman et al /4/ (kinetic energy $\sim 0.7 \text{ eV}$ for the styrene monomer) and Larciprete and Stuke /3/ (velocity $\sim 2000 \text{ ms}^{-1}$). In the latter paper although no results were presented for Kapton it was stated that in that case abundant ionic products were ablated together with the neutrals which was not the case for polystyrene. With these results in mind we suggest that an explanation for the high velocities observed here would be a combination of supersonic expansion as dealt with in the model mentioned above /8/ and Coulomb explosion of the ionised

polymer surface produced by multiphoton ionisation. This would explain the increasing velocity observed with increasing fluence, a greater fluence leading to a denser charge distribution on the surface and hence a more energetic explosion. Measurements by Srinivasan et al /2/ of the laser induced fluorescence of C_2 and CN from Kapton gave velocities of 6500 ms^{-1} for ablation with 248nm which is very similar to what we observe. It is possible that these species are formed by recombination of ejected ions with electrons which will be formed in abundance during the multiphoton ionisation.

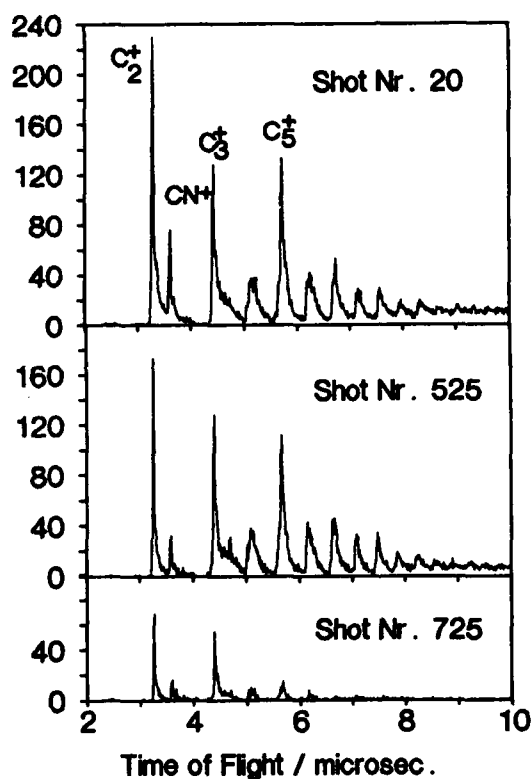


Fig. 3 Single shot ion spectra taken after different numbers of laser shots on the same surface area.

An interesting question is how the observed mass distribution changes with increasing numbers of laser shots. Single shot spectra obtained after different numbers of laser shots on the same surface area are shown in figure 3. This illustrates that the mass distribution remains constant as the sample is being etched, however the intensity of the ion signal decreases as a hole is formed in the polyimide film. When looked at under a microscope the hole formed has very sharp edges, again indicative of a photochemical rather than a photothermal process. These results are very different from previous measurements carried out in our laboratory where the polyimide film was attached to a metal plate. In this case the mass distribution at the beginning of the ablation looked very similar to what is shown in Figure 3 but as the number of laser shots increased the intensity of the C_2^+ and C_3^+ peaks increased considerably when compared with the larger masses. It was also observed that in this case the edges of the hole formed in the sample were dark brown in colour indicating that carbonisation of the sample had occurred. This would be strongly indicative of thermal processes and care should be taken when comparing measurements with free-standing samples and those with samples attached to metal or silicon substrates.

The method used here would certainly seem to be of relevance to thin film and multilayer technology as a means of investigating both the thickness of the layers and the extent of mixing between layers.

CONCLUSIONS

A direct measurement of the ionic products formed during photoablation of a polyimide (Kapton) film using a pulsed excimer laser at a wavelength of 308 nm and fluences up to 500 mJ/cm² provides strong evidence that the ablation proceeds via photochemical processes. Large amounts of ions within a very broad mass range are formed, and it is possible that the neutral species which have been the subject of most investigations so far have been produced by ionic recombination or fragmentation of larger particles.

ACKNOWLEDGEMENTS

The authors would like to acknowledge many stimulating and fruitful discussions with Prof. I.V. Hertel.

REFERENCES

- /1/ Dyer, P.E. and Sidhu, J., J. Appl. Phys. 57 (1985) 1420
- /2/ Srinivasan, R., Braren, B. and Dreyfus, R.W., J. Appl. Phys. 61 (1987) 372
- /3/ Larciprete, R. and Stuke, M., Appl. Phys. B. 42 (1987) 181
- /4/ Feldmann, D., Kutzner, J., Laukemper, J., MacRobert, S. and Welge, K.H., Appl. Phys. B. 44 (1987) 81
- /5/ Koren, G., Appl. Phys. B. 46 (1988) 147
- /6/ Ulmer, G., Bues, K., Campbell, E.E.B. and Hertel, I.V., in preparation
- /7/ Kroto, H.W., Heath, J.R., O'Brien, S.C., Curl, R.F. and Smalley, R.E., Nature 318 (1985) 162
- /8/ Garrison, B.J. and Srinivasan, R., J. Appl. Phys. 57 (1985) 2909

PART VIII

Laser-Induced Surface Modification

ULTRATHIN SILICON DIOXIDE FILMS: PHOTO-INDUCED GROWTH

IAN W. BOYD

Electronic & Electrical Engineering, University College London,
Torrington Place, London WC1E 7JE, UK.

ABSTRACT

The reaction of oxygen with silicon induced by intense photon beams at different wavelengths is described. We find different enhancement rates applying to UV and visible radiation, which can be as high as 400% for thin film growth at low temperatures. Often, however, they can be so small that they may be completely overshadowed at high temperatures by the rapid oxidation rates arising from thermal contributions. By using UV radiation projected through a mask to induce low temperature photonic oxidation of silicon, we have grown directly patterned oxide structures dispensing with the need for conventional photolithographic etching.

INTRODUCTION AND BACKGROUND

The field of laser processing of thin films and microstructures has burgeoned in recent years [1, 2]. In fact, photonicallly driven reactions in general have attracted considerable attention for two main reasons.

Firstly, there is a perceived need for new low temperature film growth techniques for future microelectronic advances to be made. For example, oxides are the corner-stone of silicon technology, and there is already a continual effort to produce thinner layers at lower temperature with higher dielectric quality and improved interface characteristics for applications in structures with dimensions well into the sub-micron level. In such devices gate oxide layers will have to be scaled down to 150 Å and below, in order to retain similar operating and control voltages. The low operating temperatures are necessary to minimise unwanted atomic diffusion from the carefully arranged doped regions, to eliminate the possibility of contamination, and to reduce wafer warpage and defect generation.

Low temperature processing is also highly desirable for the various thermally sensitive optoelectronic technologies based on compound semiconductors such as GaAs, InP, MCT etc. Photon-stimulated reactions can be induced at much lower temperatures than those currently being used in present-day production lines. Energetic photons can also initiate rapid and enhanced growth rates which can assist in reducing the total amount of high temperature processing during growth.

Table I Summary of the different photon-induced reactions that can be induced to grow thin solid films of silicon dioxide.

PHOTON SOURCE	DESCRIPTION	REACTION MECHANISM
Heated Coil Furnace	Black-Body Radiation	Photothermal: High Temperature Si-Si Bond Breaking
Tungsten Lamp	Black-Body Radiation	
CO ₂ Laser	Monoenergetic IR Photons	
Ruby, Ar Laser	Monoenergetic Visible Photons	Photothermal & Photonic: High Temperature Si-Si Bond Breaking Photo-Carrier Si-Si Bond-Breaking
Xe Arc Lamp	Wideband UV/Visible Photons	
Excimer Laser	Monoenergetic UV Photons	Photo-thermal, Photonic, Photo-chemical, Photo-ionisation: Photocarrier Si-Si Bond Breaking Photo-Dissociation of Gas Photoelectron Ionisation of Diffusant High Temperature Si-Si Bond Breaking
In-Situ Gas Discharge	Wideband VUV/UV Photons	

Secondly, the influence of specific spectral distributions or precisely defined energies of photons can give useful fundamental information on the chemistry and physics of reaction processes. A variety of photon-based methods have been used to initiate, stimulate and enhance the growth of silicon oxides, providing new mechanistic pathways bringing different angles of perspective to a field which is still surprisingly little understood, despite the enormous technological importance of the layers produced.

In this paper, a brief overview of photon oxidation of Si is given. The various reaction schemes and mechanisms that affect film growth will be outlined.

REACTION SCHEMES

Table I reviews the three major routes by which oxidation can be photon-initiated [1]. From this point of view, the traditional resistance-heated coil (hot-wall) furnace can be considered a radiant, essentially "black-body" source.

The photons, whose wavelengths span the yellow-orange to the infrared spectral regions, are absorbed strongly by the silicon. After the significant carrier excitation and free-carrier absorption the highly excited electrons relax and recombine very rapidly, transferring their energy to the lattice, through phonon scattering. This leads to an increased lattice temperature, reflecting the high degree of atomic vibration. Within this regime of "thermal processing", normally induced in furnaces, new advances include the use of high intensity lamps resulting in Rapid Thermal Processing (RTP) [3].

Questions have arisen over the years as to the importance of the spectral distribution of the photons used to induce the oxidation reactions. For example, to what degree is the photo-excited carrier population important...or the precise energy distribution of the photo-excited carrier population? This has stimulated interest in the use of intense visible and UV photon sources to oxidise silicon as well as other semiconductors [1]. The major reaction mechanisms induced in these wavelength regimes are also summarised in Table I. In the literature most secondary photon-induced reactions are often termed "photonic".

Whilst the photon sources up till now have provided surface excitation, in the deeper UV it becomes possible to directly-photodissociate gas phase molecules. In this way, more highly reactive components can be generated that can more significantly enhance the surface reactions. In addition to gas phase photo-chemical (photolytic) dissociation, photothermal (pyrolytic) cracking can occur when specific precursor molecules impinge upon the photo-heated surfaces.

It is not only the oxidising species that can be generated by these mechanisms, so can Si atoms. In this way, complete deposition of the film can be performed from the gas phase. In this regime, Si can be obtained by the dissociation of silane (SiH_4), di-silane (Si_2H_6) or trisilane (Si_3H_8), whilst oxygen atoms can be released from O_2 , N_2CO_2 , NO_2 etc.

The deposition rate will depend upon the energy range and intensity of the photons present as well as the partial pressures and flow rates of the gases chosen and the temperature of the substrate. Usually this is very much a low temperature technique that can be applied to temperature-sensitive substrates, and in general the quality of the films produced are competitively close to those obtained by other deposition methods.

THERMALLY DRIVEN SILICON OXIDATION

Thermally controlled silicon oxidation in dry oxygen (O_2) is technologically probably the most important chemical reaction used in the microelectronics industry. The reaction chemistry describing the formation of oxide films has been widely accepted as following the well-known Deal Grove model [4], first proposed more than two decades ago. The theory describes a reaction of O_2

with Si for thin oxides, where the rate is limited only by the chemistry at the Si-SiO₂ interface (linear regime) until the oxide becomes so thick that the finite diffusion of the oxidant slows down the growth, and oxidation proceeds within the diffusion limitations (parabolic growth regime). Experimentally, the theory fits all the growth data in the temperature range 700-1300°C, providing the theory is applied once an initial 200 Å or so of oxide has grown.

In the earlier days of silicon microtechnology, when gate oxides were typically well above 600 Å there wasn't much interest in this initial growth of 200 Å. Nowadays, when it is clear that gate oxides will soon dip under this level, it is potentially of great technological benefit to be able to understand the kinetics involved in this regime.

At present, there are more than 12 different models which attempt to describe the oxidation mechanism for sub-200 Å films, as shown in Table II. Many of these propose strong contributions arising from ionic species or from the accumulation of charge at the Si-SiO₂ interface, whilst some consider the effect of stress on the diffusion and/or chemical reaction. Others suggest that the oxide may contain micro-pores of specific dimensions through which the O₂ could rapidly diffuse. This situation makes it exceedingly difficult to interpret any modifications to the thermal oxidation system induced by photons, although the observations may provide important evidence for or against particular oxidation models for the Si + O₂ system.

It is perhaps important to point out at this stage that the studies summarised here have been performed in the thin film regime, where, for conventional oxidation at moderately high temperatures, diffusion is rapid. However, in our case, it is often undesirable to induce such high temperatures, and it must be borne in mind that slow diffusion may in some instances actually retard the growth of the thin films.

VISIBLE PHOTON EFFECTS

It is somewhat interesting to note that in traditional furnace oxidation, and even more so in recent Rapid Thermal Oxidation (RTO), the silicon surface is continually flooded by a range of photons from the heating source. In other words, the measured reaction rates for what has been conventionally called "thermal" oxidation, may in fact include contributions arising from the presence of photons in the visible/near IR spectral regions.

Indeed, it is well known that oxidation only reaches acceptably fast rates at temperatures above about 700°C, where the amount of black-body radiation above the Si band-gap becomes significant. Nevertheless, until it is shown that "dark" oxidation proceeds at a slower rate, we shall take the furnace-measured rates as being purely thermal.

TABLE II. Summary of Silicon Thermal Oxidation Models

DESCRIPTION OF SILICON OXIDATION MODEL	REFERENCE
Diffusion of O_2 & reaction with Si + space charge effect & tunnelling/thermionic emission	Deal & Grove [3,18]
Enhanced diffusion of O_2 through micropores	Revesz & Evans [19] Irene [20]
Stress-induced diffusion effects	Doremus [21] Farglex & Ghibaudo [22] Leroy [31]
Two independently diffusing species	Hann & Helms [33]
Diffusion variation with oxide thickness	Reisman et al. [34]
Diffusion zone near Si-SiO ₂ interface	Murali & Murarka [36]
Creation of O_2^- /hole pair, leading to enhanced diffusion of O_2^-	Grove [18] Tiller [23]
Influence of O_2^{2-} and O^-	Lora-Tamayo et al [24]
Influence of O^-	Hu [25]
Fixed charge in oxide assists diffusion charged species O_2^- , and perhaps O^-	Lu & Cheng [26]
Fixed charge in oxide reduces available Si bonds by reducing holes with band-bending	Schafer & Lyon [27]
Fixed interface potential retards charged species near the interface	Naito et al [32]
Both O_2 and 2-O react with silicon	Ghez & van der Meulen [28]
Equilibrium between O_2 and 2-O, only O reacts with Si for thin oxides	Blanc [29]
Two-step oxidation: Si \rightarrow α -SiO ₂ + Si(I) & Si(I) \rightarrow SiO ₂	Tiller [30]
Enhanced Oxygen solubility & reactivity	Orlowski & Pless [35]

Several investigations have been reported that have studied the effect of deliberately increasing the photon flux incident on the silicon during furnace oxidation. The first observations using the Ar laser as essentially the sole source of energy for the reaction noted oxide growth rates significantly above those well recorded for conventional furnace rates [5,6].

Subsequent experiments [7-9] used much lower energy densities of visible radiation superimposed upon Si samples already undergoing high temperature furnace oxidation, and were also interpreted as evidence for photonic enhancement. In these latter cases, photonic enhancement rates around 20% were extrapolated from the data. To achieve this by purely thermal oxidation would have meant an equivalent increase in temperature from 900°C to only 927°C. However, the authors state that their estimates of the temperature rise induced by the laser beam could not account for the required 27°C, so photonic mechanisms were invoked.

Rather than attempting to determine the quantitative enhancement factors, two independent groups have used a relative approach to show that there is indeed a wavelength-dependent photonic effect. By applying identical absorbed beam powers of slightly different wavelength (thus allowing for initial differences in surface reflectivity), we have shown that a faster reaction rate is achieved by the longer wavelength radiation [10]. In fact, by allowing the Fabry-Perot effect of the growing transparent oxide layer to continually feedback more energy to the reaction, over a period of about 320 min almost 50% more oxide can be grown by the green rather than the blue light from the Ar laser [10].

The observations cannot be explained by differential absorption, since the blue light is more strongly attenuated in Si and should if anything create a larger initial temperature (and hence oxidation rate). The photonic effect has clearly dominated this possibility since the blue photons always induce the slower reaction. Because the reflectivity has already been handled by initial normalisation of the beam powers, and it is known that at higher temperatures the reflection coefficient for the blue light increases less than that for the green, some other optical factor must therefore be controlling the reaction.

For equal absorbed powers, we can calculate that there are around 5% more photons in the green beam than in the blue. Thus, the number of photons incident on the Si surface during oxidation increases the density of photo-excited carriers (and hence anti-bonding state density) which would increase the reaction rate.

We have obtained a thermal equivalent to this enhancement factor [10] by applying the thermal oxidation model of Massoud et al [11], and have found that the photon flux difference of 5% between the wavelengths leads to a reaction enhancement equivalent to 20% of the thermal rate.

It is important to point out in this case, that the photonic effect only operates whilst the photo-generated carrier density remains appreciably above that of the thermally generated population. In order to illustrate this, we show in Figure 1 the equilibrium carrier population generated in Si by an intense Ar laser beam, assuming that recombination is dominated by the Auger process, as a function of the temperature rise the same laser beam would induce in the Si. Also plotted is the intrinsic carrier population that would otherwise be expected under strict

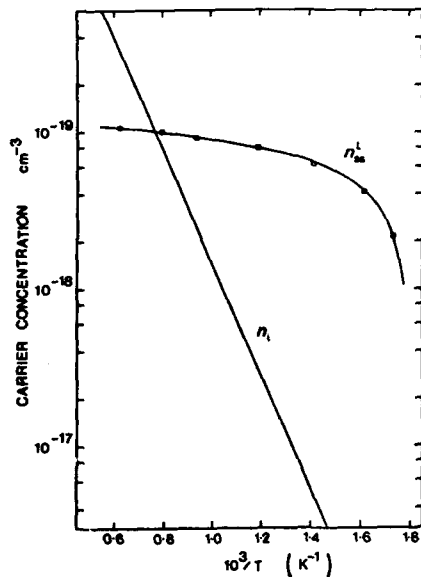


Fig. 1 The estimated steady-state carrier density photo-excited by Ar laser radiation, n_{ss}^l , versus the temperature induced by the same beam. Also plotted is n_i , the intrinsic carrier population.

thermal conditions. It is evident from this rough analysis that at temperatures much above 950°C it would be difficult to see any photonic enhancement, even with the extreme laser beam power densities used. This perhaps makes it slightly surprising that in references [7-9], where the Si was already held on average at 900°C, and where only mild beam intensities were applied, so-called photonic enhancements could be observed.

In conclusion, we note the presence of a photonic enhancement in the visible strongly associated with photo-generated carriers. Evidently, at high temperatures, any possible photonic effect on the oxidation reaction may be masked by the background carrier density occurring thermally within the lattice itself.

NEAR UV REGION

CW Irradiation

Previous experiments in this regime have used extremely powerful laser beams where melting can be induced [12, 13], or have compared pulsed heating situations with cw heating modes [13]. In either case, it is not straightforward to accurately assess the thermal and photonic contributions to the reaction, thereby making interpretation of the observations exceedingly difficult.

We have directly compared the effect of cw UV and visible light using particularly low beam intensity conditions to minimise the thermal contribution to the reaction, and also so that any significant differences in the enhancement induced by the different colours may be readily identified [14].

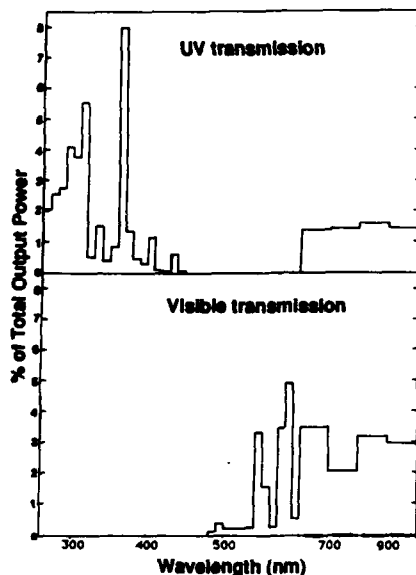


Fig. 2 The spectral composition of the two bands of incident radiation used to initiate silicon oxidation. Top (UV5 filter), Bottom (GG495).

A cw arc discharge lamp filled with a Xe:Hg gas mixture was used to provide a wide spectrum of photons (260 - 2000 nm) at a total integrated power of around 160W. The silicon samples were <100> oriented p-type (2-10 Ohm.cm) wafer portions, of 125 microns thick and some 20 x 20 mm square. All samples were cleaned identically in dilute HF, and a native oxide of 20 Å was allowed to grow prior to photon-stimulated growth. The Si was placed near the geometric focus of the lamp, which was around 10 mm in diameter, so that the samples intercepted all the incident light.

By introducing special filters into the beam path, the colour range of photons impinging upon the silicon surface was determined. Figure 2 shows the colour spectrum of the Xe/Hg arc lamp photons transmitted by two different filters used, namely UG5 (UV) and GG495 (visible). Since we are primarily looking for growth differences, the small fraction of red light transmitted by the UV filter is clearly not of significant importance. By irradiating individual silicon samples in air with the two colour bands of light, the oxide growth induced could be determined as a function of time. The oxide thickness was determined by fixed refractive index ($n=1.462$) measurements with an ellipsometer.

To isolate differences in the non-thermal contribution to the process, we performed preliminary calibration experiments to standardise the individual beam powers for the two colour ranges such that the same temperature could be induced in each case. A silicon sample into which was embedded a thermocouple was placed in the usual sample location within the beam and recorded the input power to the lamp necessary to induce a temperature of 400°C in the Si. This occurred with the visible light for 885W input and for the UV for 980W. The disparity between the two power levels is principally indicative of the difference in silicon reflectivity between the two broad wavelength regions.

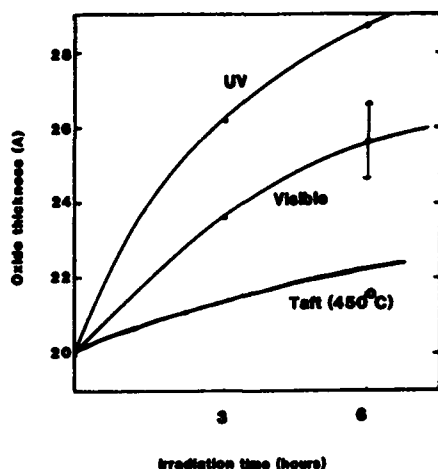


Fig.3 Oxide growth as a function of irradiation time using the two spectral bands of radiation defined in Figure 2. Also plotted is the thickness that would have grown thermally at 450°C during the same time period [Taft, 15].

Knowing that these power levels induced precisely the same temperature on the silicon, then any difference in the growth rate could be ascribed to a faster reaction rate induced by a non-thermal or "photonic" phenomena. Figure 3 shows the oxide thickness as a function of time induced by the two photon bands together with a previously published curve of the measured oxide thickness grown thermally at 450°C [15]. Whilst purely thermal oxidation at 450°C only produces about 2 Å growth in 360 min, the light-induced reactions encourage between 6 and 9 Å to grow.

Furthermore, we note that the UV light produces 50% more oxide than the visible radiation, i.e. the shorter wavelengths induce a faster reaction than do the longer wavelengths. Although the photon flux entering the Si several times larger for the visible radiation in this case, the UV radiation is much more strongly absorbed. Therefore, within the zone near the oxide interface where the Si is likely to oxidise, there are likely to be more photo-generated carriers in the UV pumped system. Again, it is important to note that since temperature has been pre-calibrated, it cannot account for the differences in growth rate.

In addition to the increase in photo-carriers, one might expect the energy distribution of these highly excited electrons also to be important above a certain energy threshold not previously achieved with visible photons. To explore such possibilities we have examined the Si-SiO₂ energy bands. The energy difference between the two conduction bands is around 3.2 eV (corresponding to a wavelength near 390 nm), while from the valence band of the Si to the conduction level in SiO₂ is 3.2 + 1.1 = 4.3 eV (around 290nm). In energy terms, the carriers generated by the UV light in these experiments contain on average 5 eV of energy whilst those photo-stimulated by the visible radiation have only around

2 eV or less. Therefore, the UV light can generate some carriers with sufficient energy to move into the oxide conduction band. Knowing that in Si the photoemission efficiency is quite small, however, (around 10^{-3}), we only expect that the highest energy tail of our conduction-band electrons to escape into the oxide.

Pulsed Excimer Irradiation

Since cw UV radiation can stimulate low temperature oxide growth, we have applied the pulsed UV output from a KrF laser to producing both large area films and discretely patterned structures [16].

A KrF excimer laser operating at 10Hz, and producing 20 ns pulses of 249 nm radiation, was focused to produce some 230 mJ/cm^2 at the sample. The energy variation over the spot size about 20 mm was within $\pm 2\%$, and the energy fall-off over the longest growth period used was around 5%. The silicon was $\langle 111 \rangle$ orientation, p-type (B doped) material with a resistivity of 6-10 Ωcm .

The growth induced is plotted in Figure 4 as a function of the number of laser pulses. After 40,000 shots around 30 Å of oxide had grown. It is interesting to note that this is very similar to the growth induced by the cw radiation in the UV, shown in Figure 3. However, although the curves are similar in nature, there is a major difference in the growth rates achieved.

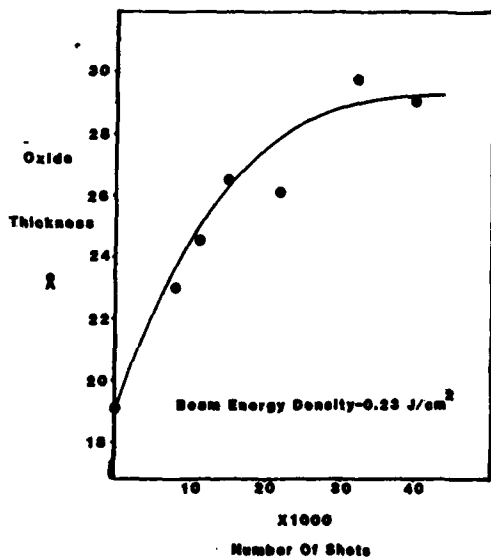


Fig.4 Oxide thickness grown as a function of the number of KrF laser pulses at an average incident beam fluence of 230 mJ/cm^2 .

For example, since the pulse duration was around 20 ns then after 40,000 shots the total illumination time of the Si is only 0.8ms. The fastest growth (19 to 25 Å) occurred after just 10,000 shots, meaning that 6 Å of oxide grew after only 0.2 ms of irradiation. This results in an apparent growth rate of 30,000 Å/s !

The induced temperature can be estimated using simple heating models and knowing that the Si melting point (1412°C) could be reached by applying pulses of around 0.5 J/cm². We thus estimate that our 0.23 J/cm² pulses induce a maximum temperature of 500°C, and that the total time the Si would be elevated close to this temperature would be around 100 ns. This produces an equivalent thermal oxidation rate of 6,000 Å/s. However, it is known that even at 600°C it would take around 500 min to thermally grow to 25 Å at the recognised growth rate of 8×10^{-4} Å/s [15]. Indeed, the reaction rate required to achieve the observed growth, could only be obtained by extrapolating the known data to a temperature of more than 2000°C, some 600°C above the silicon melting point.

Since the kinetics behind thermal oxidation of Si are not yet fully known, it is difficult to determine the precise mechanisms affecting UV oxidation. Nevertheless, four major steps must occur before SiO₂ can grow, i.e. (i) the gaseous O₂ is transported to the SiO₂ surface, (ii) the O₂ collides and sticks, (iii) the oxidising species diffuses through the existing SiO₂ to its interface with the underlying crystal Si, and (iv) it eventually reacts with Si atoms to form SiO₂. From the growth curves, we find that a linear reaction is not sustained as the oxide grows, suggesting diffusion limitations. This is consistent with the knowledge that only low temperatures are induced.

By applying the usual diffusion equation to the O₂ molecule in SiO₂ at 600K during the overestimated 0.01s of heating [17]

$$L = (t \cdot 2D_0 \cdot \exp(-E/kT))^{1/2}$$

where $D_0 = 2.7 \times 10^{-4}$ and E is 1.16 eV, we find the diffusion length of the molecule to be about 3 Å. In fact, the diffusion constant would have to be 100 times larger to have grown 30 Å in that time. Therefore, the dominant reactive species present during UV irradiation effectively diffuses much faster than O₂ to promote enhanced growth, and thus may not be O₂. Candidates for alternatives include any of the ionic oxygen species, or indeed neutral O atoms. The energy supplied by the KrF laser photons is extremely close to the known photodissociation threshold of O₂ (around 240 nm), making the photo-generation of a small fraction of highly reactive O species possible.

Since this technique encourages oxidation only where UV photons impinge the Si surface, we have applied it to induce selective oxide growth. Figure 5 shows a mask projection system used to project a pattern of photons onto a Si wafer in air. The relay lens reduces the mask pattern 10 times and oxidation only proceeds where the photons interact with the surface and produce the necessary excited state to induce the oxidation reaction.

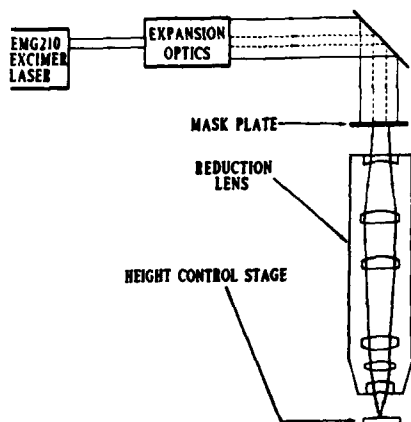


Fig. 5 Schematic configuration of the set-up used to grow directly patterned oxides on silicon.



Fig. 6 Oxide pattern grown directly on silicon using the projection system shown in Figure 5. Features below 5 microns are apparent here.

Since there was no significant temperature increase, oxide did not grow in the dark regions of the projected pattern. Figure 6 shows the selective oxidation structure grown with this method. Thus the standard lithographic definition and etching has been eliminated, and features down to the micron level are readily achieved.

In conclusion, we show that whilst visible radiation can enhance the oxidation reaction to a small degree, the enhancement can often be masked by the background thermally-controlled reaction. In the near UV, the enhancement is somewhat larger, possibly because of the larger percentage of photo-carriers with enough energy to escape from the silicon into the SiO_2 . By minimising the thermal reaction at a temperature around 400°C , we report directly patterned oxidation induced by the UV radiation.

ACKNOWLEDGEMENTS

The contributions of and many discussions with F Micheli and V. Nayar are gratefully acknowledged. This work was partly funded by SERC and by the Nuffield Foundation.

REFERENCES

1. I.W. Boyd, Laser Processing of Thin Films and Microstructures, Springer Series in Materials Science Vol.3, (Springer-Verlag, London, New York, 1987).
2. I.W. Boyd, E.F. Krimmel (eds.), Photon, Beam and Plasma Assisted Processing: Fundamentals and Device Technology, Proc. 1988 E-MRS Symposium B, (North-Holland, Amsterdam, 1988).
3. T.O. Sedgewick, T.E. Seidel, B-Y. Tsaur, Eds) Rapid Thermal Processing Materials Research Society, Pittsburgh 1986, p313.
4. B.E. Deal, A.S. Grove, J. Appl. Phys., 36, 3770 (1965).
5. J.F. Gibbons, Japan. J. Appl. Phys. Suppl., 12, 121 (1981).
6. I.W. Boyd, J.I.B. Wilson, J.L. West, Thin Solid Films
7. E.M. Young, W.A. Tiller, Appl. Phys. Lett., 42, 63 (1983).
8. S.A. Schafer, S.A. Lyon, J. Vac. Sci. Technol., 19, 494 (1981).
9. S.A. Schafer, S.A. Lyon, J. Vac. Sci. Technol., 21, 423 (1982).
10. F. Micheli, I.W. Boyd, Appl. Phys. Lett., 51, 1149 (1987).
11. H. Massoud, J.D. Plummer, E.A. Irene, J. Electrochem. Soc., 132, 1745 (1985).
12. T.E. Orlowski, H. Richter, Appl. Phys. Lett., 45, 241 (1984).
13. E.M. Young, W.A. Tiller, Appl. Phys. Lett., 50, 80 (1987).
14. V. Nayar, I.W. Boyd, (Unpublished).
15. E.A. Taft, J. Electrochem. Soc., 131, 2460 (1984).
16. V.Nayar, I.W. Boyd, F.Goodall, G.Arthur, Applied Surface Science (1988).
17. J.C.C. Tsai, in VLSI Technology ed. S.M. Sze, (McGraw-Hill, London, 1983).
18. A.S. Grove, Physics and Technology of Semiconductor Devices, (Wiley, New York, 1967).
19. A.G. Revesz, R.J. Evans, J. Phys. Solids, 30, 551 (1969).
20. E.A. Irene, J. Appl. Phys., 54, 5416 (1983).
21. R.H. Doremus, Thin Solid Films, 122, 191 (1984).
22. A. Fargeix, G.Ghibaudo, J. Appl. Phys., 54, 7153 (1983).
23. W.A. Tiller, J. Electrochem. Soc., 119, 591 (1980).
24. A. Lora-Tamayo, E. Dominguez, E. Lora-Tamayo, J. Llabres, Appl. Phys., 17, 79 (1978).
25. S.M. Hu, Appl. Phys. Lett., 42, 672 (1983).
26. Y.Z. Lu, Y.C. Cheng, J. Appl. Phys., 56, 1608 (1984).
27. S.A. Schafer, S.A. Lyon, Appl. Phys. Lett., 47, 154 (1985).
28. R.Ghez, Y.J.van der Meulen, J.Electrochem.Soc., 119, 1100 (1972).
29. J. Blanc, Appl. Phys. Lett., 33, 424 (1978).
30. W.A. Tiller, J. Electrochem. Soc., 128, 689 (1981).
31. B. Leroy, Phil. Mag. B, 55, 159 (1987).
32. M.Naito, H.Homma, N.Homma, Sol. St. Electron., 29, 885 (1984).
33. C.J. Hann, C.R. Helms, J. Electrochem. Soc., 134, 1297 (1987).
34. A. Reisman, E.H.Nicollian, C.K.Williams, C.J.Merz, J. Electron. Mater., 16, 45 (1987).
35. M. Orlowski, V. Pless, Appl. Phys. A46, 67 (1988).
36. V. Murali, S.P. Murarka, J. Appl. Phys., 60, 2106 (1986).

LASER PHYSICAL AND LASER CHEMICAL VAPOR DEPOSITION OF TiN AND TiN_xO_y FILMS

J.Narayan, N.Biunno, A.R.Srivatsa, R.Singh and B.Chen
Department of Materials Science and Engineering
North Carolina State University
Raleigh, N.C. 27695-7916.

ABSTRACT

We have investigated the formation of polycrystalline TiN and amorphous TiN_xO_y films using laser physical (LPVD) and laser chemical (LCVD) vapor deposition techniques. The LPVD method involved the ablation of a TiN hot pressed pellet and Ti in the presence of nitrogen plasma using nanosecond XeCl excimer laser pulses (wavelength 308nm, pulse duration 45×10^{-9} seconds, and energy density $\sim 4.5 \text{ J cm}^{-2}$). The films were polycrystalline (average grain size $\sim 100 \text{ \AA}$) with face-centered-cubic structure and lattice constant of 4.25 \AA . The average grain size remained constant as the substrate temperature ranged from 25 to 550°C . In the LCVD method, a pulsed CO_2 laser beam was used to crack TiCl_4 and NH_3 and form TiN films. Amorphous TiN_xO_y films were formed under poor vacuum conditions in the LPVD techniques. These amorphous TiN_xO_y films often exhibited explosive recrystallization with characteristic star patterns. Resistivity and microhardness measurements were made on these films and these results have been correlated with microstructure and chemical composition.

INTRODUCTION

Titanium nitride coatings have found a variety of applications ranging from corrosion and erosion resistant protective layers to diffusion barriers in microelectronic devices¹⁻⁴. The primary considerations in the formation of these coatings include lowering of processing temperature, spatial selectivity and control of microstructures. Laser deposition techniques offer these advantages. In this paper, we have investigated the formation of TiN and TiN_xO_y films by laser physical and laser chemical vapor deposition techniques. These films were characterized by TEM for microstructures, and RBS and Auger for chemical compositions. Electrical resistivity I-V (current-voltage), and microhardness measurements were made as a function of oxygen content of thin films.

EXPERIMENTAL

In the LPVD method, a high-power pulsed laser ($\lambda = 0.308 \text{ \mu m}$, $\tau = 45 \text{ ns}$, and energy density 4.5 J cm^{-2}) was used to ablate TiN target pellet and deposit on a substrate, kept at a distance of about 3 cm parallel to the target. The temperature of the (100) silicon substrate was varied from room temperature to 550°C during deposition to study its effect on microstructure and chemical composition. The partial pressure of nitrogen was controlled by bleeding in the nitrogen near the

target.

In the LCVD method, a mixture of $\text{TiCl}_4/\text{NH}_3$ (ratio 2-10%) was introduced near the target in the presence of NH_3 background pressure maintained at 10 millitorr. A beam of pulsed CO_2 and XeCl excimer laser was used to induce chemical reactions leading to the formation of TiN on molybdenum target.



Figure 1(a) Plan view TEM micrograph showing fine-grained structure of TiN film.

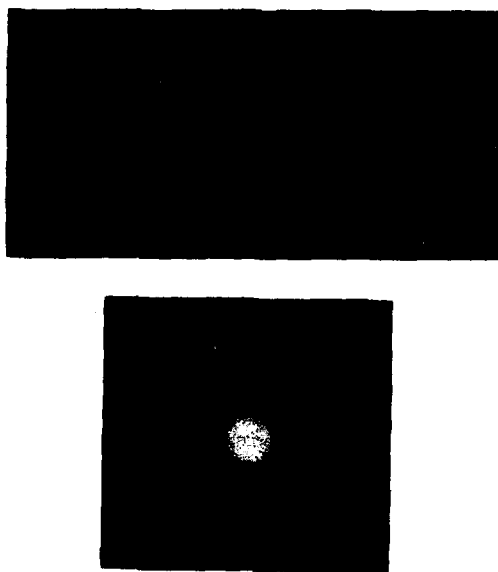


Figure 1(b) Dark field cross-section TEM micrograph and associated diffraction pattern.
Note the overlap of the polycrystalline diffraction pattern from the TiN film and
<110> diffraction pattern from the Si substrate.

RESULTS AND DISCUSSION

Figure 1(a) shows a plan-view TEM micrograph containing a polycrystalline structure of the film. The average grain size of the films was found to be 100Å. A cross-section of the same specimen under dark-field imaging conditions is shown in Fig. 1(b), which shows an interposing layer of amorphous silicon oxide, about 20Å thick, between TiN and the silicon substrate. From the section TEM micrograph, it is apparent that the grains do not have a columnar structure. The polycrystalline nature of the film is evident from the selected-area diffraction pattern. Using silicon as a standard ($a_0 = 5.43\text{Å}$) during diffraction studies, the lattice constant of the films was determined to be $4.25 \pm 0.05\text{Å}$ with a sodium chloride crystal structure. The TiN_xO_y films with a large amount of oxygen using LPVD method, were found to be amorphous. The amorphous films deposited at room temperature contained explosively recrystallized regions, as shown in Fig. 2. It is envisaged that the explosive recrystallization starts during the deposition process and the activation energy for starting the recrystallization event is derived from the kinetic energy of the bombarding ions.

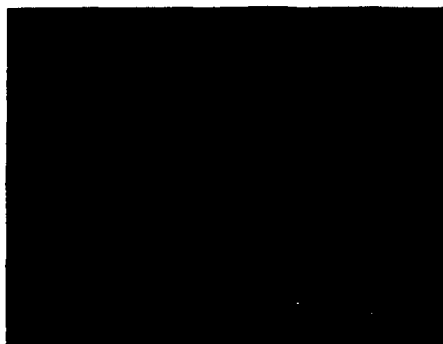


Figure 2 Dark field micrograph of explosively recrystallized TiN_xO_y film.

The chemical composition of these films was analyzed using Auger electron spectroscopy (AES) and Rutherford backscattering analyses. Fig. 3(a) shows a typical AES spectrum from a LPVD film, deposited with nitrogen pressure of 0.5m torr in the chamber. This spectrum was taken in the steady state part of the composition of the film. As is evident from the spectrum, the film contains a small amount of oxygen. It was interesting to note that this spectrum was identical to that obtained from the target TiN, shown in fig. 3(b), representing a bulk composition. The similarity in the two spectra shows that a chemical composition of TiN identical to that of the target can be obtained by LPVD in an appropriate nitrogen partial pressure.

Figure 3(c) shows Auger spectrum obtained from LCVD films. The oxygen content in these films is extremely small. The quantification of the AES spectrum is complicated by the fact that the principal nitrogen Auger peak, KL_2L_3 at 381eV, overlaps with the $\text{L}_3\text{M}_{2,3}\text{M}_{2,3}$ titanium peak at 383 eV. The titanium spectra changes in both intensity and shape with a change in the nitrogen content⁵. Furthermore, the presence of a small amount of oxygen is known to change the titanium

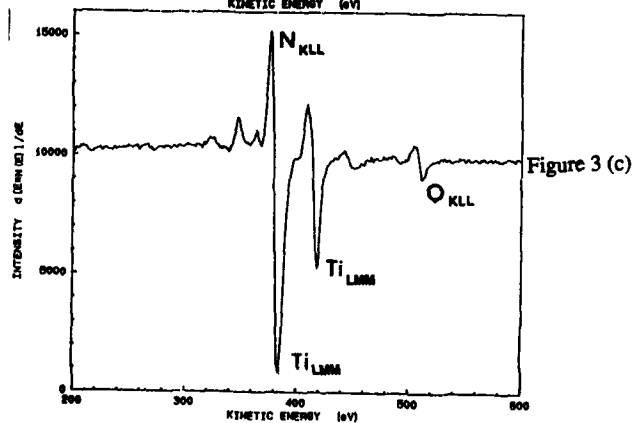
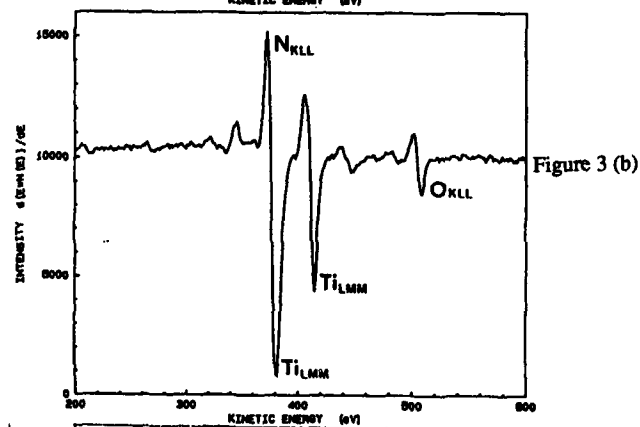
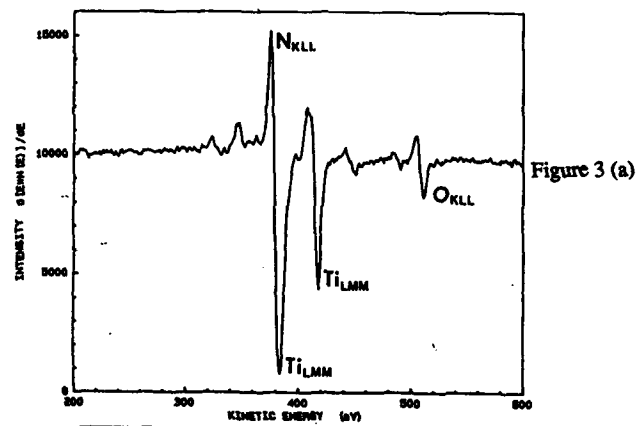


Figure 3. Auger spectra from (a) LPVD film, (b) TiN pellet and (c) LCVD film.

peak intensity⁶. Therefore, one has to resort to standards or compare the results from RBS. The RBS results showed nitrogen content > 90% in LPCVD films. Further quantification of these films is still in progress.

Measured resistivities ranged from 50 to 150 $\mu\Omega$ - cm, indicating metallic nature. The I-V characteristics showed metallic behavior, which changed to a semiconducting nature with increasing oxygen content. Microhardness measurements on TiN films showed values typically 15GPa which is in agreement with hardness values reported by others on TiN films.

In summary, we have shown that polycrystalline TiN films can be deposited by LPVD method with substrate temperature being close to room temperature. The average grain size of the film ($\sim 100\text{\AA}$) remained approximately constant with increasing substrate temperature up to 550°C. The films were metallic and showed semiconducting behavior with increasing oxygen content. The microhardness values on these films agreed with previous measurements. We have also used LCVD method to deposit high quality TiN films. The oxygen content can be eliminated in these films with a lot more ease compared to LPVD films. A detailed characterization of LCVD films is being continued.

ACKNOWLEDGEMENT

Part of this work was supported by National Science Foundation (NSF) grant MSM-8618735. The authors would like to thank Dr. Carl J. McHaurge and Michael O'Hearn, Oak Ridge National Laboratory for making the microhardness measurements.

REFERENCES

1. J.E.Sundgren, B.O.Johansson and S.E.Karlsson, *Thin Solid Films*, **105**, 353 (1983).
2. M.Wittmer and H.Melchior, *Thin Solid Films*, **93**, 397 (1982).
3. B.Zega, M.Kornmann and J.Amiquet, *Thin Solid Films*, **54**, 577 (1977).
4. E.Vulkonen, T.Karlsson, B.Karlsson and B.O.Johansson, *Proceedings of SPIE 1983 International Technical Conference*, **401**, 41 (1983).
5. P.T.Dawson and K.K.Tzatzov, *Surface Science* **149**, 105 (1985).
6. R.Pantel, D.Levy and D.Nicolas, *J. Vac. Sci. Technol. A* **6**, 2953 (1988).

REVERSIBLE LASER MODIFICATION OF HIGH TEMPERATURE SUPERCONDUCTING Y-Ba-Cu-O FILMS

Robert R. Krchnavek, Bellcore, Morristown, NJ 07960,
Siu-Wai Chan, C.T. Rogers, F. De Rosa, P.F. Miceli, and S.J. Allen, Jr., Bellcore,
Red Bank, NJ 07701

ABSTRACT

We describe a reversible technique for locally modifying the oxygen stoichiometry and electrical transport properties of superconducting thin films. A focused argon ion laser beam is scanned across the surface of a $\text{YBa}_2\text{Cu}_3\text{O}_{7-x}$ thin film, contained in a vacuum, at incident power levels well below those necessary for ablation. The change in oxygen stoichiometry is monitored in-situ by the room temperature electrical resistance. We have measured the superconducting properties of these locally modified films. The resulting R vs T curve for the composite structure (film/laser stripe/film) shows the expected double transition. The first transition, corresponding to the unmodified film, occurs at 87 K while the second transition, corresponding to the modified stripe, occurs at a lower temperature and is a function of the laser induced change in the room temperature electrical resistance. The critical current for the composite structure is depressed from the original film. The laser writing can be erased or bleached out by room temperature exposure to an oxygen plasma.

INTRODUCTION

Electronics is envisioned as one area for important future applications of the high transition temperature (T_c) superconductors based on the La-Ba cuprates discovered by Bednorz and Muller [1], and the Y-Ba cuprates discovered by Wu [2]. These potential applications will rely heavily on the ability to make and process thin films of these materials and control their local transport properties on a microscopic scale. In this paper, we report on the transport properties of superconducting $\text{YBa}_2\text{Cu}_3\text{O}_{7-x}$ films that have been locally modified by laser induced heating in a controlled ambient. In contrast to previous work [3-5], we demonstrate that the modified film need not produce an insulating region but rather a superconducting phase with a reduced transition temperature. By reducing T_c and the critical current in a micron scale region of a superconducting thin film, we have the potential of fabricating devices based upon weak link structures. Furthermore, by placing the laser modified sample in an oxygen plasma, the original film properties can be recovered leading us to believe the laser induced phase is oxygen deficient.

EXPERIMENTAL

The superconducting films used in these experiments were prepared on (110) and (001) SrTiO_3 substrates by co-evaporation of Y, BaF_2 , and Cu in the presence of O_2 . The films were subsequently annealed at 850 °C for 30 minutes in oxygen with an H_2O partial pressure of 0.02 atm for fluorine removal [6]. The thickness of the annealed films ranged from 250 nm to 900 nm. The films were then patterned as conventional Hall bars using standard photolithography and subsequent wet etching with a one-volume percent solution of nitric acid. The patterned

samples were cleaned in an oxygen plasma and Ag contacts were evaporated onto the Hall bars through a shadow mask. Gold wires were bonded to these pads using indium solder. The resistance versus temperature data for a typical film is shown in Figure 1. The film displays metallic behavior down to the transition temperature of 87 K. The transition width (90-10 %) was 3.0 K. The critical current for this film was $1.2 \times 10^4 \text{ A/cm}^2$ at 80 K.

The experimental system used to modify the film consisted of an argon ion laser tuned to 514.5 nm and focused to a spot diameter of 5 μm . The beam is directed into a vacuum cell mounted on a set of computer controlled translation stages. The typical incident laser power was in the range of 40-60 mW and the cell was evacuated to approximately 10^{-3} Torr. The lateral writing rate was 10 $\mu\text{m/s}$. The room temperature electrical resistance of the Hall bar could be monitored during the laser writing. The ability to measure the electrical resistivity in-situ proved indispensable in controlling the laser power so that the electrical properties could be slightly modified instead of producing the insulating phase.

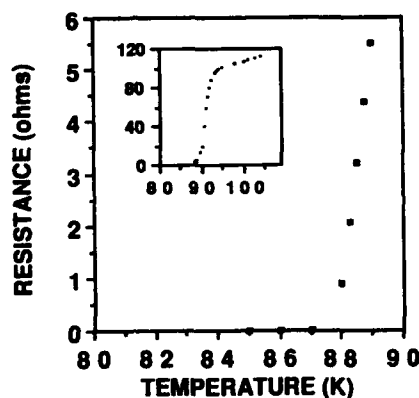


Figure 1. Resistance versus temperature data for a typical $\text{YBa}_2\text{Cu}_3\text{O}_{7-x}$ film on a SrTiO_3 substrate.

RESULTS AND DISCUSSION

Figure 2a shows an optical micrograph of a laser modified film. The modified region consists of a stripe 5 μm wide and 200 μm long and written in the direction perpendicular to the flow of current. Note that the laser modified region does not exhibit any physical degradation in the form of microscopic material removal or cracking; however, there is an obvious change in the optical reflectivity. The room temperature resistance of this leg of the Hall bar prior to laser writing was 174 ohms corresponding to a sheet resistance of 25 ohms/square. After the first laser scan, the resistance increased by 5 ohms. Assuming the laser modifies the entire thickness of the film in the exposed region, the laser modified stripe can be considered as a resistance in series with the unmodified film. The area of the stripe is 0.025 squares so the 5 ohm increase for this area infers a change in the sheet resistance from 25 to 200 ohms/square.

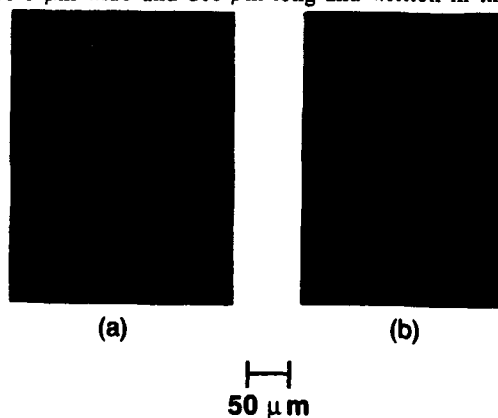


Figure 2. (a) An optical micrograph of a laser modified film showing the change in the optical reflectivity. (b) An optical micrograph of the same region of the film in Figure 2a after plasma oxidation.

Two subsequent passes with the laser beam increased the total resistance by another 9 ohms. The calculated resistance of the laser modified region increased to 560 ohms/square. Although the optical reflectivity increased after the first laser scan, subsequent scans did not produce an easily detectable change in this reflectivity. The electrical measurements, however, provided an easy means of monitoring the laser processing.

Figure 3a shows the resistance versus temperature curve for a typical laser modified superconducting thin film. The modified film shows a double transition; the first at 87 K corresponds to the unmodified regions of the film while the second corresponds to the laser modified region. The second transition, in this case occurring at 71 K, has a transition width of 9.0 K. If the laser processing was depleting oxygen from the surface region of the film and converting the superconducting phase into an insulating phase, we would not expect to see the second transition. Even if the conversion to the insulating phase was incomplete, we would not expect to see a transition at 71 K but rather see a transition at 87 K and measure a severely reduced critical current. The laser modified film has a critical current of 3.6×10^{-4} A/cm² at 65 K. This is approximately 30 times lower than the unmodified film at the same temperature below its T_c . It is well known that reducing the oxygen content of $\text{YBa}_2\text{Cu}_3\text{O}_{7-x}$ depresses T_c and makes the material more resistive. Based upon theoretical calculations, the laser induced temperature rise is approximately 375-500 °C [7-8]. This temperature rise is in agreement with previous work in terms of removing oxygen from these thin film superconductors [9]. To confirm that the superconducting phase is only deficient in oxygen content and not the metal constituents, we placed the above sample in an oxygen plasma for approximately 1 hour [10]. The plasma was formed in a barrel reactor at a power level of 50 W and an oxygen pressure of 0.02 Torr. The resulting resistance versus temperature curve for the laser modified sample is shown in Figure 3b. Note that the curve is essentially identical to the unmodified curve in Figure 1. In some cases, the room temperature resistance is still slightly above the original unmodified film possibly indicating some irreversible laser induced damage, but the double transition has clearly disappeared leaving the single, higher transition of 87 K. We have also seen the room temperature resistance after plasma oxidation become lower than the original film even though the transition temperature is identical to the original, unmodified film. Currently, we attribute this to an incompletely annealed starting film, although it is still under investigation. In addition to the transport properties returning to those of the original film, the optical reflectivity also recovers. This can be seen in Figure 2b which is an optical micrograph of the same film shown in Figure 2a after plasma oxidation. The laser induced stripe is essentially erased with only a slight trace of where the beam wrote on the surface. It is possible that this

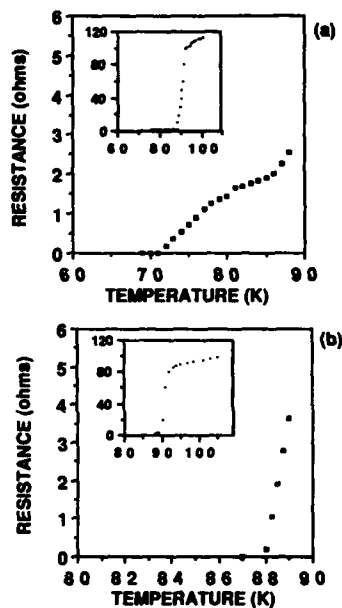


Figure 3. Resistance versus temperature data for the (a) laser modified film showing the characteristic double transition and (b) for the same film after plasma oxidation. Note the return of the electrical properties to those of the original film (Fig. 1).

slight trace is in fact some permanent laser induced damage.

The degree to which we can control the reduction of T_c using the in-situ monitoring of the room temperature electrical resistance is remarkable. In Figure 4, we have plotted the transition temperature for a variety of laser modified samples. The horizontal axis is a measure of the change in the room temperature resistivity in the laser modified region relative to the resistivity of the unmodified film. Note that slight changes in the film resistivity, e.g., less than a factor of 10, produce significant changes in T_c . Because the laser modified region is a small fraction of the total resistance being measured during the laser writing, changes in absolute resistance on typical films may only be 1-2 ohms. As a result, the in-situ monitoring is essential for controlling the degree to which the films are modified.

The data gathered for Figure 4 was obtained by a combination of varying the incident laser power and/or maintaining constant laser power and varying the number of scans. Some insight into the nature of the oxygen removal mechanism can be obtained by monitoring the change in room temperature electrical resistance as a function of the laser power or number of scans. In Figure 5, we have plotted the absolute resistance of a single sample (film/laser stripe/film) as a function of incident laser power with each data point indicating a single scan. The first scan occurs in the lower left portion of the graph with successive scans occurring at progressively higher laser powers. At a power level of 42 mW, 8 scans were made without increasing the laser power. As shown in the figure, each successive scan produced a smaller change in resistance. Not until the laser power is increased do we see another significant change in the resistance value. This change in resistance at this new power level will also decrease with successive scans as can be seen at 48.75 mW of incident laser power. The saturation of the change in resistance at a given laser power could be attributed to a diffusion mechanism where the surface oxygen atoms are readily removed while oxygen atoms deep in the film must diffuse to the surface. The increase in the resistance due to an increase in power may result from the increased laser induced temperature rise in the wings of the beam and effectively removing oxygen from a wider stripe. However, no broadening of the high reflectance stripe is seen under these conditions. At the present time, we do not understand the precise details of the laser induced oxygen removal and are continuing to explore it.

A significantly different effect from the data presented in Figure 4 can be seen in Figure 6. In this case, we have modified two independent Hall bars on the same sample. In the first case, shown by the solid line in Figure 6b, we have induced a resistivity change approximately 20 times that of the unmodified region

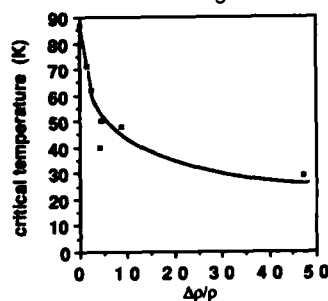


Figure 4. A graph of the variation in the critical temperature as a function of the laser induced change in room temperature electrical resistivity normalized to the unmodified film resistivity.

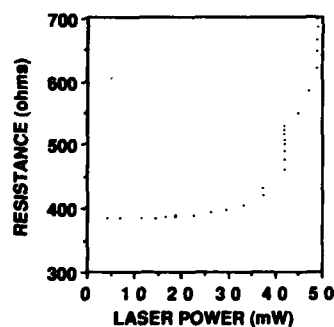


Figure 5. The resistance of a single sample as a function of each laser scan. The first scan occurs in the lower left portion of the graph with succeeding scans occurring at higher power levels.

whereas in the second case, shown by the dashed line, the resistivity change is approximately 280 times. In both of these cases, the second transition temperature, i.e., the transition corresponding to the laser modified stripe, is 76 K. Not only should a resistivity change of 20 produce a much lower T_c , the fact that both resistivity changes produce the same transition temperature is disconcerting. Critical current measurements on the first sample compared very favorably with the original film; $2 \times 10^4 \text{ A/cm}^2$ at 61 K for the laser modified film versus $4 \times 10^4 \text{ A/cm}^2$ at 75 K for the unmodified film. However, critical current measurements on the second film were impossible to obtain due to a spontaneous film failure in which the structure suddenly stopped superconducting while at cryogenic temperatures and remained in the non-superconducting metallic state. This experiment was repeated several times with the same result; over a very wide range of laser induced resistance changes, the transition temperature of the laser modified region was in the neighborhood of 76-80 K. However, on films with a large laser induced room temperature resistance change, the superconducting state was often unstable and did not last for more than a few hours. Failure of the high resistance films may be indicative of a very weakly connected superconducting path. Further analysis of the unmodified regions of the film via X-ray diffraction revealed the desired $\text{YBa}_2\text{Cu}_3\text{O}_{7-x}$ phase plus a small fraction of $\text{Y}_2\text{Ba}_4\text{Cu}_8\text{O}_{9-y}$. It is believed that the superconductivity in both the low resistivity and the high resistivity laser modified films is being carried largely by $\text{Y}_2\text{Ba}_4\text{Cu}_8\text{O}_{9-y}$ which is known to have a transition temperature near 80 K [11]. This would also agree with recent work [12] indicating that oxygen removal is considerably more difficult in $\text{Y}_2\text{Ba}_4\text{Cu}_8\text{O}_{9-y}$ than in $\text{YBa}_2\text{Cu}_3\text{O}_{7-x}$. The fraction of $\text{Y}_2\text{Ba}_4\text{Cu}_8\text{O}_{9-y}$ in this film is less than that which is required to maintain a percolation path in thin films. However, observations that the $\text{Y}_2\text{Ba}_4\text{Cu}_8\text{O}_{9-y}$ phase usually occurs as intergrowths in the $\text{YBa}_2\text{Cu}_3\text{O}_{7-x}$ phase [13] suggest that a smaller fraction of $\text{Y}_2\text{Ba}_4\text{Cu}_8\text{O}_{9-y}$ could still maintain superconductivity across the $5 \mu\text{m}$ laser modified region. One might ask how the critical current measurement could be so good for the first case if the supercurrent is being carried by a phase that is known to be only a small fraction of the total material. It must be remembered, however, that the critical current measurement on the unmodified film was measured at a temperature where the $\text{Y}_2\text{Ba}_4\text{Cu}_8\text{O}_{9-y}$ phase was barely superconducting and thus not contributing to the critical current measurement. If we have selectively removed the oxygen from the $\text{YBa}_2\text{Cu}_3\text{O}_{7-x}$ phase material and left the $\text{Y}_2\text{Ba}_4\text{Cu}_8\text{O}_{9-y}$ material intact, this opens up the possibility of some novel structures fabricated from multiphase materials. It is interesting to note that plasma oxidation of these films returned them to their

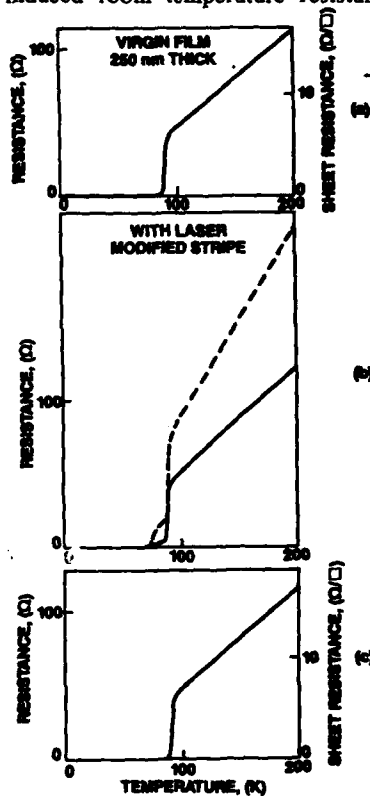


Figure 6. Transport data for a multiphase superconducting thin film. (a) Unmodified film. (b) Laser modified film. The solid line has a resistivity change of 22 while the dashed curve has a resistivity change of 280. (c) Plasma oxidized film.

original state. If we have selectively removed the oxygen from the $\text{YBa}_2\text{Cu}_3\text{O}_{7-x}$ phase material and left the $\text{Y}_2\text{Ba}_4\text{Cu}_8\text{O}_{9-y}$ material intact, this opens up the possibility of some novel structures fabricated from multiphase materials. It is interesting to note that plasma oxidation of these films returned them to their

original state as shown in Figure 6c.

CONCLUSION

We have shown that localized laser heating of $\text{YBa}_2\text{Cu}_3\text{O}_{7-x}$ thin films in a vacuum can produce a superconducting phase with a reduced transition temperature. Plasma oxidation returns the laser modified films back to their original superconducting state indicating the laser induced phase is oxygen deficient. By monitoring the room temperature electrical resistance in-situ, one can control the laser writing parameters necessary to achieve the superconducting state instead of the fully oxygen depleted semiconducting state. The laser modified region has a reduced critical current which suggests that this technique might be useful in fabricating weak link structures. The ultimate resolution of this technique is believed to be the laser induced temperature profile and under the proper conditions of incident laser power and spot size, submicron structures should be possible.

ACKNOWLEDGMENTS

We would like to acknowledge the encouragement and advice of our colleagues Philippe Barboux, Laura Greene, Jean-Marie Tarascon, Daniel Daly and John Rowell. We also acknowledge the committed technical support of Kervin Evans from Tougaloo College.

REFERENCES

1. J. G. Bednorz and K. A. Muller, *Z. Phys. B* **64**, 189 (1986).
2. M. K. Wu, J. R. Ashburn, C. T. Torng, P. H. Hor, R. L. Meng, L. Gao, Z. J. Huang, Y. Q. Wang and C. W. Chu, *Phys. Rev. Lett.* **58**, 908 (1987).
3. M. Rothschild, J.H.C. Sedlacek, J.G. Black and D.J. Ehrlich, *IEEE Elec. Dev. Lett.*, **9**, 68 (1988).
4. M. Rothschild, J.H.C. Sedlacek, J.G. Black and D.J. Ehrlich, *Appl. Phys. Lett.*, **52**, 404 (1988).
5. G. Liberts, M. Eyett and D. Bauerle, *Appl. Phys. A*, **45**, 313 (1988).
6. Siu-Wai Chan, B.G. Bagley, L.H. Greene, M. Giroud, W. L. Feldmann, K. R. Jenkin II and B. J. Wilkins, *Appl. Phys. Lett.*, **53** (1988) 1443.
7. I.D. Calder and R. Sue, *J. Appl. Phys.* **53**, 7545 (1982).
8. J. Heremans, D.T. Morelli, G.W. Smith and S.C. Strite III, *Phys. Rev. B*, **37**, 1604 (1988).
9. S. Uchida, H. Takagi, T. Hasegawa, K. Kishio, S. Tajima, K. Kitazawa, K. Fueki and S. Tanaka, in *Novel Superconductivity*, edited by Stuart Wolf and Vladimir Kresin (Plenum Press, New York 1987), p. 855.
10. B.G. Bagley, L.H. Greene, J.-M. Tarascon, and G.W. Hull, *Appl. Phys. Lett.*, **51**, 622 (1987).
11. K. Char., M. Lee, R.W. Barton, A.F. Marshall, I. Bozovic, R.H. Hammond, M.R. Beasley, T.H. Geballe, and A. Kapitulnik, *Phys. Rev.*, **B38**, 834 (1988).
12. K. Char, private communication.
13. A.F. Marshall, R.W. Barton, K. Char, A. Kapitulnik, B. Oh, R.H. Hammond and S.S. Laderman, *Phys. Rev.* **B37**, 9353 (1988).

SELECTIVE-AREA LASER PHOTODEPOSITION OF TRANSPARENT CONDUCTIVE SnO₂ FILMS

R.R. KUNZ, M. ROTHSCCHILD, and D. J. EHRLICH
Lincoln Laboratory, Massachusetts Institute of Technology,
244 Wood Street, Lexington, MA 02173

ABSTRACT

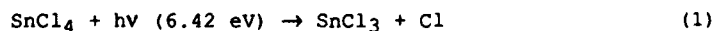
The deposition of SnO₂ films has been demonstrated using an ArF (193-nm) excimer laser to drive the photochemical reactions of mixed SnCl₄ and N₂O vapors. Without any annealing, films 100 nm thick grown on room-temperature substrates have resistivities as low as 0.04 Ω-cm. The optical bandgap of 3.20 eV and transmission cutoff wavelength of 330 nm compare favorably with films obtained using alternate higher temperature techniques. The maximum temperature excursion during the 20-ns laser pulse is estimated to be 300 to 400 °C.

Introduction

The unusual combination of high visible-wavelength transparency and good electrical conductivity has made SnO₂ films important for, among other applications, optoelectronic devices [1], resistive heating elements [2], and barrier layers for solar cells [3]. The thin films necessary for such devices can be deposited with the usual sputter, evaporation, and chemical vapor deposition techniques [4], but these require high processing temperatures or post-deposition annealing to obtain the desired properties. This letter reports the laser photochemical deposition of SnO₂ to yield highly conductive and transparent thin films of SnO₂ at low substrate temperatures and without annealing. As with other photodeposition processes [5], selective-area growth can be achieved by patterned surface irradiation.

Experimental

The films were deposited using SnCl₄ and N₂O as the reactants on room-temperature fused silica substrates which also served as input windows. An ArF excimer laser (193 nm) was the photon source. At 193 nm, SnCl₄ undergoes photodissociation via [6]



with an absorption cross section [6] in the vapor phase, of $3.8 \times 10^{-17} \text{ cm}^2$. Subsequent photochemical reactions of SnCl₃ may strip further Cl atoms from the trichloride radical. N₂O undergoes photodissociation to form N₂ and metastable oxygen



The vapor phase absorption cross section [7] at 193 nm for reaction (2) is $7.9 \times 10^{-20} \text{ cm}^2$. We note that both of these vapor reactants adsorb strongly on SiO_2 surfaces, with unknown consequences to the photochemical channels.

Results

Initial experiments were performed using 0.75 Torr SnCl_4 and 50 Torr N_2O , and a laser fluence of 20 mJ/cm^2 per pulse. Under these conditions, the photochemical reactions result in two solid products. The first is a moisture-sensitive white powder which collects on all surfaces. Fourier transform infrared spectroscopy (FTIR), Auger electron spectroscopy, and solubility analysis reveal this powder to be predominantly SnOCl_2 . Figure 1 shows the FTIR spectrum of this product, where it is shown compared to that of SnOCl_2 as previously reported [8]. The second product is observed only where the beam irradiates the fused silica surface. It is conductive and, on the basis of evidence below, is identified as primarily SnO_2 .

The resistivity of the SnO_2 films is shown as a function of laser fluence in Figure 2; the laser pulse rate was 5 Hz and the total number of pulses was 10^4 . Note that a minimum laser fluence of 10 to 20 mJ/cm^2 per pulse is needed to form conductive SnO_2 ; below this only SnOCl_2 is formed. At laser fluences greater than 70 to 80 mJ/cm^2 per pulse, ablation of the film is observed and little SnO_2 is deposited.

Figure 3 shows the SnO_2 film thickness versus the number of pulses at a laser fluence of 20 mJ/cm^2 per pulse; note that the film thickness begins to saturate with dose at $\sim 100\text{-nm}$ thickness. The 193-nm absorption coefficient of these films was measured to be $1.5 \times 10^5 \text{ cm}^{-1}$, corresponding to an absorption length of 67 nm. From Figure 3, the maximum film thickness achievable appears to be approximately two absorption lengths. This is expected since the beam irradiates the reaction volume through the growing film, and hence film growth slows when the laser irradiation becomes seriously attenuated. A slightly more detailed analysis shows that the reaction rate reduction scales approximately as the Beer's - Law attenuation and is consistent with film growth limited by a photochemical channel dependent linearly on transmitted intensity.

The curve indicating the total SnO_2 thickness in Figure 3 (squares) is not representative of the conductive SnO_2 layer thickness. Rather, a fraction of the SnO_2 layer consists of poorly adherent, powdery SnO_2 (confirmed by wet etch resistance). This layer can be easily removed via polishing, leaving behind a hard, conductive, adherent SnO_2 layer. The thickness of the hardened layer is shown in the lower curve of Figure 3 (circles),

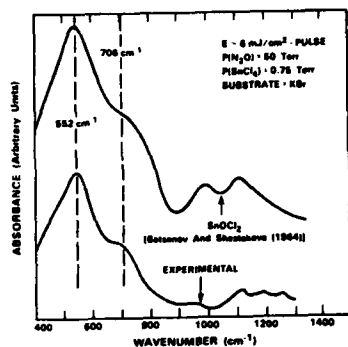


Figure 1. Fourier transform infrared spectrum of SnOCl_2 formed via photolysis of SnCl_4 and N_2O at 193 nm.

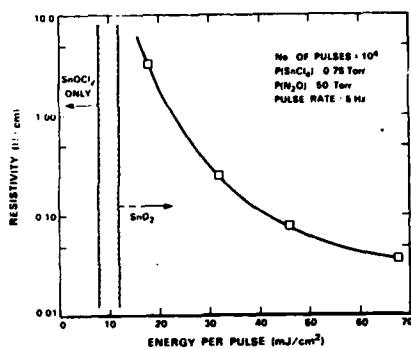


Figure 2. Tin oxide resistivity versus the laser fluence used during growth. For each point, the total number of pulses was fixed at 10^4 , the SnCl_4 pressure was 0.75 Torr, the N_2O pressure 50 Torr, and the laser pulse rate was 5 Hz.

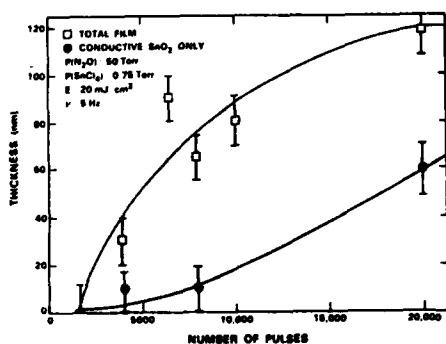


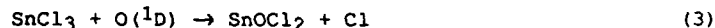
Figure 3. Tin oxide total film thickness versus the number of pulses at a constant fluence of 20 mJ/cm^2 per pulse. The gas pressures and laser repetition rate are the same as in Figure 2.

where the shaded area represents the poorly conductive SnO₂ layer thickness.

The optical absorption coefficient of a laser-deposited film versus photon energy was measured. The cutoff energy was 3.7 eV (330 nm), well within the range of good films deposited by other means. Heating to 550 °C for two hours in air is a fairly common post-deposition treatment to maximize the conductivity [9] of conventionally deposited SnO₂. It is interesting to note that this anneal had little effect on either the optical absorption or the resistivity of the laser photodeposited films. By plotting this data in a similar fashion to Spence [10], the bandgap was determined to be 3.2 eV for the as-deposited film and 3.1 eV for the annealed film. Each is quite close to the reported [11] value of 3.54 eV for pure, crystalline SnO₂. Auger spectroscopy showed there to be undetectable (less than 1%) chlorine in the as-deposited film. Although the actual concentration of chlorine was not measured, its presence even at less than 1% levels may effect the electrical properties of the films [12].

Discussion

The deposition process is initiated by the photochemical reactions (1) and (2). Among the many possible vapor-phase reactions involving the photoproducts, reaction (3)



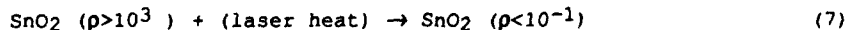
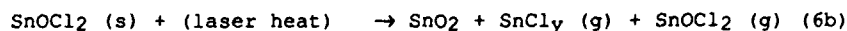
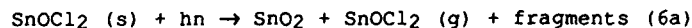
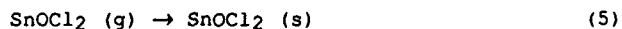
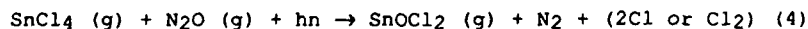
is known to occur. Calculation of the gas phase density of SnOCl₂ after each laser pulse, based on reactant pressures and absorption cross sections, photon flux, and rate constants [13] results in a calculated SnOCl₂ concentration of $3 \times 10^{15} \text{ cm}^{-3}$ (limited by the availability of atomic oxygen). If one-sixth of the SnOCl₂ were to condense on the fused silica window, this would correspond to $5 \times 10^{14} \text{ cm}^{-2}$ SnOCl₂ molecules on the surface, or approximately a half monolayer before the next pulse. Figure 3 shows that, initially, a ~0.01-nm thickness of SnO₂ is deposited per pulse. This suggests that only a small fraction (< 5%) of the SnOCl₂ molecules adsorbed on the window actually react to form SnO₂. The remaining fraction undergoes evaporation and secondary reactions resulting in revaporization.

The absorption coefficient of fused silica at 193 nm is of the order 10^{-3} cm^{-1} , whereas those of SnOCl₂ and SnO₂ are (by our measurements) $3 \times 10^5 \text{ cm}^{-1}$ and $1.5 \times 10^5 \text{ cm}^{-1}$, respectively. As a result, 193-nm substrate absorption is dominantly in an oxychloride adsorbed layer even at submonolayer thickness. The temperature rise due to the laser pulse depends strongly on the condensed-layer thickness. If it is assumed that the dominant absorbing layer is SnOCl₂, calculation of the temperature rise indicates that the maximum temperature during the laser pulse at 50 mJ/cm² per pulse is less than 150 °C for SnOCl₂ layers less

than 4 nm thick. The thermal conversion to the oxide cannot occur at these thicknesses since SnOCl_2 thermally decomposes into SnO_2 only at temperatures greater than 150 °C [8]. However, a photochemical conversion is not ruled out. Once the growing oxychloride film becomes thick enough to absorb a significant portion of the laser energy, the laser-induced temperature rise can exceed 150 °C and the formation of SnO_2 can proceed via a thermally activated mechanism. Thermal analysis places an upper bound of 300-400 °C on the peak laser-induced temperature of a fully attenuating film at the maximum laser power of the experiment which is 70 mJ/cm² per pulse.

A subsequent photoprocess, perhaps a photothermal reaction, appears to be essential to achieve good material properties since, when low-fluence laser pulses are used, the films never acquire low values of resistivity (see Figure 2). Evidence for a thermal reaction is supported by recent UV-lamp-induced growth of SnO_2 from SnCl_4 , where substrate temperatures in the range of 300-400 °C were required to obtain comparable resistivities [14]. The nature of this mechanism is unclear, but may involve out-diffusion of chlorine, recrystallization, or subtle changes in stoichiometry. The benefits of high-fluence irradiation observed here do not depend upon vapor-phase formation of oxygen atoms, as is thought to be the case for UV photochemical annealing of tantalum oxide [15]. Several samples of SnO_2 were prepared using only 5×10^3 pulses at 20 mJ/cm² per pulse (see Figure 2). The samples were then irradiated with another 10^4 pulses, one sample in 500 Torr helium, another in 500 Torr N_2O . In spite of the efficient generation of oxygen atoms in the latter case, the resulting resistivities for the two ambients were virtually identical (0.57 Ω-cm). This suggests strongly that the annealing mechanism is photothermal. Figure 3 clearly illustrates this annealing by plotting the fraction of the SnO_2 layer that exhibits good adhesion, hardness, and conductivity as a function of the annealing time (number of pulses). The conversion of the film properties due to laser exposure is evident as the conversion continues even after the net film growth stops.

The overall reaction scheme can now be summarized



where reaction (6a) represents a photochemical conversion and y is an integer ≤ 4 , and reaction (6b) represents a photothermal reaction that takes place once film growth begins. Reaction (7) is the laser annealing step.

Conclusion

In summary, selective-area photodeposition of SnO_2 with resistivity as low as $0.04 \Omega\text{-cm}$ has been demonstrated with an ArF excimer laser. Based on previous studies, even lower resistivity may be possible through the incorporation of dopants such as indium, antimony or fluorine during film growth. The mechanism for the film formation is thought to be through the photochemically activated vapor-phase reaction of SnCl_4 and N_2O to form SnOCl_2 . The SnO_2 is grown via the decomposition of thin layers of the SnOCl_2 that accumulate between laser pulses. The transient (20-ns-duration) temperature of the surface does not exceed 300 to 400 °C throughout the film growth and does not penetrate significantly into the substrate. The optical bandgap of 3.2 eV and transmission cutoff wavelength of 330 nm compare favorably with films deposited by other means.

Acknowledgment

This work was sponsored by the Defense Advanced Research Projects Agency and by the Department of the Air Force, in part under a specific program supported by the Air Force Office of Scientific Research.

References

1. H. Iida, N. Shibata, T. Mishuku, A. Ito, H. Karasawa, and Y. Hayashi, IEEE Electron Device Lett. EDL-4, 157 (1983).
2. C. Mellor and K. A. Petersen, U.S. Patent Applied Docket No. 85-1-153 (Sept. 1987).
3. D. K. Schroder, IEEE Trans. Electron Devices 25, 90 (1978).
4. J. C. Manificier, Thin Solid Films 90, 297 (1982).
5. A review may be found in Laser Microfabrication: Thin-Film Processes and Lithography, edited by D. J. Ehrlich and J. Y. Tsao, (Academic Press, New York, 1989).
6. J. Fernandez, G. Lespes, and A. Dargelos, Chem. Phys. 111, 97 (1987).
7. C. Hubrich and F. Stuhl, J. Photochem. 12, 93 (1980).
8. S. S. Batsanov and N. A. Shestakova, Izv. Akad. Nauk SSSR, Neorg. Mater. [Inorg. Mater. (USSR)] 2, 110 (1966).
9. R. Banerjee and D. Das, Thin Solid Films 149, 291 (1987).
10. W. Spence, J. Appl. Phys. 38, 3767 (1967).
11. S. Samson and C. G. Fonstad, J. Appl. Phys. 44, 4618 (1973).
12. J. A. Aboaf, V. C. Marcotte, and N. J. Chou, J. Electrochem. Soc. 120, 701 (1973).
13. S. T. Amimoto, A. P. Force, R. G. Gulotty, and J. R. Wiesenfeld, Chem. Phys. 71, 3640 (1979).
14. T. Tabuchi, K. Yamagishi, and Y. Tarui, Jpn. J. Appl. Phys. 26, L186 (1987).

15. M. Matsui, S. Oka, K. Yamegishi, K. Kuroiwa, and Y. Tarui,
Jpn. J. Appl. Phys. 27, 506 (1988).

LASER-INDUCED MULTI-CRYSTALLIZATION OF THIN GERMANIUM FILMS

C. ORTIZ,* K.A. RUBIN,* AND S. AJURIA**

*IBM Research Division, Almaden Research Center, 650 Harry Road, San Jose, California 95120-6099

**Materials Science and Engineering Department, Massachusetts Institute of Technology, Cambridge, Massachusetts 02139

ABSTRACT

We report here the crystallization kinetics of thin (35nm and 60nm) amorphous as-deposited Ge films using diffraction limited laser beam irradiation and laser pulses between 30ns and 1mS. The recrystallization of crystalline as-deposited films was also studied for similar laser conditions. Crystallization was observed for pulses as short as 50ns. We conclude that the use of small beam spots ($\sim 1\mu\text{m}$) gives a very different crystallization morphology from that observed previously for larger beam diameter and same laser pulse length. In our case for short irradiation times, the nucleation process dominates over crystal growth. Laser irradiation of as-deposited crystalline films produced grains with significantly less defects than grains crystallized from as-deposited amorphous films. Temperature calculations allow us to understand these results by showing that only the small spot irradiation sustains the material at high temperature for times comparable to the pulse width.

INTRODUCTION

We report the crystallization kinetics of thin Ge films using diffraction limited laser beam irradiation and laser pulses between 30ns and 1mS. Both amorphous and fine grain polycrystalline films were studied. The experiments presented here used thin (35nm and 60nm) films of germanium on Si_3N_4 membranes.

EXPERIMENTAL

In our study, the substrates were customized for TEM analysis: Germanium films, 35 and 60nm thick, were deposited by electron beam evaporation on 150nm thick Si_3N_4 membranes. Films deposited at room temperature were amorphous; those deposited at 500°C were polycrystalline with average grain size $\sim 20\text{nm}$.

The irradiation was carried out in air with a Krypton laser ($\lambda = 647\text{nm}$). A high quality, 0.47 NA lens was overfilled by the gaussian profile laser beam. This produced a diffraction limited spot of theoretically $1.7\mu\text{m}$ diameter ($1/e^2$). This small spot size was confirmed by optical microscopy. The focus was maintained on the sample by means of an automatic servo control using a separate GaAs laser. The Krypton laser was used to both optically monitor and induce the phase transformations. The laser irradiation was performed through the nitride layer at a variety of laser powers and pulse lengths, controlled by an extra-cavity acousto-optic modulator. The experiment consisted of single pulses whose duration and power was controlled by a computer. The laser pulses ranged between 30ns and 1mS. The maximum power incident on the sample was 40mW.

RESULTS AND DISCUSSION

Figures 1a and 1b show the effect of the laser irradiation for a 35nm thick, amorphous Ge film for laser pulses of 100ns and 100 μ s, respectively. The short pulses (under or equal to 200ns), as Fig. 1a shows, produce a crystallized area with a random distribution of crystallites in the central region, finer grain structures further away from the center, and an irregular perimeter which enclose some amorphous material. This indicates that the laser pulses have induced nucleation; a result that differs from results obtained by others in thicker unsupported films, where pulses of the same duration predominantly induced grain growth [2].



Figure 1. Crystallization of 35nm amorphous Ge. (a) 38mW, 100ns laser pulse. Outer crystallites are mixed with amorphous material. Morphology is typical of short pulse irradiation. (b) 6.5mW, 100 μ s pulse. Note helical grains forming concentric rings surrounding central ablated region. Ablation always occurred with crystallization for these long times and this thickness.

Laser pulses of 1 μ s or longer produce a crystallized area having a circular shape with smooth edges. The appearance indicates that a cooperative crystallization front propagates outward, a result reported previously [2] for nanosecond pulses and unsupported films. Figures 2a and 2b show the crystallization for a 60nm thick sample irradiated for 100 μ s at two different laser energy densities. The central area has a radial structure with elliptically shaped crystallites which contain a high density of defects. At the edge of this zone, a thin concentric area with very small crystallites is present as shown in Fig. 2a.

The most dramatic result for longer pulses and higher laser power densities was the multiple concentric crystalline rings. These were observed only in the amorphous samples and only for pulses of 10 μ s or longer. The number of rings increased with pulse width or sample thickness (60nm) as shown in Figs. 1b and 2b. The periodicity of each ring increased with distance from the irradiation center which implies that grain growth was favored over nucleation. Note that the rings which were observed previously were equally spaced and crumpled due to stress. Since our laser pulses are very long, our material has time to relax structurally. In fact, amorphous Ge has been



Figure 2. Irradiation of a 60nm amorphous Ge film. (a) 2.5mW, 100 μ s pulse. Note radial crystal growth. Edge consists of tiny crystals. (b) Effect of increase of laser power. Note central radial grains surrounded by concentric rings. Ablated spot was carried by 4.8mW incident and 100 μ s long pulse and nonablated spot was from 3.6mW, 100 μ s pulse.

found to relax continuously to a lower free energy state [3]. It has been shown by Raman spectroscopy of Si, which is very similar to Ge, that these continuous relaxation states are related to the average bond angle distortion of the lattice network [4]. The heat liberated by crystallization of germanium is 83.6 cal/gm, which is large. However, it is not enough to maintain this multi-event crystallization without additional heat from the laser. The crystals in these outer concentric rings grow with a helical direction to the interface where the small crystallites just discussed appear to play a major role in the nucleation of the crystalline rings. The strange growth direction has been interpreted in electron beam induced explosive crystallization of a-Ge films to be due to the significant radial temperature gradient [5]. A second explanation could be the presence at this interface of a convection effect due to the discontinuity of the thermal gradient defined by the beam profile, the diffused heat and the heat of crystallization. In fact, very often convective effects have been observed in crystals growing from the melt [6].

Finally, irradiation of films which were crystalline as-deposited with conditions which were similar to those used for the amorphous as-deposited case resulted in dramatically different crystalline morphologies. Figure 3 shows these results for a 30nm thick polycrystalline sample irradiated for 100 μ s. The nonirradiated area consists of grains with an average size of 140nm. The irradiated area consists of large recrystallized grains with very few defects. No extra concentric zones were ever observed. When the laser-melted spot recrystallized, there was no additional energy gain to be obtained from the polycrystalline surroundings. Thus, the diameter of the laser recrystallized region is limited in size to the area initially melted by the laser. Several grains nucleated independently and the crystal growth was competitive resulting in irregular grain boundaries and equiaxed grain shape.

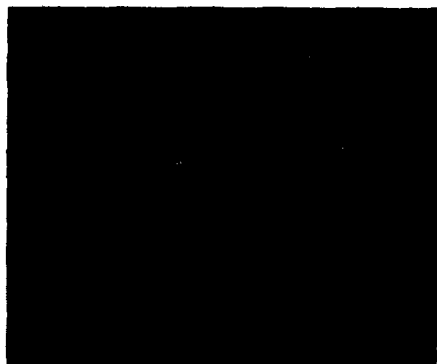


Figure 3. Laser irradiation of 30nm crystallized Ge film. The power was 9mW and the laser pulse 100 μ s. Laser recrystallization of melted region produces grains with much less defects than amorphous as-deposited film.

Finite difference calculations were performed using a three-dimensional solution to the diffusion equation to model the temperature profiles during heating and cooling due to laser irradiation.

Figure 4 presents the calculations which were performed to understand the result of short crystallization pulses for our experimental configuration and that of Bostanjoglo [7]. The structure corresponding to our experimental configuration was denoted as A and consisted of 35nm Ge/150nm Si₃N₄. Pulses of 100ns A₁ and 1000ns A₂ duration and FWHM diameter of 0.77 μ m were modelled. The structure corresponding to that of Bostanjoglo et al. was denoted as B and consisted of 90nm Ge freely suspended. A 3.7W, 25ns pulse with 15 μ m FWHM diameter was assumed to be absorbed. This is consistent with the experimental pulse used [7]. A qualitative comparison of the time the heat remained in the spot was obtained by calculating the temperature versus time for a maximum temperature rise of 700°C at the end of the pulse at radii of 0.45 μ and 9.5 μ for A and B, respectively. The actual crystallization temperature will vary with the time the heat is applied and the film thickness [8], but will be near 700°C. The temperature of A₁ cooled 20% to 560°C 15ns after the end of the 100ns pulse. However, B required 2200ns to cool to 560°C after the 25ns pulse ended. Thus, the experiments using structure B correspond to crystallization of a-Ge in the μ s regime with the configuration A. This is the reason why we observed a morphology similar to that of Bostanjoglo with pulses of 1000ns or more duration. The temperature versus time for a 1000ns pulse A₂ is also plotted. We see that the temperature is within 20% of maximum after 525ns. The majority of the heat in structure B is removed by lateral diffusion. Since the diameter of the irradiated region is approximately 20 times larger than A it takes longer for the heat to leave.

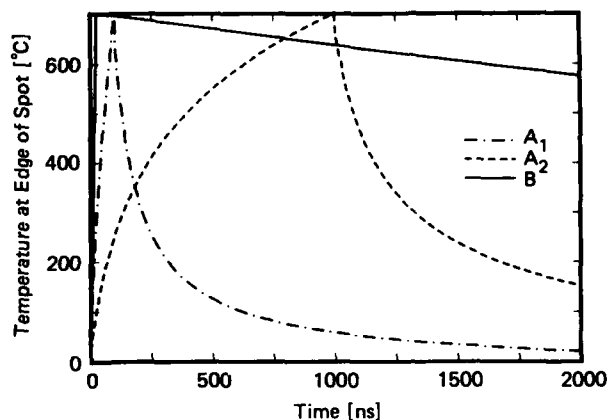


Figure 4. Calculated temperature versus time corresponding to the experimental conditions: A_1 (13.3mW, 100ns), A_2 (4.9mW, 1000ns). Sample is 35nm Ge/150nm Si_3N_4 , with a laser beam diameter of $0.77\mu\text{m}$ FWHM. Temperature measured at $0.45\mu\text{m}$ from the spot center. B (3.7W, 25ns). Powers are absorbed values. Sample is 90nm Ge irradiated with a laser beam diameter of $15\mu\text{m}$ FWHM. Temperature measured at $9.55\mu\text{m}$ from the center. Note the much longer cooling time of B compared to A_1 .

CONCLUSION

The effect of diffraction limited laser beams, pulse width and power on the crystallization morphology of germanium was examined. Crystallization was observed for 50ns pulses. Laser irradiation of as-deposited crystalline films produced grains with significantly less defects than grains crystallized from as-deposited amorphous films. Two different morphologies were evident within the laser crystallization of amorphous samples for laser pulses shorter or longer than $1\mu\text{s}$.

The length of the laser pulse determined whether nucleation or grain growth was the main crystallization process. Short or long irradiation times resulted in nucleation or grain growth dominated crystallization, respectively.

The longer pulses gave a complex morphology which is similar to the previous reported nanoseconds regime where the crystal growth process is dominant. The microstructure from shorter pulse irradiation was new. We could explain this result by calculating the temperature versus time and show that the use of diffraction limited beams and nanoseconds, results in a very different time duration of the sample at high temperature.

ACKNOWLEDGMENTS

The authors would like to thank H. Smith and M. Chen for their helpful comments.

REFERENCES

- [1] K.A. Rubin, R.W. Barton, M. Chen, V.B. Jipson and D. Rugar, *Applied Physics Letters* **50**, 1488 (1987).
- [2] O. Bostanjoglo and E. Endruschat, *Phys. Stat. Sol. (a)* **91**, 17 (1985).
- [3] E.P. Donovan, F. Spaepen, D. Thurnbull, J.M. Poate and D.C. Jacobs *J. Appl. Phys.* **57**, 1795 (1985).
- [4] W.C. Sinke, T. Warabisako, M. Miyao, T. Tokuyama, S. Roorda and F.W. Saris, "MRS Symposium A", (1987) in press.
- [5] R.K. Sharama, S.K. Bansal, R. Nath, R.M. Mehra, K. Bahadur, R.P. Mall, K.L. Chaudhary and C.L. Garg, *J. Appl. Phys.* **55**, 387 (1984).
- [6] W. Wilcox, *J. Crystal Growth* **65**, 133 (1983).
- [7] O. Bostanjoglo, R.P. Tornow and W. Tornow, *Ultra Microscopy*, **21**, 367 (1987).
- [8] P. Pierrard, B. Mustafschiev, W. Marinc, J. Marfaing and F. Salvan, *Thin Solid Films* **141**, (1984).

**PULSED LASER CLEANING OF ANTIMONY
SINGLE CRYSTAL <111> SURFACE**

Etienne J. PETIT, Roland CAUDANO
L.I.S.E., Facultés Universitaires N-D de la Paix, rue de Bruxelles, 61,
B-5000 NAMUR (Belgium)

ABSTRACT

The <111> face of an antimony single crystal was irradiated under ultra-high-vacuum conditions by the 193 nm radiation of a high-power excimer laser. The effects of the laser beam on the sample as a function of the light Energy Density (ED) and of the annealing Repetition Number are presented.

Surface studies by Auger electron spectroscopy, scanning electron microscopy and low energy electron diffraction show that an atomically clean and well ordered surface can be produced by this method. A strong chemical reduction is induced by pulsed laser annealing above 100 to 130 mJ/cm². Surface analysis shows that, for an ED less than 500 mJ/cm², the surface evaporates without melting deeper than 200 nm. Evidences for oxide modification and for organic molecule desorption were observed even after irradiations with an ED as low as 45 mJ/cm².

The surface reduction is described by a thermal model involving surface heating and subsequent evaporation of the oxide layer. The desorption and diffusion processes may involve both thermal and photolytic mechanisms.

INTRODUCTION

The native oxides on the <111> face of an antimony single crystal have been irradiated by the 193 nm radiation of a high-power excimer laser under Ultra-High-Vacuum (UHV) conditions. Surface analysis by Auger Electron Spectroscopy (AES), Scanning Electron Microscopy (SEM) and Low Energy Electron Diffraction (LEED) was performed *in-situ* to study the effects of the Pulsed Laser Annealing (PLA) parameters (i.e. the number of exposures to the laser beam, hereafter called the "Repetition Number" (RN) ; and, the Energy Density (ED) of each exposure to the laser beam). We show in section 2 that the pulsed laser annealing is a powerful technique and that it can provide flat and atomically clean surfaces. A thermal model description of the observed results is considered in the third section. The numerical simulations provide a useful insight into the basic mechanisms involved in the superficial modifications.

EXPERIMENTAL CONDITIONS

The Sb <111> surfaces from an ultra-pure single crystal were oxidized one month in air, mechanically polished with one micrometer alumina powder, and rinsed in alcohol before being introduced into the vacuum vessel (background pressure : 10⁻⁸ P during analysis, 10⁻⁶ P during PLA). The samples were irradiated with the 30 ns pulsed beam of a high-power excimer laser (emission at 193 nm). The length of the square areas side homogeneously irradiated, ranges between 0.2 and 1.2 mm. The cylindrical mirror electron analyser used for AES has 0.4 % relative resolution. The SEM analysis was performed by imaging the absorbed electronic current from the electron gun of the scanning Auger microscope (30 μm resolution). The LEED diagrams were observed by means of a four grids retarding field analyser.

EXPERIMENTAL RESULTS

SEM observations

The image showed a decrease of the secondary electron emission (SEE)

from the irradiated surface. The contrast became noticeable when the sample was irradiated three times with an ED of 45 mJ/cm^2 ; only once, at an ED of 65 mJ/cm^2 ; and always after treatment at higher ED or higher RN. Exposed surfaces looked flat and displayed sharp borders. However, over 500 mJ/cm^2 , the decrease of the SEE yield extended beyond the irradiated area. No crater formation was observed though. 200 nm deep lapping defects seemed to be sites of preferential laser sputtering and did not disappear even at the highest irradiation ED.

LEED observations

A diffuse LEED pattern could be observed after 50 PLA at 300 mJ/cm^2 . No peculiar surface reconstruction was obvious.

Auger analysis

Figures 1 and 2 present the evolution of the intensities of the Auger signal of C, O, semi-metallic Sb and Sb oxides versus RN (1, 3, 10, 50), and fig 3, versus the ED of a single irradiation, and after one (A) and fifty (B) laser shots. No other element was detected at the surface.

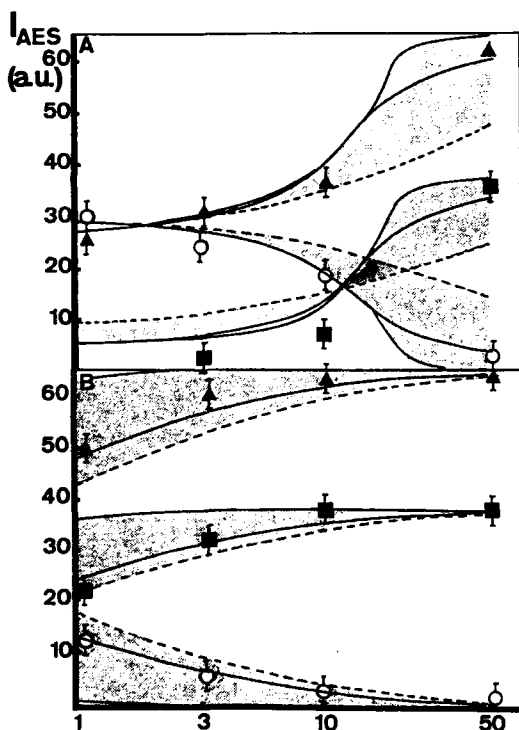


Fig 1. The effect of the repetition of the PLA on the surface composition observed by AES at 135 mJ/cm^2 (A) and 200 mJ/cm^2 (B).

The black symbols represent the semi-metallic Sb : the triangle, the Auger line at 465 eV, the square the 27 eV line. The white symbols designate Sb oxides at 442 eV (triangles) and at 25 eV (squares). The oxygen Auger signal at 510 eV is displayed by an O; the carbon one at 272 eV, by a "C".

The effect of the repetition number

Figures 1A and 1B show that a repeated laser annealing with ED greater than 135 mJ/cm^2 leads progressively to a similar surface composition free of contamination. At an ED of 500 mJ/cm^2 , the surface is completely cleaned after the first exposure.

Between 45 and 65 mJ/cm^2 (fig 2), the repetition of the irradiation contributes mainly to decrease the superficial carbon concentration. During this cleaning the Auger signal intensities of oxygen and of the NNN and the MNN lines of antimony oxides first increase slightly and reach a situation which may be interpreted as a clean oxide surface, before decreasing again.

Since the semi-metallic Auger signal remains constant, this behavior is related to a modification of the nature of the oxide.

The effect of the ED parameter

Figure 3. presents the effect of the ED parameter on the superficial atomic composition and on the chemistry after one and fifty laser shot(s) respectively. The ED scales report the ED of a single laser

irradiation. The variation of the apparent threshold ED for chemical reduction versus RN clearly appears. A general increase of the intensities of Auger signals indicated on fig 3.A. by the large dashed line is observed after the one shot PLA below 70 mJ/cm². It is caused by an increase of the yield of the electron avalanche induced by the primary electron beam excitation and by the decrease of the superficial SEE yield.

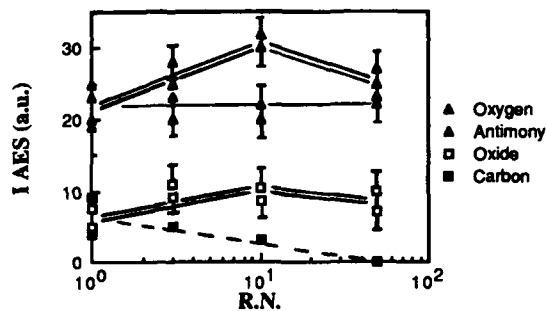


Fig 2. Same as Fig 1., between 45 and 65 mJ/cm².

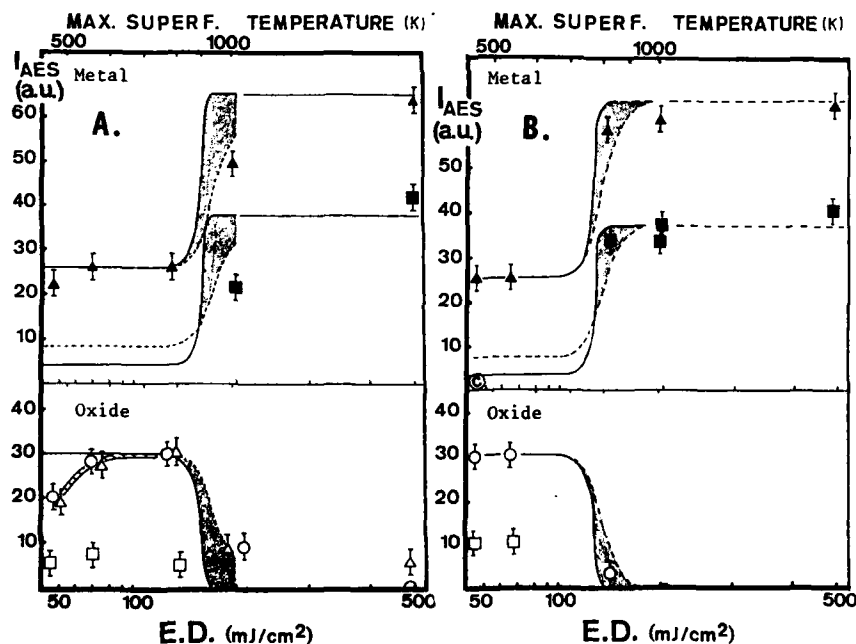


Fig 3. The effect on Auger signal of the ED, respectively, after one (A) and fifty (B) exposures to the laser beam. The lines present the results from numerical simulations (see text).

Summary of the experimental observations

The observations show that the surface is not deeply (<200nm) melted during pulsed irradiation with ED lower than 500 mJ/cm², but that heating plays a significant role, and that the oxides progressively leave the surface when ED exceeds 130 mJ/cm². These first conclusions suggest to us a thermal-model description of the ablation process.

Below 100 mJ/cm², the surface organic contamination is easily removed; however, 50 laser shots slightly modify the superficial composition of the oxide, as observed by AES. The PLA treatment seems to be more efficient than the usual thermal annealing in UHV for removing the carbon contamination [1], since no ion milling is needed.

The SEE yields of oxides are known to be larger than those of metals. The correlation between the SEE yield decrease, the modification of the nature of the oxide (fig 2), and the increase of the Auger electron yield (fig 3), observed after PLA at low fluences, is evidence of the oxide diffusion towards the bulk.

SIMULATIONS

Preliminary

Substrate heating and heat conduction are the more energy consuming mechanisms since :

- the complete reduction or evaporation of a 100 nm thick oxide layer needs a fraction less than 10⁻³ of the deposited energy.
- The photoemission process takes less than several percent of the light energy [2].

Moreover, since the oxide layer is thinner than the heat diffusion depth during the irradiation : $e < \sqrt{4Dt_p}$ ($t_p = 30$ ns), heating is driven by the thermal properties of the substrate [3].

The simple thermal modeling

Assuming constant optical and thermal properties of the material during heating up to the melting temperature, the heat equation is linear (linear maximum superficial temperature rise versus ED). In such condition, the superficial temperature rise ($dT(K)$) is related to the ED (mJ/cm²) by the following formula :

$$dT = (1-R) * \frac{ED * 5.20}{d * Cp * \sqrt{D}}$$

where R denotes the reflectivity; d , the density (6.7 g/cm³ for Sb); C_p , the specific heat (0.23 J/g K); D , the thermal diffusivity (0.12 cm²/s). The number 5.20 refers to a comparison with the GaAs thermal properties and its behavior under PLA [4]. This approximation has been confirmed by more extensive calculations as represented on figure 4. for a 30 ns-gaussian laser pulse whose width is 2 nm. In this case, the total ED is 100 mJ/cm². The center of the 30 ns long gaussian time profile of the

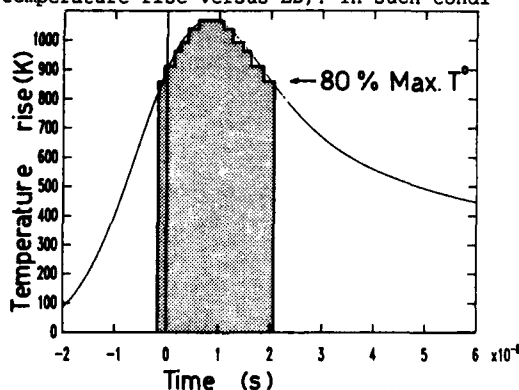


Fig 4. The computed superficial temperature rise caused by a 100 mJ/cm² exposure on an antimony single crystal.

laser pulse coincides to the origin of the time scale [5].

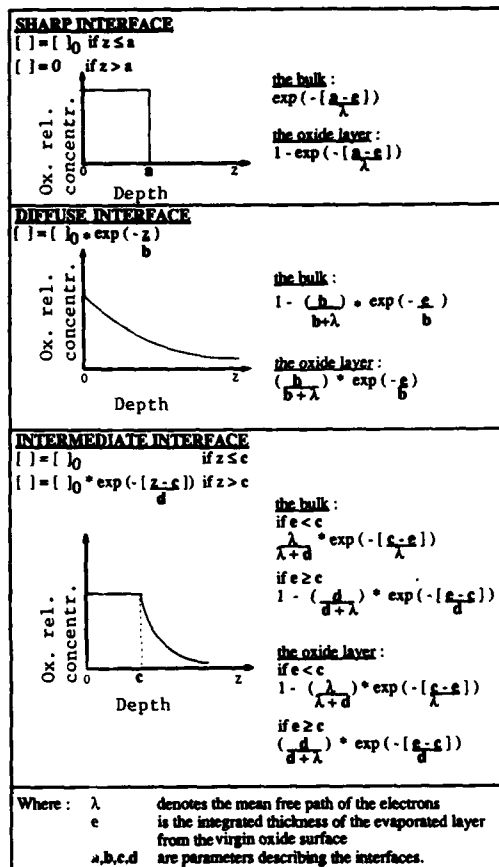


Fig 5. Analytical expressions for the computation of the Auger signal intensities relative to one from a bulk sample and coming from the bulk and from the oxide layer.

The calculation of the total amount of evaporated material, based on the LANGMUIR - KNUDSEN - HERTZ equation, includes the vapor pressure (P_v) dependance on the temperature. The total amount of material evaporated was approximated by a finite series over the temporal thermal profile of the surface as shown in Fig 4 by the bold line and grey area. We used the data from table I [6]. The evaporation rate, Q (at/s), is given by:

$$Q = P_v \cdot (2\pi \cdot m \cdot kT)^{-0.5}$$

where m is the molecular mass; k , the Boltzman constant; and, T , the absolute temperature. The vapor pressure depends strongly on temperature:

$$P_v(T) = 10^{\frac{A}{T} + B}$$

At the same temperatures the evaporation rate of antimony tetramers is 30 to 100-fold less than that of Sb_4O_6 . We have approximated the variation of the sputtering rate during the oxide layer evaporation assuming that it linearly evolves from the oxidic state rate to the one of the semi-metallic state versus the surface composition. This evaluation is exact if the evaporation of the oxide and of antimony are both first order reactions.

Table I : Data for vapor pressure calculation :
 for Sb_4O_6 for Sb

T	B		A	B
- 10360	12.19	(742-839 K)	-10320	10.59 (below 900 K)
- 9625	11.31	(742-914 K)	- 6500	6.37
- 3900	5.137	(929-1073 K)		

The computation of the Auger signal intensities assumes no modification of the shape of the interface during the irradiation, considering that, due to the evaporation, the surface recedes faster than the oxygen diffuses towards the bulk. This assumption allows us to use analytical formulae for the Auger signal intensities computation. We postulated some types of interfaces (from sharp to exponentially decreasing ones, through all the intermediate cases), assuming a uniform excitation of the interface by the 2 keV primary electrons, and an exponential decay of the

electronic signal with depth. Auger excitation cross sections were chosen to fit the Auger signal from a clean surface. The interface parameter(s) was (were) determined to fit the Auger spectrum of the native oxide-covered surface using mean free path data from the literature (Fig. 5).

Results

The model fits the observations well. The grey areas in fig 1 and fig 3 show the extension of all the possible results while continuously changing the interface shape from sharp to diffuse. The bold lines show the best fits we obtained. Note that the shape of the fitting curves depends slightly on the mean free path of the 450 eV electrons. The theoretical curve fits best the experimental results when the mean free path of the 450 eV electrons was taken to be equal to 1.2 nm.

1. The evolution of the superficial composition of a sample repeatedly exposed to 135 mJ/cm^2 irradiations (fig 1 A) was best fitted assuming that, during each exposure, the surface reaches at most 795 K. The parameters of the intermediate-type-interface were :

$$c = 0.70 \text{ nm} \quad \text{and} \quad d = 0.47 \text{ nm}$$

This result implies that only 35 % of the incident energy is transferred to the surface. The underestimation of the optical coupling of the radiation with the surface is due to the constant temporal shape of the superficial temperature rise assumed.

2. The variation of the superficial composition due to 200 mJ/cm^2 exposures (fig 1 B) was fitted assuming a maximum superficial temperature rise to 900 K. We obtained the best fit with the following parameters for the intermediate interface :

$$c = 0.22 \text{ nm} \quad \text{and} \quad d = 1.29 \text{ nm}$$

This interface appears to be more diffuse. Since the antimony single crystal starts melting below this temperature, the strong reflectivity increase on melting no longer allows us to use the linear relation between the laser beam ED and the maximum temperature rise.

3. The fitting of the third set of data would fail as soon as the ED enables surface melting since first the maximum superficial temperature rise does not vary linearly versus ED any more, and on the other hand oxygen diffusion is enhanced in the liquid phase. However our simple approximation predicts well the starting of the apparent ED threshold for oxide ablation below the melting temperature.

4. Finally, thermal modeling simulations predict no oxide sublimation below 700 K. However, partial decomposition and desorption may be expected on heating antimony oxides in UHV above 600 K [1,7], thus they may be caused by irradiations with ED between 45 and 65 mJ/cm^2 (fig 2). However, we observed both these phenomena also at lower fluences. On the other hand, hours of thermal annealing at 530 K into U.H.V. do not remove the carbon contamination. So we suggest that the oxide modification and the desorption of organic contaminants can be also stimulated by electronic excitations of the oxide [8,9].

Summary of the results from the computer simulation

In spite of its simplicity this model allows us to discriminate between thermal (evaporation process above 130 mJ/cm^2) and non-thermal processes (oxide modification and organic contaminants desorption at ED lower than 45 mJ/cm^2).

1. The predictions of this model would be improved by a more detailed study of the interface evolution under irradiation.

- As a matter of fact it was necessary to postulate a more diffuse interface to fit the superficial composition change under harder exposure to the laser beam.

- At low fluences, evidence for oxide modification were found.

2. Precise measurements of the reflectivity of the antimony native oxide versus the temperature or versus the laser beam ED would permit us to correlate these two scales.

FINAL CONCLUSIONS

Pulsed Laser Annealing (PLA) is a powerful tool for cleaning antimony single crystals. Irradiation parameters have been determined. Simple thermal modeling shows that the oxide ablation is mainly due to thermal evaporation. However the removal of carbon contamination and the oxide modification below 100 mJ/cm^2 involve photolytic processes.

ACKNOWLEDGEMENTS

This research is sponsored by the Belgian program on interuniversity research project on "Interface Sciences" initiated by the Belgian State Science Policy Programming.

E. J. PETIT is indebted to IRSIA (Institute for encouraging Scientific Research in Industry and Agriculture) for a fellowship. We are also grateful to A. Dereux and A. Peremans from LPMPS-FUNDP and LASMOS-FUNDP labs respectively for helpful discussions and the precise computation of the temporal evolution of the superficial temperature.

REFERENCES

1. F. Jona Surf. Sci. **8**, 57 (1967).
2. I. Apker Phys. Rev. **76**, 270 (1949).
3. J.F. Ready, Effects of High-power Laser Irradiation (Acad. Press, London, 1971).
4. G.J. Galvin, M.O. Thompson, J.W. Mayer, P.S. Peercy, R.B. Hammond, in Laser Processing of Semiconductor Devices, ed by C.C. Tang (SPIE Proceed. **385**, 1983).
5. A. Dereux, A. Peremans, J-P. Vigneron, J. Darville, J-M. Gilles, J. Elec. Spectr. Rel. Phen., **45**, 261 (1987).
6. C.J. Smitheels Metals Reference Book, 5th. ed (Butterworths, London & Boston, 1976).
7. S. Maroie, H. Colette, Z. Gabelica, J. Verbist, B. Nagy, J. Acta Chim. Hung. **119** (2-3) 167 (1985).
8. R.F. Haglund, M.H. Mendenhall, N.H. Tolk, G. Betz, W. Husinsky, Nucl. Instr. Meth. Phys. Res. **B32**, 321 (1988)
J. Siejka, R. Srinivasan, J. Perriere, in Energy Beam-Solid Interactions and Transient Thermal Processing (MRS 1985) ed. by V.T. Nguyen, A.G. Cullis (Les éditions de physique, Paris, 1985), p. 139.

PULSED LASER PROCESSING OF TARGETS IMMERSED IN LIQUID MEDIA

Julian P. Partridge, IBM, T.J. Watson Research Center, Box 218, Yorktown Heights, NY 10598.

Peter R. Strutt and Paul G. Klemens, The University of Connecticut, Institute of Materials Science, Box U-136, Storrs, CT 06268.

ABSTRACT

This report describes a study of the formation of TiN thin films produced by laser irradiation of titanium targets immersed in liquid nitrogen. Three fluence thresholds have been determined, corresponding to: (i) surface melting in gaseous nitrogen (0.7 J/cm^2) (ii) surface melting under liquid nitrogen with TiN formation (1.2 J/cm^2) and (iii) gross melting accompanied by the generation of periodic surface structures ($> 2.0 \text{ J/cm}^2$). Data obtained from transmission electron microscopy, Auger spectroscopy, and XPS studies show that the rapid solid-state cooling rates (10^4 deg/sec) result in a supersaturated, twinned hcp structure with solute contents up to 40 at% nitrogen.

Theoretical estimates suggest that the majority of the incident excimer laser radiation is absorbed by the target with subsequent thermal transfer to the liquid producing a high-pressure shock wave originating at the liquid-solid interface. Pressures up to 4.3 GPa are predicted with the expanding vapor layer reaching a terminal velocity after $5 \mu\text{s}$ and a total lifetime of $28 \mu\text{s}$. Such a lifetime is considerably longer than the thermal pulse in the substrate (from a 1-dimensional heat flow analysis). The results are discussed with reference to such estimates. Because the thermal diffusivity far exceeds that of the solute, the extent of nitridation is determined predominantly by the first 200 ns of the thermal pulse experienced by the target.

INTRODUCTION

Reactions occurring at laser-irradiated targets immersed in liquids can differ from those occurring under gaseous conditions. Differences include higher target quench rates following pulsed laser heating and an increase in the near-surface dopant concentration. Extremely high pressures can be generated in the liquid (1,2) and in some cases the incident fluence is sufficient to produce substrate melting. This paper addresses the phenomena that occur when a pulsed laser irradiates targets immersed in liquid media. The discussion is restricted to the specific case of titanium metal targets immersed in liquid nitrogen.

EXPERIMENTAL

A KrF excimer laser was used to produce 248 nm wavelength radiation of 22 ns pulse duration in a multimode operation. The maximum pulse energy of 700 mJ passed through a double aperture system. The apertures were 8 mm in diameter and were used to select a region of uniform intensity. Such a configuration considerably reduces the available pulse energy (to $\approx 20 \text{ mJ}$) in addition to requiring careful alignment.

A unique feature of the current arrangement is the use of a computer-interfaced calorimeter in conjunction with a beam-splitter. Such an arrangement allows the complete irradiation history of any sample to be recorded for later analysis, a feature considered to be of great importance if the nitriding mechanism is to be modeled accurately. A 5 mW Uniphase helium-neon laser was used as an aid in optical alignment and to permit successive target areas to be defined.

Electropolished titanium discs were mounted in an array-type holder before equilibrating in liquid nitrogen. Focal lengths were adjusted to change the irradiated area between 0.2 mm^2 and 3 mm^2 . The samples were irradiated for up to 500 seconds at repetition rates from 0.2 to 0.8 Hz. A low repetition rate was used to (i) permit calorimetric determination of individual pulse energies, and (ii) allow any nitrogen vapor bubbles to escape from the liquid

prior to the arrival of subsequent pulses. Various analytical techniques were used to determine the extent and nature of the nitrided near-surface region.

RESULTS

For fixed immersion depths of 5 mm, various pulse energies and focal distances were used in single-pulse experiments to determine the melt threshold. The onset of melting was determined by optical microscopy of the irradiated region: the quality of the prior jet polishing permits the irradiated region to be distinguished from the as-polished areas. In some locations grains are only partially melted. An interesting effect observed at the melt threshold is evidence of selective grain melting within the irradiated zone which has been attributed previously (3) to the orientation dependence of the thermal properties of titanium.

The value of the melt threshold fluence is relatively independent of the irradiated area over a large range. The data for 5 mm immersion are compared to zero immersion depth (i.e. N_2 vapor at 1 atmos.) in Figure 1 with thresholds corresponding to 1.2 J/cm² and 0.7 J/cm² respectively. When the fluence is increased still further, crater formation occurs and another threshold can be determined for mass transport and the occurrence of periodic surface structures (PSS). Such structures have been observed by other workers (4,5) and are attributed in this case to longer solidification times at the high fluences coupled with high pressure flow phenomena. Figure 1 shows the threshold for these instabilities to be around 2 J/cm².

AES/XPS

Auger electron spectroscopy and x-ray photoelectron spectroscopy were performed in the irradiated region. Standards of $TiN_{0.45}$ and $TiN_{0.95}$ calibrated by Rutherford Backscattering Spectroscopy were required. The AES and XPS results are summarized in Figure 2. A ratio technique was required for the AES because the 379 eV nitrogen peak is unresolved from the major titanium peak at 387 eV.

This was done by determining the ratio of the secondary 418 eV peak to the 387 eV titanium peak and subtracting this contribution from the 379/387 eV combined peak to determine the effective nitrogen yield.

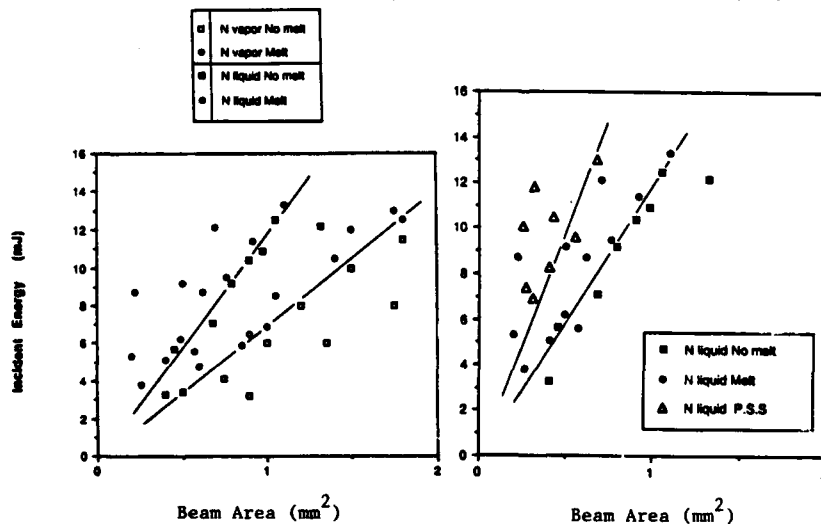


Figure 1 Melt thresholds for titanium at 248 nm irradiation.

Oxygen and carbon yields became negligible after sputtering beyond 20 Å from the surface so contaminants were not considered during composition calculations. The standards were again used in conjunction with an area ratio technique. Significant quantities of nitrogen were detected within the irradiated zone. It is interesting to note that a bulk tungsten backing considerably reduces the amount of nitrogen incorporated into the 5000 Å thick sub-surface region of the titanium. This is due to the greatly enhanced cooling rate arising from the higher thermal conductivity of tungsten.

TEM

Thin foils suitable for transmission electron microscopy (TEM) were prepared by jet-thinning from the back of the irradiated targets. Non-irradiated samples show featureless grains with an average grain size of 20 μm . Samples irradiated at 1.4 J/cm² experienced significant surface melting making thin foil preparation difficult. Frequently the nitrided layer was removed and only a highly dislocated material with equilibrium lattice constant was observed in the α phase. Foils made from targets irradiated at the melt threshold show structures which are consistent with twins induced by shock-loading, Figure 3.

The phases expected in a nitrided titanium target may be predicted from the phase diagram and since it is likely that the rapid quenching produced non-equilibrium structures, the observed phases could be hcp α -Ti, bcc β -Ti, tetragonal Ti₃N, or fcc TiN. None of the cubic or tetragonal structures were found in the selected area diffraction patterns and the spotted rings could be indexed only as distorted hcp. Although the accuracy of lattice parameter determination via TEM rarely exceeds 1%, the 2.5% increase above the observed α -phase values is real and significant. A superposition of predicted diffraction rings and observed ones gives excellent correlation. The analytical results are summarized in Table 1.

Such results are best understood by considering that each technique examines information originating from different locations. The XPS/AES data originates in the 10 Å near-surface layer but was able to yield information from greater depths by sputtering. Similarly, TEM information originates from the top 1000 Å as a consequence of the preparation technique. The TEM results are consistent with the presence of a rapidly-cooled, nitrogen-rich phase in the 1000 Å surface region.

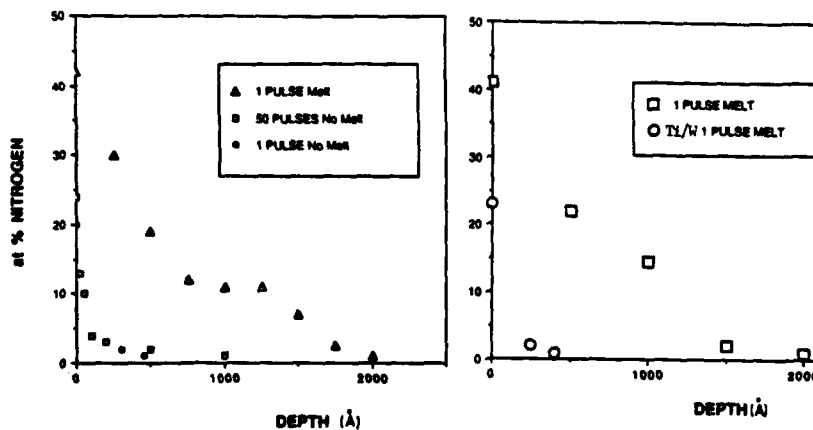


Figure 2 (a) AES and (b) XPS results from irradiated regions.

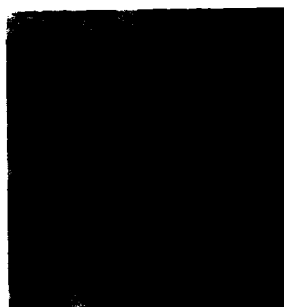


Figure 3 TEM micrographs of twins in irradiated region

Condition	LOW FLUENCE $\approx 12 \text{ J/cm}^2$	HIGH FLUENCE $> 15 \text{ J/cm}^2$
TECHNIQUE		
XPS/AES	20 at% N	49 at% N
X-ray Diffraction	α -Ti	α -Ti + TiN
T.E.M.	Distorted hcp titanium	N/A

Table 1 Analytical results

ANALYSIS

Heat flow analysis. The current conditions involve a short heating cycle (22 ns pulse duration) and a small beam dimension (around 1 mm^2) so we can assume there exists no energy loss through reradiation or convection. The differential equation for heat flow in a semi-infinite target with a boundary at $x = 0$ for a beam of diameter d propagating in the z direction is:

$$T(r,z,t) = \frac{d^2}{K} \left[\frac{\alpha}{\pi} \right]^2 \int_0^t \frac{F(t-t')}{t'^{1/2}(4\alpha t + d^2)} \exp \left[\frac{z^2}{4\alpha t} - \frac{r^2}{(4\alpha t' + d^2)} \right] dt'$$

where α = thermal diffusivity ($= K/\rho C$), K = thermal conductivity, C = specific heat, t is the pulse duration, and $F(t-t')$ is the beam power at any time during the pulse. The substrate is also considered to be semi-infinite. The absorption depth corresponds to the carrier mean free path (electron) which is 100 \AA compared to the 0.5 mm beam diameter. The heat loss from edges is therefore negligible and the heat flow is considered to be 1-dimensional. The thermal diffusion distance for the 22 ns pulse duration is only 400 \AA which means that the heat during the irradiation cycle must be considered. Using such considerations yields a generalized expression with dimensionless variables which is integrated numerically for τ over interval t . The curves for titanium assuming a 10 mJ incident pulse, 50% reflectivity, and a maximum power of $1 \times 10^7 \text{ W/cm}^2$ are plotted in Figure 4. In reality, the conduction process becomes 3-dimensional after a finite time and the predictions should only be considered useful for times below 500 ns. Note that the temperature is the temperature rise and at 800 \AA depth reaches the melting point (1670°C) after 30 ns. At greater depths the lower peak temperatures are attained after greater times. The heating and cooling rates at this depth are around 10^{10} deg/s which are typical of such laser processing.

Lifetime of pressure pulse

This may be estimated by considering the time taken for the liquid/vapor interface to move away from the irradiation zone a distance X equal to the square root of the beam area Λ . Beyond this point the 3-dimensional cooling effects cause rapid quenching of the vapor followed by collapse of the cavity. The mean interface velocity (V) can be averaged over the total time (t_c) for x to reach its final value. The initial interface location is given by the position of the interface at the end of the pulse. V_s is the velocity of sound in the liquid. The mass of liquid above the cavity is given by the product of the liquid density (ρ_l), immersion depth (h), and irradiated area ($\Lambda^{3/2}$) so an expression may be found (6) for the value of the time taken for cavity collapse as a function of the experimental values determined in the current study:

$$t_f^2 = 3 V_0 \rho_L \left[\frac{\tau h A^{3/2}}{E} \right]$$

By substituting typical experimental values into this equation, one obtains a value for the pulse duration of approximately 50 μ s. Pressures of 4×10^4 atmospheres predicted by other workers (1,2), in conjunction with the short time of 28 μ s represents conditions under which low-temperature shock loading of titanium produces the extensive twinning of the hcp structure. The important feature of this result is the fact that the gas bubble lifetime of approximately 30 μ s is considerably longer than the temperature pulse predicted above.

Diffusion considerations

Any diffusional analysis of the concentration profile must consider the variation of temperature (T) with time (t). This would need to be done numerically using the T vs t data of Figure 4 with a knowledge of the Arrhenius parameters, but there is another problem. This is the fact that the T vs t thermal cycle is also a function of depth and a simple $\int D \cdot dt$ method is invalid. Some insight may be obtained, however, by studying the relative rates of heat and chemical diffusion at, for example, 2000 K, see Table 2. This means that the relative diffusion distance of the thermal energy far exceeds that of the nitrogen species. The temperature gradient at the surface will be very small for times below 100 ns which allows a rough estimate of the diffusion distance of N in α -Ti just below the melting point (1943 K). This predicts a maximum solute penetration depth of only 40 \AA after 20 ns which increases to 60 \AA after 50 ns at the melting point. Thus the amount of nitrogen detected is too large to be attributed solely to solid state diffusion. One must consider the possibility of a thin molten layer existing for a time equal to the pulse duration (22 ns), which predicts a greater nitrogen penetration depth. The nitrogen diffusivity is approximately 3 orders of magnitude greater in the liquid phase than the solid.

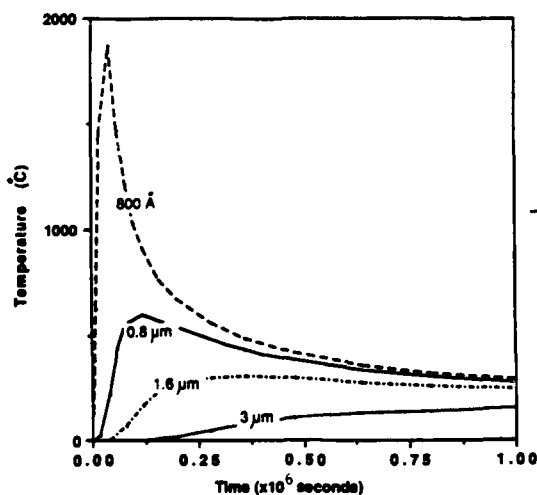


Figure 4 Ti temperature profiles

N diffusivity	Thermal diffusivity
α -Ti 1000 K	
$D = 1.3 \times 10^{-7} \text{ cm}^2/\text{s}$	$\alpha = 0.04 \text{ cm}^2/\text{s}$

Table 2

Extending the heat flow model to temperatures above the melting point and including the higher diffusivity in the liquid phase predicts surface melting to 800 Å with a lifetime of approximately 76 ns, giving a diffusion distance of only 326 Å. This result correlates well with the lower curve of Figure 1 which has previously been designated as a single pulse with no melting. The maximum diffusion distance possible in the solid state is only 80 Å for the β phase (and would be even smaller ≈ 10 Å for the α phase). This suggests that surface melting has occurred in this case even though a melt depth of 800 Å cannot be detected from microstructural observations.

CONCLUSIONS

1. Three fluence thresholds can be distinguished for the 248 nm pulse irradiation of titanium. These correspond to :
 (i) surface melting in the presence of nitrogen vapor (0.7 J/cm^2),
 (ii) surface melting under liquid nitrogen (1.2 J/cm^2), and
 (iii) gross melting accompanied by the generation of periodic surface structures ($> 2.0 \text{ J/cm}^2$)
2. Significant nitrogen incorporation to depths exceeding 100 Å requires melting of the surface layer which is not discernible by optical microscopy.
3. The rapid solid-state cooling rates ($\approx 10^{10} \text{ deg/s}$) results in a supersaturated, non-equilibrium, heavily twinned hcp structure with a nitrogen solute content up to 40 at%.
4. Because the thermal diffusivity far exceeds the solute diffusivity, the extent of nitridation is determined predominantly by the first 200 ns of the thermal cycle experienced by the target.
5. The observations of mononitrides made by other workers has been observed here only after repeated irradiation at high fluence ($> 1.5 \text{ J/cm}^2$). This is attributed to the greater melt depth and correspondingly lower cooling rates which permit the formation of near-equilibrium phases.
6. It remains unclear whether or not surface vaporization is significant at high fluences. A numerical method which includes the latent heat of fusion and the temperature dependence of the thermal diffusivity and heat capacity will be needed if more accurate analyses are to be made for diffusion in the molten state.

REFERENCES

1. G.P. Davidson and D.C. Emmony, J.Phys. E. **13**, 92 (1980).
2. S.R.J. Brueck and H. Kildal, J.Appl.Phys. **52**, (2) 1004 (1981).
3. J. Partridge and P. Strutt, Mat. Res. Soc. Symp., Dec. 1987, Symp.B Vol.101, 443 (1988).
4. D. Dijkkamp, X.D. Wu, S.W. Chan, and f. Venkatesan, J.Appl.Phys. **62**, (1) 293 (1987).
5. I. Ursu et al., J.Phys.D., 1183 (1986).
6. J. Partridge, P. Strutt and P. Klemens, To be published, J.Appl. Phys. (1989).

PART IX

**Ion-, Electron-, and
Plasma-Assisted Chemistry**

PHYSICAL AND CHEMICAL SPUTTERING AT VERY LOW ION ENERGY: THE IMPORTANCE OF THE SPUTTERING THRESHOLD

CHRISTOPH STEINBRUCHEL

Materials Engineering Department and Center for Integrated Electronics, Rensselaer Polytechnic Institute, Troy, NY 12180-3590

ABSTRACT

A variety of data for physical etching (i.e. sputtering) and for ion-enhanced chemical etching of Si and SiO₂ is analyzed in the very-low-ion-energy regime. Bombardment by inert ions alone, by reactive ions, and by inert ions in the presence of reactive neutrals is considered. In all cases the etch yield follows a square root dependence on the ion energy all the way down to the threshold energy for etching. At the same time, the threshold energy has a non-negligible effect on the etch yield even at intermediate ion energies. The difference between physical and ion-enhanced chemical etch yields can be accounted for by a reduction in the average surface binding energy of the etch products and a corresponding reduction in the threshold energy for etching. These results suggest that, in general, the selectivity for ion-enhanced etch processes relative to physical sputtering can be increased significantly at low ion energy.

INTRODUCTION

Ion bombardment of a solid is an important part of a number of modern thin film processes. Sputtering in a discharge or with an ion beam is employed widely for the deposition of thin films. Ion bombardment is also used to modify the surface properties of a film. Furthermore, in dry (plasma) etching ion bombardment often plays an essential role in the removal of material from a film. In many applications, however, and particularly in plasma etching, ion bombardment may also have a deleterious effect, by introducing damage into the film. Since damage typically increases with increasing ion energy, it is desirable to work with the minimum ion energy which achieves the desired result.

In this paper, we examine the behavior of physical and ion-enhanced chemical etch yields for Si and SiO₂ at very low ion energy. We show that there is a universal dependence of the etch yield on ion energy all the way down to the threshold energy for etching. It turns out also that chemical enhancement of etch yields can be related to a reduction of the average surface binding energy of the etch products and a corresponding reduction in the threshold energy for etching. Moreover, even at intermediate ion energies the threshold energy needs to be taken into account for a quantitative description of etch yields.

THEORY

The generally accepted picture for sputtering (i.e. physical etching) has been given by Sigmund [1]. According to Sigmund's theory the sputtering yield Y , i.e. the number of target atoms removed per incoming ion can be expressed as

$$Y(E) = C_{pt} S_n(E/E_{pt}) \quad (1)$$

In Eq. (1) C_{pt} and E_{pt} are constants depending on the target t and the projectile p , and $S_n(E/E_{pt})$ is a universal function, the nuclear stopping cross section, of the reduced energy $\epsilon = E/E_{pt}$. Furthermore, C_{pt} is inversely proportional to the surface binding energy U . Sigmund evaluated $S_n(E/E_{pt})$ on the basis of the Thomas-Fermi model but recognized that at very low ion energy, typically $E < 1$ keV or $\epsilon < 0.05$, the Thomas-Fermi model overestimated $S_n(E/E_{pt})$. Wilson et al. [2] derived a more accurate expression for $S_n(E/E_{pt})$ by taking into account the screening of the atom-atom interaction potential.

Furthermore, the result of Wilson et al. can be approximated to within 5% by

$$S_n(E/E_{pt}) \propto E^{1/2} \quad (2)$$

for $E/E_{pt} \lesssim 0.02$, as noted by Zalm [3]. The same form has been obtained very recently by Winters and Taglauer [4] using a better atom-atom interaction potential within the framework of Sigmund's theory.

It was also realized that at very low ion energy, i.e. near the threshold energy for sputtering E_{th} , data for $Y(E)$ showed a more rapid decrease than $\propto E^{1/2}$ [5-7]. This was accounted for in an empirical way by setting

$$Y(E) = C_{pt} S_n(E/E_{pt}) f(E_{th}/E) \quad (3)$$

where $f(1) = 0$ and $f(0) = 1$. For the function $f(E_{th}/E)$ several forms have been proposed [5-7]. In this paper we will use the function $f(E_{th}/E)$ suggested by Matsunami et al. [5]

$$f_M(E_{th}/E) = 1 - (E_{th}/E)^{1/2} \quad (4)$$

because it is the simplest and because it provides the best description of the available data, as will be shown elsewhere [8]. Thus, by combining Eqs. (1) to (4) one can write

$$Y(E) = A(E^{1/2} - E_{th}^{1/2}) \quad (5)$$

where A and E_{th} are constants depending on the particular projectile-target combination. This paper will explore the question to what extent Eq. (5) provides a good description of available data for sputtering yields and chemically enhanced etch yields at very low ion energy.

FIT OF THEORY TO DATA

In Figs. 1 and 2 we give least-squares fits of Eq. (5) to data of several authors for Si and SiO_2 [9-12]. The data include sputtering by noble gas ions (Ar^+ , Ne^+), sputtering by chemically reactive ions (Cl^+ , F^+ , CF^+), and ion beam assisted chemical etching (bombardment of the target by Ar^+ with simultaneous exposure to Cl_2). The fit to the data is generally very good, showing clearly the $E^{1/2}$ dependence of $Y(E)$ as well as the threshold energy E_{th} (cf. Table 1 below). We also note that a set of data for Ar^+ on Si by Harper et al. [10], agreeing closely with the data by Tachi et al. [11], has been left out of Fig. 1 for the sake of clarity (cf. Table 1 below). Very recent data for Ar^+ on SiO_2 by Todorov and Fossum [13] agree well with Harper's results [10] but cover too small an energy range (40-100eV) as to be useful for fitting.

DISCUSSION

For the purpose of discussion we list in Table 1 the values for A and E_{th} (Eq. (5)) obtained by the least-squares fit to the various sets of data. As an indication of the quality of the fit, we also give values for the square of the correlation coefficient, r . Let us point out that the form of $f(E_{th}/E)$ by Matsunami et al. [5], Eq. (4), leading to Eq. (5), in general yields a slightly better fit to the data than the form of $f(E_{th}/E)$ given by Yamamura et al. [6] ($f_Y(E_{th}/E) = [1 - (E_{th}/E)^{1/2}]^2$). In addition, Eq. (5) results in a much better fit to the data than does the form of $f(E_{th}/E)$ suggested by Bohdanský [6] ($f_B(E_{th}/E) = [1 - (E_{th}/E)^{2/3}] [1 - E_{th}/E]^2$). Furthermore, it turns out that a dependence of $Y(E)$ on E other than as $E^{1/2}$ gives an inferior fit to the data. The details of this comparison will be published elsewhere [8].

As regards the data on Figs. 1 and 2 and the fitting parameters in Table 1, we point out that there is a slight disagreement between the data of Wehner [9] and Oostra et al. [12] on the one hand and the data of Tachi et al. [11] and Harper et al. [10] on the other hand for Ar^+ on Si. In particular, the former data imply a somewhat larger value for E_{th} than the latter data. The origin of this discrepancy is not clear but may be due to slightly better background vacuum conditions for the latter sets of data. Also for CF^+ on SiO_2 , E_{th} turns out to be about zero, whether one takes all data points for the fit

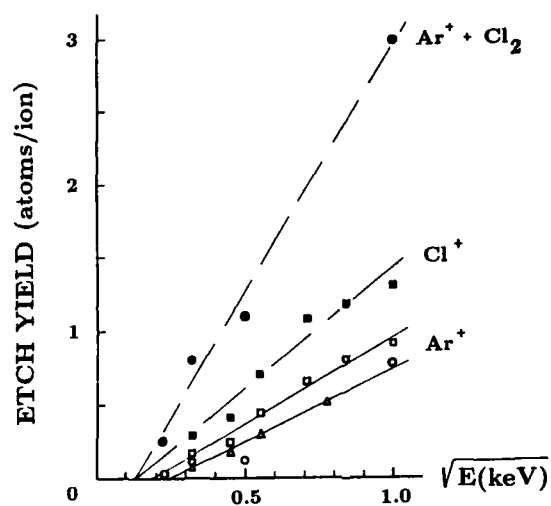


Fig. 1. Etch yields Y on Si as a function of ion energy E : plot of Y vs $(E(\text{keV}))^{1/2}$.
 Δ : Laegreid and Wehner [9]; \blacksquare : Tachi et al. [11]; \circ : Oostra et al. [12].

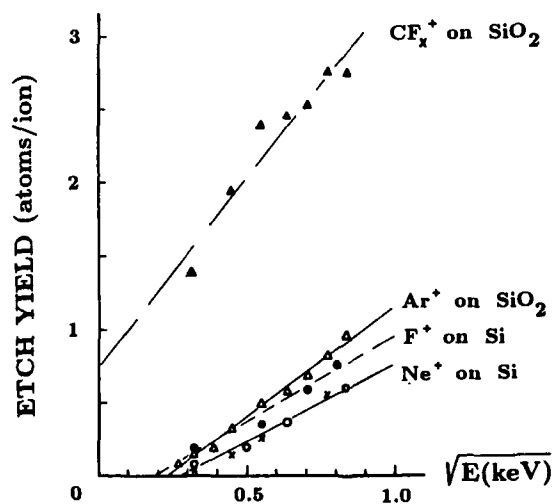


Fig. 2. Etch yields Y on Si and SiO_2 as a function of ion energy E : plot of Y vs $(E(\text{keV}))^{1/2}$.
 x : Laegreid and Wehner [9]; Δ : Harper et al. [10]; \circ : Tachi et al. [11].

Table I: Least-squares-fit parameter values for describing experimental etch yields $Y(E)$ according to Eq. 5: $Y(E) = A (E^{1/2} - E_{th}^{1/2})$

Projectile	Reactive Gas	Target	A	E_{th}	r^2	Ref.
Ar ⁺	-	Si	1.02	64	1.00	9
Ar ⁺	-	Si	1.18	27	0.98	10
Ar ⁺	-	Si	1.16	31	0.98	11
Cl ⁺	-	Si	1.64	18	0.95	11
Ar ⁺	-	Si	0.98	64	0.94	12
Ar ⁺	Cl ₂	Si	3.28	16	0.99	12
Ne ⁺	-	Si	1.13	95	0.99	9
Ne ⁺	-	Si	1.02	77	0.98	11
F ⁺	-	Si	1.14	35	0.97	11
Ar ⁺	-	SiO ₂	1.49	52	0.99	10
CF ₂ ⁺	-	SiO ₂	2.53	0	0.92	10

(as in Table 1) or only the three points at lowest ion energy.

Two features of Figs. 1 and 2 are especially noteworthy. First, ion bombardment of Si either with chemically reactive ions (Cl⁺, F⁺) or in the presence of a neutral reactant (Cl₂) leads to a much lower value for the threshold energy E_{th} than does bombardment with inert ions alone of comparable mass. Second, the slopes of the straight lines, i.e. the values of the constant A of Eq. (5), are considerably larger in the reactive cases than in the case of simple physical sputtering. Moreover, if one compares bombardment of Si by Ar⁺ alone with bombardment in the presence of Cl₂, in which case a substantial amount of Cl should be incorporated into the target surface [14], E_{th} and A^{-1} are changed roughly by the same factor. Since $E_{th} \propto U$ and $A \propto U^{-1}$, where U is the surface binding energy of removed products [1], the observed changes in E_{th} and A can both be rationalized in terms of the same change in U. It is also well established that under these conditions a large fraction of the product species is of the type SiCl_x [15]. On the other hand, bombardment with reactive ions (Cl⁺, F⁺) should give rise to a much smaller surface concentration of Cl or F, so that to first order only E_{th} should be affected.

One should keep in mind, though, that a definite relationship between E_{th} and U exists only in physical sputtering. There, the threshold condition is determined by the fact that U represents the minimum energy a surface atom must acquire in order to be ejected from the target. However, when the products are volatile as in chemical sputtering, i.e. when the binding energy of products is essentially zero, the threshold condition should derive from the minimum energy deposited at the target surface which can initiate the surface reaction forming the volatile products.

For the etching of SiO₂ by CF₂⁺ in Fig. 2 we note that CF₂⁺ refers to a beam containing a mixture of ions. Mass spectrometric analysis of such an ion beam [16,17] indicates that under the experimental conditions in [10] the "average" beam composition was about CF₂⁺. Although the fit to the data is not quite as good as in all the other cases (cf. Table 1), Fig. 2 does suggest that E_{th} is about zero. This is consistent with the picture of the etch mechanism being direct reactive ion etching [18], i.e. the ions themselves are the main chemical reactants leading to highly volatile products. In this case E_{th} for etching would be given by the minimum energy required for the ions to dissociate upon impact, which could very well be quite small.

It is clear from this as well as other work [3,4,8,19] that the etch yield $Y(E)$ depends on the ion energy E as $E^{1/2}$ at low E in all cases, whether they involve physical sputtering or reactive etching. But our analysis also demonstrates that for a quantitative description of etch yields it is essential to include the effect of the threshold energy even at ion energies

of a few hundred eV, i.e. for E way above E_{th} . In fact, the parameter values for E_{th} in Table 1 show that e.g. at $E = 500$ eV the term $\propto E_{th}$ in Eq. (5) contributes as much as 30% to $Y(E)$ for physical sputtering and as much as 20% for reactive etching.

CONCLUSIONS

Our analysis has shown that physical as well as ion-enhanced chemical etch yields on Si and SiO_2 are described well by an $E^{1/2}$ dependence on the ion energy E down to the threshold energy E_{th} for etching. Even at ion energies of several hundred eV it is important to take into account the effect of E_{th} for a quantitative description of the etch yield. The value of E_{th} turns out to be greatly reduced in ion-enhanced chemical etching as compared to physical sputtering.

Since physical sputtering is often the limiting factor in etching one material selectively with respect to another, the above results imply that the optimal conditions for selective etching require an ion energy just below the threshold energy for physical sputtering of the material which is not supposed to be etched. Unfortunately, threshold energies are not well-known for many systems of interest in plasma processing. This applies even to physical sputtering, but in particular to ion-enhanced chemical etching. Furthermore, the mechanisms giving rise to threshold behavior in cases other than physical sputtering are not understood. More work addressing these issues is clearly needed and could make an important contribution to the understanding and further improvement of plasma etch processes.

References

- [1] P. Sigmund, in *Sputtering by Ion Bombardment I*, Vol. 47 of Topics in Applied Physics, edited by R. Behrisch (Springer, Berlin, 1981) p. 9.
- [2] W. D. Wilson, L. G. Haggmark, J. P. Biersack, *Phys. Rev.* **15**, 2458 (1977).
- [3] P. C. Zalm, *J. Vac. Sci. Technol. B* **2**, 151 (1984).
- [4] H. F. Winters and E. Taglauer, *Phys. Rev. B* **35**, 2174 (1987).
- [5] N. Matsunami, Y. Yamamura, Y. Itikawa, N. Itoh, Y. Kazumata, S. Miyagawa, M. Morita, R. Shimizu, *Radiat. Eff. Lett.* **57**, 15 (1980).
- [6] Y. Yamamura, N. Matsunami, N. Itoh, *Radiat. Eff. Lett.* **68**, 83 (1982).
- [7] J. Bohdanský, *Nucl. Instrum. Methods B* **2**, 587 (1984).
- [8] Ch. Steinbrüchel (to be published).
- [9] N. Laegreid and G. K. Wehner, *J. Appl. Phys.* **32**, 365 (1961).
- [10] J. M. E. Harper, J. J. Cuomo, P. A. Leary, G. M. Summa, H. R. Kaufman, F. J. Bresnock, *J. Electrochem. Soc.* **128**, 1077 (1981).
- [11] S. Tachi, K. Miyake, T. Tokuyama, in *Proceedings of the Third Symposium on Dry Process* (Institute of Electrical Engineers of Japan, Japan, 1981), p. 17; *Jpn. J. Appl. Phys. Suppl.* **21-1**, 21, 141 (1983).
- [12] D. J. Oostra, R. P. van Ingen, A. Haring, A. E. de Vries, G. N. A. van Veen, *Appl. Phys. Lett.* **50**, 1506 (1987).
- [13] S. S. Todorov and E. R. Fossum, *Appl. Phys. Lett.* **52**, 365 (1988).
- [14] T. Mizutani, C. J. Dale, W. K. Chu, T. M. Mayer, *Nucl. Instrum. Methods B* **7/8**, 825 (1985).
- [15] A. W. Kolfshoten, R. A. Haring, A. Haring, A. E. de Vries, *J. Appl. Phys.* **55**, 3813 (1984).
- [16] T. M. Mayer and T. A. Barker, *J. Electrochem. Soc.* **129**, 585 (1982).
- [17] Ch. Steinbrüchel, *J. Vac. Sci. Technol. B* **2**, 38 (1984).
- [18] Ch. Steinbrüchel, H. W. Lehmann, K. Frick, *J. Electrochem. Soc.* **132**, 180 (1985); *Mat. Res. Soc. Symp. Proc.* **38**, 157 (1985).
- [19] Ch. Steinbrüchel, *Appl. Phys. A* **36**, 37 (1985).

THE MICROSTRUCTURE OF GOLD FILMS WRITTEN BY FOCUSED ION BEAM INDUCED DEPOSITION

Patricia G. Blauner, Jae Sang Ro, Yousaf Butt, Carl V. Thompson, and John Melngailis,
Research Laboratory of Electronics
Massachusetts Institute of Technology, Cambridge, MA 02139 USA

ABSTRACT

Focused ion beam induced deposition of gold microfeatures is accomplished by 40 keV Ga⁺ bombardment of a substrate on which dimethyl gold hexafluoro acetylacetonate is continuously adsorbed. Under optimum conditions, deposition rates exceeding 11 Å/s have been achieved as well as high aspect ratio features, linewidths of approximately 0.1 μm, and resistivities of 500–1500 μΩ-cm. The microstructure, composition, and yield of the deposits have been examined as a function of various process parameters. Improved film growth and purity are observed in deposits made with lower organometallic pressures or higher current densities.

INTRODUCTION

Ion beam induced deposition uses ion bombardment to induce the growth of a film from a precursor gas adsorbed on a substrate. Typically, a local high pressure region of the appropriate gas is created using either a small pressure cell or nozzle. The ion beam then dissociates adsorbed molecules, the undesired by-products ideally desorb from the surface and the film grows. In contrast to processes involving beam assisted deposition [1], no film growth occurs in the unbombarded region. By using a highly focused beam of ions, this process may be used for deposition of submicron features. As such, it holds promise as a microelectronics repair or prototyping tool where it can be combined with the focused beam's ability to mill material with submicron resolution.

Focused ion beam induced deposition was first demonstrated by Gamo *et al.* [2] and followed earlier work on localized deposition using lasers [3]. Highly localized deposition using electron [4–7], ion [2,8–11], and photon bombardment have now been demonstrated using a large variety of precursor gases to produce films of W, Ta, Fe, Al, Au, Cr and carbon, to name a few. The latter two materials have already found commercial application in the field of photolithographic mask repair [12–15]. Future applications now being explored for focused ion beam induced deposition include x-ray lithographic mask repair and integrated circuit restructuring [16]. Both of these would exploit the focused ion beam's potential both to deposit and mill with sub-tenth micron resolution.

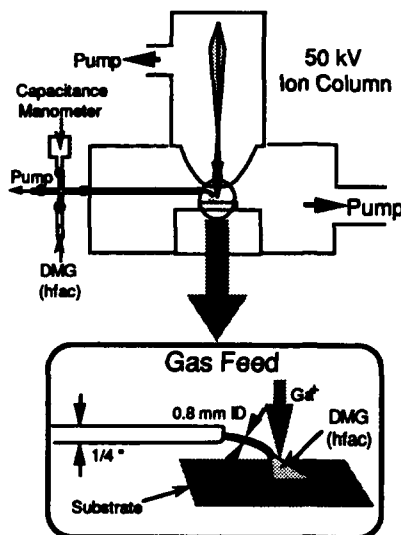
With these applications in mind, we have concentrated our work on the deposition of Au, since it is both a good x-ray absorber and a good conductor. The experimental results discussed below concentrate on the parameterization of the deposition process, and in particular, the characterization of the deposited films as a function of ion and organometallic molecular flux. These issues are of particular relevance to focused ion beam work, where the balance between these two fluxes can be quite close. In extending the deposition process from one employing broad ion beams with current densities of a few microamperes per square centimeter to one employing fo-

cused beams with current densities of amperes per square centimeter, challenging problems arise. By systematically parameterizing the process, our aim has been to develop a more complete understanding of the basic mechanisms involved in ion beam induced deposition.

EXPERIMENTAL

Thin film and microfeature deposition were accomplished using 40 keV Ga^+ bombardment of SiO_2 substrates (100 nm thermally grown oxide on Si wafers) over which dimethyl gold hexafluoro acetylacetonate vapor was introduced (hereafter referred to as DMG(hfac)). Details of the ultra high vacuum focused ion beam apparatus and the gas delivery system are described elsewhere [17]. Summarizing, referring to figure 1, a gas delivery tube creates a local pressure ambient of DMG(hfac) over the substrate and the focused ion beam (diameter 70 – 100 nm and current 25 – 100 pA) is rapidly scanned in this area. The pressure of the organometallic at the surface was measured using a stagnation tube [17] and could be varied from <0.1 mTorr to 10 mTorr by adjusting the height of the delivery tube over the surface. The scanned or averaged beam current density (beam current divided by scanned area) could be varied from $4 \mu\text{A}/\text{cm}^2$ to $>1 \text{ A}/\text{cm}^2$ (stationary beam) by adjusting the size of the scanned area. In all cases scan speeds in excess of 30 cm/s were used to avoid instantaneous depletion of the adsorbed gas coverage [9, 17].

The compositions of deposits were analyzed by Auger electron spectroscopy. Film thicknesses were measured either by stylus profilometry or high angle scanning electron microscopy. Resistivity was measured by depositing a line across a pre-evaporated metal pattern (4 point contact). Film microstructure was evaluated using both high resolution scanning electron microscopy and transmission electron microscopy. For TEM analysis, deposits were made directly onto 1000 Å thick silicon nitride membranes.



1. Schematic of the apparatus: Focused beams from a differentially pumped ion column were incident on targets in the work chamber (base pressure 5×10^{-8} Torr). During deposition, DMG(hfac) vapor was delivered through a small tube suspended over the substrate. This delivery apparatus was mounted on an XYZ manipulator so that the molecular flux could be controlled by varying the height of the tube over the substrate.

RESULTS AND DISCUSSION

An example of a $1\text{ }\mu\text{m}$ high Au deposit is shown in figure 2. This $3.4 \times 3.4\text{ }\mu\text{m}$ patch took 15 minutes to write using a 25 pA beam and a DMG(hfac) pressure of 10 mTorr, indicating a deposition yield[†] of 5.8 ± 0.6 atoms per incident ion and a deposition rate of $11\text{ }\text{\AA}/\text{s}$. Its thickness and high aspect ratio suggest the utility of this technique for x-ray mask repair. Auger analysis of this film indicates a composition of approximately 50% Au, 35% C and 15% Ga, with no F or O detectable. Figure 3 shows 2 examples of lines written with submicron widths. They were written with 50 pA, 70 nm diameter beams under conditions of various scanned current densities and hence deposition efficiencies, as will be discussed below. The measured resistivity of lines such as these, $500 - 1500\text{ }\mu\Omega\text{-cm}$, is comparable to that of polysilicon, indicating that they would be of use in many circuit restructuring applications.

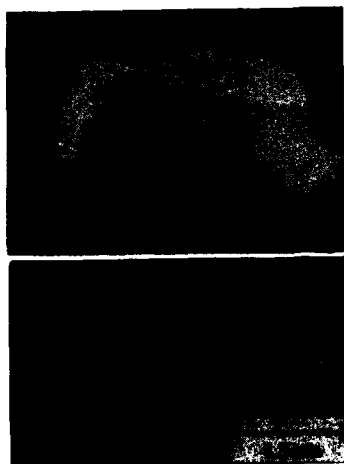


Fig. 2 SEM of a $3.4 \times 3.4\text{ }\mu\text{m}$ deposit shown in perspective (top) and in profile (bottom). This feature was written at a deposition rate of $11\text{ }\text{\AA}/\text{s}$. The height ($\sim 1\text{ }\mu\text{m}$) and high aspect ratio of the edges of this deposit are of particular interest for application in x-ray lithographic mask repair.

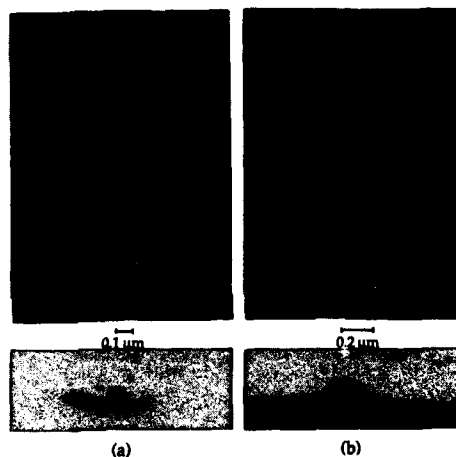


Fig. 3 SEM of deposited lines shown in perspective (top) and in cross section (bottom). These lines were written by repeatedly and continuously scanning a 50 pA ion beam over (a) $25\text{ }\mu\text{m}$ at 300 cm/s for 30 s (deposition yield[†] < 1 atoms/ion) and (b) $90\text{ }\mu\text{m}$ at 180 cm/s for 2 min. (deposition yield[†] ~ 2.5). The resistivity of lines such as (b) was measured to be $500 - 1500\text{ }\mu\Omega\text{-cm}$. The larger width of the line in (b) is believed to be due to drift in the ion beam perpendicular to the scan direction. The feature in the foreground of the cross section in (a) is an artifact of the beam not being blanked at the end of the line.

A critical sensitivity of the deposition efficiency to various process parameters was evident in these experiments and led to a study of the process as a function of both ion and DMG(hfac) flux [17]. We found that the deposition efficiency or yield (atoms/ion) increased to a limiting value both with increasing DMG(hfac) flux and decreasing ion flux [see ref. 17 for details of these measurements]. This is the expected behavior since under ion bombardment the steady-state coverage

of the adsorbate will increase with increasing molecular flux and decrease with increasing ion flux and the data have been fit qualitatively to models of the deposition mechanism which account for adsorption, beam induced adsorbate dissociation and sputtering of the growing film [17]. The latter phenomenon is of particular importance in this work since 40 keV Ga^+ sputters with high efficiency and, if adsorbate coverage is sufficiently depleted, milling rather than the desired deposition will result. Our measurements in the absence of the organometallic vapor indicate sputtering yields of 15.7 ± 1.3 and 12.6 ± 1.3 atoms/ion from evaporated Au and the deposited Au/C/Ga films, respectively.

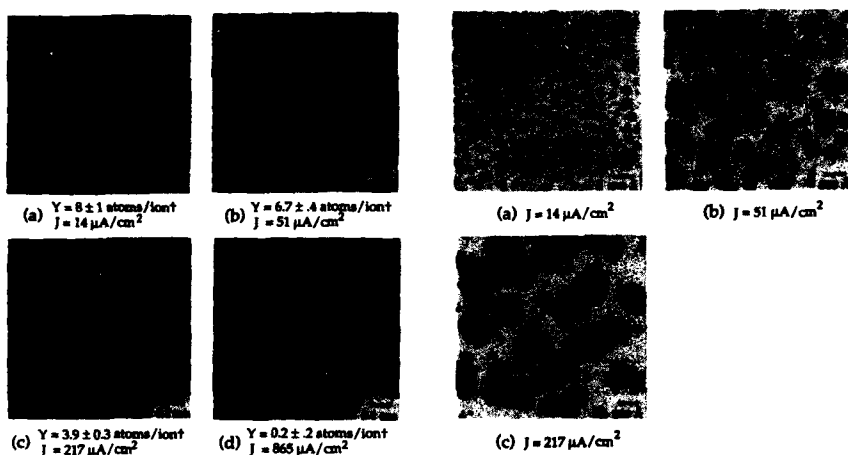


Fig. 4 SEM of films ($> 500 \text{ \AA}$ thick) deposited at various scanned current densities. All other parameters were kept fixed (a DMG(hfac) pressure of 10 mTorr, 100 pA, $0.1 \mu\text{m}$ diameter beam, scanned at 35 cm/s, and a $0.05 \mu\text{m}$ spacing between raster lines). Y is the deposition yield[†].

Fig. 5 Plan view TEM of $\sim 1000 \text{ \AA}$ thick films deposited with different current densities. All other parameters were kept fixed as in fig. 4.

In varying ion and DMG(hfac) fluxes we observed important changes in the film composition and microstructure which can be correlated with the deposition yield itself. Figure 4 shows SEM's of films deposited with scanned current densities of 14–865 $\mu\text{A}/\text{cm}^2$. These films were all deposited using 100 pA beam currents and 10 mTorr (10^{18} molecules/ cm^2) of DMG(hfac) pressure. As can be surmised from these micrographs and the composition data shown in table 1, increased ion flux and the associated decreased deposition yield correlate with lesser carbon content and increased coarsening of the crystalline islands which compose the film. As shown in figure 5, TEM analysis of films deposited onto thin membranes under identical conditions confirm that this coarsening is associated with the film microstructure and not just the surface topography.

Figure 6 shows SEM's of films deposited with DMG(hfac) pressures varying from 0.1 – 10 mTorr (10^{16} – 10^{18} molecules/ cm^2) and a scanned current density of $25.7 \mu\text{A}/\text{cm}^2$ (all other

conditions were identical to those of the films shown in figure 4). In comparing the microstructure of these films with the composition data given in table 1, we find that, again, the decreased deposition yield, this time associated with decreased DMG(hfac) flux, correlates with both a lesser carbon content and improved film growth. We note, however, that the film deposited with a yield[†] of 5.5 atoms/ion at a pressure of 0.1 mTorr is significantly purer than that deposited with a yield[†] of 3.9 atoms/ion at 10 mTorr, suggesting a more complicated relationship between carbon content and the various deposition parameters than a simple dependence on the deposition yield.

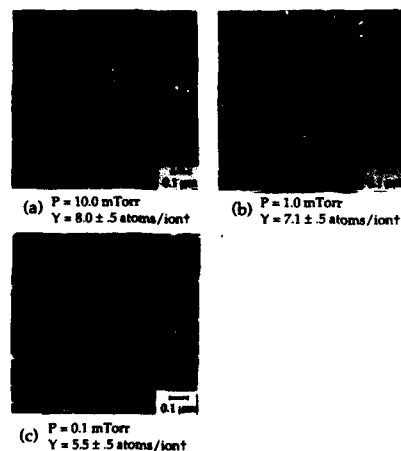


Fig. 6 SEM of films (> 1000 Å thick) deposited with various DMG(hfac) pressures. All other parameters were kept fixed (a scanned current density of 26 $\mu\text{A}/\text{cm}^2$, 100 pA, 0.1 μm diameter beam, scanned at 125 cm/s, and a 0.05 μm spacing between raster lines). Y is the deposition yield[†].

P (mTorr)	J ($\mu\text{A}/\text{cm}^2$)	Y (atoms/ion)	%Au	%C	SEM
10	14	8 ± 1	34	58	Fig. 4a
10	51	6.7 ± 0.4	38	54	Fig. 4b
10	217	3.9 ± 0.3	52	40	Fig. 4c
10	26	8.0 ± 0.5	38	55	Fig. 6a
1.0	26	7.1 ± 0.5	53	40	Fig. 6b
0.1	26	5.5 ± 0.5	64	30	Fig. 6c

Table 1 The composition of the deposited films at various scanned current densities and DMG(hfac) pressures. Composition is given in atomic % of Au and C, the remainder being Ga from the implanted beam and is based on results from Auger analysis performed after sputter removal of the first ~100 Å of material (no carbon contamination was observed outside of the deposit after this sputter cleaning). SEM micrographs of the microstructure of the corresponding films are shown in the indicated figures.

These results suggest that at high adsorbate coverage, where deposition is more efficient and more adsorbate molecules are dissociated per incident ion, the by-products of the dissociation are less efficiently desorbed from the growing film, leading to a high carbon content in these films. This carbon then impedes island growth, leading to nucleation of new islands. The resulting discontinuous microstructure explains the relatively high resistivities we have measured for deposited lines.

This interpretation agrees with the results obtained by Ro *et al.* [18] for 70 keV broad beam Ar^+ induced Au deposition. These authors examined the microstructure, carbon content and resistivity of films deposited at constant current density (0.7 $\mu\text{A}/\text{cm}^2$) and DMG(hfac) pressure but at substrate temperatures from 21°C to 160 °C (the thermal decomposition temperature of

DMG(hfac). They found that at higher temperatures carbon content and resistivity drops dramatically and film microstructure becomes continuous. From this, they concluded that at higher temperatures, where by-product desorption is aided by the additional thermal energy, the film growth is not impeded by the presence of excessive carbon and, as a result, film resistivity approaches that of bulk Au. Furthermore, the microstructure of films deposited at room temperature with Ar^+ and Ga^+ show similar characteristics. This suggests that the presence of implanted Ga in focused ion beam deposited films does not grossly affect the film growth.

CONCLUSION

We have demonstrated the utility of focused ion beam induced deposition of Au in the fabrication of submicron Au features. The microstructure, composition, and yield of the deposits have been examined for various ion current densities and various gas pressures. We suggest that the resistivity of deposited lines could be reduced below the observed value of 500 – 1500 $\mu\Omega\text{-cm}$ by modest substrate heating, as reported for broad beam induced deposition [18].

ACKNOWLEDGEMENTS

The authors thank J. Martin and E.L. Shaw for their assistance with the Auger analysis, Y.C. Lin for generously supplying thin membranes for TEM work, and J. Carter and the staff of the Submicron Structures Laboratory for their constant support. This work has been supported by U.S. Army Research Office Contract No. DAAL 03087-K-0126 and Draper Laboratory.

REFERENCES

- † The deposition yield was calculated assuming the deposit has an atomic density equal to that of bulk Au.
1. See, for example: J.M.E. Harper, J.J. Cuomo, and H.R. Kaufman, *J. Vac. Sci. Technol.* **21**, 737 (1982).
2. K. Gamo, N. Takakura, N. Samoto, R. Shimizu, and S. Namba, *Japan. J. Appl. Phys.* **23**, L293 (1984).
3. For review of the subject: D.J. Ehrlich and J.Y. Tsao, *J. Vac. Sci. Technol.* **B1**, 969 (1983).
4. S. Matsui and K. Mori, *J. Vac. Sci. Technol.* **B4**, 299 (1986).
5. R.B. Jackman and J.S. Foord, *Appl. Phys. Lett.* **49**, 196 (1986).
6. H.W.P. Koops, R. Weiel, and D.P. Kern, *J. Vac. Sci. Technol.* **B6**, 477 (1988).
7. R.R. Kunz and T.M. Mayer, *Appl. Phys. Lett.* **50**, 962 (1987).
8. K. Gamo, D. Takehara, Y. Hamamura, M. Tomita, and S. Namba, *Microel. Eng.* **5**, 163 (1986).
9. G.M. Shedd, H. Lezec, A.D. Dubner, and J. Melngailis, *Appl. Phys. Lett.* **49**, 1584 (1986).
10. F.G. Rüdener, W. Steiger, and D. Schrottmeier, *J. Vac. Sci. Technol.* **B6**, 1542 (1988).
11. L.A. Stern, D.K. Stewart, Presented at 35th Meeting of Amer. Vac. Soc. (1988).
12. J.R.A. Cleaver, H. Ahmed, P. Heard, P. Prewett, G. Dunn, H. Kaufman, *Microel. Eng.* **3**, 253 (1985).
13. N.P. Economou, D.C. Shaver, and B. Ward, *SPIE* **773**, 201 (1987).
14. M. Yamamoto, M. Sato, H. Kyogoko, K. Aita, Y. Nakagawa, A. Yasaka, R. Takasawa, O. Hattori, *SPIE* **632**, 97 (1986).
15. W.P. Robinson and D.W. Williams, Presented at 35th Meeting of Amer. Vac. Soc. (1988).
16. For review of applications of focused ion beams: J. Melngailis, *J. Vac. Sci. Technol.* **B5** 469 (1987).
17. P.G. Blauner, J.S. Ro, Y. Butt, C.V. Thompson, and J. Melngailis, to be published.
18. J.S. Ro, A.D. Dubner, C.V. Thompson, and J. Melngailis, *Mat. Res. Soc. Symp.* **101**, 255 (1988).

TEMPERATURE DEPENDENCE OF ETCH RATE AND RESIDUAL DAMAGE IN REACTIVELY ION ETCHED GaAs AND AlGaAs

S. J. PEARTON⁺, K. S. JONES⁺, U. K. CHAKABARTI⁺, B. EMERSON⁺, E. LANE⁺,
M. J. VASILE⁺, T. R. FULLOWAN⁺, W. S. HOBSON⁺, K. T. SHORT⁺
and N. M. HAEGEL⁺⁺

⁺AT&T Bell Laboratories, Murray Hill, NJ 07974

⁺University of Florida, Gainesville, FL 32611

⁺⁺UCLA, Los Angeles, CA 90024

ABSTRACT

The etch rate of GaAs and AlGaAs during $\text{CCl}_2\text{F}_2:\text{O}_2$ reactive ion etching was measured over the temperature range 50–400°C. For GaAs, the etch rate increases super-linearly from $\sim 400\text{\AA}\cdot\text{min}^{-1}$ to $\sim 3000\text{\AA}\cdot\text{min}^{-1}$ over this temperature range for a $0.56\text{ W}\cdot\text{cm}^{-2}$, 4 mTorr discharge with a 19:1 $\text{CCl}_2\text{F}_2:\text{O}_2$ mixture. The surface morphology of GaAs undergoes a smooth-to-rough transition near 150°C, and the residual damage in the near-surface region appears to decrease with increasing etch temperature. The I-V characteristics of Schottky diodes fabricated on the etched surfaces show ideality factors of 1.001 for 150°C RIE, although these worsen because of thermal degradation of higher etching temperatures. From AES and XPS data the etched GaAs shows little contamination after etching. In contrast, little temperature dependence of the etch rate of AlGaAs is observed using $\text{CCl}_2\text{F}_2:\text{O}_2$, although once again there is surface degradation for etching temperatures above 150°C.

INTRODUCTION

The plasma etching of GaAs, AlGaAs and other III-V compound semiconductors is once again becoming of critical importance, due largely to the need to achieve high resolution, anisotropic etching in device applications. There are a variety of requirements such as fast etch rate, high selectivity for example, GaAs over AlGaAs, or conversely equi-rate etching for these materials which are desirable in various fabrication schemes [1–4]. There has been a considerable effort to determine the optimum etch gas chemistries and etching conditions needed for these often diametrically opposed requirements. In the case of GaAs and AlGaAs the most common constituent of most of the gas chemistries is chlorine. This is attractive because gallium chlorides are volatile at relatively low temperatures, as opposed to the stable gallium fluorides [5,6]. Because of this, the use of CCl_2F_2 -based etching is commonly used to give high selectivities for GaAs over AlGaAs, as high as 600:1 under optimum conditions. It appears that the formation of stable AlF species is the etch-stop mechanism when etching through GaAs to an underlying AlGaAs layer.

To date, surprisingly little work has been directed toward measuring the temperature dependence of the etch rates of GaAs and AlGaAs in CCl_2F_2 mixtures, and more studies are needed on the chemical nature of the etched surfaces. In most commercial plasma etching systems, there is some rise in temperature of the sample in the first few minutes of the etch unless precautions to ensure good thermal contact to the cathode are taken [7]. In this paper we report the temperature dependence of etch rate of GaAs and AlGaAs during $\text{CCl}_2\text{F}_2:\text{O}_2$ reactive ion etching (RIE) over the temperature range 50–400°C. In addition, we have looked at the residual disorder in the GaAs using transmission electron microscopy (TEM) and studied the etched surface chemistry by X-ray Photoelectron Spectroscopy (XPS) and Auger Electron Spectroscopy (AES). The current voltage characteristics of simple Schottky diodes were used to measure the electrical quality of the etched material.

EXPERIMENTAL

The GaAs samples used consisted of bulk, LEC-grown substrates oriented in the (100) direction. The wafers were undoped with resistivities of $4\text{--}6\times 10^7\ \Omega\cdot\text{cm}$. The AlGaAs layers for etching were grown by Metal Organic Chemical Vapor Deposition (MOCVD) on semi-insulating GaAs substrates. The Al fraction was varied from 0.15 to 1 (AlAs), as measured by photoluminescence at 4K. A thin (200Å) GaAs cap was deposited on top of the 1 µm thick AlGaAs layers to prevent oxidation of the layers. This was etched off in 15–20 secs during the RIE treatment.

The samples were patterned for etching using a lithographically defined AZ1350J photoresist mask, consisting of a variety of lines and spaces of different sizes (1-100 μm). For elevated temperature etching a SiN_x mask in the same pattern was used. After RIE, the masks were stripped off in buffered HF solution, and the etch depth measured with a Dektak Stylus profilometer. The isotropy of the etch was determined from SEM examination of the etched patterns. The surface chemistry of the etched surfaces was obtained from Auger Electron Spectroscopy (AES) and X-ray Photoelectron Spectroscopy (XPS). The presence of sub-surface disorder was determined from ion channelling and cross-sectional Transmission Electron Microscopy (TEM). In some experiments we included n-type GaAs ($n = 10^{17} \text{ cm}^{-3}$) wafers with alloyed AlGeNi rear contacts, and n-type AlGaAs layers grown on n^+ GaAs substrates, also with alloyed rear ohmic contacts, during the RIE treatments. After RIE, arrays of TiPtAu Schottky contacts were evaporated onto the etched surface. These samples were used for measurement of the Schottky barrier heights and ideality factors from current-voltage characteristics. Etching was carried out in a conventional asymmetric electrode RIE system (MRC Model 51) using a $\text{CCl}_2\text{F}_2:\text{O}_2$ mixture. The samples were fixed to the cathode using a heat-sinking grease, and each RIE treatment was for 4 min.

RESULTS AND DISCUSSION

(a) GaAs

The average etch rate of GaAs as a function of sample temperature, at a $\text{CCl}_2\text{F}_2:\text{O}_2$ pressure of 4 mtorr, flow rate of 20 sccm, plasma power density of $0.56 \text{ W}\cdot\text{cm}^{-2}$, and a gas composition of 19 $\text{CCl}_2\text{F}_2:\text{O}_2$, is shown in Figure 1. The increase in etch rate is super-linear over the temperature range measured. The morphology of the etched surface changes dramatically with the temperature of the sample during the RIE treatment. For etching temperature up to $\sim 100^\circ\text{C}$, the GaAs surface remains smooth, with morphological roughness $\leq 50\text{\AA}$. Around 150°C the sample becomes rather rough, with surface roughness on the order of 200-400 \AA . Beyond $\sim 180^\circ\text{C}$ the surface undergoes a rough to smooth transition, and at 250°C the morphology is comparable to room temperature etching. Beyond $\sim 275^\circ\text{C}$ the etched surface becomes progressively rougher, until at 400°C there are morphological features up to $0.4 \mu\text{m}$ deep visible in both TEM and SEM micrographs. Figure 2 shows SEM pictures of the surfaces of unpatterned GaAs samples after RIE at 50, 150, 250 and 400°C respectively.

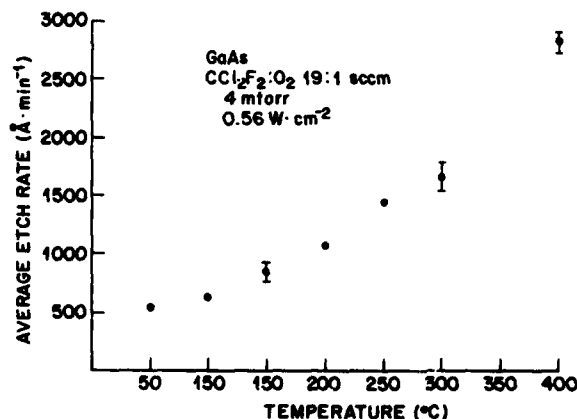


Figure 1. Average etch rate of GaAs in a $0.56 \text{ W}\cdot\text{cm}^{-2}$, 4 mTorr discharge using a 19:1 $\text{CCl}_2\text{F}_2:\text{O}_2$ mixture. The gas flow rate was 20 sccm, the self-bias on the cathode was $\sim 380\text{V}$, and the etching time was 4 min at each temperature.



Figure 2. SEM micrographs of GaAs surfaces after etching in a $0.56 \text{ W}\cdot\text{cm}^{-2}$, 4 mTorr, 19:1 $\text{CCl}_2\text{F}_2\text{:O}_2$ discharge, for 4 mins at 50°C (top left), 150°C (top right), 250°C (bottom left) and 400°C (bottom right).

Arrhenius plots of the average etch rates of GaAs under our conditions, as a function of inverse temperature are shown in Figure 3. At elevated temperatures the data can be fitted by an activation energy of 0.11 eV, but the slope of the graph changes around 160°C, and to guide the eye we show a line through the lower temperature data with a slope of 0.17 eV. We take this change in slope to indicate there are at least two mechanisms involved in the etching of GaAs by $\text{CCl}_2\text{F}_2\text{:O}_2$ over the temperature range 50–400°C. Since the microscopic etch mechanisms are not clear in semiconductors, we can only speculate on the reasons for the change in the slope, but Auger data shows that the As-to-Ga ratio in the near-surface region after RIE increases for increasing temperatures, indicating that the rate of removal of Ga chlorides becomes relatively faster than the rate of removal of As chlorides. Accounting for the surface-roughening described above, there were no significant differences in the amount of oxide or carbon remaining on the etched surfaces. In all cases, F and Cl were restricted to the immediate surface.

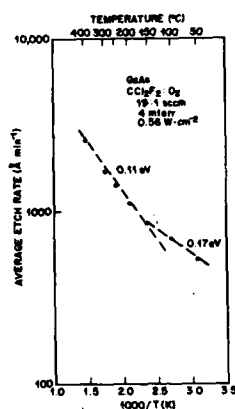


Figure 3. Arrhenius plot of average etch rate of GaAs under the conditions described in the caption of Figure 1, as a function of inverse temperature during the RIE.

We note also at this point that there was no dependence of GaAs etch rate at 4 mTorr pressure on plasma power density for elevated temperature (100–300°C) etching. This is in direct contrast to the result at ≤50°C, where there was almost a linear dependence of etch rate on the power density in the $\text{CCl}_2\text{F}_2\text{:O}_2$ discharge. This indicates that at this pressure the etch rate is not desorption limited above 100°C, so that increasing the ion energy bombarding the GaAs surface does not lead to an increase in the rate at which material is removed. For etching at 200°C, we did however, see a transition to

smoother surface morphologies upon increasing the discharge power density from $0.4 \text{ W}\cdot\text{cm}^{-2}$ to $1.3 \text{ W}\cdot\text{cm}^{-2}$. At this temperature we also observed much more outward sloping of the sidewalls of etched features as the pressure was increased from 4-40 mTorr. At a given temperature, the etch rate tended to go through a maximum near 20 mTorr, and then decrease with increasing pressure. This is probably the result of insufficient sweeping away of the etch products at higher pressures. We would then expect an increase in etch rate if the power density were increased.

Figure 4 shows the Schottky barrier heights and ideality factors obtained from I-V characteristics in etched GaAs samples. The ideality factor goes through a minimum for 150°C etching - note that even for etching at 50°C the diode ideality factor is larger than on an unetched control sample. The Schottky barrier height shows a weak increase for etching temperatures up to $\sim 250^\circ\text{C}$, and has a dramatic increase after 400°C etching. This is probably the result of the formation of a disordered near-surface "dead" region. We have seen similarly large barrier heights on GaAs samples that have been implanted with very high doses ($\sim 10^{16} \text{ cm}^{-2}$) of either As or Ga ions at low energy (20 keV). This is somewhat akin to the use of thin p^+ layers on n-type material in order to make electron conduction more difficult from semiconductor to metal. For etching at 50°C we saw a slight increase in ideality factor and a decrease in Schottky barrier height with increasing plasma power density. This is consistent with the introduction of generation-recombination centers into the near-surface region. With cross-sectional TEM no sub-surface dislocation loops associated with the etching process were observed for power densities below $0.6 \text{ W}\cdot\text{cm}^{-2}$, which implies that the changes in electrical properties of the GaAs are related to point defects inaccessible to TEM. At power densities above $\sim 1 \text{ W}\cdot\text{cm}^{-2}$ we did observe the introduction of large densities ($\sim 10^8 \text{ cm}^{-2}$) of small loops.

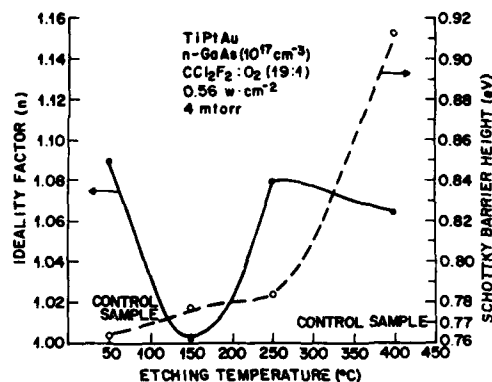


Figure 4. Schottky barrier heights and ideality factors from TiPtAu Schottky diodes on n-type GaAs etched in a 19:1 $\text{CCl}_2\text{F}_2:\text{O}_2$, $0.56 \text{ W}\cdot\text{cm}^{-2}$ discharge, as a function of the temperature of the sample during the RIE treatment.

(b) AlGaAs

The behaviour of AlGaAs during RIE with CCl_2F_2 was quite different to GaAs. Figure 5 shows the average etch rate of AlGaAs with varying Al compositions, as a function of temperature. There is basically no variation of etch rate with temperature for any composition. This kind of behaviour has been observed previously by Contolini [7] for a number of III-V materials.

We observed progressively poorer surface morphologies for increasing temperatures and for higher Al compositions for fixed etching conditions. This is somewhat unexpected because one would have thought that the removal of the relatively involatile AlF species would have been easier at elevated temperatures. The AES data showed the formation of an aluminum oxide film after etching, with lower Al content samples have a thicker film. Figure 6 shows AES depth profiles of As, Ga, Al, O, C, F and Cl in $\text{Al}_{0.25}\text{Ga}_{0.75}\text{As}$ samples after etching at 125 or 350°C . There is a more pronounced oxide in the sample etched at the higher temperature. This oxide film was approximately a factor of three thinner in $\text{Al}_{0.71}\text{Ga}_{0.29}\text{As}$ layers etched under the same conditions. There was very little F or Cl remaining in the AlGaAs surfaces after RIE.

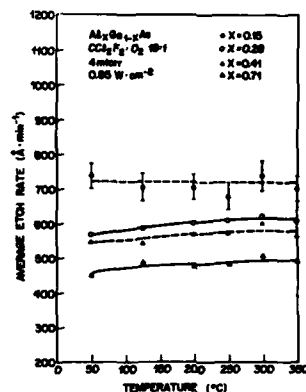


Figure 5. Average etch rate of AlGaAs in a $0.85 \text{ W}\cdot\text{cm}^{-2}$, 4 mTorr discharge using a 19:1 $\text{CCl}_2\text{F}_2:\text{O}_2$ mixture. The gas flow rate was 20 sccm. The self-bias on the cathode was $\sim 480\text{V}$, and the etching time was 4 min at each temperature.

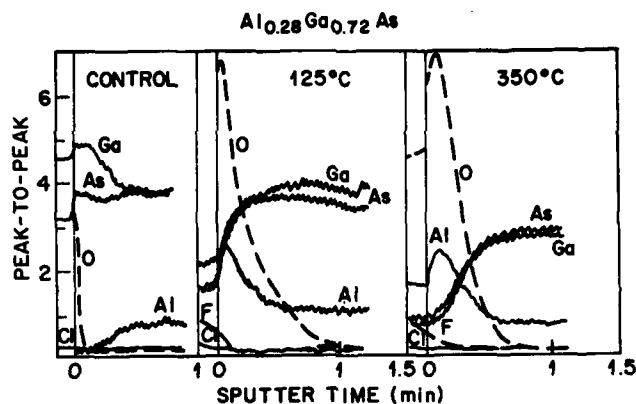


Figure 6. AES depth profiles in $\text{Al}_{0.28}\text{Ga}_{0.72}\text{As}$ samples etched in a $0.85 \text{ W}\cdot\text{cm}^{-2}$, 4 mTorr, 19:1 $\text{CCl}_2\text{F}_2:\text{O}_2$ discharge, with the sample held at 125°C or 350°C . The control sample had a capping layer of 200Å of GaAs. This is usual in the growth of GaAs, in order to prevent oxidation of the AlGaAs.

In general, for AlGaAs we saw decreasing etch rates for increasing Al contents, with the etch rate actually falling with time, presumably due to the formation of an increasing density of involatile AlF_3 species and aluminum oxide. This is consistent with the super-linear increase in etch rate with increasing plasma power density. There was also a dramatic decrease in etch rate with increasing gas pressure, indicating less efficient removal of etch products.

SUMMARY AND DISCUSSION

For Freon 12 :oxygen RIE of GaAs, we observe a strong dependence of etch rate on sample temperature during the plasma exposure. The surface morphology of the etched GaAs goes through a smooth-rough-smooth-rough series of transitions at ~ 150 , 180 and 275°C respectively. The activation energy for etching GaAs under our conditions is between 0.11-0.17 eV, and indicates there are at least two etch mechanisms present. The surfaces after RIE are chemically rather clean, although there is evidence for the introduction of near-surface disorder by ion bombardment during the etch. This would be expected from the rather high self-bias ($\sim 380\text{V}$) on the cathode under our conditions. The displacement threshold energy in semiconductors is on the order of 15-20 eV, so that in principle an ion of full energy crossing the plasma sheath at the cathode and striking the GaAs surface could displace 19-25 Ga or As atoms.

The case of Freon 12:O₂ etching of AlGaAs is quite different to that of GaAs. There is little temperature dependence of the average etch rate, with rough surface morphologies above 150°C . Although the use of CCl_2F_2 is commonly used in conjunction with AlGaAs as an etch stop in GaAs-AlGaAs heterostructures, it is worth calibrating the removal rates of AlGaAs using this chemistry, simply because in some situations one wishes to etch GaAs and subsequently to slowly remove some AlGaAs. For the case where GaAs and AlGaAs need to be etched at similar rates, the use of Cl_2 is a better choice.

REFERENCES

1. H. Tamura and H. Kuritara, *Jpn. J. Appl. Phys.* 23, L731 (1988).
2. M. B. Stern, A. G. Craighead, P. F. Liao and P. M. Mankiewich, *Appl. Phys. Lett.* 45, 410 (1984).
3. C. B. Cooper, III, S. Salimian and H. F. MacMillan, *Appl. Phys. Lett.* 51, 2225 (1987).
4. A. Scherer, H. G. Craighead and E. D. Beebe, *J. Vac. Sci. Technol.* B5, 1599 (1987).
5. S. Semura, H. Saitoh and K. Asakawa, *Proc. Symp. on Dry Process*, ed. J. Nishizawa (Inst. Electrical Engineers of Japan) pp. 68-72, (1982).
6. K. L. Seaward, N. J. Moll, D. J. Coulman and W. F. Stickle, *J. Appl. Phys.* 61, 2358 (1987).
7. R. L. Contolini, *J. Electrochem. Soc.* 135, 929 (1988).

SURFACE MORPHOLOGICAL CHANGES OF POLYIMIDE WITH OXYGEN REACTIVE ION BEAM ETCHING (RIBE)

Kyung W. Paik and Arthur L. Ruoff, Department of Materials Science and Engineering, Cornell University, Bard Hall, Ithaca, NY 14853

ABSTRACT

At the beginning of etching, surface asperities appeared on the top plane of the polyimide (PI) film. The formation of surface asperities is due to the ordered phase in PI film. The known dimension of the ordered phase measured by X-ray diffraction is consistent with the size of surface asperities, 100 Å, observed by TEM. Further ion doses made these asperities evolve into smooth bumps which then eroded into cones as a result of etch yield difference as a function of the angle of beam incidence $Y(\theta)/Y(0)$ which has a maximum at $\theta=70^\circ$. Finally cones led to the development of grass-like structure on the top plane of the PI film. The formation of plate-like structure on the cross-sectional plane of PI indicates that the structural inhomogeneity of the PI film (the ordered and disordered phase) is the main cause for the surface morphological changes of PI.

INTRODUCTION

Polyimide has been used in advanced electronic packaging technology as a dielectric material. Among the multi-level electronic packaging technologies, thin film multilayer (TFML) structures with Cu conductor and polyimide can provide high density and high speed interconnections in a multichip package.[1] However, one of the problems of Cu/PI interconnection is that Cu does not stick to fully cured PI because of its weak chemical interaction with PI. [2]

Basically, the adhesion of two materials depends on the chemical reactivity and the surface morphology at the interface. Because Cu has little chemical reactivity with PI, one way to improve adhesion of Cu/PI is the surface modification of the substrate material in order to increase mechanical interlocking.[3] Among several surface modifying techniques, plasma etching and reactive ion etching (RIE) have been used to modify PI surface to improve adhesion. However, the mechanism of morphological changes of PI film under oxygen ions has not been clearly understood.

In this study we investigate the mechanism of morphological changes of PI film with the oxygen RIBE which has several advantages-- independent control of beam energy, current density, and angle of ion incidence -- compared with oxygen plasma etching and RIE.

EXPERIMENTS

Two types of PI films, Kapton-H film and a spin-coated PI (DuPont 2540) film on a silicon wafer, were prepared. The spin-coated PI was dried at 135 °C for 30 minutes, and then cured at 400 °C for 1 hour in an Ar gas atmosphere. Oxygen reactive ion beam etching (RIBE) was carried out with various beam energies (500, 1000 eV), ion current densities (from 0.4 to 1.2 mA/cm²) and etching times. The chamber base pressure was 2×10^{-6} Torr and the operating oxygen base pressure was 2×10^{-4} Torr. Most of the etching was performed on the top plane of both films. A cross-sectional slice (normal to their surfaces) of film was also prepared and etched to find whether there were any morphological differences between the cross-sectional and the top plane of the PI film. To prepare the cross-sectional slice, a half area of the top plane was masked by a glass slide and then etched by O₂ RIBE to create a 10 µm high step on the top surface. The side of this step (the cross-section) was then subsequently etched by oxygen beams normal to this cross section. The surface morphology of the cross-section was observed by SEM.

Other spin-coated PI films were also prepared on a salt (NaCl) crystal. Dilute polyamic acid solution was used to obtain an adequate film thickness by controlling spinning speed. The film thickness was approximately 2000 Å plus the depth of etched PI under the given beam conditions. The anticipated depth of PI film etched away can be easily obtained by the curve of etch rate vs etching conditions.[4] The thickness of the PI left on a salt crystal after O₂ RIBE can be controlled to be approximately 2000 Å which is the proper thickness for TEM observation. The etched PI on salt crystal was cut by a razor blade into small square shapes with 2mm length to fit in a Cu grid for TEM, and then immersed in distilled water to dissolve the salt crystal substrate. The floating PI film was picked up by the Cu grid, and dried for TEM observation. The etched side of the PI film always faced toward the electron beams in the TEM.

The sputter yield of PI as a function of angle of ion beam incidence was carried out to explain the details of morphological change in PI. Part of PI sample masked by a glass slide was attached to various tilted specimen stages and etched to make an etch step. Sputter yield was obtained by measuring the depth of etch steps with a surface profilometer. As θ , the angle between ions and plane normal, increases, the ion flux (J) was multiplied by $1/\cos\theta$ in order that $J\cos\theta$ was kept constant as 0.5 mA/cm².

RESULTS

1. SEM observation

The surface morphology of PI changed substantially with beam energies and ion doses (beam current density times etching time). Fig. 1 shows the surface morphological changes of PI with various etching times at a fixed beam energy of 1000 eV and current density of 1.2 mA/cm². Etch pit-like

structure appeared on a smooth PI surface during the initial etching with less than 5×10^{17} ions (1 minute etching). These etch pits evolved to surface cracks during further ion etching, grew deeper and propagated, and led to the development of grass-like structure at the top plane of the PI films as shown in Fig. 2(a). The grass-like structure became deeper and wider at larger ion doses and higher beam energies due to surface erosion resulting from simultaneous chemical reaction and physical bombardment effects of oxygen ions[5]. When oxygen ions bombard normally on a cross-sectional plane, a plate-like structure with a different morphology was observed as shown in Fig. 2(b).



Fig. 1 SEM pictures illustrating surface morphological changes by O₂ RIBE (A) Unetched (B) 1, (C) 3, (D) 5 mins. (at 1000 eV, 1.0 mA/cm²)

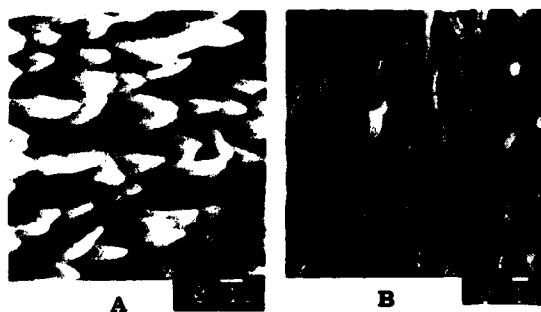


Fig. 2
Typical grass-like structure(A) on top plane and plate-like structure(B) on cross-sectional plane
(A) 1000 eV / 1.2 mA/cm² / 10 mins.
(B) 1000 eV / 1.2 mA/cm² / 5 mins.

2. TEM observation

Fig. 3 shows the finer details of the morphological changes observed by TEM as a function of etching time at constant 500 eV and 1.0 mA/cm². Fine surface bumps of approximately 100 Å at the tip were observed for up to 1.5 minutes (5.6×10^{17} ions) etching. Etching over 1.5 minutes decreases the

number of bumps and makes a bump structure erode into a cone structure as shown in Fig. 3 (e).

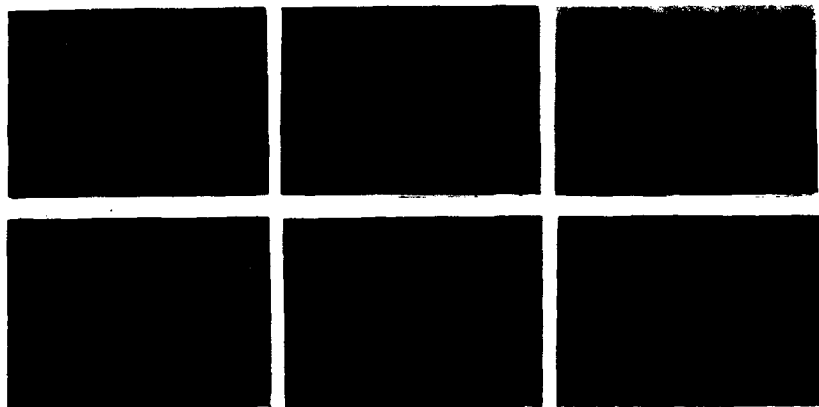


Fig.3 TEM pictures illustrating the morphological change of PI with etching times. (Ion beams : Oxygen, 500 eV, and 1.0 mA/cm²) (A) Unetched, (B) 0.5, (C) 1.0, (D) 1.5, (E) 2.5 mins.(30° tilted) and (F) Ar IBE etched, 500 eV, 0.8 mA/cm² and 2.5 mins.

3. Yield versus angle observation

Fig. 4 shows the result of etch yield, $Y(\theta) / Y(0)$, as a function of the angle between ions and plane normal. The linear rate of surface erosion[6]

$$R_n = (J \cos \theta) Y(\theta) / N$$

where

$Y(\theta)$: the sputtering yield as a function of ion angle of incidence θ

θ : the angle between ions and plane normal

J : uniform ion flux density (ions/cm².s)

N : atomic density of substrate

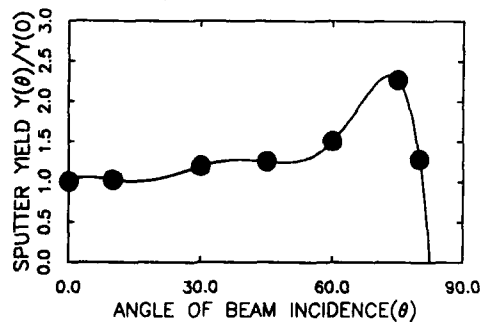


Fig. 4. Sputter yield of PI versus the angle θ
Beam conditions: 1000 eV, 0.5 mA/cm², 12 mins

is determined by the function $Y(\theta)$ which has a maximum value of 2.3 at $\theta=70^\circ$ compared with $Y(0) = 1$ at $\theta = 0$, because the ion flux falling upon the unit area of this plane, $J\cos\theta$, is kept constant as 0.5 mA/cm^2 at various angle θ . The side of bumps where the angle between ions and plane normal is about 70° was eroded faster than the top and bottom plane of the bumps where $\theta=0^\circ$, resulting in the formation of cones.

4. Reasons for morphological changes

Suggestions have been made about the change in surface morphology after oxygen ion etching. Rangelow et. al.[7] and Kogoma et. al.[8] suggested that the appearance of the surface roughness is caused by metal contaminant due to sputtering of reactor walls during O_2 reactive ion etching (RIE) and by a deposited material (CnHmOx) during O_2 plasma etching, respectively. However, the idea of surface impurities cannot explain several observed phenomena. First, different surface morphologies -- grass-like and plate-like structure -- are found at the top plane and the cross-sectional plane of the PI film, respectively. If the surface impurities during the etching were the main cause for morphological changes, there would be the same grass-like structure at the cross-sectional plane of PI film too. Second, no measurable surface metal impurities were found in our surface sensitivity enhanced XPS studies and X-ray elemental analysis in STEM. Third, as shown in Fig. 3(f) Ar IBE made no specific surface morphology appear in PI. If the shadowing effect of surface impurities were the origin of the morphological changes, there would be the same grass-like structure during Ar IBE. Furthermore, suppressing the occurrence of the grass-like structure by the addition of CF_4 to the O_2 ion beam[7] also proves that the simple shadowing effect by surface impurities cannot be the reason for morphological changes in PI with the oxygen RIBE. Thus, we suggest that structural inhomogeneities in the PI film, specifically ordered and disordered phases, are the main reason for the observed morphological changes in PI.

The microstructure of PMDA-ODA PI film has been investigated by numerous groups using scattering and diffraction.[9, 10] Long-range crystalline structure does not exist in the thermally imidized PI film. However, short range ordered structures described as crystalline were observed only in highly extended chain segments. The alignment of the polymeric chain backbone in the plane of the film during the solvent coating process, especially a molecular orientation of the PI parallel to the surface of the film has been observed.[11] The mean dimension of the ordered regions in PI film in directions normal and parallel to the lamellae are about 10-25 Å and greater than 100-130 Å, respectively.[12] In addition, the lateral alignment of chain segment in the plane of the PI film also may order along the vertical direction of the PI film.

The etch rate of the ordered phase will be less than that of the disordered

phase. This is because the ordered phase is denser and more tightly bonded and therefore less vulnerable to oxygen ions than the disordered phase. As a result, etch pits develop at the early stage of etching around ordered phases on the top plane, and then round bump shaped surface asperities originate from etch pits and evolve into cones during further etching because of erosion rate difference at various angle θ as explained in the etch yield studies. Cones were etched continuously during higher ion doses. Some small cones disappeared as a result of further etching. Finally, long and thin grasses were formed on the top plane. Plate-like structure was also formed along the ordered phase in the cross-sectional plane.

SUMMARY

1. The morphological change of PI with O₂ RIBE follows the formation of etch pits, bumps, cones, grass-like and plate-like structure.
2. The formation of surface asperities during etching is due to the structural inhomogeneities of PI film (ordered and disordered phases).
3. The erosion of bumps into cones during morphological changes in PI can be explained by the observed fact that the etch yield difference as a function of angle of beam incidence, $Y(\theta)/Y(0)$, has maximum at $\theta=70^\circ$.

ACKNOWLEDGEMENT

Support by General Electric Co. (No AGMT DTD 120886) is acknowledged.

REFERENCES

1. R. J. Jensen, J.P. Cummings, and H. Vora, IEEE Trans. Components, Hybrids, Manuf. Technol., **CHMT-7**, 384-393, (1984)
2. N.J. Chou and C.H. Tang, J. Vac. Sci. Technol., **A2**(2), 751-755, (1984)
3. D.E. Packham, in Adhesion Aspects of Polymeric Coatings, edited by K.L. Mittal, 19-44, Plenum Press, New York, (1983)
4. W.E. Vanderlinde, PhD thesis, Cornell University, (1988)
5. K.W. Paik and A.L. Ruoff, in Proc. Materials Res. Soc. Symp.: Adhesion in Solids, **119**, p 271-276, edited by J.E.E. Baglin, D.M. Mattox, C. Batich, R.J. Gottschall, (Mat. Res. Soc., Pittsburg, 1988)
6. G. Carter and M.J. Nobes, in Ion Bombardment Modification of Surfaces, O. Auciello and R. Kelly, 163-224, Elsevier, Amsterdam, (1985)
7. I.W. Rangelow, K. Macheli, L. Niewohner, R. Kassing and W. Pilz, Microelectronic Engineering, **3**, 475-481, (1985)
8. M. Kogoma, G. Turban, in Plasma Chemistry and Plasma Processing, **6**, 349-380, (1986)
9. T.P. Russell, J. Polym. Sci., Polym. Phys. Ed. **22**, 1105-1117, (1984)
10. N. Takahashi, D.Y. Yoon and W. Parrish, Macromol., **17**, 2583-2588, (1984)
11. W.M. Prest, Jr. and D.J. Luca, J. Appl. Phys., **51**(10), 5170-5174, (1980)
12. S. Isoda, H. Shimada, M. Kochi, and H. Kambe, J. of Polym. Sci., Polym. Phys. Ed., **19**, 1293-1312, (1981)

ON THE USE OF MÖSSBAUER NUCLEI AS PROBES OF RADIATION INDUCED EFFECTS AT INTERFACES

P. A. INGEMARSSON*, T. ERICSSON**, G. POSSNERT*** AND R. WÄPPLING**

*Dept. of Radiation Sciences, Uppsala University, Box 535, S-751 21 Uppsala, Sweden

**Department of Physics, Uppsala University, Box 530, S-751 21 Uppsala, Sweden

***The Svedberg Laboratory, Box 533, S-751 21 Uppsala, Sweden

ABSTRACT

Conversion electron Mössbauer spectroscopy was used as a means of investigating radiation induced changes at thin film interfaces. 25 Å thick layers of ^{57}Fe were evaporated onto substrates of Si, SiO_2 and Al_2O_3 and covered with 150 Å ^{56}Fe . Samples were then subjected to ion irradiation with 20 MeV Cl^{4+} to doses ranging from 10^{12} to 2×10^{14} ions/cm² and subsequently annealed in vacuum at 450 °C. Mössbauer spectra were recorded before and after each step. The analysis revealed chemical alterations, induced by the ion bombardment, indicative of film-substrate bond formation and reconstruction of residual surface hydrocarbons. The results are interpreted in view of accompanying enhancements in thin film adhesion.

1 INTRODUCTION

Until recently, studies of interface modifications induced by ion irradiation have focused on the use of keV ions [1,2], generally referred to as ion beam mixing. In 1982, some of the merits associated with MeV-ion beam processing of thin film interfaces became evident when Griffith *et al.* [3] reported that the electronic interactions, initiated by ions in this energy region, could be applied as a post-deposition treatment of thin metal films to improve their adhesion to supporting substrates. Large ion ranges, negligible sputtering of the metal surface and limited interface mixing (except for polymers) are benefits, compared to keV ions, from which a growing interest in this field can be derived.

The fact that the region in which the effects are taking place seems to be confined to only a few monolayers near the interface was illustrated in an RBS study of multilayer Ag-Si structures [4]. Within the resolution of this technique, no interfacial mixing could be detected, leading to the conclusion that such a mixing, if it exists, would have to be restricted to a region of less than ~20 Å from the interface. This result implies that only a few atoms per unit area are subjected to changes induced by the penetrating ions. Accordingly, any physical or chemical approach in the analysis of these effects calls for extraordinary demands with respect to sensitivity as well as depth resolution.

Conversion Electron Mössbauer Spectroscopy (CEMS) is a method which has attracted attention in thin film and interface analysis. As concerns the effects of particle beam processing, the interest in CEMS has, so far, mainly been focused on ion beam mixing [5,6]. However, appreciable progress has also been made in the characterization of MeV-ion effects at metal-polymer interfaces [7-9]; both of these types of studies are associated with comparatively large effects and have, consequently, been the subject of extensive investigations.

In the present paper, we report on the use of CEMS to characterize MeV-ion induced alterations at iron thin film interfaces. We will primarily consider systems that belong to the category in which the modifications induced by the ion beam are restricted to the near-interface region.

The thermal stability of the different components, formed as a result of the ion irradiation, were investigated by subsequent heat treatment of the samples. A comparison will be made with previous studies of the iron-Teflon interface.

2 EXPERIMENTAL

Wafers of sapphire, fused silica and silicon, 50 mm in diameter, were used as substrates for thin film deposition. Before being loaded into an evaporation chamber, they were cleaned according to the following procedure: Al_2O_3 and SiO_2 were successively washed in hot diluted detergent, de-ionized water, boiling $\text{HNO}_3\text{:H}_2\text{O}$ (1:1) solution, de-ionized water and finally methanol. The silicon substrate was dipped in $\text{HF:H}_2\text{O}$ (1:50) solution for about half a minute. Films of ^{57}Fe , 25 Å thick, were thermally evaporated at a base pressure of 2×10^{-6} torr. Without breaking the vacuum, additional 150 Å thick ^{56}Fe layers were deposited on top in order to minimize atmospheric exposure of the ^{57}Fe surface. Specimens serving as adhesion test samples were prepared in a similar way, however, the wafers were smaller ($\sim 1 \text{ cm}^2$) and the iron used for film deposition consisted of natural Fe. The film thickness was monitored by a quartz crystal oscillator.

Ion irradiation was performed using the Uppsala EN-tandem Van de Graaff accelerator. Samples were irradiated with 20 MeV Cl^{4+} to doses ranging from 10^{12} to 2×10^{14} ions/ cm^2 , although only the highest dose was considered in the Mössbauer study. The beam was electrostatically swept over an area of $50 \times 50 \text{ mm}^2$ using a scanning assembly described elsewhere [10]. The large sample area enabled us to collect Mössbauer data with relatively good statistics within a few days of measurements. The specimens were subsequently annealed in vacuum at 450 °C for one hour. Scratch tests were used to determine possible adhesion improvement of the iron films, the preferential removal of the film serving as a qualitative measure.

In the study of thin films or thin embedded layers, the detection of back-scattering conversion electrons is usually advantageous, compared to the transmission mode, for intensity and signal-to-background reasons. Accordingly, conversion electron Mössbauer spectroscopy was employed in the present study. Ambient temperature spectra were recorded for as-deposited, irradiated and, irradiated and heat treated samples. A computer controlled Mössbauer spectrometer allowing for simultaneous velocity calibration was employed using iron metal at room temperature as the standard.

3 RESULTS AND DISCUSSION

The Fe- SiO_2 and Fe- Al_2O_3 systems showed a considerable improvement in adhesion for areas exposed to irradiation at doses above $\sim 10^{13}$ ions/ cm^2 . The bond strength of iron films to silicon, however, was relatively high already before the ion bombardment was carried out and, accordingly, no clear enhancement in adhesion could be observed following ion beam exposure. The difference in behaviour between SiO_2 and Al_2O_3 on the one hand and Si on the other hand could probably be attributed to the different cleaning procedures, the rinse in methanol leaving behind a comparatively large amount of residual hydrocarbons at the surface. In order to clarify the influence of the sample pre-treatments, further studies have to be undertaken.

Not only the existence but also the actual amount of hydrocarbons on the substrate surface has been found to considerably affect the strength of adhesion. Mendenhall [4] reported the adhesion for Au and Ag films on Si as being strongly dependent on whether or not the silicon was rinsed in methanol prior to film evaporation. Similar results were reported by Baglin *et al.* [11] who exploited different cleaning procedures thereby deliberately creating certain chemical

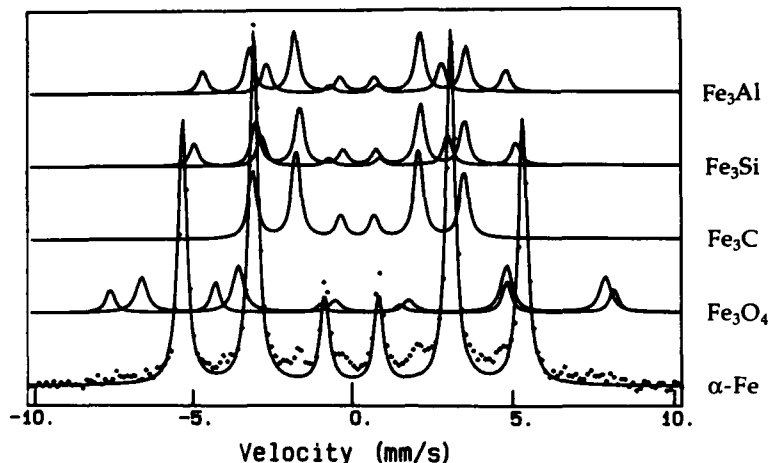


Figure 1. Mössbauer spectra for some possible iron-compounds

properties at the interface under study. The importance to adhesion of MeV ion induced bond breaking of hydrocarbons at interfaces has been stressed as this process may give rise to structures where the film atoms are in immediate contact with the substrate atoms [12-14]. Furthermore, the large number of secondary electrons ejected from such contaminants has been proposed to contribute to the adhesion improvement [15].

Radiation induced alterations were also exhibited in the Mössbauer spectra, the interpretation of which was based on models of possible compounds which might be formed as a result of the presence of different atomic species. The signals corresponding to some possible compounds, to be formed subsequent to ion bombardment, are displayed in Figure 1. In Fe_3Al and Fe_3Si , iron is located at two different sites having 4 (A-site) and 8 (B-site) nearest neighbour iron atoms, respectively, with the relative abundance 2:1. Also in the case of Fe_3O_4 , two different iron sites have to be considered. As can be seen, it is an unfortunate coincidence that the Mössbauer line positions in cementite (Fe_3C) overlap with those of the A-site in Fe_3Si (or Fe_3Al) whereas the positions of the lines originating from the B-site in Fe_3Si (Fe_3Al) are rather close to that of iron metal. Consequently, an unambiguous distinction between Fe_3C and Fe_3Si (Fe_3Al) is difficult and we will in the following denote this component Fe_3X .

Typical Mössbauer spectra corresponding to 25 Å ^{57}Fe films on Si and SiO_2 are shown in Figures 2 and 3, respectively. At a dose of 2×10^{14} ions/cm², tiny alterations can be observed in the Mössbauer spectra (Figures 2b and 3b). This implies that only a limited number of iron atoms are affected by the irradiation process. One possibility is that only those iron atoms which are close to the interface suffer an appreciable change in their local surrounding. If this is the case, one would expect to find components in the spectra characteristic for iron-silicon compounds as well as for iron-oxygen and iron-carbon species. The carbon can be introduced both from the vacuum system and from the pre-treatment of the substrate whereas the other components are constituents of the substrate. However, it is clear that most of the features found in the investigated samples can be attributed to the proposed compounds used.

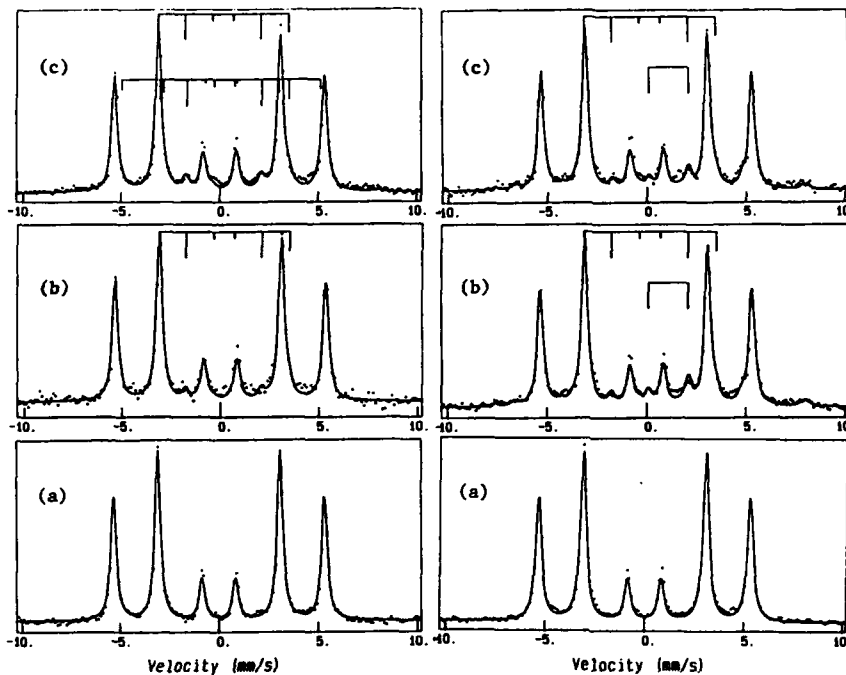


Figure 2. Mössbauer spectra for ^{57}Fe films on Si corresponding to (a) untreated, (b) irradiated to 2×10^{14} ions/cm 2 and (c) irradiated and annealed specimen

Figure 3. Mössbauer spectra for ^{57}Fe films on SiO_2 corresponding to (a) untreated, (b) irradiated to 2×10^{14} ions/cm 2 and (c) irradiated and annealed specimen

When estimating the contribution from the different components, one has to make assumptions regarding the relative line intensities of each subspectrum. The iron metal spectrum shows relative line intensities characteristic for an in-plane magnetization and, accordingly, the intensities quoted below were derived with the same assumption.

The evolution of the Mössbauer spectra for the different iron-substrate combinations show similar features in terms of the different components formed during the processing. In the case of e.g. the silicon substrate, the Mössbauer spectrum after evaporation revealed the normal metallic iron spectrum. The intensity of the Fe_3X species increases upon irradiation to about 5%. After subsequent heat treatment, the amount of Fe_3X has increased to ~8% and one sees the formation of Fe_3O_4 at the 2% level.

When fused silica is used as substrate, one observes an additional doublet in the spectra after irradiation. The hyperfine parameters, isomer shift ~1 mm/s and quadrupole splitting ~2 mm/s, are similar to those of silicate minerals. This feature was also seen in studies of ion beam mixed Fe- SiO_2 interfaces reported by Zhang *et al.* [6] who attributed their observation to Fe^{2+} in octahedral sites in a silicate phase formed during irradiation with 100 keV Ar^+ ions. The intensity of this component is, in the present case, ~3% and is unaffected by the heat treatment. The amount of both Fe_3O_4 and Fe_3X is ~6% and also these intensities are not influenced by the annealing. For sapphire, finally, the major effect of irradiation is represented by an increase in the amount of Fe_3O_4 in the spectra from ~6% to ~12% with no subsequent change upon heat treatment.

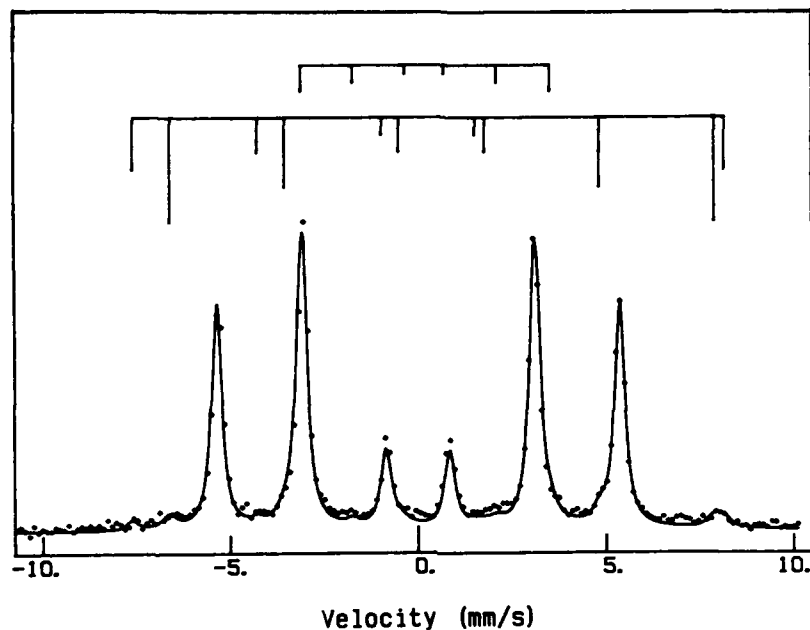


Figure 4. Mössbauer spectra for the sandwich structure (see text) irradiated to 2×10^{14} ions/cm² and annealed (450 °C, 1 h)

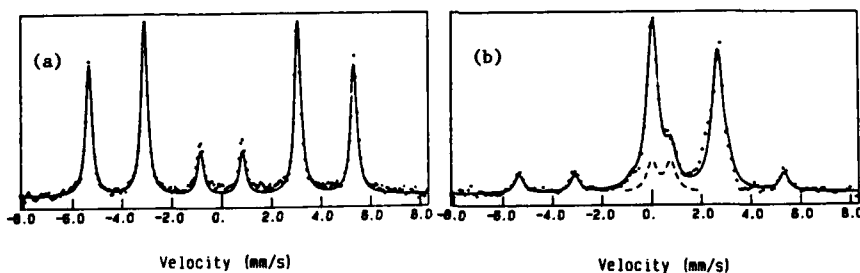


Figure 5. Mössbauer spectra recorded from ⁵⁷Fe films on Teflon PTFE (a) before and (b) after ion irradiation with 16 MeV S³⁴⁺ to a dose of 5×10^{13} ions/cm² (due to [16]).

In order to check whether the observed effects are related to interactions between the film and the underlying substrate, a separate experiment was performed using a sandwich structure consisting of three iron layers; Si/ 500 Å ⁵⁶Fe/ 25 Å ⁵⁷Fe/ 150 Å ⁵⁶Fe. The Mössbauer spectrum of the embedded ⁵⁷Fe layer after 20 MeV ³⁵Cl irradiation to 2×10^{14} ions/cm² and subsequent annealing at 450 °C is shown in Figure 4. The spectrum shows the typical metallic iron pattern

and differs considerably from those recorded from the Si, SiO₂ and Al₂O₃ samples after similar treatment (cf. Figure 2c). This indicates that the formation of cementite involving carbon from the vacuum system is not very probable. Hence, in this case, the Fe₃X component could primarily be attributed to Fe₃Si.

As mentioned above, radiation effects at polymer interfaces are comparatively more pronounced. Figure 5 shows CEMS spectra from 25 Å ⁵⁷Fe films deposited onto Teflon PTFE (due to reference 16). Data were recorded before (5a) and after (5b) irradiation with 16 MeV S³⁺ ions to a dose of 5×10¹³ ions/cm², i.e. a considerably lower dose than that providing the Mössbauer data in the present study. The two doublets formed upon irradiation were attributed to the development of Fe-F and Fe-C compounds. It is tempting to correlate these components to the substantial improvement in adhesion of the Fe film. However, the adhesive strength, though *not* the Mössbauer spectrum, was found to be equally affected when the PTFE substrates were bombarded prior to film deposition. It was therefore concluded that the Fe-F and Fe-C bond formation was only indirectly related to the adhesion enhancement, the assessment of which is rather determined by the surface strength of the Teflon.

4 CONCLUSIONS

The present study shows that MeV ion irradiation can be applied to induce chemical bonds between a deposited iron film and substrates of Si, SiC₂ and Al₂O₃. The corresponding signals are relatively weak. Furthermore, some of their peak positions coincide with those corresponding to compounds which are not associated with the presence of the substrate. Consequently, regarding these systems, special precautions must be undertaken (e.g. using a reference sample as described above) in order to extract relevant information from a CEMS interface study. Iron-polymer systems, on the other hand, exhibit pronounced alterations at relatively low doses.

ACKNOWLEDGEMENTS

Special thanks are owed to Jonas Åström for valuable help in the lab during the course of this work. Brent Fultz is gratefully acknowledged for fruitful discussions. The work was supported by The National Swedish Board for Technical Development. Travel support from Helge Ax:son Johnsons Stiftelse is much appreciated.

REFERENCES

1. Marc-A. Nicolet, T. C. Banwell and B. M. Paine
Mat. Res. Soc. Symp. Proc., **27**, 3 (1984).
2. F. Besenbacher, J. Bøttiger, S. K. Nielsen and H. J. Whitlow
Appl. Phys., **A22**, 141 (1982).
3. J. E. Griffith, Yuanxun Qiu and T. A. Tombrello, Nucl. Instr. Meth., **198**, 607 (1982).
4. M. H. Mendenhall, Ph.D. Thesis, California Institute of Technology, 1983.
5. S. B. Ogale, Rekha Joshee, V. P. Godbole, S. M. Kanetkar and V. G. Bhide
J. Appl. Phys., **57**, 2915 (1985).

6. P. Q. Zhang, G. Principi, A. Paccagnella, S. Lo Russo and G. Battaglin
Nucl. Instr. Meth., B28, 561 (1987).
7. M. Carbucicchio and A. Valenti, Hyperfine Interactions 42, 981 (1988).
8. P. A. Ingemarsson, T. Ericsson, A. Gustavsson-Seidel, G. Possnert, B. U. R. Sundqvist
and R. Wäppling, *Application of Ion Beams in Materials Science*, Edited by T. Sebe and
Y. Yamamoto, (Hosei University Press, Tokyo, 1987) pp. 323.
9. P. A. Ingemarsson, T. Ericsson, G. Possnert and R. Wäppling
Accepted for publication in Hyperfine Interactions.
10. A. Hallén, P. A. Ingemarsson, P. Håkansson, G. Possnert and B. U. R. Sundqvist
Accepted for publication in Nucl. Instr. Meth.
11. J. E. E. Baglin, Mat. Res. Soc. Symp. Proc. 47, 3 (1985).
12. R. L. Headrick and L. E. Seiberling, Mat. Res. Soc. Symp. Proc. 35, 539 (1985).
13. P. Anders Ingemarsson and T. A. Tombrello
Adhesion in Solids, Edited by D. M. Mattox, J. E. E. Baglin, C. Batich and
R. J. Gottschall, (Mater. Res. Soc. Proc., 119, Pittsburgh, PA, 1988) pp. 103
14. M. Carbucicchio, A. Valenti, G. Battaglin, P. Mazzoldi and R. Dal Maschio
Radiation Effects, 98, 21 (1986).
15. T. A. Tombrello, Nucl. Instr. Meth., B24/25, 517 (1987).
16. P. A. Ingemarsson, T. Ericsson, G. Possnert and R. Wäppling
Submitted to J. Adhesion Sci. Technol.

EPITAXIAL RELATIONSHIPS IN ESD PROCESSES ON OXIDE SURFACES

M.R. MCCARTNEY AND DAVID J. SMITH
Department of Physics and Center for Solid State Science
Arizona State University, Tempe, AZ 85287

ABSTRACT

During intense electron irradiation inside the electron microscope, the electron-stimulated desorption of oxygen from the surfaces of several maximally-valent transition-metal oxides (TiO_2 , V_2O_5 , Nb_2O_5 , and WO_3) has been observed [1]. The irradiated surfaces become covered with a crystalline layer of the corresponding monoxide phase. These reduced phases, which are all based on cubic structures and have metallic conductivity, grow with a well-defined epitaxial relationship with the bulk oxide. Computer-drawn models of the crystal structures have been used to study the atomic arrangements implied by the epitaxial relationship, and certain structural features were found to be common to the oxides studied.

INTRODUCTION

It is well-known that many compound materials suffer the preferential loss of one of the atomic species present during electron irradiation [2]. As several damage mechanisms may be operating simultaneously, the final product of the irradiation will depend on the prevailing mechanism given such variable parameters as damage cross-sections, electron beam current densities and accelerating voltages, as well as other experimental parameters. For example, work by Lin and Lichtman [3] showed that when crystals of WO_3 were irradiated by a relatively low-energy, low-density beam of electrons (3keV, $0.1\text{A}/\text{cm}^2$) during Auger Electron Spectroscopy (AES), the proportion of oxygen at the surface was greatly reduced but not completely removed. Berger et al. [4] found that titanium oxides of several stoichiometries, when exposed to high-energy, high-current-density electron beams (100keV, $2 \times 10^4 \text{A}/\text{cm}^2$) developed pits covered by thin layers of material whose Ti:O ratio was very much less than one.

Our particular interest here is in the reduction of several maximally-valent transition-metal oxides (TiO_2 , V_2O_5 , and Nb_2O_5) which occurs under the conditions prevailing during high-resolution electron microscope (HREM) observation. We have already shown that the electron-stimulated desorption (ESD) of oxygen under these conditions results in the development of a layer of the crystalline monoxide phase on the surfaces of the beam-damaged crystals [1]. All these surface phases have structures which are basically of the rock-salt type, but with varying amounts of anion and cation vacancy ordering. The metallic conductivity of these oxides is a crucial attribute which effectively stifles the further loss of oxygen through an interatomic Auger process [5] and thereby prevents the accumulation of a pure metal phase on the surface. The monoxide phases were found to grow with a strong tendency for three-dimensional epitaxy with the bulk crystal. In this paper we consider these epitaxial relationships, certain features of which were found to be common to all systems studied. We show that profile imaging, which gives information on a local scale unavailable with other techniques, can provide insight on the epitaxial growth of the monoxide phases.

EXPERIMENTAL DETAILS AND RESULTS

The oxide materials were prepared for electron microscopy by crushing the respective powders under ethanol with an agate mortar and pestle, and allowing a drop of suspension to dry on a holey carbon support film. Unless otherwise noted, microscope observations were made with a JEM-4000EX HREM,

operated at 400keV. Typical magnifications were 600kX and 800kX, with current densities at the specimen in the range 10-50A/cm² for sample irradiation and 3-6A/cm² for recording electron micrographs. A standard laser optical bench was used to provide optical diffraction patterns (ODMs) from the electron micrographs corresponding to sample areas as small as 1000Å². By reference to lattice fringes from the bulk oxide, the spacings in the surface phase could be measured with an accuracy of ~2-3%.

High-resolution electron micrographs from the edge of an irradiated crystal of V₂O₅ in a [001] projection, as shown in Fig. 1, display the formation and growth of a new phase with finely spaced, orthogonal fringes. Analysis using ODMs from the electron micrographs reveals that these 2.08±0.05Å fringes correspond to the {200} spacings of VO, which has a NaCl-structure with disordered vacancies. The monoxide phase develops readily on the surface of the bulk crystal despite the presence of a 20Å layer of amorphous contamination. It should also be noted that the reduction proceeds rapidly at an accelerating voltage of 100keV, indicating that the predominant damage mechanism for this material is non-ballistic. The crossed fringes of VO₂ have a well-defined epitaxial relationship with the V₂O₅ lattice, with the VO {200} planes parallel to the comparably spaced V₂O₅ {600} planes and the VO {020} planes parallel to the V₂O₅ {020} planes. Fig. 2 shows a schematic model for the proposed epitaxy where the large/small spheres represent vanadium/oxygen atoms respectively. The alignment of the lattice planes is such that the *a*, *b* and *c* axes of the two oxides are parallel.

In order to test whether this apparent three-dimensional relationship persisted for crystals of V₂O₅ in other orientations, the epitaxy at the reduced edge region of a crystal of V₂O₅ tilted to a [011]-projection was also examined. The fringes in this region were found to have spacings of 2.08±0.05Å and 2.39±0.05Å with an angular separation of 55°. These values are consistent with the {200}- and {111}-planes for a crystal of VO in a [011] projection except for the absence of the {011} planes. Reference to structural models indicates that when the bulk V₂O₅ crystal is tilted to this projection, the unit cell of the epitaxial VO is rotated away from its [011]-projection by about 6° in such a way that the VO {011} planes are not perpendicular to the beam direction and therefore would not be expected to be visible in the image.

Electron-beam-irradiated crystals of Nb₂O₅ similarly developed fringes on their surfaces which could be identified with the reduced monoxide.



Fig. 1. High-resolution electron micrograph from crystal of V₂O₅ in [001] projection showing the development of the metallic lower oxide "VO" following electron irradiation at 400keV.



Fig. 2. Models of [001] V_2O_5 and [001] VO confirming the well-defined epitaxial relationship between the major lattice planes of the two oxides.

Fig. 3a shows the edge of a crystal of Nb_2O_5 in a [010]-projection at the start of the period of observation and Fig. 3b shows the same area after irradiation for 20 min. with a current density of $14A/cm^2$. The crossed fringes of the new phase, with spacings of $2.09 \pm 0.04A$, correspond to the [200]-spacings of NbO. NbO has a rock-salt structure with vacancies ordered in such a way that the Nb sub-lattice is missing an ion from the corner position and the O sub-lattice is missing an ion from a face-centered position. This ordering of vacancies would destroy the expected symmetry and allow the kinematically forbidden {100} and {110} spacings to appear. In our case, the reduced phase did not apparently have this ordering of vacancies.

The well-defined epitaxial relationship between the bulk and surface phases for the [010] projection of Nb_2O_5 is clearly visible in the selected-area-electron-diffraction (SAED) pattern shown in Fig. 4a. Nb_2O_5 has a large unit cell and monoclinic symmetry ($a=21.153$, $b=3.82A$, $c=19.356A$, $\alpha=\beta=90^\circ$, $\gamma=119.8^\circ$). The {100} and {010} planes of the NbO phase appear to be oriented along the (209) and (1003) directions of the bulk crystal, and not along either of the monoclinic a and c axes of the Nb_2O_5 . The two systems then

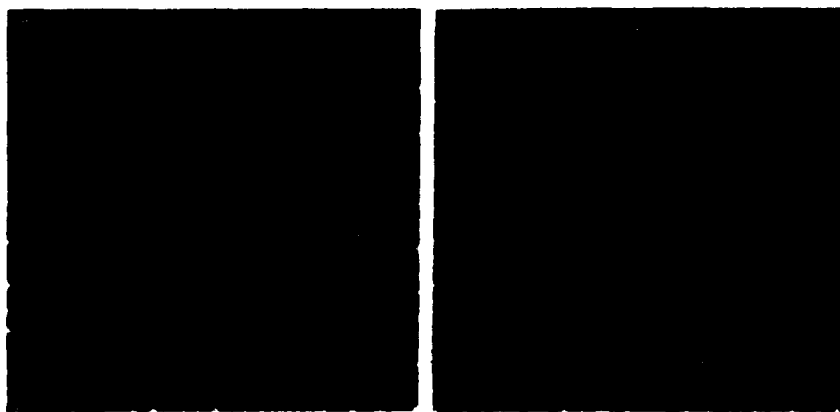


Fig. 3. Profile images from Nb_2O_5 crystal in [010] projection: (a) at onset of irradiation; (b) following irradiation for 20 min. at 400keV with electron current density of $-14A/cm^2$.

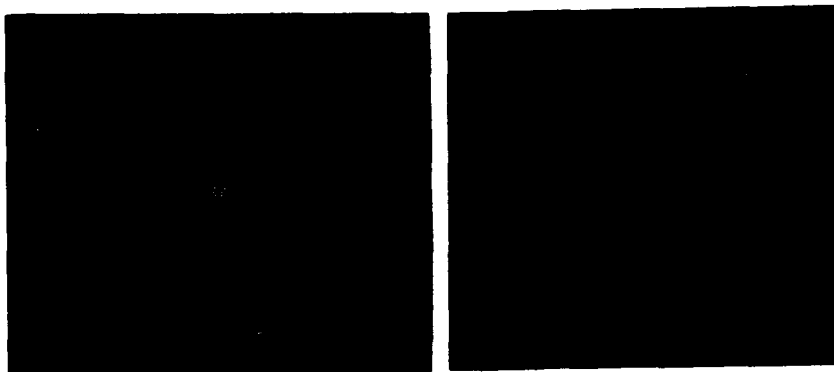


Fig. 4. Selected-area electron diffraction patterns from crystals of Nb_2O_5 following electron irradiation at 400keV. (a) [010]; (b) [100]. Extra spots (arrowed) come from NbO surface phase.

have their *b* axes parallel. Fig. 4b shows the SAED of an electron-beam-reduced crystal of Nb_2O_5 in the [100] orientation. Images of the damaged edge of this crystal contained only one-dimensional 2.09Å fringes which were parallel to the Nb_2O_5 (010) planes. The three-dimensional epitaxy implied by Fig. 4a is corroborated by the lack of development of crossed fringes due to the reduced phase on bulk crystals tilted to a [100] orientation: the (001) planes of the two phases are simultaneously parallel to each other and perpendicular to the [100] Nb_2O_5 direction, but the (001) planes of the NbO phase are tilted by about 20° away from the direction of the (001) planes of the Nb_2O_5 and are thus not perpendicular to the electron beam.

Extensive studies of ESD of oxygen from TiO_2 (rutile) during irradiation in HREM have been made [6]. It has been observed that the loss of oxygen from the rutile lattice results in the formation of TiO on the edge and surfaces of the TiO_2 bulk crystals, again with a very strong tendency toward a three-dimensional epitaxy [7]. In certain projections, the collapse of the rutile planes has been found to proceed via the formation of an intermediate phase which we have identified [6] as TiO_2 -II, the high-pressure modification of TiO_2 [8]. These findings are in disagreement with other workers [9] who have reported the formation of α - Ti_2O_3 in certain projections. Fig. 5 shows the edge region of a crystal of TiO_2 in a [001] projection with both the intermediate and final phases present. OCM analysis of the very edge of this micrograph gives spacings which correspond to those of TiO in a [113] projection with the (211) planes of TiO aligned with the (200) planes of the TiO_2 . TiO also has a defective rock-salt structure with metal and oxygen vacancies ordered on alternate (110) planes of a pseudocubic lattice, giving it monoclinic symmetry. Careful analysis based on OCM's and image simulations of the somewhat disordered intermediate phase reveals that this region corresponds to the [010] projection of TiO_2 -II with the (200) planes of TiO_2 -II aligned with the rutile (200) planes. TiO_2 -II has the α - PbO structure and, once formed, it is thermodynamically stable at atmospheric pressure [8]. Fig. 6 shows a computer-drawn model of the proposed epitaxies between the three oxides again with cations/anions as large/small spheres respectively (unit cells outlined). When these models are viewed at a glancing angle from below, along respectively TiO_2 (200)/ TiO_2 -II (200)/ TiO (211) planes, the most striking feature of the epitaxy becomes evident. During the collapse of planes which results from the loss of oxygen from the bulk TiO_2 , the tendency for metal atom planes parallel to the TiO_2 (200) direction to remain parallel to metal atom planes in the final TiO phase is mediated through similarly spaced and oriented planes of metal

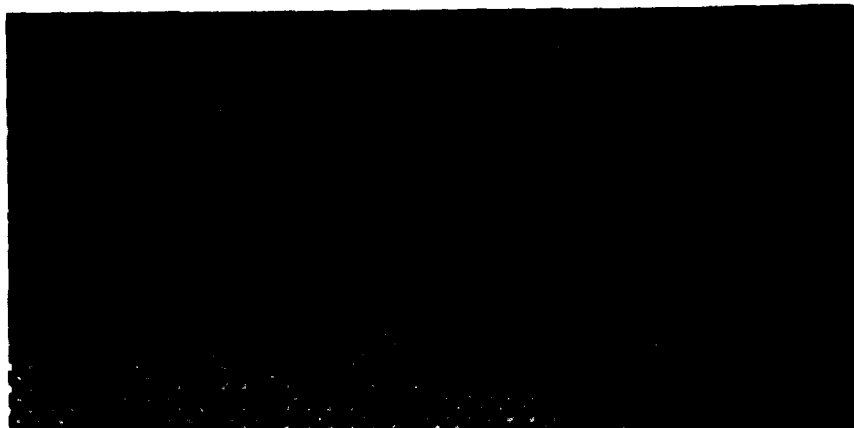


Fig. 5. High-resolution electron micrograph from crystal of [001] rutile following electron irradiation, showing the intermediate $\text{TiO}_2\text{-II}$ phase (A) and the surface TiO (B).

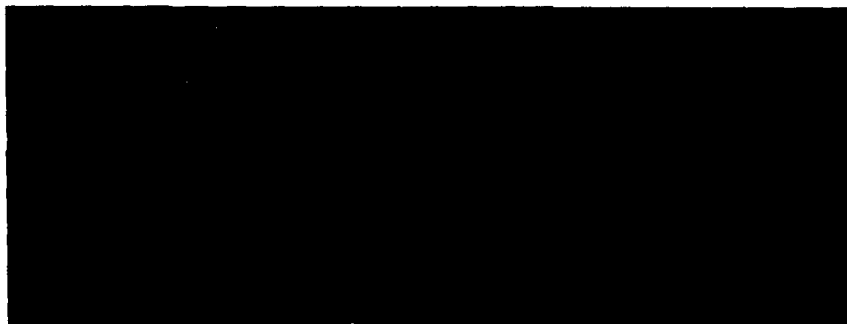


Fig. 6. Schematic model, from left to right, of [001] TiO_2 , $\text{TiO}_2\text{-II}$ and TiO , showing the epitaxial relationship between the three oxides.

atoms in the intermediate phase. The three-dimensional nature of the epitaxy between the original TiO_2 and the final TiO product was also confirmed by observations in other projections where both materials were in low-index zones, such as [100] rutile [6,7].

DISCUSSION

The electron-stimulated desorption of oxygen from maximally-valent transition-metal oxides, which is due to electron irradiation within the high-resolution electron microscope, results in the formation of an epitaxial layer of the corresponding lower (metallic) oxide, with a rock-salt structure [1]. For all the oxide systems studied, it appears that the Knotek-Feibelman mechanism involving an Auger decay process [5] is the initiating mechanism for reduction of the surface and near-surface regions, directing both the epitaxy and the final material formed. The basically orderly collapse of atomic planes observed for all of the oxides indicates that the primary desorption process is neither ballistic nor explosive,

while the continued absence of a pure metal layer at the surface, combined with the metallic conductivity of the various monoxide phases, suggests that while other damage-initiating mechanisms may certainly be operating, the predominant process is not inconsistent with core-hole decay.

The damage rates were found to be different for the various starting materials, with V_2O_5 damaging most readily and Nb_2O_5 the least readily. For TiO_2 in the [001] projection, an electron-current density threshold of $\sim 14A/cm^2$ was measured [6] for the desorption with no reduction apparently taking place below this value even when the rutile crystals had received total electron doses in excess of those received by crystals damaged by a higher current density beam. This particular result indicates that electron-beam-assisted diffusion of oxygen from the interior of the bulk crystal must play an important role in the competing processes of desorption and recrystallization.

The observed three-dimensional epitaxy for all of these oxide systems appears to originate with the tendency of the fundamental high-symmetry crystallographic planes of the maximally-valent oxide to persist through to the final monoxide phase. By juxtaposing structural models of each parent oxide and its respective end-product, it was invariably seen that the development of the lower oxide only involved comparatively minor movements of the cation sublattice. Moreover, in some cases, it was even possible to predict in advance of actual imaging with the microscope what the relative orientations of the two phases should be.

Finally, it seems worthwhile to reiterate the invaluable role played by surface profile imaging in these studies. When an HREM is operated under optimum imaging conditions, interpretable resolution limits of better than 2\AA are nowadays available. Furthermore, details can be obtained about atomic configurations in the vicinity of any surfaces which are orientated such that they are parallel to the electron-beam direction [10]. Thus, it has been straightforward to chart, at the atomic level, the progressive development of the monoxide phases and their epitaxial relationship with the original maximally-valent oxide.

ACKNOWLEDGEMENTS

This research was supported by the Office for Naval Research MAPS Special Focus Program Grant N00014-86-K-0319.

REFERENCES

1. D.J. Smith, M.R. McCartney and L.A. Bursill, *Ultramicroscopy* **23**, 299 (1987).
2. L.W. Hobbs, in *Quantitative Electron Microscopy*, edited by J.N. Chapman and A.J. Craven (Scottish Universities Summer Schools in Physics, Edinburgh, 1984).
3. T.T. Lin and D. Lichtman, *J. Appl. Phys.*, **50**, 1298 (1979).
4. S.D. Berger, J.M. Macaulay and L.M. Brown, *Phil. Mag. Letts.*, **56**, 179 (1987).
5. M.L. Knotek and P.J. Feibelman, *Surface Sci.*, **90**, 78 (1979).
6. M.R. McCartney and D.J. Smith, submitted.
7. M.R. McCartney, in *Proc. 46th Ann. Meet. EMSA*, edited by G.W. Bailey (San Francisco Press, San Francisco, 1988) p. 684.
8. P.Y. Simons and F. Dachele, *Acta Cryst.*, **23**, 334 (1967).
9. M.I. Buckett, J. Strane, D.E. Luzzi, J.P. Zhang, B.W. Wassels and L.D. Marks, *Ultramicroscopy*, in press.
10. D.J. Smith, R.W. Glaisher, P. Lu and M.R. McCartney, *Ultramicroscopy*, in press.

HIGH CURRENT DENSITY ELECTRON BEAM INDUCED DESORPTION

S.D. BERGER*, J.M. MACAULAY†, L.M. BROWN† AND R.M. ALLEN†

*AT&T Bell Laboratories, 600 Mountain Ave., Murray Hill, NJ 07974.

†Cavendish Laboratory, Madingley Road, Cambridge, CB3 0HE, UK.

ABSTRACT

High current density electron beam irradiation with a small probe can lead to the production of holes in a variety of inorganic materials. We review some of the experimental observations of the hole formation process and compare these to the predictions of a simple model.

INTRODUCTION

Electron beam irradiation using small probes (~ 1 nm) with high current densities ($\sim 10^7$ Am $^{-2}$) results in the formation of holes ~ 2 nm in diameter in a variety of materials [1,2,3]. The materials in which this effect occurs are all highly ionic in their bonding and include NaCl, Al $_2$ O $_3$, MgF $_2$, CaF $_2$, AlF $_3$, TiO $_2$, TiO, MgO and many others. An example of such a hole in Na- β -Al $_2$ O $_3$ is shown in Figure 1.

Although the incident beam power is extremely high the formation of holes is not associated with specimen heating. It can be shown using well established theory that the temperature rise under the beam is only of the order of a few K. Rather, the hole is formed by some type of electron beam damage, either ionization or direct momentum transfer (knock-on). Indeed both types of damage mechanism have been studied extensively in ionic materials. For a good introductory discussion to the subject see the article by Hobbs [4]. However, many of the features peculiar to hole drilling are not yet understood. In this article we review some of the more consistent results of the hole drilling process. Further, we present a simple model of hole formation and compare the theoretical predictions with the experimental results.

The motivation for this work lies in the potential application of the hole drilling to nanometre scale electron beam lithography.

EXPERIMENTAL OBSERVATIONS

Current Density Threshold

It is observed that for a given electron probe size the incident beam current can be reduced until even extended irradiation fails to produce significant mass loss in the material. This implies that the hole drilling process is current density (J) limited. The current density threshold has been measured as a function of accelerating voltage and the results for CaF $_2$ and amorphous Al $_2$ O $_3$ are shown in Figure 2, taken from the work of Salisbury et al [5]. Clearly the two materials show very different behaviour, the CaF $_2$ having a much stronger variation in threshold than alumina. However, in both cases the threshold increases with increasing accelerating voltage. Although not shown in the figure the error associated with the threshold measurement can be substantial ($\sim 50\%$) since the observed threshold is not a sharp transition.

The current density threshold can also be investigated by determining the minimum time taken to produce a hole as a function of probe current density. The results of such an experiment in amorphous AlF $_3$ are shown in Figure 3. The plot shows essentially two regions. At high values of J the minimum time taken to drill a hole is only slowly varying while at low current densities the time varies very rapidly. This rapid variation at low values of J explains why the observed threshold is not a sharp transition.

If the process were truly current density limited, then we would expect a plot of t_{\min} vs J to approach infinite time at some positive value of J . It is difficult to deduce any non-zero value of

J from the data of figure 3. The implication is that the measured threshold may be only an apparent threshold.



Figure 1. An Example of a hole drilled in Na-β-Alumina.

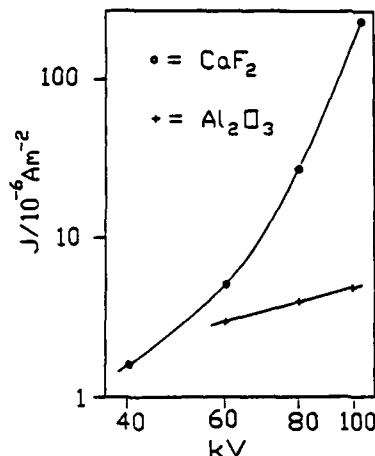


Figure 2. A plot of current density threshold vs. accelerating voltage.

Electron Energy Loss Spectroscopy Studies

The hole formation process has been studied using electron energy loss spectroscopy (EELS) by a number of workers [6,7,8] and the results show that drilling proceeds by the separation of the anion and cation species and their subsequent removal away from the irradiated region.

In the majority of cases EELS measurements reveal that as mass loss occurs the remaining material becomes chemically reduced, i.e. the cation to anion ratio increases. At the same time a distinct signal from the cation in its metallic form can be observed.

In some instances particularly when the starting material is in an amorphous form, a different sequence is observed. In this case we observe the build up of the anion in the form of gas bubbles [6]. The formation of a gas phase is accompanied by the rapid removal of the cation from the irradiated volume.

Further information can be obtained by studying the material after hole formation. Both EELS and high angle scattering measurements [8] suggest that a large proportion of the cations removed from the hole concentrate in the volume surrounding the hole rather than being desorbed into the vacuum.

Rate of Mass Loss

For a variety of materials we have measured the transmitted beam current as a function of time during hole drilling. For the thicknesses of material used in our experiments, the transmitted current is approximately proportional to the mass loss. We tend to see two distinct types of drilling rate curve and these are illustrated in Figure 4. Figure 4a shows continuous mass loss up to hole formation and this type of curve is associated with the EELS spectra which show a gradual chemical reduction.

In Figure 4b we see a small initial mass loss followed by a plateau region and finally an extremely sharp rise leading to hole formation. This type of curve tends to be associated with gas bubble formation [6]. We have looked at materials in which we see either or, or both types of drilling rate, but so far we have been unable to correlate this to any physical property.

Metallization

One common observation during high current density irradiation in these materials is the formation of metallized regions. This can occur in a number of circumstances. For example, when a hole or line is cut in AlF_3 the edge of the feature is converted almost entirely to aluminium metal [9]. In the same material rapid scanning or using a defocused probe results in metallic colloid formation [7]. In single crystallites of many materials we have observed that metallic plugs rather than holes are formed. It is also worth noting that broad beam irradiation such as conventional or high resolution transmission electron microscopy of these materials can result in a large area metal formation [10].

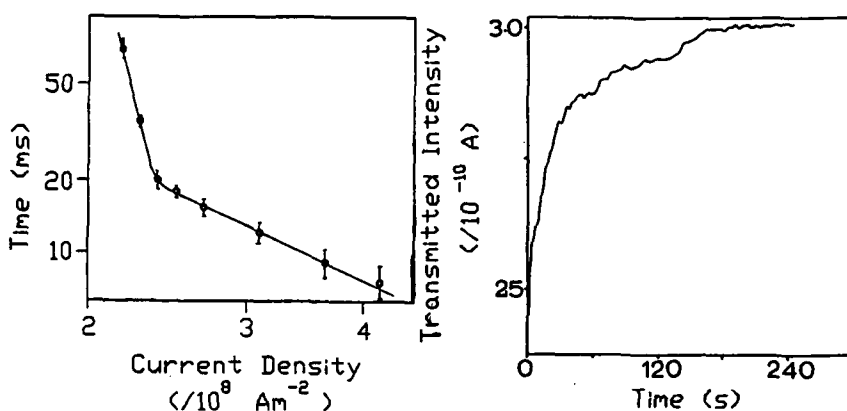
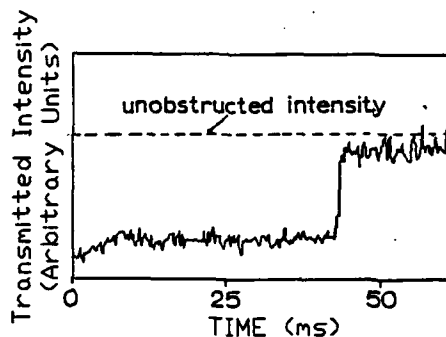


Figure 3. Plot of minimum time taken to form a hole as a function of current density for AlF_3 at 100 kV accelerating voltage.

Figure 4. Plots of transmitted current as a function of irradiation time.

Figure 4a (top right) for CaF_2 .

Figure 4b (bottom right) for MgF_2 .



MODELLING THE HOLE FORMATION PROCESS

It seems clear that the basic damage mechanism operating in this case is some form of ionization induced damage. The main evidence for this is that holes can be drilled, in all cases, with incident electron beam energies significantly below the cut-off energy for knock-on damage to the perfect lattice.

In our model we assume that some initial ionizing interaction leads to the formation of vacancies and interstitials. Conceptually the interstitial ion may be either a cation or an anion or both. If the anion is taken to be mobile it is possible to explain the damage behaviour at both very low and very high current densities. At low current densities the population of mobile anions is sparse and there is little chance for anion molecule (di-interstitial) formation. Thus the

anions escape leaving a metal rich region under the beam. At high current densities, the anions rapidly form molecules, and are trapped as a gas under the beam. It is this trapped gas that can lead to the formation of a hole. This reaction can also result in the production of interstitial cations [12]. This latter process is not modelled in the equations. Thus we can see the origin of a threshold for drilling.

If the cation is taken to be mobile, at very low current densities cations are liberated and escape, leaving anions which are easily lost as halogen gas. At very high current densities, the cations form a solid plug of metal under the beam. Thus the assumption of mobile cations seems to produce hole drilling at low current densities and metallisation at high current densities, contrary to observation.

To simplify the argument we shall only consider the subsequent behavior of one of these species, the anion say, imagining that the other plays no further part. Thus there will be an atomic fraction of vacancies, p , and interstitials, n , present in the irradiated volume at some time, t . We further assume that the interstitials are free to diffuse but the vacancies are not.

It is well known that in certain materials interstitials have an activation energy for motion and hence a cut-off energy for knock-on damage that is very much lower than that for ions in lattice sites. Thus both thermal diffusion and ionic displacement due to momentum transfer from the primary beam may occur. These can be characterized by a hopping frequency ν , where ν is of the form

$$\nu = \nu_D \exp(-E/kT) + \Phi J(V_c^{-1} - V^{-1})V^{-1} \quad 1$$

Thermal hopping Beam assisted hopping
(see Chadderton [11])

Here ν_D may be taken to be the Debye frequency, Φ is a constant, J is the beam current density, V the beam accelerating voltage, E the activation energy and V_c the cut-off beam accelerating voltage for displacement. If we take the activation energy is taken to be 0.76eV for fluorine in AlF_3 , we would expect V_c to be $\sim 7kV$, thus well within the range of our experiment.

We now imagine three mechanisms where by the interstitials are removed from the irradiated volume. First, if they come into contact with a vacancy they recombine. The rate at which recombination occurs will be proportional to the product pn . Second, if they come into contact with another interstitial they form a di-interstitial which we take to be a halogen molecule. The rate of formation of di-interstitials will be proportional to n^2 . Finally, if the interstitial hops outside of the irradiated volume we assume it has escaped. The rate at which this event occurs will be determined by the product of the number of interstitials and the ratio of surface area to volume of the irradiated region. Therefore, at some time there will be an atomic fraction of halogen molecules, c , and an atomic fraction of escaped interstitials, e .

Using this model we can delineate a set of rate equations to describe the hole drilling process. In a simplified form these are

$$\frac{dp}{dt} = \sigma J(1-p) - Znp\nu \quad 2$$

$$\frac{dn}{dt} = \sigma J(1-p) - Znp\nu - Z'n^2\nu - \frac{2a}{r}n\nu \quad 3$$

$$\frac{dc}{dt} = Z'n^2\nu \quad 4$$

$$\frac{de}{dt} = \frac{2a}{r}n\nu \quad 5$$

Where p , n , c and e are the atomic fractions of vacancies, interstitials, di-interstitials (molecules) and escaped interstitials respectively. σ is the cross-section of the 'primary' event, J the current density, ν the hopping frequency, t the time, r the radius, and a the interionic distance. Z and Z' are constants. The term $(1-p)$ represents the volume of undamaged material remaining.

We have solved these equations numerically and investigated the non-steady state behaviour for different values of the parameters.

Figure 5 shows a plot of the various atomic fractions as a function of time for two values of the excitation rate. Figure 5a is typical of 'low' and 'intermediate' excitation rates and shows an initial rise in the number of vacancies which then slowly decays as they diffuse out of the irradiated volume. There is also some small fraction of di-interstitial formation. We can consider curve c, i.e. the fraction of di-interstitials, to represent a plot of the mass loss which can be compared to the experimental drilling rate curves. At 'high' values of excitation rate a different behaviour starts to occur as illustrated in Figure 5b. Here the initial rate of production of interstitials is so high that they are unable to escape quickly enough and thus concentrate in the irradiated volume. This results in an increased di-interstitial population leading to hole formation. Compare curve c of Figure. 5b with Figure. 4a.

The model permits us to produce plots of the minimum time for hole formation as a function of current density, see Figure 6. The curve shows a fairly linear region bounded at low current densities by an apparent threshold. Figure 6 should be compared with figure 3. The form of the theoretical curve does not depend upon the detailed values of the parameters, and is clearly in agreement with experiment. It is probable that the experimental curve relates to the near threshold part of the theoretical curve, and a study of the drilling behaviour over a wider range of current density is highly desirable.

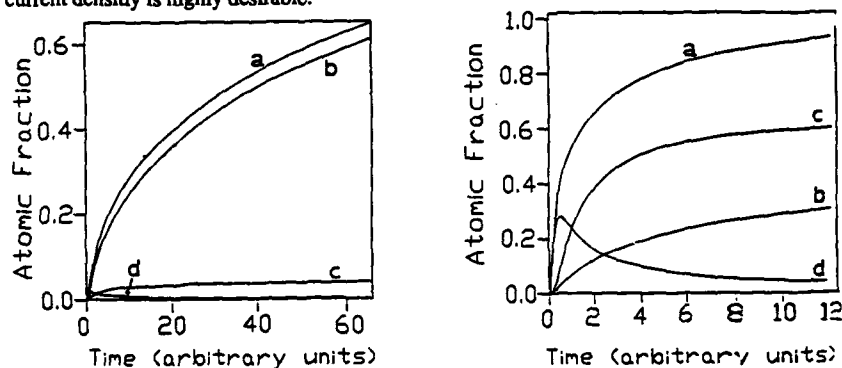


Figure 5. Plots of the various atomic fractions as a function of irradiation time. Figure 5a (left) is for 'low' values of excitation and figure 5b (right) is for 'high' values. In both cases the curve a) represents the fraction of vacancies, b) escaped interstitials, c) di-interstitials and d) interstitials, as discussed in the text.

Figure 7 shows a plot of the predicted current density threshold as a function of accelerating voltage, assuming a maximum drilling time of 60 seconds. The behaviour is highly non-linear. At low accelerating voltages, thermal hopping predominates, and linear behaviour is observed, because the primary cross-section is approximately inversely proportional to V . At a voltage which permits beam induced hopping, the current density rises rapidly because of the increasing interstitial mobility. When the voltage is sufficiently high that the beam induced hopping predominates, another linear region is encountered (at around 60 kV in Figure 7) because the cross section for interstitial motion is again approximately proportional to V (see equation 1). Finally at high voltages the cross-section becomes so small that the hole drilling is very slow and the required current density becomes very large. Figure 7 should be compared with Figure 2. The main point is that the observed rapid variation of threshold current density with voltage can be explained over the voltage range from 5 kV to 100 kV at room temperature.

DISCUSSION

The reaction rate equations 2,3,4 and 5 presented here are very similar to many earlier theories of radiation damage, particularly perhaps that of Jain and Lidiard [13] for metal colloid growth in irradiated ionic crystals. However equation 5 which arises from the finite beam size

has no counterpart in the earlier theories. It is equation 5 which is essential for hole formation. The reaction rate equations are not by themselves sufficient to model the observed non-linear behaviour of drilling rate with voltage and beam current density. For this, it seems essential to introduce a voltage dependant cross-section such as that of equation 1, where there is an onset of beam induced defect mobility over the accessible range of accelerating voltage.

Of course the proposed theory is grossly simplified, and omits many factors such as surface desorption and the effect of defect concentration gradients in the neighbourhood of the beam. Clearly it is critical to explore the temperature dependence of the hole drilling process.

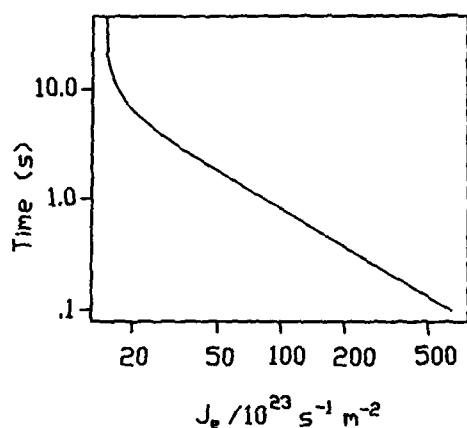


Figure 6. Theoretical plot of time to produce a hole as a function of current density.

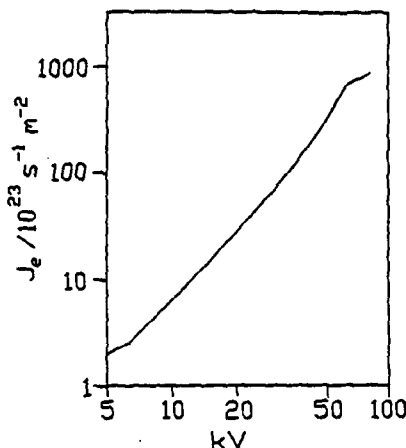


Figure 7. Theoretical plot of current density threshold as a function of accelerating voltage.

ACKNOWLEDGEMENTS

J.M.M and R.M.A acknowledge the support of the SERC and the Cambridge Philosophical Society (J.M.M)

REFERENCES

- [1] A.N. Broers, Proc. R. Soc. Lond. A, **416**, 1 (1988)
- [2] A. Murray, M. Isaacson and I. Adesida, Appl. Phys. Lett., **45**, 5, 589 (1984)
- [3] C.J. Humphreys, I.G. Salisbury, S.D. Berger, R.S. Timsit and M.E. Mochel, Inst. Phys. Conf. Ser. No. 78, 1 (Published by the Institute of Physics: Bristol and Philadelphia 1985)
- [4] L.W. Hobbs in *Quantitative Electron Microscopy* edited by J.M. Chapman and A.J. Craven (Scottish Universities Summer School in Physics Publications, Edinburgh, 1984)
- [5] I.G. Salisbury, R.S. Timsit, S.D. Berger and C.J. Humphreys, Appl. Phys. Lett., **45**, 12, 1289 (1984)
- [6] S.D. Berger, I.G. Salisbury, R.H. Milne, D. Ineson and C.J. Humphreys, Phil. Mag. B, **55**, 3, 341 (1987)
- [7] A. Murray, M. Scheinfein and M. Isaacson, J. Vac. Sci. Technol. B, **3**, 1, 367 (1985)
- [8] S.D. Berger, J.M. Macaulay and L.M. Brown, Phil. Mag. Lett., **56**, 5, 179 (1987)
- [9] J.M. Macaulay and S.D. Berger, Microelectronic Engineering **6**, 527 (Published by North-Holland 1987)
- [10] See the article by D.J. Smith in this volume.
- [11] L.T. Chadderton in *Radiation Damage in Crystals* (Methuen: London, 1965)
- [12] C.R.A. Catlow, K.M. Diller and L.W. Hobbs, Phil. Mag., **42**, 2, 123 (1980)
- [13] U. Jain and A.B. Lidiard, Phil. Mag., **35**, 1, 245 (1977)

FORMATION OF A Ni_3O_4 SPINEL PHASE ON THE SURFACE OF NiO
DURING ELECTRON IRRADIATION

MARY I. BUCKETT AND L. D. MARKS, Department of Materials Science and Engineering,
Northwestern University, Evanston, IL 60208.

ABSTRACT

Structural changes occurring at the surface of NiO during electron irradiation were examined in-situ with a variable voltage high resolution electron microscope. The interaction of the specimen with the electron beam was found to be highly dependent on the state of the surface prior to irradiation. It was observed that by varying the sample preparation conditions, the Ni on the surface of NiO could either be oxidized to Ni_3O_4 spinel phase or reduced to islands of metallic Ni . The formation of the Ni_3O_4 spinel phase is in agreement with previous surface science studies, where chemical shift information identified the presence of Ni^{3+} species at the surface. This has previously been interpreted as the formation of Ni_2O_3 .

INTRODUCTION

It is well known that beam-induced structural and chemical changes may occur in materials during observation in the electron microscope [1]. In most cases, attempts are made to minimize the damaging effect of the electron beam. Under certain circumstances, however, electron microscopy has proven useful for studying the ionizing radiation damage of materials. With the development of better instruments and new techniques for imaging surfaces, high resolution electron microscopy (HREM) has been shown to be a complimentary technique in the study of surface radiation damage [2]. We present an example of HREM applied to surface studies of irradiation-induced structural and chemical changes in NiO .

The behavior of NiO and oxidized Ni surfaces under electron irradiation has been investigated by a number of conventional surface science techniques [3-6]. Desorption studies of this material have produced conflicting results. The original work by Knotek and Feibelman found NiO to be stable against O^+ desorption [3]. They proposed a core excitation mechanism by which O^+ desorption should occur only from maximum valence transition metal (TM) oxides. The K-F model has successfully predicted whether O^+ desorption is observed in many of the transition metal oxides, the most notable exception being NiO . Conflicting studies have reported on O^+ desorption [3,4] and the lack of O^+ desorption in this non-maximum valence TM oxide [5,6]. Previous HREM investigations of NiO have contributed a number of interesting observations, but have not shown conclusive structural evidence revealing the nature of the desorption process, unlike the results obtained for maximum valence oxides such as TiO_2 [7] and V_2O_5 [8].

We have performed a detailed HREM investigation of the in-situ, beam-induced changes occurring at the surface of NiO under various operating conditions and sample preparations. Our

results indicate that clean NiO is stable to ESD of oxygen under ionizing radiation. Ballistic damage in the form of mass loss occurs at 300 keV incident electron energy but not at 100 keV. When surface defects are introduced or if the surface is not free of carbon contamination, two specific electron-stimulated reactions are observed: the formation of a Ni_3O_4 spinel phase and the rapid decomposition to metallic Ni. These reactions are dependent not only on the beam energy and flux, but the condition and environment of the sample surface.

EXPERIMENTAL

Standard HREM specimens were prepared by grinding (in methanol) single crystal bulk NiO into powder form and dispersing onto holey carbon films supported on Cu grids. Some specimens were dry ground to produce more highly defective surfaces. Just prior to insertion into the microscope, the specimens were baked on a 150 W light bulb for 10–15 minutes, achieving a maximum temperature of 240 ± 5 °C. All irradiation experiments were performed in a Hitachi H9000 operating at 100 kV or 300 kV in a vacuum of $< 5 \times 10^{-7}$ Torr. Electron flux was qualitatively controlled by varying the filament bias and the condenser aperture setting. Two flux conditions will be reported here - 'low' and 'high'. The 'low' flux condition represents operation at 8 μA or less filament current with the condenser aperture in. The 'high' flux condition represents a filament current of 8 μA with the condenser aperture out.

RESULTS AND DISCUSSION

Formation of the Ni_3O_4 Spinel Phase

Clean NiO showed mainly ballistic erosion in the form of mass loss during 'high' flux irradiation at 300 kV, as shown in Figure 1. Along isolated areas of the surface, a doubling of the unit cell was also observed and verified by optical diffraction (OD), but was not evident in selected area diffraction (SAD). The second phase was identified as a Ni_3O_4 spinel structure by electron diffraction in three different orientations and by extensive image matching with computer simulations, as shown in Figures 2 and 3 respectively. At 'low' flux the surface-initiated formation of the second phase predominated (Figure 3).

Reconstruction of the immediate surface was noted almost instantaneously, and the initial transformation to the spinel phase occurred rapidly. Surface diffusion and rearrangement were apparent, but neither significant mass loss nor volume change were associated with its appearance. Growth of the spinel phase into the bulk, however, required a threshold flux and appeared to be diffusion-controlled. The growth characteristics inward from the surface fit a \sqrt{Dt} type behavior. Further work is presently underway to confirm this result and will be reported elsewhere [9].

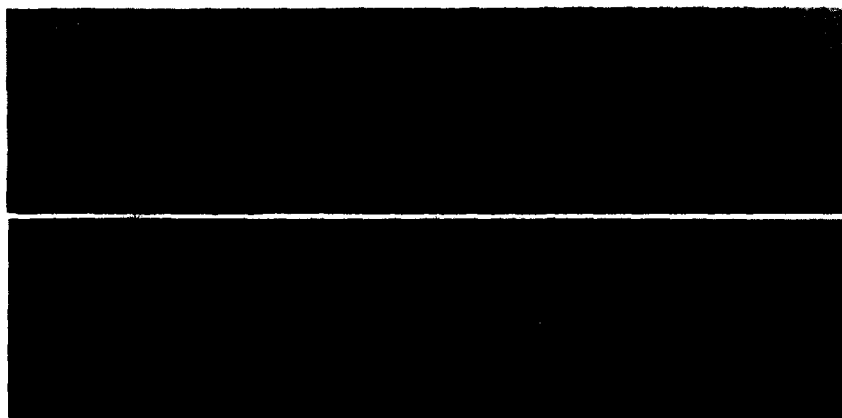


Figure 1.

- a) NiO (100) after 1 hr, 'high' flux at 300 kV.
- b) NiO (110) after 1 hr, 'high' flux at 300 kV.

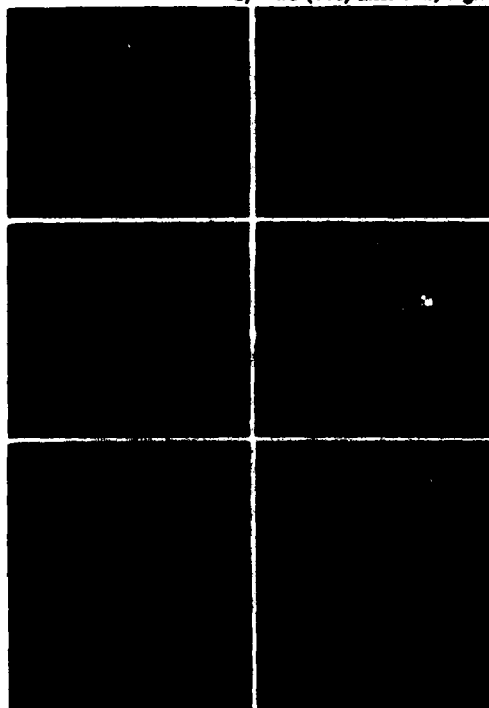


Figure 2.

NiO Diffraction patterns
before (left) and after (right)
 Ni_3O_4 formation.

- a) NiO (001)
- b) NiO (011)
- c) NiO ($\bar{1}11$)



Figure 3. NiO (110) at 'low' flux after 1 hour. Computer image calculations of the Ni_3O_4 spinel phase are inset. Defocus values are in Å.

Variation of the sample preparation conditions to produce more highly defective initial surfaces, or surfaces with a larger proportion of high index faces, resulted in enhanced spinel phase formation. Sample orientation did not seem to play a major role in the initial transformation to the spinel phase, as it appeared under similar conditions in three independent orientations. The presence of amorphous carbon contamination also had no effect on the transformation to the spinel phase, indicating that the surface environment did not play a major role. Encapsulating graphitic layers quenched its formation, thus showing the process to be surface-initiated.

The mechanism by which the Ni_3O_4 spinel phase forms seems to be governed, at least initially, by an electronic mechanism other than the electron-stimulated desorption of oxygen. Subsequent growth of the phase may be via migration of Ni vacancies into the bulk. In consideration of the possible driving forces, we find the most plausible explanation to be the loss of Ni from the surface, creating Ni site surface defects as well as oxidizing some Ni^{2+} to Ni^{3+} . Previous surface science studies have reported similar results of a surface Ni^{3+} species in the oxidation of Ni to NiO [10]. A doubling of the surface unit cell has also been observed by LEED studies of NiO and interpreted to be ferromagnetic NiO [11]. Our computer image simulations of this structure did not match the experimental images in any of the three orientations which were investigated.

At 100 kV, clean NiO showed no ballistic damage in agreement with the study of Luzzi, et al., who reported a threshold beam energy of 115 ± 5 keV for ballistic damage [12]. A doubling of the unit cell at the surface appeared within minutes after the start of irradiation, much more rapidly than at 300 kV. OD and SAD identified this structure to be the same Ni_3O_4 spinel phase as observed at 300 kV.

'Dirty' NiO

At both 100 and 300 kV, NiO in contact with reactive (non-graphitic) carbon underwent a rapid decomposition. The products of this reaction ranged from the appearance of non-wetting, epitaxial islands of metallic Ni to more extensive bulk changes such as recrystallization, rapid disintegration, and apparent melting of the sample. An example of this process is shown in Figure 4. The degree of the reaction was seen to vary inversely with incident electron energy. This reaction has also been observed to varying extents by others [12-15]. In all cases, it appears that the interaction of the electron beam and reactive carbonaceous species cause severe degradation to the surface of NiO.

CONCLUSIONS

Although NiO is subject to ballistic damage under ionizing radiation conditions at 300 kV, evidence of oxygen desorption is not observed. The behavior of NiO surfaces during electron irradiation depends on the condition of the surface and the surface environment in addition to the electron beam energy and flux. Two prevalent electron-stimulated surface reactions are observed. In agreement with previous surface science results, a surface transformation is observed with a confirmed structure of the form $[\text{Ni}^{2+}(\text{2Ni}^{3+})\text{O}_4]$ spinel phase with double the NiO unit cell size.

The occurrence of this phase depends heavily on the defect nature of the surface. In the presence of reactive carbonaceous species, the surface of NiO decomposes. Depending on the degree of reaction, products range from epitaxial islands of metallic Ni to the apparent melting of the crystal.



Figure 4. 'Dirty' NiO (110) samples which, at the onset of irradiation at 300kV, had undergone spontaneous reaction to form Ni islands on all exposed surfaces.

ACKNOWLEDGEMENTS

This research is supported by the Air Force Office of Scientific Research under Grant Number AFOSR 8609344 DEF.

REFERENCES

1. L.W. Hobbs, Ch. 11 in Quantitative Electron Microscopy ed: J. N. Chapman and A. J. Craven, SUSSP Publications, Edinburgh (1984).
2. M.I. Buckett, et al., Ultramicroscopy (in press).
3. H.H. Madden, J. Vacuum Sci. Technol. **13**, 228 (1976).
4. H.C. Gerritsen, et al., Surface Sci. **139**, 16 (1984).
5. H. Niehus and W. Losch, Surface Sci. **111**, 344 (1981).
6. M.L. Knotek and P.J. Feibelman, Phys. Rev. Letters **40**, 964 (1978).
7. D. J. Smith, M. R. McCartney, and L. A. Bursill, Ultramicroscopy **23**, 299 (1987).
8. H. Fan, L.D. Marks, Northwestern University, to be published.
9. M.I. Buckett, S. Singh, L.D. Marks, Northwestern University, to be published.
10. K.S. Kim and N. Winograd, Surface Science **43**, 62 (1974).
11. T. Suzuki, et al., J. Phys. Soc. Vol. 30 888, (1971).
12. D.E. Luzzi, et al., Mater. Res. Soc. Symp. Proc. Vol. 100, 635 (1988).
13. D.J. Smith, et al., Surface Science **175**, 673 (1986).
14. K.M. Oslyn and C.B. Carter, Electron Microscopy 1982, Vol. 2, p.191.
15. J. Liu and J.M. Cowley, Proc. of EMSA, 176 (1987).

ELECTRON-BEAM ASSISTED CVD OF SILICON HOMOEPITAXIAL FILMS

J. P. WEST* AND C. B. FLEDDERMANN**

*Department of Electrical Engineering and Computer Engineering, University of New Mexico, Albuquerque, NM 87131[†]

**Sandia National Laboratories, Division 1126, P. O. Box 5800, Albuquerque, NM 87185 and the Center for High Technology Materials, University of New Mexico, Albuquerque, NM 87131

ABSTRACT

The use of a wide-area electron beam to aid the deposition of epitaxial silicon films has been studied. The electron beam used in this study is generated using a cold cathode, abnormal-glow discharge which allows a wide variation of electron energy and beam current. Depositions are performed on single crystal silicon substrates which are prepared using standard wet chemical silicon cleaning techniques and an *in situ* plasma etch using nitrogen tri-fluoride diluted in hydrogen. The beam diameter is approximately 10 cm and can readily be scaled up to accommodate larger diameters, allowing great potential for large area single wafer deposition. Using electron beams generated in this system, we have demonstrated enhanced growth rates and improved crystalline quality for films grown with electron-beam enhancement.

INTRODUCTION

Electron-beam-assisted chemical vapor deposition (CVD) is one of the family of low temperature stimulated CVD processes whose potential benefits are due to reduced processing pressures and temperatures. Like laser-assisted CVD and plasma enhanced CVD, electron-beam-enhanced deposition can increase film growth rates and improve crystalline structure by stimulating surface reactions and increasing the mobilities of adsorbed species. For example, it has been shown that at temperatures typical for growing amorphous films (300°C), crystalline films can be deposited with sufficient discharge or laser power [1]. Electron-beam deposition is unique, however, in that stimulation is provided predominantly by high speed ballistic electrons, which can induce chemical reactions, break chemical bonds, increase reaction rates by ionizing and exciting reaction products, and heat the substrate. These processes can be done directly by ballistic electrons emanating from the cathode or indirectly by low-energy secondary electrons created when ballistic electrons collide with the sample surface, ejecting an electron in the process. Temperatures for stimulated CVD processes are typically 200-300°C below those required by thermal CVD for the production of epitaxial films [2,3]. The lower thermal energy is compensated for by the energy imparted to the gas and sample surface by electrons.

The purpose of the research described here is to evaluate the impact of a broad-area electron beam generated in a glow discharge on the deposition of silicon thin films. The impact of electron bombardment is demonstrated by comparing silicon films deposited with and without electron beam enhancement. A comparison is also made between films deposited with the beam normal to the substrate surface and those deposited with the beam parallel to the surface, to isolate the effect of the beam on the surface from its effect on the gas above the surface during deposition. This study complements previous work on electron-beam stimulated CVD of silicon thin films [4] which focussed on producing narrow lines using an electron gun rather than large area films using a broad beam.

[†]Current address: Motorola, Inc., Austin, TX

EXPERIMENTAL APPARATUS

The apparatus used in this research is similar to that used in previous studies of electron-beam annealing [5,6], growth of amorphous silicon films [7], and the growth of other materials for microelectronic applications [8] and is shown in Fig. 1. The system is capable of generating a wide area electron-beam with energies up to 12 keV and currents up to 60 mA. The operating pressure ranges from a few tens of mTorr up to 400 mTorr. The reaction chamber is a 4" inner diameter pyrex cross. The cathode is a flat aluminum plate with an optical viewport that provides a means for optical temperature measurement using a pyrometer. The cathode surface is roughened by a wet chemical etch to increase the secondary electron emission rate and is coated with a silicon film to inhibit sputtering of the aluminum into the growing film. A stainless steel ring anode is separated from the cathode by a 7" long pyrex tube, and the chamber is oriented in a horizontal position (the cathode was level with the substrate) to minimize fallout of particulates to the substrate surface. The chamber is evacuated by a turbomolecular pump which is backed by a rotary vane pump, achieving pressures after bakeout in the mid 10^{-7} Torr range. Gas flow and chamber pressure are maintained using mass flow controllers and a downstream control valve. Purge and diluent gases used (He and H_2) were research grade, while electronic grade silane (10% in H_2) was used for film growth, and electronic grade NF_3 for *in situ* pre-deposition etching. The substrate is held on a heated molybdenum cylinder approximately 1" in diameter and 1" tall, wrapped with flexible heating cable composed of a nichrome heating element, a BaO insulator and an inconel sheath, which is brazed to the molybdenum cylinder. Good thermal contact between substrate and heater is maintained using indium solder. The heater is grounded to prevent charge build-up which would reduce the flux of electrons to the sample.

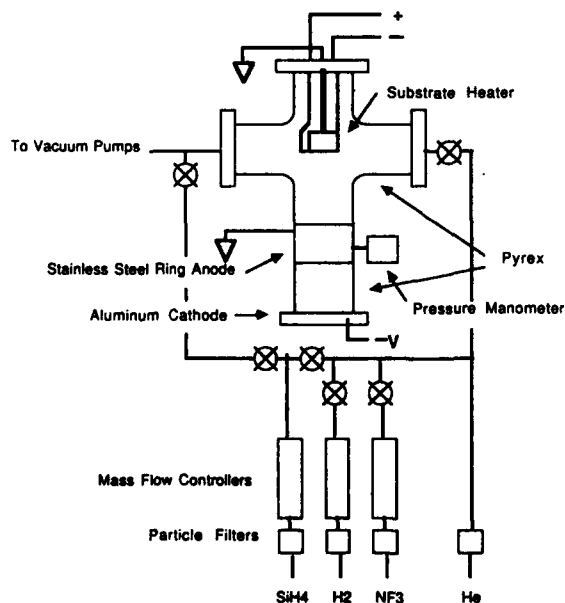


Fig. 1. Experimental apparatus for electron-beam assisted silicon CVD.

In this configuration, energy from the electron-beam is deposited in a very thin layer near the substrate surface, possibly causing a locally higher temperature at the surface. The pyrometer measures the temperature integrated over the volume from the surface to a depth of approximately 500 μm , leading to the possibility that the surface is much hotter than measured, and any beneficial effects of the electron-beam bombardment are due solely to heating of the substrate surface. Calculations have been performed taking into account the deposition of energy into the substrate and the diffusion of heat from the surface into the bulk material. These estimates show that at the power levels used in this experiment, the increased temperature at the surface is negligible.

SAMPLE PREPARATION AND EXPERIMENTAL PROCEDURE

Probably the most critical aspect of growing epitaxial films is the quality of the silicon surface upon which deposition is initiated: it must be free of the native oxide and any impurities. The substrates used in this research were 1x2 cm rectangles cut from 2-5 ohm-cm n-type (100) silicon. Initially, any gross hydrocarbons stemming from packaging materials or handling are removed using hot solvents: trichloroethylene, followed by acetone and isopropyl alcohol. The degreasing is followed by a 5 minute rinse in overflowing deionized water. After degreasing, surface contaminants are removed by a 10 minute oxidation/etch in hot sulfuric acid/hydrogen peroxide (5:1) followed by a 10 second HF etch. After a rinse in DI water, the wafers are dipped in isopropyl alcohol and are blown dry with filtered UHP nitrogen.

Several measures are taken to inhibit the adsorption of water and oxygen on the chamber walls during sample installation. The chamber is hot when opened, which drastically reduces the oxygen and water removal time. In addition, a positive pressure is maintained with helium during the brief period when the chamber is open. After sample installation, the chamber is evacuated to 10^{-4} Torr, backfilled to 100 Torr with helium, and then evacuated. This is repeated three times to purge any air that entered the chamber during sample installation.

Following chamber bakeout, the native oxide and any impurities at the oxide/bulk interface are removed using a dilute NF_3 plasma etch. The discharge is maintained with hydrogen flowing at 80 sccm mixed with 2 sccm of NF_3 at a pressure of 80 mT. Discharge power is maintained at approximately 70 Watts for a 1 minute etch. Under these conditions approximately 100 Å of material is removed, which should leave the surface free of both the native oxide and any impurities residing on the surface. After the etch, the heater is slowly ramped to the desired temperature while 200 sccm of hydrogen flows through the chamber. Once the desired temperature is reached, the hydrogen flow is reduced to 60 sccm, the electron beam is initiated (for the beam-enhanced studies), and 2.5% silane in hydrogen at a flow rate of 80 sccm is introduced. For thermal CVD depositions, the procedure is the same except for the initiation of the glow discharge. After deposition, another purge takes place in hydrogen at 400 sccm to prevent contamination of the surface while the sample is being cooled.

EXPERIMENTAL RESULTS

Four diagnostic techniques were used to evaluate the films: surface profiling using a Dektak profilometer to evaluate the film thickness; TEM to study the interface properties and crystallinity of the materials; laser Raman spectroscopy, also to determine the crystallinity of deposited films;

and Auger spectroscopy to identify impurities present in the films. The film growth rate as a function of temperature and deposition conditions is shown in Fig. 2. Three different conditions are shown here, growth without an electron-beam (thermal CVD), growth with the electron-beam normal to the substrate surface, and growth with the substrate surface parallel to the electron beam in order to separate the surface effects of the beam from effects caused by electrons interacting with gas phase species above the surface. This figure clearly indicates that there is a substantial increase in growth rate for both electron-beam deposition configurations.

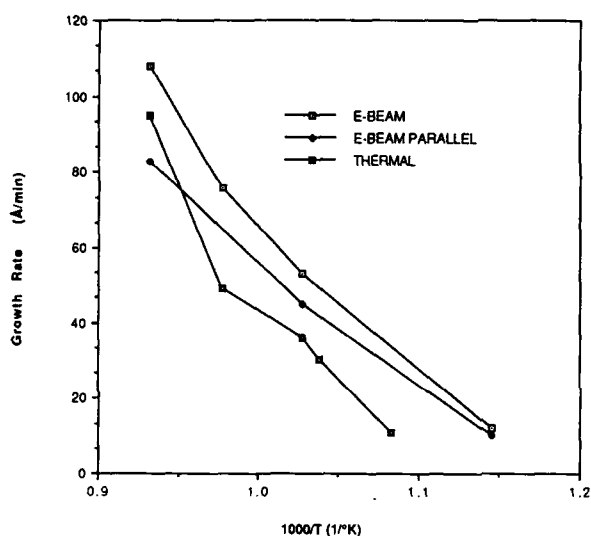


Fig. 2. Growth rate for thermal and electron-beam assisted films.

The TEM measurements, performed on a few films grown at 800°C, indicate that the interface between the bulk silicon and the deposited film contains a thin (approximately 50 Å thick) layer of amorphous material, probably SiO₂. The films also exhibited fine scale porosity of approximately 50 Å dimension.

The Raman scattering measurements show films ranging from crystalline to amorphous depending on the deposition conditions. These results are tabulated in Table I, which shows the growth conditions, the quality of the deposited film as determined by the broadening of the crystalline peak and the presence of the broad 480 cm⁻¹ peak corresponding to amorphous silicon, and the height of the crystalline silicon Raman signal at 519 cm⁻¹ for normal-incidence electron-beam enhanced films and thermal films. The height of the 519 cm⁻¹ peak is related to the relative amount of crystalline phase material that is present along with microcrystalline and amorphous material. The smaller the peak (corrected for shine through from the substrate), the smaller the amount of crystalline phase material that is present. From the results shown in Table I, it can be seen that the crystalline quality is higher for the films grown with electron-beam stimulation.

TABLE I

Temperature (°C)	Electron-Beam Deposited Films		Thermally Deposited Films	
	Structure	Relative Height of 519 cm ⁻¹	Structure	Relative Height of 519 cm ⁻¹ peak
800	crystalline	0.89	crystalline	0.67
750	microcrystalline	0.59	microcrystalline and crystalline	0.48
700	microcrystalline	0.54	microcrystalline	0.33
650	microcrystalline	0.54		
600	amorphous	0.26	amorphous	0.27
550	amorphous	0.20		

Auger spectra indicate very little contamination of the films. Candidate impurities include indium, the materials in the braze used to attach the heating cable to the heater, aluminum from the cathode, or molybdenum from the heater. One film did show the presence of a small amount of chromium (presumably from the braze) but molybdenum, aluminum and indium were not detectable in the films tested.

DISCUSSION

The beam-enhanced films used in this study were deposited using an electron energy of 2.7 keV with a substrate current of 6.8 mA. The results of the TEM studies unfortunately show that the cleaning procedure used was inadequate to ensure a clean surface for the deposition of a crystalline film. However, although high quality epitaxial films were not grown, the Raman results do indicate that the use of the electron-beam did have a significant effect on the quality of the material that was deposited. Improvement would also be expected for films deposited on a clean silicon surface when electron beams are present.

The surface profiling measurements show clearly that the growth rate for these films is enhanced when an electron beam is present. The reason for this is two-fold. When the substrate is held parallel to the beam so that there is no direct impact of the ballistic electrons on the surface, the growth rate is enhanced compared to thermal deposition probably due to gas phase reactions initiated by the beam electrons, leading to more easily decomposed silicon bearing species at the surface. The enhancement is even higher when the beam impinges directly on the surface, indicating that the beam electrons, or more likely the secondary electrons emitted from the substrate, have a role in increasing the decomposition of the silane molecules or radicals.

The Raman results also show the value of the electron impact on the substrate surface. At all temperatures, the quality of the material, indicated by the width of the 519 cm⁻¹ signal and by the height of this signal compared to bulk material, is higher for the electron-beam enhanced samples compared to the thermally grown material, showing that the electron-beam is effective in inhibiting the formation of microcrystalline and amorphous silicon. This probably indicates that the beam is effective in creating more mobile species on the surface or in imparting some momentum to them.

CONCLUSION

We have shown that electron-beam bombardment can be a viable tool for the enhancement of the deposition of semiconductor thin films. In our work, electron beams have enhanced the growth rate and the quality of films deposited both through gas phase reactions leading to more easily decomposed silicon precursors, and also by enhancing reactions at the surface of the growing film. More work needs to be done to grow high quality silicon epitaxial films and to determine the ultimate low temperature at which high quality thin films can be grown with electron-beam enhancement.

ACKNOWLEDGEMENTS

The authors wish to express their thanks to Paul Pochan for expert technical help, and D. Tallant and T. Headley of Sandia National Laboratories for performing the Raman and the TEM studies, respectively. This work, performed at Sandia National Laboratories, was supported by the U.S. Department of Energy under Contract Number DE-AC04-76DP00789.

REFERENCES

1. R. Reif, J. Vacuum Sci. Technol. A2, 429 (1984).
2. W. R. Burger and R. Reif, J. Appl. Phys. 63 368 (1988).
3. B. S. Meyerson, E. Ganin, D. A. Smith and T. N. Nguyen, J. Electrochem. Soc. 133, 1232 (1986).
4. E. S. Faber, R. N. Tauber, and B. Broyde, J. Appl. Phys. 40, 2958 (1969).
5. N. J. Ianno, J. T. Verdeyen, S. S. Chan, and B. G. Streetman, Appl. Phys. Lett., 32, 622 (1981).
6. C. B. Fleddermann, N. J. Ianno, J. T. Verdeyen, and B. G. Streetman, in Laser and Electron-Beam Interactions with Solids, edited by G. K. Celler and B. R. Appleton (Mater. Res. Soc. Proc. 4 Pittsburgh, PA 1982) pp. 795-800.
7. P. J. Hargis, Jr. and J. M. Gee, Solid State Tech. 27(11), 127 (1984).
8. C. A. Moore, J. J. Rocca, G. J. Collins, P. G. Russel, and J. D. Geller, Appl. Phys. Lett. 45, 169 (1984).

THE INITIAL STAGES OF PLASMA SYNTHESIS OF DIAMOND FILMS*

R. Melunas, M.S. Wong, K. Sheng, T.P. Ong, and R.P.H. Chang
Dept. of Materials Science and Engineering, Northwestern University, Evanston, IL 60208

ABSTRACT

The effects of plasma starting conditions on the initial stages of diamond nucleation and growth in a microwave plasma have been studied as a function of important deposition parameters. The influence of the substrate temperature on the diamond nucleation rate, quality, and final film morphology has been elucidated through various analytical measurements. The diamond films are characterized with Raman spectroscopy, X-ray diffraction, and scanning electron microscopy. Finally, methods are described for reproducibly controlling the grain size and morphology of the diamond films for tribological and abrasive applications.

INTRODUCTION

Following the discoveries of Deryaguin et al. [1] there has been a large interest in recent years in the science and technology of plasma enhanced chemical vapor deposited diamond films [2,3]. Thin diamond films have potential applications in optics, electronics, and protective coatings. The ability to control the final diamond film morphology is important for its eventual utilization in these various applications. In an attempt to understand and better control the grain size and morphology of polycrystalline diamond films, we have studied the question of how initial synthesis parameters influence the early stages of nucleation and growth of diamond on various substrates.

EXPERIMENTAL

A microwave plasma system has been constructed for the purpose of studying diamond film growth kinetics. The microwave (2.4 gigahertz) power from a kilo-watt generator is coupled through a rectangular waveguide to a one inch diameter quartz tube which perpendicularly bisects the guide (see Figure 1). Samples are placed on a graphite substrate holder beneath which a thermocouple is mounted. Typical deposition conditions for all samples in this paper are pressure of 40mbar, and gas composition of 0.5% methane and 0.2% oxygen in hydrogen gas at a total flowrate of 200sccm. Addition of small amounts of oxygen to the hydrogen/methane plasma increased the diamond deposition rate as has been previously reported [4] and also contributed to the removal of graphitic and amorphous deposits which form during the initial stages of nucleation. Small amounts of oxygen and water vapor have been shown to effectively increase the concentration of atomic hydrogen in hydrogen plasmas [5]. This greater concentration of atomic hydrogen enhances both the deposition of the diamond phase and the etching away of the unwanted amorphous and graphitic components codeposited.

All substrates used are first uniformly polished in an automatic polisher with 1/4 micron diamond paste, then cleaned ultrasonically in methanol and DI water until no polishing grits are observed under SEM. Although a large series of different substrate materials have been studied for diamond nucleation and growth, only results on silicon (Si) substrates are presented. Results from molybdenum (Mo) substrates are similar to that of silicon.

RESULTS AND DISCUSSION

In the following, we shall discuss the effects due to substrate temperature and the plasma starting conditions on nucleation and film morphology. Various types of diamond film morphologies have previously been identified and are found to be strong functions of both hydrocarbon concentration and deposition temperature. At low methane concentrations ($< 0.4\%$) it has been shown that a (111) habit predominates in a film grown at 800 C, while at slightly higher percentages ($> 0.5\%$) a (100) habit prevails. At even greater concentrations ($> 1.4\%$) a microcrystalline diamond form is observed [6]. The orientation of the diamond grains is also a function of deposition temperature with a preferred (111) orientation observed at low temperatures (900 C) while a (100) form is exhibited at higher values [7].

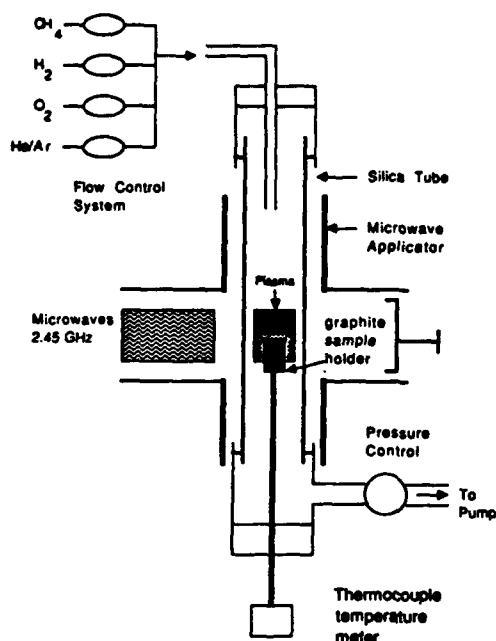


Figure 1. Schematic illustration of the microwave plasma enhanced CVD system.

For mechanical and tribological applications of diamond films, it is desirable to control in a reproducible manner the grain size or texture present in the polycrystalline films while retaining a distinct morphology. In a polycrystalline film the final grain size is more a function of the initial nucleation density on the substrate surface than that of crystallite growth rate. The simplest method for controlling the diamond nucleation density is by polishing the substrate with selective diamond grits. This method is not an acceptable solution for practical process applications. Alternatively, we have studied the control of nucleation through adjustment of the substrate temperature.

Initial studies with the microwave plasma system indicate that the nucleation stage of diamond deposition occurs rapidly during the first minutes of plasma deposition. Our studies indicate that the temperature of the substrate at the point where diamond deposition is initiated has a crucial effect on the nucleation density and final film morphology. In our microwave system the substrate is heated both inductively via the microwave and from interaction with the hydrogen plasma. It takes two minutes to reach 900 C linearly from room temperature and about another minute to reach 1000 C. Thus, within the first few minutes one has a choice of how the gas mixture is introduced. We define Ramp 1 as the case when all gases are introduced from the very beginning, while for Ramp 2, the methane gas is introduced only when the substrate has reached the desired temperature for diamond deposition.

The difference in these two start-up conditions is revealed in the final film morphology. Within one hour, diamond films grown on silicon substrates under Ramp 1 conditions will have a continuous film with crystallite sizes between 0.5 to 2 microns. On the other hand, silicon samples grown under Ramp 2 conditions have a lower initial nucleation density and hence take longer to form continuous films. The final film consists of much larger crystallites. The micrographs of resulting surface morphologies from both Ramps 1 and 2 are shown in Figure 2. Low temperature and high temperature deposition cases are presented, wherein it can be seen clearly that a distinct crystal habit is maintained. The grain size is considerably different from the Ramp 1 and Ramp 2 cases. Similar results also have been obtained for Mo substrates.

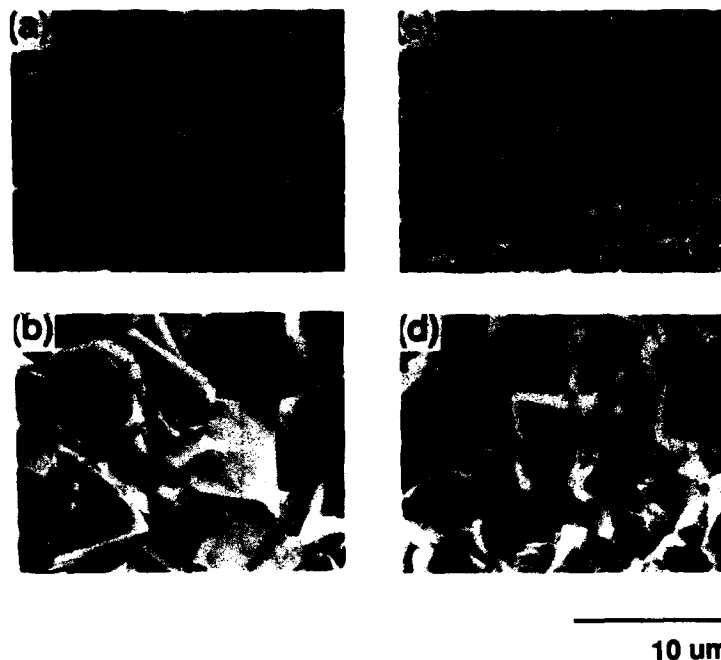


Figure 2. Final diamond film morphology, (a) Ramp 1, 1000C; (b) Ramp 2, 1000C; (c) Ramp 1, 925C; (d) Ramp 2, 925C.

These initial results indicate that there is an optimal temperature at which maximum nucleation takes place on the silicon substrate. It might be argued that during a Ramp 2 type deposition one is merely observing the results of prolonged hydrogen etching of the substrate. Indeed, during the initial 2-3 minutes of Ramp 2, the sample is heated in a hydrogen plasma. This initial etching could modify the substrate surface in a manner which suppresses diamond nucleation. To test this hypothesis, a sample is first heated up under a Ramp 2 condition for 3 minutes. The hydrogen discharge is extinguished and the sample is allowed to cool in vacuum. Diamond deposition is then initiated on the same sample under Ramp 1 conditions. In this case a high nucleation density is still obtained indicating the effect is largely due to favorable conditions present during the initial starting conditions.

To determine the optimal nucleation temperature, a series of diamond film samples have been prepared as a function of nucleation temperature under Ramp 2 conditions (i.e. after the substrate has reached a predetermined temperature, methane is introduced into the discharge). The deposition time is only twenty minutes, so that continuous films are not formed allowing the nucleation density to be evaluated using SEM. Figure 3 shows the measured nucleation density as a function of substrate temperature. From this plot we can easily conclude that the maximum nucleation density occurs around 925 C which is about 75 degrees lower than the reported maximum film growth temperature [8,9].

The "quality" of the above diamond crystallites samples have also been studied by Raman spectroscopy (see Figure 4). These Raman spectra are taken with a laser excitation of 5145 Å. There are several interesting features in these spectra. The sample prepared at 1000 C has the largest diamond phonon signal at 1332 cm^{-1} and a near flat background. We may say that this is the highest "quality" diamond. The sample prepared at 850 C has the smallest diamond phonon signal and a broad shoulder at 1550 cm^{-1} attributed to a graphitic phase. The lower temperature spectra also show the presence of a feature at 1430 cm^{-1} . Analysis of the samples with 4880 Å laser excitation does not

show the existence of this feature, confirming that it is not a Raman signal. The origin of this fluorescence at 1430 cm^{-1} has not been fully identified so far. A peak in this region has also been observed in Raman analysis of ion bombarded SiC [10] and also microcrystalline diamond [11], though in these cases the feature was found to be due to Raman scattering. The feature at 980 cm^{-1} in the spectra is due to second order Raman scattering from the Si substrate [12].

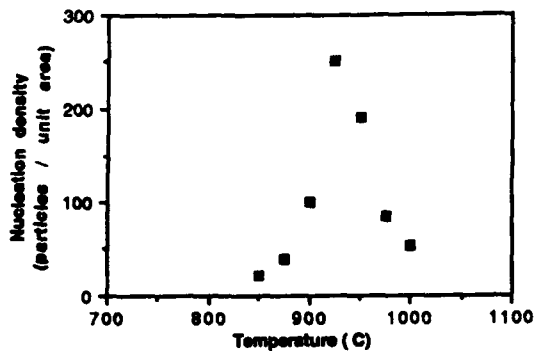
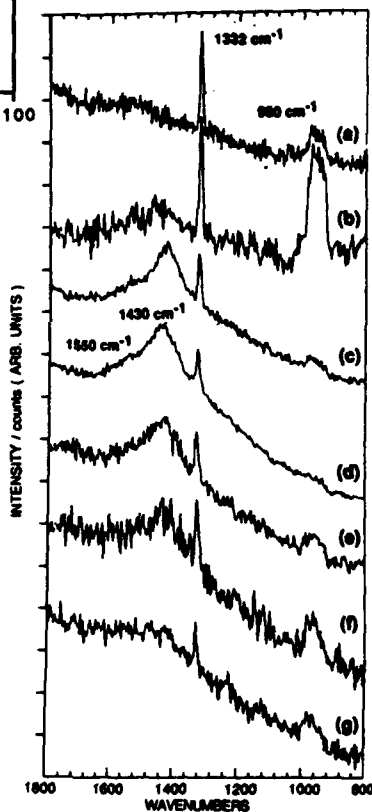


Figure 3. Nucleation Density vs. Temperature.

Figure 4. Raman spectra of Si substrates used in nucleation density/temperature study (Fig. 3). (a) 1000°C, (b) 975°C, (c) 950°C, (d) 925°C, (e) 900°C, (f) 875°C, (g) 850°C.



A comparison of figures 3 and 4 reveals that the diamond with the highest nucleation density does not necessarily possess the best quality. For some applications such as tribological coatings, though, a lower film purity is less a critical concern as that of obtaining a desired film morphology. The main difference between using a diamond film as a protective coating against wear and as that of an abrasive coating is one of film morphology and texture [11]. With some insight into the influence of plasma

starting conditions on the diamond nucleation rate, various two stage depositions have been attempted on Si and Mo substrates. Figure 5 shows the results of some of these tests. Diamond is first deposited

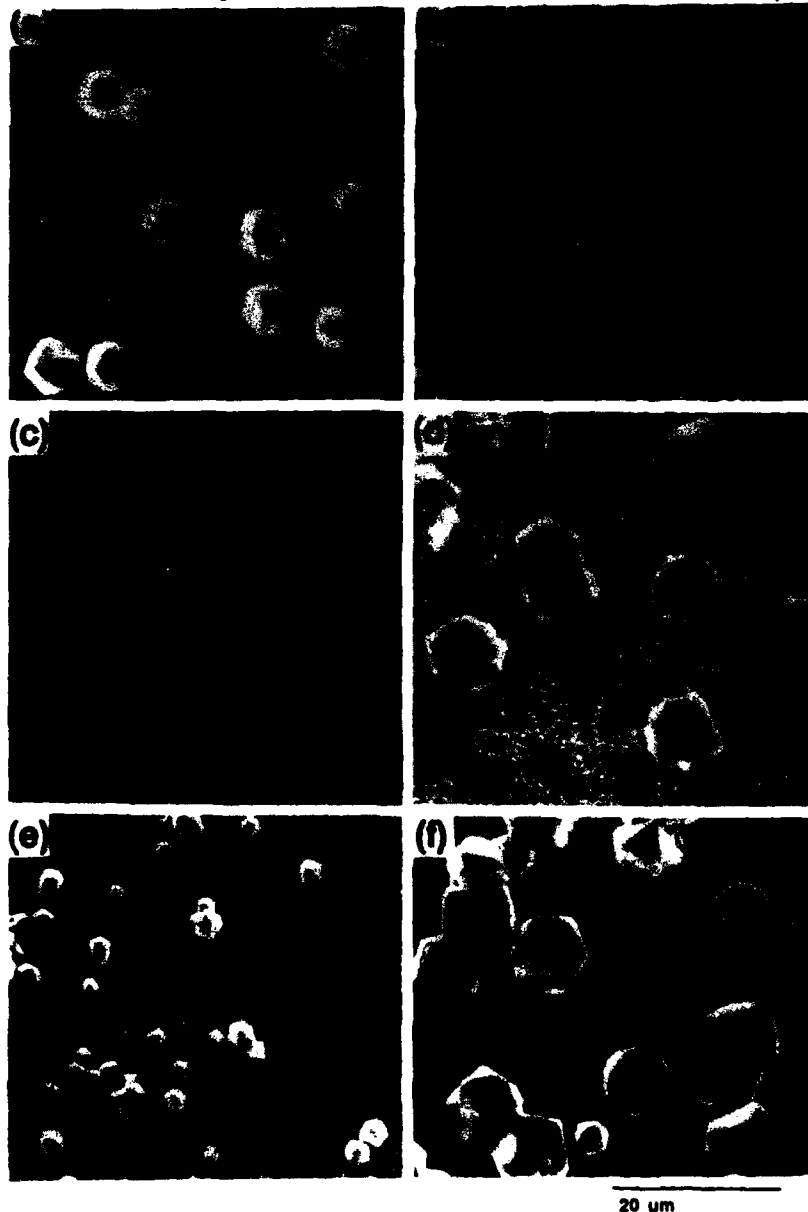


Figure 5. Two stage diamond deposition; Ramp 2 on Si (a) and Mo (c) followed by Ramp 1 on same Si (b) and Mo (d) substrates. Final film morphology after two stage deposition on Si (e) and Mo (f) showing variation in grit size.

on Si (a) and Mo (b) substrates under Ramp 2 type conditions for 3 hours to form large crystallites. Next diamond is deposited on the same samples under Ramp 1 type conditions. Much smaller crystallites are nucleated between the larger diamond crystals (b, d) which over time coalesce into a continuous film. We envision such two stage deposition processes can be used to produce diamond coated grinding surfaces for abrasive applications. By varying the growth time during the Ramp 2 deposition either small (e) or large (f) diamond crystals can be produced to function as a desired grit size. Then with a Ramp 1 deposition stage the remaining exposed substrate surface can be coated with a smaller grained diamond film to protect the surface from mechanical or chemical wear. Efforts are underway to study the tribological properties of these various surfaces.

In conclusion, we have studied the initial stages of diamond nucleation on silicon and molybdenum substrates. The initial plasma starting conditions are shown to have a critical influence on diamond nucleation and final film morphology. It is shown that the maximum nucleation density occurs at 925 C and that the highest quality diamond crystallites nucleate at near 1000 C. A previously unreported fluorescence feature at 1430cm^{-1} is found in diamond films deposited below 975 C. Efforts are underway to study further the effects of various temperature ramps on the evolution and control of diamond morphology.

* This research is sponsored by DOE Basic Energy Science Division.

REFERENCES

1. D. V. Fedoseev, V. P. Vamin, and B. V. Deryagin, *Russ. Chem. Rev.* **53**, 435 (1984).
2. G. H. Johnson, A.R. Badzian and M.W. Geis, editors, *Extended Abstract Diamond and Diamond-like Materials Synthesis*, (Mater. Res. Soc., Pittsburgh, PA 1988).
3. R.C. DeVries, *Ann. Rev. Mater. Sci.* **17**, 181 (1987) and references therein.
4. T. Kawato and K. Kondo, *Jap. J. App. Phys.* **28** (9), 1428 (1987).
5. V. V. Zaitsev, *Russ. J. Phys. Chem.* **47**, 781 (1973); **51**, 318 (1977).
6. K. Kobashi, K. Nishimura, Y. Kawata, T. Horichi, *Phys. Rev. B* **38** (6), 4067 (1988).
7. S. Matsumoto, *J. Mat. Sci. Lett.*, **4**, 600 (1985).
8. B. V. Spitsyn, L. L. Bouilov and B. V. Derjaguin, *J. Cryst. Growth* **52**, 219 (1981).
9. B. V. Derjaguin, L. L. Bouilov and B. V. , *Spitsyn Archivum Nauk O Materialtech* **2**, 111 (1986).
10. R. B. Wright and D. M. Gruen, *Rad. Effects* **33**, 133 1977.
11. W.A. Yarbrough and R. Roy in *Extended Abstract Diamond and Diamond-like Materials Synthesis*, edited by G. H. Johnson, A. R. Badzian and M. W. Geis. (Mater. Res. Soc., Pittsburgh, PA 1988) pp. 33-38.
12. J. H. Parker, Jr., D. W. Feldman, and M. Ashkin, *Phys. Rev.* **155**, (3), 712 (1967).
13. M.S. Wong, R. Melunas, T.P. Ong, and R.P.H. Chang, in *New Materials Approaches to Tribology: Theory and Applications*, MRS Proceeding for Symposium S, Boston 1988, to be published.

RF Plasma CVD Using Hollow Cathode Discharge

SHIN ARAKI, HIDEKI KAMAJI, AND KAZUO NORIMOTO

Fujitsu Laboratories Ltd., 10-1, Morinosato-Wakamiya, Atsugi 243-01, Japan

ABSTRACT

We have made a-Si photoreceptors at low pressure to prevent the formation of Si_mH_n powders and by separating the growing surface from the high density plasma. A new plasma CVD method using a hollow-cathode discharge, where the discharge electrode is the cathode, is described. There is a hollow region in the discharge electrode. Hollow-cathode discharge enables a high density plasma to form at low pressure. The gas is decomposed in the hollow cathode preventing plasma damage to the film. This method allows us to achieve a high deposition rate (10 $\mu\text{m}/\text{h}$) and good quality films for photoreceptors.

INTRODUCTION

Amorphous silicon photoreceptors last a long time [1], but their productivity should be increased. The creation of Si_mH_n powders must be prevented and the film deposition rate must be increased. The a-Si photoreceptors are fabricated by rf (radio frequency) plasma CVD. The amorphous Si photoconductive layer is 10 to 30 μm thick, and must be deposited quickly. To achieve a high deposition rate, the gas flow rate and gas pressure and the rf power must be increased. Under these conditions, however, the disilane and its radicals (SiH_3 , Si_2H_5 , etc.) collide with each other more frequently, and form many Si_mH_n powders. These powders will cause defects on a-Si photoreceptors, and high rf power causes plasma damage on the photoreceptor.

BACKGROUND

Figure 1 shows the relationship between deposition rate and gas pressure in conventional rf plasma CVD. This rate increases with pressure and then stabilizes. Conventionally, photoreceptors are fabricated around 1 Torr, where the deposition rate saturates. Under these high pressures, the disilane and its radicals often collide, cluster, and form Si_mH_n powder. This

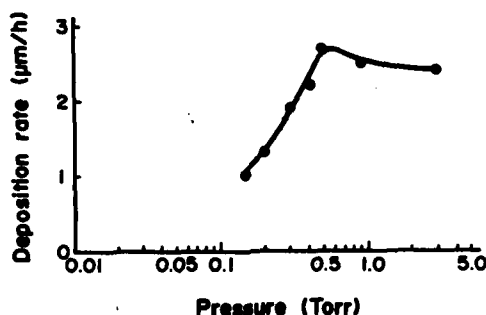


Figure 1 Relationship between deposition rate and gas pressure in conventional rf plasma CVD

powder sticks to the discharge electrode and to the ceiling and bottom of the chamber and causes defects in the amorphous silicon photoreceptor. The chamber must be cleaned after each deposition, and cleaning takes longer than deposition. We have confirmed that Si_mH_n powder does not form at pressures under 0.3 Torr.

But, in this region, the deposition rate decreases abruptly with pressure.

To prevent these powders from forming, we need to keep the pressure low, but at low pressures the deposition rate decreases. We increased the deposition rate by using a dense plasma and limited the dense plasma region to avoid plasma damage.

Our goal was to fabricate a thick film at a low enough pressure to prevent powder formation, and yet at a high enough gas decomposition for a high deposition rate. To solve these problems, we developed a method to produce rf hollow-cathode discharge plasmas at low pressures, and to prevent plasma damage, we isolated the substrate from the dense plasma.

EXPERIMENT

Hollow-cathode discharge produces a high density plasma [2-4] and is suitable for our purposes. Figures 2 and 3 show the equipment. By making the area of the discharge electrode smaller than that of the ground electrode and by using a blocking capacitor between the rf power supply and discharge electrode, the discharge electrode is negatively self-biased and becomes the cathode. The high density plasma then forms only in the hollow region in the discharge electrode, even at low pressures. Disilane gas is supplied through holes in the hollow. The high-density gas passes through the high-density plasma and decomposes in the hollow, which is far enough from the film that the plasma does not damage it. The gas is further decomposed by conventional rf glow discharge.

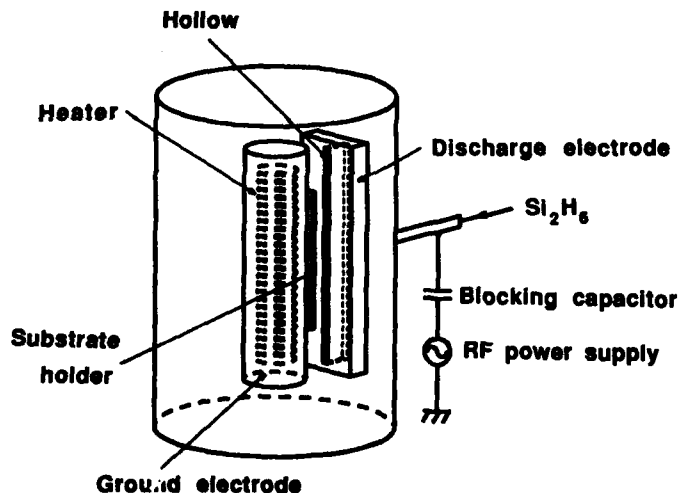


Figure 2 RF hollow cathode discharge equipment

Figure 4 shows the discharge electrode voltages. The greater part of the rf waveform is less than zero.

The electrode is 134 mm wide and 464 mm tall. The hollow region in the cathode discharge is 8 mm wide, 28 mm deep, and 462 mm tall, and is divided by stainless steel nets 40 mm apart, the same spacing as the holes. The stainless steel nets allow the plasma to be produced at pressures below 100 mTorr (Table 1). We observed the radiation of the rf plasma from the window of the chamber and confirmed the existence of both strong hollow-cathode discharge radiation and weak rf glow discharge radiation. But the dense plasma in the hollow region did not extend to the substrate.

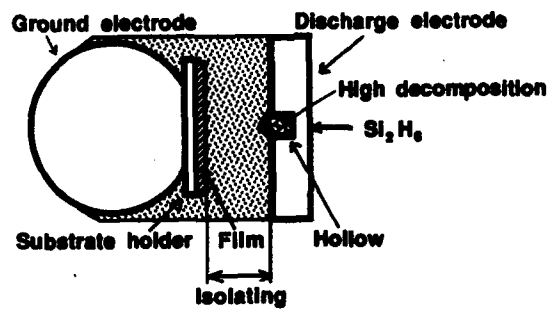


Figure 3 Cross section of the equipment

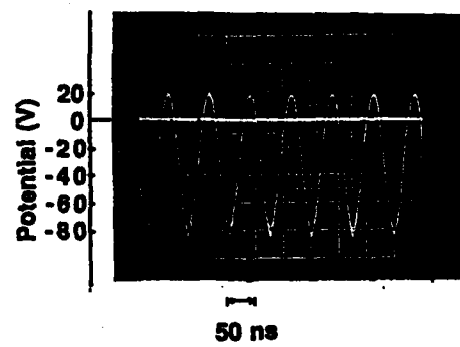


Figure 4 Discharge electrode voltages

Table 1 Deposition parameters

RF power	100 W
Pressure	15 to 70 mTorr
Gas	Si_2H_6 , 50 sccm
Substrate temperature	270 °C

Figure 5 shows the deposition rates in conventional rf plasma CVD and the new method. We tried to deposit films at less than 0.3 Torr. The deposition rate increases rapidly between 15 and 30 mTorr and saturates at more than 30 mTorr. At 50 mTorr, our deposition rate is 3 times faster than conventional rf plasma CVD of high pressure. At 15 mTorr, the plasma becomes unstable, and deposition rate decreases. We achieved a high deposition rate without Si_3H_8 powders at more than 30 mTorr.

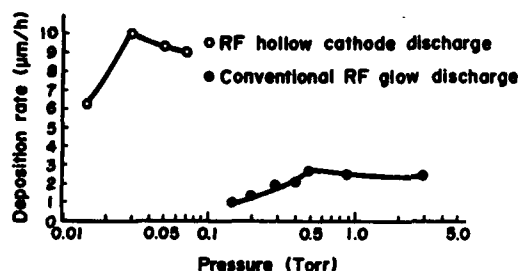


Figure 5 Deposition rate

Figure 6 shows the photoconductivity and dark conductivity and their ratio as a function of gas pressure for a deposited a-Si sample. The ratio increases with pressure until 50 mTorr and then saturates. At 50 mTorr, the photoconductivity-to-dark conductivity ratio is nearly 10^4 , which is adequate for a photoreceptor.

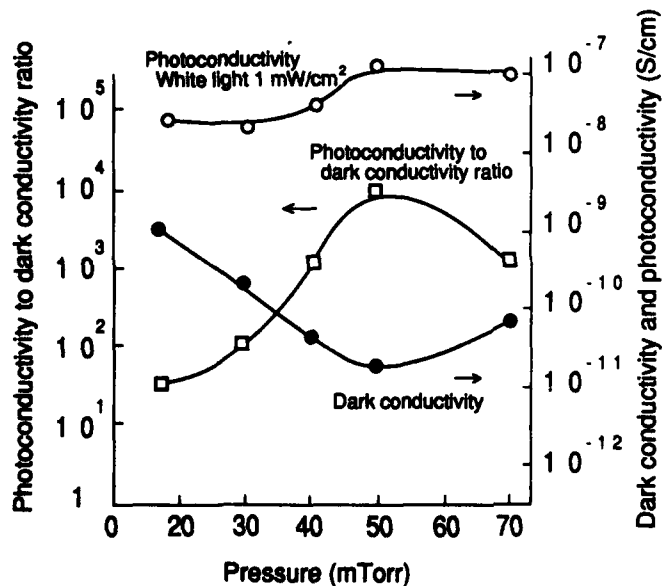


Figure 6 Photoconductivity and dark conductivity and their ratio as a function of gas pressure.

CONCLUSION

We have developed a new method for fabricating a-Si photoreceptors using rf hollow-cathode discharge. This method enables a high deposition rate at low pressures which inhibit the formation of Si_mH_n powders. The deposition rate is high, about 10 $\mu\text{m}/\text{hour}$, because a dense plasma is used. Plasma damage does not occur because the dense plasma is isolated from the a-Si film. The photoconductivity-to-dark conductivity ratio is nearly 10^4 under a 1 mW/cm^2 white light.

ACKNOWLEDGEMENT

We thank Dr. Y. Inagaki, general manager of Electromechanics Division, Mr. K. Kiyota, deputy manager of Printer Technology Laboratory, Mr. Y. Aida, section manager of Printer Technology Laboratory, and Dr. M. Kimura, senior researcher of Printer Technology Laboratory, for their advice and encouragement.

REFERENCE

1. S. Araki, H. Nou, H. Kamaji, and K. Kiyota, in *Materials Issues in Amorphous-Semiconductor Technology*, edited by D. Adler, Y. Hamakawa, and A. Madan (Mater. Res. Soc. Proc. 70, Pittsburgh, PA, 1986) pp. 677-682.
2. A. Güntherschulze, *Z. Tech. Phys.* **11**, 49 (1930).
3. B. Chapman, *Glow Discharge Processes*, (John Wiley & Sons, New York, 1980) p. 172.
4. T. Sato, M. Tada, and Y. C. Huang, *Thin Solid Films* **54**, 61(1978).

PART X

I. C. Fabrication Technology

SELECTIVE-AREA LASER-ASSISTED PROCESSING FOR MICROELECTRONIC MULTI-CHIP INTERCONNECT APPLICATIONS

ROBERT F. MIRACKY

Microelectronics and Computer Technology Corp. (MCC)
12100 Technology Blvd., Austin, TX 78727

Abstract

Laser direct-write processes are attractive complements to traditional methods of fabricating microelectronic circuitry. This paper is a summary of our work in applying such processes to high-density inter-chip interconnection modules, such as those using copper conductors on polyimide dielectric layers. We begin by discussing the requirements which laser processes must satisfy in order to be useful in this application. An analytical model of laser heating is then described, which aids in understanding the thermal problem of absorption of visible-wavelength laser light by polyimide. Calculations using this model are consistent with experimental observations. Finally, we focus on one laser processing technique: laser chemical vapor deposition. We describe a new process for laser chemical vapor deposition of tungsten on polyimide, which enables the formation of low resistance contacts ($\approx 0.1 \Omega$) between the deposited tungsten films and pre-patterned nickel-coated copper conductors. Lines approximately $30 \mu\text{m}$ wide and $3\text{--}4 \mu\text{m}$ thick were deposited at a scan rate of $93 \mu\text{m/s}$. From four-point resistance measurements of different lengths of deposited films, the tungsten film resistivity is estimated to be two to three times the bulk value.

Introduction

Laser-assisted chemical processing has matured to a level where its use in engineering or manufacturing applications can now be contemplated. "Selective-area", or "direct write", processes, in which the spatial confinement of the etch or deposition reaction is accomplished by virtue of the focused nature of the laser beam, have already been employed in integrated circuit (IC) repair and customization [1,2,3]. Here, conductors on the IC's are either etched or deposited by laser-assisted chemistry (oftentimes *both* processes are performed sequentially in a single process cycle). While these are certainly convincing demonstrations of the utility of laser methods for maskless patterning of integrated circuits, there are other areas within microelectronics in which laser processing might also prove beneficial.

One interesting potential application for laser direct-write is the formation of electrical connections *between* individual integrated circuits. But the laser processes must be tailored to the specific interconnect technology, which in turn is dictated by the system-level packaging strategy. There are basically two approaches: monolithic circuitry, and hybrid assemblies. "Wafer-scale integration" is an example of the former. However, low yield for this technology has dampened the prospects for employing monolithic IC's which are larger

than a centimeter or two on a side. On the other hand, hybrid approaches, in which IC's are individually bonded to a separate, high-density interconnect module, or "substrate", are not susceptible to these yield limitations. By achieving near-wafer-scale densities of circuits, these assemblies are capable of creating high performance computer *systems*. An example of an emerging technology in this latter group is copper conductors on polyimide interlayer dielectric [4,5,6].

This paper is a summary of our investigations into applying laser chemical processes to copper-polyimide technology. By way of introduction, we shall describe the key features of copper-polyimide, highlighting the materials and process concerns which are important for laser processing. Then we will present an analytical model of laser heating which describes how pyrolytic, visible-wavelength laser processes occur with polyimide as the dielectric. Finally, we devote the bulk of the paper to discussing results of applying laser chemical vapor deposition of tungsten to copper-polyimide, and how it can be used to form low resistance conductor links.

Copper-Polyimide Interconnect Technology

Figure 1 is a schematic representation of copper-polyimide (Cu/PI) technology, showing typical values for the design parameters. The Cu/PI samples used in these investigations were fabricated by means of pattern electroplating and mechanical polish-planarization processes [6]. Beginning with a 10-cm oxidized silicon wafer, DuPont 2525 polyimide was spun on, dried, cured, and polished to a thickness of about 18 μm . A 5- μm thick layer of copper was formed by electroplating through a patterned layer of photoresist, over sputtered layers of chromium and copper. (The Cr and Cu layers were used to supply cathode current during electroplating, and were eventually removed from the field areas.) A thicker layer of copper was then electroplated through a different photoresist pattern, to form the interlayer vias, or "pillars". The tops and sides of the copper features were coated with a thin layer of nickel, to protect the copper during subsequent processing. Polyimide was applied, cured, and mechanically polished to a final thickness of about 15 μm , exposing the tops of the pillars in the process. The conductor formation and polyimide deposition/polish processes were then repeated to form the desired number of interconnect layers (see Figure 2).

As with integrated circuits, direct repair or customization of interconnection module conductors is most efficiently accomplished using laser techniques. Laser chemical vapor deposition (LCVD) is an attractive approach, because of its versatility and linewidth resolution. LCVD of copper [7] and nickel [1,8] has been demonstrated, but neither process is optimal for this application: Copper is susceptible to corrosion during subsequent processing steps, and $\text{Ni}(\text{CO})_4$, the most common CVD precursor for nickel, is extremely toxic. Tungsten, on the other hand, is attractive because of its low resistivity, corrosion resistance, and simple deposition chemistry. While tungsten LCVD has previously been used with integrated circuits [2,3], it has not been employed with copper-on-polyimide interconnection modules (or "substrates"). This paper reports the first effort to extend tungsten LCVD to this interconnect technology.

LCVD of tungsten for copper-polyimide substrates presents new challenges compared to those for aluminum-on-silicon dioxide IC's. Some of the differences between the two technologies are summarized in Table I. First, the contact metallurgy is entirely different. Second, polyimide decomposes at a much lower temperature (below about 500 $^{\circ}\text{C}$) than silicon dioxide, so the substrate surface cannot be heated to as high a temperature. This

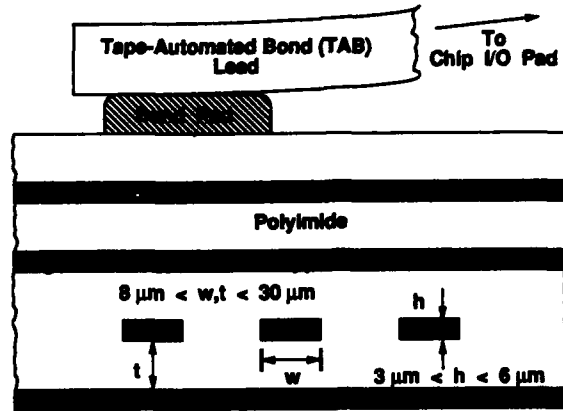


Figure 1: Cross-section of multi-layer interconnection module, composed of copper conductors (dark shaded regions) and polyimide interlayer dielectric (white regions). "Ref" layers are ground plane reference layers, while the "Sig" layers contain patterned signal wires. The parameter ranges indicated are typical values for this technology.

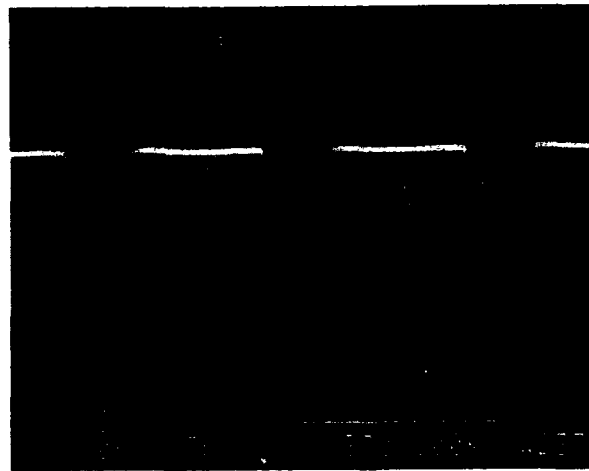


Figure 2: Scanning electron micrograph of cross-section of multi-layered interconnection module with copper conductors (light regions) and polyimide interlayer dielectric (dark regions). The bright film on the top of the uppermost conductors is gold, to provide a layer for bonding chips to the substrate. The substrate is ceramic. The narrowest conductor lines (between the bond pad columns) are $5\text{ }\mu\text{m}$ thick and $10\text{ }\mu\text{m}$ wide. (from Ref. [6])

impedes the attainment of high tungsten deposition rates. Recent studies have shown that bulk CVD of tungsten onto polyimide is just as selective as onto other dielectrics (such as SiO_2), at H_2 pressures in the 1–10 Torr range and for temperatures below 216 °C [9]. A major objective of tungsten LCVD as we shall describe it here is to achieve selectivity *loss* at high reactant compositions or localized substrate temperatures: We wish to deposit tungsten *directly* on polyimide, without requiring nearby tungsten to initiate the process.

Table I: LCVD process constraints for IC and multi-chip substrate applications

	Chip	Substrate
Metals to Contact	Al, Si, W	Cu, Ni/Cu
Interlayer Dielectric	SiO_2	Polyimide
Maximum Dielectric Temperature	1600 °C	500 °C
Conductor Thickness	$< 1 \mu\text{m}$	$\approx 5 \mu\text{m}$
Conductor Width	1–5 μm	10–30 μm
Module Size	1 cm	5–10 cm

Analytical Model for Laser Heating

To obtain a quantitative understanding of laser heating of polyimide at visible wavelengths, we have analyzed a simple model which embodies the key features. The geometry we considered is illustrated in Figure 3. Here is shown a layer of a dielectric of thickness L (light, cross-hatched region), which is taken to be polyimide, situated above a good thermal conductor, such as copper or silicon (dark, hatched region at the bottom). This allows the boundary conditions to be simplified, by imposing the constraint that $T = 0$ at the bottom of the polyimide layer, where T is defined as the temperature elevation above ambient due to the laser heat input. The polyimide-copper slab is taken to extend indefinitely in the lateral directions.

The laser is incident normally on the top surface, within the circular shaded region of radius R . Although the radial distribution of the laser energy is typically Gaussian, we simplify the problem by assuming a uniform input power density of $P/(2\pi R^2)$ for $r < R$, and zero for $r > R$. We have measured the absorption length λ at 488 nm of Dupont 2525 polyimide to be about 29 μm , which is comparable to the thickness of the polyimide layer; hence, it *cannot* be neglected. This is taken into account by assuming that the laser heating is volumetrically distributed throughout the thickness of the layer, with an exponential dependence $\exp(-z/\lambda)$. The complete form for the volumetric heat generation p resulting from the laser is then:

$$p = \frac{P}{\pi R^2 \lambda} \Theta(R - r) \exp(-z/\lambda) \Theta(t). \quad (1)$$

We have solved this problem using the Green's function method [10]. The solution at any point located laterally a distance r from the beam center, at a depth z below the top surface of the polyimide, at any time t , can be written as:

$$T(r, z, t) = \frac{2\epsilon P}{\pi k L R} \sum_{n=0}^{\infty} \cos(\gamma_n z) f_n(\lambda, L, a) \int_0^{\infty} \frac{J_0(\beta r) J_1(\beta R)}{\beta^2 + \gamma_n^2} \{1 - \exp[-\alpha(\beta^2 + \gamma_n^2)t]\} d\beta \quad (2)$$

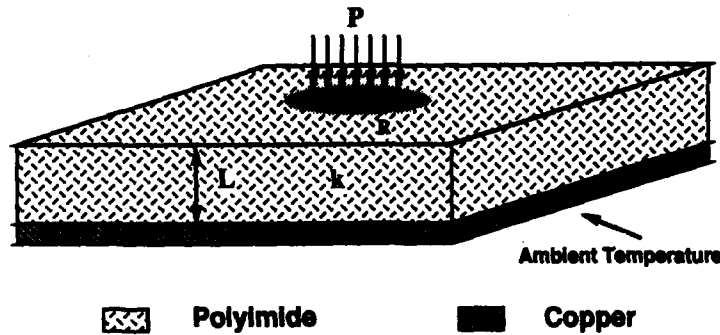


Figure 3: Simplified geometry used in analysis of laser heating of polyimide. See text for definitions of parameters.

where:

P = incident laser power

k = thermal conductivity of dielectric

a = reflectivity of bottom conductor

R = laser beam radius

L = thickness of dielectric

ϵ = emissivity of dielectric

α = thermal diffusivity of dielectric

λ = absorption length of dielectric at laser wavelength

$\gamma_n = (2n + 1) \frac{\pi}{2L}$

f_n accounts for the exponential heating due to the laser, and is given by the expression:

$$f_n(\lambda, L, a) = \frac{1}{1 + (\gamma_n \lambda)^2} [1 + (-1)^n (1 + a)(\gamma_n \lambda) \exp(-L/\lambda) - a \exp(-2L/\lambda)] \quad (3)$$

For the laser processing applications of interest to us, such as laser direct write, in which the beam is scanned continuously across the surface, the steady-state limit $t \rightarrow \infty$ is the most relevant case. The most significant parameter is the maximum temperature rise, which occurs at the beam center, $r = z = 0$. In this case, the expression for T reduces to a rather simple form:

$$T(0, 0, \infty) = \frac{2eP}{\pi k L} \sum_{n=0}^{\infty} f_n(\lambda, L, a) \frac{1}{(\gamma_n R)^2} [1 - (\gamma_n R) K_1(\gamma_n R)] \quad (4)$$

where K_1 is the modified Bessel function of order one. The summation in n converges rapidly, making numerical estimates straightforward to obtain using a short computer program.

Taking $k = 1.7$ mW/cm-K, $\epsilon = 0.92$, and $\lambda = 29$ μ m as the parameters for polyimide, we have computed the temperature increase for various values of the remaining parameters. We also attempted to correlate these calculations with laser heating experiments. For one type of sample, with a 24- μ m thick layer of polyimide over a uniform, 5- μ m thick layer of

copper, we observed experimentally that the threshold for polyimide softening was about 7.6 mW of incident laser power, with a beam diameter of about 10 μm . Using this value of laser power, we calculate temperature increases T from Equation 4 of 375 °C, 428 °C, and 481 °C, corresponding to values of a equal to 0.0, 0.5, and 1.0, respectively. Although the temperature at which polyimide softening occurs is not as universal as, say, the melting point of a crystalline solid, our calculations are seen to be generally consistent with the known materials properties of polyimide, for which the softening temperature can lie in the range 325–525 °C [11].

To emphasize the importance of assuming an exponential distribution for the heating in the polyimide, we also calculated what the maximum temperature might be for the same power level, 7.6 mW, but with $\lambda = 1 \mu\text{m}$ (we set a equal to 0.0, although the importance of a is very small at this level of absorption). We obtain $T = 1994 \text{ }^\circ\text{C}$, which is clearly unphysical in light of our experimental observations. Thus, we see that to understand pyrolytic laser processing on partially transparent materials such as polyimide, one must appreciate the thermal conduction problem as we have described it here.

Laser CVD of Tungsten

LCVD of tungsten, which in our process occurs via the hydrogen reduction of tungsten hexafluoride, is similar to bulk tungsten CVD, with two major differences. First, the "selectivity" for LCVD arises not because of differential nucleation rates for different materials, but rather from the temperature gradient resulting from the focused laser beam. Secondly, LCVD is generally performed at much higher reactant partial pressures (the H_2 partial pressure can be several hundred Torr), in order to get sufficiently high localized reaction rates. As a consequence of this, and that the volume rate of conversion of reactants is considerably lower than the corresponding bulk CVD case, LCVD of tungsten does not depend significantly on macroscopic flow characteristics.

Our experimental setup is generically similar to others which have already been described in the literature (see, for example, [1]). It comprises a microscope head which has been modified to allow a CW argon ion laser beam to be introduced into its optical path. An individual laser experiment used a portion of a copper-polyimide wafer (approximately 3-cm \times 3-cm), which had been fabricated as described above, but with only a single patterned conductor layer over polyimide. The copper-polyimide sample was placed inside a stainless steel reaction chamber which had been mounted on computer-controlled x- and y-translation stages. After evacuating the chamber, H_2 and WF_6 were introduced into the chamber at controlled rates. The all-lines, TEM₀₀ output of the laser (whose dominant lines are at 514 and 488 nm) was first expanded, then directed into one port of the microscope head. The beam was finally focused, by means of a 20X microscope objective, through a glass window in the reaction chamber to a spot size of typically 15 μm at the sample surface. The precise location of the tungsten deposition was controlled by manipulating the translation stages to position the sample at the desired location underneath the focused laser beam; we refer to this a laser "scan". The time interval during which the laser beam was exposed to the sample was controlled by means of a computer-driven mechanical shutter.

The most important application of the LCVD process is the formation of a low-resistance electrical connection between two pre-patterned nickel-copper multi-chip substrate conductors. To accomplish this, tungsten must be deposited on both the polyimide and the conductors at sufficiently high rates. This is indeed a challenge, if for no other

reason than that CVD of tungsten occurs much more slowly on polyimide than on metals [9]. But another important consideration is that LCVD at fixed laser power is not an isothermal process, due to the inhomogeneous thermal conductance of a typical copper-polyimide interconnection module. Therefore, there are two process constraints. On the one hand, the laser power must be kept at a low enough level to prevent significant ablation of the polyimide. On the other hand, the laser power must be high enough so that sufficient tungsten is deposited on the nickel-copper to form a low-resistance contact.

These materials complications were accommodated by performing the LCVD in two laser scans. After the desired reactant partial pressures had been reached in the chamber, and with the shutter closed, the laser beam focal point was positioned at the end of the first conductor. With the beam stationary, the shutter was opened for an interval of approximately one second, which we refer to as the "dwell" interval. At the end of the dwell interval and without closing the shutter, scanning of the laser beam from the first to the second conductors was begun, at a speed of about 100 $\mu\text{m/s}$. Once the second conductor had been reached, the scanning ceased, but the shutter was held open for a second dwell interval, after which it was finally closed. The laser power was then increased, typically by at least a factor of two. The laser was once again positioned on the first conductor, and the process was repeated: shutter open, dwell, scan, dwell, shutter closed. The two-scan process is important to obtain both thick deposits on the polyimide and good contacts between the nickel-copper and the deposited tungsten.

After the laser processing for a single wafer sample had been concluded, the sample was removed from the reaction chamber, and cleaned with a 40-s dip in 0.1 N KOH. This cleaning removes small particles of tungsten which nucleate on the polyimide in the vicinity of the scan region [9], as well as any tungsten oxide which might form on the surface of the nickel, or the polyimide itself [12]. Finally, four-point resistance measurements were made to classify the effects of process variables.

A number of representative tungsten LCVD scans are shown in Figures 4 through 6. They were all formed with $P(\text{H}_2) = 181$ Torr, $P(\text{WF}_6) = 7$ Torr, a first-scan power of 125 mW, and at a scan rate of 93 $\mu\text{m/s}$ (from left to right). Figure 4(a) shows a scan formed with a second-scan power of 280 mW and a dwell time of 2 s. Note the uniform character of the deposit. Figure 4(b) is a close-up of the right-side contact of Fig. 4(a). Observe that tungsten has readily nucleated on the surface of the nickel-copper, and has spread in a uniform fashion onto the surface of the polyimide. The surface of the tungsten is not at all smooth, obviously being quite nodular instead. We do not have sufficient data to infer the exact relationship between process parameters and surface topography, but we can make a couple of general statements. First, higher scan rates lead to smoother line profiles. Second, a combination of higher scan rates and higher power levels can result in "undulating" line profiles, whose spatial frequency along the scan direction is approximately equal to the deposited film linewidth. This phenomenon has been observed previously [12].

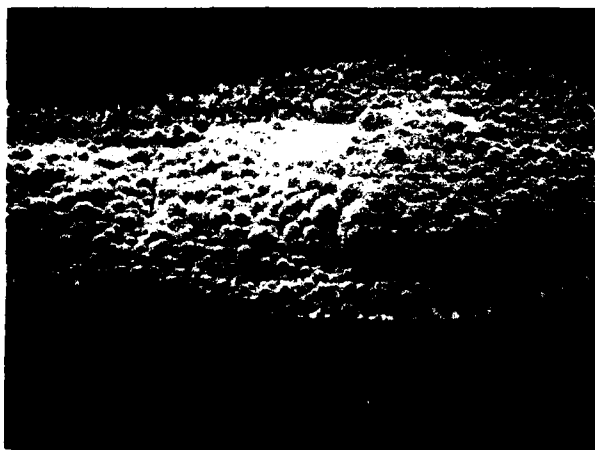
Figure 5(a) shows a similar-looking scan, except that here the dwell time had been reduced from 2 s to 1 s. Note that the lateral extent of the tungsten deposit at the nickel-copper contacts has been reduced from that in Fig. 4(a). The resistance has gone down slightly, from 0.65 Ω in Fig. 4(a) to 0.58 Ω in Fig. 5(a). From a practical perspective, we observe that the 1-s dwell interval creates a deposited tungsten line whose width is well within the 60- μm pitch of the conductor lines, and thus is not likely to short out to a nearest-neighbor.

In Fig. 5(b), the power of the second scan had been increased by about 10% to 310 mW,



(a)

280 mW 2-s Dwell 0.65 Ω



(b)

Figure 4: (a) Scanning electron micrograph of a 300- μm long LCVD tungsten film joining two 350- μm long nickel-copper conductors on polyimide: 2 s dwell, 280 mW second-scan power, 0.65 Ω link resistance; (b) close-up of right-side contact in (a).

from 280 mW in Fig. 5(a). The resistance has decreased from $0.58\ \Omega$ to $0.53\ \Omega$, a difference of about 9%. However, this trend does not continue indefinitely: For a power of 370 mW, the resistance increases to $1.35\ \Omega$. Fortunately, the power dependence of the resistance is relatively flat at the minimum, which is important for process control in a practical application.

We also investigated whether or not there is an asymmetry in the nature of the contact formed at either conductor, determined by the direction of the scan. We did this by forming a link similar to those in Figs. 4 and 5, except that it was formed by scanning the laser from both contacts toward the center, overlapping by about $100\ \mu\text{m}$ in the center of the link. The measured resistance in this case was $0.53\ \Omega$, the same as that in Fig. 5(b), which suggests that the direction of the scan is probably not a crucial factor.

Finally, we tried forming a link by scanning twice at a second-scan power of 280 mW, preceded by a single 125-mW scan. In this case, although the tungsten was noticeably thicker on the polyimide, the resistance was slightly higher, $0.62\ \Omega$. This could be due to a degradation of the contact at one or both ends, caused by excessive heating and stress. Whatever the source of the extra resistance, it apparently dominates any reduction in resistance due to the lower sheet resistance of the tungsten on the polyimide.

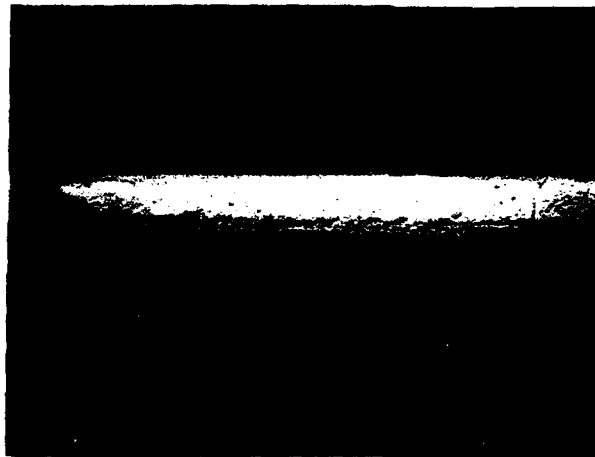
Figure 6(a) shows a longer link formed between two nickel-copper conductors, about $880\ \mu\text{m}$ long. The dwell was 3-s here, but the conditions were otherwise the same as those for the scan of Fig. 5(a) (with the scan running from upper right to lower left). The resistance went up as expected, to $2.61\ \Omega$. With this second link length, we can now crudely estimate the sheet- and contact-resistances for the tungsten links. The resistance estimates of $0.58\ \Omega$ and $2.61\ \Omega$ must first be corrected for the non-negligible lengths of nickel-copper included in the measurement structure (estimated to be $0.06\ \Omega$ and $1.43\ \Omega$, respectively). If we assume that the links of Figs. 5(a) and 6(a) have the same width ($30 \pm 5\ \mu\text{m}$) and thickness ($3.5 \pm 0.5\ \mu\text{m}$), as well as identical resistivities and contact-resistances, we calculate that the resistivity is $12 \pm 3.5\ \mu\Omega\text{-cm}$, and that the contact resistance is $0.09\ \Omega/\text{contact}$. The measured tungsten resistivity is about two to three times the bulk value, $5.6\ \mu\Omega\text{-cm}$, which is comparable to that measured by other researchers with other types of substrates, where values of 2-5 times the bulk value are typical [3].

Figure 6(b) shows a magnified view of the interior of the link in Fig. 6(a). While we have not performed quantitative estimates of film adhesion, films similar to those in Figs. 4-6 do pass the Scotch-tape pull test. Excellent adhesion between bulk tungsten and polyimide has also been observed by Pattee *et al.* [9].

Summary

We have illuminated the opportunities and challenges for the application of laser process methods to multi-chip interconnection wiring, especially for copper-polyimide interconnect substrates. We have used an analytical thermal model of the process of laser heating of polyimide, to test and verify our understanding of the phenomenon of laser-heating of a partially transparent film. We have described a novel laser CVD process for forming low-resistance tungsten links between nickel-coated copper conductors on polyimide dielectric. This maskless "direct-write" deposition technique permits direct repair or customization of inter-chip interconnects on copper-polyimide substrates. The use of tungsten is attractive because the CVD chemistry is well-understood, and tungsten interconnects do not require passivation or protective overcoats.

280 mW 1-s Dwell 0.58 Ω



(a)

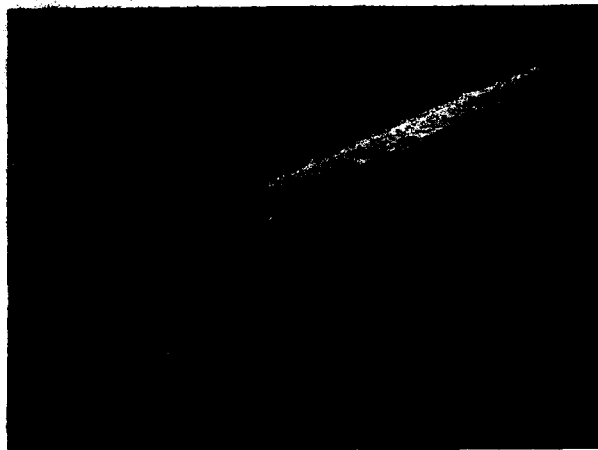
310 mW 1-s Dwell 0.53 Ω



(b)

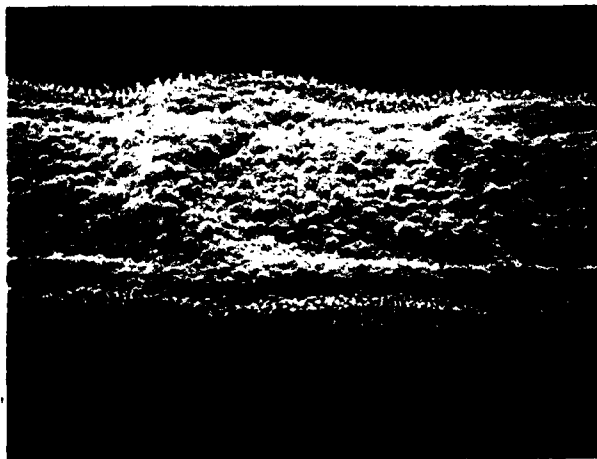
Figure 5: Scanning electron micrographs of 300- μm long LCVD tungsten films joining two 350- μm long nickel-copper conductors on polyimide. (a) 1 s dwell, 280 mW second-scan power, 0.58 Ω link resistance. (b) 1 s dwell, 310 mW second-scan power, 0.53 Ω link resistance.

280 mW 3-s Dwell 2.61 Ω



(a)

280 mW 3-s Dwell 2.61 Ω



(b)

Figure 6: (a) Scanning electron micrograph of an 880- μm long LCVD tungsten film joining two lengthy nickel-copper conductors on polyimide: 3 s dwell, 280 mW second-scan power, 2.61 Ω link resistance. (b) Close-up of middle portion of link in (a).

Acknowledgements

We gratefully acknowledge the assistance of the following individuals: J. Eisele, F. Prado, A. Sparkman, and J.E. Yater, for assisting in the construction of the LCVD apparatus; J.T. Pan and J. Pistor, for providing the copper-polyimide samples; D. Nelson and R. Reyes, for performing the SEM microscopy; and T. Hirsch, E. Lillie, C. MacKay, and L. Smith, for helpful discussions.

References

- [1] A.F. Bernhardt, B.M. McWilliams, F. Mitlitzky, and J.C. Whitehead, in *Photon, Beam, and Plasma-Stimulated Chemical Processes at Surfaces*, edited by V. Donnelly, I. Herman, and M. Hirose (Mater. Res. Soc. Proc. 75, Pittsburgh, PA 1987), pp. 633-644.
- [2] A.W. Johnson and K.E. Greenberg, in *Photon, Beam, and Plasma-Stimulated Chemical Processes at Surfaces*, edited by V. Donnelly, I. Herman, and M. Hirose (Mater. Res. Soc. Proc. 75, Pittsburgh, PA 1987), pp. 645-649.
- [3] J.G. Black, S.P. Doran, M. Rothchild, J.H.C. Sedlacek, and D.J. Ehrlich, in *Photon, Beam, and Plasma-Stimulated Chemical Processes at Surfaces*, edited by V. Donnelly, I. Herman, and M. Hirose (Mater. Res. Soc. Proc. 75, Pittsburgh, PA 1987), pp. 651-655.
- [4] R.J. Jensen, J.P. Cummings, and H. Vora, *IEEE Trans. Components, Hybrids, and Manufacturing Technology* CHMT-7, 384 (1984).
- [5] H.J. Levinstein, C.J. Bartlett, and W.J. Bertram, Jr., in *Proc. IEEE International Solid State Circuits Conference*, 224-225 (1987).
- [6] J.T. Pan, S. Poon, and B. Nelson, *Proc. Eighth Annual International Electronics Packaging Conf.*, 174-189 (1988).
- [7] F.A. Houle, C.R. Jones, T. Baum, C. Pico, and C.A. Kovac, *Appl. Phys. Lett.* 46, 204 (1985).
- [8] S.J. Bezuk, R.J. Baseman, C. Kryzak, K. Warner, and G. Thomes, in *Photon, Beam, and Plasma-Stimulated Chemical Processes at Surfaces*, edited by V. Donnelly, I. Herman, and M. Hirose (Mater. Res. Soc. Proc. 75, Pittsburgh, PA 1987), pp. 75-81.
- [9] R.W. Pattee, C.M. McConica, and K. Baughman, *J. Electrochem. Soc.* 135, 1477 (1988).
- [10] M. N. Özisik, *Heat Conduction*, (J. Wiley and Sons, New York, 1980).
- [11] M.I. Bessonov and N.P. Kuznetsov, in *Polyimides: Synthesis, Characterization, and Applications, Volume I*, edited by K.L. Mittal (Plenum Press, New York, 1984), pp. 385-399.
- [12] W.M. Grossman and M. Karnesos, *J. Vac. Sci. Tech.* B5, 843 (1987).

PROCESS MARGINS FOR LASER PLANARIZATION OF 1 TO 5 μ m GOLD FILMS

A. F. BERNHARDT, R. J. CONTOLINI, D. B. TUCKERMAN AND
A. H. WEISBERG, Lawrence Livermore National Laboratory,
P.O. Box 5503, M/S L-271, Livermore, CA 94550

ABSTRACT

A pulsed excimer laser or flashlamp-pumped dye laser is used to melt 1 to 5 μ m Au layers. The size of feature which can be filled by laser planarization is limited because of the finite melt duration, but the basic goal of levelling local surface topography is accomplished.

Laser reflow of thicker films reveals fundamental differences between the excimer laser and the flashlamp-pumped dye laser, resulting from the order-of-magnitude difference in pulse duration. The excimer pulse is short compared to the thermal diffusion time of the metal layer and this can create voids and craters in the metal above discontinuities in the underlying structure. For Au thicknesses greater than about 3 μ m, void formation occurs at fluences at or below that necessary to planarize the film. The dye laser has a planarization threshold similar to that of the excimer but it takes over 60% greater energy to create voids than to planarize a 5 μ m film.

A second damage mode, common to both laser sources, occurs where adjacent planarization zones overlap in a patterned area: thin spots can be created by the first planarization pulse which are vaporized by the second pulse.

INTRODUCTION

In multilevel interconnect, the surface topography of a given level of metallization is determined by that of underlying layers. Abrupt steps in surface topography can lead to non-uniformities in the electrical properties of the interconnect as well as to processing difficulties. Most multilevel interconnect fabrication processes planarize the dielectric layers to mitigate these problems. We explore pulsed-laser melting of the metal layers to produce a smooth surface over vias and trenches, without dielectric planarization.

Laser planarization of 1 μ m thick Au [1] and Al [1-4] has been reported. While there is much interest in laser planarization of VLSI metallization, our interest lies primarily in metallization for wafer-scale hybrid packaging. Since chip-to-chip conductor lengths tend to be much greater than on-chip distances, transmission line interconnect is desirable. This restricts the line resistance to a value less than about twice the line impedance and requires relatively large conductor thickness, as well as large cross-section [5].

The planarization process is initiated by the absorption of laser radiation at the metal surface. If the laser pulse duration is long compared to the thermal time constant of the metal but short with respect to the thermal time constant of the underlying layers, then the metal heats approximately uniformly. Surface tension provides the force which reshapes the surface. If the metal surface initially has a sinusoidal profile, for example, minima will rise and maxima will decline, commencing an oscillation which would, in the absence of damping, continue until the metal refreezes. Viscosity provides the damping which flattens the surface. Assuming that the wave amplitude is small compared to both the fluid depth, h , and the wavelength, λ , and that the oscillation is sufficiently underdamped (low viscosity and short wavelength), the damping time is given by [6]:

$$t_d = \frac{\lambda^2}{8\pi^2\nu}$$

where ν is the kinematic viscosity ($\nu = 2.9 \times 10^{-3} \text{ cm}^2/\text{s}$ for Au at 1337 K). The oscillation period is given by

$$t_{osc} = \frac{\lambda^{3/2}}{(2\pi)^{1/2}} \left[\frac{\alpha}{\rho} \tanh\left(\frac{2\pi h}{\lambda}\right) \right]^{-1/2}$$

where α is the surface tension ($\alpha = 1130 \text{ erg/cm}^2$ and $\rho = 19.3 \text{ g/cm}^3$ for Au at 1337 K). Thus, for example, if a $2 \text{ }\mu\text{m}$ film of Au has a melt duration of $2 \text{ }\mu\text{s}$, small amplitude waves shorter than about $6 \text{ }\mu\text{m}$ will damp out while $16 \text{ }\mu\text{m}$ waves will move through half an oscillation cycle.

For longer wavelengths, a more general treatment is required [7].

The melt duration will determine the maximum wavelength that can be damped. The melt duration is determined by how much energy is stored in the liquid (including latent heat of melting) and how rapidly it diffuses into the underlying structure. Heating the entire sample prior to laser irradiation [3,4] decreases the temperature gradient between the metal and the substrate and extends the melt time. A similar description applies to the planarization of vias, trenches and other surface features encountered in multilevel interconnect.

We have used an excimer laser to planarize 1 to $5 \text{ }\mu\text{m}$ thick Au over vias and trenches of similar depth. The thermal time constant of the thicker Au layers (about 250 ns for $5 \text{ }\mu\text{m}$ Au) significantly exceeds the laser pulse duration ($30 - 40 \text{ ns}$ FWHM) so that a significant temperature gradient is generated across the Au. In the thickest metal ($5 \text{ }\mu\text{m}$), the energy required to melt the layer also vaporizes the surface of the Au. The vapor pressure generated at the surface drives undesirable hydrodynamic effects discussed below. Flashlamp-pumped dye lasers have 0.5 to $2 \text{ }\mu\text{s}$ pulse durations, allowing a reasonable operating margin for the thicker films.

We have numerically modelled the laser heating process using a 1-D finite-difference heat flow code which incorporates both melting and vaporization. The model results support the

postulated presence of high temperatures and, therefore, high vapor pressures at the melt surface during laser planarization of thick films with the excimer laser.

EXPERIMENTAL

We report here on the laser planarization of Au on patterned SiO_2 . The fabrication sequence shown in Figure 1 produces conductors embedded in the dielectric and a substantially planar surface. A SiO_2 layer is deposited by plasma-enhanced chemical vapor deposition (PECVD) and trenches are formed by reactive ion etching (RIE). A 400 Å adhesion layer of $\text{Ti}_{0.3}\text{W}_{0.7}$ is sputtered onto the patterned wafer followed by various thicknesses of Au. We find that W, Mo, and $\text{Ti}_{0.3}\text{W}_{0.7}$ provide the best adhesion layers for laser planarization. Materials such as Cr and Nb which are commonly used for adhesion fail under conditions of laser planarization.

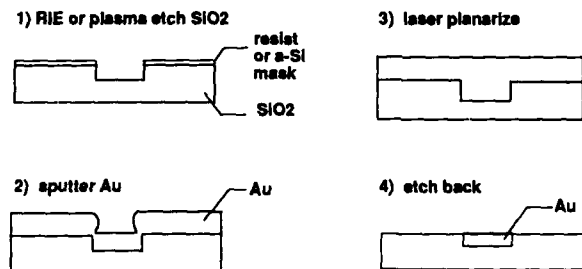


Figure 1. Fabrication of Au lines embedded in SiO_2 .

Planarization of Au up to 3 μm thick used an excimer laser with pulse energy up to 400 mJ and pulse duration of 30 ns full width at half maximum (FWHM), while experiments on 5 μm thick Au were conducted with a 1 J, 40 ns FWHM excimer laser. The dye laser had pulse energy up to 1 J at 495 nm and pulse duration of 1500 ns FWHM. In all cases, the beam spatial profile was homogenized so that its intensity was flat across most of its area. The laser fluence was measured using a current injection detector (CID) camera and beam profiling software.

Etch back of the excess Au was carried out using ion milling or a combination of electropolishing and ion milling. The last 0.5 μm or so of the Au was always ion milled at 45 degrees, for which the etch rates of Au and SiO_2 are equal.

RESULTS

Figure 2 shows SEMs of a planarized SiO_2 surface containing embedded Au conductors. The planarization was accomplished by

excimer laser melting a 2.5 μm thick layer of sputtered Au over a 5 μm thick SiO_2 surface which contained trenches 2.5 μm deep. Note that each line terminates in a pad centered on a via that connects it to a lower conductor level. The planarization step fills the via so that its presence is not evident from the surface.



Figure 2. SEM of Au lines embedded in SiO_2 . Initial Au depth was 2.5 μm .

Figure 3 shows profilometer traces across the set of four lines of Figure 2 before and after planarization. Local planarization (line to line) leaves only 3000 \AA of local surface relief out of the original 2.5 μm , but the area containing the lines subsides 6000 \AA due to conservation of volume. The subsidence means that the etch-back of 2.5 μm to remove unwanted Au in unpatterned areas will leave a rippled surface with about 1.9 μm deep Au lines in the trenches.

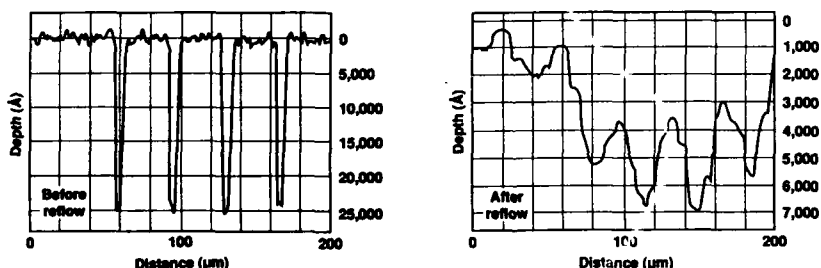


Figure 3. Profilometer traces of 2.5 μm Au over 2.5 μm trenches before and after excimer laser planarization. Trench filling is accompanied by a 6000 \AA subsidence in the patterned area.

Work at 2.5 μm could not be successfully extended to 5 μm Au films over 5 μm deep trenches using an excimer laser. Repeated attempts to planarize such thick metal produced trenches which were filled but contained numerous craters in the surface of the trenches, such as in Figure 4. The craters occurred only in the trenches, not in Au over flat SiO_2 . SEMs of cross-sectioned trenches revealed the presence of voids.

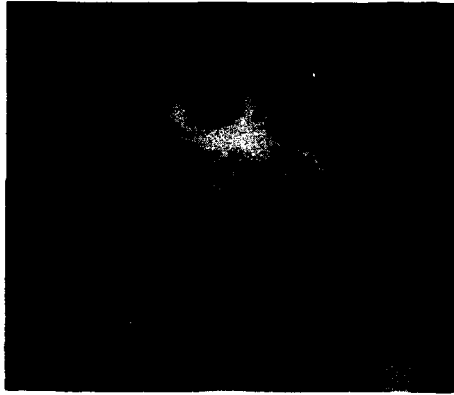


Figure 4. SEM of the surface of 5 μm thick laser-melted Au over 5 μm deep trenches showing crater formation. The location of the border of the trench is revealed in the crystal structure of the Au. The trench is 10 μm wide.

This void formation is associated with vaporization of the surface of the Au during the excimer pulse. As mentioned above, the excimer pulse is much shorter than the thermal time constant of the Au at this thickness, so a significant temperature gradient develops across the Au. At laser fluences sufficient to melt the Au layer, surface temperatures are quickly reached at which high vapor pressure develops as shown in the 1-D numerical simulation [8] of Figure 5. The top curve represents the temperature history of the surface. Each lower curve represents the temperature history 1/4 μm deeper into the Au. At these laser fluences, energy is available for further vaporization but the existing vapor has no time to move, so surface temperature and pressure continue to increase as the laser fluence is increased [9]. Figure 5 also shows that as peak surface temperatures and pressures are reached, only about 2 μm of the Au have melted.

While these high temperatures and pressures occur on horizontal surfaces which see the full laser fluence, the trench side walls are much cooler at the peak of the laser pulse. Thus the high pressure above the trench can be relieved by sideways motion of the liquid as suggested in Figure 6. In the simplest analysis, a pressure gradient on the order of a 100 MPa will generate an initial velocity of about 100 m/s in a slug of liquid of depth comparable to the melt depth (2 μm) and of lateral dimension (20 μm) on the order of the speed of sound times the duration of the vapor pressure excursion. Neither viscosity nor surface tension will significantly retard this flow and a 10 μm trench will be bridged in a matter of 100 ns or so. Since mainly the top of the Au layer is moving, voids will be trapped by the flow.

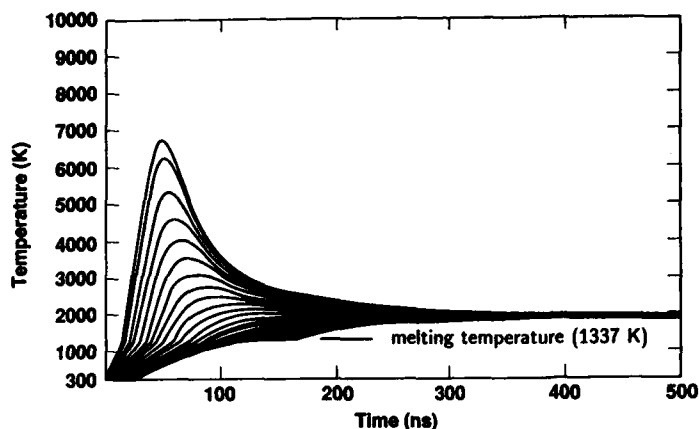


Figure 5. Numerical simulation of heat flow in excimer laser heating of 5 μm of Au over 10 μm SiO_2 .

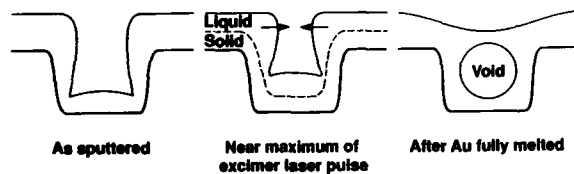


Figure 6. Schematic cross-sections of a trench covered by 5 μm of Au. The laser energy incident across the top of the trench is spread over the the walls and bottom of the trench. Thus, the walls are heated much more slowly by the laser than horizontal top surfaces. The resulting pressure gradient near the peak of the excimer laser pulse commences lateral motion in the melted portion of the Au (center), which continues until the trench is bridged and a void is formed (right).

Figure 7 shows experimental thresholds for excimer surface melting, planarization and damage as a function of metal thickness. We identify the melt threshold fluence by a sudden change in surface specularly. There is a factor of two margin in energy between planarization, which is associated with complete melting of the Au, and damage associated with vaporization of the bulk of the Au. The onset of damage is sudden, about a 10% change in laser fluence causes essentially all of the Au to be removed where no significant removal is observed at the lower fluence.

Figure 7 also includes data on void generation with excimer laser planarization. The factor of two operating margin observed for 1 μm thick Au disappears for 3 μm Au when void generation is considered. For 5 μm thick films voids were formed at 60% of the fluence necessary to planarize a pattern.

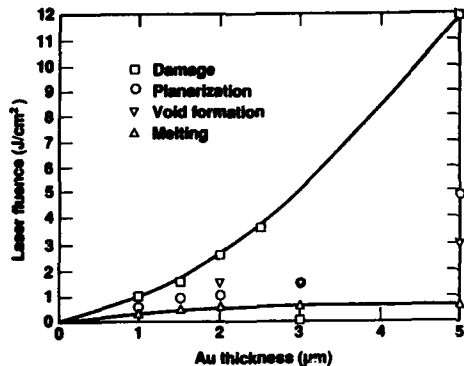


Figure 7. Experimental excimer laser melt, planarization, void formation and damage thresholds.

The void formation and damage thresholds are increased dramatically using the dye laser. For 5 μm films, the planarization threshold is only slightly higher than with the excimer, about 5.5 J/cm^2 , but void formation does not occur until above 9 J/cm^2 . The damage threshold is about 1/3 higher for the dye laser.

Large areas must be planarized with many contiguous pulses. A second pattern-sensitive defect occurs near the edge of the planarization zone where adjacent pulses overlap. The laser fluence falls more or less quickly to zero, depending on the precautions taken in beam homogenization. In this transition zone the melt time of the Au is shorter than that in the uniform intensity part of the beam, and partial planarization may leave thin areas adjacent to the lines. This effect is most pronounced on inside corners of bends in trenches where metal flows in two directions into the trench (instead of only one direction as occurs along a straight section of trench). When a second pulse hits this area, the thin Au can be vaporized, leaving a bare spot as pictured in Figure 8. This problem is common to all metal thicknesses and laser sources, although it may be somewhat less severe for dye laser planarization due to the lack of the pressure-driven effects described above.

The pulse overlap damage can also occur simply because a dense pattern presents an excessively large ratio of volume to be filled to volume of available metal. For example, the planarized structure of Figure 9 [1], though perfectly planarized, will not survive a second pulse without damage.

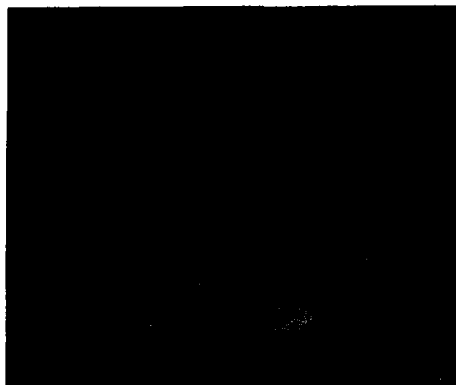


Figure 8. SEM of surface (left) shows exposed SiO_2 at the inside corner of a 90 degree bend in a trench when pulse edges overlap. A cross-sectional drawing is shown below.

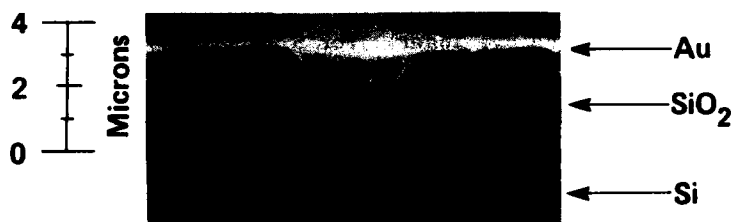


Figure 9. The perfectly planarized structure shown here will also be damaged if a second pulse strikes this area.

The best strategy for avoiding pulse overlap damage is to planarize entire dice with a single pulse. With good homogenization, the edges of the beam will fall only on the area between die. The kerf generally contains no underlying structure and will not be damaged. Even if some damage occurs on the kerf, wafer yield should not be reduced.

CONCLUSIONS

In excimer laser planarization, voids are formed in patterned areas by pressure-induced hydrodynamic effects. As a result, factor-of-two process margins for 1 μm of Au over 1 μm trenches erode almost to zero for 3 μm thick Au over 3 μm trenches. For 5 μm Au over 5 μm trenches, voids form at 60% of the energy required to planarize 10 μm wide trenches.

The fundamental problem with commercial excimer lasers in this application is that their pulse duration is short compared to the thermal diffusion time through the Au layer. Use of a flashlamp-pumped dye laser with 1.5 μ s pulse duration restores a 60% process margin for 5 μ m Au planarization.

Finally, damage can occur in patterned areas where planarization pulses overlap. The overlap region should be confined to unpatterned (eg. kerf) or sparsely patterned areas of the wafer and its area limited by sharp truncation of the beam edge.

ACKNOWLEDGEMENTS

We would like to thank Dr. Randal L. Schmitt of the Combustion Research Facility of the Sandia National Laboratories for the use of the flashlamp-pumped dye laser used in this work.

This work performed under the auspices of the U.S. Department of Energy by the Lawrence Livermore National Laboratory under Contract W-7405-Eng-48.

REFERENCES

1. D.B. Tuckerman and A.H. Weisberg, IEEE Electr. Dev. Lett. EDL-7, 1 (1986).
2. R. Mukai, N. Sasaki, and M. Nakano, IEEE Electr. Dev. Lett. EDL-8, 76 (1987).
3. R. Mukai, N. Sasaki, and M. Nakano, in Beam-Solid Interactions and Transient Processes, Materials Research Society Symposium Proceedings Volume 74, edited by S.T. Picraux, M.O. Thompson, J.S. Williams (Materials Research Society, Pittsburgh, 1987), p. 229.
4. R.J. Baseman, J.C. Andreshak, A. Gupta, C-Y. Ting, in Selected Topics in Electronic Materials, Materials Research Society Symposium Extended Abstracts, edited by B.R. Appleton, D.K. Biegelsen, W.L. Brown and J.A. Knapp, (Materials Research Society, Pittsburgh, 1988), p. 259.
5. C.W. Ho, D.A. Chance, C.H. Bajorek and R.E. Acosta, IBM J. Res. Develop. 26, 286 (1982).
6. L.D. Landau and E.M. Lifshitz, Fluid Mechanics, (Pergamon Press, New York, 1959), p. 240.
7. P.F. Marella, D.B. Tuckerman and R.F. Pease, in Laser and Particle Beam Chemical Processing on Surfaces, Materials Research Society Symposium Proceedings Volume 129, edited by A.W. Johnson, G.L. Loper and T.W. Sigmon, in press.
8. A.F. Bernhardt, unpublished.
9. J.F. Ready, J. Appl. Phys. 36, 462 (1965).

FLASHLAMP-PUMPED DYE AND EXCIMER LASER PLANARIZATION OF THIN METAL FILMS

PAUL F. MARELLA*, DAVID B. TUCKERMAN**, R. FABIAN PEASE*

*Stanford Solid-State Electronics Laboratory, Stanford University, Stanford, CA 94305

**LP Program, Special Studies Division, Lawrence Livermore National Laboratory, Livermore, CA 94550

ABSTRACT

The fundamental differences between excimer (≈ 30 ns pulse duration) and flashlamp-pumped dye (≈ 500 ns pulse duration) laser planarization are examined for 1.5-2 μm thick gold films over SiO_2 layers. Test structures containing bar patterns (square waves) of 5000 \AA peak-to-trough amplitude with spatial periods ranging from 10 μm to 100 μm were prepared and laser-irradiated. A linear model is presented which describes the time-evolution of the film's surface topography when melted with a dye laser pulse. Excimer laser planarization is found to be susceptible to evaporative recoil effects which may cause undesired pattern amplification.

INTRODUCTION

Multilevel thin-film metal interconnections, both on-chip and off-chip, are becoming essential in high-performance circuits and systems. Planarization techniques are necessary elements of a modern multilevel metallization process. A novel technique for planarizing thin, nonrefractory metal films by momentarily melting them with an 0.5-1.0 μs dye laser pulse has been demonstrated by Tuckerman and Weisberg[1]. More recently, Mukai *et al* planarized aluminum thin films with 15-ns excimer laser pulses [2,3]. The absorbed energy fluence in each case was $\sim 1 \text{ J/cm}^2$ per μm metal thickness. In this letter we examine (theoretically and experimentally) the differing effects produced by such different pulse durations on thin (1.5-2 μm) gold films over insulating SiO_2 layers. Also, we present a model employing the linearized Navier-Stokes equation which describes the transient flow leading to planarization.

THEORY

A flashlamp-pumped dye laser pulse heats the metal nearly uniformly since the thermal diffusion length δ_{dye} is much greater than the metal thickness h ($\delta_{\text{dye}} = 2\sqrt{\kappa_{\text{Au}}\tau_{\text{dye}}} \approx 12 \mu\text{m}$, where $\kappa_{\text{Au}} \approx 0.7 \text{ cm}^2/\text{s}$ [4] is the thermal diffusivity of Au, and τ_{dye} is the dye laser pulse duration [FWHM] ≈ 500 ns) and the underlying SiO_2 layer acts as a thermal barrier ($\kappa_{\text{Au}}/\kappa_{\text{SiO}_2} \sim 10^2$ [4], where K is thermal conductivity). In contrast, the 30-ns excimer laser pulse induces a large (~ 4000 K), brief temperature differential across the metal since $\delta_{\text{ex}} \approx 2.9 \mu\text{m} \sim h$. The surface temperature may allow sufficient evaporation pressure to generate a recoil impulse which deforms the molten surface [5,6]. The magnitude of such hydrodynamic mass redistribution normally far exceeds any mass loss due to evaporation [5]. Consider a metal film having the initial cross section shown in Fig. 1. For $L > 2\delta_{\text{ex}}$, a uniform-intensity excimer laser pulse will raise the temperature of the troughs somewhat more than the peaks because of the local thickness difference. The near-exponential relationship between evaporation rate and temperature implies a larger impulse in the troughs than at the peaks, which tends to increase the peak-to-trough amplitude. This recoil effect is most important over a particular range of pattern wavelengths (about 30-50 μm in this work). Much longer wavelengths experience lateral pressure gradients that are too small to cause appreciable flow. For much shorter wavelengths, surface tension and viscous forces become effective at both opposing the recoil impulse and attenuating (as described below) the disturbance after the recoil impulse.

The subsequent time evolution (i.e., after the recoil impulse, if any) of small-amplitude $\alpha(x,t)$, long-wavelength L surface waves (Fig. 1) in molten metal can be described by the two-dimensional linearized (i.e., neglecting the convective term due to (3) below), incompressible Navier-Stokes (N-S) equation [7].

$$(1) \quad \rho \frac{\partial v}{\partial t} = -\nabla P + \eta \nabla^2 v \quad (\text{linearized N-S})$$

$$(2) \quad \nabla \cdot v = 0 \quad (\text{continuity, incompressibility})$$

Here $v = (v_x, v_y)$ is the velocity field, P is pressure, ρ is the density of the melt (18 g/cm^3 at 1337 K[8]), and η is its dynamic viscosity (5.4 cP at 1337 K[8]). The system is subject to the following conditions:

$$(3) \quad \alpha \ll h, L \quad (\text{small amplitude, long wavelength})$$

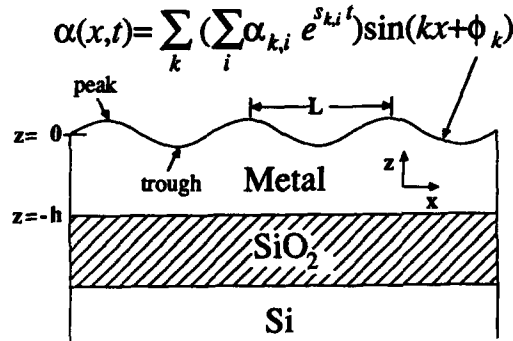


Fig. 1. Cross section of a metal film over SiO_2 having a small surface disturbance $\alpha(x,t)$. A general initial surface pattern can be Fourier-decomposed into sinusoidal shapes. In the case of an aperiodic disturbance the sum would be replaced by an integral.

- (4) $\frac{\partial \alpha}{\partial t} = 0$ at $t = 0$ (no initial motion)
- (5) $v_x, v_z = 0$ at $z = -h$ (no-slip condition)
- (6) $\frac{\partial v_x}{\partial z} + \frac{\partial v_z}{\partial x} = 0$ at $z = 0$ (zero shear at the melt surface)
- (7) $\gamma \frac{\partial^2 \alpha}{\partial x^2} = -P + 2\eta \frac{\partial v_z}{\partial z}$ at $z = 0$ (normal force balance at the melt surface)

where γ is the surface tension (1130 erg/cm² at 1337 K[8]). We assume that $\partial \alpha / \partial t = v_z$ at $z=0$ by virtue of (3). The system of equations is linear and separable. Any general initial surface disturbance $\alpha(x)$ may be decomposed into independent spatial Fourier components, each of which evolves as a sum of complex exponentials:

$\alpha_k(x,t) = (\sum_i \alpha_{k,i} e^{s_{k,i} t}) \sin(kx + \phi_k)$, where $k = 2\pi/L$ and i is the mode number; v has a homogeneous ($e^{\pm m_{k,i} z}$) and a particular ($e^{\pm kx}$) component, where $m_{k,i} = \sqrt{k^2 + \rho s_{k,i} / \eta}$. Application of (6) and (7) yields a characteristic determinant (8) whose zeros define the allowed natural frequencies $s_{k,i}$.

$$(8) \begin{vmatrix} 2 \sinh kh - \left(\frac{m_{k,i}}{k} + \frac{k}{m_{k,i}} \right) \sinh m_{k,i} h & 2 \cosh kh - \left(1 + \frac{m_{k,i}^2}{k^2} \right) \cosh m_{k,i} h \\ \frac{k\gamma}{\eta} \left(\sinh kh - \frac{k}{m_{k,i}} \sinh m_{k,i} h \right) + s_{k,i} \left(\left(1 + \frac{m_{k,i}^2}{k^2} \right) \cosh kh - 2 \cosh m_{k,i} h \right) & \frac{k\gamma}{\eta} (\cosh kh - \cosh m_{k,i} h) + s_{k,i} \left(\left(1 + \frac{m_{k,i}^2}{k^2} \right) \sinh kh - 2 \frac{m_{k,i}}{k} \sinh m_{k,i} h \right) \end{vmatrix} = 0$$

Using Newton recursion in the complex plane [9], the frequencies of the two least damped modes (i.e., smallest $|\text{Re } s_k|$) are plotted as a function of wavelength in Fig. 2 for a 1.75 μm thick gold film. These frequencies form a complex conjugate pair for $L \leq 50 \mu\text{m}$, implying underdamped motion. A corresponding plot for 1.75 μm thick aluminum ($\rho = 2.4 \text{ g/cm}^3$ [8], $\eta = 1.4 \text{ cP}$, $\gamma = 520 \text{ erg/cm}^2$ at 1073 K [10]) also becomes underdamped for $L \leq 50 \mu\text{m}$ and exhibits natural frequencies about twice that of gold (the two least damped frequencies scale as $\sqrt{\eta}$ and η/ρ for overdamping, and as $\sqrt{\gamma/\rho}$ and η/ρ for underdamped oscillation and damping, respectively). Note that for $L > 50 \mu\text{m}$, the longest damping time constant $\tau = 1/s_{k,1}$ is asymptotic to that derived by Tuckerman and Weisberg [1]. Their inertia-free analysis becomes invalid for $L < 50 \mu\text{m}$, where the inertial term $(\partial v/\partial t)$ in (1) becomes non-negligible. For $L \leq 10 \mu\text{m}$, s_k is asymptotic to the solution derived by Levich [11] for a liquid of infinite depth; this is because the motion of such a liquid is confined to a scale depth of $L/2\pi < 1.6 \mu\text{m}$ and so is insensitive to the presence of a solid surface at $z = -1.75 \mu\text{m}$. The preceding analysis could be extended to handle three-dimensional structures such as vias.

Most of the planarizing action occurs while the metal is completely melted (an interval t_{molten} , typically 1-5 μs). Some planarization also occurs during the melting and freezing processes (which take $\sim \tau_{\text{laser}}$ and $t_{\text{freeze}} \sim 1 \mu\text{s}$, respectively), but this flow is significantly impeded by the presence of the solid metal phase. Thus for the purpose of calculating the degree of planarization, we consider the flow duration to be longer than t_{molten} but shorter than $\tau_{\text{laser}} + t_{\text{molten}} + t_{\text{freeze}}$.

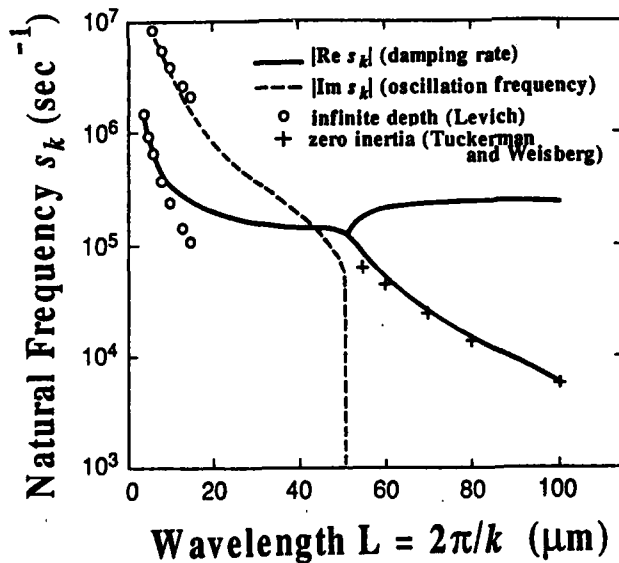


Fig. 2. Plot of the two least damped (i.e., $i = 1, 2$) complex natural frequencies $s_{k,i}$ as a function of wavelength $L = 2\pi/k$ for a 1.75 μm thick molten gold film. At short wavelengths, s_k approaches the infinite depth solution of Levich [11]. At long wavelengths, the lower (dominant) branch is asymptotic to the result of Tuckerman and Weisberg [1].

The following analytical, one-dimensional, model is used to calculate bounds on t_{melt} and estimate t_{freeze} for flashlamp-pumped dye laser pulses (excimer laser pulses can be treated with a few small modifications). The model allows for cooling by conduction only, and assumes an infinitely conductive metal (since $K_{\text{Au}} / K_{\text{SiO}_2} \sim 10^2$, see above). We assume T independent $\kappa_{\text{SiO}_2} = 0.008 \text{ cm}^2/\text{s}$, $(\rho C)_{\text{SiO}_2}$ (volumetric heat capacity) = $2.8 \text{ J/cm}^3\cdot\text{K}$, $K_{\text{SiO}_2} = 0.05 \text{ W/cm}\cdot\text{K}$ [4] and hence we have

$$(9) \quad \frac{\partial T}{\partial t} = (\kappa_{\text{SiO}_2}) \frac{\partial^2 T}{\partial x^2}$$

throughout the SiO_2 . We consider the case in which the laser melts the entire thickness of the metal. The near-gaussian temporal profile of the laser pulse is replaced with the "box" profile shown in Fig.3a. This approximation allows us to break the problem into two parts: I. Laser On (Heating), and II. Laser Off (Cooling).

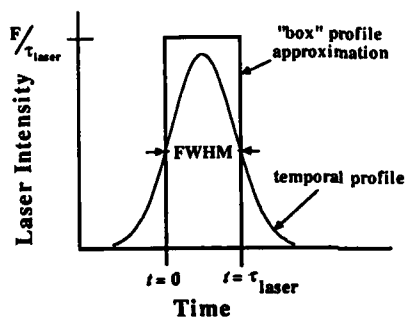


Fig.3a) Figure illustrating the temporal "box" profile approximation to the near-gaussian laser pulse. This approximation allows for division of the calculation of t_{melt} (the time interval in which the metal is completely molten) and t_{freeze} (the time interval in which the metal freezes) into separate parts (i.e., Laser On [heating], and Laser Off [cooling]).

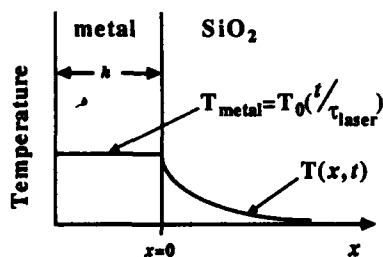


Fig.3b) A metal layer (thickness h) in contact with an infinite slab of SiO_2 at $x=0$. This approximation to the situation depicted in Fig.3c is used to calculate the temperature rise, in both the metal and the SiO_2 , during the laser pulse (i.e., Laser On).

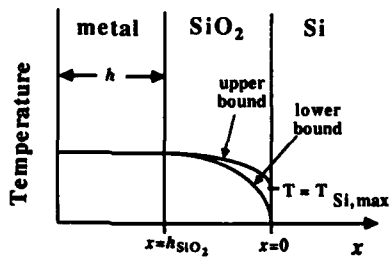


Fig.3c) The one-dimensional, layered metal- SiO_2 -Si system employed in the Laser Off (Cooling) calculations; these calculations provide upper and lower bounds for t_{melt} and an estimate of t_{freeze} .

I. Laser On (Heating)

For heating we consider a metal film of thickness h in contact (at $x=0$) with an infinite slab of SiO_2 (Fig.3b). The SiO_2 thickness need not be finite here since the temperature rise, during heating, for $x \geq 2 \mu\text{m}$ (the nominal SiO_2 thickness) is very small. The following boundary condition follows from the infinite conductivity of the metal:

$$(10) \quad T(x=0, t) = T_0 \left(\frac{t}{\tau_{\text{dye}}} \right) \quad 0 \leq t \leq \tau_{\text{dye}}.$$

Solving (9) (Laplace Transform Method [12]), we obtain

$$(11) \quad T(x, t = \tau_{\text{dye}}) = T_0 \left(\left(1 + 2u^2 \right) \text{erfc}(u) - \frac{2}{\sqrt{\pi}} u e^{-u^2} \right),$$

where $u = x/2\sqrt{\kappa_{\text{SiO}_2} \tau_{\text{dye}}}$. T_0 is found by simple heat balance according to (12).

$$(12) \quad (F - Hh) = T_0 h \left((\rho C)_{\text{metal}} + \frac{(\rho C)_{\text{SiO}_2}}{T_0 h} \int_0^{\infty} T(x, t = \tau_{\text{dye}}) dx \right)$$

F is the absorbed laser fluence and H is the volumetric latent heat of melting for the metal layer.

II. Laser Off (Cooling)

For the subsequent cooling, we consider a molten metal film (h) in contact with an SiO_2 layer of thickness h_{SiO_2} over an infinite slab of Si (Fig.3c). To obtain a lower bound on t_{molten} we solve (9) with the following boundary conditions:

$$(13) \quad T(x, t = 0) = T_0 \left(\frac{x}{h_{\text{SiO}_2}} \right)^2$$

$$(14) \quad T(x = 0, t) = 0 \text{ (}^\circ\text{C)}$$

$$(15) \quad -K_{\text{SiO}_2} \left(\frac{\partial T}{\partial x} \right) = (\rho C)_{\text{metal}} \left(\frac{\partial T}{\partial t} \right) \quad \text{at } x = h_{\text{SiO}_2}.$$

(13) is a parabolic approximation to (11) (accurate to $\leq 10\%$), (14) insures maximum conduction and therefore provides the lower bound for t_{molten} , (15) is a statement of the metal's infinite conductivity (i.e., the metal acts like a thermal capacitor). Solving with Laplace transforms, we obtain

$$(16) \quad T(x, t) = 4T_0 \sum_{n=1}^{\infty} \frac{\left(1 + \frac{1 - \cos \alpha_n}{q} - \frac{\sin \alpha_n}{\alpha_n} \right) \sin(\alpha_n \frac{x}{h_{\text{SiO}_2}}) e^{-t/\tau_n}}{\alpha_n^2 \left(1 + \frac{\alpha_n^2}{q^2} + \frac{1}{q} \right) \sin \alpha_n}$$

where $q = \frac{(\rho C)_{\text{SiO}_2} h_{\text{SiO}_2}}{(\rho C)_{\text{metal}} h}$, $\tau_n = \frac{h_{\text{SiO}_2}^2}{\kappa_{\text{SiO}_2} \alpha_n^2}$, and the α_n are the roots of $q = \alpha_n \tan \alpha_n$. $T(h_{\text{SiO}_2}, t_{\text{molten}}) = T_{\text{freeze}}$ provides the lower bound on t_{molten} (t_{molten}). An upper bound on t_{molten} is found by first calculating the maximum temperature rise $T_{\text{Si,max}}$ for the surface of an infinite Si slab when heated by the flux provided by (16) at $x=0$, and then re-solving the cooling problem with (13) replaced by (13') and (14) replaced by (14').

$$(13') \quad T(x, t = 0) = (T_0 - T_{\text{Si,max}}) \left(\frac{x}{h_{\text{SiO}_2}} \right)^2 + T_{\text{Si,max}}$$

$$(14') \quad T(x = 0, t) = T_{\text{Si,max}}$$

$T(h_{\text{SiO}_2}, t_{\text{molt}}) = T_{\text{freeze}}$ then yields the upper bound on t_{molt} ($t_{\text{u,molt}}$). We have

$$(17) \quad t_{\text{molt}} < t_{\text{molt}} < t_{\text{u,molt}}$$

We estimate t_{freeze} by employing the heat flux from (16) at $x = h_{\text{SiO}_2}$, $t = t_{\text{molt}}$; here we assume that this flux stays constant while the metal freezes (i.e. (18)).

$$(18) \quad Hh = \left(-K_{\text{SiO}_2} \left(\frac{\partial T}{\partial x} \right) \right) \Big|_{x=h_{\text{SiO}_2}, t=t_{\text{molt}}} t_{\text{freeze}}$$

For Au ($(\rho C)_{\text{Au}} = 2.8 \text{ J/cm}^3\cdot\text{K}$, $T_{\text{freeze}} = 1064^\circ\text{C}$ [4], $H = 1.2 \text{ kJ/cm}^2$ [13]) of thickness $h = 1.75 \text{ }\mu\text{m}$, $h_{\text{SiO}_2} = 2.0 \text{ }\mu\text{m}$ and an incident dye laser pulse of 2.4 J/cm^2 (57% absorbed energy at $\lambda = 490 \text{ nm}$ for evaporated Au [5]) we obtain $T_0 = 1700^\circ\text{C}$, $T_{\text{Si,max}} = 170^\circ\text{C}$, $t_{\text{molt}} = 2.3 \text{ }\mu\text{s}$, $t_{\text{u,molt}} = 2.7 \text{ }\mu\text{s}$, $t_{\text{freeze}} = 0.8 \text{ }\mu\text{s}$. We choose $t_{\text{molt}} = 2.5 \text{ }\mu\text{s}$ (the average of t_{molt} , $t_{\text{u,molt}}$). So, for these conditions we obtain flow time bounds of $2.5 \text{ }\mu\text{s}$ (t_{molt}) and $3.8 \text{ }\mu\text{s}$ ($t_{\text{laser}} + t_{\text{molt}} + t_{\text{freeze}}$). These values agree (to within 10%) with those recently calculated, using a more accurate finite-difference technique, by Bernhardt [6].

EXPERIMENTS

Test structures were fabricated by first depositing LPCVD SiO_2 ($1.9 \text{ }\mu\text{m} \pm 5\%$) on silicon wafers and then sputter-depositing $500 \text{ }\text{\AA}$ of $\text{Ti}_{0.3}\text{W}_{0.7}$ followed by $2.0 \text{ }\mu\text{m} (\pm 5\%)$ of Au. Parallel trenches (square waves) having spatial periods varying from $10 \text{ }\mu\text{m}$ to $100 \text{ }\mu\text{m}$ were photolithographically defined and wet-etched to a depth of $5000 \text{ }\text{\AA}$. The rough, optically absorbant surface texture of the etched regions would cause non-uniform reflectance (an undesired experimental variable), so we smoothed them by exposing the wafers to low-fluence (0.7 J/cm^2) Xe^+Cl excimer laser pulses. The relatively low energy, but high peak power, of these pulses induces shallow melting at the etched regions which smooths the high spatial frequency roughness in the troughs but leaves the basic square wave shapes intact (peak-to-trough amplitudes of $5000 \text{ }\text{\AA} \pm 4\%$ over a 70 mm square test area).

The square wave patterns were then irradiated with either excimer (Xe^+Cl , $\lambda = 308 \text{ nm}$, $\tau_{\text{ex}} = 30 \text{ ns}$) or flashlamp-pumped dye (coumarin, $\lambda = 490 \text{ nm}$, $\tau_{\text{dye}} = 500 \text{ ns}$) laser pulses. Beams were homogenized to produce uniform flux profiles. Incident energy fluences were determined by imaging with a digitizing camera and then measuring the total pulse energy with a volume calorimeter (for the UV) or a surface absorber (for the visible wavelength). Spot uniformity was $\pm 4\%$ across a $3 \text{ mm} \times 4 \text{ mm}$ spot for the excimer laser, and $\pm 7\%$ over a $2.5 \text{ mm} \times 3 \text{ mm}$ spot for the dye laser. The entire thickness of the Au film melted (as evidenced by a marked increase in grain size after melting [14]) at all fluences used here ($\geq 1.2 \text{ J/cm}^2$ for the excimer laser, 2.4 J/cm^2 for the dye laser). All surface profiles were measured with a Dek-Tak™ profilometer.

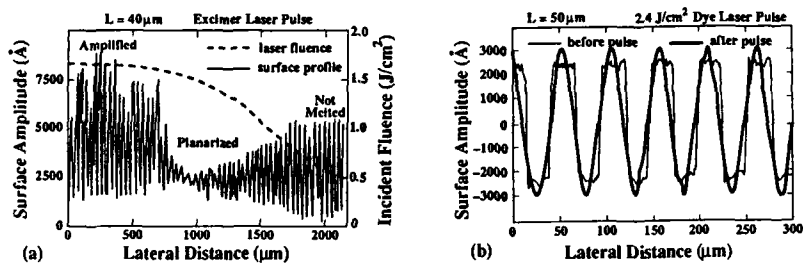
RESULTS

The excimer laser planarization results (peak intensity $\sim 10^8 \text{ W/cm}^2$) were influenced by evaporative recoil; resultant profiles did not exhibit smooth shapes or uniform, reproducible amplitudes. Patterns irradiated at 1.7 J/cm^2 had larger final amplitudes than those treated with less energy (1.2 J/cm^2 , 1.55 J/cm^2) for $L = 30, 40 \text{ }\mu\text{m}$. In fact, pattern amplification (e.g., a 40% amplitude increase induced by the excimer laser pulse) was observed at $L = 40 \text{ }\mu\text{m}$ (Fig. 4a). There was no significant mass loss due to evaporation for these fluences ($\leq 2.2 \text{ J/cm}^2$). These results cannot be explained by our linear flow model, in which a higher fluence yields a longer melt time and hence more damping. Rather, they can be explained by the evaporative recoil concept in which a higher fluence can yield a large pressure impulse which increases the pattern amplitude. In fact, the excimer laser caused surface roughening of an initially planar region; a surface roughness of $\sim 500 \text{ }\text{\AA}$ increased to $\sim 1 \text{ }\mu\text{m}$ after a single 2.2 J/cm^2 pulse. In a more extreme case, a 3.0 J/cm^2 pulse caused melt ejection [5] near the beam edges.

Irradiation with a flashlamp-pumped dye laser did not give rise to evaporative recoil, because of the relatively low peak intensity ($\sim 10^6 \text{ W/cm}^2$). The laser planarization can then be viewed simply as a low-pass spatial filtering process for the Fourier surface components, in accordance with (8). For $10 \text{ }\mu\text{m} \leq L \leq 60 \text{ }\mu\text{m}$, only the fundamental Fourier component (a smooth sinusoid as in Fig. 4b) remains significant after irradiation. For $L = 100 \text{ }\mu\text{m}$, the unattenuated fundamental and the 3rd harmonic (attenuated about 50%) are evident after melting (Fig. 4c). At $L = 20 \text{ }\mu\text{m}$, substantial planarization occurred; note also that the peaks and troughs of the irradiated surface traded positions, confirming the predicted underdamped behavior (Fig. 4d). The measured amplitudes, after a single pulse, of the fundamental Fourier components (normalized to their initial values) are plotted as a function of wavelength L in Fig. 5. The predictions of our linear theory for the flow time limits of $2.5 \text{ }\mu\text{s}$ and $3.8 \text{ }\mu\text{s}$ are also plotted. The effects of a sequential planarizing pulses could be estimated by raising these curves to the n th power.

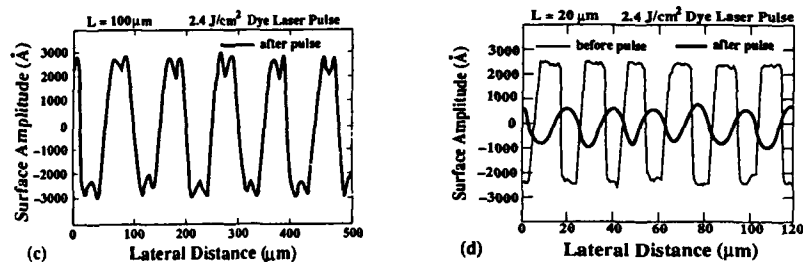
CONCLUSION

The physics of pulsed laser planarization of thin metal films has been investigated theoretically and experimentally. Excimer lasers, due to their relatively short pulse durations, produce an evaporative recoil effect which can cause pattern amplification. For this reason, small process margins (e.g., Fig.4a) and multiple-pulse damage are obtained with these lasers[6]. Flashlamp-pumped dye lasers provide more desirable, reproducible results owing to their longer pulses. A linear theory has been presented which accurately models the recoilless transient flow. The use of multiple sequential dye laser pulses could provide further planarization in accordance with our model.



a) Effect of an excimer laser pulse on an initial square-wave pattern of amplitude 5000 Å and spatial period 40 μm in the vicinity of the beam edge. We find an initial (unmelted) square wave pattern outside the beam area, an adjacent planarized region near the beam edge, and an *amplified* pattern in the center of the beam.

b) For flashlamp-pumped dye laser irradiation an initial square wave of 50 μm spatial period exhibits only a smooth sinusoidal fundamental frequency component after exposure to 2.4 J/cm².



c) An initial square wave (not shown) of 100 μm spatial period which exhibits both the fundamental and its third harmonic (which is responsible for the dimples in the peaks and troughs) after a 2.4 J/cm² dye laser pulse.

d) An initial square wave of 20 μm spatial period which exhibits a vestigial fundamental sinusoid after a 2.4 J/cm² dye laser pulse. Note the interchanged positions of the peaks and troughs, an inertial overshoot predicted by our theory.

Fig.4. Surface profiles of gold films of average thickness equal to 1.75 μm before and after irradiation with a laser pulse.

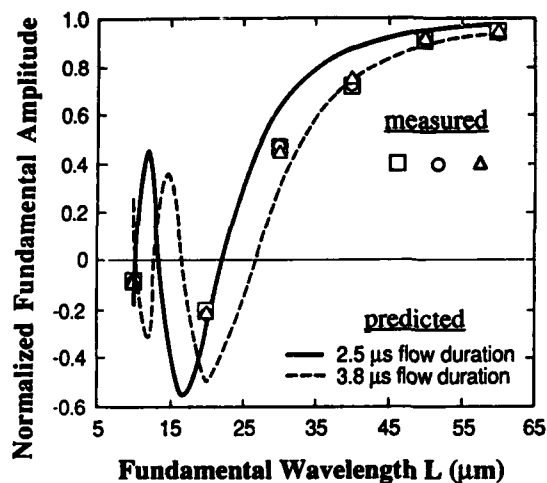


Fig.5. Plot of the measured fundamental Fourier component amplitudes as a function of wavelength L for a gold film of mean thickness $1.75 \mu\text{m}$, after exposure to a 2.4 J/cm^2 flashlamp-pumped dye laser pulse. Also plotted are the predictions of our linear hydrodynamic model for the calculated flow duration bounds of 2.5 and $3.8 \mu\text{s}$.

ACKNOWLEDGMENT

The authors wish to thank A. F. Bernhardt for many invaluable discussions, A. H. Weisberg for helpful discussions and assistance with the experiments, R. J. Contolini for his help in the laboratory, and J. H. Feikert, G. E. Griggs, B. W. Langley, and S. M. Taylor for their help with test sample fabrication. P. F. Marella is an SRC Fellow. This work was supported in part by the DOD VHSIC Program, and in part by the U.S. Department of Energy under Contract W-7405-Eng-48 as well as by the SRC under Contract 87-MJ-103.

REFERENCES

1. D. B. Tuckerman and A. H. Weisberg, *IEEE Electron Device Letters*, EDL-7, 1(1986).
2. R. Mukai, N. Sasaki and M. Nakano, *IEEE Electron Device Letters*, EDL-8, 76(1987).
3. R. Mukai, K. Kobayashi and M. Nakano, in *Proc. 1988 VLSI Multilevel Interconnection Conf.(V-MIC)*, IEEE Cat. 88CH2624-5, June 1988, pp. 101-107.
4. Y. S. Touloukian and C. Y. Ho, *Thermophysical Properties of Matter*, New York: IFI / Plenum, 1973.
5. M. von Allmen, *Laser-Beam Interactions with Materials*, Springer-Verlag, 1987, pp. 163-170, pg.17.
6. A. F. Bernhardt, R. J. Contolini, D. B. Tuckerman, A. H. Weisberg, in *Laser and Particle Beam Chemical Processes on Surfaces, Materials Research Society Symposium Proceedings*, volume 129, A. Wayne Johnson, G. L. Loper, T. W. Sigmon, Ed's, this volume.
7. L. D. Landau and E. M. Lifshitz, *Fluid Mechanics*, Great Britain: Pergamon Press Ltd., 1959, Chapter II.

8. E. T. Turkdogan, Physical Chemistry of High Temperature Technology, UK: Academic Press inc., 1980, Chapter 3.
9. J. Stoer and R. Bulirsch, Introduction to Numerical Analysis, New York: Springer-Verlag, 1980, pp. 246-248.
10. R. N. Lyon, ed., Liquid Metals Handbook. Washington, D.C.: U.S. Government Printing Office, June 1952, p.41.
11. V. G. Levich, Physicochemical Hydrodynamics, Prentice-Hall Inc., 1962, pp.599-608.
12. H. S. Carslaw and J. C. Jaeger, Conduction of Heat in Solids, Clarendon Press, Oxford, 1959, Chapter XII.
13. O. Kubaschewski, E. LL. Evans, and C. B. Alcock, Metallurgical Thermochemistry, Pergamon Press, 1967, pg. 366.
14. D. B. Tuckerman and R. L. Schmitt, in *Proc. 1985 VLSI Multilevel Interconnection Conf. (V-MIC)*, IEEE Cat. 85CH2197-2, June 1985, pp. 24-31.

LASER SURFACE MODIFICATION FOR COPPER DEPOSITION ON POLYIMIDE

Y.S. Liu and H.S. Cole
GE Research and Development Center
P.O. Box 8, Schenectady, New York 12345

ABSTRACT

Selective modification of surface reactivities with lasers, using either direct writing or projection method, is intrinsically a sensitive method to prepare a surface for high-resolution and high-speed area selective thin film deposition. In this paper, we demonstrated the use of laser direct-writing and projection patterning techniques for selective modification of the electrochemical property of a polyimide surface. High quality and high-resolution copper patterns on polyimide surfaces are produced when the surface-modified sample is subsequently placed in an electroless plating solution. These results demonstrated that the use of laser-selective-modification of surface properties in conjunction with other batch thin film deposition processes provides an attractive approach for area-selective metallization for a variety of applications in which high writing speed and high sensitivity are required.

INTRODUCTION

The demands for application-specific IC design and fabrication, yield enhancement, circuit restructuring and fast turnaround prototyping have significantly increased the interest in adaptive processing techniques using direct energy sources such as lasers [1]. Previous studies in laser processing have focused mostly on semiconductors, solid dielectrics, and metals [2]. Recent interests in multilevel and multichip high-performance electronic packaging have attracted attention on laser processing of polymeric materials such as polyimide, which has a low dielectric constant and relatively stable thermal properties [3]. The low dielectric constant reduces capacitance coupling which often determines the ultimate speed and frequency of the packaged electronic devices. Standard thin film metallization and photoresist patterning processes are being used for fabrication of interconnects layouts, followed by either additive or subtractive processes to make final multichip interconnects. Topographical nonuniformity often limits the interconnect line width to greater than 25 μm using present thin film techniques. Laser-selective metal deposition on polymers, either direct-write or projection patterning, is a key processing technology for the development of a viable laser direct-interconnect for high-density and high-performance multichip interconnects for ASICs and quick turnaround prototyping applications.

A fast writing speed exceeding several millimeters per second is a key requirement for the development of a direct-write process for interconnect paths over several meters. Slower direct writing processes are useful only for short-run interconnects such as circuit alternations, local restructuring, and repairs. The laser scan speed V_s is related to the film growth rate, V_g by [4]

$$V_s = D/(dV_g)$$

where D is the beam diameter and d is the film thickness. This equation shows that with a beam diameter of 10 μm to deposit a 1- μm -thick film, a film growth rate of 100 $\mu\text{m}/\text{sec}$ is required in order to achieve a writing speed of 1 $\mu\text{m}/\text{sec}$. In gas phase photolysis, growth rates are limited by the transport of reactants and products to and away from the reaction

zone. The proper wavelength must be used in order to couple the spectral properties of gaseous phase compounds or adsorbates for photodissociation with efficient quantum yields. In spite of the fact that many interesting photochemical reactions have been reported, none of these processes appeared fast enough for direct writing applications. In the pyrolytic approach, reactants of higher concentrations can be used to enhance the writing speed. As a result, higher film growth rates have been demonstrated [4].

In this study, a two-step process was used to achieve a fast writing speed. In this two-step process, laser radiation is first used to selectively modify the polymer surface, followed by a batch thin film process to form interconnect patterns. Surface modification of surface reactivities with lasers, using either direct writing or projection patterning technique, is intrinsically a sensitive method for area-selective thin film deposition [5]. Surface modifications can be achieved via a variety means such as

- Physical vs Chemical
- Photolytic vs Pyrolytic
- Additive vs Subtractive
- Catalytic vs Inhibitive
- Adsorptive vs Desorptive

In the present study, we applied surface modification to copper deposition on polyimide using both direct writing and excimer laser projection techniques. In the former case, an argon laser was used to selectively deposit a trace amount of Pd on polyimide surfaces such that electroless copper deposition takes place in the surface areas exposed to laser irradiation (positive process). In the latter case, an excimer lasers was used to desensitize a polyimide surface such that a negative metal pattern was formed after electroless deposition (negative process).

EXPERIMENTAL

Argon-Laser-Activated Copper Deposition - a Positive Process

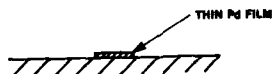
In this work, an argon laser at 351 nm was used to selectively decompose an organometallic Pd-containing compound [6,7]. In these experiments, the substrates were either spun on polyimide on glass or 50- μm -thick Kapton films laminated on glass. Palladium acetate (PdAc) was dissolved in chloroform as the palladium precursor and was spun on the polyimide substrate. The surface concentration of Pd was controlled by varying the initial amounts of PdAc dissolved in the solvent, and final surface Pd concentrations were determined by the Rutherford back-scattering technique. After irradiation, the sample was immersed in an electroless copper plating solution. The process sequence is shown in Figure 1. The advantage of this approach is that only a few monolayers of palladium atoms are needed for initial surface sensitization, which led to a fast writing speed of several centimeters per second. At 351 nm, polyimide has an absorption coefficient of about 10^4 cm^{-1} , so over 90% of incident energy is absorbed in the top 1- μm surface [8]. When a sample is exposed to laser irradiation, local heating of the polymer substrate causes thermal decomposition of PdAc, which has a decomposition temperature of 225 °C, while the substrate is thermally stable to above 400 °C. Figure 2 shows optical micrographs taken at each of the process steps: Figure 2-1.-spin-coated sample with PdAc dissolved in chloroform; Figure 2-2-irradiated sample with a 20-mW argon laser at 351 nm scanned at 2 mm/sec; Figure 3-3-irradiated sample after chloroform rinse to remove PdAc in the surface areas not exposed to laser radiation (a trace amount of Pd on the exposed area was barely visible); Figure 2-4-sample after being placed in an electroless copper plating solution and with copper lines selectively deposited on the polyimide surface. Depending upon the laser power and scanning speed, copper line-widths of about 7 μm to 50 μm with a thickness to 1.5 μm were achieved.

LASER-ACTIVATED COPPER DEPOSITION — THIN FILM APPROACH

1. DISSOLVE ORGANOMETALLIC IN SOLUTION
AND SPIN ON, THEN LASER-ACTIVATE



2. RINSE



3. ELECTROLESS Cu DEPOSITION



Figure 1. A schematic of laser-activated metal deposition process.

Laser-Activated Cu Deposition on Polyimide

Process

1. Coat PdAc on
Polyimide

2. Argon Laser
Irradiation

3. Chloroform
Rinse

4. Electroless Cu
Deposition



Figure 2. Optical micrographs taken at each of the process steps: (2) sample irradiated with 351 nm argon laser (20 mW, 2 mm/s); (3) unirradiated PdAc removed with chloroform rinse; and (4) after immersion in electroless Cu plating solution.

Excimer-Laser Patterning Copper on Polyimide—a Negative Process

A negative patterning process has also been demonstrated using an excimer laser [9]. The process is schematically illustrated in Figure 3. In this case, a pd-containing compound is first spun on the polyimide surface. The sample surface was then exposed to an excimer laser through a mask or using a projection method. The exposed surface area becomes totally desensitized once the irradiating fluence is above a threshold level, which depends upon wavelength of the excimer laser used. After immersing the sample in an electroless copper plating solution, a copper pattern is formed and is shown in Figure 4. Because of strong absorption of polyimide at both 193 nm and 248 nm, a threshold fluence less than 20 mJ/cm² was found to be sufficient to cause total desensitization. Once the irradiating fluence exceeds the threshold level, identical copper patterns were formed regardless of the number of irradiation pulses. Figure 5 shows x-ray photoluminescence spectra (XPS) of a sample sensitized with a Pd-containing precursor and irradiated with an excimer laser at a fluence level above the threshold. Figure 5(a) is the XPS spectrum of a sample after sensitization with Pd-containing precursor. Figure 5(b) shows the spectrum after the surface area was exposed to excimer laser irradiation for one single pulse, and Figure (c) shows the spectrum after exposure to 10 excimer laser pulses at the same fluence level. Figure 5(b) and 5(c) have identical XPS spectra in which Pd peaks are absent after the samples were exposed to excimer laser irradiation. Both samples resulted in identical copper patterns after being placed in electroless copper deposition.

EXCIMER LASER SELECTIVE METALLIZATION

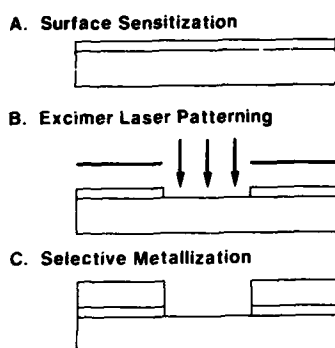


Figure 3. Schematic of excimer laser metal patterning.

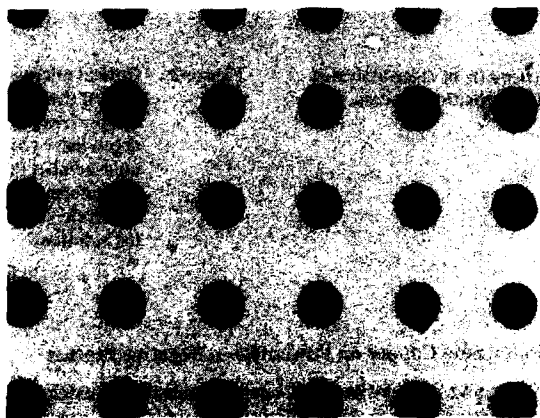


Figure 4. A metal pattern fabricated on the UtemTM surface using an excimer laser. The metal was prevented from electroless copper deposition in the areas exposed to the laser pulses. The diameter of the circular areas is about 2 mm. (UtemTM is a trademark of GE.)

CONCLUSION

We have shown that surface modification using lasers provides a sensitive technique for area-selective metallization. The present study demonstrated the use of both direct write and projection patterning techniques for selective modification for metal patterning. In the former case, an argon laser was used to selectively deposit a trace amount of Pd on polyimide surfaces such that electroless copper deposition takes place in the surface areas exposed to laser irradiation (positive process). In the latter case, an excimer laser was used to desensitize a polyimide surface such that a negative metal pattern was formed after electroless deposition (negative process). Since only a very thin surface layer of Pd catalyst was required for copper deposition, both techniques were highly sensitive, and a fast writing speed was achieved.

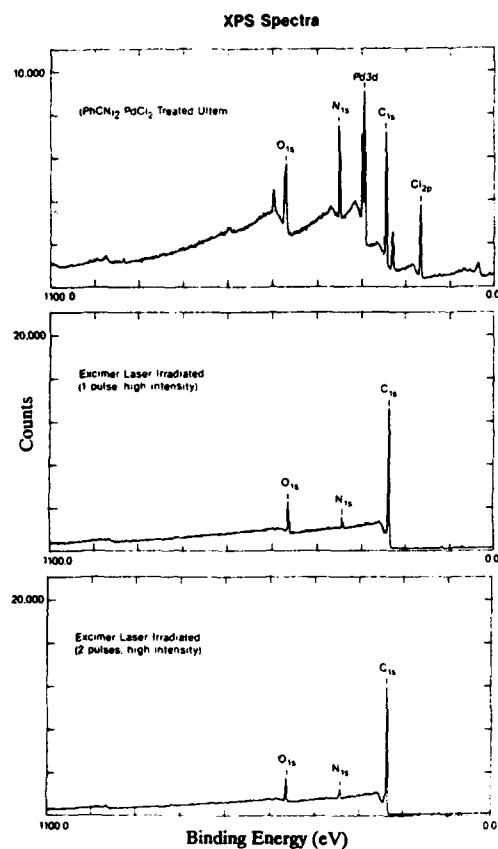


Figure 5. XPS spectra of (a) an UltemTM sample spin-coated with a Pd precursor (b) after the sample was exposed to single excimer laser pulse at a fluence exceeding about 20 mJ/cm², and (c) after exposed to 10 pulses at the same fluence level as that for (b).

ACKNOWLEDGMENT

We thank R. Guida and J.W. Rose for their excellent technical assistance, and Dr. Mike Burrell for XPS analysis. This work was in part sponsored by ONR/SDIO under the contract No. N00014-85-C-0890.

REFERENCES

1. D. V. Smart and D. M. Stewart, Proc. of SPIE, Conf. on *Lasers in Microlithography*, Santa Clara, CA, 774, (1987), p. 88.
2. *Laser Microfabrication and Thin Film Processing*, edited by D. J. Ehrlich and J. Y. Tsao, (Academic Press, to be published, 1989).
3. H. S. Cole, Y. S. Liu, J. W. Rose, R. Guida, L. M. Levinson and H. R. Philipp, *Electrochem. Soc. Conf. on Laser Processing for Microelectronic Applications*, Honolulu, Hawaii, (1987).
4. Y. S. Liu, in *Tungsten and Other Refractory Metals Deposition for VLSI Applications*, edited by R. L. Blewer, (Materials Research Society, Pittsburgh, PA, 1985), p. 43.
5. M. Stuke, Y. Zhang and S. Kuper, *Laser and Particle Beam Chemical Processing for Microelectronics*, edited by D. J. Ehrlich, G. S. Higashi, and M.M. Oprysko, (Materials Research Society, 101, Pittsburgh, PA, 1988), p. 139.
6. H. S. Cole, Y. S. Liu, J. W. Rose, and R. Guida, *Appl. Phys. Lett.*, (21), 2111 (1988).
7. M.E. Gross, G.J. Fisanick, P.K. Gallager, K.J. Schnoes, and M.D. Fennell, *Appl. Phys. Letts.*, 47(7), 669, (1985).
8. H. R. Phillip, H. S. Cole, Y. S. Liu, and T. A. Sitnik, *Appl. Phys. Lett.*, 48, 192 (1986).
9. Y. S. Liu, W. T. Grubb and H. S. Cole, *Tech. Digest of Conf. on Lasers and Electro-Optics, WX-5* (7), 286 (1988).

PATTERNED EXCIMER LASER ETCHING OF GaAs WITHIN A MOLECULAR BEAM EPITAXY SYSTEM

P. A. MAKI and D. J. EHRLICH
Lincoln Laboratory, Massachusetts Institute of Technology,
244 Wood St. Lexington, MA 02173

ABSTRACT

We have utilized an ArF excimer laser in a projection imaging geometry to etch GaAs layers grown *in situ* within a molecular beam epitaxy (MBE) system. Clean epitaxial surfaces were prepared using standard MBE growth procedures, then etched in a second chamber isolated by a gate valve. We report studies of the etching dependence on pulse rate (0.2 Hz to 150 Hz) and chlorine pressure (10^{-6} , 10^{-4} , and 5×10^{-3} Torr). We discuss the etching mechanism in terms of previous studies of the reaction between GaAs surfaces and molecular chlorine under high vacuum conditions. We show that the pulse rate and Cl_2 pressure dependencies of the etching can be explained by the progress of the reaction at the instant of pulse exposure. Etch morphology is found to vary with the repetition rate, with the smoothest surfaces obtained at low repetition rates. We discuss the implications of the results in the context of *in situ* thin layer processing and epitaxial overgrowth.

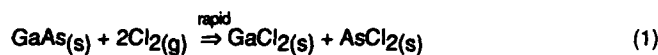
Introduction

Processing of thin layer structures in GaAs requires *in situ* patterned etching in combination with epitaxial growth to avoid contamination resulting from air exposure. Excimer projection etching is promising for this application because of its direct, maskless patterning capability. In this paper, we demonstrate an excimer laser etching process which can be used in combination with MBE to fabricate GaAs structures entirely in a vacuum environment.

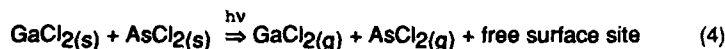
Previous studies have examined excimer laser etching of GaAs [1,2,3] at pressures where gas-phase radical generation contributes to the etching process. In the present work, we examine the etching process in a low pressure chlorine ambient, where gas-phase photolysis is negligible and the surface reaction is dominant. We report data on the etching process as a function of pulse repetition rate, fluence, and chlorine pressure using an ArF excimer laser as a UV light source. We show that the dependence on these parameters can be explained by a model which relates etch rate to the progress of the reaction between the molecular chlorine and the GaAs surface at the instant of pulse exposure. In addition, we demonstrate controlled bilayer etching. The resulting surfaces under many conditions are of sufficient quality that epitaxial overgrowth is possible without the formation of any unusual growth morphologies.

The interaction between GaAs and chlorine is thought to occur through a first step in which a rapid reaction forms monochlorides or dichlorides of gallium and arsenic followed by a second step which proceeds more slowly and forms gallium and arsenic trichlorides [4,5,6]. Since the arsenic trichloride is more volatile than the

gallium trichloride, the preferential evaporation of the former leaves the surface with a gallium trichloride layer which tends to limit the reaction by reducing the available active sites. The complete mechanism as suggested by Ha *et al.* [6] is as follows:



Our experiments suggest that the excimer laser assists the etching by the photodesorption of the reaction products from the surface:



By varying the laser repetition rate, it is possible to probe the different stages of these reactions.

Experimental

The basic setup, as shown up in Fig. 1, consists of an excimer laser and a loadlocked vacuum system with GaAs MBE capability. The system has two ultrahigh-vacuum chambers which are isolated by a gate valve. A sample holder can be transferred between the two chambers without air exposure using a magnetically coupled transfer rod. In one chamber, GaAs can be grown by elemental-source MBE. In the second chamber, gas can be introduced using a leak valve, and the sample can be exposed to an excimer laser through a single-element optical projection system.

Prepolished (100) GaAs substrates are degreased and etched with 5:1:1 H_2SO_4 , H_2O_2 , H_2O , mounted on a molybdenum sample holder using indium solder, and loaded into the vacuum system through a load lock. An epitaxial film of GaAs is prepared using typical MBE growth procedures. After the sample has cooled to room temperature, it is transferred into the etching chamber. At this point the sample surface is free from any substantial oxides or impurities and exhibits a reflection electron diffraction (RED) pattern indicative of a smooth surface.

In the etching chamber the sample is exposed to Cl_2 gas through a leak valve while the pressure is monitored using a cold cathode gauge. During etching, the ion pump is valved off, and the chamber is not exhausted except for residual pumping by the cold cathode gauge. To avoid transient effects in the composition of the gas ambient due to reactions between residual water vapor and chlorine gas, the chamber is filled with chlorine gas prior to sample loading and pumped out. After the

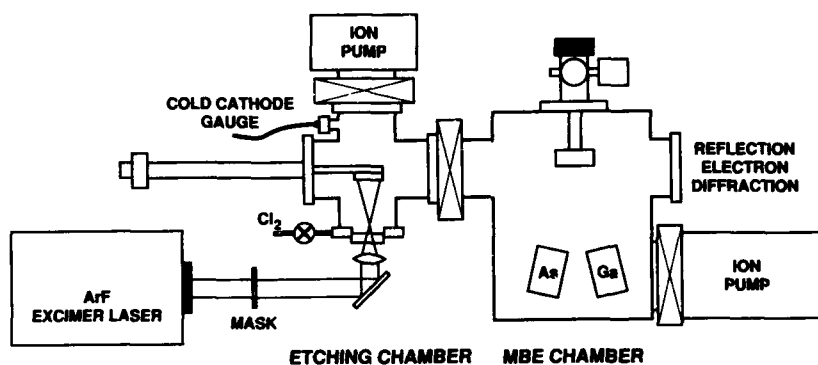


Figure 1 Schematic diagram of excimer laser and vacuum system.

etching process (~15 min) the chamber is evacuated using the ion pump. While the chlorine gas is present, the excimer laser beam is introduced through a UV-grade fused silica window with the beam axis normal to the sample surface. Laser fluences were measured using a pyroelectric detector at the sample position in order to measure the transmission losses, and then these losses were used to determine the fluence using a detector external to the vacuum system. We assume that the temperature of the sample holder is at the ambient temperature of the etching chamber, which is typically near 25 °C.

After etching, the depth of the etched region was measured using a surface profilometer. Variations in the fluence across the etched regions sometimes caused local variations in the etch rate. These variations were averaged for each etch step in a consistent way so that within each set of experiments, the averaging method is the same. The etched surfaces were examined using optical microscopy in order to determine the degree of smoothness of the surface and its suitability for epitaxial overgrowth.

Results and Discussion

Figure 2 shows the dependence of the etch rate as a function of the excimer laser pulse repetition rate for Cl₂ pressures of 5×10^{-3} Torr, 10^{-4} Torr, and the background pressure after etching (10^{-6} Torr) plotted on a log-log scale. For 5×10^{-3} Torr and 10^{-4} Torr, the etch rate shows three distinct dependences on the repetition rate f . For repetition rates less than 10 pps, the dependence follows a $f^{1/2}$ dependence for both pressures. For pulse repetition rates above 10 pps, but below 60 pps, the dependence is approximately linear. Above 60 pps, saturation appears for 10^{-4} Torr, while the data for 5×10^{-3} Torr shows no saturation up to 150 pps. We explain the etch rate dependencies as follows. At low pulse rates, the period between laser pulses is sufficiently long that the reaction approaches the point of the gallium trichloride layer formation. The $f^{1/2}$ dependence corresponds to a square root of time dependence, which suggests a rate-limiting diffusion process in the

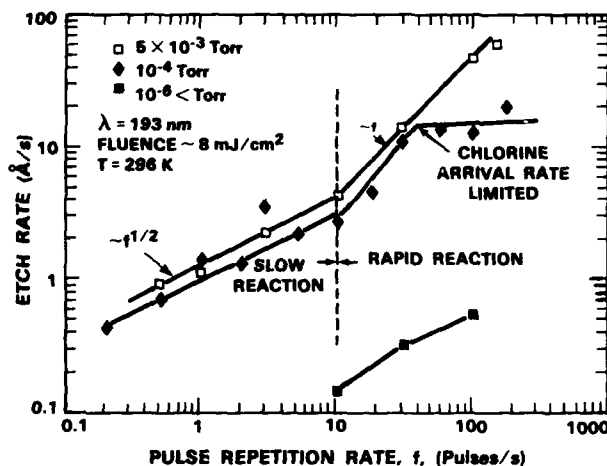


Figure 2
Dependence of
the GaAs etch rate
on repetition rate
and Cl_2 pressure.
Time scales of the
reaction steps are
indicated in the
figure.

reaction [Eq. (2)]. Above 10 pps, the products on the surface are only those of the fast reaction [Eq. (1)] because the gallium trichloride layer does not have time to accumulate between pulses. Since this reaction proceeds quickly, the quantity of reaction products formed between pulses is relatively constant, so that the etch rate varies linearly with the repetition rate. Above 60 pps, the etch rate at 10^{-4} Torr is limited by the chlorine arrival rate. The etch rate saturation begins when the pulse period approaches the chlorine monolayer arrival time. At the higher pressure of 5×10^{-3} Torr, no saturation is observed in the etch rate because the laser repetition rate is not high enough to reach the monolayer arrival rate. Chlorine is necessary for etching, as the 10^{-6} Torr etch rate is 20 and 90 times less than the etch rate for 10^{-4} and 5×10^{-3} Torr, respectively, at 100 pps.

If this model is correct, then the dependence of the etch rate on the fluence should show some saturation when the fluence is high enough to desorb all the reaction products from the surface. We have, in fact, observed a corresponding saturation in fluence at $\sim 15 \text{ mJ/cm}^2$ for Cl_2 pressures of 5×10^{-3} Torr and repetition rates of 0.5 and 25 pps. From the previous work [4] on the GaAs-chlorine reaction, we expect that there should be a limiting thickness of the product layer for very long times. At a chlorine pressure of 5×10^{-3} Torr, we have observed saturation in the etch rate of 4.4 Å per pulse for repetition rates ≤ 0.2 pps and a fluence of 11 mJ/cm^2 . This suggests that the layer thickness consumed by the reaction may approach 5.6 Å per pulse, which would correspond to a GaAs removal rate of two monolayers per pulse, or a monolayer coverage of gallium trichloride.

The morphology of the etched surface varies significantly with the pulse repetition rate, chlorine pressure, and fluence. Smoothness of the surface tends to degrade at very high pulse energies ($> 18 \text{ mJ/cm}^2$) or high repetition rates (> 10 pps). As shown in Fig. 3, smooth surfaces are obtained at low pulse repetition rates.

Figure 4 shows an optical micrograph of a GaAs surface after a complete growth, etching, and overgrowth sequence. The pattern was projected onto the surface using a mask and a lens external to the etching chamber. The sequence of

steps was a growth of 0.5 μm of GaAs, followed by etching of 0.1 μm , and then overgrowth with 0.3 μm of GaAs. The interior of the cloverleaf pattern is the etched area. The overgrown film is smooth and epitaxial in appearance and is free of any abnormal nucleated defects. The oval defect density is comparable to the unetched regions of the surface. The surface was etched at 0.5 pps, 5×10^{-3} Torr of Cl_2 , at a fluence below saturation. The ripple observed on the surface results from a spatial variation in the laser pulse fluence during etching.



20 μm

Figure 3 Optical micrograph of the etched surface morphology for 0.5 pps, 5×10^{-3} Torr, 12 mJ/cm^2 . MBE oval defect is visible near center.



660 μm

Figure 4 Optical micrograph of an etched and overgrown epitaxial GaAs film.

Conclusions

This work demonstrates a controllable etch process which can be used *in situ* to spatially pattern GaAs. Our results demonstrate that controlled bilayer etching of GaAs is possible, which is the etching analog of atomic layer epitaxy. At low repetition rates, the morphology of the etched surface is of sufficient quality that epitaxial overgrowth of GaAs occurs without the formation of any unusual defects. Further studies are required to evaluate the electrical and optical properties of the laser etched surface and overgrown interface. Among many applications, this etching process can be used to define the active area of a laser, or spatially adjust the thickness of quantum wells in 2 monolayer increments. Combined with epitaxial growth, laser etching can be used to fabricate a wide variety of complex structures *in situ*. Our preliminary studies suggest that parts of this work can be extended to other III-V materials, making *in situ* processing of heterostructures possible.

Acknowledgments

We wish to acknowledge the expert technical assistance of T. Evans and helpful discussions with D. C. Shaver. This work was sponsored by the Department of the Air Force, in part under a specific program supported by the Air Force Office of Scientific Research, and by the Defense Advanced Research Projects Agency.

References

1. P. D. Brewer and R. M. Osgood, Jr., Proc. SPIE, **611**, 62, (1986), and references therein.
2. P. D. Brewer, D. McClure, and R. M. Osgood, Jr., Appl. Phys. Lett. **49**, 803 (1986).
3. M. Hirose, S. Yokohama, and Y. Yamakage, J. Vac. Sci. Technol. B **3**, 1445 (1985).
4. M. Balooch, D. R. Olander, and W. J. Siekhaus, J. Vac. Sci. Technol. B **4**, 794 (1986).
5. M. S. Ameen and T. M. Mayer, J. Appl. Phys. **63**, 1152 (1988).
6. J. H. Ha, E. A. Ogryzlo, and S. Polyhronopoulos, J. Chem. Phys. **89**, 2844 (1988).

BORON DOPING OF SILICON USING EXCIMER LASERS

A. SLAOUL, F. FOULON, M. BIANCONI*, L. CORRERA, R. NIPOTTI*, R. STUCK, S. UNAMUNO, E. FOGARASSY AND S. NICOLETTI*
 CRN (IN2P3), Laboratoire PHASE (ER du CNRS n° 292), 23 rue du LOESS, F-67037 STRASBOURG CEDEX (France)
 *CNR-LAMEL, Via Castagnoli 1, I-40126 BOLOGNA (Italy)

ABSTRACT

The use of lasers in the doping of semiconductors has been investigated extensively these last years both for photovoltaic and microelectronic applications. In this work, doping of single-crystal silicon in BCl_3 ambients using a pulsed UV laser has been studied as a function of laser wavelength and fluence in order to investigate the effects of photochemical decomposition of the BCl_3 gas and the effects of thermal decomposition of adsorbed layers on the doping process. Different parameters involved in the process (laser energy density, number of pulses per frame, BCl_3 gas pressure) were investigated. The electrical characteristics of the doped layers were discussed.

INTRODUCTION

Recently, there has been considerable interest in impurity doping into semiconductor materials using an excimer laser /1, 5/. Since virgin silicon has a large absorption coefficient in the ultraviolet region, an intense pulsed excimer laser irradiation in a suitable chemical atmosphere can locally melt the near surface region and produce a significant incorporation of dopant from the environment into the molten surface layer. The dopant distribution is then driven by simple thermal diffusion. This feature gives an advantage in forming very shallow junctions. However, the mechanism of excimer laser doping is dependent on the interaction of the doping gas and the laser wavelength as well as on the reaction of the gas with the silicon surface.

Recently, Correra et al. /6/ have described phosphorous doping into silicon by decomposing PCl_3 gas using an XeCl (308 nm) excimer laser. In this case, PCl_3 has no absorption at 308 nm and it has been shown that only the thermal decomposition (pyrolysis) of the adsorbed layers contributes to the incorporated dopant atoms. Thus, the supply of dopant atoms from adsorbed layers limits the doping process. On the other hand, Foulon et al. /7/ have reported the fabrication of a shallow boron junction by the irradiation of an ArF (193 nm) excimer laser into the silicon immersed in BCl_3 . Since in this case the doping gas is absorbed at 193 nm, the influence of photochemical decomposition (photolysis) of both gas ambient and adsorbed layers on doping characteristics have been demonstrated.

In order to separate the effects of photochemical decomposition of the doping gas from those of thermal decomposition, it is important to perform the excimer laser doping using two different wavelength and the same gas.

In this work, we report boron doping into silicon by decomposing BCl_3 using ArF and XeCl excimer lasers. We investigate the influence of doping conditions on the sheet resistance and the impurity concentration profiles, and discuss the mechanism of excimer laser doping. Finally, we present the electrical properties of some laser doped layers.

EXPERIMENTAL

The samples used in this study were n-type <100> single crystal silicon with resistivity of 1 ohm cm. The sample surface was cleaned with an HF dip and a

deionized H_2O rinse, and then immediately enclosed in the stainless-steel gas chamber. The chamber is normally evacuated below 10^{-4} mbar, purged and evacuated again before filling with the active gas (BCl_3). The pressure was varied in the range 0.1 to 50 mbar. Two different lasers were used to melt the silicon surface and to produce dopant incorporation simultaneously: an ArF (193nm) and a XeCl (308nm) excimer lasers with pulse duration of 21ns and 70ns, respectively. The laser energy density at the sample surface was varied between 0.8 and $1.8 J/cm^2$, which is well above the melting threshold of c-Si. This laser fluence takes into account the loss by the gas absorption in the case where the ArF laser is used since it is well established now that the BCl_3 gas is absorbed at 193 nm [8,9] but not at 308 nm [9].

Characterization of the doped layer has been carried out using the four point probe and secondary ion mass spectroscopy (SIMS). Profiles of carrier concentration were obtained by the automatic resistivity-Hall stripping techniques (ARHS).

As for the electrical characterization of the doped layer, some samples irradiated at 193 nm wavelength were post-annealed in order to remove point defects eventually introduced during the rapid solidification.

Some large area samples were doped with the 308 nm laser process. Changes in the defect densities of the depletion region due to changes in the substrate temperature were investigated.

RESULTS AND DISCUSSION

Figures 1a and 1b report the experimental values of the boron concentrations as a function of the depth in silicon for 193 nm and 308 nm wavelength irradiations. Both profiles were obtained at fixed BCl_3 pressure (5mbar) and different number of pulses per frame ($n = 1-50$). The fluences were 1.5 and $1.1 J/cm^2$ respectively, corresponding to computed melt depth of 1280 Å for XeCl and 3000 Å for the ArF. The melting time was about 120 nsec for both laser pulses, as shown by the computer simulation reported in Figure 2.

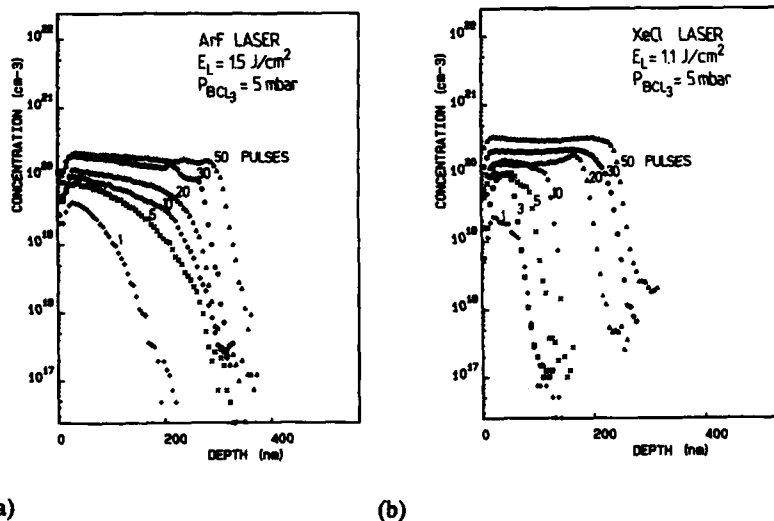


Figure 1 Boron concentration profiles by SIMS measurements: (a) doping with ArF (193 nm) laser; (b) doping using XeCl (308 nm) laser.

In the XeCl case a gradual increase of the incorporated boron can be observed up to 10 pulses per frame, without any significant change of the junction depth. After this value, corresponding to a surface concentration of about 1×10^{20} at/cm³, an important increase of the melt depth occurs. This behavior, already observed /10, 11/, is probably due to the solid and liquid reflectivity change as well as to the variations in the thermodynamic parameters of heavy doped silicon. Using a numerical simulation program /12/, we have shown that 5% change in reflectivity can induce an increase of the melt depth of about 50%.

In the ArF case a similar trend of the dopant profiles verse n is observed, but a relatively less important change of the melt depth occurs.

The common trend is the sharp increase of the total amount of incorporated material (I) with n . Due to the fast diffusion of the dopant into the molten layer, square shape profiles are obtained within a few pulses. As already studied /6/, the total incorporation I is determined by the total melting time t_m , whereas the incorporation rate depends both on the diffusivity of the dopant into the melt and on the dopant supply at the silicon-ambient interface:

$$I = \int_0^{t_m} D_1 \frac{\partial C(x, t)}{\partial x} \bigg|_{x=0} dt$$

where D_1 is the diffusivity in liquid silicon and $C(x, t)$ is the boron concentration at depth x and time t .

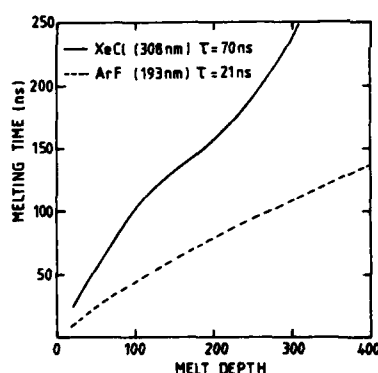


Figure 2 Melt time versus melt depth. Calculation for 308 nm, FWHM = 70 ns and 193 nm, FWHM = 21 ns. See ref 12 for optical and thermodynamic parameters.

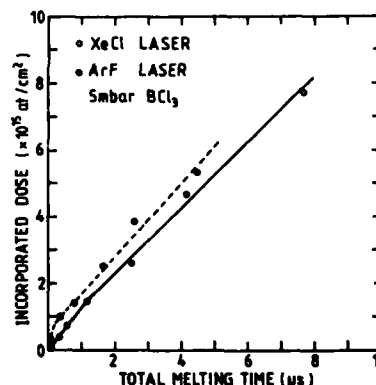


Figure 3 Total quantity of impurity as a function of the total melting time.

As the BCl absorption coefficient at 193 nm is much higher than it is at 308 nm, any effect on the source term due to the dopant-vapor photolysis should be evidenced by the comparison between the XeCl and ArF incorporation rates.

The actual values of the incorporated boron as a function of the total melting time are reported in Figure 3.

Two different incorporation regimes can be remarked for both wavelengths, i.e., a first rapid dopant incorporation followed by a slower linear increase with time t_m . This

behavior is particularly evident for the ArF results, whereas the XeCl data exhibit a smoother trend.

As for the first regime, it must be noted that the short times (low n values) correspond to a junction depth lower than the melt depth. In the case of XeCl irradiation, the displayed trend can be attributed to a nearly complete incorporation of the layer of adsorbate which forms onto the silicon surface /6/. In these conditions the incorporation can be described as limited by the dopant source.

When ArF data are considered, a very sharp increase of boron incorporation during the first regime is observed. As it can be assumed that the actual diffusion-controlled transport mechanism of the dopant into the silicon is dependent on the laser wavelength and pulse duration, it can be concluded that the I values observed are due to a larger amount of material available for the incorporation. This additional supply can be attributed to the photolytic dissociation of the ad-layer and/or of the ambient gas molecules. In this case the dopant source can be considered about infinite, and the incorporation process is mainly diffusion limited.

The second incorporation regime occurs after the junction depth reaches the melt depth. This condition is attained after many laser pulses; the dopant profile vs depth is rather flat, and the incorporation process becomes flux limited. Any further increase of dopant incorporation is hindered by the small concentration gradient giving rise to a slow diffusion draining. The ultimate dopant concentration is limited by the solubility in liquid silicon. For these reasons when the number of pulses is increased, the larger dopant source available in the case of 193 nm irradiation becomes less effective than for the first irradiation, and the incorporation rate for the ArF doping approaches the XeCl value.

In order to get more information about the surface status and the doping mechanism, the dependence of the incorporated dose on BCl_3 pressure was investigated by irradiating c-Si samples at a fixed fluence and for 30 shots. The results are displayed in Figure 4. The curve corresponding to ArF laser takes the absorption in the gas into account. Different pressure ranges can be distinguished. At pressures lower than about 0.1 mbar the incorporation is constant, whereas a remarkable dependence on the pressure appears in the higher range. For both wavelengths, the evidence of the chemisorbed saturated layer on the silicon surface is provided by the constant incorporation versus pressure in the 10^{-4} - 10^{-1} mbar range. This layer, which probably saturates all the adsorption sites such as surface impurities and defects, has been evaluated to be not less than the maximum incorporation per pulse of about 10^{14} BCl_3 molecules/ cm^2 . As for the higher pressure range, the increase of I as a function of the pressure follows a logarithmic law. The same trends have been obtained for XeCl irradiating c-Si in PCl_3 ambients with, however, formation of physisorbed layers above 1 mbar in presence of BCl_3 . This difference may be because BCl_3 has a higher vapor pressure than PCl_3 . The logarithmic trend has been shown to be related to the successive formation of weakly bounded physisorbed layers /13/. This explanation is valid for the two wavelengths. However, when using the ArF laser, it appears that saturation occurs for pressures higher than 10 mbar. More experiments will be necessary in order to confirm this trend.

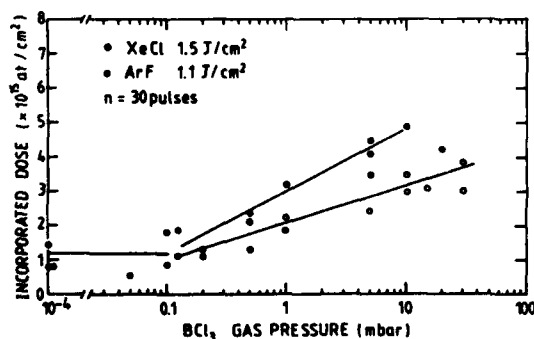


Figure 4. The total amount of incorporated boron as a function of the BCl_3 pressure p for XeCl and ArF lasers.

Figure 5 shows the mobility and carriers profiles versus depth as obtained by ARHS measurements for two samples irradiated at 193 nm, 1.1 J/cm^2 , and $n=10$. One of them was post-annealed in a "HEATPULSE" incoherent light system at 1000°C for 10 seconds. The comparison between the as-irradiated and post-annealed samples shows that the rapid thermal treatment essentially improves the mobility values without affecting the dopant profile. The small differences in the dopant distribution between the two samples can be ascribed to random fluctuations during the laser irradiation process. This improvement results probably from the annealing of high point defects induced by thermal quenching in the emitter region during the melt regrowth. The presence of these electrical microscope defects induced by laser irradiation in virgin silicon has been confirmed by DLTS technique. The results will be published elsewhere.

As test devices, 4-cm^2 solar cells were obtained on low resistivity wafers doped by the XeCl laser. Figure 6 shows the dark I-V plots for two cells processed at the same fluence and number of pulses per frame (1.8 J/cm^2 , $n=9$), one kept at room temperature and the other at 300°C during the irradiation. The cell processed at high temperature has reverse current one order of magnitude lower than the cell irradiated at room temperature. Correspondingly the shunt resistance changes from 0.44 to 5.1 Kohm . The higher shunt resistance suggest that there are fewer defects in the depletion region in the P-N junction.

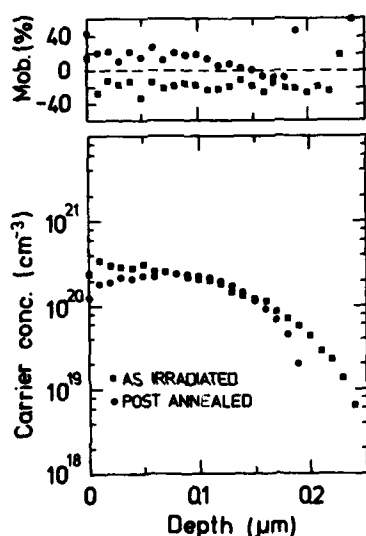


Figure 5 Mobility and carrier concentration profiles for samples doped in 5 mbar BCl_3 ambients without and with rapid thermal annealing (1000°C , 10 sec) done after the doping.

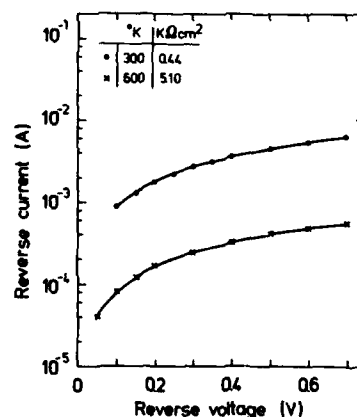


Figure 6 Reverse I-V characteristics of the laser processed diodes showing the effect of heating of the sample (300°C) during the doping process.

CONCLUSION

In this work, it has been shown that multipulse excimer laser (ArF or XeCl) irradiation of silicon in BCl_3 ambients allows the attainment of both controlled junctions depths and doping levels. As for the doping mechanism, the experimental

data indicate that the process is rate limiting in the case of XeCl whereas it is diffusion limiting for the ArF laser.

Moreover, the evolution of the total amount of incorporated boron with the pressure shows that at pressure lower than 0.1 mbar, the incorporation is caused by the presence of a strongly bounded chemisorbed layer, whereas at high pressure, the supply is the successive formation of weakly bounded physisorbed layers.

ACKNOWLEDGMENTS

This work was partially financially supported by the Centre National d'Etudes des Telecommunications (CNET, France) and the Italian Program of Electronic and Microelectronic Material Devices.

REFERENCES

1. T.F. Deutsch, *Mat. Res. Soc. Sym. Proc.* **17**, 225 (1983); K.G. Ibbs and M.L. Lloyd, *ibid.*, **17**, 243 (1983).
2. T.W. Sigmon in Photon Beam and Plasma Stimulated Chemical Processes at Surfaces, edited by V.M. Donnelly, I.P. Herman, M. Hirose (*Mat. Res. Soc. Proc.* **75**, Pittsburg, 1987) pp. 619-623.
3. G.G. Bentini, M. Bianconi, and S. Matsumoto, *Appl. Phys.* **A45**, 317 (1988).
4. S. Kato, T. Nagahori, S. Matsumoto, *J. Appl. Phys.* **62**, 3656 (1987).
5. S. Kato, H. Saeki, J. Wada, and S. Matsumoto, *J. Electrochem. Soc.* **135**, 1030 (1988).
6. L. Corraera, G.G. Bentini, M. Bianconi, R. Nipoti, and D.A. Patti, to be published in *Appl. Surf. Sci.* **36** (*European Mat. Res. Soc. Symp.*, Strasbourg, 1988).
7. F. Foulon, A. Slaoui, E. Fogarassy, C. Fuchs, and P. Siffert, ref. 6.
8. H.J. Maria, J.R. McDonald, and S.P. McGlynn, *J. Am. Chem. Soc.* **95**, 1050 (1973).
9. A. Slaoui, F. Foulon, C. Fuchs, E. Fogarassy, and P. Siffert, submitted to *J. Chem. Phys.*
10. A. Slaoui, E. Fogarassy, and P. Siffert in Springer Ser. Chem. Phys. on Laser Processing and Diagnostics, edited D. Bauerle (*Springer Verlag*, **39**, Heidelberg, 1984) pp. 65-69.
11. E.P. Fogarassy, D.H. Lowdnes, J. Narayan, and C.W. White, *J. Appl. Phys.* **58**, 2167 (1985).
12. S. Unamuno, and E. Fogarassy, ref. 6.
13. C.J. Chen, *J. Vac. Sci. Technol.*, **A5**, 3386 (1987).

HEAVILY DOPED ULTRA-SHALLOW JUNCTIONS FORMED BY AN ArF EXCIMER LASER

S. Yoshioka, J. Wada, H. Saeki and S. Matsumoto
Department of Electrical Engineering, Keio University
Hiyoshi, Yokohama, 223 Japan

ABSTRACT

Boron doping of single crystal silicon using an argon fluoride excimer laser with diborane gas has been performed. Diborane gas has an absorption at 193nm, which leads to gas phase photodecomposition of the diborane. Utilizing the photolytic effect, we obtained high surface concentration and ultrashallow junctions of $5 \times 10^{20} \text{ cm}^{-3}$ and $0.1 \mu\text{m}$, respectively. The photolytic effect enhances the incorporation of the dopant species.

INTRODUCTION

With the reduction of device geometry, ultrashallow and heavy doping has become more important to avoid the short channel effects of MOS devices. In the ion implantation method, it is difficult to form the heavily doped ultrashallow junctions for p^+ layer because of the inherent channeling effect by light ions like boron. Then excimer laser doping is attractive for formation of ultrashallow junctions[1-7]. Since silicon has a large absorption coefficient in the ultraviolet region[8], excimer laser light is strongly absorbed in the near-surface region of silicon. Then only the shallow region of the surface can be melted by the laser beam. The laser beam produces dopant species through pyrolytic and/or photolytic dissociation of the doping gas. The species diffuse into the molten region caused by the laser beam.

Deutsch et al.[2] performed the boron doping with BCl_3 and an ArF excimer laser in a photolytic process, while Carey et al.[3] reported the fabrication of ultrashallow junctions by the irradiation of XeCl excimer laser on the silicon immersed in B_2H_6 through a pyrolytic process.

In a previous work, boron doping was carried out using an ArF excimer laser with a transparent BF_3 gas[5]. It was confirmed that dopant species were supplied from only the adsorbed layer on the silicon surface through a pyrolytic process. On the other hand, a photolytic process[6], which used an ArF excimer laser with POCl_3 gas which absorbs strongly at 193 nm, was found to incorporate the dopant species from the gas phase into silicon at a level greater than could be obtained by only the adsorbed layer.

In order to fabricate heavily doped ultrashallow junctions utilizing photolytic processes and to compare with pyrolytic processes, we have carried out boron doping into silicon using an ArF excimer laser with B_2H_6 gas, which has an absorption at 193 nm[9]. From the dependence of the sheet resistance on the incident energy and the number of pulses, we have found that the doping with B_2H_6 is significantly different from the doping with BF_3 .

EXPERIMENTAL

The 5% B_2H_6 gas diluted with N_2 was used as a dopant source. The diborane absorption peak is near 193 nm[9]. An ArF excimer laser with a 17-ns-long pulse at 193 nm was operated at 2Hz. The laser beam was focused onto the silicon surface by quartz lenses. The beam size at the sample surface was 2.5mm wide by 7.2mm long. The sample was set at 4-cm length from the quartz window in a stainless steel chamber. The absorption coefficient of diborane is $0.00150\text{--}0.00304 \text{ cm}^{-1}\text{Torr}^{-1}$ [9]. Thus, for 5 Torr of diborane, the absorption in the cell is 3.0-5.9 %.

Samples were $\langle 100 \rangle$ Cz n-type single-crystal silicon with resistivity of 3-5 ohm-cm. After a standard RCA cleaning, the chamber was pumped to below 0.01 Torr. Laser irradiation was performed in two ways: (1) the irradiation was performed with B_2H_6 .

ambient; (2) the sample were irradiated after the B_2H_6 was loaded and pumped to below 0.01 Torr several times successively to form adsorbed layers. The sheet resistance of the doped area was measured using the four-point probe method. We obtained the dependence of the sheet resistance on the incident energy and the number of pulses. Carrier concentration profiles were determined by the differential resistivity measurement with an anodic oxidation using the Irvin curve[10]. Boron concentration profiles were obtained by secondary ion mass spectrometry (SIMS).

RESULTS AND DISCUSSION

In Fig. 1, we show plots of the sheet resistance versus the incident laser energy for a pressure of 5-Torr diborane and for different numbers of pulse. The data obtained for BF_3 ambients[5] are also plotted in the figure. The steep rise of the curves at $0.6J/cm^2$ is probably due to the threshold for melting of single-crystal Si.

Although the partial pressure of diborane is 5 Torr and that of boron trifluoride is 50 Torr, the sheet resistance for diborane is lower by two orders of magnitude. This result suggests that the boron doping with diborane is carried out through not only the pyrolytic dissociation of adsorbed layers but also the photolytic process of adsorbed layers and gas phase molecules.

The sheet resistance decreases with incident laser energy in Fig.1. Since the depth of the molten region and the diffusion time are determined by the incident energy, then the total quantity of impurity increases with the incident energy. To clarify this point, carrier concentration profiles are investigated.

The carrier concentration profiles for 1 pulse irradiation are shown in Fig. 2 for the incident fluences of 0.7, 0.8, and 1.0 J/cm^2 . It is found that the surface concentration increases slightly and the junction depth increases with the incident fluence. That is, the total quantity of carriers increases with the fluence. Thus the decrease of the sheet resistance with the fluence in Fig. 1 is understood.

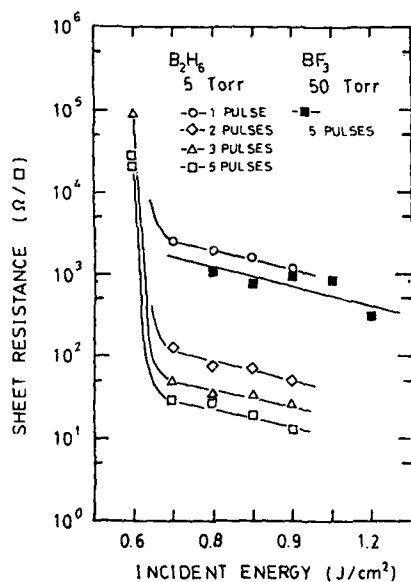


Fig. 1 Sheet resistance vs incident energy.

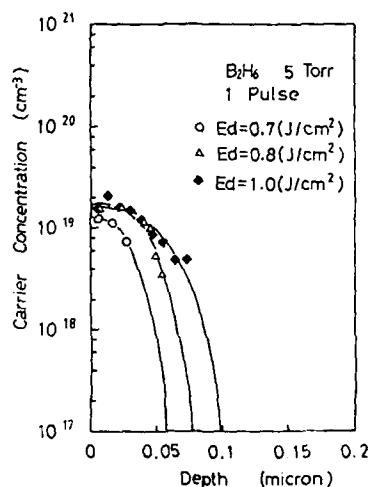


Fig. 2 Carrier concentration profiles for different incident energies

The dependence of sheet resistance on the number of laser pulses is shown in Fig. 3. The laser incident fluence and the gas pressure are 0.7 J/cm^2 and 5 Torr. In this figure, the data of BF_3 at 0.8 J/cm^2 and 50 Torr [5] are also included. The sheet resistance decreases with the number of pulses, which increase the total quantity of impurity.

In general, the diffusion length L is given by $L = (Dt)^{0.5}$, where D is the time averaged diffusion coefficient and t is the diffusion time. Assuming the diffusion time to be the product of the pulse duration time and the number of pulses (N), the sheet resistance R_s is proportional to $N^{-0.5}$ with a constant surface concentration. Consequently when the doping process is limited only by the diffusion, the sheet resistance is proportional to $N^{-0.5}$. Deutsch et al. [2] carried out the doping using an ArF excimer laser with BCl_3 gas which has significant absorption at 193 nm. They found that R_s varied as $N^{-0.6}$ and concluded that the doping process was limited by the diffusion of the incorporated dopant atoms in molten silicon.

However, the sheet resistance R_s varies as N^{-1} for BF_3 . For diborane the sheet resistance R_s cannot be expressed with $N^{-0.5}$, indicating that the doping mechanism for diborane is different from that of BF_3 and BCl_3 . These results suggest that both doping mechanisms are not subject to the simple diffusion limitation but are dominated by the supply of dopant atoms from the outside.

There is a tendency of a saturation in Fig. 3 for diborane near 5 pulses. This result is attributed to the saturation of the surface carrier concentration and to the depth of the molten region as shown in Fig. 4.

Figure 4 also shows carrier concentration profiles for 0.7 J/cm^2 and 5 Torr for different pulse numbers. The surface carrier concentration increases with the number of pulses. Thus the supply of dopant atoms from the outside limits the doping process.

An interesting point is that the very high concentration of $5 \times 10^{20} \text{ cm}^{-3}$ and the ultrashallow junctions below $0.1 \mu\text{m}$ are performed by multipulsed irradiation. The other distinct feature is that the profile shapes change from a complementary error function-like to a box-like profile with an increase in the number of pulses. This indicates that boron atoms diffuse into the molten silicon and do not diffuse into the solid region substantially.

In Fig. 5, boron concentration profiles obtained by SIMS are shown. For 1 pulse and 2 pulses, the profiles are similar to those of carrier profiles. Both measurement techniques are about 30% accurate. For 10 pulses the surface concentration reaches above 10^{21} cm^{-3} , but the concentration is so high that the activity decreases and carrier concentration is limited to $5 \times 10^{20} \text{ cm}^{-3}$. The tendency of the sheet resistivity to saturate above 5 pulses in Fig. 3 results in the

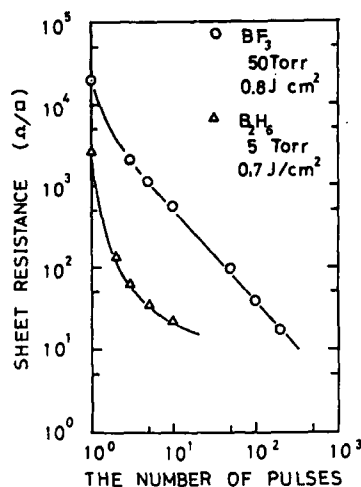


Fig. 3 Sheet resistance vs the number of pulses.

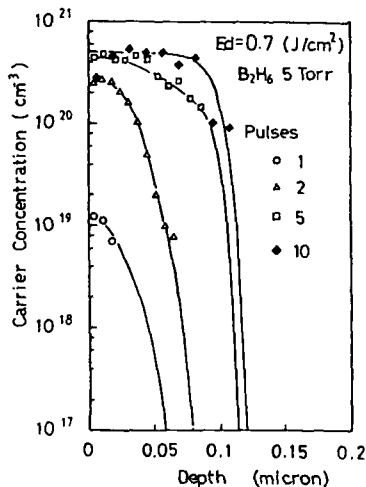


Fig. 4 Carrier concentration profiles for various number of pulses.

In order to investigate the role of the gas phase, we carried out doping using only an adsorbed layer; that is, the laser irradiation was performed after diborane gas was pumped to below 0.01 Torr as mentioned above. Figure 6 shows the results with the adsorbed layer only as well as that combined with gas ambients. In the figure the results of BF_3 are also included.

In the case of BF_3 , the two techniques gave the same results. This suggests that the doping was performed only through the pyrolytic process of adsorbed layer[5]. But in the case of diborane, the two techniques gave significantly different results. The absorption of the laser by the diborane in the gas phase contributes to the doping level. That is to say, the difference in the two curves for diborane is attributed to the photolytic process which produces boron atoms by photodissociation of the diborane gas.

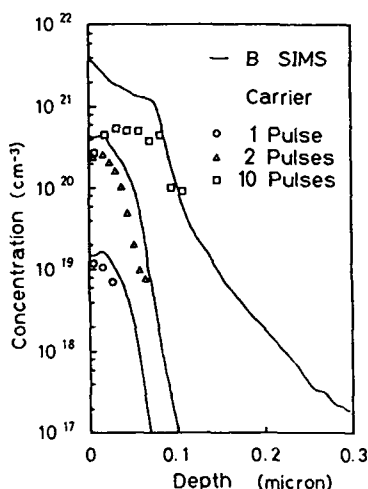


Fig. 5 Boron concentration profiles by SIMS and carrier concentration profiles.

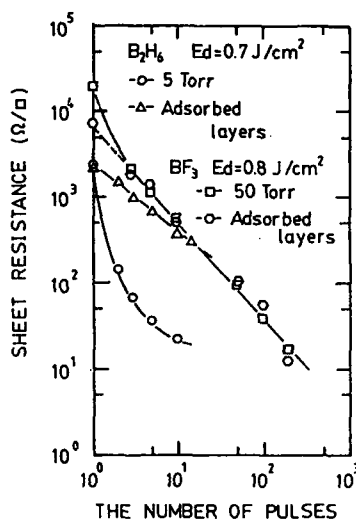


Fig. 6 Sheet resistance of doping using only adsorbed layer and gas

SUMMARY

The boron doping of silicon using an ArF excimer laser and diborane, which has an absorption at 193 nm, has been performed. The sheet resistance for diborane is much lower than that of transparent BF_3 . We obtained high surface concentration of about $5 \times 10^{20} \text{ cm}^{-3}$ and shallow junctions of $0.1 \mu\text{m}$ as determined from carrier concentration profiles at 10 pulses irradiation. The shape of the carrier profile changes from a complementary error function-like to a box-like profile with the increase of number of pulses. The mechanisms of laser doping with diborane involve pyrolytic processes of adsorbed layers and photolytic processes of dopant gas.

ACKNOWLEDGMENT

We would like to thank K. Uwasawa, S. Inui and T. Matuso for help with this work and M. Miyake of NTT LSI Laboratories for SIMS measurement.

References

1. Y.Rytz-Ftoidevaux, R.P.Salathe, and H.H.Gilgen, Appl. Phys. A37, 121 (1985).
2. T.F.Duesch, D.J.Ehrlich, D.D.Rathman, D.J.Silversmith, and R.M.Osgood, Jr., Appl. Phys. Lett. 39, 825 (1981).
3. P.G.Carey, T.W.Sigmon, R.L.Press, and T.S.Fahlem, IEEE Electron Device Lett. EDL-6, 291
4. P.G.Carey, K.Bezjian, T.W.Sigmon, P. Gildea, and T.J.Masgee, IEEE Electron Device Lett.
5. S.Kato, T.Nagahori, and S.Matsumoto, J. Appl. Phys. 62, 3656 (1987).
6. S.Kato, H.Saeki, J.Wada, and S.Matsumoto, J. Electrochem. Soc. 135, 1030 (1988).
7. K.G.Ibbs and M.L.Lloyd, in CHARACTERISTICS OF LASER IMPLANTATION DOPING, edited by R.M.Osgood, S.R.J.Brueck, H.R.Schlossberg (Mater. Res. Soc. Proc. 17, Boston, PA1982) pp.243-248.
8. G.E.Jellison, Jr., and F.A.Modine, Appl. Phys. Lett. 41, 180 (1982).
9. M.P.Irion and K.L.Kompa, J. Chem. Phys. 76, 2338 (1982).
10. W.E.Beadle, J.C.C.Tsai, and R.D.Plummer, QUICK REFERENCE MANUAL, John Wiley & Sons, New York, 1985). pp.2-37.

LASER PATTERNING OF HIGH TEMPERATURE SUPERCONDUCTING OXIDE FILMS

A. Gupta, B. W. Hussey, R. Jagannathan, E. I. Cooper, and E. A. Giess
IBM Thomas J. Watson Research Center, Yorktown Heights, NY 10598

ABSTRACT

A focused argon ion laser (514 nm) beam has been used for patterning superconducting lines of $\text{YBa}_2\text{Cu}_3\text{O}_{7-\delta}$ using films prepared from metal trifluoroacetate solution precursors. A stoichiometric mixture of the precursors is dissolved in methanol, and the solution is spun on yttria-stabilized zirconia substrate to form a film. The film is patterned by irradiating in selected areas by direct laser writing to convert the irradiated layers to an intermediate fluoride state, the nonirradiated areas being unchanged. The nonirradiated areas are then dissolved away, leaving a pattern of the fluoride material. This patterned layer is converted to the superconducting oxide in a subsequent high temperature step involving reaction with water vapor.

INTRODUCTION

Since the discovery of high temperature oxide superconductors, many techniques have been developed for depositing films of these materials [1]. For eventual application of these films in fabrication of devices and high-speed interconnects, it is necessary to develop suitable patterning techniques for these films. The reactivity of the superconducting oxides with most wet chemicals has made it difficult to apply standard photolithographic techniques for fine line patterning. A possible solution is to pattern precursor films of the superconductor, which are not sensitive to the wet chemicals, and then convert the patterned precursor to the superconducting oxide [2]. We report on a maskless patterning process for high T_c superconducting oxide films using a focused cw argon ion laser beam. The process involves localized photothermal decomposition of metallo-organic precursor films using laser direct writing, in which patterning is accomplished prior to attainment of a superconducting state in the layer.

Recently a number of different solution precursors, containing mixtures of Y, Ba, and Cu metallo-organics, have been developed for preparation of superconducting films of $\text{YBa}_2\text{Cu}_3\text{O}_{7-\delta}$ (1-2-3) by spin coating [3-6]. Typically, a mixture of the precursors with the right cation stoichiometry is deposited on the substrate and is converted to the oxides by thermal decomposition at temperatures of 300-500°C. The superconducting phase is formed by subsequent annealing in oxygen at a higher temperature. Besides process simplicity, the use of solution precursors allows accurate control of composition and intimate mixing for a multi-component system. Moreover, there is a potential of patterning these films by photothermal or photochemical decomposition using a focused beam source. Laser direct writing techniques have been used in the past for patterned deposition of metals, such as palladium and copper, by decomposition of metallo-organic films [7,8]. We have used the direct writing process for patterning 1:2:3 trifluoroacetate precursor films to deposit 1:2:3 fluoride intermediates. The patterned fluoride layer is converted to the superconducting oxide in a subsequent step involving reaction with water vapor. Preliminary results on this process were reported by us in an earlier publication [9]. Direct writing of superconducting lines using metal nitrate and neodecanoate precursor films have also been recently reported [10,11].

EXPERIMENTAL

The preparation of the metal trifluoroacetates has been described in an earlier publication [6]. The fluorine substitution in the carboxylates makes them readily soluble in a variety of organic solvents, including alcohols. A spin-on solution of Y-Ba-Cu trifluoroacetate (TFA) was prepared by dissolving stoichiometric amounts of the three trifluoroacetates (Y:Ba:Cu=1:2:3) in methanol. Some solutions containing copper in excess of the stoichiometric ratio were also prepared. The concentration of the metal ions in solution was confirmed by inductively coupled plasma emission spectroscopy (ICP). Films were spin-coated on randomly oriented single crystals of yttria-stabilized zirconia (YSZ). The concentration of the solution was adjusted so as to produce 4-4.5 μm thick films at a spin speed of 2000 rpm. The spun-on films were baked at 200°C to remove the water of crystallization and any residual solvent. The dried films were amorphous, as determined by x-ray diffraction, and were featureless.

The TEM₀₀ output at 514 nm from an Ar⁺ (Spectra Physics 171) was used as the excitation source. The laser beam was attenuated with neutral density filters, or a variable filter polarizer, and then reflected onto a cube beamsplitter residing inside a microscope (Cambridge Instruments). The beamsplitter reflected 80% of the laser beam onto a Leitz Wetzlar 20X infinity corrected microscope objective (NA = 0.4). The beam waist was measured using the scanning knife-edge technique. A plot of the beam waist as a function of distance between sample and objective lens yields a minimum value of 1.8 μm for the focused beam waist (1/e). The beam was focused onto the sample placed on a scanning X-Y stage with a maximum scan speed of 10 mm/sec and a resolution of 0.1 μm .

After exposure to the laser, the undeveloped material was removed by rinsing in methanol. The as-written features were insulating and had to be converted to the superconducting oxide by reacting with water vapor and subsequent annealing. To form the superconducting phase the film was placed in an oven at 850°C under flowing helium saturated with water vapor for 30 min. This was followed by a short anneal (5-10 min) in dry helium at 900-920°C. The helium flow was then replaced with oxygen flow and the sample was slowly cooled down to room temperature. The water vapor was required to convert the fluorides to the oxides through formation of hydrogen fluoride.

For measuring the resistivity of the lines as a function of temperature, a continuous flow cryostat with a temperature controller was used. The details of the sample preparation and measurement have been described in a previous publication [10]. A temperature controlled silicon diode (± 0.1 K accuracy) was mounted next to the sample for accurate temperature measurement.

RESULTS AND DISCUSSION

Thermogravimetric analysis (4°C/min) of the individual trifluoroacetates, and their 1:2:3 mixture, was carried out in oxygen and argon ambient to study the thermal decomposition behavior under slow heating condition. Weight loss and x-ray analysis were used to identify the products. The results showed that all the trifluoroacetates decomposed over a relatively narrow range of temperature (250-360°C) and lead to formation of the respective fluorides. Some copper oxide was also formed during decomposition, the fraction of which increased when the decomposition was carried out in oxygen. Decomposition of copper trifluoroacetate also resulted in loss of a small amount of copper through volatilization, particularly when decomposed in argon atmosphere. Complete decomposition of the 1:2:3 TFA mixture occurred at a lower temperature ($\sim 310^\circ\text{C}$) in oxygen than in argon ($\sim 360^\circ\text{C}$). The results of the thermogravimetric analysis of the 1:2:3 mixture in argon and oxygen atmosphere are shown Fig. 1.

The absorption spectra of the spun-on 1:2:3 TFA film, before and after dehydration, are shown in Fig. 2. The as spun-on films are light blue in color and show a broad band in the near-infrared and red region of the spectrum due

to Cu^{2+} absorption, with increasing absorbance in the ultraviolet region from the fluorocarboxylate ligand absorption. On dehydration at 200°C , the UV absorption band extends to longer wavelengths, which is reflected in a change in color of the films to light green. The Cu^{2+} absorption band shows no changes on dehydration. The laser radiation at 514 nm falls in between the two absorption bands, and is absorbed only weakly. Decomposition of relatively thick films is possible because of the large absorption depth. The dehydrated films slowly absorb moisture from the atmosphere and revert back to the hydrated form. This requires processing the films soon after baking at 200°C to avoid changes in the absorption characteristics. The changes can also be avoided by processing the films at an elevated temperature on a hot stage ($150\text{--}200^\circ\text{C}$). This also results in significantly reducing the laser power density required for patterning the films.

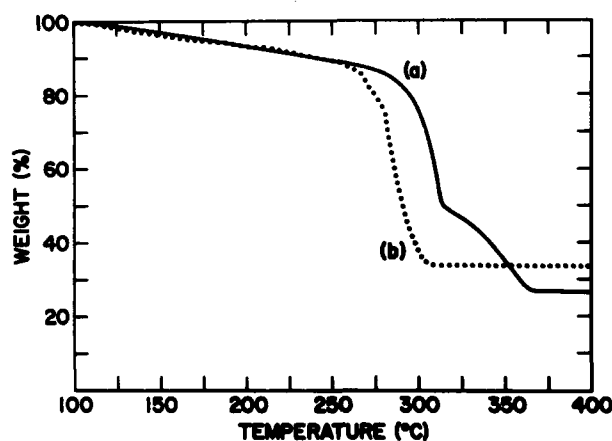


Fig. 1. Thermogravimetric analysis of the 1:2:3 TFA mixture in: (a) argon and (b) oxygen atmosphere.

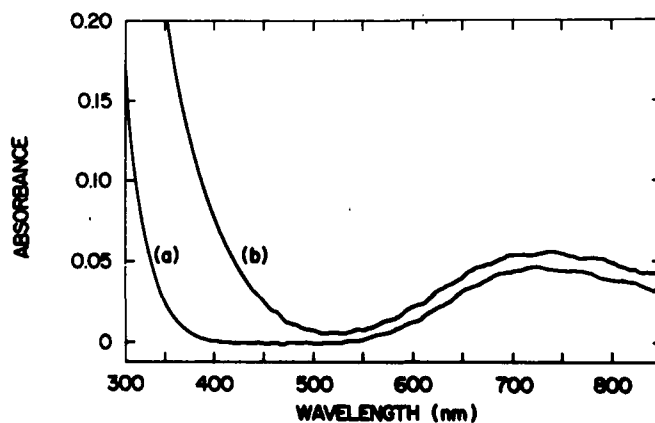


Fig. 2. (a) Absorption spectrum of $4.2\text{ }\mu\text{m}$ thick 1:2:3 TFA film; (b) spectrum after dehydration at 200°C .

The line width of the as-written features varies linearly with laser power density in the range of $(0.2-1.5) \times 10^6 \text{ W/cm}^2$, when the films are patterned at room temperature. The dependence of line width on scan speed for three different laser power densities is shown in Fig. 3. The line width is fairly independent of scan speeds up to 1 mm/sec and then starts decreasing. The observed dependence of line width on laser power density and scan speed can be qualitatively understood by considering the thermal conduction of heat after absorption of radiation. Assuming that the thermal conductivity of the deposit is similar to that of the YSZ substrate ($1.4 \text{ Wm}^{-1}\text{K}^{-1}$), most of the heat will be lost through the substrate, and the temperature distribution will be relatively insensitive to the geometry of the deposit [12]. The temperature will increase linearly with absorbed energy, and a steady-state temperature will be reached quite rapidly, regardless of scan speed. Only when the residence time of the laser beam approaches the thermal diffusion time will the effect of scan speed on line width be noticeable.

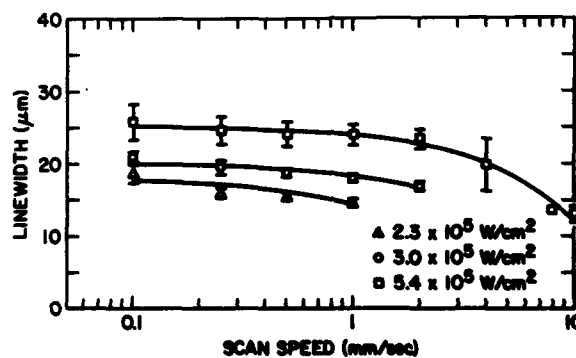


Fig. 3. Variation of line width as a function of scan speed for three different laser power densities.

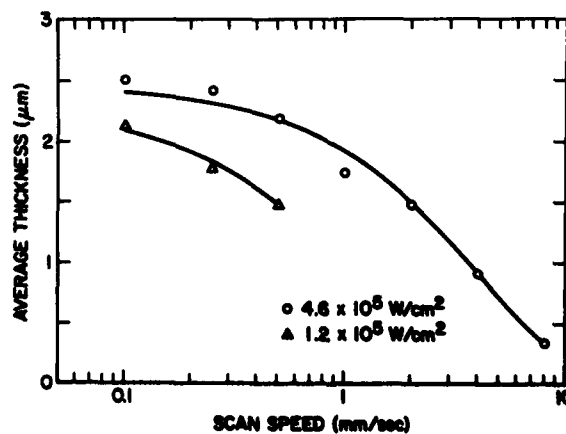


Fig. 4. Variation of average thickness of developed lines as a function of scan speed for two different laser power densities.

The fractional decomposition of the film, or thickness of the deposit during laser writing, is determined primarily by the kinetics of decomposition. The average thickness of the deposit after development is plotted as a function of scan speed in Fig. 4. For a fixed laser power density, the average thickness of the deposit is found to increase rapidly with decreasing scan speed until it reaches its limiting value. The temperature and time dependence of the kinetics are both reflected in the observed variation in thickness of the deposit as a function of scan speed and laser power density.

On annealing the laser written features to form the superconducting oxide, the width and thickness of the lines decreased by about 10-15%. Figure 5 shows typical superconducting lines prepared on a YSZ substrate. X-ray diffraction pattern of the lines (not shown) clearly showed the formation of the 1-2-3 phase. The major peaks in the pattern corresponded to the (001) reflections of the superconducting oxide phase, indicating a c-axis normal preferred orientation. Unreacted barium fluoride was also observed in the diffraction pattern.

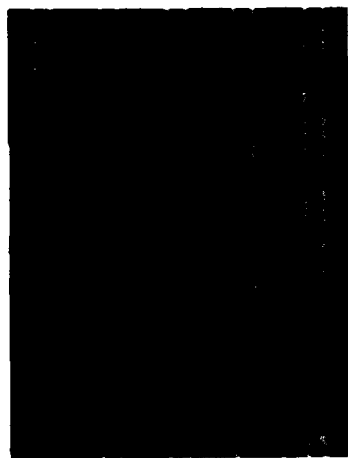


Fig. 5. Scanning electron micrograph of 10 μm superconducting lines.

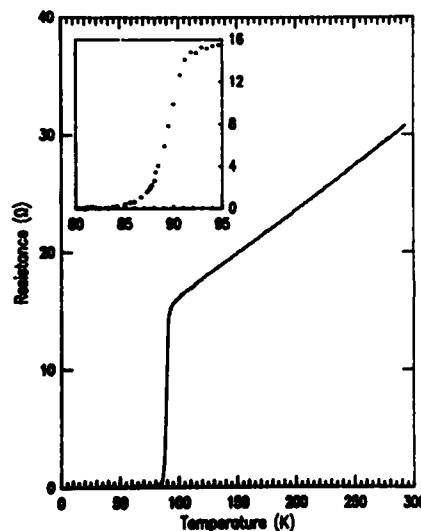


Fig. 6. Resistance vs temperature of lines shown in Fig. 5 (TFA film composition of 1:2:3.5).

For measuring the resistivity of the lines as a function of temperature, a number of parallel lines were written with connecting pads for four-point probe measurement. Lines patterned using TFA films with 1:2:3 stoichiometry exhibited superconducting onset temperatures in the range of 90-95 K. However, the resistive transition was quite broad, with zero resistance achieved at 70-75 K. These results were obtained consistently over a relatively wide range of laser process parameters. Chemical (ICP) analysis showed that while the ratio of barium to yttrium was 2:1 in the patterned lines, the concentration of copper relative to yttrium was lower than the expected 3:1 ratio. This suggested that copper was being selectively removed from the films during laser writing. The removal of copper is believed to be due to formation of the volatile Cu(I) TFA during decomposition. To compensate for the removal of copper, the composition of the spun-on films was made copper rich. This narrowed down the transition width significantly, as shown in Fig. 6 for lines prepared from 1:2:3.5 TFA composition. Superconducting lines down to 10 μm width (1 μm thickness) have

been patterned from 4 μm TFA films which routinely show zero resistance temperatures in the range of 80-85 K. Finer lines ($\sim 5 \mu\text{m}$) have been patterned from 2 μm thick TFA films. While the superconducting onset temperature of these lines remains the same as those of wider lines, the zero resistance temperature drops to about 65 K. This is probably due to the increased effect of the interaction with the substrate of the thinner films during the high temperature annealing step.

CONCLUSIONS

We have shown that laser direct writing is a viable technique for patterning superconducting oxide films using solution precursors. The technique has been used for depositing features several centimeters in length and 10-15 microns wide, which are superconducting above liquid nitrogen temperature. The selective removal of copper from the film during laser writing causes deviation from stoichiometry in the developed features, and has to be compensated for by adjusting the composition of the precursor film. This can possibly be avoided by patterning the films in an atmosphere of oxygen to reduce the formation of the volatile Cu(I) TFA intermediate.

ACKNOWLEDGMENTS

We thank J.I. Landman for the electrical measurements, B.L. Olson for the chemical analysis, and P.J. Bailey for the scanning electron micrographs.

REFERENCES

1. Thin Film Processing and Characterization of High Temperature Superconductors, edited by J.M.E. Harper, R.J. Colton, and L.C. Feldman (American Physical Society Proceedings No. 165, New York, NY 1988) pp. 2-211.
2. M. Gurvich and A.T. Fiory, *Appl. Phys. Lett.* **51**, 1027 (1987).
3. C.E. Rice, R.B. van Dover, and G.J. Fisanick, *ibid.*, **51**, 1842 (1987).
4. A.H. Hamdi, J.V. Mantese, A.L. Micheli, R.C.O. Laugel, D.F. Dungan, Z.H. Zhang, and K.R. Padmanabhan, *ibid.*, **51**, 2152 (1987).
5. M.E. Gross, M. Hong, S.H. Liou, P.K. Gallagher, and J. Kwo, *ibid.*, **52**, 160 (1988).
6. A. Gupta, R. Jagannathan, E.I. Cooper, E.A. Giess, J.I. Landman, and B.W. Mussey, *ibid.*, **52**, 2077 (1988).
7. M.E. Gross, A. Appelbaum, and P.K. Gallagher, *J. Appl. Phys.* **61**, 1628 (1987).
8. A. Gupta and R. Jagannathan in Laser and Particle-Beam Chemical Processing, edited by D.J. Ehrlich, G.S. Higashi, and M.M. Oprysko (Mater. Res. Soc. Proc. **101**, Pittsburgh, PA 1988) pp. 95-100.
9. A. Gupta, B.W. Mussey, G. Koren, E. I. Cooper, and R. Jagannathan in Processing and Applications of High T Superconductors, edited by W.E. Mayo (The Metallurgical Society, Warrendale, PA 1988) pp. 73-82.
10. A. Gupta and G. Koren, *Appl. Phys. Lett.* **52**, 665 (1988).
11. J.V. Mantese, A.B. Catalan, A.M. Mance, A.H. Hamdi, A.L. Micheli, J.A. Sell, and M.S. Meyer, *Appl. Phys. Lett.* **53**, 1335 (1988).
12. K. Piglmayer, J. Doppelbauer, and D. Bäuerle in Laser-Controlled Chemical Processing of Surfaces, edited by A. Wayne Johnson, D.J. Ehrlich, and H.R. Schlossberg (Mater. Res. Soc. Proc. **29**, Pittsburgh, PA 1984) pp. 47-54.

EPITAXIAL SILICON LAYERS MADE BY REDUCED PRESSURE/TEMPERATURE CVD

J.L. REGOLINI, D. BENSACHEL, J. MERCIER(*), C.D'ANTERROCHES and A. PERIO

Centre National d'Etudes des Telecommunications
BP 98 - 38243 - Meylan Cedex - France

(*) LEPES/CNRS, Av. des Martyrs, 38042 Grenoble Cedex - France

ABSTRACT

In a rapid thermal processing system working at a total pressure of a few Torr, we have obtained selective epitaxial growth of silicon at temperatures as low as 650°C. When using SiH_2Cl_2 (DCS) as the reactive gas, no addition of HCl is needed. Nevertheless, using SiH_4 below 950°C a small amount of HCl should be added.

Some kinetic aspects of the two systems, DCS/HCl/ H_2 and SiH_4 /HCl/ H_2 , are presented and discussed. For the DCS system, we show that the rate-limiting reactions are slightly different from those commonly accepted in the literature, where the results are from systems working at atmospheric pressure or in the 20-100 Torr range.

Our model is based on the main decomposition of DCS, $\text{SiH}_2\text{Cl}_2 \rightarrow \text{SiHCl} + \text{HCl}$, instead of the widely accepted reaction $\text{SiH}_2\text{Cl}_2 \rightarrow \text{SiCl}_2 + \text{H}_2$. This is the main reason why no extra HCl is required in the DCS/ H_2 system to obtain full selectivity from above 1000°C down to 650°C.

INTRODUCTION

Conventional silicon chemical vapor deposition (CVD) is in the 1000°C-1200°C temperature range. Very large scale integrated circuits (VLSI) need smaller geometries for both vertical and lateral dimensions. Thus, the development of shallow junctions is heading towards low temperature processing since the dopant profile has to be perfectly controlled.

According to Srinivasan and Meyerson [1], silicon CVD epitaxial temperatures down to 1000°C can produce perfect device quality films. In the temperature range between 650°C and 1000°C, it is less certain that perfect device quality films will be produced, thus suggesting that plasma-enhanced CVD [2] or the ultra high vacuum CVD [3] techniques be used.

Another technique, developed by J.F. Gibbons et al. [4], has proved to give good quality devices. They use a rapid thermal processing (RTP) system to grow epitaxial silicon layers on one minute time-scale and below 1000°C, thus, minimizing contamination and dopant diffusion. We present the experimental results obtained in a similar set-up using silane or dichlorosilane diluted in hydrogen as the main gases. We have previously reported experimental results and kinetic aspects of Si epitaxial growth using the same system with SiH_4 /HCl/ N_2 / H_2 [5,6,7]. Selectivity was also discussed as well as layer characterizations by electrical measurements, transmission electron microscopy (TEM), and chemical decoration.

The aim of the present paper is to report the selective epitaxial growth of Si using only DCS diluted in H_2 in the 1100°C-650°C temperature range. A comparison of some kinetic aspects of the two systems, SiH_4 /HCl/ H_2 and SiH_2Cl_2 /HCl/ H_2 , at pressures around 2 Torr and temperatures between 1100°C and 650°C is also presented. Selectivity will also be discussed throughout the whole temperature range for the two systems. The so-called loading effect is discussed as well as TEM observations made on layers grown at 650°C.

EXPERIMENTAL

Our experimental set-up consists of a rapid thermal CVD system using a bank of tungsten lamps as a source of radiant heat. This system was pioneered by J.F. Gibbons [4] and the process was named "Limited REaction Processing". The actual reactor is a horizontal cold-wall air-cooled silica chamber where the base pressure is about 2 m Torr obtained simply by a mechanical oil pump with a molecular sieve oil trap. The substrate temperature rather than the gas flow is used as a switch to turn the CVD reaction on and off. The substrate is heated only while the surface reaction should be occurring.

After loading a sample, the system is purged using H_2 , which is also used as a carrier gas. Short cycles or power pulses of a few seconds to two minutes are used for "in situ" cleaning and growth in order to avoid heating the reactor wall, thus minimizing contamination. The H_2 flow is permanent during the whole process. Multiple processes can be accomplished without removing the sample from the reaction chamber. The cleaning of the wafers prior to deposition is carried out using a chemical procedure followed by an "in situ" thermal process as previously described [5,7].

Four-inch (100) or (111) wafers, with a patterned SiO_2 layer, were used in this study. The thickness of the growth layers was measured by a profilometer. The surface temperature was measured by a thin thermocouple attached to a test wafer under the same experimental conditions. Reactive and carrier gases are all electronic grade and no special purification was used, their flow being established by flowmeters prior to the temperature cycles.

RESULTS AND DISCUSSION

All the experiments were carried out in H_2 as a carrier gas at 2 slm with a total pressure of about 2 Torr in a reacting gas dilution from 10% to 0.1% in volume unless otherwise specified. Figure 1 shows the growth rate G as a function of the reciprocal temperature $1/T$ in an Arrhenius type plot for two different samples.

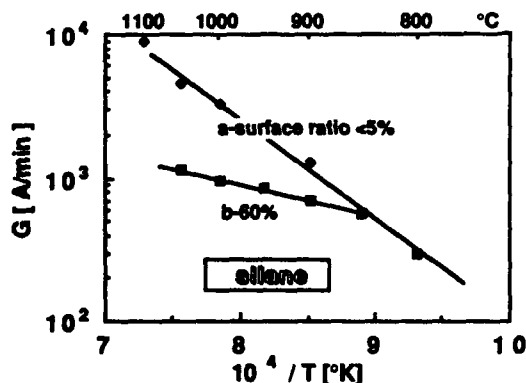
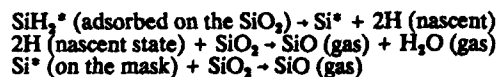


Figure 1.
Silane/hydrogen
system showing
the loading
effect only at
temperatures
above 850°C.

The growth rate for the patterned sample, which has less than 5% bare Si as the total exposed silicon surface, is shown as curve (a). Its growth rates are higher than the corresponding ones in curve (b), where the surface ratio is about 60%. Curve (b) follows a "normal" behaviour, i.e. a high temperature ($T > 850^\circ\text{C}$) region where the growth rate is fairly constant and mainly controlled by the gas phase reactions. The low temperature ($T > 850^\circ\text{C}$) side is characterized by a surface-reaction-controlled regime

where it is possible to measure an activation energy, as will be shown later. The particular behaviour followed by curve (a), as observed in the high temperature side, can be explained by the proposed qualitative scheme [6]:



The second reaction is a hydrogen consuming one, thus the main SiH_4 decomposition,



is shifted toward the right giving rise to a higher growth rate. In the present case the surface controlled regime extends beyond 1000°C . Moreover, this loading effect is only observed when the seed to mask ratio is below 5% and it does not depend on the chlorine species present during the reaction as proposed by Ishitani et al. [8]. Below 850°C , this effect is not present because the $\text{SiO} (\text{gas})$ production requires higher temperatures.

Just the opposite is observed with the $\text{SiH}_2\text{Cl}_2/\text{H}_2$.

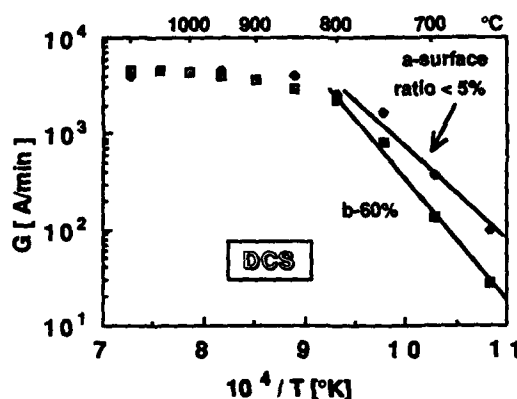


Figure 2.
Dichlorosilane/
hydrogen system.
The loading effect
is only observed
at temperatures
below 800°C .

As shown in Figure 2 the loading effect is present in the low temperature side and according to our previous paper [9], the main DCS decomposition is:



Since there is no H_2 production, there is no loading effect observed at temperatures above 850°C as previously discussed. Nevertheless, below 800°C , there is an important difference between the two samples. In the Torr pressure regime (our case), the DCS/H_2 system is fully selective; thus, at the silica mask, the formed silicon nuclei are etched away through the SiCl_4 formation by the reaction:



The SiCl_2 then formed has enough mobility to migrate into the Si seed giving a higher growth rate than in the case where there is no mask. The apparent activation energy (E_a) is 46 kcal/mol for the first case and 59 kcal/mol for the other. The latter is in total agreement with the DCS molecule dissociation energy as proposed by Ishitani et al. [10]

Coming back to the silane system, selectivity can be obtained with no addition of HCl using the SiH_4/H_2 system at temperatures above 900°C . Only 10% of the silane flow is needed for the HCl concentration when working below 900°C .

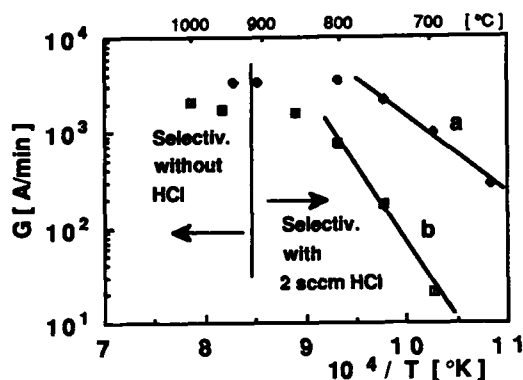


Figure 3.
Silane / hydrogen
system. (a) no HCl
addition. (b) with
HCl (see text).

Figure 3 shows the growth rate vs $1/T$ for the two systems: (a) 40 sccm silane in 2 slm hydrogen and (b) 20 sccm silane plus 2 sccm HCl in 2 slm hydrogen. The E_a value is 38 kcal/mol for the first case and 74 kcal/mol for the second. The first one is a normal value encountered for silane decomposition. However, a small amount of HCl drives the E_a to a value higher than what we obtained for DCS, i.e. 60 kcal/mol.

By using DCS diluted in hydrogen, selectivity is obtained throughout the temperature range (650 – 1000°C). Only a low percentage of HCl is required when using silane below 950°C . In all the cases studied, the surface morphology, observed under optical microscopy, is always specular and shiny. The crystalline quality of the epilayers grown in the low temperature range has been investigated by TEM.



Figure 4.
TEM plane view of
a layer grown at
 650°C .

Figure 4 is a TEM plane view of a layer grown at 650°C with a diffraction pattern showing a single crystal layer. Precipitates and isolated dislocations are observed in a density evaluated at a maximum value of $10^6/\text{cm}^2$. However, a large part of these defects can be explained since no special care is taken with the laboratory environment and/or sample handling.

CONCLUSION

Full selectivity has been obtained with only DCS diluted in H_2 . However, in the silane system, a small percentage of HCl concentration in silane is sufficient to obtain selectivity up to 650°C. This is the main characteristic of our system working in the Torr pressure regime. The etching of silicon by the presence of HCl is enhanced by this reduced pressure regime. The observed loading effect depends on the reacting gases and it is qualitatively explained. The crystalline quality of the epi-layers observed by TEM is acceptable for device applications. The remaining defects are under study.

REFERENCES

1. G.R.Srinivasan and B.S.Meyerson, *J. Electrochem. Sci.* **134**, 1518 (1987)
2. T.J.Donahue and R.Reif, *J. Appl. Phys.* **57**, 2757 (1985)
3. B.S.Meyerson, E.Ganin and D.A.Smith, "Reduced Temperature Processing for VLSI," ed. by R.Reif and G.R.Srinivasan, p. 285. The Electrochem. Soc. softbound Proceedings Series, Pennington, NJ (1986).
4. J.F.Gibbons, C.M.Gronet and K.E.Williams, *Appl. Phys. Let.* **47**, 721 (1985)
5. J.L.Regolini, D.Bensahel, I.Nissim, J.Mercier, E.Scheid, A.Perio and E.Andre, *Electronics Letters* **24**, 408 (1988)
6. J.Mercier, J.L.Regolini, D.Bensahel and E.Scheid, submitted to *J. Crystal Growth*
7. J.L.Regolini, D.Bensahel, E.Scheid, A.Perio and J.Mercier, to be published with the Proceedings of the E-MRS 1988 in "Applied Surface Science"
8. A.Ishitani, N.Endo and H.Tsuya, *J.J. Appl. Phys.* **23**, L391 (1984)
9. J.L.Regolini, D.Bensahel, J.Mercier and E.Scheid, submitted to *J. Appl. Phys.*
10. A Ishitani, T.Takada and Y.Ohshita, "Proc. of the 10th Inter. Conf. on CVD," ed. by G.W.Cullen, (The Electrochem. Soc. **87**, Honolulu, HA 1987) p.91

X-RAY LITHOGRAPHY STUDIES OF POLYSILANE USING A LASER PLASMA X-RAY SOURCE*

GLENN D. KUBIAK[‡], DUANE A. OUTKA[‡], AND JOHN M. ZEIGLER[†]

[‡]Sandia National Laboratories, Livermore, CA 94551-0969

[†]Sandia National Laboratories, Albuquerque, NM 87185.

ABSTRACT

A laser-generated plasma source of monochromatized soft x-rays has been used to study the x-ray lithographic resist properties of poly(cyclohexylmethylsilane-co-dimethylsilane). X-ray absorption spectra near the Si L_{2,3} edge of unexposed samples were measured to guide the choice of exposure photon energy. We find that poly(cyclohexyl-methylsilane-co-dimethylsilane) exhibits positive tone at x-ray energies near 105 eV (Si 2p resonance), a sensitivity of 1000 mJ/cm² and a contrast of 1.5. Sensitivity is found to increase markedly when exposed samples are held in air before development. Using simple wire mesh masks, estimates of the minimum achievable linewidth have been made.

INTRODUCTION

X-ray lithography in the region near 1keV photon energy (12.4 Å) is capable of producing high-resolution (< 0.2 μm) structures in resist layers with extremely wide process latitude and low sensitivity to low-atomic-number particulate defects [1,2]. To achieve these impressive results, proximity printing is performed through delicate reticles at unit magnification. One of the major obstacles to widespread implementation of this patterning technology resides in the difficulty in fabricating, inspecting and repairing the reticle blanks. This problem is exacerbated by the fact that at unit magnification, pattern fidelity tolerances on the reticle must be as good as or better than those to be achieved in the resist. An alternative approach, which has received far less study, is to develop 5x-10x demagnifying projection printing by using reflective optics in the region from 100-500 eV [3]. This would achieve extremely high resolution using reticle sizes comparable to those being produced now. The availability of relatively inexpensive laser plasma x-ray sources, which achieve high average power production of such soft x-rays using commercially available lasers, makes the approach particularly attractive. At present, however, little is known regarding the sensitivity, contrast, and resolution of candidate resists in the 100-500 eV spectral region[4,5].

We have chosen a polysilane resist, poly(cyclohexyl-methylsilane-co-dimethylsilane) (PCMDS) as the focus of the present study. This material exhibits several lithographically useful properties as a mid- and deep-UV positive photoresist for feature sizes ≥ 0.8 μm; it has an exposure sensitivity of 260 mJ/cm² at an exposure wavelength of 248 nm, is photovolatilized readily at fluences above 50 mJ/cm² (using ~25 ns pulses), and is etch-resistant in reactive ion etch plasmas containing oxygen[6]. Although the lithographic properties of the polysilanes have been studied extensively in the UV, little work has been reported in the soft x-ray region[5]. Absorption coefficients of the polysilanes in this region are large, making high resolution applications in thick films impossible. However, bilayer lithography strategies utilizing very thin films of these etch-resistant materials have already been demonstrated in the UV [7,8] and should be possible in the soft x-ray region also. In addition, spectral structure near the Si L_{2,3} absorption edge at 105 eV may permit the radiation chemistry to be varied in useful ways as a function of exposure wavelength.

We present here a brief summary of our initial studies of the soft x-ray absorption spectrum and the exposure sensitivity, contrast, and resolution at hv = 105 eV of PCMDS. Using synchrotron radiation, the near edge x-ray absorption fine structure (NEXAFS) spectrum of this material has been measured at the Si L_{2,3} absorption edge. We have performed all exposure sensitivity and resolution experiments with a monochromatized laser plasma source (LPS) of soft x-rays. Sensitivity curves measured at 105 eV are presented for samples developed immediately after x-ray exposure as well as for samples "cured" in air between exposure and development. Coarse resolution estimates have been made for both broadband and monochromatic exposures using simple Ni mesh masks.

EXPERIMENTAL

Samples of PCMDS were obtained from Petrarch Chemical Systems with an average molecular weight of approximately 1×10^5 g/mole and a polydispersity of 5. The polymer was dissolved without further purification in xylenes to a concentration of 5 wt. % and spin-coated onto silicon wafers to depths of 0.2 - 0.3 μm . Samples were *not* baked at any time before or after x-ray exposures.

NEXAFS spectra of the untreated polysilane at the Si $L_{2,3}$ edge were measured at beamline VIII-II at the Stanford Synchrotron Radiation Laboratory with a toroidal grating monochromator. The NEXAFS spectra were obtained by measuring secondary and Auger electrons produced by the decay of the Si 2p core hole. In order to avoid interference from photoemission peaks, only those electrons with a kinetic energy of 40 eV were collected using a hemispherical electron energy analyzer. Unfortunately, at the time of the NEXAFS measurement, it was not possible to measure the monochromator transmission function, so the background in the raw NEXAFS spectra had to be estimated by comparing spectra taken with two different gratings, 822.6 and 2400 lines/mm. While this leads to uncertainty regarding weak spectral features, the large peak at 105 eV, which is the primary interest of this study, was quite apparent in the raw spectra.

Monochromatized soft x-ray exposures were performed in the LPS diagrammed schematically in Fig. 1 and described in more detail in Ref. 9. In the present configuration, an injection-seeded excimer laser (Lambda Physik EMG 150) operating with KrF at a wavelength of 248 nm is focused with a 1000 mm focal length lens onto a rotating gold-coated target. The laser

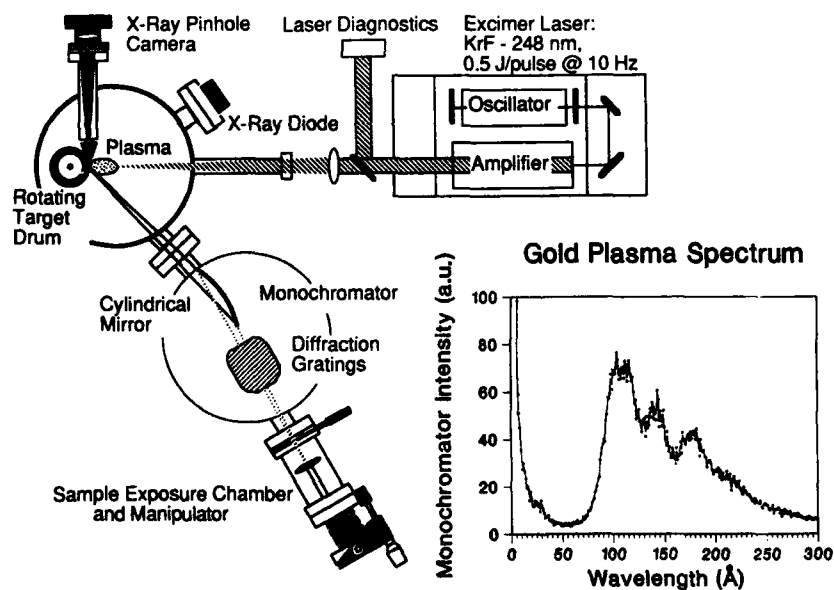


Fig. 1 Schematic diagram of the Laser Plasma X-Ray Source, monochromator and sample exposure chamber. Shown in the inset is a typical output spectrum recorded with the 800 l/mm diffraction grating.

pulse energy on target and FWHM pulsewidth are typically 0.5 J and 25 ns, respectively. A portion ($\sim 3.8^\circ \times 0.75^\circ$) of the radiant XUV and soft x-ray flux is monochromatized by a high throughput stigmatic monochromator described in detail in Ref. 10. The spectral variation of the monochromatized output flux was calibrated absolutely for the specified laser parameters using a double ion chamber containing neon gas. A typical spectrum is shown in the inset of Fig. 1. At 100 eV, the source produces 1.5×10^{10} photons/mm²-1% BW per pulse. Repetition rates range from 3-10 Hz. No attempts were made to measure the *in situ* flux incident on the sample during exposures. Instead, an aluminum x-ray diode, filtered with an Al:Si filter, was used to monitor long-term variations in the spectrally integrated (15-73 eV) radiant flux during exposures and the appropriate corrections were applied to the absolute flux values obtained earlier. We believe this procedure is accurate to within a factor of two.

Sample exposures were made on a small region of the resist layer for a specified number of laser pulses in vacuum; the sample was then translated to expose a virgin region and the procedure repeated. After exposure, the samples were developed in 10% tetrahydrofuran (THF) in isopropanol for 3-5 minutes at room temperature. As has been noted previously for deep-UV exposures performed in air [6], increasing concentrations of THF improve the apparent sensitivity of PCMDS but degrade resolution. We find this effect to be even more pronounced for x-ray exposures performed *in vacuo*. Film thickness measurements were performed with a profilometer (Tencor Inst. Alpha-Step 200) scanned through the center of the ~ 300 μ m wide spot formed by the focused x-ray beam. To obtain pattern resolution estimates, exposures were made through a simple Ni mesh (12.7 μ m period) held in tension and in close proximity to the wafer surface. These latter samples were developed in 30% THF in isopropanol solvent.

RESULTS AND DISCUSSION

In Fig. 2 is shown the NEXAFS spectrum of unexposed PCMDS along with the X-ray absorption and electron energy loss spectra of five silicon-containing model compounds [11,12]. The spectrum of the polysilane strongly resembles that of the tetramethylsilane in that both contain a prominent and broad peak at 105 eV, whereas it is distinct from that of the other simple silicon containing compounds in the number and position of the peaks observed. The peak at 105 eV in tetramethylsilane has been attributed to final states involving Si-C σ^* orbitals [11] which are also present in polysilane, so the similarity between the two NEXAFS spectra is understandable. The polysilane also contains Si-Si bonds, however, which should be manifest in the NEXAFS spectrum. Calculations indicate that the lowest unoccupied orbitals of alkyl-substituted polysilanes are of predominantly Si-Si σ^* antibonding character, with the Si-C σ^* orbitals nearby in energy but only weakly intermixed [13]. Therefore, the NEXAFS features associated with the Si-Si bonds are apparently also located at 105 eV and are not distinctly resolved. The spectrum of tetramethylsilane also has a low broad peak at 122 eV which was not resolved in the polysilane spectrum because of the uncertainty in the background.

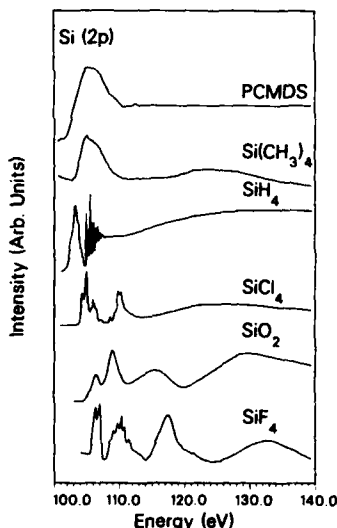


Fig. 2 X-ray absorption spectrum of PCMDS in the Si L_{2,3} absorption edge region compared with x-ray absorption and electron energy loss spectra taken from Refs. 11 and 12 of five silicon-containing model compounds. The peak at 105 eV is assigned to a Si-Si and Si-substituent σ^* bond resonance.

To exploit the existence of the Si-Si, Si-substituent σ^* resonance feature observed in the NEXAFS at 105 eV, monochromatic exposures were performed at this energy. The solid line in Fig. 3 shows an exposure sensitivity curve for a 0.23 μm thick film developed a few minutes after removal from vacuum. This material exhibits positive tone and a sensitivity, defined here as the dose required to remove 50% of the film, $D_{0.5}$, of approximately 1000 mJ/cm^2 . The corresponding contrast (γ) is approximately 1.5. This behavior is analogous to that observed under 20 keV electron beam exposure, where crosslinking was thought to play a significant role [6]. When the films are "cured" in air for a period of several days or weeks before development, the exposure sensitivity curve shown as the dashed line in Fig. 3 is obtained. In this case, the apparent sensitivity is increased to $D_{0.5} = 200 \text{ mJ}/\text{cm}^2$, but γ is reduced to ~ 0.5 . This difference is likely to be caused by the diffusion of oxygen to unreacted or partially reacted polymer radical chain ends, consistent with earlier photovolatilization studies at 248 nm [8]. These studies also demonstrated that exposures *in vacuo* produced silylenes ($\text{R}-\text{Si}-\text{R}''$), which are known to be unstable with respect to oxidation, and small amounts of chain fragments [8]. In contrast, exposures in air produced stable cyclic siloxanes $(\text{RCH}_2\text{SiO})_n$.

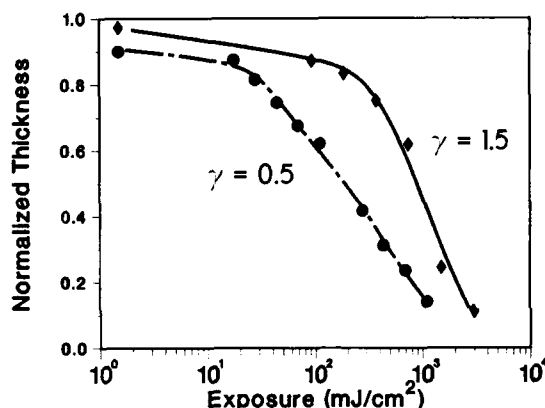


Fig. 3 Sensitivity curves of PCMDs exposed to 105 eV radiation. Curves are shown for development immediately following exposure in and removal from vacuum (\diamond , solid line); and for development after the exposed sample was allowed to remain in air for a prolonged period (\circ , dashed line).

Our choice of 105 eV photon energy was dictated in part by the assumption that photochemistry following resonant x-ray absorption would be similar to that observed with direct $\sigma-\sigma^*$ excitation in the deep UV. PCMDs exhibits a chain scission quantum yield of 0.24 [ref. 6] at 248 nm, via rupture of the Si-Si backbone. Following such UV photoexcitation, intersystem crossing from the singlet to a strongly vibrationally coupled, localized triplet manifold results in multiple Si-Si bond ruptures [8,14]. Therefore, if the same triplet manifold is accessed through x-ray absorption via the σ^* resonance, the depolymerization should exhibit analogous "gain". We have not yet verified this with detailed studies of the x-ray photochemistry at 105 eV, but it is interesting to note that the exposure sensitivity expressed in photons/ cm^2 is ~ 5 times greater at 105 eV than at 5 eV. This suggests that the solid state photochemical quantum yield is greater at 105 eV, perhaps due to the larger total energy available for bond breaking. Based on photoemission experiments which show little admixture between alkyl side-group and silicon-backbone levels [15], we expect alkylated organopolysilanes such as PCMDs to be more sensitive upon resonant x-ray absorption than their arylated counterparts.

Continuing to compare the UV and soft x-ray response of PCMDs, we note that the contrast measured in the deep-UV ($\gamma \approx 3.1$) [6] is much greater than that found in the present work. We attribute this to an increase in crosslinking relative to chain scission for the *in vacuo* 105 eV exposures, and not to differences in film absorption. For both deep-UV and 105 eV exposures, film absorption remains high throughout exposure (in contrast to the mid-UV, where absorption is bleached during exposure). At 105 eV, this is evident from the fact that the resonance seen in the NEXAFS resides on a large Si absorption continuum. Because of this

high film absorption, PCMDS is likely to be most useful in surface imaging bilayer resist schemes. For example, from the mass absorption coefficients of Si and C at 105 eV [16], a film density of 0.9 g/cm^3 and a Si weight fraction of 30.4 %, we estimate the "nonresonant" film absorption coefficient to be $2.7 \mu\text{m}^{-1}$. For the $0.23 \mu\text{m}$ film thickness used here, the fraction of the incident x-ray flux reaching the bottom of the film is therefore 0.5, not far from the optimum value of ~ 0.37 [17]. These results suggest that polysilane films $\leq 0.2 \mu\text{m}$ thick can be utilized as etch-resistant surface imaging layers in bilayer soft x-ray lithography. Films thicker than $\sim 1 \mu\text{m}$ would absorb too strongly in this spectral region to be useful.

Figure 4 shows scanning electron micrographs of a $\sim 0.35 \mu\text{m}$ thick film exposed through a thin nickel wire mesh to: a) a dose of 2.3 J/cm^2 of monochromatic 105 eV radiation, and b) broadband radiation from the zero-order (specular) reflection of the monochromator. Sample development was performed immediately after exposure and removal from vacuum. For samples exposed at 105 eV, micrographs show fairly shallow wall profiles, except near the corners of the illuminated square, where film perforation and webbing have occurred. The film exposed to broadband XUV and soft x-ray radiation exhibits substantial linewidth loss from the combined effects of diffraction and overexposure. Residue can be seen in the bottom of the square illuminated regions. In these initial experiments, no attempt has been made to optimize the development procedure, nor has a descumming treatment been applied. Even under these less-than-optimal conditions, however, resolution of $\sim 1 \mu\text{m}$ appears feasible. Experiments are in progress to optimize resist processing procedures. We also plan to employ masks having smaller feature sizes and to control mask-wafer gap better so that resolution can be assessed more meaningfully.

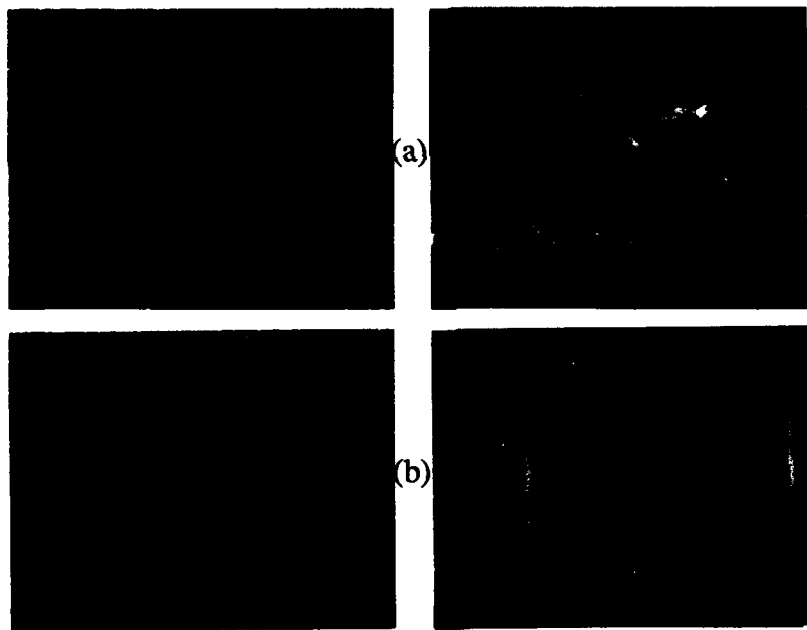


Fig. 4 Scanning electron micrographs of PCMDS exposed through a Ni-wire mesh to: a) 105 eV radiation, and b) broadband radiation from the specular reflection of the monochromator. The mesh period is $12.7 \mu\text{m}$.

CONCLUSIONS

The polysilane co-polymer poly(cyclohexylmethylsilane-co-dimethylsilane) exhibits an x-ray absorption resonance feature at 105 eV which we have assigned to excitation into silicon-silicon and silicon-substituent σ^* orbitals. Using a laser plasma x-ray source, monochromatic exposures have been performed at this resonance. The resulting sensitivity curves show that uncured PCMDS is a positive resist, of moderate sensitivity and contrast. Curing exposed samples in air before development yields higher sensitivity but lower contrast, probably due to the formation of stable and more soluble oxidation products. We estimate that a resolution of $\sim 1 \mu\text{m}$ can be achieved with this material, based on the formation of grid patterns in the resist following exposure through a wire mesh mask. We suggest that this material is a good candidate as an etch-resistant top resist layer in bilayer soft x-ray lithography schemes.

ACKNOWLEDGEMENTS

Dr. T. P. Tooman is acknowledged for his efforts in successfully establishing the laser plasma source. The valuable comments of Drs. J. L. Durant and T. E. Felter and expert technical assistance of Kurt Berger are gratefully acknowledged. We also thank Robert D. Pilkey for performing profilometer measurements. This work is supported by the U. S. Department of Energy under contract #DE-AC04-76DP00789 and was performed in part at the Stanford Synchrotron Radiation Laboratory which is supported by the Office of Basic Energy Sciences of the DOE and the Division of Materials Research of NSF.

REFERENCES

1. A. Heuberger, *J. Vac. Sci. Technol. B* **6**, 107 (1988).
2. D. W. Peters, J. P. Drumheller, R. D. Frankel, A. S. Kaplan, S. M. Preston, and D. N. Tomes, *Proc. SPIE* **923**, 28 (1988).
3. B. Lai, F. Cerrina, and J. H. Underwood, *SPIE* **563**, 174 (1985); F. Cerrina, *J. Imag. Sci.* **30**, 80 (1986).
4. K. Mochiji, T. Kimura, H. Obayashi, and H. Maezawa, *Proc. SPIE* **539**, 56 (1985).
5. D. Mancini, J. W. Taylor, R. C. West, J. Maxka, and F. Cerrina, Abstracts of the 1985 Univ. of Wisconsin Synchrotron Radiation Center User's Mtg.
6. G. N. Taylor, M. Y. Hellman, T. M. Wolf, and J. M. Zeigler, *Proc. SPIE* **920**, in press (1988).
7. D. C. Hofer, R. D. Miller, C. G. Willson, and A. Neureuther, *Proc. SPIE* **469**, 108 (1984).
8. J. M. Zeigler, L. A. Harrah, and A. W. Johnson, *Proc. SPIE* **539**, 166 (1985).
9. T. P. Tooman, *J. Opt. Soc. Amer. A*, in press (1989).
10. M. C. Hettrick and J. H. Underwood, *Appl. Opt.* **25**, 4228 (1986).
11. For the compounds $\text{Si}(\text{CH}_3)_4$ and SiH_4 , see R.N.S. Sodhi, S. Daviel, and C.E. Brion, *J. Electron. Spectrosc. Relat. Phenom.* **35**, 45 (1985).
12. For the compounds SiCl_4 , SiO_2 and SiF_4 , see J. L. Dehmer, *J. Chem. Phys.* **56**, 4496 (1972).
13. K. Takeda, M. Fujino, K. Seki, and H. Inokuchi, *Phys. Rev. B* **36**, 8129 (1987).
14. L. A. Harrah and J. M. Zeigler, *Macromol.* **20**, 601 (1987).
15. G. Loubriel and J. M. Zeigler, *Phys. Rev. B* **33**, 4203 (1986).
16. B. L. Henke, P. Lee, T. J. Tanaka, R. L. Shimabukuro, and B. K. Fujikawa, *Atom. Data Nuc. Data Tables* **27**, 1 (1982).
17. A. R. Gutierrez and R. J. Cox, *Polym. Photochem.* **7**, 517 (1986).

LASER TRIM REVISITED IN THE LIGHT OF AN EXCIMER LASER^{a)}

MICHEL GAUTHIER,* RICHARD BOURRET,**
GERARD GAVREL,*** and RICHARD CARNEGIE***

*Laser Chemistry Group, Division of Chemistry, National Research Council of Canada, Ottawa, Canada, K1A 0R6

**NRC Summer Student 1988

***Network Access Division, Northern Telecom Canada Limited, P.O. Box 1000, Aylmer, Québec, Canada, J9H 5M6

ABSTRACT

In the Laser Chemistry Group's program aimed at understanding the basic mechanisms involved in the fabrication and characterization of integrated circuits, we have converted an infrared laser-based, thick film trimming technique, which is over 15 years old, to UV light. It is known that excimer lasers can be used for microfabrication of semiconductors and ceramics. Much cleaner ablations than those obtainable with the infrared lasers have been demonstrated in a large variety of materials. This, together with the fact that excimers with repetition rates over 1 kHz are presently on the market, leads us to propose that better accuracies and smaller drifts, should be achievable using excimer laser-based thick film hybrid circuit trimming. Results of XeCl laser trimming of over four hundred resistors, including temperature coefficient of resistance measurements and life tests at elevated temperatures, demonstrate that UV trimming is a factor of 10 better than the presently used infrared process.

INTRODUCTION

Laser trimming of printed resistors in thick film hybrid circuits is a well developed technology.¹⁻³ The suppliers of trimming systems are now focusing on high production rates of millions of resistors per day, but with a precision limited in most cases to 1%. This is satisfactory for most applications, but increased trimming accuracies together with a significant reduction in post-trimming resistance drift⁴ would be welcome for special applications.

Excimer laser machining of ceramics has been demonstrated to give promising results for applications in microfabrication.⁵ With excimer lasers, the wavelength is sufficiently short that the photon energy is comparable to the binding energy of many materials, so that "cold-machining" becomes a possibility.⁶ The very small number of publications on excimer laser processing of materials may be surprising considering the availability of commercial excimers for over 10 years. Poulin *et al* presented a convincing demonstration of the superiority of excimer lasers for processing free-standing films, for polymer photolithography, and for the removal of thin metal films over polymers.⁷ Another process of interest concerned the ablation of Se films.⁸

The industrial workhorses for laser processing of materials are, and will remain, according to all predictions, the CO₂ and Nd:YAG infrared lasers. They dominate the market to a point that only these industrial leaders were included in Sona's perspective on laser machining, although he recognized the promising future of excimer lasers.⁹ On the other hand, Humphries *et al* underlined the growing importance of the market for excimer lasers with a doubling of the number of installed lasers worldwide in just over 3 years, reaching 2000 in early 1986,¹⁰ and approaching 3000 at the end of 1988.¹¹

^{a)}Issued as NRCC # 29822

Laser machining of ceramics has been done almost exclusively in the infrared. Silicon nitride ceramics can be cut,¹²⁻¹⁴ and joined¹⁵ with CO₂ lasers. Ceramic materials up to 7 mm thickness have been cut successfully with a Nd:YAG laser.¹⁶ High thermal stresses caused cracks in the specimens.^{16,17} Nd:YAG laser processing of ceramics immersed in a liquid has been presented as an effective method for avoiding the formation of a recast layer and the appearance of cracks in the machined part.^{18,19}

The trimming of thick film hybrid circuits is presently done with Nd:YAG lasers, where the absorbed energy tends to spread out to the bothersome "heat-affected-zone", responsible for most of the drift. Sturrett stated that the primary cause of that drift was microcracking of the resistor material outside the laser kerf into the current path.²⁰ The effects of microcracking increase as the value of the paste increases, making the higher value paste the most critical. Sturrett described a process including closed-loop, real-time process monitoring and control yielding resistor drifts of less than 1% of the final trimmed value.

With the intention of improving significantly on this 1% figure, we thus set up to find the optimum trimming conditions for adjusting standard test resistors with an excimer laser. Short to medium time drifts, covering times 20 ms to several weeks after the trim, and TCRs²¹ have been measured, and are reported here.

EXPERIMENTAL

Test boards were positioned close to the focus of a 40 mm focal length UV lens which concentrated the light from a spatially filtered excimer laser beam. A Lumonics Model 860 XeCl laser, $\lambda = 308$ nm, was used in the unstable resonator configuration, at a pulse repetition frequency of 50 Hz. The beam size and energy density at the target were adjusted with a combination of the following methods: the positioning of properly sized apertures before and after the spatial filter; adjustment of the beam intensity using attenuators; and by a proper choice of the focusing lens to target distance. The beam was stationary and the boards were moved on an Aerotech XYZ microstepping motor driven translation stage. The beam profile at the target was as shown in Fig. 1, determined by scanning a 5 μ m wide slit across the beam, along a line perpendicular to both the beam direction and the trim cut. Test resistors from 10 and 100 kilohms Dupont Birox pastes were all trimmed the same way, cutting a single straight line across the resistors midway between the two ends, and cutting through half the width, as in the sketch, Fig. 2.

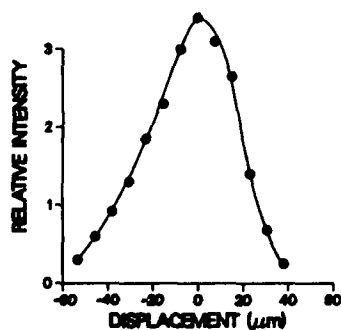


Fig. 1 Beam profile at the target position as a function of distance from beam axis.

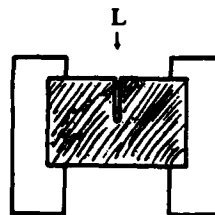


Fig. 2 Schematic illustration of the laser cut position, L, at the center of a printed resistor, (shaded area).

The test boards included resistors of various dimensions and aspect ratios as listed in Table I, where w is the width, and l is the length.

Table I. Resistor sizes used in this study, in mm.

w	1	1	1	1	1	1.5	2.5	2.5	2.5	2.5	2.5	2.5	2.5	5
l	1	2	3	4	5	1.5	1	1.5	2	2.5	3	4	5	5

The cut width was arbitrarily adjusted to $40\text{ }\mu\text{m}$, and the energy density was adjusted to 10 J cm^{-2} , in order to give visually acceptable clean ablations of the $15\text{ }\mu\text{m}$ thick resistors. The lateral displacement speed of the target was $18\text{ }\mu\text{m s}^{-1}$. Trimmed resistances were in the range 4 - 400 kilohms. Ablation rates, or speed of vertical penetration through the cermet in nm of resistor thickness per pulse, were obtained from Dektak profile measurements of partial ablations performed at various energy densities in the range $0.3 - 9.0\text{ J cm}^{-2}$. Results are shown in Fig. 3 for the 100 kilohm resistor paste.

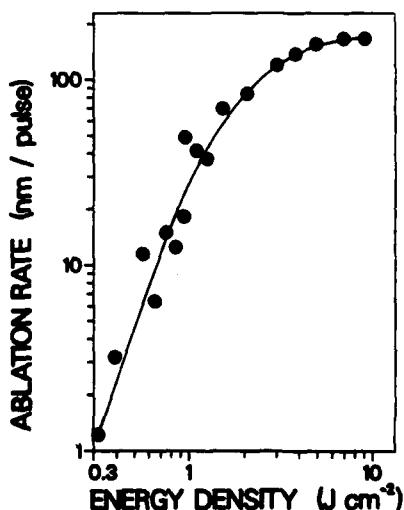


Fig. 3 Ablation rate of resistors from 100 kilohms paste, in nm of resistor thickness per laser pulse vs incident UV laser energy density.

RESULTS AND DISCUSSIONS

The main series of tests consisted of measuring the TCR of 432 resistors of various aspect ratios, before and after excimer laser trimming. A life test at $125\text{ }^{\circ}\text{C}$ was also performed for 130 hours.

The initial TCRs are displayed in Fig. 4, as open symbols. An overall mean TCR of 100 ppm was obtained which agrees perfectly with Dupont's specifications. The usual variation with resistor length, i.e. smaller TCRs for longer resistors, was also obtained. The after-trim TCRs are displayed in Fig. 4, as filled symbols. TCRs were systematically reduced in value after the trim. These results show that the trimming simply changed the aspect ratio of the resistors without any effect on their basic properties in the critical area of the current path ahead of the trim cut.

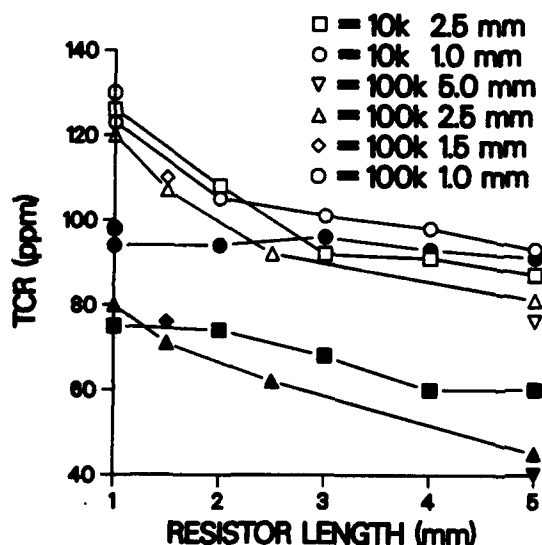


Fig. 4 Temperature Coefficient of Resistance, TCR, vs resistor length. Open symbols: before trim; filled symbols: after trim. Widths of 10 and 100 kilohms per square resistors are given in insert.

Since microcracking has been observed previously in infrared trimmings,²⁰ several trims were carefully examined with a scanning electron microscope, and no sign of any cracking has been detected. Figure 5 is a sample SEM picture of the end of a trim. This trim was 28 μm wide at the bottom of the cut, and 37 μm at the top. Voids in the cermet are opened up by the laser ablation. The important observation is the absence of cracks, and the very smooth appearance of the walls.

A life test was done with the 432 resistors, for 130 hours at 125 °C. Resistance drifted on average $0.058 \pm 0.037\%$ for the 320 resistors of 10 kilohms per square. In this set, the 1.0 mm wide resistors all drifted the same, independent of their length, except the shortest, 1.0 mm long, which drifted 0.094 %. The 2.5 mm wide resistors in the same set displayed a trend, where the longest drifted 24 % less than the shortest. The 100 kilohms per square resistors drifted more, as is usually the case: 112 resistors drifted an average of $0.105 \pm 0.074\%$. This second set contained a series of square resistors from 1 x 1 mm to 5 x 5 mm. The largest ones drifted 8 % less, on average, than the smallest.

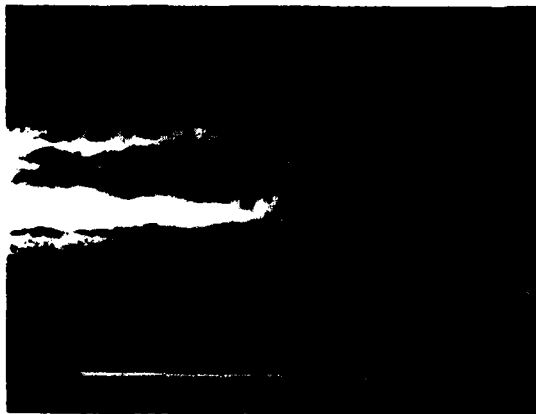


Fig. 5 SEM picture of an excimer laser trim. The white 28 μm wide portion at the center left is the alumina substrate. The white bar at the bottom is 100 μm long.

A 1000 hour life test was also performed on another smaller set of UV laser trimmed resistors of 10 kilohms per square, where the drift was observed to be significantly less. In this case, the trim cut was narrower at $30\text{ }\mu\text{m}$, and this is expected to reduce the drift as was observed in previous work.²⁰ The test consisted of passing a DC current of 50 mA through the resistors maintained at a constant temperature of $125\text{ }^{\circ}\text{C}$. Resistance was measured before and after the test, and at an intermediate time of 280 hours. No significant drift was observed in the second period between 280 and 1000 hours. The resistors drifted on average by 0.02 %, a factor of 10 less than is usually observed for infrared trimmed resistors.

The very small short-term drift, for times shorter than 10 minutes, resulting from excimer laser trimming is illustrated in Fig. 6. In this case, the resistance drifted 1 ohm, or 0.005 %, in the first minute after the trim. After 30 minutes, the total drift was 0.007 %. The resistance was monitored before, during, and after the trimming with an HP 3456A Digital Voltmeter and a microcomputer. During, and shortly after the trimming, the measurements were done at a rate of $44\text{ readings s}^{-1}$, then at 3 readings s^{-1} for the next 30 minutes. The translation stages and the sample holder were enclosed in an insulated box to maintain the ambient temperature constant at $24\text{ }^{\circ}\text{C}$, thus the variations in resistance observed are real variations in the electrical and mechanical properties of the trimmed resistors.

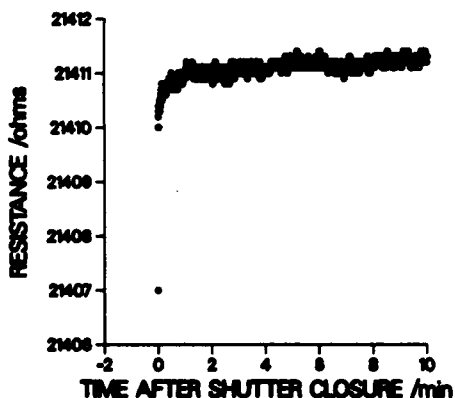


Fig. 6 Short-term resistance variations measured with a 6 digit multimeter during and shortly after the trim. The resistance was adjusted at 21,410.0 ohms.

All the several dozen trims monitored displayed the same small increase in resistance in the first minute after the end of the trim, as in Fig. 6, possibly resulting from a thermalization of the cermet. This very small short-term drift is evidence of the almost non-existent "heat affected zone", characteristic of infrared laser trimming. An additional lesser amount of drift during the following 30 minutes was present in all resistors.

CONCLUSION

This preliminary study on the ultraviolet laser trimming of printed resistors demonstrated that an improvement by a factor of 10 is achievable in the reliability of the trimming as well as in the long term drift in resistance.

Since the post-trim drift was observed to be only slightly dependent on resistor size, UV laser trimming should be the specified process in applications such as implantable devices or hearing aids where size is important, and where a trimming process giving very low drift and high stability after burn-in is essential.

Even though the UV laser trimming in this study was done at relatively slow speeds and modest laser power (6 mW), the same positive results should be obtained using a more powerful laser (30 W), at typical trim speeds (as used in the industry).

ACKNOWLEDGMENTS

We wish to express our thanks to Dr. J.B. Webb of NRC's Laboratory for Microstructural Sciences for the SEM pictures.

REFERENCES

- ¹M.C. Crawley, in Industrial Applications of Lasers, edited by H. Koebner (Wiley, Chichester, 1984) pp. 177-190.
- ²For the use of cermet pastes in the fabrication of thick film resistors, the reader is referred to textbooks such as: C.A. Harper, editor, Handbook of Thick Film Hybrid Microelectronics: A Practical Sourcebook for Designers, Fabricators, and Users, (McGraw-Hill, New York, 1974).
- ³Thin film circuits, formed by chemical etching of 0.1 μm thick coatings can also be laser trimmed. This is a different technology, not addressed in the present paper.
- ⁴The drift is the change in resistance with time, and is usually given in percent of the initial resistance value.
- ⁵K.J. Schmatjko and G. Endres, *Fachber. Metallbearb.* 64, 294 (1987).
- ⁶I.J. Spalding, in Proc. 4th Int. Conf. Lasers in Manufacturing, edited by W.M. Steen (IFS Ltd, Bedford, UK, 1987) pp. 229-234.
- ⁷D. Poulin, J. Reid, and T. Znotins, in Laser Materials Processing: Proc. 6th Int. Congress on Applications of Lasers and Electro-optics, edited by S.L. Ream, (IFS Publications, Bedford, UK, 1988) pp. 135-141.
- ⁸A. Jadin, M. Wautelet, and L.D. Laude, *Semicond. Sci. Technol.* 3, 499 (1988).
- ⁹A. Sona, in Laser Advanced Materials Processing, (High Temperature Soc. Japan, Osaka, Japan, 1987) pp. 661-673.
- ¹⁰M. Humphries, H.-J. Kahlert, and K. Pippert, in Proc. 4th Int. Conf. Lasers in Manufacturing, edited by W.M. Steen (IFS Ltd, Bedford, UK, 1987) pp. 255-262.
- ¹¹R. Sandwell (private communication).
- ¹²P.R. Soni and T.V. Rajan, *Trans. Indian Ceramic Soc.* 44, 42 (1985).
- ¹³R.L. Wallace and S.M. Copley, *Adv. Ceramic Materials* 1, 277 (1986).
- ¹⁴J. Yamamoto and Y. Yamamoto, in Laser Advanced Materials Processing, (High Temperature Soc. Japan, Osaka, Japan, 1987) pp. 297-302.
- ¹⁵I. Miyamoto, H. Maruo, K. Kuriyama, and Y. Horiguchi, in Laser Advanced Materials Processing, (High Temperature Soc. Japan, Osaka, Japan, 1987) pp. 237-242.
- ¹⁶R. Harrysson and H. Herbertsson, in Proc. 4th Int. Conf. Lasers in Manufacturing, edited by W.M. Steen (IFS Ltd, Bedford, UK, 1987) pp. 211-220.
- ¹⁷K.P. Cooper and J.D. Ayers, in Laser Materials Processing: Proc. 6th Int. Congress on Applications of Lasers and Electro-optics, edited by S.L. Ream, (IFS Publications, Bedford, UK, 1988) pp. 179-187.
- ¹⁸S. Ito, M. Nakamura, and W. Kanematsu, *Bull. Japan Soc. Precision Engg* 21, 167 (1987).
- ¹⁹N. Morita, S. Ishida, Y. Fujimori, and K. Ishikawa, *Appl. Phys. Lett.* 52, 1965 (1988).
- ²⁰M.S. Sturrett, in Proceedings of the 1987 International Symposium on Microelectronics, (Int. Soc. for Hybrid Microelectronics, Reston, VA 1987) pp. 140-146.
- ²¹The Temperature Coefficient of Resistance, TCR, is the fractional change in resistance with temperature, and is usually given in parts per million, ppm, of the initial resistance value, per degree Celsius.

SINGLE & MULTIPLE PULSE ABLATION OF POLYMERIC AND HIGH
DENSITY MATERIALS WITH EXCIMER LASER RADIATION AT 193NM AND
248NM

DAVID J. ELLIOTT AND BERNHARD P. PIWCZYK

DAVID J. ELLIOTT, IMAGE MICRO SYSTEMS, INC., 900 Middlesex
Turnpike, Bldg #8, Billerica, Massachusetts 01821

BERNHARD P. PIWCZYK, IMAGE MICRO SYSTEMS, INC., 900
Middlesex Turnpike, Bldg #8, Billerica, MA 01821

ABSTRACT

The evolution of the excimer laser from a research tool in the 1970's to the industrial models of the 1980's has opened up numerous applications in semiconductor manufacturing, materials processing, and biological and medical research. Present production-capable, computer-controlled excimer systems with handling equipment enabling efficient automation can now operate for up to 50 million shots before undergoing scheduled maintenance, with fluences remaining within $\pm 10\%$ in most cases. Thus, although many uses for the excimer laser are still research-oriented, production applications are rapidly emerging.

INTRODUCTION

Excimer lasers offer several key advantages as energy sources:

- o First, they can provide deep-ultraviolet radiation at relatively high average power. Early UV lasers, such as double or triple harmonic Nd:YAG and ion lasers, had output power of less than one watt. Excimers, at similar wavelengths, deliver up to 50 watts: energy levels consistent with the production throughput rates needed for many processes [1] [2].
- o Excimers have been shown to be essentially speckle-free, unlike earlier lasers operating in the ultraviolet spectrum. Speckle, an interference effect caused by high spatial coherence, causes localized excursions in the beam intensity profile which can result, for example, in non-uniform ablations in micro-machining applications. Excimers have relatively low spatial coherence, and are therefore essentially free of speckle.
- o Excimers, as sources of deep ultraviolet radiation, are much more efficient than alternative light sources. The mercury arc lamp, with strong G-line, H-line and I-line peaks, falls off dramatically in the far ultraviolet region, just where the excimer begins. While mercury vapor and mercury

halide lamps may have high conversion efficiencies (~50%), their high infrared content requires considerable output filtering. The excimer lasers on the other hand, produce essentially monochromatic radiation without the requirement of filtering.

The application of excimer lasers for microelectronic fabrication processes is particularly promising. The continued reduction of VLSI circuit geometries, together with increasingly higher levels of circuit integration create a demand for new circuit fabrication technologies. One of limitations of current IC fabrication technology is the use of high temperature processing. High temperatures distort silicon wafers, causing a loss of alignment control and resulting in a significant reduction in device yield. Excimer laser technology at very short ultra-violet wavelengths offers the possibility of low temperature processing, including the following major applications: Photoresist ablation over alignment marks, annealing, doping, and etching. In addition, applications in IC packaging, circuit personalization and fiber optics appear as very promising new applications for excimer laser technology in the electronics industry.

The most significant advantage of the excimer laser as a light source in VLSI processing is the range of short wavelengths available. This translates directly into better resolution. Argon Fluoride, for example, offers a 193nm wavelength at power levels exceeding those of the mercury lamp at G, H and I-lines.

ABLATION

Several years after the invention of the excimer laser, a light absorption phenomenon termed "ablative photodecomposition" or "photoablation" was discovered [3]. This phenomenon occurs when pulsed ultraviolet radiation is absorbed on the surface of an organic solid; the high energy of UV photons is intensely absorbed by the polymer molecules, resulting in excitation within the molecules.

This energetic absorption results in bond breaking when the incoming UV energy exceeds the molecular bonding energy. The point at which such bond breaking occurs is termed the "ablation threshold". The ablation thresholds for a number of materials are given in the following table [4]:

ABLATION THRESHOLDS FOR 193NM EXCIMER LASER
PULSE ENERGY (MJ/CM²)

PHOTOLYTIC:

Nitrocellulose	Less than 20
Novolak-Based Photoresist	30
Polycarbonate	40
Polyimide	45

PYROLYTIC:

Polysilicon	100
Silicon Nitride	195
Spin-on-Glass	200
Silicon Dioxide	350
Silicon	Greater than 1000

The principal advantage of photoablation is the low thermal component of this process at low fluence levels. This property avoids undesirable melting or carbonization of organic molecules, a problem that often exists when visible or infrared laser radiation is used.

Organic polymer molecules consist of chains of smaller molecular units called monomers. A typical polymer chain will contain in the range of 1000-100,000 atoms of carbon, hydrogen, oxygen and nitrogen. These molecules absorb 95% of the incident energy at 193nm, and undergo a radiative lifetime (excited state) of about 0.1 nanosecond duration. The bond breaking lifetime is estimated to be in the 1-10 picosecond range [5]. The depth of the absorption is less than 3000 angstroms, typically about 2000 angstroms, depending upon the particular polymer type, the fluence, and the area being exposed.

In photoablation reactions, the polymer molecules undergo bond scission, with excess energy remaining in the fragments in the form of thermal and kinetic energy. The rapid expansion created by this excitation and bond cleavage gives rise to the ejection of ablation products, gases and often small particles; the material transport time is estimated at about 10 microseconds. The accompanying fluorescence of ejected material often causes a plume of luminescence that can be readily observed. A scavenging nozzle designed to capture the by-products of ablative photodecomposition may be used to remove debris which can be a result of photoablation [6]. Figure 1 shows the amount of material removed as a function of fluence for 3 excimer wavelengths. The target was polyimide.

ALIGNMENT MARK ABLATION

Polymer ablation is also applicable in IC manufacturing for removing photoresist over the alignment marks on wafers prior to the patterning step, in order to avoid partial obscuration of the marks by the resist. Avoiding such obscuration of the alignment marks improves the overlay registration accuracy of the exposure system, in turn

increasing the yield during device production. More importantly, it also permits the development of even higher resolution chip designs: since IC devices now require up to 20 individual masking steps, overlay registration, the precise alignment of the current layer with those that lie under it, has become as important as resolution.

Initial tests have shown that overlay can be improved from 0.3um (3 sigma) using die-by-die alignment with resist left above the marks to as little as 0.05um, by first removing the resist with pulses of excimer laser light at 193nm. The typical beam fluence used to ablate the alignment marks is 500 mJ, an average of 15 pulses being sufficient to remove most layers of resist without damage to the underlying mark. Figure 2A shows an ablated alignment mark, while Figure 2B shows the overlay improvement possible with this technique. [6]

FIBER OPTIC COMMUNICATIONS

Optical fiber communications is another rapidly growing field in which the excimer laser is beginning to play an important role. Excimer laser micromachining of optical fibers can be used to create "tap" locations at which light signals can be extracted through the side of the fiber. The feasibility of welding optical fibers by means of a small number of excimer laser pulses has also been demonstrated.

These micromachining and fusing experiments were performed using a IMS XLR-100 system at 193 nanometers within a fluence range of 5-12 J/cm², at various pulse repetition rates and with a computer controlled aperture shaping the beam in areas ranging from 10 to 140 microns on a side. The system is shown in Figures 2A and 2B, while the results of one such experiment are depicted in Figure 3.

CIRCUIT PERSONALIZATION AND REPAIR

Patterning of gold for electronic conductors and interconnects is a key manufacturing process usually requiring multiple process steps. Gold on a hybrid circuit device can be structured in a single, "dry" step using the energetic photons from an excimer laser exposure system. The SEM photo shown in Figure 4 illustrates the resolution and edge acuity possible with photo-thermal ablation at 248 nanometers (Krypton Fluoride). Photo-thermal reactions use thermal effects of photons rather than ablative photodecomposition for material removal.

Figure 4 shows a square hole made in a gold film by shaping the excimer laser beam with a computer controlled, multi-bladed aperture. A fluence of approximately 12J/cm² was used at a repetition rate of up to 200 Hz. Typical applications for this capability are integrated circuit

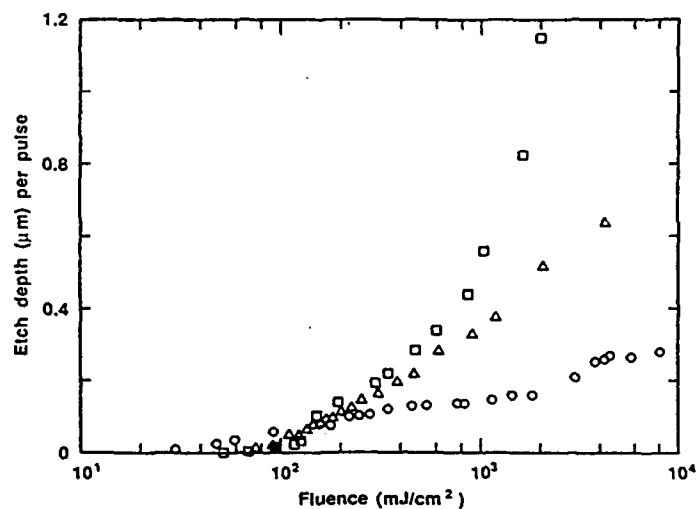


FIGURE 1.

A plot of depth of material removed per pulse as a function of fluence; sample: polyimide film, 125 μm thick. Laser pulse: \circ , 193 nm; Δ , 248 nm; \square , 308 nm. Each data point averaged more than ten to several hundred pulses; uncertainty, $\pm 8\%$.

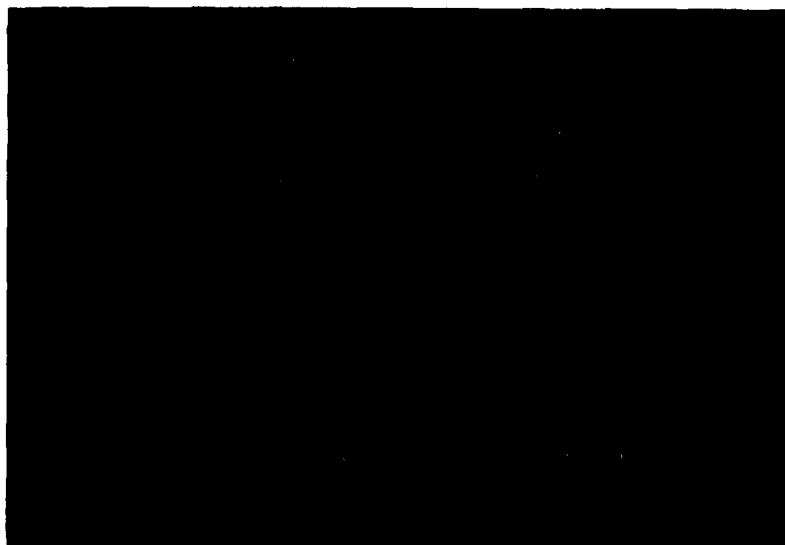
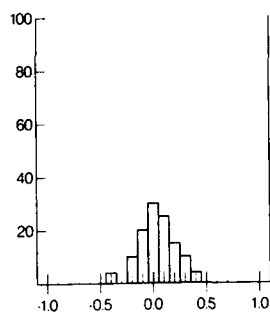


FIGURE 2A.
ABLATED ALIGNMENT MARK USING 10 PULSES OF 193NM
RADIATION FROM LAMBDA PHYSIK 105i EXCIMER LASER
IN ALPHA SYSTEM

Before Ablation
0.159 μm Standard Deviation, 3



After Ablation
0.041 μm Standard Deviation.

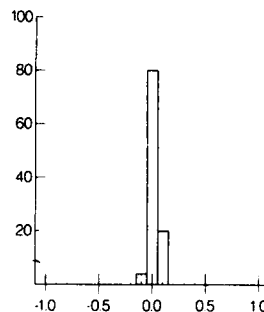


FIGURE 2B.
OVERLAY IMPROVEMENT USING RESIST ABLATION OF
ALIGNMENT MARKS: 1) BEFORE ABLATION, 0.159 μm
STANDARD DEVIATION; AND 2) AFTER ABLATION WITH
0.041 STANDARD DEVIATION

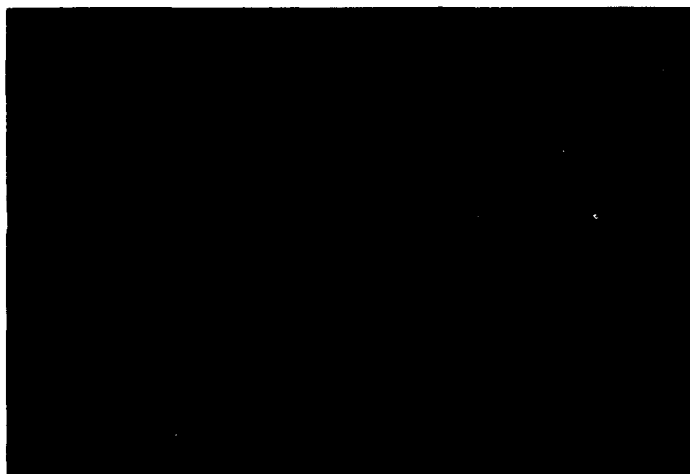


FIGURE 3.
ABLATED STRUCTURES IN AN OPTICAL FIBER USING
IMS EXCIMER LASER SYSTEM

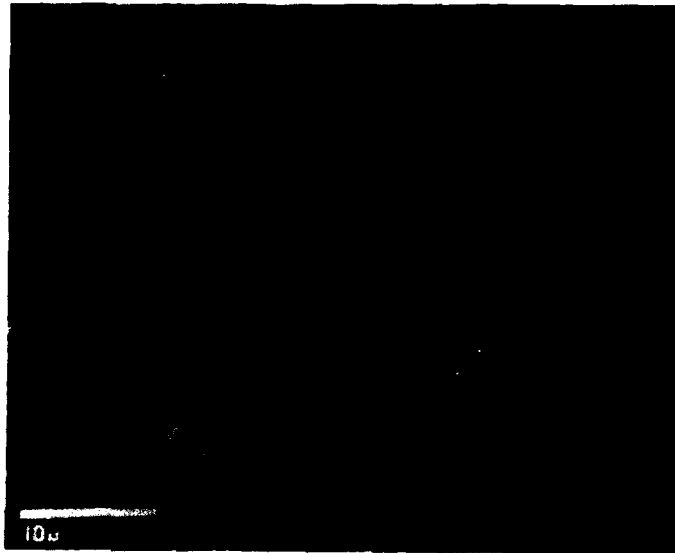


FIGURE 4.
GOLD LAYER 15 MICRONS THICK ABLATED WITH HIGH FLUENCE
DELIVERY SYSTEM AT 193NM

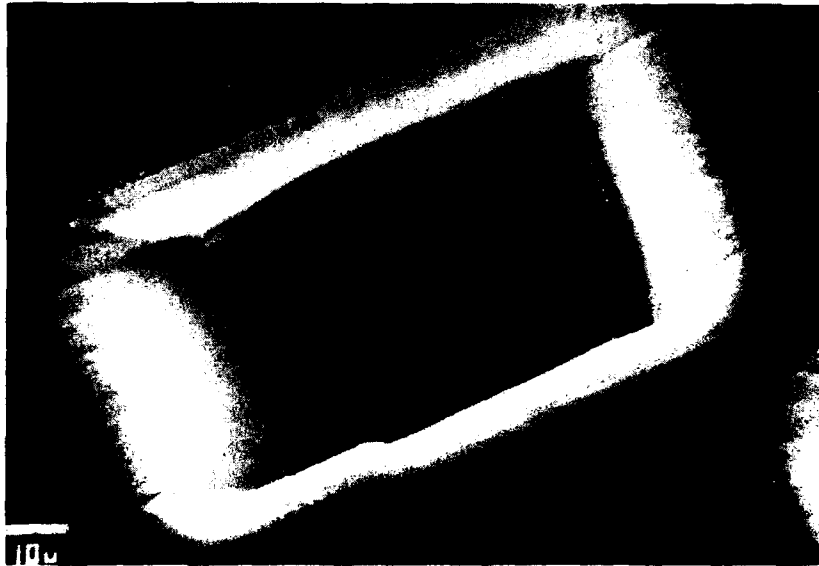


FIGURE 5.
POLYIMIDE LAYER ABLATED DOWN TO COPPER LEAD USING
248NM EXCIMER LASER DELIVERY SYSTEM

personalization (link cutting) and removal of short circuits to repair interconnect patterns.

INTEGRATED CIRCUIT PACKAGING

VLSI devices with more than one or two hundred connections create a demand for new IC packages. In order to interconnect today's advanced integrated circuits, a new strategy involving the use of alternating layers of a dielectric material and a metallic conductor is emerging.

Frequently, the combination of choice is a thick (3-15 μ m) dielectric layer of polyimide, together with a copper conductive layer. The excimer laser is used to create a series of openings or vias in the dielectric material, permitting electrical access to the conductor. Copper conductors can also be cleanly cut with the excimer. Figure 5 illustrates the sharp side walls in a copper conductor and the surrounding polyimide obtained by utilizing an excimer laser at a wavelength of 193 nm and a fluence of approximately 12 Joules/cm².

BIOMEDICAL RESEARCH

Because of the relatively minor thermal contribution in the action of the excimer laser as compared with the larger effect of ablative photodecomposition, such a system is an ideal tool for incising delicate specimens without significant thermal or structural damage. This property is of great advantage in genetic and biological research, permitting fine sectioning of living tissue with a minimum of collateral damage to the surrounding tissues.

Figure 6A is a SEM photograph of a human red blood cell, showing a cut performed by means of a finely focused excimer laser exposure at a wavelength of 193nm. A sharp, clean, high resolution cut is observed. Similarly, Figure 6B shows 0.3 micron punctures made in the cell membrane using a submicron beam size.

SUMMARY AND CONCLUSIONS

This paper has touched upon some promising new applications for excimer lasers in the fields of electronics manufacturing, fiber optic communications, and biomedical research. In most cases, results demonstrating the applicability of excimers to these fields have been presented.

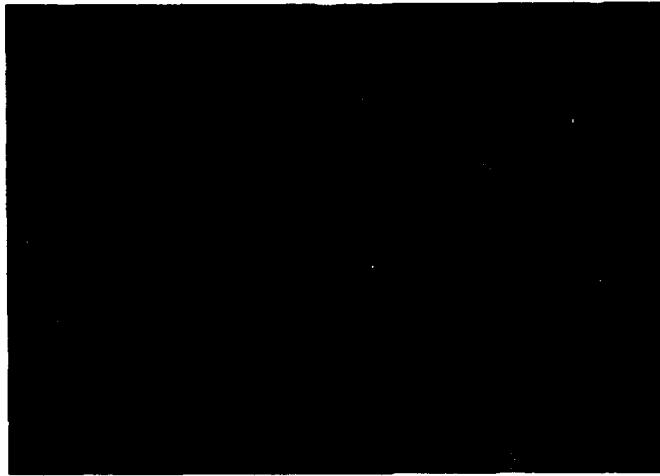


FIGURE 6A.
RED BLOOD CELL CUT AT 193NM



FIGURE 6B.
SUB-MICRON PUNCTURES OF A RED BLOOD CELL WALL
USING 193NM EXCIMER LASER SYSTEM

Excimer laser light pulses at wavelengths of 193nm and 248nm have been used experimentally to improve alignment accuracy for wafer exposure systems; to micromachine fiber components for fiber optic networks; to incise cells for biological research; and to perform high resolution micromachining for superconductor applications.

Future generations of excimer laser systems will address as yet unforeseen production applications which are the outgrowth of current research. In the semiconductor manufacturing field alone, laser-assisted etching, deposition, doping and direct lithography are all techniques that show potential for significantly improving production efficiency and allowing products of vastly greater sophistication to be created. Today's excimer laser systems have reached a level of maturity which permits the groundwork to be laid for such future progress.

REFERENCES

1. H. Egger, H. Pummer, and C.K. Rhodes, EXCIMER LASERS FOR THE GENERATION OF EXTREME ULTRAVIOLET RADIATION, Laser Focus, June, 1982.
2. H. Pummer, THE STATUS OF COMMERCIAL EXCIMER LASER DEVELOPMENT, Lambda Physik, 289 Great Road, Acton, MA July, 1985.
3. B. Garrison, R. Srinivasan, LASER ABLATION OF ORGANIC POLYMERS: MICROSCOPIC MODELS FOR PHOTOCHEMICAL AND THERMAL PROCESSES, J. Appl. Phys. 57 (8), 15 April, 1985.
4. R. Srinivasan and Bodil Braren, ABLATIVE PHOTODECOMPOSITION OF POLYMER FILMS BY PULSED FAR-ULTRAVIOLET (193NM) LASER RADIATION: DEPENDENCE OF ETCH DEPTH ON EXPERIMENTAL CONDITIONS, Journal of Polymer Science: Polymer Chemistry Edition, Vol. 22, 2601-2609 (1984), John Wiley & Sons, Inc.
5. D.J. Ehrlich, EARLY APPLICATIONS OF LASER DIRECT PATTERNING: DIRECT WRITING AND EXCIMER PROJECTION, Solid State Technology, December, 1985.
6. K.J. Polasko, D.J. Elliott, B.P. Piwczyk, VLSI PATTERN REGISTRATION IMPROVEMENT BY PHOTOABLATION OF RESIST-COVERED ALIGNMENT TARGETS, IEEE Triple Beams Meeting, Woodland Hill, CA, 1987.

Author Index

Adler, E.L., 399
 Ajuria, S., 455
 Al-Jumaily, G.A., 17
 Allen, Jr., S.J., 441
 Allen, R.M., 515
 Aoyagi, Y., 171
 Arai, H., 315
 Araki, S., 539
 Ashby, C.I.H., 269
 Aylett, M.R., 285

Bachmann, F., 91
 Baller, T.S., 299
 Baum, T.H., 119
 Bedair, S.M., 165
 Beeson, K.W., 321
 Bensahel, D., 609
 Berger, S.D., 515
 Bernhardt, A.F., 559
 Beuermann, Th., 79
 Bianconi, M., 591
 Biunno, N., 435
 Blackmore, G.W., 183
 Blauner, P.G., 483
 Boch, E., 195
 Bonnell, D.W., 353
 Bcuree, J.E., 251
 Bourret, R., 399, 621
 Boyd, I.W., 421
 Boyer, L.L., 17
 Braren, B., 405
 Bresse, J.F., 251
 Brown, L.M., 515
 Buckett, M.I., 521
 Bues, K., 411
 Burke, H.H., 291
 Butt, Y., 483

Cai, P.Y., 73
 Campbell, E.E.B., 411
 Carnegie, R., 621
 Caudano, R., 461
 Chakabarti, U.K., 489
 Chan, S-W., 441
 Chang, R.P.H., 533
 Chen, B., 435
 Chow, G-M., 393
 Clements, N.S., 321
 Cody, N.W., 177, 233
 Cole, H.S., 579
 Collins, G.J., 227, 239
 Collins, R., 219
 Comita, P.B., 125
 Cong, Y., 219
 Contolini, R.J., 559

Cooper, E.I., 603
 Correra, L., 591

D'Anterrosches, C., 609
 De Rosa, F., 441
 de Zwart, S.T., 299
 Dickinson, J.T., 385
 Dieleman, J., 3, 299
 Dodson, B.W., 29
 Donnelly, V.M., 147, 159
 Dosluoglu, T., 177
 Durose, K., 285

Eden, J.G., 201
 Ehrlich, D.J., 259, 447, 585
 El-Masry, N.A., 165
 Elliott, D.J., 627
 Emerson, B., 489
 Ericsson, T., 501
 Eschbach, P.A., 385

Fahmy, A.A., 165
 Feil, H., 299
 Fleddermann, C.B., 527
 Flicstein, J., 251
 Fogarassy, E., 195, 591
 Foulon, F., 591
 Freedman, A., 57
 Fuchs, C., 195
 Fullowan, T.R., 489
 Furuno, S., 73

Gauthier, M., 399, 621
 Gavrel, G., 621
 Giess, E.A., 603
 Goto, Y., 213
 Gupta, A., 603

Haegel, N.M., 489
 Hagerhorst, J.M., 347
 Hailgh, J., 285
 Hails, J.E., 183
 Hanabusa, M., 73
 Hastie, J.W., 353
 Helvajian, H., 359
 Hess, P., 85
 Hill, H., 183
 Ho, W., 245
 Hobson, W.S., 489
 Hussey, B.W., 603
 Hussien, S.A., 165

Iguchi, S., 73
 Ingemarsson, P.A., 501
 Inoue, G., 371

Irvine, S.J.C., 183
Iwai, S., 171

Jackson, R.L., 119
Jagannathan, R., 603
Jasim, K.M., 139
Jen, C-K., 399
Jensen, K.F., 107
Jones, C., 201
Jones, K.S., 489

Kamaji, H., 539
Karam, N.H., 165
Kasatani, K., 69
Kasuya, A., 365
Kawasaki, M., 69, 305, 371
Kiely, C.J., 201
Kisker, D.W., 239
Klemens, P.G., 469
Kodas, T.T., 125
Konstantinov, L., 85
Krchavek, R.R., 441
Krishnaswamy, J., 219
Kubiak, G.D., 615
Kunz, R.R., 447
Küper, S., 375

Lane, E., 489
Langan, J., 311
Larson, C.E., 119
Liu, Y.S., 579
Lu, Y.F., 333, 339

Macaulay, J.M., 515
Maki, P.A., 585
Mannhart, J.D., 347
Marella, P.F., 569
Marks, L.D., 521
Matsushashi, H., 63
Matsumoto, S., 189, 597
Matsumura, T., 315
McCartney, M.R., 509
McCaulley, J.A., 147, 159
McCrary, V.R., 147, 159
McNally, J.J., 17
McNeil, J.R., 17
Meguro, T., 171
Meilunas, R., 533
Meisner, G.P., 133
Melngailis, J., 483
Mercier, J., 609
Meyer, M.S., 133
Miceli, P.F., 441
Miracky, R.F., 547
Moylan, C.R., 327
Mullin, J.B., 183
Murahara, M., 315

Nagahori, T., 189
Nagai, H., 213

Nagatomo, S., 333, 339
Namba, S., 171
Namba, S., 333, 339
Narayan, J., 219, 435
Nicoletti, S., 591
Nipoti, R., 591
Nishi, N., 69, 305
Nishikawa, S., 63
Nishina, Y., 365
Norimoto, K., 539
Nowak, R., 85

O'Neill, J., 45
Ohno, S., 63
Oikawa, A., 73
Ong, T.P., 533
Oprysko, M.M., 347
Ortiz, C., 455
Osgood, Jr., R.M., 45, 279, 291
Outka, D.A., 615

Paik, K.W., 495
Partridge, J.P., 469
Pearson, S.J., 489
Pease, R.F., 569
Pederson, L.R., 385
Perio, A., 609
Petit, E.J., 461
Pihlstrom, B., 239
Piwczyn, B.P., 627
Podlesnik, D.V., 279
Possnert, G., 501
Pougnat, A.M., 251
Price, Jr., P.E., 107
Purohit, P.V., 259

Rager, B., 91
Regolini, J.L., 609
Reicher, D.W., 17
Rengan, A., 219
Rieger, D., 91
Ro, J.S., 483
Rogers, C.T., 441
Rommelueire, J.F., 251
Rothschild, M., 259, 447
Ruberto, M.N., 279
Rubin, K.A., 455
Ruoff, A.L., 495

Saeki, H., 597
Sanchez, E., 45
Sato, A., 69
Sato, H., 69, 305, 371
Scarmozzino, R., 291
Schenck, P.K., 353
Scheuermann, M.R., 347
Schnoes, M.L., 239
Sell, J.A., 133
Shaw, P., 45

Sheng, K., 533
Sheng, T.Y., 227
Shimo, N., 99
Short, K.T., 489
Shorter, J.A., 311
Siffert, P., 195
Singh, R., 435
Slaoui, A., 591
Smith, D.J., 509
Solanki, R., 177, 233
Srinivasan, R., 405
Srivatsa, A.R., 219, 435
Steinbruchel, C., 477
Steinfeld, J.I., 311
Stinespring, C.D., 57
Strongin, D.R., 125
Strutt, P.R., 207, 393, 469
Stuck, R., 591
Stuke, M., 79, 375
Sudarsan, U., 177, 233
Summersgill, J.P.L., 285

Takai, M., 333, 339
Tavitian, V., 201
Thompson, C.V., 483
Tokuda, K.L., 239
Treyz, G.V., 291
Tsuei, C.C., 347
Tu, C.W., 147
Tuckerman, D.B., 559, 569
Tyndall, G.W., 327

Ulmer, G., 411
Unamuno, S., 591

van Veen, G.N.A., 299
van Zwol, J., 299
Vasile, M.J., 489
Vedam, K., 219

Wada, J., 597
Wäppling, R., 501
Weisberg, A.H., 559
Welle, R.P., 359
West, D.R.F., 139
West, J.P., 527
Williams, F.L., 17
Willner, A.E., 279
Wong, M.S., 533
Wu, Z., 45

Xiao, T.D., 207
Xin, X., 311

Yagi, T., 213
Ying, Z.C., 245
Yoshihara, K., 99
Yoshioka, S., 597
Yu, Z., 227

Zarnani, H., 227
Zeigler, J.M., 615

Subject Index

- ablation, ArF laser
 - of photoresists 627
 - of $\text{YBa}_2\text{Cu}_3\text{O}_{7-x}$ film patterning 347
- ablation, KrF laser
 - of Ag, prod. energies 359
 - of Al, prod. energies 359
 - of Au 625
 - of C (graph.), opt. spectrom., spatial/temporal 365
 - of Ge, opt. spectrom., spatial/temporal 365
 - of $\text{Na}_2\text{O}-3\text{SiO}_2$, mass/opt. spectrom., spat./tempor. 385
 - of NaCl
 - pulsewidth depend. 375
 - of Pd-containing films
 - in Cu film patterning 579
 - of poly(methyl methacrylate)
 - pulsewidth depend. 375, 405
 - of poly(tetrafluoroethylene)
 - pulsewidth depend. 375
 - of polyimide
 - pulsewidth depend. 405
 - of Si, opt. spectrom., spatial/temporal 371, 365
- ablation, Nd-Yag laser (532nm)
 - of C (graphite), masses/energies, product 353
 - of $\text{YBa}_2\text{Cu}_3\text{O}_{7-x}$, masses/energies, product 353
- ablation, XeCl laser
 - ceramic resistor trimming 621
 - of Al
 - patterning of Al on PVD 399
 - of polyimide films, masses/energies, ionic product 411
- ablation, XeF laser
 - of Ag, product energies 359
 - of Al, product energies 359
- activation energy 63, 69, 91, 107, 159, 189
- atomic layer epitaxy (ALE), laser assisted 171
- Arrhenius behavior 63, 107, 159, 189
- Arrhenius parameters
 - coverage dependent 159
- bilayer etching 585
- boron doping 591, 597
- Bremsstrahlung process 365
- C_1^+ , C_2^+ , C_3^+ 353
- carrier photogen., Ar^+ laser
 - in GaAs/AlGaAs multilayers
 - etching, aq. HNO_3 279
- ceramics 333, 621
- chain reaction 99
- characterization of surfaces
 - see:surface characterization
- chemical vapor deposition
 - see:deposition, chemical vapor
- chemical vapor transport 393
- chemisorption, dissociative
 - of Br_2 on Ni
 - etching, Ni films 327
 - of CF_3 on Si 311
 - of Cl_2 on GaAs 585
 - of Cl_2 on Si
 - etching, Si films 3, 299
 - of NF_3 on Si 311
 - of $\text{TiCl}_4/\text{Al}(\text{CH}_3)_3$ on surfaces
 - TiAl catalyst formation 259
 - of XeF_2 on Si 311
- cladding, CO_2 laser assisted
 - of steel substrate with
 - Ni-Fe-Cr-Al alloy 139
- clusters, large size 365
- co-evaporation 393
- collisional relaxation 91
- Coulomb explosion 411
- crystallization kinetics 455
- CuO^+ 353
- CVD, electron-beam assisted
 - see:deposition, electron-beam assisted
- CVD ion-beam assisted
 - see:deposition, ion-beam assisted
- CVD, lamp-induced
 - see:deposition, lamp-ind.
- CVD, laser-induced
 - see:deposition, laser-ind.
- decomposition, Ar^+ laser induced
 - of $\text{Ga}(\text{C}_2\text{H}_5)_3$ and AsH_3
 - surface effect, photochem. 171
 - of Y/Ba/Cu trifluoroacetate films
 - depos. $\text{YBa}_2\text{Cu}_3\text{O}_{7-x}$ lines 603
- decomposition, electron beam induced
 - of SiH_4 and H_2
 - depos. epitaxial Si 527

- decomposition, ion induced
 of $\text{Au}(\text{CH}_3)_2(\text{hfac})$ by Ga^+ ions
 depos. Au lines 483
- deposition, electron assisted
 cold cathode discharge, using
 of Si epitaxial films 527
- deposition, ion assisted
 focused Ga^+ ions, using
 of Au lines 483
- low energy ions, epitaxial growth
 dynamics modeling 29
- O_2^+ ion assisted deposition,
 metal oxide opt. films 17
- deposition, ion sputtered
 Ar^+ ions, using
 of $\text{Pb}_{(1-x)}\text{La}_x(\text{Zr,Ti})_{1-x/4}\text{O}_3$ 17
- deposition, lamp induced
 H plasma disk lamp, using
 of ZnSe films 239
- Hg lamp, using
 of $\text{Hg}_{(1-x)}\text{Cd}_x\text{Te}$ epitaxial
 films 233
- of Ti/Al catalysts 259
- VUV windowless lamp, using
 of AlN films 227
- of Si (amorphous) films 227
- of Si_3N_4 films 227
- Xe lamp, using
 of Mo films 245
- deposition, lamp/laser
 Hg lamp and Ar^+ laser, using
 of Al lines 251
- deposition, laser induced
 Ar^+ laser (257 nm), using
 of CdTe epitaxial films 183
- Ar^+ laser (351 nm), using
 Pd pattern for Cu depos. 579
- Ar^+ laser, using
 of Al, kinetics method 125
- of Al lines 119, 251
- of Au, kinetics method 125
- of Au lines 107, 133
- of GaAs ALE 171
- of GaAs epitaxial films 165,
 171
- of GaP epitaxial lines 177
- of Pd lines 107
- of Si lines 189
- of W lines 547
- of $\text{YBa}_2\text{Cu}_3\text{O}_{7-x}$ 603
- ArF laser, using
 of Al films 73
- of Bi metal particles 99
- of C (diamond) films 213
- of Cd films 45, 57
- of Ga (GaAs) films 147, 159
- of GaP epitaxial films 177
- of Ge epitaxial films 201
- of In, $\text{In}(\text{CH}_3)_3$ photophys. 69
- of Pb metal particles 99
- of Si, $\text{Si}(\text{CH}_3)_4$ photochem. 195
- of Si, $\text{Si}_2(\text{CH}_3)_6$ photochem. 195
- of SnO_2 films 447
- of W films 63
- of Zn films 45
- CO_2 laser, using
 of Au lines 133
- of GeSe films 207
- of W/SiO₂ fiber composite 393
- dye laser (200-320 nm), using
 of Al, $\text{Al}(\text{CH}_3)_3$ photophys. 79
- KrF laser, using
 of Bi metal particles 99
- of Cr, Cr^* kinetics 91
- of Cr films 85
- of GaP films 177
- of Pb metal particles 99
- of Pd pattern for Cu dep. 579
- of Te films 57
- XeCl laser evaporative
 of C (diamondlike) films 219
- XeCl laser, using
 of TiO_xN_y films 435
- XeF laser, using
 of Ga (GaAs) 147, 159
- deposition, chemical vapor
 rapid thermal processing, by
 of Si epitaxial films 609
- deposition, plasma enhanced
 microwave plasma, using
 of C (diamond) films 533
- RF plasma, using
 of Si (amorphous) films 539
- deposition precursors
 see: precursors, deposition
- deposition, UV to IR assisted
 245
- desorption, ArF laser
 of surface oxides from Sb 461
- desorption, electron beam
 of metal oxides/fluorides
 experiments/modeling 515
- of oxygen from metal oxides,
 monoxide growth epitaxy 509
- desorption, XeCl laser
 of SiCl_x from Si surface 299
- deuterium lamp 73
- diamond and diamondlike films
 213, 219, 533
- dielectrics
 AlN, deposition 227
- ceramics, ablation 621
- LiNbO_3 , etching 321
- metal oxide coatings, depos. 17
- metal oxides/fluorides 515
- Mn-Zn ferrite, etching 339
- Mn-Zn ferrite/sendust
 composite, etching 333
- $\text{Na}_2\text{O}-3\text{SiO}_2$, ablation 385
- NaCl , ablation 375

- Ni_3O_4 , formation 521
 $\text{Pb}_{1-x}\text{La}_x(\text{Zr}_y\text{Ti}_{1-y})_{1-x/4}\text{O}_3$
 electro-optic film, depos. 17
 poly(methyl methacrylate),
 ablation 375, 405
 poly(tetrafluoroethylene),
 ablation 375
 polyimide, ablation 411
 polyimide, ion etching 495
 Si_3N_4 deposition 227
 SiO_2 photo-induced growth 421
 SiO_2 , phys. sputtering, ion 477
 SiO_2 react., CF_x radicals 311
 SnO_2 , depos. films 447
 $\text{TiN}/\text{TiN}_x\text{O}_y$, depos. films 435
 TiN , formation 469
 diffraction-limited laser 455
 diffusion constants gas 91
 direct write, deposition
 Ar^+ laser (351nm) induced
 of Pd on polyimide 579
 Ar^+ laser (488nm) induced
 of W on polyimide 547
 Ar^+ laser induced
 finite element model 107
 of Al lines 119
 of Au lines 107, 133
 of GaAs epitaxial lines 165
 of GaP epitaxial lines 177
 of Pd lines 107
 of Si lines 189
 of $\text{YBa}_2\text{Cu}_3\text{O}_{7-x}$ lines 603
 CO_2 laser induced
 of Au lines 133
 Ga^+ ion beam induced
 of Au 483
 Hg lamp/ Ar^+ laser induced
 of Al lines 251
 direct write, etching
 Ar^+ laser (257nm) induced
 of InP 285
 direct write, reaction
 Ar^+ laser induced
 O-depletion from
 $\text{YBa}_2\text{Cu}_3\text{O}_{7-x}$ 441
 directly patterned oxide 421
 disk-plasma VUV lamp 227, 239
 dissociative chemisorption
 see: chemisorption, dissociative
 doping, ArF Laser assisted
 of Si with boron atoms
 by B_2H_6 photol./pyrol. 597
 by BCl_3 photol./pyrol. 591
 doping, XeF laser assisted
 of Si with boron atoms
 by BCl_3 pyrol. 591
 doping precursors
 see: precursors, doping
 electro-optical materials 29
 electron assisted deposition
 see: deposition, electron asst.
 electron beam damage 515
 electron beam decomposition
 see: decomposition, elec. beam
 electron beam desorption
 see: desorption, electron beam
 electron microscope 509
 epitaxial, growth
 CdTe on CdTe, GaAs, or Si 177
 Ga on GaAs 165, 171, 585
 GaP on Si and GaP 177
 Ge on GaAs 201
 $\text{Hg}_{1-x}\text{Cd}_x\text{Te}$ on CdTe, GaAs,
 and GaAs/Si 233
 ion induced, dynamics model 29
 monoxide phase,
 transition metal oxides 509
 Si on Si 527, 609
 etching, Ar^+ laser
 of GaAs and Ga(AsP)
 surface carrier
 dependence 269
 of GaAs/AlGaAs multilayers 279
 of LiNbO_3 321
 of Mn-Zn ferrite 339
 of Mn-Zn ferrite/sendust 333
 etching, Ar^+ laser (257 nm)
 of InP
 direct write/patterning 285
 etching, Ar^+ laser (350-360 nm)
 of Si
 via formation 291
 etching, ArF laser
 of GaAs
 patterned, in MBE system 585
 of Si
 mass spectrom., TOF 305
 etching, ion
 of AlGaAs
 by $\text{CCl}_2\text{F}_2^+/\text{O}_2^+$ ions 489
 of GaAs
 by $\text{CCl}_2\text{F}_2^+/\text{O}_2^+$ ions 489
 of polyimide films
 by O_2^+ ions 495
 of Si
 by $\text{Ar}^+, \text{Cl}^+, \text{F}^+, \text{Ne}^+$ ions 477
 of SiO_2
 by $\text{Ar}^+, \text{CF}_x^+$ ions 477
 etching, ion-assisted chemical
 of Cu
 by Ar^+ ions and Cl_2 3
 of Si
 by Ar^+ ions and Cl_2 3, 477

- etching, KrF laser
 - of LiNbO_3
 - fluence/etch gas depen. 321
 - of Ni
 - fluence/ Br_2 press. depen. 327
- etching, KrF/XeF laser
 - of SiC
 - patterned etching 315
- etching precursors
 - see:precursors, etching
- etching, XeCl laser
 - of Cu
 - mass spectrom., TOF 3
 - of Si
 - mass spectrom., TOF 3, 299
- explosive reaction 99
- femtosecond scale laser pulses 375
- ferrite 333, 339
- focused ion beam 483
- free radicals 99, 311
- grain boundaries 347
- grass-like structure 495
- Group IV semiconductors
 - see:semiconductors, Group IV
- growth epitaxial
 - see:epitaxial growth
- high T_c superconductors 347, 353
 - 441, 603
- hole drilling 515
- hollow-cathode discharge 539
- hybrid circuit 621
- in situ processing 421, 585
- inter-chip interconnections 547, 559, 569
- interconnects 547, 559, 569, 579
- interface modification
 - ion beam, adhesion improvement
 - of Fe films 501
- ion assisted chemical etching
 - see:etching, ion-assisted chem.
- ion assisted deposition
 - see:deposition, ion assisted
- ion beam sputtering 17, 29, 477
- ion etching
 - see:etching ion
- ion induced decomposition
 - see:decomposition, ion induced
- ion sputtered deposition
 - see:deposition, ion sputtered
- lamp induced deposition
 - see:deposition, lamp induced
- lamp induced photolysis
 - see:photolysis, lamp-induced
- laser cladding 139
- laser cleaning 461
- laser decomposition
 - see:decomposition, laser
- laser desorption
 - see:desorption, laser
- laser doping
 - see:doping, laser
- laser etching
 - see:etching, laser
- laser induced deposition
 - see:deposition, laser induced
- laser induced thermochemistry
 - see:thermochem. laser-induced
- laser induced fluorescence
 - TOF
 - KrF laser abl. $\text{Na}_2\text{O}-3\text{SiO}_2$ 385
 - KrF laser abl. Si 371
- laser photochemistry
 - see:photochemistry, laser
- laser photolysis
 - see:photolysis, laser
- laser pyrolysis
 - see:pyrolysis, laser
- laser planarization 559, 569
- lattice distortion 165
- lithography, X-ray
 - laser plasma source
 - polysilane resists, for 613
- mass spectroscopy
 - TOF
 - ArF laser etch. Si in Cl_2 305
 - ArF/KrF laser photol. of
 - ads. $\text{In}(\text{CH}_3)_3$ 69
 - dye laser (200-320nm) photol.
 - of $\text{Al}(\text{CH}_3)_3$ 79
 - KrF laser abl. of
 - $\text{Na}_2\text{O}-3\text{SiO}_2$ 385
 - KrF/XeF laser abl. Ag, Al 359
 - Nd-Yag (532nm) etch. of
 - $\text{YBa}_2\text{Cu}_3\text{O}_{7-x}$ and
 - C (graphite) 353
 - XeCl laser abl. of
 - polyimide 411
 - TOF, angular resolved
 - Ar^+ ion etching Si in Cl_2 3
 - XeCl laser etch. Si and Cu
 - in Cl_2 3, 299

metals

Ag, energies abl. species 359
 Al, energies abl. species 359
 Al, film depos. 73, 119, 251
 Al or Ni/Al film ablation 399
 Au, ablation 627
 Au, ion beam direct write 483
 Au, laser planariz. 559, 569
 Au, line depos. 107, 133, 483
 Bi, particle formation 99
 Cd, film depos. 45
 Cr, Cr(C,O) film depos. 85
 Cr, film depos. 91
 Ga (GaAs), depos. 147, 159
 Mo, deposition 245
 Ni, film etching 327
 Pb, particle formation 99
 Pd, line depos. 107
 Sb, ArF laser annealed 461
 Te, film depos. 57
 W, film depos. 63
 W, line depos. 547
 Zn, film depos. 45
 microwave plasma 483
 modeling, direct-writing 107
 modification of surfaces
 see: surface modification
 MOS capacitors 63
 multilayers 279

optical coatings 29
 opto-electronic devices 285

patterning, selected area
 see: selected area patterning
 plasma enhanced deposition
 see: deposition, plasma enhanced
 photochem., Ar⁺ laser induced
 of Mn-Zn ferrite in
 aq. H₃PO₄ 339
 photogenerated carriers 245, 269,
 291
 photolysis, Ar⁺ laser (257nm)
 of Cd(CH₃)₂ with Te(C₂H₅)₂ or
 Te₂(CH₃)₂, CdTe epitaxy 183
 of CH₃I with H₂
 etching InP, patterned 285
 photolysis, Ar⁺ laser (350-360nm)
 of Cl₂
 etching, Si 291
 photolysis, ArF laser
 of AlH(CH₃)₂
 deposition, Al films 73
 of Bi(CH₃)₃
 deposition, Bi particles 99

of C₂F₂
 behavior, CF₂ on Si 311
 behavior, CF₂ on SiO₂ 311
 of CCl₄ with H atoms
 deposition, C (diamond) 213
 of Cd(CH₃)₂
 deposition Cd films 45
 of Cl₂
 etching Si (prod. energ.) 305
 of Ga(C₂H₅)₃
 deposition Ga(GaAs) films 159
 of Ga(CH₃)₃
 deposition Ga(GaAs) films 159
 of Ga(CH₃)₃ with PH₂(t-C₄H₉)
 deposition GaP epit. films 177
 of GeH₄ with NH₃ sensitizer
 deposition, Ge on GaAs 201
 of Pb(CH₃)₄
 deposition, Pb particles 99
 of SiH₄ or Si₂H₆
 deposition Si films 195
 of SnCl₄ and N₂O
 deposition SnO₂ films 447
 of WF₆
 deposition W films 63
 of Zn(CH₃)₂
 deposition Zn films 45
 of B₂H₆
 doping Si with B atoms 597
 of BCl₃
 doping Si with B atoms 591
 photolysis, CO₂ laser
 of C₂F₆
 behavior, CF₃ on Si 311
 behavior, CF₃ on SiO₂ 311
 photolysis, dye laser (200-320nm)
 of Al(CH₃)₃, [Al]/[AlCH₃],
 wavelength depend. 79
 photolysis, H plasma disk lamp
 Zn(C₂H₅)₂, deposition of
 ZnSe films 239
 photolysis, Hg (low press.) lamp
 of Al(CH₃)₃, deposition of
 Al lines 251
 of Te(CH₃)(C₂H₅), Cd(CH₃)₂, Hg
 deposition, Hg_{1-x}Cd_xTe 233
 of TiCl₄ and Al(CH₃)₃
 deposition, Ti/Al 259
 photolysis, KrF laser
 of Bi(CH₃)₃, deposition
 Bi fine particles 99
 of Br₂
 etching, Ni films 327
 of Cr(CO)₆ (multiphoton)
 deposition Cr films,
 Cr⁺ kinetics 91
 deposition Cr(C,O) films 85
 of Pb(CH₃)₄, deposition
 Pb fine particles 99
 of Te(CH₃)₂
 deposition Te 57

- photolysis, KrF laser induced
 of $\text{In}(\text{CH}_3)_3$
 masses/energies product 69
 photolysis, VUV windowless lamp
 of $\text{Al}(\text{CH}_3)_3$ and NH_3
 deposition, AlN films 227
 of Si_2H_6
 deposition, Si films 227
 of SiH_4 and N_2
 deposition, Si_3N_4 films 227
 photolysis, Xe lamp
 of $\text{Mo}(\text{CO})_6$ coadsorbed with K
 deposition, Mo films 245
 photolysis, XeF laser
 of ClF_3 , etching
 SiC with KrF laser 315
 piezoelectric 399
 polyvinylidene difluoride 399
 precursors, deposition
 $\text{Al}(\text{CH}_3)_3$ 79, 125, 251, 259
 $\text{Al}(\text{CH}_3)_3$ and NH_3 for AlN 227
 $\text{AlH}(\text{CH}_3)_2$ 73
 $\text{AlH}_2[\text{N}(\text{CH}_3)_3]_2$ 119
 Au ink 107, 133
 $\text{Au}(\text{CH}_3)(\text{hfac})$ 125, 483
 $\text{Bi}(\text{CH}_3)_3$ 99
 CCl_4/H_2 for C (diamond) 213
 $\text{Cd}(\text{CH}_3)_2$ 45
 CH_4/H_2 for C (diamond) 533
 $\text{Cr}(\text{CO})_6$ 85, 91
 $\text{Ga}(\text{C}_2\text{H}_5)_3$, AsH_3 for GaAs ALE 171
 $\text{Ga}(\text{CH}_3)_3$, AsH_3 for GaAs 165
 $\text{Ga}(\text{CH}_3)_3$ or $\text{Ga}(\text{C}_2\text{H}_5)_3$
 for Ga 147, 159
 GeH_4 and NH_3 for Ge 201
 GeCl_4 and Se_2Cl_2 for Ge-Se
 films 207
 $\text{In}(\text{CH}_3)_3$ 69
 $\text{Pb}(\text{CH}_3)_4$ 99
 $\text{Pd}(\text{C}_2\text{H}_3\text{O}_2)_2$ 107, 579
 $\text{Mo}(\text{CO})_6$ 245
 Si_2H_6 195, 227, 539
 SiH_2Cl_2 609
 SiH_4 189, 195, 527, 609
 SiH_4 and N_2 for Si_3N_4 227
 SnCl_2 and N_2O for SnO_2 447
 $\text{Te}(\text{CH}_3)(\text{C}_2\text{H}_5)_2$, $\text{Cd}(\text{CH}_3)_2$, and Hg
 for $\text{Hg}_{1-x}\text{Cd}_x\text{Te}$ 233
 $\text{Te}(\text{CH}_3)_2$ 57
 $\text{Te}(\text{CH}_3)_2$ or $\text{Te}(\text{C}_2\text{H}_5)_2$, $\text{Cd}(\text{CH}_3)_2$,
 for CdTe 183
 TiCl_4 259
 TiCl_4 and NH_3 for TiN and
 TiN_{0.7}O_{0.3} 435
 WF_6 53, 547
 Y/Ba/Cu trifluoroacetates
 for $\text{YBa}_2\text{Cu}_3\text{O}_{7-x}$ 603
 $\text{Zn}(\text{C}_2\text{H}_5)_2$ and $\text{Se}(\text{C}_2\text{H}_5)_2$
 for ZnSe 239
 $\text{Zn}(\text{CH}_3)_2$ 45
- precursors, doping
 B_2H_6 for B doping of Si 597
 BCl_3 for B doping of Si 591
 precursors, etching
 Br_2 for Ni 327
 C_2F_4 for Si and SiO_2 269
 C_2F_6 for Si 269
 $\text{CCl}_2\text{F}_2^+/\text{O}_2^+$ ions for GaAs,
 AlGaAs 489
 CH_3I for InP 285
 Cl_2 for GaAs 585
 Cl_2 for GaAs, Ga(As,P), Cl
 by glow discharge 269
 Cl_2 for Si 291, 299, 305, 477
 ClF_3 for SiC 315
 NF_3 for Si 311
 O_2^+ ions for polyimide 495
 XeF_2 for Si 311
 pyrolysis, Ar⁺ laser
 of $\text{Al}(\text{CH}_3)_3$
 deposition, Al lines 239
 of $\text{AlH}_2[\text{N}(\text{CH}_3)_3]_2$
 deposition Al lines 189
 of Au-ink
 deposition Au lines 107, 133
 of SiH_4
 deposition Si lines 189
 pyrolysis, Ar⁺ laser (351nm)
 of $\text{Pd}(\text{C}_2\text{H}_3\text{O}_2)_2$, Pd patterns
 for Cu deposition 579
 pyrolysis, Ar⁺ laser
 of CCl_4 , etching
 Mn-Zn ferrite/sendust 333
 of $\text{Ga}(\text{CH}_3)_3$ and AsH_3 ,
 GaAs epitaxy 165
 of $\text{Ga}(\text{CH}_3)_3$ with $\text{PH}_2(\text{t-C}_4\text{H}_9)$
 deposition GaP epit. films 177
 pyrolysis, ArF laser
 of $\text{Ga}(\text{C}_2\text{H}_5)_3$
 deposition Ga(GaAs) films 159
 of $\text{Ga}(\text{CH}_3)_3$
 deposition Ga(GaAs) films 159
 of B_2H_6
 doping Si with B atoms 597
 of BCl_3
 doping Si with B atoms 591
 pyrolysis, CO_2 laser
 of Au ink
 deposition, Au lines 133
 of GeCl_4 and Se_2Cl_2
 deposition Ge-Se films 207
 pyrolysis, XeF laser
 of BCl_3 , doping
 Si with B atoms 591
 of $\text{Ga}(\text{C}_2\text{H}_5)_3$, deposition
 Ga(GaAs) films 147, 159
 of $\text{Ga}(\text{CH}_3)_3$, deposition
 Ga (GaAs) films 147, 159

quartz crystal microbalance 327

rapid thermal processing 609

reactions, surface

behavior of

CF₂ on Si and SiO₂ 311

CF₃ on Si and SiO₂ 311

NF₃ on Si and SiO₂ 311

XeF₂ on Si and SiO₂ 311

excimer laser stimulated

mechanisms review 3

noble ion stimulated

mechanisms review 3

of Cu with

Cl₂ and XeCl laser beams 3

Cl₂ beams 3

of Si with

Cl₂ and XeCl laser beams 3

Cl₂ beams 3

temperature modulation method

react. energ./kinetics 125

relaxation techniques 125

selected area patterning

Ar⁺ laser (257nm) growth

of GaP epit. films 177

Ar⁺ laser (351 nm) induced

of Pd for Cu depos. 579

Ar⁺ laser induced

of GaAs ALE 171

ArF laser ablation

of YBa₂Cu₃O_{7-x} films 405

ArF laser deposition

of SnO₂ films 447

ArF laser etching

of GaAs in MBE system 585

ArF laser growth

of GaP epitaxial films 177

ArF/XeF laser deposition

of Ga epitaxial lines 165

KrF laser growth

of SiO₂ films 421

KrF/XeF laser etching

of SiC 315

XeCl laser ablation

of Al from PVD 399

XeF laser growth

of GaAs films 147

self-limiting mechanism 171

semiconductors, Group IV

C (diamond) growth 213

C (diamondlike) evaporative

deposition 411

C (graphite) ablation 353

Ge epitaxial film depos. 201

Ge film crystallization 455

Ge-Se film deposition 207

Si ablation 371

Si deposition 527, 609

Si, doping with B 591, 597

Si, etching 3, 291, 299, 305, 477

Si phys. sputtering

with ions 477

Si reactions with CF_x

radicals 311

SiC etching 315

semiconductors, II-VI

CdTe, epitaxial depos. 183

Hg_{1-x}Cd_xTe, epitax. depos. 233

InP, etching 285

ZnSe, deposition 239

semiconductors, III-V

AlGaAs etching 489

Ga(As,P), etching 269

GaAs, atomic layer

epitaxy 171

GaAs, epitaxy 165

GaAs, etching 269

GaP, epitaxial growth 177

site-selective decomposition 171

SQUIDS 347

surface characterization

Auger spectroscopy 45, 125

of annealed Sb surface 461

of deposited Al lines 119, 251

of deposited AlN films 227

of deposited Au lines 483

of deposited Ge

epitaxial films 201

of deposited Si films 527

of deposited Si lines 189

of deposited SnO₂ films 447

of deposited TiN and

TiN_xO_y films 435

of etched GaAs and

AlGaAs surfaces 489

of etched LiNbO₃ films 321

of formed TiN films 469

of grown GaP epitax. films 177

electron energy loss spectros.

desorption metal oxides/

fluorides, electron beam 509

high resolution:CO₂ laser

deposited Ge-Se films 245

electron probe microanalysis

of clad layers of Ni-Fe-Cr-Al

alloy on steel 139

surface characterization (cont.)

- high energy electron diffraction
 - of GaAs by ALE 171
- high resol. electron microscopy
 - formation of Ni_3O_4 521
 - growth, epitaxial monoxide 509
- infrared absorption spectrosc.
 - of chemisorbed metal alkyls 45
 - of deposited AlN films 227
 - of deposited C
 - (diamondlike) films 219
 - of deposited Ge-Se films 245
 - of depos. polyethylene 259
 - of deposited SnO_2 films 447
- low energy electron diffraction
 - of chemisorbed $\text{Cd}(\text{CH}_3)_2$,
 - $\text{Te}(\text{CH}_3)_2$, thermal/
 - photolytic behavior 57
 - of laser annealed Sb 461
- Mössbauer spectroscopy
 - of interfaces 501
- optical absorption
 - of deposited metal oxide
 - optical coatings 17
 - of deposited SnO_2 films 447
- photoluminescence
 - of grown ZnSe films 239
- photon induced desorption
 - spectroscopy: of deposited
 - Ge-Se films 245
- profilometry
 - of deposited Au lines 483
 - of deposited Si films 527
 - of etched GaAs and
 - AlGaAs surfaces 489
 - of etched InP surfaces 285
 - of etched polymer films 375
 - of etched/overgrown
 - GaAs patterns 585
 - of melt planarized Au
 - films 559, 569
- Raman spectroscopy
 - of deposited C (diamond)
 - films 213, 533
 - of deposited C (diamondlike)
 - films 219
 - of deposited Si films 527
- reflection electron diffraction
 - of etched/overgrown
 - GaAs patterns 585
- reflection high energy
 - electron diffraction, of depos.
 - C (diamond) films 213

surface characterization (cont.)

- Rutherford backscatt. spectrom.
 - of deposited metal
 - oxide films 17
 - of deposited Pd, for
 - Cu deposition 579
 - of deposited TiN and
 - TiN_xO_y films 435
 - of formed TiN films 469
- scanning acoustic microscopy
 - of ablated Al or
 - Ni-Al films 399
- secondary ion mass spectrometry
 - of depos. Ge epit. films 201
 - of dopant B profiles in
 - Si 591, 597
 - of grown CdTe epit. films 183
- scanning electron microscopy
 - of ablated Al or
 - Ni-Al films 399
 - of ablated ceramic 621
 - of annealed Sb surface 461
 - of depos. Au lines 133, 483
 - of deposited C (diamond)
 - films 213, 533
 - of deposited Ge-Se films 245
 - of deposited Si lines 189
 - of deposited W lines 547
 - of etched GaAs and
 - AlGaAs surfaces 489
 - of etched LiNbO_3 321
 - of etched polyimide 495
 - of etched polymer films 375
 - of etched vias in Si 291
 - of melt planarized Au 559
 - of patterned $\text{YBa}_2\text{Cu}_3\text{O}_{7-x}$
 - films 347
 - of X-ray exposed polysilane
 - resists 613
- scanning electron microscopy/
 - energy dispers. X ray anal.
 - of deposited
 - $\text{Pb}_{1-x}\text{La}_x(\text{Zr}_{1-x}\text{Ti}_x)_{1-x/4}\text{O}_3$
 - electro-optic films 17
- spectroscopic ellipsometry
 - of depos. ^ (diamondlike)
 - films 4, 358
- thermal desorption mass
 - spectrometry
 - of CF_x radical/Si or SiO_2
 - reaction products 311
 - of chemisorbed metal
 - alkyls 45
 - of deposited Ge-Se films 245

surface characterization (cont.)

transmiss. electron microsc.
 of crystallized Ge films 455
 of deposited Au lines 483
 of deposited C (diamondlike) films 219

of deposited Ge-Se films 245
 of deposited $\text{Hg}_{1-x}\text{Cd}_x\text{Te}$ epitaxial films 233

of deposited Si epitaxial films 527, 609

of deposited TiN and TiN_xO_y films 435

of etched GaAs and AlGaAs surfaces 489

of etched polyimide 495

of formed TiN films 469

of grown GaP epit. films 177

work function change measurements: of deposited Ge-Se films 245

X-ray absorption spectroscopy of polysilane resists 613

X-ray analysis: of deposited Ge-Se films 245

X-ray diffraction

of deposited Au lines 133
 of deposited C (diamond) films 533

of deposited $\text{Hg}_{1-x}\text{Cd}_x\text{Te}$ epitaxial films 233
 of deposited

$\text{Pb}_{1-x}\text{La}_x(\text{Zr,Ti})_{1-x/4}\text{O}_3$ electro-optic films 17

of grown ZnSe films 239

of patterned $\text{YBa}_2\text{Cu}_3\text{O}_{7-x}$ 603

X-ray photoelectron spectroscopy

of CF_x radical/Si or SiO_2 reaction products 311
 of chemisor. $\text{Cd}(\text{CH}_3)_2/\text{Te}(\text{CH}_3)_2$, thermal/photol. behavior 57

of deposited Au lines 133

of deposited Ga (GaAs) films 159

of deposited Ge epitaxial films 201

of deposited Pd, for Cu deposition 579

of etched GaAs and AlGaAs surfaces 489

of formed TiN films 469

of grown Ga (GaAs) films 147

X-ray diffraction

of clad layers Ni-Fe-Cr-Al alloy on steel 139

of deposited Ge-Se films 245

topography of grown GaAs epitaxial lines 165

Surface Modification

Ar^+ laser induced

of $\text{YBa}_2\text{Cu}_3\text{O}_{7-x}$, reversible oxidation 441

dye laser induced

of Au films, planarization 569, 559

electron beam induced

of NiO surfaces, Ni_3O_4 formation 521

excimer laser induced

of Au films, planariz. 559

Kr^+ laser induced

of Ge films, multicrystallization 455

KrF laser induced

TiN formation, liq. N_2 469

laser or lamp induced

of SiO_2 films, growth 421

XeCl laser induced

of Au films, planariz. 569

surface reactions

see: reactions, surface

tactile sensors 399

thermochemistry, Ar^+ laser induced

of Mn-Zn ferrite

in aq. H_3PO_4 339

of Mn-Zn ferrite/sendust

in aq. KOH/NaOH 333

thermal decomposition

$\text{Cd}(\text{CH}_3)_2$ 57

$\text{Cr}(\text{CO})_6$ 91

$\text{Te}(\text{CH}_3)_2$ 57

thin film adhesion 501

thin film interfaces 501

ultra shallow junctions 597

ultrasonic transducers 399

via production 291

Volmer-Weker film growth 207

windowless disc plasma lamp 227

X-ray lithography

see: lithography, X-ray

$\text{YBa}_2\text{Cu}_3\text{O}_{7-x}$ films 353, 441, 603

ablation of 353, 347

metal trifluoroacetate,

laser decomposition 603